

566p

NASA CR-61849

DOCUMENT NO. 63SD801
15 OCTOBER 1963

GPO PRICE \$ _____
CFSTI PRICE(S) \$ _____
Hard copy (HC) 8.66
Microfiche (MF) 2.75

FACILITY FORM 602

N 66-13403

(ACCESSION NUMBER) <u>566</u>	(THRU) <u>1</u>
(PAGES) <u>CL 51839</u>	(CODE) <u>31</u>
(NASA CR OR TMX OR AD NUMBER)	(CATEGORY)

ff 653 July 65

VOYAGER DESIGN STUDY.

VOLUME IV SYSTEM DESIGN

(copy Oct. 6, 1963)

(NASA Contract NASw-696)

Prepared Under Contract NAS W-696

for

NATIONAL AERONAUTICS AND SPACE ADMINISTRATION
OFFICE OF SPACE SCIENCES
WASHINGTON, D.C.



GENERAL ELECTRIC

MISSILE AND SPACE DIVISION
Valley Forge Space Technology Center
P.O. Box 8555 • Philadelphia 1, Penna.

SECTION 1. ENTRY LANDER

VOLUME SUMMARY

The Voyager Design Study report is contained in six volumes, an appendix, and subcontractor reports. The volume numbers and their titles are as follows:

Volume No.

- I Voyager Design Summary
- II Mission and System Analyses
 - 1. Mission Analysis
 - 2. Parametric System Performance
 - 3. Voyager Systems
 - 4. Reliability
- III Subsystem Design
 - 1. Communications
 - 2. Television
 - 3. Radar
 - 4. Guidance and Control
 - 5. Propulsion
 - 6. Power Supply
 - Appendix (Classified)
- IV System Design
 - 1. Entry/Lander
 - 2. Orbiter
- V Sterilization
- VI Program Development Plans

Separate Reports from the following Companies are also included:

Aerojet-General Corp.
Barnes Engineering
Bell Aerosystems Co.
Conductron Corp.
Electro-Mechanical Research Inc.
General Electric Co.
Light Military Electronics Dept.
General Precision Inc.
Hazeltine

North American Aviation Inc.
Autonetics Division
Rocketdyne Division
Radio Corporation of America
Rocket Research Corp.
Texas Instruments Corp.
Thiokol Chemical Corp.
Elkton Division
Reaction Motors Division



Frontispiece - Mars Entry Lander Deployed

TABLE OF CONTENTS

Section	Page
1. ENTRY LANDER	1-1
1.1 INTRODUCTION	1-1
1.1.1 Objectives	1-1
1.1.2 Design Criteria and Limitations	1-1
1.2 SUMMARY OF RESULTS	1-3
1.2.1 System Description	1-3
1.2.2 Basic Trajectories.	1-6
1.2.3 Subsystem Description	1-8
1.2.4 Sequence of Events.	1-14
1.2.5 Summary Parallel Study with Low Pressure Atmosphere	1-19
1.3 ANALYSIS AND STUDY RESULTS	1-69
1.3.1 Configuration Matrix	1-69
1.3.2 Aeromechanics	1-73
1.3.3 Entry Heat Protection.	1-135
1.3.4 Structural Analysis	1-211
1.3.5 Retardation	1-244
1.3.6 Thermal Control	1-273
1.3.7 Materials.	1-301
1.3.8 Configuration Optimization	1-331
1.3.9 Vehicle Design	1-348
2. ORBITER SYSTEM INTRODUCTION	2-1
2.1 Summary	2-4
2.2 Configuration Selection and Sequence of Events	2-13
2.2.1 Sequence of Events	2-19
2.3 Orbiter Configuration Design and Integration.	2-32
2.3.1 General	2-32
2.3.2 Orbiter Description	2-32
2.3.3 View Angle	2-37
2.3.4 Revisions for Other Years.	2-69
2.3.5 Titan III-C Conceptual Configuration	2-70
2.3.6 Saturn V Configuration	2-71
2.4 Thermal Control	2-87
2.4.1 Orbiter (Main Body)	2-87
2.4.2 Planetary Horizontal Package.	2-108
2.4.3 Venus Thermal Studies	2-122
2.4.4 References, Thermal Control.	2-130

2.5	Structural and Dynamic Criteria of Orbiter	2-131
2.5.1	Structural Description	2-131
2.5.2	Structural Loads Criteria	2-142
2.5.3	Load Analysis	2-150
2.5.4	Stress Analysis	2-158
2.5.5	References	2-161
2.6	Weight Analysis	2-164
2.6.1	Summary	2-164
2.6.2	Subsystem Detail Weight (Mars 1969)	2-169
2.6.3	Structure Detail Parts	2-177
2.6.4	Equipment Packaging	2-182
2.6.5	Power Supply and Solar Array Weights.	2-186

LIST OF ILLUSTRATIONS

Figure		Page
1. 1. 3-1	Mars Atmospheres - Pressure	1-31
1. 1. 3-2	Mars Atmospheres - Temperature	1-31
1. 1. 3-3	Mars Atmospheres - Density	1-32
1. 1. 3-4	Venus Atmospheres - Pressure	1-32
1. 1. 3-5	Venus Atmospheres - Temperature	1-33
1. 1. 3-6	Venus Atmospheres - Density	1-33
1. 2. 1-1	Altitude Histories for Martian Entry	1-34
1. 2. 1-2	Altitude Histories for Venusian Entry	1-34
1. 2. 1-3	Mars Lander with Aft Cover Attached	1-35
1. 2. 1-4	Mars Lander with Radiator-Adapter Section Attached	1-36
1. 2. 2-1	Peak Axial Deceleration Vs. Entry Angle for $W/C_{DA} = \text{PSF}$	1-37
1. 2. 2-2	Peak Axial Deceleration Vs. Entry Angle for Various Velocities and Martian Lower Atmosphere	1-37
1. 2. 2-3	Peak Axial Deceleration Vs. W/C_{DA} for Several Martian Entires.	1-38
1. 2. 2-4	Peak Axial Deceleration for Two Venusian Atmospheres Where $W/C_{DA} = 40 \text{ psf}$ and $V = 38,000 \text{ Ft/Sec}$	1-38
1. 2. 2-5	Peak Axial Deceleration W/C_{DA} for Two Venusian Atmospheres Where $V = 38,000 \text{ Ft/Sec}$	1-39
1. 2. 2-6	Mach Number Vs. Altitude for Several Martian Entires	1-40
1. 2. 2-7	Altitude of Occurrence at $M = 2.5$ for Entry into Mars Lower Atmosphere	1-40
1. 2. 3-1	Mars 1969 Lander Block Diagram	1-41
1. 2. 3-2	Sequence Diagram - Mars Entry	1-43
1. 2. 3-3	Sequence Diagram - Venus Entry	1-45
1. 2. 3-4	Thermal Control System for Mars Lander	1-47
1. 2. 3-5	Thermal Control System for Venus Lander	1-47
1. 2. 5-1	Density-Altitude Profile, 15 Millibar Atmosphere	1-48
1. 2. 5-2	Pressure-Altitude Profile, 15 Millibar Atmosphere	1-48
1. 2. 5-3	Temperature-Altitude Profile, 15 Millibar Atmosphere	1-49
1. 2. 5-4	Entry Path Angle Restriction for Voyager in the 11 Millibar Model Atmosphere	1-50
1. 2. 5-5	Vehicle Weight (Entry) Vs. W/C_{DA}	1-50
1. 2. 5-6	Mars 1969 Lander - 11 to 30 Millibar Atmosphere.	1-51
1. 2. 5-7	Altitude of Occurrence of $M = 2.5$ for Entry into Martian 11 Millibar Atmosphere - 21,000 Ft./Sec.	1-53
1. 2. 5-8	Altitude of Occurrence of $M = 2.5$ for Entry into Martian 11 Millibar Atmosphere - 15,000 Ft./Sec.	1-53
1. 2. 5-9	Altitude of Occurrence of $M = 2.5$ for Entry into Martian 30 Millibar Atmosphere - 21,000 Ft./Sec.	1-54
1. 2. 5-10	Altitude of Occurrence of $M = 2.5$ for Entry into Martian 30 Millibar Atmosphere - 15,000 Ft./Sec.	1-54
1. 2. 5-11	Peak Axial Deceleration Vs. γ_e for Martian Entry	1-55
1. 2. 5-12	Peak Axial Deceleration Vs. γ_e for Martian Entry	1-55
1. 2. 5-13	Martian Descent Velocity Vs. Earth W/C_{DA} in Final Descent With Surface Density as a Parameter	1-56
1. 2. 5-14	Drag Area of Main Descent Parachute(s)	1-56
1. 2. 5-15	Assembly Weight of Main Descent Parachute(s).	1-57
1. 2. 5-16	Packing Volume of Main Descent Parachute(s)	1-57
1. 2. 5-17	Descent Time as a Function of Deployment Altitude, 11 Millibar (Lower) Atmosphere	1-58
1. 2. 5-18	Decelerator Parachute State-of-the-Art, Mars 11 Millibar Atmosphere	1-58

LIST OF ILLUSTRATIONS (Cont'd)

<u>Figure</u>	<u>Page</u>
1.2.5-19 Drag Area of the Hyperflo Canopy as a Function of Constructed Diameter and Mach Number	1-59
1.2.5-20 Estimated Assembly Weight of Hyperflo Decelerator Parachute(s)	1-59
1.2.5-21 Percent Vehicle Entry Weight Necessary for the Retardation System	1-60
1.2.5-22 Optimization of Impact Velocity for Parachutes and Crush-up Landing System	1-60
1.2.5-23 Optimization of Descent Velocity for Parachute-Retrorocket System	1-61
1.2.5-24 Optimization of Descent Velocity for Parachute-Retrorocket System	1-61
1.2.5-25 Optimization of Descent Velocity for Parachute-Retrorocket-Crush-up Landing System	1-62
1.2.5-26 Normal Impact Velocity.	1-62
1.2.5-27 Required Stroke Vs. Normal Velocity for Various Deceleration Rates	1-63
1.2.5-28 Shock Attenuation System Weight.	1-63
1.2.5-29 Shock Attenuation System Weight.	1-64
1.2.5-30 Shell Structure Weight Variation - Mars Lander	1-64
1.2.5-31 Bulkhead Weight Variation - Mars Lander	1-65
1.2.5-32 Shield Weight Vs. Base Diameter	1-65
1.2.5-33 Structure Weight Vs. Base Diameter	1-66
1.2.5-34 Payload Weight Vs. Base Diameter	1-66
1.2.5-35 Retardation Weight Vs. Base Diameter	1-67
1.2.5-36 Ballistic Parameter and Entry - Vehicle Weight Vs. Base Diameter	1-67
1.2.5-37 Payload Fraction Vs. Base Diameter	1-68a
1.2.5-38 Sketches Depicting Side-Oriented (A) and Base Oriented (B) High Drag Vehicle - Mars	1-68b
1.3.2-1 Voyager Entry Configurations.	1-86
1.3.2-2 Voyager Drag Coefficient Vs. Mach Number	1-86
1.3.2-3 Voyager Drag Coefficient Vs. Mach Number	1-87
1.3.2-4 Voyager Drag Coefficient Vs. Mach Number	1-87
1.3.2-5 Voyager Drag Coefficient Vs. Mach Number	1-88
1.3.2-6 Voyager Drag Coefficient Vs. Altitude	1-88
1.3.2-7 Voyager Drag Coefficient Vs. Altitude	1-89
1.3.2-8 Voyager Drag Coefficient Vs. Altitude	1-89
1.3.2-9 Voyager Drag Coefficient Vs. Altitude	1-90
1.3.2-10 Voyager Pressure Distribution	1-90
1.3.2-11 Voyager Pressure Distribution	1-91
1.3.2-12 Voyager Pressure Distribution	1-91
1.3.2-13 Voyager Pressure Distribution	1-92
1.3.2-14 Voyager Shock Shape Variation with Mach Number	1-92
1.3.2-15 Trajectory Parameters for Entry into Mars Lower Atmosphere	1-93
1.3.2-16 Trajectory Parameters for Entry into Mars Lower Atmosphere	1-93
1.3.2-17 Peak Axial Deceleration Vs. W/C_{DA} for Several Martian Entries.	1-94
1.3.2-18 Peak Axial Deceleration Vs. W/C_{DA} for Several Martian Entries.	1-94
1.3.2-19 Peak Axial Deceleration Vs. W/C_{DA} for Several Martian Entries.	1-94
1.3.2-20 Peak Dynamic Pressure Vs. W/C_{DA} for Several Martian Entries.	1-94
1.3.2-21 Peak Dynamic Pressure Vs. W/C_{DA} for Several Martian Entries.	1-95
1.3.2-22 Peak Dynamic Pressure Vs. W/C_{DA} for Several Martian Entries.	1-95
1.3.2-23 G_{xMax} Vs. W/C_{DA} for Two Venusian Atmospheres Where $V = 38,000$ Ft./Sec.	1-95
1.3.2-24 G_{xMax} Vs. γ for $W/C_{DA} = 40$ for a Velocity of 21,000 Ft./Sec. at Various Martian Atmospheres	1-96

LIST OF ILLUSTRATIONS (Cont'd)

<u>Figure</u>	<u>Page</u>
1.3.2-25 G_{xMax} Vs. γ for $W/C_{DA} = 20$ psf for a Velocity of 23,000 Ft./Sec. at Various Martian Atmospheres	1-96
1.3.2-26 G_{xMax} Vs. γ for $W/C_{DA} = 40$ psf for a Velocity of 23,000 Ft./Sec. at Various Martian Atmospheres	1-97
1.3.2-27 G_{xMax} Vs. γ for $W/C_{DA} = 60$ psf for a Velocity of 23,000 Ft./Sec. at Various Martian Atmospheres	1-97
1.3.2-28 G_{xMax} Vs. γ for $W/C_{DA} = 40$ psf for a Velocity of 25,000 Ft./Sec. at Various Martian Atmospheres	1-98
1.3.2-29 G_{xMax} Vs. γ for $W/C_{DA} = 20$ psf for Various Velocities and Martian Lower Atmosphere	1-98
1.3.2-30 G_{xMax} Vs. γ for $W/C_{DA} = 20$ psf for Various Velocities and Martian Upper Atmosphere	1-98
1.3.2-31 Velocity Vs. γ for $W/C_{DA} = 20$ psf and Mean Martian Atmosphere at Various Peak Axial Decelerations in Earth G's	1-99
1.3.2-32 Velocity Vs. γ for $W/C_{DA} = 40$ psf and Lower Martian Atmosphere at Various Peak Axial Decelerations in Earth G's	1-99
1.3.2-33 Velocity Vs. γ for $W/C_{DA} = 40$ psf and Mean Martian Atmosphere at Various Peak Axial Decelerations in Earth G's	1-100
1.3.2-34 Velocity Vs. γ for $W/C_{DA} = 40$ psf and Upper Martian Atmosphere at Various Peak Axial Decelerations in Earth G's	1-100
1.3.2-35 Velocity Vs. γ for $W/C_{DA} = 60$ psf and Mean Martian Atmosphere at Various Peak Axial Decelerations in Earth G's	1-101
1.3.2-36 Altitude at G_{xMax} Vs. γ for Various Martian Atmospheres Where $W/C_{DA} = 40$ psf and Velocity = 21,000 Ft./Sec.	1-101
1.3.2-37 Altitude at G_{xMax} Vs. γ for Various Martian Atmospheres Where $W/C_{DA} = 20$ psf and Velocity = 23,000 Ft./Sec.	1-101
1.3.2-38 Altitude at G_{xMax} Vs. γ for Various Martian Atmospheres Where $W/C_{DA} = 40$ psf and Velocity = 23,000 Ft./Sec.	1-102
1.3.2-39 Altitude at G_{xMax} Vs. γ for Various Martian Atmospheres Where $W/C_{DA} = 60$ psf and Velocity = 23,000 Ft./Sec.	1-102
1.3.2-40 Altitude at G_{xMax} Vs. γ for Various Martian Atmospheres Where $W/C_{DA} = 40$ psf and Velocity = 25,000 Ft./Sec.	1-102
1.3.2-41 Trajectory Parameters for Entry into Venus Standard Atmosphere	1-103
1.3.2-42 Trajectory Parameters for Entry into Venus Standard Atmosphere	1-103
1.3.2-43 G_{xMax} Vs. γ for Two Venusian Atmospheres Where $W/C_{DA} = 40$ psf and Velocity = 32,000 Ft./Sec.	1-104
1.3.2-44 G_{xMax} Vs. γ for Two Venusian Atmospheres Where $W/C_{DA} = 20$ psf and Velocity = 38,000 Ft./Sec.	1-104
1.3.2-45 G_{xMax} Vs. γ for Two Venusian Atmospheres Where $W/C_{DA} = 40$ psf and Velocity = 38,000 Ft./Sec.	1-104
1.3.2-46 G_{xMax} Vs. γ for Two Venusian Atmospheres Where $W/C_{DA} = 60$ psf and Velocity = 38,000 Ft./Sec.	1-105
1.3.2-47 Altitude at G_{xMax} Vs. γ for Various Venusian Atmospheres Where $W/C_{DA} = 40$ psf and Velocity = 32,000 Ft./Sec.	1-105
1.3.2-48 Altitude at G_{xMax} Vs. γ for Various Venusian Atmospheres Where $W/C_{DA} = 20$ psf and Velocity = 38,000 Ft./Sec.	1-105
1.3.2-49 Altitude at G_{xMax} Vs. γ for Various Venusian Atmospheres Where $W/C_{DA} = 40$ psf and Velocity = 38,000 Ft./Sec.	1-106
1.3.2-50 Altitude at G_{xMax} Vs. γ for Various Venusian Atmospheres Where $W/C_{DA} = 60$ psf and Velocity = 38,000 Ft./Sec.	1-107
1.3.2-51 Venus Trajectory	1-107
1.3.2-52 Venus Trajectory	1-107
1.3.2-53 Venus Trajectory	1-108
1.3.2-54 Venus Trajectory	1-108

LIST OF ILLUSTRATIONS (Cont'd)

Figure	Page
1.3.2-55 Venus Trajectory	1-109
1.3.2-56 Venus Trajectory	1-109
1.3.2-57 Venus Trajectory	1-110
1.3.2-58 Voyager Configuration	1-110
1.3.2-59 Variation of Drag Coefficient with Mach Number, Altitude 0-250,000 Feet (Mars Lower Atmosphere)	1-111
1.3.2-60 Variation of Drag Coefficient with Altitude - Mars	1-111
1.3.2-61 Variation of Axial Force Coefficient with Angle of Attacks, Altitude 0 to 250,000 Feet (Mars Lower Atmosphere)	1-112
1.3.2-62 Variation of Axial Force Coefficient with Angle of Attacks, Altitude 0 to 250,000 Feet (Mars Lower Atmosphere)	1-112
1.3.2-63 Variation of Axial Force Coefficient with Angle of Attack at Various Altitudes (Mars Lower Atmosphere)	1-113
1.3.2-64 Variation of Normal Force Coefficient with Angle of Attack, Altitude 0 to 250,000 Feet (Mars Lower Atmosphere)	1-113
1.3.2-65 Variation of Normal Force Coefficient Slope with Mach Number, Altitude 0 to 250,000 Feet (Mars Lower Atmosphere)	1-114
1.3.2-66 Variation of Normal Force Coefficient with Angle of Attack at Various Altitudes (Mars Lower Atmosphere)	1-114
1.3.2-67 Variation of Pitching Moment Coefficient with Angle of Attack, Altitude 0 to 250,000 Feet (Mars Lower Atmosphere)	1-115
1.3.2-68 Variation of Pitching Moment Coefficient Slope with Mach Number, Altitude 0 to 250,000 Feet (Mars Lower Atmosphere)	1-115
1.3.2-69 Variation of Pitching Moment Coefficient with Angle of Attack at Various Altitudes (Mars Lower Atmosphere)	1-116
1.3.2-70 Variation of Center of Pressure Location with Mach Number, Altitude 0 to 250,000 Feet	1-116
1.3.2-71 Variation of Dynamic Damping with Mach Number	1-117
1.3.2-72 Variation of Dynamic Damping with Angle of Attack	1-117
1.3.2-73 Normal Acceleration Due to Pitch, Axial Acceleration and Total Angle of Attack Vs. Altitude.	1-118
1.3.2-74 Mach Number, Normal Loads, and Dynamic Pressure Vs. Altitude	1-118
1.3.2-75 Total Angle of Attack Envelope History Comparison for Various Spin Rates.	1-119
1.3.2-76 Total Angle of Attack Envelope History Comparison for Various Spin Rates.	1-119
1.3.2-77 Total Angle of Attack Envelope Vs. Altitude with c.g. Offset and Product of Inertia	1-120
1.3.2-78 A_{Xp} Altitude History Comparison for Symmetric and Asymmetric Vehicle.	1-120
1.3.2-79 Upper Envelope of Pitch Rate and Frequency for Entry into Mars Lower Atmosphere.	1-121
1.3.2-80 Capture Angle as Function of Velocity and W/C_{DA} for Entry into Mars Mean Atmosphere	1-121
1.3.2-81 Capture Angle as Function of Velocity and W/C_{DA} for Entry into Venus Standard Atmosphere.	1-122
1.3.2-82 Capture Angle as Function of Velocity and W/C_{DA} for Entry into Venus Extreme Atmosphere.	1-122
1.3.2-83 Venus Standard Atmosphere Capture Angle Trajectory	1-123
1.3.2-84 Venus Standard Atmosphere Capture Angle Trajectory	1-123
1.3.2-85 Effect of Drag Modulation on Maximum Loads	1-124
1.3.2-86 Effect of Drag Modulation on Maximum Loads	1-124
1.3.2-87 Resultant Load Vs. Entry Path Angle	1-125
1.3.2-88 Resultant Load Vs. Entry Path Angle	1-125

LIST OF ILLUSTRATIONS (Cont'd)

Figure		Page
1.3.2-89	Altitude of Maximum Resultant Loads Vs. Path Angle	1-126
1.3.2-90	Mach Number, Axial Acceleration, and Path Angle Vs. Time	1-126
1.3.2-91	Dynamic Pressure, Velocity, and Altitude Vs. Time	1-127
1.3.2-92	Resultant Loads Vs. Lift/Drag	1-127
1.3.2-93	Resultant Loads Vs. Lift/Drag	1-128
1.3.2-94	Resultant Loads Vs. Entry Path Angle	1-128
1.3.2-95	Resultant Loads Vs. Lift/Drag	1-129
1.3.2-96	Altitude of Maximum Resultant Loads Vs. Path Angle	1-129
1.3.2-97	Resultant Loads Vs. Lift/Drag	1-130
1.3.2-98	Altitude, Path Angle, and Velocity Vs. Time	1-130
1.3.2-99	Axial Acceleration and Mach Number Vs. Time	1-131
1.3.2-100	Orbiter Braking	1-131
1.3.2-101	Effects of Products of Inertia on Spin-Up	1-132
1.3.2-102	Lander Response to Initial Rotational Rates	1-132
1.3.2-103	Steady State Conditions Following Spin-Up Caused by a Separation (Lateral Rate = 0.25 Deg./Sec.)	1-133
1.3.2-104	Angular Deviation Vs. Thrusting Time	1-133
1.3.2-105	Angular Deviation Vs. Spin-Up Rate	1-133
1.3.2-106	Angular Deviation Vs. Spin-Up Rate	1-133
1.3.3-1	Local Pressure Distribution (Air and N ₂ -CO ₂)	1-158
1.3.3-2	Local Temperature Distribution (Air and N ₂ -CO ₂)	1-158
1.3.3-3	Local Density Ratio (Local Density/Reference Density).	1-159
1.3.3-4	Static Pressure Behind Normal Shock Wave (25% CO ₂)	1-159
1.3.3-5	Static Density Behind Normal Shock Wave (25% CO ₂)	1-159
1.3.3-6	Figure Deleted	1-160
1.3.3-7	Stagnation Convective Heating (25% CO ₂)	1-160
1.3.3-8	Comparative Heating Around Body (Air and N ₂ -CO ₂)	1-160
1.3.3-9	Hypervelocity Stagnation Point Heat Transfer in Simulated Planetary Atmospheres (Gruszczynski and Warren)	1-161
1.3.3-10	Comparative Radiative and Convective Heating, Mars Mean Atmosphere	1-161
1.3.3-11	Instantaneous Heating, Mars Mean Density Atmosphere	1-162
1.3.3-12	Instantaneous Heating, Mars Mean Density Atmosphere	1-162
1.3.3-13	Instantaneous Heating, Mars Mean Density Atmosphere	1-162
1.3.3-14	Instantaneous Heating, Mars Mean Density Atmosphere	1-162
1.3.3-15	Instantaneous Heating, Mars Mean Density Atmosphere	1-163
1.3.3-16	Instantaneous Heating, Mars Mean Density Atmosphere	1-163
1.3.3-17	Instantaneous Heating, Mars Mean Density Atmosphere	1-163
1.3.3-18	Instantaneous Heating, Mars Mean Density Atmosphere	1-163
1.3.3-19	Instantaneous Heating, Mars Mean Density Atmosphere	1-164
1.3.3-20	Instantaneous Heating, Mars Mean Density Atmosphere	1-164
1.3.3-21	Instantaneous Heating, Mars Mean Density Atmosphere	1-164
1.3.3-22	Instantaneous Heating, Mars Mean Density Atmosphere	1-164
1.3.3-23	Instantaneous Heating, Venus Standard Atmosphere (25% CO ₂)	1-165
1.3.3-24	Instantaneous Heating, Venus Standard Atmosphere (25% CO ₂)	1-165
1.3.3-25	Instantaneous Heating, Venus Standard Atmosphere (25% CO ₂)	1-166
1.3.3-26	Instantaneous Heating, Venus Standard Atmosphere (25% CO ₂)	1-166
1.3.3-27	Instantaneous Heating, Venus Standard Atmosphere (25% CO ₂)	1-167
1.3.3-28	Instantaneous Heating, Venus Standard Atmosphere (25% CO ₂)	1-167
1.3.3-29	Instantaneous Heating, Venus Standard Atmosphere (25% CO ₂)	1-168
1.3.3-30	Instantaneous Heating, Venus Standard Atmosphere (25% CO ₂)	1-168
1.3.3-31	Instantaneous Heating, Venus Standard Atmosphere (25% CO ₂)	1-169
1.3.3-32	Instantaneous Heating, Venus Standard Atmosphere (25% CO ₂)	1-169
1.3.3-33	Instantaneous Heating, Venus Standard Atmosphere (25% CO ₂)	1-170

LIST OF ILLUSTRATIONS (Cont'd)

<u>Figure</u>		<u>Page</u>
1.3.3-34	Instantaneous Heating, Venus Standard Atmosphere (25% CO ₂) . . .	1-170
1.3.3-35	Instantaneous Heating, Venus Standard Atmosphere (25% CO ₂) . . .	1-171
1.3.3-36	Velocity Normalized Heating, Mars Lower Atmosphere	1-171
1.3.3-37	Stagnation Integrated Heating, Mars Upper Density Atmosphere . . .	1-172
1.3.3-38	Stagnation Integrated Heating, Mars Mean Density Atmosphere . . .	1-172
1.3.3-39	Stagnation Integrated Heating, Mars Lower Density Atmosphere . . .	1-173
1.3.3-40	Martian Atmospheric Models	1-173
1.3.3-41	Atmospheric Density Effect on Total Heating, Mars Stagnation Point	1-174
1.3.3-42	Hypervelocity Stagnation Point Heat Transfer in 90% CO ₂ -91% N ₂	1-174
1.3.3-43	Integrated Convective Heating, Venus Standard Atmosphere	1-175
1.3.3-44	Integrated Radiative Heating, Venus Standard Atmosphere.	1-175
1.3.3-45	Total Integrated Heating, Venus Standard Atmosphere	1-176
1.3.3-46	Radiant Heating Contribution, Venus Standard Atmosphere	1-176
1.3.3-47	Integrated Convective Heating, Venus Standard Atmosphere	1-177
1.3.3-48	Integrated Radiative Heating, Venus Standard Atmosphere.	1-177
1.3.3-49	Radiant Heating Contribution, Venus Standard Atmosphere	1-178
1.3.3-50	Total Integrated Heating, Venus Standard Atmosphere	1-178
1.3.3-51	Integrated Convective Heating, Venus Standard Atmosphere	1-179
1.3.3-52	Integrated Radiative Heating, Venus Standard Atmosphere.	1-180
1.3.3-53	Total Integrated Heating, Venus Standard Atmosphere	1-180
1.3.3-54	Radiant Heating Contribution, Venus Standard Atmosphere	1-180
1.3.3-55	Integrated Total Heating, Mars Mean Atmosphere, Stagnation Point	1-181
1.3.3-56	Integrated Total Heating, Mars Mean Atmosphere, Maximum Turbulent Heating Point.	1-181
1.3.3-57	Integrated Total Heating, Mars Mean Atmosphere, Mid Cone Point	1-182
1.3.3-58	Initial Venusian Radiation Data (Breene and Nardone)	1-182
1.3.3-59	Venus Heat Fluxes Used in REKAP Ablation Study, Standard Atmosphere.	1-183
1.3.3-60	Latest Venusian Radiation Data (Breene and Nardone)	1-183
1.3.3-61	Radiation from CO ₂ -N ₂ Mixture	1-184
1.3.3-62	Venus Trajectory, Best Model Atmosphere.	1-184
1.3.3-63	Hot Gas Radiation Intensity (25% CO ₂)	1-185
1.3.3-64	Stagnation Radiative Heating (25% CO ₂)	1-185
1.3.3-65	Comparative Heating Around Body (Air and N ₂ -CO ₂)	1-186
1.3.3-66	Stagnation Point Radiation in Simulated Venusian Atmosphere Experimental Results Obtained with the Cavity Gage Compared to the Theoretical Predictions	1-186
1.3.3-67	Average Heat of Ablation, Malta Pit I Facility.	1-187
1.3.3-68	Typical ESM Ablation Performance Data	1-187
1.3.3-69	Ablation Material Performance (Hypersonic Arc Facility).	1-188
1.3.3-70	Aerodynamic Shear Stress, Mars Mean Atmosphere.	1-188
1.3.3-71	Heat Fluxes Due to Earth Satellite Re- entry	1-189
1.3.3-72	Sum of Five Carbon Species, Partial Pressure Vs. Wall Temper- ature	1-189
1.3.3-73	Latent Heat of Sublimation (.5 Carbon Species)	1-190

LIST OF ILLUSTRATIONS (Cont'd)

Figure		Page
1.3.3-74	Venus Heat Fluxes Used in REKAP Ablation Study, Standard Atmosphere.	1-190
1.3.3-75	Aerodynamic Shear Stress for Conditions Used in REKAP Study.	1-191
1.3.3-76	Limiting Char Thicknesses for Conditions Used in REKAP Study	1-191
1.3.3-77	Typical Analog Results - Temperature	1-192
1.3.3-78	Typical Analog Results - Ablation and Char Thicknesses	1-192
1.3.3-79	Typical Analog Results - Heat Flux Partitioning	1-193
1.3.3-80	Typical Analog Results - Heat Flux Partitioning	1-193
1.3.3-81	REKAP Heat of Ablation Correlation	1-193
1.3.3-82	Effect of Radiant Heating on Ablation Performance (Summary of REKAP Data)	1-194
1.3.3-83	Typical Energy Absorption Partitioning	1-195
1.3.3-84	Comparison of REKAP Ablation Prediction with Ground Test Data	1-195
1.3.3-85	Mars Shield Ablation Requirements, Mean Atmosphere.	1-196
1.3.3-86	Mars Shield Ablation Requirements, Mean Atmosphere.	1-196
1.3.3-87	Mars Shield Ablation Requirements, Mean Atmosphere.	1-197
1.3.3-88	Mars Shield Ablation Requirements, Mean Atmosphere.	1-197
1.3.3-89	Mars Shield Ablation Requirements, Mean Atmosphere.	1-198
1.3.3-90	Mars Shield Ablation Requirements, Mean Atmosphere.	1-198
1.3.3-91	Mars Shield Ablation Requirements, Mean Atmosphere.	1-199
1.3.3-92	Mars Shield Ablation Requirements, Mean Atmosphere.	1-199
1.3.3-93	Mars Shield Ablation Requirements, Mean Atmosphere.	1-200
1.3.3-94	Ratio of Laminar to Total Time Integrated Heating, Mars Mean Atmosphere	1-200
1.3.3-95	Atmospheric Model Effect on Total Heating, Mars	1-201
1.3.3-96	Stagnation Point Ablation Thickness, Mars Mean Atmosphere	1-201
1.3.3-97	Stagnation Point Ablation Thickness, Mars Mean Atmosphere	1-202
1.3.3-98	Stagnation Point Ablation Thickness, Mars Mean Atmosphere	1-202
1.3.3-99	Stagnation Point Ablation Thickness, Mars Mean Atmosphere	1-203
1.3.3-100	Radiant Heating Distribution.	1-203
1.3.3-101	Venus Shield Ablation Requirements, Standard Atmosphere (25% CO ₂)	1-204
1.3.3-102	Venus Shield Ablation Requirements, Standard Atmosphere (25% CO ₂)	1-204
1.3.3-103	Venus Shield Ablation Requirements, Standard Atmosphere (25% CO ₂)	1-205
1.3.3-104	Venus Shield Ablation Requirements, Standard Atmosphere (25% CO ₂)	1-205
1.3.3-105	Venus Shield Ablation Requirements, Standard Atmosphere (25% CO ₂)	1-206
1.3.3-106	Venus Shield Ablation Requirements, Standard Atmosphere (25% CO ₂)	1-206
1.3.3-107	Venus Shield Ablation Requirements, Standard Atmosphere (25% CO ₂)	1-207
1.3.3-108	Venus Shield Ablation Requirements, Standard Atmosphere (25% CO ₂)	1-207
1.3.3-109	Venus Shield Ablation Requirements, Standard Atmosphere (25% CO ₂)	1-208
1.3.3-110	Insulation Requirements, Mars Mean Atmosphere	1-209
1.3.3-111	Insulation Requirements, Mars Mean Atmosphere (W/C _D A = 40)	1-209
1.3.3-112	Insulation Requirements, Mars Mean Atmosphere (W/C _D A = 60)	1-210
1.3.3-113	Typical Venus Insulation Requirements	1-210

LIST OF ILLUSTRATIONS (Cont'd)

<u>Figure</u>		<u>Page</u>
1.3.4-1	Blunt Vehicle Configurations	1-220
1.3.4-2	Structural Loads and External Pressure - Mars Lander	1-220
1.3.4-3	Structural Loads and External Pressure - Mars Lander	1-220
1.3.4-4	Structural Loads and External Pressure - Mars Lander	1-221
1.3.4-5	Structural Loads and External Pressure - Venus Lander	1-221
1.3.4-6	Structural Loads and External Pressure - Venus Lander	1-222
1.3.4-7	Structural Loads and External Pressure - Venus Lander	1-222
1.3.4-8	Dynamic Pressure Vs. Ballistic Parameter - Mars Standard Atmosphere.	1-223
1.3.4-9	Peak Dynamic Pressure Vs. Ballistic Parameter - Venus Standard Atmosphere.	1-223
1.3.4-10	Effect of Vehicle Shapes on Weight (1500 Lb. Vehicle, Honeycomb Sandwich Shell Construction of Aluminum.	1-223
1.3.4-11	Effect of Vehicle Shapes on Weight (Honeycomb Sandwich Shell Construction of Aluminum - Mars Lander)	1-223
1.3.4-12	Effect of Vehicle Shapes on Weight (Honeycomb Sandwich Shell Construction of Magnesium)	1-224
1.3.4-13	Construction Effects (Ring-Stiffened Stainless Steel).	1-224
1.3.4-14	Construction Effects (Monocoque Shell, Stainless Steel)	1-224
1.3.4-15	Construction Effects (Honeycomb Sandwich, Stainless Steel)	1-224
1.3.4-16	Effect of Materials on Weight (Honeycomb Sandwich Shell, Titanium)	1-225
1.3.4-17	Effect of Materials on Weight (1500 Lb. Vehicle, Honeycomb Sandwich, Stainless Steel)	1-227
1.3.4-18	Impact Attitude of Vehicle	1-233
1.3.4-19	Normal Impact Velocity	1-233
1.3.4-20	Required Stroke Vs. Normal Velocity for Various Deceleration Rates.	1-233
1.3.4-21	Vehicle Kinetic Energy Vs. Normal Velocity	1-233
1.3.4-22	Material Energy Absorption Properties	1-233
1.3.4-23	Vehicle Geometry	1-234
1.3.4-24	Primary Impact Support Structure Weight	1-235
1.3.4-25	Primary Impact Volume	1-235
1.3.4-26	Secondary Impact Volume	1-235
1.3.4-27	Mars Lander Impact System Weight	1-235
1.3.4-28	Venus Lander Impact System Weight	1-243
1.3.4-29	Optimization Program Chart	1-243
1.3.4-30	Structures Studied	1-243
1.3.5-1	Mach 20 Altitude Vs. Entry Velocity	1-257
1.3.5-2	Required Impulse as a Function of Velocity Increment and Vehicle Weight	1-257
1.3.5-3	Retro Rockets	1-258
1.3.5-4	Effect of Drag Modulation	1-258
1.3.5-5	Drag Area Vs. Maximum Diameter of 80° Ballute with Ram-Air Inflation.	1-259
1.3.5-6	Drag Area Vs. Base Diameter of 80° Airmat Cone Attached Directly to Vehicle	1-259
1.3.5-7	System Weight Vs. Base Diameter of 80° Airmat Cone.	1-260
1.3.5-8	System Weight Vs. Base Diameter of 80° Airmat Cone.	1-260
1.3.5-9	System Weight Vs. Maximum Diameter of 80° Ram-Inflated Ballute	1-261
1.3.5-10	System Weight Vs. Maximum Diameter of 80° Ram-Inflated Ballute	1-261
1.3.5-11	Altitude Vs. Vehicle W/C _{DA} for Mach 1.0, 2.0 and 5.0	1-262
1.3.5-12	Martian Touchdown Velocity Vs. Earth W/C _{DA} in Final Descent With Surface Density as a Parameter	1-262

LIST OF ILLUSTRATIONS (Cont'd)

Figure		Page
1.3.5-13	Drag Area of Main Descent Parachute(s)	1-263
1.3.5-14	Assembly Weight of Main Descent Parachute(s)	1-263
1.3.5-15	Packing Volume of Main Descent Parachute(s)	1-264
1.3.5-16	Parachute Deployment State-of-the-Art Main Descent Parachutes .	1-264
1.3.5-17	Decelerator Parachute State-of-the-Art, Mars Lower Atmosphere.	1-265
1.3.5-18	Decelerator Parachute State-of-the-Art, Mars Upper Atmosphere .	1-265
1.3.5-19	Drag Area of the Hyperflo Canopy as a Function of Constructed Diameter and Mach Number	1-266
1.3.5-20	Estimated Assembly Weight of Hyperflo Decelerator Parachute . .	1-266
1.3.5-21	Retardation System Weight for Given Parameters	1-267
1.3.5-22	Parachute Diameters Vs. Final Descent Weight	1-267
1.3.5-23	Parachute Weights Vs. Final Descent Weights.	1-267
1.3.5-24	Decelerator Chute Pack Volume Vs. Final Descent Weight - Mars Lander	1-267
1.3.5-25	Main Chute Pack Volume Vs. Final Descent Weight - Mars Lander.	1-268
1.3.5-26	Deceleration Vs. Time from 8 g's - Mars Entry	1-268
1.3.5-27	Deceleration Vs. Time from 8 g's - Mars Entry	1-269
1.3.5-28	Deceleration Vs. Time from 8 g's - Mars Entry	1-269
1.3.5-29	Deployment Point Diagram - Mars Entry	1-270
1.3.5-30	Functional Block Diagram, Retardation System	1-270
1.3.5-31	Programmer Functional Events for Mars Entry	1-271
1.3.5-32	Descent Time to Impact Vs. Entry Path Angle - Mars Entry . . .	1-271
1.3.5-33	Descent Time with Main Parachute Vs. Deployment Altitude - Mars Lower Atmosphere	1-272
1.3.6-1	Absolute Viscosity Vs. Temperature.	1-287
1.3.6-2	Absolute Viscosity of Ethylene Glycol Solutions	1-287
1.3.6-3	Absolute Viscosity Vs. Temperature.	1-288
1.3.6-4	Kinematic Viscosity Vs. Temperature	1-288
1.3.6-5	Kinematic Viscosity of Ethylene Glycol Solutions.	1-289
1.3.6-6	ρC_p Vs. Temperature.	1-289
1.3.6-7	Specific Heat Vs. Temperature	1-290
1.3.6-8	Specific Heat of Ethylene Glycol Solutions	1-290
1.3.6-9	Density Vs. Temperature	1-291
1.3.6-10	Density Vs. Temperature for Ethylene Glycol Solutions	1-291
1.3.6-11	Thermal Conductivity Vs. Temperature.	1-292
1.3.6-12	Thermal Conductivity of Ethylene Glycol Solutions	1-292
1.3.6-13	Prandtl Number Vs. Temperature.	1-293
1.3.6-14	Prandtl Number Vs. Temperature.	1-293
1.3.6-15	Vapor Pressure Vs. Temperature.	1-294
1.3.6-16	Vapor Pressure of Ethylene Glycol Solutions	1-294
1.3.6-17	Mars Design Surface Temperatures	1-295
1.3.6-18	Required Optical Surface Properties for Temperature Control During Transit from Earth to Venus with Sun Orientation . . .	1-295
1.3.6-19	Thermal Shroud Insulation Thickness for Shade-Oriented Vehicle .	1-296
1.3.6-20	Weight of Environmental Control Systems for Venus Landing Craft.	1-296
1.3.6-21	Weight of Environmental Control Systems for Venus Landing Craft.	1-297
1.3.6-22	Weight of Expendable Coolant for Venus Landing Craft	1-297
1.3.6-23	Weight of Internal Thermal Environment for Optimum Insulation Thickness	1-298
1.3.6-24	Weight of Internal Thermal Environment System for Constant Insulation Thickness.	1-298
1.3.6-25	Ammonia Expendable Coolant Weight (Optimum Insulation Thickness)	1-299

LIST OF ILLUSTRATIONS (Cont'd)

<u>Figure</u>		<u>Page</u>
1.3.6-26	Ammonia Expendable Coolant Weight (Constant Insulation (Thickness)	1-299
1.3.6-27	Optimum Insulation Thickness Vs. Time (in Hours)	1-300
1.3.7-1	Phenolic Nylon - Modulus of Elasticity and Coefficient of Thermal Expansion	1-304
1.3.7-2	Effect of Aging Tape Wound Phenolic Nylon at 250 ^o F on Room Temperature Properties	1-305
1.3.8-1	Variation of Structural and Insulation Weight With Backface Temperature	1-335
1.3.8-2	Variation of Structural and Insulation Weight With Backface Temperature	1-335
1.3.8-3	Variation of Structural and Insulation Weight With Backface Temperature	1-335
1.3.8-4	Variation of Structural and Insulation Weight With Backface Temperature	1-335
1.3.8-5	Variation of Structural and Insulation Weight With Backface Temperature	1-336
1.3.8-6	Variation of Structural and Insulation Weight With Backface Temperature	1-336
1.3.8-7	Variation of Structural and Insulation Weight With Backface Temperature	1-336
1.3.8-8	Variation of Structural and Insulation Weight With Backface Temperature	1-336
1.3.8-9	Variation of Structural and Insulation Weight With Backface Temperature	1-337
1.3.8-10	Shield Structure Optimization	1-337
1.3.8-11	Shield Structure Optimization	1-337
1.3.8-12	Shield Structure Optimization	1-337
1.3.8-13	Bluntness Ratio Vs. Weight - Venus Entry	1-338
1.3.8-14	Bluntness Ratio Vs. Weight - Venus Entry	1-338
1.3.8-15	Bluntness Ratio Vs. Weight - Venus Entry	1-338
1.3.8-16	Bluntness Ratio Vs. Weight - Venus Entry	1-338
1.3.8-17	Bluntness Ratio Vs. Weight - Venus Entry	1-339
1.3.8-18	Bluntness Ratio Vs. Weight - Venus Entry	1-339
1.3.8-19	Impact Velocity Optimization on the Basis of Weight (Vehicle Weight = 300 Lbs).	1-340
1.3.8-20	Impact Velocity Optimization on the Basis of Weight (Vehicle Weight = 1500 Lbs)	1-340
1.3.8-21	Impact Velocity Optimization on the Basis of Weight (Vehicle Weight = 2500 Lbs)	1-341
1.3.8-22	Impact Velocity Optimization on the Basis of Volume (Vehicle Weight = 300 Lbs)	1-341
1.3.8-23	Impact Velocity Optimization on the Basis of Volume (Vehicle Weight = 1500 Lbs)	1-342
1.3.8-24	Impact Velocity Optimization on the Basis of Volume (Vehicle Weight = 2500 Lbs)	1-342
1.3.8-25	Secondary Impact Attenuation Weight Vs. Wind Velocity	1-343
1.3.8-26	Payload Fraction Optimization (Vehicle Weight = 300 Lbs).	1-343
1.3.8-27	Payload Fraction Optimization (Vehicle Weight = 1500 Lbs)	1-343
1.3.8-28	Payload Fraction Optimization (Vehicle Weight = 2500 Lbs)	1-343
1.3.8-29	Variation of W/CDA With Configuration (Vehicle Weight = 300 Lbs).	1-344
1.3.8-30	Variation of Entry Vehicle Density With Configuration (Vehicle Weight = 300 Lbs).	1-344

LIST OF ILLUSTRATIONS (Cont'd)

Figure		Page
1.3.8-31	Variation of W/C_{DA} with Configuration (Vehicle Weight = 1500 lbs).	1-345
1.3.8-32	Variation of Entry Vehicle Density with Configuration (Vehicle Weight = 1500 lbs)	1-345
1.3.8-33	Variation of W/C_{DA} with Configuration (Vehicle Weight = 2500 lbs).	1-346
1.3.8-34	Variation of Entry Vehicle Density with Configuration (Vehicle Weight = 2500 lbs)	1-346
1.3.8-35	Variation of V/D^3 with Configuration.	1-347
1.3.8-36	Design Restraints on Configuration Optimization	1-347
1.3.9-1	Entry/Lander - Side Orientation Scheme	1-373
1.3.9-2	Entry/Lander - Nose-Up Orientation Scheme	1-375
1.3.9-3	Surface Loads on Mars 1969 Vehicle - Nose in Wind.	1-377
1.3.9-4	Surface Loads on Mars 1969 Vehicle - Base in Wind.	1-377
1.3.9-5	Mars Vehicle Oriented and Deployed	1-378
1.3.9-6	Mars 1969 Entry/Lander	1-379
1.3.9-7	Mars 1971 Entry/Lander	1-383
1.3.9-8	Mars 1973 Entry/Lander	1-385
1.3.9-9	Venus 1970 Entry/Lander	1-391
1.3.9-10	Entry Loads - Mars 1969 Vehicle	1-391
1.3.9-11	Lander Gross Weight vs. Base Diameter	1-391
1.3.9-12	Center of Gravity vs. Vehicle Length.	1-392
1.3.9-13	Mars Lander - Vehicle Inertia (Gross Weight Configuration) vs. Gross Weight	1-392
1.3.9-14	Mars Lander - Vehicle Inertia (Entry Configuration) vs. Gross Weight	1-393
1.3.9-15	Payload Compartment Volume vs. Base Diameter	1-393
1.3.9-16	Gross Weight vs. Total Shield Weight	1-394
1.3.9-17	Structural Weight vs. Gross Weight	1-394
1.3.9-18	Retardation Weight vs. Gross Weight.	1-395
1.3.9-19	Ground Orientation System Weight vs. Gross Weight	1-395
1.3.9-20	Gross Weight vs. Payload Weight - Venus Landers	1-396
1.3.9-21	Gross Weight vs. Payload Weight - Mars Lander.	1-396
1.3.9-22	Venus Lander - Insulation Area vs. Gross Vehicle Weight.	1-397
1.3.9-23	Thermal Control System Weight	1-397
1.3.9-24	Adapter Structure and Radiator Weight vs. Gross Vehicle Weight	1-398
1.3.9-25	Propulsion System Weight vs. Gross Vehicle Weight	1-398
1.3.9-26	Detailed Weight Breakdown - Mars Lander.	1-399
1.3.9-27	Detailed Weight Breakdown - Venus 1970 Lander.	1-401

LIST OF ILLUSTRATIONS

Figure No.

2-1	Saturn B + S VI Preliminary Nose Fairing and Spacecraft Envelope . . .	2-3
2.2.1-1	Sequence of Events - Mars 1969	2-25
2.2.1-2	Voyager Orbiter System Block Diagram	2-27
2.2.1-3	Voyager Orbiter Axes	2-29
2.2.2-1	Voyager plus 45 in. Adapter Within Saturn Shroud	2-30
2.2.2-2	Voyager Mounted on Combined Instrument Unit - Adapter Within Saturn Shroud	2-31
2.3.2-1	Voyager Launch Configuration	2-33
2.3.2-2	Voyager Transit Configuration	2-33
2.3.3-1	High Gain Antenna	2-39
2.3.3-2	Antenna Elevation Angle (θ) in Relation to Earth Ecliptic Plane	2-41
2.3.3-3	Antenna Azimuth Angle (α) in Relation to Vehicle Sun Line	2-42
2.3.3-4	Earth, Sun, Mars Angles (α), Launch Through 360 Days	2-42
2.3.3-5	Determination of Angle (Limiting Case)	2-43
2.3.3-6	PHP Component Layout	2-45
2.3.3-7	Angular Position and Altitude of Orbiter in Relation to Mars	2-47
2.3.3-8	PHP Support and Drive Mechanism	2-49
2.3.3-9	Lander Flight Path	2-52
2.3.3-10	Magnetometer	2-55
2.3.3-11	Lander/Orbiter Interface	2-59
2.3.3-12	VHF Antenna Deployment Mechanism	2-61
2.3.3-13	Active Cell Area vs Overhand	2-65
2.3.3-14	Engine Mounting	2-67
2.3.4-1	Mars 1971 Voyager Configuration	2-73
2.3.4-2	Mars 1973 Voyager Configuration	2-75
2.3.4-3	Venus 1970 Voyager Configuration	2-77
2.3.4-4	Venus 1972 Voyager Configuration	2-79
2.3.5-1	Titan III C Orbiter	2-81
2.3.5-2	Titan III C Fly-By Bus	2-83
2.3.6-1	Saturn V Voyager Configuration	2-85
		2-88
2.4.1-1	Voyager Configuration	2-91
2.4.1-2	Planetary Geometric Factors (Orbiter Sides to Mars)	2-91
2.4.1-3	Albedo Geometric Factors (Orbiter Sides to Mars)	2-92
2.4.1-4	Orbiter Surface Coating Pattern	2-93
2.4.1-5	Effective Emittance vs Louver Angle	2-96
2.4.1-6	Base Plate Weigh vs Heat Dissipation	2-98
2.4.1-7	Paddle Temperature vs Distance from Sun	2-99
2.4.1-8	Wall Temperatures of Compartments 2 and 3 vs Distance from Sun . . .	2-101
2.4.1-9	Wall Temperature of Compartment 1 vs Distance from Sun	2-102
2.4.1-10	Tank Temperature vs Distance from Sun	2-102
2.4.1-11	F-14 Tank Temperature vs Power Required	2-103
2.4.1-12	He Tank Temperature vs Power Required	2-103

LIST OF ILLUSTRATIONS (Cont'd)

2.4.2-1	PHP Positions in Mars 1969 Orbit	2-110
2.4.2-2	Sun Angle vs Maximum Heat Rejection	2-115
2.4.2-3	Distance from Sun vs PHP Temperature and Heat Required	2-120
2.4.2-4	PHP Geometric Factors for Mars $1 \times 19 \times 10^3$ NM Orbit	2-123
2.4.2-5	PHP Temperature History in a Mars $1 \times 19 \times 10^3$ NM Orbit	2-124
2.4.3-1	Venus PHP Configurations Chosen for Passive Temperature Control Analysis	2-126
2.4.3-2	Venus PHP Analog Circuit for Passive Temperature Control Studies	2-128
2.5-1	Voyager - Mars 1969 Orbiter Structure, Fix Tank M. T. G.	2-133
2.5-1	Voyager - Mars 1969 Orbiter Structure, Fix Tank M. T. G. (cont) . .	2-135
2.5-1	Voyager - Mars 1969 Orbiter Structure, Fix Tank M. T. G. (cont) . .	2-137
2.5-2	Voyager - Mars 1969-1B (Orbiter Structure and Panel Assy)	2-139
2.5-3	Major Mass Item Weight and Location, End View	2-151
2.5-4	Major Mass Item Weight and Location, Plan View	2-152
2.5-5	Dynamic Transmissibility Factors vs Frequency (cps)	2-157
2.5-6	Qualification Test Input G's (RMS) at Vehicle Resonance	2-157
2.5-7	Dynamic Response in G's (RMS) vs Frequency (cps)	2-159
2.6.1-1	Orbiter Axes	2-164
2.6.1-2	Orbiter Reference Data	2-165
2.6.2-1	Parts Location for Detail Weight Analysis, Orbiter Structural Arrangement (No Scale)	2-173
2.6.2-2	General Location of Removable Honeycomb Panels	2-174
2.6.2-3	Parts Location for Detail Weight Analysis, PHP Structural Arrangement (No Scale)	2-175
2.6.2-4	Parts Location for Detail Weight Analysis, High Gain Antenna Structural Arrangement	2-176
2.6.4-1	Payload Packaging Arrangement (No Scale)	2-185
2.6.5-1	Definitation of Area Used in Calculating Solar Array Weights	2-187
2.6.5-2	Typical Solar Cell Construction	2-188

LIST OF TABLES

<u>Table No.</u>	<u>Title</u>	<u>Page</u>
1.3.9-1	Matrix of Vehicle Structures	1-349
1.3.9-2	Design Parameters for Vehicles Presented in Study.	1-369
1.3.9-3	Lander - Summary Weight Breakdown	1-370
2-1	Mission Analysis Requirements	2-2
2.4.1-1	Orbiter and Planetary Horizontal Package Temperature Limits	2-90
2.4.1-2	Summary of Maximum Heater Requirements During Normal Cruise (Watts)	2-90
2.4.1-3	Orbiter Component Power Dissipations	2-90
2.4.1-4	Standard Values of Solar Array Thermal Constants	2-97
2.4.1-5	Local Antenna Temperatures	2-105
2.4.1-6	Nominal Coating Properties	2-106
2.4.1-7	Irradiated Coating Properties	2-106
2.4.1-8	Irradiation Test Results for D4D on Aluminum	2-107
2.4.2-1	PHP Component Power Dissipations	2-117
2.4.2-2	Maximum Heat Rejection Rate (Watts/ft ² Base Radiator) at Mars	2-117
2.4.3-1	Constants and Fluxes for Venus PHP	2-127
2.4.3-2	Passive PHP Parameter Values	2-127
2.6.1-1	Weight, Center of Gravity and Inertia Variation, Mars 1969	2-165
2.6.1-2	Mars 1969 3% Off-Ratio-Propulsion System	2-166
2.6.1-3	Weight, Center of Gravity and Inertia Variation, Mars 1969	2-166
2.6.1-4	Mars 1971 3% Off-Ratio Propulsion System	2-167
2.6.1-5	Subsystem Weight Matrix	2-168

SECTION 1.0 ENTRY/LANDER DESIGN

1.1 INTRODUCTION

In the past two years many studies have been conducted by GE/MSD to determine the system characteristics required for entry into the Venus or Mars atmospheres. Two representative studies are Reference 1 & 2. The first study, Ref. 1, investigated the use of a GE designed Discoverer or Nerv capsule for entry into the Mars atmosphere. The conclusion reached was that a Discoverer-type capsule could be used for direct ballistic entry, and that retardation in the unknown, but very thin, Mars atmosphere would be one of the more difficult design problems. The second study, Ref. 2, extended the first study to include entry into the Venus atmosphere. Again the conclusion reached was that the Discoverer shape could be used for entry into the thick Venus atmosphere and that high deceleration loads during entry and high atmospheric temperatures would be the limiting design problems for Venus.

Both of the above studies were limited to Discoverer shapes to utilize a proven aerodynamic configuration. The size range was limited from 200 to 500 lb. vehicles because the studies were performed for the Mariner program. For the Voyager Study no shape limitations have been assumed. The weight limitations have been extended to cover the range from 200 to 6000 lbs.

1.1.1 OBJECTIVES

The objectives of the Voyager Lander Program have been three-fold: first, to define Lander Systems that meet mission analysis requirements, second, to study Lander designs parametrically and, third, to investigate areas of technical uncertainty. The design effort to accomplish the first two of these objectives was carried on concurrently, but due to timing limitations, the feedback from the parametric analysis is not fully incorporated in the systems proposed for the specific missions. Thus the specific systems proposed represent near optimum systems that will require further optimization in the preliminary design phase of the Voyager program. The third objective has been accomplished as an integral part of efforts in each technical discipline.

1.1.2 DESIGN CRITERIA & LIMITATIONS

Five specific Lander Systems were investigated. The system requirements for each Lander, as defined in the Mission Analysis, (Volume II), are as follows:

	Mars			Venus	
	1969	1971	1973 *	1970	1972
Number of Landers	2	2	2	1	1
Lander Weight (lbs.)	1,450	2,000	2,000	525	2,600
Entry Velocity (lbs.)	21,500	18,900	19,200	38,800	37,900
Entry Angle	← No Limit →				
Design Life	← 6 Months →			10 Min on Surface	6 Hrs on Surface
Power Supply	RTG + BATT	RTG + BATT	RTG + BATT	BATT	BATT
Primary Communication	Relay	Relay	Direct	Relay	Relay

*Mars 1975 Lander will be identical to the 1973 vehicle.

The Entry/Lander conceptual design was carried out to meet the environmental limitations listed below:

Characteristics	Design Load	Time of Occurrence
Pressure	760 to 10^{-10} mm Hg.	Surface - Space
Axial & Shock	125 Mars 325 Venus	Entry & Impact
Vibration frequency (cps)	5 - 50 50-100 100-2k	Powered Flight
Sinusoidal	1.3 2.5 3.5	
Random (cps)	.015 .015 .035	
Noise (db.)	160	Entry

The Lander and all installed equipment must be sterilizable by thermal means (145° C @ 36 hrs. for qualification) and chemical means (exposure to Ethylene Oxide). In addition to sterilization, the Lander and all installed equipment must be able to function after exposure to the transit environment for periods up to 325 days for Mars systems and up to 190 days for Venus systems.

The design atmospheres used in this study were supplied by NASA. The Mars atmospheres are the "Upper Limit", "Mean" and "Lower Limit" atmospheres of Shillings Model II atmospheres, Reference 3. The Venus atmospheres are the "Standard" and "Extreme" atmosphere defined by L. D. Kaplan in Reference 4. The pressures, temperatures and densities used in the study are presented in Figures 1.1.3-1 thru 1.1.3-6. The Mars atmospheres were not significantly different from the atmospheres used on the previous Mariner Studies. The Venus atmospheres used in this study did not include the high (54 atmosphere) pressure model atmosphere used in the Venus/Mars capsule study which had a significant effect on both the maximum entry deceleration loads and the thermal control system.

However, a few investigations in this study were begun early in the program and are based on planetary atmospheric models other than those above. Where this occurs, the particular atmospheric model is noted. The "old" Venus Best, Extreme I and Extreme II model atmosphere have been obtained from Reference 2, and the "old" Mars Model A, B, and C atmospheres have been taken from Reference 1.

New Mars model atmosphere characterized by very low surface pressures (11 millibar) were introduced towards the end of the study. These atmospheres will be treated separately in the study and, unless otherwise stated, the low pressure atmospheres are not used in the bulk of this report.

To insure consistency throughout the Study, the nature of the Martian Surface had to be defined. The surface of both planets was assumed to be a hard rocky crust with slopes up to 20degrees. For design purposes, free water in the form of lakes or oceans was assumed improbable. Surface winds of up to 40 mph (58.6 fps) were assumed to exist on both planets.

The designs presented to support specific missions, represent a state-of-the-art which will be available in the 1969 time period. Since later opportunities utilize subsystems developed for the first opportunity, later systems also represent the 1969 state-of-the-art. Wherever possible commonality between the Mars and Venus vehicle was a design goal.

References

1. "Suitability of Discoverer and NERV for Mars Atmospheric Entry", P. G. Thome, final report for work performed under JPL Contract # 950226 (1962).
2. "Venus Mars Capsule Study", P. G. Thome, Final report for work performed under JPL Contract 950250 (1962).
3. "Limiting Model Atmospheres of Mars", G. F. Schilling, R-402-JPL a report prepared for JPL by the Rand Corp.
4. "A Preliminary Model of the Venus Atmosphere", L. D. Kaplan, Report Number 32-379 from JPL.

1.2 SUMMARY OF RESULTS

1.2.1 SYSTEM DESCRIPTION

In support of the concepts presented in Volume II, Mission & System Analysis, five Entry/Landers have been examined in some detail. The physical characteristics are described in the matrix table, Table 1.2.1-1.

TABLE 1.2.1-1 LANDER SYSTEM - CHARACTERISTICS

	← Mars →			← Venus →	
	1969	1971	1973	1970	1972
Gross Weight, Lbs.	1450	2000	2000	525	2600
Entry Weight, Lbs.	1270	1768	1768	447	2358
Base Diameter, In.	92	108	108	58	123.5
Nose Radius, In.	16.1	16.1	16.1	10.0	21.6
Base Area, Ft ²	46.1	63.6	63.6	18.3	83.1
Bluntness Ratio RN/RB	0.35	0.30	0.30	0.35	0.35
Drag Coefficient	0.78	0.77	0.77	0.65	0.65
W/C _D A	35	35.5	35.5	45	44
Length, In.	45.94	55.44	55.44	40.5	71.50
Semi Cone Angle, Deg.	40	40	40	30	35
Communications	Direct Relay	Direct Relay	Direct	Relay	Relay
Power Supply	RTG & Batt.	RTG & Batt.	RTG & Batt.	Primary Batt.	Primary Batt.
Retardation	3 Stage Parachute	→		Atmos & Aft Cover	→

TABLE 1.2.1-2. ENTRY LANDER SCIENTIFIC EXPERIMENTS

DATA	← Mars →			← Venus →	
	1969	1971	1973	1970	1972
<u>ENTRY & DESCENT</u>					
Temperature	X	X	X	X	X
Pressure	X	X	X	X	X
Density	X	X	X	X	X
Composition of Atmosphere					
Mass Spectrometer	X	X			
Gas Chromatograph	X		X		X
Altitude	X	X	X	X	X
Electron Density	X		X		
UV Multichannel Radiometer		X			
8 446 A Radiometer		X			
UV Solar Spectrum			X		X
Cloud Properties				X	X
Electrostatic Potential Gradient					X
TV					X
<u>SURFACE</u>					
			<u>LANDER</u>		
			<u>A</u>	<u>B</u>	
Temperature	X	X	X	X	X
Pressure	X	X	X	X	X
Density	X	X	X	X	X
Composition of Atmos.					
Mass Spectrometer	X	X			
Gas Chromatograph	X	X	X	X	X
Wind Speed & Direction	X	X	X	X	X
TV Panorama	X	X	X	X	X
TV Microscopic	X	X	X		
Surface Sounds	X	X	X		X
Precipitation	X				
TV-Light Source				X	
Skylight Analyzer		X	X	X	X
Light Level Indicator	X				
Surface Penetrability	X	X			X
Soil Moisture	X				
Seismic Activity	X	X			X
Surface Gravity	X				
Radioisotope Growth Detector	X				
Turbidity & PH Growth Detector	X				
Multiple Chamber Growth Detector	X	X	X	X	
Photoautotroph Detector	X	X	X	X	
Microscopic Analysis	X	X	X		X
Drill	X	X			
Pulverizer	X	X			
Sample Handling Equipment	X	X	X		
X-Ray Diffractometer		X			X
α - Particle Scattering		X			X
Thermal Conductivity of Ground		X			X
Electrical Conductivity of Ground		X			
Insolation		X			X
Surface Radioactivity		X			X
Meteor Trails		X	X		X
Ionospheric Profile		X	X		X
Eclipse by Phobos		X			
Insect Attractor		X	X	X	
Pulse Light		X	X	X	
Rocket Soundings of Atmosphere				X	
Distance to Phobos		X			
Seismic Properties			X		

All Mars vehicles have been designed using a Radioisotope Power Supply. The radioisotope was chosen because the expected low temperature Mars environment requires vehicle payload heating, and because of the ready availability of a good low temperature junction for the thermoelectric generator. The Radioisotope Thermoelectric Generator (RTG) makes possible the long surface life for Mars vehicles which in turn makes direct communication capability from the Lander to the Earth, in addition to Orbiter relay capability necessary for long life reliable communication capability.

Venus vehicles must survive temperatures of 1050° F on the planet surface. Even after optimization, the weight of the Venus thermal control system is the largest single subsystem weight for a design life in excess of 4 or 5 hours. For the Venus 1970 system, the Orbiter period is 3.6 hours; therefore, small vehicles (Venus 1970) are designed for survival to impact plus 10 minute life before loss of line-of-sight. Large vehicles - having the capacity for a larger thermal control system - are designed to survive until the Orbiter regains communications line-of-sight on its first complete orbit (6 hours).

Table 1.2.1-2 lists the scientific experiments to be carried aboard the Mars and Venus Entry/Landers. The primary mission of the Mars vehicles is biological life detection on the planet. The secondary mission is the measurement of geophysical and atmospheric data of the planet. The Venus 1970 mission will concentrate on obtaining atmospheric and surface environmental data. The Venus 1972 mission includes experiments to determine if forms of life exist in the upper atmosphere. Specific experiments have been selected to fulfill the requirements of the individual missions. A more complete description of the scientific payload and scientific objectives can be found in Volume II, Section 1.0.

The Lander systems proposed are designed to enter the Mars and Venus atmospheres ballistically from an interplanetary transfer trajectory. Entry from orbit was studied briefly but eliminated from further consideration because of the high weight penalty for orbit injection. Although the system requirements specify target areas on Mars, the Entry/Landers for both Venus and Mars are designed to enter at any entry angle from the "skip" limit to vertical entry. Entry at path angles less than 20 degrees are not desirable because of the very high integrated aerodynamic heating near the capture angle and because of the uncertainties involved in defining the capture angle in the unknown atmospheres. Figures 1.2.1-1 and 1.2.1-2 show the altitude time history envelopes of possible entry trajectories. Note the long ballistic descent times in the thick Venus atmosphere compared to the short times in the thin Mars atmospheres.

Although the commonality of the Landers for Venus and Mars was originally a goal, the penalty for commonality proved to be too great. The Venus vehicle is characterized by high entry deceleration loads, high structural temperatures at impact, rudimentary retardation system and a cooling type thermal control system. The Mars vehicle is characterized by relatively low entry deceleration loads, a multistage supersonic parachute system, and a heating type thermal control system. The Mars 1969 Lander is shown in Figures 1.2.1-3 and 1.2.1-4.

A typical weight distribution for a 1500 lb. gross weight vehicle is shown on Table 1.2.1-3. Note that Venus vehicles are characterized by high thermal control system weight despite short (6 hr.) life limitations, and Mars vehicles are characterized by high retardation system weight. For further discussion of weight trends, see Section (1.3.9).

Both the Venus and Mars systems are designed for minimum descent time consistent with reliability requirements. At other than the limiting condition - thin Mars atmosphere, vertical entry - a radar altimeter will be used to prevent deployment of the parachute system on the Mars Lander above 30,000 ft. Deployment of the aft cover of the Venus vehicle to gain additional drag similarly will be delayed until the Lander is within 5000 ft. of the surface of the planet. These minimum descent times are necessary to insure line-of-sight between the Lander and Orbiter at the time of impact of the Lander.

Although the subsonic descent time on the Mars vehicle can be very short, both the Venus and Mars Landers can perform atmospheric experiments after blackout and prior to impact.

TABLE 1.2.1-3. TYPICAL LANDER SUMMARY WEIGHT BREAKDOWN

	Mars	Venus
	% Total	% Total
Shield	5.8	14.0
Structure	16.1	20.5
AFT Cover & Separation	4.4	5.8
Retardation & Crush Up	19.8	6.0
Thermal Control	5.0	23.8
Electrical Power	7.3	1.2
Communications	9.7	4.5
Orientation	4.6	3.6
Scientific Payload	11.0	8.4
Payload Deploy & Installing	3.9	2.9
Total Entry Lander	87.6	90.7
Spin & Separation	1.8	1.1
ΔV Rocket	6.7	6.2
Adapter & Radiator	3.9	2.0
Total Lander	100.0	100.0

1.2.2 BASIC TRAJECTORIES

Both point mass and six degree of freedom trajectories are discussed in Section 1.3.2. This section of the summary is included to acquaint the reader with the characteristic entry deceleration loads as a function of various parameters.

A. Maximum Axial Deceleration

The axial decelerations experienced by vehicles entering the Martian and Venusian model atmospheres are presented graphically in Figures 1.2.2-1 through 1.2.2-5. The trends that would be expected from linear theory, such as: the relative magnitudes of axial deceleration and the altitude of occurrence, are borne out by these figures. For example, peak deceleration (earth g's) varied directly as the square of the entry velocity, path angle, and the density gradient of the atmosphere.

For a Venus entry, the ballistic parameter effect on maximum deceleration is shown for a nominal velocity of 38,000 fps for the Venus Standard and Extreme atmospheres (Figure 1.2.2-5).

The variation of the maximum deceleration rate with planetary atmosphere is shown for Mars on Figure 1.2.2-1 and for Venus on Figure 1.2.2-4. The maximum deceleration loads occurred on the Mars Lower atmosphere and the Venus Standard atmosphere. Maximum deceleration loads occurred in the model atmosphere with the steepest density gradient in the 100,000 to 500,000 foot range.

The variation of peak deceleration with entry velocity for Mars is shown on Figure 1.2.2-2, while the variation of peak deceleration with entry angle for Venus and Mars are shown on Figures 1.2.2-1 through 1.2.2-4. Entry at shallow entry angles can be used as a mechanism of reducing the peak deceleration during entry on either Venus or Mars.

The maximum design deceleration load for Mars was taken as 125 g's and for Venus as 325 g's. These figures correspond to a higher entry velocities than is predicted for either system. Figures 1.2.2-1 and 1.2.2-4 predict the maximum entry decelerations for Mars to be about 87 g's and for Venus about 314. The difference between the design and predicted "g" level was due to variations in initial entry conditions and a conservative margin of safety. Both Mars and Venus vehicles have been designed for 125g impact load.

B. Envelope of Altitude vs. Time

An altitude-time history envelope is presented in Figure 1.2.1-1 based on a nominal entry velocity of 21,500 F. P. S. and a ballistic parameter of 35 psf. If the true atmospheric profiles are not appreciably more dense than the Mars Upper or appreciably less dense than the Mars Lower, all altitude time histories should fall between the two bounds shown for path angles between 20 and 90 degrees as the altitude history based on the Mars Mean atmosphere suggests.

Figure 1.2.1-2 shows a similar altitude time history envelope for Venus based on a nominal entry velocity of 38,000 F. P. S. and a ballistic parameter of 40 psf. For this entry velocity and ballistic parameter all vehicles should have an altitude history falling between this upper and lower bound. The band of altitudes is somewhat narrower than those for the analogous Martian entry due to the greater agreement in the two Venusian atmosphere profiles at lower altitudes.

C. Occurrence of Parachute Deployment Mach Number

Mach number-altitude histories for four point mass trajectories, based on a nominal velocity of 21,500 fps and a nominal ballistic parameter of 35 psf, appear on Figure 1.2.2-6. The effect of the atmosphere on altitude of occurrence of a Mach number of 2.5, the maximum parachute deployment altitude, is readily seen by noting the intersection of the dashed 2.5 line with the various Mach numbers curves.

The actual altitudes at which a Mach number of 2.5 occurs is presented as a function of ballistic parameter with path angle as a parameter in Figure 1.2.2-7 for a nominal entry velocity of 21,500 ft./sec. into the Mars Lower Atmosphere. The Lower Atmosphere allows the deepest penetration before a Mach number of 2.5 is reached. As the path angle and ballistic parameter increase, the altitude at a Mach number of 2.5 decreases. It is seen that for a ballistic parameter of 60 psf and path angle of 90 degrees, the vehicle impacts at a Mach number above 2.5. Corresponding results for the Mean and Upper Martian atmospheres show that the altitudes are higher for the same entry velocity and for a constant atmosphere the altitudes decrease as the velocities increased.

For the supersonic parachute system proposed, approximately 17,000 feet will be lost during deployment staging; therefore, to insure that the main stage parachute is fully deployed at 5,000 feet a Mach number of 2.5 must occur at altitudes higher than 22,000 feet. Figure 1.2.2-7 shows that the vehicle must have a ballistic parameter of 35 psf or less to insure full deployment of the parachute system.

1.2.3 SUBSYSTEM DESCRIPTION

This section of the report summarizes the more important subsystem conclusions reached during the study and the interaction of the subsystem design on the Lander System. The details of the analyses and more complete explanation of the logic involved in reaching the conclusions are found in the Analysis Section of the Report, Section 1.3.1 thru 1.3.9. The System block diagram Figure 1.2.3-1 shows the various subsystems and their interrelation.

A. Vehicle Subsystem

The Vehicle Subsystem includes all subsystems of the Lander except the power supply, communications and scientific payload.

B. Shape Selection

Blunt sphere cones were selected for both the Venus and Mars Landers because they avoid the potential dynamic stability problems of very blunt (Apollo) shapes, and because the need for a high drag shape outlaws the use of very sharp nosed vehicles. Aerothermodynamic analysis has not shown the need for sharp nosed vehicles to avoid radiative heating problems on a steep Venus entry. Thus, the mid-range of sphere cones was selected for this study to fully utilize the wealth of flight experience obtained on GE RVX, Mark 2, Mark 6, Discoverer and other programs.

A ballistic coefficient of 35 psf was selected for the Mars Lander to insure successful deployment of multistage supersonic parachute systems. With ballistic coefficients greater than 35 psf, the parachute system cannot be fully deployed and achieved terminal velocity in the lower Limit Atmosphere with a vertical entry.

A ballistic coefficient of 45 psf was selected for the Venus Lander to insure as fast a descent as is consistent with surface impact velocity of 50 to 60 feet per second. The aft cover of the Venus Lander is deployed to further arrest the touchdown velocity of the Venus Lander.

The bluntness ratio, cone angle and base diameter was selected to achieve the desired weight vehicle, the ballistic coefficient specified by retardation, and a reasonable packaging density simultaneously. As shown in the configuration tradeoff and optimization section cone angles in the range of 40 degrees and bluntness ratios in the range of 0.6 result in the most efficient vehicle. As discussed in Section 1.3.9 lower bluntness ratios are required for reliable side orientation on the surface of the planet. The optimum bluntness ratio for a given vehicle depends on the location of the vehicle center of gravity, the vehicle cone angle and the depth of the crushable material in the region of the nose cap. For the types of vehicles discussed in this study, a bluntness ratio of 0.4 to 0.5 is appropriate. The vehicle presented in Table 1.2.1-1 show a conservative bluntness ratio of 0.35 which was chosen early in the study before the optimization and trade off studies were completed.

Packaging densities were used as a guide in selecting vehicles because of the uncertainties in the size and weight of the scientific payload. Based on gross vehicle volume a density of 15 pounds per cubic foot was assumed to be a maximum, and on more detailed studies within the payload compartment a packaging density of 20 pounds per cubic foot was assumed to be a maximum.

C. Thermal Protection

The thermal protection system for the Venus and Mars Landers must protect the Landers from the typical heating conditions tabulated below:

	Mars		Venus	
	Mean Atmosphere		Standard Atmosphere	
Entry Path Angle, Deg DFH	20	90	15	90
Heating Time, Sec.	150	25	55	10
Peak Heating Rate \dot{Q} , Btu/Sec - $f+^2$	180	460	1190	2,750
Integrated heating Q Btu/ $f+^2$	9000	4200	2750	10,200

The shield selected for the Mars Lander is a GE developed Elastometric Shield Material (ESM). This material was selected because of its high heat of ablation, its tolerance to thermal gradients, its high insulating properties, and because it appears it can be made radar transparent. The ESM shield is particularly well suited to the long relatively low heat pulse encountered on a Mars entry.

The elastometric nature of the material leads to other advantages such as resistance to handling damage and protection against micrometeorite damage during the long transit. The shield designs quoted in the weight analysis contain a 50% ablation margin and an insulation layer required to hold the shield bond temperature to 300°F - a limit established for the fiberglass crushable material. The shields were designed to enter at any path angle greater than 20 degrees computed at 10⁶ feet. The required shield for entry angles between the capture angle ($\gamma_e = 18.5$) and 20 degrees were not calculated because the shield weights become unreasonably high near the capture path angle. (See Section 1.3.3.F).

Phenolic nylon was selected for the Venus thermal shield because of the flight-proven characteristics of the material at high heat loads. Phenolic nylon is a member of an all-organic class of materials whose ablation performance improves with increasing heat rates. Phenolic graphite is selected as an alternate for phenolic nylon because of the potential performance improvement of the phenolic graphite with respect to the phenolic nylon.

Further analysis of the shield design is found in Section 1.3.3 and of the material selection is found in Section 1.3.7.

D. Lander Structural Subsystem

The Mars and Venus Landers have been designed to enter the planetary atmospheres with no restriction on entry path angles. Vertical entry imposes the limiting design conditions with maximum deceleration rates of 125 earth "g's" for the Mars Lander and 325 earth "g's" for the Venus Lander. The Landers were designed to survive impact on the planetary surface with the impact "g" load equal to the maximum entry deceleration load.

The basic construction of the Mars vehicle consists of a heat shield bonded to the fiberglass crush-up structure which is in turn bonded to the aluminum honeycomb sandwich primary structure. As mentioned above, the shield thickness includes insulation to maintain the shield/crush-up bond line temperature below 300°F. The fiberglass honeycomb crush-up structure was selected because of its high energy absorption characteristics, because it can be made radar transparent, and because of its insulating value on the planetary surface. The primary structure can be made from a low temperature light-weight

material such as Aluminum, Magnesium or Beryllium. Aluminum was selected over Magnesium or Beryllium because of cost and state-of-the-art considerations. The honeycomb construction technique was selected because of its weight advantage over other conventional construction techniques because the double seal protection offered by the two face sheets, and because the honeycomb is in itself a crushable material. Parametric curves of other materials and construction techniques are included in Section 1.3.4.

The Venus Lander is similar to the Mars Lander except that high temperature materials have been substituted for the crush-up structure and the primary structure. The high (1050° F) surface temperatures of Venus require the use of stainless steel or titanium honeycomb for both the crush-up material and the primary structure. Stainless steel was selected in preference to titanium because of state-of-the-art considerations.

E. Retardation Subsystem

The difference in the Mars and Venus atmospheres is graphically illustrated by the difference in the retardation system of the Venus and Mars Entry/Landers. The terminal descent velocities of the surface of the Venus and Mars Landers are tabulated for ballistic vehicles without auxiliary drag devices.

	<u>Maximum Terminal Ballistic Impact Velocity</u>	<u>Minimum Terminal Ballistic Impact Velocity</u>
Venus (fps)	260	120
Mars (fps)	690	480

The retardation system must reduce the velocity of the vehicle at impact so that the shock attenuation system can absorb the remaining energy without exceeding the maximum entry deceleration loads - 125 g's for Mars and 325 for Venus. As shown in Section 1.3.8, the optimum weight combination of parachutes and shock absorption material occurs at impact velocities of about 70 feet per second. The depth of the crushable material at this impact velocity however is approximately 9 inches which may pose practical problems in manufacturing and vehicle design. Pending further study, it is felt that the optimum impact velocity will be in the range of 50 to 60 feet per second.

The parachute system proposed for the Mars Vehicle consists of a Mach number 2.5 supersonic decelerator parachute which is ejected from a mortar tube to provide the first stage. Drag from the decelerator parachute is then used to separate the aft cover, extract the main parachute and remove the deployment bag from the main parachute canopy. A second stage of deceleration is then accomplished by the reefed main canopy. Final deceleration is provided after the main parachute is disreefed and the canopy inflates to the fully inflated configuration. This sequence is shown on Figure 1.2.3-2. The Mach number 2.5 parachute was chosen as a conservative estimate of the state-of-the-art in supersonic parachutes.

The thick Venus atmosphere makes possible the use of very simple retardation devices to achieve impact velocities of 50 to 60 feet per second. The retardation of the Venus vehicle is accomplished by deployment of the vehicle aft cover as a drag plate - See Sketch Figure 1.2.3-3.

The deployment for the Mars landing sequence is initiated by the retardation programmer. The programmer uses a series of "g" switches and timers to sense the Mach number 2.5 flight speed regardless of the entry angle or the atmosphere encountered. The retardation programmer block diagram is illustrated in Section 1.3.5. In order to prevent excessive descent times, the radar altimeter is used to prevent deployment of the parachute system at altitudes above 30,000 ft.

F. Orientation Subsystem

Since the prime objective of the Voyager program is the collection and transmission of surface data from the planets, orientation of the ground sampling equipment and communication antennas is vitally important.

Four basic orientation modes were evaluated for this study - nose-up, nose-down, side with vehicle orientation, side with payload orientation. The nose-up and nose-down orientation systems were discarded because of the difficulty in bringing the Lander to the final position from any other position. By limiting the bluntness ratio as a function of the vehicle cone angle, the vehicle can be made unstable in the nose-down position, which makes the vehicle most likely to come to rest on its side. Once the vehicle has come to rest, it is preferable to orient the payload with respect to the ground rather than re-orient the vehicle, since by definition the vehicle comes to rest in a minimum energy position.

The orientation sequence is as follows. A position sensor determines the position of the vehicle and determines the next step in the orientation sequence. If the vehicle is nose down, rockets are used to tip the vehicle on its side, if the vehicle is on its base, the tip bars are extended to tip the vehicle on its side. Once on its side, the aft bulkhead of the vehicle is rotated to a predetermined position with respect to the ground. The tip bar is fully deployed until it contacts the ground. Explosive anchors mounted to the tip bars are then fired to stake the vehicle in position.

G. Packaging and Deployment

Packaging studies were conducted on assumed scientific payloads and the power supplies and communication equipment recommended for the various opportunities. Based on past experience in packaging scientific payloads, a maximum permissible packaging density of 20 pounds per cubic foot was used in this study. As mentioned above, the shape of the vehicle was varied to maintain the maximum packaging density.

In the course of the study, several important packaging considerations were uncovered.

- (1) The radiation hazard of the Radioisotope Thermoelectric Generator power supply requires heavy shielding or insertion of the radioactive fuel as one of the last operations prior to launch. Insertion just prior to launch is most easily accomplished on the launch pad by removal of a nose cap. Therefore, the RTG should be located in the nose of the vehicle.
- (2) Installation of components that cannot be thermally sterilized require careful attention to location so that remote handling techniques or glove-box techniques can be accomplished.
- (3) Because of the relative rigidity of the antenna coaxial cables, all communication equipment must be located on the rotating bulkhead to avoid twisting the cables.

The radar altimeter for the Mars vehicle is located in the crush-up material between the shield and structure since both the shield and crushable material can be made radar transparent. The radar altimeters must be deployed on the Venus vehicle because the shield and crush-up structure required for the Venus Lander are not radar transparent equipment requiring contact with the surface of the planet will be deployed with the tip bars.

H. Mars Thermal Control Subsystem

Because of the Radioisotope power supply the Mars Lander vehicle requires a thermal control system to be operative during the prelaunch, launch, transit, entry and surface modes of the mission. The system must serve the dual purpose of cooling the RTG unit

and providing heat to the payload within the vehicle as required. Since the high temperature RTG is located inside the vehicle, a coolant loop is necessary to connect the RTG with an external radiator during the transit period. The existence of this loop provides the feasibility of a secondary loop for localized payload temperature control. A schematic drawing of the proposed control system is shown on Figure 1.2.3-4.

In the prelaunch phase, the RTG will be cooled by an externally supplied coolant flowing through the RTG heat exchanger.

During the powered flight, while the booster nose fairing covers the Voyager vehicle, RTG cooling will be accomplished by an evaporative heat exchanger using an on-board water supply as the cooling agent. In transit, the RTG coolant releases its heat either to the payload coolant or to the transit radiator which is mounted on the Orbiter-Lander adapter. The flow path of the RTG coolant is controlled to maintain payload temperatures.

During entry, after the transit radiator has been separated from the Lander, the RTG will again be cooled directly by a water boiler. This allows additional use of the heat exchanger which is used for the launch phase RTG cooling.

After entry and vehicle orientation, nose section segments are separated from the vehicle to expose the RTG. Cooling is accomplished by radiation to the surrounding environment. Payload thermal control is maintained, as before, through the use of a heat exchanger and closed loop coolant system.

Components (battery, biological experiments) with maximum allowable temperatures below the limits for the electronic and communication equipment are controlled by waxes which attain a two-phase (liquid-solid) state at these maximum temperatures.

I. Venus Thermal Control Subsystem

The Venus Lander will require transit, entry and surface thermal control systems. From system considerations the Lander will be shade oriented during transit therefore electrical heaters using power from the spacecraft solar panels will be used to maintain the internal temperatures between 50 and 100° F. An aluminized mylar insulation blanket over the heat shield will be used to minimize the power requirements for internal heaters and to minimize the thermal stresses that exist between the shield and structure.

On the surface of the planet the hot (1050° F) environment will require a cooling system to maintain the payload within acceptable bounds. Of the four cooling systems evaluated - thermoelectric, heat pump, vapor compression, and expendable phase change working fluid - the expendable system was found to be the lightest. The choice of the working fluid depends on the design surface pressure. For atmospheric pressures greater than 10 atmospheres an ice-water system was found best, while for pressures below 10 atmospheres a liquid ammonia proved to be best. In the model atmosphere specified for this study the ammonia system is recommended. The liquid ammonia system is capable of removing approximately 500 BTU per pound of coolant expended. The Venus Cooling System block diagram is shown in Figure 1.2.3-5.

J. Power Supply Subsystem

As discussed in Vol. III the power supply selected for the Mars Lander is a Radioisotope Thermoelectric Generator (RTG) with rechargeable Nickel Cadmium batteries. The batteries will handle peak loads with the RTG supplying the power required to maintain the Lander and the power required to recharge the batteries. The power rating the Mars RTG is 82 watts of electrical energy based on a 5 percent efficient thermoelectric generator.

The use of the radioisotope power supply introduces numerous problems such as failure mode protection both on Earth entry and Mars entry, ground handling radiation precautions, cooling problems etc. Use of the radioisotope power supply does provide thermal energy for use in the thermal control of the Lander in space and in the cold Mars environment.

Dose rates expected from the unshielded isotope indicate that considerable shielding is required to protect personnel during handling and prelaunch operations.

The Venus power supply consists of a primary silver-zinc battery since operating times on the surface are only 30 minutes and 5.5 hours respectively for the 1970 and 1972 missions. Silver-zinc batteries have been specified and are based on the assumption that with development they can be made heat sterilizable. Nickel cadmium batteries (proven heat sterilizable) can be used as a replacement but, at a weight penalty factor of three.

K. Communications Subsystem

As described in Vol. III, Section 1 there are 7 basic communication modes in the typical Mars Lander. These links and their more important characteristics are presented below.

Link	Data Rate (bits/sec)	Transmitted Power (watts)	Antenna (Transmitting Receiving)
Primary data Link, Lander to Orbiter	16,000	25	Turnstile
Data Link, Lander to Earth used as backup to 1 & after Orbiter life is over	1,000	70	21 db Helix
Omnidirectional Data link, Lander to Earth, emergency mode	4	70	Turnstile
Data Link, Lander to Orbiter, after separation to Lander impact	500	25	"Transmission Line"
Prime Command Link from Orbiter to Lander	10	5	Turnstile
Backup Command Link Orbiter to Lander using Omni Antenna	1	10 K	Turnstile
Command Link from Earth to Lander using Lander high gain antenna	1	10 K	21 db Helix

On the Venus vehicles only two communication links are used. The characteristics of these two links are listed below and more fully explained in Vol. III, Section I.

Link	Data Rate Bits/Sec	Frequency (mc)	Antenna
Data Link Lander to Orbiter after separation	500 pre Entry 8000 post Entry	95	"Transmission Line"
Data Link Lander to Orbiter from planet surface	8000 Venus 70 16000 Venus 72	95	"Transmission Line"

1.2.4 SEQUENCE OF EVENTS

For a typical Mars mission, Table 1.2.4-1 summarizes in detail the major events which take place from the prelaunch phase to the commencing of the surface experiments. The mission profile is separated into the prelaunch, launch, parking, orbit, transit, approach, entry, descent, and surface phases of operation. Throughout the flight, selected diagnostic instruments will be programmed to monitor and telemeter information back to Earth via the Orbiter relay communications system. All signals to begin an event on the Lander, will be given through the Orbiter programmer while the Lander & Orbiter are physically attached. The only deviation from this is the release of the Lander sterility barrier which is released when the booster nose fairing is separated.

Four minutes before separation, on signal from the Orbiter, the Lander separation sequencer is activated. Separation events are triggered through a series of timer. Immediately after separation (event 4.10), the cold gas spin system is activated to stabilize the vehicle during thrusting. Seventeen minutes later, the change of velocity rocket is fired. The delay of 17 minutes is made to allow a distance of approximately 1000 feet between the Lander and Orbiter at the time of thrusting. This distance is considered sufficient to prevent large perturbations to the Orbiter and clouding of the solar panels due to the Lander rocket exhaust.

Entry time has been arbitrarily started at one million feet. Prior to Lander separation, the Lander separation sequencer receives a computed cruise time which will place the Lander at the entry altitude. Upon reaching entry altitude, the sequencer timer activates various sensors, instruments, and atmospheric experiments to be monitored during entry.

The retardation programmer is started at 8.0 g's (decreasing). The decelerator parachute is deployed at a Mach number of 2.5 on signal from the programmer. Should a Mach number of 2.5 occur above 30,000 feet, the radar altimeter will delay the signal until the vehicle has descended to 30,000 ft. The radar altimeter will be set to start the retardation sequence at 20,000 ft as a back-up for the retardation programmer (10) and as an emergency mode. Terminal velocity with the open main parachute occurs at a minimum altitude of 4000 feet.

On impact, the parachute is released in a two stage sequence, one pair of shroud lines are cut at a time, to spill the chute to one side of the vehicle. The vehicle orients itself using tip rockets and/or the tip over bar. The aft bulkhead is then unlocked and rotated to the proper position. A command is stored in the Lander programmer to repeat the orientation procedure if the position sensing switch calls for it. The tip bar is then permanently deployed along with the antennas and deployable scientific experiments.

The sequence of events for a Venus mission from prelaunch to the beginning of the entry phase is essentially the same as the Mars mission. Table 1.2.4-2 shows a list of the major events and their associated time and altitude limits which occur during a Venus entry.

TABLE 1.2.4-1. SEQUENCE OF EVENTS - MARS MISSION

Lander Sequence of Events	Signal	Time to Begin Sequence	Operating Time	Culm. Time
1.0 Prelaunch Checkout				
1.1 Communications Checkout	Command thru orbiter	0	10 min.	10 min.
1.2 Power Supply and Thermal Control System Checkout	Command thru orbiter	10 min.	10 min.	20 min.
1.2.1 RTG inlet and outlet temperature				
1.2.2 Cooling system pump motor temperature				
1.2.3 Cooling water temperature and flow rate (sensor on AGE)				
1.2.4 Modulation valve temperature				
1.2.5 Water boiler pressure				
1.2.6 Differential pressure across pump				
1.2.7 Pump motor power and RPM check				
1.3 Propulsion System Checkout	Command thru orbiter	20 min.	5 min.	25 min.
1.3.1 Cold gas temperature and pressure				
1.3.2 Ignition checkout (AV rocket)				
1.3.3 Spin Rocket valve checkout				
1.4 Scientific Payload Checkout	Command thru orbiter	25 min.	10 min.	35 min.
1.4.1 Temperature checkout of experiments				
1.5 Vehicle Structure Checkout	Command thru orbiter	35 min.	5 min.	40 min.
1.5.1 Monitor structural temperatures				
1.5.2 Monitor payload compartment temperature				
Lander Sequence of Events	Signal	Time to Begin Sequence	Operating Time	Culm. Time
1.6 Aero-Thermodynamic Sensor Checkout	Command thru orbiter	40 min.	15 min.	55 min.
1.6.1 Pressure transducer and temperature instrument checkout				
1.6.2 Char sensor check				
1.6.3 Ablation sensor check				
1.7 Motion Sensor Checkout	Command thru orbiter	55 min.	10 min.	65 min.
1.7.1 Three axis rate gyro checkout - fine and coarse				
1.7.2 Three axis accelerometer checkout - fine and coarse				
2.0 Launch Phase				
2.1 Motion sensors on and telemetering thru in-flight disconnect	Command thru orbiter	L-10 min.		65 min.
2.2 Selected diagnostic instruments on and telemetering thru IFD	Command thru orbiter	L-10 min.		
2.3 Release of nose fairing. Release of sterility bag.	Nose fairing release (Command to booster)	300 K ft.		
3.0 Parking Orbit and Entry into Transit Phase		L+6 min.		L 30 min.
3.1 Motion sensors on and telemetering thru IFD	Orbiter programmer (timed)			
3.2 Selected diagnostic instruments on and telemetering thru IFD				

TABLE 1.2.4-1. SEQUENCE OF EVENTS - MARS MISSION(CONT'D)

Lander Sequence of Events	Signal	Time to Begin Sequence	Operating Time	Culm. Time
4.0 Transit Phase		L+40 min.		L+40 min
4.1 Motion Sensors off	Command thru orbiter	L+40 min.		
4.2 Periodic diagnostic monitoring	Command thru orbiter			
4.3 Exercise thermal control correction when and if required	Command thru orbiter	as required		
4.4 Exercise power switching when and if required	Command thru orbiter	as required		
4.5 Assume terminal mode of transit phase	Command thru orbiter	S-30 min.		
4.6 Motion sensors and diagnostic instrumentation on	Command thru orbiter	S-30 min.		
4.7 Start separation sequencer (located on Lander)	Command thru orbiter	S-4 min.		
4.8 Selected communications equipment turned on	Command from sequencer	S-3-1/2 min.		
4.9 Fire in-flight disconnect (IFD)	Command from sequencer	S-5 sec.		
4.10 Fire explosive separation bolts	Command from sequencer	S		
5.0 Approach Phase				280 days
5.1 Fire cold gas separation jets	Sep. sequencer	S+1/2 sec.	30 sec.	
5.2 Activate cold gas spin system	Sep. sequencer	S	1 min.	
5.3 Read out accelerometers and rate gyros	Sep. sequencer	S	30 sec.	
5.4 Fire delta V rocket	Sep. sequencer	S+17 min.		
5.5 Read out accelerometers and rate gyros	Sep. sequencer	S+16 min.	20 min.	

Lander Sequence of Events	Signal	Time to Begin Sequence	Operating Time	Culm. Time
5.6 Periodic diagnostic monitoring	Command thru lander programmer	S+18 min.	1 min.	
5.7 Recorder playback of separation	Stored command	E-1 min.	3 sec.	
5.8 Switch from radiator to boiler	Stored command	E-2 min.		
5.9 Read out thermal control system diagnostic instrumentation	Stored command	E-2 min.		
5.10 Activate retardation battery	Stored command	E	1 sec.	
5.11 Fire thruster bolts - shed adapter	Stored command			

Lander Sequence of Events	Signal	Time* Shortest	Time* Longest	Altitude Ft* Highest	Altitude Ft* Lowest
6.0 Entry Phase		E			1000K
6.1 Assume entry phase	Stored command	E			1000K
6.2 Recorder on transmit	Stored command	E+3 sec	978K	978K	935K
6.3 Motion sensors on	Stored command	E+3 sec	978K	978K	935K
6.4 Diagnostic instruments on	Stored command	E+3 sec	978K	978K	935K
6.5 Entry scientific experiments on	Stored command	9 sec	78 sec	800K	500K
6.6 Enter blackout	"g" switch	38 sec	159 sec	342K	132K
6.7 Arm retardation programmer	Peak heating	41 sec	161 sec	155K	113K
6.8 Peak heating	Peak "g"	43 sec	173 sec	330K	79K

TABLE 1.2.4-1. SEQUENCE OF EVENTS - MARS MISSION(CONT'D)

Lander Sequence of Events	Signal	Time		Altitude-Ft *		Lander Sequence of Events	Signal	Time to Begin Sequence	Operating Time	Culm. Time
		Shortest	Longest	Highest	Lowest					
6.10 Radar altimeter on	Peak "g"	43 sec	173 sec	330K	79K	8.0 Surface Phase	Impact switch	0		
6.11 Start retardation	"g" switch	52 sec*	192 sec	303K	22.5K	8.1 Begin surface diagnostic monitoring		0	30 sec	1-1/2 min.
6.12 End blackout		47 sec	160 sec	250K	36K	8.2 Upset vehicle to side; a. rocket if nose down b. tip-over bar if nose up	Programmer, position switch	1 min. 1-1/2 min.	1 min. 2-1/2 min.	1-1/2 min. 2-1/2 min.
6.13 Switch from transit antenna to descent antenna	Retardation programmer	47 sec	160 sec	250K	36K	8.3 Unlock bulkhead	Programmer	2-1/2 min.	30 sec.	3 min.
6.14 Decelerator chute deployed	"	54 sec	358 sec**	30K*	22.5K	8.4 Orient rotating bulkhead	Programmer, position switch	3 min.	1 min.	4 min.
6.15 Jettison decelerator chute and aft cover. Main chute deployed in reefed condition	"	65 sec	383 sec			8.5 Repeat 8.2, 8.3, 8.4 if necessary	Programmer position switch	4 min.	2 min.	6 min.
** Limited by radar altimeter * Extremes of time and altitude in most instances do not occur on the same trajectory						8.6 Deploy tip bar	Programmer	6 min.	30 sec.	6-1/2 min.
7.0 Descent Phase						8.7 Fire tip bar harpoons to anchor vehicle	"	6-1/2 min.	2 sec.	6-1/2 min.
7.1 Main parachute disreefed		73	391	15K	4K	8.8 Separate nose section to	"	7 min.	3 sec.	7 min.
7.2 Play back entry data		73	391	15K	4K	8.9 Switch off boiler	"	9 min.	2 sec.	9 min.
7.3 Begin real time telemetry		73	391	15K	4K	8.10 Deploy and erect 5 ft. turnstile	"	9 min.	2 min.	11 min.
7.4 Impact		155 sec	15 min		0	8.11 Deploy and orient backup antennas	"	11 min.	2 min.	13 min.
7.5 Spill and release main parachute						8.12 Playback descent and initial surface phase information	"	13 min.	10 min.	23 min.
						8.13 Deploy surface TV	"			
						8.14 Begin surface experiments	"	23 min.		

TABLE 1.2.4-2. ENTRY SEQUENCE OF EVENTS - VENUS ENTRY

	TIME		VENUS ALTITUDE- FT	
	SHORTEST	LONGEST	HIGHEST	LOWEST
Begin Entry			1000K	
Begin Blackout			1000K	
Peak Heating	16 sec	76 sec	400K	315K
Peak "g"	18 sec	82 sec	407K	287K
End Blackout	22 sec	102 sec	301K	239K
Begin Atmospheric Experiments	22 sec	102 sec	301K	239K
Velocity - Subsonic	29 sec	125 sec	340K	225K
Deploy aft cover	1000 sec	1494 sec	5000	5000
Playback Entry Data	1000 sec	1494 sec	5000	5000
Impact	18.4 min	26.7 min		0

1.2.5 SUMMARY PARALLEL STUDY WITH LOW PRESSURE ATMOSPHERE

A. Summary

The design model atmospheres used in the parallel study effort are defined in Table 1.2.5-1 and Figures 1.2.5-1 through 3. The tabulation below shows the comparison of the 15 millibar atmospheres - four atmospheres - with the Upper limit, Mean, and Lower Limit atmospheres used in the study.

	Parallel Study (15mb Atmos)				Main Study		
	11mb-A	11mb-B	15 mb	30 mb	Upper Limit	Mean	Lower Limit
Surface Pressure mb	11	11	15	30	41	85	133
Surface Temperature °K	260	260	230	210	200	250	300

Retardation and parachute deployment was a major problem area with the atmospheres used for the Main Voyager Study. The parallel study with lower pressure and density accentuated the difficulty of the retardation problem.

Figure 1.2.5-4 shows the restriction required on entry path angle to achieve successful deployment of a Mach number 2.5 parachute system as a function of ballistic parameter. Because of high heating and capture uncertainties a minimum entry path angle of 20 degrees was established for the Voyager vehicle. Error analysis has shown that ± 14 degrees is a reasonable tolerance on entry path angle, therefore from this standpoint the maximum ballistic parameter is 22 psf. Further reduction of the ballistic parameter is desirable to gain design margin and to permit aiming at selected landing sites.

To achieve the lowest ballistic parameter, the maximum drag shape known to be dynamically stable was selected. This shape is a spherically blunted cone with a 52° half cone angle and bluntness ratio of 0.47 which has been used successfully on GE designed Mark 2 ballistic Re-entry Vehicle. As explained in Section 1.2.5-F, having defined an entry shape (Section 1.2.5-B) and a maximum packaging density, the ballistic parameter is a function of the entry vehicle weight as shown on Figure 1.2.5-5.

Use of conventional parachutes and impact attenuation equipment in the low density atmosphere results in unreasonably high retardation system weights and impractical depths of crushable material. The use of retro rockets in conjunction with the parachutes and impact attenuation structure was found to result in approximately 100 pounds net weight saving (see Section 1.2.5-D). The reliability of the system using retro rockets is inherently lower because of the additional functions introduced in the retardation sequence and the sensing required to fire the retro rockets.

The shock attenuation system weight required for the high drag vehicle is higher than the weight of the Main Study configuration, due to the change in vehicle shape for the same impact velocities. As shown in Section 1.2.5-E, the shock attenuation system required for 200 feet per second wind velocity will be 3 to 4 times the weight of shock attenuation equipment required for 40 miles per hour. The design for the high wind velocities must be omni-directional and will result in a data capsule concept. Since it has been postulated that the high winds occur only during the daylight hours, landing during the hours of darkness is recommended to avoid the severe penalty of designing for the high winds.

TABLE 1.2.5-1. MARS ATMOSPHERE AND UNCERTAINTIES

Property		11 mb-A	11 mb-B	15 mb	30 mb
Surface Pressure, mb	ρ_0	11	11	15	30
Stratosphere Temperature, °K	T_s	130	230	180	130
Surface Temperature, °K	T_0	260	260	230	210
Acceleration of Gravity at Surface, cm/sec ²	δ	375	375	375	375
Composition, molar concentration %					
CO ₂		65	65	43	11
A		35	35	32	13
N ₂		0	0	25	76
Molecular Weight	M	42.7	42.7	38.7	31.2
Specific Heat Ratio	γ	1.40	1.40	1.42	1.42
Adiabatic Temp. Lapse Rate Troposphere, deg K/km	Γ	5.30	5.30	4.81	3.93
Tropopause Altitude, km	h_T	24.5	5.66	10.4	23.5
Inverse Scale Height, km ⁻¹	β	.148	.0838	.0970	.108
Surface Density, gm/cm ³	$\rho_0/10^{-5}$	2.17	2.17	3.04	5.36
Artificial Surface Density gm/cm ³	$\rho_0/10^{-5}$	13.2	2.53	4.37	14.1
Density at Tropopause, gm/cm ³	$\rho_{TP}/10^{-5}$.347	1.57	1.60	1.55

The proposed high drag vehicle is shown on Figure 1.2.5-6. This (1270 lbs. entry weight) vehicle is designed to have a ballistic parameter of 16 psf which restricts the entry path angles between 20 and 35 degrees computed at 10^6 feet. The high cone angle (52°) and bluntness ratio (0.47) require base orientation rather than side orientation as discussed in Section 1.2.5-F.

The conclusions reached in the parallel study are:

1. An entry Lander can be designed for the 15 mb atmospheres without significant sacrifice in payload capability.
2. Severe entry corridor limitations are required to insure successful parachute deployment.
3. The proposed Lander system is inherently less reliable because of corridor restrictions, more complex retardation systems, and a less desirable orientation system.
4. Design for 200 feet per second wind velocities at impact will require extensive development and a data capsule concept as discussed in Section 1.2.5-E.

B. Trajectory Analysis 15 mb Model Atmospheres

(1) Trajectory Matrix

In order to define the magnitude of the design changes imposed by the 15 mb Model Atmospheres, a limited matrix of point mass ballistic entry trajectories were computed. The matrix consisted of all combinations of the characteristics listed below:

Entry Velocity V_e 21,000 ft/sec and 15,000 ft/sec

Entry Path Angles = 20, 30, 60 and 90° dth

Ballistic Parameters $W/C_D A = 5, 10, 15, 20$ and 35 PSF

Atmospheres 11 mb-A, 11 mb-B, 15 mb, and 30 mb.

The lower velocity of 15,000 ft/sec was included to simulate possible out-of-orbit trajectories and the choice of lower ballistic parameters were based on the knowledge that the lower ballistic parameters reduce the descent rate into the less dense atmospheres allowing more time for parachute deployment.

(2) Parachute Deployment Altitude

The most dense of the 15 mb Model Atmospheres (30 mb) allows the entry vehicle to penetrate more deeply into the Mars atmosphere for significant events to occur than the least dense atmosphere used in the Main Voyager Study. Figures 1.2.5-7 and 1.2.5-8 show the altitude of occurrence of a Mach number of 2.5 (supersonic parachute deployment altitude) as a function of ballistic parameter with path angle as a parameter for entry velocities of 21,000 ft/sec and 15,000 ft/sec into the 11 mb-A atmosphere. Considering 20,000 ft to be a minimum chute deployment altitude, it is shown that the path angle entry corridor is severely limited for the higher ballistic parameters, and further, that very little is gained in reducing initial velocity to 15,000 ft/sec. An increase of 35 - 45,000 ft. in altitude of occurrence results if the 30 mb atmosphere is assumed. Those results appear in Figures 1.2.5-9 and 1.2.5-10.

(3) Maximum Deceleration Rates

The magnitude of key events, such as peak accelerations and peak heating, depends on the rate of change of density with altitude. Of the four low density model atmospheres used in the parallel study, the 11 mb-A atmosphere (possessing the largest density gradient) yielded the highest maximum axial deceleration rates. The lower ballistic parameters, $W/C_{DA} = 10$ psf, curve gives slightly higher decelerations than the broken curve for $W/C_{DA} = 15$ psf. This same ballistic parameter effect was noticed on the more dense Mars Lower, Mean and Upper atmospheres. These results appear in Figure 1.2.5-11.

Figure 1.2.5-12 presents maximum deceleration as a function of path angle with atmosphere as a parameter for a constant entry velocity of 21,000 ft/sec. The density gradient effect for the various atmospheres yields the expected result of having the higher maximum decelerations occurring for the 11 mb-A model atmosphere. The ballistic parameter trend observed on the other model atmospheres (i. e., maximum loads inversely proportional to W/C_{DA}) does not hold for the larger path angles for the 15 mb and 30 mb atmospheres, but the differences in magnitudes are negligible.

(4) Capture Angles

For the low density model atmospheres the following capture angle results were noted where the initial path angle is at 10^6 ft.

- (a) For a particular entry velocity and atmosphere the capture angle increases approximately 0.5° as W/C_{DA} increases from 5 to 35.
- (b) Between a nominal entry velocity of 21,000 ft/sec and a nominal out-of-orbit entry velocity of 15,000 ft/sec, the capture angle decreases approximately 4.0° .
- (c) The 15 mb and 30 mb atmospheres had the same effect on capture angle.

(5) Capture Angles for Low Density Martian Atmospheres

<u>Velocity</u>	<u>Atmosphere</u>	<u>Capture Angle Range</u>
21,000 ft/sec	11 mb-A	$18.0^{\circ} - 18.5^{\circ}$ dfh
21,000 ft/sec	15 mb	$17.5^{\circ} - 18.0^{\circ}$ dfh
21,000 ft/sec	30 mb	$17.5^{\circ} - 18.0^{\circ}$ dfh
15,000 ft/sec	11 mb-A	$14.0^{\circ} - 14.5^{\circ}$ dfh
15,000 ft/sec	15 mb	$13.5^{\circ} - 14.0^{\circ}$ dfh
15,000 ft/sec	30 mb	$13.5^{\circ} - 14.0^{\circ}$ dfh

(6) Multiple Degree of Freedom Trajectories

No multiple degrees of freedom trajectories were analyzed for the supplementary study but certain trends can be predicted based on a comparison of the density profiles. The angle of attack convergence as the vehicle descends into a particular model atmosphere will depend largely on the density gradient. Two atmospheres having the same density gradients cause a vehicle entering with an initial angle of attack to converge in angle of attack in direct proportion to the relative magnitudes of the densities at corresponding altitudes. This influence is smaller than the density gradient effect. It should be expected, therefore, that a 6 degree of freedom trajectory using the 11 mb-A atmosphere

will have a slightly more rapidly converging total angle of attack (for some initial conditions) than for the same trajectory calculated using the Mars lower atmosphere due to the slightly larger density gradient. Further, the maximum transverse loads would be slightly decreased. This situation will not exist for the 11 mb-B atmosphere with its lower density gradient.

C. Configuration Analysis

As noted in the preceding trajectory parametric analysis, unless the entry path angle is severely restricted the ballistic coefficient must be reduced to achieve successful parachute deployment. Three ways of reducing this parameter ($W/C_D A$) are 1) Reduce the weight W , 2) Increase the base area A , and 3) Increase the drag coefficient C_D .

Reduction of the total vehicle weight is generally undesirable, since a large portion of this weight will come directly out of the payload. While a slightly lighter Lander shell weight will result with lower ballistic coefficients, this method leads rapidly to prohibitively small payloads.

Increasing the base area also leads to a point of diminishing returns. The added heat shield and structural weight required for a larger diameter vehicle tends to increase more rapidly than the base area so that the net effect is an increase in the ballistic coefficient.

While a slight decrease in vehicle weight combined with a slight increase in vehicle diameter may aid the situation, a major factor in modifying the ballistic parameter will be the drag coefficient. Barring dominant radiative heating, an increase in drag will result in a corresponding decrease in ballistic coefficient without any adverse static effect. This implies one would like to fly as high a drag shape as possible. However, when considering highly blunted shapes, such as Apollo type configurations, dynamic characteristics become important. Following entry at possible high angles of attack, density damping will occur initially. As the dynamic pressure increases, the aerodynamic characteristics will tend to dominate. After peak dynamic pressure, the aerodynamics must overcome the effect of decreasing dynamic pressure if vehicle oscillations are to converge. The question of possible large or divergent oscillations in regions of high heating, normal loads or at parachute deployment and their influence on system design is of interest.

Linear theory (Ref. 1) shows that the dynamic stability factor

$$\zeta = C_D - C_{L_\alpha} + (C_{M_q} + C_{M_{\dot{\alpha}}}) \left(\frac{D}{\sigma} \right)^2$$

where

ζ = dynamic stability factor

C_D = drag coefficient

C_{L_α} = lift curve slope

$C_{M_q} + C_{M_{\dot{\alpha}}}$ = dynamic damping coefficient

D = reference dimension ~ vehicle diameter

σ = radius of gyration

will control angle of attack envelope where ζ must be negative for convergence. Considering blunt body characteristics at near zero angles of attack; C_D is strongly positive, C_{L_α} is negative and $(C_{M_q} + C_{M_\alpha})$ is at best near zero if not positive. While characteristics at higher angles of attack are more conducive to convergence, dynamic oscillations may be severe. The problem is increased with any adverse pitch or spin rate during initial entry at high angles of attack.

The solution utilized on manned earth re-entry vehicles is to provide an active rate damping system. Another possible solution is to trail a small "stabilizing" device. Apart from the problem of ejection and deployment of such a device, it is not evident without extensive investigation that a trailing body is "a priori" stabilizing. Tests have shown that the complex motion of two bodies (up to 13 degrees of freedom) may in fact couple such as to increase divergent tendencies. It is strongly felt that early unmanned planetary Landers should be passive in every possible aspect.

Six degree of freedom trajectories, Section 1.3.2-E, have shown that angles of attack up to 24 degrees can occur during peak heating and normal loads on a vehicle with reasonably favorable aerodynamic characteristics. Prior trajectory analyses have shown Apollo type configurations may in fact tumble far into a Martian entry. Even assuming that a catastrophic oscillation history will not result, i. e., angles of attack near 180 degrees during peak heating, peak loads, or at parachute deployment, the design penalty for higher angles of attack during heating and increased normal loads must be evaluated in view of the potential drag coefficient increase.

If the limit of adequate dynamic characteristics is somewhat arbitrarily set at a proven earth re-entry configuration (a blunted sphere-cone $R_N/R_B = 0.5$ and $\theta_c \approx 50^\circ$ with $C_L \gtrsim 0$ and $(C_{M_q} + C_{M_\alpha}) \lesssim 0$), several conclusions can be drawn. The hypersonic drag coefficient for this configuration is approximately 1.3. While an Apollo type shape could increase this value to near 1.5, it appears the 15 per cent increase in drag (or decrease in ballistic coefficient) would be largely consumed by increased heat shield and structural weight due to higher integrated heating and normal loads. Thus if a conservative Lander design approach is to be followed, highly blunted Apollo type configurations do not appear acceptable. To confidently utilize higher drag shapes, further parametric ground and flight test data are required. Another approach to increasing the drag coefficient is to utilize an auxiliary drag device. This concept is discussed under Retardation Analyses (Section 1.2.5-D) and is not recommended for early Voyager missions.

Therefore, the highest possible drag configuration with proven acceptable dynamic characteristics ($R_N/R_B = 0.5$ $\theta_c \approx 50^\circ$) has been selected for further investigation.

D. Retardation

A general discussion of the retardation of Voyager Lander vehicle entering the atmospheres of Mars and Venus has been given in the main body of the Voyager Study Report. Conclusions drawn from this discussion were that parachutes appeared to represent the optimum choice of retardation device based on performance and state-of-the-art considerations. In this parallel study, it is desired to show the effect of lower density atmospheric models, 11 to 30 millibar surface pressure, on the Voyager Lander system design.

From the retardation point of view, consideration of the lower density atmospheric models results in two problem areas. First, for a given vehicle and trajectory, the vehicle velocity at deployment of the retardation devices is much higher as illustrated in previous sections. Secondly, the required drag area of the final descent parachute(s) is considerably increased. These two effects of the lower density atmospheres result in a more difficult retardation problem which can only be satisfied by increasing the weight and/or complexity of the retardation system.

For the 11, 15, and 30 millibar atmospheres, Figure 1.2.5-13 provides the information necessary to determine the required drag area (C_{DA}) for a given vehicle weight and desired impact velocity. Once the required C_{DA} of the Parachute(s) is known, the size and number of parachutes, main descent parachute weight and volume can be obtained from Figures 1.2.5-14 through 1.2.5-16, respectively. Descent time of the vehicle after main parachute deployment is given in Figure 1.2.5-17 as a function of deployment altitude and descent velocity in the 11 millibar atmospheres.

A drogue parachute is recommended for purposes of main parachute deployment, vehicle stabilization and deceleration. Use of a supersonic decelerator allows a larger basic vehicle ballistic parameter to be employed for a given altitude of main parachute deployment. Figure 1.2.5-18 presents the approximate decelerator parachute state-of-the-art as referenced to the Mars 11-B model atmosphere. In Figure 1.2.5-18 the line representing a dynamic pressure of 1.0 PSF defines a lower limit at which parachute inflation would be expected to be erratic. Also the Mach number 2.2 line represents the approximate upper Mach number limit based on performance of past recovery systems. At the present time, a new parachute, the Hyperflo, is being developed which has performed satisfactorily, aerodynamically, in tests at Mach numbers up to 6.0. At these high Mach numbers, aerodynamic heating of the parachute becomes significant, resulting in a materials problem since normal parachute material, nylon, loses considerable strength at elevated temperatures. An alternate parachute material, HT-1, capable of retaining approximately 50 per cent strength to 600°F is presently being incorporated into the Hyperflo design. Thus, this temperature limit, 600°F, based on the temperature increase across a normal shock is shown in Figure 1.2.5-18. In recent flight tests of a Hyperflo canopy constructed of HT-1 material, deployment Mach numbers up to 4.0 were successfully obtained in which satisfactory operation occurred. Therefore, for this study, a design deployment Mach number 2.5, corresponding to the Main Voyager Study, has been selected realizing that considerable growth in Mach number capability is possible.

The estimated C_{DA} of the Hyperflo as a function of diameter and Mach number is presented in Figure 1.2.5-19. The drag coefficient (C_D) of the canopy is based on wind tunnel, free-flight and rocket sled tests. In Figure 1.2.5-20, the weight of the Hyperflo canopy as a function of drag area and deployment dynamic pressure is estimated.

Combining the weights of the Hyperflo decelerator and the main descent parachute and allowing for such items as deployment bags, suspension lines, risers, use of HT-1 material, sterilization, radiation and vacuum soak, results in an estimate of retardation system weight. This weight as a percentage of Lander vehicle weight at entry is presented in Figure 1.2.5-21 as a function of impact velocity.

From Figure 1.2.5-21, it can be seen that the retardation system weight will decrease with increasing impact velocity. At the same time the weight of an impact attenuation system increases with increasing impact velocity since more energy must be dissipated, as explained in more detail in Section 1.2.5-E. Since both the retardation and impact attenuation systems are a direct function of impact velocity and varying in opposite directions, the combined weight of the two systems should indicate an optimum landing velocity. For the material deformation type of attenuation system, Section E, Figure 1.2.5-22 gives the combined retardation and crushup weight as a function of impact velocity for a vehicle weight of 1270 lb. and maximum impact deceleration of 125 g's. From Figure 1.2.5-22 the optimum velocity, based on total weight, is 85 f.p.s. At this velocity, considerable depth (stroke \approx 14 inches) of crushable material is necessary if the deceleration is not to exceed 125 g's. This stroke in combination with secondary impact considerations, consumes a significant portion of the total vehicle volume, resulting in unrealistic payload packing densities or a reduction in payload. Seeking to reduce the attenuation system volume, three approaches can be taken: lower the impact velocity, increase the impact deceleration design limit, or consider an alternate attenuation system.

Lowering the impact velocity would decrease the required stroke or depth of the crushup material, thereby decreasing the vehicle volume necessary for crushup material. However, the weight of parachute necessary to reduce the impact velocity increases rapidly as indicated in Figure 1.2.5-22. The increase in retardation system weight must be balanced by a decrease in payload weight in order to hold the total vehicle weight constant. This course of action is undesirable.

An alternate solution to reducing crushup material volume is to increase the "g" load at impact. This, of course, will decrease the crushup volume without an increase in landing system weight since the same impact velocity is used, resulting in the same amount of energy to be absorbed. The increased "g" load can be detrimental to the design of the payload and violates one of the initial assumptions of the study. Therefore, a change in impact "g" load was ruled out as a solution to the crush-up volume problem.

In considering alternate attenuation systems, the least complex and highest performance system appeared to be retro-rockets. The type of retro-rocket system considered consisted of three solid propellant rockets attached to the main parachute risers above the vehicle which fire in a direction ≈ 30 degrees from the vertical to avoid extensive plume impingement on the vehicle. The three rockets would be connected together in a cluster with thrust vectors at 120 degree angle of roll from each other.

Initially, the parachutes and retro-rockets were sized to give zero vertical velocity in the Mars 11 millibar atmosphere with crushable material absorbing the horizontal energy. Figure 1.2.5-23 presents the combined weight for this type of system as a function of parachute terminal descent velocity. The optimum parachute terminal descent velocity appears to be 150 f.p.s., which gives a system weight of just over 200 lbs. This is a reduction in weight of about 100 lbs. or 30 per cent over the parachute-crushup system shown in Figure 1.2.5-22.

Unlike the crush-up system which is passive, the solid propellant retro-rocket system cannot be easily designed to operate in a range of atmospheric models since it must be designed for a given terminal descent rate. It is then of interest to determine the effect of atmospheric model on the system design. Figure 1.2.5-24 presents the retardation and retro-rocket weight (including crush-up for secondary impact) as a function of parachute terminal descent velocity for the 30 millibar atmosphere. It can be seen that the optimum descent velocity is reduced to approximately 120 f.p.s. and the total weight is about 180 lbs.

The design solution chosen for use in the range of atmospheric models (11 to 30 millibar) is to design the parachute - retro-rocket system such that zero vertical velocity is encountered at impact if the actual Mars atmosphere proves to be the 30 millibar model. If the actual atmospheric model turns out to be the 11 millibar value, then a residual impact velocity would be encountered after retro-rocket firing due to the higher terminal descent velocity in the lower density atmosphere. This residual vertical velocity and any horizontal velocity would be absorbed by crushup material. The trade-off of total weight (parachutes, retro-rocket and crushup) with terminal descent velocity in the 11 and 30 millibar atmospheric models is given in Figure 1.2.5-25. Note in Figure 1.2.5-25 that the optimum descent velocity is about 90 f.p.s. in the 30 millibar model which corresponds to 139 f.p.s. in the 11 millibar model. The optimized weight is lower than that for parachute retardation and crushup alone by almost 100 lbs. Also, the crushup volume is reduced considerably since the velocity to be absorbed is only the difference between the two atmospheric models (49 f.p.s.) and not 85 f.p.s. as in the non retro-rocket case. This system, though more complex than that recommended in the main Voyager study, is felt to be more effective in view of the reduced density of the nominal 15 mb atmospheric models. It is therefore the recommended system for use on the Voyager Lander vehicle in this parallel study.

E. Shock Attenuation

As shown by the parachute sizes and weights in the previous section, a careful analysis of shock attenuation devices is required to achieve an optimized retardation system. Unfortunately, many assumptions are required to predict the behavior of the entry vehicle on impact such as wind speeds, ground slope and texture, and the inelastic behavior of the energy absorbing materials. This section treats each variable in an attempt to arrive at a suitable conclusion regarding shock attenuation equipment.

Figure 1.2.5-26 shows graphically the resultant impact velocity of the entry vehicle as a function of vertical descent velocity, and ground slope for a fixed - 40 mile per hour - wind velocity. The analyses in the Retardation section show that the vertical descent velocities from 40 to 80 feet per second are of interest. Figure 1.2.5-27 shows the depth of the shock attenuation material required to decelerate the vehicle to rest at various deceleration rates as a function of the resultant or normal velocity. These curves illustrate that at high impact velocities and low deceleration rates deep crushable material is required. Very deep crushable material results in small internal vehicle volumes and packaging density problems.

Figures 1.2.5-28 and 1.2.5-29 define the shock attenuation system weight as a function of impact velocity and deceleration rate for the vehicles designed in the Main Study ($W/C_{DA} = 35$) and "15 mb" parallel study ($W/C_{DA} = 15$) atmospheres. The matrix below tabulates the weight increase for a normal velocity of 70 feet per second.

SHOCK ATTENUATION SYSTEM WEIGHT

VEHICLE	DECCELERATION RATE			
	100 G's	200 G's	300 G's	400 G's
Shock Attenuation wt - Main Study Vehicle	104 lbs	100 lbs	95 lbs	90 lbs
Shock Attenuation wt - High Drag Vehicle	130 lbs	126 lbs	119 lbs	110 lbs

The tabulation above shows that the payoff for designing to higher deceleration rates is small for the impact velocities in the range of this study. Figures 1.2.5-30 and 1.2.5-31 show the effect of designing to higher "g" loads on structural weights. The net result of designing to higher "g" loads for a given impact velocity is a gain in weight due to the increase in structural weights. A design entry deceleration rate of 125 g's was established for the Mars by trajectory analysis of a vertical entry in the thicker atmosphere. This limit will not be changed because of the uncertainties of the Mars atmospheres.

All of the analysis thus far has been based on a horizontal impact velocity of 40 miles per hour (58 f.p.s.) combined with vertical descent rates of 40 to 150 feet per second. For a vertical descent the topographical features of the surface of the planet are relatively unimportant. When the horizontal velocity of the entry vehicle is higher than the vertical descent rate it is necessary to better define the surface of the planet.

Such systems as skids and shaped vehicles appear most favorable for a high horizontal velocity impact design. However, unless the landing area is well defined, they cannot be properly engineered, and the design will be only as valid as the assumed landing area definition. Since very little is known, at the present time, about other planetary surfaces, developments in these impact systems can only progress with better knowledge of the surface and an increased assurance of landing on a desirable site. Therefore, the above

systems are not recommended as a design solution to the high horizontal velocity problem at the present time.

Since the surface characteristics of the planet are unknown, and since the reduction of the horizontal velocities with retro-rockets requires stabilization and control, an omnidirectional impact system is recommended. This design will have the highest reliability of any system for landing on unknown terrain; however, payload weight will be sacrificed for impact system weight. Both a spherical and an ellipsoidal shaped capsule appear promising with deformable material either external or internal to the capsule support structure. An impact system weight increase of 50-75 per cent for this approach over that used for the Main Study Voyager design is anticipated using the same design conditions as for the Voyager study. This is due to the fact that the entire surface is covered with crushable material and two independent structures for capsule and shield are required. An impact system weight increase of 300-400 per cent is expected if the horizontal design velocity increases from 58 f. p. s. to 200 f. p. s. for either the Voyager design or an omnidirectional design approach.

F. Vehicle Design

The design of the Entry/Lander is fixed by the parameters defined in the previous sections. The vehicle design must meet the following requirements.

- gross vehicle weight 1450 lbs. Mars 1969 vehicle (entry weight 1270 lbs.)
- shape - $R_N/R_B = 0.47$
 $\theta_c = 52^\circ$
- design impact velocity 49 f. p. s.
- packaging density 15 lbs/ft³ (see Section 1.3.9-F).

Since the vehicle shape is fixed as the maximum drag shape consistent with dynamic stability requirements, the vehicle surface area and volume can easily be determined as a function of base diameter. The shield and structure weights can then be determined as functions of the base diameter (Figures 1.2.5-32 and 1.2.5-33). The vehicle volume and the payload packaging density determine the payload weight as a function of base diameter (Figure 1.2.5-34).

Summing up shield, structure and payload permits an estimate of retardation system weight as a function of diameter (Figure 1.2.5-35). Summation of all the above weights, Figures 1.2.5-32 through 1.2.5-35, results in a vehicle entry weight. Since the hypersonic drag coefficient is constant for a given shape and the base area is a function of the base diameter for a given entry weight, the optimum ballistic parameter is easily determined (Figure 1.2.5-36). The relationship between gross weight and ballistic parameter exists for this design because the vehicle external geometry was held constant. Finally, the payload fraction as a function of base diameter is shown on Figure 1.2.5-37.

G. Orientation and Deployment

The high drag shape of the vehicle proposed for the 15 mb atmosphere results in a geometry that is not favorable for side orientation (Figure 1.2.5-38). Alternatively, base down orientation is proposed. Rockets through the side of the vehicle, Figure 1.2.5-6, will be used to tip the vehicle over from its side to its base as required by a position sensor. Multiple rockets will be used for redundancy and multiple opportunities to repeat the orientation procedure.

Once the vehicle has been oriented on its base, the nose cap will be ejected to uncover the RTG and permit deployment of the scientific payload (Figure 1.2.5-38). Surface sampling for this vehicle will be accomplished through the aft bulkhead.

The estimated weight breakdown of the high drag vehicle is shown on Table 1.2.5-2. Note the relatively small change in payload capacity from the vehicle proposed in the main study. This is explained by (1) severe limitations on the vehicle entry corridor, (2) a more complicated retardation system including retro-rockets rather than the relatively simple all parachute system proposed in the main study, and (3) because of the weight economies involved with the base down orientation system. The two vehicles presented in the weight break-down are not strictly comparable because they are designed to have different capability and different inherent reliability. The 15 mb vehicle is less reliable because of the more complicated retardation system and the base orientation versus side orientation.

H. Lander Dispersion and Line-of-Sight Times for 15 mb Mars Atmosphere

Lander studies, for the case of the 11 mb Mars atmosphere, place limitations on the permissible values for entry angle. Entry angle, in turn, influences both Lander dispersion and line-of-sight time. The permissible entry angle corridor covers the range of 20° to 35° . In order to place each Lander on its previously selected landing site, Syrtis Major (7°N) and Pandora Fretum (24°S), and at the same time meet the entry angle corridor conditions for the case of simultaneous Lander separation, it is necessary to select the time of entry such that both landing sites are east of the Orbiter ground track. For example, Pandora Fretum could be reached by a plane change of 19.9° with an entry angle of 31° ; Syrtis Major would require a plane change of 59° and an entry angle of 27° , thereby satisfying the entry angle corridor requirements.

It is estimated that, under the worst conditions, line-of-sight from Pandora Fretum to the Orbiter will be maintained for at least 8.5 minutes after Lander impact. However, Syrtis Major is so far out of the plane of the trajectory that line-of-sight to the landing site is lost long before the time of entry. Thus, under these circumstances, data can be obtained from only the Pandora Fretum Lander during the approach phase.

An examination of landing site dispersion for Syrtis Major (worst case) indicates that in-plane errors in impact location can increase to more than 20° (planet central angle) for separation attitude errors of 4° . An attitude error of less than 3° would be required in order to insure impact for the case studied ($\Delta V = 312 \text{ ft./sec.}$).

It is clear that the 11 mb Mars atmosphere introduces Lander problems in the areas of line-of-sight time and dispersion for the case studied. The resulting constraints on choice of landing sites and orbit selection can be defined with further studies.

TABLE 1.2.5-2. WEIGHT STATEMENT 15 MB VEHICLE

	15 mb Vehicle	Voyager Mars 1969 Vehicle
Shield	100	84
Structure	274	234
Aft Cover	66	57
Retardation & Crushup	280	288
Crushup Structure	126	133
Parachutes	83	127
Parachute Housings	11	12
Programmmer Batteris, etc.	12	8
Harness	10	4
Hardware	5	4
Retro-rockets	33	-
Ground Orientation	40	67
Separation	6	6
Payload	504	534
Thermal Control	72	72
Power Supply	100	106
Communications	145	141
Scientific Payload	187	215
TOTAL ENTRY WEIGHT	1270	1270
Adapter	71	71
ΔV Rocket	97	97
Spin System	12	12
Gross Entry Lander Weight	1450	1450

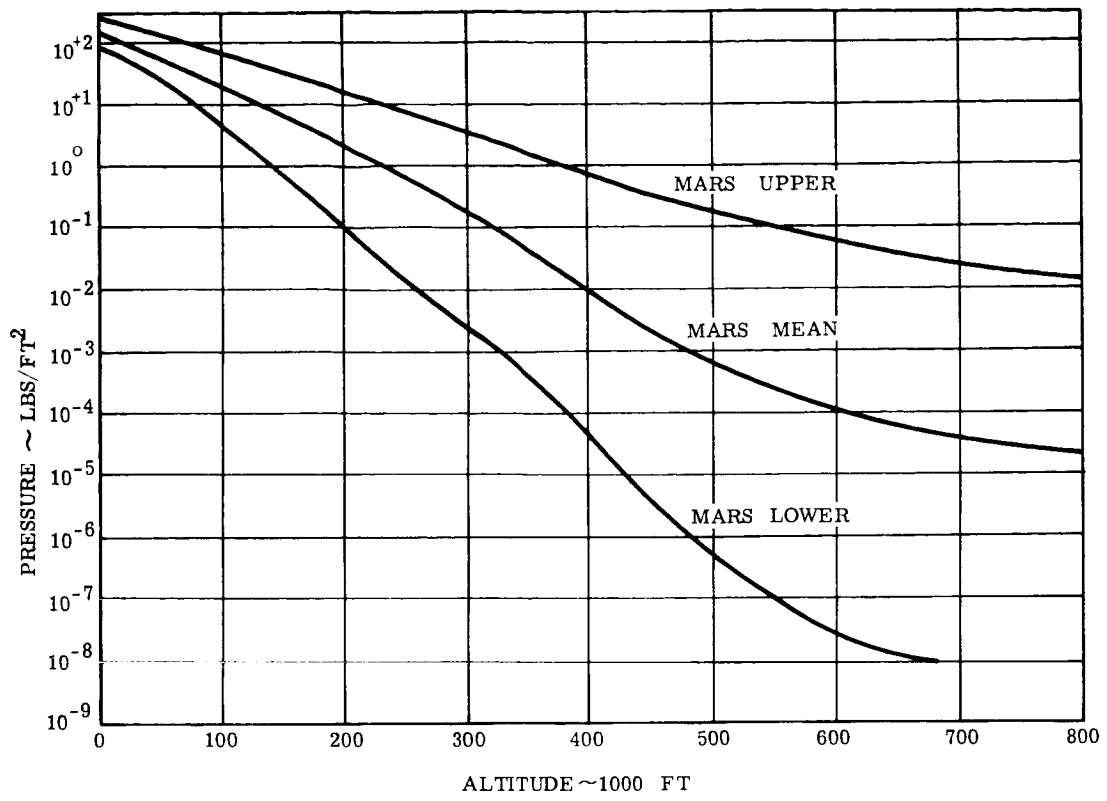


Figure 1.1.3-1. Mars Atmospheres - Pressure

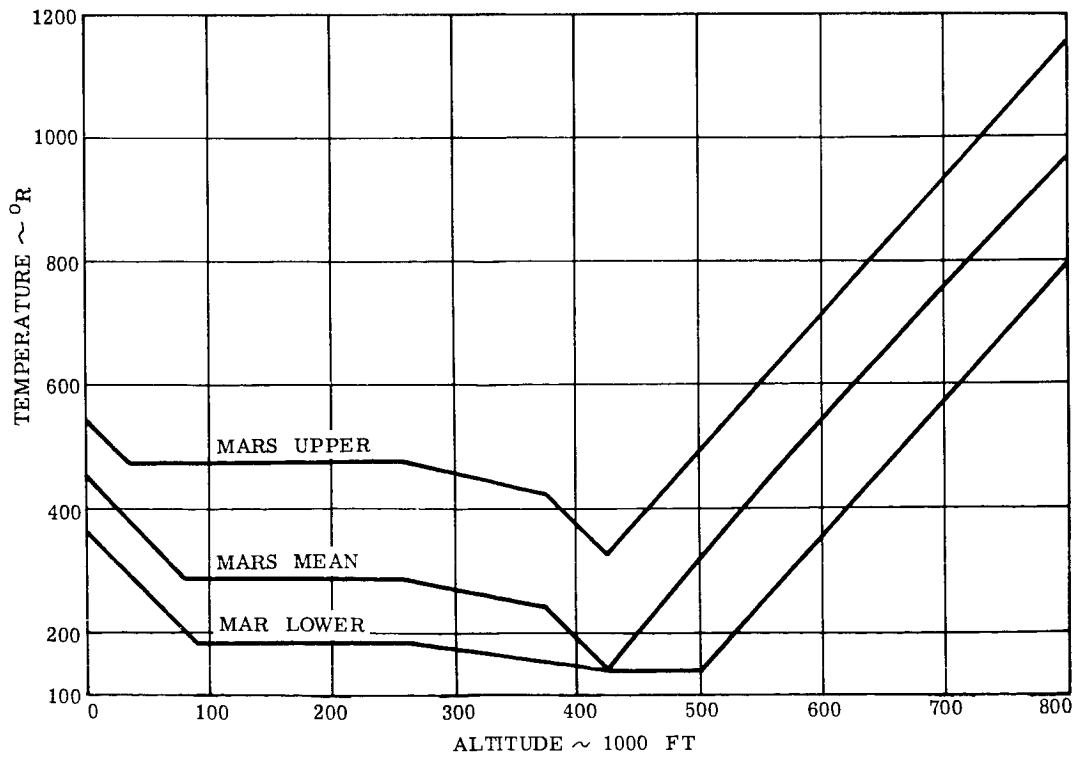


Figure 1.1.3-2. Mars Atmospheres - Temperature

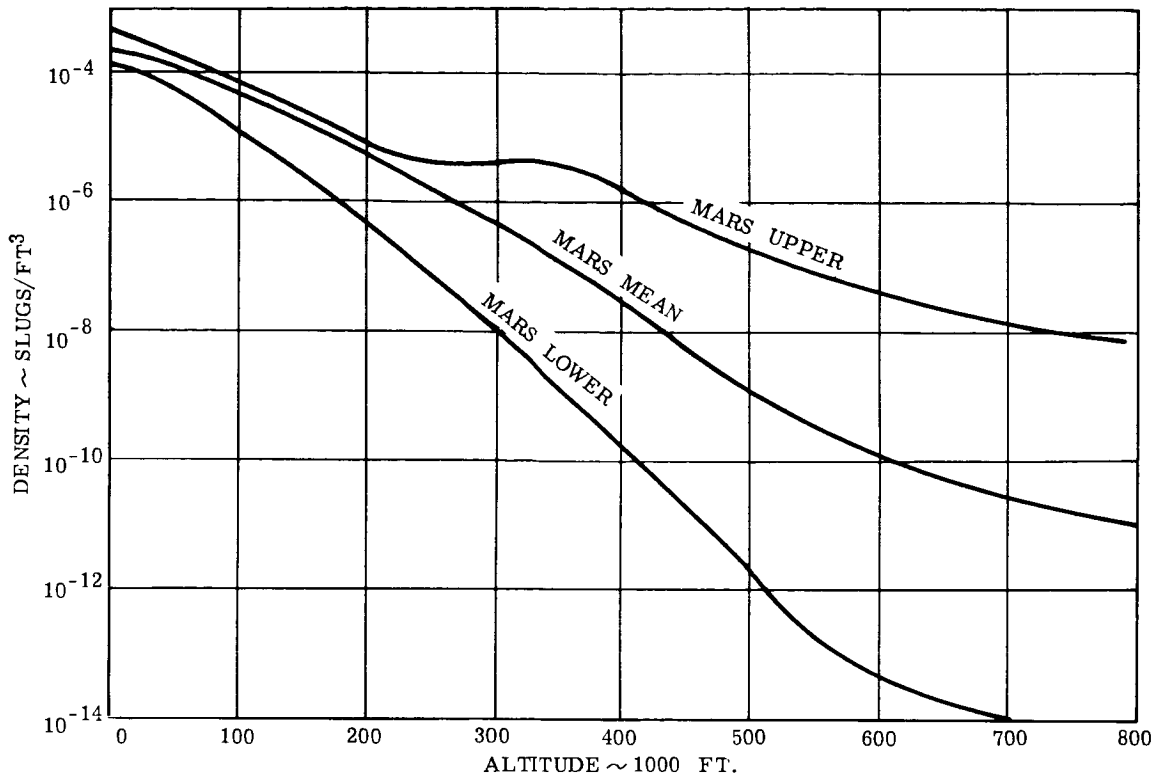


Figure 1.1.3-3. Mars Atmospheres - Density

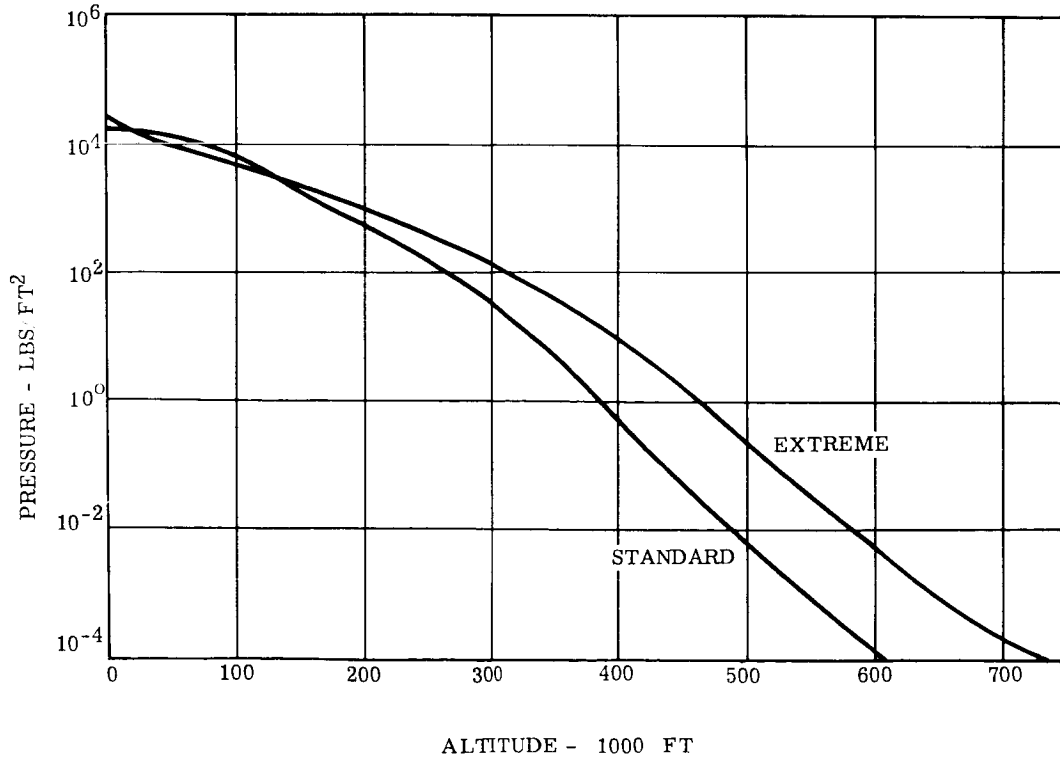


Figure 1.1.3-4. Venus Atmospheres - Pressure

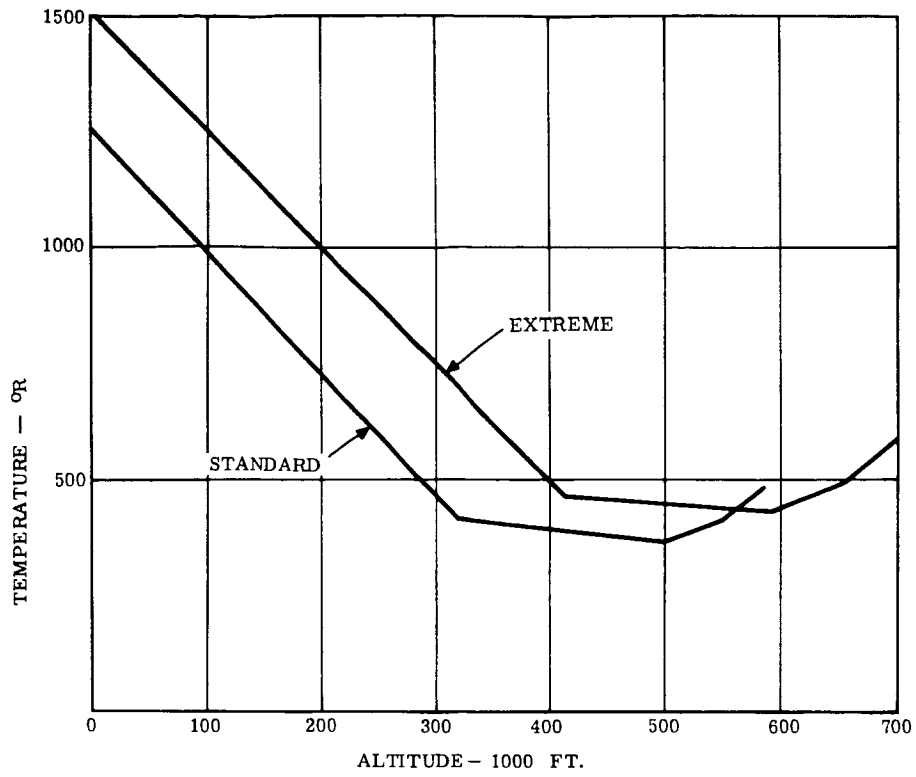


Figure 1.1.3-5. Venus Atmosphere - Temperature

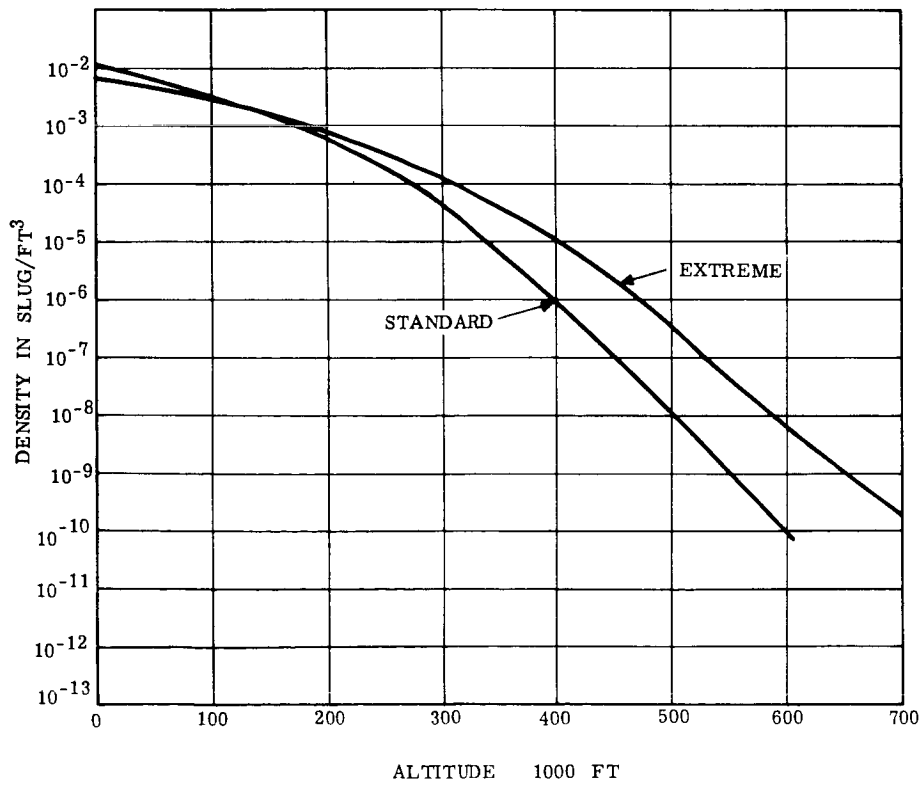


Figure 1.1.3-6. Venus Atmospheres - Density

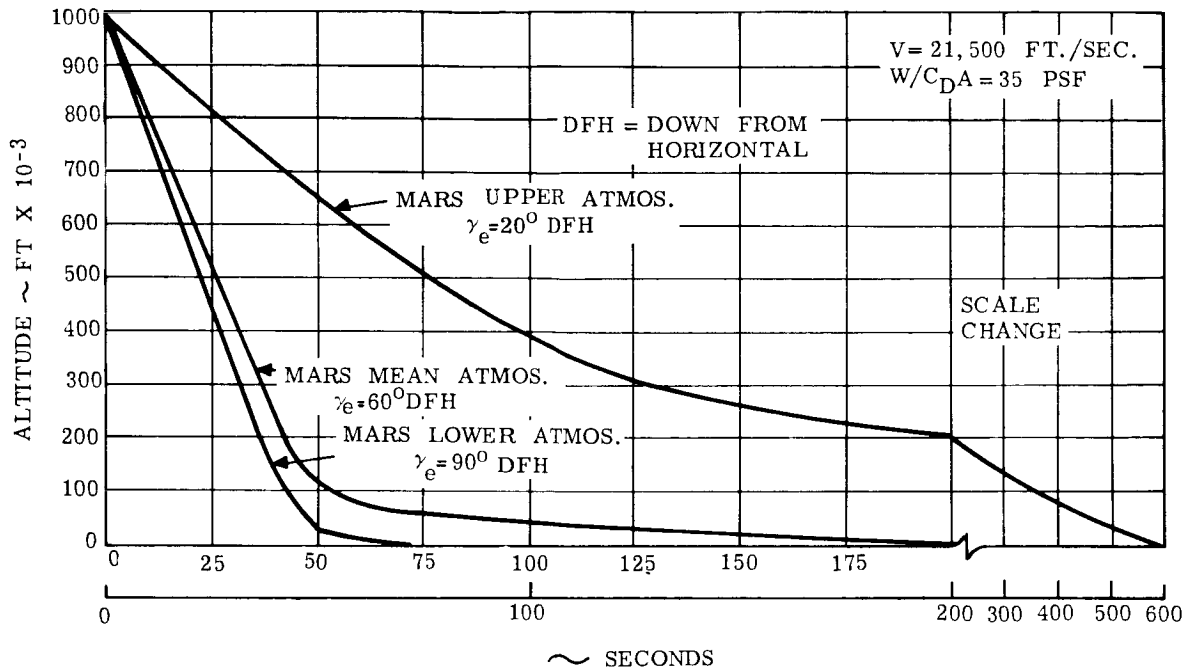


Figure 1.2.1-1. Altitude Histories for Martian Entry

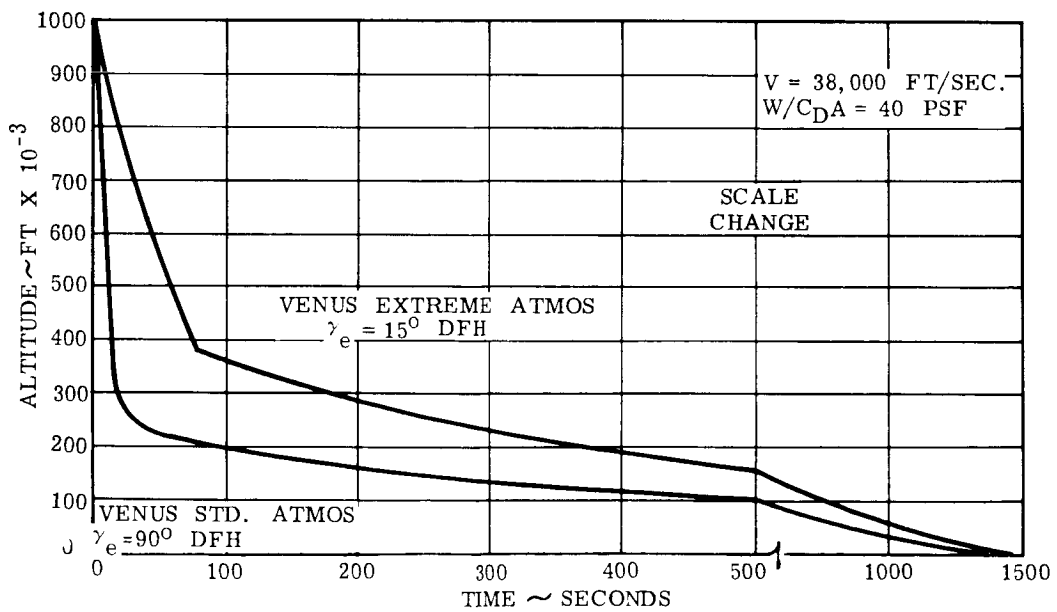


Figure 1.2.1-2. Altitude Histories for Venusian Entry

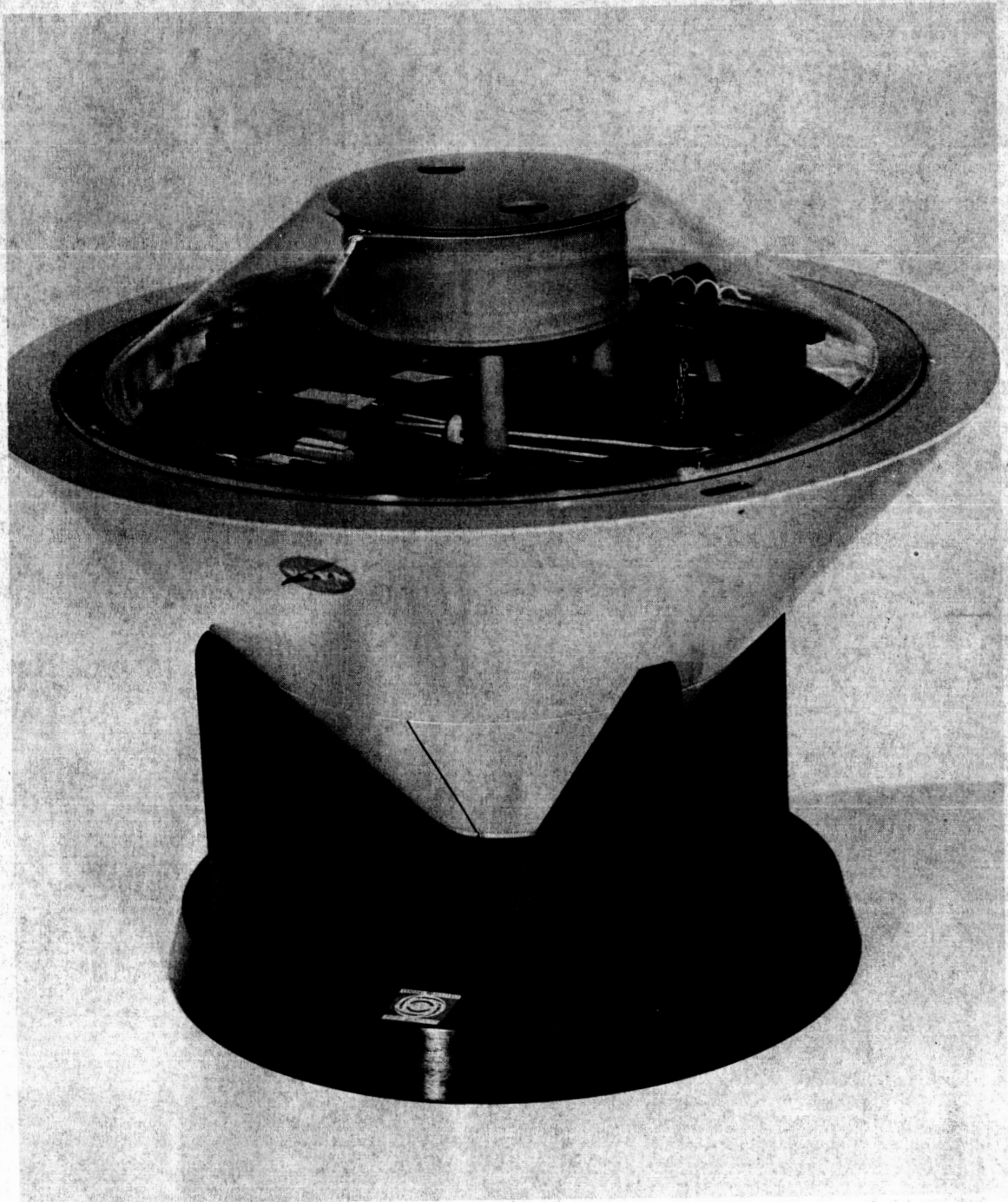


Figure 1.2.1-3. Mars Lander With Aft Cover Attached

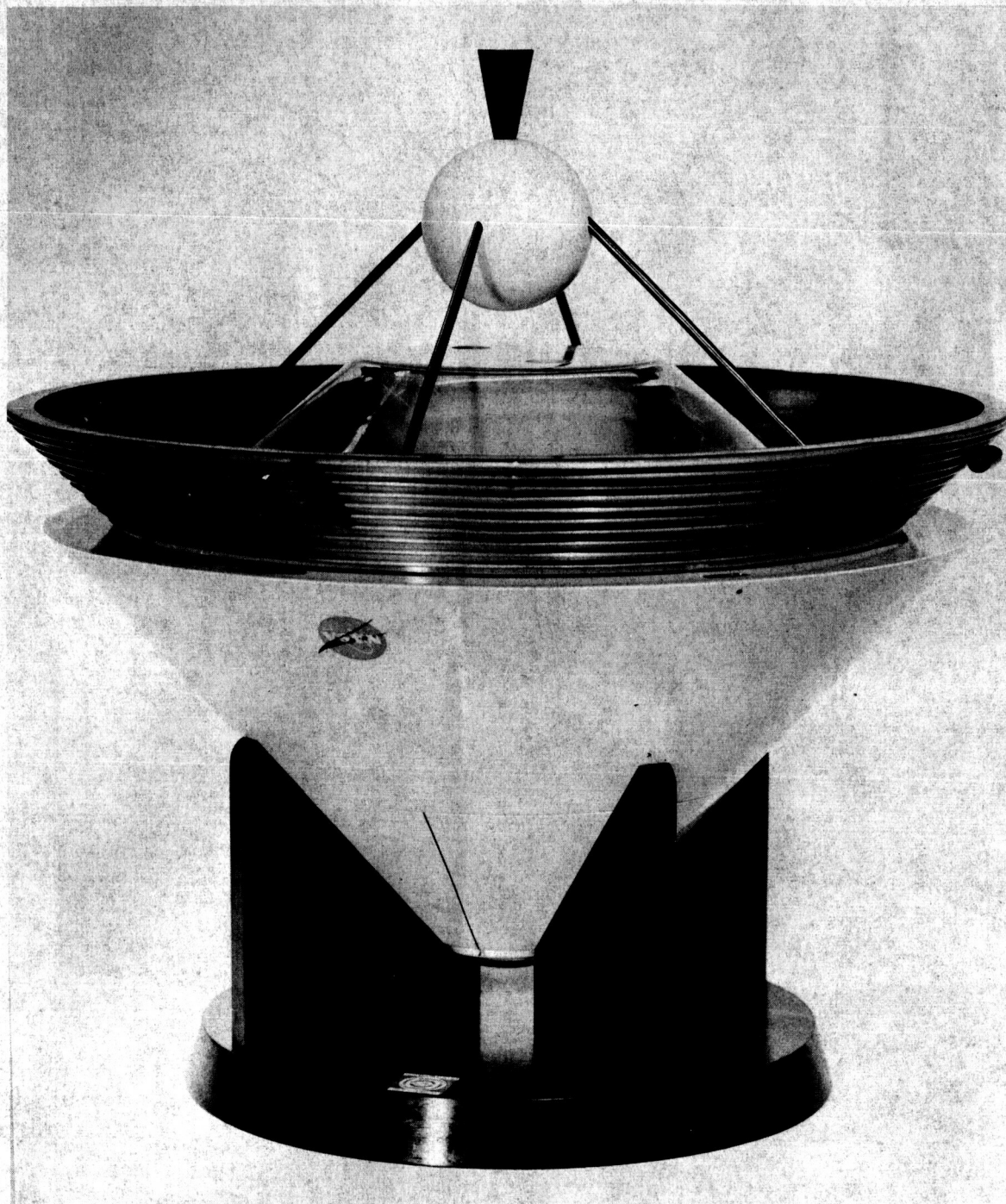


Figure 1.2.1-4. Mars Lander With Radiator-Adapter Section Attached

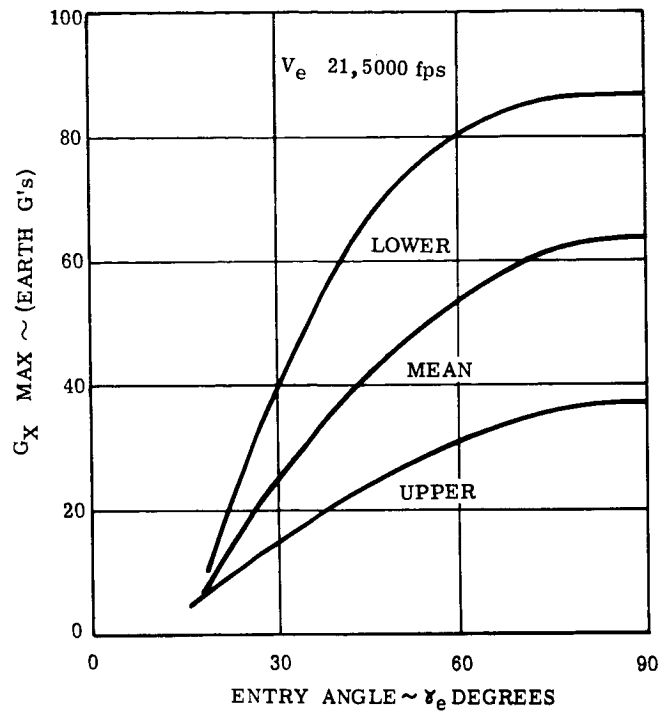


Figure 1.2.2-1 Peak Axial Deceleration vs. Entry Angle for $W/C_D A = 35 \text{ PSF}$

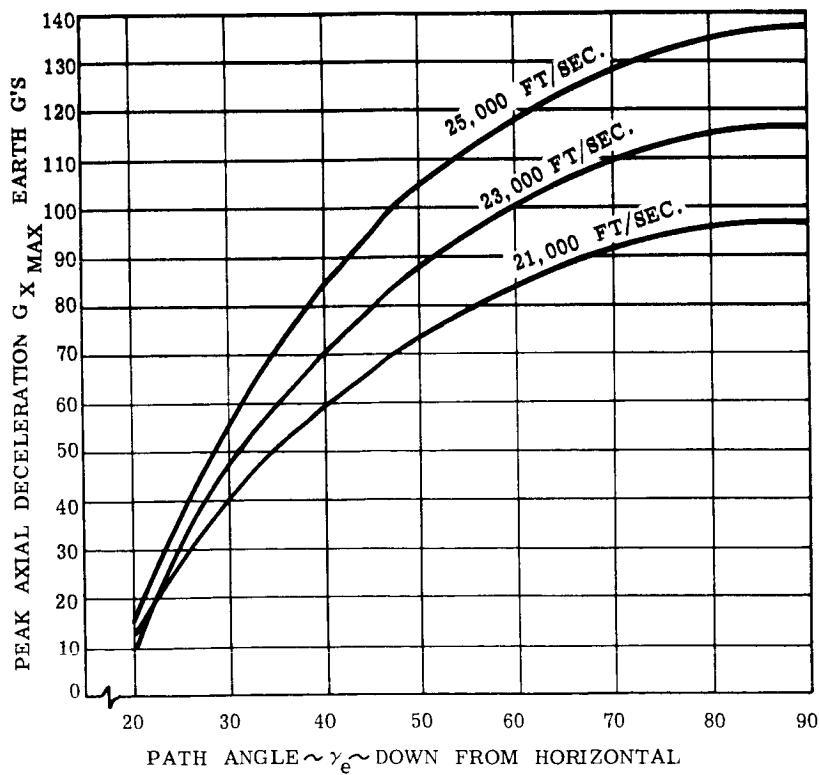


Figure 1.2.2-2 Peak Axial Deceleration vs. Entry Angle for Various Velocities and Martian Lower Atmosphere

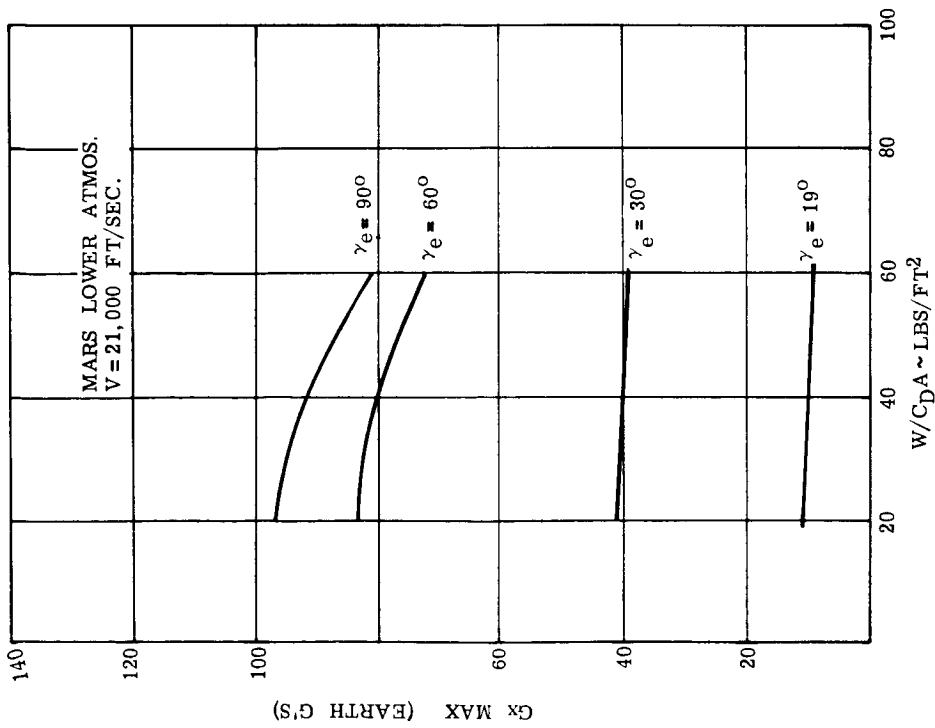


Figure 1.2.2-3 Peak Axial Deceleration vs. W/C_{DA} for Several Martian Entries

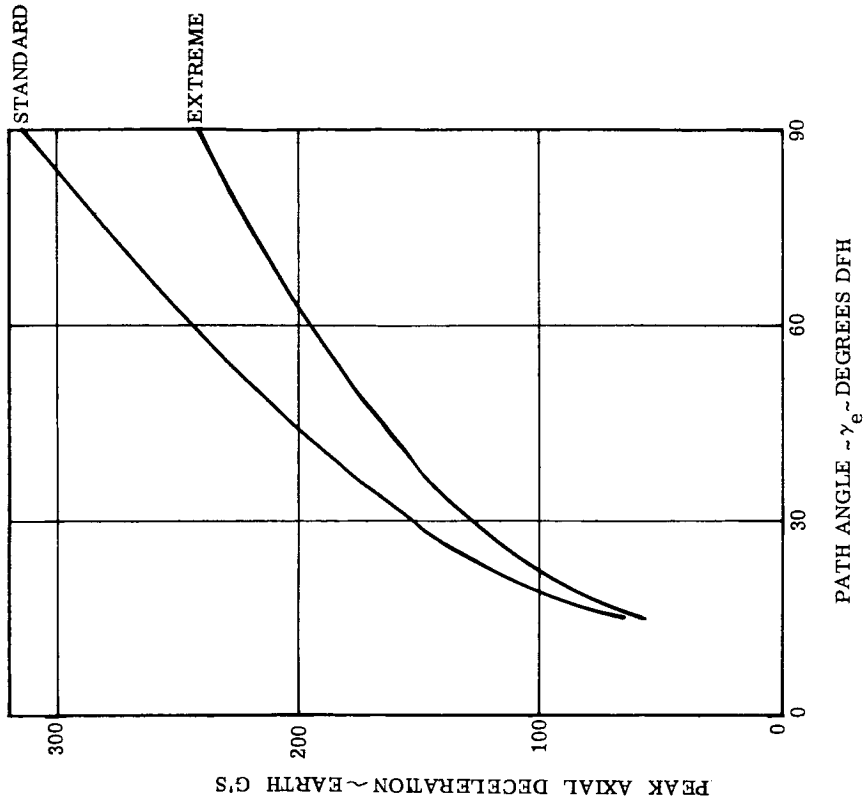


Figure 1.2.2-4 Peak Axial Deceleration for Two Venusian Atmospheres Where $W/C_{DA} = 40$ psf and $V = 38,000$ Ft/Sec...

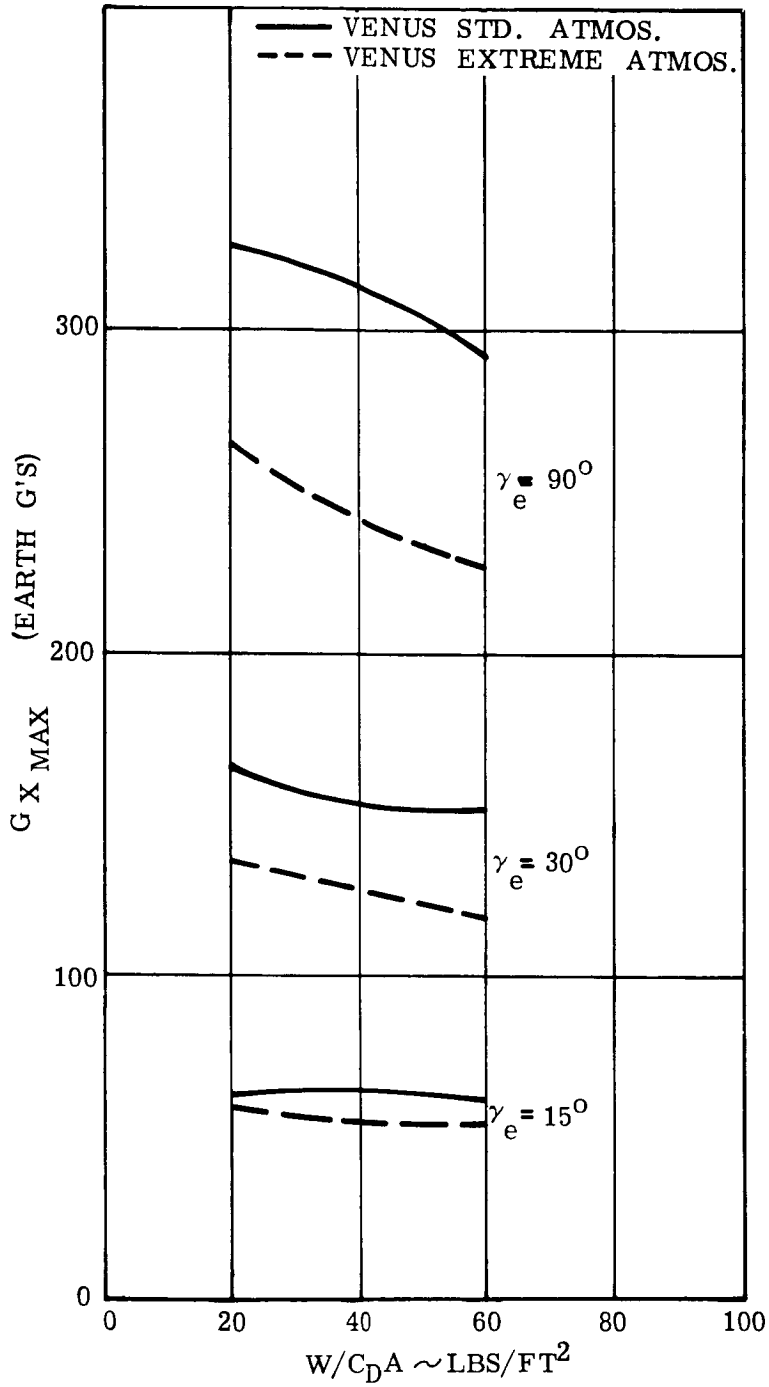


Figure 1.2.2-5 Peak Axial Deceleration $W/C_D A$ for Two Venusian Atmospheres Where $V = 38,000 \text{ Ft/Sec.}$

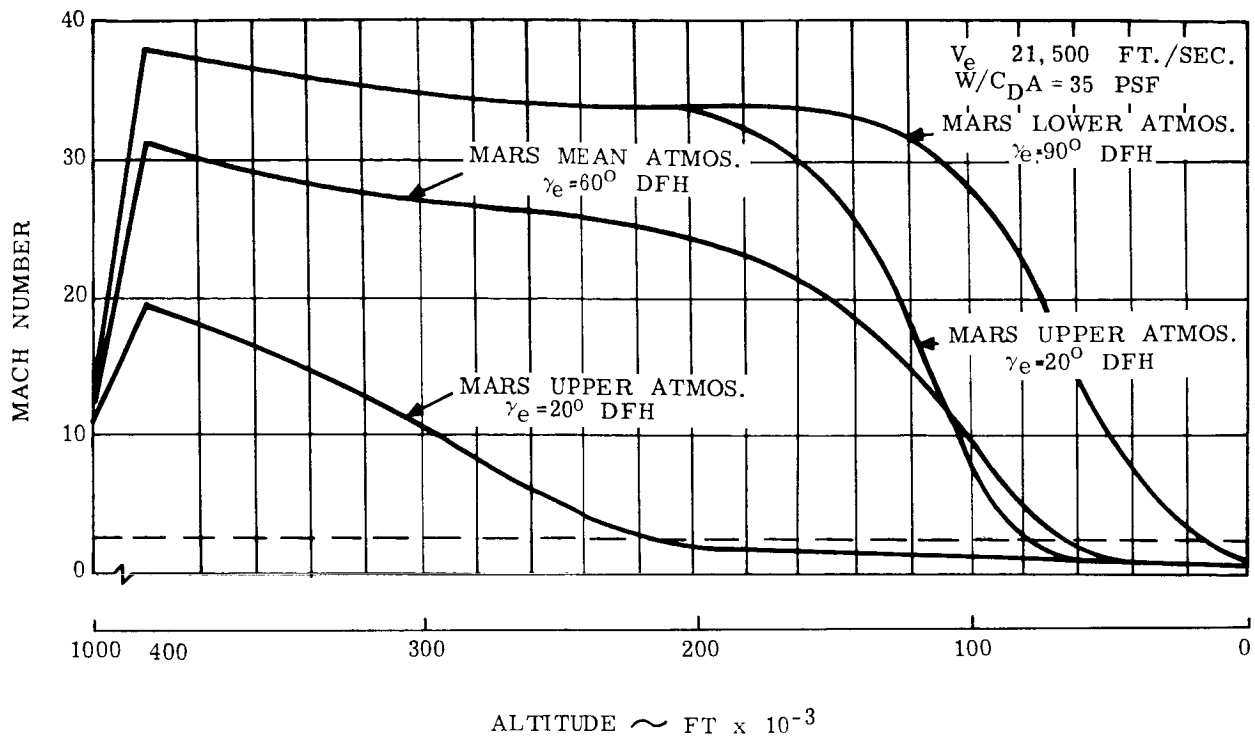


Figure 1.2.2-6 Mach Number vs. Altitude for Several Martian Entries

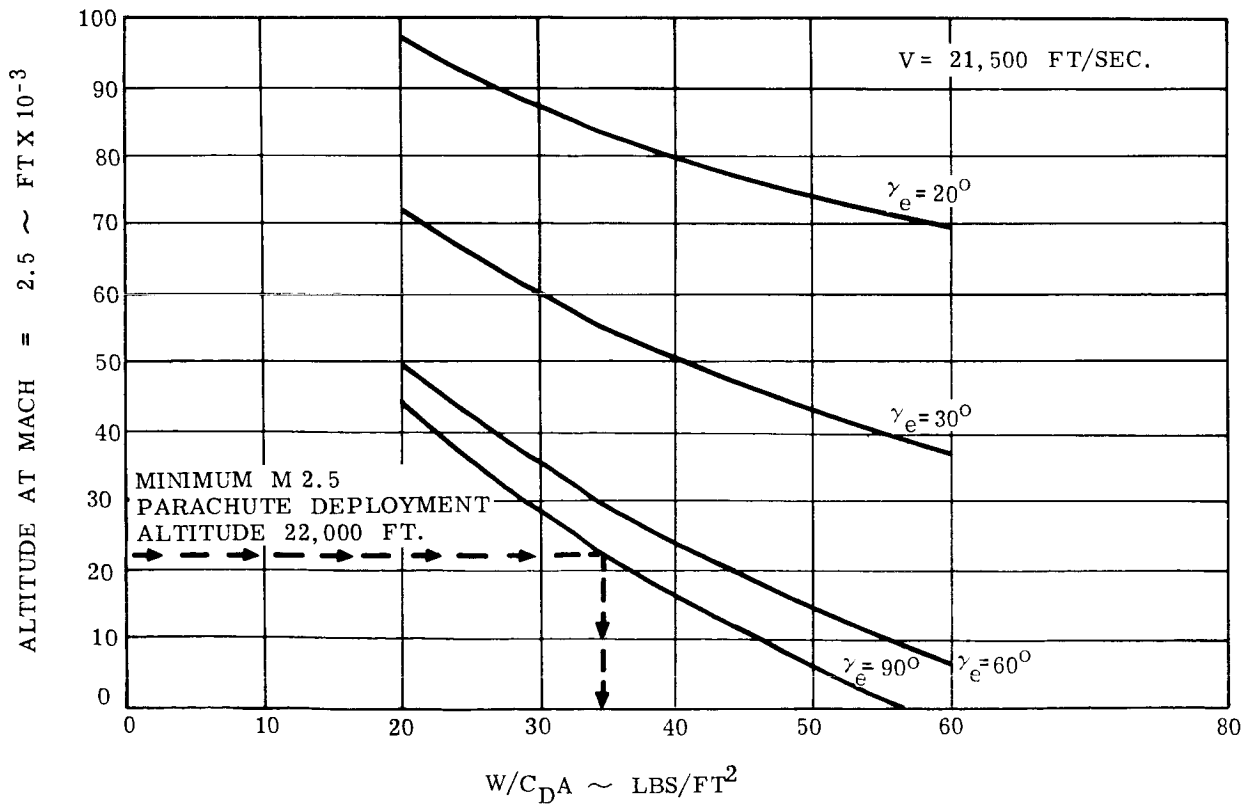
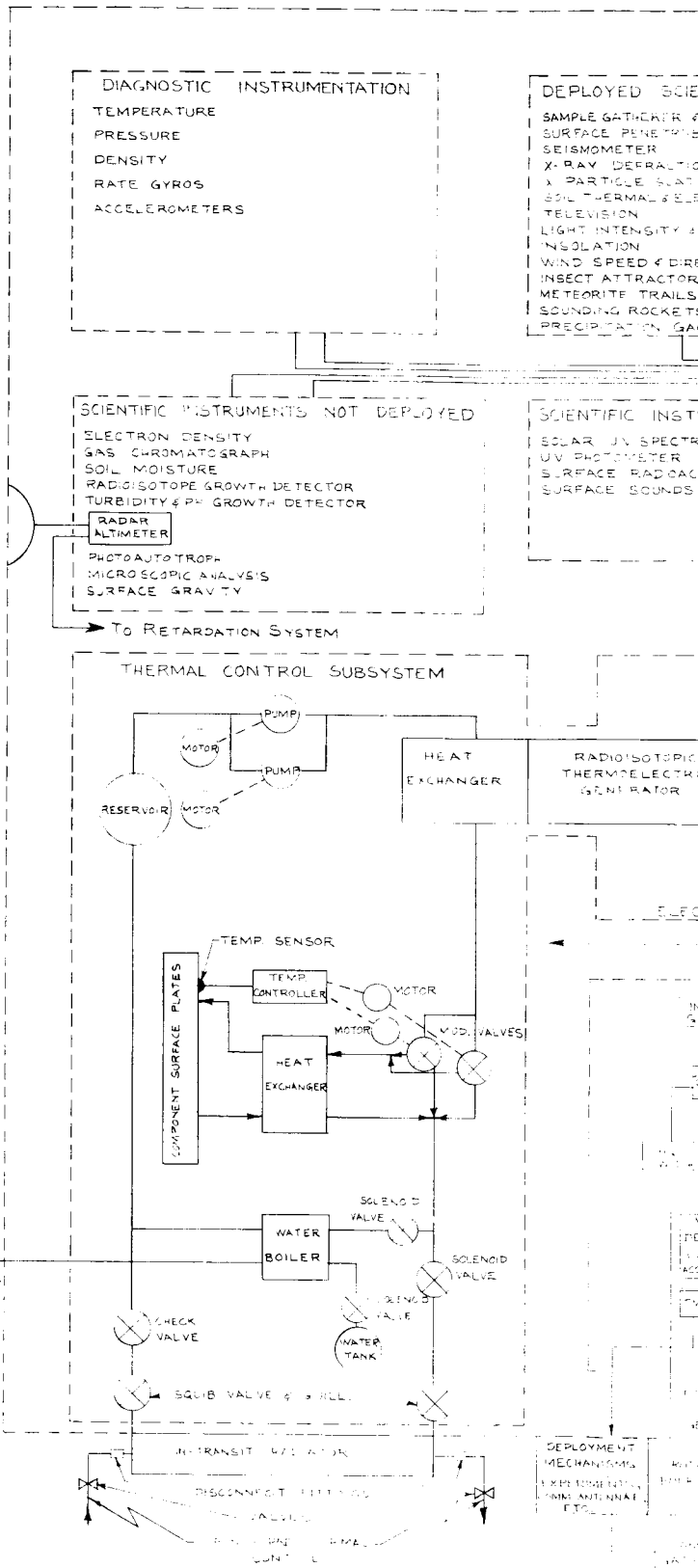


Figure 1.2.2-7 Altitude of Occurrence at M - 2.5 for Entry Into Mars Lower Atmosphere



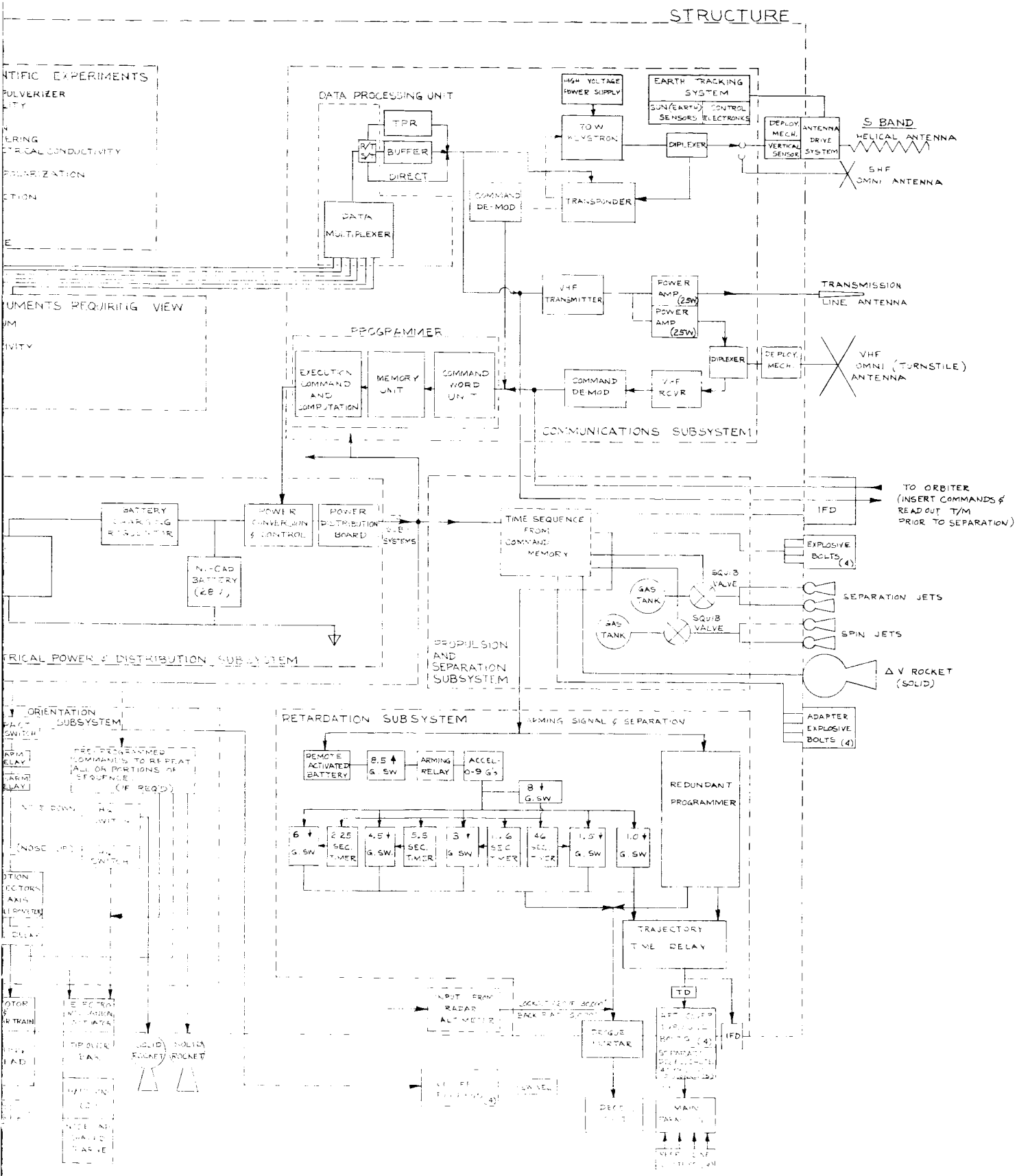
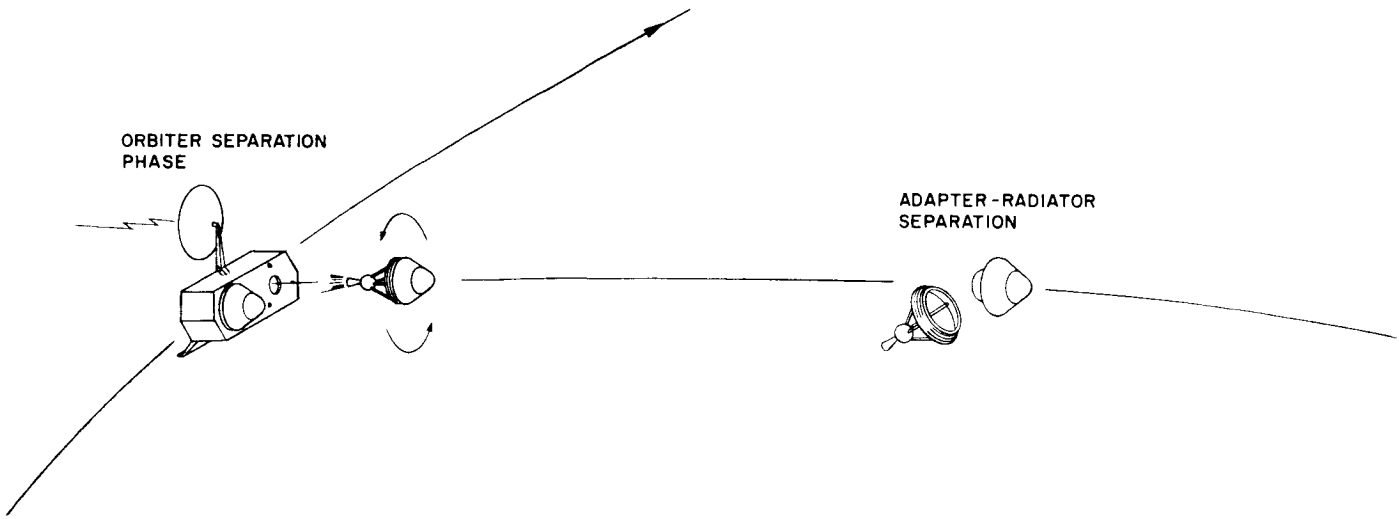


Figure 1.2.3-1 Mars 1969 Lander Block Diagram



EN
(1,
S

TRY
100,000 FT. FROM
IRFACE OF MARS)

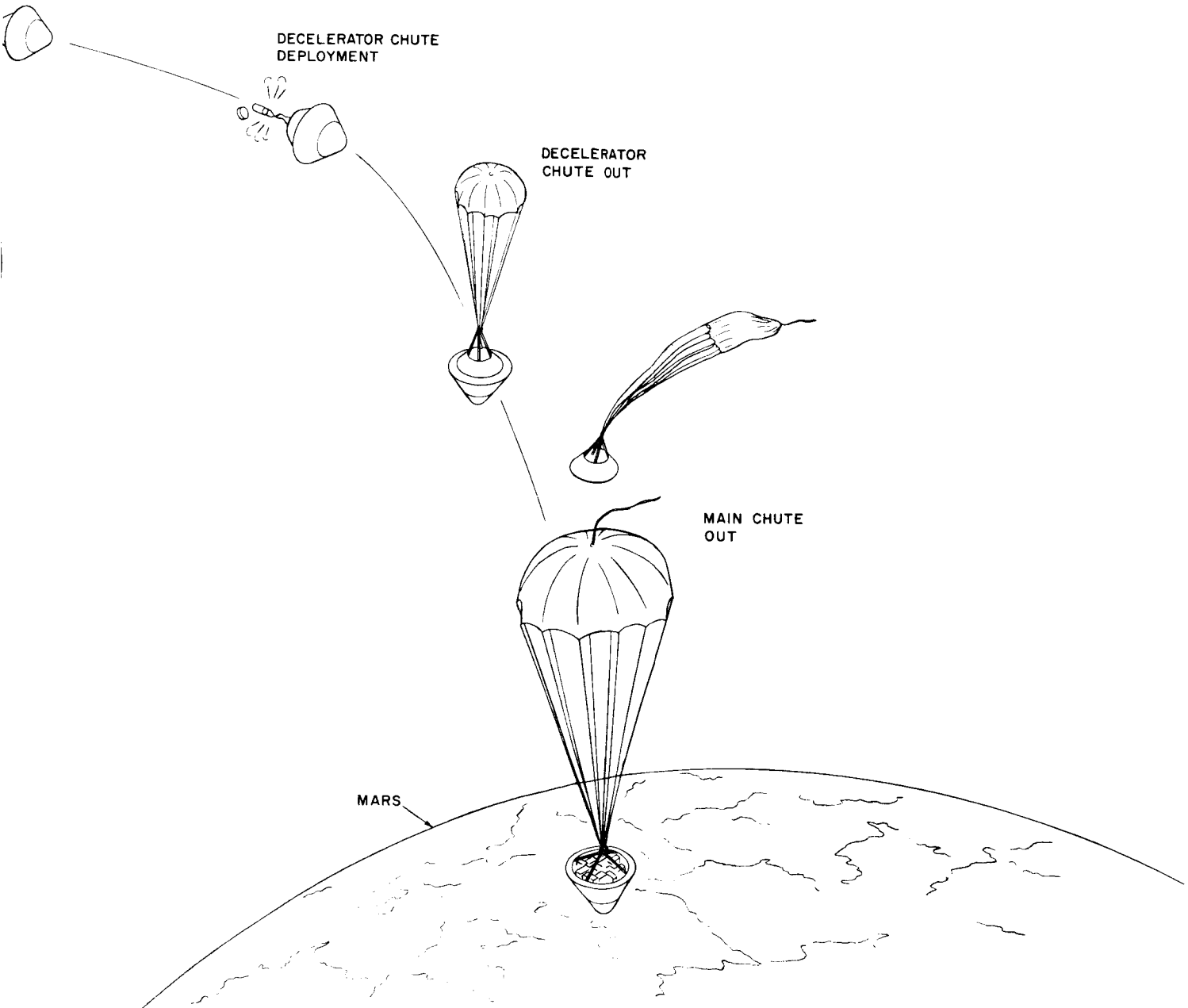
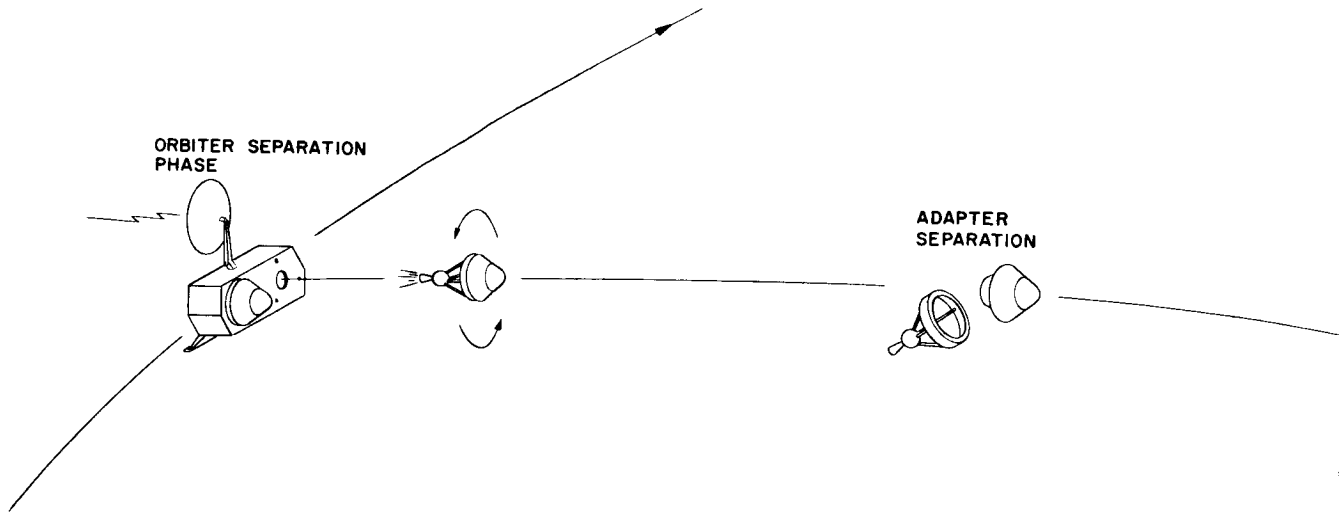


Figure 1.2.3-2 Sequence Diagram - Mars Entry



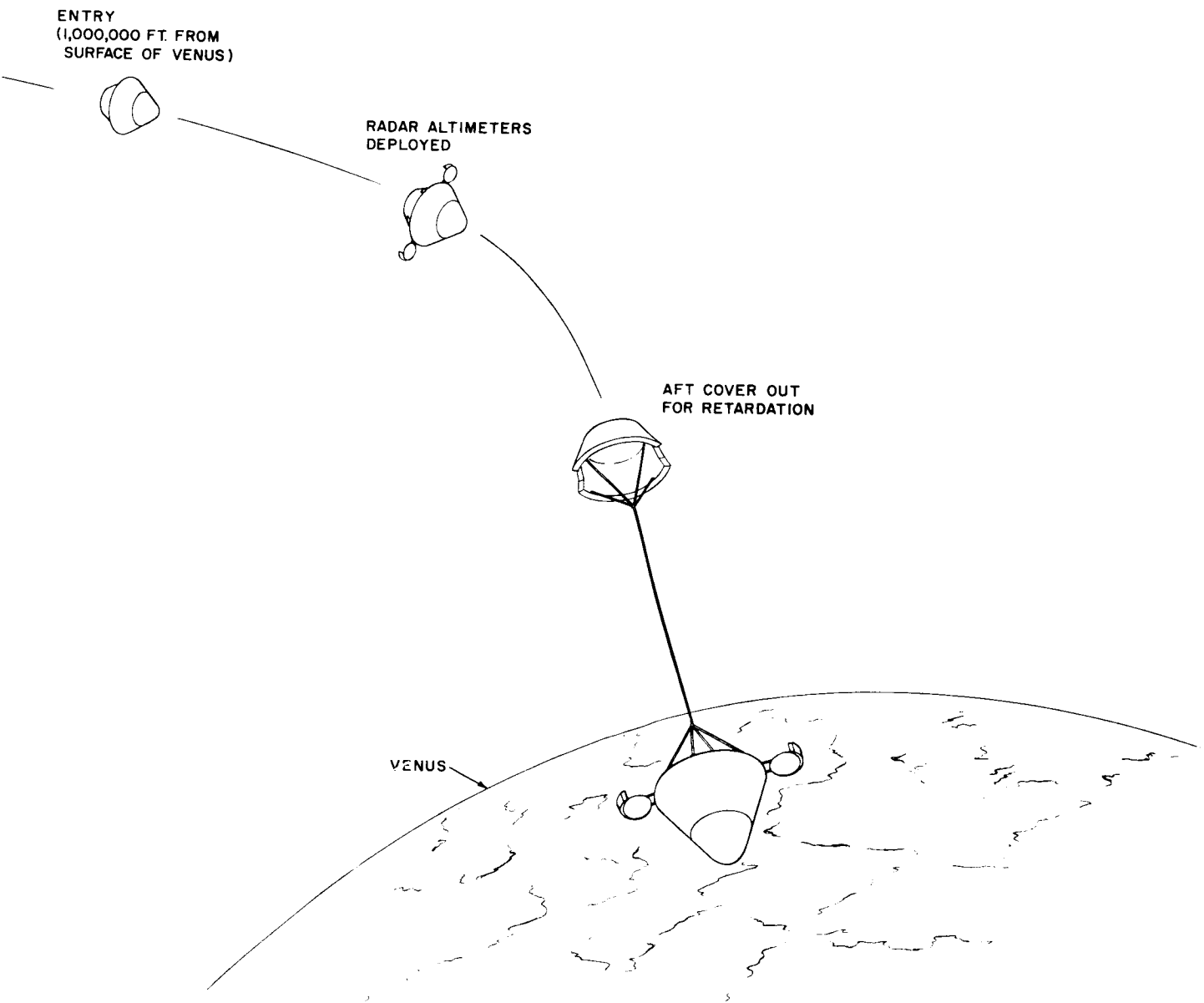


Figure 1.2.3-3 Sequence Diagram - Venus Entry

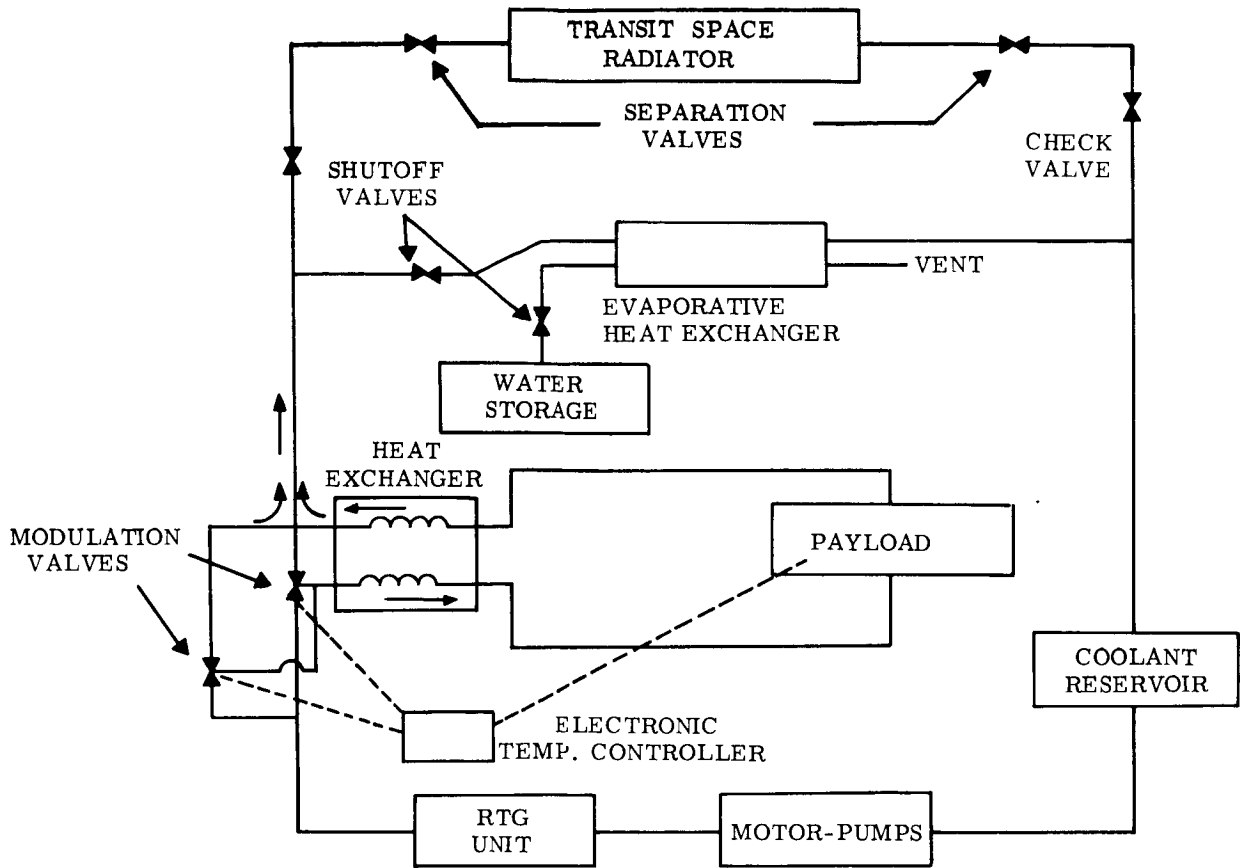


Figure 1.2.3-4 Thermal Control System for Mars Lander

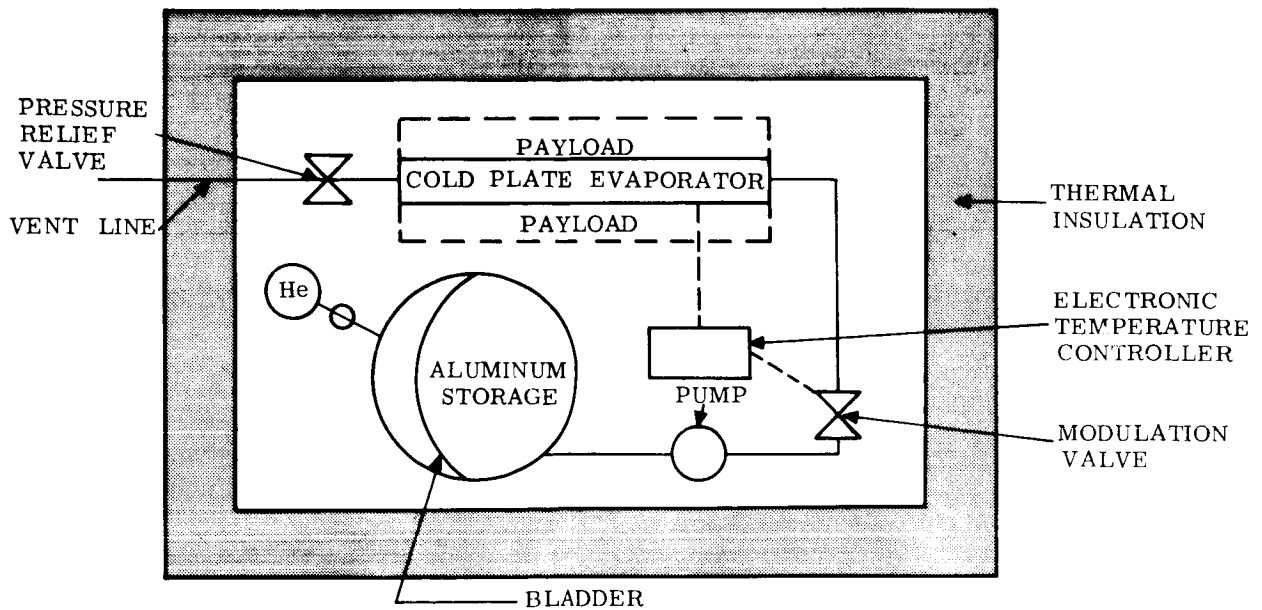


Figure 1.2.3-5 Thermal Control System for Venus Lander

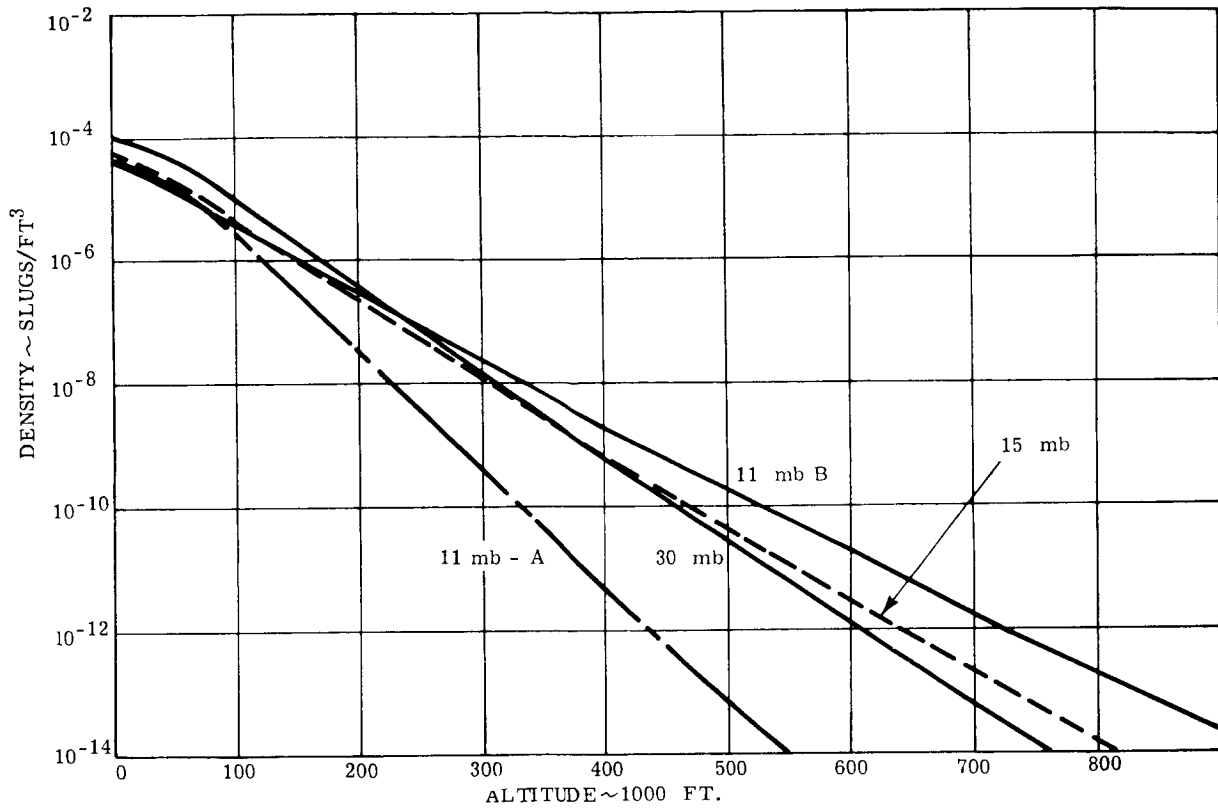


Figure 1.2.5-1 Density - Altitude Profile, 15 Millibar Atmosphere

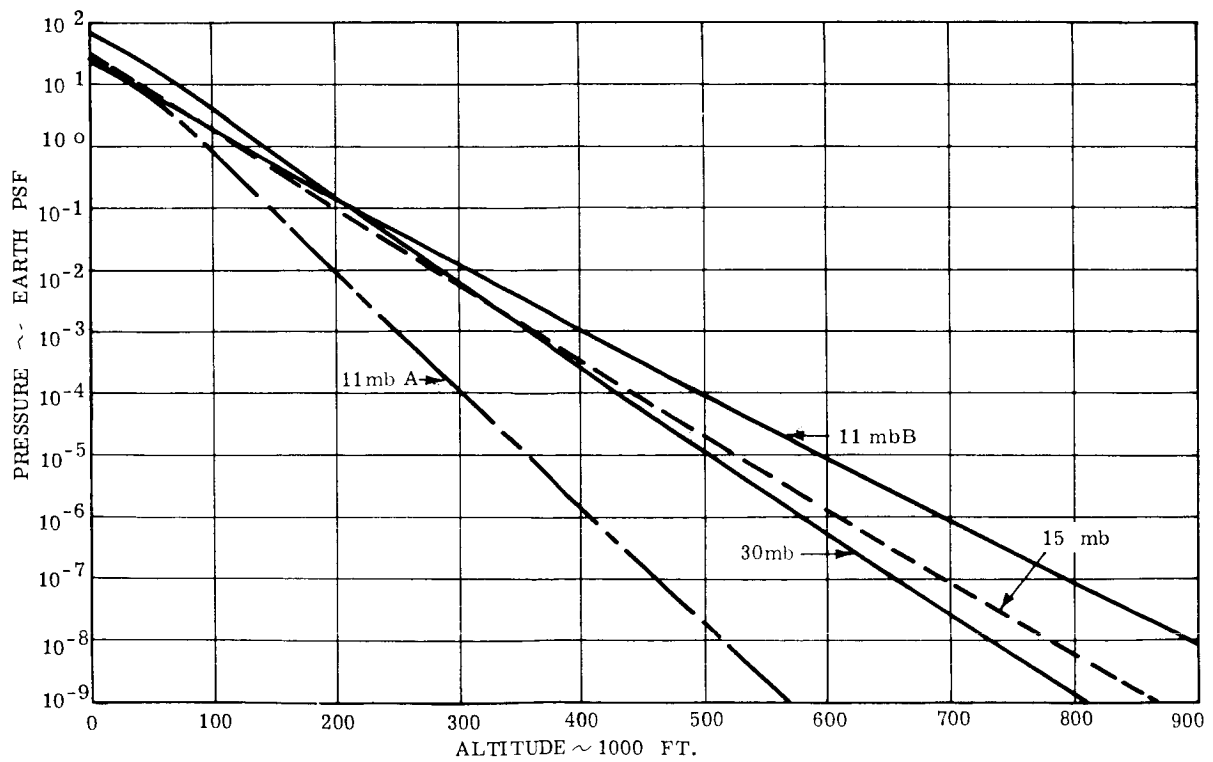


Figure 1.2.5-2 Pressure - Altitude Profile, 15 Millibar Atmosphere

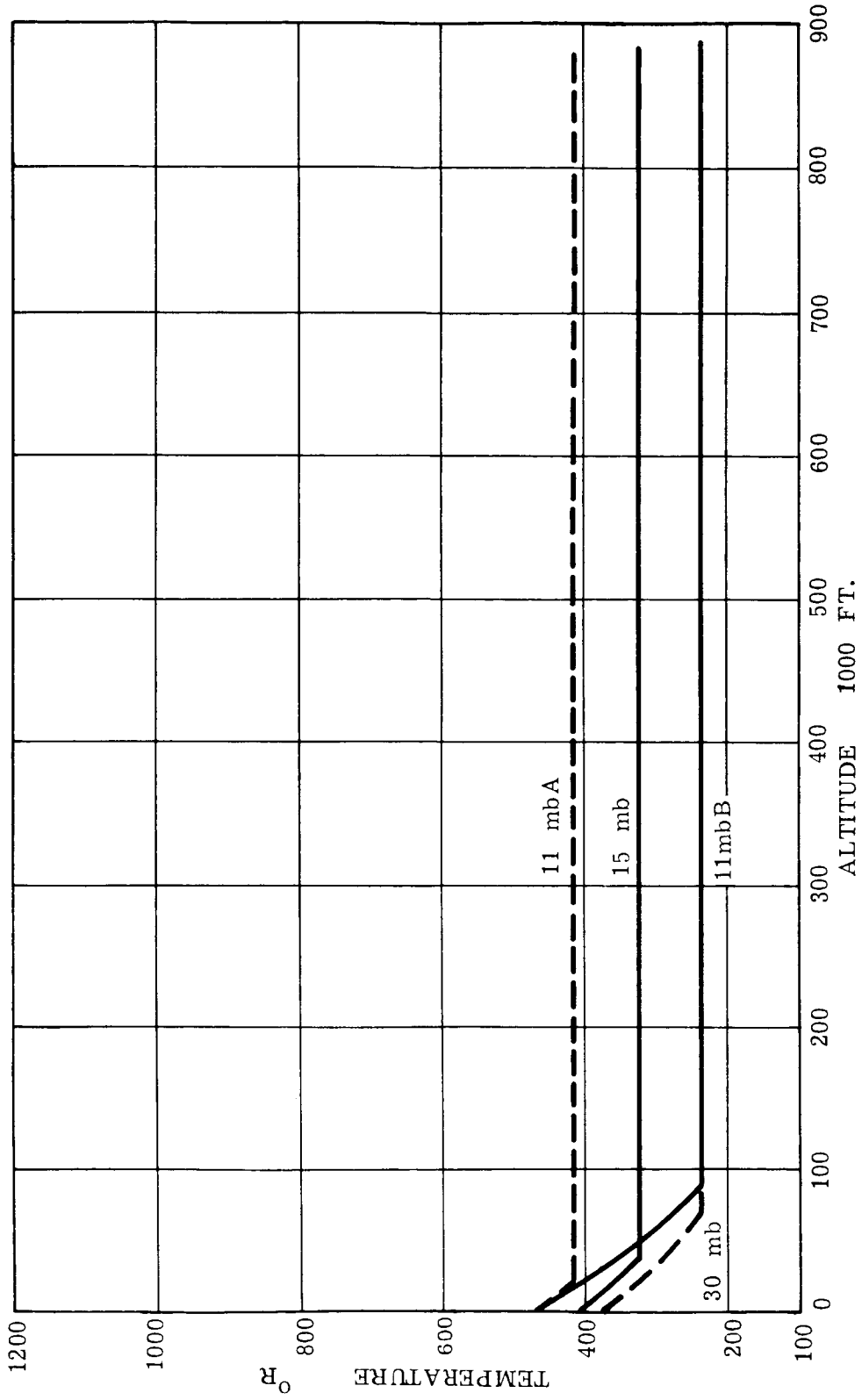


Figure 1.2.5-3 Temperature - Altitude Profile, 15 Millibar Atmosphere

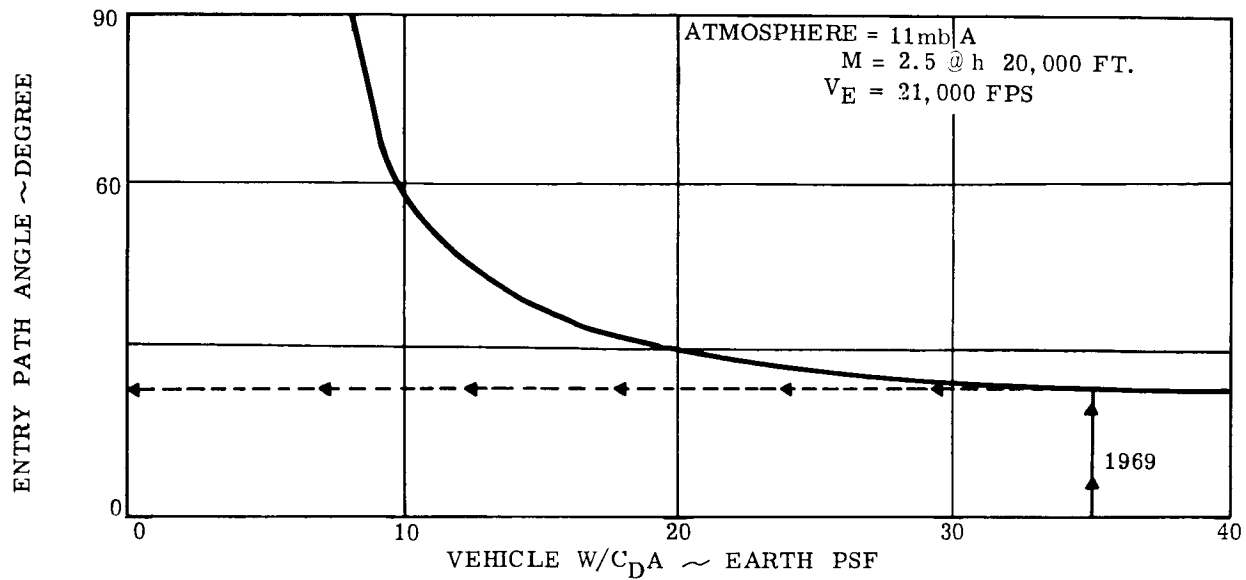


Figure 1.2.5-4 Entry Path Angle Restriction for Voyager in the 11 Millibar Model Atmosphere...

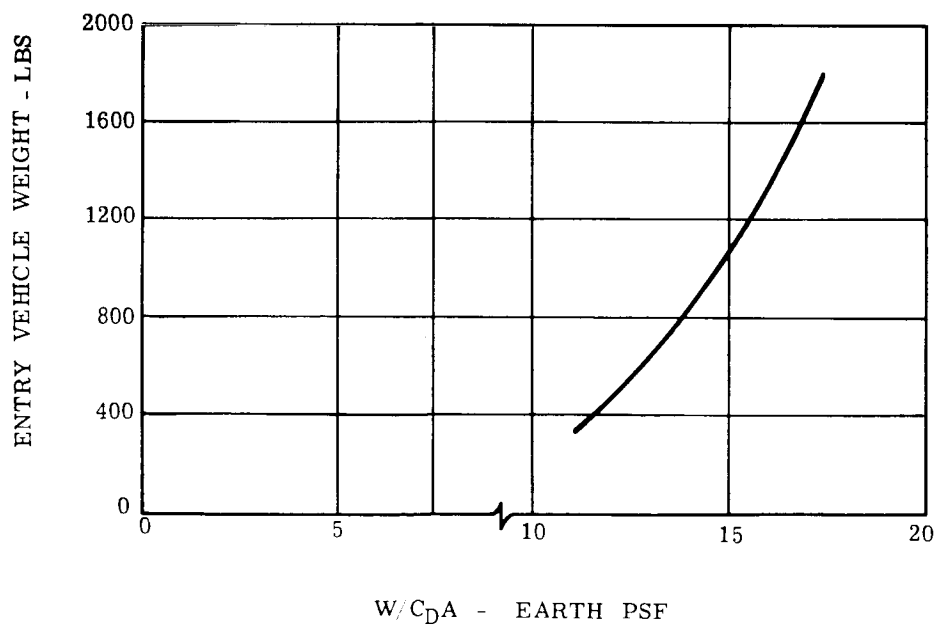
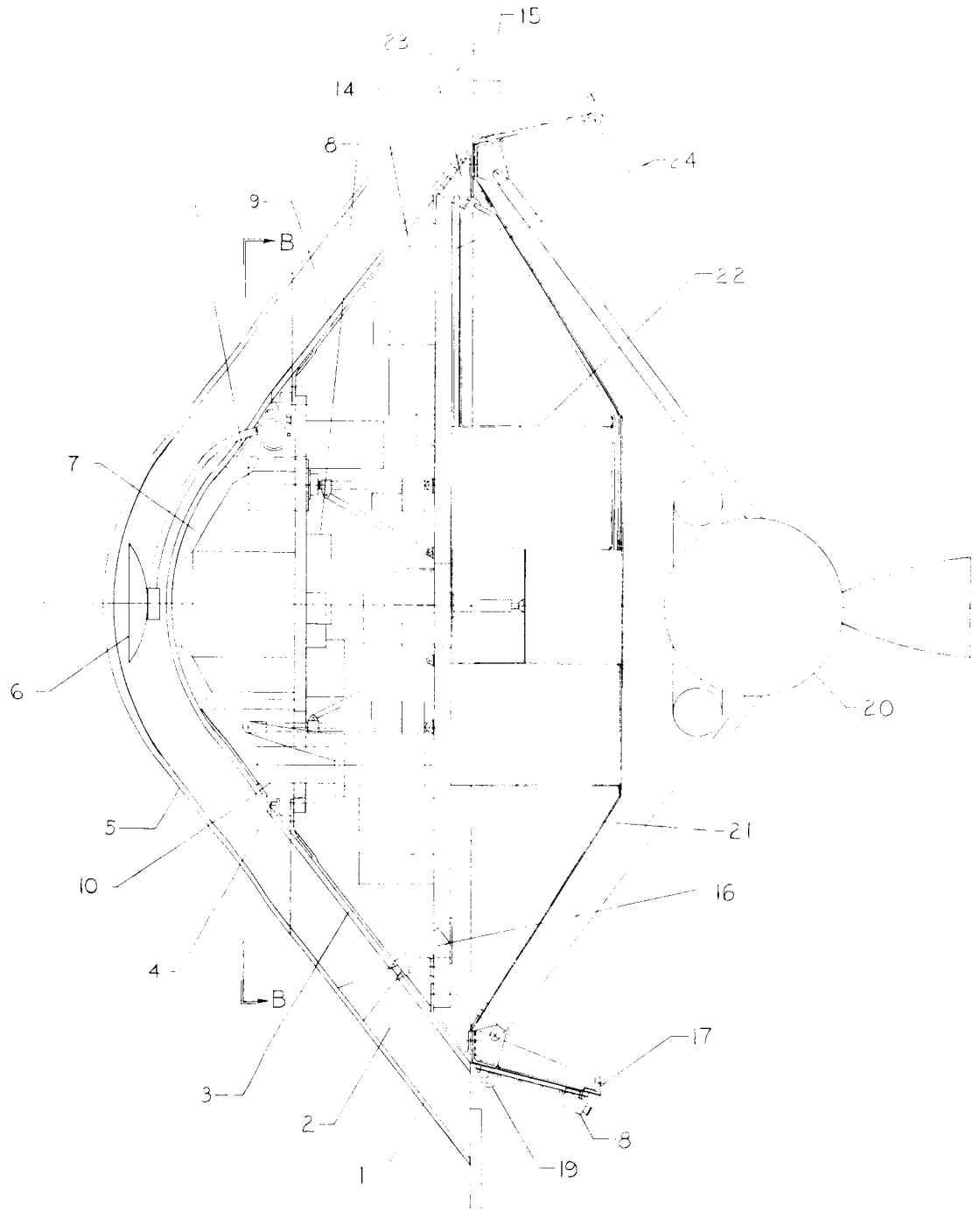
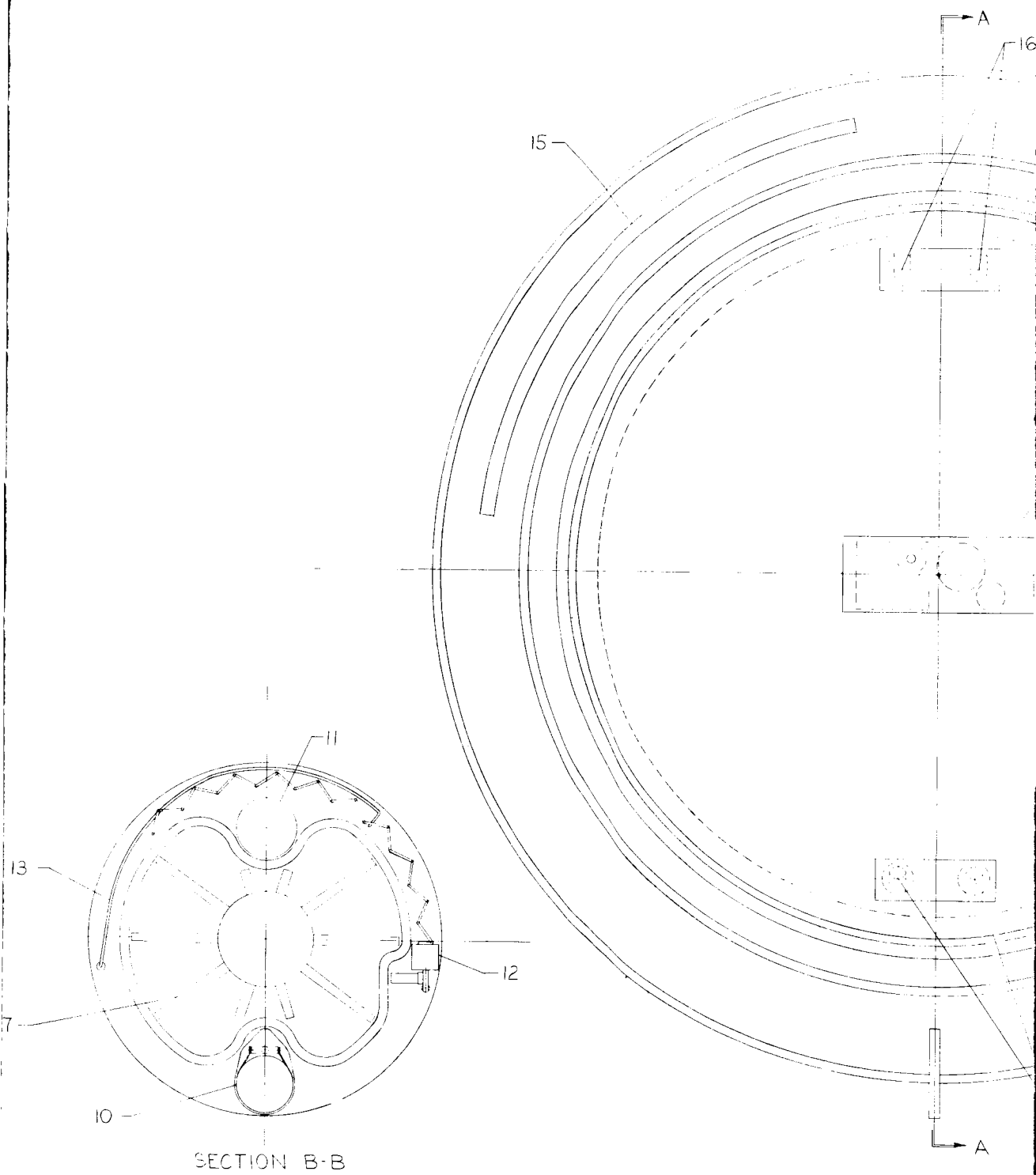


Figure 1.2.5-5 Vehicle Weight (Entry) vs. W/C_{DA}



SECTION A-A



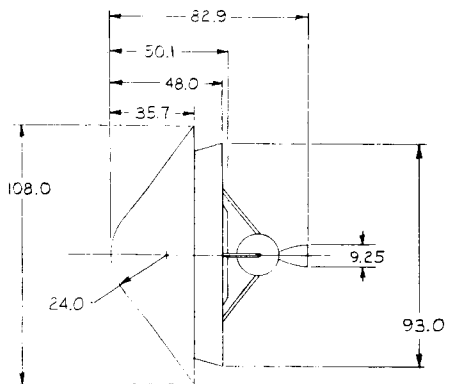
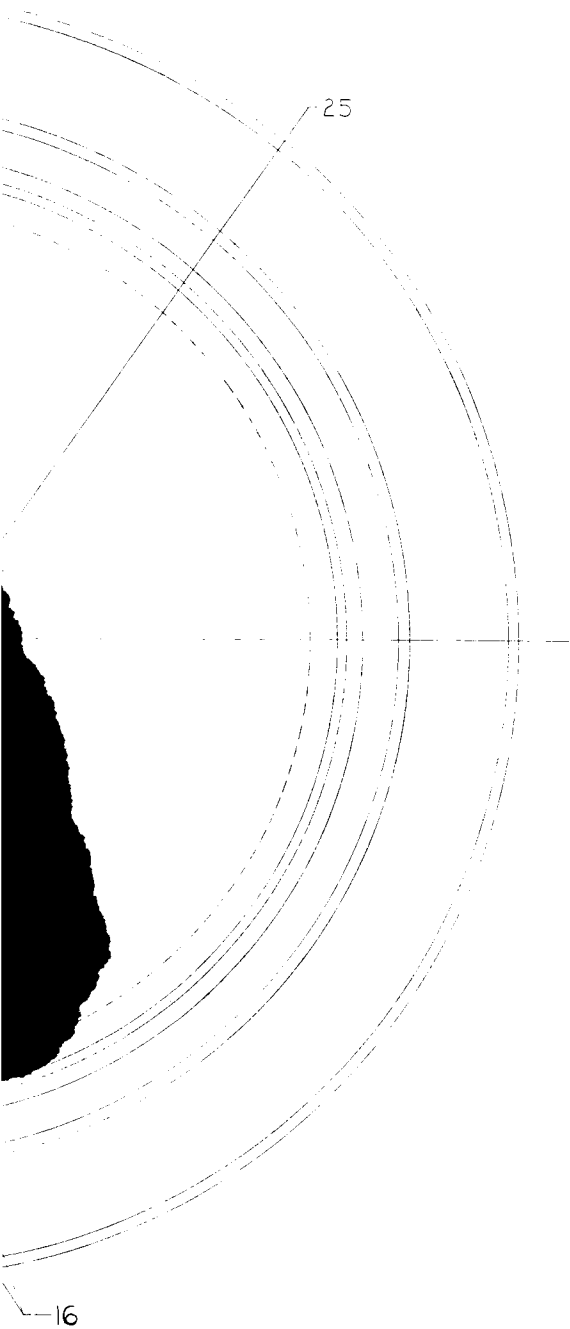


Figure 1.2.5-6 Mars 1969 Lander 11 to 30 Millibar Atmosphere

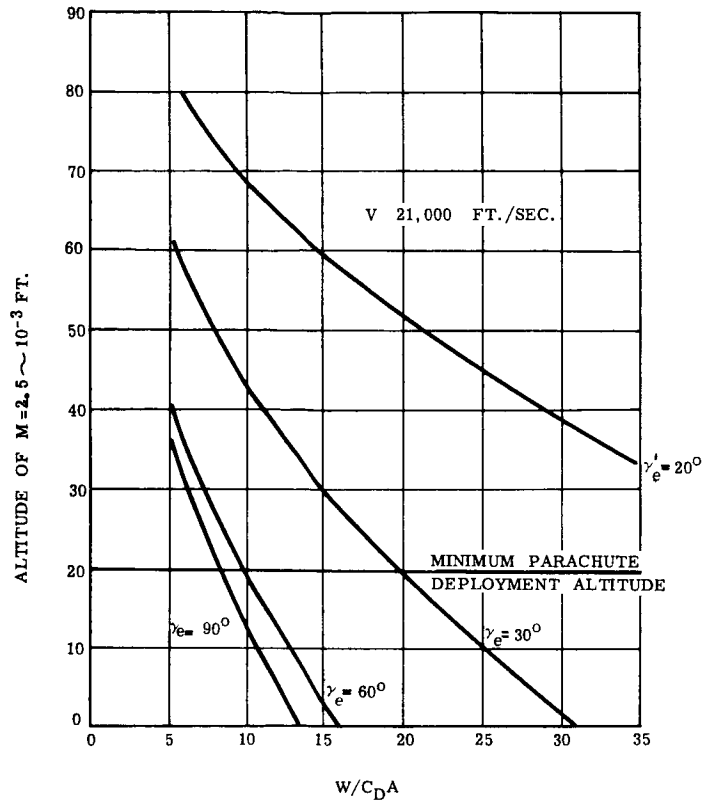


Figure 1.2.5-7 Altitude of Occurrence of $M=2.5$ for Entry Into Martian 11 Millibar Atmosphere - 21,000 Ft/Sec.

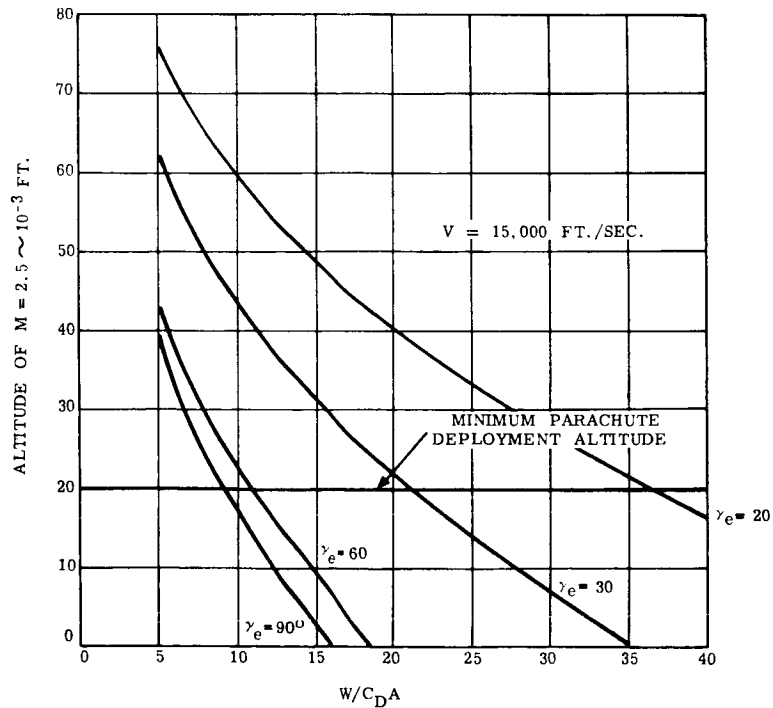


Figure 1.2.5-8 Altitude of Occurrence of $M=2.5$ for Entry Into Martian 11 Millibar Atmosphere - 15,000 Ft/Sec.

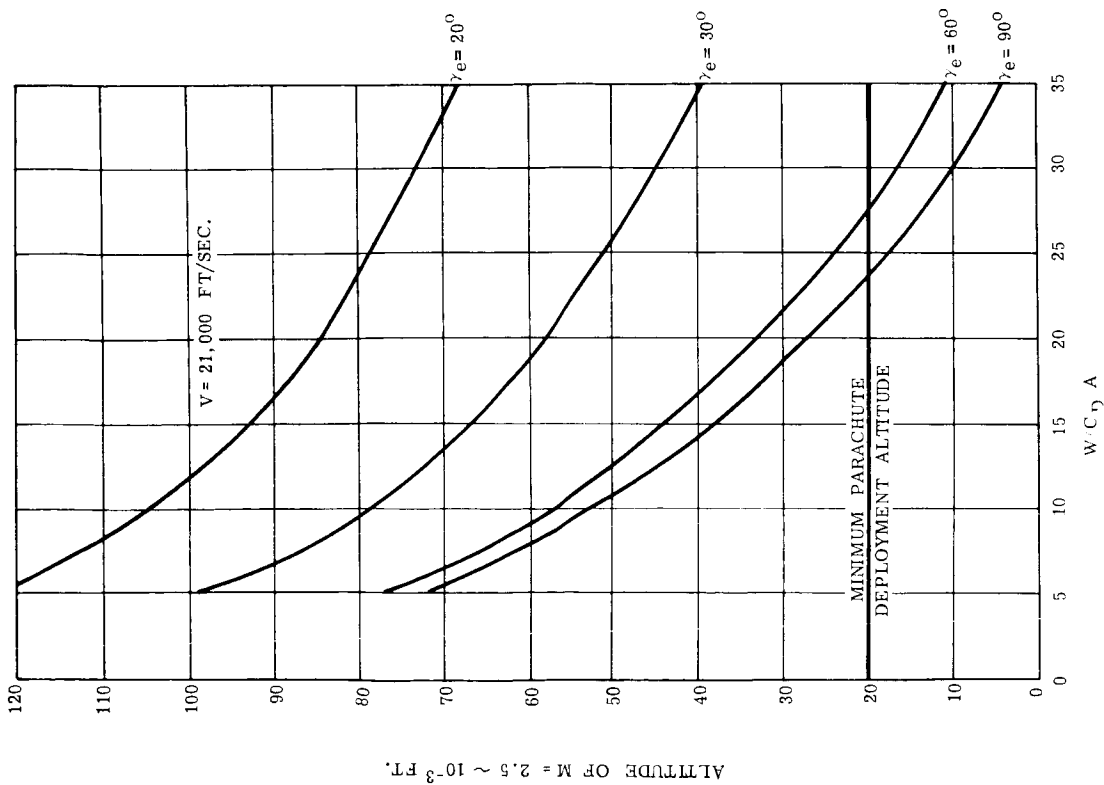


Figure 1.2.5-9 Altitude of Occurrence of $M = 2.5$ for Entry Into Martian 30 Millibar Atmosphere - 21,000 Ft/Sec.

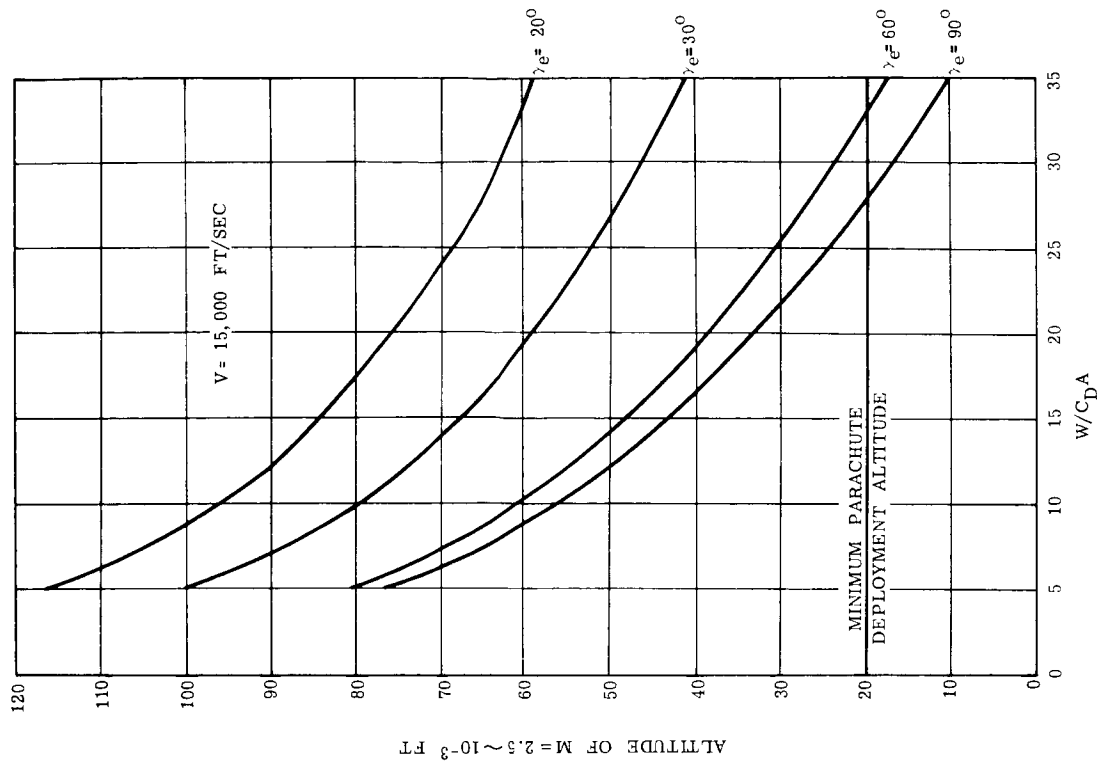


Figure 1.2.5-10 Altitude of Occurrence of $M = 2.5$ for Entry Into Martian 30 Millibar Atmosphere - 15,000 Ft/Sec.

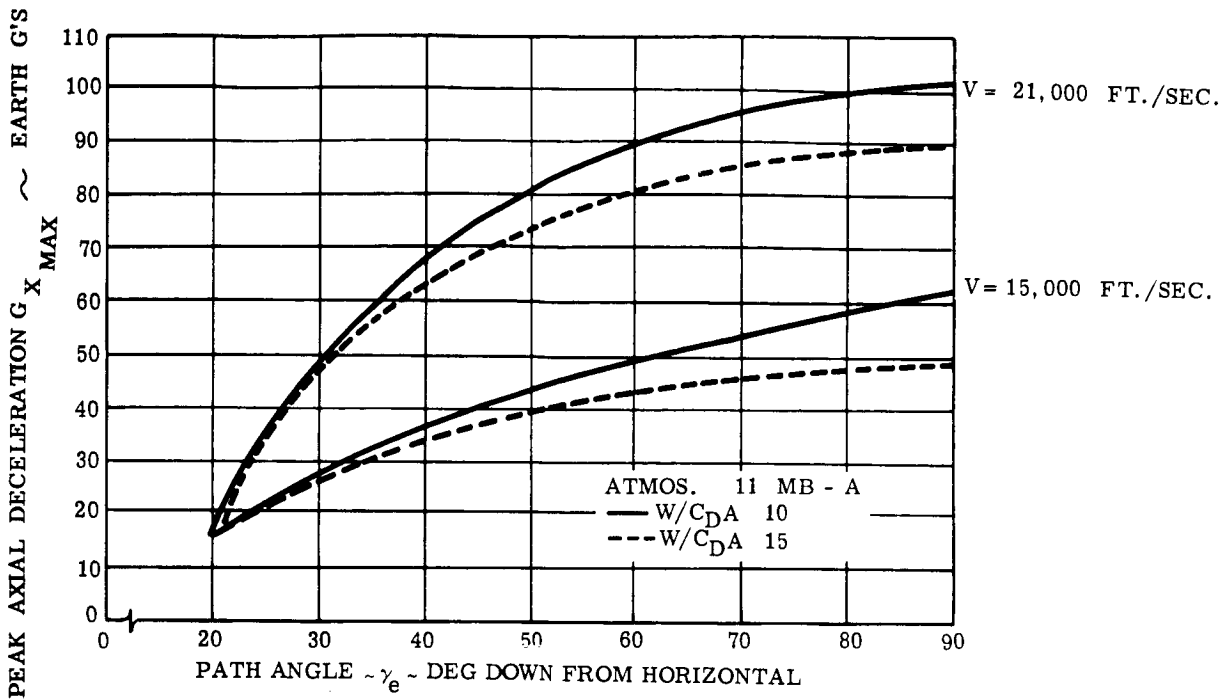


Figure 1.2.5-11 Peak Axial Deceleration vs. γ_e for Martian Entry

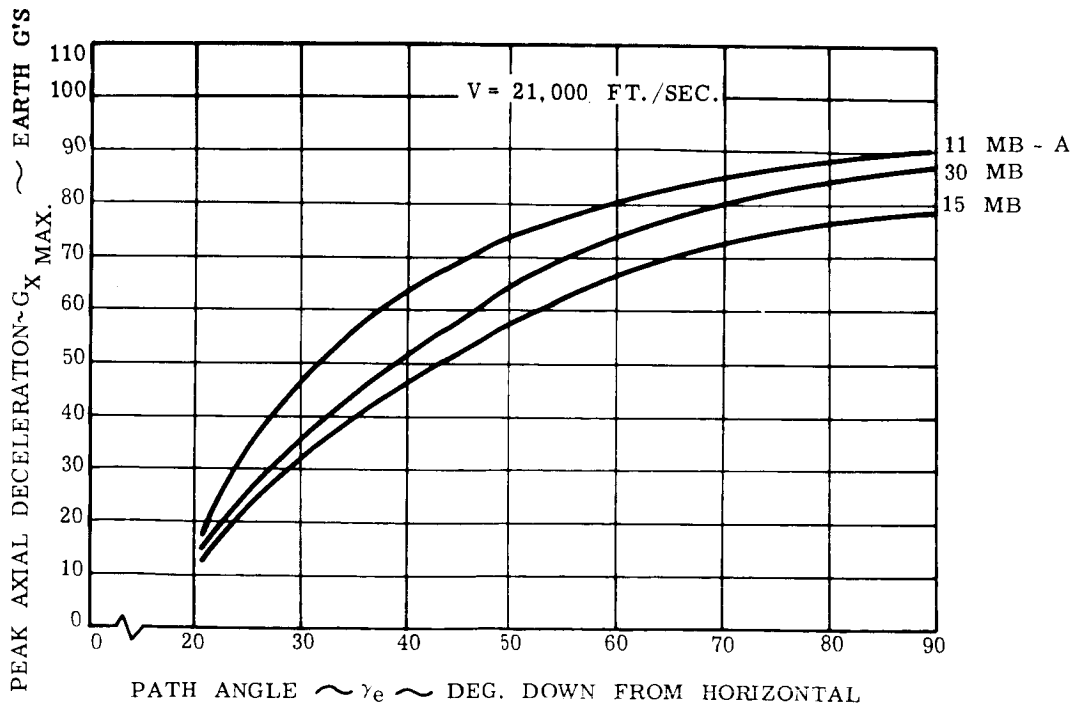


Figure 1.2.5-12 Peak Axial Deceleration vs. γ_e for Martian Entry

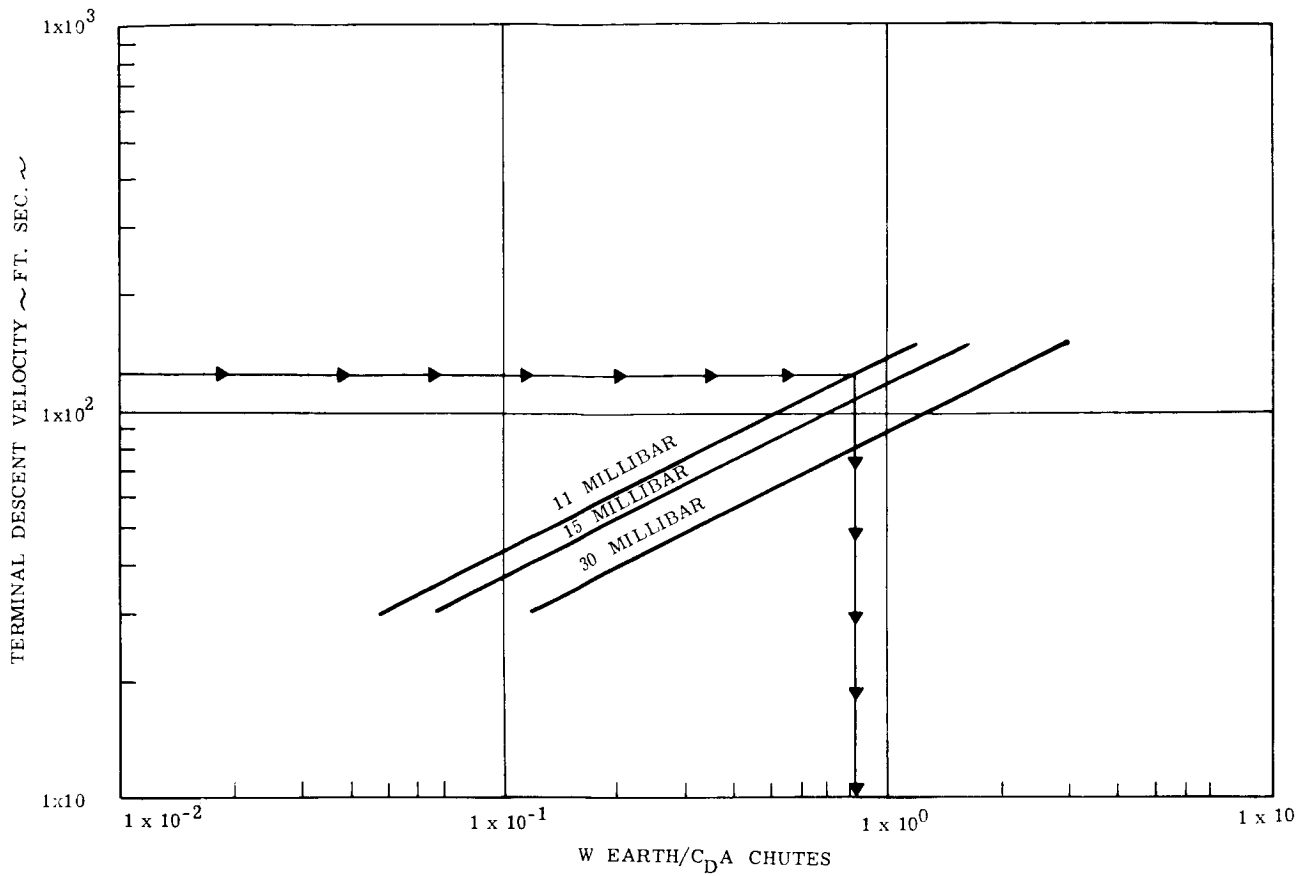


Figure 1.2.5-13 Martian Descent Velocity vs. Earth $W/C_D A$ in Final Descent With Surface Density as a Parameter

$$C_{D0} = 0.7$$

EFFICIENCY OF CLUSTER = f (NUMBER OF PARACHUTES)

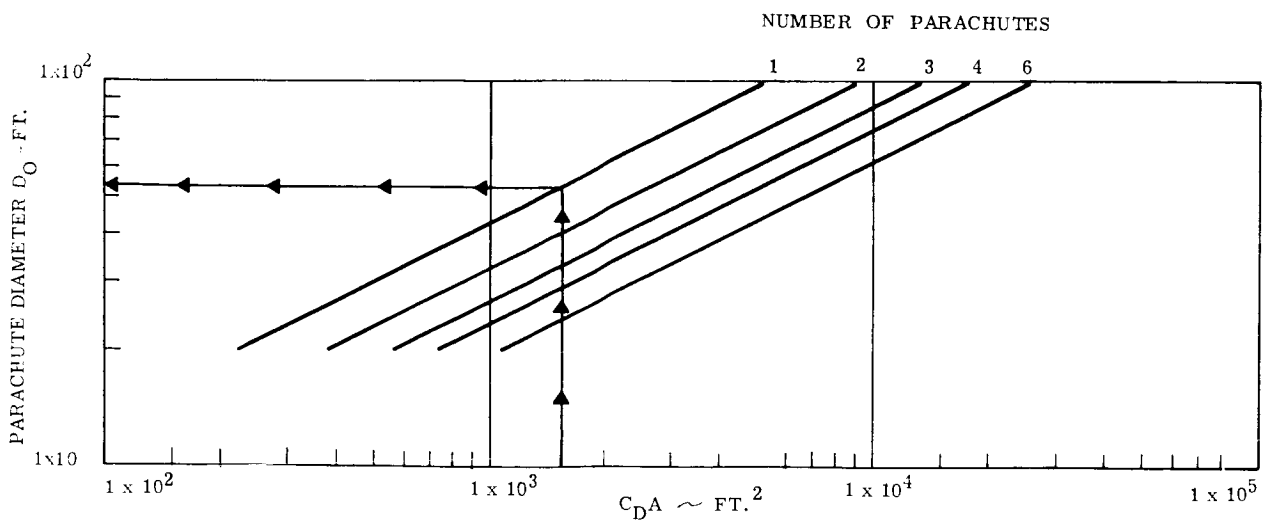


Figure 1.2.5-14 Drag Area of Main Descent Parachute(s)

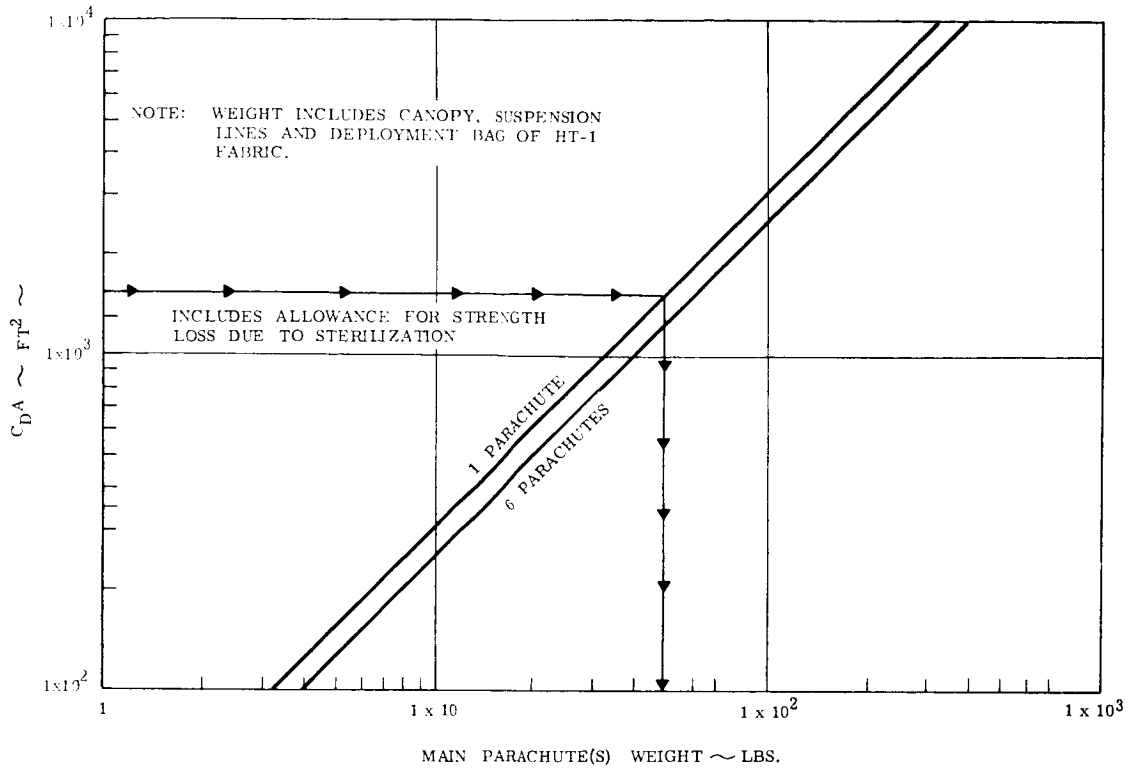


Figure 1.2.5-15 Assembly Weight of Main Descent Parachute(s)

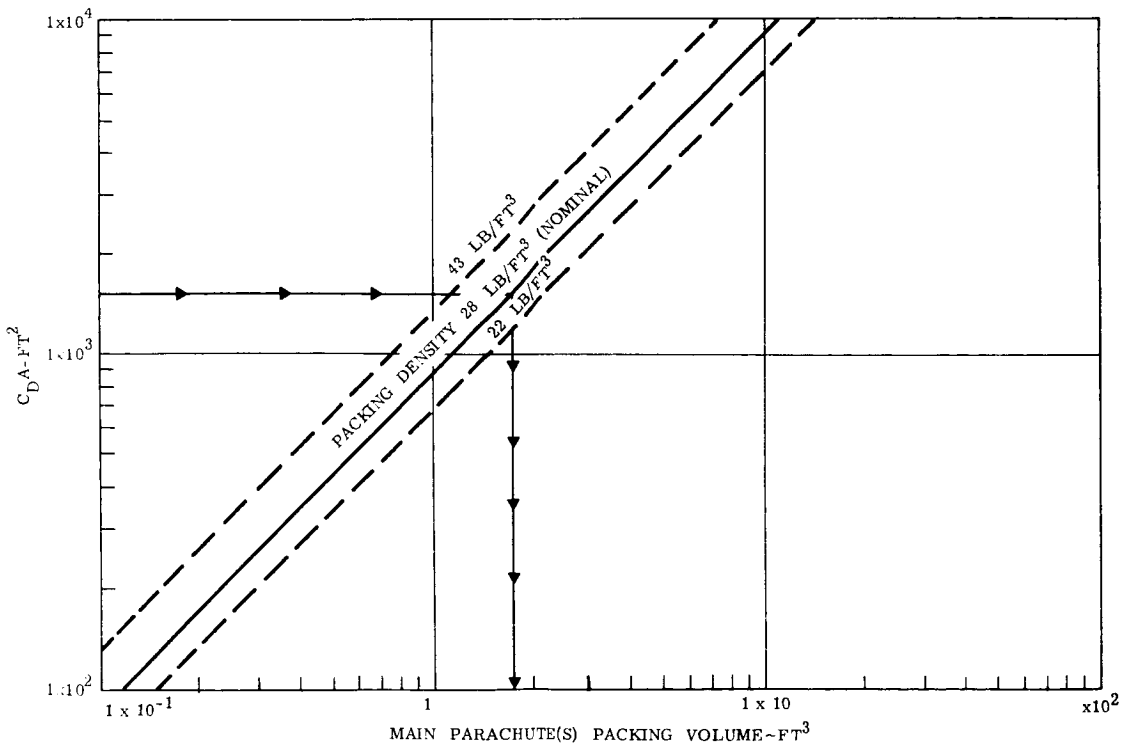


Figure 1.2.5-16 Packing Volume of Main Descent Parachute(s)

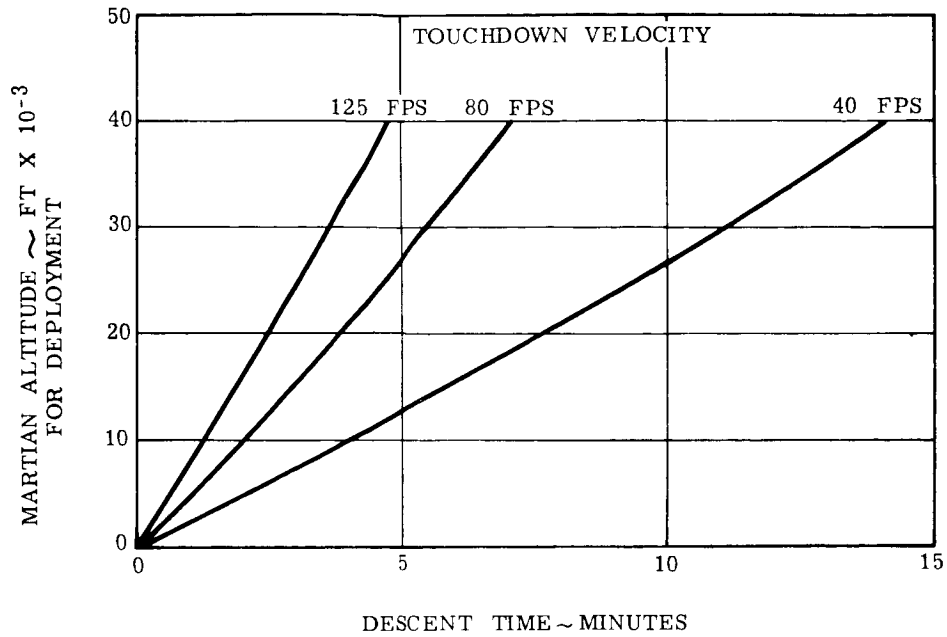


Figure 1.2.5-17 Descent Time as a Function of Deployment Altitude, 11 Millibar Atmosphere

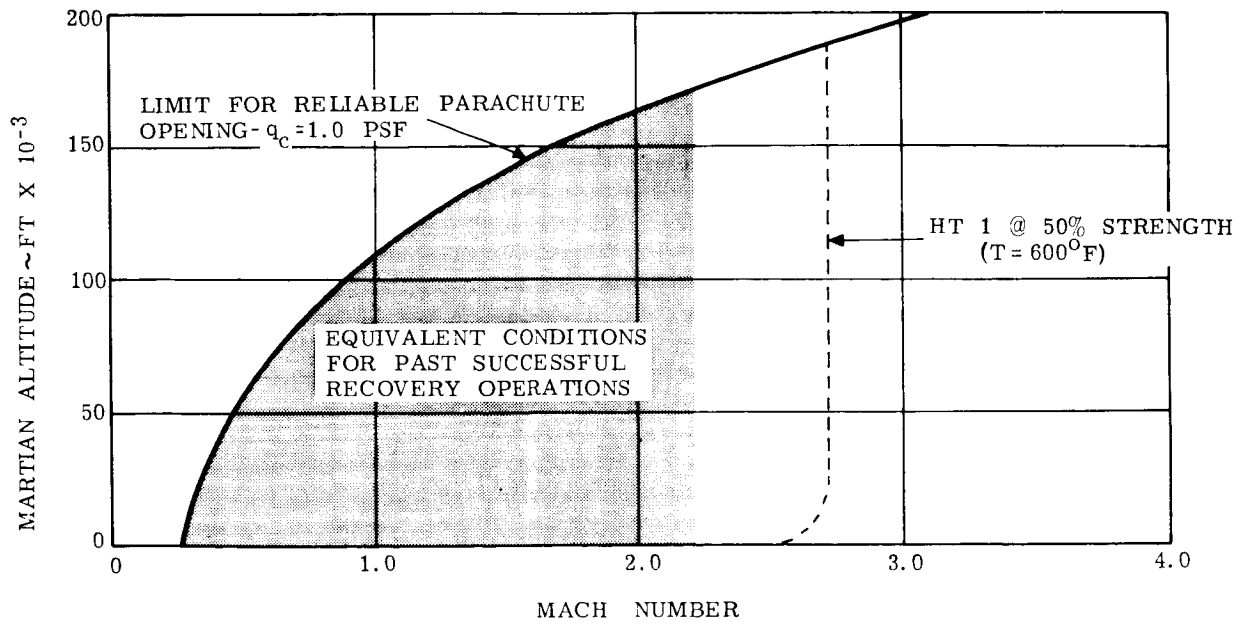


Figure 1.2.5-18 Decelerator Parachute State-of-the-art, Mars 11 Millibar Atmosphere

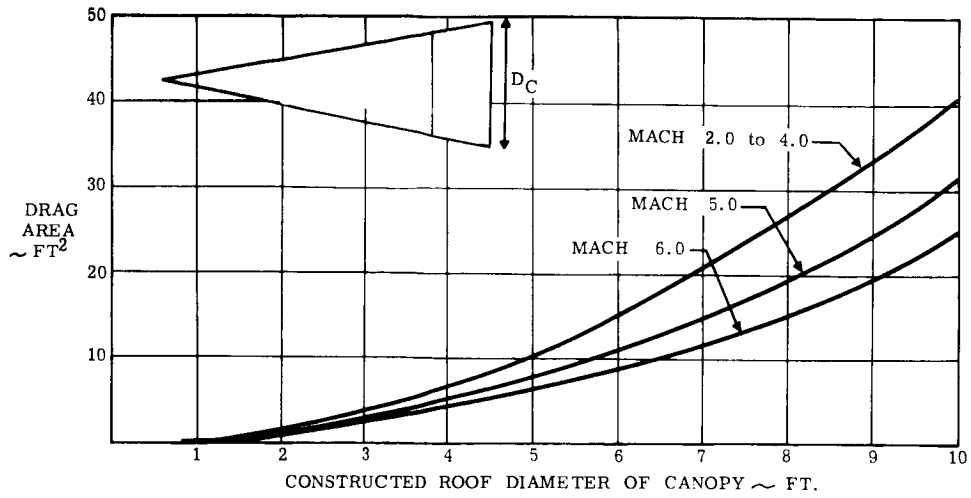


Figure 1.2.5-19 Drag Area of the Hyperflo Canopy as a Function of Constructed Diameter and Mach Number

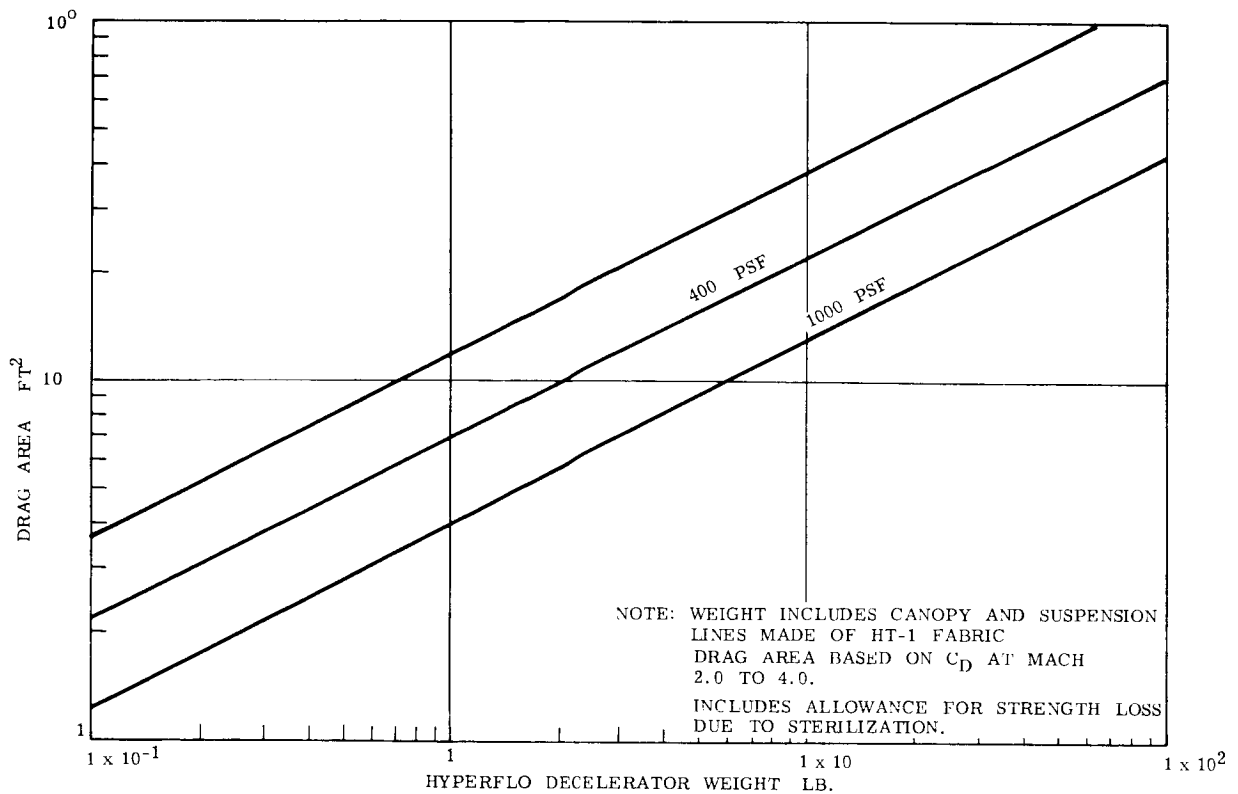


Figure 1.2.5-20 Estimated Assembly Weight of Hyperflo Decelerator Parachute(s)

RETARDATION SYSTEM WEIGHT ~ PERCENT
ENTRY VEHICLE WEIGHT

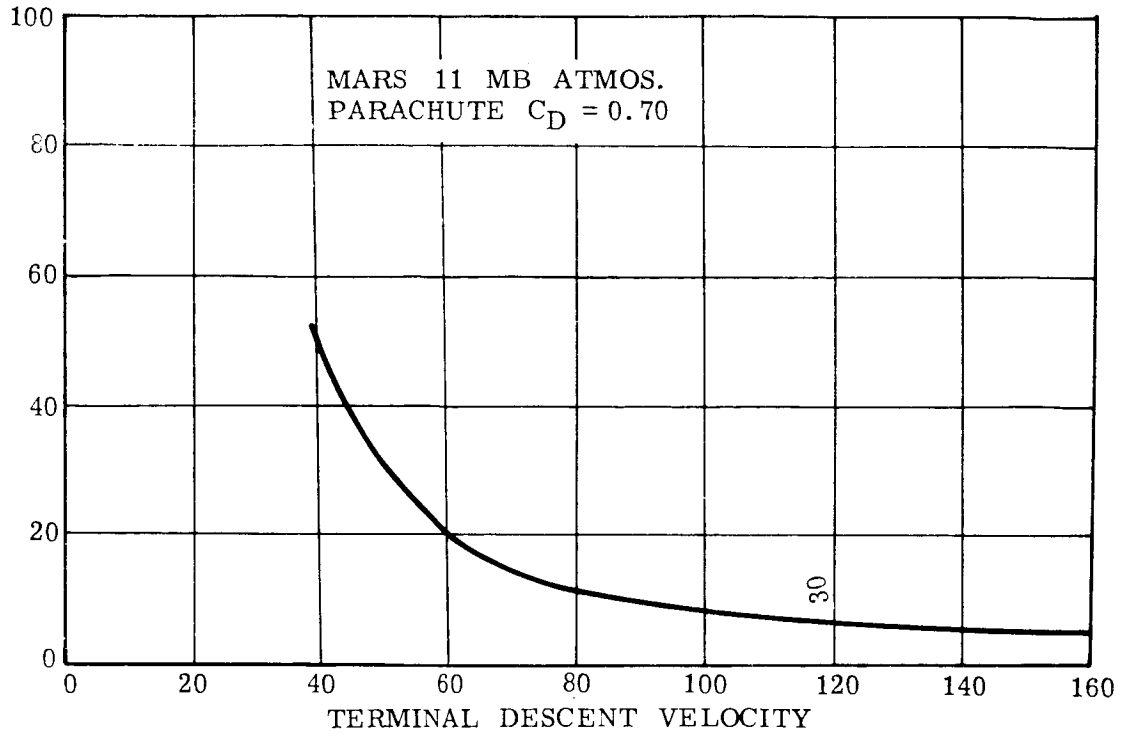


Figure 1.2.5-21 Percent Vehicle Entry Weight Necessary for the Retardation System

RETARDATION & CRUSHUP WEIGHT ~ LB.

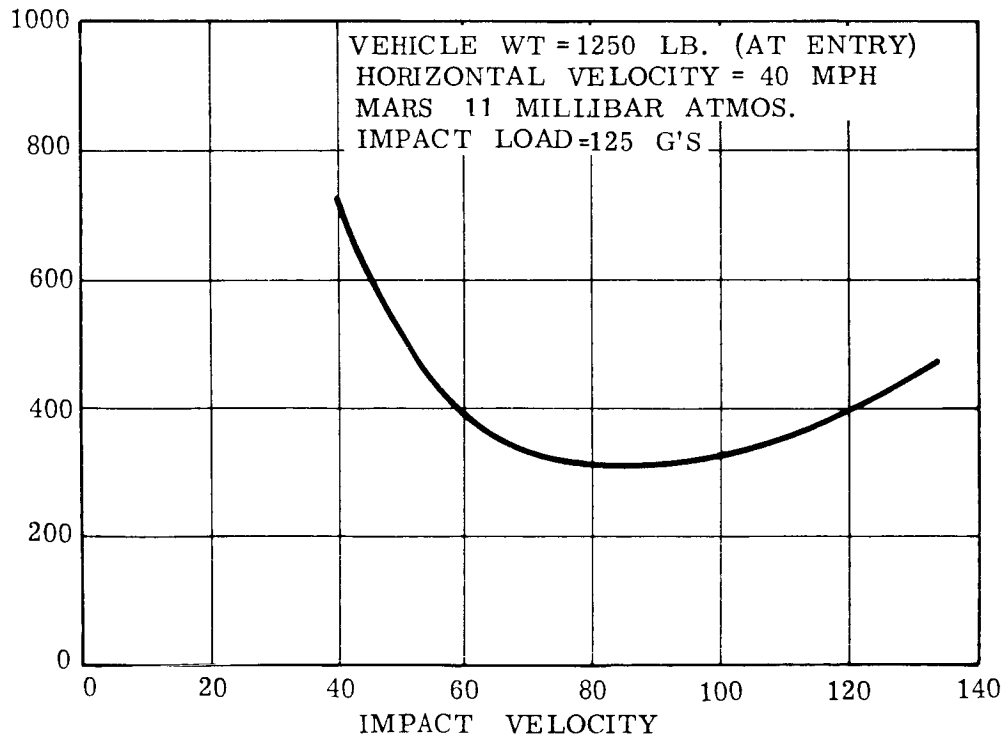


Figure 1.2.5-22 Optimization of Impact Velocity for Parachutes and Crush-up Landing System

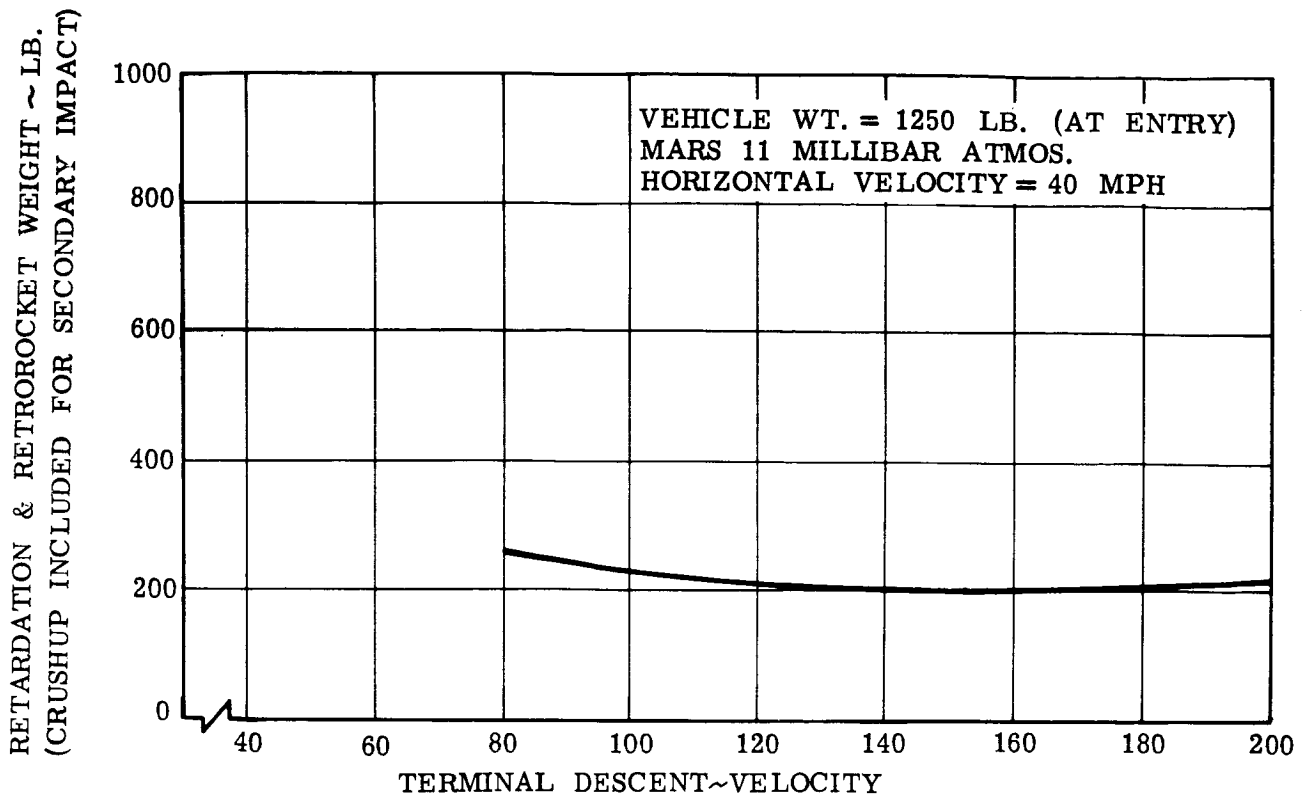


Figure 1.2.5-23 Optimization of Descent Velocity for Parachute-Retrorocket System

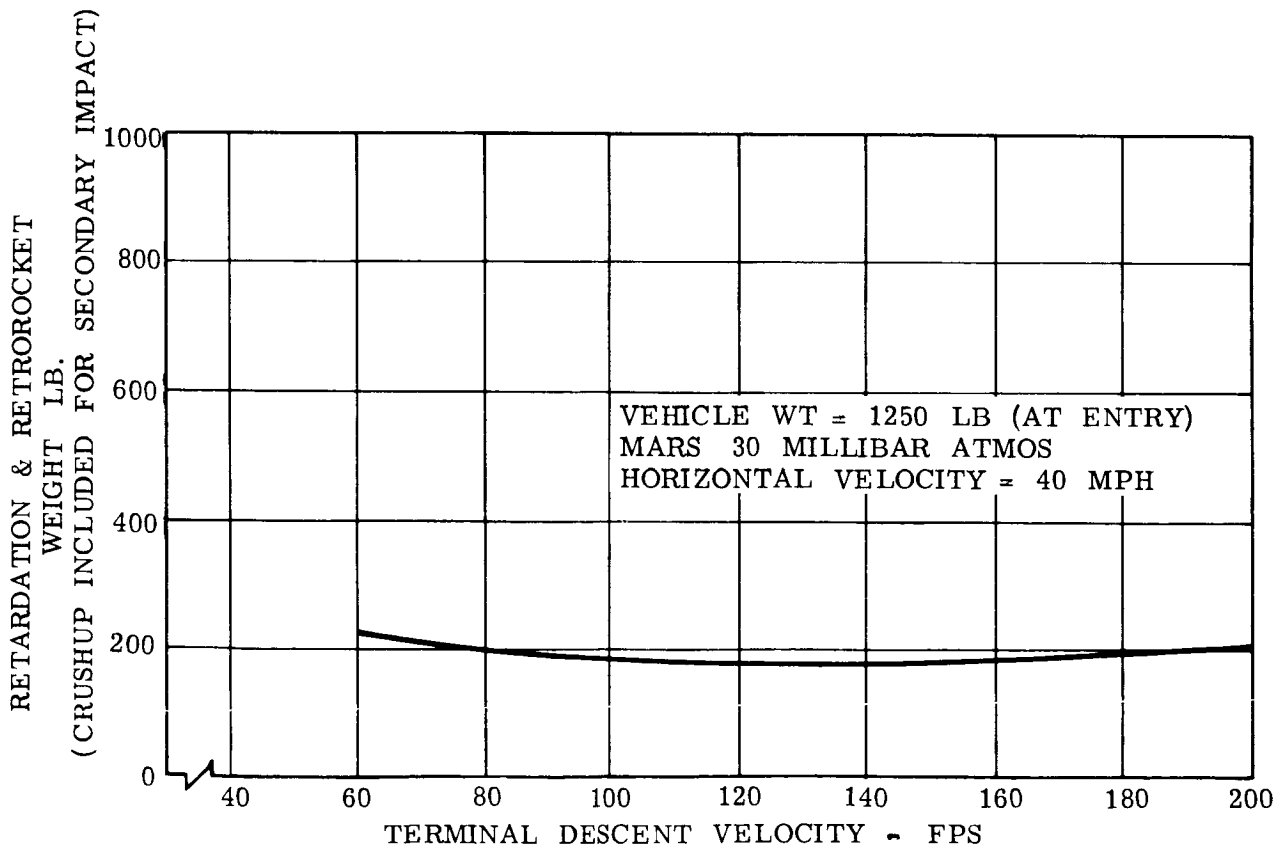


Figure 1.2.5-24 Optimization of Descent Velocity for Parachute-Retrorocket System

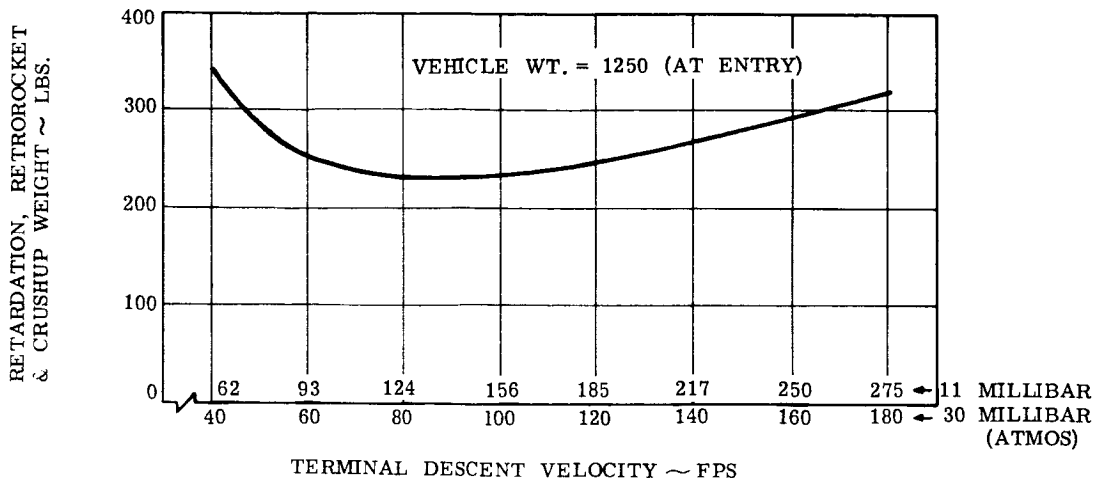


Figure 1.2.5-25 Optimization of Descent Velocity for Parachute-Retrorocket-Crushup Landing System...

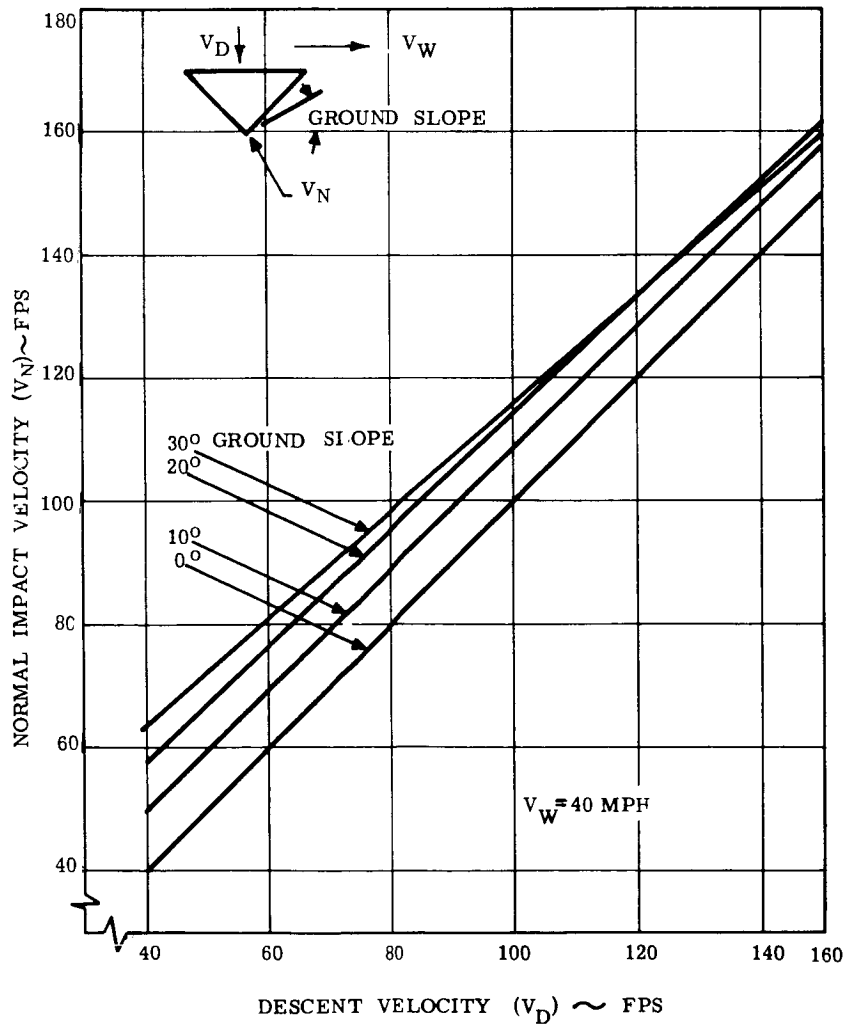


Figure 1.2.5-26 Normal Impact Velocity

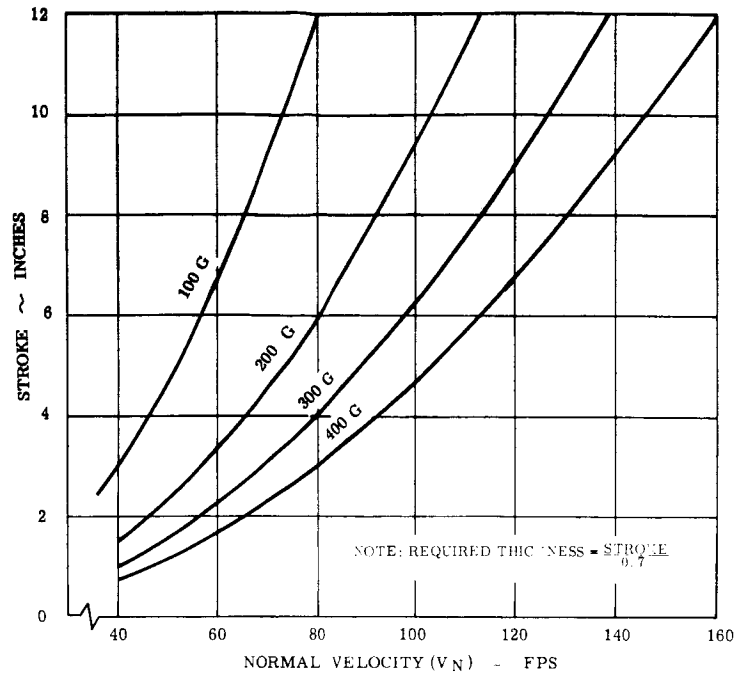


Figure 1.2.5-27 Required Stroke vs. Normal Velocity for Various Deceleration Rates

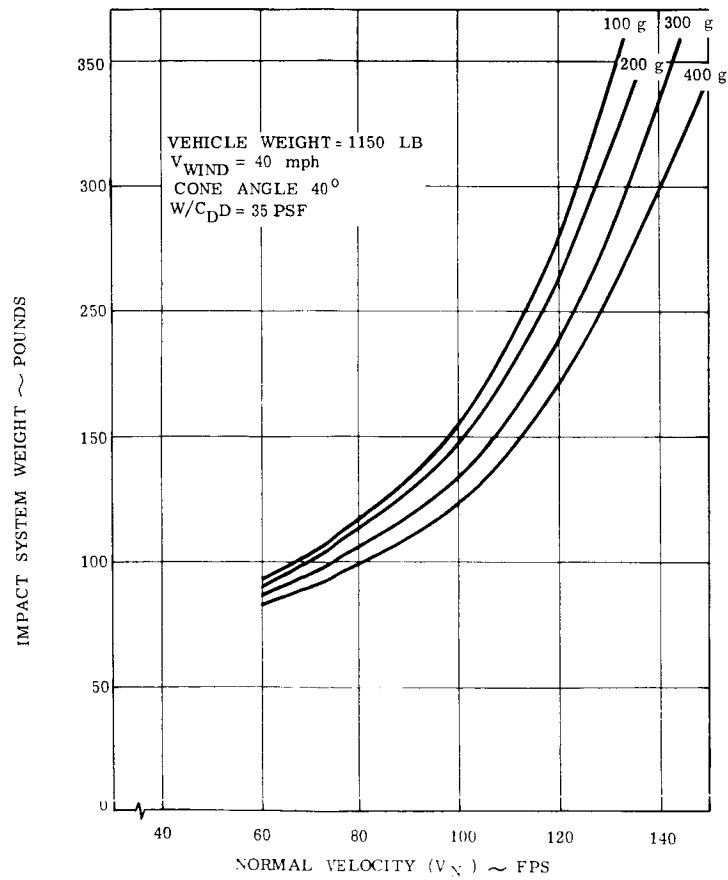


Figure 1.2.5-28 Shock Attenuation System Weight

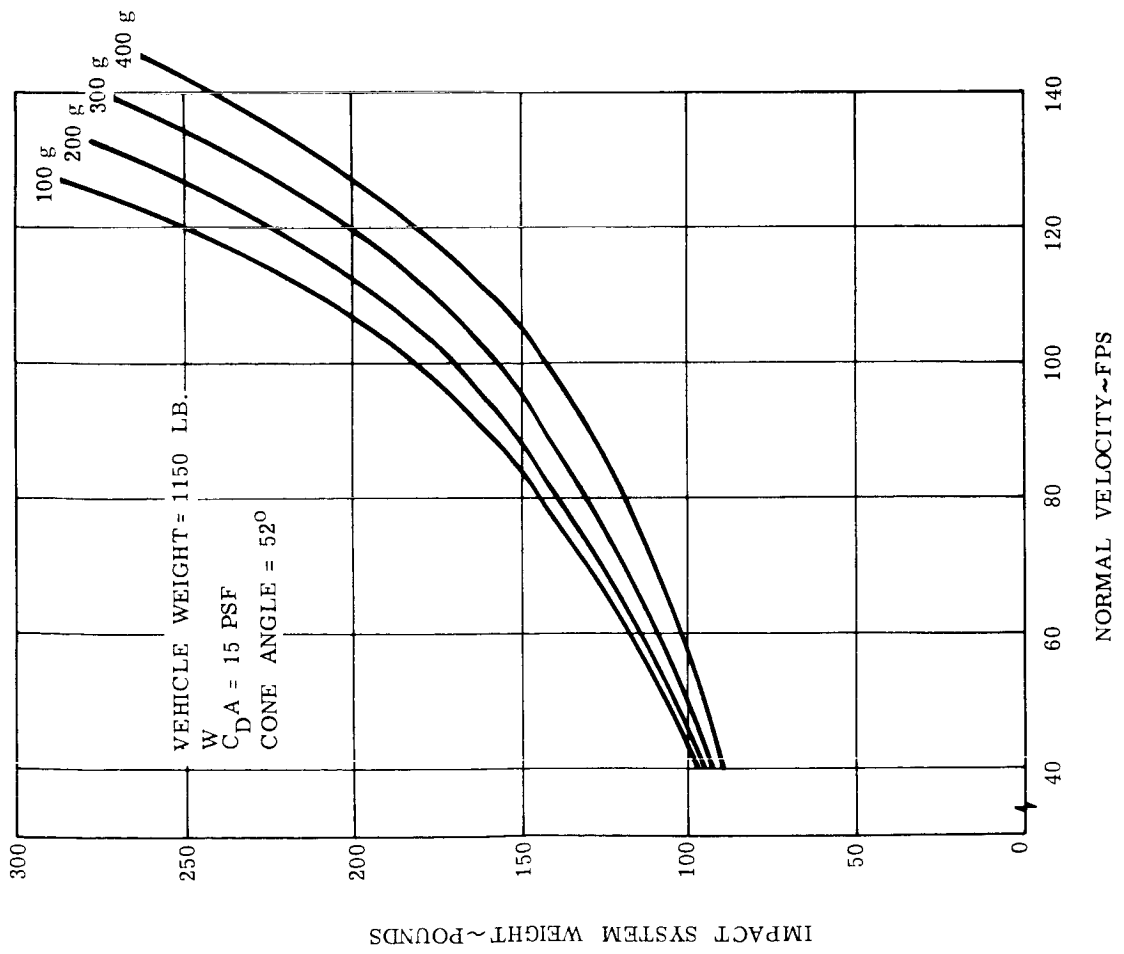


Figure 1.2.5-29 Shock Attenuation System Weight

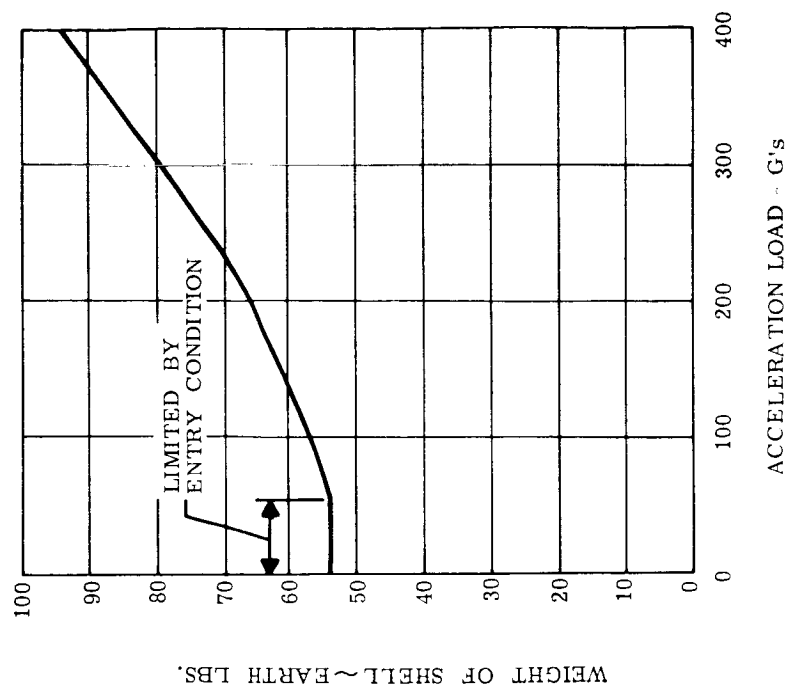


Figure 1.2.5-30 Shell Structure Weight Variation-Mars Lander

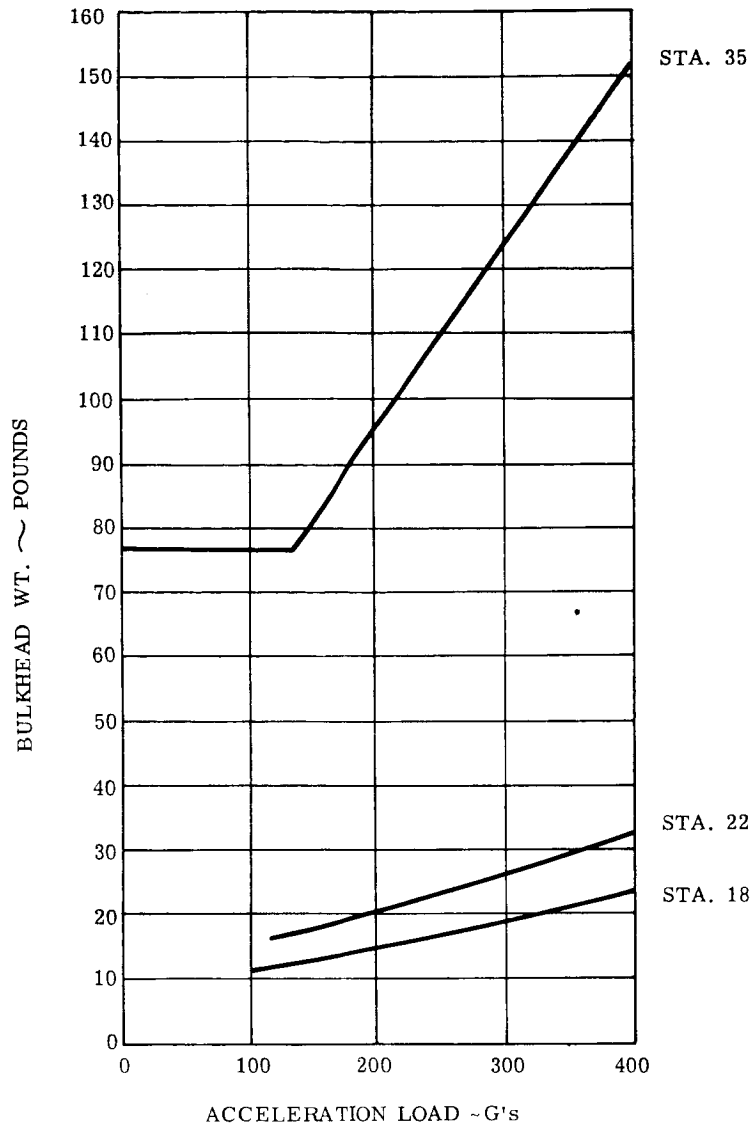


Figure 1.2.5-31 Bulkhead Weight Variation - Mars Lander

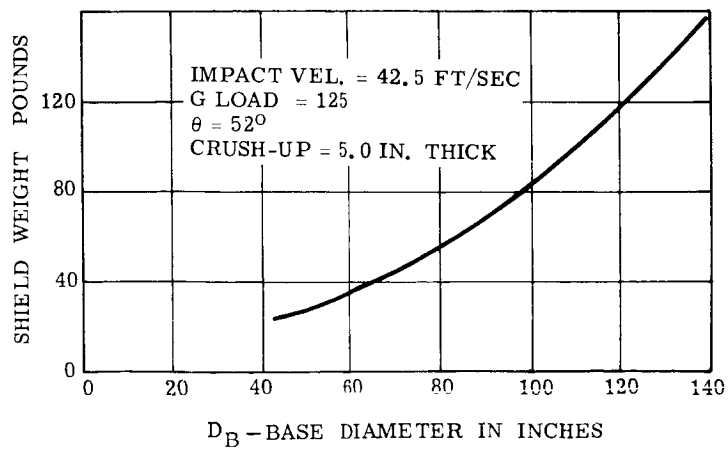


Figure 1.2.5-32 Shield Weight vs. Base Diameter

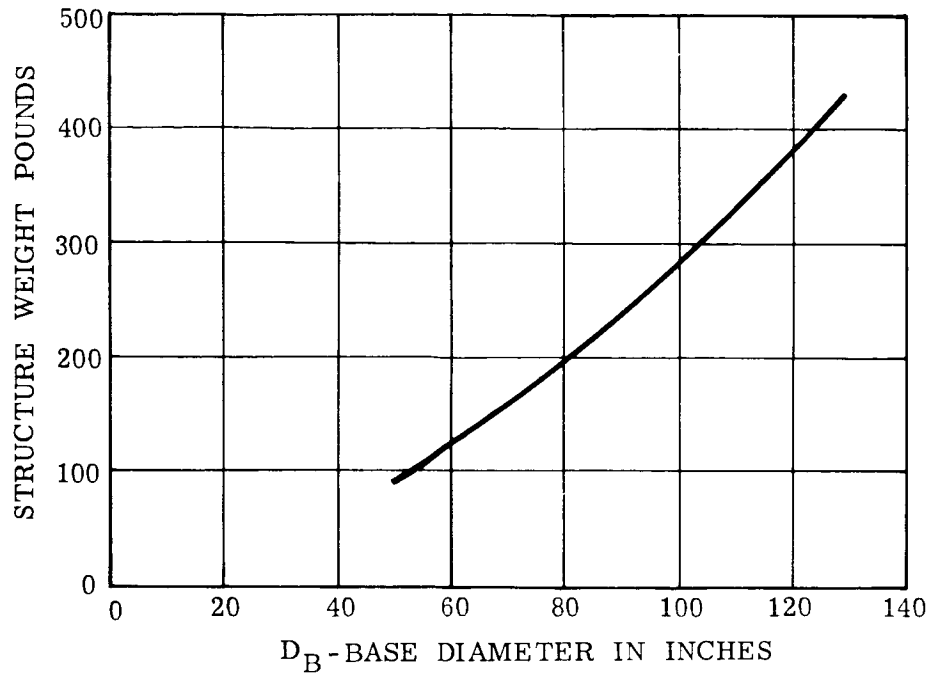


Figure 1.2.5-33 Structure Weight vs. Base Diameter

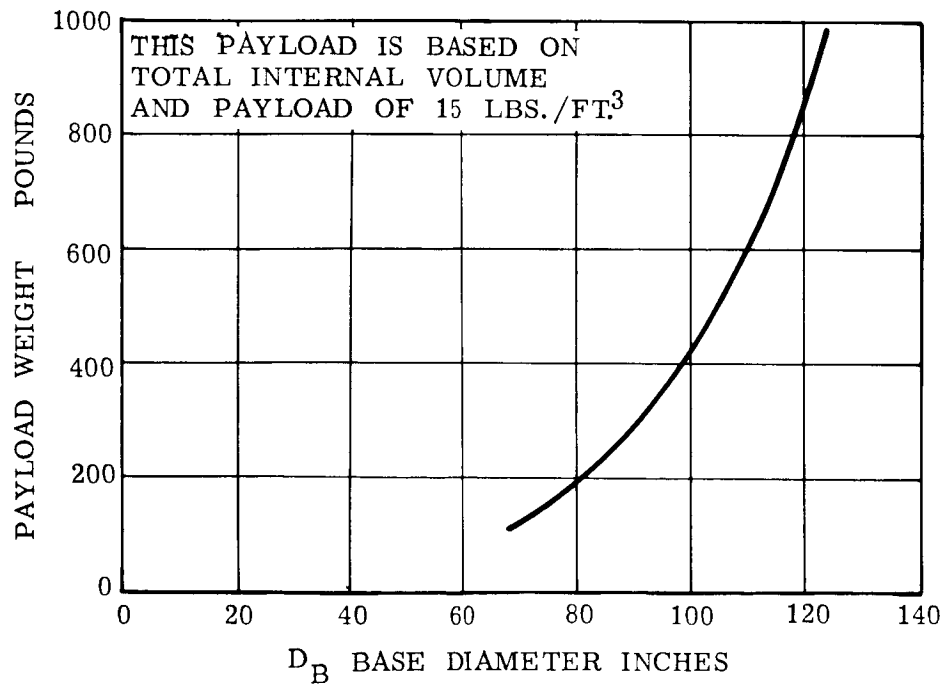


Figure 1.2.5-34 Payload Weight vs. Base Diameter

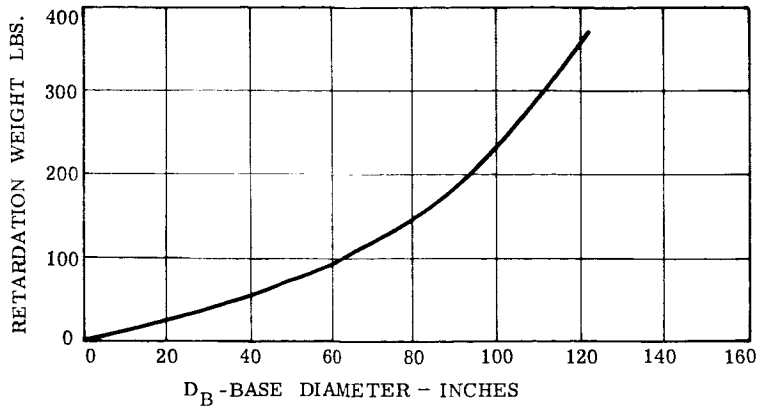


Figure 1.2.5-35 Retardation Weight vs. Base Diameter

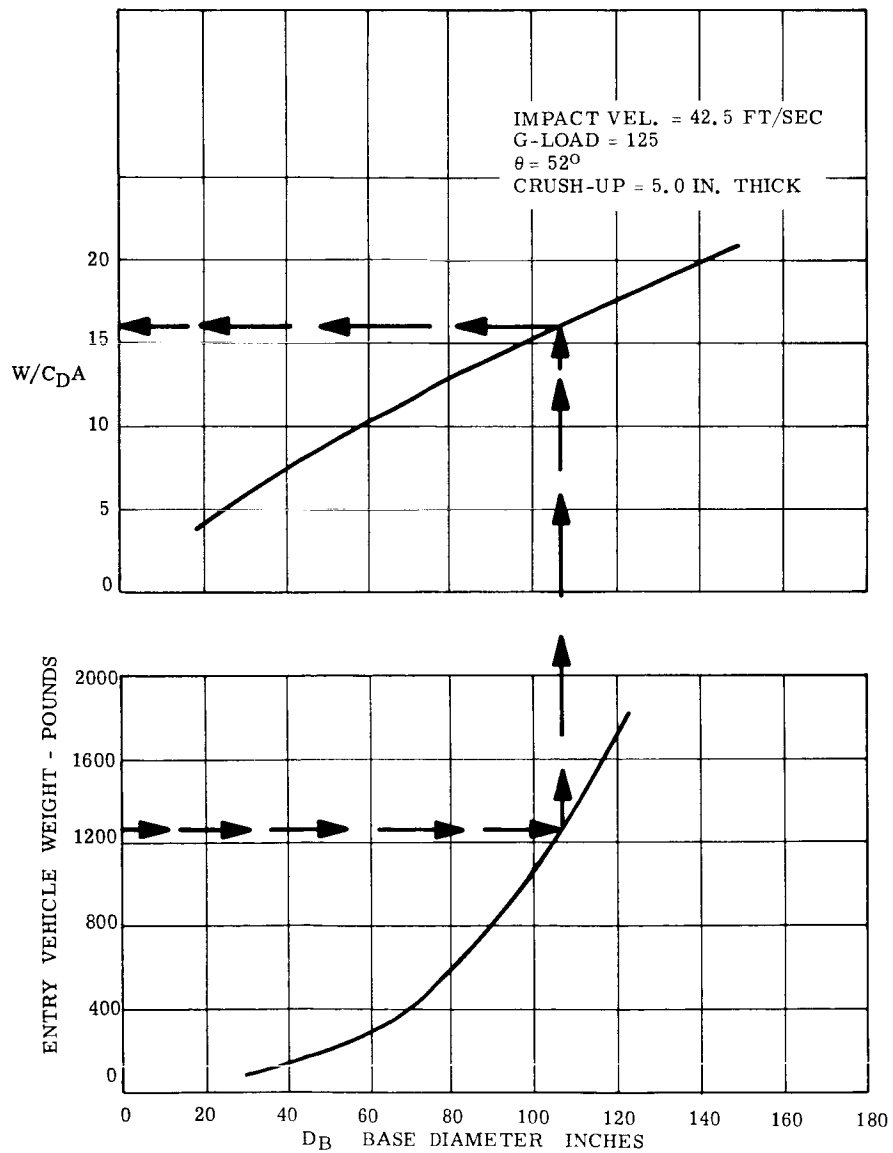


Figure 1.2.5-36 Ballistic Parameter and Entry Vehicle Weight vs. Base Diameter

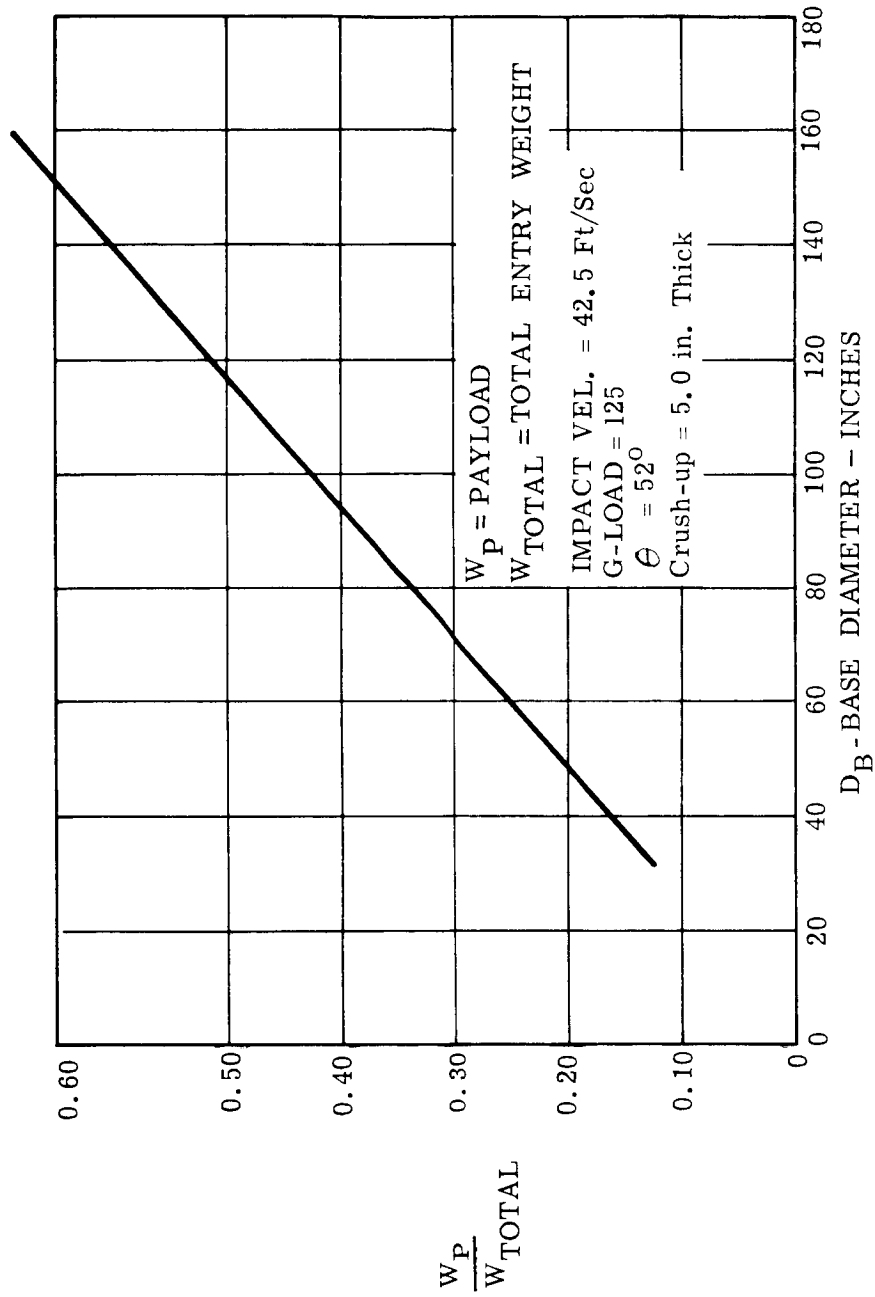


Figure 1.2.5-37 Payload Fraction vs. Base Diameter

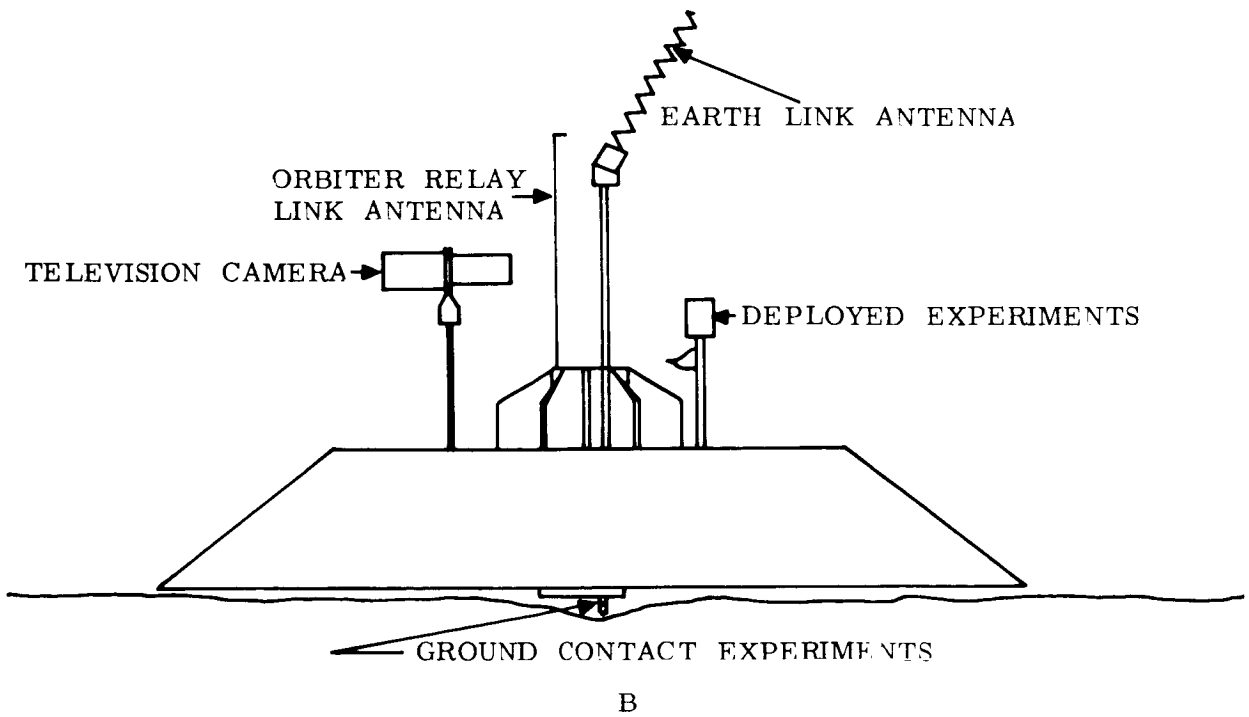
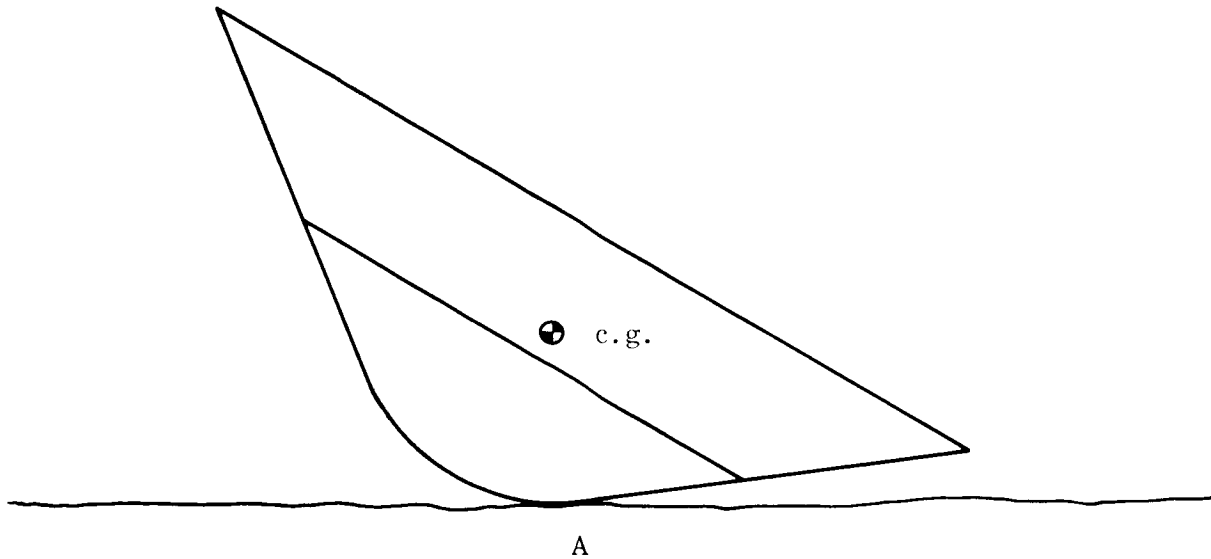


Figure 1.2.5-38 Sketches Depicting Side-Oriented (A) and Base-Oriented (B) High Drag Vehicle - Mars

1.3 ANALYSIS AND STUDY RESULTS

Detailed analyses have been conducted in the various technical disciplines relating to Lander technology. These analyses are presented by subject area to assist those primarily interested in specific disciplines. The effect of study parameters; such as, initial entry conditions, atmospheric models and configuration variables have been investigated. Subsystem designs have been developed and integrated into realistic conceptual Lander designs. In addition, subsystem results have been parametrically evaluated to indicate optimization trends.

1.3.1 CONFIGURATION MATRIX

A. General Classes of Configurations

In determining a range of configurations for detailed technological investigation, consideration must be given to mission requirements, planetary entry environment, and potential design confidence. Mission requirements include impact survival and sufficient payload capability to perform the desired experiments and communicate the resulting data. The low density Mars atmosphere provides severe retardation problems, while the Venus entry environment is characterized by high decelerations and thermal loads. Design confidence must be evaluated in terms of projected state-of-the-art based on the Voyager timetable. Several general classes of configurations have potential planetary entry capability.

(1) Lifting Configurations

A lifting entry body can provide corridor modulation to reduce the severity of the Venusian entry loads and heating on the vehicle. If sufficient lift/drag ratio is available, the possible impact points can be expanded into "footprints" containing horizontal and lateral range capability. The Martian retardation problem can be eased by utilizing vehicle lift capability to reduce the vertical descent rate at the expense of increased horizontal velocity. While the lifting body can reduce the severity of the entry and increase vehicle performance, it requires a sophisticated guidance and control system to accomplish these benefits. As indicated by trajectory analyses, the entry corridor to provide extensive load or thermal reduction is extremely limited. Theoretical techniques are greatly increased in complexity when dealing with lifting bodies, other than those with simple center of gravity offsets. Combining these factors with lack of flight test experience, lower design confidence must be assigned this class of configuration.

Lifting bodies are still several years away from extensive hardware application for Earth re-entry. Projecting the state-of-the-art, it appears that adequate lifting entry technology will not be available for initial Voyager flights in 1969. During the later part of the Voyager schedule, that is during the mid-seventies, lifting vehicles may be more feasible. They provide excellent growth capability into later manned systems, or systems that include more g-sensitive equipment.

(2) Modified Drag Configurations

A configuration which includes drag modulation capability can reduce the severity of the entry loads and peak heating and also ease the retardation problem. Drag modulation can vary from continuous modulation to a simple one step drag change. The variation in drag has the effect of spreading the entry loads and heating over a longer period of the entry time cycle and thus reducing the peaks. The ability to provide increased drag over a portion of the trajectory aids the vehicle retardation.

Trajectory analysis indicates that continuous modulation is required to obtain significant reduction in the severity of the entry. This dictates the use of a rapid sensing and actuating system. Since the atmosphere of the two planets is unknown, it appears that not

only the magnitude of the deceleration but its rate of change is needed to adequately modulate the drag. To obtain sufficient drag area, large and heavy actuators must be utilized. The increased weight and reduced reliability of such a system tend to overshadow possible advantages. Lack of flight test experience with this type of configuration also leads to lack of design confidence. One-step drag modulation is considered in more detail under Retardation Analysis (Section 1.3.5).

(3) Ballistic Configurations

The highest design confidence can be placed in axisymmetric ballistic configurations based on extensive Earth re-entry capability. Ballistic entry vehicles can survive the planetary entry environments with adequate variation of configuration geometry and ballistic parameter. For early Voyager applications ballistic entry vehicles provide the most realistic class of configurations because of their basic simplicity and passive nature.

B. Sphere Cone Selection

Within the general class of flight tested ballistic configurations are sphere-cones and sphere-cone-cylinder-flares. Possible adverse aerodynamic stability effects on the flared shapes, due to atmospheric CO₂ content, and overall higher design confidence dictate the choice of sphere-cones. Limits of the sphere-cone configurations can vary from sharp-pointed cones to very blunt segmented spheres. Both of these extremes are worthy of comment for specific applications.

Pointed sphere cones, which maintain an attached bow shock wave, have been suggested by Allen of NASA Ames as desirable, if not the required, entry shapes when the heating due to radiation becomes dominant. For Venusian entry velocities up to 40,000 f.p.s., radiative heating may become a significant (but not dominant) factor particularly at steep entry angles. The lower drag of these pointed bodies tends to increase the ballistic coefficient which increases the severity of the entry. In view of the problems in maintaining a pointed nose, in addition to the fact the most severe Venusian entry conditions are just approaching the range where extremely high radiative heating is observed, the pointed sphere-cones do not appear attractive for the Voyager mission.

Very blunt configurations, such as the Apollo type, are also of interest particularly for Mars entry. The high drag shapes lower the ballistic coefficient so that the retardation problem is eased. However, they also present large areas with near stagnation values of loads and heating. Perhaps the largest question mark on these shapes is their dynamic characteristics and the resultant capability to converge to near zero angle of attack during regions of high loads and heating. During initial portions of the entry while the dynamic pressure is increasing, density damping will occur. When the dynamic pressure rises to significant values, the aerodynamic characteristics of the configuration will influence oscillation convergence. After peak dynamic pressure any aerodynamic instability will be even more pronounced. While some differences in test data exist concerning the exact value of aerodynamic damping ($C_{m\dot{q}} + C_{m\dot{\alpha}}$) for these shapes at high Mach numbers, they at best have near zero damping for small angles of attack. Combining this with extremely small or even negative values of $C_L \alpha$, the dynamic stability factor $[C_D - C_L \dot{\alpha} + (C_{m\dot{q}} + C_{m\dot{\alpha}}) (\frac{L}{\dot{\sigma}})^2]$ will be positive for these high drag shapes indicating dynamic instability. While the situation may improve at higher angles of attack, six-degree-of-freedom trajectories have shown with relatively small initial pitch rates ($q < 10^\circ/\text{sec}$), high angles of attack or even tumbling can occur well into the entry trajectory even with reasonable spin rates. In view of the existing uncertainties in the Voyager mission (i.e. atmosphere, possible Lander orientation at initial entry etc.), it is felt that unless absolutely necessary for accomplishment of mission requirements, very blunt segmented sphere shapes should be avoided.

This process of elimination leaves a rather broad family of blunted sphere-cone configurations for possible lander configurations. It is proposed to investigate this family of blunted sphere-cones by parametrically varying bluntness ratio and cone angle to determine near optimum configurations providing maximum payload capability. (See tabulation below)

CONFIGURATION ANALYSIS PARAMETERS

$\frac{R_N}{R_B}$	0.25, 0.60, 0.90
θ_c	20°, 30°, 40°
Wt	300, 1500, 2500 lbs (Nominal D = 3.5, 8.0, 10.5 Ft)
$W/C_D A$	20, 40, 60 psf
λ_e	Capture to 90°
V_e Mars:	14,500 to 25,000 ft/sec.
V_e Venus:	32,000 to 40,000 ft/sec.
Atmospheres - Mars:	Upper, Mean, Lower
Venus:	Standard, Extreme

The lower end of the bluntness ratio and cone angle range has been limited to 0.25 and 20 degrees respectively to provide sufficient drag to prevent the ballistic coefficient from becoming too large. The higher end of the range, 0.90 and 40 degrees, is felt to approach the dynamic stability limit for very blunt configurations. The exact dynamic characteristics of these shapes can only be determined by a comprehensive wind tunnel program since analytical techniques are not presently sufficiently accurate. Higher cone angles are less desirable for Venusian configurations in view of the potentially high radiative heating. Some consideration has been given 50 degree cone angles for Martian application.

When combined with the hypersonic drag coefficients, resulting from the configuration matrix, a range of ballistic parameters, ($\frac{W}{C_D A}$) obtained. Previous studies have shown a reasonable ballistic parameter range of interest is from 20 to 60 psf.

This family of configurations will be investigated over a parametric range of entry conditions to determine near optimum configurations and their payload capability.

DEFINITION OF SYMBOLS

A	reference area, ft ²		
A _N	normal acceleration, Earth g's		
A _{Np}	normal acceleration due to pitching, Earth g's		
A _X	axial deceleration, Earth g's		
A _{Xp}	axial deceleration due to pitching, Earth g's		
C _D	aerodynamic drag coefficient, $\frac{D}{1/2 \rho V^2 A}$		
C _L	aerodynamic lift coefficient, $\frac{L}{1/2 \rho V^2 A}$		
C _N	aerodynamic normal force coefficient, $\frac{N}{1/2 \rho V^2 A}$		
C _M	aerodynamic moment coefficient, $\frac{M}{1/2 \rho V^2 A \ell}$		
(C _{Mq} + C _{Mq'})	dynamic damping coefficient, /rad		
C _{Mq}	aerodynamic moment coefficient due to pitching, /deg		
C _{Mq''}	aerodynamic moment coefficient due to angle of attack rate, /deg		
D	base diameter, inches		
F	aerodynamic drag force, lbs.		
d/h	down from horizontal		
G _{XMAX}	maximum axial deceleration, Earth g's		
h	altitude, ft.		
h _c	entry altitude, ft.		
I _X	roll moment of inertia, slug-ft ²		
I _Y	pitch moment of inertia, slug-ft ²		
I _Z	yaw moment of inertia, slug-ft ²		
I _{XY}	roll-pitch product of inertia, slug-ft ²		
I _{XZ}	roll-yaw product of inertia, slug-ft ²		
I _{YZ}	pitch-yaw product of inertia, slug-ft ²		
L	aerodynamic lift force, lbs.		
l	body length, reference length, ft.		
L/D	lift to drag ratio		
M	Mach number; aerodynamic moment, ft.-lbs.		
N	aerodynamic normal force, lbs.		
p	spin rate about roll axis, rpm		
q ₀	initial pitch rate, rad/sec		
q	dynamic pressure, 1/2 ρ V ² , lbs/ft ² ; pitch rate, rad/sec		
Q̇	stagnation point heating rate, BTU/FT ² -Sec		
r ₀	initial yaw rate, rad/sec		
R _N /R _B	bluntness ratio		
R _B	base radius, inches		
R _N	nose radius, inches		
t	time, seconds		
V = V _T	total velocity, ft/sec		
V _l	velocity component along vehicle center line, ft/sec		
V _e	entry velocity, ft/sec		
W	weight, lbs.		
W/C _D A	ballistic parameter, lbs/ft ²		
α	angle of attack, deg		
δ	rate of angle of attack, deg/sec		
Δβ	lateral angular error, deg		
γ	entry angle measured positive down from horizontal at h _e , deg		
δ	total angle of attack, deg		
α	Euler angle, deg		
θ _c	semi cone angle, deg		
ρ	density, slugs/ft ³		
r	radius of gyration, ft		
τ	Euler angle, deg.		

1.3.2 AEROMECHANICS

A. Introduction

(1) Planet Characteristics

The planetary entry trajectory information presented herein is based on the following physical characteristics:

	<u>MARS</u>	<u>VENUS</u>
Radius	3392 km 11.128 x 10 ⁶ ft	6148 km 20.17 x 10 ⁶ ft
Surface Gravity	373 cm/sec ² 12.24 ft/sec ²	860 cm/sec ² 28.215 ft/sec ²
Oblateness	0	0

For this study, no winds were considered and the sensible atmosphere for both planets was assumed to extend one million feet from the surface of the planets.

(2) Model Atmospheres

Two model atmospheres were considered for Venus; Venus Standard and Venus Extreme. For Mars the three atmospheres used were designated Mean, Upper Limit, and Lower Limit to indicate the relative densities of the profiles. Since deceleration, aerodynamic heating, flight path, etc., depend mainly on the atmosphere encountered, and since so much of the detailed atmospheric information on Venus and Mars is fragmentary, several profiles are necessary for purposes of vehicle design. Although the absolute value of density at a particular altitude is uncertain, the density gradient which controls peak heating and axial loads is reasonably well defined.

Calculated trajectories use linear interpolation for speeds of sound between tabulated values, and logarithmic interpolation for density between tabulated values. Charts showing density, pressure, and temperature vs. altitude can be found in Section 1.1.

B. Preliminary Aerodynamics

Preliminary aerodynamic characteristics are presented for the matrix of configurations discussed in Section 1.3.1-B and illustrated in Figure 1.3.2-1. Nominal base diameters of 3.50, 8.00, and 10.50 feet are considered for each shape corresponding to nominal weight classes of 300, 1500, and 2500 pounds, respectively.

The variation of zero angle of attack drag coefficient with Mach number for continuum flow is presented in Figures 1.3.2-2 through 1.3.2-5 for cone semi-vertex angles of 20°, 30°, 40° and 50°. Characteristics of the three bluntness ratios under consideration are presented in each figure. Drag coefficient variations with altitude have been determined on the basis of a rarefied gas Knudsen number analogy with viscous considerations included for the more slender configurations. These altitude effects as referenced to the Earth's atmosphere are presented in Figures 1.3.2-6 through 1.3.2-9. The conversion to the appropriate Martian atmosphere has been made on the basis of a density ratio.

Hypersonic pressure distributions are presented in Figures 1.3.2-10 through 1.3.2-13 for the matrix of sphere-cone configurations. The base of the vehicle is indicated for each bluntness ratio in these figures.

For purposes of determining heat shield requirements, shock shapes for a typical vehicle have been determined for a range of Mach numbers. See Figure 1.3.2-14.

C. Point Mass Trajectories

(1) Matrix of Trajectories

A large number of point mass trajectories were examined to determine the effects of entry velocity, path angle, $W/C_D A$, and atmosphere. A preliminary matrix for Mars consisted of the following combinations:

$$V_e's = 21 \text{ K ft/sec}; 23 \text{ K ft/sec}; 25 \text{ K ft/sec}$$

$$\gamma_e's = 20^\circ, 30^\circ, 60^\circ, 90^\circ \text{ (down from horizontal)}$$

$$W/C_D A's = 20; 40; 60 \text{ lbs/ft}^2$$

Atmosphere = Upper, Lower, and Mean

For Venus the initial matrix contained the following:

$$V_e's = 32 \text{ K ft/sec}; 35 \text{ K ft/sec}; 38 \text{ K ft/sec}; 40 \text{ K ft/sec}$$

$$\gamma_e's = 15^\circ, 30^\circ, 90^\circ \text{ (down from horizontal)}$$

$$W/C_D A's = 20, 40, 60 \text{ lbs/ft}^2$$

Atmosphere = Standard and Extreme

These matrices yielded design information for thermal protection, structures, retardation, communications, etc. and showed trends which caused the V_e , γ_e , and $W/C_D A$ parameters to be expanded as the study developed. For example, velocities were extended down to 14,500 ft/sec (to simulate a de-orbit type entry) for Mars.

Trajectory parameters are presented in Figures 1.3.2-15 and 1.3.2-16 for a typical direct entry into the Mars Lower Atmosphere for entry conditions of:

$$\begin{array}{ll} V_e = 21,500 \text{ ft/sec} & h_e = 10^6 \text{ ft} \\ \gamma_e = 90^\circ \text{ down from horizontal} & W/C_D A = 35 \text{ lbs/ft}^2 \end{array}$$

The figures show that there is: a slight increase in velocity initially, due to the planet's gravitational force; negligible drag force at the higher altitudes. As the vehicle penetrates further the density increases rapidly and the resultant drag begins to decrease the velocity. The axial deceleration, A_x , varies directly as the product of the density (increasing) and the square of the velocity (decreasing). At some point, however, the velocity begins to decrease more rapidly than the density increases causing a maximum deceleration with subsequent decreasing deceleration. The stagnation point heating rate, \dot{Q} , was calculated for each trajectory as explained in Section 1.3.3 (Entry Heat Protection). Axial deceleration was explicitly calculated in the point mass trajectories by the expression $A_x = q C_D A/W$.

Any differences in trajectories, for the same $W/C_D A$, arising from different shapes were insignificant.

One interesting result not encompassed by linear theory was a slight variation of the magnitude of maximum g's with $W/C_D A$. This is especially evident in Figures 1.3.2-17 to 1.3.2-19 at the higher entry angles.

Linearization assumes a practically straight line trajectory and an exponential atmosphere, both of which are generally true for this study. It also assumes, however, a drag coefficient which varies only with Mach number. In this study each trajectory uses a drag coefficient which varies with altitude as well.

Figures 1.3.2-20 through 1.3.2-22 illustrate corresponding values of peak dynamic pressure as a function of $W/C_D A$ and path angle for the three Martian atmospheres.

For Venus, the $W/C_D A$ effect on maximum g's is shown for a nominal velocity of 38,000 fps. For the Venus Standard and Extreme atmospheres, see Figure 1.3.2-23. Like the case of Mars, the effect is more pronounced for the steeper path angles.

Peak axial deceleration vs. path angle, with atmosphere as a parameter, is presented for representative $W/C_D A$'s and velocities in Figures 1.3.2-24 through 1.3.2-28. From these plots, it can be seen that peak axial deceleration increases with increasing entry angle, is largest for the lower atmosphere, and decreases for higher $W/C_D A$'s.

For a constant $W/C_D A$ of 20 psf, the path angle/velocity effect is shown in Figure 1.3.2-29 and 1.3.2-30.

Some typical cross plots were made to obtain lines of constant peak g's vs. path angle and entry velocity. (See Figures 1.3.2-31 through 1.3.2-35.) These results can be used to determine a specific entry condition if it is desired to limit the peak deceleration loads. The altitude of occurrence of peak deceleration is shown in Figures 1.3.2-36 through 1.3.2-40.

Trajectory parameters for entry with the Venus Standard atmosphere are presented in Figures 1.3.2-41 and 1.3.2-42. For the Venus trajectory:

$$\begin{array}{ll} V_e = 38,000 \text{ ft/sec} & h_e = 10^6 \text{ ft} \\ \gamma_e = 90^\circ \text{ dfh} & W/C_D A = 20 \text{ lbs/ft}^2 \end{array}$$

Peak axial deceleration for the Venus Standard and Extreme atmospheres is shown vs. path angle, for an entry velocity of 32,000 fps and $W/C_D A$'s of 40 psf, in Figure 1.3.2-43. Peak axial deceleration is shown for an entry velocity of 38,000 fps and $W/C_D A$'s of 20, 40, and 60 psf in Figures 1.3.2-44 through 1.3.2-46. The altitudes at which maximum axial load occurs for $V_e = 32,000$ fps and a $W/C_D A$ of 40 psf is shown in Figure 1.3.2-47. Figures 1.3.2-48 through 1.3.2-50 shows the corresponding altitudes for an entry velocity of 38,000 fps and $W/C_D A$'s of 20, 40 and 60 psf.

The Venus atmospheric model is sufficiently dense near the surface so that, even for a direct entry, peak deceleration occurs at so high an altitude that terminal velocity is almost reached at 250,000 feet. Peak g's is approximately 325 Earth g's occurring at 315,000 feet. Below 300,000 feet the path angle rapidly approaches 90° down from horizontal and impact velocity is approximately 62 ft/sec. Some atmospheric effects for Venus can be noted by observing the velocity and altitude time histories presented in Figures 1.3.2-51 through 1.3.2-57. These are based on an entry velocity of 38,000 ft/sec. Some trends are:

- that total flying time is longer for entry into the Standard Atmosphere for comparable path angles and $W/C_D A$'s;
- that the differences in flying time between atmospheres decrease as the $W/C_D A$'s increase;
- that both atmospheres cause the vehicle to approach terminal velocity at relatively high altitudes.

The heating trends encountered during entry on both Mars and Venus are similar to Earth's, namely:

- a) $\dot{Q}_{\max.}$ increases as path angle becomes steeper
- b) $\dot{Q}_{\max.}$ increases as $W/C_D A$ increases
- c) $\dot{Q}_{\max.}$ occurs at lower altitudes as path angle increases
- d) $\dot{Q}_{\max.}$ occurs at lower altitudes as $W/C_D A$ increases

D. Complete Aerodynamics Characteristics

Estimated aerodynamics for a typical Mars configuration are presented. The configuration, Figure 1.3.2-58, is a sphere cone with a semi-vertex angle of 42° and bluntness ratio of 0.24. The base diameter is 86" with the nominal center of gravity location at 32.1 inches from the nose.

The estimated variations of zero angle of attack drag coefficient with Mach number and altitude are presented in Figures 1.3.2-59 and 1.3.2-60. The variation with Mach number, Figure 1.3.2-59, represents continuum flow or altitudes below 250,000 feet in the Martian lower atmospheric model. Altitude effects have been determined on the basis of a rarefied gas Knudsen number analogy.

$$C_D = C_{D_{\text{CONT}}} + \frac{K}{K+1} (C_{D_{\text{FM}}} - C_{D_{\text{CONT}}})$$

where

$$K = \frac{\lambda}{D}$$

K = Knudsen number

λ = Mean Free Path

D = Max. Diameter

CONT = Continuum

FM = Free Molecule

Skin friction effects, within the continuum flow regime, appear relatively small for this type configuration. Transition from continuum to free molecule flow occurs between 300,000 and 500,000 feet for the vehicle in the Martian lower atmospheric model. The limiting value of free molecule flow has been calculated by a digital program. All altitude effects have been referenced to Earth's atmosphere and converted to the Martian lower model on the basis of a density ratio.

Variation of axial force coefficient with angle of attack for various Mach numbers is shown in Figures 1.3.2-61 and 1.3.2-62. The hypersonic variation has been computed by a digital program based on modified Newtonian theory. The axial force coefficient at supersonic speeds has been assumed to vary with angle of attack similar to the hypersonic case. Subsonic and transonic axial force coefficient have been assumed constant for small ($\alpha < 20^\circ$) angles of attack. Altitude effects on axial force coefficient as a function of angle of attack are given in Figure 1.3.2-63. Rarefied gas effects were determined as discussed in previous paragraphs.

Normal force coefficient as a function of angle of attack for various Mach numbers is presented in Figure 1.3.2-64. Slope of the normal force coefficient for small angles of attack is given in Figure 1.3.2-65. The hypersonic value of normal force coefficient slope is based on modified Newtonian theory. The effect of altitude on the normal force coefficient variation with angle of attack is shown in Figure 1.3.2-66.

Figure 1.3.2-67 presents the variation of pitching moment coefficient with angle of attack for various Mach numbers in continuum flow about a nominal center of gravity location of 0.3740 (32.1 inches from the nose). The slope of the pitching moment coefficient for small angles of attack is given as a function of Mach number in Figure 1.3.2-68. Altitude effects on pitch moment coefficient, as based on the previously discussed Knudsen number analogy, is shown in Figure 1.3.2-69 as a function of angle of attack. In continuum flow, modified Newtonian theory predicts that the vehicle will have a positive pitching moment for angles of attack greater than 110° , resulting in a statically stable condition for a backward orientation. Consideration of altitude effects, however, indicates that this "backward stability" will not occur under rarefied gas conditions. Since the 6-degree of freedom trajectories of Section 1.3.2-C indicate that under certain entry conditions the continuum flow regime can be reached prior to significant vehicle pitch-over, it is recommended that entry angle of attack be restricted if possible.

Figure 1.3.2-70 shows that for small angles of attack the vehicle is statically stable through out the Mach number range for the nominal center of gravity location.

An estimate of dynamic damping as a function of Mach number is presented in Figure 1.3.2-71. The estimate is based on consideration of damping data of a blunt body (Mercury capsule) and a blunt-sphere-cone. Neutral damping at hypersonic speeds is felt to be a conservative estimate while the value at supersonic speeds is relatively unimportant due to the proposed parachute deployment at Mach 2.5, which would stabilize the vehicle below Mach 2.5. An estimate of dynamic damping of the vehicle at angle of attack is given in Figure 1.3.2-72. The important trend illustrated in this figure is that damping would occur at angle of attack.

E. Multiple Degree of Freedom

Point mass trajectory analysis assumed zero angle of attack; it yielded no information about lateral loads. In order to describe the motion of and about the vehicle's center of gravity and to determine some effects of system errors (say, guidance or separation) a few Martian entry trajectories with six-degrees of freedom were examined. These trajectories were based on a vehicle with $W/C_{DA} = 35$ psf and with the aerodynamic characteristics and shape described in Section 1.3.2 and a nominal velocity of 21,500 ft/sec. The study was limited to a Martian Lower atmosphere which would yield the worst aerodynamic decelerations. Initial conditions were:

$$\begin{aligned}
 V_e &= 21,500 \text{ ft/sec} \\
 \gamma_e' &= 20^\circ \text{ and } 90^\circ \text{ (down from horizontal) @ } h_e = 10^6 \text{ ft} \\
 \delta &= 90^\circ \\
 I_x &= 92.0 \text{ slugs ft}^2 \\
 I_y &= I_z = 106.0 \text{ slugs ft}^2 \\
 W &= 1160 \text{ Earth lbs} \\
 D_B &= 7.16 \text{ ft Base Diameter (reference length)} \\
 p &= 0, 40, \text{ and } 80 \text{ rpm} \\
 &\text{Zero c.g. offset, products of inertia, pitch and yaw rates} \\
 &\text{Mars Lower Atmosphere}
 \end{aligned}$$

Aerodynamic coefficients were used as a function of altitude and angle of attack as well as Mach number and angle of attack.

Figures 1.3.2-73 and 1.3.2-74 show significant parameters for a 90° entry with spin rate of 80 rpm. The figures show that the total angle of attack envelope remains practically constant until 330,000 feet due to the constant path angle and high spin which causes the vehicle to maintain a fixed orientation. As the aerodynamic forces increase they overcome this gyroscopic effect and cause the angle of attack to slowly converge to approximately 11° at 40,000 feet. It should be noted that there is no lower envelope indicating that the motion is circular, i. e., the vehicle center line cones around the velocity vector. At the altitude of $M = 2.5$ (22,500 feet) angle of attack has converged to 12.2° ; this is not excessive from a parachute deployment standpoint.

A_{N_p} (where A_N is the peak transverse loads) describes how the normal deceleration measured at the vehicle c. g. decreases for a point forward of the c. g. and increases for a point aft of the c. g. for a trajectory of this type. The transverse loads curve also has no lower envelope thus implying that the vehicle experiences sustained lateral load rather than pulsating lateral load.

The angle of attack referred to in the preceding paragraphs is the total angle of attack, δ , (always positive) which is defined as the angle between the vehicle center line and the relative velocity vector; it is body fixed. The normal (sometimes called lateral or transverse) loads refers to the resultant of the loads perpendicular to the vehicles center line. That is:

$$\delta = \arccos (V_1/V_T) \quad (0^\circ \text{ to } 180^\circ) \text{ for no winds}$$

$$A_N = \frac{q C_N A}{W}$$

Figure 1.3.2-75 compares the total angle of attack envelopes vs. altitude for spin rates of 80, 40, and 0 rpm, for entry into the Mars Lower atmosphere, and for path angle of 90° . In all cases, no atmospheric effect is felt above 400,000 feet but, as the vehicle descends, the angle of attack converges at a rate inversely proportional to the spin rate. Indeed, for a zero spin rate the vehicle starts to turn around above 375,000 feet and the total angle of attack starts oscillating between an upper and lower bound indicating the planarity of the motion. The 40 and 80 rpm cases indicate circular motion.

Figure 1.3.2-76 compares angle of attack altitude histories for a path angle of 20 and the same spin rate effect is observed. The initial increase in angle of attack for all cases is due to the change in path angle and inertial central angle while the vehicle is above the sensible atmosphere. This kinematic change allows the angle of attack to increase to between 92° and 93° before aerodynamic forces can overcome the tendency of the vehicle to remain inertially fixed in space for 40 and 80 rpm spin rates. As the restoring moment increases during descent the total angle of attack converges, as it did in the 90° path angle case.

The attitude of the vehicle at various critical points on the trajectory is a function of the entry conditions. Too large an angle of attack at lower altitudes could affect the performance of delicate instruments. The magnitude of angle of attack at a few key regions for an entry into Mars lower atmosphere with an initial angle of attack of 90° appear in the following table.

TOTAL ANGLE OF ATTACK AT KEY EVENTS

EVENT	$\gamma_e = 90^\circ$ dfh			$\gamma_e = 20^\circ$ dfh		
	p = 80 rpm	p = 40 rpm	p = 0 rpm	p = 80 rpm	p = 40 rpm	p = 0 rpm
Q_{\max}	23°	16°	$0-10.1^\circ$	38.7°	24.6°	$0-8.5^\circ$
$A_{N_{\max}}$	16°	12°	$0-8.3^\circ$	29.7°	21.0°	$0-7.7^\circ$
$A_{X_{\max}}$	14.2°	11.2°	$0-8.3^\circ$	22.2°	15.0°	$0-7.3^\circ$
M = 2.5	12.2°	10.6°	$0-12^\circ$	13.7°	11.5°	$0-10.3^\circ$

Maximum normal loads which vary directly with entry angle of attack and path angle are tabulated in the following table. Since this study was limited to one angle of attack of 90° the maximum normal loads vary with spin rate which affects the convergence of angle of attack.

Also peak axial deceleration varies inversely as entry angle of attack and directly as the path angle. The axial deceleration due to pitch A_{xp} varies as the sum of the squares of the pitch and yaw rates. The transverse rates do not have maximum amplitude at the altitude of occurrence of peak g's but are included below to show order of magnitude and trends. Units of A_{xp} are Earth g's/ft causing a decrease in A_x for points forward of the c.g. and an increase for points aft of the c.g.

MAXIMUM LOADS

LOADS	$\gamma_e = 90^\circ$ dfh			$\gamma_e = 20^\circ$ dfh		
	p = 80 rpm	p = 40 rpm	p = 0 rpm	p = 80 rpm	p = 40 rpm	p = 0 rpm
Max A_x	95	96.2	99.2	14.1	14.1	14.7
A_{xp} at Max A_x	3.5	2.4	1.5	1.0	.6	.2
Max A_N	28.7	23.	17.3	7.1	4.8	2.3
Max A_{N_p}	14.5	12.7	10.2	2.7	2.3	1.3

In general, the altitude of occurrence of peak axial deceleration, Mach 2.5, etc. agreed with those altitudes calculated on a corresponding point mass trajectory with the same velocity, path angle, and $W/C_D A$.

Figure 1.3.2-77 displays the total angle of attack envelope resulting from the same initial conditions of 21,500 ft/sec; $\gamma = 90^\circ$, p = 40 rpm but includes a mass asymmetry and c.g. offset. A c.g. offset of 0.1 inches and a product of inertia (I_{xp}) equal to 1% of the pitch moment of inertia was deemed reasonable. It is seen that at the higher altitudes the upper and lower envelope are wider apart than at the lower altitudes indicating that the change in angle of attack is due to precessional-type motion uninhibited by aerodynamic forces. As the vehicle penetrates more deeply the difference between upper and lower envelope decreases.

The parameter A_{xp} , axial deceleration due to pitch, does not appear to present a problem for the trajectories investigated for this report, Maximum A_{xp} occurs at altitudes above any critical g-sensing altitude and A_{xp} decreases as the M = 2.5 altitude is approached. An altitude history comparison for a symmetric and asymmetric vehicle appears in Figure 1.3.2-78 where it is seen that the vehicle with a c.g. offset and product of inertia gives higher A_{xp} .

The pitching frequency (f) as a function of altitude is shown in Figure 1.3.2-79 for a typical trajectory and is seen to reach a maximum of 7.8 cycles per second in the neighborhood of $\max A_x$, 80,000 feet. At 20,000 feet the frequency has decreased to 2 cps. Also shown is the upper envelope of pitch rate (\dot{q}), which exceeds $535^\circ/\text{sec}$ in absolute value in the neighborhood of 100,000 feet. Because of roll rate the same type plot would represent yaw rate. It should be noted that these rates result from a trajectory which assumes no initial transverse rates.

F. Capture Analysis (Method and Parametric Results)

Theoretically, to trap a ballistic interplanetary vehicle in the planetary gravitational field, the vehicle must experience enough atmospheric braking to remove the hyperbolic excess velocity. In order to accomplish this braking, the vehicle must enter the planetary atmosphere at an entry path angle greater than the capture path angle. This "capture angle" is defined as the path angle at entry above which the trajectory would have a monotonic decreasing altitude history.

As the altitude, velocity and W/C_{DA} increase, and the atmospheric density decreases, a vehicle would tend to escape or skip. A matrix of high altitude trajectories were calculated starting at 1,000,000 feet with variable velocities, W/CDA 's, and atmospheres. The trends of these results appear in Figures 1.3.2-80 through 1.3.2-82. The effect of W/CDA on capture for Venus is smaller than that for Mars since the more rapidly increasing atmosphere during descent causes a rapid drag build up. The smallest capture angle for Mars for this study is approximately 15° , occurring for the Mars Upper atmosphere, $W/CDA = 20$ psf, and $V = 21,000$ ft/sec; the largest was approximately 19.5° , occurring for the Mars Lower atmosphere, $W/CDA = 60$ psf, and $V = 25,000$ ft/sec.

Since there are many uncertainties in the planetary atmospheres it is considered unwise to design a vehicle to enter too near capture, since at this point the total integrated heating is prohibitively large and since a guidance error could result in an "undershoot" causing the vehicle to escape.

Significant trajectory parameters for a minimum capture trajectory appear in Figures 1.3.2-83 and 1.3.2-84. It is readily apparent that the descent rate is very small between 50 and 300 seconds. The heating rate (Q) while not having a particularly large maximum value does have a long duration resulting in very high integrated aerodynamic heating. The double peaks in dynamic pressure (q), and axial deceleration (A_x), is caused by the different rates of increasing density and decreasing velocity in this region.

It should be recalled that the capture angle values given are based on the assumption of zero angle of attack. Should the vehicle enter with an angle of attack the effective drag coefficient would increase, the integrated $W/C_D A$ decrease, and the tendency to escape would decrease.

G. Modulated Drag

The reduction in peak load during entry to Mars and Venus by drag modulation was investigated. Both single stage drag change and perfect drag modulation were studied. It should be noted that this study was made using the Mars A and C atmospheres and the Venus Extreme I atmosphere. The trends that resulted apply equally as well to the "new" atmospheres used in this report.

Perfect modulation involves using the maximum drag coefficient (C_D) until a desired level of deceleration is obtained then changing C_D to maintain this desired level until peak dynamic pressure (q_{\max}) is reached. After q_{\max} the C_D can be kept at the minimum level obtained at q_{\max} or allowed to increase to maintain the constant deceleration up to the point where the maximum C_D is again being used.

The maximum deceleration obtained using a single drag change depends on the altitude at which C_D is staged. If C_D is staged at too high an altitude the second peak in deceleration exceeds the first. For staging at too low an altitude the first exceed the second. Therefore, there is an optimum altitude for staging.

The maximum load versus the change in C_D for a $\gamma_e = 90^\circ$ entry to Mars for both perfect and one step drag modulation at the optimum altitude is shown in Figure 1.3.2-85. A 30% decrease in deceleration can be obtained with a perfect modulated C_D change of 2. For a single step change in drag at the optimum altitude only a 20% reduction was obtained. Similar results were obtained for Venus for the Extreme I atmosphere.

The reduced load ratio versus the ratio of maximum to minimum C_D is shown in Figure 1.3.2-86. This figure contains both Venus and Mars calculated points which show good agreement. The single drag stage curve is for Venus 90° entries with the Extreme I atmosphere.

Drag modulation has one distinct advantage over lift for the reduction of entry loads: it is effective at all entry path angles as long as capture is not a problem. Lift is effective only for the shallow entry angles.

H. Lifting Entry

A parametric study was performed for determining the effects of lift on maximum resultant load (A_R) reduction during entries to Venus and Mars. Entries were calculated for lift to drag ratios (L/D) of 0, .3, .6, and .9 for entry path angles (γ_e) from near capture to vertical. The effects of entry velocity (V_e) and atmospheric uncertainties on A_R were determined for both planets. The study was carried out using the Venus Best and Extreme I atmospheres and the Mars A and C atmospheres.

The effect of $W/C_D A$ (from 30 to 90 lb/ft^2 for Venus and 20 to 60 lb/ft^2 for Mars) on A_R were found to be small. For this study a $W/C_D A$ of 60 lb/ft^2 for Venus and 40 lb/ft^2 for Mars were used.

(1) Venus Entries

The maximum resultant load (A_R) versus entry path angle (γ_e) is shown in Figures 1.3.2-87 and 1.3.2-88 for the Extreme I atmosphere and various L/D with entry conditions of $h_e = 600,000$ feet, $V_e = 40,000$ ft/sec. Lift is effective in reducing A_R only for γ_e less than about 50 degrees as shown in Figure 1.3.2-87. Similar results were found for the Best model atmosphere.

The capture angle is between 7.5 and 8 degrees for $W/C_D A$ of 30 to 90 lb/ft^2 with $h_e = 600,000$ ft and $V_e = 40,000$ ft/sec. For $L/D = .3$ and greater, entry capture exceeds 50 degrees. Entries with constant L/D are, therefore, impractical and some control over L/D must be used in order to realize any advantages.

A reduction of A_R of about 50% can be recognized for the lower entry angles as shown in Figure 1.3.2-88. By using negative lift a capture angle of about 0.5 degrees less than the ballistic can be obtained. Reduced heating and landing site selection are other advantages of lifting vehicles. To obtain these advantages lift must be controlled in some manner. Lift modulation control methods are beyond the scope of this initial study, but possible control systems would include a pull-out to ballistic flight after passing peak g or a constant g descent beyond peak g .

The altitude of maximum resultant loads vs. path angle is shown in Figure 1.3.2-89 for various L/D . In each of these cases subsonic flight exists below 220,000 feet giving very long flight times. For the $\gamma_e = 8^\circ$ ballistic case the flight time from peak g to

impact was about 2450 seconds as shown in Figures 1.3.2-90. Time histories of the entry parameters for the $\gamma_e = 8^\circ$ ballistic case are shown in Figures 1.3.2-90 and 1.3.2-91.

The effect of V_e and atmosphere are shown in Figures 1.3.2-92 and 1.3.2-93. The large effect of the uncertainty in atmospheric properties are demonstrated by the 50% increase in A for $\gamma_e = 8^\circ$ case using the Extreme I atmosphere rather than the Best.

(2) Mars Entries

The effect of L/D in reducing A_R is shown in Figure 1.3.2-94 for $h_e = 800,000$ feet and $V_e = 25,000$ ft/sec. As noted for Venus, lift is effective in reducing A_R only for the shallower entries. The atmosphere A used in this figure is not the most critical atmosphere for loading as demonstrated in Figure 1.3.2-95. The atmosphere C gives about 70% higher loads than A.

The altitude at maximum resultant loads for atmosphere A is shown in Figure 1.3.2-96. A similar plot for atmosphere C would show altitudes about 30% lower. The effect of entry velocity on A_R is shown in Figure 1.3.2-97.

The major part of the load reduction due to lift can be recognized with $L/D = 0.5$ (see Figures 1.3.2-97 and 1.3.2-92). Such an L/D could be obtained from blunt cones using a c.g. offset.

The capture angle for the Mars A atmosphere is between 14 and 15 degrees and for the Mars C between 15 and 16 degrees for ballistic flights. With lift, escape occurs at ≈ 40 degrees and is dependent on L/D and $W/C_D A$. As in Venus a control system is required in order to utilize lift.

Time histories of the entry parameters for a Mars A ballistic entry are given in Figures 1.3.2-98 and 1.3.2-99. For this trajectory the vehicle goes subsonic at about 50,000 feet. For a $\gamma_e = 90$ degrees with the Mars A atmosphere the vehicle goes subsonic near 20,000 feet and with the Mars C atmosphere near 40,000 feet.

I. Orbiter Braking

A study was made to determine the feasibility of atmospheric braking of a Venus Orbiter. Figure 1.3.2-100 shows the velocity change that may be obtained by a single skip of the Orbiter vehicle through the Venus Extreme I atmosphere. Although this velocity decrement is primarily dependent on the depth of penetration into the atmosphere, this figure shows it versus entry path angle since this is a more easily controlled variable. The curve for a $W/C_D A$ of 150 psf represents the Orbiter with the entry Lander attached and that of 10 psf is for the Orbiter alone. It appears that atmospheric braking for the Orbiter is unfeasible for two reasons:

- (1) The sensitivity of entry angle (as determined by Figure 1.3.2-100).
- (2) The uncertainty of Venusian atmospheric characteristics.

J. Spin Requirements

The successful flight of the lander vehicle requires the transfer of the vehicle from a hyperbolic orbit to an elliptical orbit which intersects the planet. This transfer may be achieved by the addition of an incremental velocity to the lander at a prescribed position along the hyperbolic orbit. While the orbiter control system can align the lander vehicle initially to the proper orientation for velocity addition, during and following separation the vehicle may be subjected to unwanted torques which destroy this orientation, with the result that the desired velocity and direction are not attained.

The motion of the vehicle may be contained by spinning the vehicle about its longitudinal, or thrusting, axis. The gyroscopic forces associated with spin prevent the vehicle from tumbling and thereby permit the attainment, within limits, of the desired velocity vector.

The system producing separation of the lander from the orbiter is presently envisioned as a pair of cold gas jets which provide sufficient thrust to produce a separation velocity of 1 foot/sec. During this sequence, misalignments of the jet nozzle and vehicle mass asymmetries could produce a moment which could cause a misorientation of the vehicle. A preliminary study indicated that an angular rate of no more than 1/8 deg/sec and an attitude error of no more than 0.1 degree would occur in the presence of a c.g. offset of 0.1 inch. These values have been doubled and used as design criteria for the phases following separation in order to obtain a conservative result. It appears that separation rates of this magnitude produce no appreciable effect on the spin-up phase and are, therefore, of no great concern. In order to insure a safe clearance between the orbiter and the lander before spin-up occurs, the lander will coast at the velocity of separation for a period of 4 seconds during which time it has travelled approximately 4 feet from the orbiter. An angular rate of 1/8 deg/sec could therefore cause a misalignment of the thrust axis of 1/2 degree. This misalignment must be considered as a bias of the final velocity vector attained during retro.

(1) Spin-Up

The spin-up phase of the Mars landers' mission should provide a sufficient rotational velocity such that the vehicle will maintain a constant inertial position in space. Thus, the velocity increment to be added during the retro phase will produce the proper total velocity vector for a successful entry trajectory.

It becomes apparent that residual rotational rates accruing from the separation phase as well as mass asymmetries (products of inertia) may have deleterious effects upon both the orientation and dynamic motion of the vehicle during the spin-up procedure. Through the use of a six-degree-of-freedom computer program, vehicle dynamic motion was analyzed for three spin-up rates; 40, 60, and 80 rpm. Since the separation system is to be designed to impart no more than 0.25 deg/sec pitch or yaw rate, this value was used for those runs with non-zero initial-rate conditions. The torque application time, limited to a maximum of 30 seconds, was varied from 20 to 30 seconds with a corresponding variation in torque level thus maintaining a constant total torque impulse for each case. The product of inertia (I_{xz}) was assumed to be 1 1/2% to 3% of the rotational inertia (I_x) which are somewhat larger values than normal production tolerances on mass distribution would engender. Accordingly, therefore, the precessional characteristics shown in Figure 1.3.2-101 are slightly more severe than those that would result from a more conventional high $W/C_D A$ vehicle.

The effect of both spin-rate and torque application time may be seen in Figure 1.3.2-102. The diagram represents the steady-state coning angle in inertial space of the vehicle's longitudinal axis expressed in terms of the Euler angles θ , and ψ , for the three spin-up rates investigated. This diagram represents a view of the angular deviation of the vehicle's longitudinal axis as seen by an inertial observer. It also shows the steady precession cone angle experienced by the vehicle along with a typical transient response (for one case) during the spin-up period.

Each of the nine cases shown initially possessed residual pitch and yaw rates resulting from the separation phase. The trace of ψ vs. θ during the torqueing interval is shown for one of the 60 rpm cases and is typical for all. The magnitude of the ordinate and abscissa for the various spin-rates indicates that for a constant torque application time the coning angle becomes smaller with increasing rpm. This is a direct result of the

gyroscopic action of spin. A slightly different representation of these effects is shown in Figure 1.3.2-103. The steady-state conditions following spin-up are depicted therein. For the same steady-state spin-rate the magnitude of the offset angle becomes smaller with decreasing torque application time since the vehicle is captured more rapidly by gyroscopic action. This offset angle represents the initial misalignment of the retro phase thrust vector with the desired orientation.

For those cases where products of inertia were considered, the resulting motion indicated as a torus, (see Figure 1.3.2-101) is essentially unaffected by initial pitch or yaw rates since the effect of product of inertia completely masks the contribution of the extremely small body rates. While Figure 1.3.2-101 represents vehicle motion in the absence of initial lateral rates the effect of introducing such rates would merely shift the center of each torus a fraction of a degree from its presently shown origin.

The effects of products of inertia cause the type of motion to change considerably from that caused by initial angular rates, and the vehicle now moves in all four quadrants in space. Since the lander must be at a distance of approximately 1000 feet before the ΔV rockets are fired in order to reduce the effect of rocket jet impingement on the orbiter, the lander will coast for a period of approximately 15 minutes. The vehicle motion during this period will be contained by gyroscopic action to the angular deviations shown in Figure 1.3.2-101. Since one cannot tell exactly where the vehicle axis is at the time of rocket firing, the ΔV firing was assumed to take place at a position of maximum angular deviation along with the corresponding angular rates. In this manner, the angular deviation of the resultant velocity caused by rocket thrust is maximized, and a conservative estimate obtained. It is also apparent that with this type of motion, the thrusting time should be chosen as an integral multiple of frequency, which will permit a nullification of the acceleration components along axes normal to the vehicle longitudinal axis.

(2) ΔV Rocket Firing

Utilizing the resulting vehicle precessional characteristics from the spin-up phase, the ΔV portion of the landers' mission was analyzed. Clearly, the most important criterion for measuring system performance is the retro velocity vector deviation angle, $\Delta\beta$. Minimizing the deviation depends upon selecting that spin rate, spin-up time, and thrusting time which will minimize the adverse effects caused by residual pitch and yaw rates, products of inertia, and c.g. offset.

The employment of a cold gas propulsion system for spin-up will permit an accurate alignment of the roll torque jets and will thus preclude any additional precessional perturbations due to roll torque offset.

In the absence of angular and thrust-offset errors, a total impulse of 18,000 lb/sec will produce an incremental velocity of 400 ft/sec on a 1450 pound vehicle. As previously mentioned, the thrusting time chosen should be an integral multiple of vehicle frequency in order to permit a nullification of the acceleration components along axes normal to the vehicle's rotational axis. For the 1450 pound vehicle under consideration, frequency calculations indicated that a retro thrusting time of 17.2 seconds would be required. Actually, a number of retro thrusting times, each providing the same total impulse of 18,000 lb/sec were analyzed. Figure 1.3.2-104 represents the effect of thrusting time (T_{HT}) upon $\Delta\beta$ for the three spin-up rates investigated. Figures 1.3.2-105 and 1.3.2-106 show the relationship between $\Delta\beta$ and spin-up rate for the recommended thrusting time. Although 60 or 80 rpm would seem to be the preferred spin-rate for the case where no mass asymmetries are present (Figure 1.3.2-105), an inspection of Figures 1.3.2-104 and 1.3.2-106 shows that in the presence of products of inertia a spin rate of 40 rpm should be chosen. It should be noted that the choice of the lowest rpm would provide the

benefits of lower lateral loads and a lower angle of attack of planetary entry. In view of the fact that products of inertia are never quite eliminated in manufacture it is clearly evident that their magnitude must be reduced to the lowest possible value in order to ensure satisfactory system performance. The seriously degrading effect of products of inertia upon $\Delta\beta$ can be seen in Figure 1.3.2-106. Although a spin-up torque application time (T_t) of 20 seconds appears to be better for the case when $I_{xz} = 0$ (Figure 1.3.2-105), the severity of the effect of products of inertia upon $\Delta\beta$ (Figure 1.3.2-106) indicate that a torque application time of 30 seconds is necessary. It can be seen that when, in the presence of mass asymmetries, the vehicle is brought to final rpm in a shorter time duration, the ensuing ΔV sequence terminates with larger errors in $\Delta\beta$. This effect is due to the propagation of larger lateral rates (at the end of spin-up) as the torque application time is decreased. Thus a small benefit is achieved in $\Delta\beta$ by the choice of a 30 second torque application time.

It should be noted that the results shown include the effects of c.g. offset and are therefore slightly conservative. Also, as in the spin-up phase, the effects of residual pitch or yaw rates were found to be of extremely minor significance. It must be concluded that to minimize $\Delta\beta$ or direction errors of the time of retro firing the most important single requirement is the balance of the vehicle to minimize products of inertia. Small errors introduced in separation are negligible compared to the effects of products of inertia.

K. Recommendations, Problem Areas, Study Areas, Development Programs, Etc.

Having arrived at a reasonable configuration and weight to satisfy design requirements through the use of point mass trajectories the logical extension is to investigate certain critical areas based on multiple degree of freedom trajectories. When system tolerances (e.g. guidance, separation, spin-up, weight and balance, etc.) are factored in, the likelihood of entering a planet with zero angle of attack and zero transverse rates is very small. The small matrix of six-degree of freedom trajectories included in this study only show trends for a few special cases. It is suggested, therefore, that future analyses include several partial trajectories, with selected initial conditions, which would yield "representatively bad" effects (not worst case) on individual items. There could be 3-sigma type trajectories for heating, normal loads, retardation-chute deployment, etc. calculated only down to the region of interest.

The aerodynamic reported in Section 1.3.2-B indicate that with large entry angles of attack the vehicle could become stable backwards. This could occur under several conditions of entry path angle, entry angle of attack, and spin rate and should be investigated to establish safeguards. Tolerances on aerodynamics, like pitching moment coefficient and dynamic damping coefficient which affect vehicular oscillatory motion after entry, should be studied. Similarly, the starting altitude (assuming a specific set of initial conditions) can have an effect on loads and angle of attack history. This tolerance on altitude can be compensated for by varying the initial conditions provided the vehicle is out of the sensible atmosphere and this of course varies with each model atmosphere.

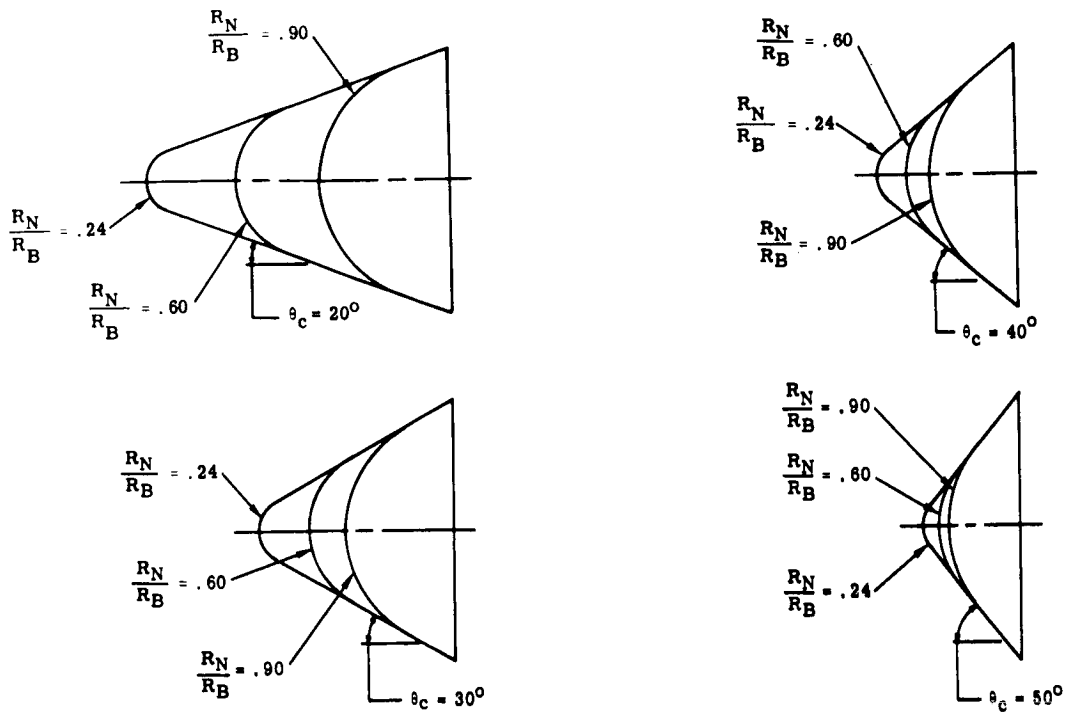


Figure 1.3.2-1. Voyager Entry Configurations

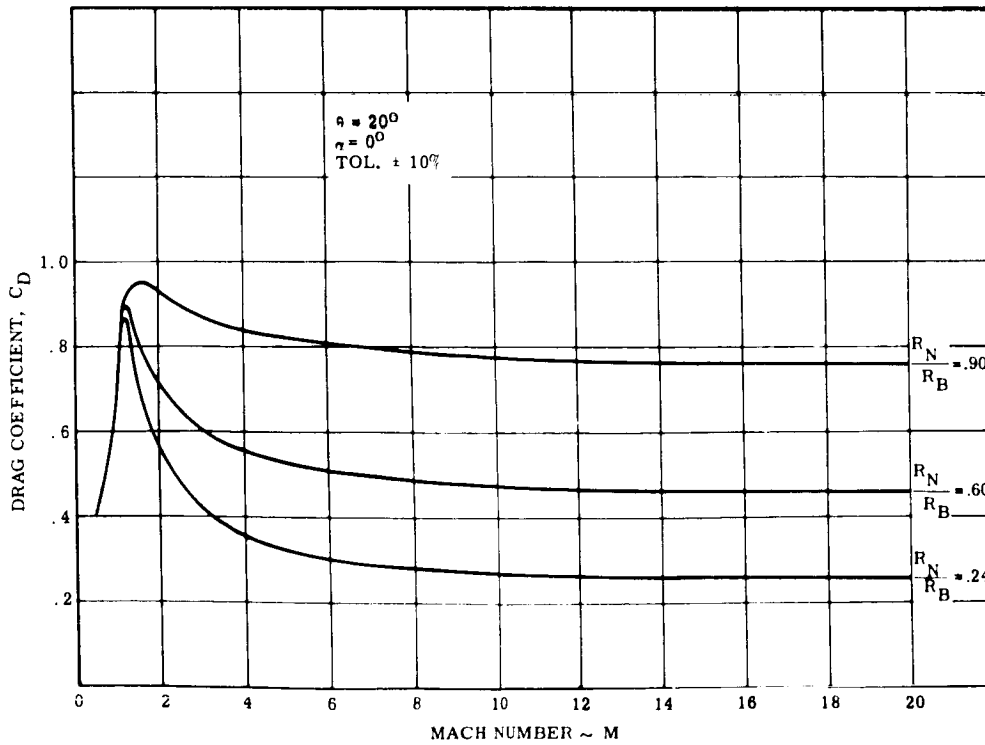


Figure 1.3.2-2. Voyager Drag Coefficient vs. Mach Number

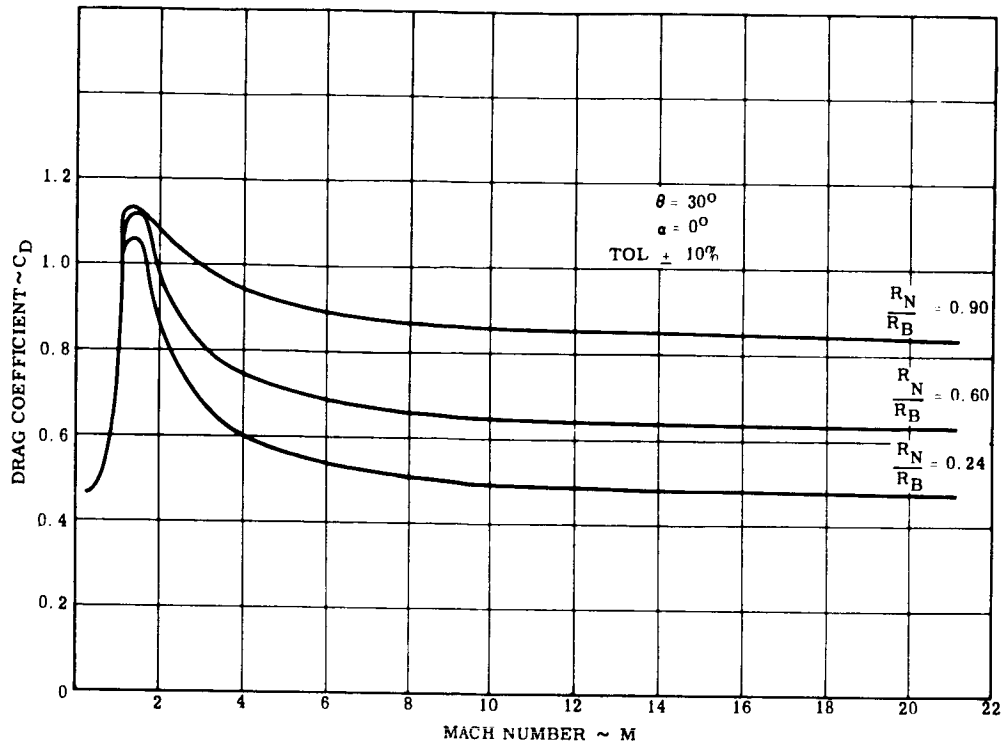


Figure 1.3.2-3. Voyager Drag Coefficient vs. Mach Number

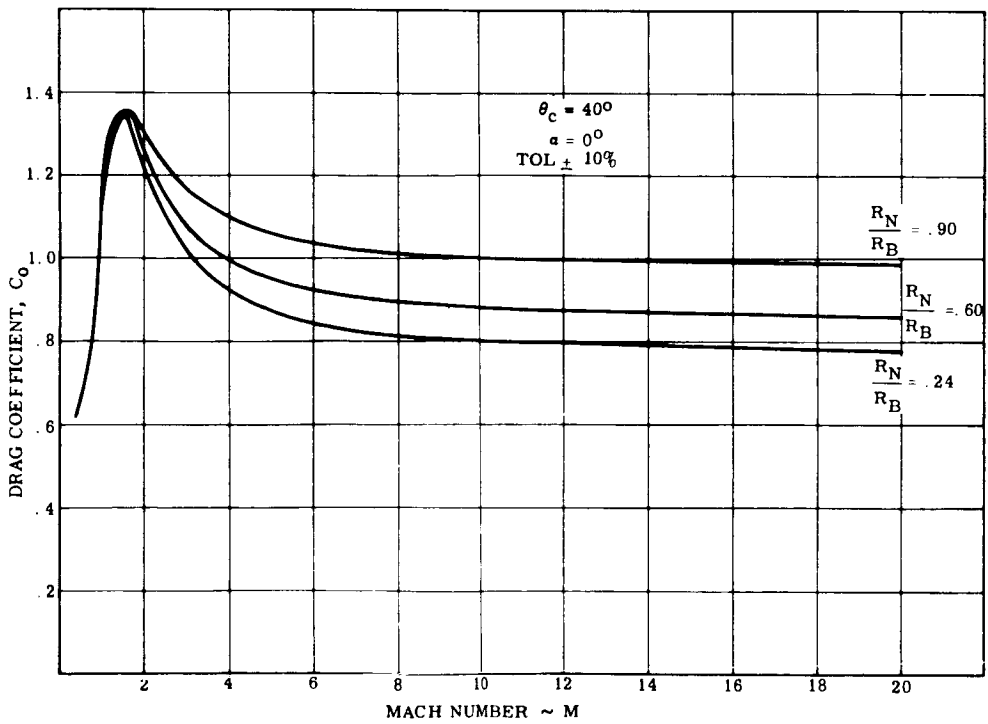


Figure 1.3.2-4. Voyager Drag Coefficient vs. Mach Number

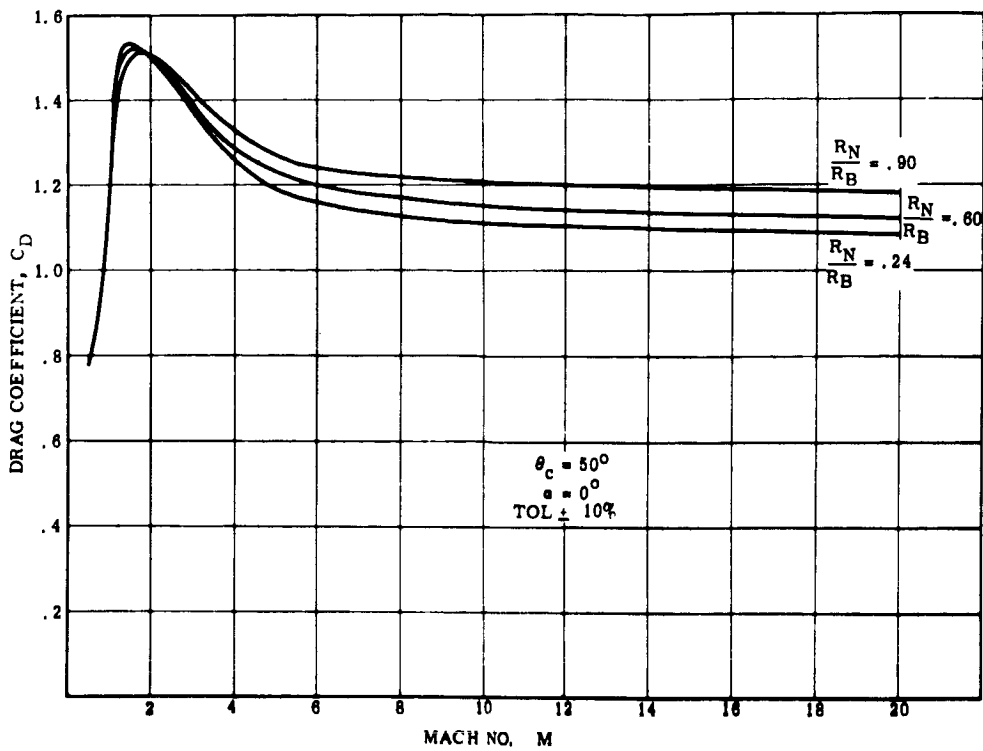


Figure 1.3.2-5. Voyager Drag Coefficient vs. Mach Number

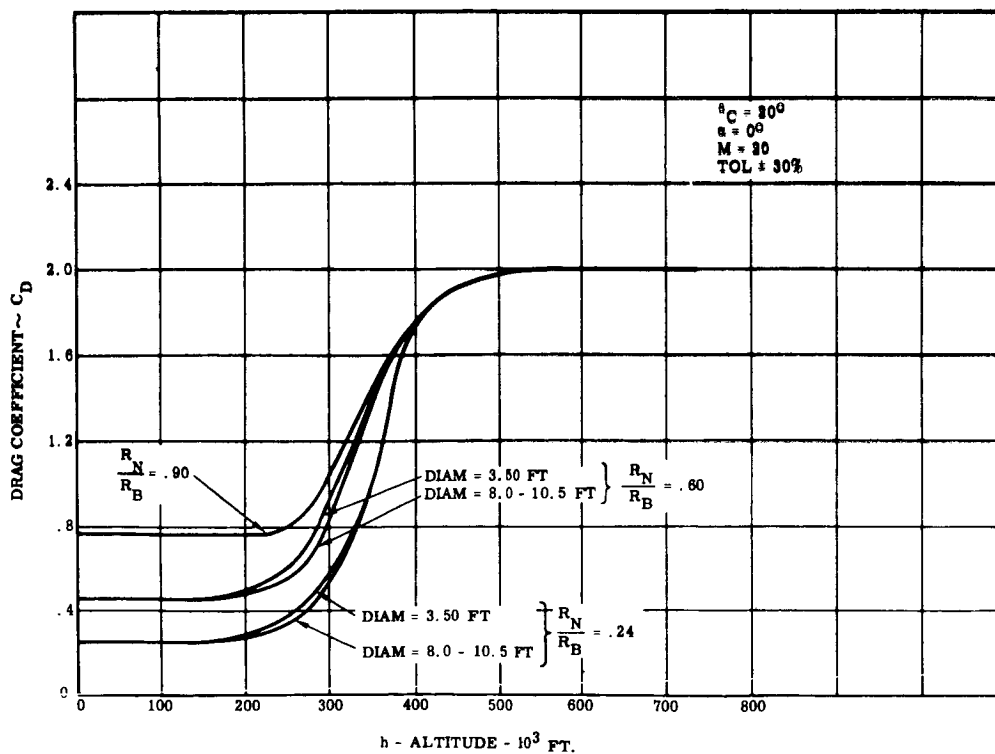


Figure 1.3.2-6. Voyager Drag Coefficient vs. Altitude

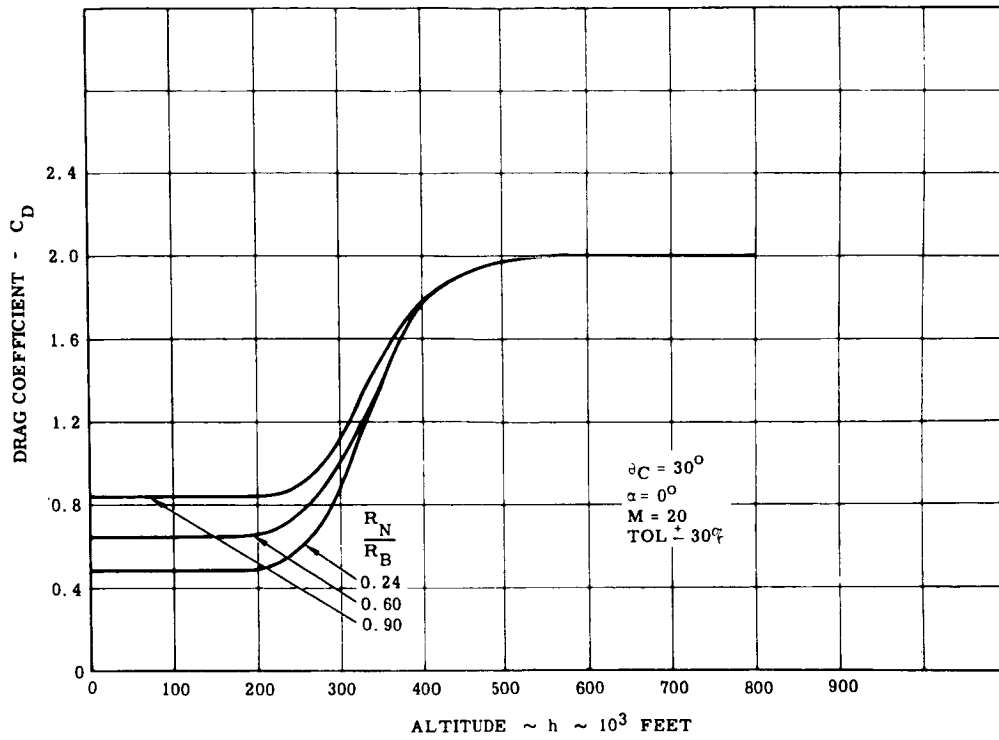


Figure 1.3.2-7. Voyager Drag Coefficient vs. Altitude

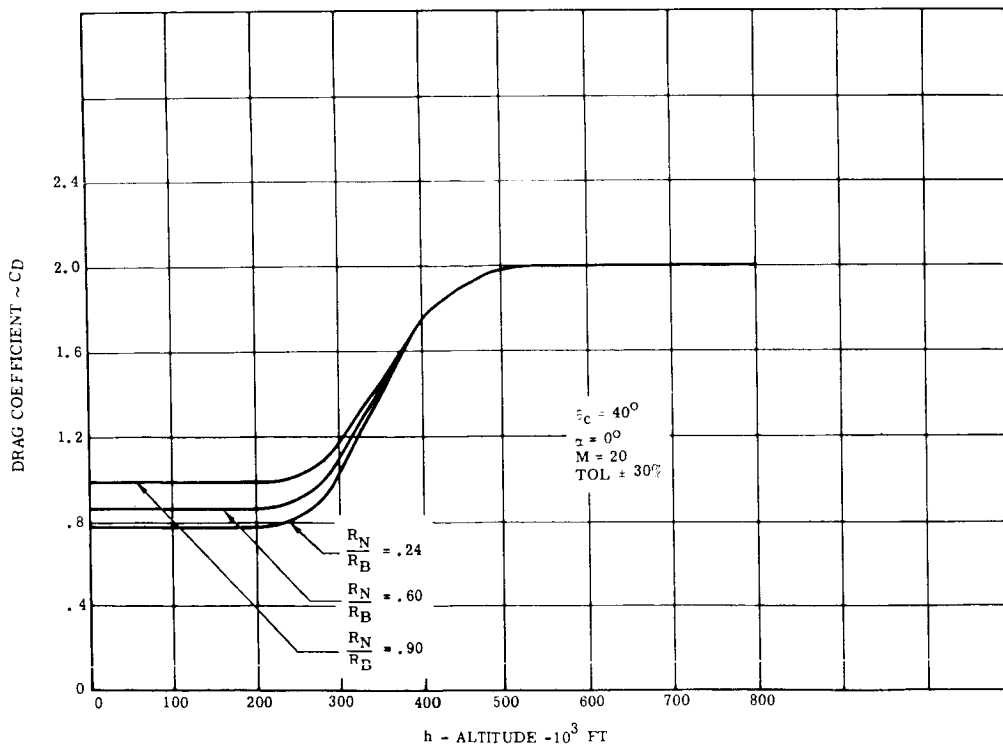


Figure 1.3.2-8. Voyager Drag Coefficient vs. Altitude

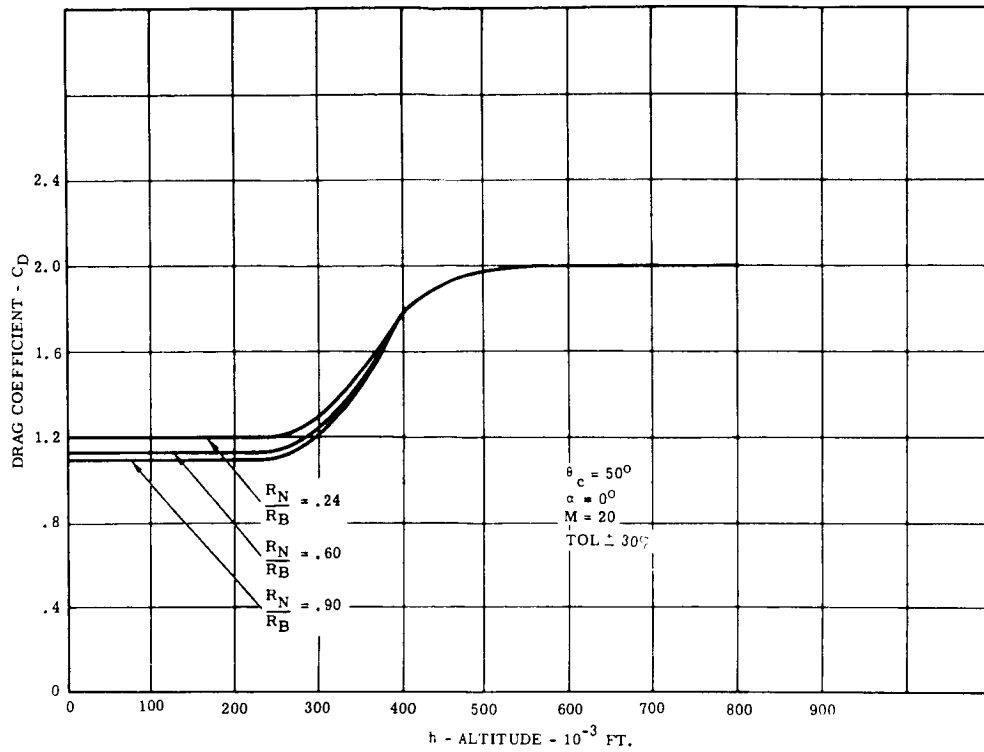


Figure 1.3.2-9. Voyager Drag Coefficient vs. Altitude

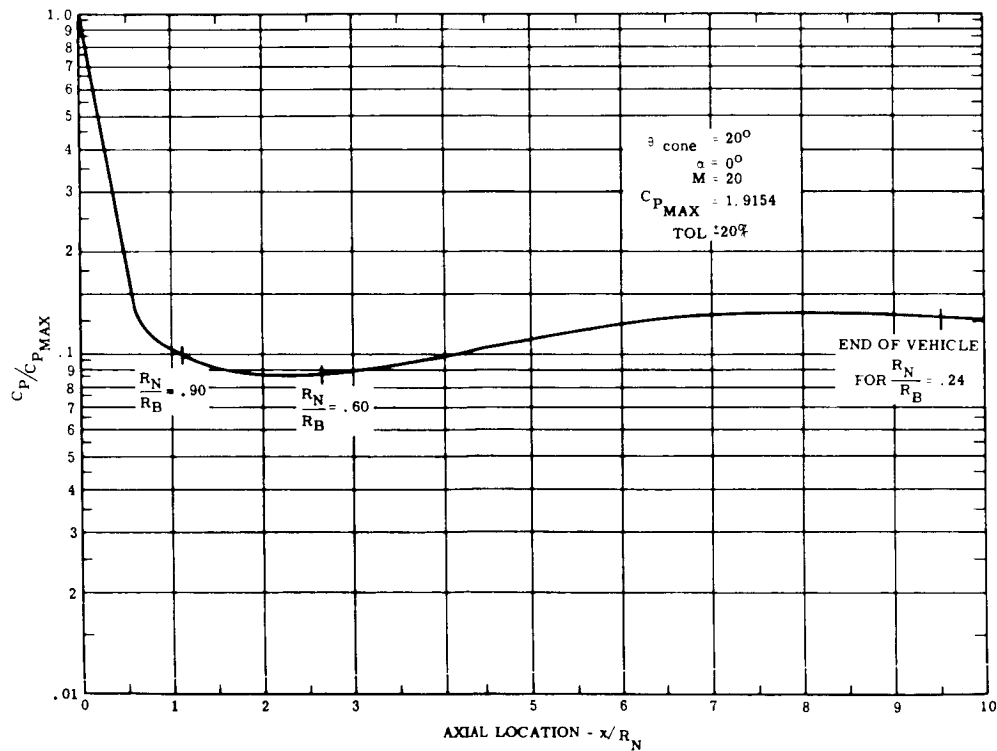


Figure 1.3.2-10. Voyager Pressure Distribution

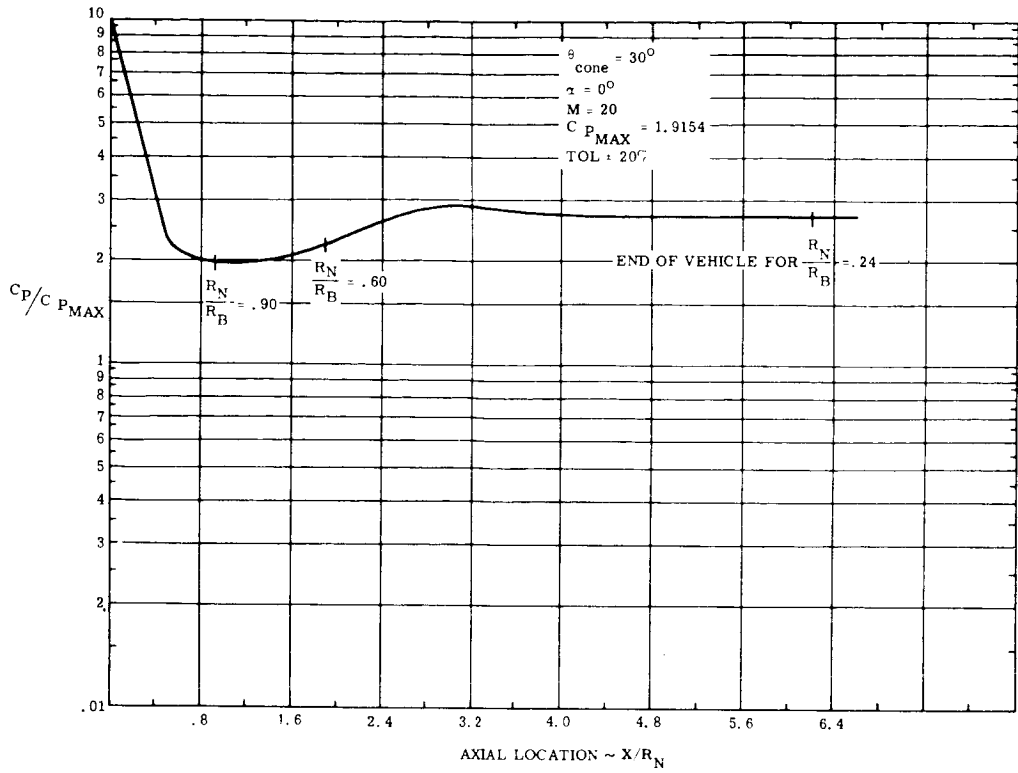


Figure 1.3.2-11. Voyager Pressure Distribution

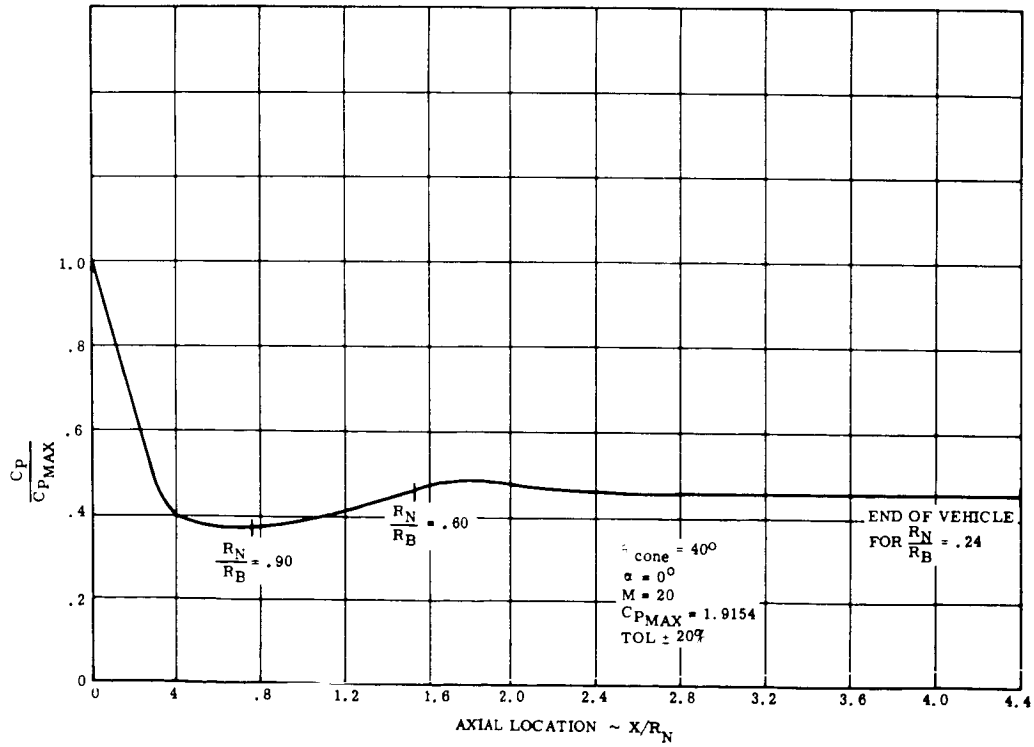


Figure 1.3.2-12. Voyager Pressure Distribution

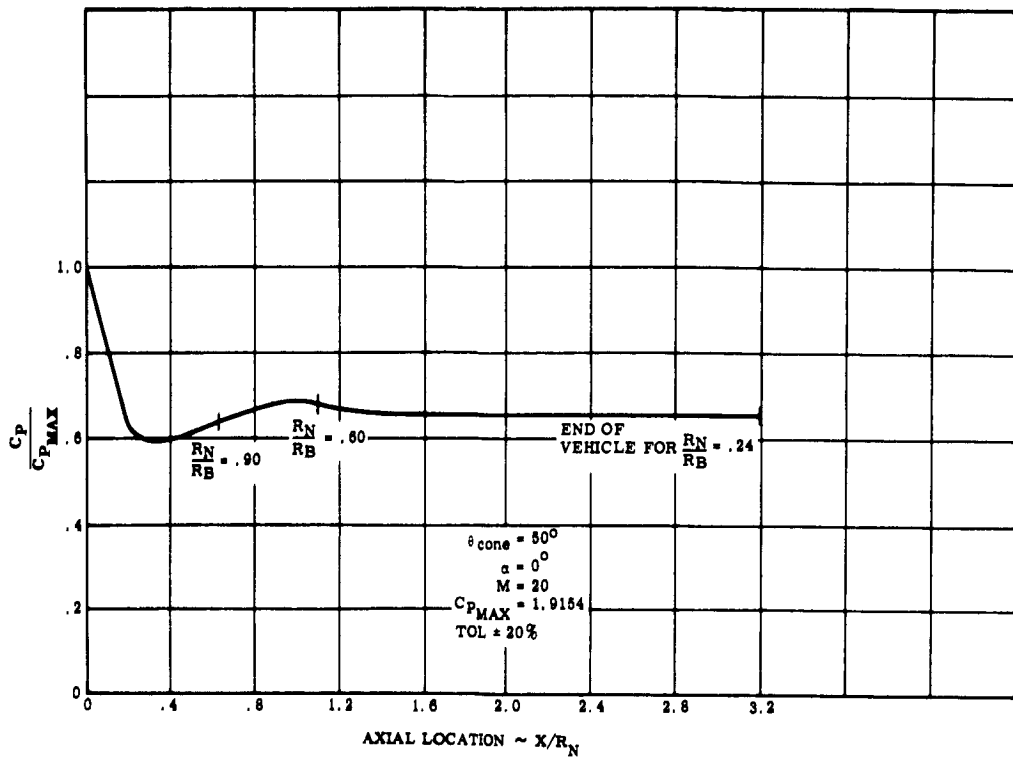


Figure 1.3.2-13. Voyager Pressure Distribution

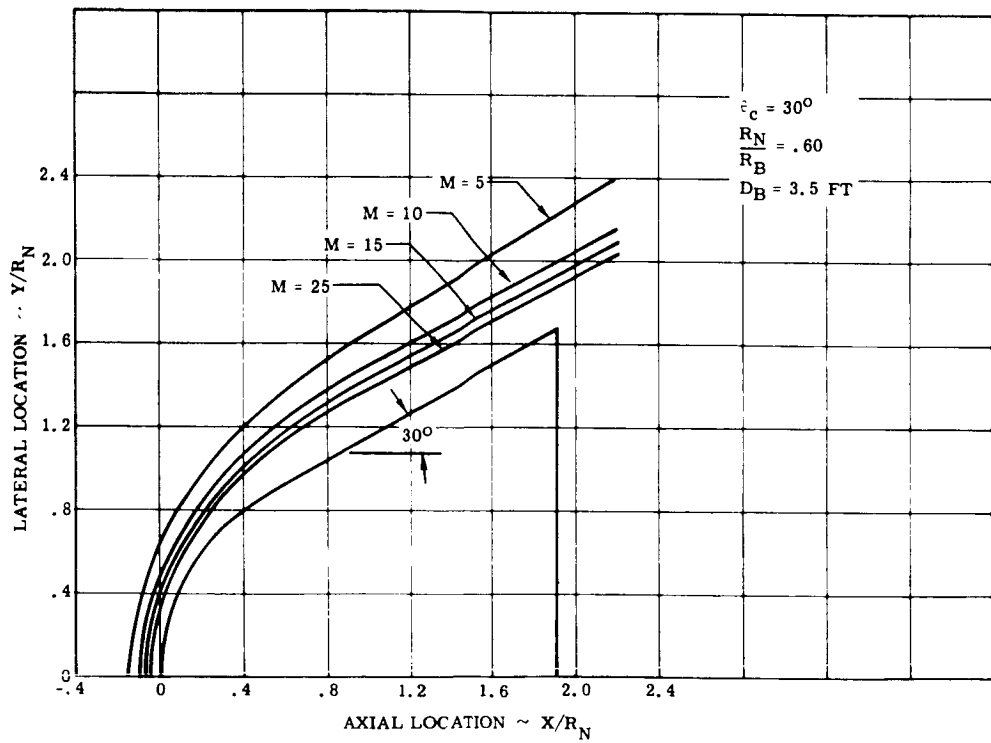


Figure 1.3.2-14. Voyager Shock Shape Variation with Mach Number

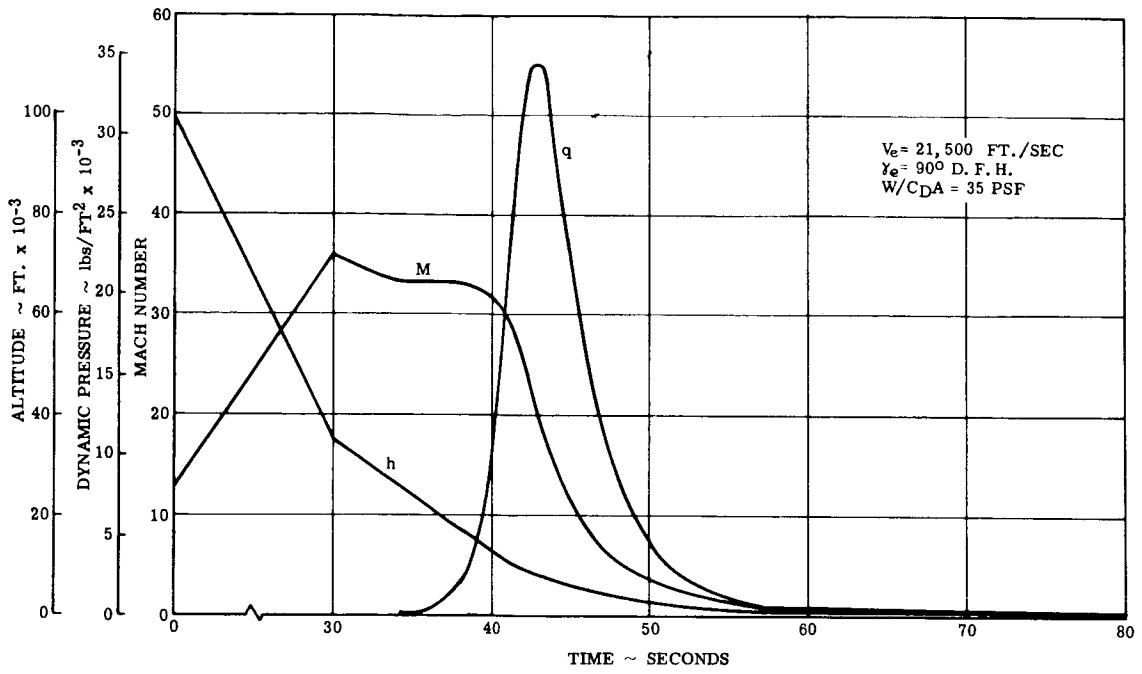


Figure 1.3.2-15. Trajectory Parameters for Entry into Mars Lower Atmosphere

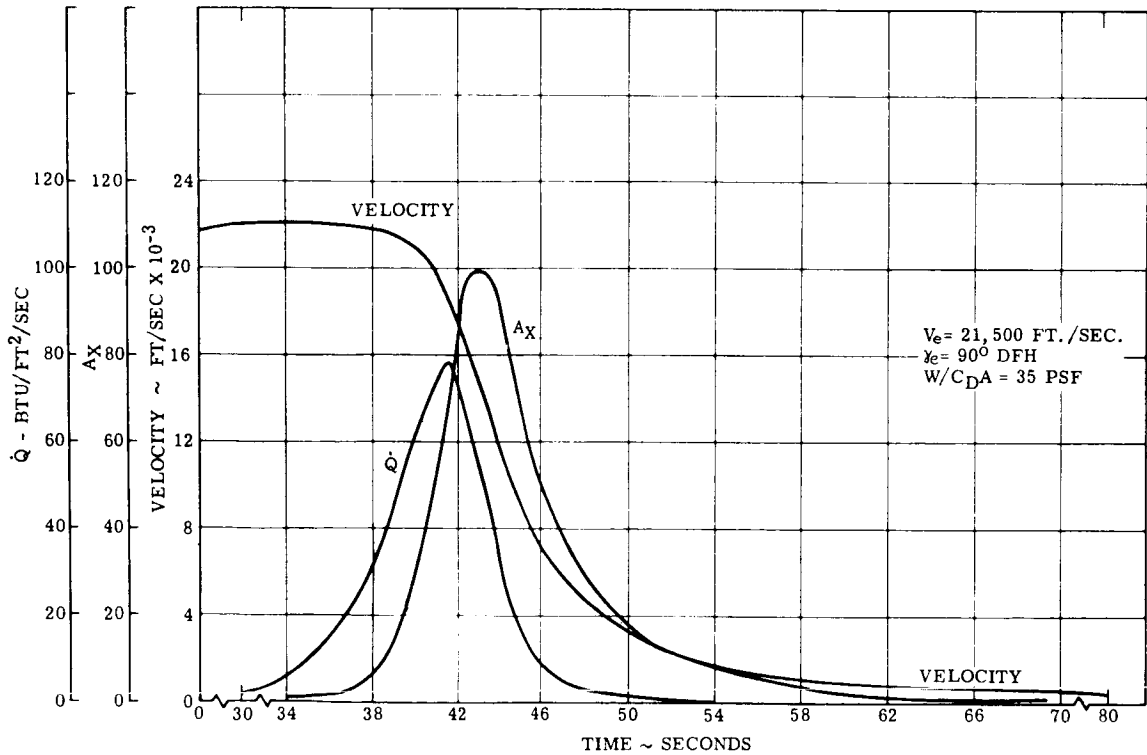


Figure 1.3.2-16. Trajectory Parameters for Entry into Mars Lower Atmosphere

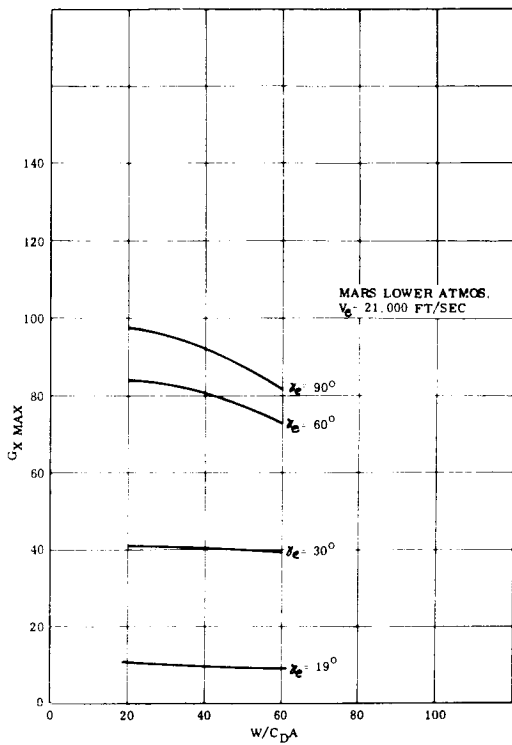


Figure 1.3.2-17. Peak Axial Deceleration vs. W/C_{DA} for Several Martian Entries

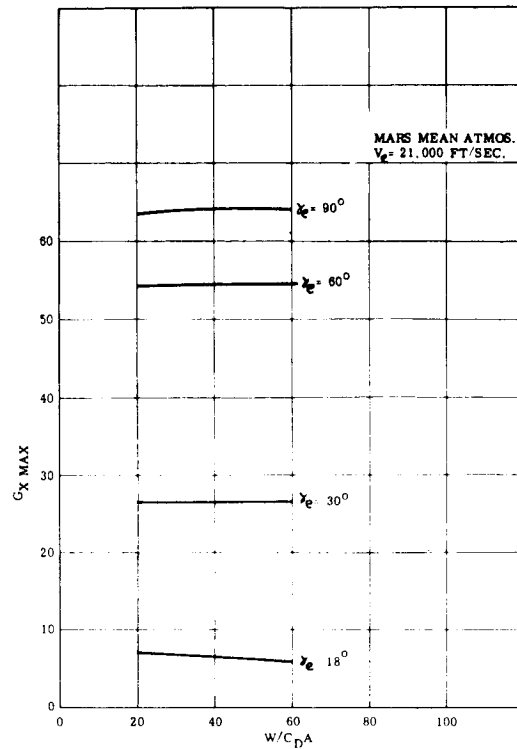


Figure 1.3.2-18. Peak Axial Deceleration vs. W/C_{DA} for Several Martian Entries

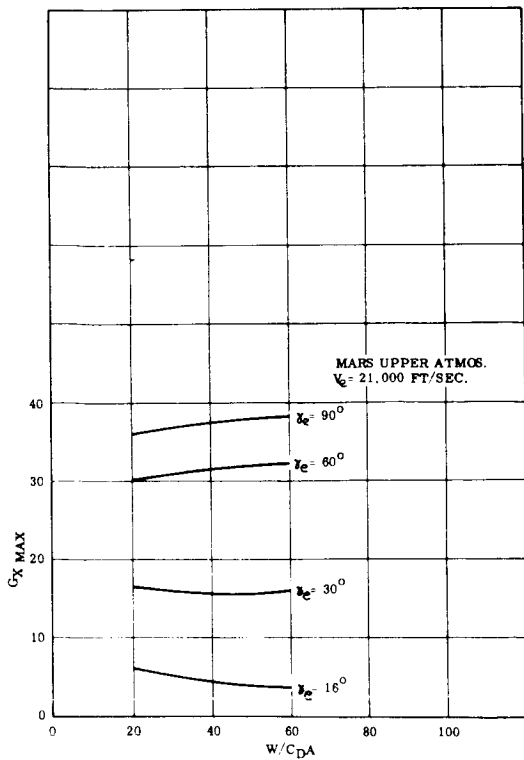


Figure 1.3.2-19. Peak Axial Deceleration vs. W/C_{DA} for Several Martian Entries

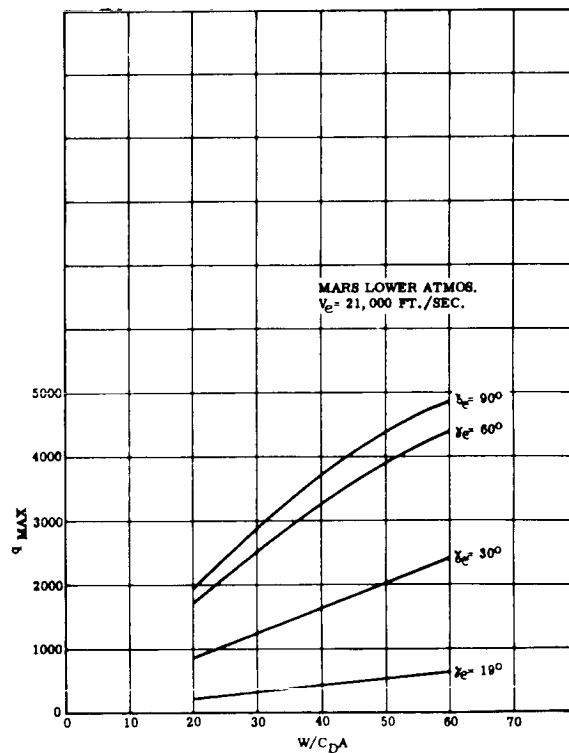


Figure 1.3.2-20. Peak Dynamic Pressure vs. W/C_{DA} for Several Martian Entries

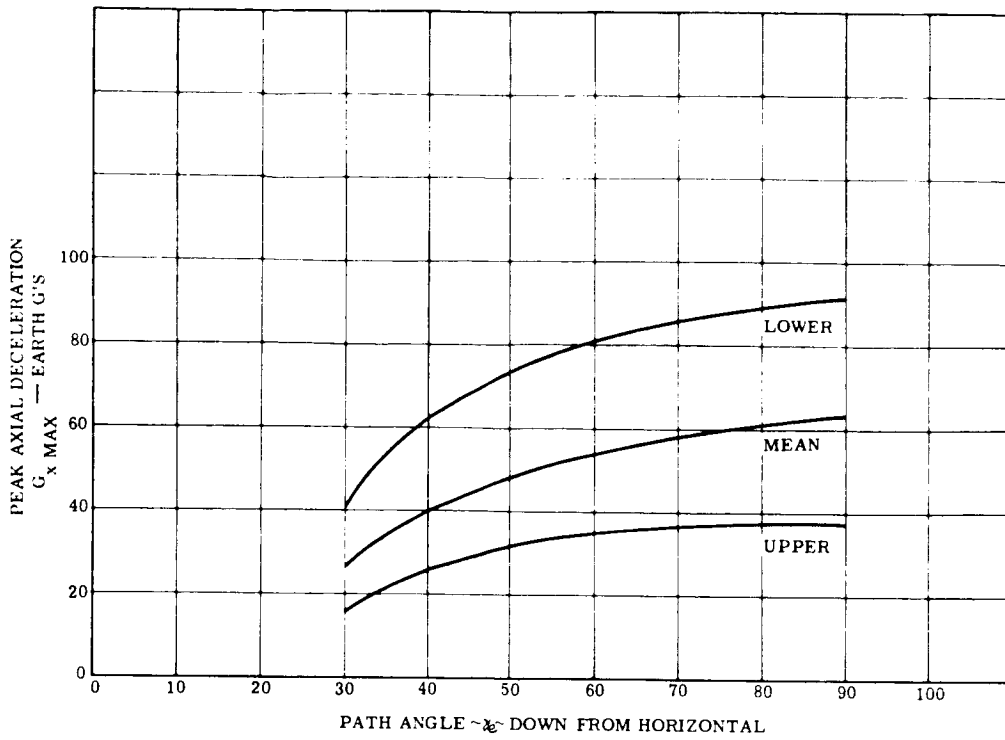


Figure 1.3.2-24. G_{xMax} vs. γ_e for $W/C_D A = 40$ psf for a Velocity of 21,000 ft./sec. at Various Martian Atmospheres

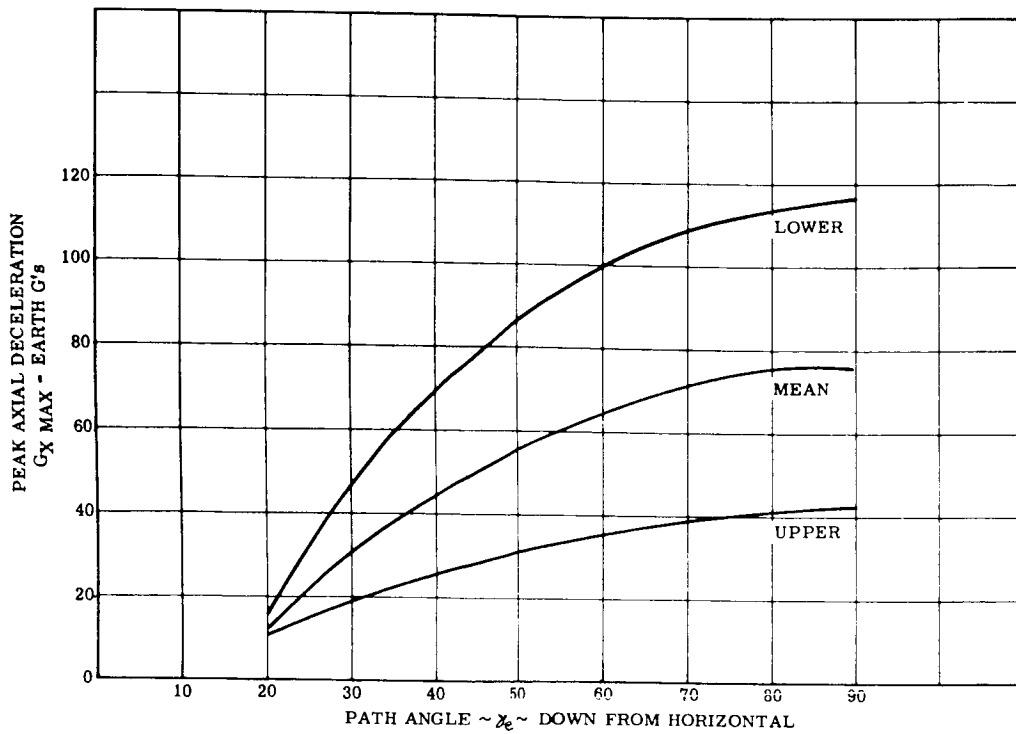


Figure 1.3.2-25. G_{xMax} vs. γ_e for $W/C_D A = 20$ psf for a Velocity of 23,000 ft./sec. at Various Martian Atmospheres

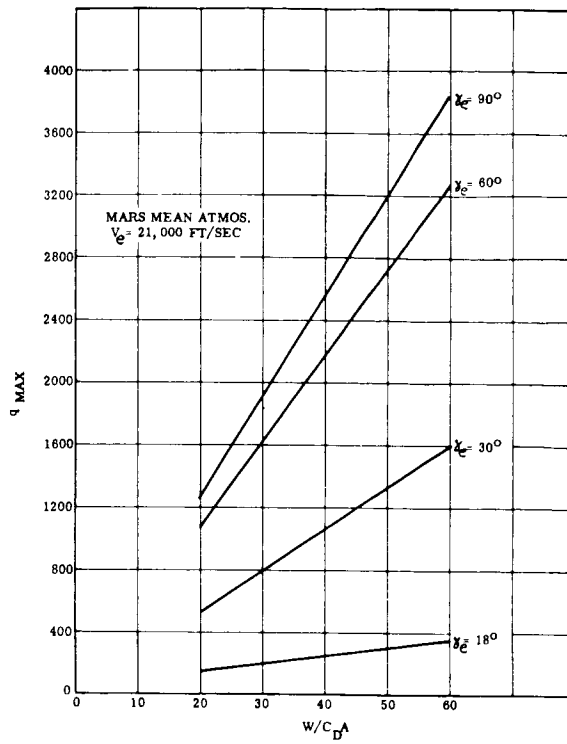


Figure 1.3.2-21. Peak Dynamic Pressure vs. W/C_{DA} for Several Martian Entries

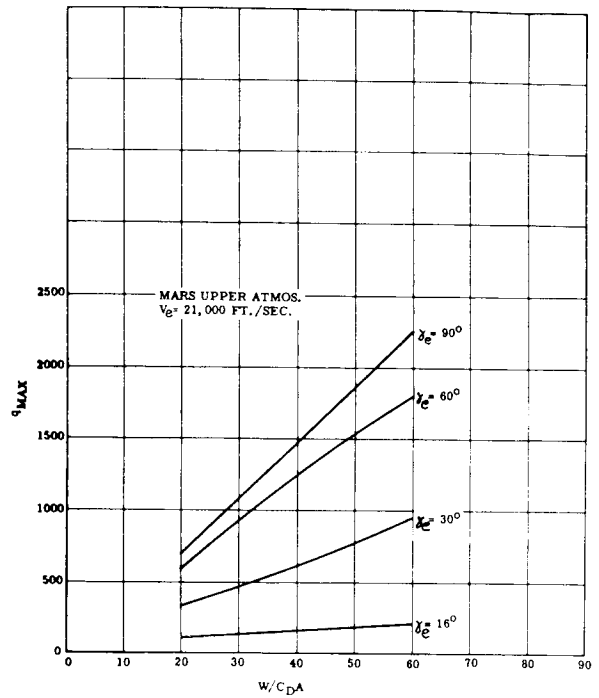


Figure 1.3.2-22. Peak Dynamic Pressure vs. W/C_{DA} for Several Martian Entries

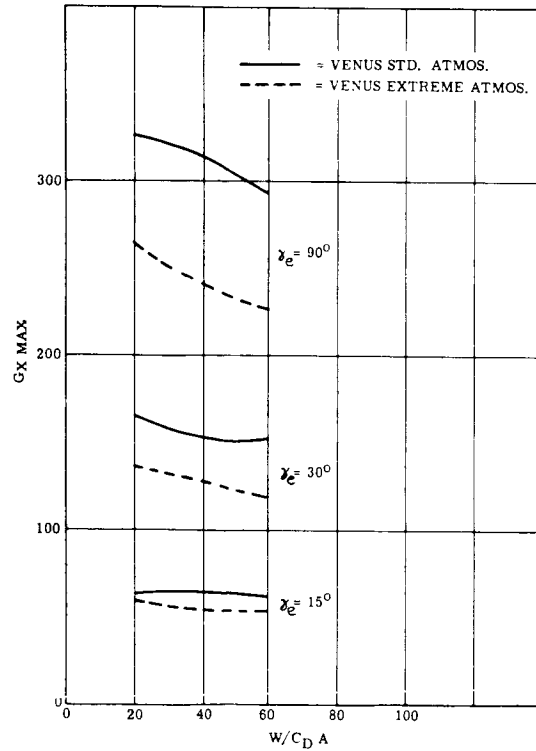


Figure 1.3.2-23. $G_{X_{Max}}$ vs. W/C_{DA} for Two Venusian Atmospheres where $V = 38,000$ ft./sec.

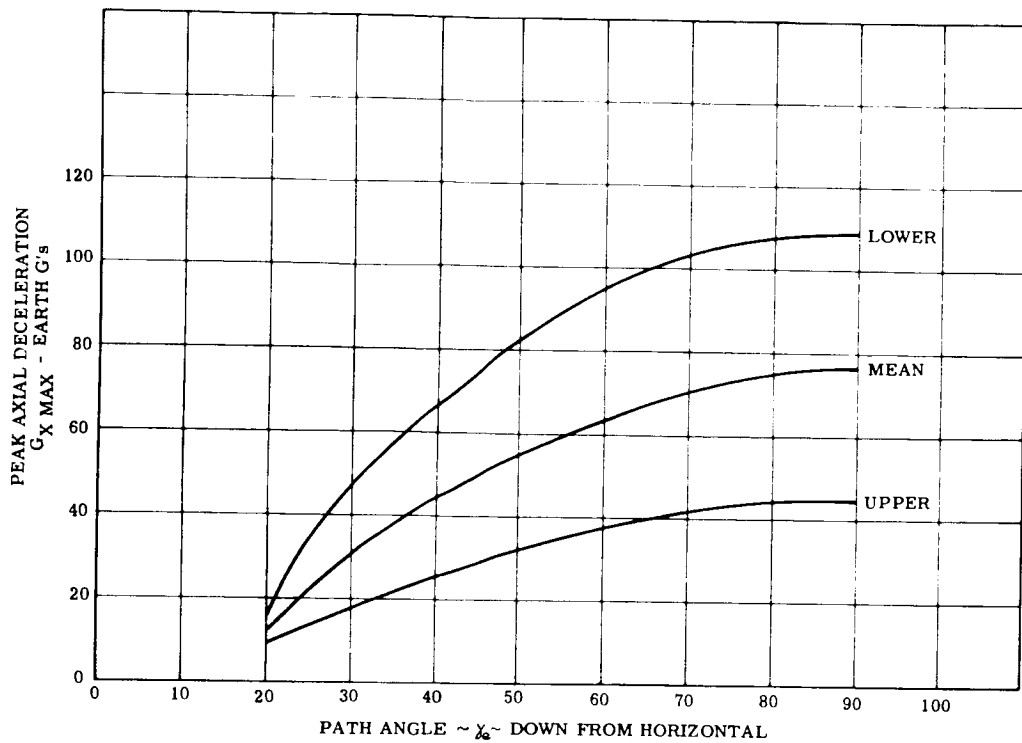


Figure 1.3.2-26. $G_{x_{Max}}$ vs. γ_e for $W/C_{DA} = 40$ psf for a Velocity of 23,000 ft./sec. at Various Martian Atmospheres

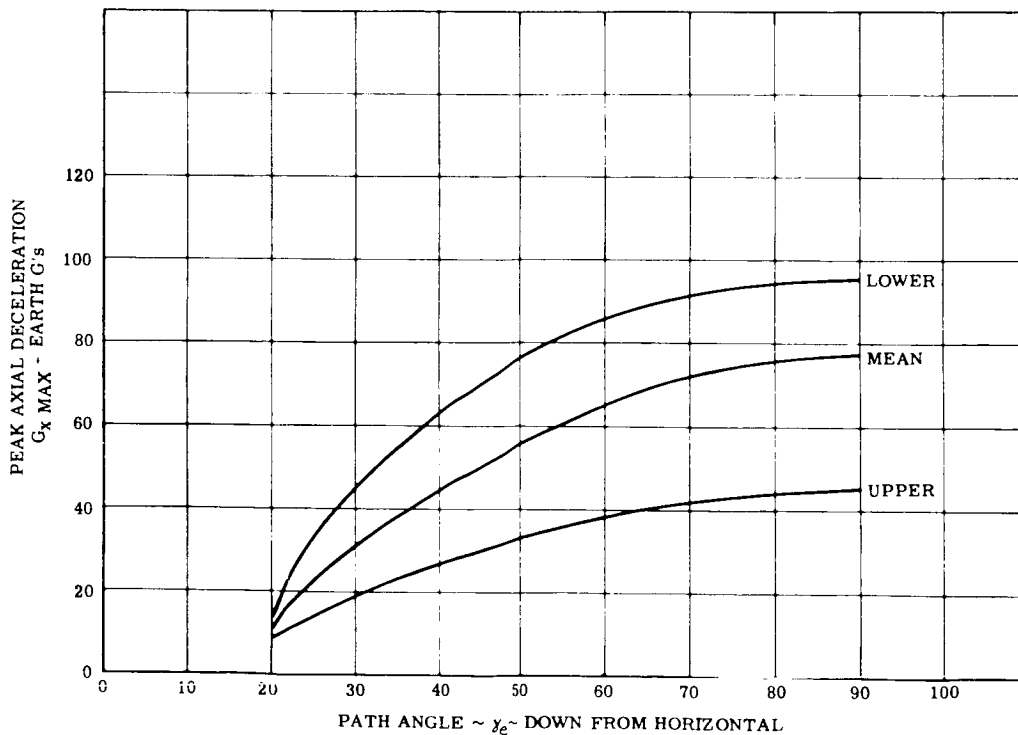


Figure 1.3.2-27. $G_{x_{Max}}$ vs. γ_e for $W/C_{DA} = 60$ psf for a Velocity of 23,000 ft./sec. at Various Martian Atmospheres

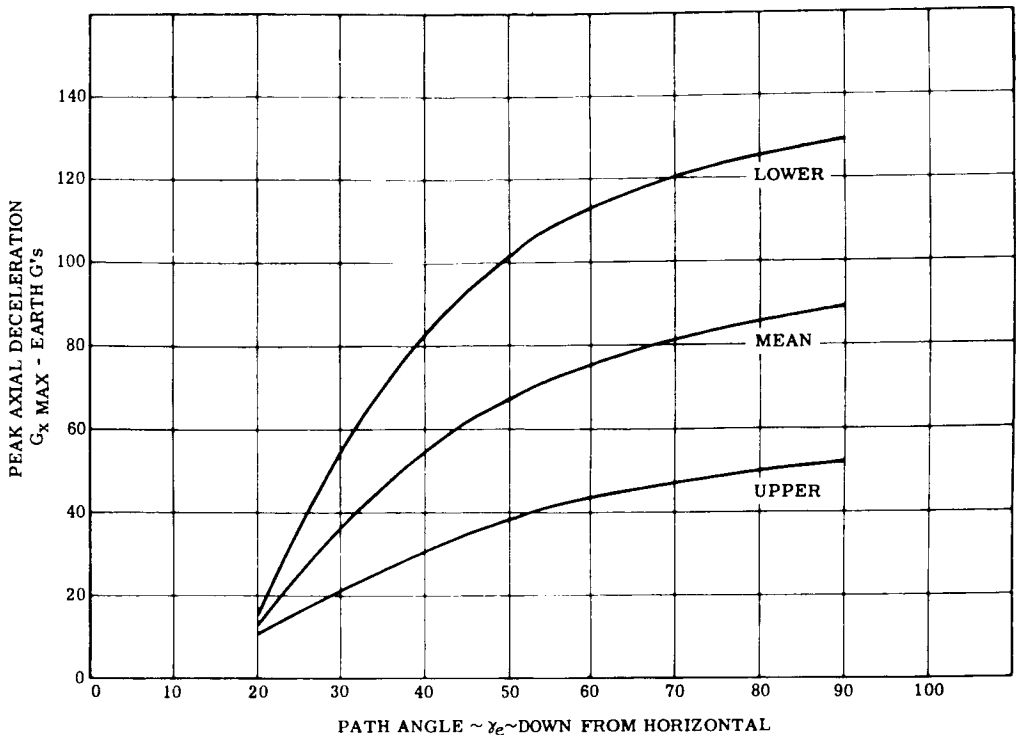


Figure 1.3.2-28. G_{xMax} vs. γ_e for $W/C_{DA} = 40$ psf for a Velocity of 25,000 ft./sec. at Various Martian Atmospheres

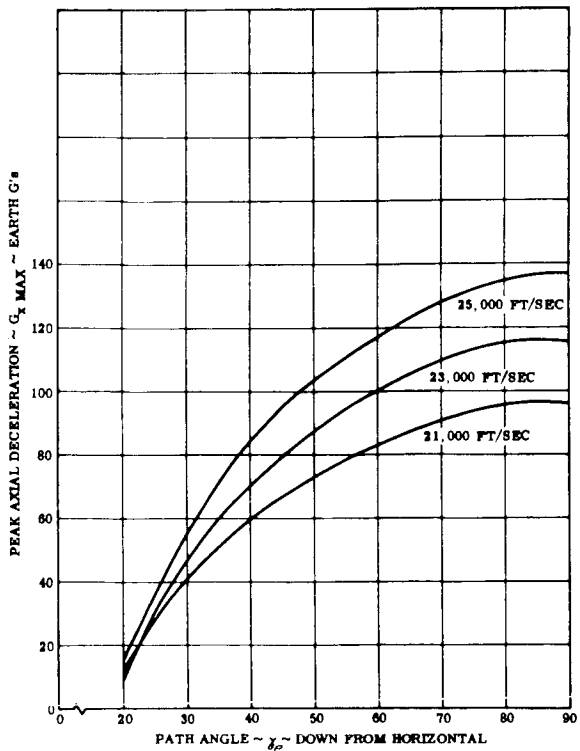


Figure 1.3.2-29. G_{xMax} vs. γ_e for $W/C_{DA} = 20$ psf for Various Velocities and Martian Lower Atmosphere

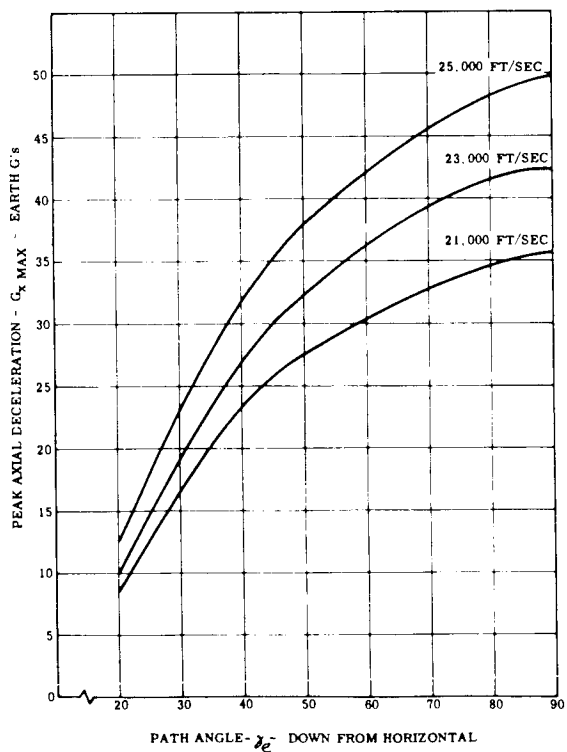


Figure 1.3.2-30. G_{xMax} vs. γ_e for $W/C_{DA} = 20$ psf for Various Velocities and Martian Upper Atmosphere

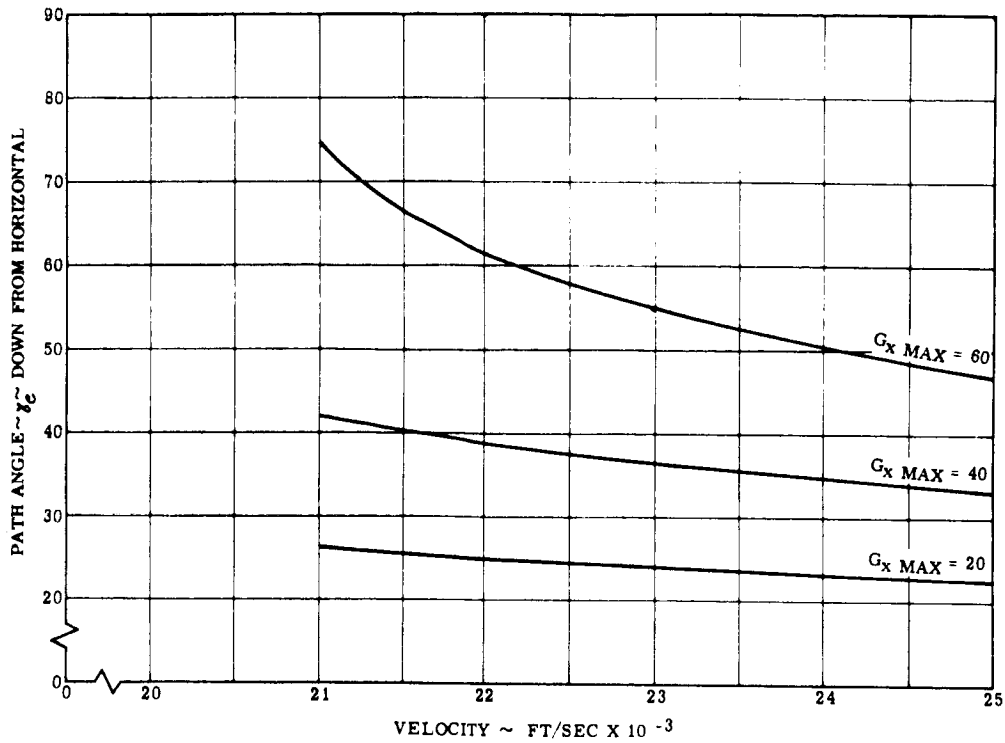


Figure 1.3.2-31. Velocity vs. γ_c for $W/C_D A = 20$ psf and Mean Martian Atmosphere at Various Peak Axial Decelerations in Earth G's

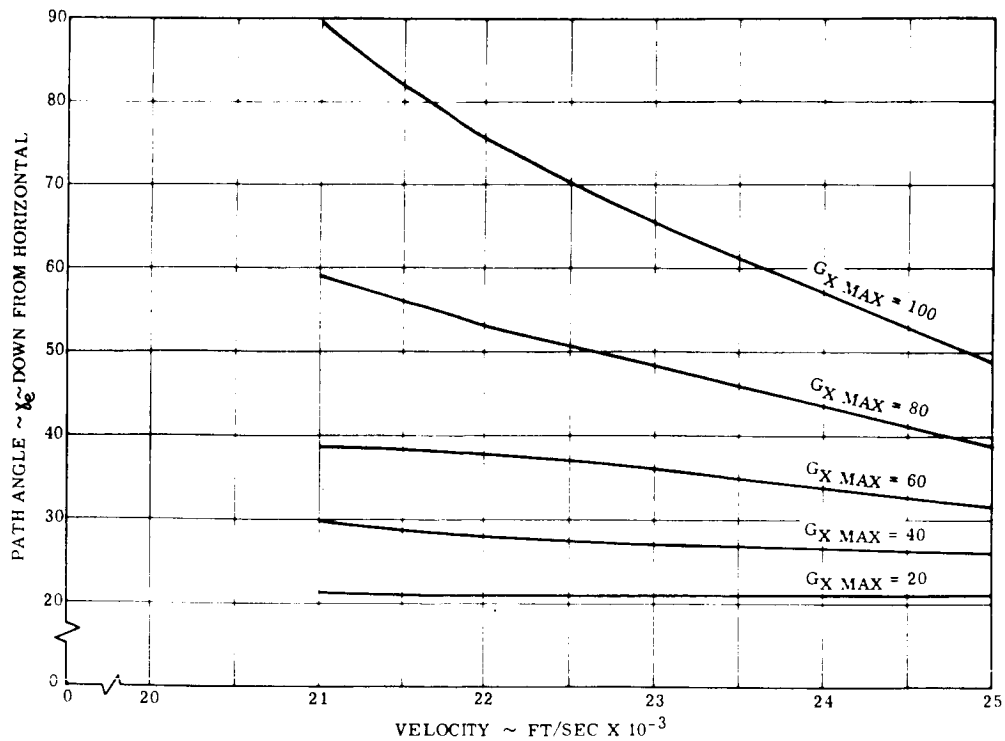


Figure 1.3.2-32. Velocity vs. γ_c for $W/C_D A = 40$ psf and Lower Martian Atmosphere at Various Peak Axial Decelerations in Earth G's

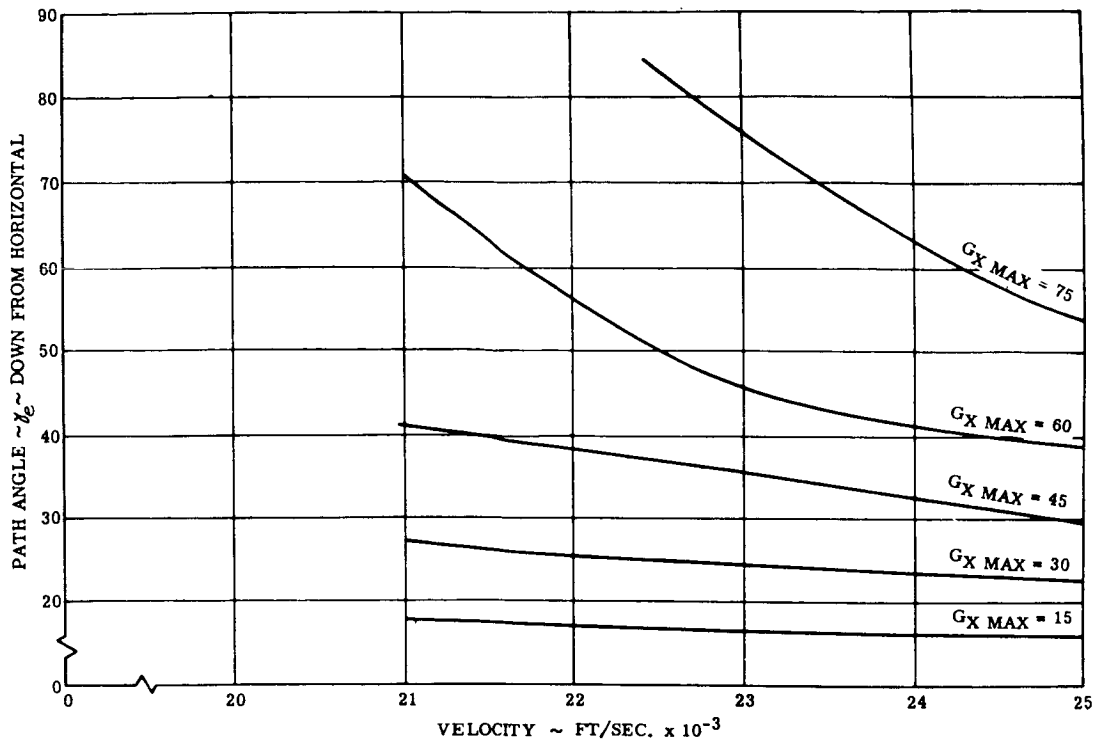


Figure 1.3.2-33. Velocity vs. γ_e for $W/C_D A = 40$ psf and Mean Martian Atmosphere at Various Peak Axial Decelerations in Earth G's

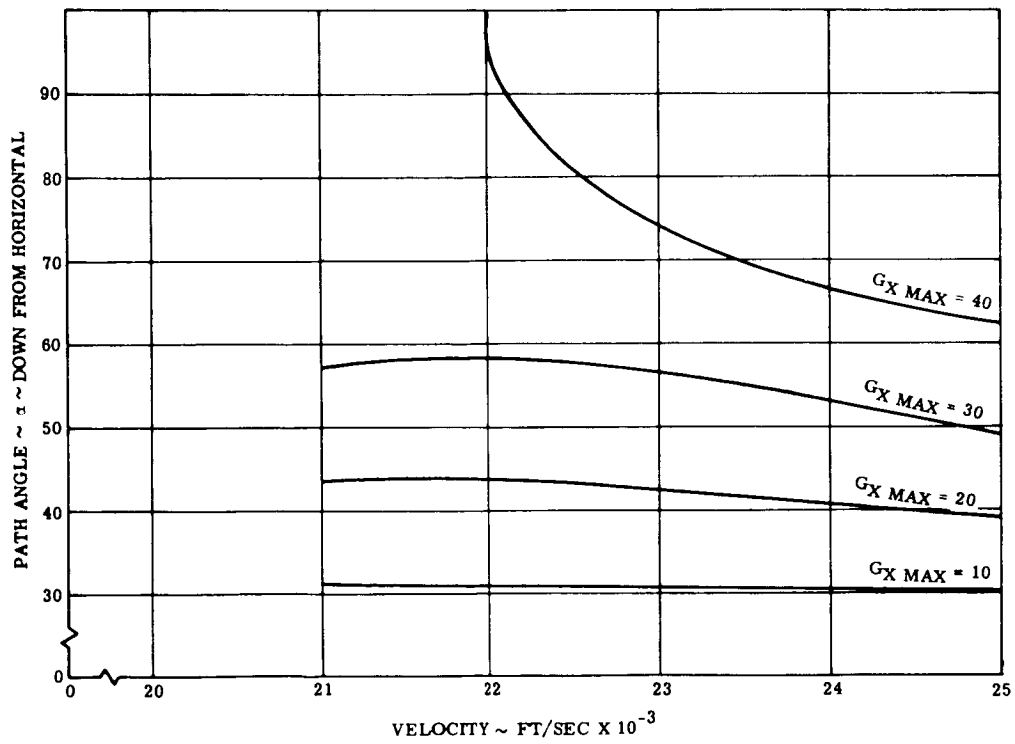


Figure 1.3.2-34. Velocity vs. γ_e for $W/C_D A = 40$ psf and Upper Martian Atmosphere at Various Peak Axial Decelerations in Earth G's

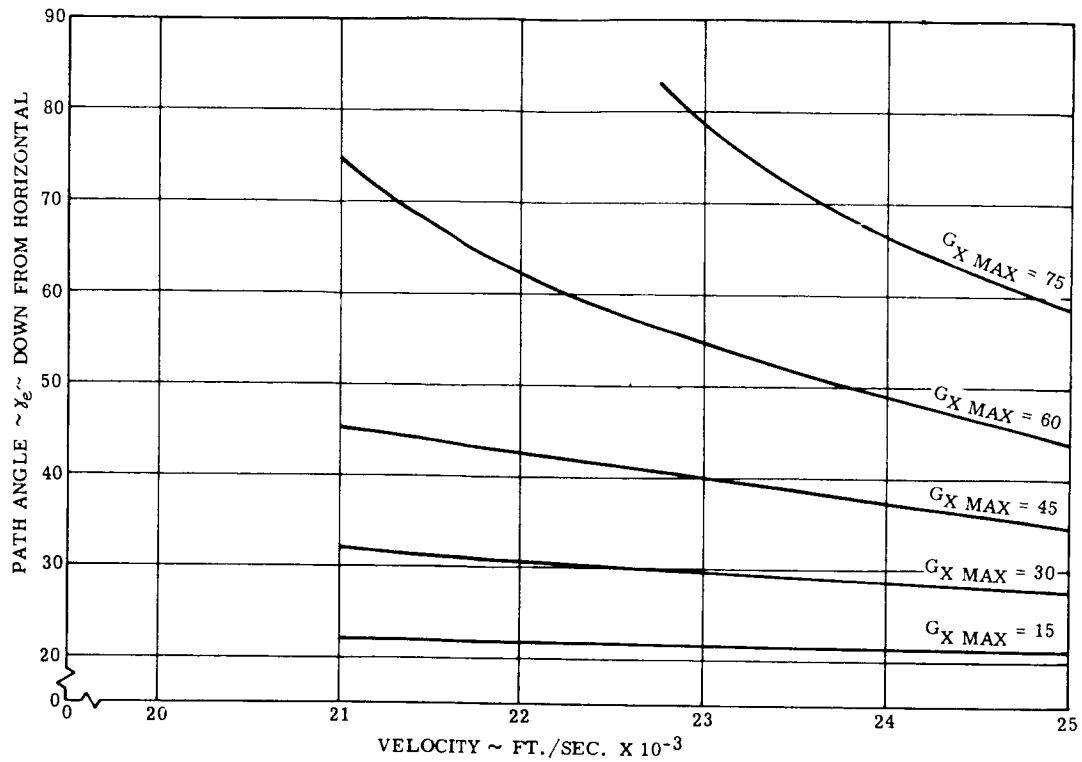


Figure 1.3.2-35. Velocity vs. γ_e for $W/C_{DA} = 60$ psf and Mean Martian Atmosphere at Various Peak Axial Decelerations in Earth G's

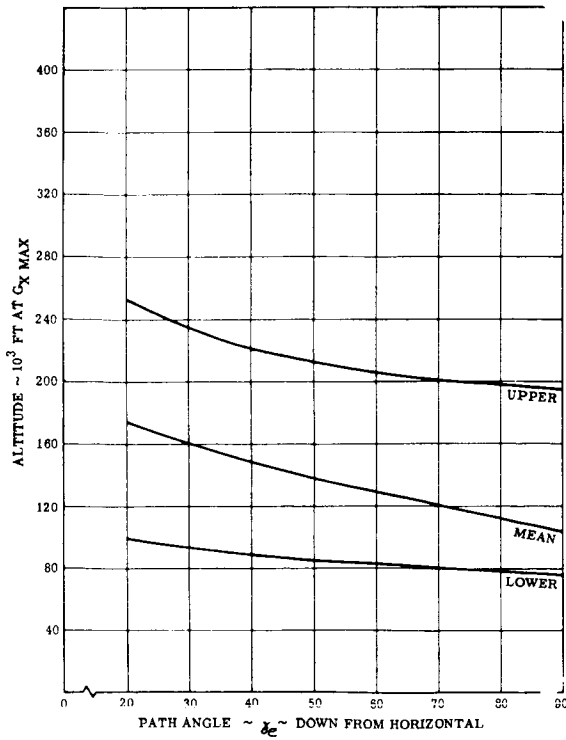


Figure 1.3.2-36. Altitude at $G_{X \text{ Max}}$ vs. γ_e for Various Martian Atmospheres where $W/C_{DA} = 40$ psf and Velocity = 21,000 ft./sec.

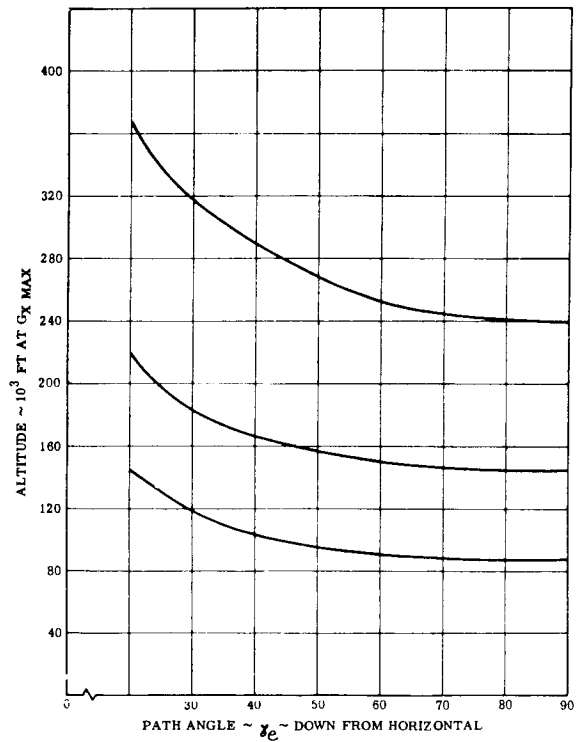


Figure 1.3.2-37. Altitude at $G_{X \text{ Max}}$ vs. γ_e for Various Martian Atmospheres where $W/C_{DA} = 20$ psf and Velocity = 23,000 ft./sec.

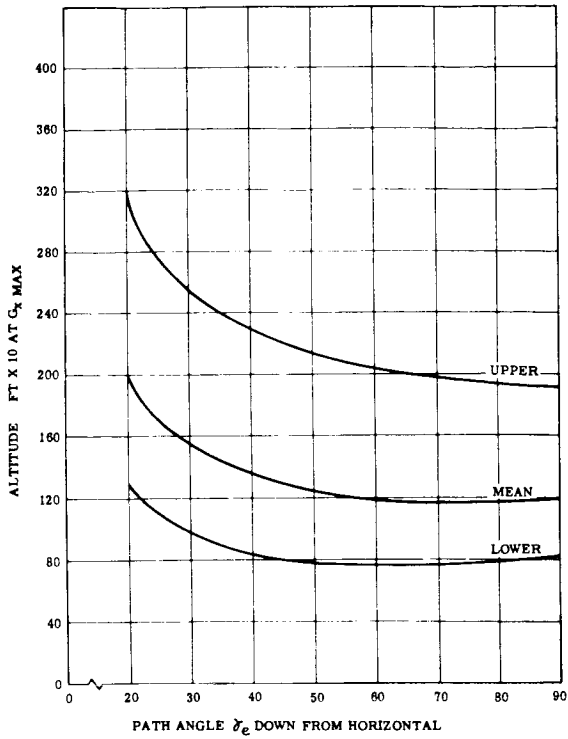


Figure 1.3.2-38. Altitude at $G_{x, \text{Max}}$ vs. γ_e for Various Martian Atmospheres where $W/C_{DA} = 40$ psf and Velocity = 23,000 ft./sec.

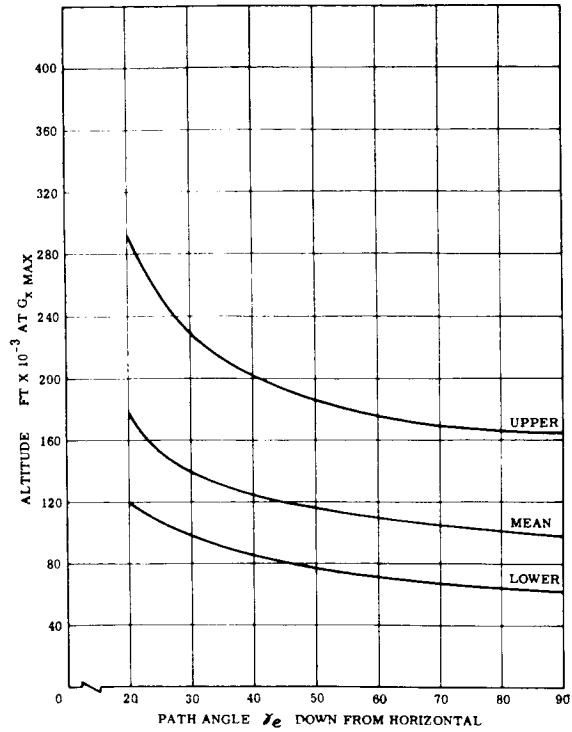


Figure 1.3.2-39. Altitude at $G_{x, \text{Max}}$ vs. γ_e for Various Martian Atmospheres where $W/C_{DA} = 60$ psf and Velocity = 23,000 ft./sec.

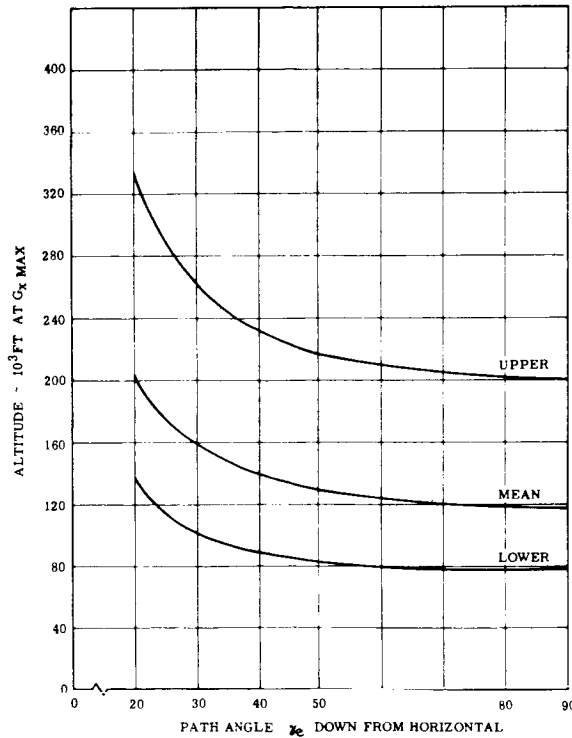


Figure 1.3.2-40. Altitude at $G_{x, \text{Max}}$ vs. γ_e for Various Martian Atmospheres where $W/C_{DA} = 40$ psf and Velocity = 25,000 ft./sec.

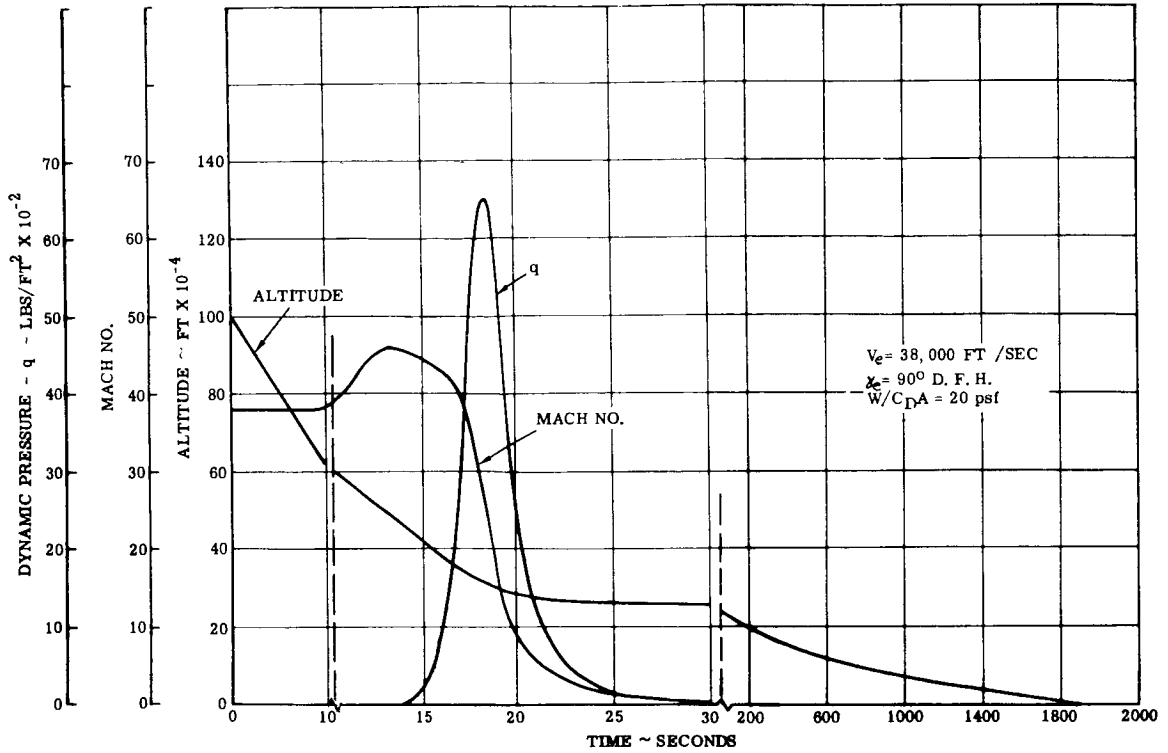


Figure 1.3.2-41. Trajectory Parameters for Entry into Venus Standard Atmosphere

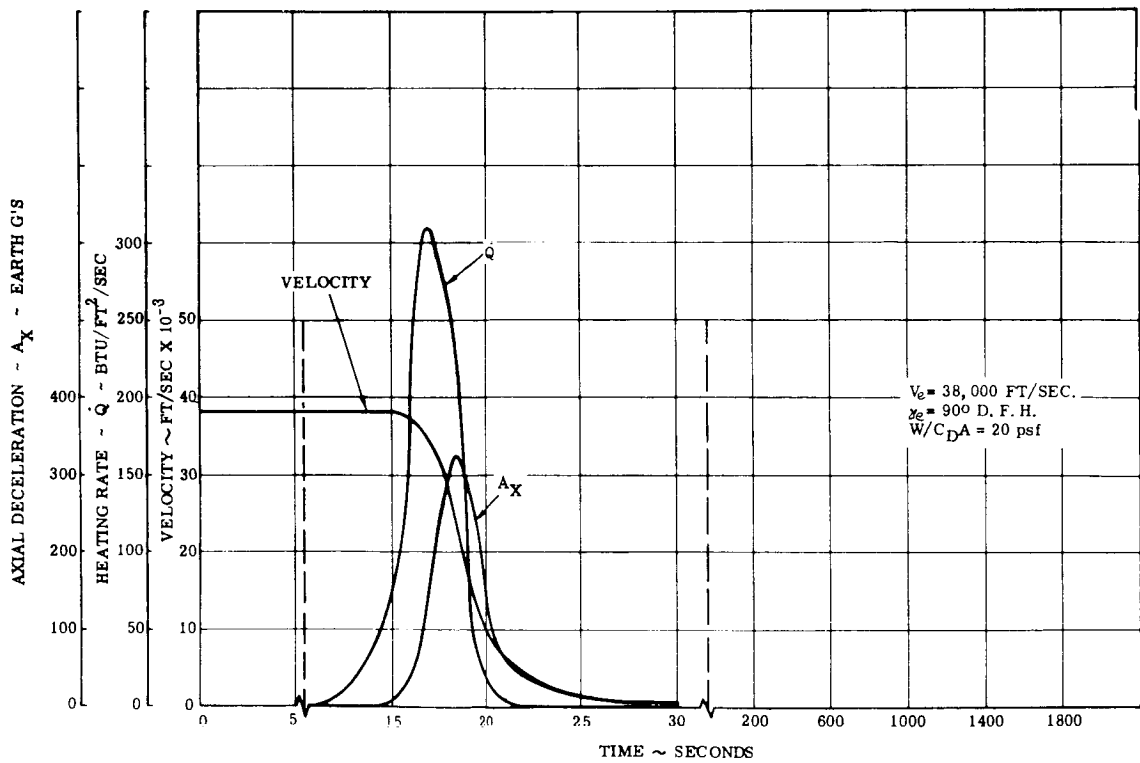


Figure 1.3.2-42. Trajectory Parameters for Entry into Venus Standard Atmosphere

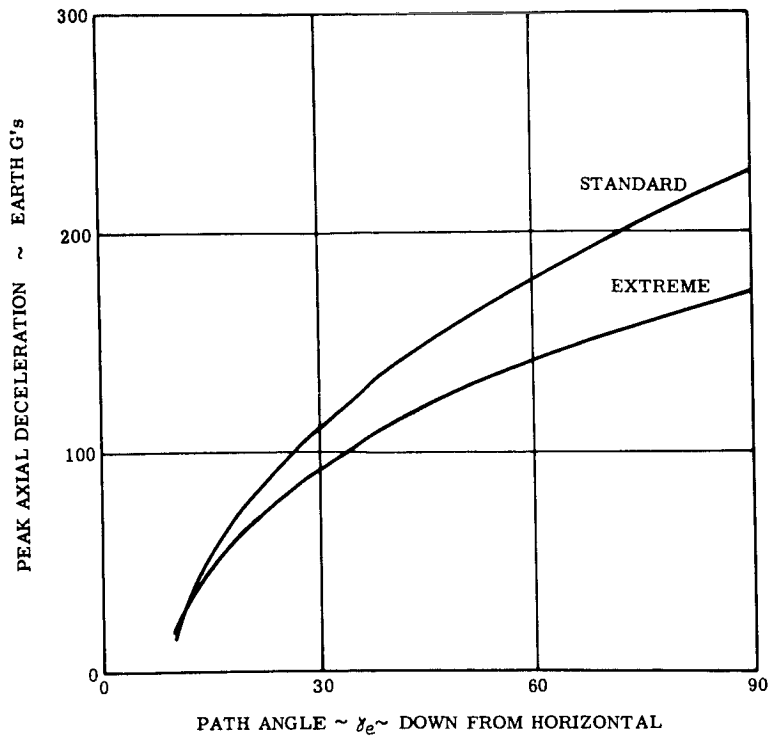


Figure 1.3.2-43. $G_{x_{Max}}$ vs. γ_e for Two Venusian Atmospheres where $W/C_{DA} = 40$ psf and Velocity = 32,000 ft./sec.

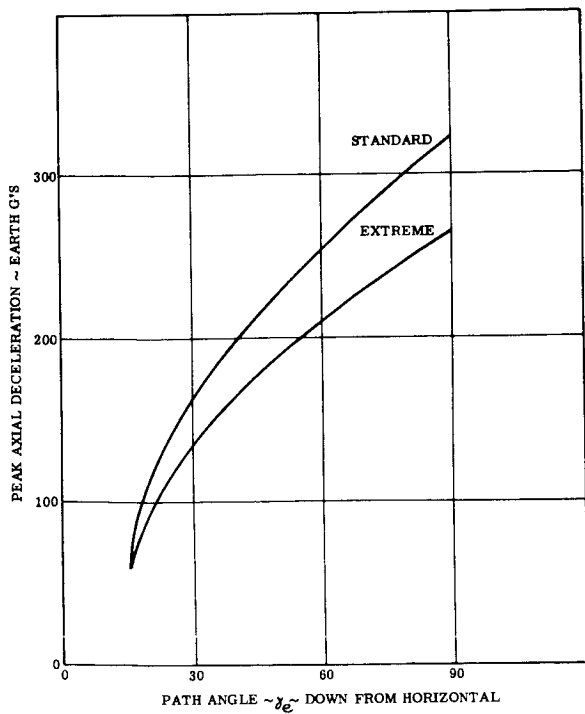


Figure 1.3.2-44. $G_{x_{Max}}$ vs. γ_e for Two Venusian Atmospheres where $W/C_{DA} = 20$ psf and Velocity = 38,000 ft./sec.

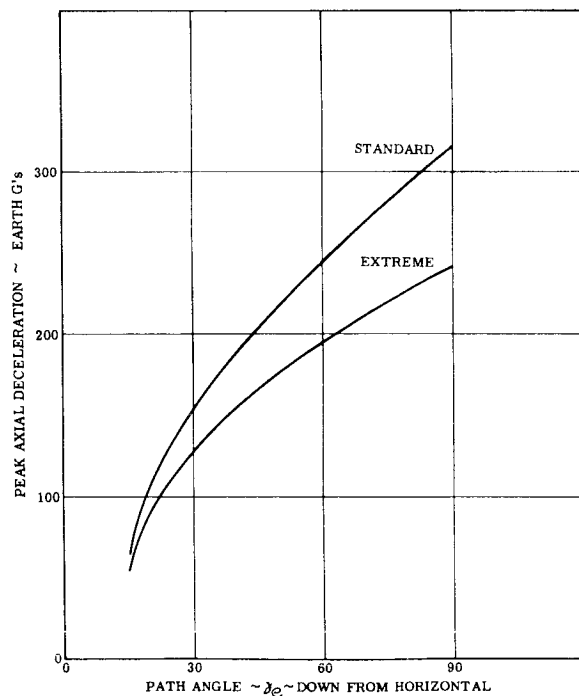


Figure 1.3.2-45. $G_{x_{Max}}$ vs. γ_e for Two Venusian Atmospheres where $W/C_{DA} = 40$ psf and Velocity = 38,000 ft./sec.

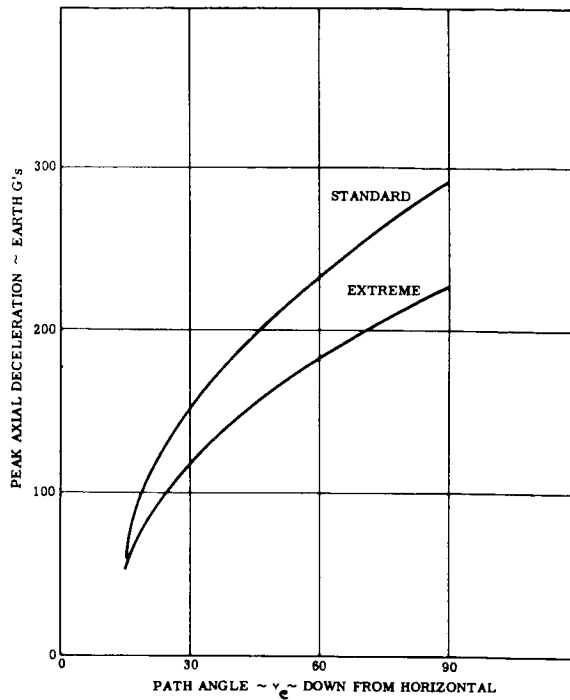


Figure 1.3.2-46. $G_{x,Max}$ vs. γ_c for Two Venusan Atmospheres where $W/C_{DA} = 60$ psf and Velocity = 38,000 ft./sec.

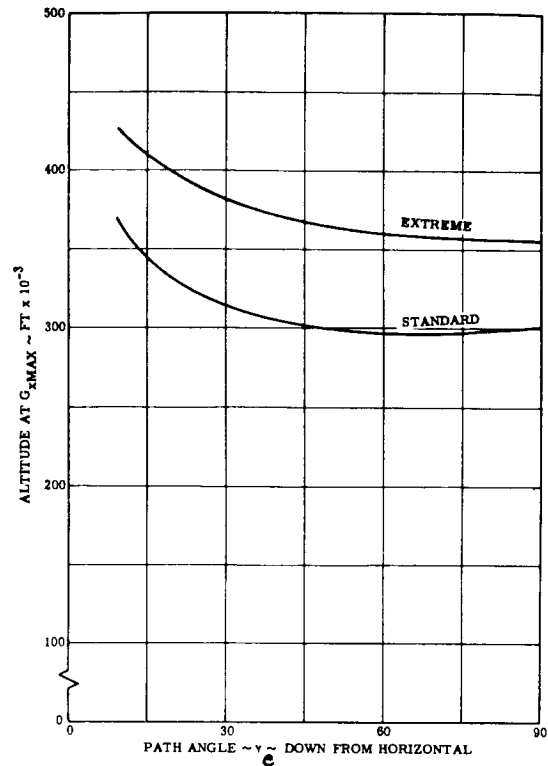


Figure 1.3.2-47. Altitude at $G_{x,Max}$ vs. γ_c for Various Venusan Atmospheres where $W/C_{DA} = 40$ psf and Velocity = 32,000 ft./sec.

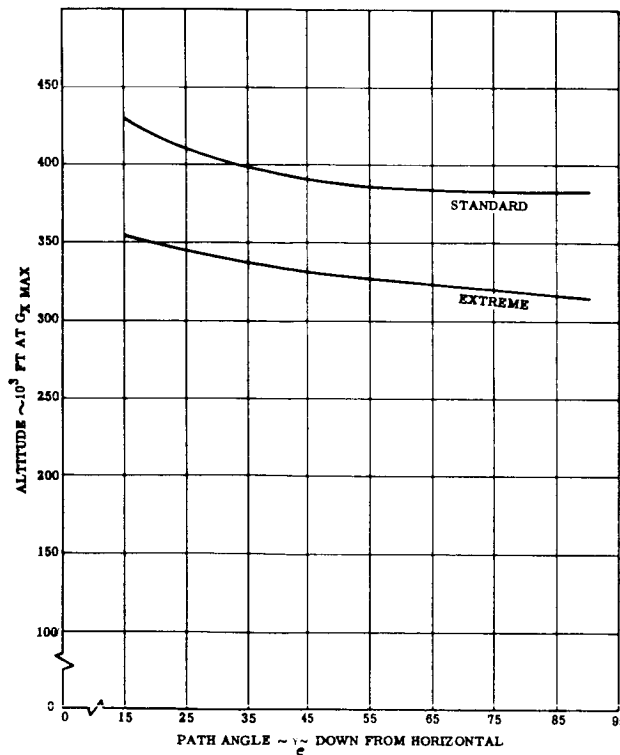


Figure 1.3.2-48. Altitude at $G_{x,Max}$ vs. γ_c for Various Venusan Atmospheres where $W/C_{DA} = 20$ psf and Velocity = 38,000 ft./sec.

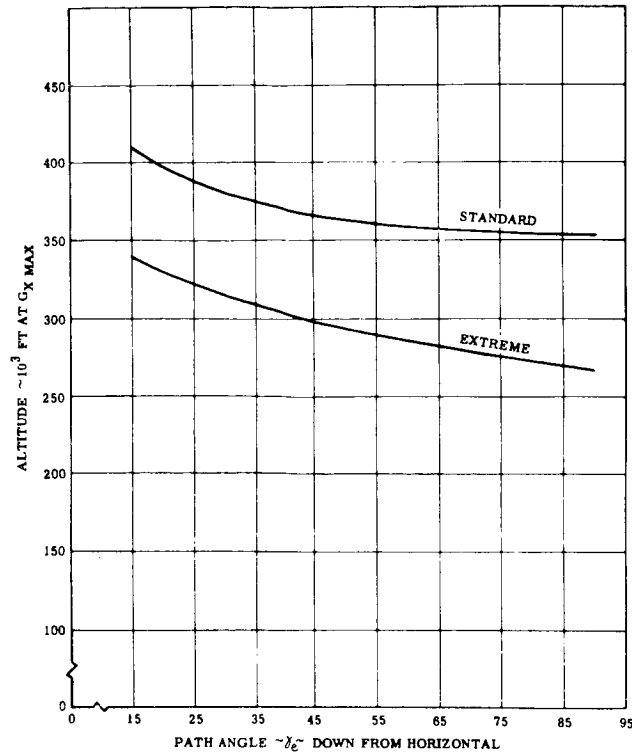


Figure 1.3.2-49. Altitude at $G_{x \text{ Max}}$ vs. γ_e for Various Venusian Atmospheres where $W/C_{DA} = 40$ psf and Velocity = 38,000 ft./sec.

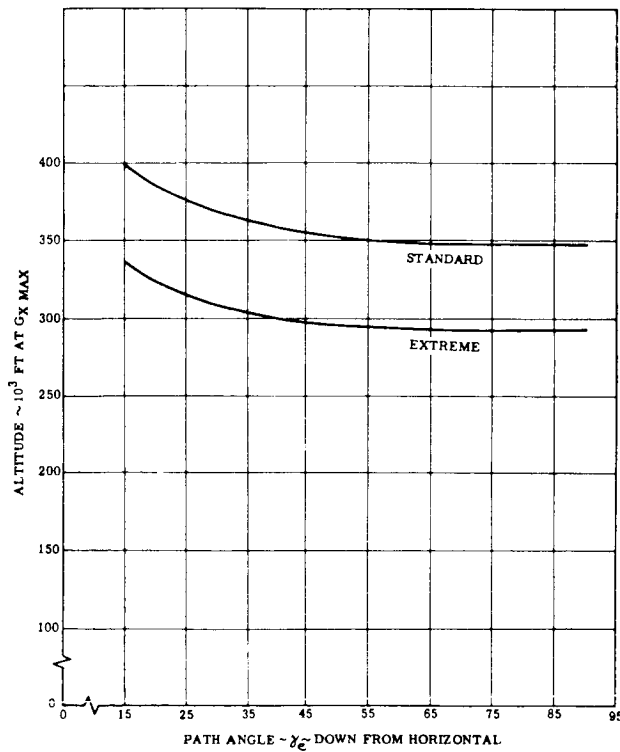


Figure 1.3.2-50. Altitude at $G_{x \text{ Max}}$ vs. γ_e for Various Venusian Atmospheres where $W/C_{DA} = 60$ psf and Velocity = 38,000 ft./sec.

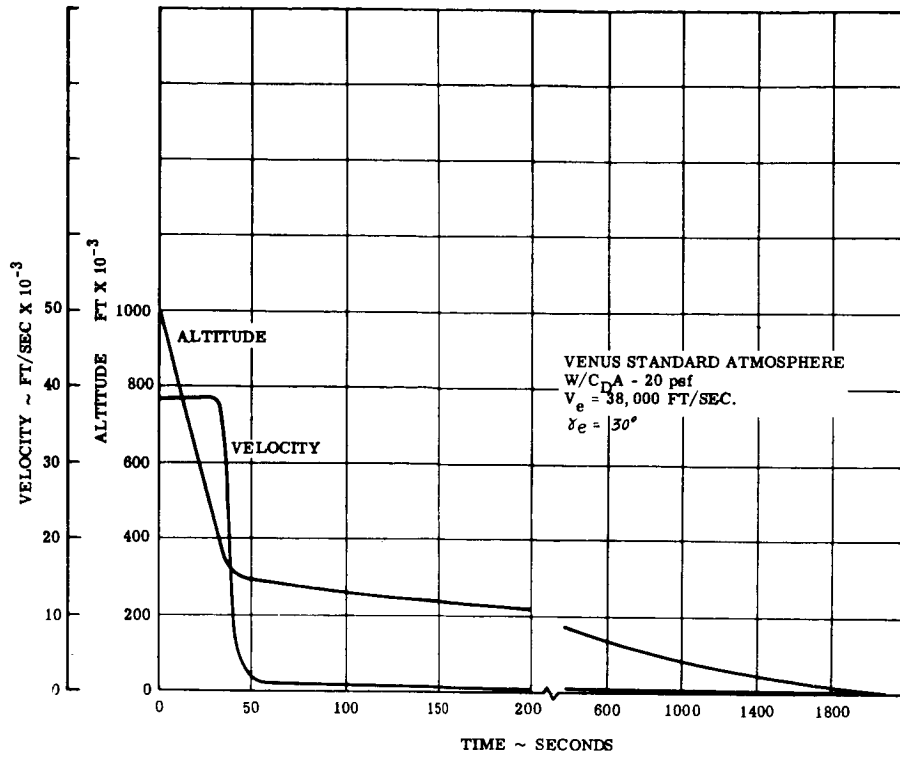


Figure 1.3.2-51. Venus Trajectory

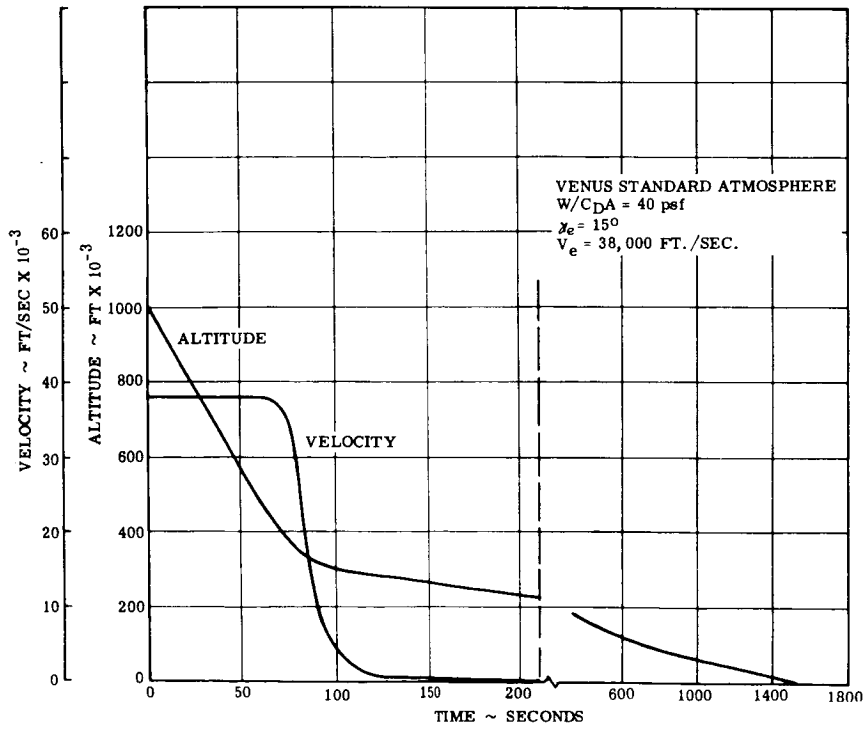


Figure 1.3.2-52. Venus Trajectory

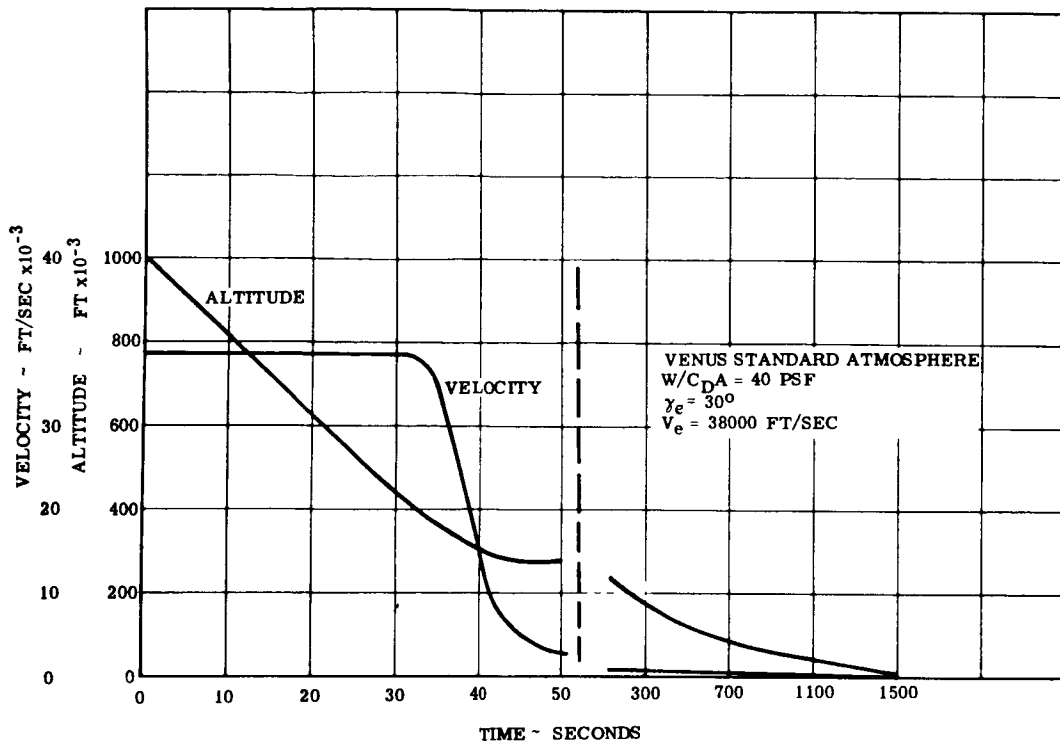


Figure 1.3.2-53. Venus Trajectory

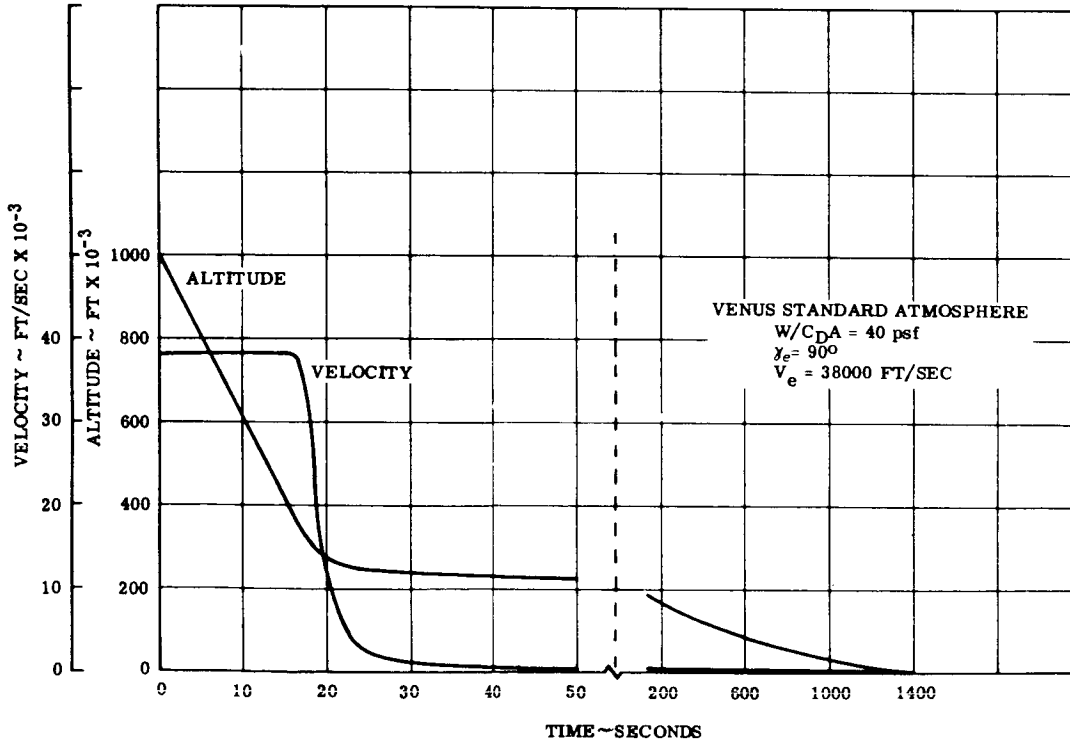


Figure 1.3.2-54. Venus Trajectory

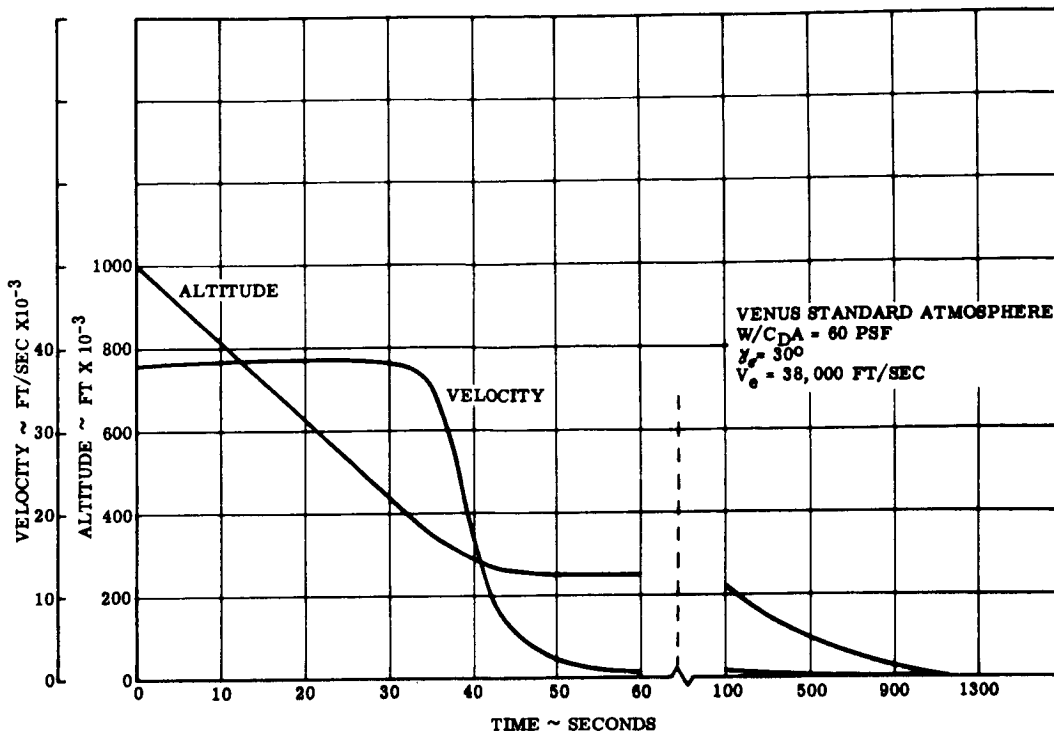


Figure 1.3.2-55. Venus Trajectory

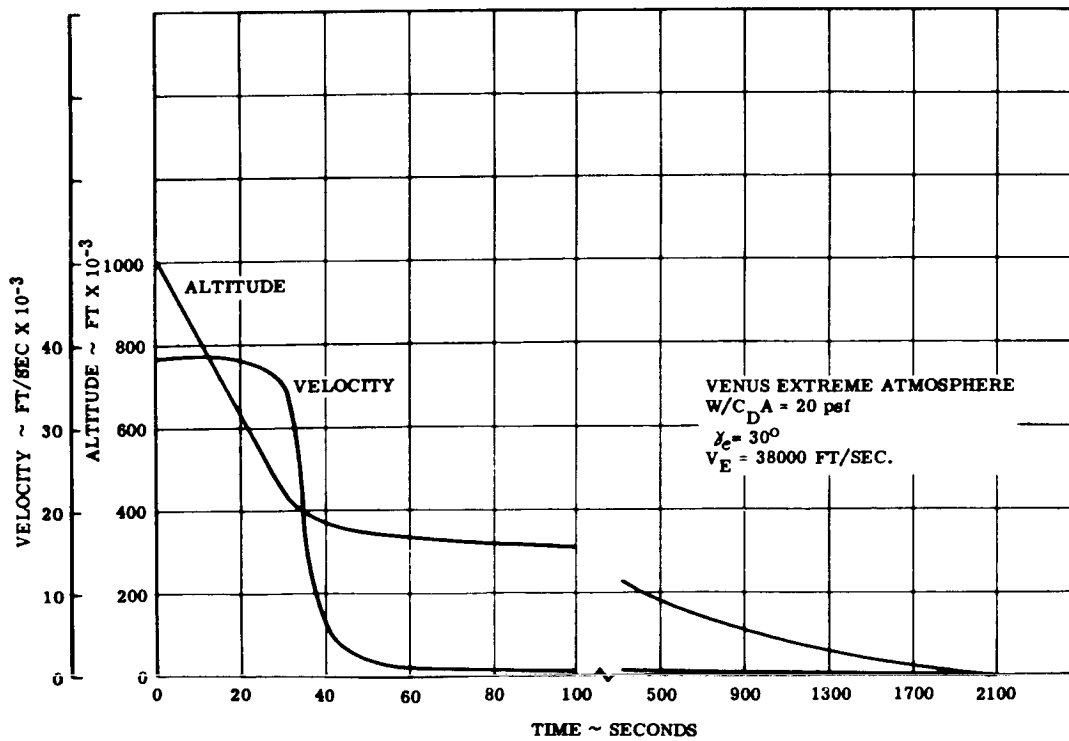


Figure 1.3.2-56. Venus Trajectory

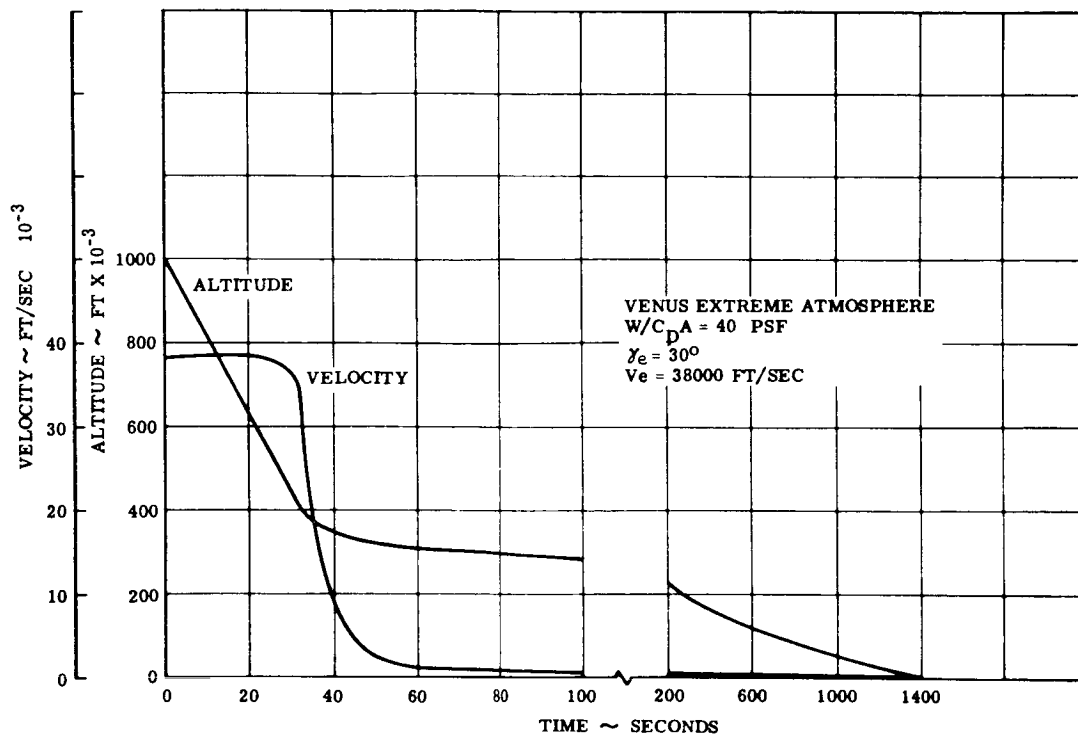
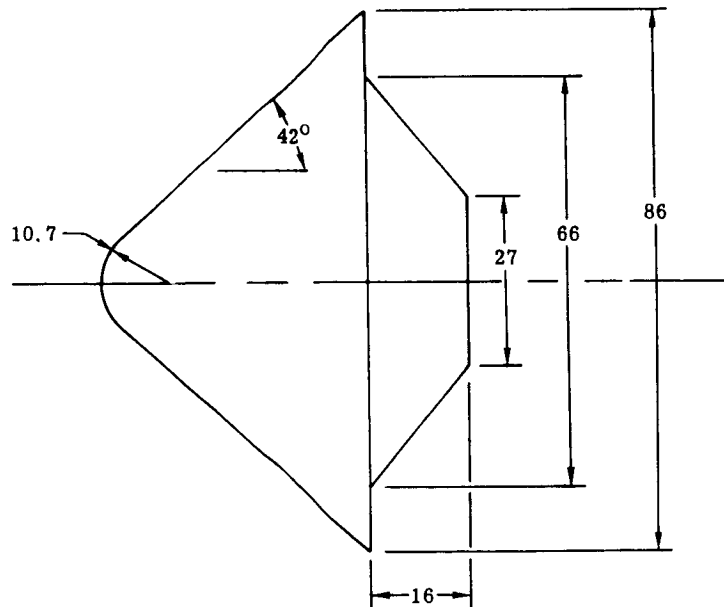


Figure 1.3.2-57. Venus Trajectory

$X_{C.G.} = 32.1 \text{ INCHES FROM NOSE}$



ALL DIMENSIONS IN INCHES

Figure 1.3.2-58. Voyager Configuration

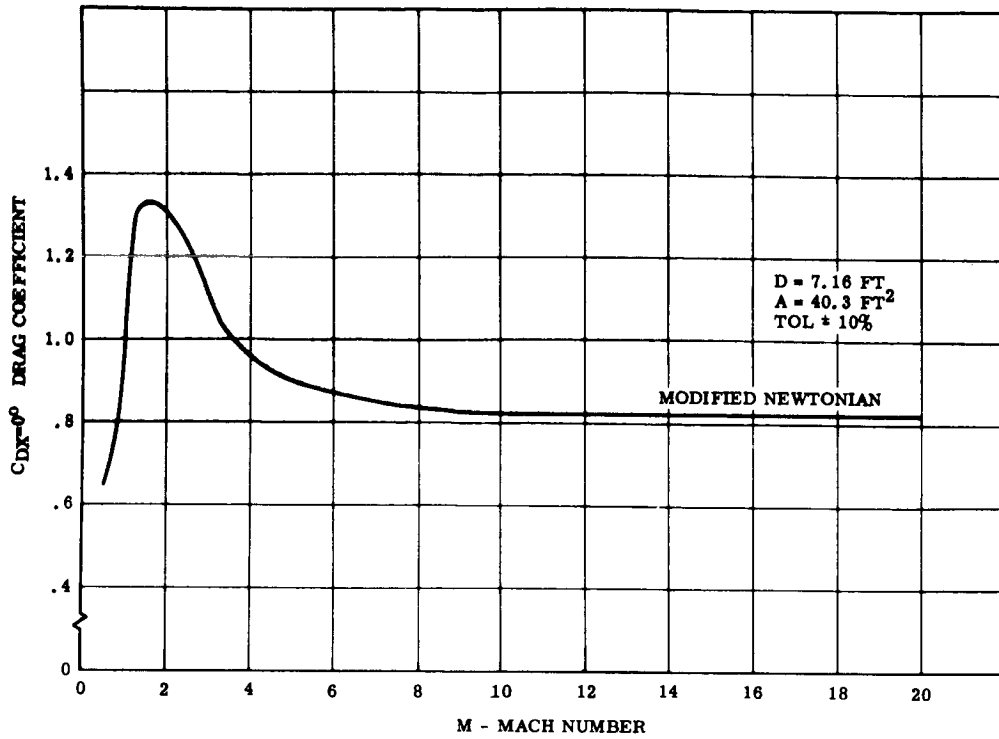


Figure 1.3.2-59. Variation of Drag Coefficient with Mach Number, Altitude 0-250,000 Feet (Mars Lower Atmosphere)

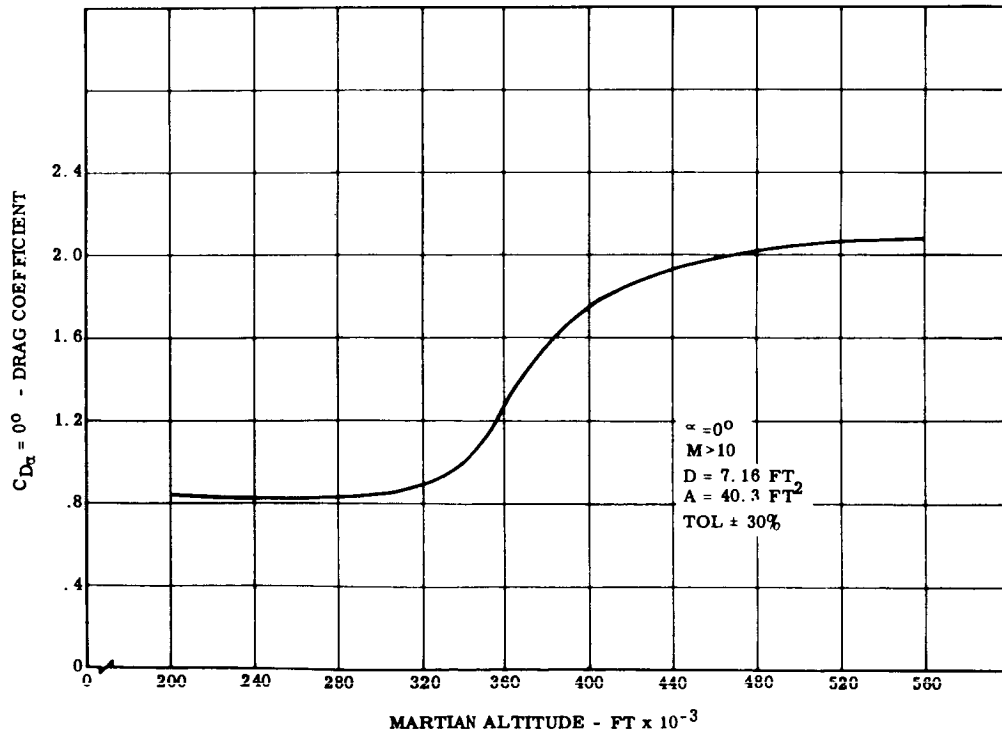


Figure 1.3.2-60. Variation of Drag Coefficient with Altitude - Mars

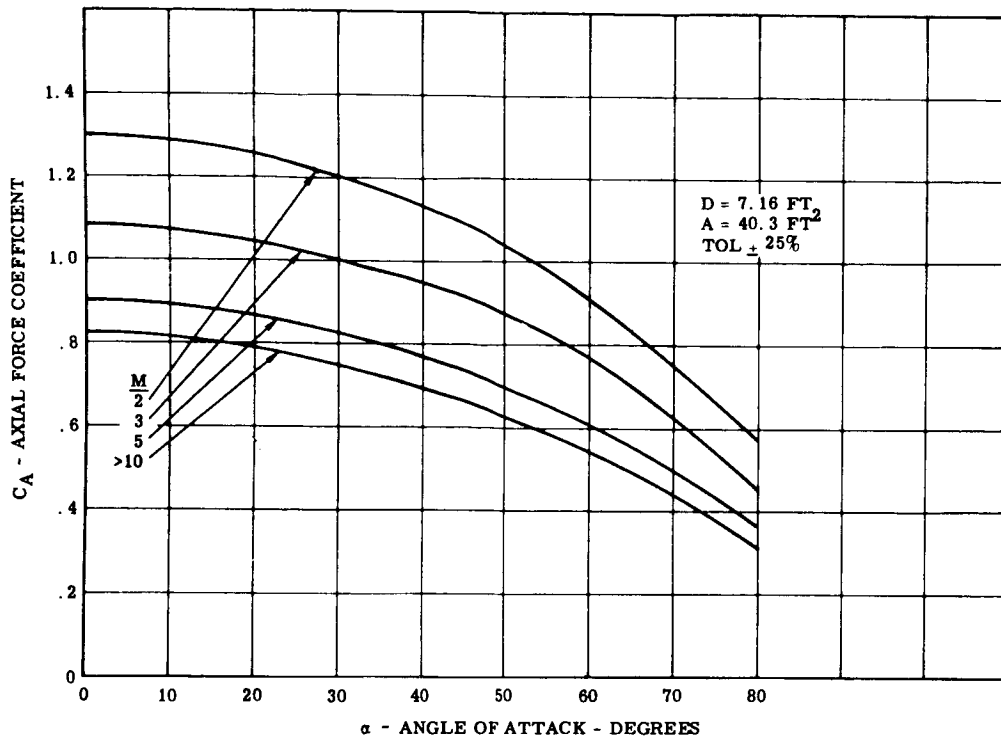


Figure 1.3.2-61. Variation of Axial Force Coefficient with Angle of Attack, Altitude 0 to 250,000 Feet (Mars Lower Atmosphere)

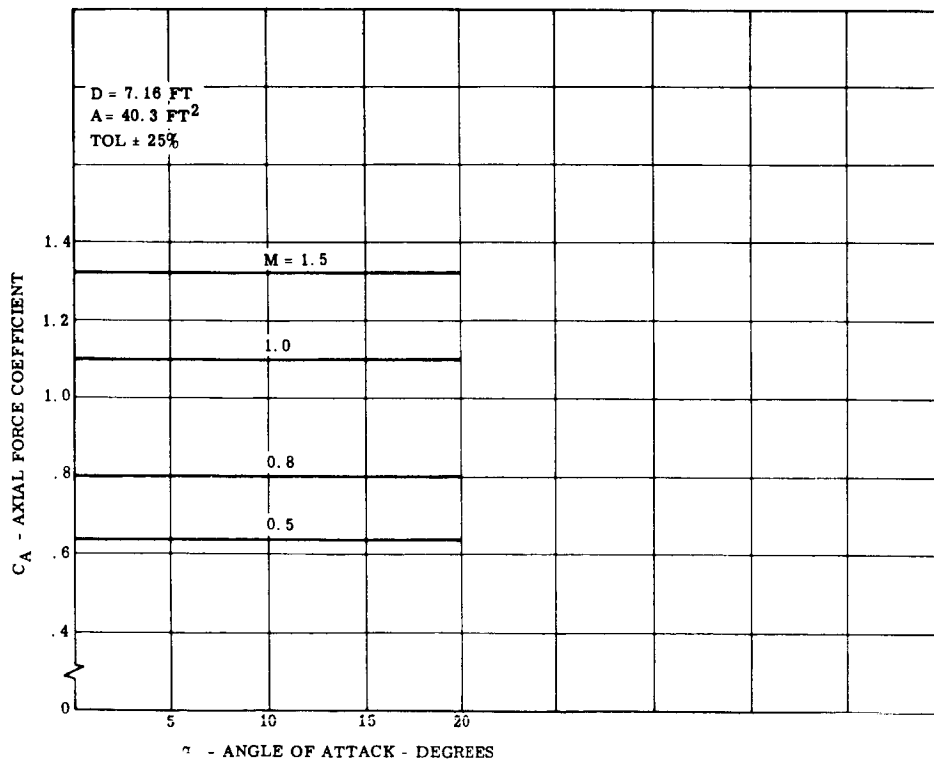


Figure 1.3.2-62. Variation of Axial Force Coefficient with Angle of Attack, Altitude 0 to 250,000 Feet (Mars Lower Atmosphere)

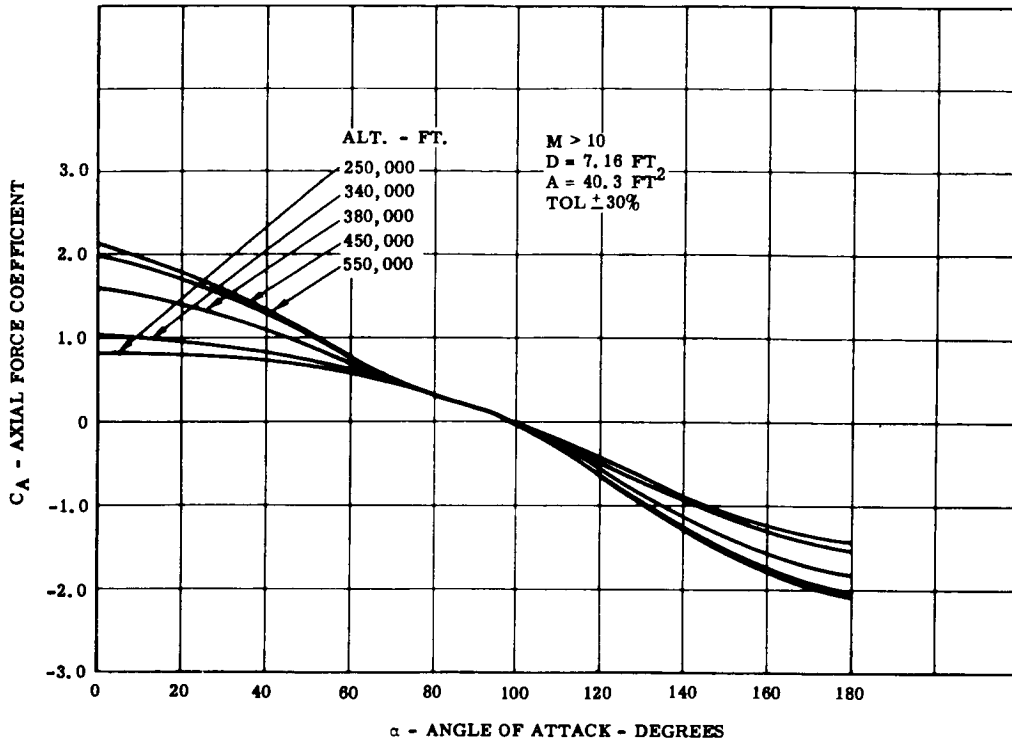


Figure 1.3.2-63. Variation of Axial Force Coefficient with Angle of Attack of Various Altitudes (Mars Lower Atmosphere)

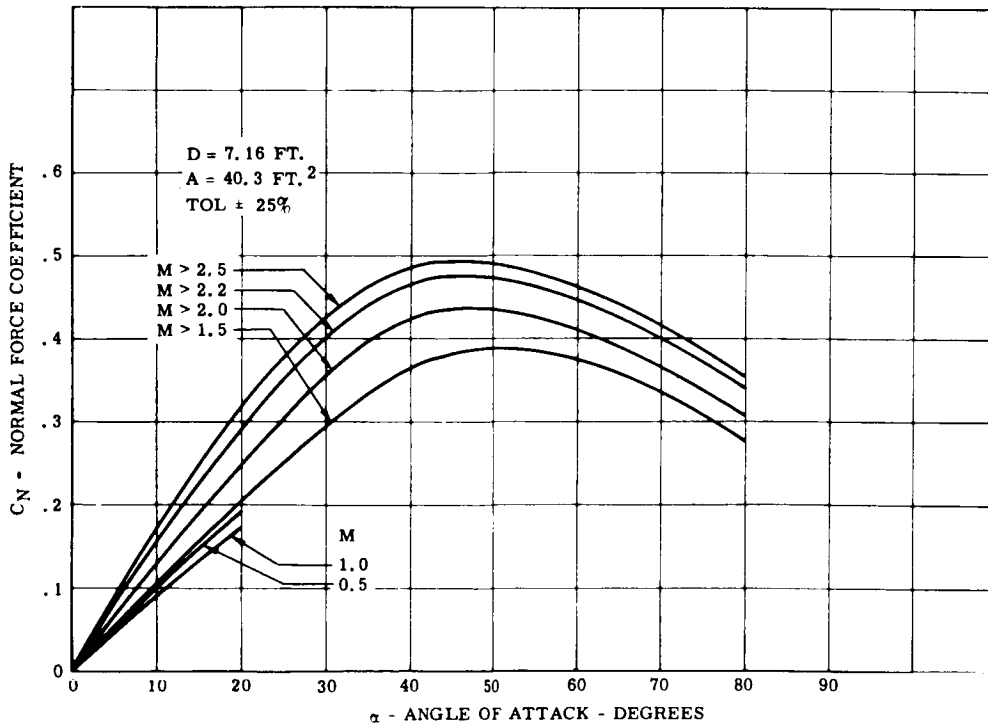


Figure 1.2.2-64. Variation of Normal Force Coefficient with Angle of Attack, Altitude 0 to 250,000 Feet (Mars Lower Atmosphere)

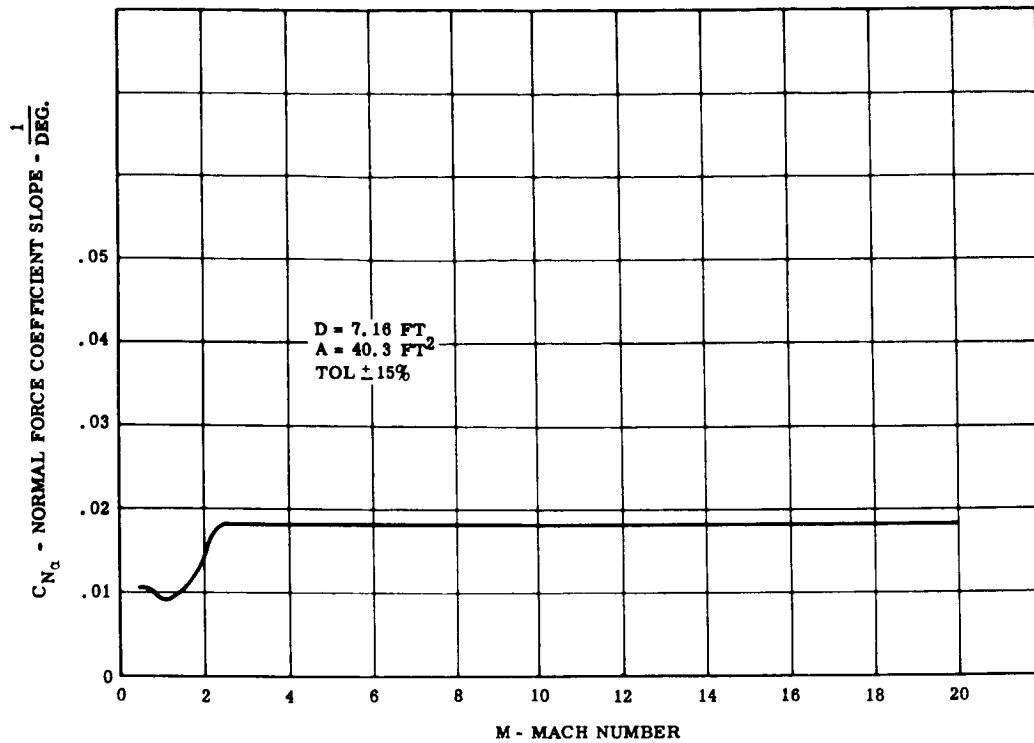


Figure 1.3.2-65. Variation of Normal Force Coefficient Slope with Mach Number, Altitude 0 to 250,000 Feet (Mars Lower Atmosphere)

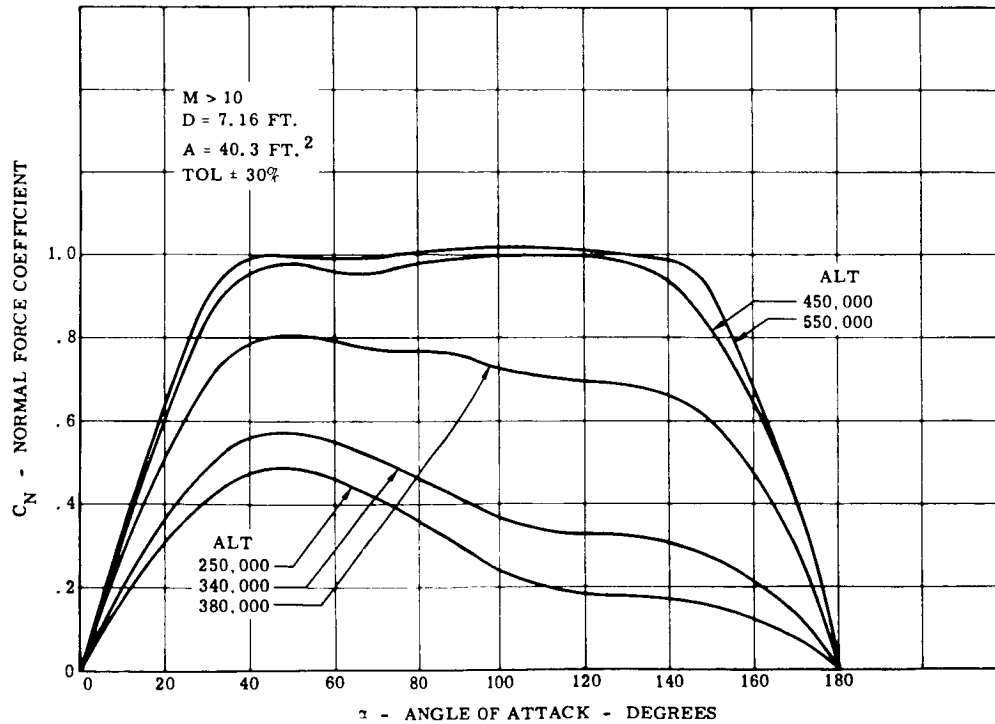


Figure 1.3.2-66. Variation of Normal Force Coefficient with Angle of Attack at Various Altitudes (Mars Lower Atmosphere)

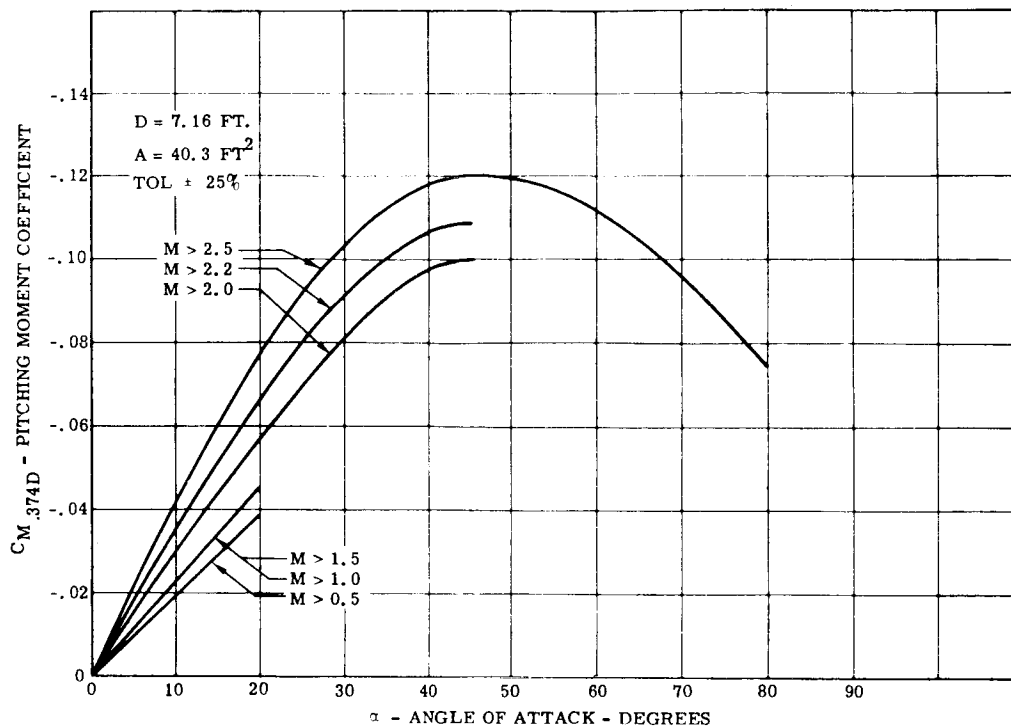


Figure 1.3.2-67. Variation of Pitching Moment Coefficient with Angle of Attack, Altitude 0 to 250,000 Feet (Mars Lower Atmosphere)

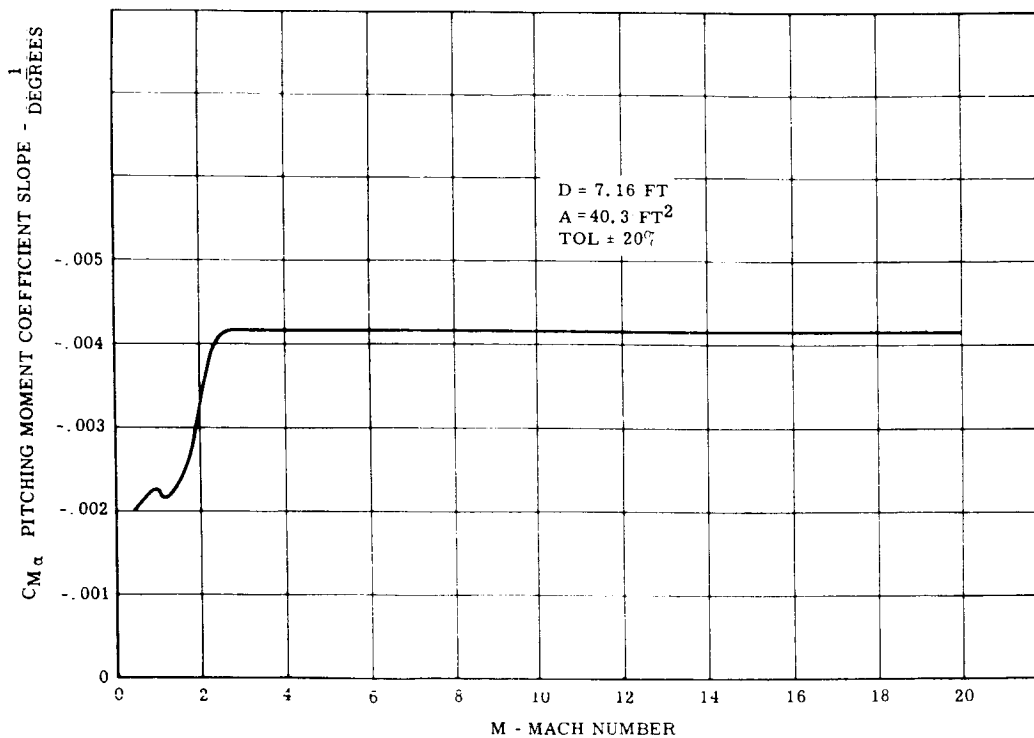


Figure 1.3.2-68. Variation of Pitching Moment Coefficient Slope with Mach Number, Altitude 0 to 250,000 Feet (Mars Lower Atmosphere)

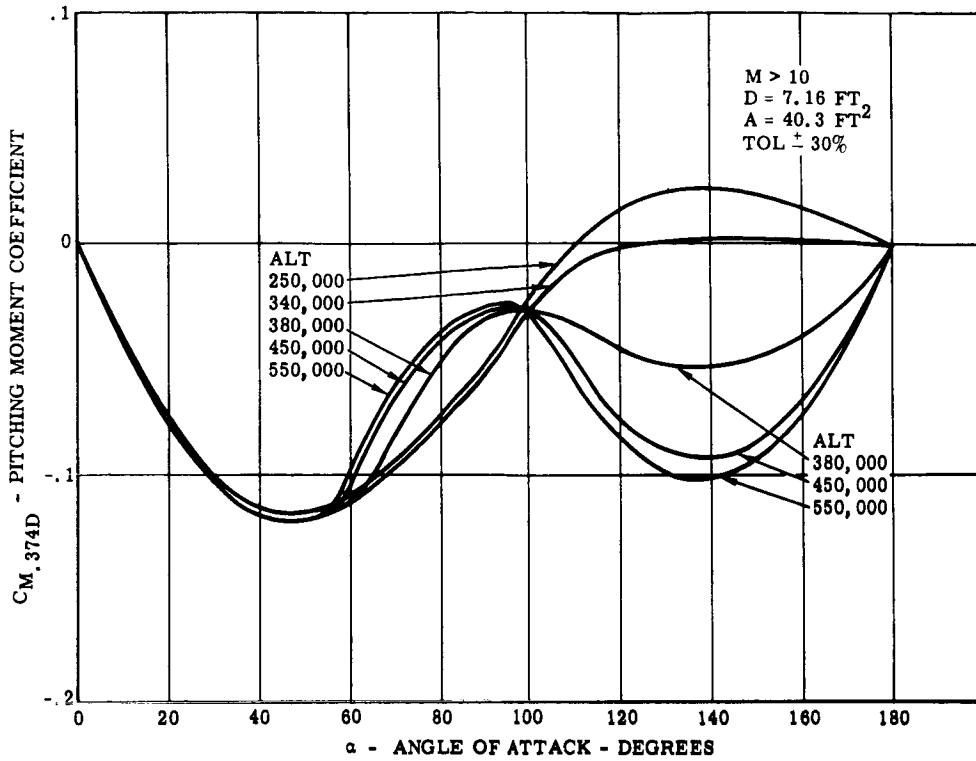


Figure 1.3.2-69. Variation of Pitching Moment Coefficient with Angle of Attack at Various Altitudes (Mars Lower Atmosphere)

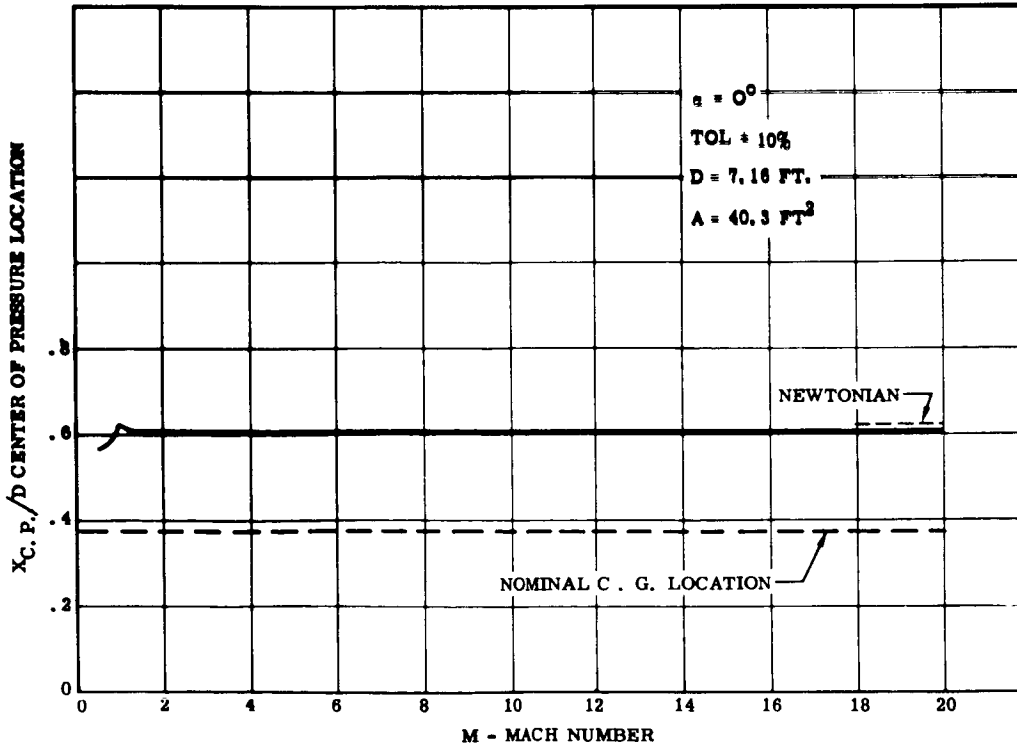


Figure 1.3.2-70. Variation of Center of Pressure Location with Mach Number, Altitude 0 to 250,000 Feet

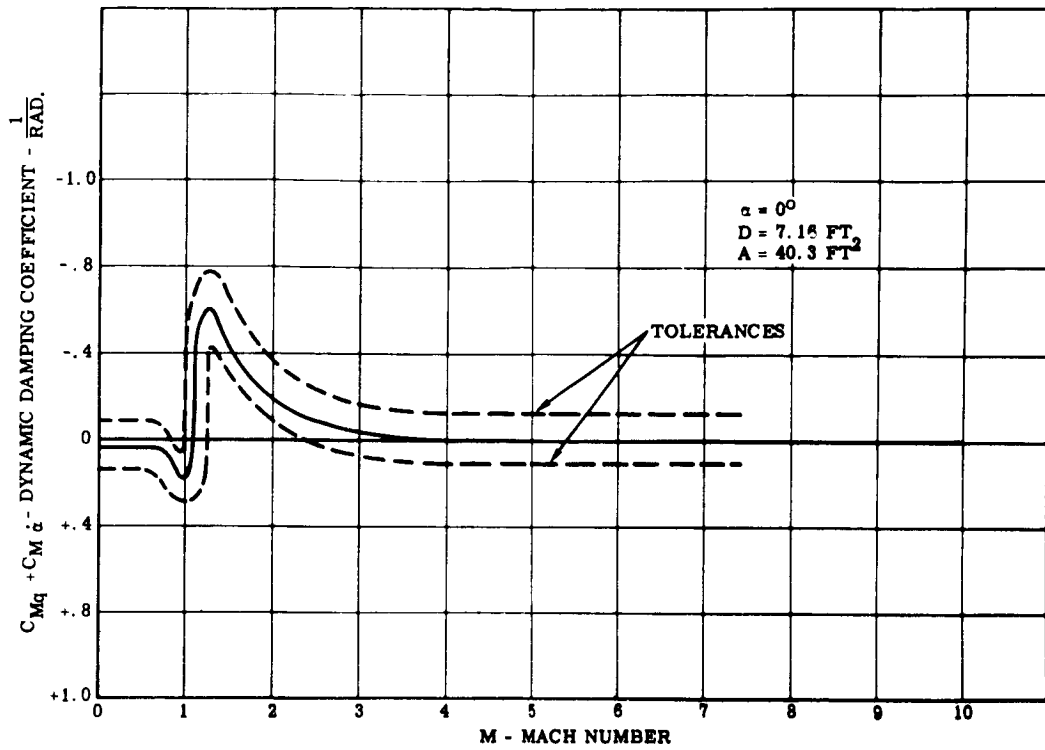


Figure 1.3.2-71. Variation of Dynamic Damping with Mach Number

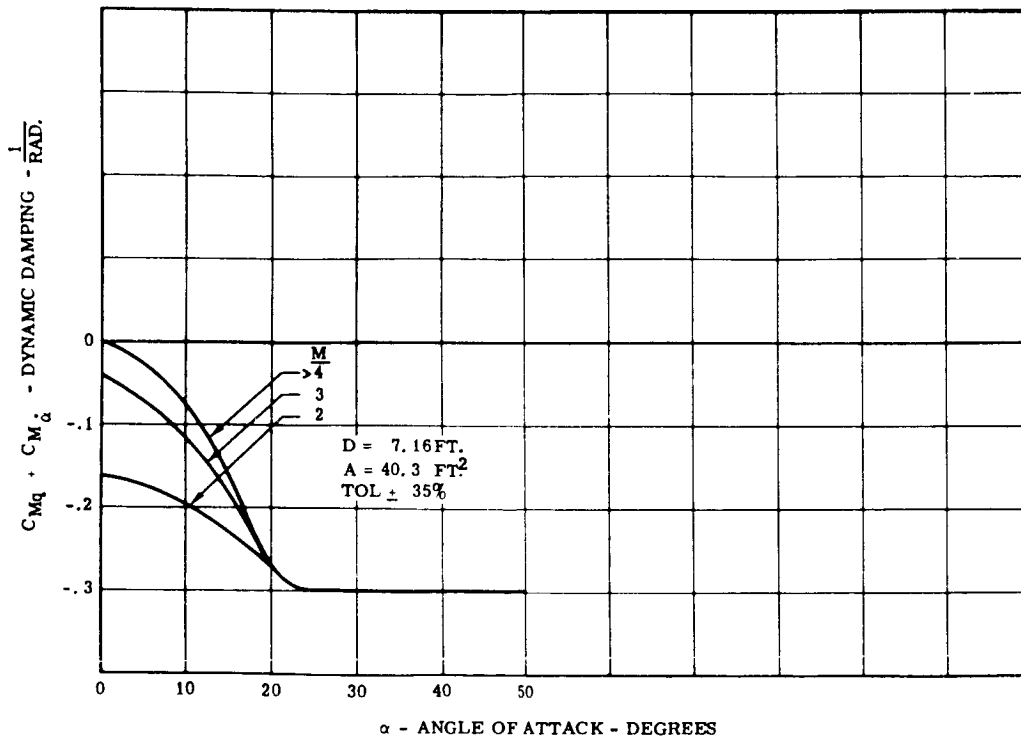


Figure 1.3.2-72. Variation of Dynamic Damping with Angle of Attack

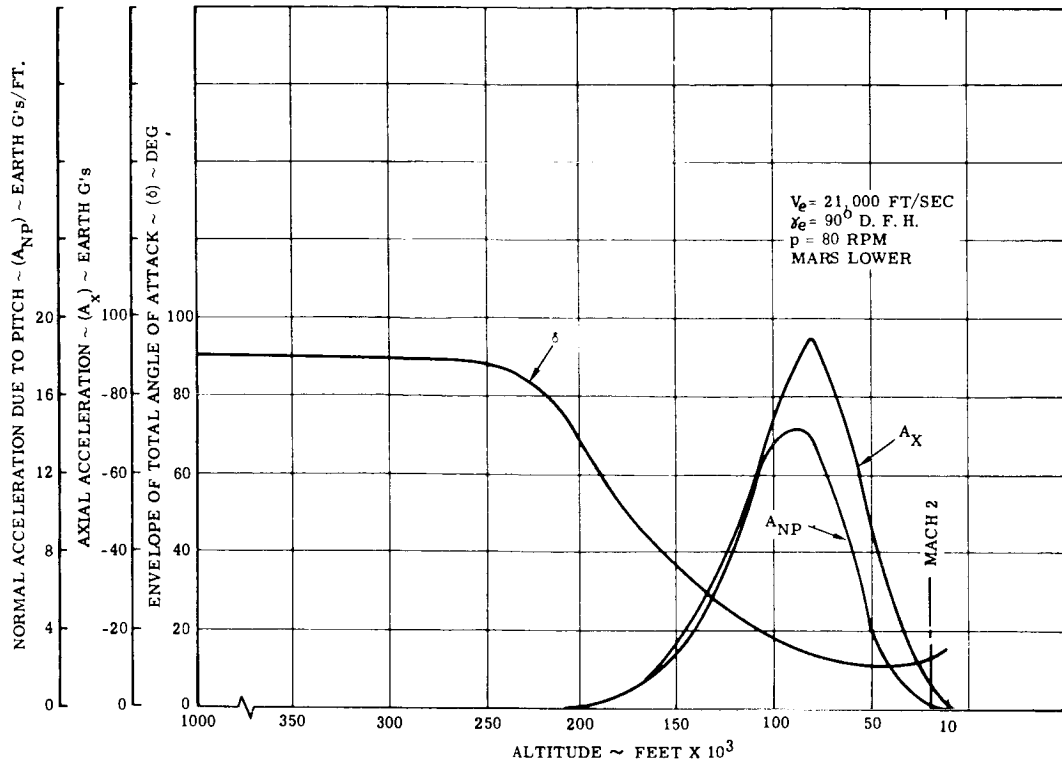


Figure 1.3.2-73. Normal Acceleration Due to Pitch, Axial Acceleration and Total Angle of Attack vs. Altitude

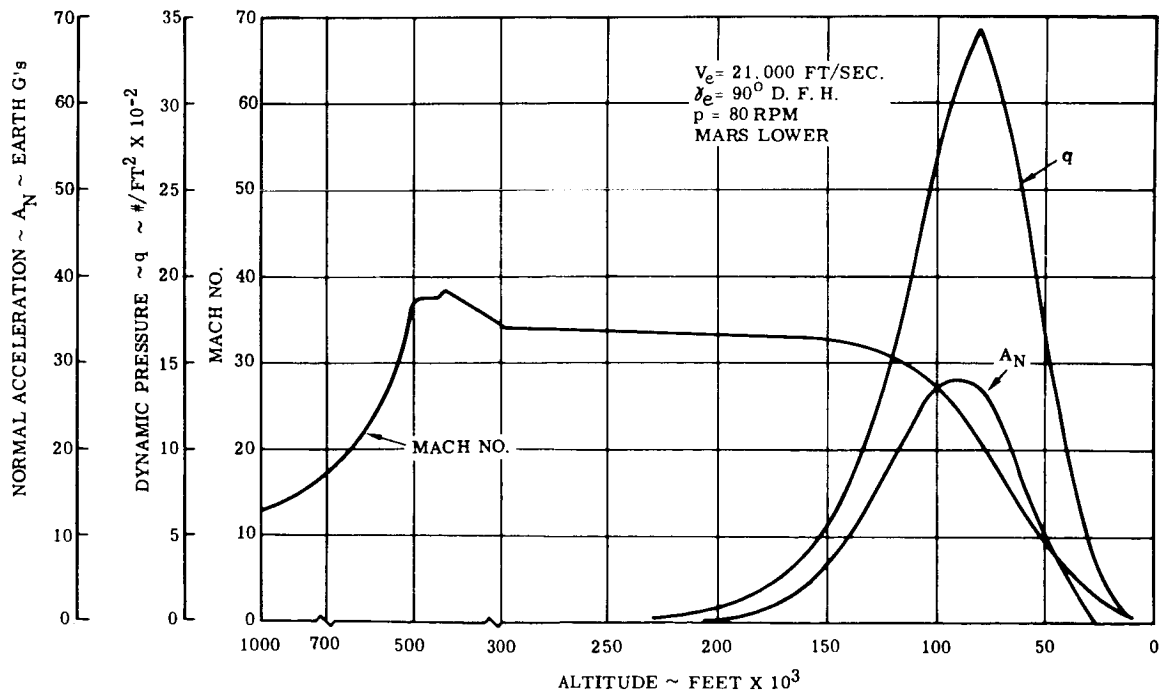


Figure 1.3.2-74. Mach Number, Normal Loads, and Dynamic Pressure vs. Altitude

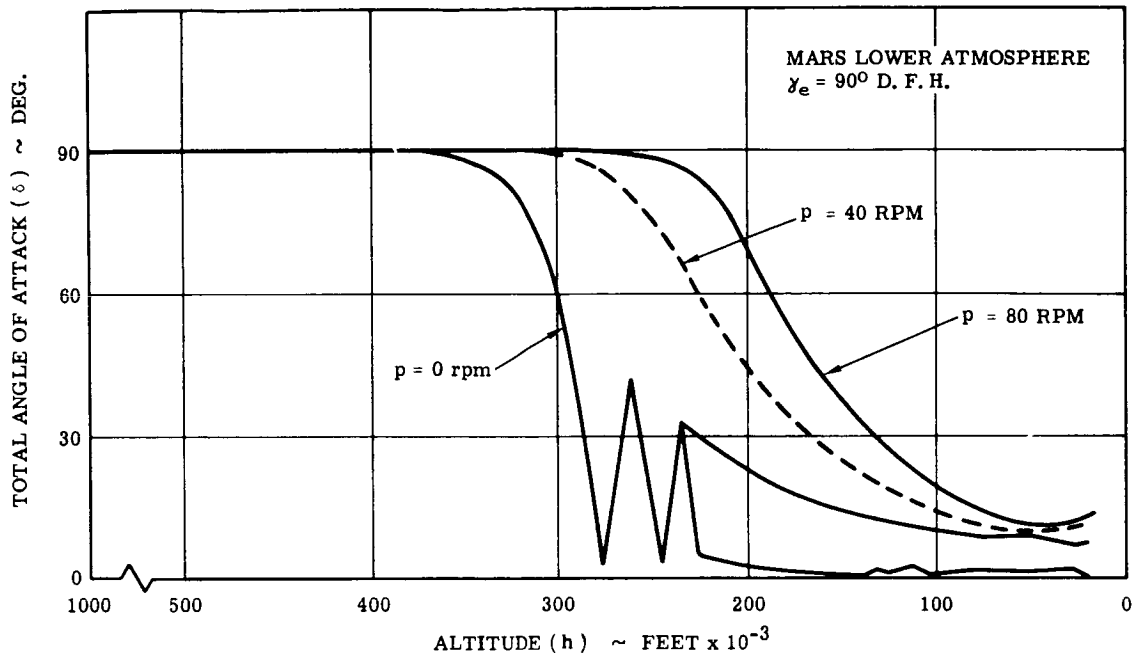


Figure 1.3.2-75. Total Angle of Attack Envelope History Comparison for Various Spin Rates

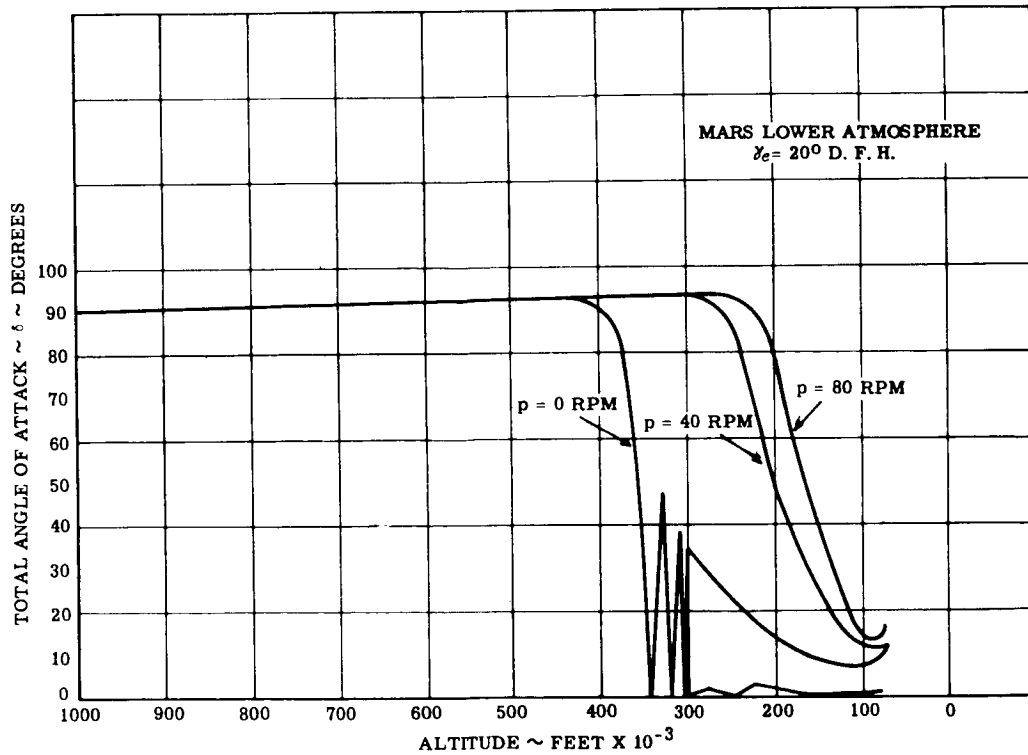


Figure 1.3.2-76. Total Angle of Attack Envelope History Comparison for Various Spin Rates

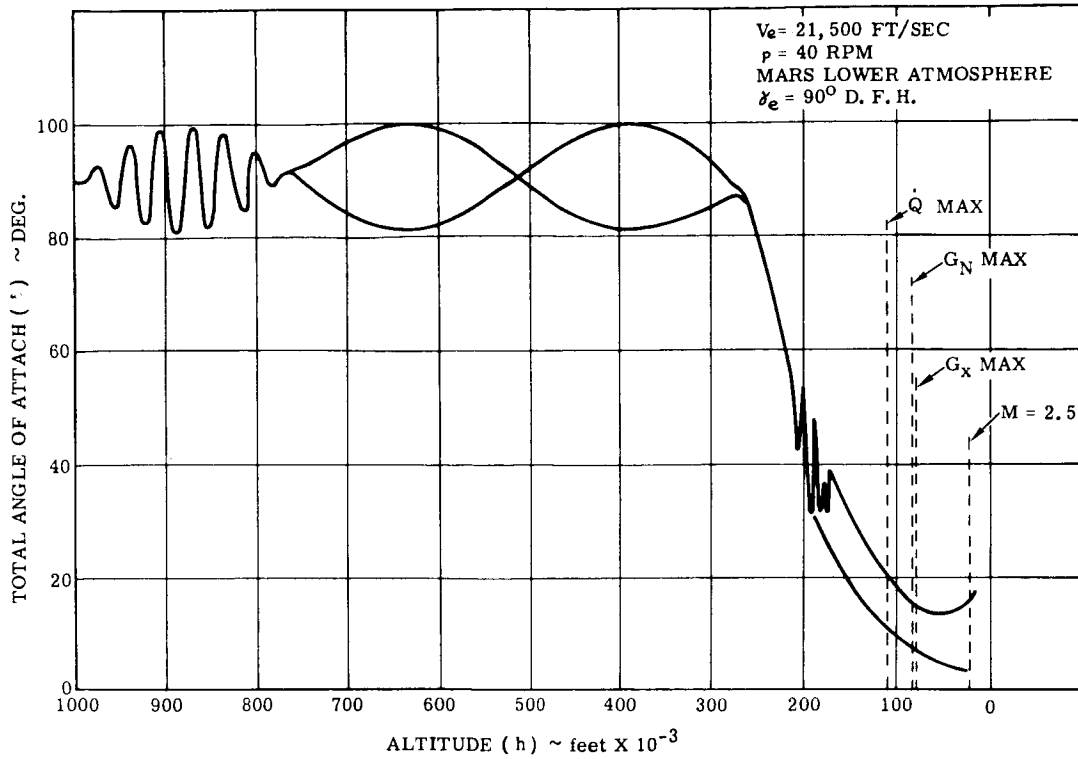


Figure 1.3.2-77. Total Angle of Attack Envelope vs. Altitude with c.g. Offset and Product of Inertia

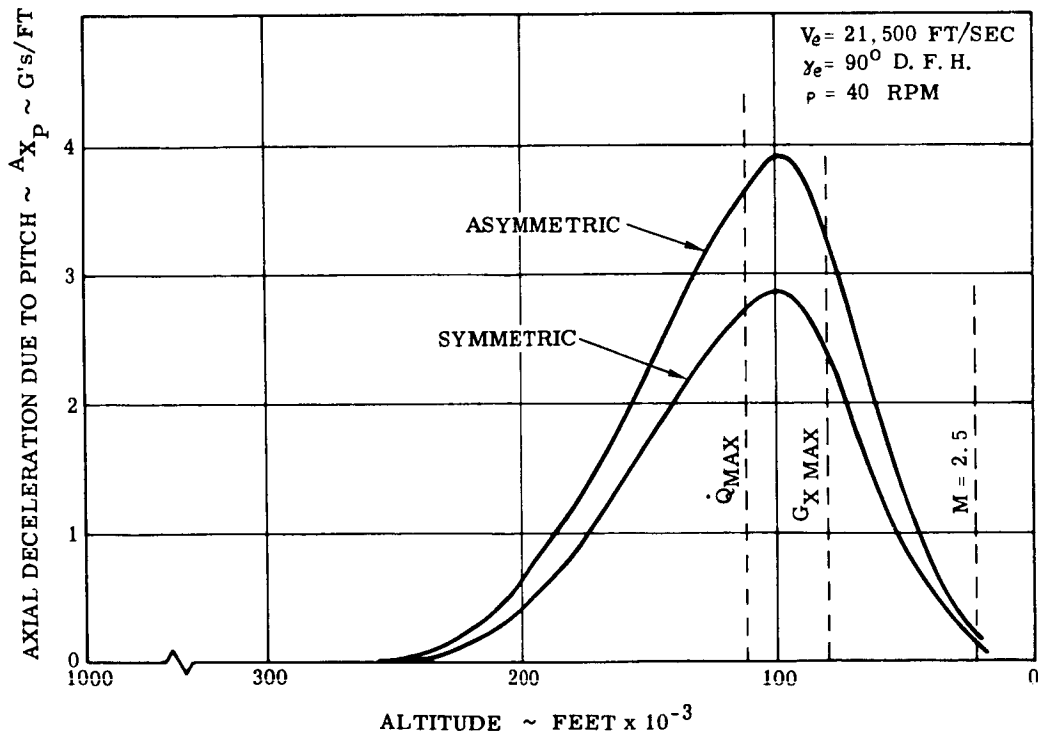


Figure 1.3.2-78. A_{Xp} Altitude History Comparison for Symmetric and Asymmetric Vehicle

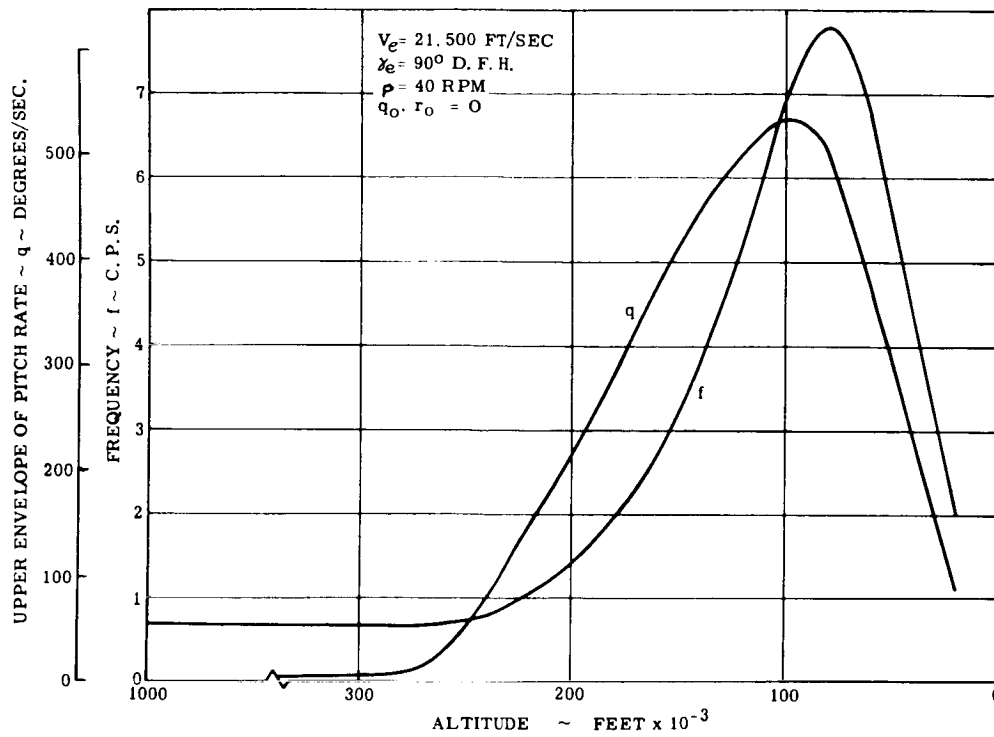


Figure 1.3.2-79. Upper Envelope of Pitch Rate and Frequency for Entry into Mars Lower Atmosphere

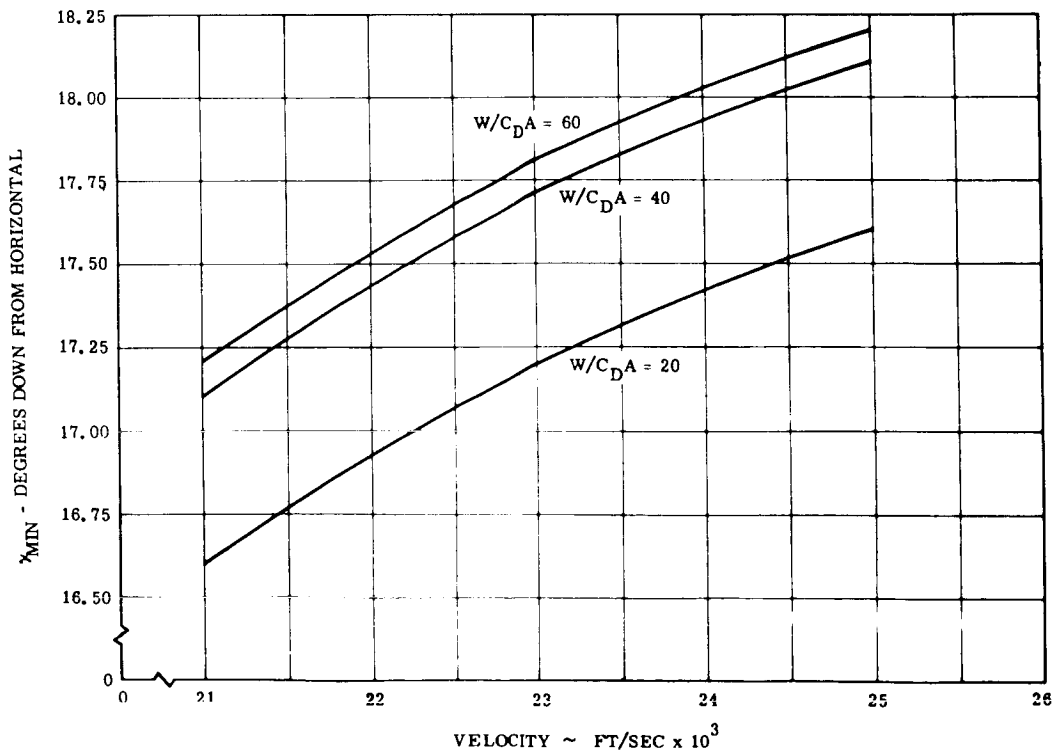


Figure 1.3.2-80. Capture Angle as Function of Velocity and W/C_{DA} for Entry into Mars Mean Atmosphere

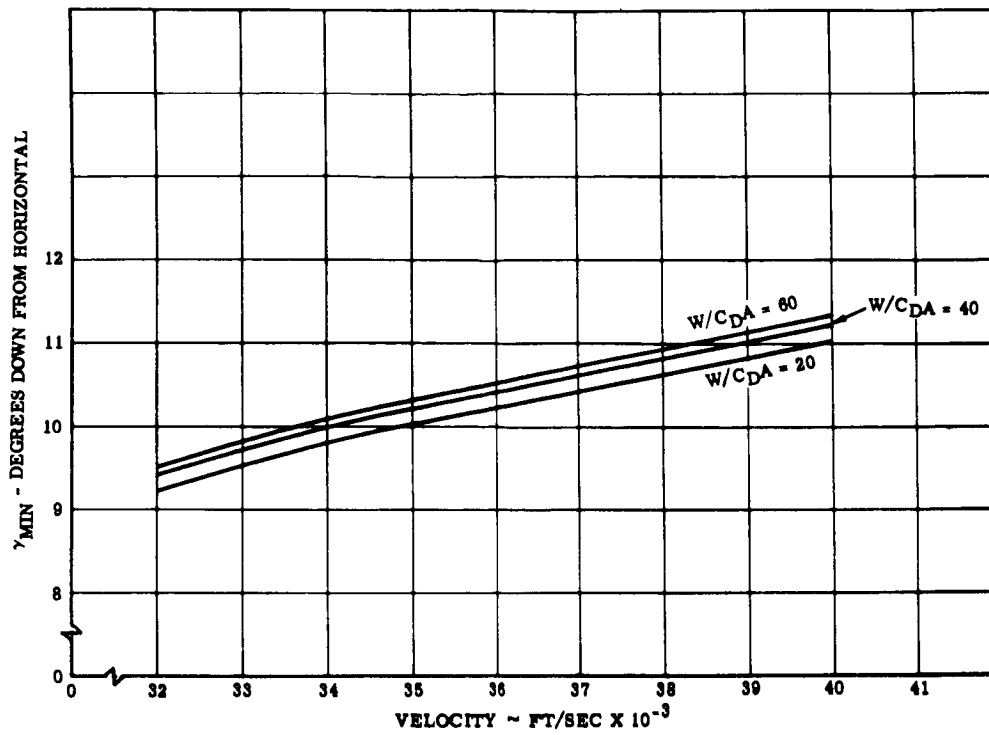


Figure 1.3.2-81. Capture Angle as Function of Velocity and W/C_{DA} for Entry into Venus Standard Atmosphere

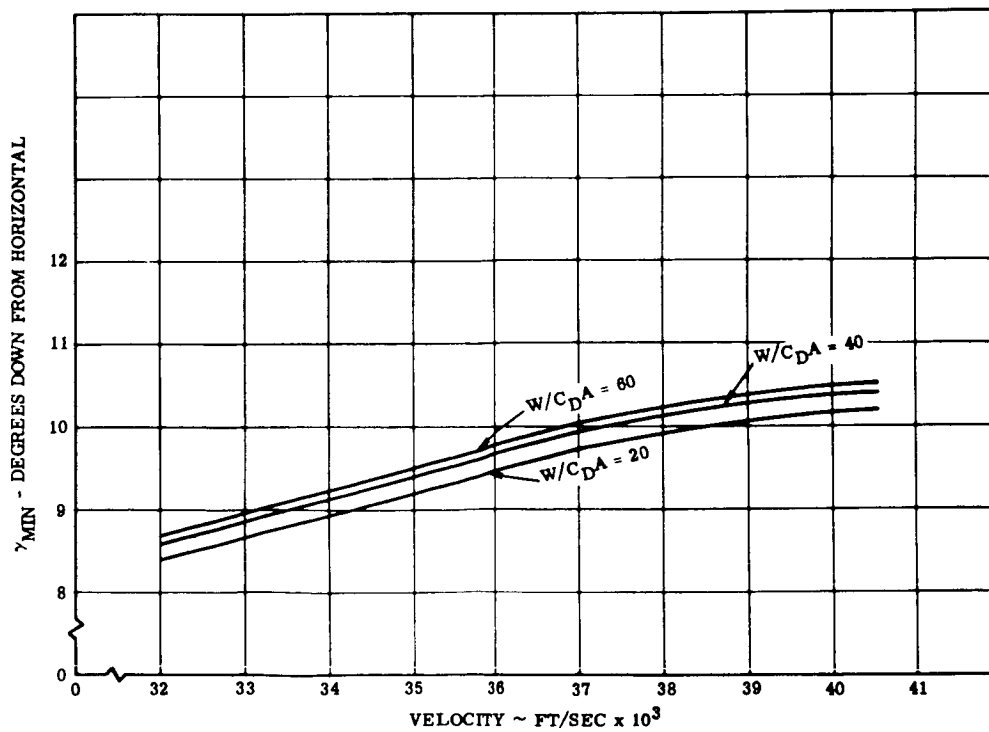


Figure 1.3.2-82. Capture Angle as Function of Velocity and W/C_{DA} for Entry into Venus Extreme Atmosphere

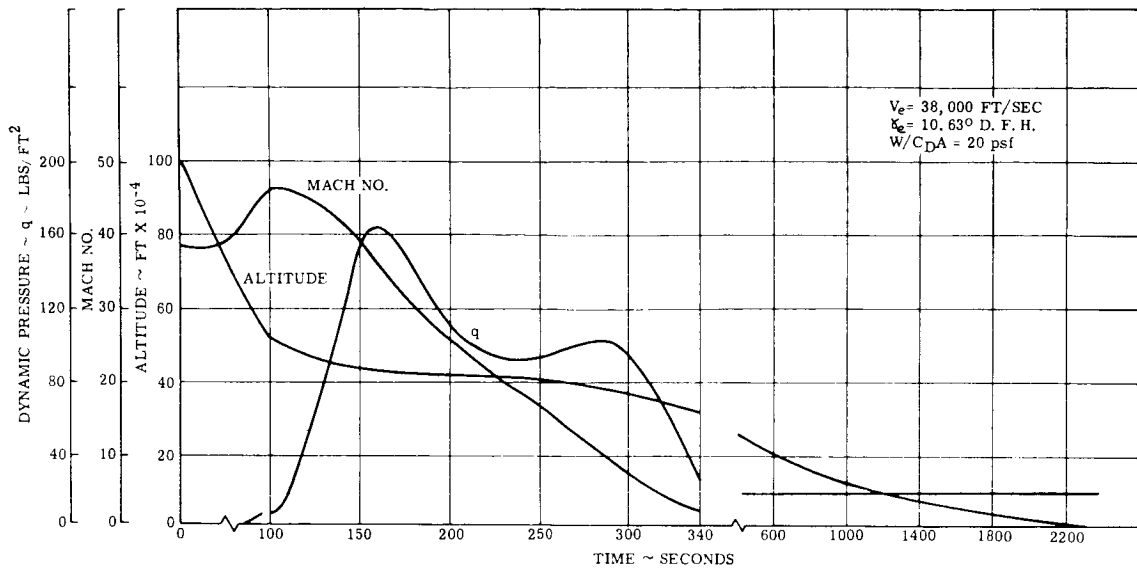


Figure 1.3.2-83. Venus Standard Atmosphere Capture Angle Trajectory

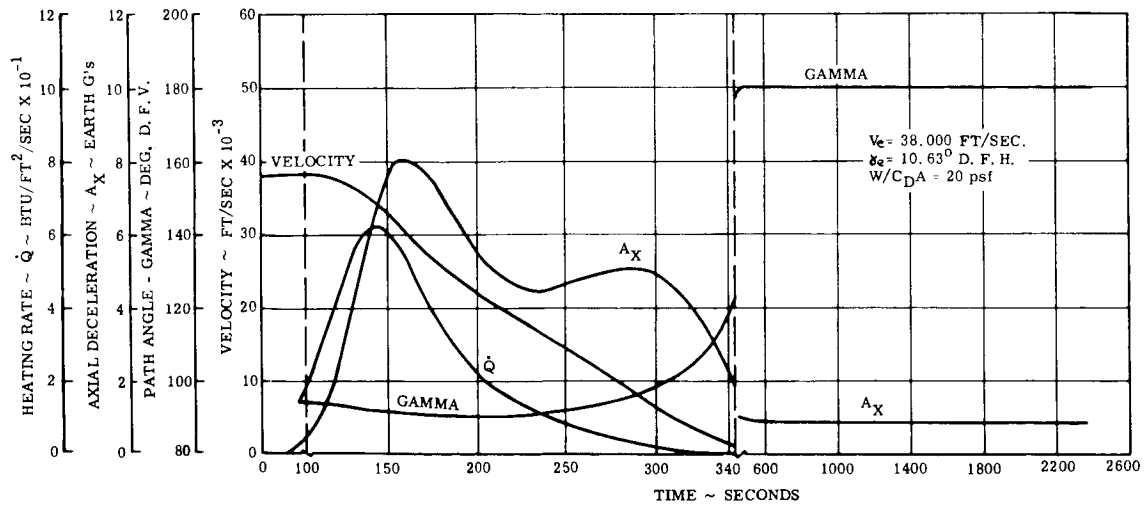


Figure 1.3.2-84. Venus Standard Atmosphere Capture Angle Trajectory

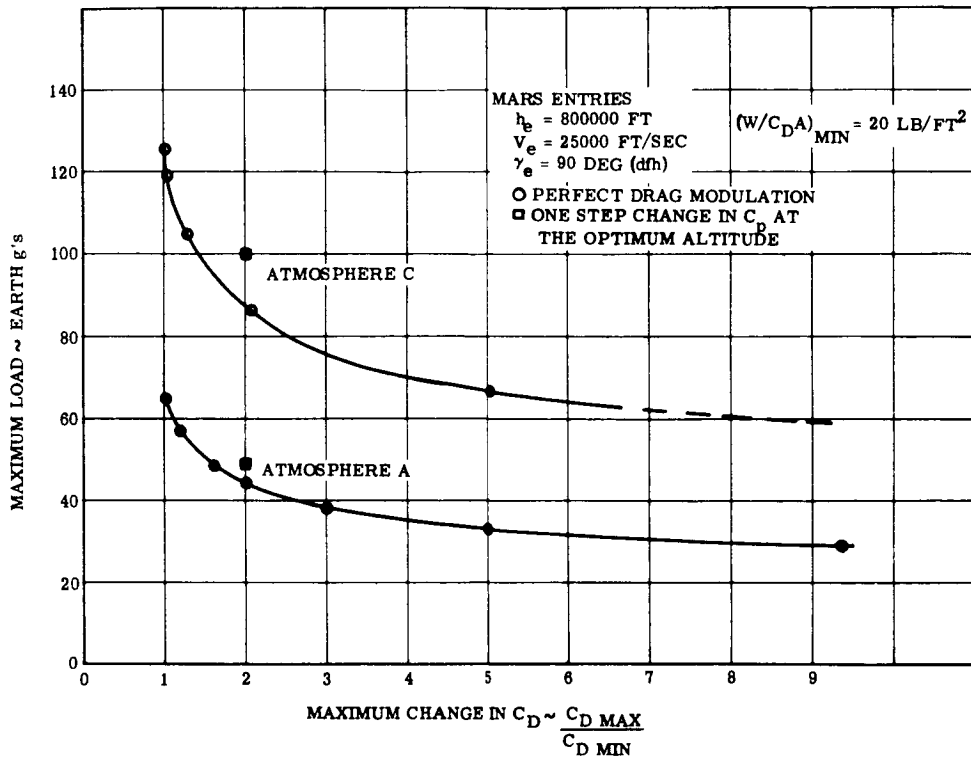


Figure 1.3.2-85. Effect of Drag Modulation on Maximum Loads

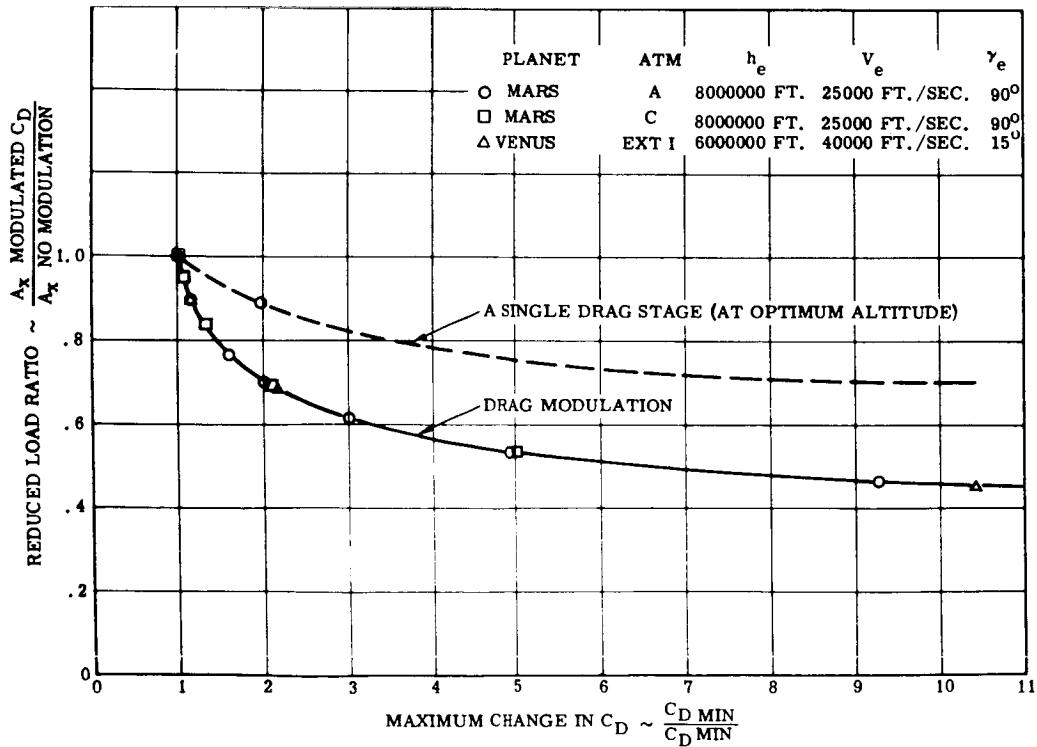


Figure 1.3.2-86. Effect of Drag Modulation on Maximum Loads

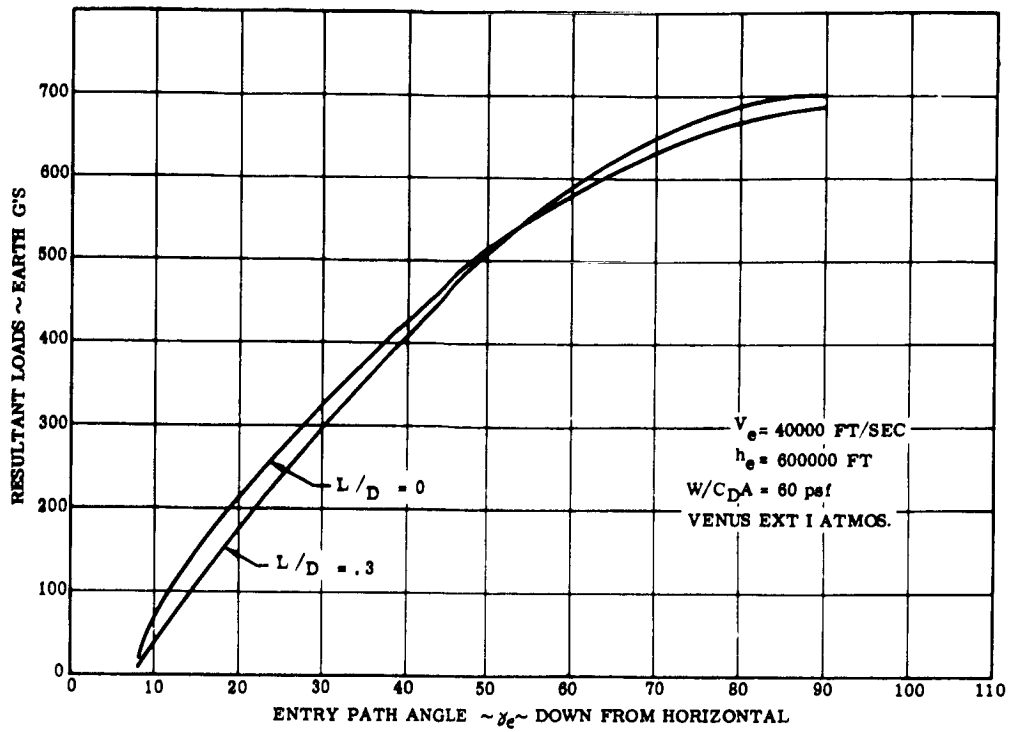


Figure 1.3.2-87. Resultant Load vs. Entry Path Angle

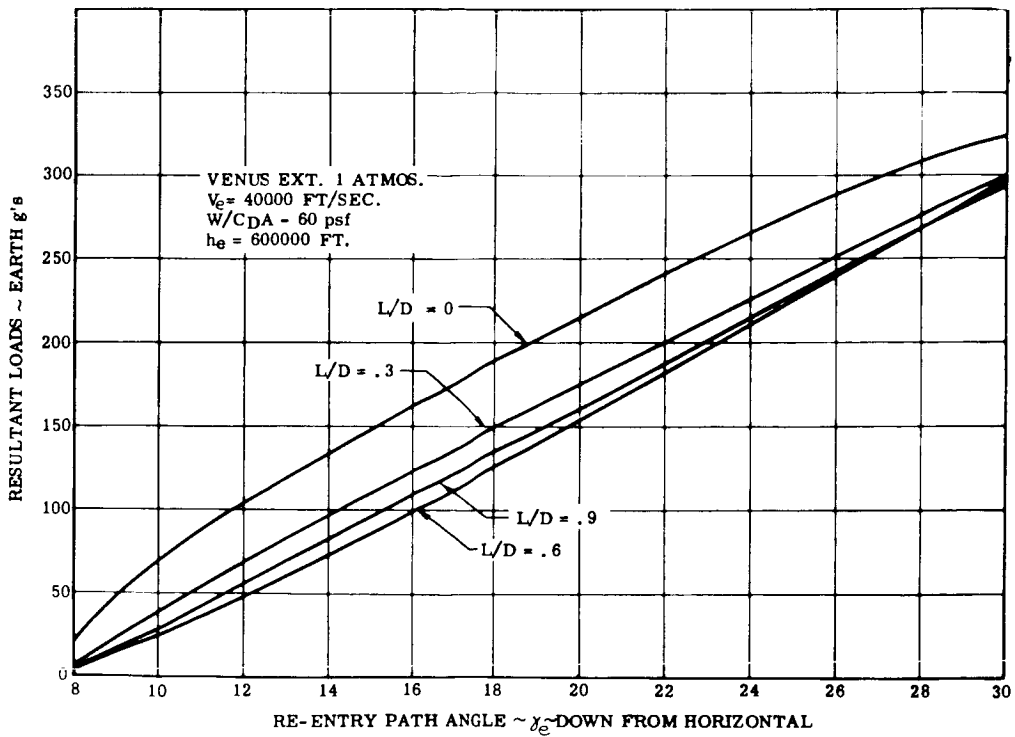


Figure 1.3.2-88. Resultant Load vs. Entry Path Angle

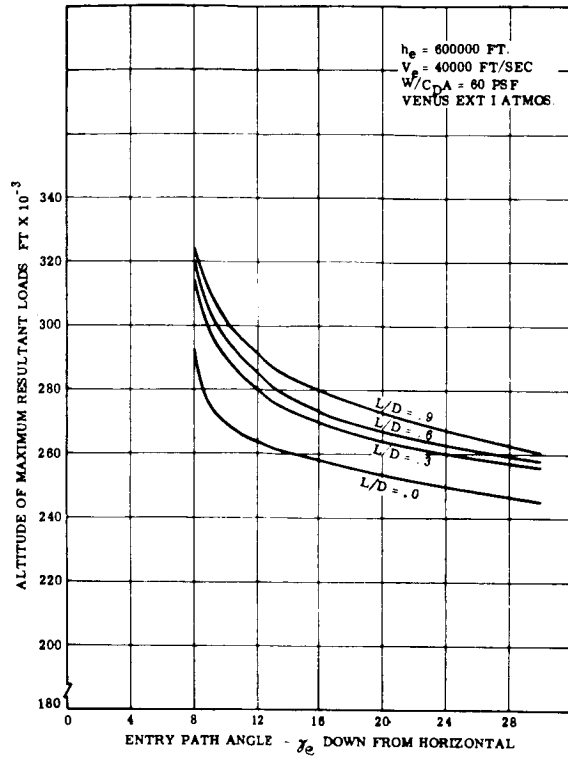


Figure 1.3.2-89. Altitude of Maximum Resultant Loads vs. Path Angle

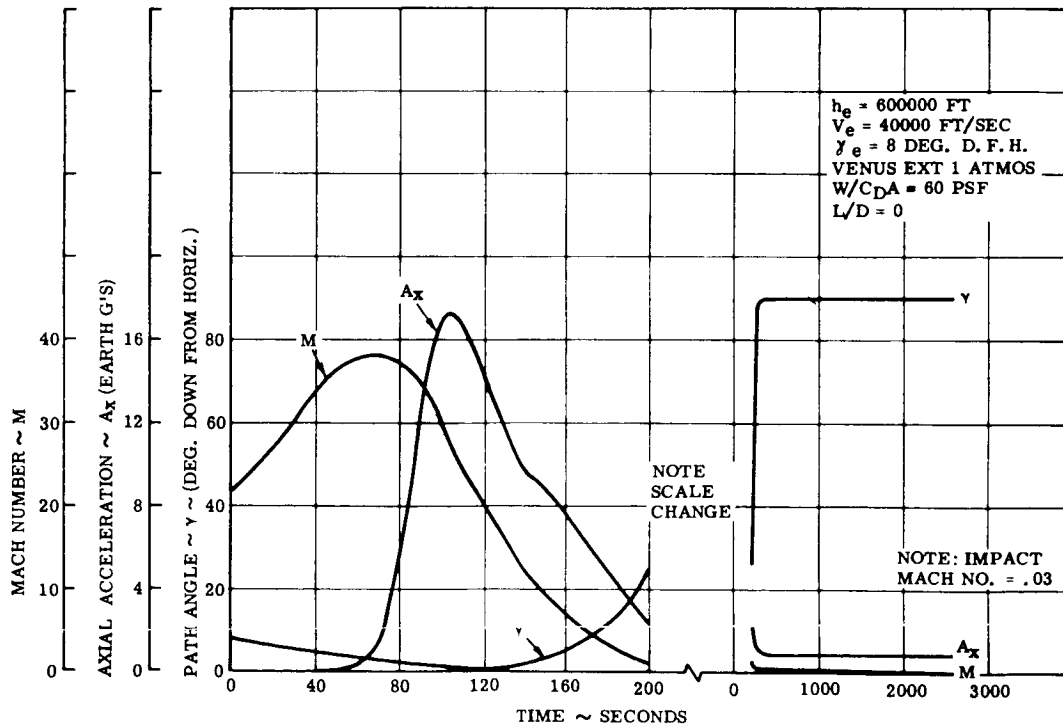


Figure 1.3.2-90. Mach Number, Axial Acceleration, and Path Angle vs. Time

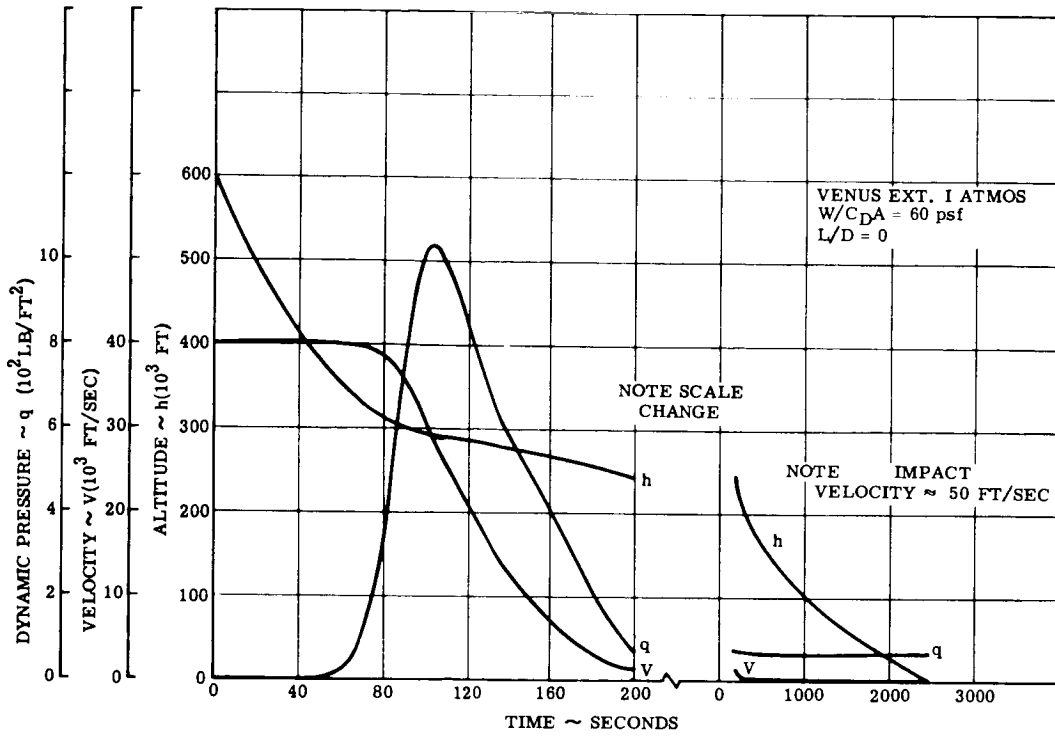


Figure 1.3.2-91. Dynamic Pressure, Velocity, and Altitude vs. Time

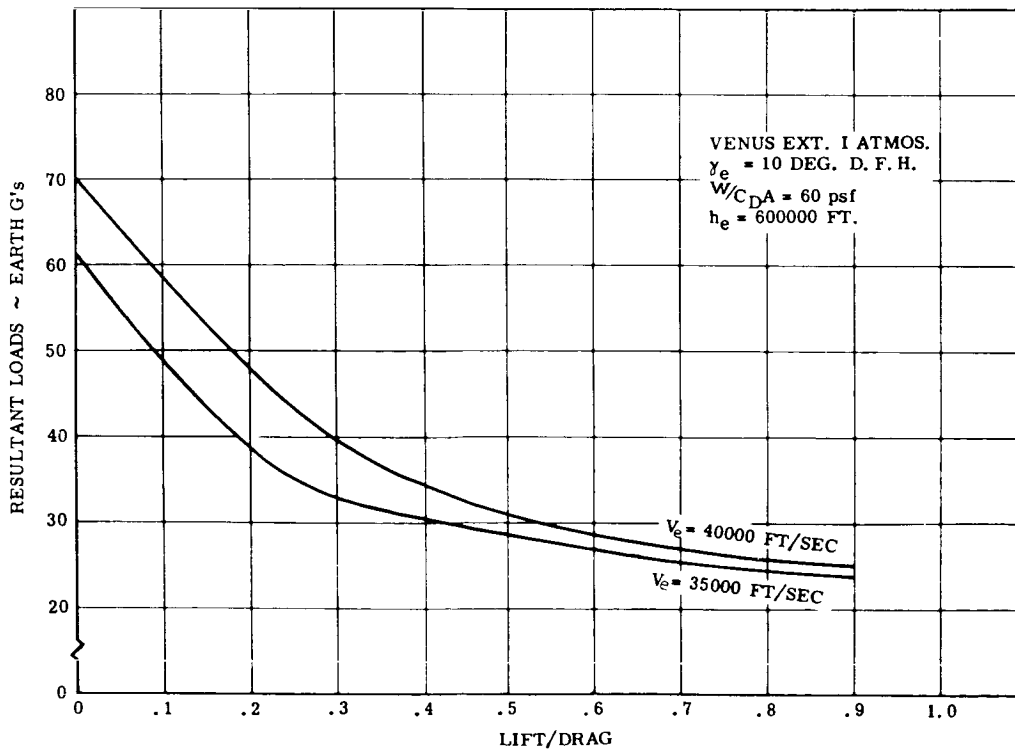


Figure 1.3.2-92. Resultant Loads vs. Lift/Drag

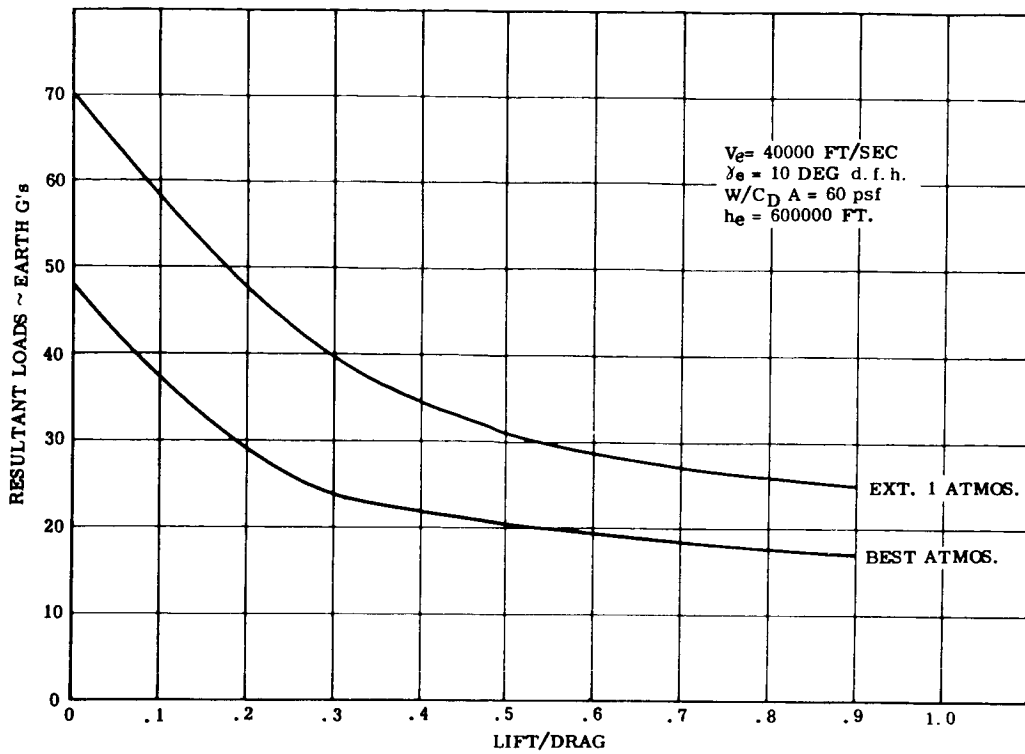


Figure 1.3.2-93. Resultant Loads vs. Lift/Drag

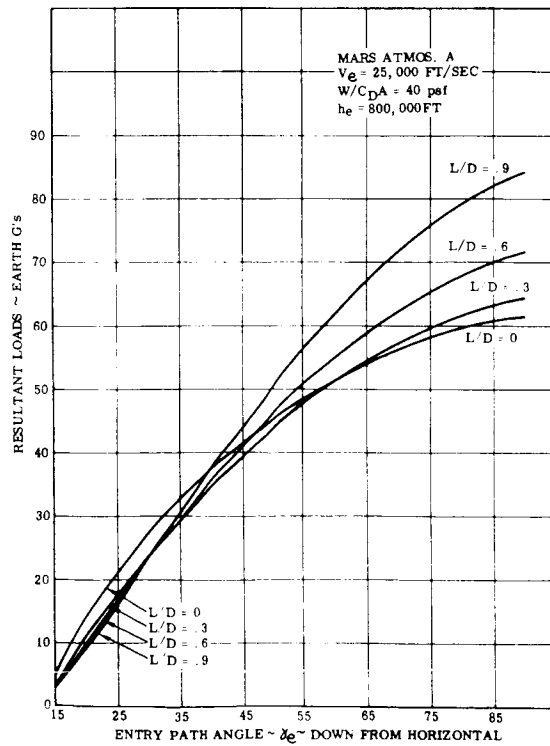


Figure 1.3.2-94. Resultant Loads vs. Entry Path Angle

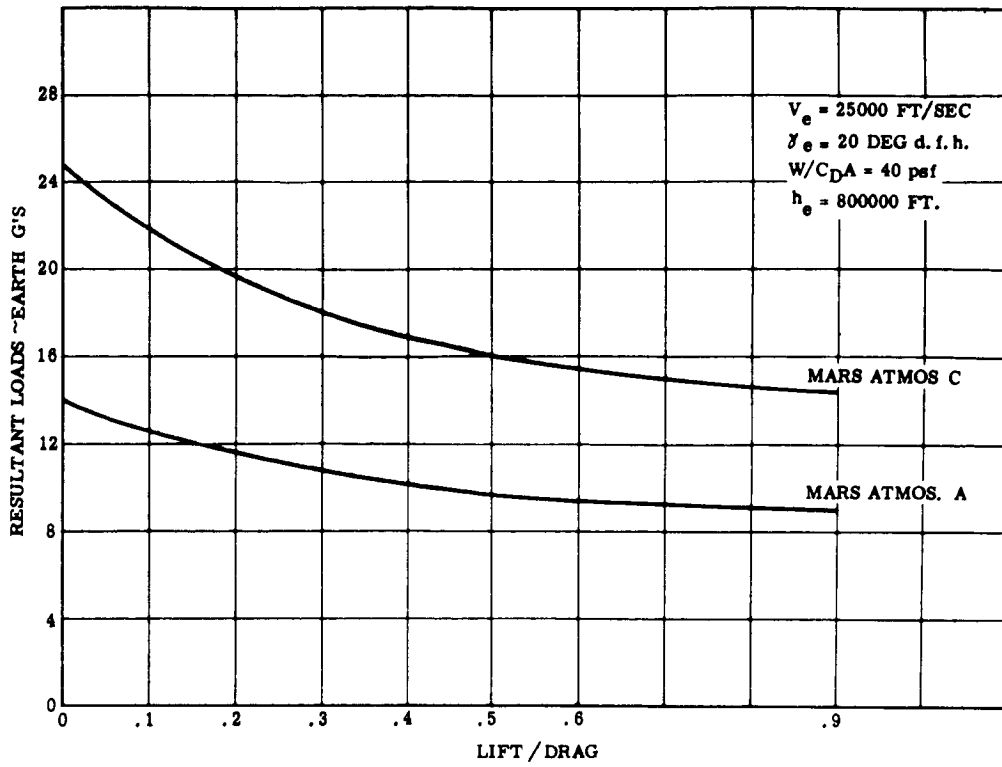


Figure 1.3.2-95. Resultant Loads vs. Lift/Drag

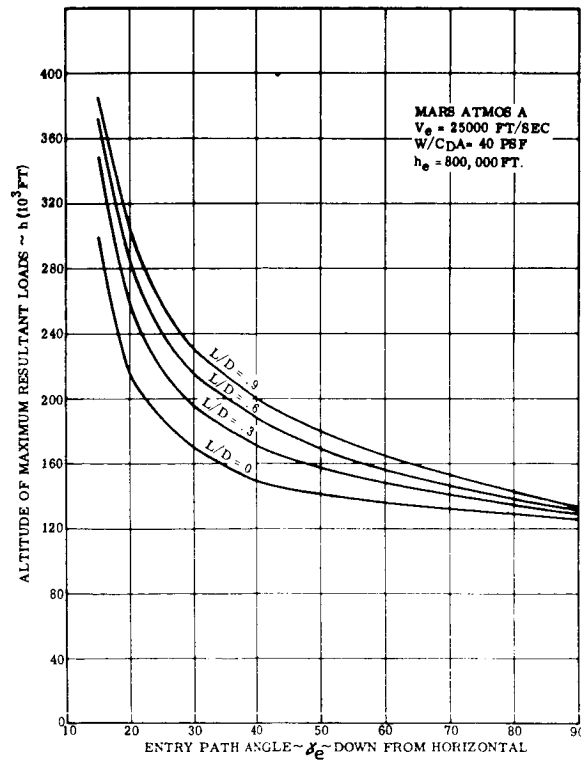


Figure 1.3.2-96. Altitude of Maximum Resultant Loads vs. Path Angle

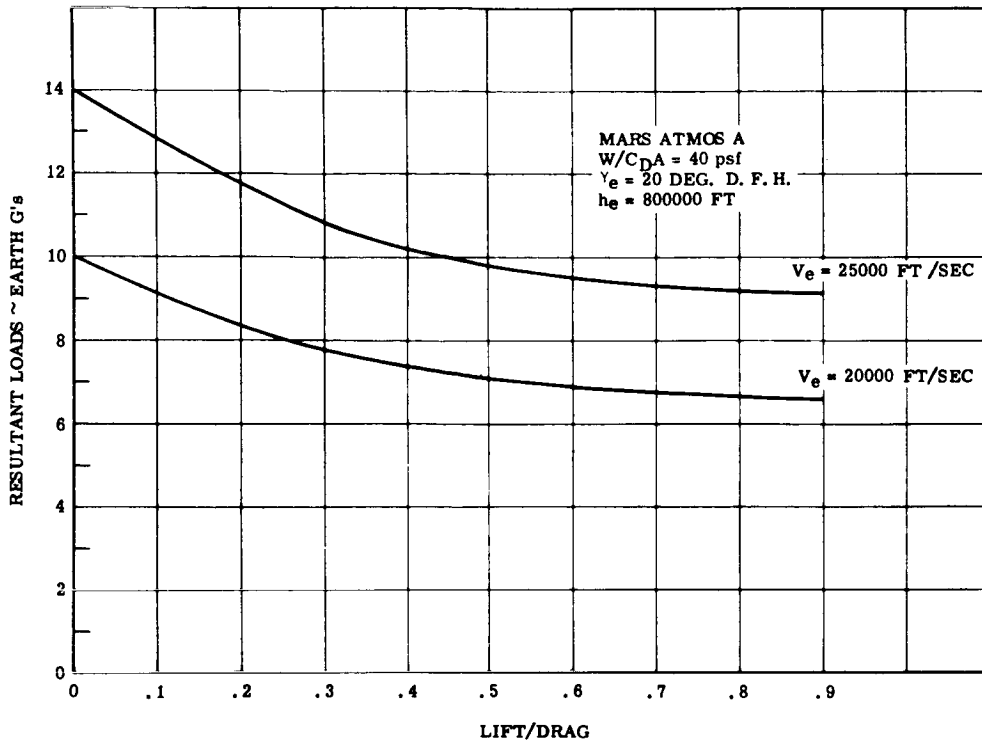


Figure 1.3.2-97. Resultant Loads vs. Lift/Drag

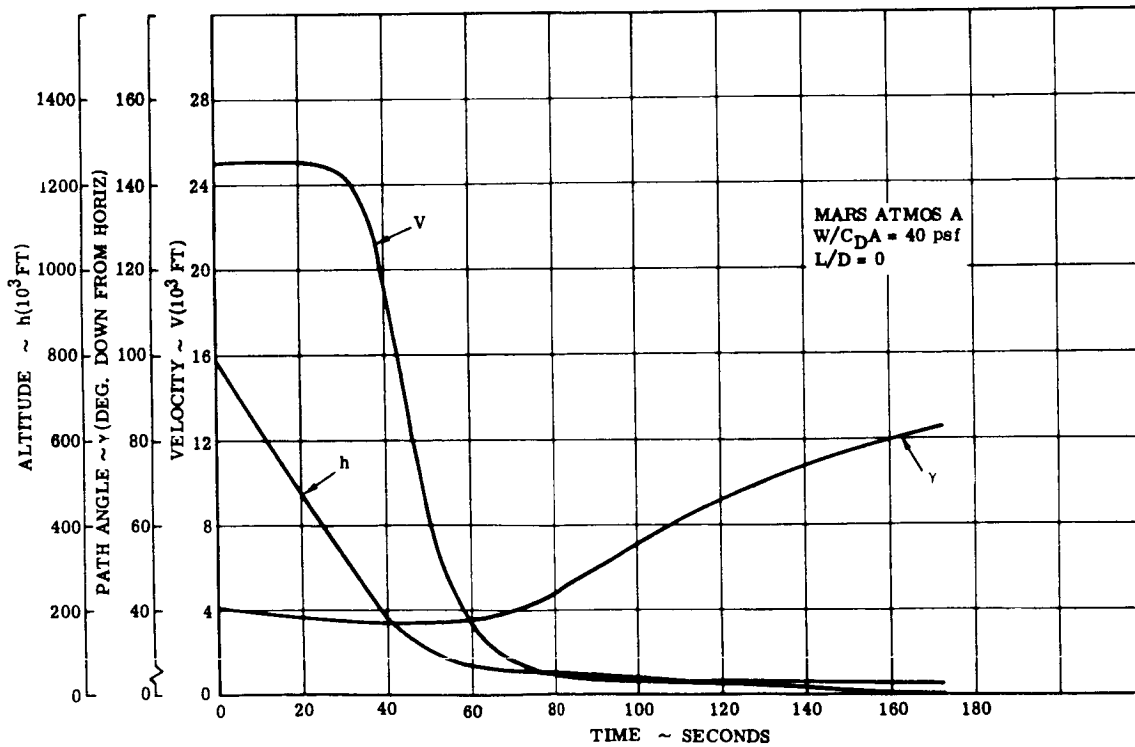


Figure 1.3.2-98. Altitude, Path Angle, and Velocity vs. Time

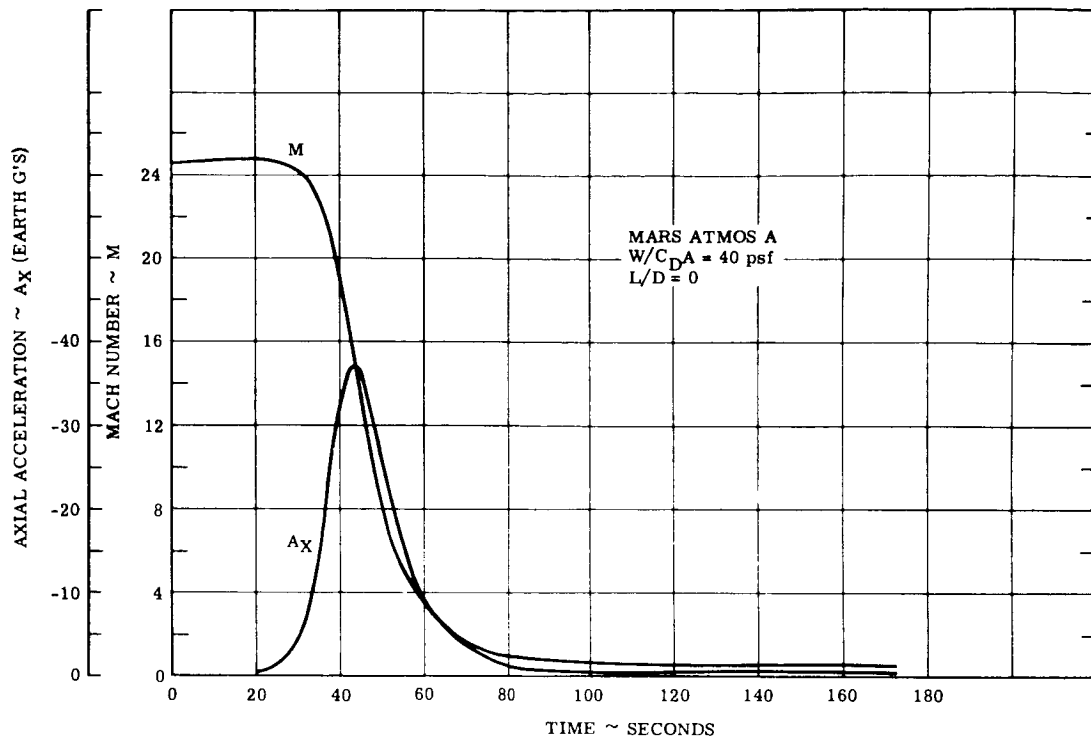


Figure 1.3.2-99. Axial Acceleration and Mach Number vs. Time

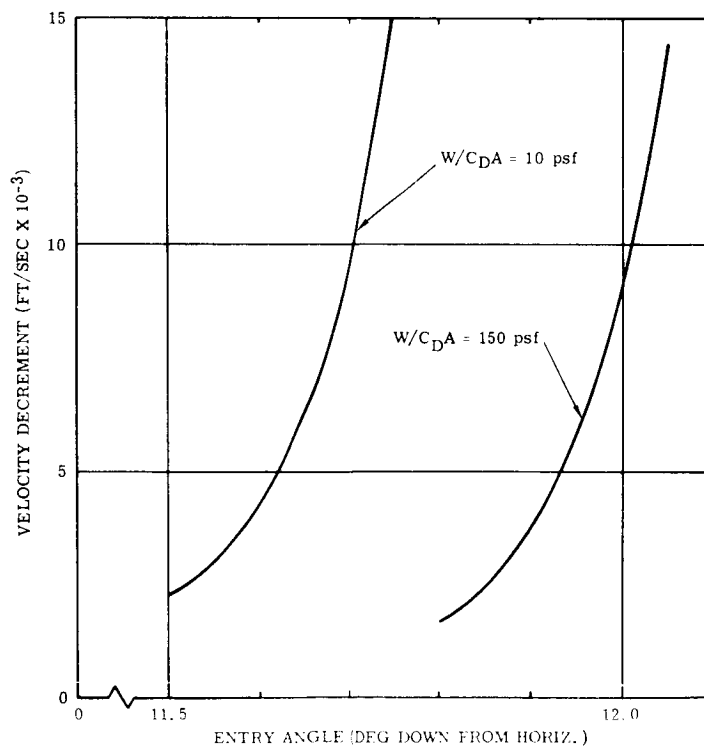


Figure 1.3.2-100. Orbiter Braking (Venus)

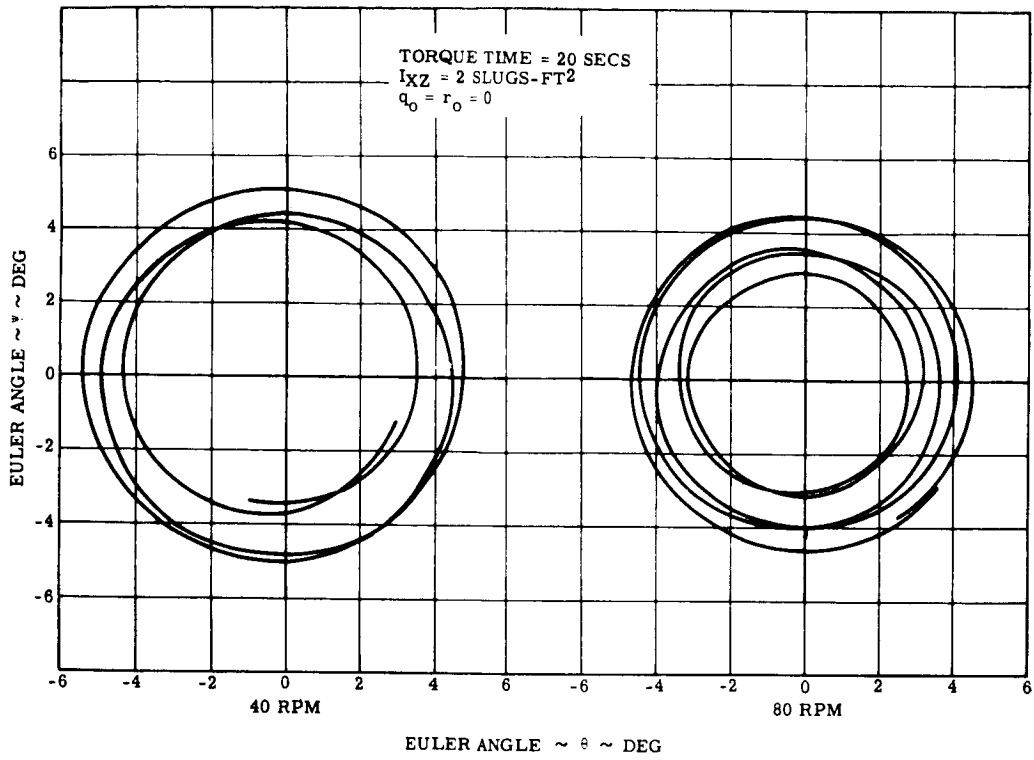


Figure 1.3.2-101. Effects of Products of Inertia on Spin-up

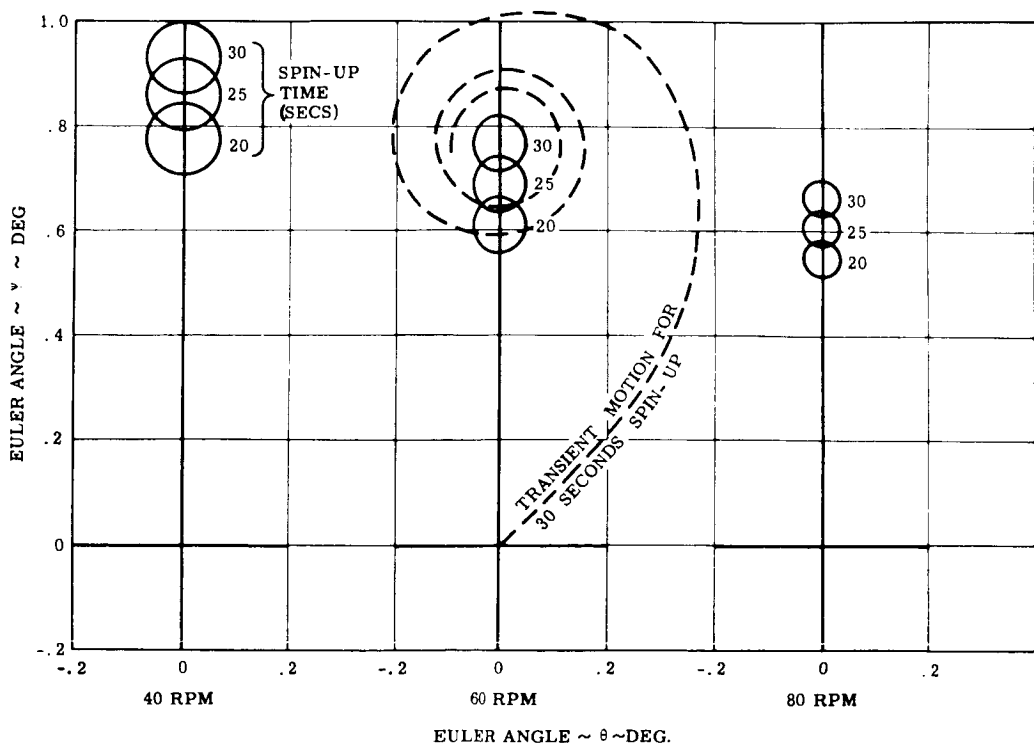


Figure 1.3.2-102. Lander Response to Initial Rotational Rates During Spin-up

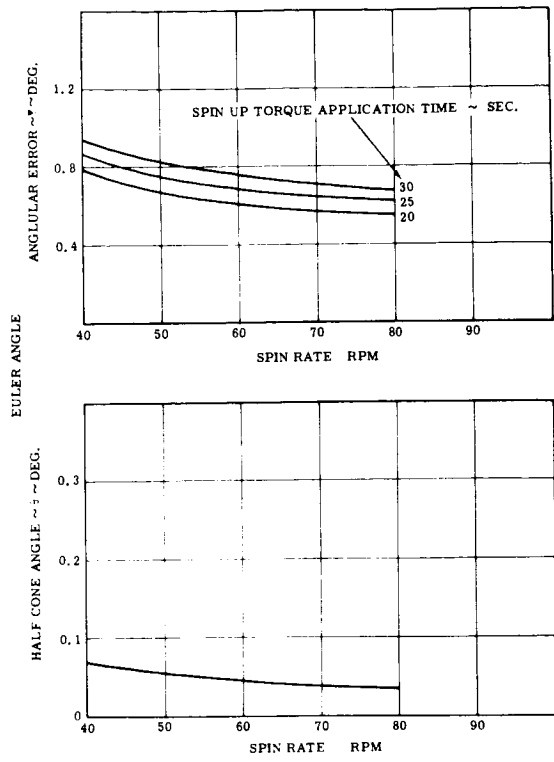


Figure 1.3.2-103. Steady State Conditions Following Spin-up Caused by a Separation (Lateral Rate = .25 deg/sec)

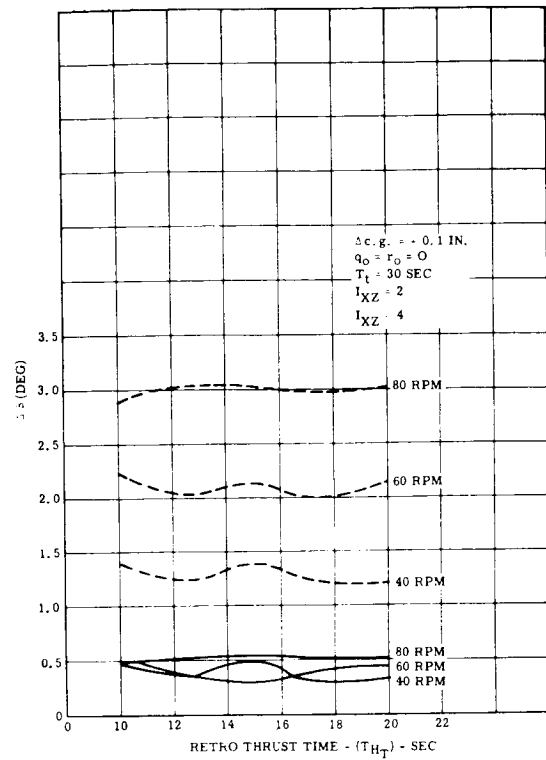


Figure 1.3.2-104. Angular Deviation vs. Thrusting Time

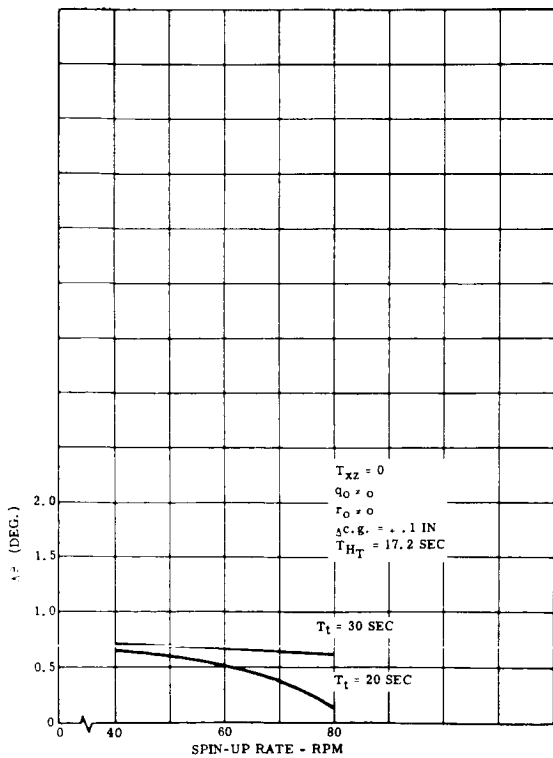


Figure 1.3.2-105. Angular Deviation vs. Spin-up Rate

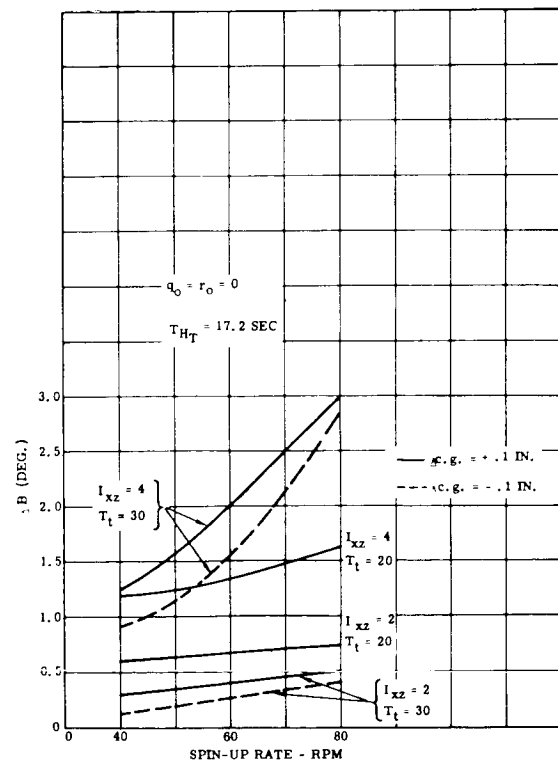


Figure 1.3.2-106. Angular Deviation vs. Spin-up Rate

1.3.3 ENTRY HEAT PROTECTION

A. Introduction

To effectively determine and present the results of the heat shield analysis for Mars and Venus it was necessary to:

- Define the thermal environment during entry, as characterized by convection, radiation, and ionization.
- Determine generalized shield requirements for a configuration selection study.
- Indicate areas requiring further study and development.

Consideration of the thermal environment encountered during entry in the atmosphere of Mars or Venus was essential for selection of suitable ablation materials, and the determination of ablation and insulation thicknesses for heat shield design. Instantaneous heating rates, and time-integrated heating, provided the basis for material selection and thickness requirements. The significant variables contributing to the determination of heat fluxes were 1) trajectory conditions, 2) atmospheric models and, 3) contribution of the various modes of heat transfer (convection, radiation, and ionization).

Utilizing ablation material properties based on past performance, and the current analytical technique (REKAP Analysis), it was possible to generalize the heat shield requirements, based on the time-integrated heating during several entry trajectories for Mars and Venus. Although the predicted heating rates were for a single vehicle configuration, generalization of the shield thickness requirements was accomplished by the application of laminar and turbulent heating distributions, with corrections for wetted length, and radiation. Shield thickness generalizations are presented in the form of shield thicknesses parametrized with respect to nose radius for the stagnation point and the maximum turbulent point (Mars only), for the complete range of entry conditions. In addition, ablation shield requirements have been determined for the following matrix of vehicle configurations which were factored into the configuration selection study.

$$\theta_C = 20^\circ, 30^\circ, \text{ and } 40^\circ$$

$$R_N/R_B = 0.24, 0.60, \text{ and } 0.90$$

$$D_B = 3.5, 8.0, \text{ and } 10.5 \text{ feet}$$

Areas requiring further analysis and development have been considered throughout this study. Attention has been given to analytical techniques, simulation of the planetary entry environment, and ablation material performance in the planetary entry environment.

B. Aerodynamic Heat Transfer (Techniques)

(1) Ablation Design Program

To determine the instantaneous convective heating rates for a vehicle entering the atmosphere of Mars or Venus, calculations were performed using the Ablation Design Program (Reference 1). The Ablation Design Program was initially developed by the Missile and Space Division for the calculation of convective and radiative heating around a blunt body during Earth re-entry.

The program uses both laminar and turbulent heat transfer equations, depending upon a trip Reynolds Number assigned by the user. For local values in excess of the trip Reynolds Number (150,000 for the current study), the program uses turbulent relation-

List of symbols used in this Section are on Page 1-155.

ships. A Lee's type equation, with properties evaluated at Eckert's reference enthalpy state, is used to calculate stagnation point convective heating. This equation is

$$\dot{Q}_s = \frac{.78}{Pr^{0.667}} (\rho_e^* \mu_e \cdot u_o^1)^{1/2} (h_s - h_w)$$

Quantities with asterisk superscripts are evaluated at the stagnation pressure; and reference enthalpy, defined as:

$$h^* = 0.5 h_w + (0.5 - .22r) h_e + 0.22 r h_o$$

For body angles greater than thirty degrees, off stagnation laminar heating is calculated by a Lee's hemispherical distribution using a Prandtl-Meyer pressure distribution. Laminar heating, for body angles less than thirty degrees, is calculated using a compressible reference enthalpy Lee's equation. This equation is

$$\dot{Q}_r = \frac{.39}{Pr^{0.667}} \frac{\rho_e^* \mu_e^* u_e y_2}{\left(\int_0^s \rho_e^* \mu_e^* u_e y_2 ds \right)^{1/2}} (h_r - h_w)$$

When the Reynolds Number for an off stagnation point exceeds the specified trip value, a turbulent relationship is used to calculate the local convective heat flux. The relationship which is used, is the G. E. axisymmetric compressible turbulent heat transfer equation, given as:

$$\dot{Q}_T = \frac{.0296}{Pr^{0.667}} \left[\frac{\rho_e^{0.2} u_e^{0.05} (\mu_e^*)^{0.2} u_e y^{0.25} (\rho_e^*)^{0.8}}{\left(\int_0^s \rho_e \mu_e u_e y^{1.25} ds \right)^{0.2}} \right] (h_r - h_w)$$

Although the basic heat transfer relationships remained unchanged for the prediction of heating during Martian and Venusian entry, appropriate constants and equations were changed. In accordance with the physical characteristics, and the predicted atmospheres of Venus and Mars, the equations for geopotential altitude, free stream density, and the velocity of sound have been changed. The change in geopotential altitude accounts for the radius of each planet. Changes in the velocity of sound, and free stream density equations include the gas constant as calculated for each gaseous mixture (Mars .868N₂, .072 CO₂, and .06A; Venus .09 CO₂, .90N₂, and .01A and .25 CO₂, .74N₂, and .01A) at ambient conditions, and an average isentropic exponent for each mixture. Air thermodynamic properties, in the form of curve fits to the Cornell Tables, were retained in the program.

Utilizing the modified version of the Ablation Design Program for a Venus 25% CO₂ atmosphere; calculations were made and compared with previous results obtained by S. Scala (Reference 4) and by detailed hand calculations using N₂ - CO₂ properties. The purpose of these comparisons was to determine the suitability, without further modifications, of the Ablation Design Program for Mars and Venus entry heating calculations. Although local pressure (Figure 1.3.3-1) remained unaffected by the use of air properties, temperature (Figure 1.3.3-2) and density (Figure 1.3.3-3) were affected. During the significant heating period, the Ablation Design Program calculated temperatures which were too high, and densities lower than for comparable N₂ - CO₂ conditions. Comparisons for static pressure (Figure 1.3.3-4) and density (Figure 1.3.3-5) behind a normal shock wave indicated that the normal shock relationships, as programmed for air, were adequate for N₂ - CO₂ mixtures. Figures 1.3.3-3 and 1.3.3-5 indicate that the two methods of calculation (using exact N₂ - CO₂ thermodynamic properties, and using air thermodynamic properties) give very good density comparisons; with density values not differing by more than 10%. Comparisons between Scala's results (without ionization effects) and the Ablation Design Program (Figure 1.3.3-7), as well as between hand calculations and the Ablation Design Program (Figure 1.3.3-8) indicates that the Ablation Design Program comes within 25% of the corresponding value of convective heating for an N₂ - CO₂ mixture. Considering accuracy of this order adequate for preliminary design purposes, no further alterations were made in the program for calculations of convective heating.

In addition to comparisons with Scala's theoretical results and manual calculations using $N_2 - CO_2$ thermodynamic properties, additional comparisons were made with the experimental shock tube data obtained by Gruszczynski and Warren (Reference 6).

Convective heating rates were obtained from several Venus trajectories, normalized with respect to nose radius and stagnation pressure, and plotted with the available experimental data as a function of driving enthalpy ($h_s - h_w$). These results were compared to Scala's theoretical predictions of convective heating with and without ionization (Reference 7). The comparison (Figure 1.3.9-9) indicated that 1) ionization need not be considered to obtain adequate convective heating predictions, and 2) a further substantiation of the previous comparison with Scala non-ionized results. It should be noted that the referenced work of Gruszczynski and Warren (Reference 6), indicated no observation of an ionization contribution to recent tests, and that therefore, for engineering, design purposes ionization is negligible.

(2) Trajectory Heating Parameter

Due to the necessity of considering a number of atmospheric models for Mars, it was found useful to resort to a heating parameter available in the Flight Mechanics' Round Earth Point Mass Program (the program used to calculate the trajectories for Venus and Mars). The heating parameter used is an approximate laminar stagnation point heat transfer equation, derived by G. Walker in Reference 8. The equation as obtained by Walker is:

$$\dot{Q}_L = f_L \rho_\infty^{0.5} u_\infty^3$$

where

$$f_L = \frac{1.67 \times 10^{-5}}{Pr^{0.667}} \left(\frac{\gamma_\infty - 1}{\gamma_\infty} \right)^{0.25} \left(\frac{\gamma + 1}{\gamma - 1} \right)^{0.25} \left(\frac{u_\infty}{a_\infty} \right)^{0.5} (R_N)^{-0.5}$$

It may be noted that Walker's heating parameter is similar to the more general form obtained by Scala in Reference 10. Scala's equation is:

$$\dot{Q}_L = C \rho_\infty^{0.5} u_\infty^3 R_N^{-0.5}$$

where C is a function of the molecular weight of the ambient gas given as:

$$C = (9.18 + 0.663 \bar{m}) \times 10^{-10}$$

Using the gaseous mixture previously quoted for Mars, an average molecular weight of 29.88 is obtained resulting in a C of 2.90×10^{-9} . In Reference 9, Walker evaluated f_L for constant values of $\gamma_\infty = 1.4$, $\gamma = 1.2$, $Pr = 0.72$, and $T = 500^\circ R$ to be $3.16 \times 10^{-9} (R_N)^{-0.5}$, and is used as such in the Round Earth Point Mass Program. With the evaluated constants the two equations are:

$$\text{Walker} - \dot{Q}_L \cdot R_N^{0.5} = 3.16 \times 10^{-9} \rho_\infty^{0.5} u_\infty^3$$

$$\text{Scala} - \dot{Q}_L \cdot R_N^{0.5} = 2.90 \times 10^{-9} \rho_\infty^{0.5} u_\infty^3$$

It is readily apparent from the two equations that convective heat rates based on Walker's equation could not exceed values for the Martian mixture by more than 11%. Therefore it was considered appropriate to utilize the heating parameter available in the Round Earth Point Mass Program, for determination of the effects of entry velocity and model atmospheres. The heating parameter was used only for Mars where radiant heating is insignificant (Figure 1.3.3-10).

(3) Aerodynamic Heat Transfer (Results)

Utilizing the Ablation Design Program, the heating to a 30 degree sphere-cone, with a bluntness ratio of 0.60 and a base diameter of 3.5 feet, was calculated for both Martian and Venusian entry. Since a surface temperature of 560°R, and a surface emissivity of zero were assumed for the ablation shield, heat fluxes calculated were cold wall values with no re-radiation. The calculations were made for a trajectory matrix as follows:

Mars -

$$\gamma_e = 20, 30, 60 \text{ and } 90^\circ$$

$$W/C_D A = 20, 40, \text{ and } 50 \text{ psf}$$

$$V_e = 23,000 \text{ f. p. s.}$$

Atmospheric Model - Mean Limit Atmosphere

Venus -

$$\gamma_e = 15, 30, \text{ and } 90^\circ$$

$$W/C_D A = 20, 40, \text{ and } 60 \text{ psf}$$

$$V_e = 38,000 \text{ f. p. s.}$$

Atmospheric Model - Standard Atmosphere/25% CO₂

$$\gamma_e = 15, 30 \text{ and } 90^\circ$$

$$W/C_D A = 40 \text{ psf, and } V_e = 38,000 \text{ f. p. s.}$$

In addition, the heating parameter previously discussed was evaluated for the complete matrix of Martian trajectories, including the three atmospheric models (Upper, Mean, and Lower Limit atmosphere). Although only stagnation heating will be discussed here, Figures 1.3.3-11 through 1.3.3-34 represent results from the Ablation Design Program, including heating to a point on the sphere, and the mid-point of the cone. Sharp breaks in the curves indicate transition to turbulent heating. Radiant heating is shown on the same curves, but will be discussed separately (for Venus only).

(4) Entry Angle Effects

As could reasonably be expected, similar entry angle effects were observed for Mars and Venus, as for Earth re-entry. Choosing a ballistic parameter of 40 psf as representative for both Mars and Venus, the magnitude of entry angle effects may be seen. A 20° entry into the Martian Mean Atmosphere on the Venus Standard atmosphere results in heating as follows:

	Mars		Venus	
	Mean Atmosphere		Standard Atmosphere	
Entry Angle - γ_e	20	90	15	90
Heating Time - Sec.	150	25	55	10
Peak Heating Rate (\dot{Q}) BUT/Ft. Sec.	180	460	1190	2750
Integrated Heating Q BTU/Ft. ²	9000	4200	21000	10,200

(5) Ballistic Parameter Effects

As in the case of entry angle effects, Mars and Venus show effects on convective heating when the ballistic parameter is varied, as previously encountered during Earth re-entry. Choosing an entry angle of 30° as typical, the effects of variation in the ballistic parameter may be seen.

Ballistic Coefficient $W/C_D A$	Mars		Venus	
	Mean Atmosphere Peak Heating	Integrated Heating	Standard Atmosphere Peak Heating	Integrated Heating
20	200	4100	1320	8800
60	354	7650	2350	15,900
Ballistic Coefficient - $W/C_D A$	20	60	20	60
Heating Time - Sec.	60	65	60	23
Peak Heating Rate (\dot{Q}) BTU/Ft. ² Sec.	200	354	1320	2350
Integrated Heating Q (BTU/Ft. ²	4100	7650	8800	15,900

(6) Entry Velocity Effects

Although all computations for Mars using the Ablation Design Program were made for an entry velocity of 23,000 f.p.s. the effects of a variation in entry velocity were evaluated. Using the heating parameter previously mentioned, heating has been evaluated for a vehicle having a one foot nose radius, and a $W/C_D A$ of 40, and entering the Lower Limit Model Atmosphere of Mars at a 90° entry angle. Stagnation heat pulses for entry velocities of 25,000, 23,000, 21,000, 19,000, 17,000, and 14,500 f.p.s. are presented in Figure 1.3.3-35. The integrated heating has been determined and normalized with respect to the heating value at a nominal velocity of 23,000 f.p.s. The theoretical basis for such a normalization procedure is discussed by Brunner in Reference 11. Figure 1.3.3-36 demonstrates the effects of entry velocity on heating and serves as a basis for modifying shield ablation requirements as a result of changes in desired entry velocity. Although no similar results are available for Venus, heating during entry will increase even more rapidly for Venus with increases in velocity, than it does for Mars.

(7) Atmospheric Effects

Because of the undetermined nature of the Martian Model Atmosphere, two approaches to the problem of variations in heating due to different model atmospheres were required. A specific approach, accounting for variations in heating due to the three atmospheric models, was required for possible effects on shield design requirements. Since all the results from the Ablation Design Program for Mars were based on the Mean Limit Model, it was necessary to be able to convert results to the Upper Limit Model or Lower Limit Model. This was done through the utilization of the heating parameters for the three Martian atmospheric models. The integrated values of stagnation heating which had been plotted, for the three atmospheres, as a function of entry angle and ballistic parameter (Figures 1.3.3-37 through 1.3.3-39) were divided by corresponding values for the Mean Limit Model. The resulting values were plotted as a function of entry angle for the extremes of ballistic parameter (Figure 1.3.3-42) to give a set of curves for determining changes in heating when considering the outer limit models.

Although the previous approach is suitable for consideration of the specific models in question, a more general approach better illustrates effects of variations in atmospheric parameters. Utilizing the density variation with altitude for the three models supplied (Figure 1.3.3-40), the density variation in the altitude where the heat pulse occurs was extrapolated to fit an isothermal model atmosphere. The density profile for an isothermal atmosphere being given by (Reference 12):

$$\rho = \rho_0 e^{-\left\{ (h-h_0)/RT \right\} \bar{m}_\infty g}$$

Assuming no variation in temperature or molecular weight with altitude the above expression simplifies to:

$$\rho = \rho_0 e^{-Kh}$$

Using density values at 100,000 and 400,000 feet (Reference 14), the density decay constant (K) was determined for each corresponding isothermal model atmosphere. The calculated density decay constant, and the densities at 100,000 feet of the model atmospheres supplied, were then used to calculate the sea level densities of the corresponding isothermal models (Table 1.3.3-1). The density decay constants and sea level densities thus obtained were used to normalize the integrated stagnation heating obtained from the heating parameters. Normalization was achieved by plotting the integrated stagnation heating divided by the square root of the pseudo - sea level density $[Q/(\rho_0')^{1/2}]$ previously obtained as a function of the density decay constant. The resulting curve (Figure 1.3.3-41) is used by taking any given model atmosphere and 1) extrapolating the straight line segment of the density-altitude curve (plotted on semi-logarithmic co-ordinates) to sea level, 2) determining the slope of the resulting curve (K), and 3) entering Figure 1.3.3-41 with the values of K and ρ_0' to obtain heating at the reference entry condition of $W/C_D A = 40$ and $V_e = 23,000$ f.p.s.

No similar approaches have been taken for Venus because of the significant contribution of radiation to the total heating. However, the effects of the Extreme Atmosphere have been evaluated for three Venusian conditions. The results shown in Figures 1.3.3-32 through 1.3.3-34 are typical, and would apply in a similar manner to $W/C_D A$'s other than 40.

TABLE 1.3.3-1. MARS "ISOTHERMAL" MODEL ATMOSPHERES

True Model (Reference 14)	True Sea Level Density (Slugs/ft ³)	Pseudo-Sea Level Density (Slugs/ft ³)	Density Decay Constant K (ft ⁻¹)	Isothermal Model Atmospheric Temp. (°R)
Lower Limit Atmosphere	1.453 x 10 ⁻⁴	7.238 x 10 ⁻⁴	3.774 x 10 ⁻⁵	178.6
Mean Limit Atmosphere	2.345 x 10 ⁻⁴	4.919 x 10 ⁻⁴	2.342 x 10 ⁻⁵	287.9
Upper Limit Atmosphere	2.942 x 10 ⁻⁴	3.065 x 10 ⁻⁴	1.378 x 10 ⁻⁵	489.3

NOTE: Mars' "Isothermal" Model Atmospheres do not represent true Martian atmospheric models. Instead they are modifications, which have been found useful in determining effects of atmospheric characteristics on integrated heating, of the original models supplied (Reference 14).

(8) Ionization Effects

At the velocities encountered during a planetary entry the free stream gas becomes dissociated and partially ionized by the shock wave preceding the vehicle. With ionization the thermal conductivity rapidly increases, along with additional energy transfer by diffusion of charges in the form of ionization energy. Stagnation point heat transfer has been calculated by Hoshizaki and Scala for velocities up to 50,000 f.p.s. Hoshizaki assumed chemical equilibrium and made use of the equilibrium transport properties for air given by Hansen (Reference 16). Scala, on the other hand calculated the convective heating assuming equilibrium chemistry, and primarily considering dissociation and ionization of pure nitrogen. Although Scala's results were significantly higher than the results of others, the difference was not a result of analytical procedures but, rather, the transport properties employed. The early results of Warren seemed to substantiate Scala's results (Reference 17). However, later data (Figure 1.3.3-42) obtained by Gruszczynski indicated shock tube results significantly lower than Scala's predictions. Comparing Gruszczynski's test data and the extrapolated theory for air, the difference was attributed to ionization. The convective heating for a typical Venusian trajectory was upgraded, based on Figure 1.3.3-42, to include the effect of ionization. Consequently, integrated heating around the body was increased by 8% to include ionization. Although

the previously mentioned results of Gruszczynski and Warren (Reference 6) seems to indicate a negligible effect due to ionization, the 8% increase in convective heating for Venus entry was retained for heat shield requirements. (Figures 1.3.3-23 through 1.3.3-34 and 1.3.3-43 through 1.3.3-54 do not include any effects due to ionization.) Because of the much lower entry velocities for Mars than for Venus, no ionization effects have been considered in the ablation shield requirements or convective heating for Mars.

In addition to the calculation and presentation of convective heat pulses for Mars and Venus, integrated values of convective heating have been obtained and are presented (Mars - Figures 1.3.3-55 through 1.3.3-57, Venus - Figures 1.3.3-43 through 1.3.3-54) for the three previously mentioned body locations. Mars convective heating has been treated as total heating, whereas the Venus curves also show radiation (to be discussed under radiative heating). All the curves are plotted as a function of entry conditions (v_e and $W/C_D A$), and serve as a basis for determining shield ablation requirements.

C. Radiative Heat Transfer

In addition to the determination of convective heating rates, it was necessary to predict the radiative energy transfer to the entry vehicle from the hot gas cap (shock layer). Such predictions require a knowledge of 1) atmospheric composition, 2) radiant contribution of each radiating specie as a function of temperature and density, and 3) shock layer characteristics such as temperature, density, and shock detachment distance. Consequently, attention has been given to the definition of radiation properties for the chemical compositions of the atmospheres of Mars and Venus, while shock layer characteristics have, of necessity, been based on the thermodynamic properties of air.

(1) Radiation Intensities

Modifications of the Ablation Design Program for application to Martian and Venusian entry included tables of radiation intensity for each gaseous mixture. Radiation data for Venus was for a 9% and 25% CO_2 mixture (References 18 and 19) based on appropriate species concentrations for each atmosphere (Reference 25). Initial data supplied (Figure 1.3.3-58), which was used in the calculations of heat pulses for the REKAP analysis (Figure 1.3.3-59), did not include the spectral region below 0.2μ and only approximately treated the temperature dependence of the free-free continua cross-sections. More recent radiation data replaced the initial data in the Ablation Design Program, and was used to calculate the radiative heat pulses for the Venusian trajectory matrix. The more recent radiation data included the following radiating species:

- C_2 band systems
- CO band systems
- CN red and violet
- N_2 band systems
- O_2 band systems
- N_2^+ band systems
- NO band systems
- Free-free continua of O, N, C, N^+ , and C^+
- Deionization continua of O^+ , N^+ , and C^+ (including the spectral region below 0.2μ)
- Free-bound continua of O^- and C^-

The utilization of new cross-sections for the free-free continua, and the consideration of spectral regions below 0.2μ for the deionization continua resulted in comparatively higher radiation intensities, as a comparison of Figures 1.3.3-58 and 1.3.3-60 will demonstrate.

Total intensities of radiation for the Martian gaseous mixture were also evaluated (Reference 18) based on species concentrations given by Reference 24. The radiation data for Mars represents initial efforts in this area, similar in scope to the previously mentioned initial values for Venus. More comprehensive considerations of the Martian species and con-

tributing spectral regions could be expected to result in similar intensity changes over the same regions as for the Venusian mixtures.

Although non-equilibrium radiation effects have not been specifically considered in this study, a preliminary examination of the problem (Reference 29) indicated only a very minor contribution by non-equilibrium radiation. For engineering purposes this contribution may be ignored.

(2) Radiative Heat Transfer (Results)

For the prediction of radiant heat transfer rate to a vehicle entering a planetary atmosphere it is necessary to know precisely the percentage gas composition. Since this was not available a series of gas mixtures with variable CO₂ content between 3% and 100% (with the balance being N₂) were studied. The radiant heat flux was calculated for entry velocities of 40,000 ft/sec and 25,000 ft/sec and at ambient density ratio $\rho_s/\rho_o = 10^{-2}$. The necessary calculations of shock relations were done using the iterative procedure described in Reference 30. The solutions were obtained with the help of equilibrium thermodynamic properties for mixtures with 3%, 9%, 25%, 80% and 100% CO₂ content under room conditions (Reference 31). The resulting stagnation point temperatures and pressures determined the molar composition of the shock layer gas.

The radiant flux was finally calculated by summing up the contribution from all principal radiators (Reference 32) corresponding to the particle density and temperature. The theory of Serbin (Reference 33) was used to obtain standoff distance of the shock wave and hence determine the volume of radiating gas layer.

At a flight velocity of 40,000 ft/sec there is only a small effect of different amounts of CO₂ in the atmosphere on the total radiation (see Figure 1.3.3-61). This is mainly due to the fact that the gas in the shock layer is completely dissociated and even partially ionized. Hence the bulk of the radiation comes from free-bound and free-free transitions. At the lower entry velocity the dissociation is not complete and molecular radiation dominates the total radiation. Mixtures with low CO₂ content will have a large number of CN molecules which are strong radiators while the CO₂ rich mixture will contain less CN but a higher proportion of CO. Since these systems have widely different radiative properties the strong influence of gas compositions on radiation is evident at the lower entry velocity. Heating at the lower velocities however will not represent limiting design for the heat shield.

Following an approach similar to that for convective heating, radiative heating results from the Ablation Design Program for a Venus trajectory (Figure 1.3.3-62) have been compared to corresponding results obtained by Scala. Because the same trajectory and the model atmosphere previously discussed were selected, the comparison of local properties and normal shock relationships for air and an N₂ - CO₂ mixture remains unchanged. It can be seen from Figures 1.3.3-63 through 1.3.3-65 that the Ablation Design Program, using the thermodynamic properties of air, gives a higher radiative heating than Scala's calculations using the appropriate N₂ - CO₂ thermodynamic properties. The higher values obtained by the Ablation Design Program were attributed to the higher temperatures caused by using air thermodynamic properties.

Results indicating a similar trend were observed by plotting data from an Ablation Design Program run simulating shock tube conditions obtained by Gruszczynski and Warren. The data from the Ablation Design Program is shown on Figure 1.3.3-66 with Gruszczynski's data from Reference 6. It should be noted that, whereas the data from the Ablation Design Program is for a 25% CO₂ - 74% N₂ mixture, the majority of Gruszczynski's data and all of Nardone's calculations were for a 9% CO₂ - 91% N₂ mixture. Consequently, the correlation between the Ablation Design Program values and the experimental results of Gruszczynski's is closer than is at first evident.

Having determined the degree of correspondence between the radiative heating calculated by the Ablation Design Program for N₂ - CO₂ mixtures and the experimental values, radiative heating values for Martian and Venusian entry trajectories were obtained. Because the

Ablation Design Program calculates convective and radiative heating simultaneously, additional runs were not required. Radiative heating values were obtained from the output for the trajectory matrix and body geometry previously used to determine convective heating. Although radiative heating was calculated for Mars, the results for the worst trajectory (i. e., greatest radiation contribution to total heating) indicated that the relatively small contribution to the total heating from radiation did not warrant consideration in determining shield thickness requirements (Figure 1.3.3-10).

(3) Entry Angle Effects

As previously demonstrated for convective heating, radiative heating indicated trends similar to those previously observed for Earth re-entry. Choosing a $W/C_D A$ of 40 as typical, it was observed that a 15° entry angle results in a radiative heat pulse of 30 seconds duration reaching a peak value of 1165 BTU/ft² sec, and an integrated value of 9000 BTU/ft². The radiation contribution to total heating amounted to 30 per cent. Conversely, a 90° entry, which had a radiative heat pulse lasting 7 seconds, reached a peak value of 8250 BTU/ft² sec., and an integrated value of 1450 BTU/ft². The radiation contribution accounted for 58% of the total heating.

(4) Ballistic Parameter Effects

Similar effects are also observed for variations in ballistic parameter. For an entry angle of 30° and a ballistic parameter of 20, the radiative heat pulse lasts 13 seconds for a peak value of 1360 BTU/ft² sec, and an integrated value of 5000 BTU/ft². The radiation contribution to total heating is 36 per cent. Keeping the entry constant at 30° , but increasing the ballistic parameter to 60, caused the duration of radiative heating to become 12 seconds. The peak value reached was 6400 BTU/ft² sec, with an integrated value of 21,000 BTU/ft². The resulting contribution of radiant to total heating was 57 per cent.

(5) Entry Velocity Effects

Although no quantitative results are available to describe the effect of entry velocity on radiative heating for Venus, the trend will be similar to effects observed for Earth re-entry. Just as convective heating (instantaneous and integrated) increases with increased entry velocity, so will the radiative heating. It is anticipated however, that the radiant heating will increase more rapidly than the convective heating, resulting in a greater radiation contribution to total heating at higher entry velocities.

An interesting and perhaps significant phenomenon may be noted on all the curves presenting radiative heat pulses (Figures 1.3.3-23 through 1.3.3-34). As the radiative heat pulse decreases toward the end of its duration, a second minor peak occurs (indicated in Figure 1.3.3-27). Gruszczynski (Reference 6) has attributed this secondary peaking action to the contribution of the CO and CN band radiation during that portion of the flight regime. Gruszczynski has brought out the significance of the secondary peaks in that "It is only after this point [labeled "A" in Figure 1.3.3-27] that the strong differences in radiation between air and the 9% CO₂ - 91% N₂ mixture -- that due to CO and CN band radiation -- become important. This is reflected in the shape of the radiative pulses after point A. Thus for initial entry velocities of the order of 40,000 f.p.s. or more, the complexity of the equilibrium radiation problem during the time of important vehicle heating, caused by our lack of knowledge of gas composition, may be considered reduced."

(6) Atmospheric Effects

An approach similar to that for convective heating was not possible for radiative heating. Consequently, the trajectories used to evaluate the effects of the Extreme Model Atmosphere for Venus on convective heating were also used to evaluate the atmospheric effect on radiative heating. As anticipated, the Extreme Atmosphere resulted in higher values of radiative heating, and a lesser contribution of radiation to the total heating. The magnitude of the effects are apparent when Figures 1.3.3-32 through 1.3.3-34 are compared with Figures 1.3.3-26 through 1.3.3-28.

D. Total Heating

As previously mentioned, total integrated values of convective heating (for the stagnation point, sphere point or maximum turbulent heating point, and the mid-cone point of the basic vehicle) have been evaluated. The results for both Mars and Venus are presented in Figures 1.3.3-55 through 1.3.3-57 and Figures 1.3.3-43 through 1.3.3-54. In addition, the integrated values of radiant heating, the sum of integrated convective and radiative heating, and the fractional contribution of radiant heating to total heating were evaluated for Venus, and are included in Figures 1.3.3-43 through 1.3.3-54. Whereas convective heating was so overwhelmingly dominant for Mars as to preclude any detailed consideration of radiation, this was not true for Venus. It is, therefore, much more difficult to specify the worst Venusian entry condition from a thermal protection standpoint, as the situation will vary with respect to the body location being considered.

E. Ablation Material Performance

Prior to the determination of ablation shield thickness requirements, a knowledge of the ablation material to be used and its properties was required. Several ablation materials were initially considered (i. e., phenolic Nylon, elastomeric shield material, phenolic graphite, and phenolic refrasil). Preliminary investigations based on cold wall heats of ablation indicated elastomeric shield material as a primary material, and phenolic Nylon as an alternative material for Martian heat shield studies. Phenolic Nylon appeared to be the most suitable ablation material for Venusian heat shield applications. The performance of these materials in the planetary environments being considered was determined by comparison with suitable test data where such data was available, and by the REKAP analysis where appropriate test data was not available.

(1) Martian Ablation Performance

(a) Elastomeric Shield Material

To determine the heats of ablation to be used for ESM and phenolic Nylon, a basic trajectory was chosen for later use in heat shield calculations. The trajectory chosen had an entry angle of 20° , and a $W/C_D A$ of 40. This trajectory represented the severest heating case with respect to entry angle and a median heating value with respect to $W/C_D A$. Ablation tests conducted in a hypersonic arc tunnel (Reference 22) for ESM 1001P-S (density = 41 lb/ft^3) indicated heats of ablation of 6250, 7600, 8800, 9100, and 9350 for five stations along the axial centerline of the test specimen. The average heat of ablation arrived at was 8220 BTU/lb, which demonstrates reasonable agreement with the 8500 BTU/lb heat of ablation based on preliminary analysis, and used for ESM heat shield calculations. The referenced test resulted in a peak heating of $47 \text{ BTU/ft}^2 \text{ sec.}$, which agrees favorably with cone values of Figure 1.3.3-15 for the basic vehicle and trajectory later used for heat shield calculations. Other heat fluxes, 23.5, 36, 44.5, 46 and $38.5 \text{ BTU/ft}^2 \text{ sec.}$, along the centerline of the test sample, which influenced previously quoted test heats of ablation, also agree favorably with heat fluxes presented in Figure 1.3.3-15 for the cone section.

Other tests conducted on ESM 1003 (Reference 23) in a rocket exhaust facility also indicated favorable comparisons with a heat of ablation of 8500 BTU/lb, when it is noted that rocket exhaust facilities generally give significantly lower enthalpies, resulting in lower apparent heats of ablation at a given heat flux. Figures 1.3.3-67 through 1.3.3-69 demonstrate heats of ablation which are typical of the ESM family of materials.

It should be pointed out that although Figure 1.3.3-70, indicates shear stress levels as high as 18 psi, this was done for the worst shear conditions. The other entry conditions would experience shear levels much lower than those indicated. Therefore, the heats of ablation shown for ESM at the lowest shear levels (0 - 8 psf) of Figure 1.3.3-68 are still typical of the Martian entry environments.

(b) Phenolic Nylon

The heat of ablation used for phenolic Nylon was based primarily on data from a recovered satellite, which resulted in a heat of ablation of 6000 BTU/lb. It is apparent from Figure 1.3.3-15 (for the basic trajectory and body used for heat shield calculations) and Figure 1.3.3-71 (representing heat flux levels encountered by the entry vehicle and the recovered satellite) that the entry environments were somewhat similar. Consequently, utilization of the 6000 BTU/lb heat of ablation as determined from the recovered satellite would seem justified. Further justification for the phenolic Nylon heat of ablation chosen is apparent in Table 1.3.3-2 and Figure 1.3.3-69 representing the previously discussed tests in a hypersonic arc facility, and rocket exhaust facility.

TABLE 1.3.3-2. MATERIAL PROPERTIES

	<u>Phenolic Nylon</u>	<u>Elastomeric Shield Material</u>
Density (lb/ft ³)	75	45
Specific Heat (BTU/lb ^o F)	.380	.360
Thermal Conductivity (BTU/hr Ft ² ^o F/ft)	.00004	.000025
Heat of Ablation (cold wall) (BTU/lb)	6000	8500
Degradation Temperature (^o R)	1100	1300

(2) Venus Ablation Performance

Previous studies of heat protection materials performance for Venus entry have introduced a new effect in ablation material performance, that of sublimation of the char surface. Conventional environments such as ballistic and satellite re-entries result in maximum surface temperatures on the order of 5000-6000^oR. Since carbon does not sublime below about 7000^oR, the consideration of surface absorption of heat by sublimation has not been required. In many cases the Venusian entry heat pulses are characterized by very high rates over short time periods. As a result of the high heating rates, the surface temperatures tend to reach very high values. The high surface temperature tends to increase the ablation material effectiveness through:

- . reduction of heat input
- . re-radiation of more heat
- . absorption of more heat by surface sublimation

In addition to the above problem, the Venusian atmosphere results in radiant heating rates which are in some cases equal to or greater than the convective rates. Since the ablation effectiveness is less for radiative heating (due to no "blocking action" or mass addition effect), it follows that the "heat of ablation" is dependent on the ratio of radiant to convective heating. Finally, the Venusian entry conditions result in stagnation enthalpy values up to 32,000 BTU/lbs, which is far outside the reaches of a sound extrapolation of present correlations of heat of ablation with stagnation enthalpy.

The performance of ablation materials is often described by the gross "heat of ablation" quantity, usually obtained by ground tests. This concept is often inadequate, especially for char forming plastics. In order to better understand the phenomena involved, General Electric has developed an applied engineering technique or model for the ablation of

thermosetting plastics designated as the Reactions Kinetics Ablation Program. For Venusian entry, such a procedure is a must since ground test facilities for establishing ablation material performance are completely inadequate in simulating the conditions of heat flux, shear stress, and enthalpy.

These problems were investigated to some extent during the previous Venus - Mars Capsule Study (Reference 4) by artificial modifications to allow fixing the surface temperature and absorption of heat at the surface. Since the previous studies resulted in very high heats of ablation (15,000 to 27,000 BTU/lbs), it was necessary that additional studies be accomplished to substantiate these results and determine the extent to which they can be applied. The additional study has been accomplished with a more rigorous modification to the REKAP program where carbon vapor pressure data and local pressure time histories are utilized to control the sublimation processes. This study was funded by the General Electric Development Authorization Program.

The REKAP Program used in this analysis was modified to include temperature and vapor pressure data and temperature - latent heat of sublimation data as developed from Reference 21 and presented in Figures 1.3.3-72 and 1.3.3-73. The local pressure was then supplied as an input for calculation in addition to the usual heating rates, thereby determining the surface temperature and heat of sublimation during sublimation periods. Sublimation was therefore an important mode of char surface recession and char thickness control. The modified program also included an over-riding char thickness control as a function of shear stress based on extensive investigation at GE-RSD, which has resulted in a shear stress - char thickness correlation from both ground and flight test data.

The above described program was used to study phenolic Nylon ablation performance for a range of Venusian entry conditions. The conditions covered a matrix of three entry angles (15° , 30° , 90°), three body locations (stagnation point, maximum turbulent heating point, mid-cone point), and four levels of hot gas radiant heat input for each of the above cases, resulting in 36 cases. The heat fluxes used in the study are given in Figures 1.3.3-59 and 1.3.3-74. The standard atmosphere and a vehicle with $R_N/R_B = 0.6$, $\theta = 24^\circ$ and $R_B = 3.5$ feet, was used as the basis for the study. As pointed out in a previous section, the radiation results are based on the preliminary radiation intensities and are not the final results which would have been predicted. The parametric variation of the gas radiation level was sufficient to cover the change. The aerodynamic shear stresses are given in Figure 1.3.3-75. The shear stresses are not severe, being of the same magnitude as blunt body ICBM re-entry into Earth atmosphere. The char-thickness limitations based on the shear correlation are given in Figure 1.3.3-76. Typical analog results are shown in Figures 1.3.3-77 through 1.3.3-80 giving in order the char and virgin material temperatures, the ablation and char thickness histories, and the heat flux partitioning.

The REKAP results were reduced to time integrated levels of degradation through use of the final degradation thickness and the total integrated gross heat input. Heat of ablation correlations with both gross heat input and the ratios of radiation to total heating (Q_R/Q_T) were devised as given in Figures 1.3.3-81 and 1.3.3-82. The data appears to correlate much better with gross heat input for all off-stagnation point locations than with radiation levels provided the radiation levels are limited to $(Q_R/Q_T) < 0.4$. In the range of Q_R/Q_T from 0 to 0.4, the loss in blocking action with radiant heat input is apparently offset by other phenomena so that the material maintains the usual characteristics of a charring plastic of increased performance when "pushed" harder.

The summary of REKAP ablation results as presented in Figure 1.3.3-82 obviously does not lead to an all inclusive correlation with Q_R/Q_T , as was developed in the previous Venus - Mars Capsule study. It does appear, however, that different body locations can be correlated with some success so that heats of ablation can be selected for parametric design studies with confidence in basing the correct level of performance and a knowledge of the range of error. The procedure adopted for parametric design studies was to 1) use

the correlation of Figure 1.3.3-81 for all cone locations due to usually low Q_R/Q_T values, 2) use a similar procedure for the nose maximum turbulent location except switch to the Q_R/Q_T correlation (Figure 1.3.3-82) at $Q_R/Q_T > 0.4$, and 3) use Figure 1.3.3-82 entirely for the stagnation point.

Analysis of the REKAP results at specific times during a trajectory was accomplished to develop instantaneous ablation rates and heats of ablation for correlation with stagnation enthalpy. Such a correlation could not be developed, however, due to the complexities of the ablation phenomena of a charring plastic. The mass addition effects which would be expected to introduce the relationship with enthalpy is reduced to 30-50% of the over-all ablation effectiveness. The remaining ablation effectiveness is directly dependent on the char layer thickness which varies widely throughout the trajectory, thereby obscuring the blocking action efforts. The partitioning of the energy absorption modes is shown in Figure 1.3.3-83.

A comparison of REKAP prediction with ground test data is shown in Figure 1.3.3-84. The data was obtained from the GE Space Sciences Laboratory air arc facility and was reported in the previous Venus - Mars Capsule study as well as Reference 27. The REKAP program was run in the exact form used in the Venus parametric ablation study. The char thickness was controlled by sublimation. It is noted that steady state ablation was obtained in approximately one second. The excellent agreement between theory and data substantiates the REKAP approach to ablation performance.

F. Ablation Requirements

(1) Martian Heat Shield Analysis

The heat shield analysis for Mars was based on the integrated heating to the basic vehicle used for previously discussed entry heating calculations, at entry conditions $\gamma = 20^\circ$, $W/C_{DA} = 40$, and $V_e = 23,000$ f.p.s. As previously discussed, the entry conditions chosen represent the extreme integrated heating with reference to entry angle, and a median value with respect to W/C_{DA} . The entry condition selected was virtually entirely laminar, therefore it was decided to apply laminar wetted length corrections to obtain heat shield thickness for other vehicles. The laminar corrections were obtained from Reference 11, as a function of S/R_N (wetted length/nose radius), and cone angle. However, rather than calculate the specific integrated heating to each vehicle, the heating to the basic vehicle was used to obtain a heat shield for the basic vehicle (Figure 1.3.3-85). The laminar corrections of Brunner were then used to determine heat shield thicknesses, without any safety margin, for the other vehicles (Figures 1.3.3-85 through 1.3.3-93).

To obtain the heat shield thicknesses for the basic vehicle, the following relationship was used:

$$X = \frac{12 Q_T}{\rho H_e} \quad (\text{Inches})$$

where X is ablation thickness in inches (no safety margin), Q_T is total time - integrated heating (BTU/ft²), ρ is ablation material density (LB/ft³), and H_e is the effective heat of ablation (BTU/lb). From the equation it is apparent that shield thickness is directly proportional to integrated heating, and that therefore, it was justifiable to apply the laminar corrections based on wetted lengths directly to shield thicknesses. Although turbulent conditions are encountered for other entry conditions, Figure 1.3.3-94, indicating the ratio of laminar to total heating, demonstrates that the major portion of the trajectory matrix experiences laminar heating. Consequently, the heat shield calculations, based on laminar corrections, are justifiable not only for the basic trajectory, but for others as well.

(2) Trajectory Corrections

Although the results obtained (Figures 1.3.3-85 - 1.3.3-93) were for the basic trajectory condition considered, ablation thicknesses for a given vehicle may be modified to obtain shield thicknesses for other trajectories. This could be done by ratioing heating for the three significant body points (stagnation point, sphere point, and mid-cone point) at the trajectory conditions for which heat shield thicknesses are desired, to the heating at the same points (S/R_N values as in Figures 1.3.3-11 through 1.3.3-22) for the basic trajectory conditions. The ratio thus obtained should be multiplied times the shield thicknesses for the given vehicle at the basic trajectory conditions. The results obtained would then be shield thicknesses for the same vehicle, but for a different trajectory. To correct for changes in entry velocity, the new entry velocity divided by the 23,000 f.p.s. should be entered into Figure 1.3.3-36 and the corresponding $Q/Q @ 23,000$ f.p.s. value determined. Using the Q/Q value thus obtained to multiply the shield thicknesses for the vehicle under consideration (with an entry velocity of 23,000 f.p.s.), shield thicknesses may be obtained for the same vehicle, but at the new entry velocity.

(3) Atmospheric Corrections

All Martian shield calculations have been made with reference to the Mars Mean Atmosphere, consequently it could be necessary to determine the effects of the Upper and Lower Limit Model Atmospheres on the heat shield requirements. Figure 1.3.3-95 has been derived for this purpose from integrated heating plots of Walker's Heating Parameter for the three atmospheres being considered. For any entry condition and vehicle being considered, heat shield thicknesses as determined for the Mars Mean Atmosphere should be multiplied by the heating ratio ($Q_{\text{upper}}/Q_{\text{mean}}$, or $Q_{\text{lower}}/Q_{\text{mean}}$) for the atmosphere in question.

(4) Parametric Plots

In addition to shield thicknesses for the general vehicle matrix, parametric shield thickness curves have been generated for ESM and Phenolic Nylon. Figures 1.3.3-96 through 1.3.3-99 are for the stagnation point, and a point on the sphere ($S/R_N = .60$), and are normalized with respect to the square root of the nose radius. As previously, these curves are based primarily on the majority of heating being laminar (Figure 1.3.3-94). To use these curves it is simply necessary to enter with an entry angle and ballistic parameter. The corresponding ablation thickness value should then be multiplied by the square root of the nose radius (in feet) to obtain the appropriate shield thickness in inches. Velocity and atmospheric corrections may be applied in the manner already discussed. A similar normalization procedure could not be used for Venus because of the significant role played by radiant heating.

(5) Venus Heat Shield Analysis

The Venus heating calculations (parametric with $H, W/C_{DA}$) are indicated in a previous section, for a basic shape with $\theta_c = 30^\circ$, $R_N/R_B = 0.6$, and $R_B = 3.5$ ft. To obtain a heat shield input to vehicle optimization requires application of these results to different shapes. Obviously, it was not possible to obtain shield thicknesses for a 27 vehicle matrix for all entry angles and W/C_{DA} 's. A nominal W/C_{DA} of 40 LB/ft² and the maximum heating entry angle of 15° was selected as the design case.

The problem remained to take the integrated convective heat and the integrated radiant heat at the selected body locations on the basic configuration and adjust them for configuration changes. The body locations selected to give adequate definition of the heat shield thickness distribution was the stagnation point, maximum turbulent heating point, tangency point, mid-cone point and end of cone point. The off-stagnation point convective heating was handled by developing correction factors from wetted length and pressure changes. The stagnation point was, of course, corrected by the $\sqrt{R_N}$. On the smaller configurations, the nose section was assumed to remain laminar and the heating of the "maximum turbulent

point" was actually obtained by Lee's distribution. The cone section was in all cases treated as all turbulent heating, although for the smaller configurations transition would not always occur early in the trajectory.

The correction of radiant heating was accomplished by developing the radiation distribution correlation shown in Figure 1.3.3-100. The relationship was devised by plotting from computer results for the basic shape, the radiation intensity (per unit shock layer thickness) versus the local pressure distribution. The development of this distribution curve with a straight line variation with such a basic quantity as the pressure distribution is considered a minor breakthrough in radiation techniques. Using this data and the local shock layer thickness and pressure distribution, the radiant heating distribution can be described for any configuration. A table of shock layer thicknesses normalized with nose radius is given in Table 1.3.3-3. It should be recognized that the basic radiation calculations used throughout this study do not account for non-isothermal shock layer and therefore the predicted radiation levels on the cone section are likely to be considerably higher than the actual values. This situation is not aggravated or attributed to in any way, however, by the present radiation distribution technique.

TABLE 1.3.3-3. SHOCK DETACHMENT AT CONE LOCATIONS

R_N/R_B	θ_c	$\frac{L}{R_N}$	
		Mid-Cone	End Cone
.24	20	.26	.35
	30	.19	.34
	40	.19	.34
.6	20	.32	.32
	30	.19	.17
	40	.165	.145
.9	20	.26	.28
	30	.17	.19
	40	.15	.175

The results of the heating distribution calculations are tabulated in Table 1.3.3-4, including integrated convection and radiation and the ratio of radiant to total heating. Also included are the heats of ablation and the predicted ablation thickness. The results were plotted as shield ablation requirements versus axial station and are presented in Figures 1.3.3-101 through 1.3.3-109.

F. Insulation Requirements

(1) Martian Insulation Requirements

Insulation requirements for a Martian entry vehicle were determined by a conduction solution using the Air-Gap Program. Using the heat fluxes obtained from the basic matrix of Martian runs, and the elastomeric shield material thermal properties of Table 1.3.3-4 as input, peak backface temperatures at the stagnation point were plotted as a function of insulation thickness for each entry condition. The resulting curves were then cross-plotted to obtain insulation thickness as a function of entry angle for several peak backface temperatures. To use these curves it is necessary to select a desired bond line temperature and enter the curves (Figures 1.3.3-110 through 1.3.3-112) with the desired entry conditions, to read off the required stagnation thicknesses. It is recommended that insulation thicknesses obtained be used around the entire body.

It is to be noted that all the curves are for ESM in the Martian Mean Atmosphere. Due to changes in entry time with changes in atmosphere, corrections would be necessary for application to the other Martian model atmospheres. It is suggested that correction factors

D _B	$\frac{R_N}{R_B}$	e _C	STAG POINT							MAX HT POINT					
			R _N	Q _C	Q _R	Q _T	$\frac{Q_R}{Q_T}$	H _e	X _{abl} inches $\frac{12 Q_T}{\rho H_e}$	Q _C	Q _R	Q _T	$\frac{Q_R}{Q_T}$	H _e	X _a
3.5	.24	20	.42	35820	3740	39560	.095	22200	.286	29130	2100	31230	.067	12300	.40
		30		35820	3740	39560	.095	22200	.286						
		40		35820	3740	39560	.095	22200	.286						
	.60	20	1.05	22660	9340	3200	.292	19900	2.57	18560	5250	23810	.220	10200	.37
		30					.292	19900							
		40				.292	19900		X = .169'						
	.90	20	1.575	18470	14010	32480	.431	17400	.299	16670	7880	24550	.321	10400	.37
		30					.431	17400							
		40				.431	17400		X = .254'						
8.0	.24	20	.96	23710	8540	32250	.265	20300	.254	19420	4800	24220	.198	10300	.37
		30					.265	20300							
		40				.265	20300		X = .154'						
	.60	20	2.40	14980	21350	36330	.588	13700	.424	14350	12010	26360	.456	11600	.36
		30					.588	13700							
		40				.588	13700		X = .387'						
	.90	20	3.60	12210	32030	44240	.724	9900	.715	14170	18010	32180	.560	11100	.46
		30					.724	9900							
		40				.724	9900		X = .581'						
10.5	.24	20	1.26	20190	11210	31400	.357	18800	.267	16310	6300	22610	.279	9800	.36
		30					.357	18800							
		40				.357	18800		X = .203'						
	.60	20	3.15	12750	28020	40770	.687	10900	.598	13490	15760	29250	.539	11200	.41
		30					.687	10900							
		40				.687	10900		X = .508'						
	.90	20	4.725	10420	42030	52450	.801	8300	1.011	13460	23640	37100	.637	10600	.56
		30					.801	8300							
		40				.801	8300		X = .762'						

TABLE 1. 3. 3-4. HEATING AND ABLATION RESULTS FOR MATRIX OF VEHICLES

TANGENCY POINT						MID CONE						END OF CONE					
Q _C	Q _R	Q _T	$\frac{Q_R}{Q_T}$	H _e	X _{abl}	Q _C	Q _R	Q _T	$\frac{Q_R}{Q_T}$	H _e	X _{abl}	Q _C	Q _R	Q _T	$\frac{Q_R}{Q_T}$	H _e	X _{abl}
8320	210	8530	.025	5900	.231	6680	230	6910	.033	5500	.201	7000	370	7370	.050	5600	.211
12130	560	12690	.044	7100	.286	11520	980	12500	.078	7000	.286	11040	1550	12590	.123	7000	.288
16300	1310	17610	.074	8400	.335	14450	2730	17180	.159	8300	.331	14080	4370	18450	.237	8700	.339
6930	460	7390	.062	5600	.211	5910	360	6270	.057	5300	.189	5910	350	6260	.056	5300	.189
10100	1280	11380	.112	6700	.272	9440	1100	10540	.104	6500	.259	10330	1330	11660	.114	6900	.270
13570	2980	16550	.180	8200	.323	13460	3550	17010	.209	8300	.328	14180	4440	18620	.238	8700	.343
7330	630	7960	.079	5800	.220	6460	600	7060	.085	5500	.205	6660	540	7200	.075	5500	.209
12980	2010	14990	.134	7700	.311	10390	1530	11920	.128	6900	.276	9910	1520	11430	.133	6700	.273
15100	4150	19250	.216	8900	.346	13880	4500	18380	.245	8700	.338	13830	5070	18900	.268	8800	.344
7060	420	7480	.056	5700	.210	6460	450	6910	.065	5500	.201	5930	720	6650	.108	5400	.197
10280	1150	11430	.101	6700	.273	9810	1930	11740	.164	6900	.272	9390	2980	12370	.241	7000	.283
13813	2750	16560	.166	8200	.323	12250	5390	17640	.306	8400	.336	11910	8400	20310	.679	9200	.353
5870	840	6710	.125	5400	.199	5030	610	5640	.108	5100	.177	5010	590	5600	.105	5100	.176
8570	2380	10950	.217	6400	.274	8030	2020	10050	.201	6300	.255	8770	2400	11170	.215	6600	.271
11500	5860	17360	.338	8400	.331	11410	6760	18170	.372	8600	.338	12060	8510	20570	.414	9300	.354
6250	1080	7330	.147	5600	.209	5500	850	6350	.134	5300	.192	5680	790	6470	.122	5400	.192
11040	3140	14180	.221	7500	.303	8840	2730	11570	.235	6700	.273	8430	2650	11080	.239	6600	.269
12920	7970	20890	.382	9400	.356	11870	8190	20060	.408	9100	.353	11840	9020	20860	.433	9400	.355
6680	530	7210	.074	5600	.206	5340	560	5900	.095	5200	.182	5620	870	6490	.134	5400	.192
9740	1440	11180	.129	6600	.271	9290	2420	11710	.207	6700	.280	8880	3630	12510	.290	7000	.286
13080	3450	16530	.209	8200	.323	11590	6740	18330	.368	8600	.341	11300	10220	21520	.475	9500	.362
5560	1010	6570	.154	5400	.195	4730	640	5370	.119	5000	.172	4750	620	5370	.115	5100	.168
8110	2880	10990	.262	6600	.266	7610	2420	10030	.241	6400	.251	8310	2880	11190	.257	6600	.271
10900	7240	18140	.399	8600	.338	10780	8140	18920	.430	8800	.344	11600	10350	21950	.472	9700	.362
5890	1090	6980	.156	5500	.203	5190	1120	6310	.177	5300	.190	5350	1030	6380	.161	5300	.193
10490	3700	14190	.261	7500	.303	8390	3140	11530	.272	6700	.275	8010	2620	10630	.246	6500	.262
12110	9650	21760	.443	9600	.363	11120	9590	20710	.463	9300	.356	11090	10350	21440	.483	9500	.361

might be obtained by ratioing entry times for the other atmospheres with those for the mean model, and applying the ratios to the insulation thickness at a particular entry condition (the greater entry time requiring the greater insulation thickness).

To obtain total shield thickness, it would be necessary to specify ablation thicknesses for the vehicle being considered, and then add to this the insulation requirements around the vehicle. The values obtained would represent minimum requirements, and should be multiplied by the desired safety factor.

(2) Venus Insulation Requirements

The heat shield insulation thickness for Venus is required only to protect the bond line so that the shield remains intact throughout the heating period. After the heating period, the outer surface is expected to rise approaching the ambient air temperature during the extended flight time before reaching the surface. The shield insulation thickness required was determined from the shield temperature response data generated in the REKAP studies. The 15° entry case was taken as the design case due to the longest heating period. The temperature gradient through the shield at the end of heating is shown in Figure 1.3.3-113. Assuming a conservative bond line temperature limit of 500°F for a silicone tube bond, the insulation thickness is only 0.03 inches. The value was used for all body locations and entry conditions.

G. Development Recommendations

Although the present study has resulted in the development of techniques and capabilities for the design of Mars and Venus entry heat protection systems further investigations are recommended. Continued investigations should include analytical development and experimental development.

(1) Analytical Development

As already noted, it was necessary to use air as the basis for thermodynamic properties to be used in heating predictions. Although the resulting inaccuracies were not considered intolerable for application to preliminary heat shield design, they are avoidable. With a further substantiation of the "true" chemical make-up of the Martian and Venusian atmospheres, it is recommended that the corresponding thermodynamic properties be utilized. Incorporation of the appropriate N₂-CO₂ thermodynamic properties in the calculation procedure would result in more accurate convective and radiative heating predictions. In addition the basic radiation intensities should be further analyzed 1) for possible additional contributing species or 2) to reflect any changes in the chemical model for the Martian and Venusian atmospheres. In particular, the Martian radiation data should be extended to include those additional contributing species already considered for Venus. The radiation calculation procedure could be further refined by using a calculation method which accounts for the effect of a non-isothermal shock layer (Reference 28).

Further analytical development in the ablation materials area is indicated with an emphasis on the REKAP approach. The present study evaluated only the thermal performance of PN in the Venusian atmosphere. Consequently, it would be advisable to further the analysis by considering other possible ablators for application to Venusian entry. It should also be noted that the present REKAP analysis considered only the Venus Standard Model Atmosphere. Unless further information becomes available indicating that this is the most probable Venusian atmosphere, the effects on material performance of entry in the Venusian Extreme Model Atmosphere should be investigated using the REKAP procedure.

(2) Experimental Development

Concurrently with any further attempts at predicting heating during entry to Mars and Venus, continued experimental shock tube studies are recommended. Such tests should be used to substantiate and support the theoretical heating predictions for Mars and Venus.

Although ground test facilities may be used to simulate the Martian entry environment, the same cannot be said for Venus. Because of the high enthalpy levels and heating rates, already discussed, no existing ground facilities can adequately simulate the Venusian entry environment. Facilities to simulate the Venusian entry environment not only must provide significantly higher enthalpy levels than those heretofore obtained; but in addition a definite need exists for a facility capable of providing convective and radiant heating in varying proportions. Consequently, it will be necessary to develop appropriate environmental facilities.

Using existing facilities (for Mars) and facilities not yet in existence (for Venus) materials tests should be conducted. The purpose of such tests, simulating the planetary entry environments, would be to experimentally determine ablation material performance. The results of these tests could be used to further refine theoretical ablation and insulation estimates for the materials being investigated. In addition test results could be used in support of a continued REKAP materials performance analysis.

SYMBOLS

D	diameter
h	enthalpy, altitude
H _e	heat of ablation
I	radiation intensity
K	density decay constant
K _r	emissivity correction factor for non-optically thin gas layer
L	shock detachment distance
m	mean molecular weight
P _r	Prandtl Number
\dot{Q}	heat transfer rate
Q	time integrated heating
R	universal gas constant, radius
r	recovery factor, radius
T	isothermal layer temperature
s	wetted length
u, v	velocity
u _o	velocity gradient
W/C _D A	ballistic parameter
X	ablation thickness
y	radial co-ordinate of body location
y ₂	streamline divergence
α	absorptivity
γ	entry angle, ratio of specific heats
σ	Boltzmann's constant
ϵ	emissivity
θ_c	half-cone angle
ρ_1	density
ρ_0	pseudo-sea level density
μ	viscosity, microns
t _e	time of entry heating

Subscripts

c	convective
e	local edge of boundary layer, entry conditions
L	laminar
O	stagnation point, sea level
S	stagnation point
r	recovery conditions
R	radiative
T	turbulent, total heating
w	wall
∞	free stream

Superscripts

*	reference conditions
---	----------------------

REFERENCES

1. Dewees, L. , "Re-entry, Vehicle Design (Ablating) Program," GE TIS R59SD391, July 1959.
2. Dunn, J. E. , "Using the Ablation Design Program to Calculate Heat Transfer Experienced By Bodies Traveling With Superorbital Velocities," CA-117-463, 2/17/63.
3. Simons, R. , "Modification of Hot Gas Subroutines, "PIR-ARSTA-8151-016, 5/29/63.
4. Volume II, "Venus-Mars Venus Capsule Study," GE-JPL Contract No. 950250, 7/30/63.
5. Simons, R. , "Venus Heating Comparisons," PIR-ARSTA-017, 6/18/63.
6. Gruszczynski, J. S. , and Warren, W. R. , "Experimental Heat Transfer Studies of Hypervelocity Flight in Planetary Atmospheres," AIAA Paper No. 63-450, August 1963.
7. Gruszczynski, J. S. , and Warren, W. R. , "Measurements of Hypervelocity Stagnation Point Heat Transfer in Simulated Planetary Atmospheres," GE-TIS R63SD29, March 1963.
8. Walker, G. K. , "Some Comments on Laminar and Turbulent Heat Transfer Equations," AETM 147, December 1959.
9. Walker, G. K. , and Schumann, B. A. , "Some Aero-Thermodynamic Information in Convenient Curve Form," AETM 183, January 1961.
10. Scala, S. , and Gilbert, L. , "Theory of Hypersonic Laminar Stagnation Region Heat Transfer in Dissociating Gases," ASTM 188, November 1962.
11. Brunner, M. , and Gallagher, P. A. , "A Simplified Analysis of the Aerodynamic Heating of a Blunt Body Re-Entering the Earth's Atmosphere at Hypersonic Velocity," GE-TIS R58SD227, January 1958.
12. Rasool, S. I. , "Structure of Planetary Atmospheres," AIAA Journal, Vol. 1, No. 1, pp. 6-17, January 1963.
13. Vachon, D. N. , "The Density Structure of the Upper Atmosphere of Mars," GE-TIS R62SD58, May 1962.
14. Chamberlin, S. , "Mars Model Atmospheres," PIR 8021-048, 5/22/63.
15. Cheng, Hsien K. , "Recent Advances in Hypersonic Flow Research," Vol. 1, No. 2, pp. 295-310, February 1963.
16. Hansen, C. F. , "Approximations for the Thermodynamic Transport Properties of High Temperature Air," NACA TN 4150, March 1958.
17. Scala, S. , "Heating Problems of Entry into Planetary Atmospheres from Supercircular Orbiting Velocities," GE-TIS R61SD176, October 1961.
18. Nardone, M. , "Current Estimates of Radiation from Earth, Venus and Mars," PIR No. 313, 2/7/63.

19. Nardone, M. , "Radiation Predictions for Venusian Atmosphere," PIR No. 2680-409, 6/21/63.
20. Mayer, H. , LA-647 Los Alamos Scientific Laboratory, 1947.
21. Viadale, G. , "The Vaporization of Graphite, TiC, ZrC, and HfC," GE-TIS R61SD010, January 1961.
22. Bierman, R. L. , "Ablation Testing of Shield Materials for the A-45 Program" TTE (TPL)-8151-039, 8/19/63.
23. Bierman, R. L. , "Evaluation of Phenolic Graphite, T-24, T-24 WFAG, and ESM 1003 in the Malta Pit #1 Rocket Exhaust Facility," Thermo. Tech. Data Rpt. No. 63SD257, 4/5/63.
24. Browne, W. G. , "Equilibrium Thermodynamic Properties of the Environment of Mars," APTM Memo. No. 2, 3/26/62.
25. Browne, W. G. , "Thermodynamic Properties of the Venusian Atmosphere," APTM Tech. Memo No. 13, Part I, 6/11/62.
26. Browne, W. G. , "Thermodynamic Properties of the Venusian Atmosphere," ATM Tech. Memo. No. 13, Part II, 6/6/63.
27. Sheridan, R. , Diaconis, N. , and Warren, W. , "Performance of Several Ablation Materials in Simulated Planetary Atmospheres," GE-TIS R63SD35, April, 1963.
28. Dohner, C. V. , "Hot Gas Radiation Program Procedure," PIR HTT-8151-081, 3/11/63.
29. Page, W. A. , "Shock-Layer Radiation of Blunt Bodies Travelling at Lunar Return Entry Velocities," IAS Paper No. 63-41, January, 1963.
30. Gruszczynski, J. S. , "Gas Dynamic Charts for Several CO₂-N₂ Mixtures in Thermochemical Equilibrium," to be published as GE-MSD TIS.
31. Browne, W. G. , "Thermodynamic Properties of the Venusian Atmosphere," GE-AAP Tech. Memo 13, June, 1962.
32. Nardone, M. C. , Breene, R. G. , Zeldin, S. S. , and Riethof, R. R. , "Radiance of Species in High Temperature Air," GE-MSD TIS No. R63SD3, June, 1963.
33. Serbin, H. , "Supersonic Flow Around Blunt Bodies," JAS 25, No. 1, January, 1953.

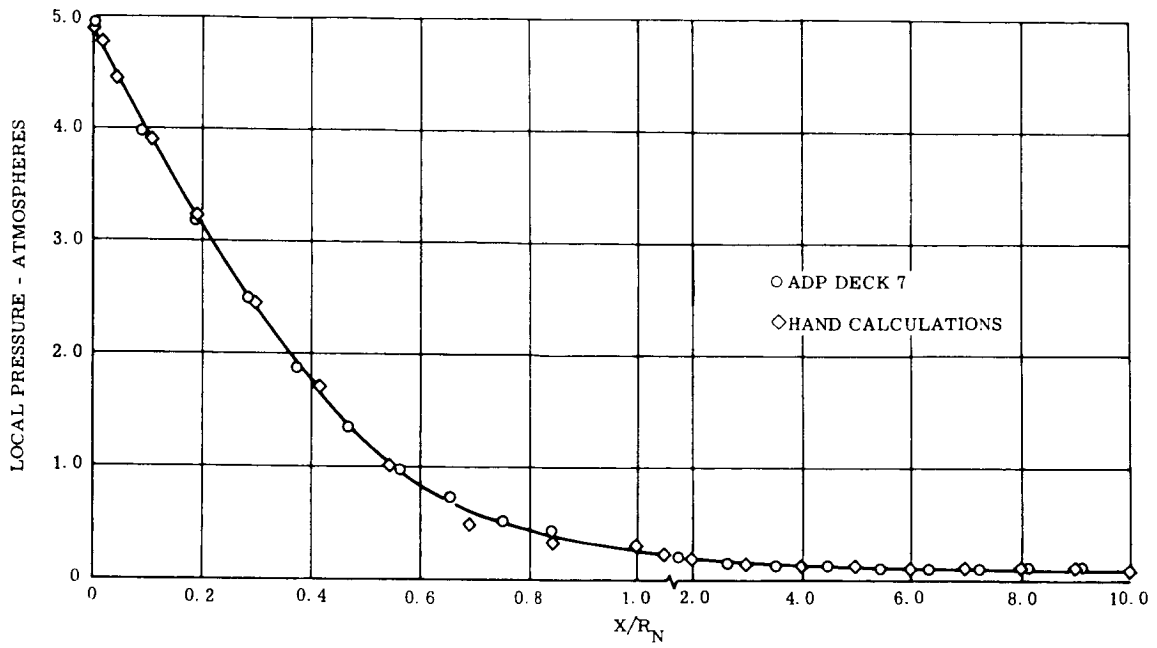


Figure 1.3.3-1. Local Pressure Distribution (Air and N₂-CO₂)

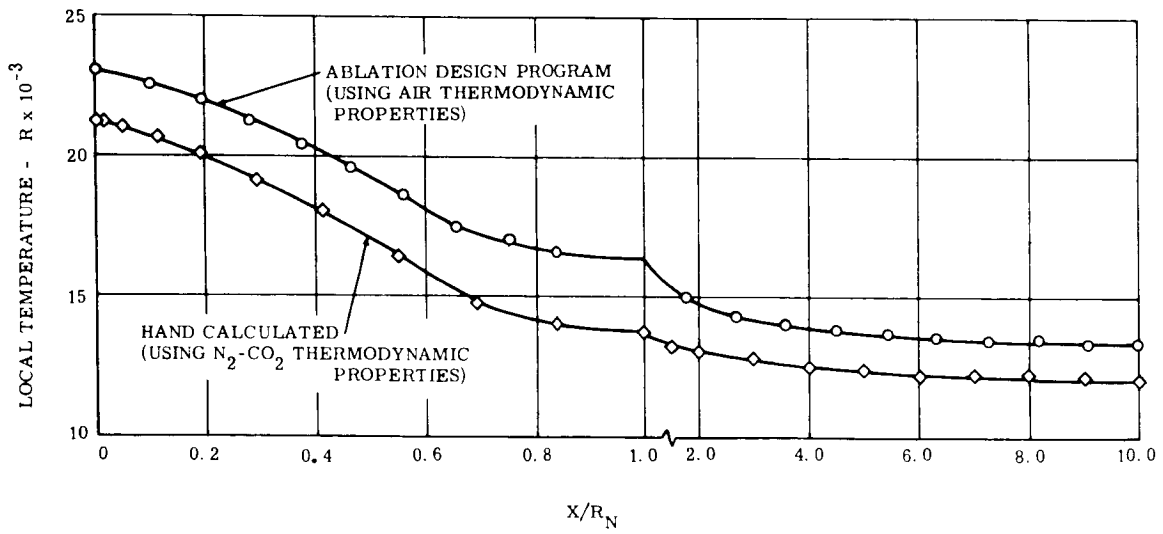


Figure 1.3.3-2. Local Temperature Distribution (Air and N₂-CO₂)

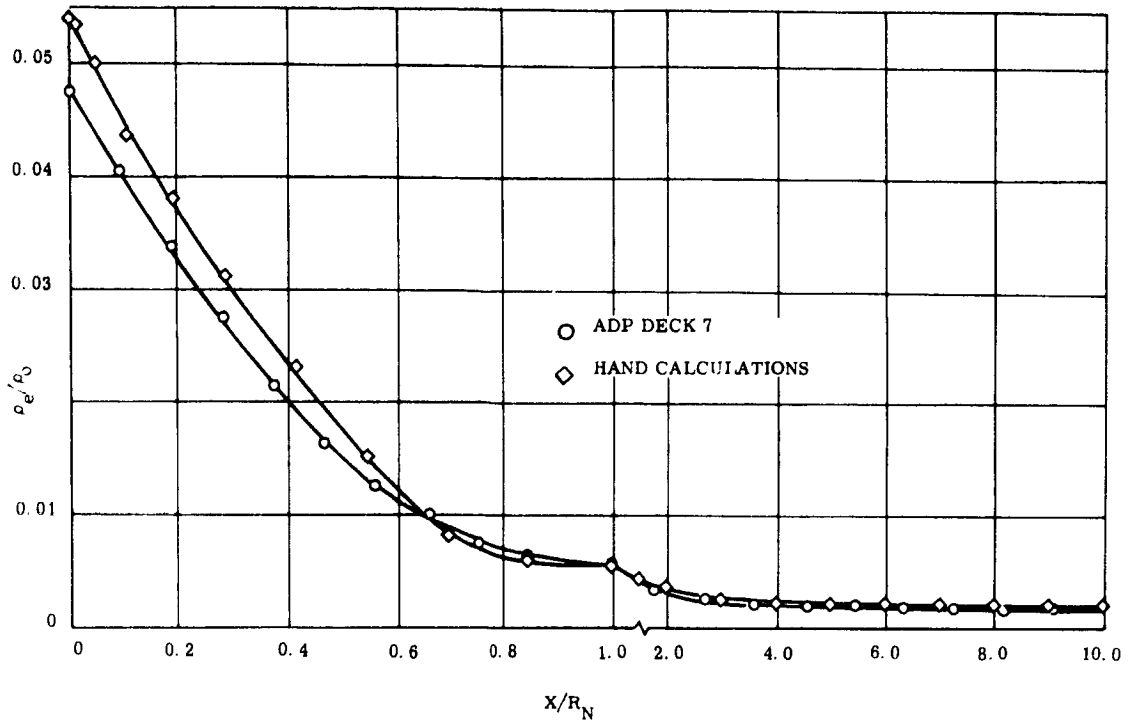


Figure 1.3.3-3. Local Density Ratio (Local Density/Reference Density)

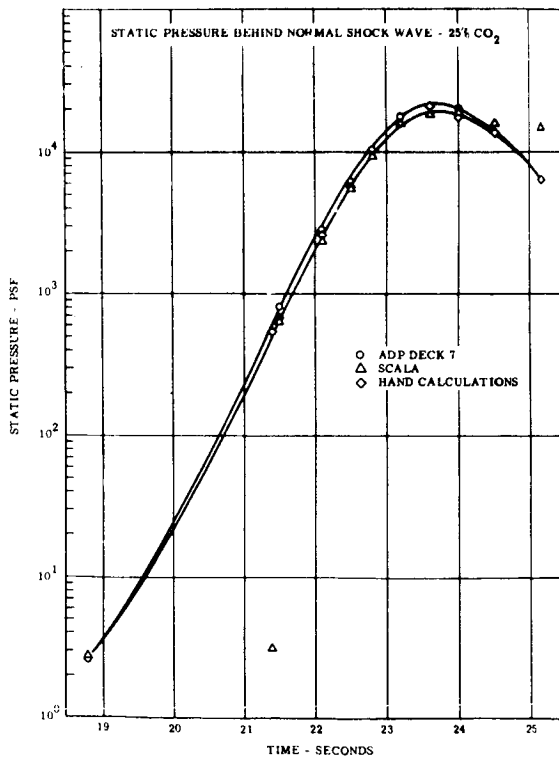


Figure 1.3.3-4. Static Pressure Behind Normal Shock Wave (25% CO₂)

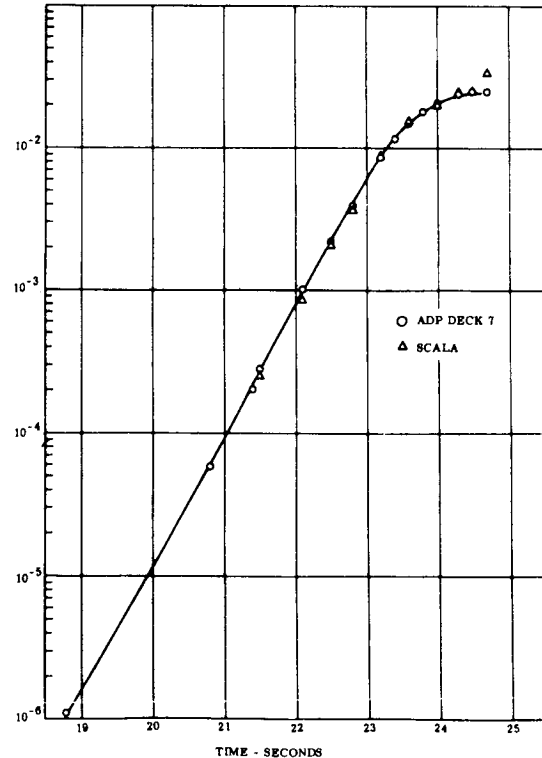


Figure 1.3.3-5. Static Density Behind Normal Shock Wave (25% CO₂)

Figure 1.3.3-6. Figure deleted

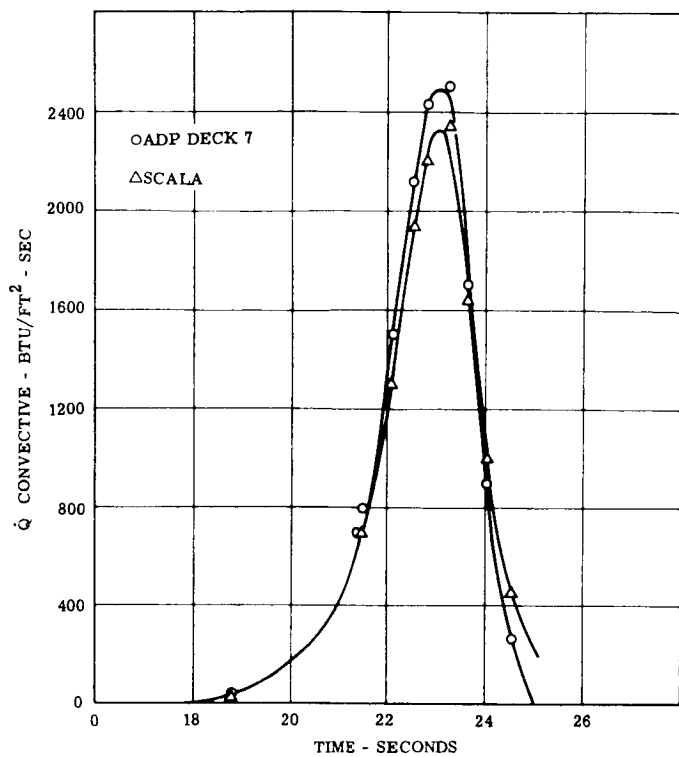


Figure 1.3.3-7. Stagnation Convective Heating (25% CO₂)

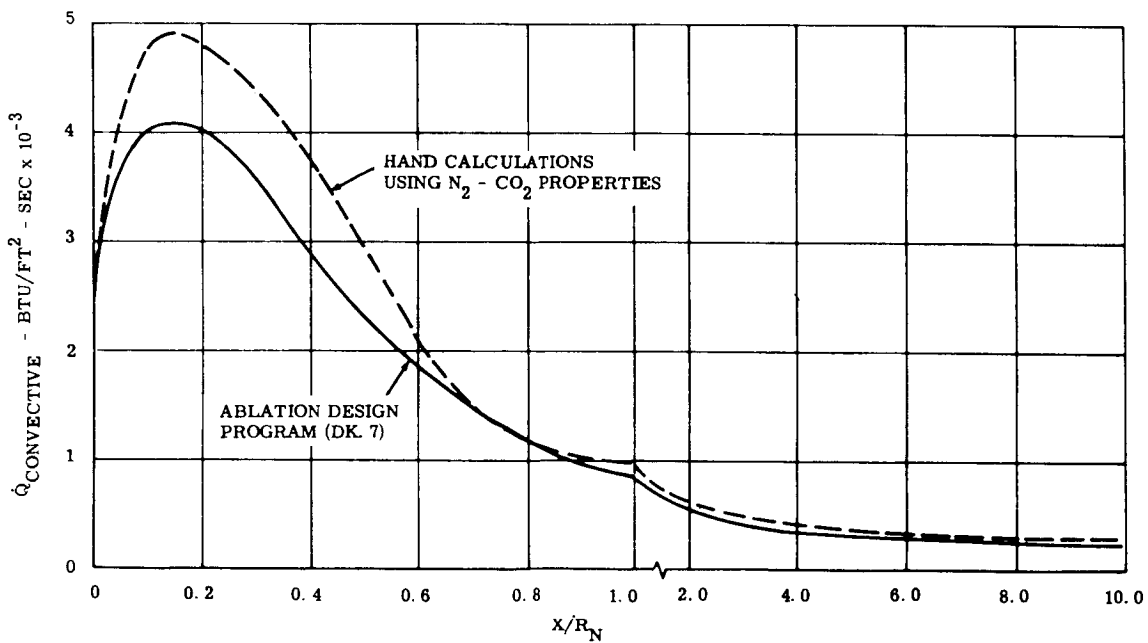


Figure 1.3.3-8. Comparative Heating Around Body (Air and N₂-CO₂)

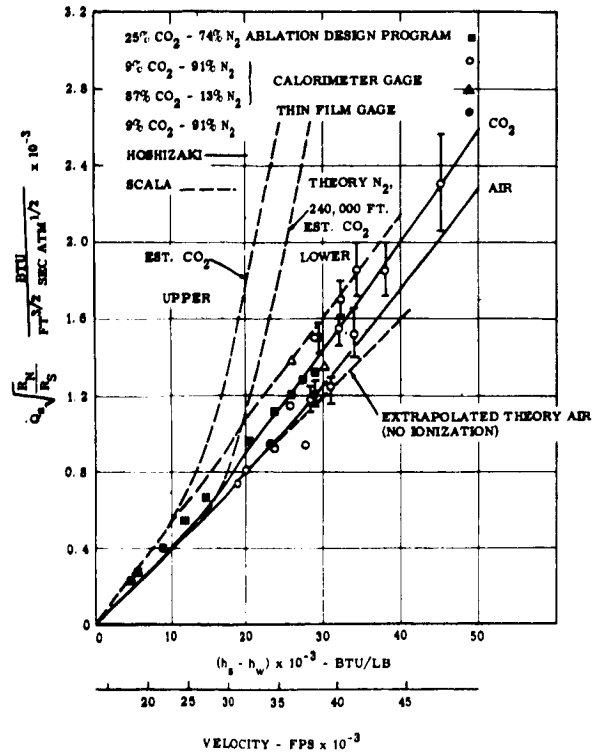


Figure 1.3.3-9. Hypervelocity Stagnation Point Heat Transfer in Simulated Planetary Atmospheres (Gruszczynski and Warren)

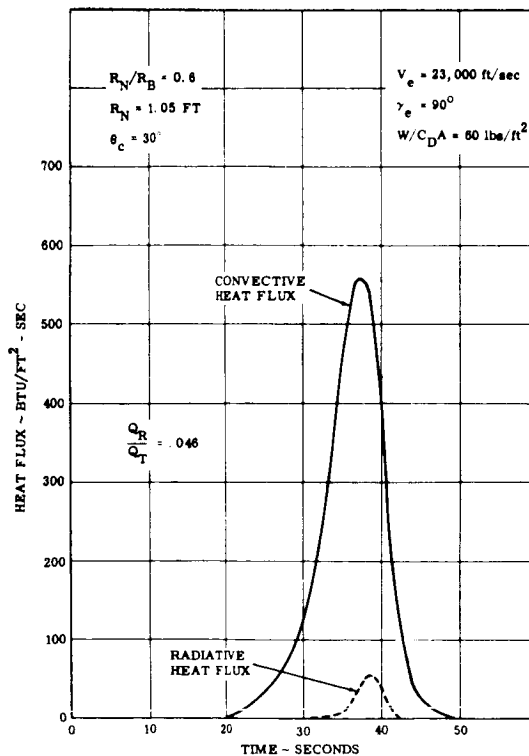


Figure 1.3.3-10. Comparative Radiative and Convective Heating, Mars Mean Atmosphere

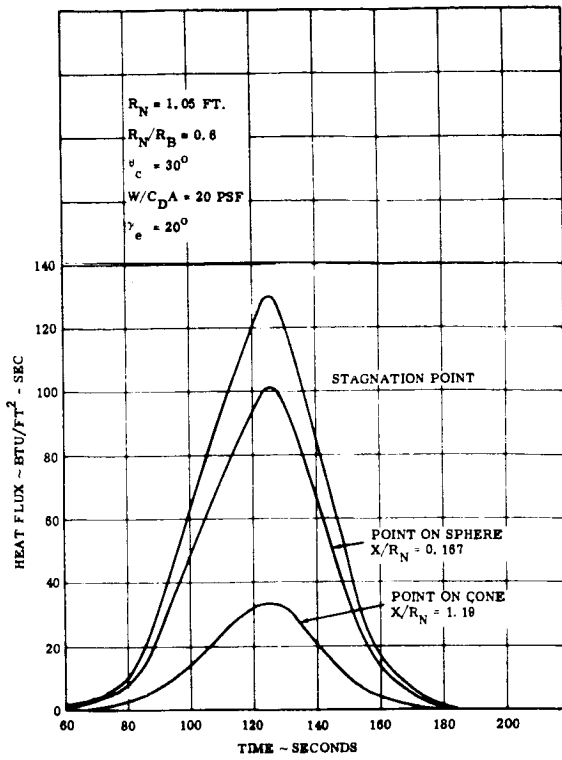


Figure 1.3.3-11. Instantaneous Heating, Mars Mean Density Atmosphere

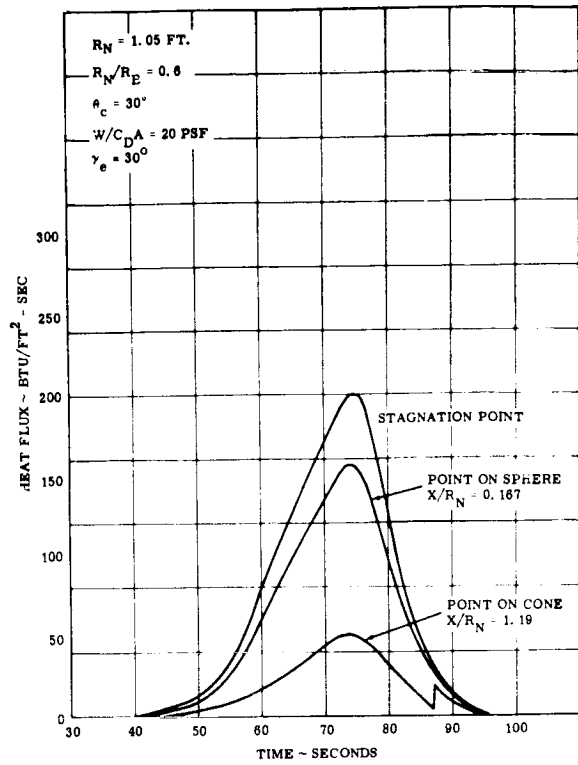


Figure 1.3.3-12. Instantaneous Heating, Mars Mean Density Atmosphere

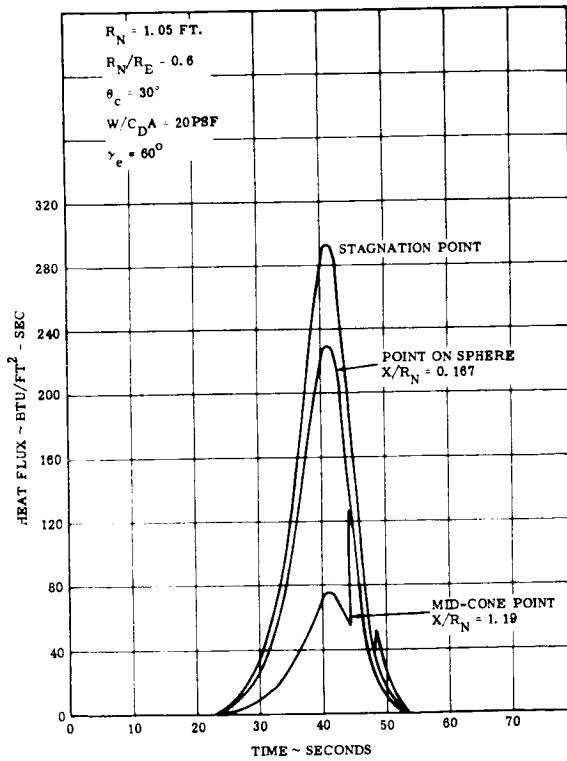


Figure 1.3.3-13. Instantaneous Heating, Mars Mean Density Atmosphere

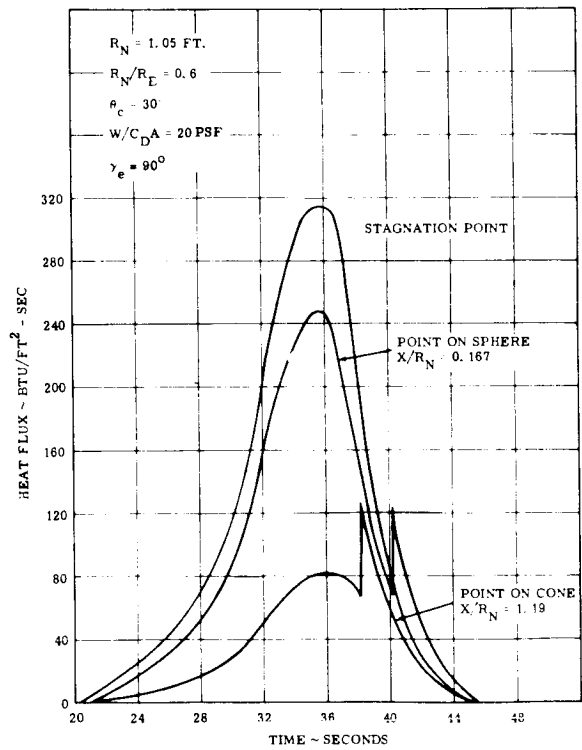


Figure 1.3.3-14. Instantaneous Heating, Mars Mean Density Atmosphere

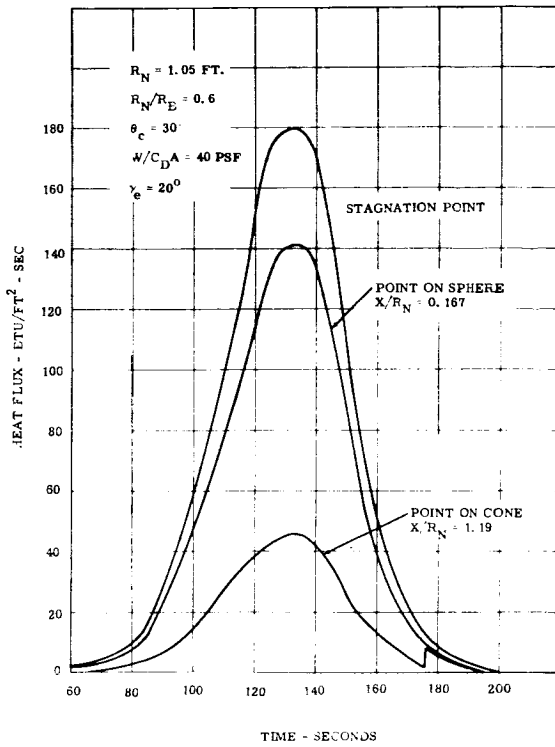


Figure 1.3.3-15. Instantaneous Heating, Mars Mean Density Atmosphere

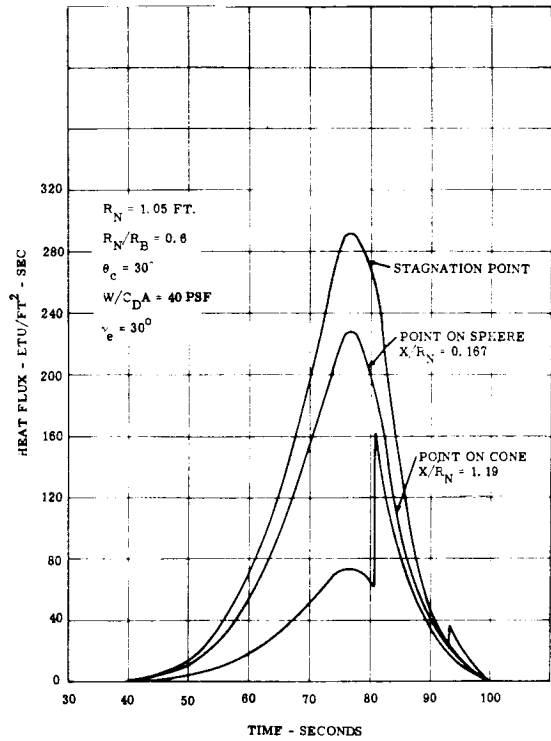


Figure 1.3.3-16. Instantaneous Heating, Mars Mean Density Atmosphere

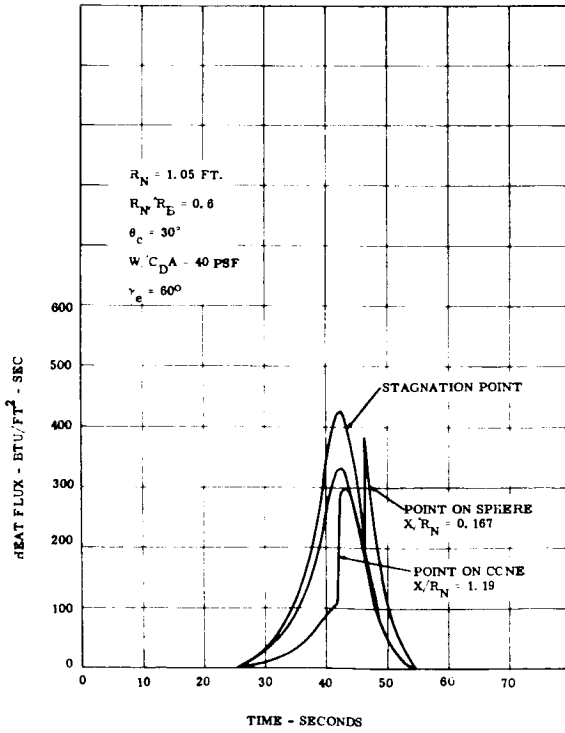


Figure 1.3.3-17. Instantaneous Heating, Mars Mean Density Atmosphere

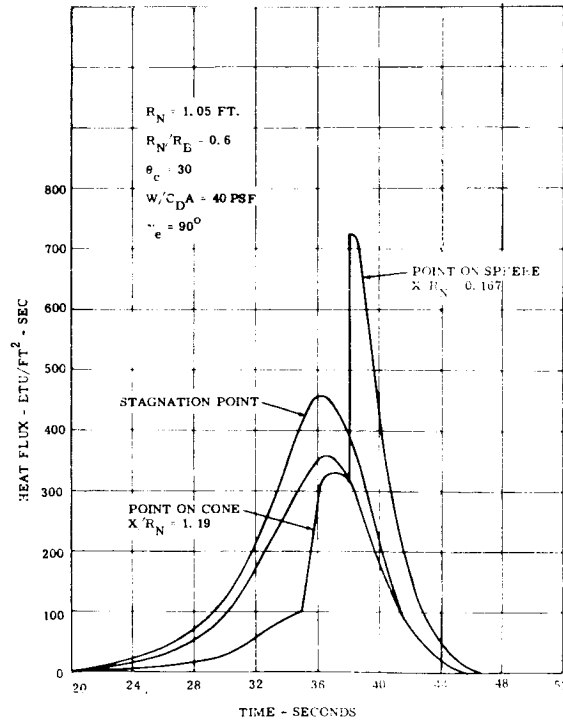


Figure 1.3.3-18. Instantaneous Heating, Mars Mean Density Atmosphere

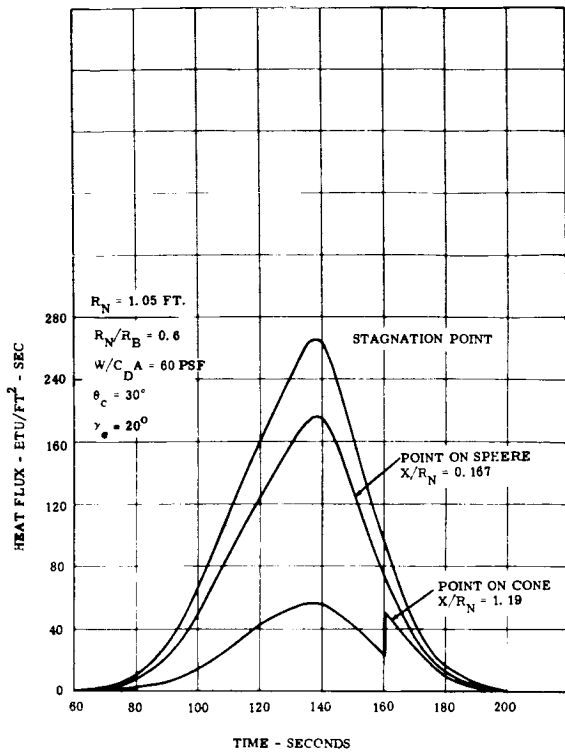


Figure 1.3.3-19. Instantaneous Heating, Mars Mean Density Atmosphere

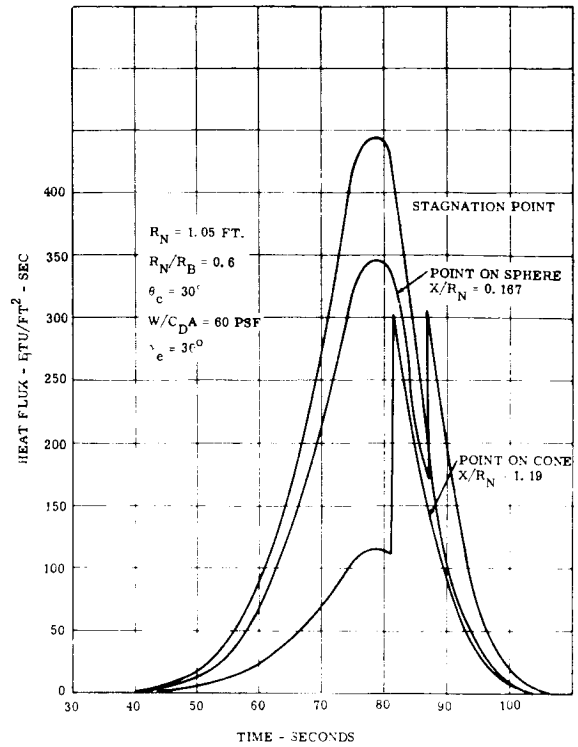


Figure 1.3.3-20. Instantaneous Heating, Mars Mean Density Atmosphere

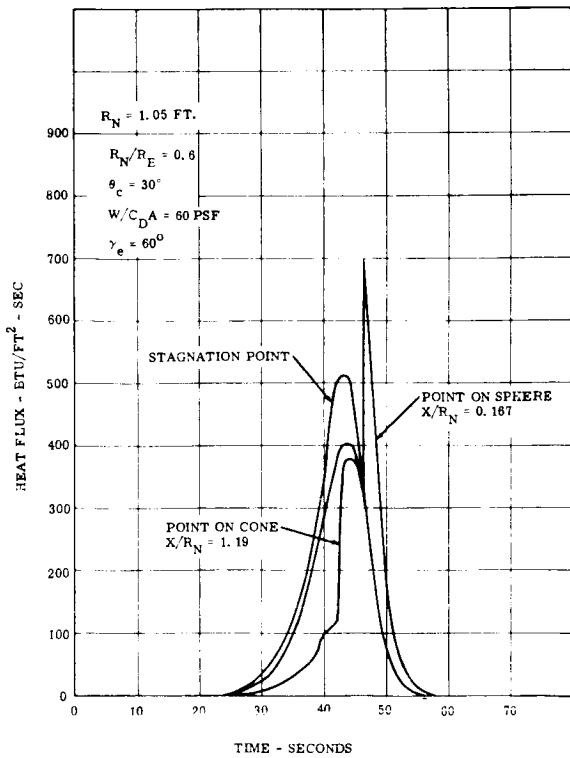


Figure 1.3.3-21. Instantaneous Heating, Mars Mean Density Atmosphere

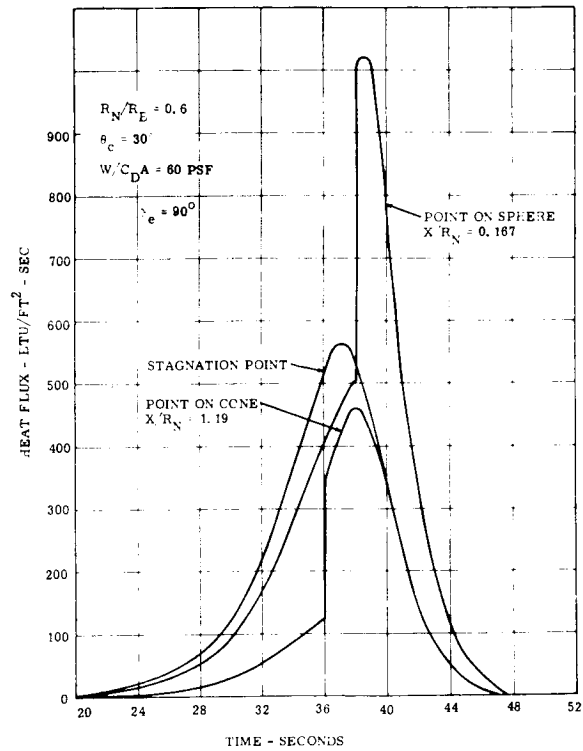


Figure 1.3.3-22. Instantaneous Heating, Mars Mean Density Atmosphere

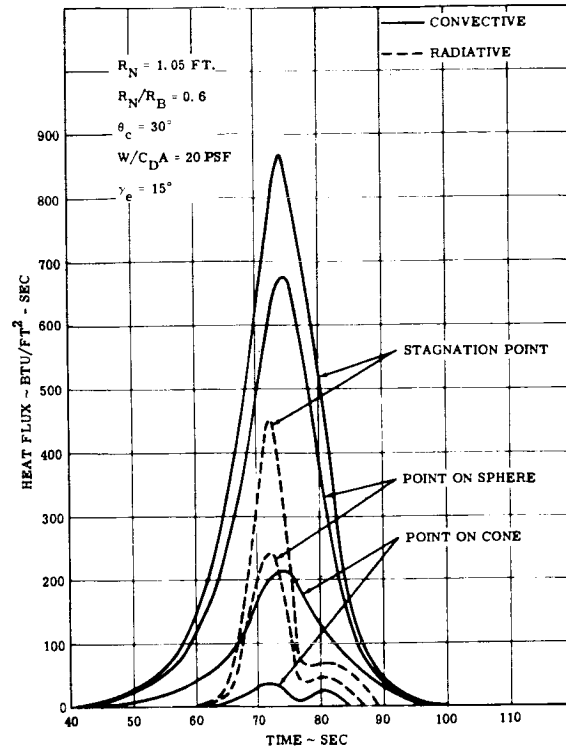


Figure 1.3.3-23. Instantaneous Heating, Venus Standard Atmosphere (25% CO₂)

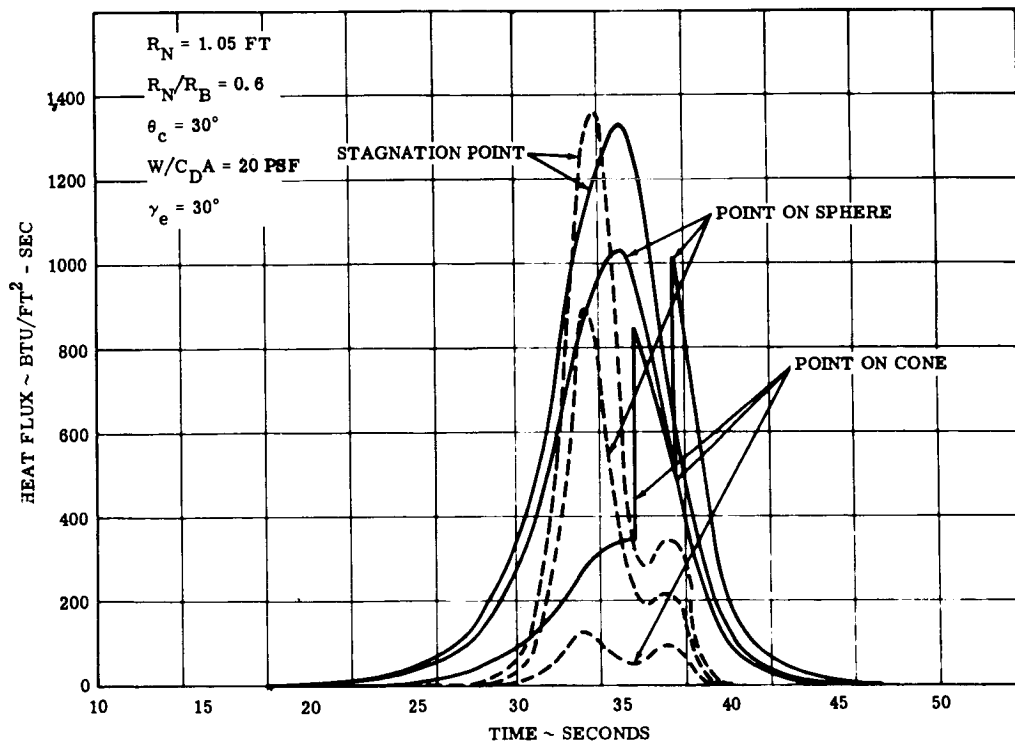


Figure 1.3.3-24. Instantaneous Heating, Venus Standard Atmosphere (25% CO₂)

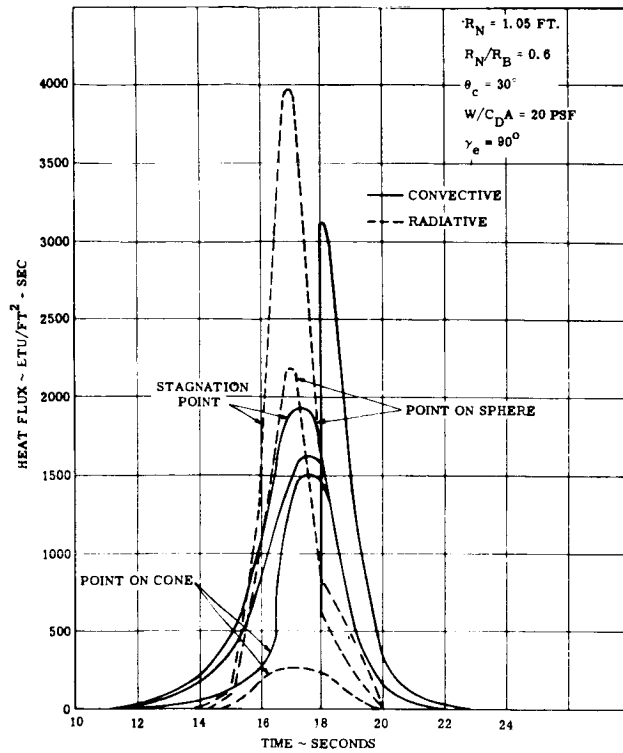


Figure 1.3.3-25. Instantaneous Heating
 Venus Standard Atmosphere
 (25% CO₂)

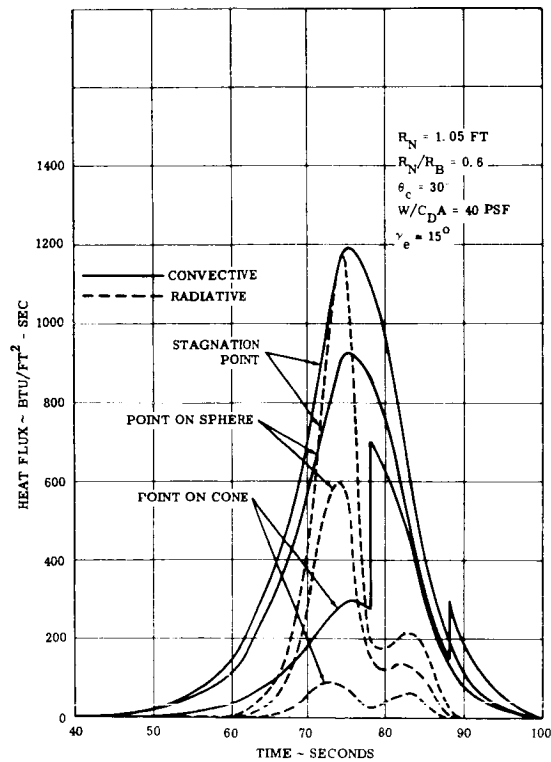


Figure 1.3.3-26. Instantaneous Heating,
 Venus Standard Atmosphere (25% CO₂)

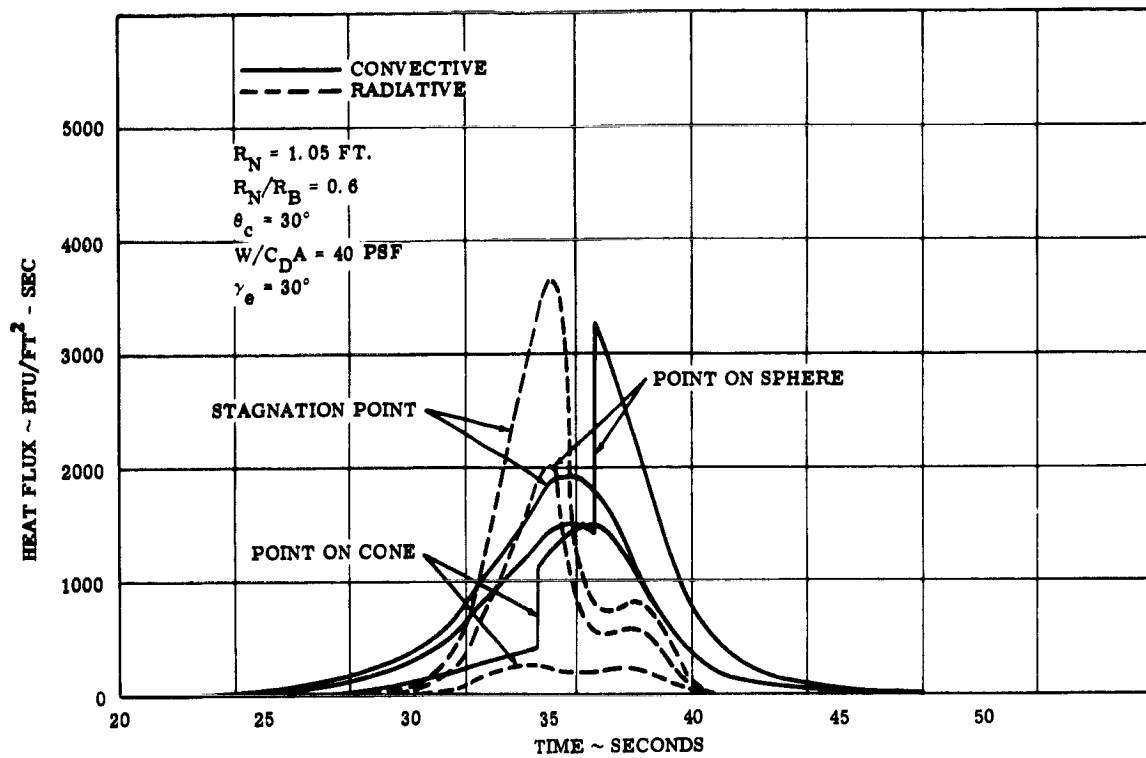


Figure 1.3.3-27. Instantaneous Heating, Venus Standard Atmosphere (25% CO₂)

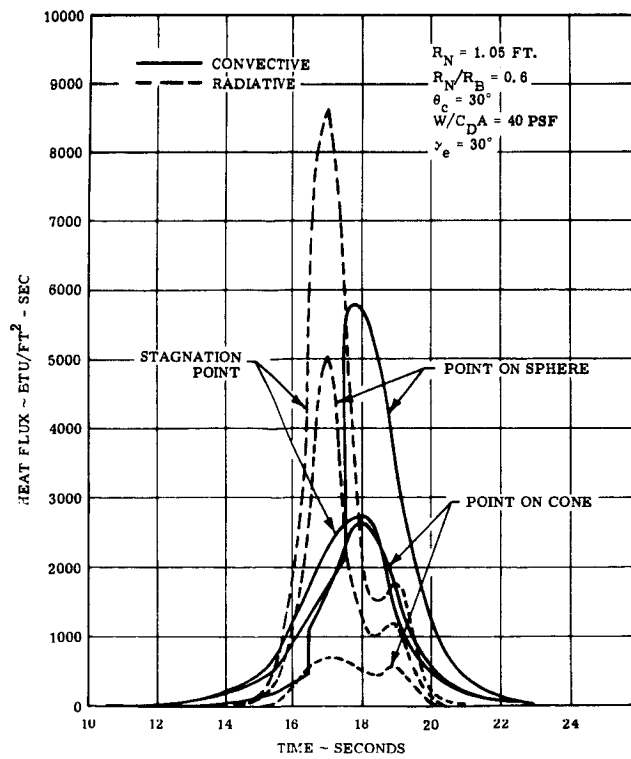


Figure 1.3.3-28. Instantaneous Heating, Venus Standard Atmosphere (25% CO₂)

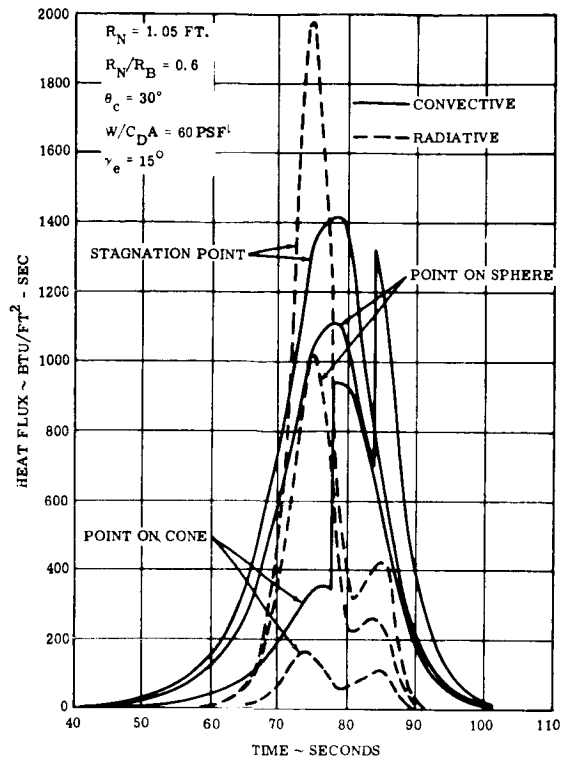


Figure 1.3.3-29. Instantaneous Heating, Venus Standard Atmosphere (25% CO₂)

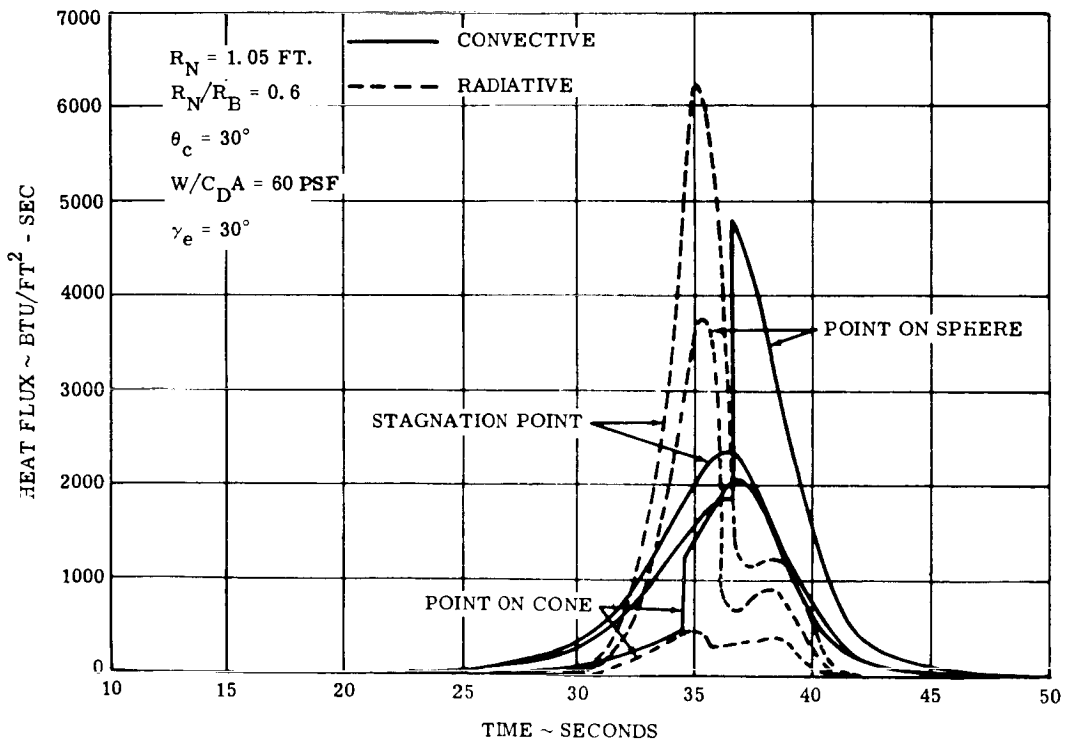


Figure 1.3.3-30. Instantaneous Heating, Venus Standard Atmosphere (25% CO₂)

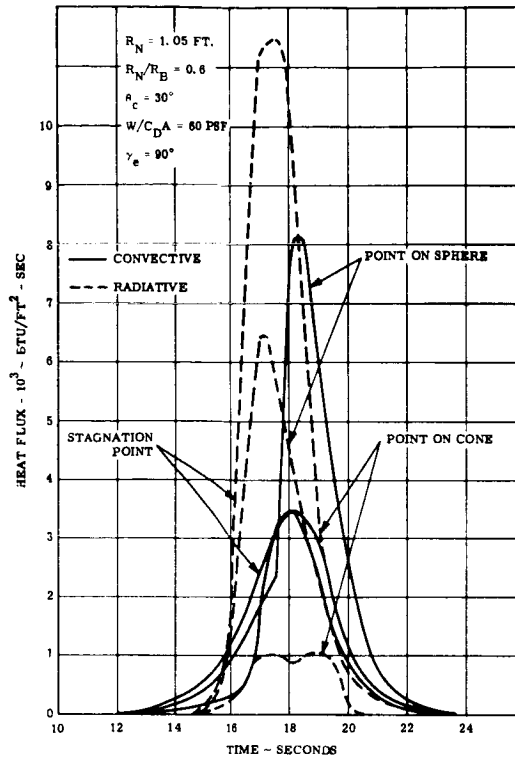


Figure 1.3.3-31. Instantaneous Heating, Venus Standard Atmosphere (25% CO₂)

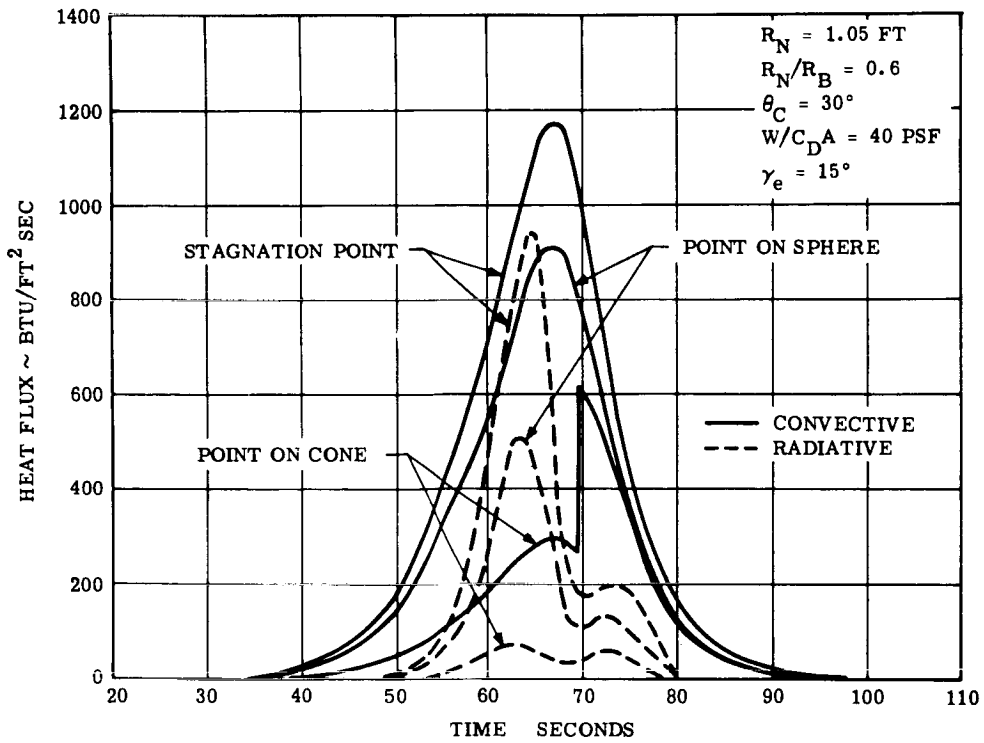


Figure 1.3.3-32. Instantaneous Heating, Venus Standard Atmosphere (25% CO₂)

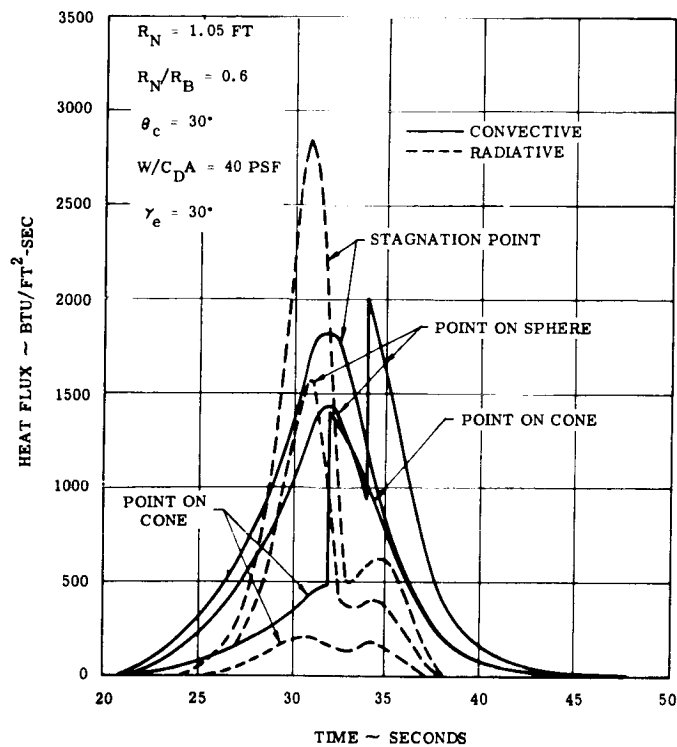


Figure 1.3.3-33. Instantaneous Heating, Venus Extreme Atmosphere (25% CO₂)

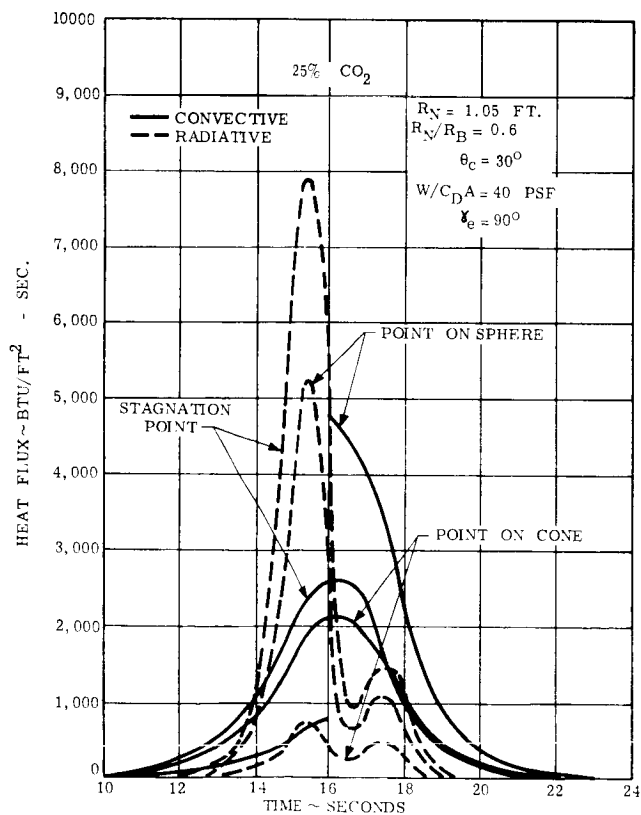


Figure 1.3.3-34. Static Pressure Behind Normal Shock Wave (25% CO₂)

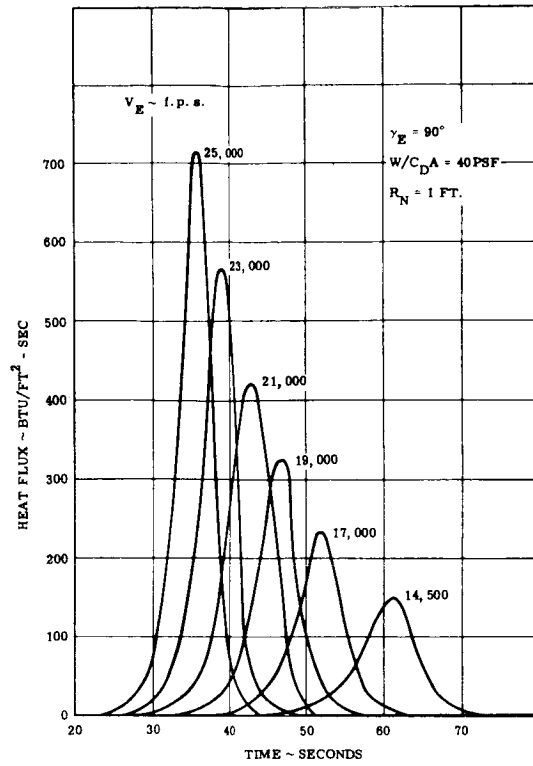


Figure 1.3.3-35. Stagnation Heat Pulses, Mars Lower Atmosphere

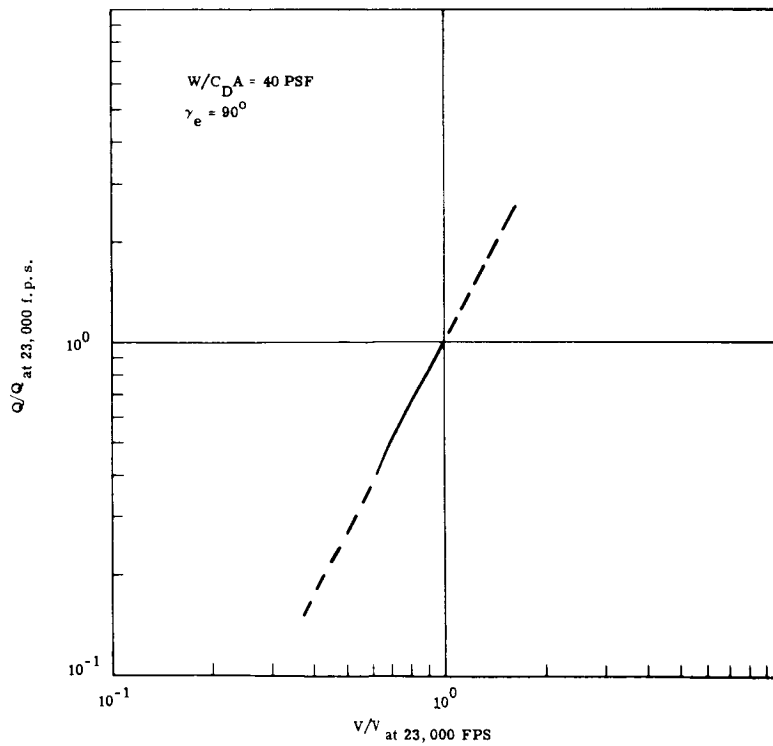


Figure 1.3.3-36. Velocity Normalized Heating, Mars Lower Atmosphere

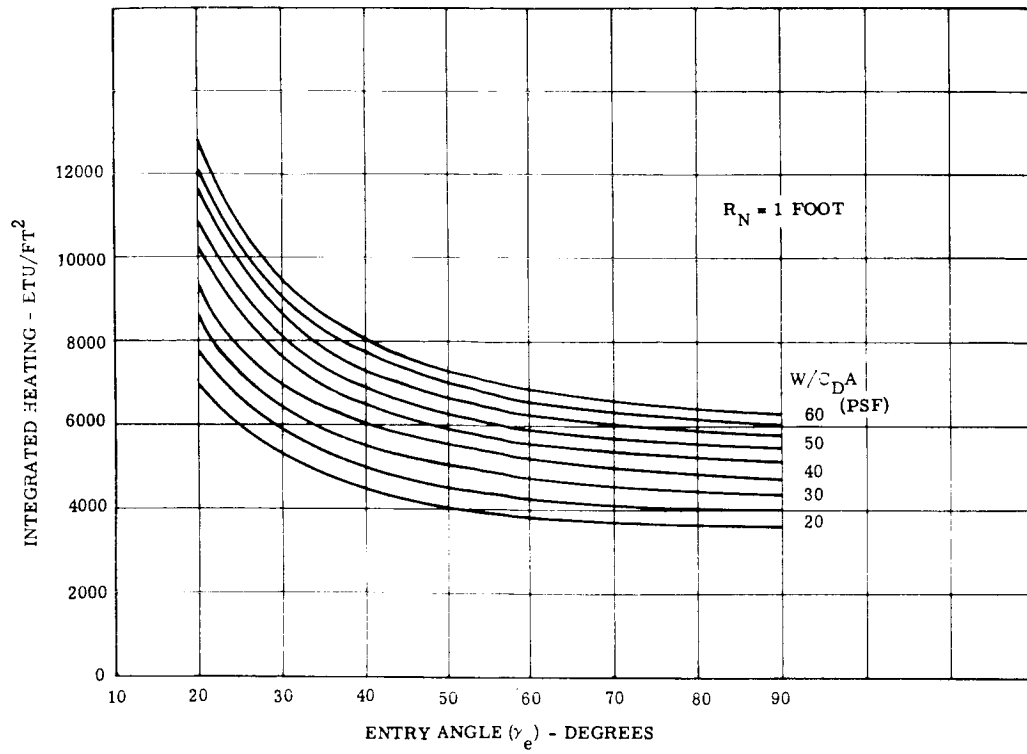


Figure 1.3.3-37. Stagnation Integrated Heating, Mars Upper Density Atmosphere

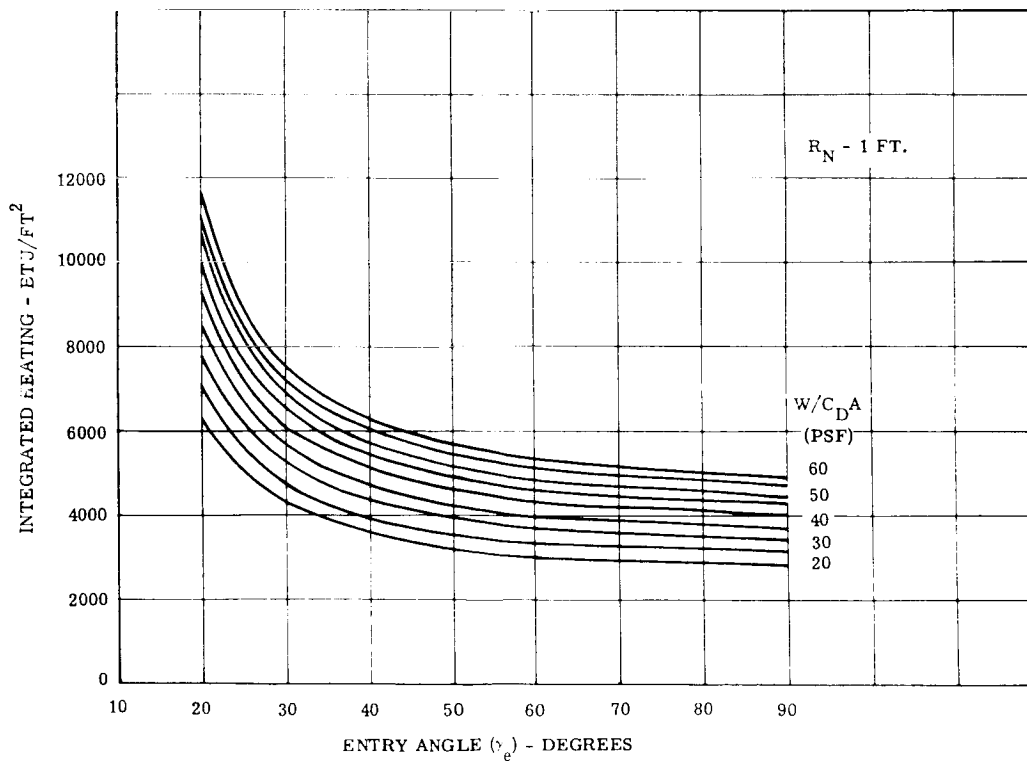


Figure 1.3.3-38. Stagnation Integrated Heating, Mars Mean Density Atmosphere

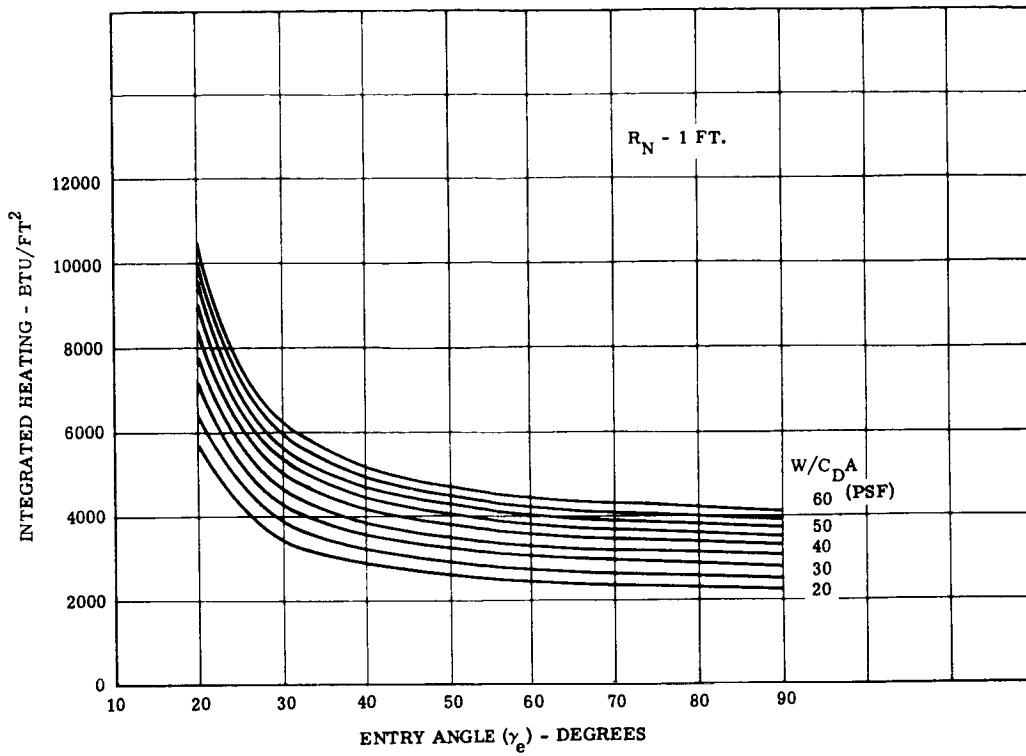


Figure 1.3.3-39. Stagnation Integrated Heating, Mars Lower Density Atmosphere

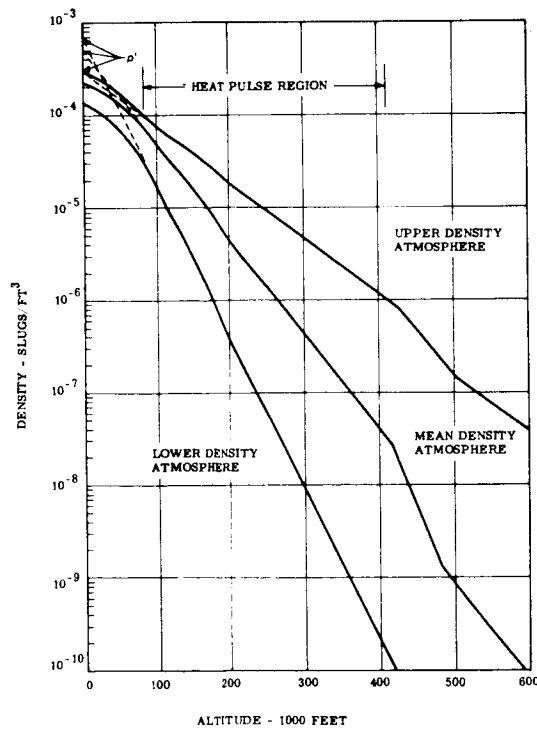


Figure 1.3.3-40. Martian Atmospheric Models

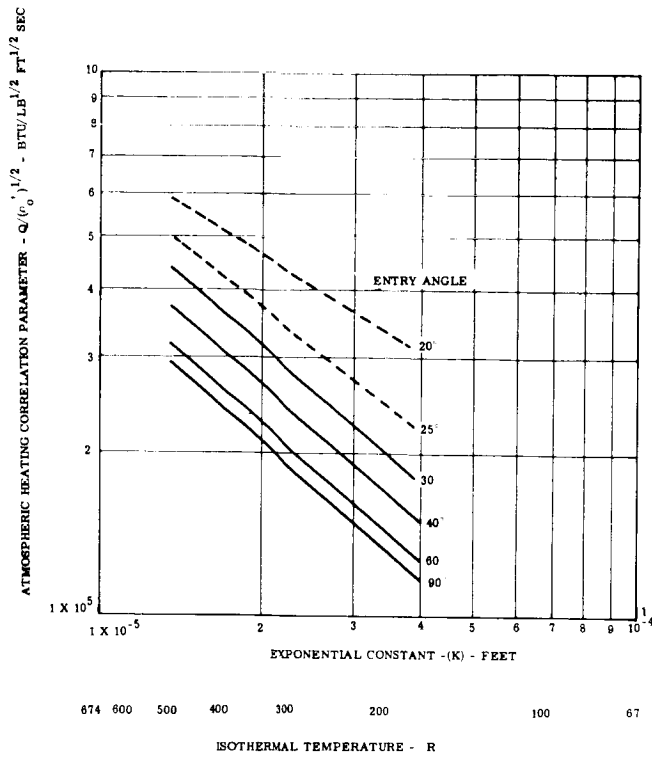


Figure 1.3.3-41. Atmospheric Density Effect on Total Heating, Mars Stagnation Point

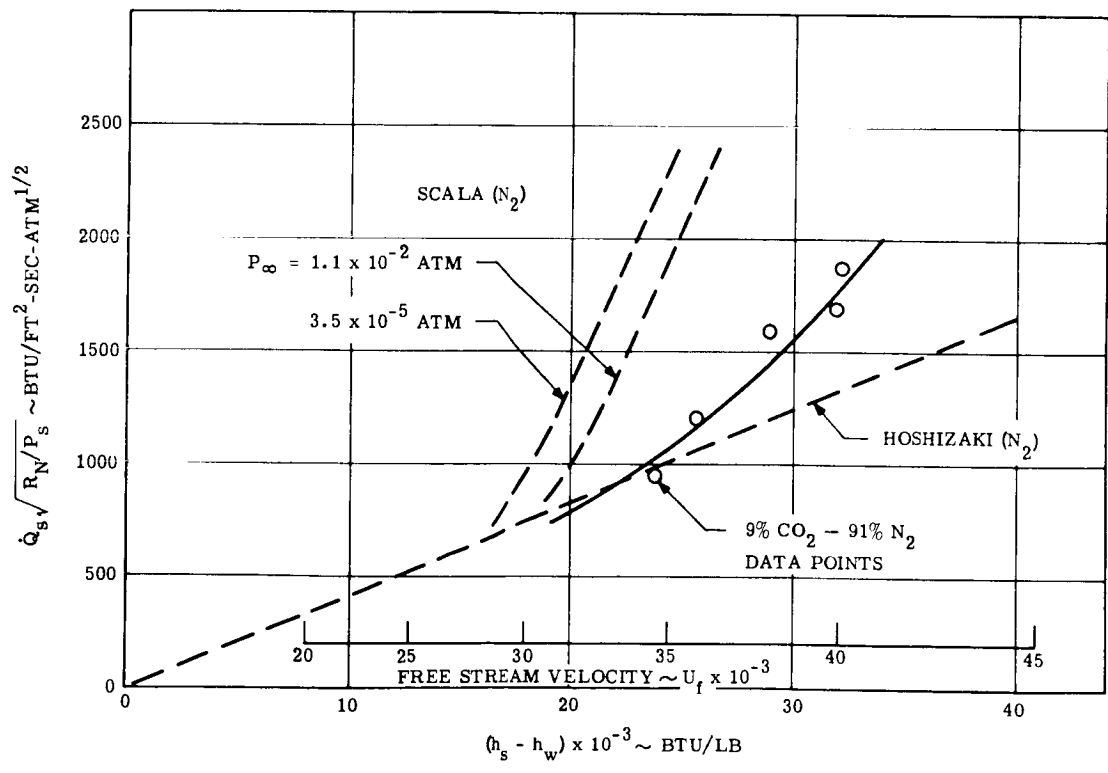


Figure 1.3.3-42. Hypervelocity Stagnation Point Heat Transfer in 9% CO₂ - 91% N₂

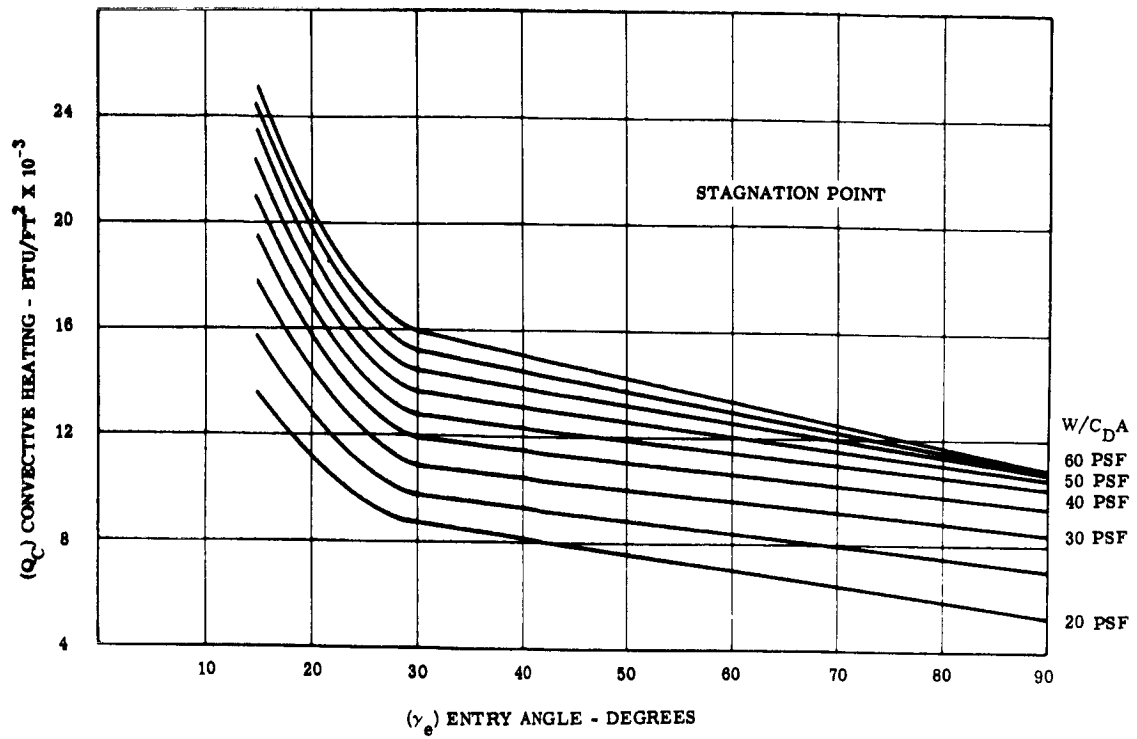


Figure 1.3.3-43. Integrated Convective Heating, Venus Standard Atmosphere

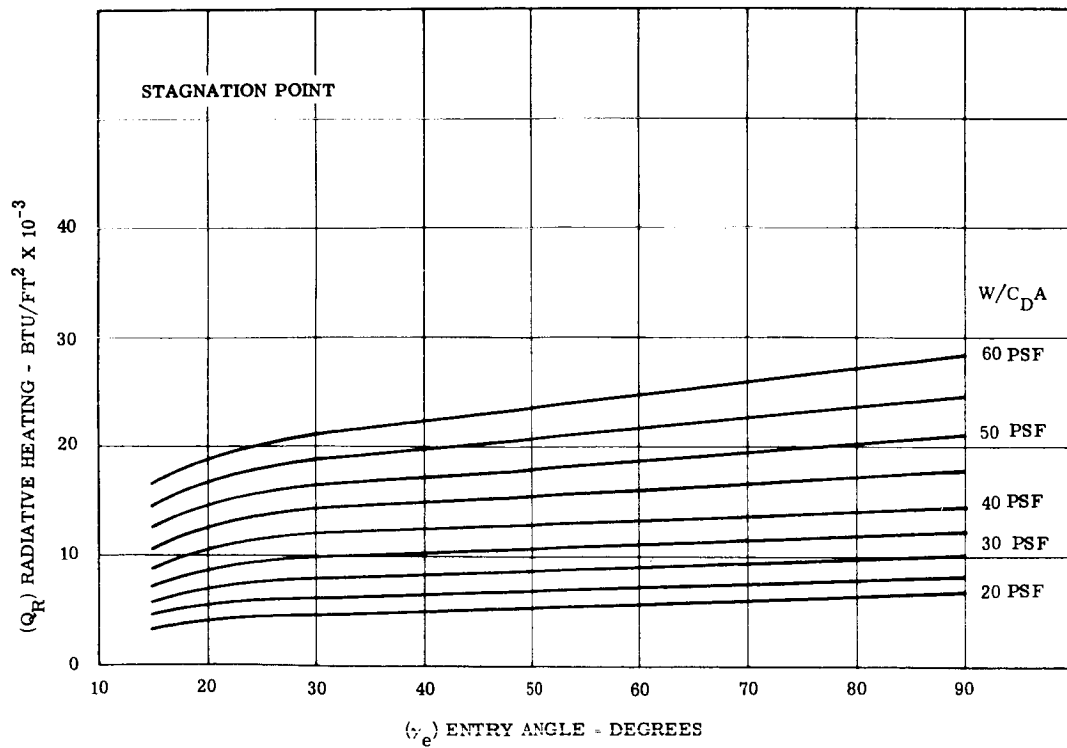


Figure 1.3.3-44. Integrated Radiative Heating, Venus Standard Atmosphere

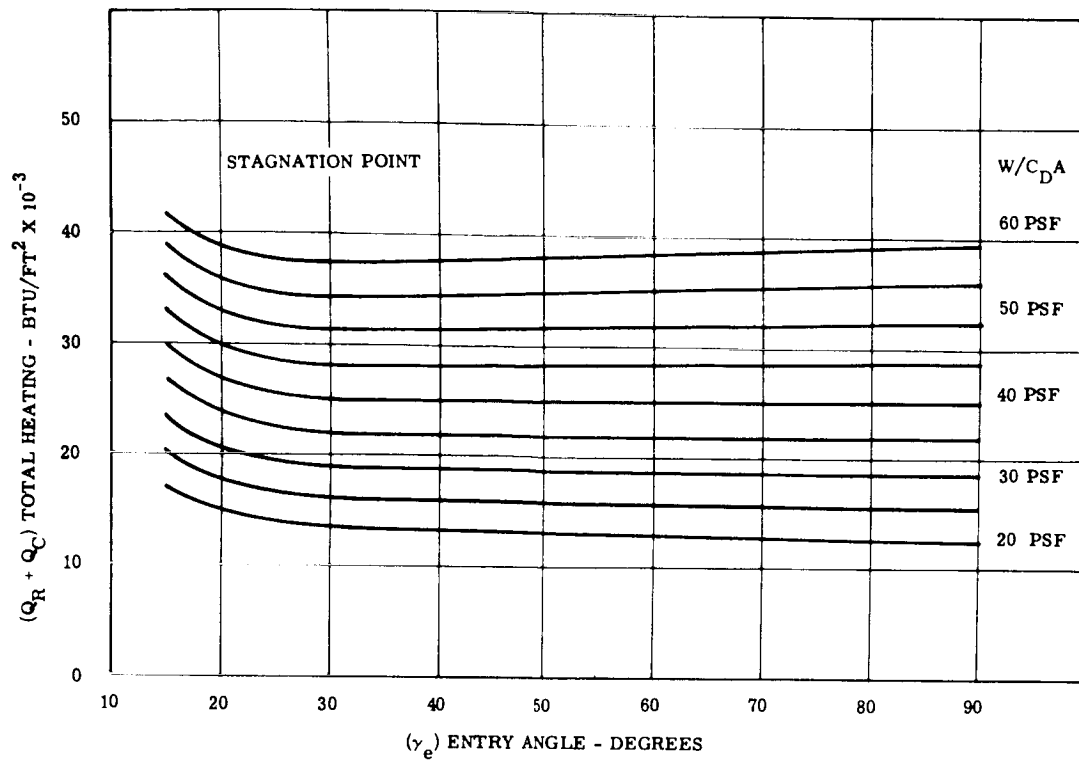


Figure 1. 3. 3-45. Total Integrated Heating, Venus Standard Atmosphere

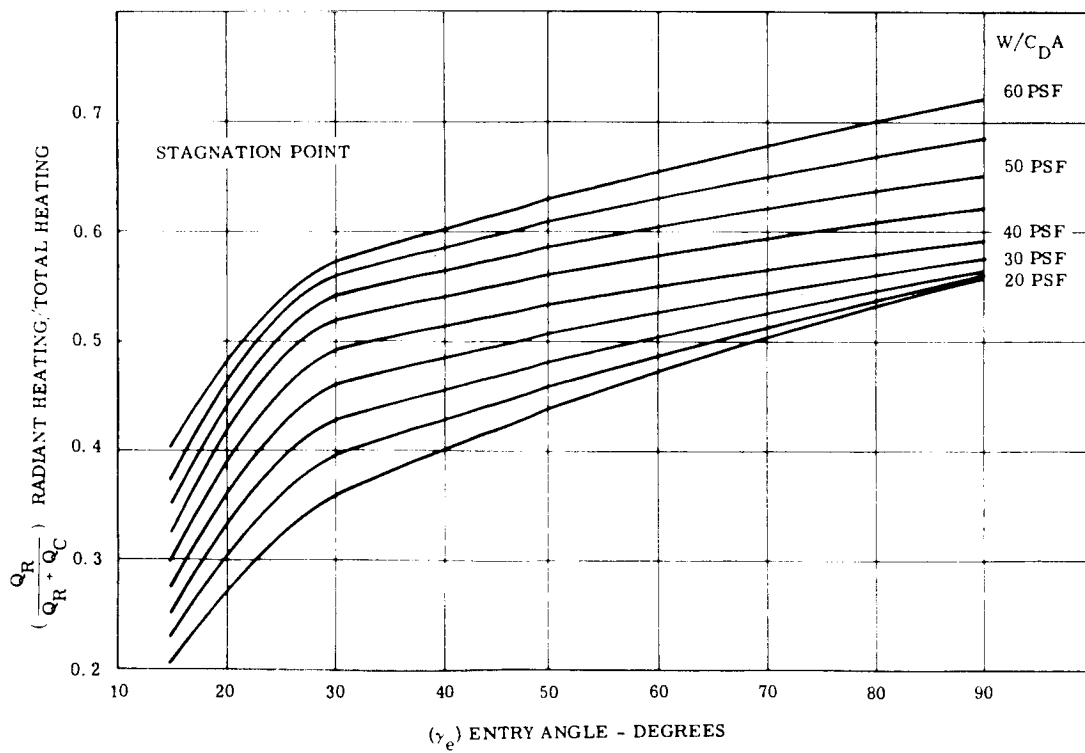


Figure 1. 3. 3-46. Radiant Heating Contribution, Venus Standard Atmosphere

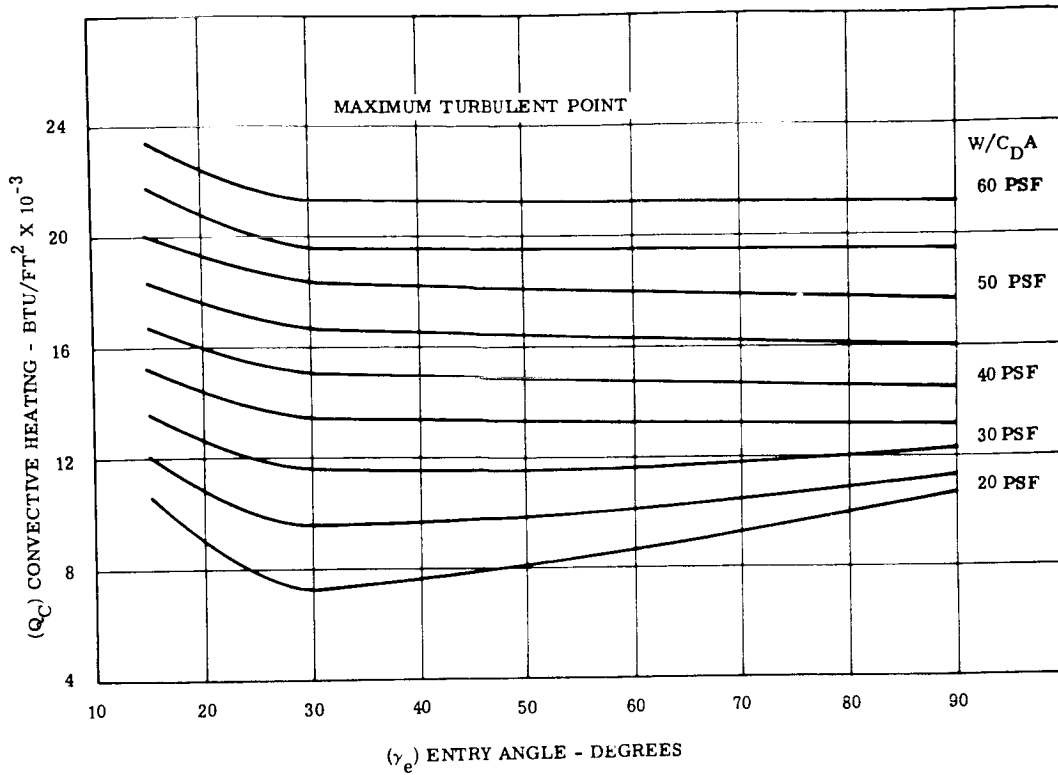


Figure 1.3.3-47. Integrated Convective Heating, Venus Standard Atmosphere

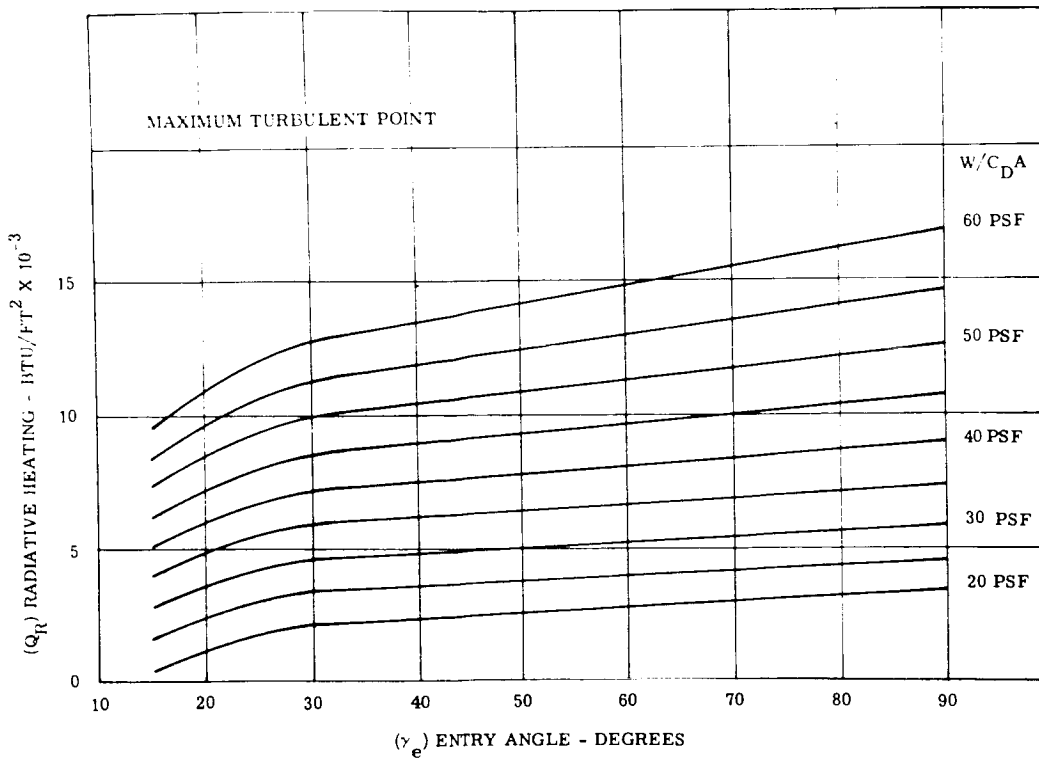


Figure 1.3.3-48. Integrated Radiative Heating, Venus Standard Atmosphere

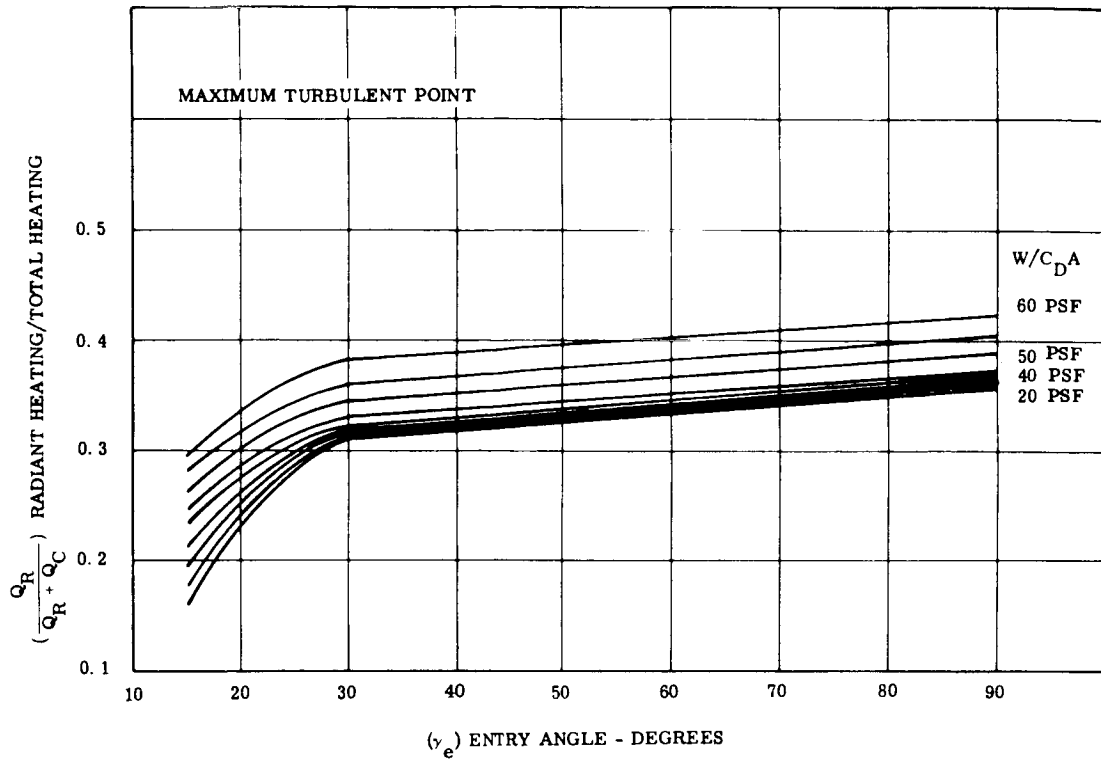


Figure 1.3.3-49. Radiant Heating Contribution, Venus Standard Atmosphere

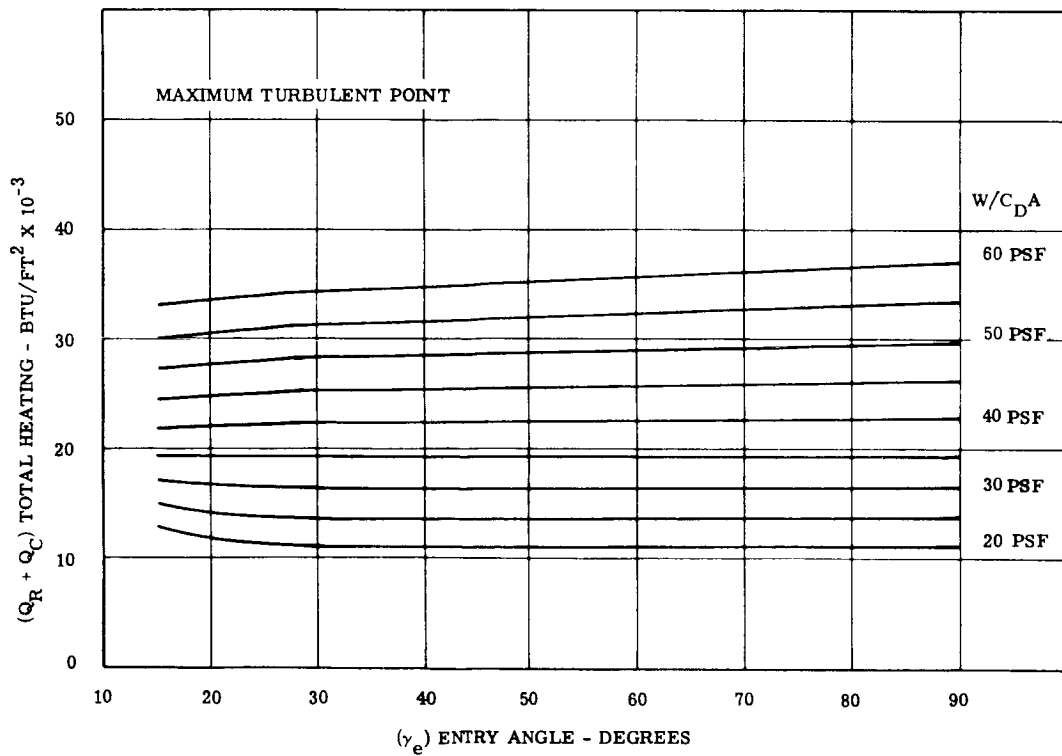


Figure 1.3.3-50. Total Integrated Heating, Venus Standard Atmosphere

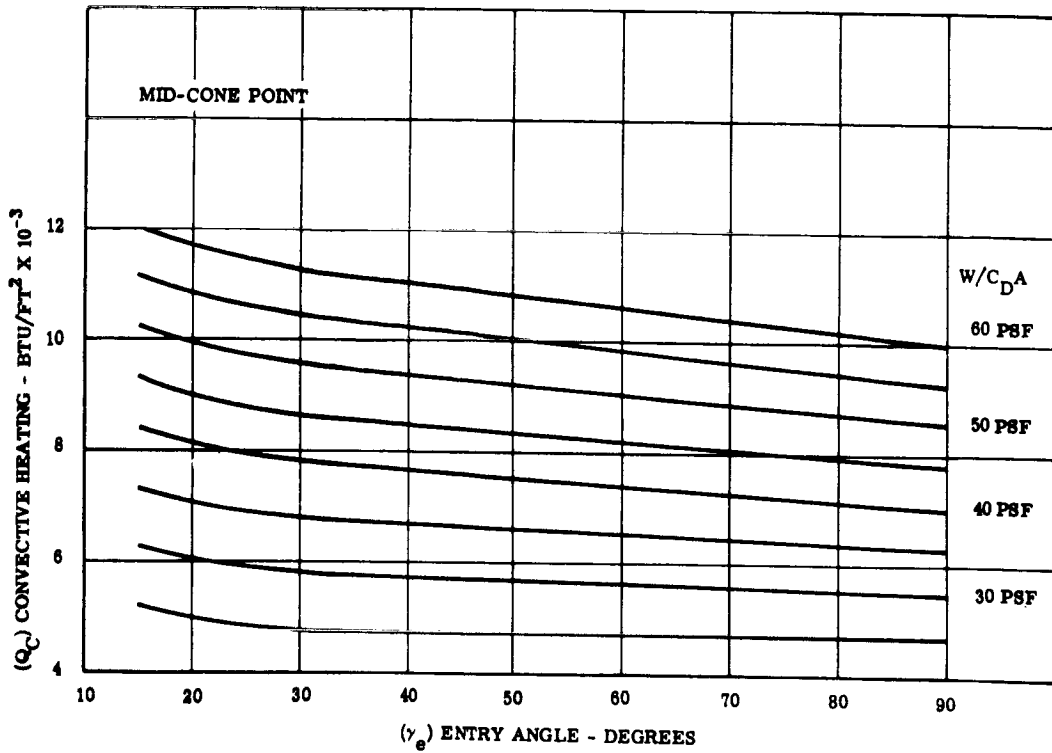


Figure 1. 3. 3-51. Integrated Convective Heating, Venus Standard Atmosphere

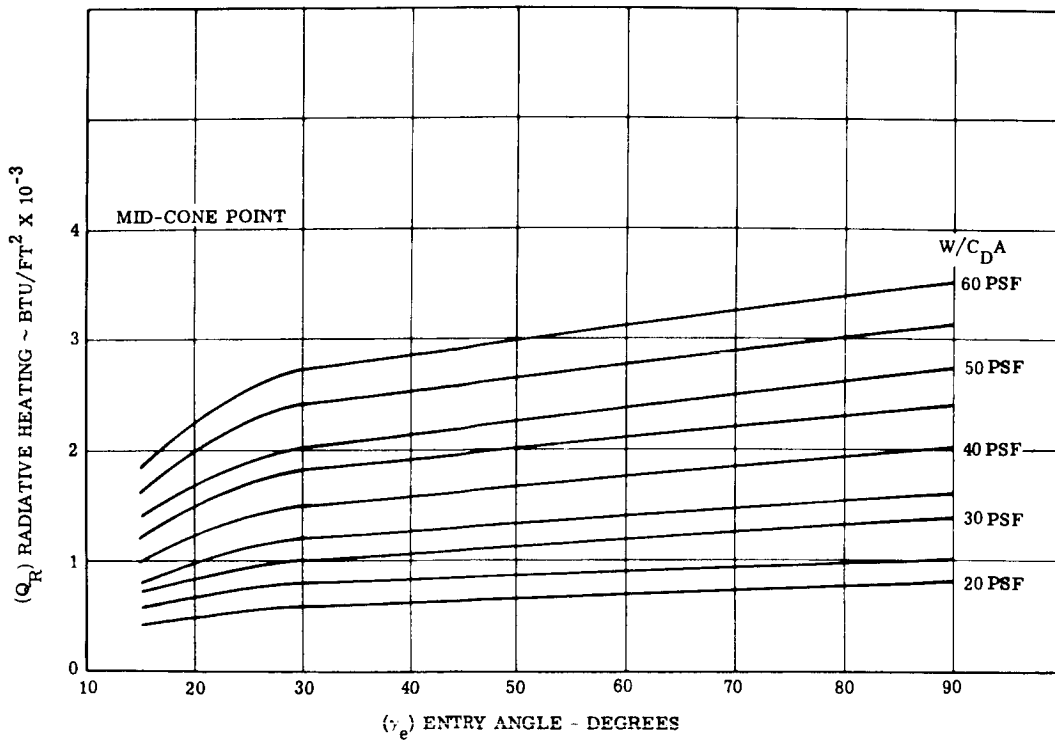


Figure 1. 3. 3-52. Integrated Radiative Heating, Venus Standard Atmosphere

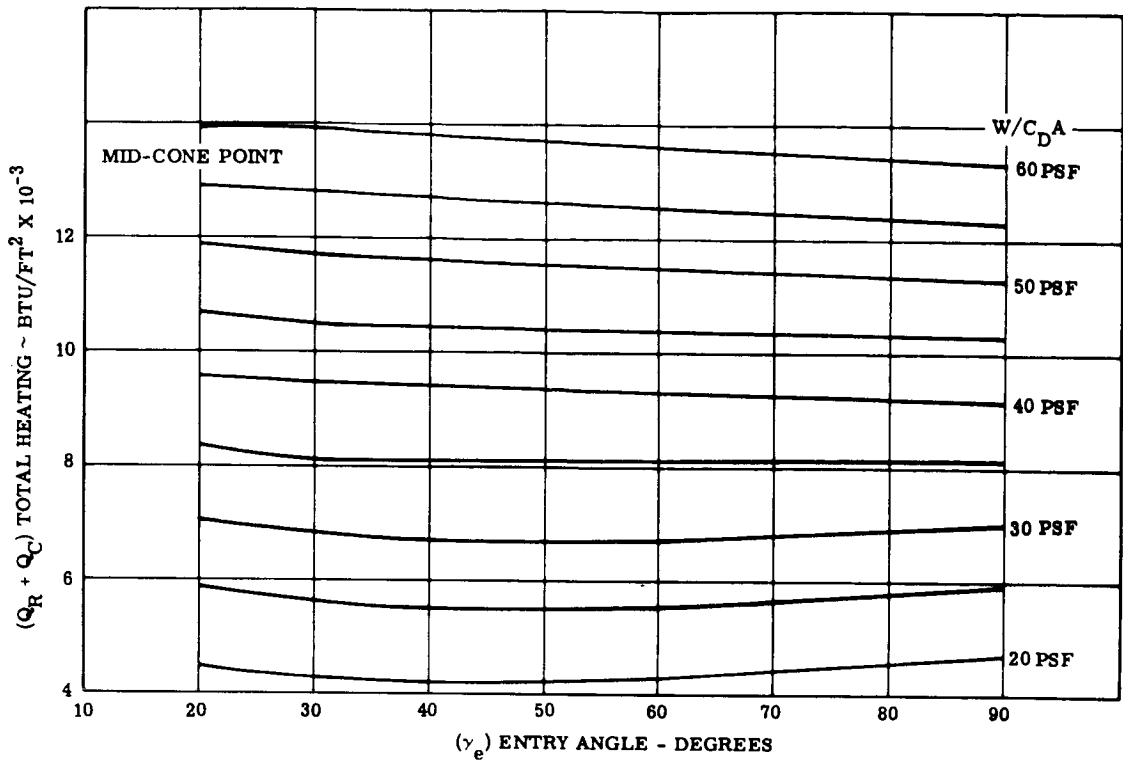


Figure 1.3.3-53. Total Integrated Heating, Venus Standard Atmosphere

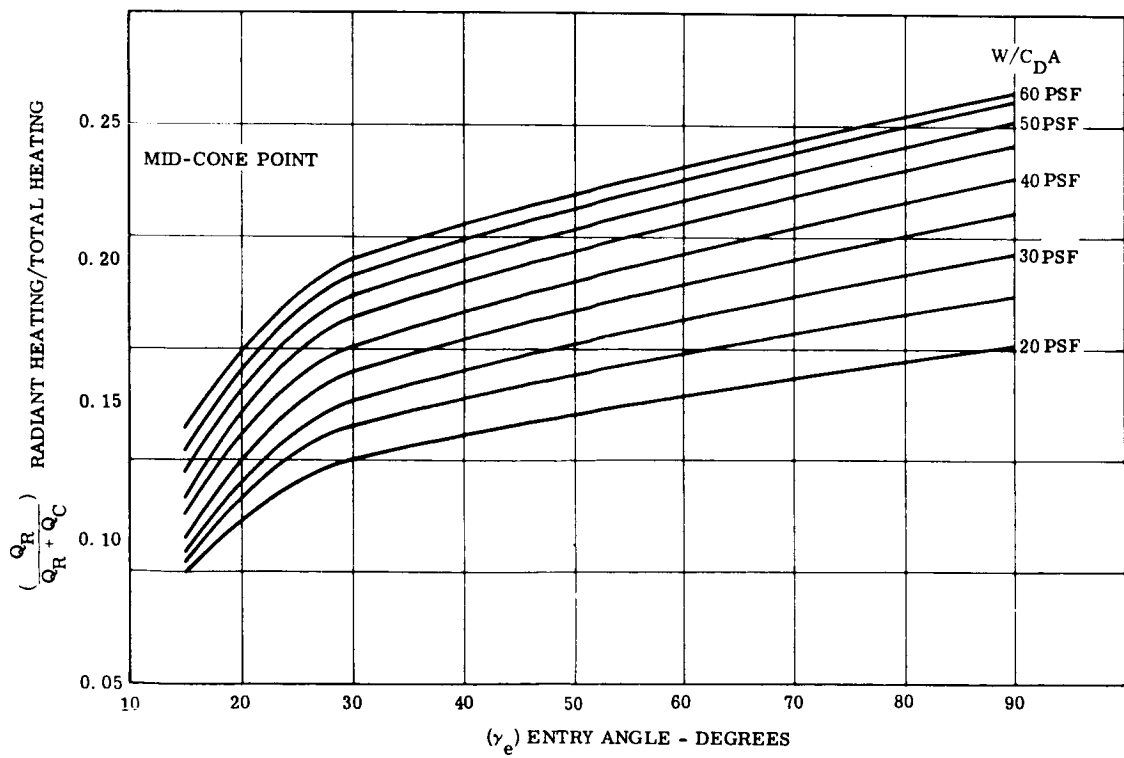


Figure 1.3.3-54. Radiant Heating Contribution, Venus Standard Atmosphere

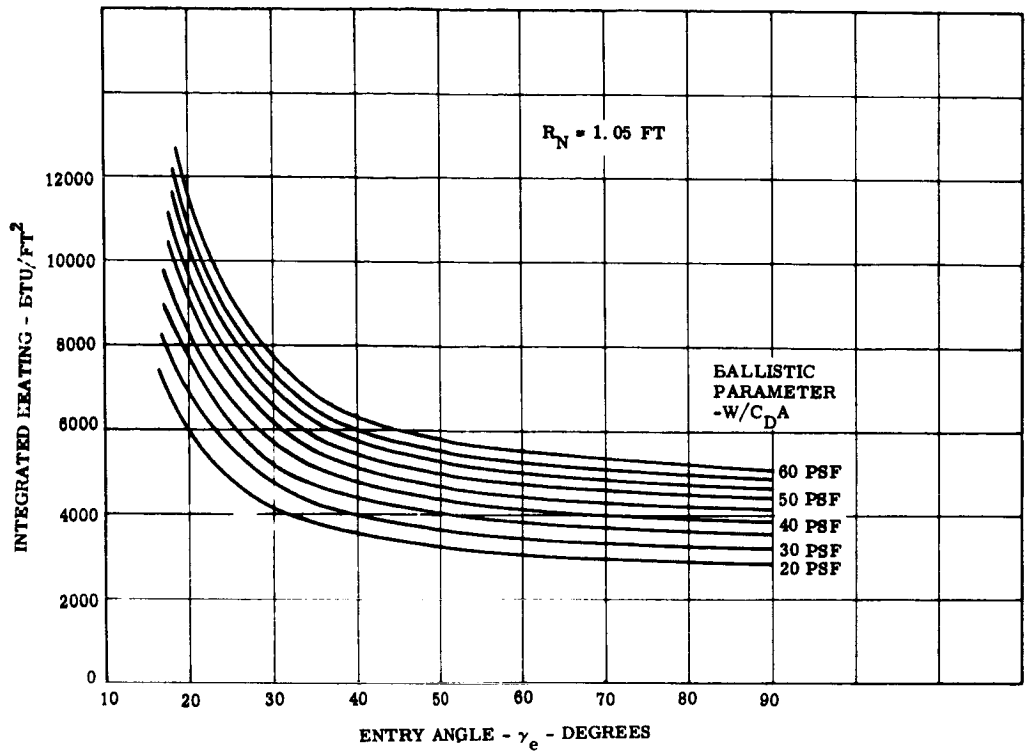


Figure 1.3.3-55. Integrated Total Heating, Mars Mean Atmosphere, Stagnation Point

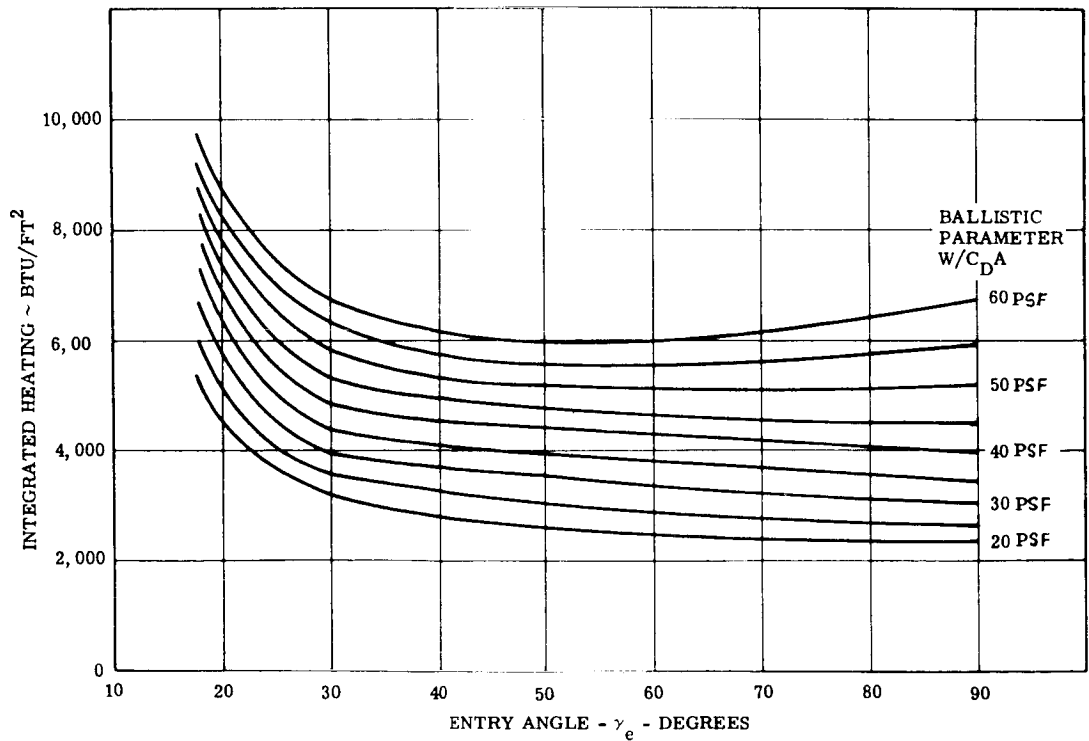


Figure 1.3.3-56. Integrated Total Heating, Mars Mean Atmosphere, Maximum Turbulent Heating Point

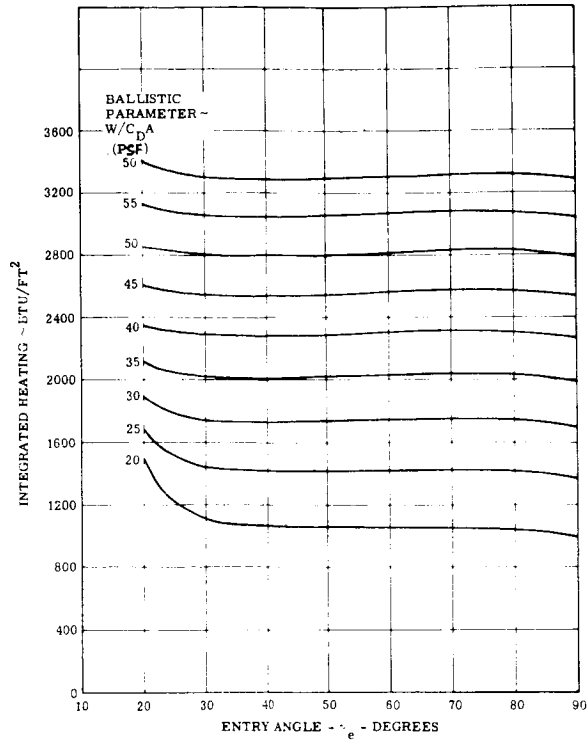


Figure 1.3.3-57. Integrated Total Heating, Mars Mean Atmosphere, Mid Cone Point

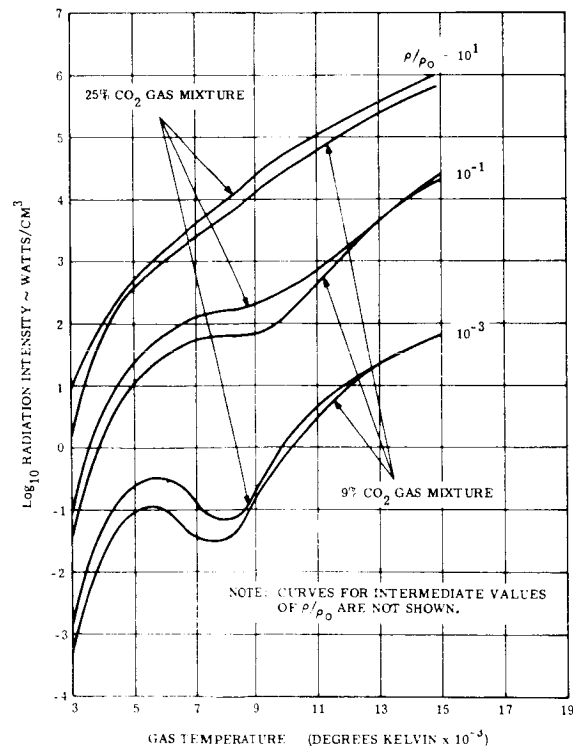


Figure 1.3.3-58. Initial Venusian Radiation Data (Breene and Nardone)

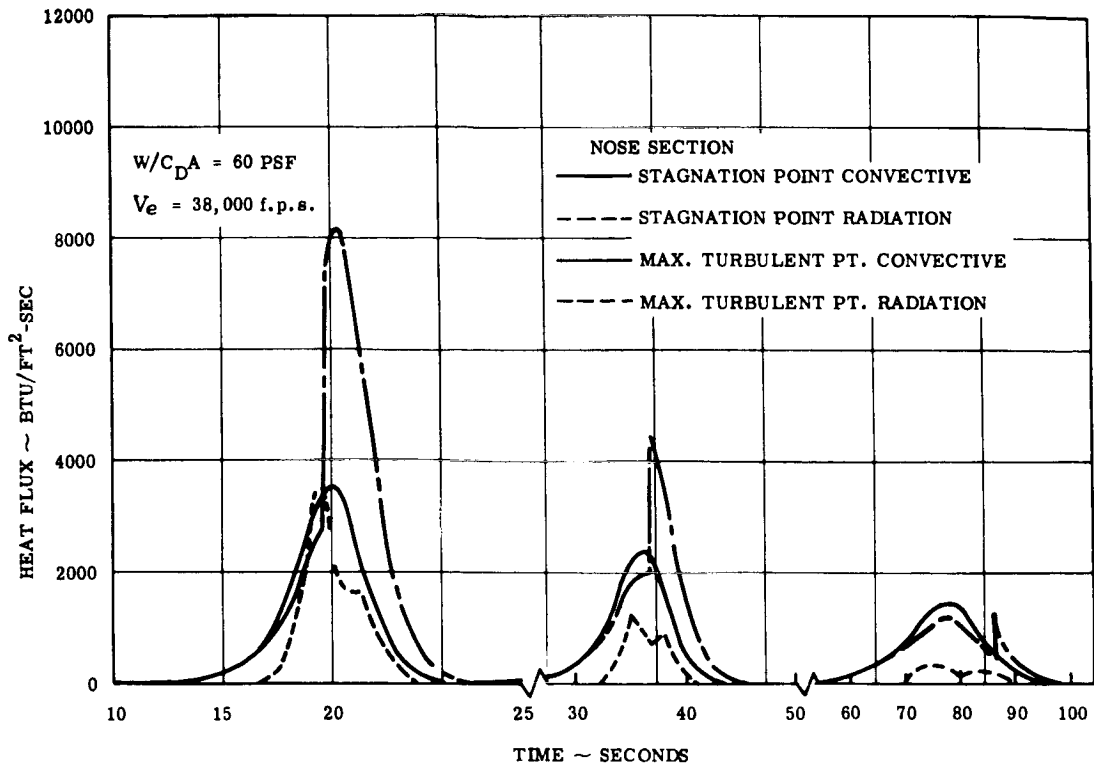


Figure 1.3.3-59. Venus Heat Fluxes Used in REKAP Ablation Study, Standard Atmosphere

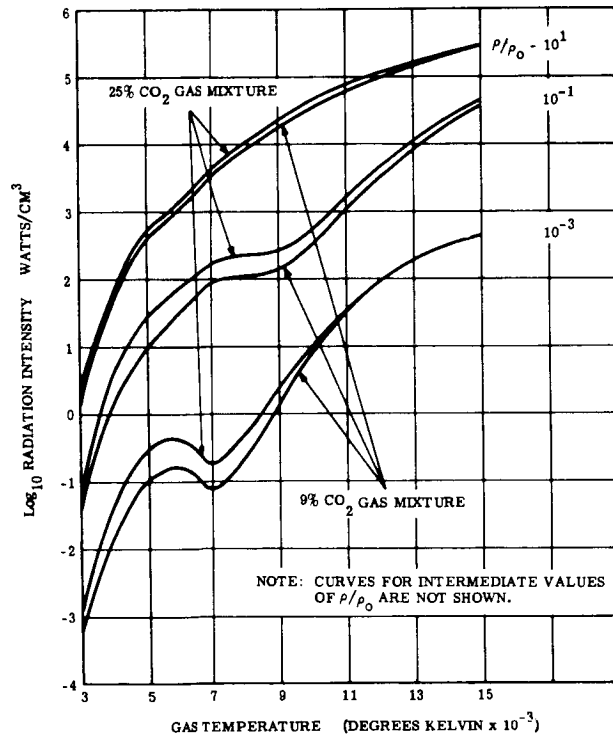


Figure 1.3.3-60. Latest Venusian Radiation Data (Breene and Nardone)

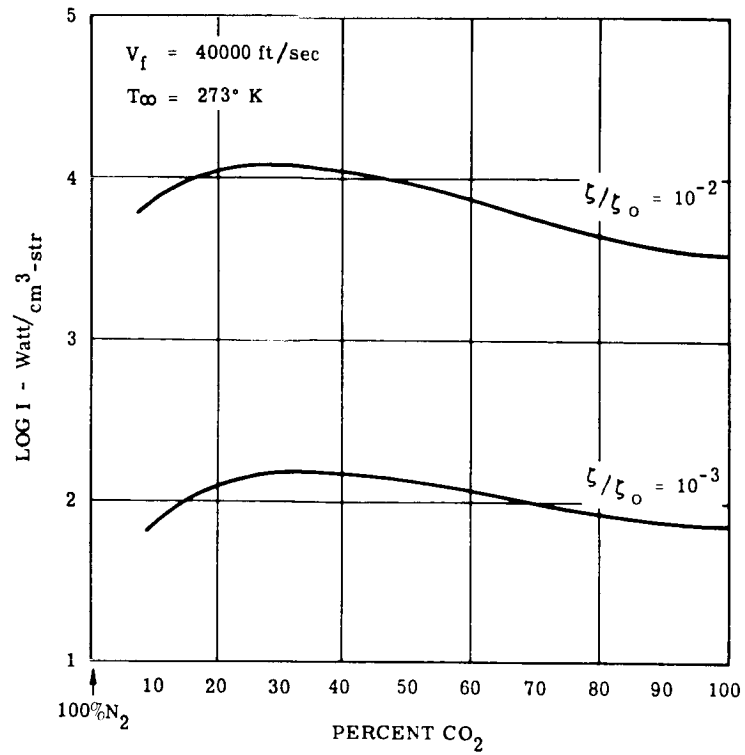


Figure 1.3.3-61. Radiation from $\text{CO}_2\text{-N}_2$ Mixture

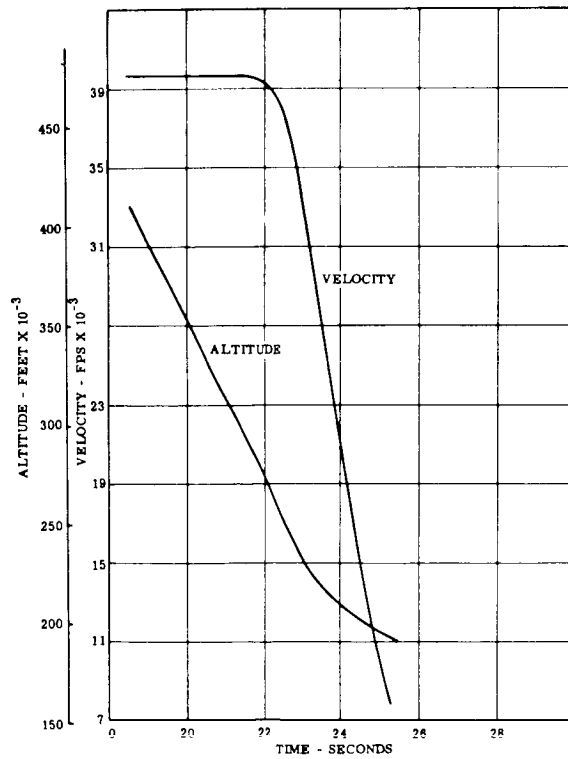


Figure 1.3.3-62. Venus Trajectory, Best Model Atmosphere

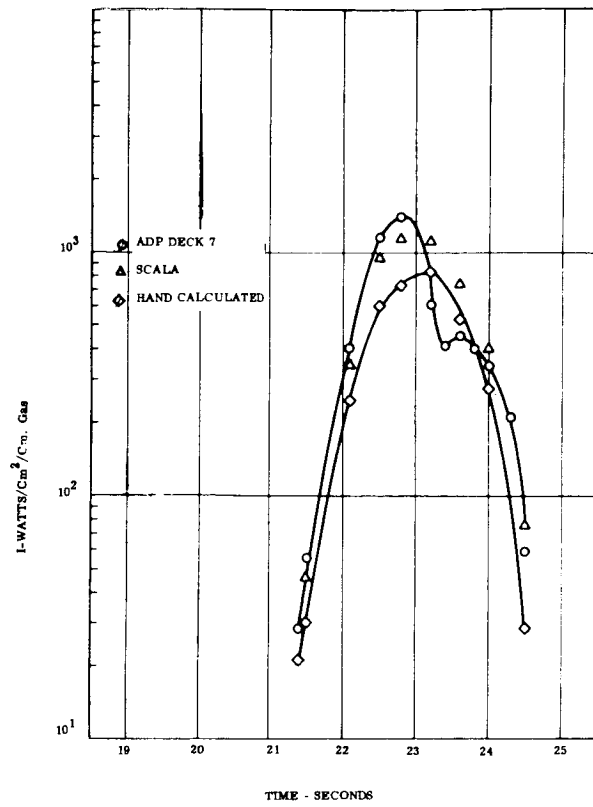


Figure 1.3.3-63. Hot Gas Radiation Intensity (25% CO₂)

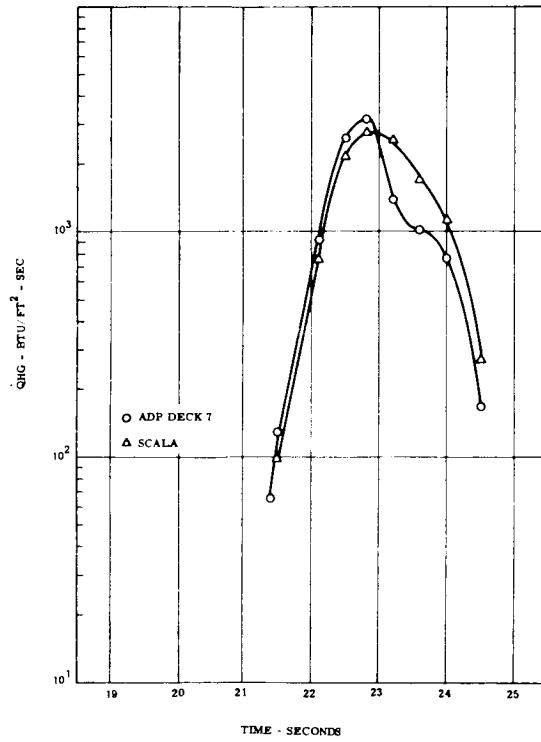


Figure 1.3.3-64. Stagnation Radiative Heating (25% CO₂)

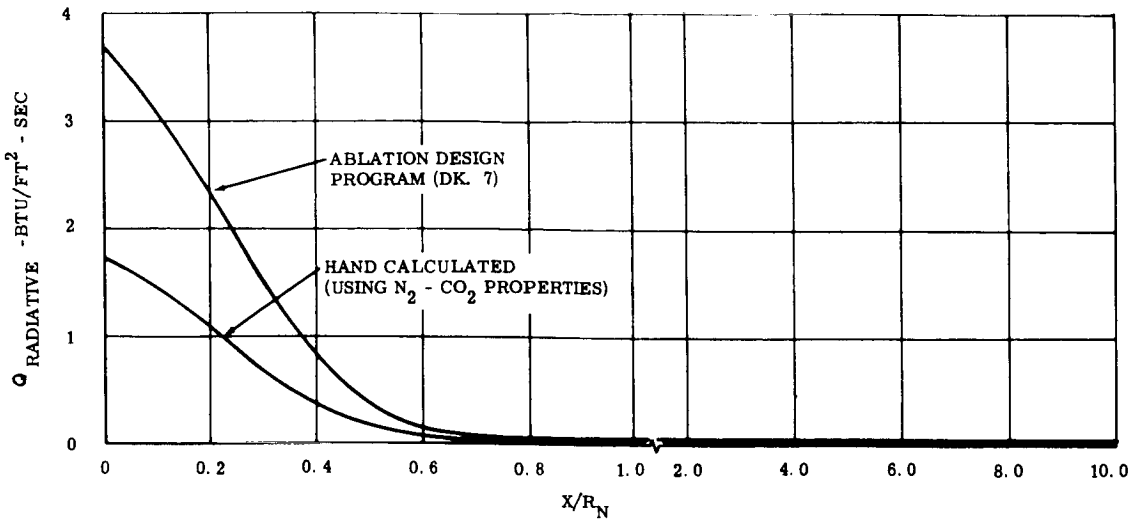


Figure 1.3.3-65. Comparative Heating Around Body (Air and N₂-CO₂)

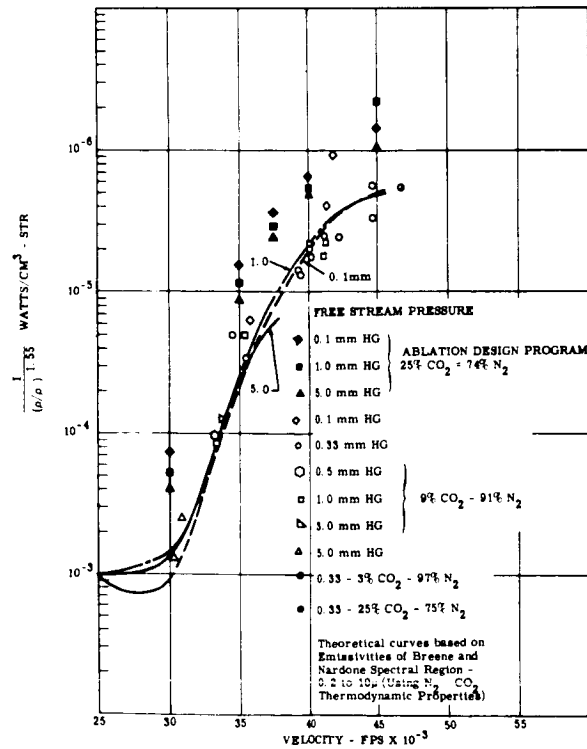


Figure 1.3.3-66. Stagnation Point Radiation in Simulated Venusian Atmosphere- Experimental Results Obtained with the Cavity Gage Compared to the Theoretical Predictions

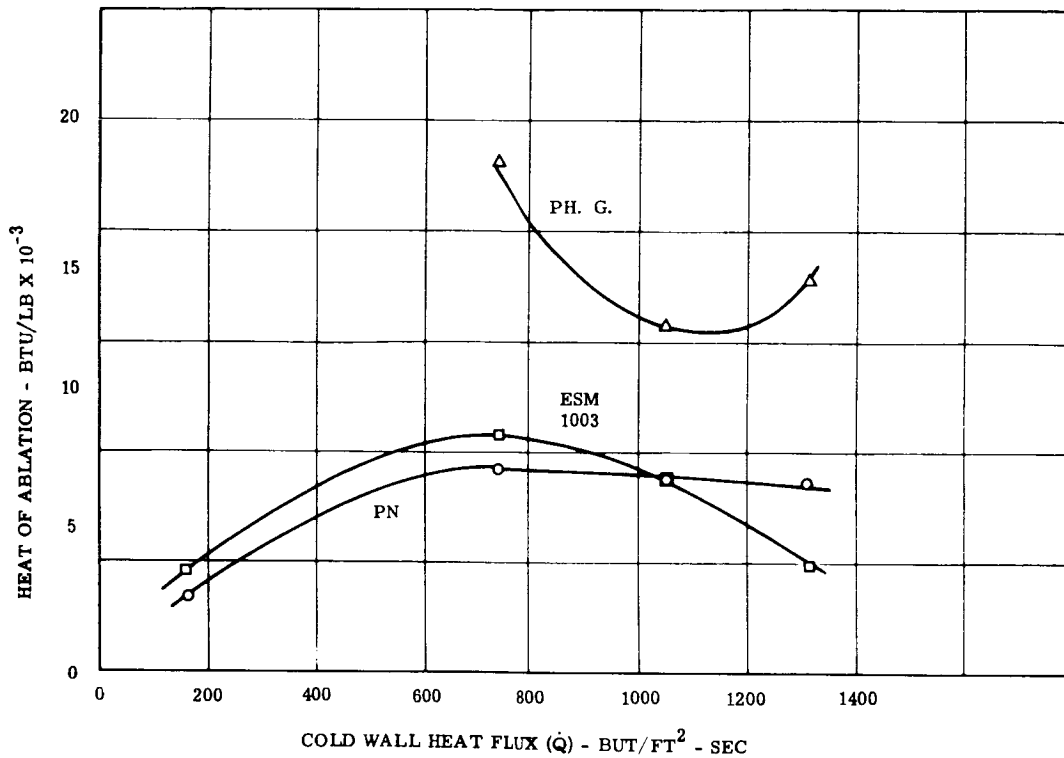


Figure 1.3.3-67. Average Heat of Ablation, Malta Pit I Facility

NOTE: Closed Symbols denote $75 \leq \rho \leq 77$ LB/FT³
 Open Symbols Denote $45 \leq \rho \leq 53$ LB/FT³
 Other Densities as Notes

UNITS: ρ , LB/FT³ of Virgin Material
 \dot{q} , BTU/FT² - SEC
 t , Time - SECS
 h_s , Enthalpy - BTU/LB

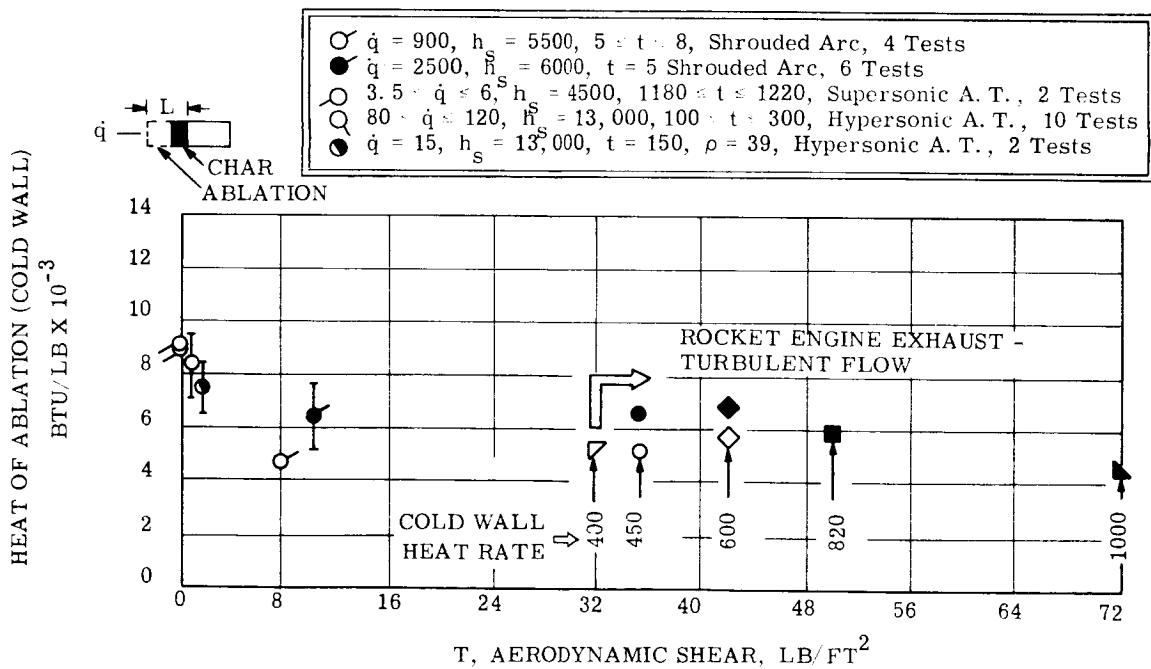


Figure 1.3.3-68. Typical ESM Ablation Performance Data

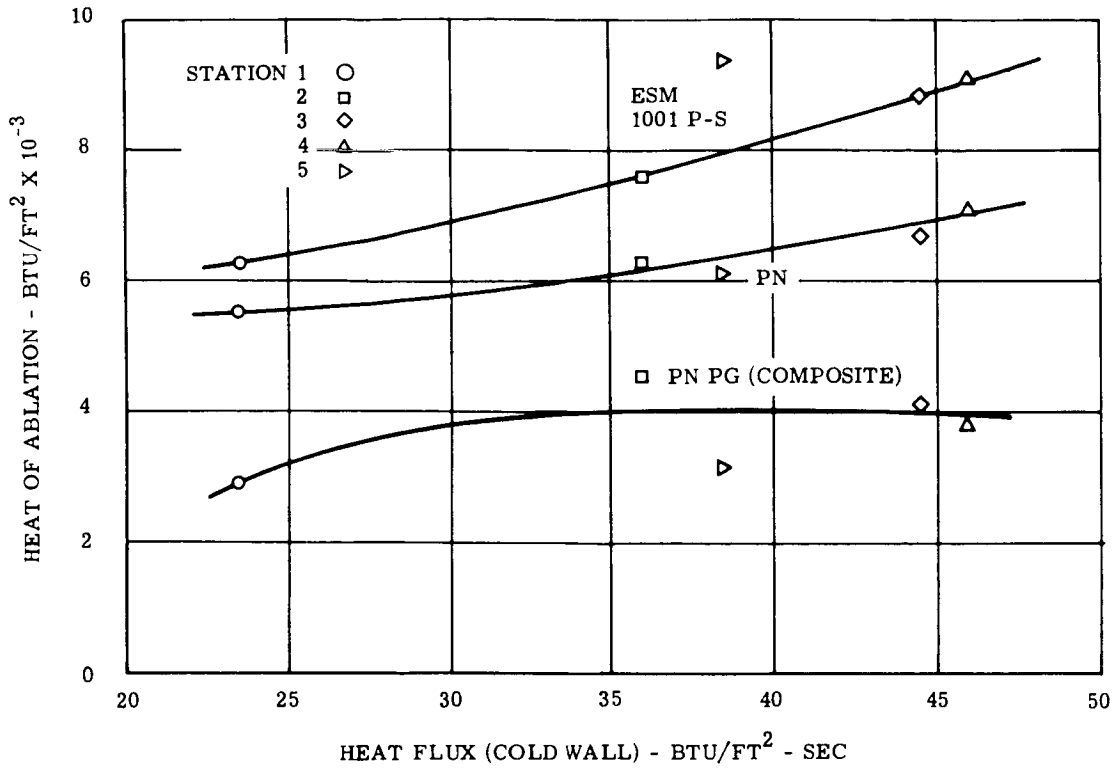


Figure 1.3.3-69. Ablation Material Performance (Hypersonic Arc Facility)

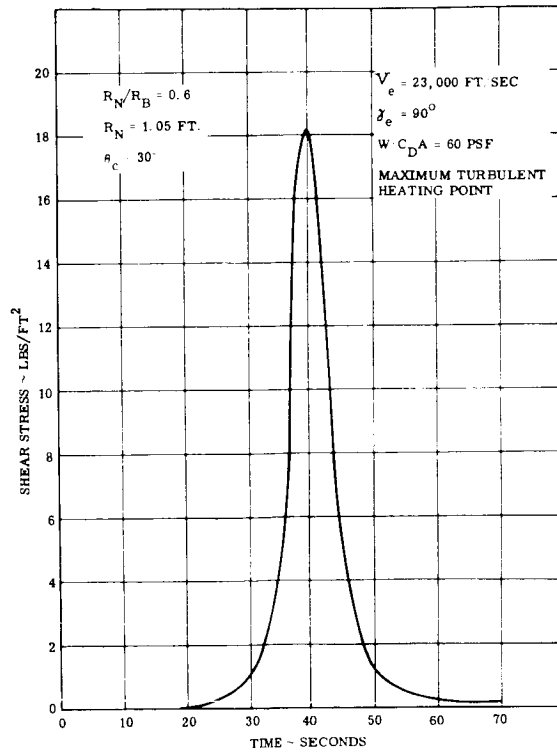


Figure 1.3.3-70. Aerodynamic Shear Stress, Mars' Mean Atmosphere

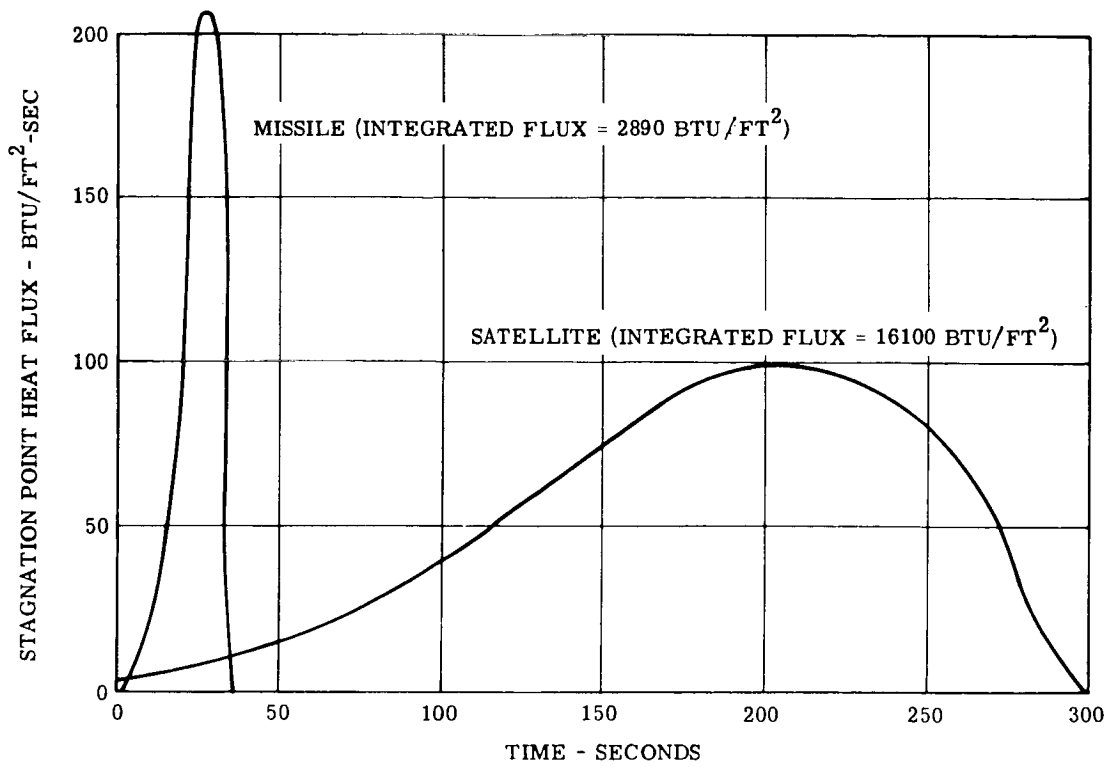


Figure 1.3.3-71. Heat Fluxes Due to Earth Satellite Re-entry

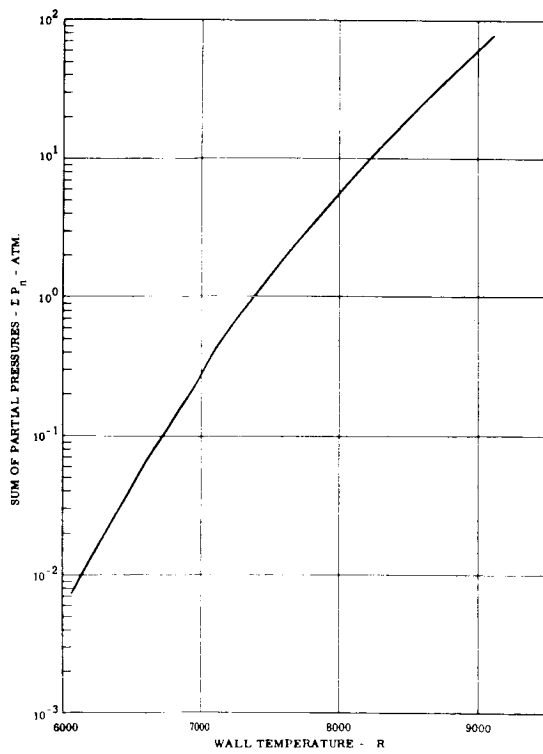


Figure 1.3.3-72. Sum of Five Carbon Species, Partial Pressure vs. Wall Temperature

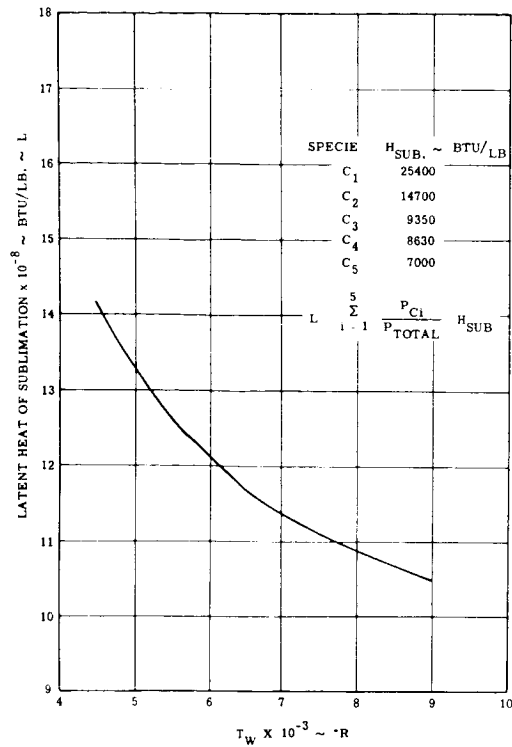


Figure 1.3.3-73. Latent Heat of Sublimation (.5 Carbon Species)

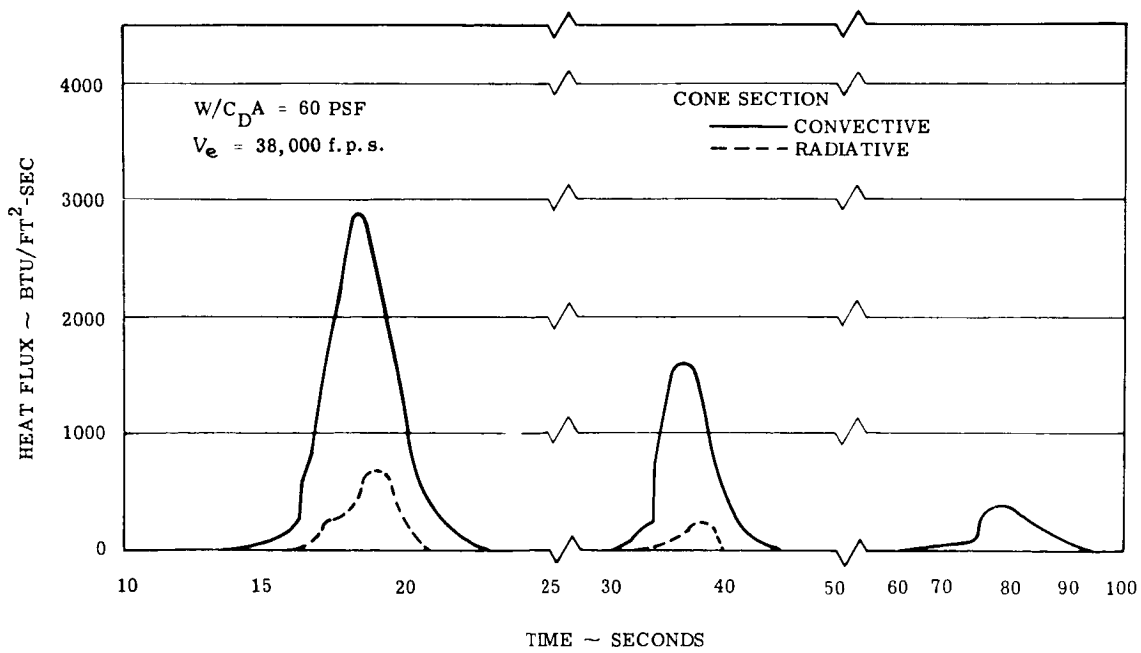


Figure 1.3.3-74. Venus Heat Fluxes used in REKAP Ablation Study, Standard Atmosphere

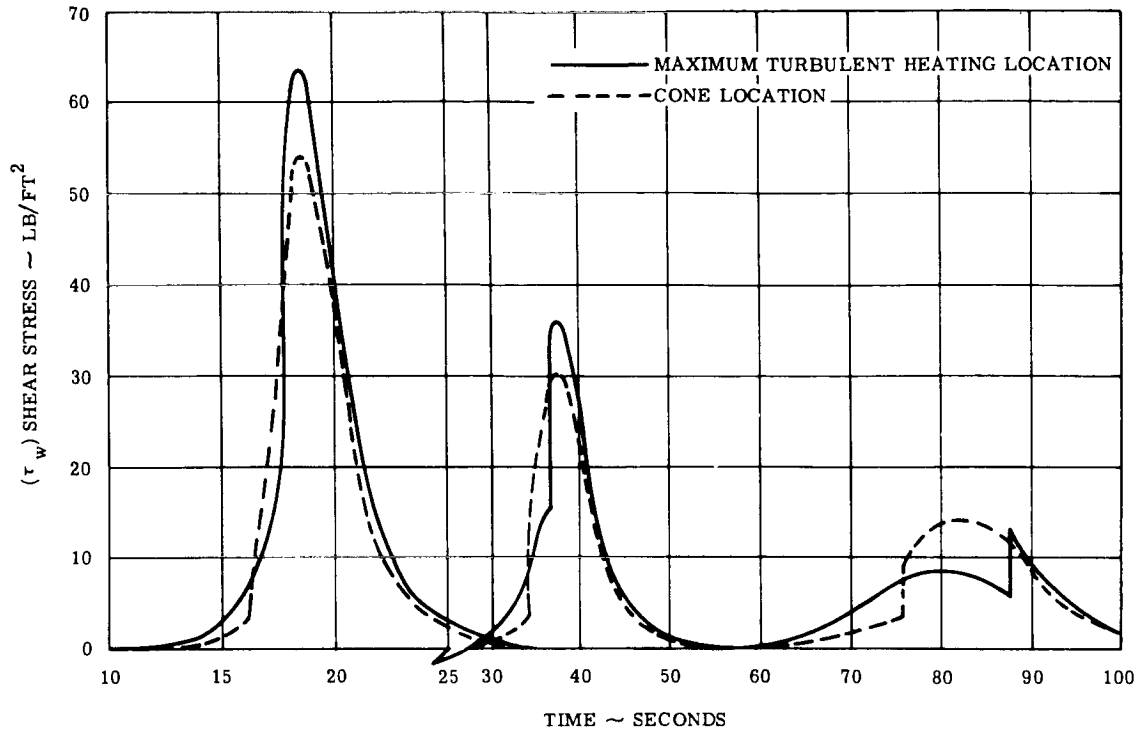


Figure 1.3.3-75. Aerodynamic Shear Stress for Conditions used in REKAP Study

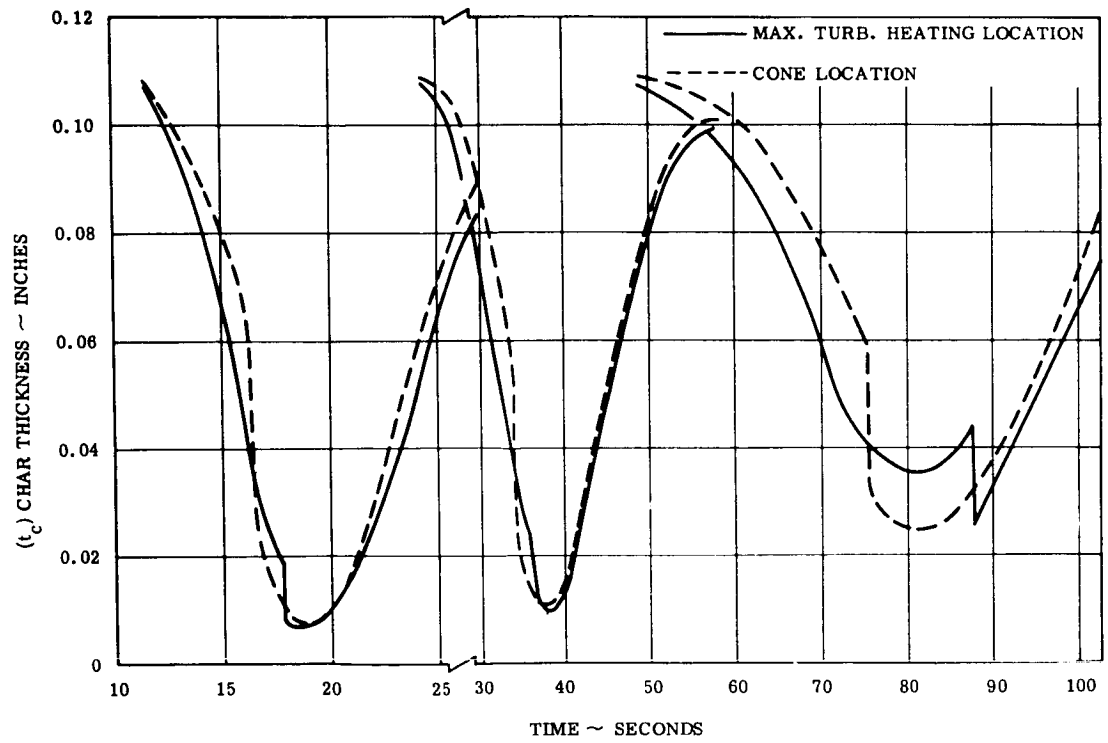


Figure 1.3.3-76. Limiting Char Thicknesses for Conditions used in REKAP Study

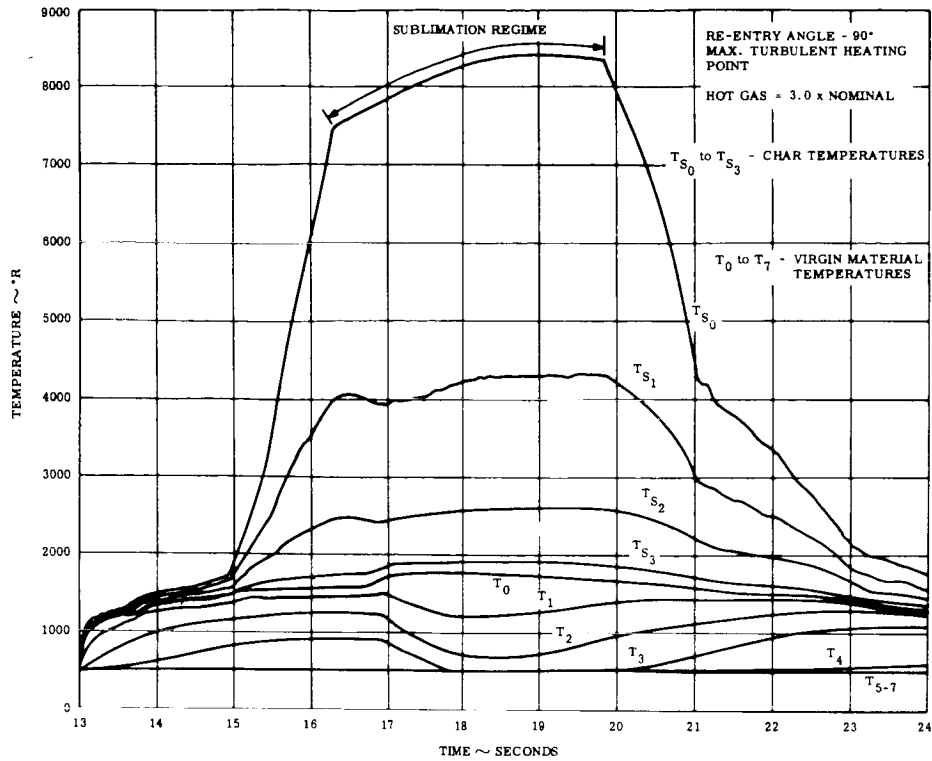


Figure 1.3.3-77. Typical Analog Results - Temperature

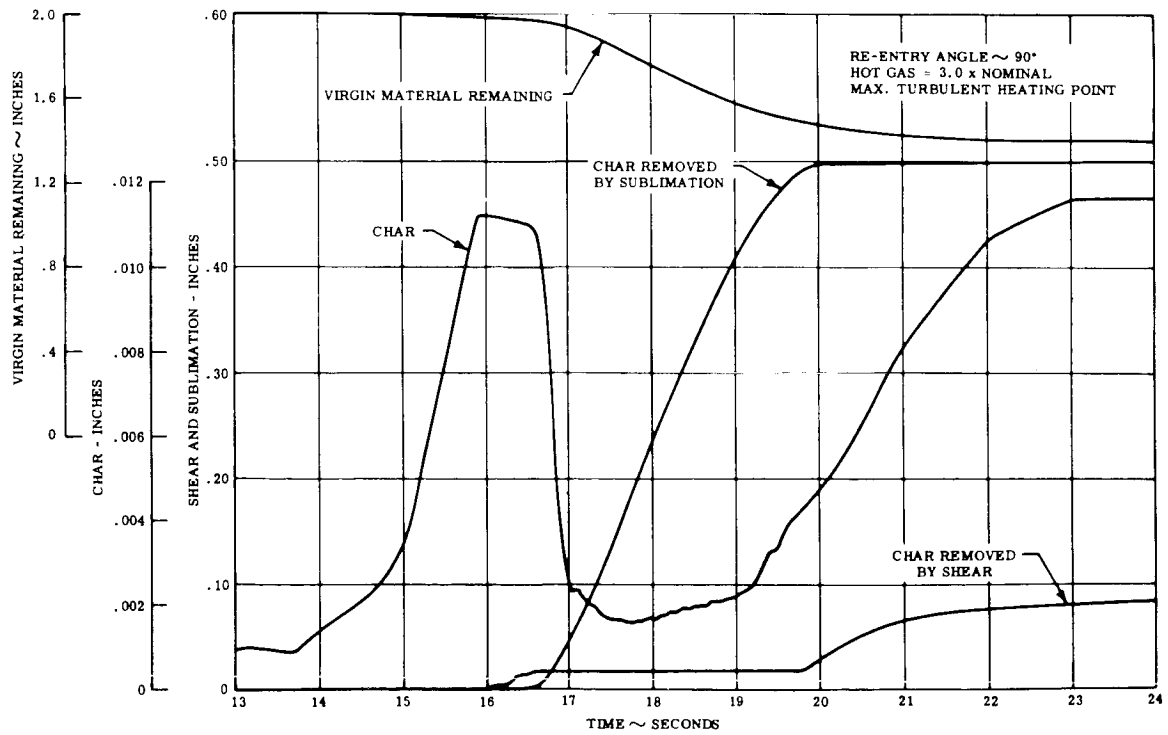


Figure 1.3.3-78. Typical Analog Results - Ablation and Char Thicknesses

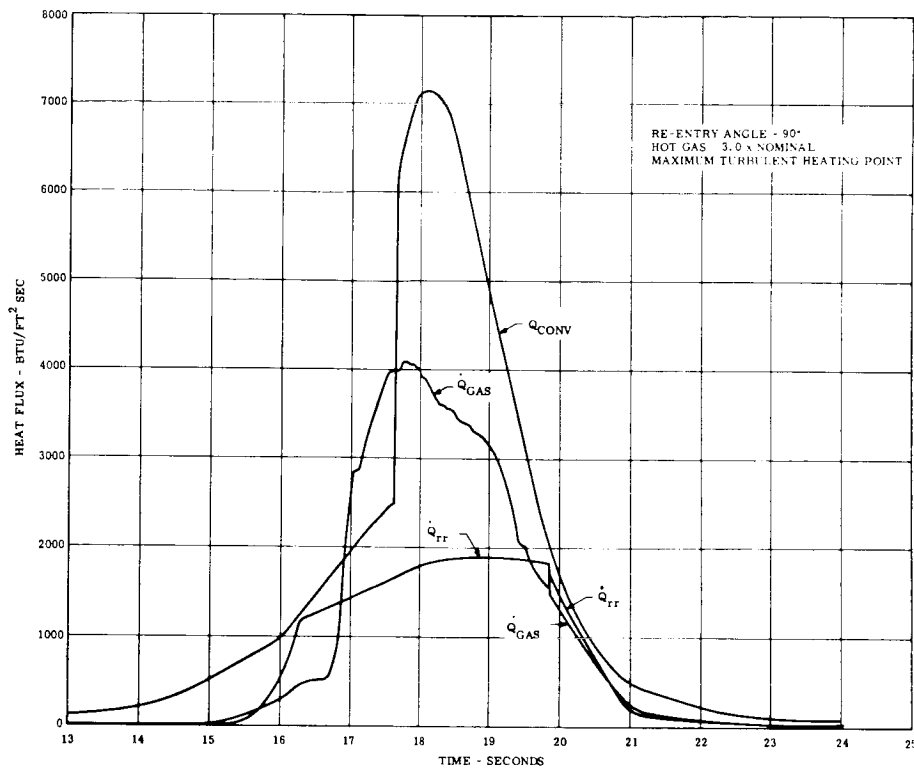


Figure 1.3.2-79. Typical Analog Results - Heat Flux Partitioning

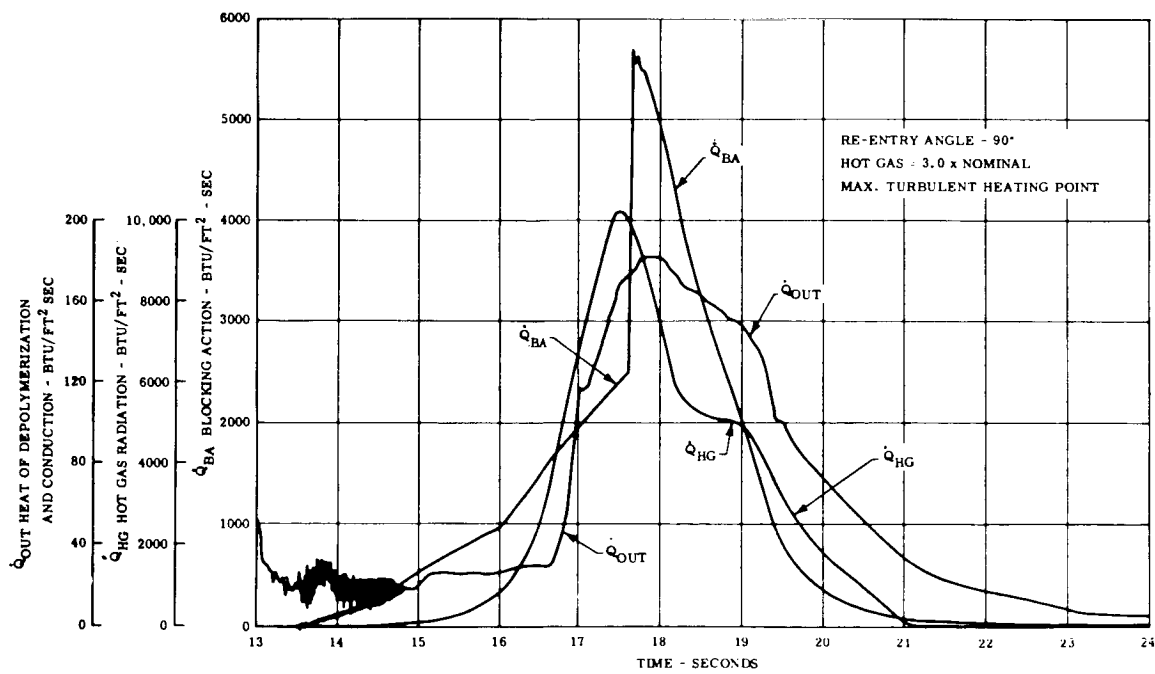


Figure 1.3.3-80. Typical Analog Results - Heat Flux Partitioning

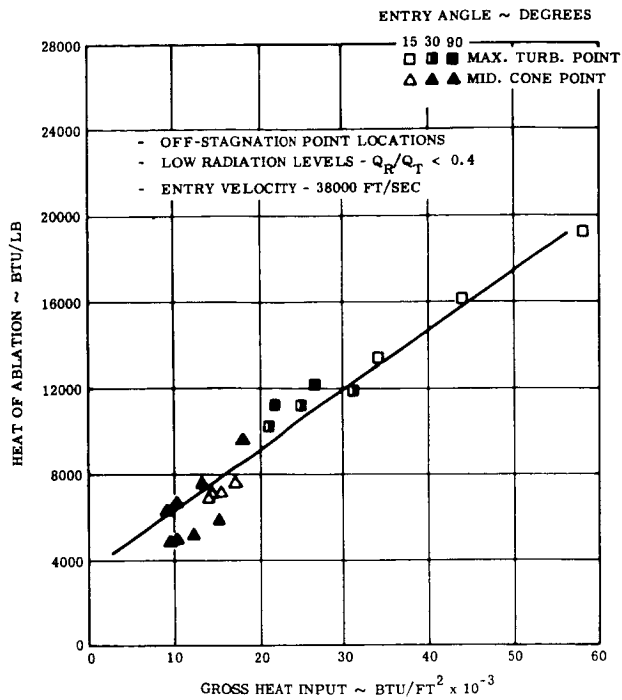


Figure 1.3.3-81. REKAP Heat of Ablation Correlation

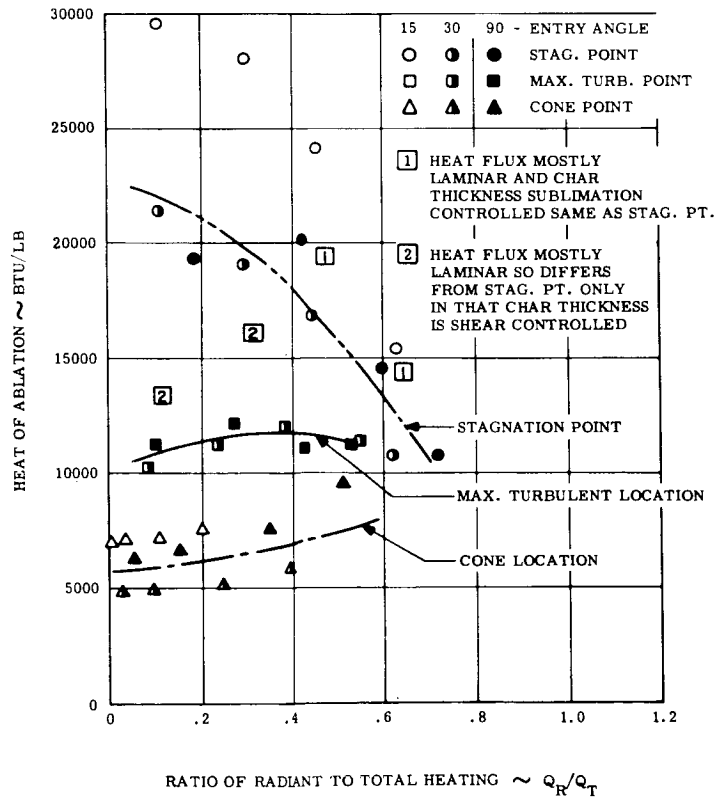


Figure 1.3.3-82. Effect of Radiant Heating on Ablation Performance (Summary of REKAP Data)

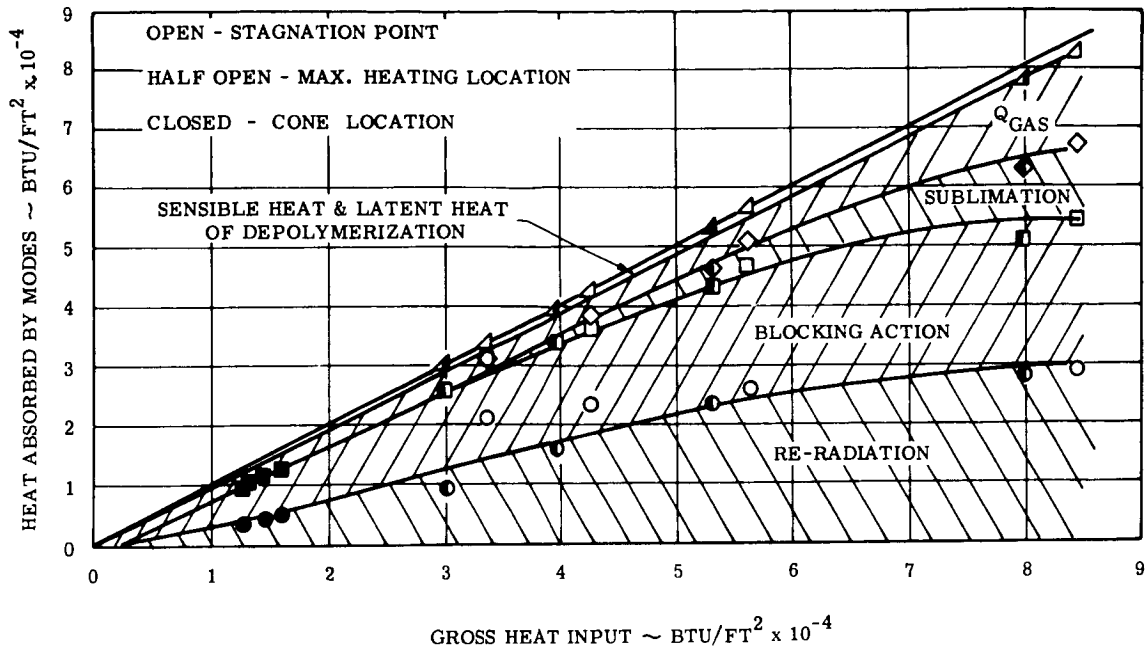


Figure 1.3.3-83. Typical Energy Absorption Partitioning

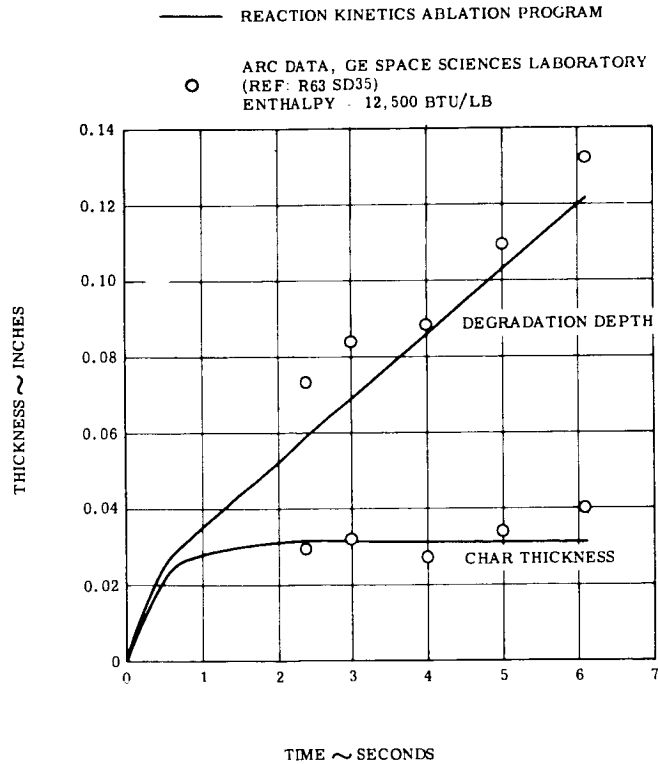


Figure 1.3.3-84. Comparison of REKAP Ablation Prediction with Ground Test Data

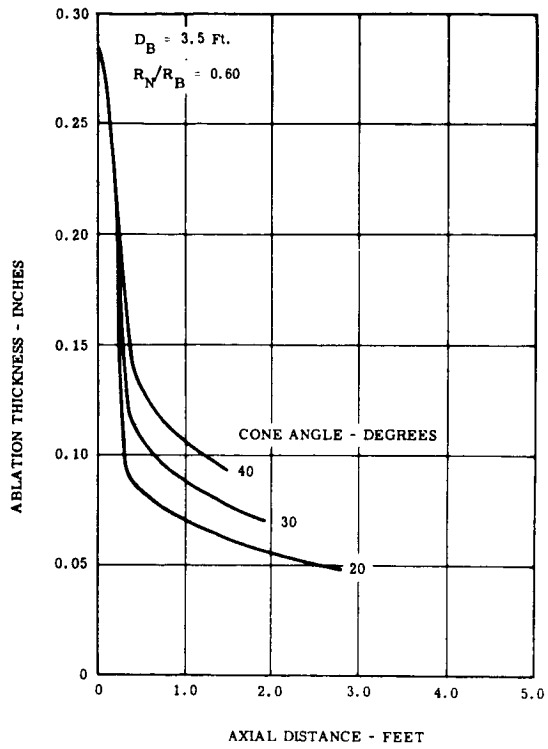


Figure 1.3.3-85. Mars Shield Ablation Requirements, Mean Atmosphere

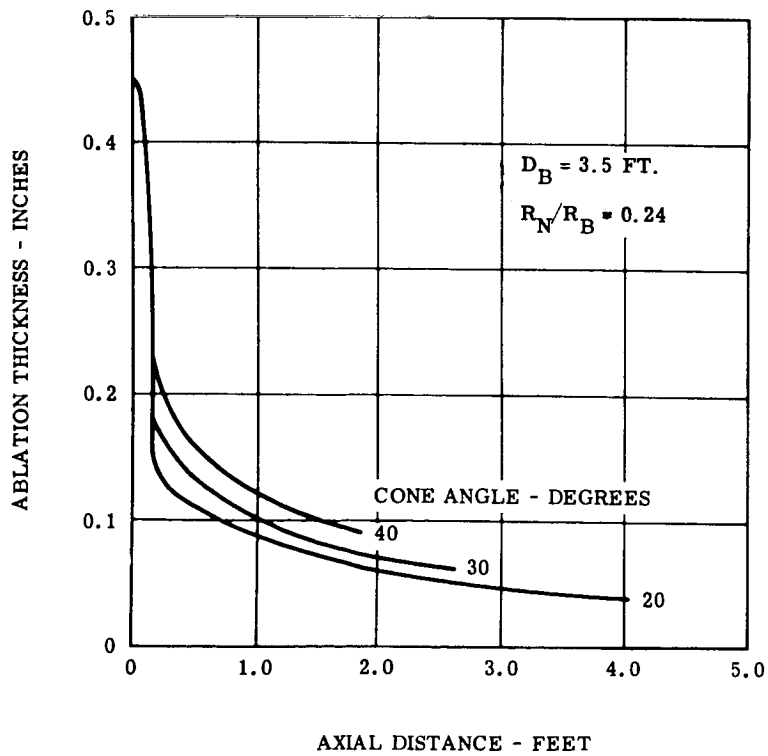


Figure 1.3.3-86. Mars Shield Ablation Requirements, Mean Atmosphere

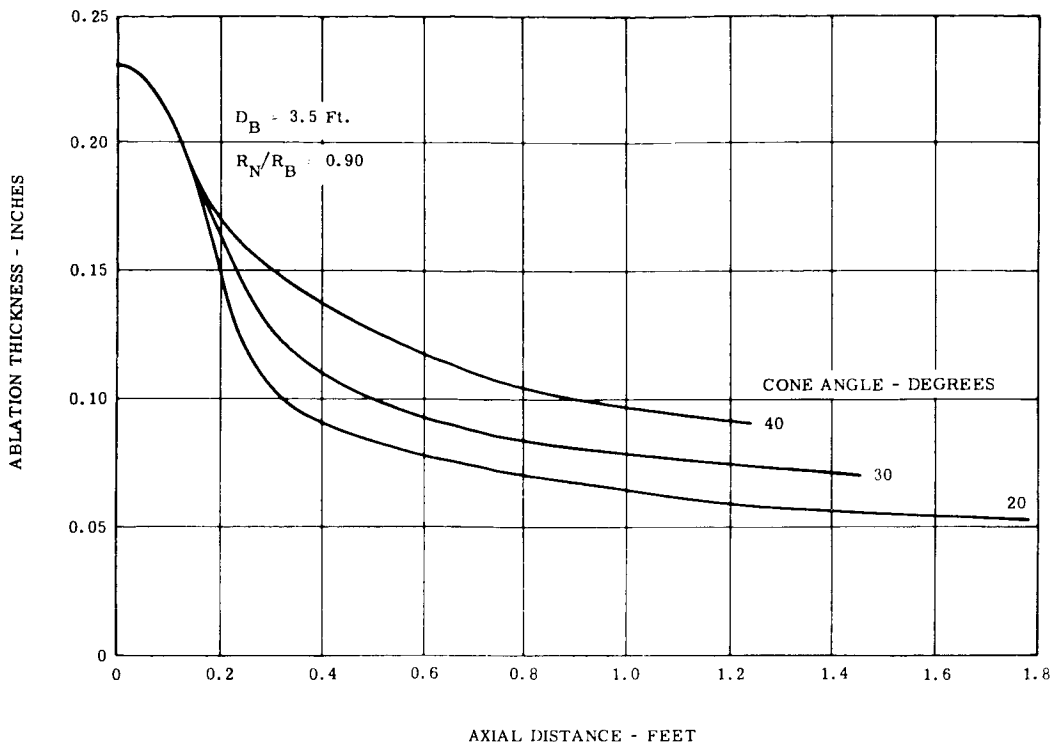


Figure 1.3.3-87. Mars Shield Ablation Requirements, Mean Atmosphere

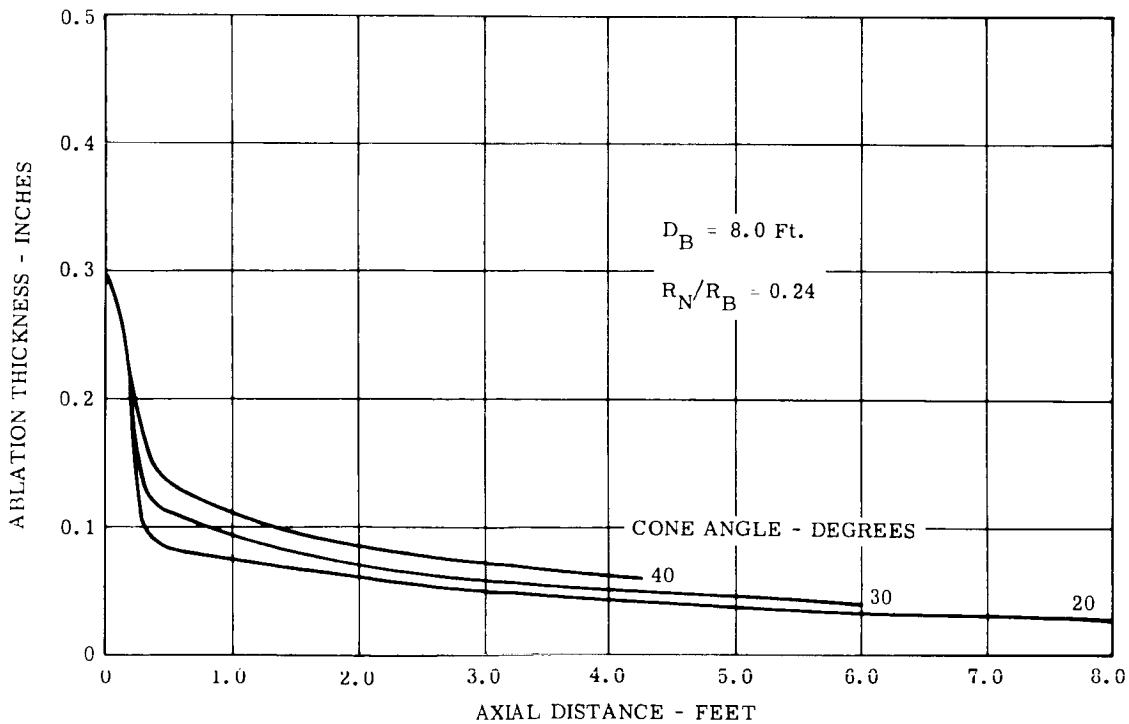


Figure 1.3.3-88. Mars Shield Ablation Requirements, Mean Atmosphere

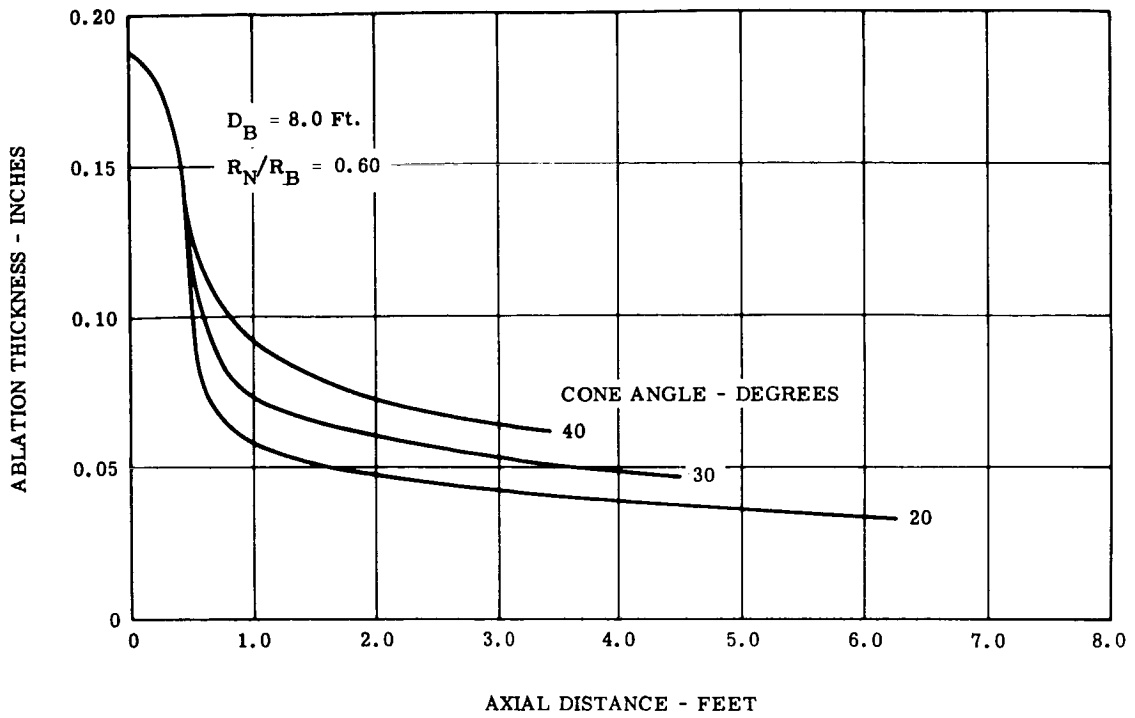


Figure 1.3.3-89. Mars Shield Ablation Requirements, Mean Atmosphere

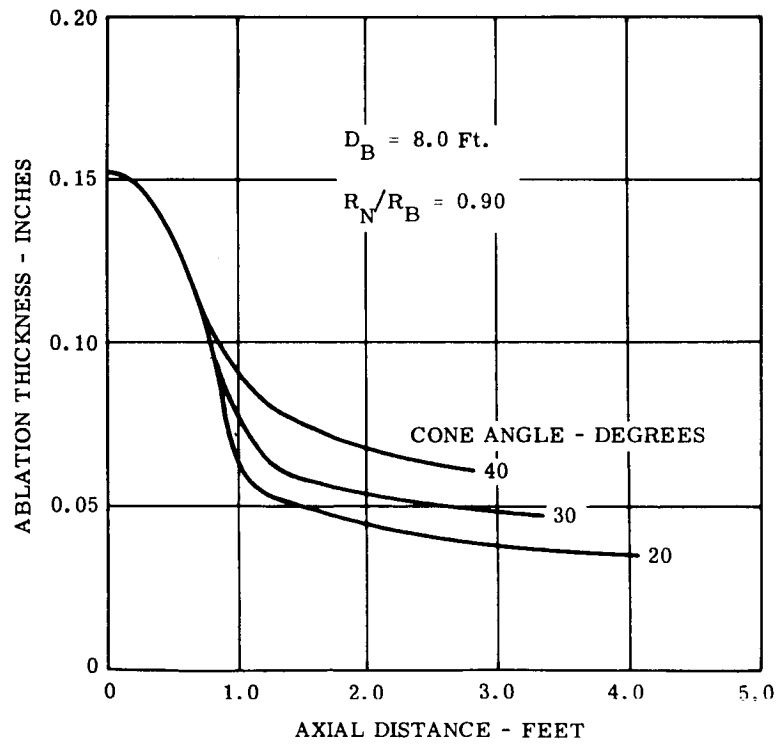


Figure 1.3.3-90. Mars Shield Ablation Requirements, Mean Atmosphere

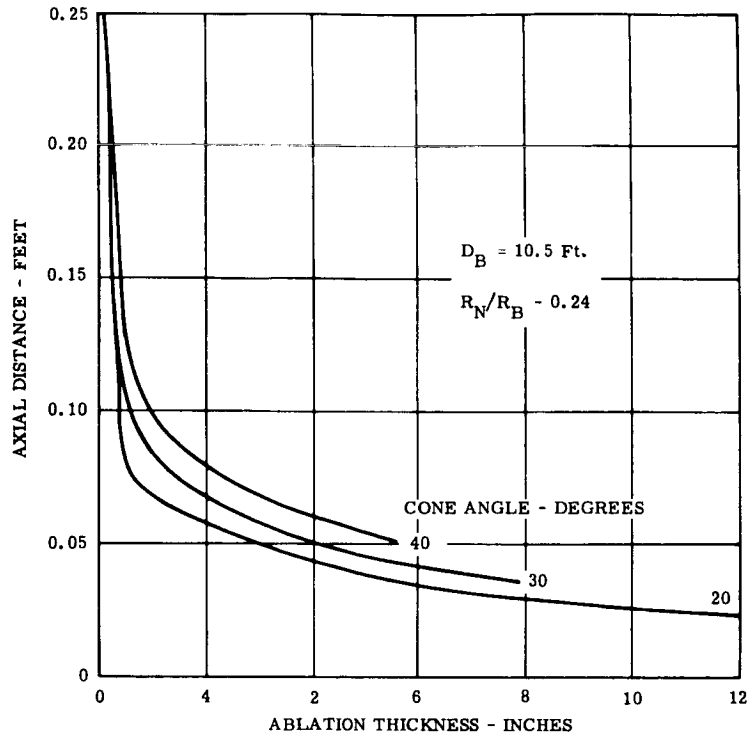


Figure 1.3.3-91. Mars Shield Ablation Requirements, Mean Atmosphere

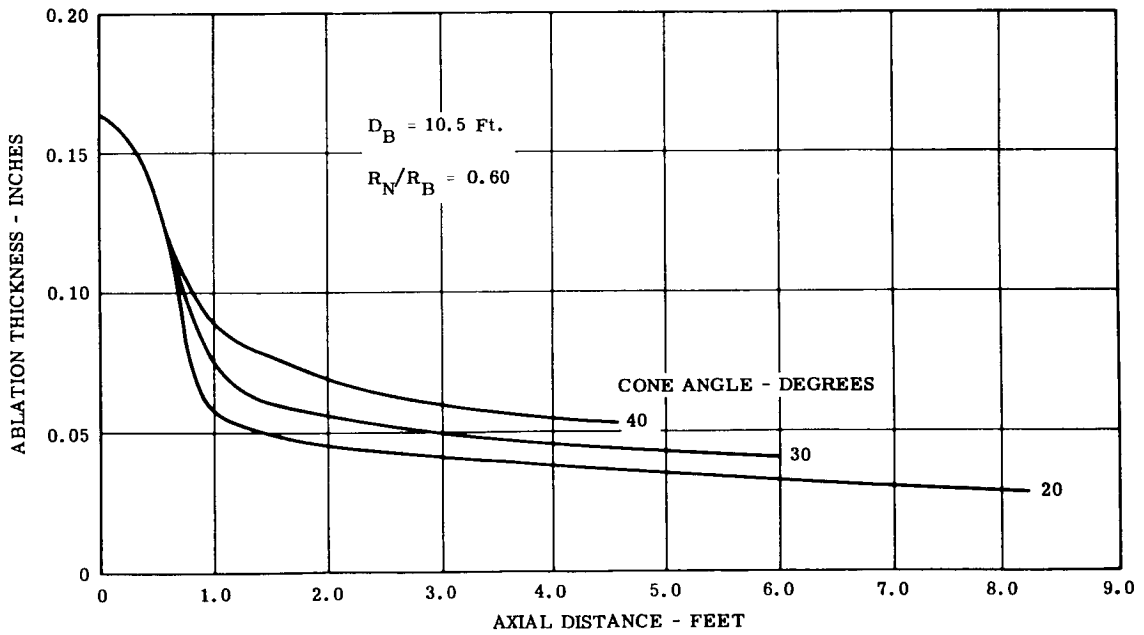


Figure 1.3.3-92. Mars Shield Ablation Requirements, Mean Atmosphere

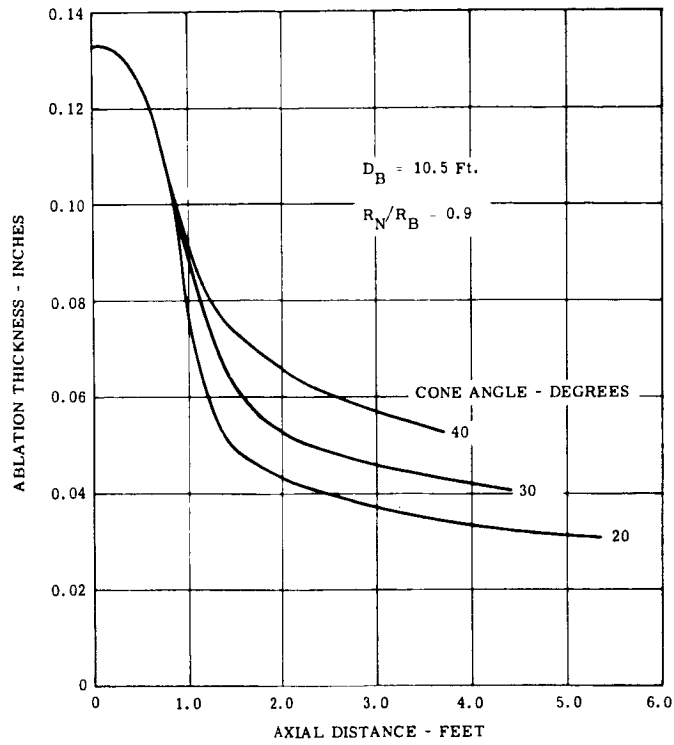


Figure 1.3.3-93. Mars Shield Ablation Requirements, Mean Atmosphere

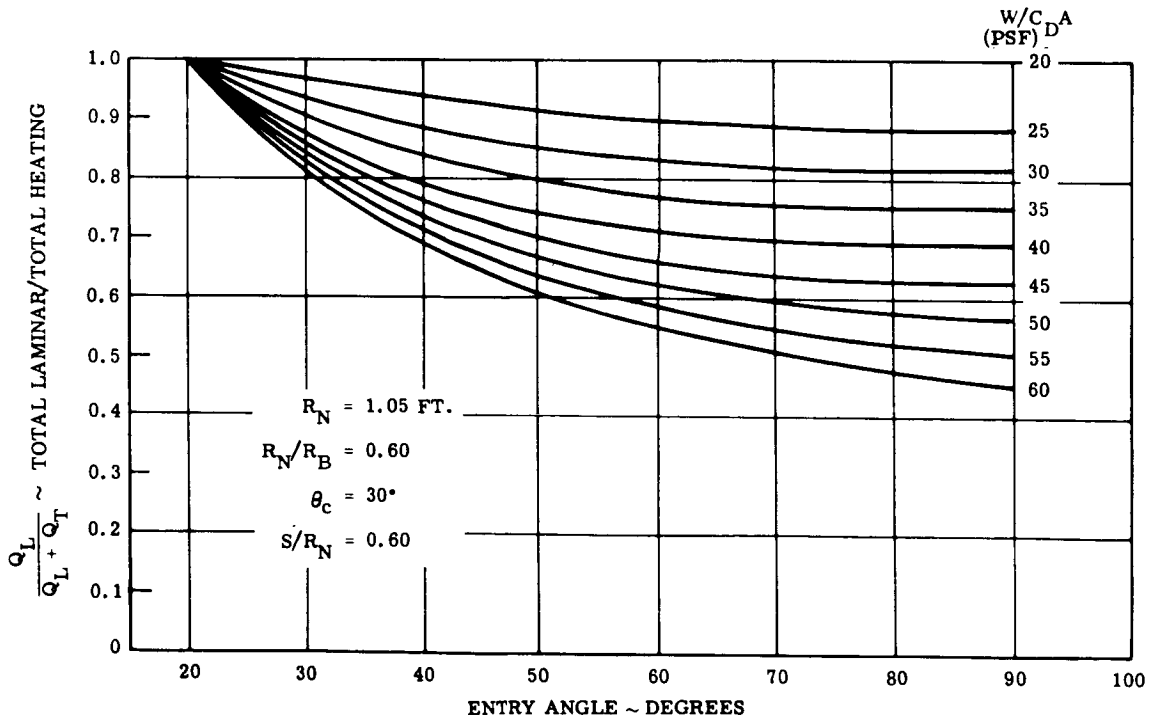


Figure 1.3.3-94. Ratio of Laminar to Total Time Integrated Heating, Mars Mean Atmosphere

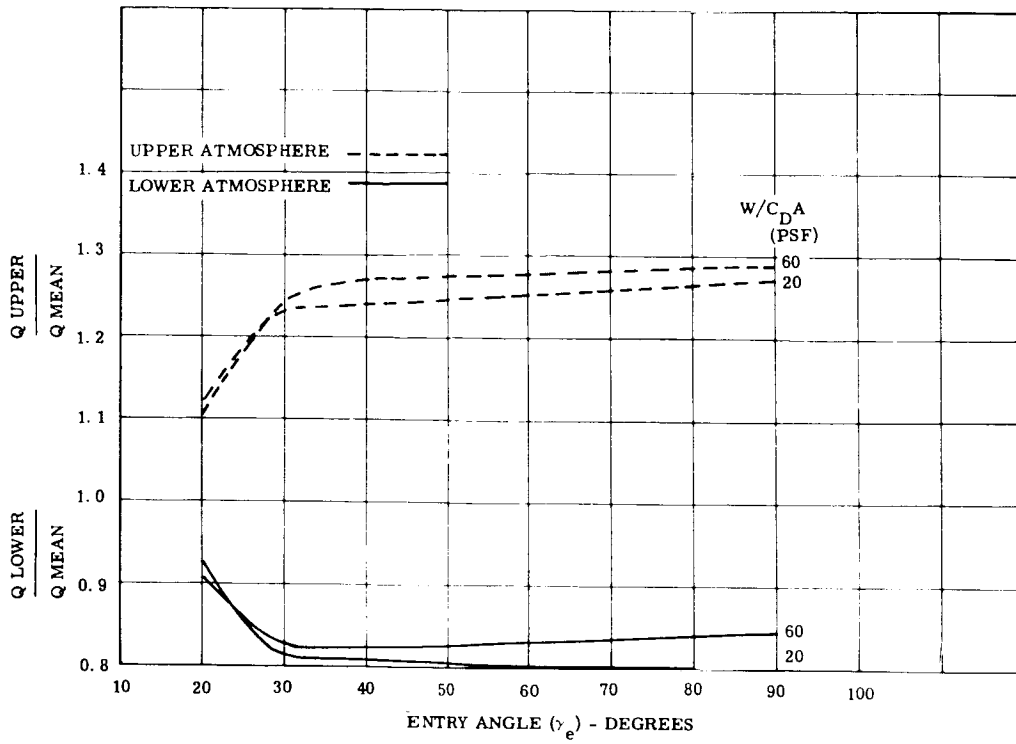


Figure 1.3.3-95: Atmospheric Model Effect on Total Heating, Mars

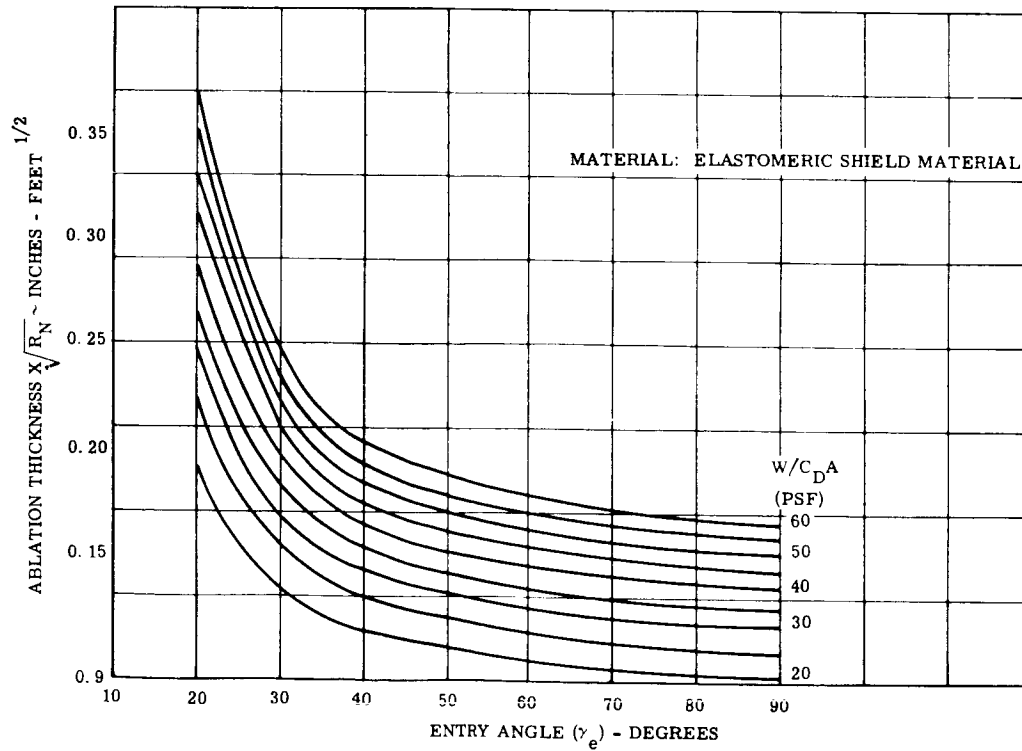


Figure 1.3.3-96: Stagnation Point Ablation Thickness, Mars Mean Atmosphere

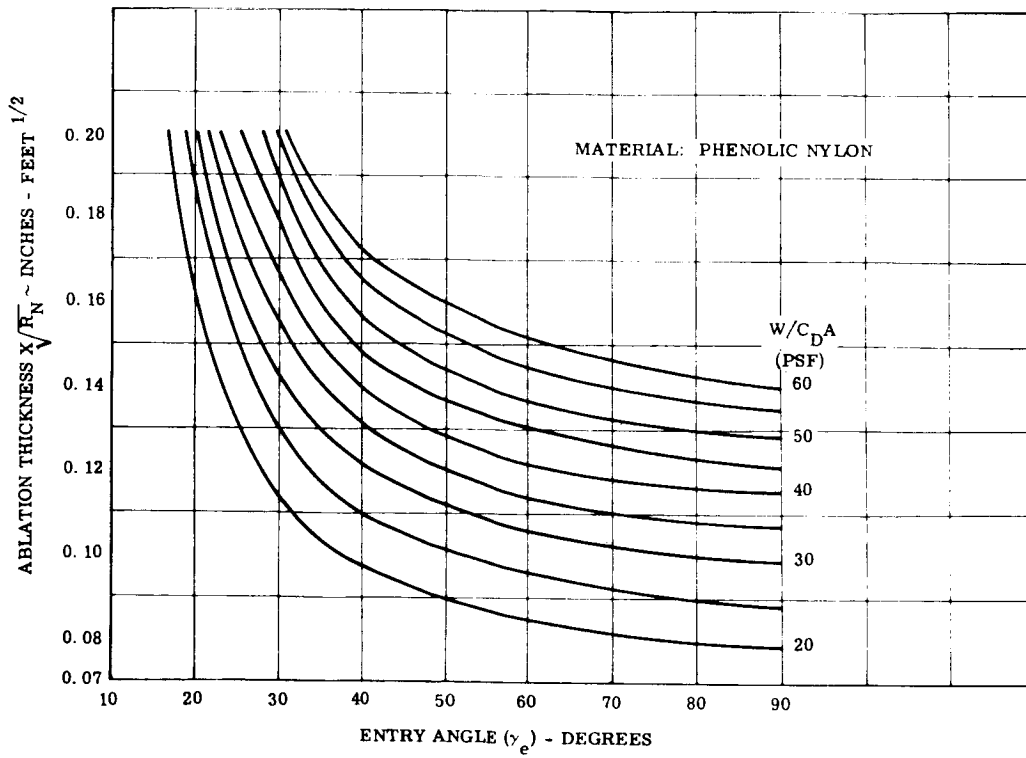


Figure 1.3.3-97 Stagnation Point Ablation Thickness, Mars Mean Atmosphere

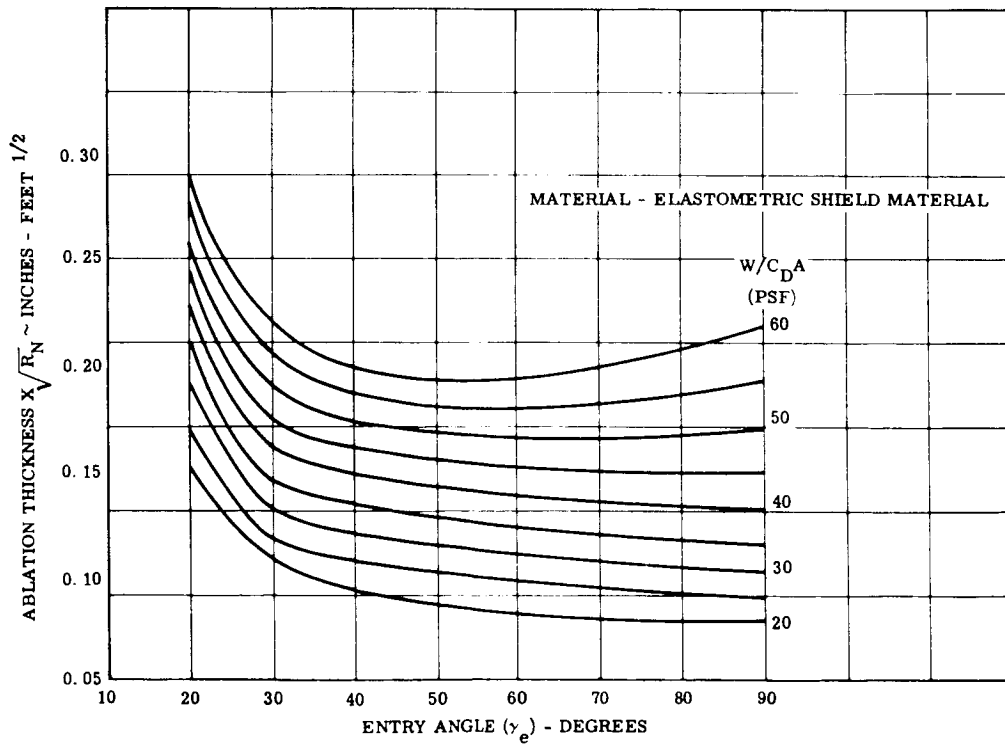


Figure 1.3.3-98 Stagnation Point Ablation Thickness, Mars Mean Atmosphere

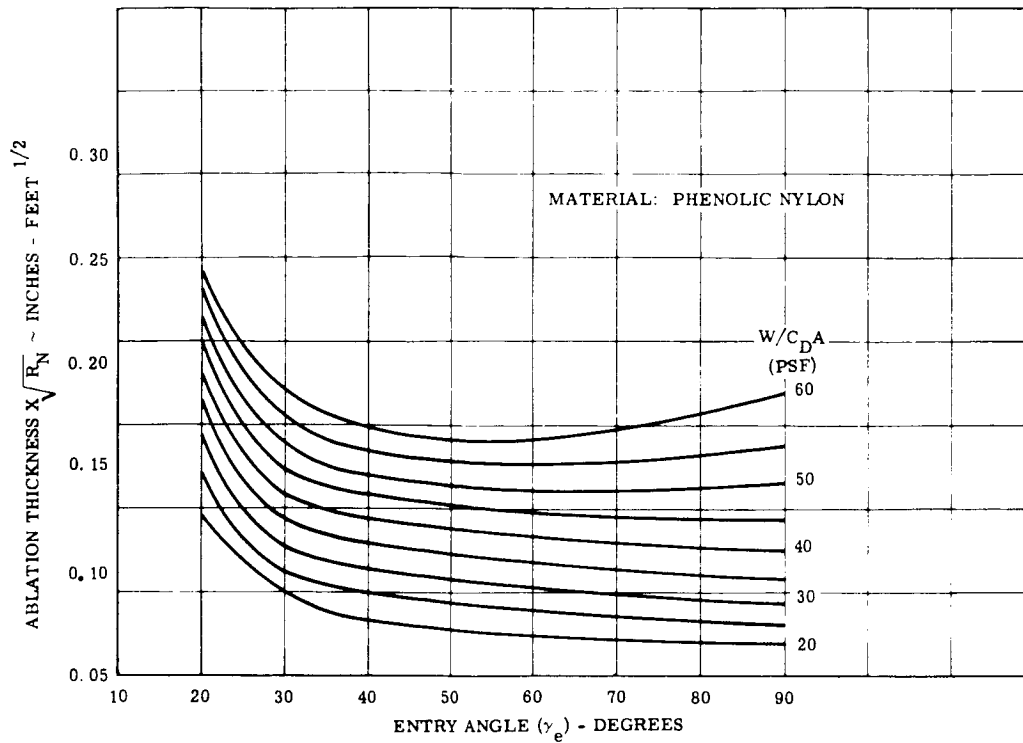


Figure 1.3.3-99 Stagnation Point Ablation Thickness, Mars Mean Atmosphere

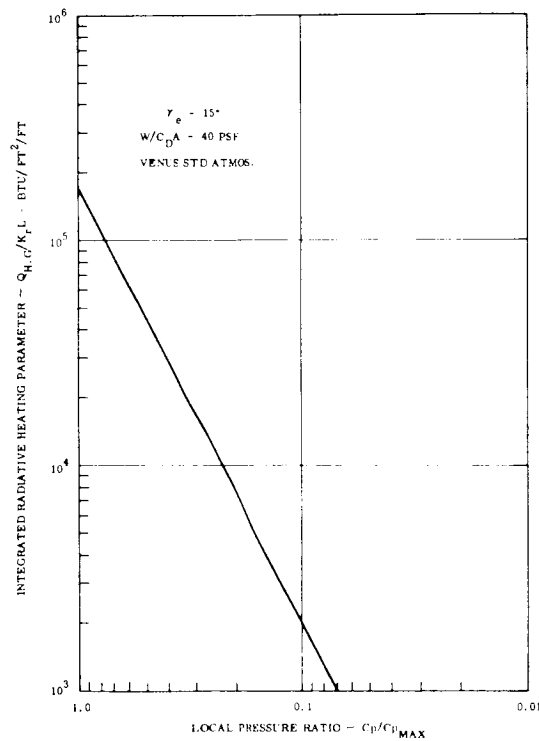


Figure 1.3.3-100 Radiant Heating Distribution

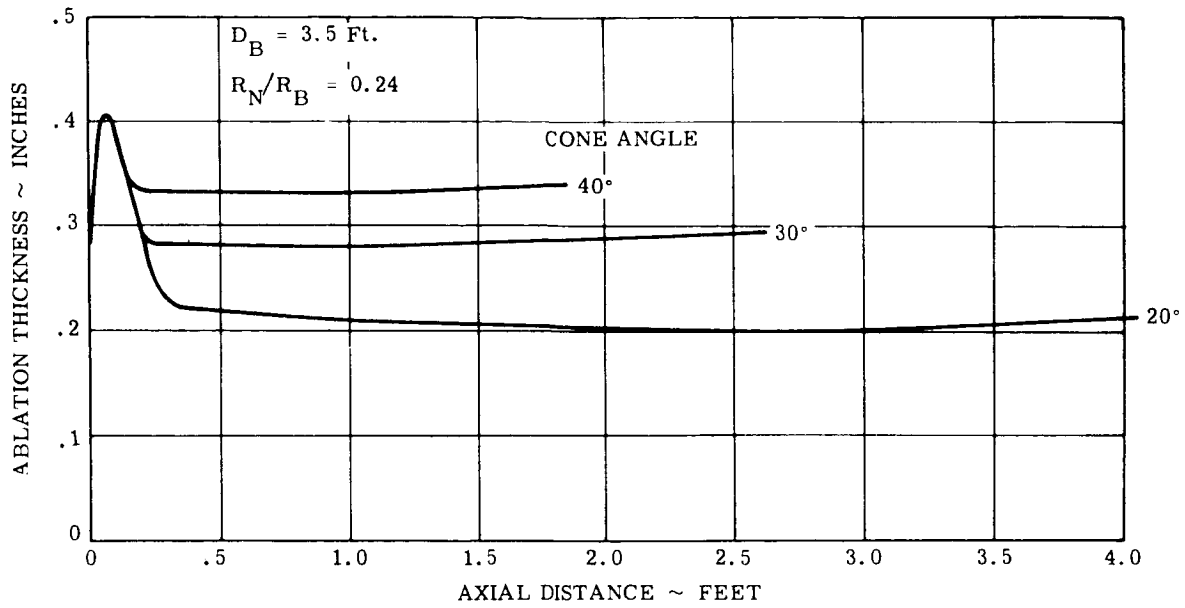


Figure 1.3.3.-101 Venus Shield Ablation Requirements, Standard Atmosphere (25% CO₂)

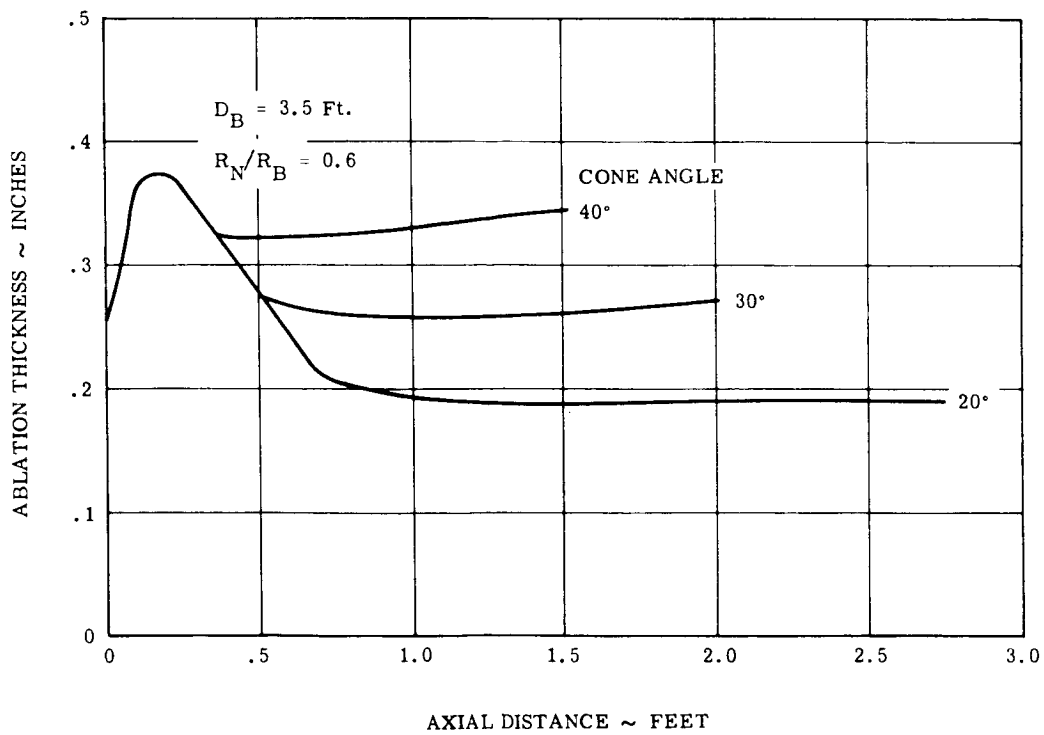


Figure 1.3.3-102 Venus Shield Ablation Requirements, Standard Atmosphere (25% CO₂)

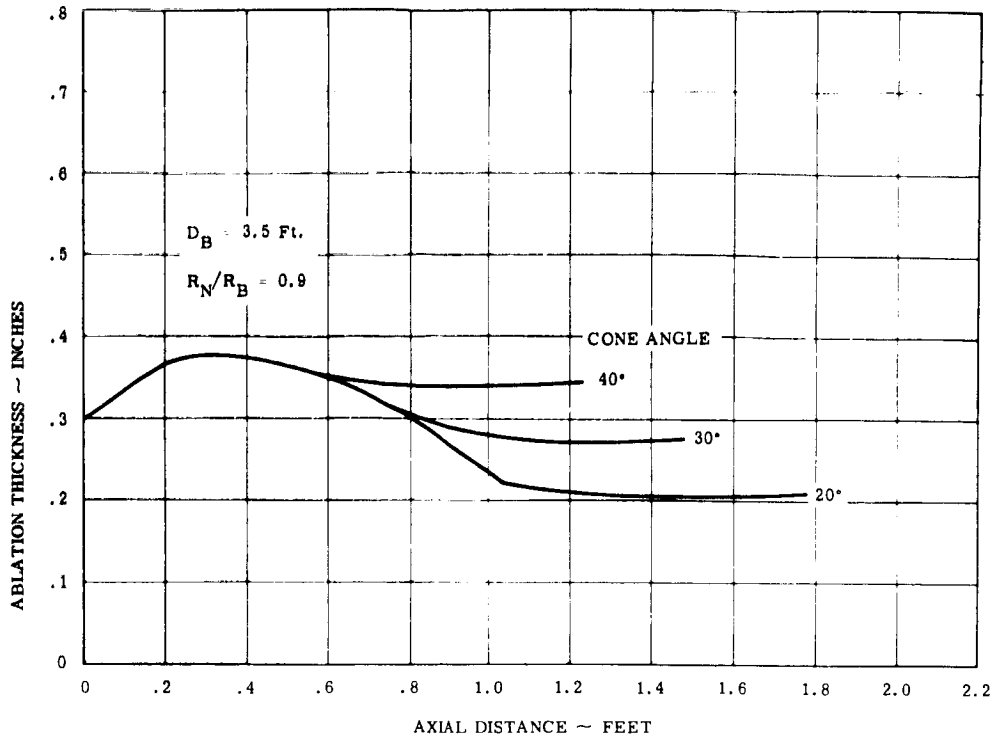


Figure 1.3.3-103 Venus Shield Ablation Requirements, Standard Atmosphere (25% CO₂)

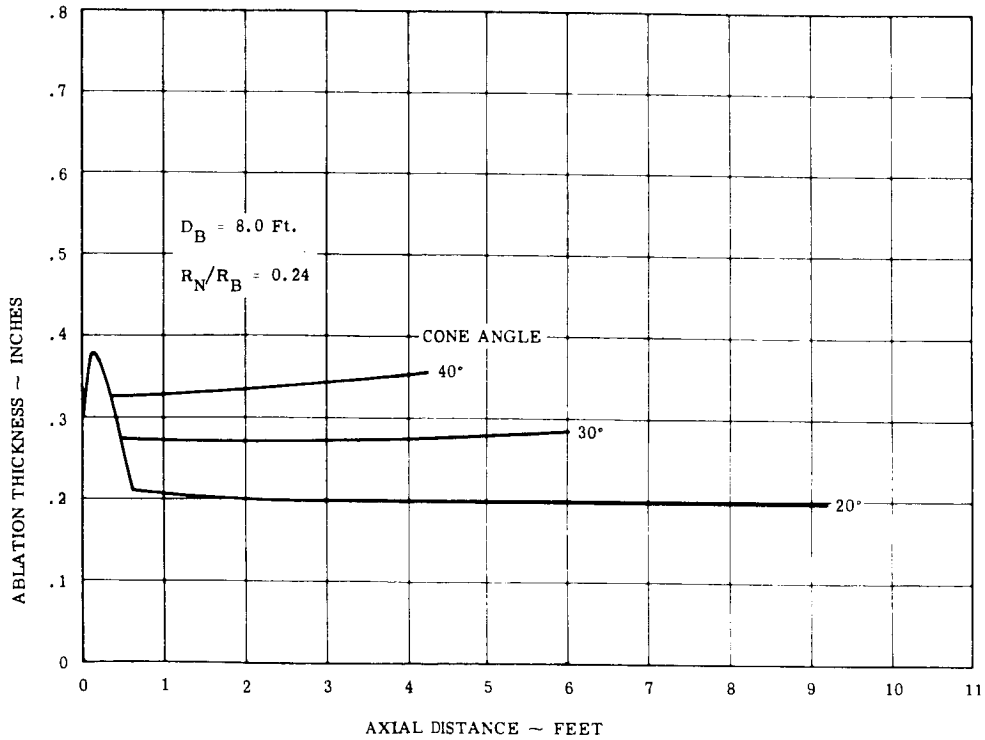


Figure 1.3.3-104 Venus Shield Ablation Requirements, Standard Atmosphere (25% CO₂)

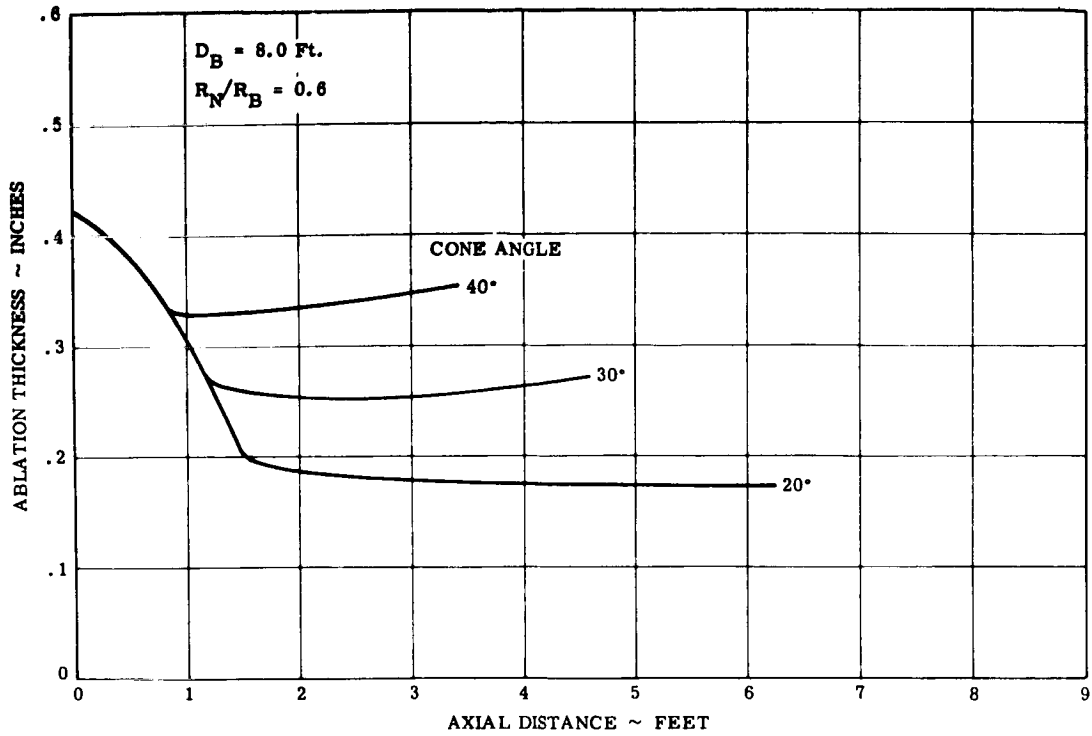


Figure 1.3.3-105 Venus Shield Ablation Requirements, Standard Atmosphere (25% CO₂)

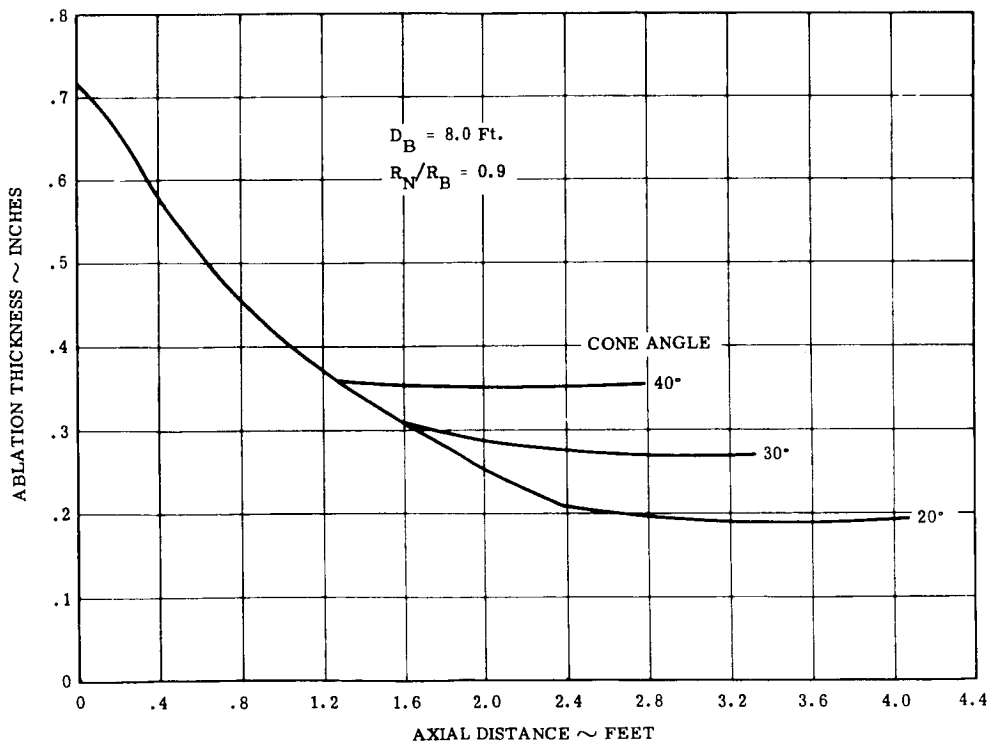


Figure 1.3.3-106 Venus Shield Ablation Requirements, Standard Atmosphere (25% CO₂)

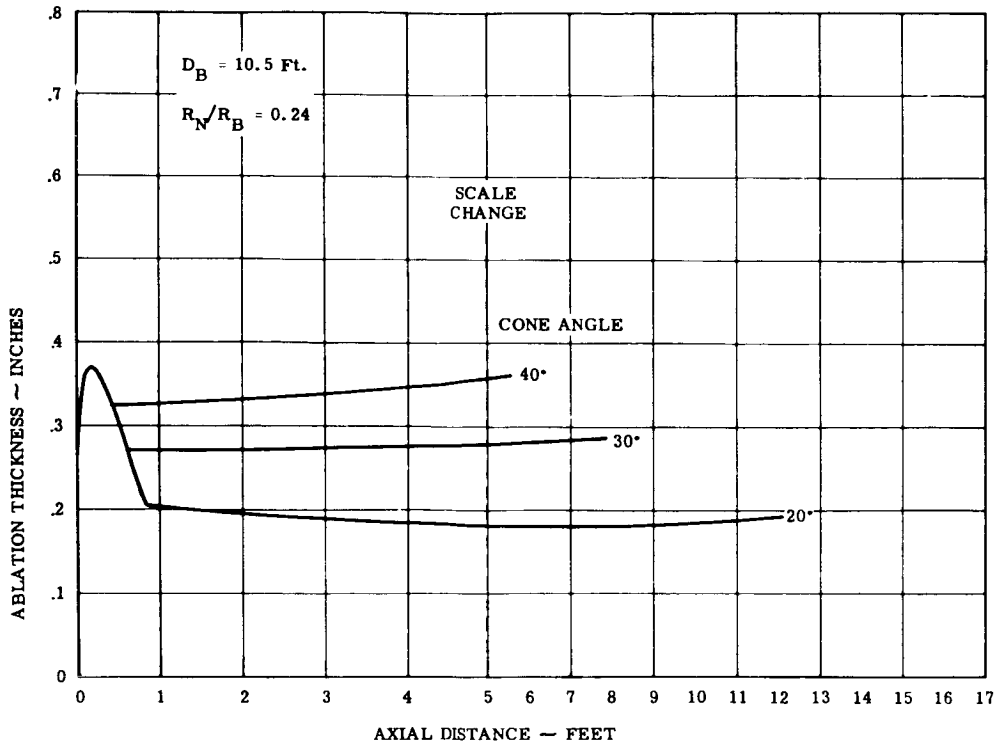


Figure 1.3.3-107 Venus Shield Ablation Requirements, Standard Atmosphere (25% CO₂)

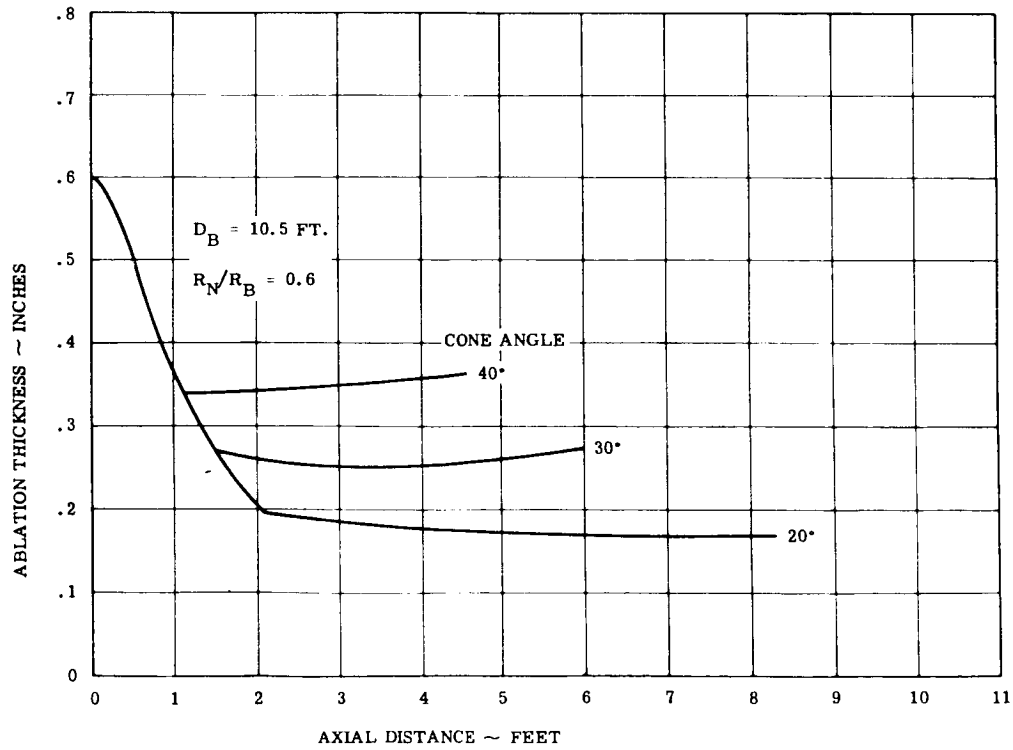


Figure 1.3.3-108 Venus Shield Ablation Requirements, Standard Atmosphere (25% CO₂)

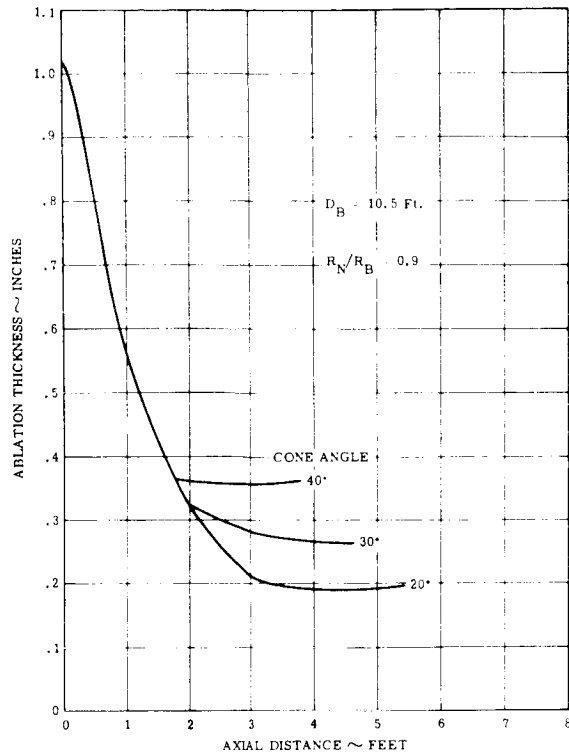


Figure 1.3.3-109 Venus Shield Ablation Requirements, Standard Atmosphere (25% CO₂)

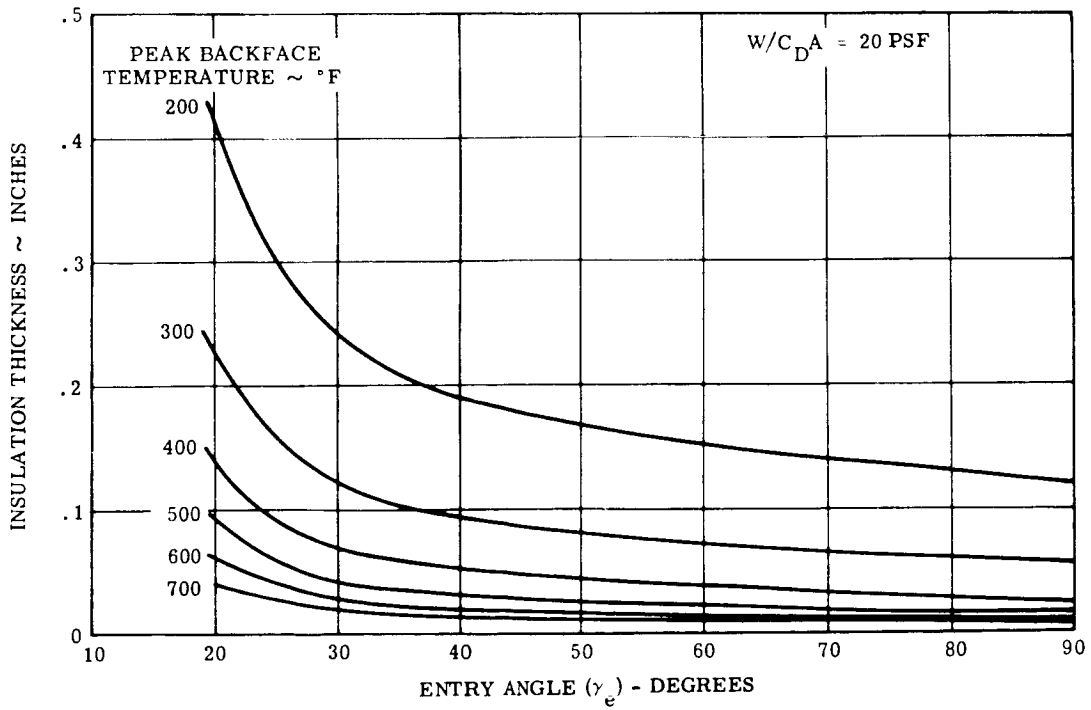


Figure 1.3.3-110 Insulation Requirements, Mars Mean Atmosphere

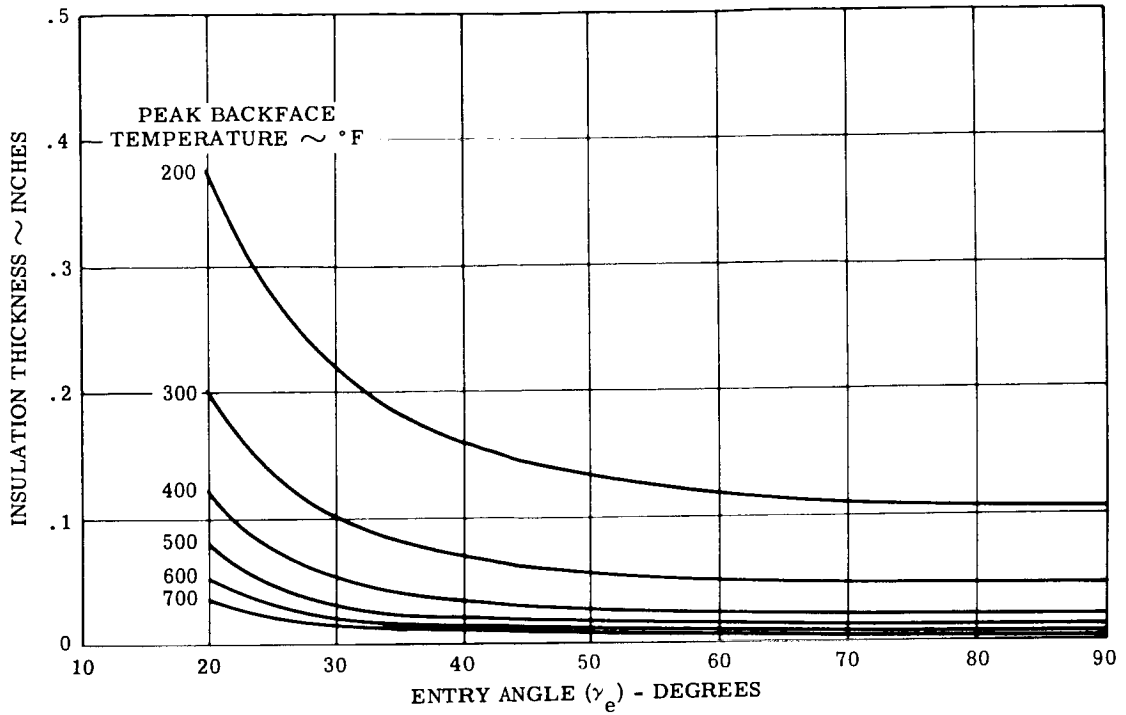


Figure 1.3.3-111 Insulation Requirements, Mars Mean Atmosphere ($W_{C DA} = 40$)

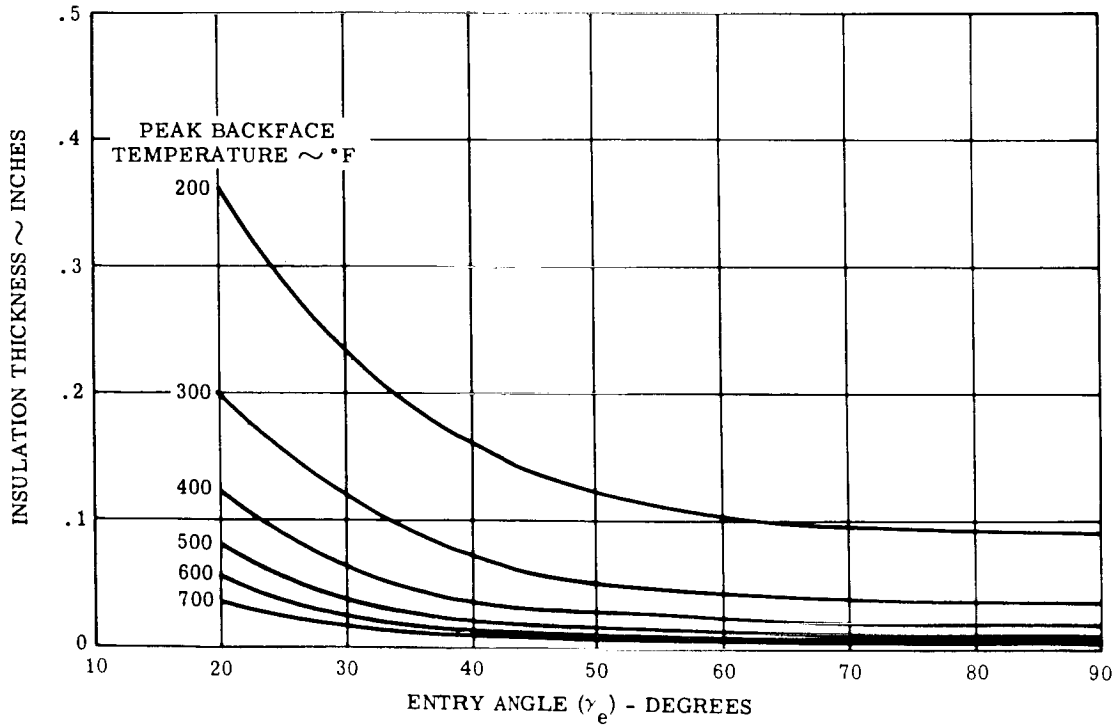


Figure 1.3.3-112 Insulation Requirements, Mars Mean Atmosphere ($W_{C DA} = 60$)

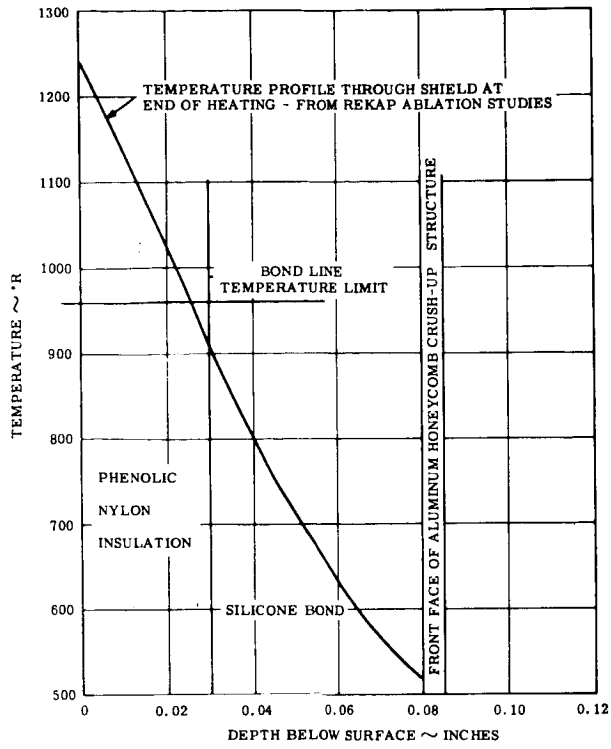


Figure 1.3.3-113 Typical Venus Insulation Requirements

1.3.4 STRUCTURAL ANALYSIS

A. Introduction

The structural analysis objective for the Voyager Study was to determine the type of structure and type of material that best suits the Lander requirements and the penalties for "off optimum" design. The results presented are for structural optimization and do not encompass the system considerations. See Section 1.3.8 for the system trade-off involving structural weight.

The structural analysis section also covers the analysis of impact structures, shield and structural compatibility; recommendations for further study are included.

(1) Design Philosophy

The Venus and Mars Lander structure was selected to withstand the following load condition:

Entry Angle, 90°
Peak axial load condition, $\left\{ \begin{array}{ll} G_{ax.} & \text{Max.} \\ G_{lat.} & 0 \end{array} \right.$
Angle-of-attack, 0°

For the range of vehicles considered the maximum g force varied from 69 to 113 for Mars entry and 185 to 340 for Venus entry.

The structural temperature was varied during the study since this characteristic is subject to system trade-off and optimization.

The impact structure was selected to maintain an impact g level equal to or less than 125 Earth g. This value was selected since it is representative of that which could be sustained by critical components. This value was treated, however, as a variable during the course of the study to obtain system trends trade-offs.

Boost loads (for the adapter design) were used as follows:

Axial 10 g's

Lateral 5 g's

The load factors used in the parametric systems studies for shell weight were:

Limit load factor 1.00

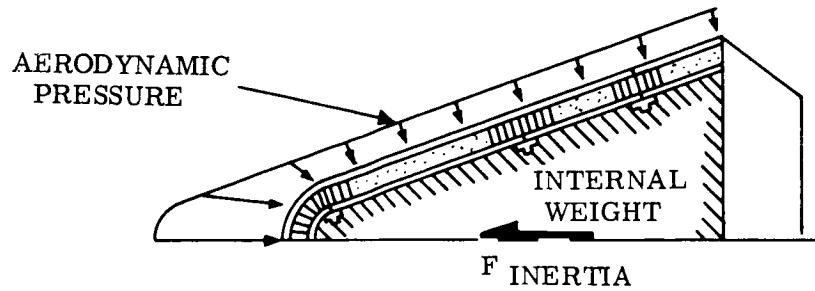
Ultimate load factor 1.25

For the bulkhead and adapter designs a 1.5 load factor was used. This factor was selected since the loading on these members could not be precisely defined. The materials and types of construction selected were those which had reliable design data and analysis. Exotic materials such as tungsten, tantalum, etc. and unusual methods of construction (fiber-reinforced plastics, etc.) were not considered because of state-of-the-art considerations.

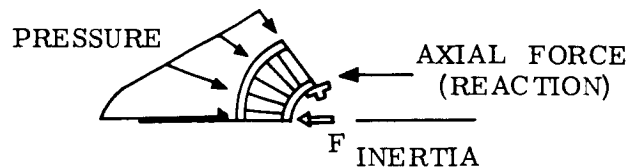
(2) General Vehicle Description

The vehicles investigated were all members of the general blunted sphere-cone family. The outer shell consisted of the thermal shield, crush-up material or filler, and metallic load carrying structure. The thermal shield provided heat protection only and was not assumed to resist any loading. The filler was provided to serve as a continuous back-up for the shield and to transfer the external pressure loads to the structural shell.

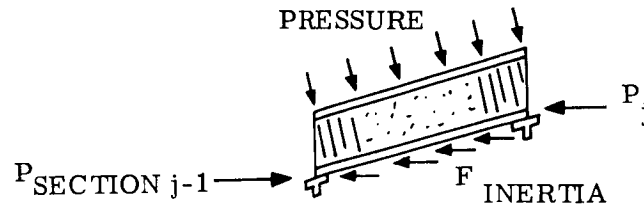
For the purposes of the parametric weight study, all internal equipment was assumed to be reacted along the shell. This condition is shown in the sketch below.



Considering each section of the vehicle; nose:

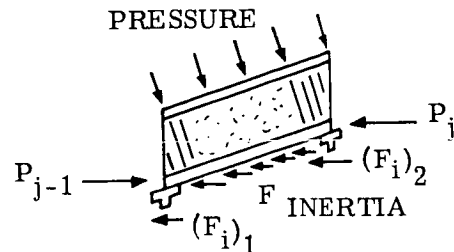


typical conical section (j)



Thus, all aerodynamic pressures are applied to the shield and transferred to the shell, and all inertia forces are applied directly to the shell. Crush-up forces are applied through the "hard spots" of crush-up material and reacted by the nose shell and support rings. In the actual hardware design, bulkheads are at this location.

The inertia loading is then revised as shown below for the conical section.



f_i = INERTIA FORCE DUE TO SHELL WEIGHT
 $(F_i)_n$ = BULKHEAD REACTIONS

B. Re-entry Vehicle Structural Optimization Program

The Re-entry Vehicle Structural Optimization Program is a preliminary design computation scheme programmed for use on the IBM 7094. Needing only the basic vehicle shape and loading environment (in terms of pressure distribution history), the program determines net structural loads. Using these loads, the program calculates for each section into which the vehicle is divided the required thicknesses and resulting structural weight as a function of structural temperature. This may be done for any combination or combinations of structural material and type of construction as follows:

<u>TYPES OF CONSTRUCTION</u>	<u>MATERIALS</u>
Monocoque	7075 aluminum
Honeycomb sandwich	2024 aluminum
Waffle-reinforced skin	Magnesium
Corrugated-sheet-stiffened single face	Beryllium
Corrugated-core sandwich	Phenolic glass
Ring-stiffened sheet	Stainless steel
	Vascojet steel
	Titanium

While the properties of the above materials are presently built into the program, any material may be studied by adding its properties to the program.

The objective of this Re-entry Vehicle Optimization Program is to develop a completely computerized IBM program which could be used to compare quickly the weight trends of many combinations of structural material and structural configurations (type of construction), as a function of structural temperature, so that the best combination for a particular application could be selected or the weight trade-offs among the various combinations could be run. In order to obtain realistic results, failure modes were considered which are as close as possible to those considered in the detailed stress analysis of a re-entry vehicle structure. These include over-all buckling, local buckling where applicable, and stress level including thermal stress. The von Mises yield criteria was used for the combined stress condition. Another important feature has been built into the program in order to obtain realistic results, namely, practical limits. For each material considered, a minimum sheet gage was specified which is a lower limit even if less thickness is actually required for strength. For all types of construction considered, minimum manufacturing requirements are imposed where applicable, such as minimum pitch and minimum depth on the corrugations, minimum thickness on the honeycomb sandwich core, etc.

Because the weights calculated in this program are primary load-carrying structure weights, they do not include such things as rivets, doublers, splices, bonds, and so on. However, a so-called "fabrication factor" has been included for each type of structure in order to make up for these miscellaneous items. These fabrication factors were determined based on past experience with each type of structure. Table 1.3.4-1 shows the predicted structural weight using the Optimization Program and the actual weight data from hardware programs.

TABLE 1.3.4-1. ACTUAL VERSUS PREDICTED WEIGHTS

Program	Predicted Weight (lb)	Actual Weight (lb)	Per Cent Difference
Mark 6 (Honeycomb)	186	202	7.9%
Skybolt (Ring-stiffened)	23	25	8.0%

A further discussion of the computer program is presented in Appendix A of this section.

(1) Matrix Studied

The vehicles evaluated during the parametric study phase were blunt sphere-cone vehicles. Bluntness ratios of .24, .60 and .90 were used. A sketch of these shapes is shown in Figure 1.3.4-1. The base diameter is variable and was selected to correspond to the gross weight of the vehicle as shown in Table 1.3.4-2. Cone half-angles of 20°, 30° and 40° were also considered. The specific vehicle weight-bluntness ratio-cone half-angle combinations investigated are shown in Table 1.3.4-3.

A more complete description of the configuration selection is given in Section 1.3.1.

TABLE 1.3.4-2. VEHICLE WEIGHT-DIAMETER RELATIONSHIP

Vehicle Gross Weight (lbs.)	Base Diameter (in.)
300	42
1500	96
2500	126

TABLE 1.3.4-3. VEHICLES STUDIED

Vehicle Weight (lbs.)	Bluntness Ratio Cone Half-angle (Deg.)		
	.24	.60	.90
300	30	30	30
1500	20	20	20
	30	30	30
	40	40	40
2500	30	30	30

The type of construction and material combinations initially investigated were:

<u>TYPE OF CONSTRUCTION</u>	<u>MATERIALS</u>
Monocoque	Aluminum
Honeycomb Sandwich	Magnesium
Waffle-reinforced skin	Beryllium
Corrugated-sheet-stiffened single face	Phenolic Glass
Ring stiffened sheet	Stainless Steel
	Titanium

All combinations were investigated in their applicable temperature range in the 70°-1000°F bracket. The specific combination of construction-material-temperature is shown in Table 1.3.4-4.

TABLE 1.3.4-4. STRUCTURAL MATRIX

Type of Construction	Material					
	Aluminum (°F)	Magnesium (°F)	Beryllium (°F)	Phenolic Glass (°F)	Titanium (°F)	Stainless Steel (°F)
Monocoque	100	100	100	100	100	100
	300	300	500	500	500	500
	500	500	900	900	900	900
	600	600	1000		1000	1000
Honeycomb Sandwich	100	100	100	100	100	100
	300	300	*	500	500	500
	*	*		*	900	900
					1000	1000
Waffle	100	100	100	100	100	100
	300	300	500	500	500	500
	500	500	900	900	900	900
	600	600	1000		1000	1000
Circumferential Corrugation	100	100	100	100	100	100
	300	300	500	500	500	500
	500	500	900	900	900	900
	600	600	1000		1000	1000
Ring-Stiffened	100	100	100	100	100	100
	300	300	500	500	500	500
	500	500	900	900	900	900
	600	600	1000		1000	1000

*Stress due to thermal gradient through thickness exceeded yield stress of material at next higher temperature investigated.

When considering the lower temperature regime of Mars, materials such as phenolic glass, stainless steel and titanium result in heavier structures than those obtained by aluminum, magnesium and beryllium. This consideration along with the fact that no gain is achieved in either the cost or manufacturing area by using the heavier metals, resulted in the emphasis of aluminum and magnesium for Martian vehicles. Beryllium, even with its attendant cost and fabrication penalties, was included because of its appreciable weight savings.

The 1050°F Venusian surface temperature dictates the choice of a medium temperature range material such as titanium, stainless steel and beryllium. Table 1.3.4-5 indicates the combinations studied for both the Mars and Venus entry.

TABLE 1.3.4-5. STRUCTURAL MATRIX (PLANETARY APPLICATION)

Type of Construction	Material					
	Aluminum	Magnesium	Beryllium	Phenolic Glass	Titanium	Stainless Steel
Monocoque	MARS	MARS	MARS VENUS	MARS VENUS	VENUS	VENUS
Honeycomb Sandwich	MARS	MARS	MARS VENUS	MARS VENUS	MARS VENUS	MARS VENUS
Waffle	MARS	MARS	-	-	-	-
Circumferential Corrugation	MARS	MARS	-	-	-	MARS VENUS
Ring-Stiffened	MARS	MARS	MARS VENUS	MARS VENUS	VENUS	VENUS

(2) Structural Loads

The load condition selected for the preliminary design of the study vehicles was that corresponding to the peak axial g condition at a zero degree angle-of-attack. The vehicle weight was assumed to be distributed throughout the internal volume at a constant packaging density. The choice of a zero degree angle-of-attack is considered realistic for this study, since investigation was conceptual by nature. The uniformly distributed internal weight will not be obtained in an actual hardware design. Packaging here will place the components on specific bulkheads with discrete load transfer points into the load-carrying shell. This perturbation will change the axial load condition but is not considered severe, since the external pressure, in general, is the more severe load contributor.

In a more detailed vehicle design analysis phase, the bulkhead locations and weight distributions can be considered.

Figures 1.3.4-2 through 1.3.4-7 present typical structural load results for the vehicles shown in Table 1.3.4-3 and for a 90° entry into the Mars Lower and Venus Standard atmospheres. Figures 1.3.4-8 and 1.3.4-9 illustrate the variation in peak dynamic pressure as a function of $W/C_D A$ for the previously stated conditions.

Figure 1.3.4-10 illustrates the effect of vehicle shapes on structural weight for the Mars vehicle. From a structural shell stand point an optimum bluntness ratio is about .7 regardless of cone angle, and the higher the cone angles the more efficient the structure. The evaluation of the optimum structure must be tempered by aerodynamic and vehicle system considerations and trade-offs

Figure 1.3.4-11 illustrates the effect of temperature and size on a basic structural weight. Note that temperature is not an important variable on the structural weight of small vehicles. Figure 1.3.4-12 is included for comparison with Figure 1.3.4-11 to illustrate the effects of material selection on structural weight. As mentioned above the trends are valid, but the results must be evaluated as part of a system trade-off.

The radius of structure was assume equal to the outside radius of the vehicle. When an appreciable difference in radii is obtained, as is the case when impact crush-up thicknesses becomes large, a correction must be applied to these weight values. For the honeycomb sandwich shell, this correction is

$$\text{Corrected Weight equals } \left(\frac{R_{\text{struct.}}}{R_{\text{shield}}} \right)^2 \cdot (\text{Weight given})$$

For the monocoque and ring-stiffened shells, this becomes

$$\text{Corrected Weight equals } \left(\frac{R_{\text{struct.}}}{R_{\text{shield}}} \right)^{1.6} \cdot (\text{Weight given})$$

where R is the radius to the respective elements.

The results of this study indicate the following trends.

- (1) Minimum weight structures for the aerodynamic load condition investigated occur for vehicles with a bluntness greater than .50. The minimum weight bluntness ratios for aluminum honeycomb sandwich (100°F) are:

Vehicle Gross Weight (lbs)	Cone Half-angle (deg)	Minimum Bluntness Ratio
300	30	.90
1500	20	.70
	30	.65
	40	.65
2500	30	.65

- (2) The honeycomb sandwich construction provides, in most cases, the minimum weight shell. The circumferential corrugation stiffened shell is competitive in weight only; difficulties in design, manufacturing and assembly make it much less desirable.
- (3) Beryllium provides the lightest material. It, however, has not progressed sufficiently to date for serious hardware application. Magnesium and aluminum are the next light-weight contenders with the emphasis being placed on aluminum for the primary material in this study because of its manufacturing ease. Magnesium is applicable for ring and fitting applications.
- (4) In almost all cases considered, an increasing cone half-angle resulted in a decreasing vehicle weight. This is shown in Figure 1.3.4-10.

Similar studies as those previously reviewed for Mars were conducted for a Venus entry. The primary difference in the two investigations was the use of higher temperature materials for the Venusian vehicles, namely, stainless steel and titanium. The vehicle weights were heavier due to the increased loading over the Mars entry. The types of construction-material combinations reported are

$\left. \begin{array}{l} \text{monocoque} \\ \text{honeycomb sandwich} \\ \text{ring stiffened} \end{array} \right\}$	$\left. \begin{array}{l} \text{beryllium} \\ \text{titanium (6AL-4V)} \\ \text{stainless steel (PH-15-7Mo)} \end{array} \right\}$
---	---

Comparison of Figures 1.3.4-13, 1.3.4-14, and 1.3.4-15 illustrates the effect of construction on the Venus Lander. Honeycomb sandwich construction shows a distinct advantage over ring-stiffened shell or monocoque. Comparison of Figures 1.3.4-15 and 1.3.4-16 illustrates the effect of materials on the shell weight of the Venus Lander. The use of titanium results in a lighter vehicle but as stainless steel is selected for the Venus Lander. Finally, Figure 1.3.4-17 illustrates the effects of shape on the structural shell weight. Unlike the Mars vehicle the optimum cone angle from a structural weight standpoint is 30° not 40°.

The pattern for minimum weight bluntness was not as consistent as that for the Mars vehicles. For the monocoque and honeycomb sandwich shells, the minimum weight bluntness is greater than .50. The ring-stiffened shell, however, has a minimum weight bluntness which varied through the range considered (.24 to .90). The additional variable of ring spacing is influential in this comparison.

(3) Conclusions and Discussion

The Mars Landers were able to utilize the common low temperature alloys such as aluminum and magnesium. Phenolic glass, beryllium, titanium and stainless steel were also investigated. The first phase minimum weight study eliminated all materials with the exception of aluminum, magnesium and beryllium. A further study of these materials was conducted for use in the monocoque, ring-stiffened and honeycomb sandwich types of construction. This resulted in the following comparison where the numbers 1, 2 and 3 indicate the weight in ascending order, 1 being the lightest.

Type of Construction	Operating Temperature	Beryllium	Magnesium	Aluminum
Monocoque	100°F	1	2	3
	500°F	1	2	3
Ring-stiffened	100°F	1	2	3
	500°F	1	2	3
Honeycomb Sandwich	100°F	-	1	2
	300°F	-	2	1

The surprising superiority of the magnesium sandwich construction is due to the fact that the Martian entry, even at a 90° entry angle, results in a low load environment. This in turn results in the utilization of minimum gage material. A minimum gage of .012 is used herein for both aluminum and magnesium. At an elevated temperature (300°F), where minimum gages are no longer applicable, aluminum is the lighter material.

On the basis of these studies, the selection of an aluminum honeycomb sandwich is recommended. This structure allows the reduction of thermal shield thickness to that which provides an outside face temperature of 300°F and provides the lightest structural weight at that temperature.

The effect of aerodynamic load carrying structure on vehicle geometry indicates the use of a 40° cone half-angle and a bluntness ratio of .65 from a structural standpoint.

The Venus Landers required the use of higher temperature materials such as stainless steel, titanium and beryllium. These materials when used in the previously discussed types of construction resulted in the following comparison (1 representing the lightest approach).

Type of Construction	Operating Temperature	Beryllium	Titanium	Stainless Steel
Monocoque	100°F	1	2	3
	800°F	1	2	3
Ring-Stiffened	100°F	-	1	2
	800°F	-	1	2
Honeycomb Sandwich	100°F	-	1	2
	800°F	-	1	2

Of the above combinations, titanium honeycomb sandwich represents the minimum weight approach. A study of the 1500 pounds vehicle indicates that the minimum weight combination for bluntness less than .6 requires the use of 40° cone half-angle.

The above selection of titanium was on a minimum weight basis only. Stainless steel does not represent an appreciable weight increase and in the final analysis (when material "know-how", cost, development, etc. is considered), this may be the most feasible material.

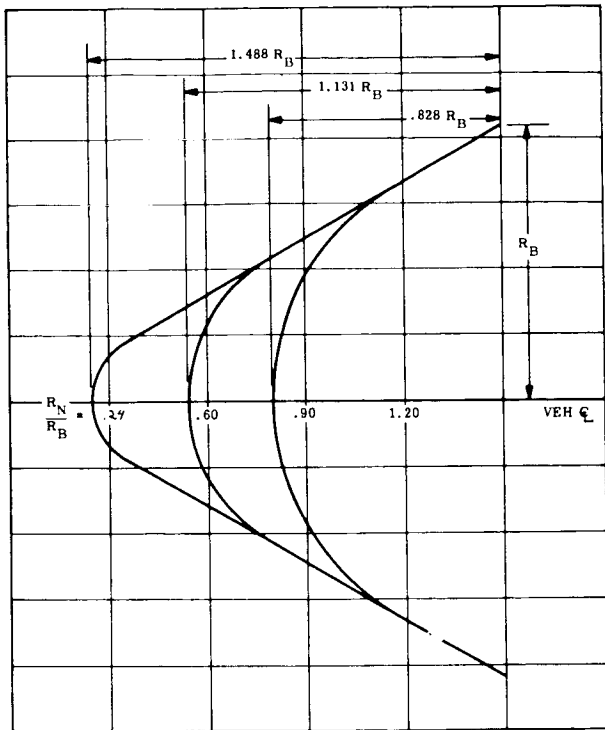


Figure 1.3.4-1. Blunt Vehicle Configurations

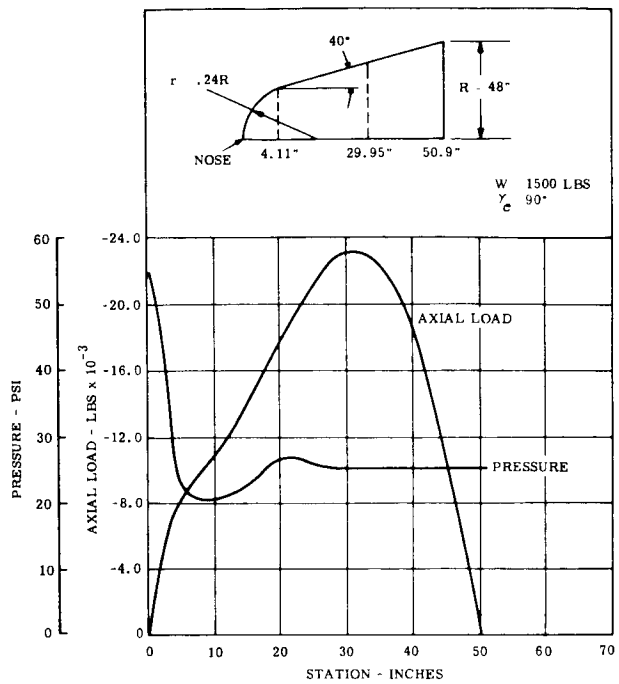


Figure 1.3.4-2. Structural Loads and External Pressure - Mars Lander

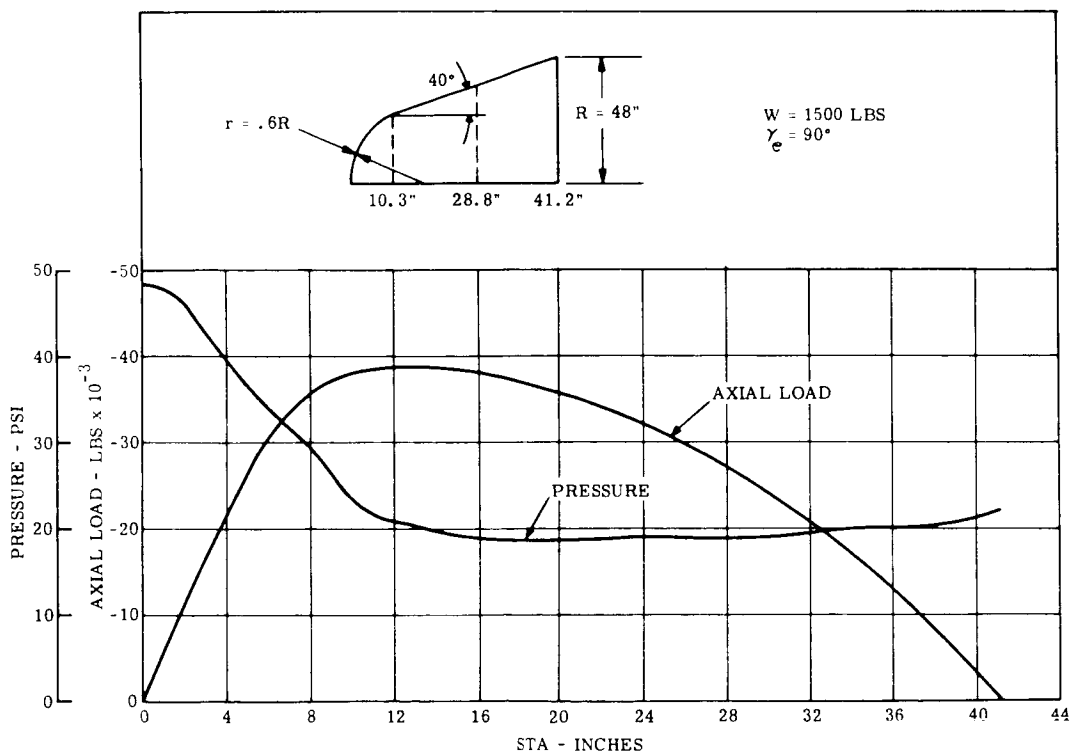


Figure 1.3.4-3. Structural Loads and External Pressure - Mars Lander

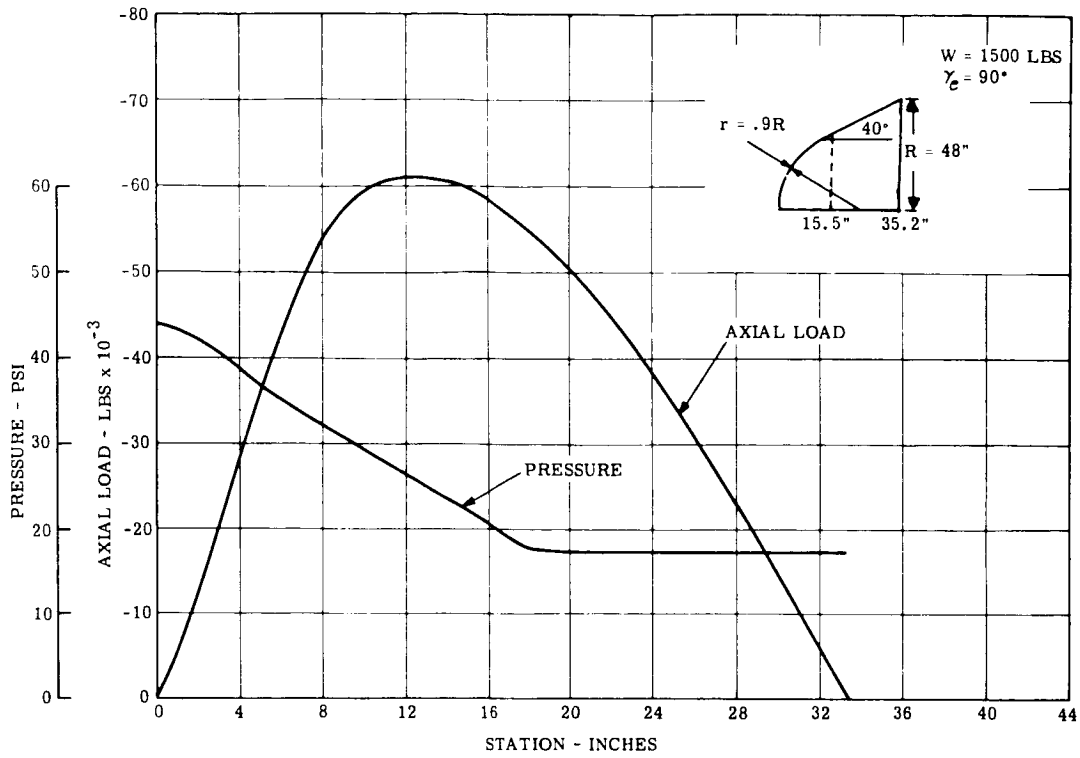


Figure 1.3.4-4. Structural Loads and External Pressure - Mars Lander

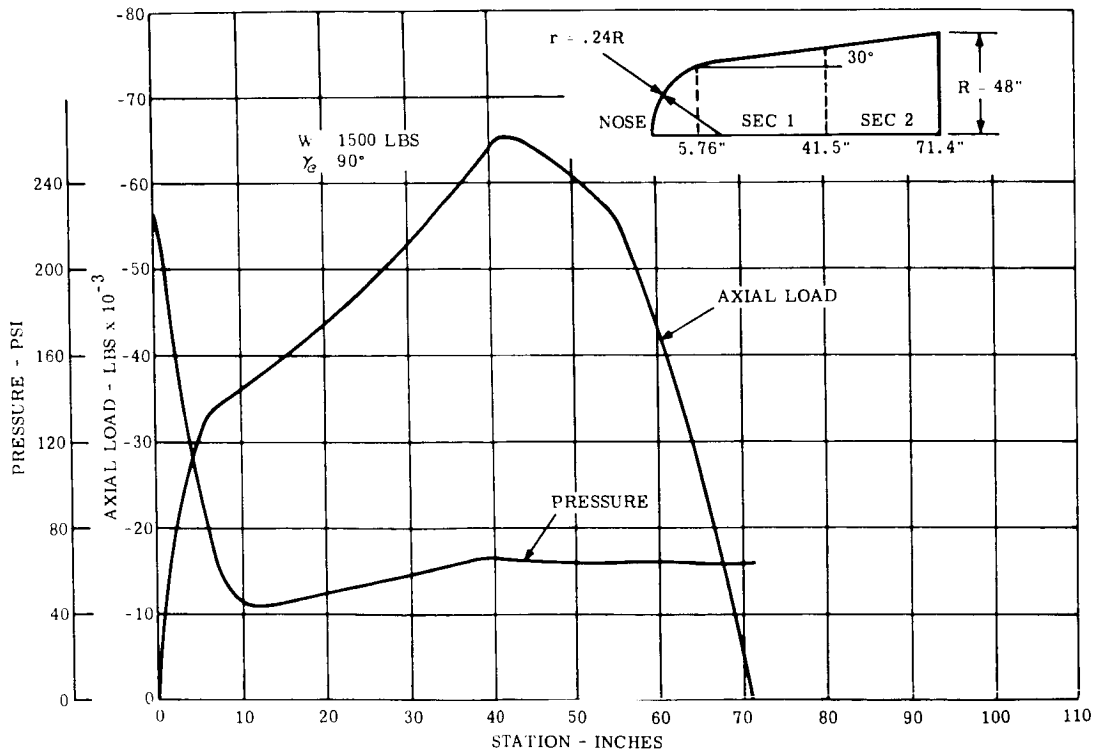


Figure 1.3.4-5. Structural Loads and External Pressure - Venus Lander

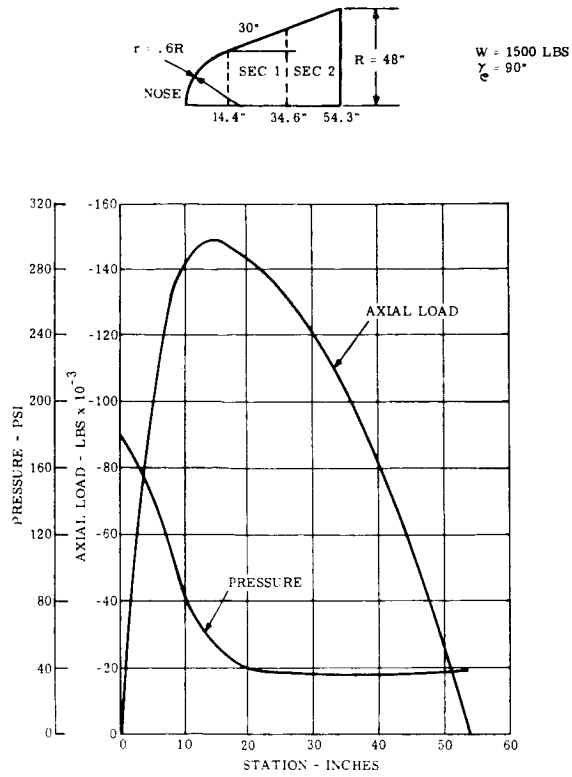


Figure 1.3.4-6. Structural Loads and External Pressure - Venus Lander

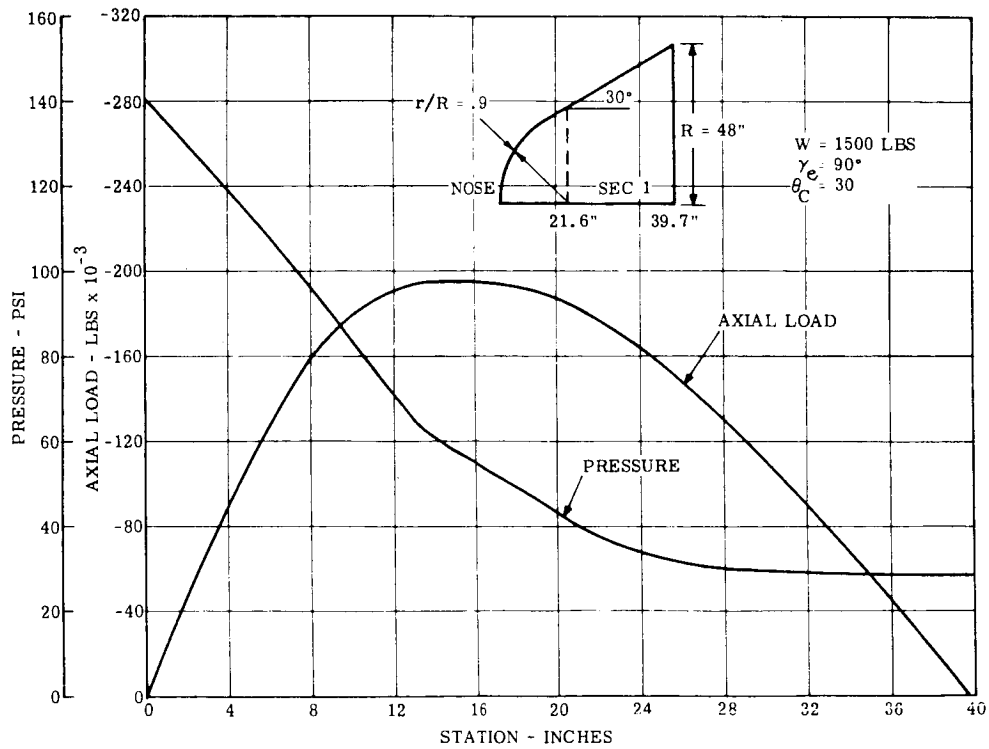


Figure 1.3.4-7. Structural Loads and External Pressure - Venus Lander

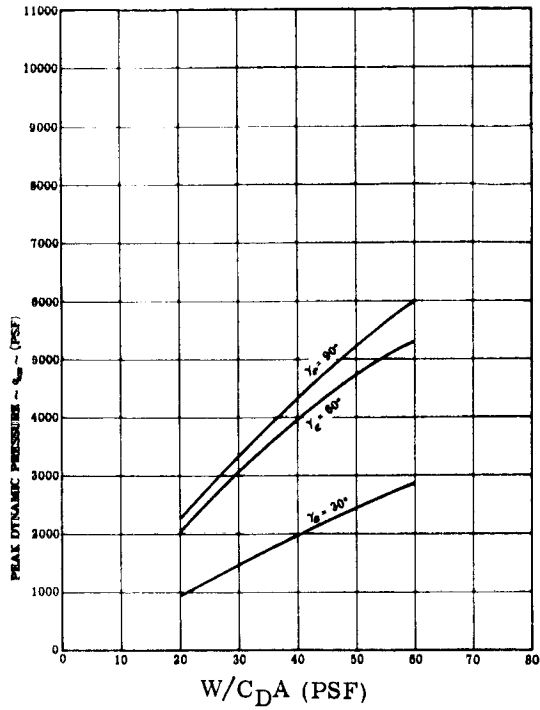


Figure 1.3.4-8. Dynamic Pressure Vs Ballistic Parameter - Mars Standard Atmosphere

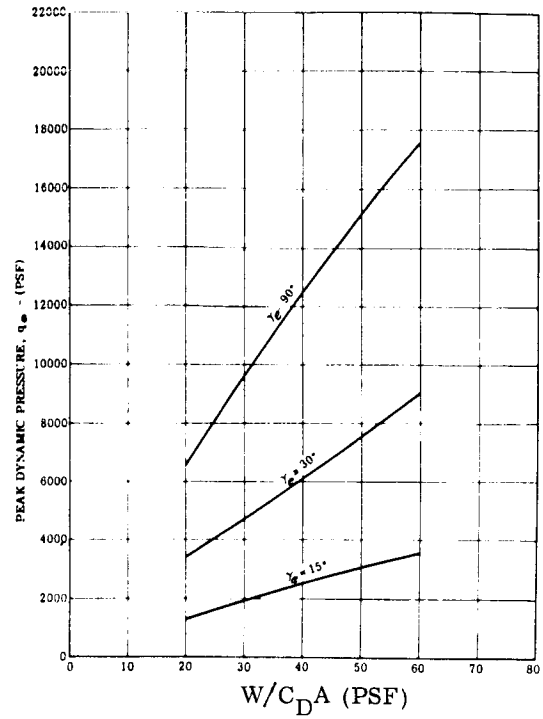


Figure 1.3.4-9. Peak Dynamic Pressure Vs Ballistic Parameter, Venus Standard Atmosphere

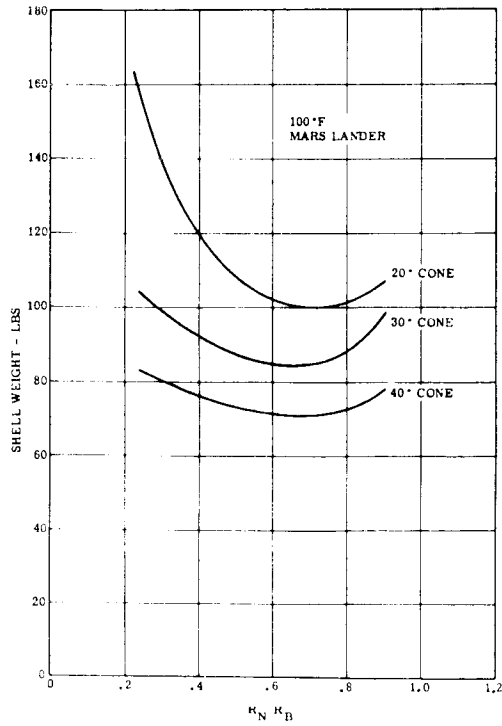


Figure 1.3.4-10. Effect of Vehicle Shapes on Weight (1500 lb. Vehicle, Honeycomb Sandwich Shell Construction of Aluminum)

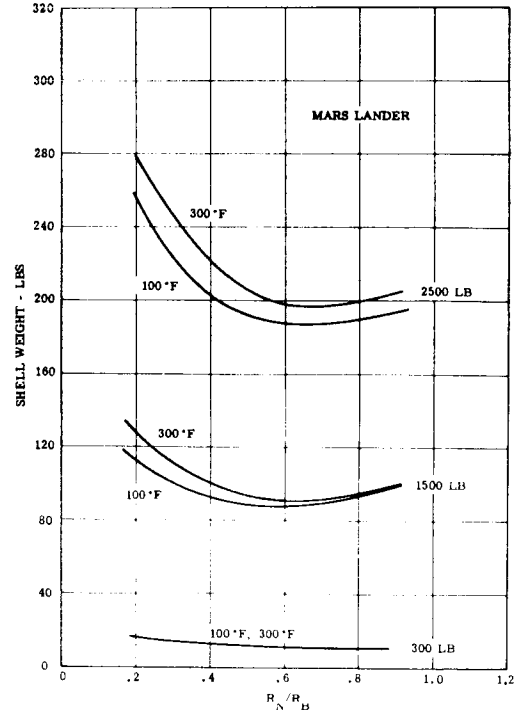


Figure 1.3.4-11. Effect of Vehicle Shapes on Weight (Honeycomb Sandwich Shell Construction of Aluminum)

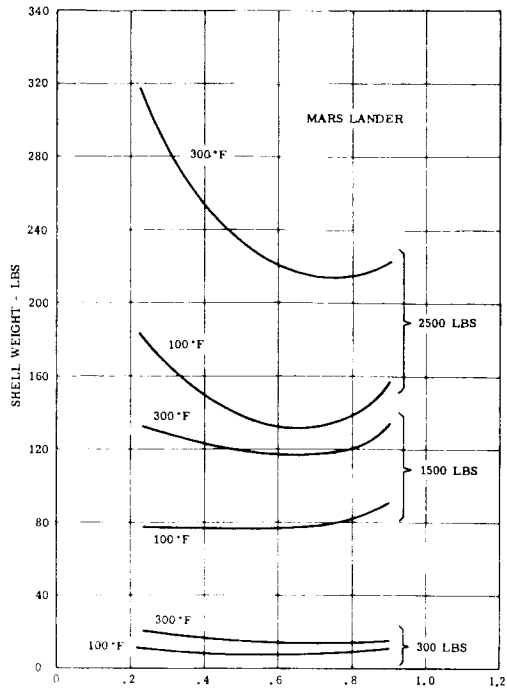


Figure 1.3.4-12. Effect of Vehicle Shapes on Weight (Honeycomb Sandwich Shell Construction of Magnesium)

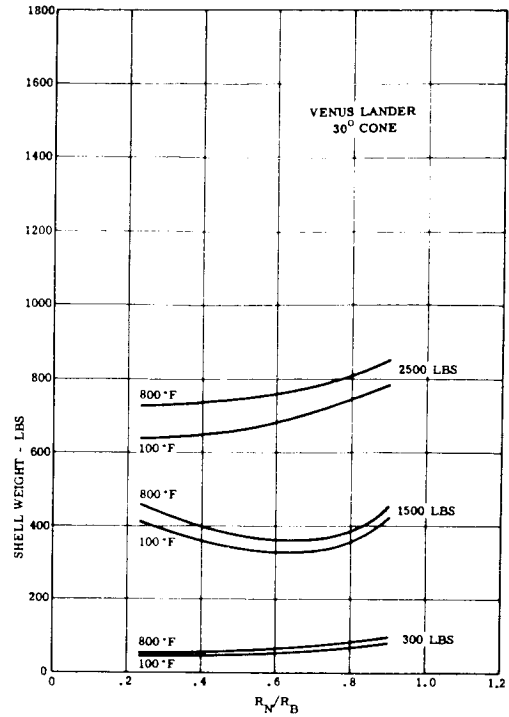


Figure 1.3.4-13. Construction Effects (Ring-Stiffened Stainless Steel)

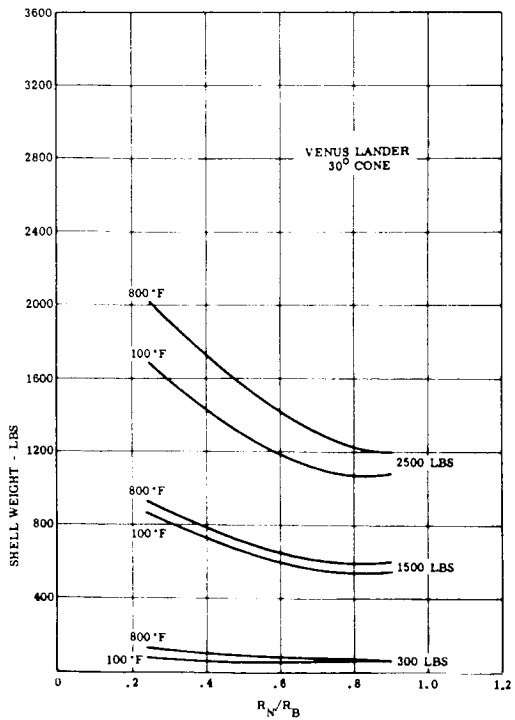


Figure 1.3.4-14. Construction Effects (Monocoque Shell, Stainless Steel)

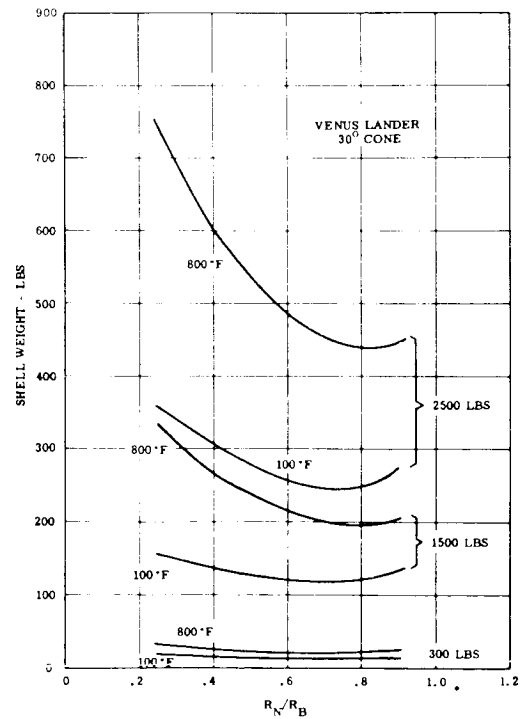


Figure 1.3.4.15. Construction Effects (Honeycomb Sandwich, Stainless Steel)

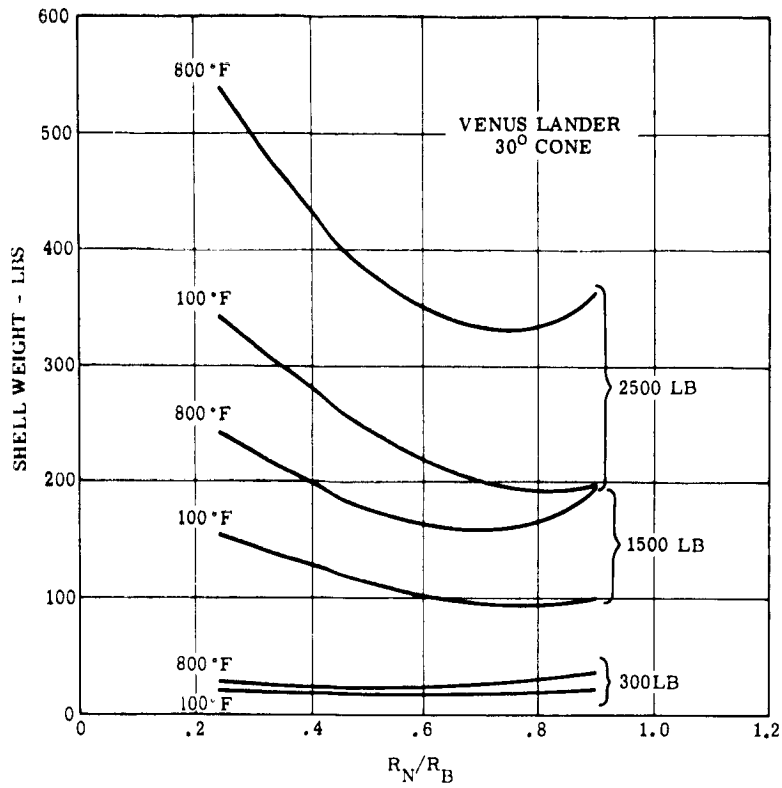


Figure 1.3.4-16. Effect of Materials on Weight (Honeycomb Sandwich Shell, Titanium)

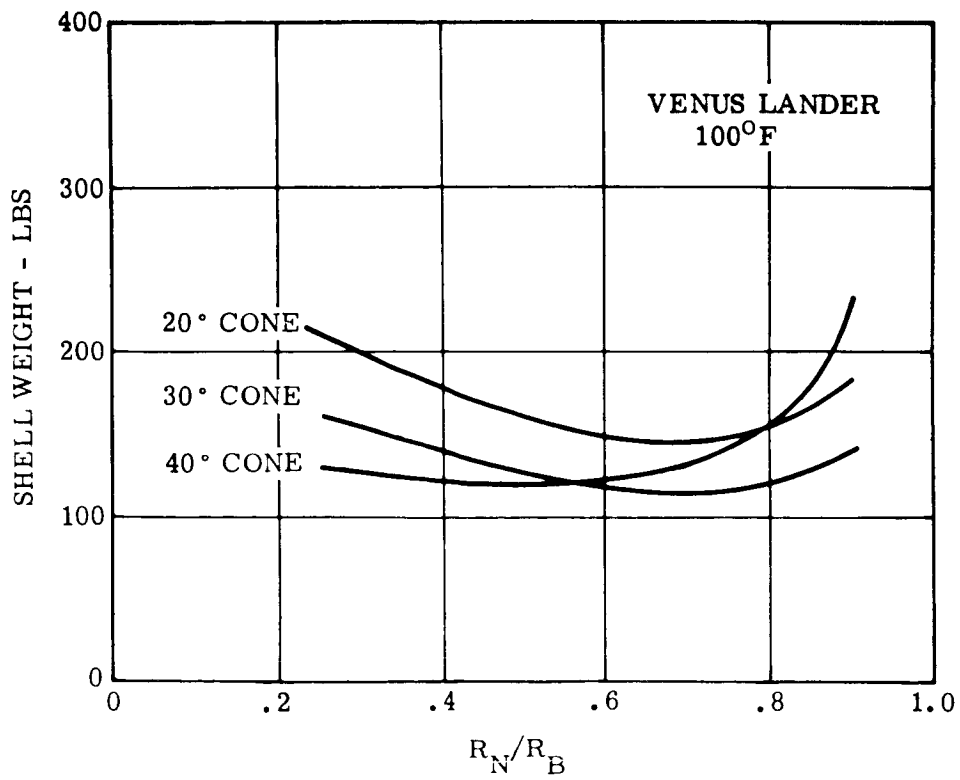


Figure 1.3.4-17. Effect of Materials on Weight (1500 lb. Vehicle, Honeycomb Sandwich, Stainless Steel)

C. Impact Structure

(1) Discussion

The function of an impact landing system for space vehicles is to absorb and dissipate the kinetic energy of the vehicle by decelerating it in such a manner that the forces transmitted to the components do not exceed the component capability. Superimposed on this basic requirement are additional requirements such as the ability to function under non-ideal impact surface conditions, low weight and package volume, the ability to perform other functions than its primary one during the transit phase, and it must have a high degree of predictability and reproducibility. In the case of a particular planetary landing, the impact system must be optimized with the parachute system for the best compromise of weight and reliability for the given required performance.

Apart from the engineering problems associated with an impact system there is also the problem of impact surface definition. Although some estimates for Martian surface indicate that it is probably covered with a thin layer of fine sand or silt, for design purposes the surface crust is assumed to be composed of a random mix of hard rock in a relatively flat setting with an average slope of 30 degrees. The design maximum surface winds were 40 mph. A surface temperature of -40 F is expected.

Even less is known about the Venusian surface. The best estimate at present is a surface similar to Mars or Earth with the possibility of winds up to 200 mph. A surface temperature of 1050 F is expected.

A number of impact landing systems have been developed or proposed as a result of engineering activities spent in the field of air-dropped cargo protection, instrumented packages from missiles, data capsules from nose cones, and manned and unmanned satellite recovery. General Electric Company has successfully employed foam material as the primary impact protection for its data capsule and performed design and testing work on crushable aluminum honeycomb for primary impact of unmanned satellite. The landing-impact energy dissipation for the various systems depends on the normal velocity of the vehicle at contact, the stroke geometry of the system, and the useable energy of the dissipation material. In the case of parachute letdown, where descent velocity is greater than the wind velocity, such systems as gas-filled bags, collapsible struts, foams, honeycombs, braking rockets, and collapsible and frangible tubes appear feasible. When the wind velocity exceeds the descent velocity and long runout is of primary concern, such systems as skids, landing gears, and strain-strap shock absorbers must be considered. The combination of wind and descent velocity for a Mars landing is felt to be within the former systems. Due to a lack of wind velocity definition on Venus, the assumption is made that it is no more severe than the Martian wind, hence, no further discussion of the above latter system will be made. If the 200 mph wind on Venus is confirmed, then a design study will be initiated on these latter systems.

A cursory review of available literature on the advantages and disadvantages of the remaining energy dissipating systems was made. References 1, 2, 3 and 4 were utilized for this review. Some of the items considered were: packaging efficiency, weight, pulse shape, stroke range, temperature range, simplicity, possible dual function in mission, springback, load orientation sensitivity, material state of the art and how each system could be incorporated in the going design. The conclusions reached after this study are:

1. For primary impact, or that portion of the impact sequence from initial touchdown up to the point of vehicle side contact, a crushable honeycomb design should be given prime consideration. A gas-filled bag system is good back-up design to be carried along until the feasibility of the honeycomb system is proven.

2. For secondary impact, or side contact of the vehicle and ground, the same approach as above should be used, although the gas-filled bag system looks much more promising for secondary impact than for primary impact.

Having made the selection for both primary and secondary impact systems, a parametric study must be made to evaluate the weight of the impact systems as a function of descent velocity, deceleration, stroke and vehicle total weight such that an optimum parachute-impact system can be found.

The vehicle is assumed to approach the impacting surface at a vertical velocity equal to the descent velocity (V_D) and a horizontal velocity equal to the wind velocity (V_W). The resultant velocity is then resolved into components parallel (V_T) and normal (V_N) to the ground surface. The maximum normal velocity occurs when the vehicle-ground orientation is as shown in Figure 1.3.4-18 (a). The maximum tangential velocity would occur when the vehicle-ground orientation is as shown in view (b). However, in this configuration a large part of the energy is expected to be absorbed in sliding friction. Hence, view (c) is assumed to represent the configuration at which all the tangential velocity is converted into rotational energy. Thus, the primary impact structure will be designed using the maximum normal velocity as shown in view (a), Figure 1.3.4-18 and given in Figure 1.3.4-19. The secondary impact structure will be designed for a normal velocity at impact equal to the wind velocity of 40 mph. However, there is indeed a definite need for further study in this area of vehicle body motion from primary to secondary impact, upon impacting an inclined surface.

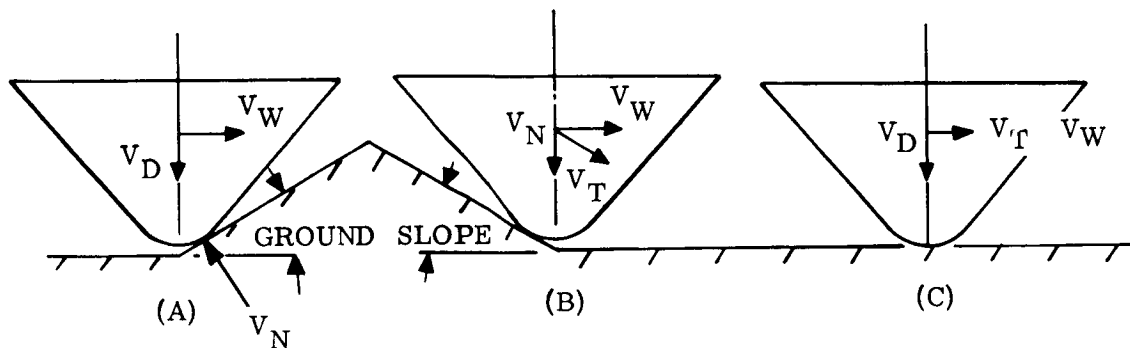


Figure 1.3.4-18. Impact Attitude of Vehicle

(2) Generalized Curves

The following curves represent that portion of the detail impact system design which is applicable to both Mars and Venus Landers. These curves show the trade-offs between wind velocity, descent velocity, deceleration, stroke, vehicle weight and kinetic energy. Figure 1.3.4-19 represents the variation of the maximum velocity normal to the structure surface, with descent velocity, and ground slope for a wind velocity of 40 mph. Figure 1.3.4-20 shows the variation in stroke, deceleration and maximum normal velocity, and Figure 1.3.4-21 represents the kinetic energy to be absorbed for a given vehicle weight and normal velocity.

(3) Mars Vehicle

(a) Design Conditions and Concept

The following represents a list of the design conditions and assumptions made in order to obtain the detailed design parameters of an impact system for the Mars Lander.

Primary Impact

1. Properties of the crushable material are isotropic and are represented by Figure 1.3.4-22. This data was obtained from References 5 and 6.
2. Design wind velocity is 40 mph or 58.6 f.p.s.
3. Maximum ground slope angle of 30 degrees.
4. Expected chute sway angle of 5 degrees will be neglected in this study, since it has no effect on normal impact velocity and only shifts the point of impact on the vehicle.
5. Efficiency of crushable honeycomb material is 70%, although slightly higher values have been observed.
6. Honeycomb is vented and precrushed
7. A rectangular pulse shape can be achieved.
8. Impacted surface is rigid, thus, the crushable structure will be designed to absorb all the kinetic energy at impact.
9. Temperature effects are secondary.
10. Velocity normal to vehicle structure is absorbed by primary impact structure.
11. Design concept is to provide a sufficient thickness and volume of crushable material in the 30 degree half cone region as indicated in Figure 1.3.4-23.

Secondary Impact

1. Design concept is to provide a sufficient thickness and volume of crushable material adjacent to the hard points at the bulkheads as indicated in Figure 1.3.4-23.
2. Design velocity at secondary impact is the wind velocity of 40 mph.

(b) Material Selection and Construction

This study is based on the material property data given in Figure 1.3.4-22. This data is assumed to be representative of either an aluminum or a fiberglass honeycomb and, through mechanical construction, to be insensitive to loading direction. Available energy absorption property data on fiberglass honeycomb is scarce; however a recent contract awarded to G.E. from JPL to determine these properties for several configurations of fiberglass honeycomb should provide the data verification needed. In addition, efforts are currently being made to obtain similar data on titanium, and steel honeycombs as well as foams. As this data becomes available, it will be factored into the design, should a higher temperature material be required.

The vehicle geometry and construction is shown in Figure 1.3.4-23. By holding the outer contour essentially fixed and varying t_p , t_s , S , P_p , and P_s various vehicle weights, impact velocities, and decelerations can be accommodated.

The inner radius (R_i) represents the contour of the honeycomb shell design that supports the primary crush-up. A weight study was made on this back-up structure as a function of the radius and the crushing stress of the honeycomb. The results are given in Figure 1.3.4-24. The bulkheads required to mount components are felt to be adequate for supporting the secondary crush-up.

Finally, having selected sufficient parameters from Figures 1.3.4-21 to define the stroke for both primary and secondary impact, the volume that is actually crushed during both primary and secondary impact as well as the total volumes required to accommodate the random orientation of the vehicle can be determined. These volumes are plotted on Figure 1.3.4-25 for primary impact and Figure 1.3.4-26 for secondary impact for the geometry shown in Figure 1.3.4-23.

(c) Design Parameters

Figures 1.3.4-19 through 1.3.4-26 represent the curves required to determine the total weight of an impact system as a function of deceleration and normal impact velocity. An example calculation follows:

Data Given:

Vehicle Impact Weight = 1150 lb.

Velocity wind = 40 mph

Nose Radius = 16 in.

Assumed Data:

Max. Normal Velocity = 80 fps

Deceleration = 300 g's

From Figure 1.3.4-19

$V_D = 58.6$ fps

From Figure 1.3.4-20 for primary impact

Stroke = 4 in

Thickness = $\frac{4}{0.7} = 5.7$ in

From Figure 1.3.4-20 for secondary impact at $V_n = 40$ mph

Stroke = 2.15 fps

Thickness = $\frac{2.15}{0.7} = 3.1$ in

From Figure 1.3.4-21

Primary Impact KE = 115,000 ft-lb

Secondary Impact KE = 62,000 ft-lb

From Figure 1.3.4-25 for primary impact

Volume crushed = 1400 in³

Total volume = 4000 in³

From Figure 1.3.4-26 for secondary impact

$$\text{Volume crushed} = 400 \text{ in}^3$$

$$\text{Total volume} = 4200 \text{ in}^3$$

For Primary Impact

$$\frac{\text{K. E.}}{\text{Vol. Crushed}} = \frac{115,000}{1400} = 82 \frac{\text{ft-lb}}{\text{in}^3}$$

and from Figure 1.3.4-22

$$\text{Crushing stress} = 1280 \text{ psi}$$

$$P_p = 15.2 \text{ lbs/ft}^3$$

For Secondary Impact

$$\frac{\text{K. E.}}{\text{Vol. Crushed}} = \frac{62,000}{400} = 155 \frac{\text{ft-lb}}{\text{in}^3}$$

and from Figure 1.3.4-22

$$\text{Crushing stress} = 2420 \text{ psi}$$

$$P_s = 22.2 \text{ lb/ft}^3$$

From Figure 1.3.4-24 at crushing stress = 1280 psi and nose radius = 16.0 in.

$$\text{Weight Primary Support Structure} = 13 \text{ lbs.}$$

$$\begin{aligned} \text{Wt. Primary Honeycomb} &= (V_T) (P_p) = \frac{4000}{1728} (15.2) \\ &= 35.2 \text{ lbs} \end{aligned}$$

$$\begin{aligned} \text{Wt. Secondary Honeycomb} &= V_T (P_s) = \frac{4200}{1728} (22.2) \\ &= 54 \text{ lbs} \end{aligned}$$

$$\text{Total Weight} = 54 + 35.2 + 13 = 102.2 \text{ lbs.}$$

Similar calculations were made varying the deceleration and max. normal velocity for primary impact. The results are shown in Figure 1.3.4-27

(4) Venus Vehicle

(a) Design Conditions and Concept

The design conditions and concepts outlined for the Mars Lander also pertain to the Venus Lander. The main concern here is the possibility of a much higher wind velocity which may dictate a different type impact system.

(b) Material Selection and Construction

Again the material selection and construction is similar to the Mars Lander. However, due to the 1050° F surface temperature expected, the energy absorption properties of higher temperature honeycombs such as titanium and steel must be obtained.

(c) Design Parameters

Because of the more dense atmosphere on Venus, only a drag plate is required to regulate the descent velocity of the Lander, and thus there is no requirement to optimize the parachute-impact systems. The 550 pound Venus Lander was investigated to show the variation of impact system weight due to normal velocity and deceleration. The same curves were used as for the Mars Lander, and the results are given in Figure 1.3.4-28

(5) Problem Areas

The main problem area encountered during this study was in the area of impact motion and attenuation devices. This problem area encompassed:

- (1) landing terrain definition,
- (2) environmental force (continuous winds and gust) definition,
- (3) component performance level (maximum impact G's),
- (4) motion analysis (including energy absorption) of vehicle after impact, and
- (5) reliable performance estimates (including test data) of the many primary and secondary concepts.

(6) Development Programs

The following analytical tools must be developed in the area of vehicle impact.

- (1) A vehicle motion computer program which incorporates vehicle geometry (such as cone angle, bluntness ratio), velocity (vehicle and horizontal), terrain (energy absorption capacity, slope, etc.) and energy absorption variables.
- (2) Methods of analysis for energy absorption system comparison, including vehicle geometry influence.

Structural and material test programs must be conducted to:

- (1) determine energy absorption properties of elevated temperature crush-up materials; phenolic glass honeycomb, steel or titanium honeycomb, etc.,
- (2) substantiate present design approach by drop tests of "boiler plate" models,
- (3) substantiate stability predictions of honeycomb sandwich conical shells,
- (4) determine mechanical data of ESM and foam materials,
- (5) evaluate other impact concepts.

REFERENCES

1. Fisher, Jr., Lloyd, J., "Landing-Impact-Dissipation Systems," NASA TN D-975, December, 1961.
2. Fisher, Jr., L. J., "Landing Energy Dissipation for Manned Re-Entry Vehicles," NASA TN D 453, September, 1960.
3. Coppa, A. P., "Collapsible Shell Structures for Lunar Landings," American Rocket Society 2156-61, October, 1961.
4. O'Bryan, T. C., Hatch, Jr., H. G., "Limited Investigation of Crushable Structures for Accel. Protection of Occupants of Vehicles at Low Speeds," NASA TN D158, October, 1959.
5. Hexcel TSB-110, "Energy Absorption Properties of Aluminum Honeycomb," January, 1960.
6. Lewallen, J. M. and Ripperger, E. A., "Energy-Dissipating Characteristics of Trussgrid Aluminum Honeycomb," SMRL RM-5, March, 1962.

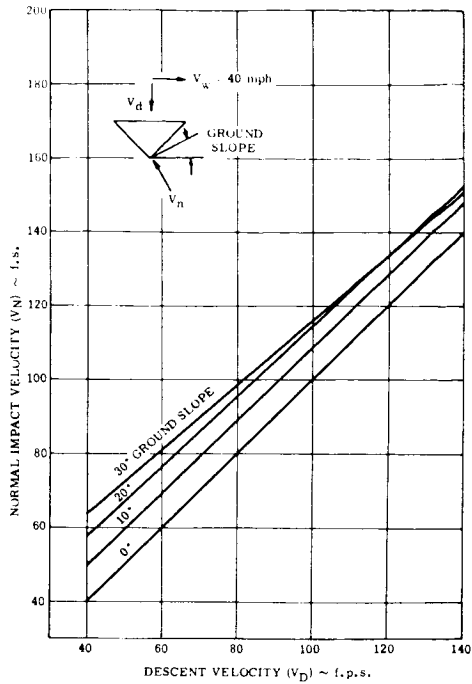


Figure 1.3.4-19. Normal Impact Velocity

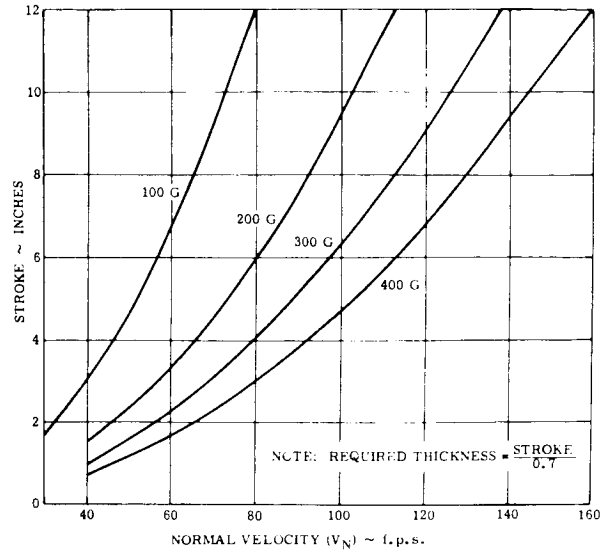


Figure 1.3.4-20. Required Stroke Vs Normal Velocity for Various Deceleration Rates

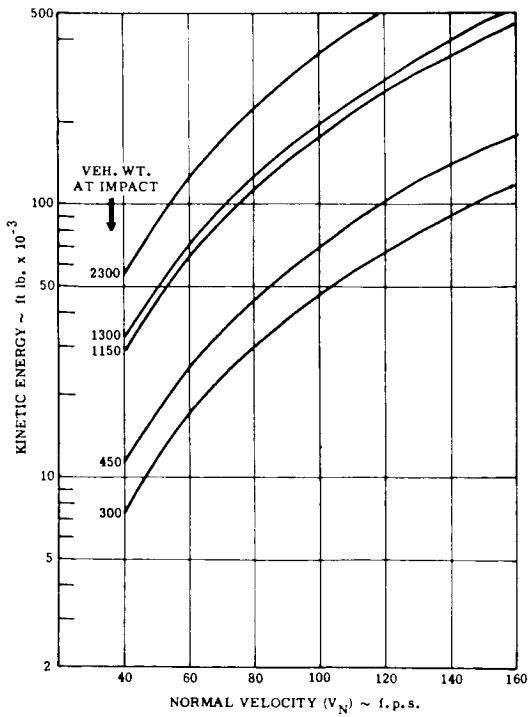


Figure 1.3.4-21. Vehicle Kinetic Energy Vs Normal Velocity

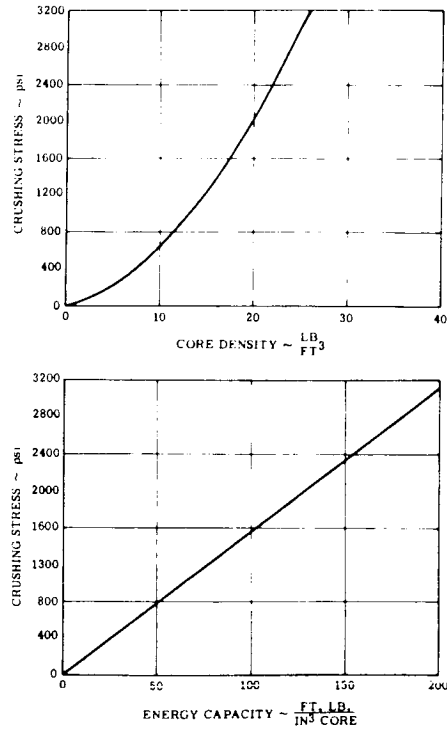


Figure 1.3.4-22. Material Energy Absorption Properties

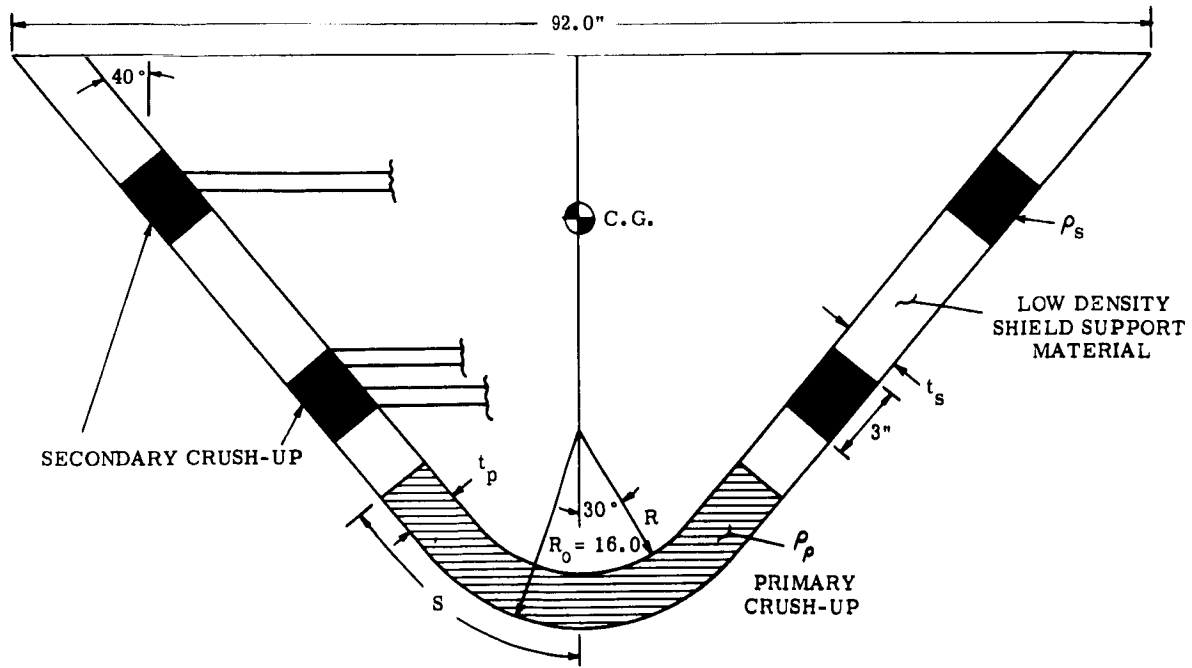


Figure 1.3.4-23. Vehicle Geometry

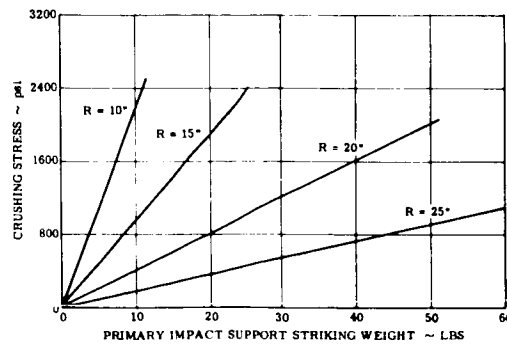
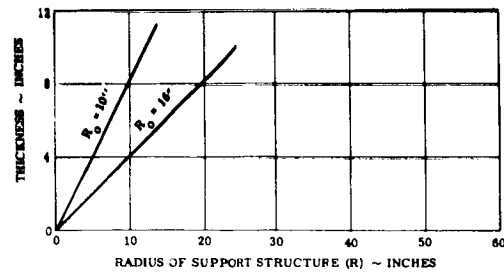


Figure 1.3.4-24. Primary Impact Support Structure Weight

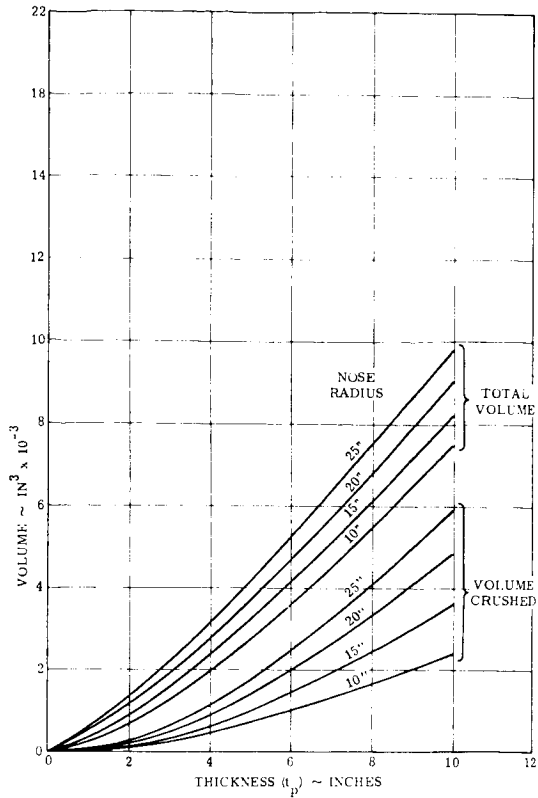


Figure 1.3.4-25. Primary Impact Volume

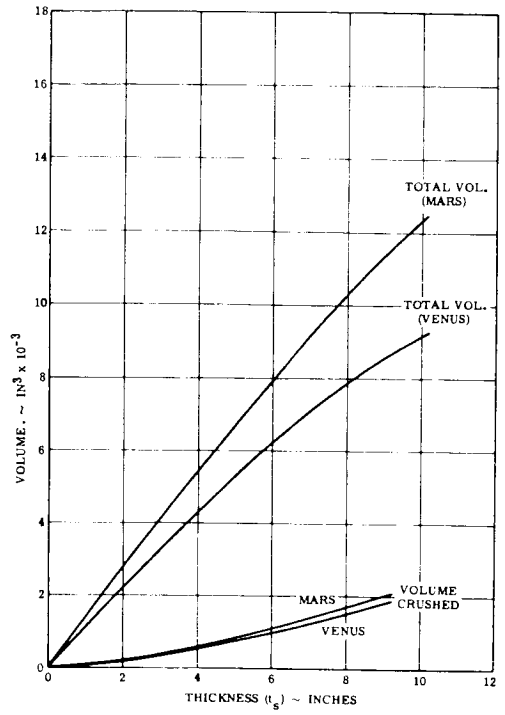


Figure 1.3.4-26. Secondary Impact Volume

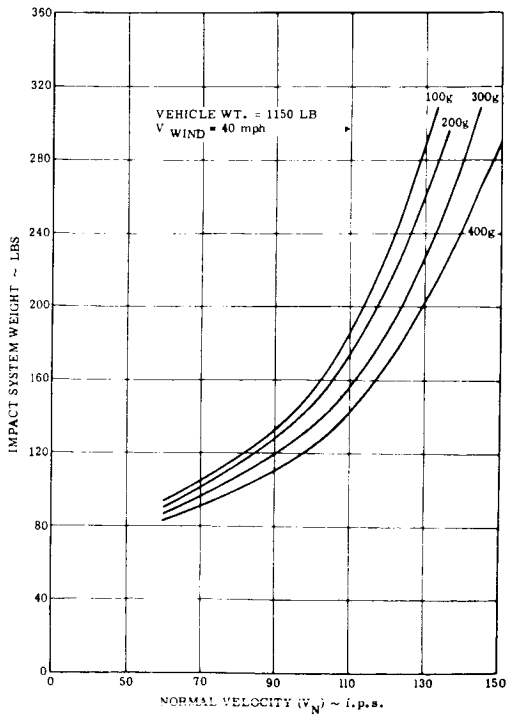


Figure 1.3.4-27. Mars Lander Impact System Weight

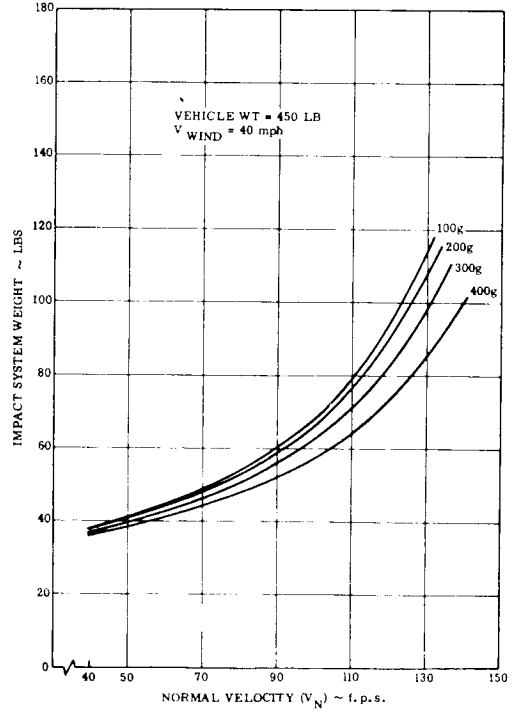


Figure 1.3.4-28. Venus Lander Impact System Weight

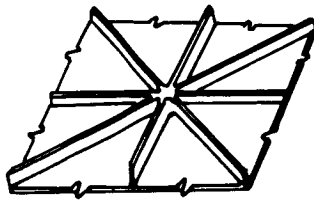
APPENDIX A

STRUCTURAL OPTIMIZATION PROGRAM

A schematic diagram of the Program is shown in Figure 1.3.4-29 (Reference 1). A description of the types of construction incorporated in this program follows. Three types of structures have been considered but present difficulties in utilization (especially when considering titanium alloys) are:

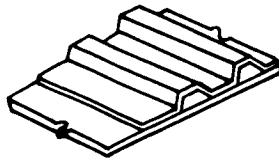
(1) Waffle Construction

This type of construction has become more prominent with the advancing technique of chemical milling. With this type of construction, the axial and hoop loads will be directed by oriented ribs providing optimum load paths.



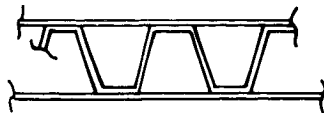
(2) Single-Face Circumferentially Corrugated Shell

In a pure monocoque structure the material is not being worked to its maximum allowable stress, therefore, material is carried as a weight penalty. Ring stiffening aids in the reduction of this weight by attempting to close the gap between failure in buckling and failure in yield. Often the number of rings and their spacing required is not practical. A corrugated-stiffened sheet optimizes this condition.



(3) Longitudinally Corrugated Sandwich Shell

This type of construction basically acts with the same concept advantages as honeycomb sandwich. However, the limitations of adhesive bonded or brazed sandwich are avoided by utilizing the welded corrugated sandwich.



A. Construction Studied

(1) Monocoque Shell

This is the most conventional type of shell considered. It is a conical shell of uniform thickness supported only at its ends. The fabrication of this type of shell is relatively simple, since the shell consists merely of rolled sheet material spliced longitudinally and stiffened at the ends by the addition of rings or bulkheads.

The primary disadvantage of this shell is its weight. Because of the long cylinder length commonly encountered in vehicle design, buckling is the main design consideration. Thus, the shell thickness is large and the material is working well below its yield stress. A sketch of this type of construction is given in Figure 1.3.4-30(a).

The equations used in the analysis of this type of structure are as follows. The buckling equation represents a linear interaction between axial load and external pressure. This equation is

$$q_{cr} = \frac{-2.63 E \left(\frac{h}{2R_c}\right)^{2.5}}{\frac{L_e}{2R_e} - .45\left(\frac{h}{2R_e}\right)^{.5}} \left\{ 1 - \frac{P}{2\pi R_e E h \left[.16 \left(\frac{h}{L_e}\right)^{1.3} + 9 \left(\frac{h}{R_e}\right)^{1.6} \right]} \right\}$$

The axial compression buckling equation of Kanemitsu and Nojima (Reference 2) and the pressure buckling equation of Windenburg and Trilling (Reference 3) are used. These equations are also the basis of the Garber Hess buckling curves (Reference 4) presently being used at GE-MSD. The bi-axial stress yield equation is used in the form

$$h = \sqrt{\frac{N_x^2 + N_x N_\theta + N_\theta^2}{\sigma_{y.p.}}}$$

+ indicates axial compressive load, internal pressure.

The unit weight of the shell is given as

$$w = 144 \rho h F_b$$

where F_b is a fabrication factor which increases the weight of the basic shell to include end rings, doublers, fasteners, etc. For the monocoque shell, F_b equals 1.10.

The symbols used are

- E = Modulus of Elasticity in Compression, lbs./sq. in.
- F_b = Fabrication Factor
- h = Shell Thickness, in.
- L_e = Equivalent Length of Cylinder, in.
- N_x = Axial load, lbs./in.
- N_θ = Hoop Load, lbs./in.

- P = Axial Load, lbs./P equals $(2\pi R) N_x$
 q_{cr} = Uniform pressure required to cause instability of shell, lbs./sq. in.
 R_e = Equivalent Radius of Cylinder, in.
 W = Shell Weight per unit Surface Area, lbs./sq. ft.
 π = 3.1416
 ρ = Density of Material, lbs./cu. in.
 $\sigma_{y.p.}$ = Yield stress of material, lbs./sq. in.

(2) Ring-Stiffened (Semi-Monocoque) Shell

This shell is essentially a monocoque shell supported at various lengthwise locations. The intermediate supports are usually rings of sufficient rigidity to cause the buckling failure to occur in the shell between the rings. This structure has been commonly accepted because of its significant weight savings over the monocoque shell and its relative ease of fabrication as compared to the sandwich and corrugated structures. However, it does not result in as light a structure as the sandwich or corrugation shells because of the practical limitation on the closeness of the rings.

The design of this type of shell is accomplished by first selecting a ring with sufficient rigidity to stabilize the shell and then determining the shell thickness necessary to prevent local skin buckling and yielding. In common practice the ring required to resist the non-axisymmetric pressure distributions imposed on the vehicle in flight is greater than that needed to stabilize the shell against axial compression only. The ring is generally designed to resist this pressure (Reference 5). For the load condition used in this study (angle-of-attack equals 0°), the ring was selected to withstand a uniform compressive load.

The shell between rings is analyzed as a monocoque shell with a length equal to the ring spacing. The equations are those given for the monocoque shell design. A sketch of the ring-stiffened shell showing integral stiffeners, is given in Figure 1.3.4-30(b). A fabrication factor of 1.20 is used in this design.

(3) Honeycomb Sandwich Shell

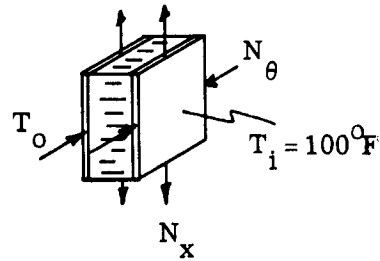
The sandwich structure (see Figure 1.3.4-30(C)) consists of two high density faces separated by a low density core material. Many core materials, such as cork, foamed plastic, etc. have been used with the most widely accepted being the cellular core of honeycomb configuration. Therefore, the shell considered herein is a honeycomb sandwich shell.

For many of the commonly encountered shell designs, the honeycomb sandwich configuration results in the lightest structure.

The honeycomb shell analysis is performed by selecting a face thickness which allows the material to work at its yield stress and then determining the core depth required to stabilize the shell. The bi-axial stress equation for yielding of the face material is

$$\sigma_{y.p.}^2 = \sigma_1^2 - \sigma_1 \sigma_2 + \sigma_2^2$$

Axial, hoop and thermal loads are applied to the sandwich shell. These loads are shown acting on the element below. All forces shown are positive.



Therefore,

$$\sigma_1 = -\sigma_x + (\pm \quad t \sigma_x)$$

$$\sigma_2 = \sigma_\theta + (\pm \quad t \sigma_\theta)$$

where

σ_x is the stress due to the axial load, N_x

σ_θ is the stress due to the hoop load, N_θ

$t \sigma_x$ is the thermal stress in the axial direction, and

$t \sigma_\theta$ is the thermal stress in the hoop direction.

The \pm sign is included to differentiate the thermal bending stresses in the inner and outer sandwich faces. Substituting for σ_1 and σ_2 in the yield equation we get

$$\sigma_{y.p.}^2 = \sigma_x^2 - (\sigma_x)(\pm t \sigma_x) + \sigma_x \sigma_\theta + \sigma_\theta^2 + (\sigma_\theta)(\pm t \sigma_\theta) + (t \sigma_\theta)^2$$

For ν equals 0.33 and T_i equals 100°F , the thermal stresses due to a thermal gradient $T_o - T_i$ is

$$t \sigma_x = t \sigma_\theta = \frac{1.50^\alpha (T_o - T_i) E_o E_i}{E_o + E_i}$$

The stresses due to the applied axial and hoop loads are

$$\sigma_x = \frac{.5N_x}{h_f}$$

$$\sigma_\theta = \frac{.5N_\theta}{h_f}$$

Substituting these relationships, the bi-axial yield equation becomes

$$\begin{aligned} \sigma_{y.p.}^2 = & \left(\frac{.5 N_x}{h_f} \right)^2 - \left(\frac{.5 N_x}{h_f} \right) \left(\pm \frac{1.50 E_o E_i \alpha (T_o - 100)}{E_o + E_i} \right) \\ & + \left(\frac{.5 N_x}{h_f} \right) \left(\frac{.5 N_\theta}{h_f} \right) + \left(\frac{.5 N_\theta}{h_f} \right)^2 \\ & + \left(\frac{.5 N_\theta}{h_f} \right) \left(\pm \frac{1.50 E_o E_i \alpha (T_o - 100)}{E_o + E_i} \right) \\ & + \left(\frac{1.50 E_o E_i \alpha (T_o - 100)}{E_o + E_i} \right)^2 \end{aligned}$$

For the buckling analysis the honeycomb sandwich is reduced to a fictitious monocoque shell of thickness \bar{t} and modulus \bar{E} with extensional and flexural rigidities equal to the honeycomb shell. The equations used to accomplish this are

$$\begin{aligned} \bar{t} &= \sqrt{3} (c_h + h_f) \\ \bar{E} &= \frac{2 E_f h_f}{\sqrt{3} (c_h + h_f)} \end{aligned}$$

\bar{E} and \bar{t} are then used in the monocoque buckling equation to determine the honeycomb core depth c_h . This equation is

$$q_{cr} = \frac{-2.63 \bar{E} \left(\frac{\bar{t}}{2R} \right)^{2.5}}{\frac{L}{2R} - .45 \left(\frac{\bar{t}}{2R} \right)^{.5}} \left\{ 1 - \frac{P}{2\pi R \bar{E} \bar{t} \left[.16 \left(\frac{\bar{t}}{L} \right)^{1.3} + 9 \left(\frac{\bar{t}}{R} \right)^{1.6} \right]} \right\}$$

+ indicates axial compressive load, internal pressure.

So far, little consideration has been given to the core itself. The previous stability calculations assumed that the core material is rigid in shear. In order to minimize the non-conservative effects of actual core shearing, the following criteria was used to determine the core modulus and density required.

$$G_c \geq \frac{E_f h_f}{9.5} \quad \rho_c = 3.42 \left(\frac{G_c}{G} \right) \rho$$

This criteria resulted in the following core densities.

MATERIAL	DENSITY (LBS/CU. IN.)
Aluminum	.0035
Stainless Steel	.0035
Titanium	.0035
Magnesium	.0035

The unit weight of the honeycomb sandwich shell is

$$W = 144 (2 H_f \rho_f + c^h \rho_c) F_b$$

A fabrication factor of 1.90 is used to include the weight of bond material, core fillers, doublers, etc.

The notation used in the previous discussion is as follows.

- E_f, E_i, E_o = Modulus of Elasticity in Compression of Face Material, lbs./sq. in. Subscripts f, i and o refer to face sheet, inner face and outer face.
- F_b = Fabrication Factor
- G = Modulus of Elasticity in Shear, lbs./sq. in.
- c^h = Depth of Honeycomb core, in.
- h_f = Thickness of Face Material, in.
- L = Length of Cylindrical Shell, in.
- N_x = Axial Load, lbs./in.
- N_θ = Hoop Load, lbs./in.
- P = Axial Load, lbs.
- q_{cr} = Uniform Pressure to Cause Instability of Shell, lbs./sq. in.
- R = Radius of Cylinder, in.

T_i, T_o	=	Temperature of inner and outer faces, Degrees Fahrenheit
W	=	Shell Weight per Unit Surface Area, lbs./sq. ft.
α_i, α_o	=	Coefficient of Thermal Expansion for Inner and Outer Face Materials, in./in./ $^{\circ}$ F
ϵ_i, ϵ_o	=	Strain in Inner and Outer Faces, in./in.
ν	=	Poisson's Ratio
π	=	3.1416
ρ	=	Density of Face Material, lbs./cu. in.
ρ_c	=	Density of Core Material, lbs./cu. in.
σ_x, σ_θ	=	Stress in Axial and Hoop Directions, lbs./sq. in.
$t\sigma_x, t\sigma_\theta$	=	Thermal Stress in Axial and Hoop Directions, lbs./sq. in.
$\sigma_{y.p.}$	=	Yield Stress of Material, lbs./sq. in.

REFERENCES

1. Hess, Bailey, Most, "Ballistic Re-entry Vehicle Thermo-Structural Optimization," GE TIS 62SD199, October 23, 1962.
2. Kanemitsu, S. and Nojima, N., "Axial Compression Tests of Thin Circular Cylinders, M. S. Thesis, California Institute of Technology, 1939.
3. Windenburg, D. F. and Trilling, C., "Collapse by Instability of Thin Cylindrical Shells Under External Pressure," Transactions of the American Society of Mechanical Engineers, Vol. 56, No. 11, pp 819-825, and Vol. 57, No. 5, 1934, pp 259-265.
4. Garber, A. M. and Hess, T. E., "Stability of Ring-Stiffened Conical Shells Under Simultaneous Pressure and Axial Compression," GE TIS R58SD226, April 30, 1958.
5. Garber, A. M., "On the Behavior of Circular Frames in Stiffened Cylinders Subjected to Nonaxisymmetric Pressure Distributions," GE TIS R59SD435, October, 1959.

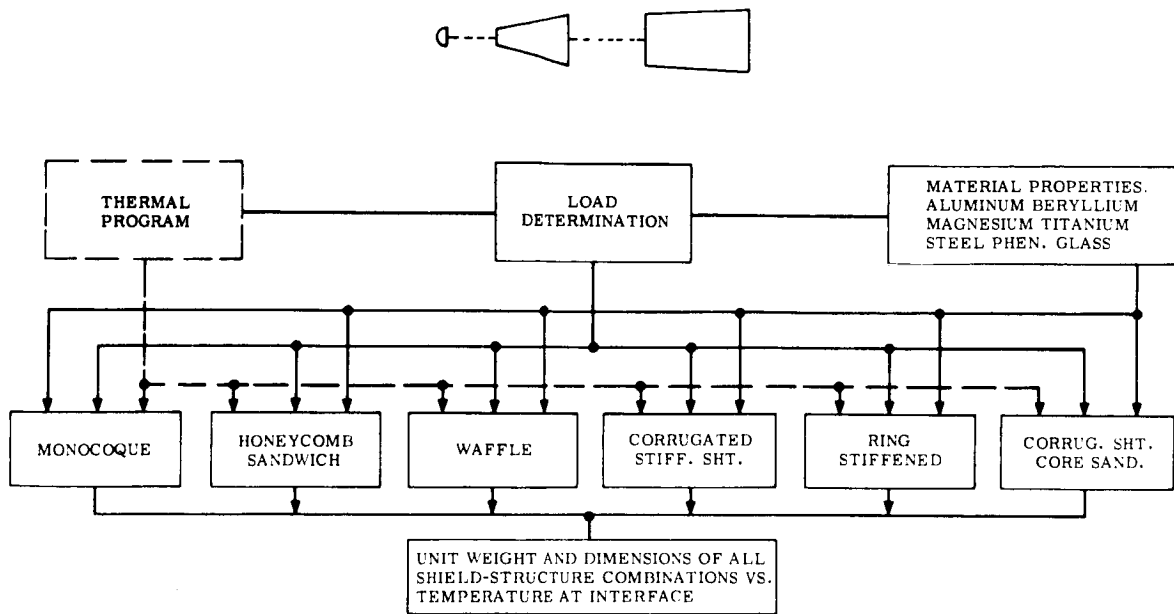
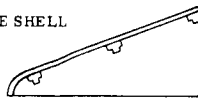
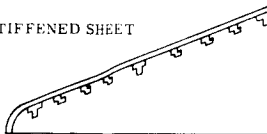


Figure 1.3.4-29. Optimization Program Chart

a) MONOCOQUE SHELL



b) RING STIFFENED SHEET



c) HONEYCOMB SANDWICH SHELL

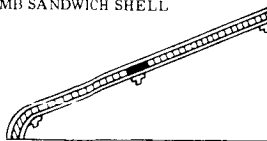


Figure 1.3.4-30. Structures Studied

1.3.5 RETARDATION

A. General Discussion

The retardation of Lander vehicles entering the atmospheres of Mars and Venus can be optimized through use of atmospheric braking. This section presents trade-offs related to vehicle retardation prior to, during, and after the occurrence of the entry heating and deceleration pulse of the basic Lander configuration.

The requirement of survival after impact with the planet surface requires that the impact velocity not exceed approximately 100 f. p. s. and preferably be much less than this maximum for state-of-the-art load attenuation techniques. This upper limit on impact velocity combined with planetary atmospheric characteristics defines the retardation requirements. Because of uncertainties in planetary atmospheric characteristics it has been found necessary in past studies (i. e., GE's Mars Entry Capsule Study, GE's Venus - Mars Entry Capsule Study, and in-house Voyager studies) to consider a broad range of possible atmospheric models for design purposes. The retardation requirements must be based on the atmospheric model having the lowest density at the planet surface. More specifically this study was concerned with a lower surface density of 1.45×10^{-4} slugs/ft.³ on Mars and 6.25×10^{-3} slugs/ft.³ for Venus. For comparison, the density at the surface of Earth is 2.38×10^{-3} slugs/ft.³. Thus, from the relationship of the above surface densities it can be seen that Mars presents a greater terminal retardation problem than Earth, while on Venus the retardation problem is less pronounced based on the required drag area. Because of its prominence the Mars retardation problem has been emphasized.

B. High Altitude Retardation

The conditions under which deployment of terminal retardation devices occurs in planetary entry are dependent upon initial entry conditions and integrated effects of entry. In order to determine trends that would result if entry conditions were modified at or during entry, the use of retro-rockets and drag modulation have been considered. The worse-case entry path angle ($\gamma_e = 90^\circ$) and Mars atmospheric model (lower) have been used.

The use of retro-rockets to reduce the vehicle velocity into the Martian atmosphere will decrease the velocity of the vehicle at any given altitude where deployment of a terminal retardation device might be desirable. A nominal supersonic Mach number ($M = 2.0$) was chosen for initiation of terminal retardation. The effect of the entry velocity upon the altitude at which a terminal retardation device might be deployed is illustrated in Figure 1.3.5-1. This figure indicates a large decrease in entry velocity which is necessary in order to substantially affect deployment altitude. For an entry velocity of 23,000 f. p. s. a vehicle using retro-rockets reaches $M = 2.0$ at 11,200 feet. The corresponding altitude for a vehicle without retro-rockets is 10,700 feet. The total retro-rocket impulse required to decrease the vehicle velocity is presented in Figure 1.3.5-2. Figure 1.3.5-3 relates the total required impulse to retro-rocket weight, independent of a separate requirement for a stabilization and control system to properly align the vehicle for firing. Combining the results of these three figures leads to the conclusion that use of retro-rockets for significant deployment altitude gain would require a large percentage of the total entry vehicle weight. In addition, weight would have to be allotted for a system to properly orient the vehicle prior to firing of the retro-rocket. The gains from retro-rockets are small; the added weight and complexity of the rockets become limiting factors. Therefore, retro-rockets are not recommended for Voyager-type Mars entry vehicles at this time. If future estimates indicate a lower Mars atmospheric density, this approach may be considered again.

A second method of modifying the Voyager entry trajectory is to reduce the vehicle W/C_{DA} . The vehicle W/C_{DA} can be variable (continuous or stepwise) or designed for a low value. An example of a light weight type of drag modulation device would be one that would be effective during the entry until loads or heating caused it to be destroyed. This device would lower the overall vehicle W/C_{DA} while it is attached. Figure 1.3.5-4 presents the effect of a

one step, drag area change, at peak heating, upon the altitude at which $M = 2.0$ occurs for the lower atmosphere, $V_e = 23,000$ f. p. s. and $\gamma_e = 90^\circ$. The initial W/C_{DA} of this figure represents that W/C_{DA} of the vehicle and drag device combined; the basic W/C_{DA} is that of the vehicle alone. The figure shows that only small gains in altitude for the Mach number condition can be expected for a one step change in drag area at the time of peak heating. It also appears that any altitude gains are diminished as the basic vehicle W/C_{DA} is reduced. Thus, in order for a drag modulation device to significantly affect the terminal retardation deployment altitude, it must be effective throughout a large portion of the entry heating pulse. This requires a design capable of withstanding loads and integrated heating comparable to that experienced by the entry vehicle itself.

Two types of drag devices have been considered, inflatable and non-inflatable. The non-inflatable device would trail the entry vehicle on a cable and be constructed similar to the entry vehicle heat shield. A variety of configurations have been suggested for the trailing devices, (cones, frustums, sphere modified cones) and some of these are presently undergoing small scale wind tunnel testing by the NASA and Air Force. Current studies on such a system indicates that W/C_{DA} can be halved at the cost of about 24% of the vehicle weight. Inflatable drag devices can be inflated from a self-contained unit or from the free stream dynamic pressure, as currently being investigated by the Goodyear Aircraft Company. Two inflatable devices which might be used to reduce entry vehicle W/C_{DA} are illustrated in Figures 1.3.5-5 and 1.3.5-6. The drag areas, as a function of maximum diameter, are also presented in these figures as determined from wind tunnel test results. Figures 1.3.5-7 and 1.3.5-8 give estimated system weights for an 80° air-mat cone constructed of Rene' 41 and Dacron fabric respectively. Included in the weight estimate are fabric, lines and inflation and control equipment. Similar weight estimates for the 80° ram-inflated Ballute are given in Figures 1.3.5-9 and 1.3.5-10.

The solid or non-inflatable drag device is now only in its conceptual stage. However, initial free-flight tests of forced inflation drag devices, as first stages of recovery systems, have been carried out. Thus research into trailing drag devices for planetary entry has only begun. If development of inflatable drag devices continues at its present pace, incorporation of such a device in a 1969 Voyager mission is feasible. The desirability of using such a device will depend on ensuing Martian atmospheric model perturbations and further weight and performance trade-offs. However, at the present time trailing drag devices for planetary entry must be considered as concepts. Significant development is necessary to produce state-of-the-art systems. Therefore, trailing drag devices have not been recommended for use in this initial study.

C. Terminal Retardation

In the previous sections the desirability of maintaining a Mars entry vehicle W/C_{DA} of 40 psf or less has been indicated. In this section the reason for this W/C_{DA} goal will be pointed out. Also, the results of a parametric retardation study for a range of Voyager Lander vehicle weights will be presented.

Based on the matrix of entry trajectories considered, previous sections have shown that from a terminal velocity viewpoint (at the Mars surface), a "straight in" ($\gamma = 90^\circ$) trajectory into the lower model atmosphere represents the worst case. Figure 1.3.5-11 presents the altitude at which Mach numbers 1.0, 2.0, and 5.0 occur as a function of vehicle W/C_{DA} . Since the Voyager mission requires survival of the payload through impact of the vehicle on the Mars surface, the impact velocity (based on state-of-the-art) should not exceed approximately 100 f. p. s. It can be seen from Figure 1.3.5-11 that an extremely low vehicle W/C_{DA} is required in order to satisfy this impact velocity constraint. Through the use of an auxiliary retardation device the basic weight W/C_{DA} can be much higher. The problem is then one of determining the maximum vehicle W/C_{DA} that can be tolerated within the retardation state-of-the-art.

For the terminal phase of retardation, three general classes of devices can be considered. They are: 1) deployable lifting surfaces such as the parawing, 2) L/D devices with flare-out

capability such as rotor systems, and 3) "pure" drag devices such as parachutes.

Parawings represent more than retardation devices. They provide considerable maneuverability, permit landing site selection, and provide a flare-out capability which theoretically gives no vertical impact velocity. Associated with parawing landing, however, is a considerable horizontal velocity requiring, for a stable landing, relatively flat terrain. In addition, the landing flare requires considerable instrumentation. Though it is felt that the parawing concept will be state-of-the-art at the time of proposed Voyager flights, it is not recommended as the method for landing unmanned entry vehicles.

Devices with small to moderate lift-to-drag ratios can be represented by autorotational rotor systems. In these systems the kinetic energy of the vehicle is converted to rotational energy of the rotor blades. By cyclic and collective pitch of the blades, maneuverability can be obtained. Just prior to vehicle impact on the planet surface the blade angle of attack is increased suddenly, converting the rotational energy of the blades to lift. Through proper sensing of altitude and velocity it is theoretically possible to touchdown on the surface without a vertical or horizontal velocity. Though this type of system appears promising, it suffers from complexity, sensing problems, and a slow rate of development. Thus, rotor systems cannot be recommended for use on the early Voyager missions.

The "pure" drag devices are characterized by parachutes. These devices provide a large amount of aerodynamic drag for a small cost in weight and volume. Due to their susceptibility to wind drift, parachutes allow both large vertical and horizontal impact velocities ($V_V = 100$ f. p. s and $V_H =$ surface wind velocity). Because of their simplicity of operation, and since they are in an advanced state-of-the-art, parachutes have been chosen as the terminal retardation system.

The design of a parachute retardation system is based upon a desired rate of descent at a particular altitude or a desired total descent time. For the Voyager mission, survival of surface impact is necessary. The rate of descent at impact, therefore, is the primary design parameter. The selection of the desired rate of descent is based upon considerations of the method of impact attenuation. Several attenuation schemes appear feasible for a 1969 Mars Voyager mission. They are material deformation, gas bags, and retro-rockets. The passive system (material deformation) would be the most reliable. Gas bags and retro-rockets are the active systems.

Gas bags represent a variety of systems that can be utilized for energy absorption by gas compression. The principal factors to consider are bag geometry, gas pressure control, and design considerations. Important design considerations are non-vertical descent, oblique or faulty impact, and the possibility of bag puncture from impacting objects on the planet's surface. Of the above considerations the probability of non-vertical descent would most likely limit the use of gas bags. In addition, sterilization might cause a materials problem in the bag design.

A retro-rocket landing device has the primary advantage that deceleration and deceleration-onset rates can be kept arbitrarily low by proper thrust control. Further, this type of system is adaptable to landing on almost any type of surface, whether planetary or lunar. In the Voyager concept, instrumentation is the suggested payload, not man. Thus the primary advantage of the retro-rocket system is meaningless, since reasonably high deceleration (100 to 200 g's) can be tolerated. Further, the retro-rocket system requires accurate data as to the lander's position in relationship to the surface of the planet and the rate of descent. In the Mars environment where the atmospheric density is unknown, the rate of descent is variable. This fact alone would greatly complicate a retro-rocket system.

Material deformation is characterized by fairly high deceleration loads and rates of onset. Systems of this type are passive and state-of-the-art at the present time. Since reasonable

deceleration loads and rates of onset are not detrimental to the Voyager payload, this type of attenuation system appears most attractive. A more detailed discussion of this type of system can be found in Section 1.3.4.C.

The choice of material deformation for a Mars Lander vehicle places practical restrictions upon the vehicle rate of descent just prior to impact. In order to keep the deceleration stroke down to a matter of inches, it is required that impact velocities be less than 100 f. p. s. if deceleration levels are not to exceed 100 to 200 g's. Thus, retardation considerations have represented impact velocities ranging from 20 to 100 f. p. s.

The size of the final stage parachute can be obtained from Figures 1.3.5-12 and 1.3.5-13. Figure 1.3.5-12 gives the W/C_{DA} ratio needed to achieve a given impact velocity on Mars for the range of atmospheric models considered. Knowing the landing vehicle weight results in the required L/D of the parachute(s), which can be converted to number of parachutes and their individual size. The maximum parachute size considered is $D_0 = 100$ feet, which is felt to represent state-of-the-art. The required drag area of the final stage parachutes can also be related to required parachute weight and packing volume as in Figures 1.3.5-14 and 1.3.5-15. For main descent parachutes, Figure 1.3.5-16 represents the present deployment state-of-the-art. Note that an upper limit in deployment Mach number ($M = 1.0$) is placed upon final stage parachutes having large drag areas and being relatively lightweight.

For purposes of main parachute deployment, vehicle stabilization, and deceleration a drogue parachute is recommended. In addition, if a supersonic deceleration is employed, a larger vehicle W/C_{DA} is allowable for a given altitude of main parachute deployment.

The ballistic coefficient constraint imposed by the decelerator is perhaps the most severe limit imposed on the Voyager Lander system by the retardation subsystem. Figures 1.3.5-17 and 1.3.5-18 present decelerator Mach number state-of-the-art at the present time. The temperature limits for nylon and HT-1 fabrics as given in these figures are only approximate since they are based upon stagnation condition behind a normal shock. However, the limits are felt to represent points at which parachute aerodynamic heating may provide a problem area. Thus, Mach 2.5 has been chosen as the upper limit for parachute deployment in this study.

The recommended decelerator is a parachute of the Hyperflo design. This design offers a Mach number growth capability due to the extensive development program being carried out at the present time. The drag area of the Hyperflo is presented in Figure 1.3.5-19 as a function of diameter (D_C) and Mach number. The estimated weight of the Hyperflo is given in Figure 1.3.5-20 as a function of the drag area at Mach numbers from 2.0 to 4.0. In applying the Hyperflo to the Voyager Lander, it has been assumed that the ratio of decelerator projected diameter to vehicle diameter should not be larger than 1.0 for operation at supersonic speeds. This ratio is conservative since wind tunnel tests of Hyperflo models indicate that values of as much as 3 might be used. However, a ratio of 1.0 provides sufficient drag area for main parachute extraction and stabilization requirements.

Combining the main descent parachute(s) and the Hyperflo decelerator into a retardation system capable of the following performance:

$$20,000 \leq V_e \leq 25,000 \text{ f. p. s.}$$

$$20 \leq \gamma_e \leq 90^\circ$$

$$20 \leq W/C_{DA} \leq 40 \text{ p. s. f.}$$

Mars Lower Atmosphere

Mach 2.5 deployment

results in a system weight which includes the following:

Parachutes and deployment bags

Suspension lines and risers

HT-1 material

Allowances for sterilization, radiation and vacuum soak,

and is presented in Figure 1.3.5-21. From this figure it can be seen that the weight of the retardation system is a function of the vehicle weight and the desired impact velocity. With an impact velocity of 40 f. p. s, approximately 13% of vehicle weight is devoted to the retardation system, and for 80 f. p. s., 4.5% of the vehicle weight is devoted to the retardation system.

Descent times for entry into the study atmospheres as a function of entry path angle are presented in Figure 1.3.5-32. The effect of varying impact velocity for the limiting $\gamma_e = 90^\circ$ entry into the lower atmosphere is shown in Figure 1.3.5-33. It should be noted that terminal descent times can be as low as 1.5 minutes for the worst case. If a higher density atmosphere is encountered, maximum descent times will be limited to Orbiter line of sight values by modifying initial deployment conditions as discussed under sensing and deployment.

Establishing an optimum impact velocity which directly affects the final drag area required — and hence the main chute size — must be the result of a weight and volume trade off between the retardation system and impact shock attenuation material requirements. This optimum impact velocity will vary significantly with configuration and volume limitations of crush-up material. For the Lander configuration, the optimum velocity for a combined minimum weight system will be approximately 65 ft/sec, which is prohibitive from a practical standpoint since impact shock material thicknesses would be excessive. Decelerator sizes, weights and pack volumes have therefore been computed for an impact velocity of 40 ft/sec; considered to be more practical to minimize impact material volume requirements.

The recommended system accomplishes three stages of deceleration from the time of deployment to the point where a final equilibrium velocity is attained. The supersonic decelerator is first ejected from a mortar tube to provide the first stage. Drag from the decelerator is then used to separate the aft cover, extract the main chute and remove the deployment bag from the main chute canopy. A second stage of deceleration is then accomplished by the reefed main canopy. Final deceleration is provided after the main chute disreefs and inflates to its fully inflated configuration.

Figure 1.3.5-22 presents constructed chute diameters vs. final descent weight of the Lander. The Lander weight includes the weight of the main chute but does not include weights of the supersonic decelerator, aft cover, or any components jettisoned prior to decelerator deployment. Required sizes have been established using drag coefficients of $C_D = 0.7$ for the main chutes. Heavier vehicles will require more than one main chute deployed in a cluster to avoid excessively large canopy diameters ≥ 100 ft.

Data on chute weights vs. final descent weights for the Mars Lander are shown on Figure 1.3.5-23. Chute weights include canopies, lines and all fabric components, such as deployment bags and risers, normally required for the system. HT-1 nylon has been considered as the material to be used for both the Hyperflo decelerator and main chute. This material appears to be the most suitable from the standpoint of withstanding sterilization temperatures. Weight data on HT-1, as reported in Ref. 1, appears to indicate that the material may not be much heavier than conventional parachute nylon when woven into fabrics and webbing to meet chute material MIL Spec requirements. In some cases, a lighter finished

product is indicated depending on the weave, fiber size, etc. Some weight increase may be recognized, however, since higher safety factors may be used during the detail design phase to compensate for strength loss during the high temperature soak period for sterilization. For this reason, a 20% increase in weight has been allowed to compensate for this loss. From rather limited data (Ref. 2) it seems that at least 15% strength loss can be expected after a soak period of 24 hours at 400°F.

Since the Hyperflo decelerator is currently in the experimental stage of development and therefore somewhat flexible in design, the weight of this decelerator has been considered as being comparable to a FIST Ribbon Chute with a canopy constructed of 500 lb. tensile strength webbing. Selection of a canopy roof design (e.g., mesh, ribbon, etc.) may induce variations in system weights but this is expected to be minor when the total system weight is considered.

For the main chute, it is anticipated that a Ring Sail or similar design will be used. Weights have been based on the use of medium weight materials in construction of the canopy. A 20% increase in weight over the use of conventional parachute nylon has also been allowed to compensate for strength loss of the HT-1 nylon during sterilization.

Figures 1.3.5-24 and 1.3.5-25 show pack volumes vs. final descent weight for the decelerator and main chutes. Pack volumes as shown on these curves have been determined from pressure pack densities and may be used to establish outside container dimensions. Sufficient allowance has been made for packing lines, deployment bags, etc., into the container. Also, additional volume has been added to the decelerator chute pack to compensate for a pressure chamber and sabot in the ejection mortar.

Utilizing the data as described above, retardation devices can be defined for each Voyager configuration designed for Mars landing. Table 1.3.5-1 presents this data for the major configurations.

Although retardation devices impose the greatest weight and volume restriction on the overall vehicle system design, it must be recognized that supporting components would also be provided in the retardation system to sense deployment and accomplish the various events in systematic order. These components as listed below would remain essentially constant in physical configuration for each Lander.

- Decelerator Ejection Mortar
- Ejection Mortar Squib and charge
- Main Chute Reefing Cutters
- Cover Release bolts
- Programmer with g sensors and timers
- Battery Power Supply
- Main Chute Swivel
- Decelerator and Main Chute cut-off fittings
- Electrical Harness and Cabling

Weights of the above components which significantly affect total vehicle system weights are listed in the detailed weight breakdown for each Lander.

TABLE 1.3.5-1. RETARDATION SYSTEM SPECIFICATIONS

ITEM	LANDER NOMENCLATURE		
	'69	'71 & '73	'73
Lander Weight at Entry	1450 lb	2000 lb	4000 lb
Lander Impact Weight	1213 lb	1711 lb	3340 lb
HYPERFLO DECELERATOR:			
Diameter	7.5 ft	9.0 ft	12.5 ft
No. Required	1	1	1
Weight	9.0 lb	13.2 lb	28.5 lb
Pack Volume	470 in ³	670 in ³	1360 in ³
Pack Configuration	Cylinder	Cylinder	Cylinder
C _D A	24.3 ft ²	35.0 ft ²	67.5 ft ²
MAIN CHUTE:			
Diameter	84.0 ft	70.4 ft	81.2 ft
No. Required	1	2	3
Weight	118 lb	165 lb	328 lb
Pack Volume	6000 in ³	8550 in ³	17100 in ³
Pack Configuration	Torus	Torus	Torus
C _D A (Reefed)	565 ft ²	794 ft ²	1590 ft ²
C _D A (Open)	3880 ft ²	5450 ft ²	10900 ft ²

REFERENCES

1. Technical Documentary Report No. ASD-TDR-63-248.
2. Technical Documentary Report No. ASD-TDR-63-329.

D. Retardation Sensing and Deployment

(1) Problem Definition and General Approach

Programming and sensing for retardation device deployment after entry into the atmosphere of Mars necessitates that a unique system be devised which will not only function over a wide range of possible atmospheric variables, but which will also function for various entry path angles, that is, from minimum capture to direct entry normal to the planet surface. The fact that the physical properties of the Martian atmosphere are not precisely known underscores the need for a system which will be as insensitive as possible to direct measurement of pressure or density for correlation with Mach number and altitude. With this in mind, a programming system has been investigated which senses vehicle deceleration during entry and, by monitoring decreasing g's in conjunction with times from a reference g point, can select a deployment condition within prescribed limits of the retardation system design.

Two major conditions must be satisfied to assure that successful retardation system deployment and landing will occur. First, the initial decelerator must be deployed within a given Mach number limit with due consideration to opening loads which will be induced on the vehicle. Second, the altitude of deployment must be sufficiently high to assure that all stages of deceleration will be completed prior to impact.

The programming system evaluated assumes that at least two parachutes will be used to retard the vehicle. One will be a relatively small decelerator with a Hyperflo canopy design capable of deployment at Mach number ≤ 2.5 and the other a main chute (or cluster) with a Ringsail canopy design sized to attain the required impact velocity. Deployment of the supersonic decelerator is the critical item to be considered since sensing of the ejection point must be accomplished over a wide range of trajectory conditions, which will be strongly influenced by entry angle and atmospheric density variations.

It is anticipated that main chute deployment can be accomplished by standard methods utilizing a suitable time interval for initial deceleration from supersonic to subsonic velocities. This interval would be nearly constant for various decelerator deployment conditions up to Mach 2.5 and should present no severe programming problem once the initial deployment can be selected. The programming problem, therefore, is primarily one of selecting a suitable supersonic deployment point rather than establishing the sequence timing for subsequent deceleration stages.

(2) Performance Limitations and Deployment Variables Considered

Mach number 2.5 is the maximum considered for deployment of a supersonic decelerator. Data accumulated from various test programs on supersonic deployment appears to substantiate the feasibility of developing a reliable system for deployment within this Mach number limit for Project Voyager. Any forthcoming advancements in chute technology increasing this limit would alleviate the problem of deploying the system within Mach number/altitude bounds to decelerate the Lander. Various trajectories for a vehicle W/C_{DA} of 40 lbs/ft² and entry velocity of 23,000 ft/sec were evaluated with respect to programming for the maximum Mach number limit. The available trajectories included entry angles 20°, 30°, 60° and 90° (down from horizontal) for each of the three atmospheres (lower, mean, and upper) considered to bracket the actual profile.

Since the vehicle designs presently considered have W/C_{DA} ratios approximating 35 lbs/ft^2 , the trajectories for a $W/C_{DA} = 40 \text{ lb/ft}^2$ represent a somewhat severe case with respect to successful deployment and maximum descent time. Changes in the design for reduced values of W/C_{DA} will permit additional deployment flexibility by providing altitude increases within the Mach 2.5 limit.

For all entry conditions, regardless of the atmospheric profile, steep entry angles approaching 90° present the most severe condition for deployment. Although the programming system presented will initiate deployment at or below Mach 2.0 for each trajectory case, this transition point may not occur at an altitude sufficiently high to decelerate the vehicle to the required velocity prior to impact. This dictates that the vehicle be designed with a $W/C_{DA} < 40 \text{ psf}$, if the entry angle cannot be controlled to eliminate the steep entry angle cases.

Even though the upper deployment limit is considered to be Mach 2.5 from a chute system development standpoint, the programming evaluation has been completed based on a conservative maximum of Mach 2.0. This is considered realistic to insure that circuit element tolerances will not cause sufficient deviation in the g-sensing and timing settings, such that an extreme deployment limit of Mach 2.5 will not be exceeded.

(3) Programming System Discussion

The programming system presented is based on utilizing the rate of change in deceleration g's with respect to time after peak entry g's have occurred to establish an initial decelerator deployment point. Figures 1.3.5-26, 1.3.5-27 and 1.3.5-28 present plots of g vs. time to show trends that can be expected for a gamut of four initial entry angles and three atmospheric profiles. Each curve is referenced from 8 g's, a selected level which must be below the peak entry load levels for all trajectories considered. This is to assure that a common reference point can be used for each possible trajectory.

Observed trends for the twelve trajectory cases examined indicate that the slope of the g vs. time curve will be consistently less for shallow entry angle cases. Also, it can be seen that for a given entry angle, the slope will generally increase from the 8 g reference point if the atmospheric profile becomes less dense.

Constant Mach Number plots superimposed on the data shown in these three figures indicate bounds which must be observed in determining the initial deployment point. Since the constant Mach Number and g vs. time plots have dissimilar slopes for given time increments after 8 g's, a series of deployment bands have been established in which timing intervals can be used to limit the Mach Number. During these intervals, actual deployment would be initiated by an accelerometer selected to close the firing circuits at various levels below 8 g's.

Timing intervals must be selected from the worst case condition (Figure 1.3.5-26) where the atmosphere profile is least dense and t is less from the reference point ($t=0$) to the Mach number bound for a given g level less than 8.0.

Figure 1.3.5-29 graphically illustrates the points at which deployment will occur for a selected group of timing bands (shown by the shaded area). The actual deployment point for a given entry angle (γ_e) would be at the intersection of the g vs. time curve with the shaded area. Deployment initiation would thus occur in one of five timing bands depending on the initial path angle and its influence on the slope of the g vs. time curve.

(4) Functional Description

A functional block diagram of the programming system is shown in Figure 1.3.5-30. The symbol "G" represents a sensing circuit which produces an output at a specified g level unless inhibited by its associated timer (T). G_0 senses the reference 8.0 g level

from which a family of acceleration vs. time curves have been determined. The inhibit timers are initiated at this g level.

The system is self-contained except for the requirement of a "battery-activate" signal at the adaptor separation event. Arming is accomplished during the period of increasing entry acceleration, and deployment of the deceleration and main parachutes is initiated at the appropriate time as the acceleration level subsequently decreases. A combination of g-sensing circuits and inhibit timers compares the actual entry trajectory with a family of predicted trajectories, and initiates deployment of the deceleration parachute at a Mach number ≤ 2.5 . Main parachute deployment then occurs following a selected time interval.

The system sequence of events is as follows:

(a) Battery Activate Event -

Near the time of adaptor separation, a signal activates the battery power supply. The battery has sufficient capacity to operate electronic circuitry in the programmer and to supply squib firing energy at the parachute deployment events.

(b) Arm Event

As the vehicle approaches the planet, deceleration is experienced at entry into the atmosphere. The g-level will increase from zero to some peak value dependent on the entry angle. The minimum peak value will occur during a shallow trajectory. Therefore, the arm event is programmed to occur at a g-level less than the minimum predicted peak value (9.4 g's) for the trajectories considered. Arming is accomplished by activation of an inertia switch at approximately 8.5 g's. An arming relay is operated and battery voltage is applied to the remaining elements in the programmer.

(c) Accelerometer Output

Voltage is now being supplied to an accelerometer having a g-range of 0-9 g's. However, the acceleration level after the arm event increases above 9 g's and the accelerometer output voltage is restricted to a preset minimum value. Acceleration now reaches a peak value and then decreases. When the acceleration level decays below 9 g's, the accelerometer produces an increasing DC voltage output.

(d) Trajectory Reference Event (G_0)

When the acceleration level decreases to a reference value of 8.0 g's, the voltage sensing and triggering circuit G_0 supplies a pulse which initiates the inhibit timers (T_1 to T_4).

(e) Deceleration Parachute Event

With timers T_1 to T_4 now operating, acceleration decreases with respect to G_0 at a rate dependent on the entry angle. If one of the g-levels, G_1 to G_4 , is experienced prior to timeout of the associated inhibit timer, a sensing and triggering circuit will operate, providing a pulse output to initiate firing of the decelerator mortar squibs. The hyper-flow decelerator is then deployed.

If G_4 (1.5 g's) has not occurred prior to timeout of inhibit timer T_4 , the vehicle is descending in a very shallow trajectory. Therefore, when the G_5 circuit produces an output indicating a deceleration load of 1.0 g, the deceleration parachute is deployed satisfying all deployment conditions for γ close to the minimum capture angle and no time limit is required for the 1.0 g timing-band.

(f) Decelerator Drag Internal Time Delay

Following decelerator parachute deployment, a time delay is inserted which delays the main chute deployment event until the vehicle velocity is sufficiently reduced. This time delay can be varied as a function of altitude if it is desired to reduce descent time for the high altitude (or shallow entry angle) deployment cases.

(g) Radar Altimeter Signal

The radar altimeter signal is intended to restrict the initial deployment altitude to prescribed maximum and minimum limits. Maximum deployment altitude control would be required if communication difficulties are encountered from long descent times. In such a case the Orbiter would travel beyond the line-of-sight region prior to impact of the Lander. Minimum altitude control would be used as a back-up for the programming system to insure that the deployment point occurred for all trajectory cases above the minimum value required for complete deceleration. In both cases the programmer would function normally to select initial deployment at Mach ≤ 2.5 and the Radar Altimeter would override the programmer signals to insure deployment within the preset altitude bounds and below the Mach number limit.

(h) Main Parachute Deployment

At completion of the selected timing interval for retardation of the Lander on the Hyperflo decelerator, the programmer will supply an electric pulse which will release the aft cover and decelerator from their attachment points on the vehicle. Drag from the decelerator will then separate the cover and main chute pack. At full line extension of the main chute, the main chute deployment bag will be removed from the canopy and inflation of the reefed canopy will occur. The Hyperflow chute, aft cover, and main chute deployment bag all become detached from any physical tie with the vehicle and are expended. The timing of the reefed drag interval will be controlled by pyrotechnic reefing line cutters and time delays activated mechanically when the main chute is initially deployed.

Figure 1.3.5-31 shows the various signals and events which will be sensed by the programmer during the initial entry phase. Utilizing the g-sensing and timing interval combinations as shown on the block diagram, Figure 1.3.5-30 satisfactory deployment conditions will be programmed for the range of entry angles and atmospheric profiles considered. The actual conditions for each of twelve selected trajectories are presented in Table 1.3.5-2. The table shows that actual deployment conditions as selected from computer runs are below the upper Mach number limit established for successful deployment. This limit would be reached only when the g-level was at its prescribed value very near the point of inhibit timer timeout for each band. The deployment points, however, all occur at sufficient altitude for complete deceleration with the exception of the most extreme case where the entry angle is 90° and the atmospheric density is least. This would indicate that in order to assure successful deployment under all cases, the W/C_{DA} of the Lander must be reduced. A subsequent check of computer runs indicated that with a W/C_{DA} of $\approx 35\text{psf}$ and the same atmospheric profiles (lower, mean and upper) deployment conditions of Mach number and altitude would be satisfied for a corresponding entry angle range from minimum capture ($\gamma_e \approx 20^\circ$) to normal to the planet surface ($\gamma_e = 90^\circ$).

TABLE 1.3.5-2. DECELERATOR DEPLOYMENT CONDITIONS

$W/C_{DA} = 40 \text{ psf}$

ATMOSPHERE	γ_e (degrees from horiz)	V (Ft./Sec.)	H (Ft.)	M (Mach Number)	q (Lbs./Ft.)	T (seconds from 8 g's)	γ (degrees from horiz)
Lower	20	960.0	73,700	1.40	18.0	60.0	24.7
	30	1290.0	45,600	1.65	59.0	11.2	28.2
	60	1440.0	16,400	1.65	118.0	2.0	59.3
	90	1355.0	8,200	1.50	118.0	1.5	90.0
Mean	20	1089.0	116,800	1.30	18.5	67.6	25.6
	30	915.0	83,800	1.10	30.2	19.3	32.5
	60	1452.0	57,718	1.63	118.0	1.9	59.4
	90	1330.0	49,300	1.43	112.0	1.6	90.0
Upper	20	1344.0	189,938	1.24	18.0	88.2	27.0
	30	1240.0	146,300	1.14	30.0	28.6	33.0
	60	1520.0	104,000	1.40	84.0	5.2	60.1
	90	1660.0	94,400	1.52	115.0	2.1	90.0

E. Suggested Areas of Further Investigation

The following retardation areas warrant further investigation and study:

1. Incorporation of hyperflo parachutes capable of deployment at high Mach numbers into the Voyager system study. Tests being conducted at the present time indicate that this parachute may eventually be capable of hypersonic operation. As development of the Hyperflo chute progresses, the results should be factored into the Voyager system's study.
2. In order to obtain low descent rates ($V = 40 - 60$ f. p. s.) on Mars, operation of the main descent parachute(s) at very low dynamic pressures is required. The effect of this low dynamic pressure upon parachute performance should be determined.
3. The effect of tolerances upon operation of the deployment sensing system should be investigated. These tolerances include g switches, timers, and entry trajectories (i. e., representative 6 degree of freedom trajectories providing vehicle angle of attack, etc.).
4. The Mars mission will require retardation system material to withstand sterilization, long vacuum soak and radiation then operate properly. The effect of these environmental factors upon retardation system design and operation should be determined through a comprehensive test program coupled with analysis to obtain applicable design factors.
5. Based on present estimates of the Martian atmosphere, deployment of the retardation parachutes will occur under low gas density conditions. Tests in the Earth's atmosphere have shown that parachute opening shock factors do vary with gas density. For accurate load predictions, the density effect on opening shock factors is required. Additional study in this area is suggested.

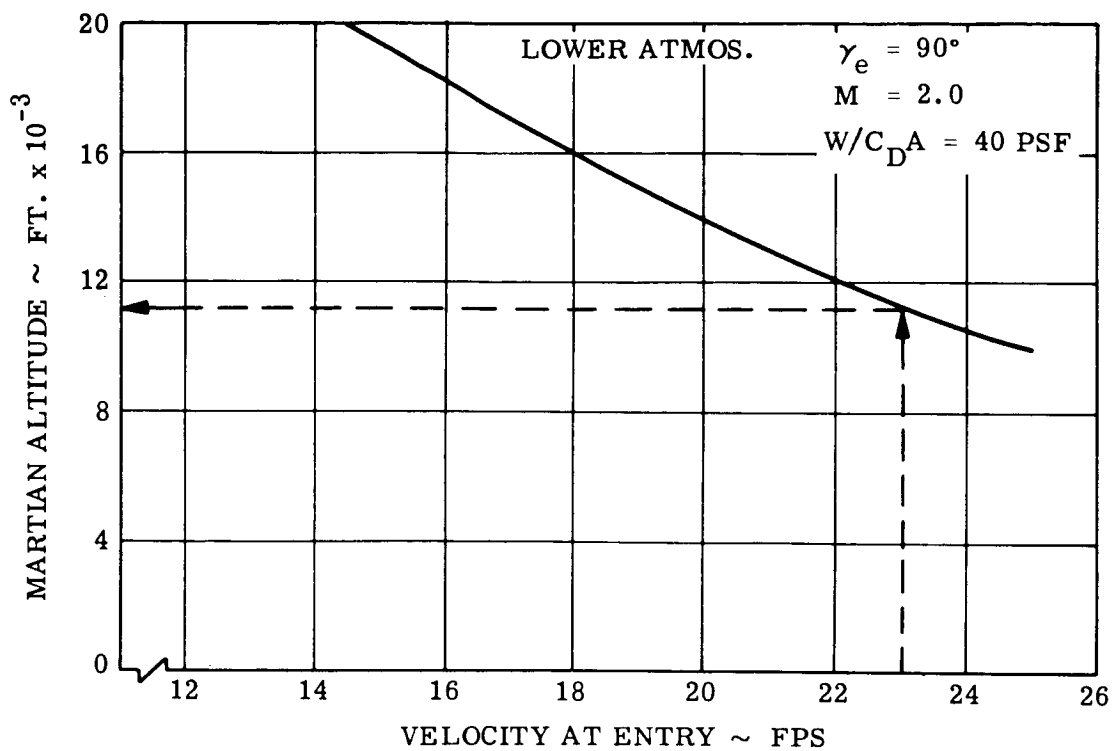


Figure 1.3.5-1. Mach 20 Altitude vs. Entry Velocity

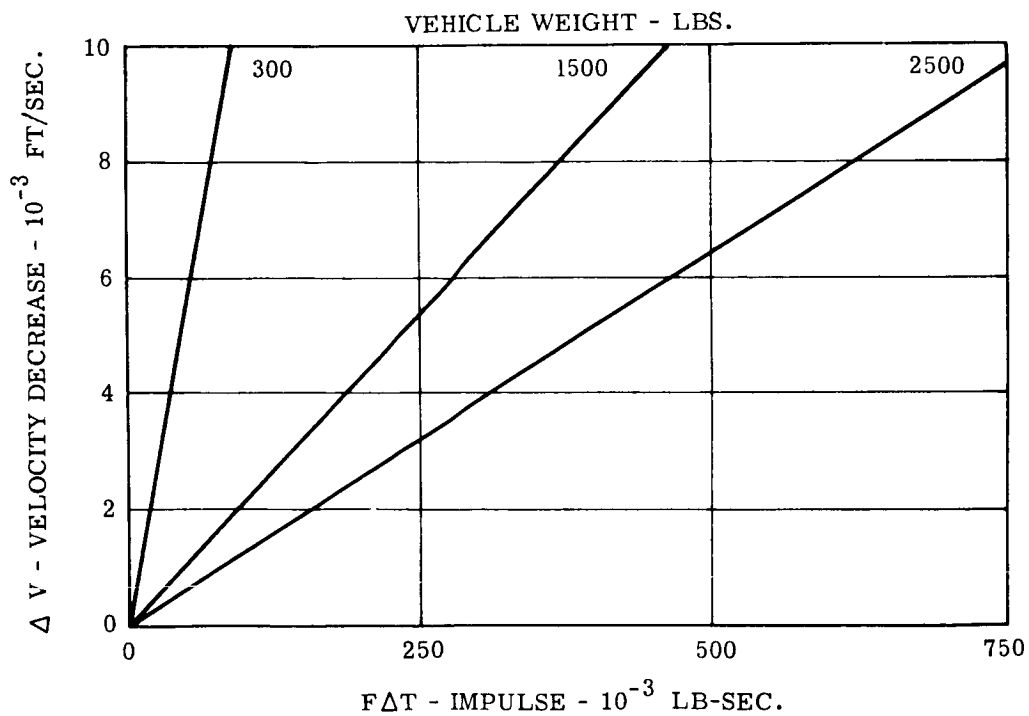


Figure 1.3.5-2. Required Impulse as a Function of Velocity Increment and Vehicle Weight

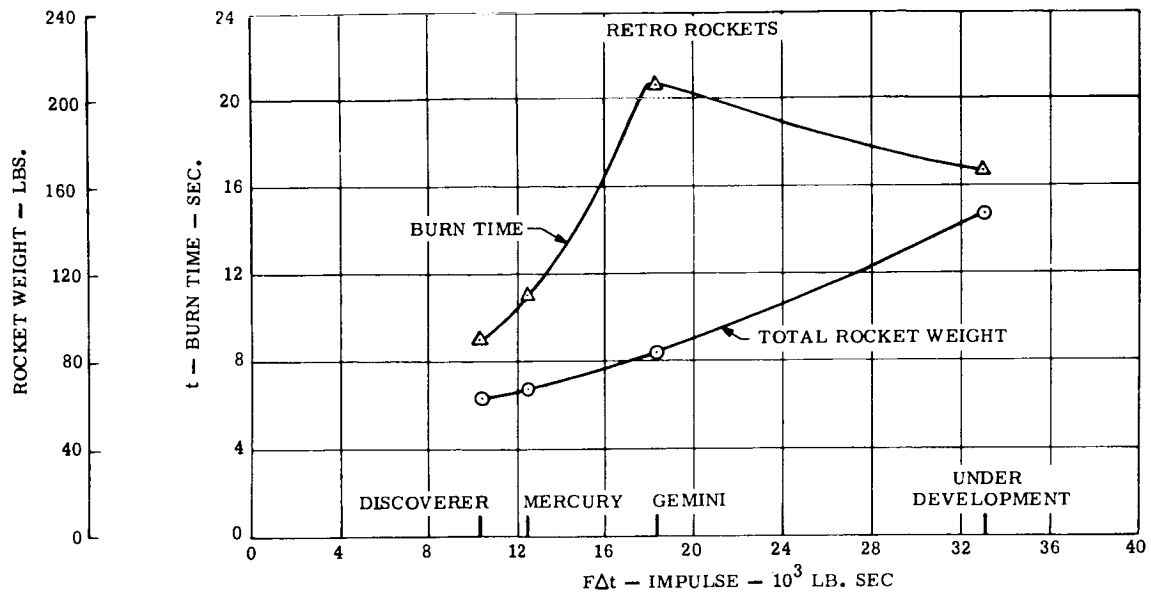


Figure 1.3.5-3. Retro Rockets

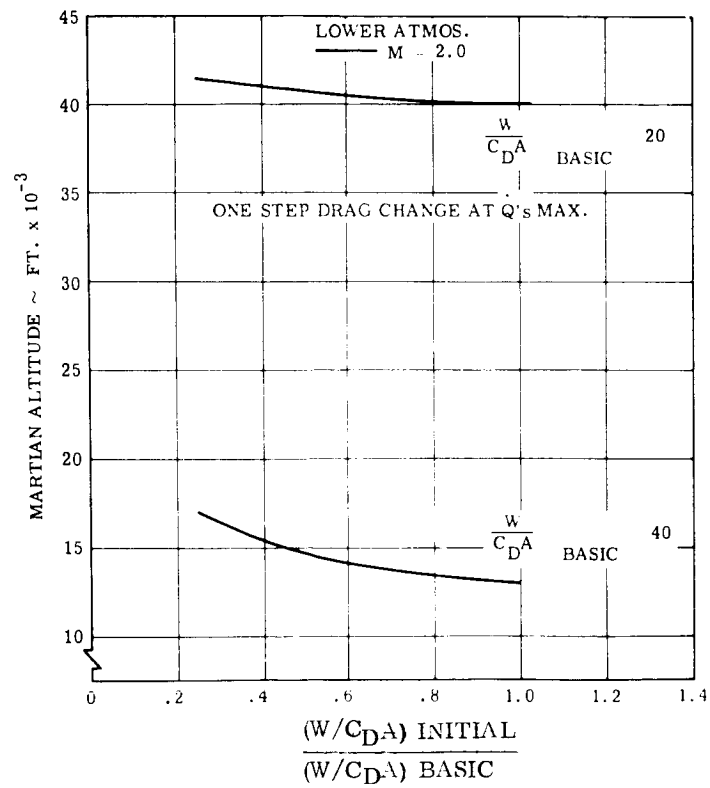


Figure 1.3.5-4. Effect of Drag Modulation

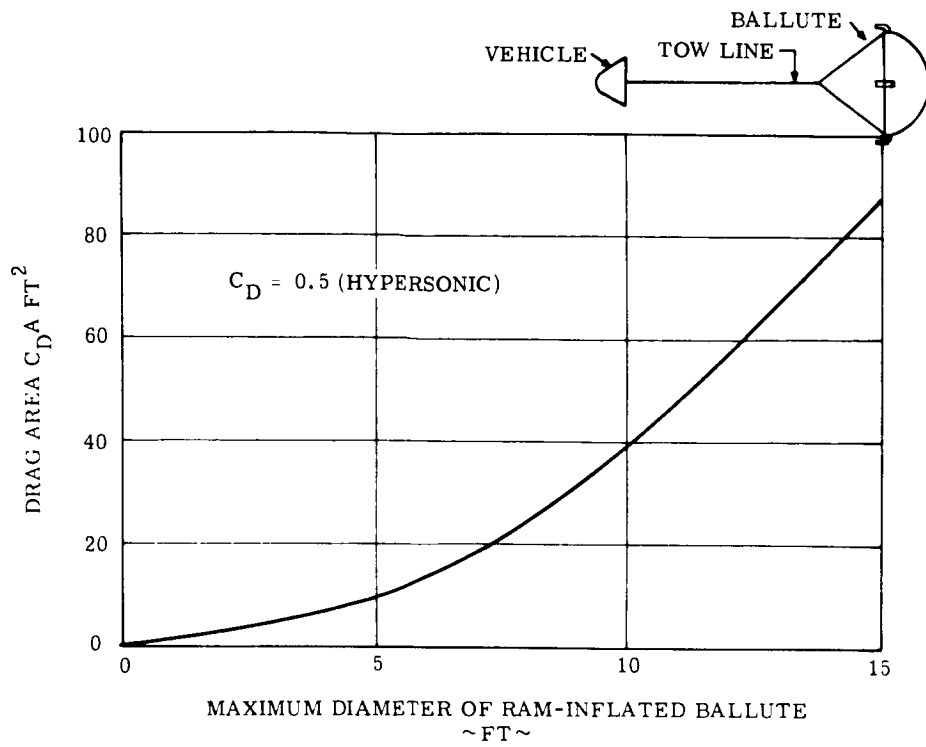


Figure 1.3.5-5. Drag Area vs. Maximum Diameter of 80° Ballute with Ram-air Inflation

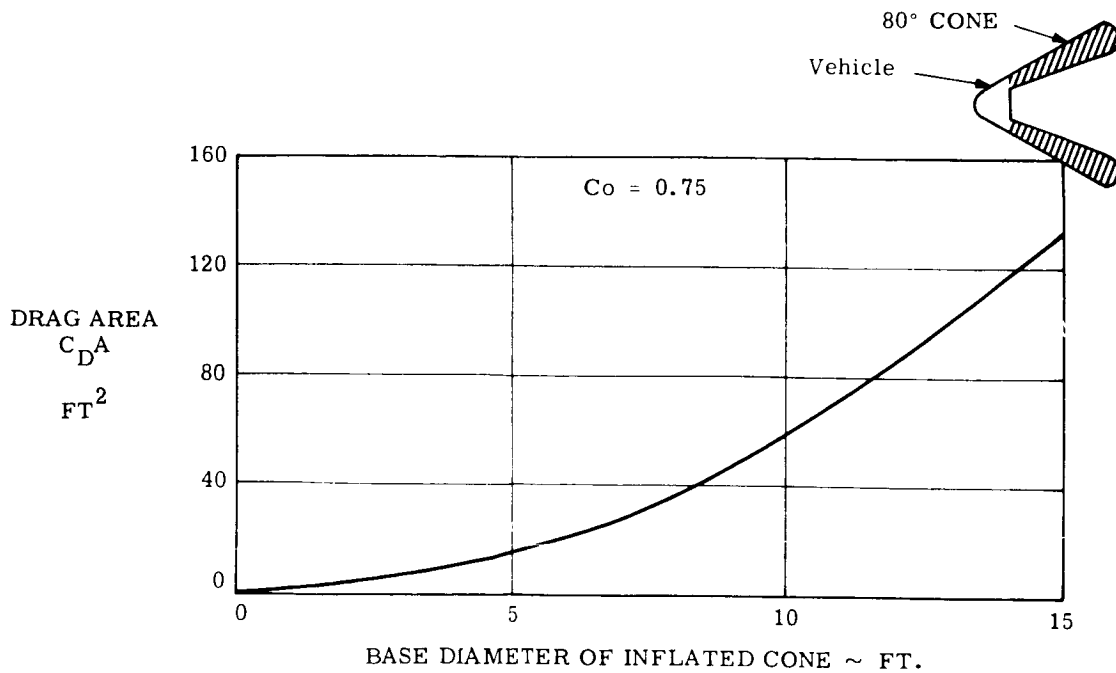


Figure 1.3.5-6. Drag Area vs. Base Diameter of 80° Airmat Cone Attached Directly to Vehicle

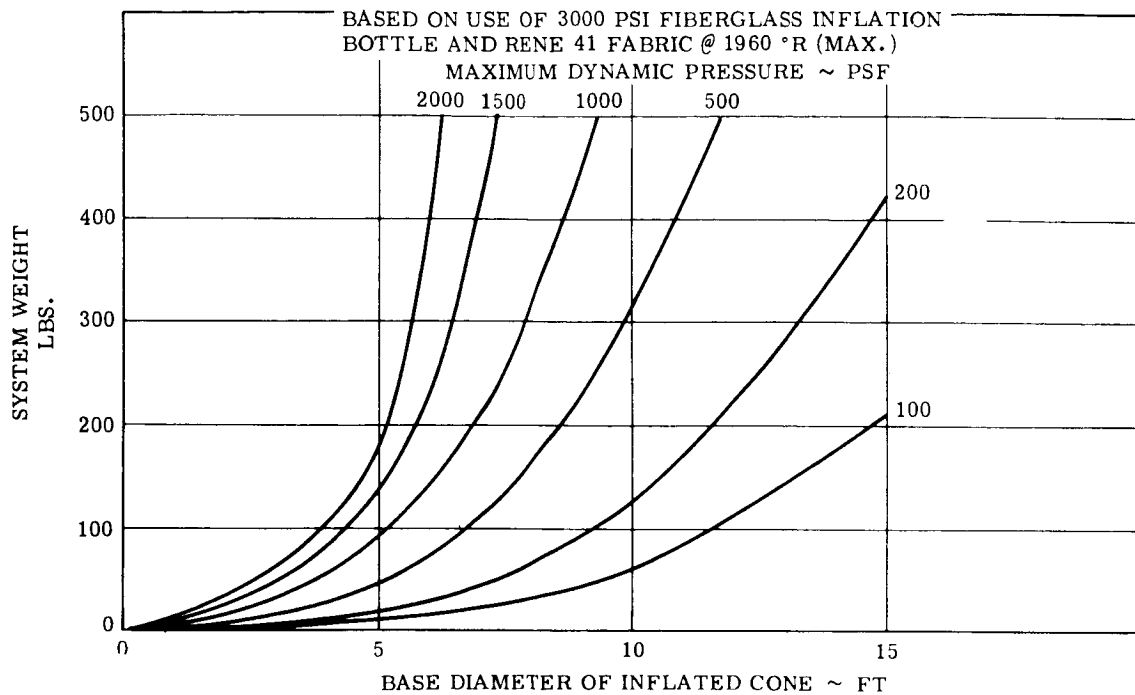


Figure 1.3.5-7. System Weight vs. Base Diameter of 80° Airmat Cone

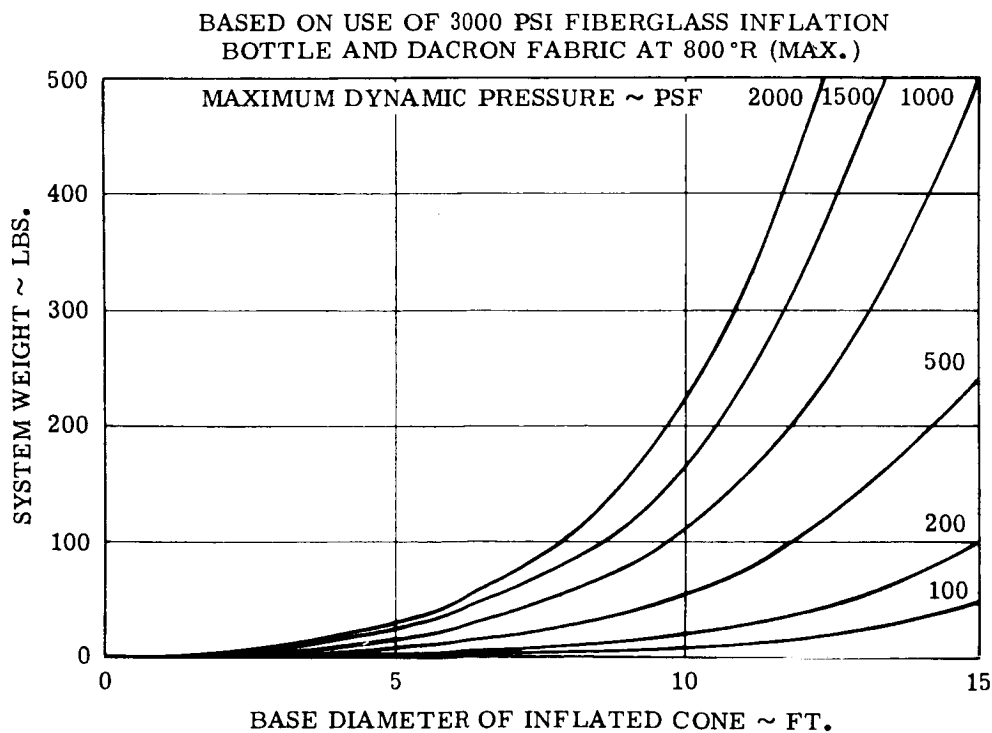


Figure 1.3.5-8. System Weight vs. Base Diameter of 80° Airmat Cone

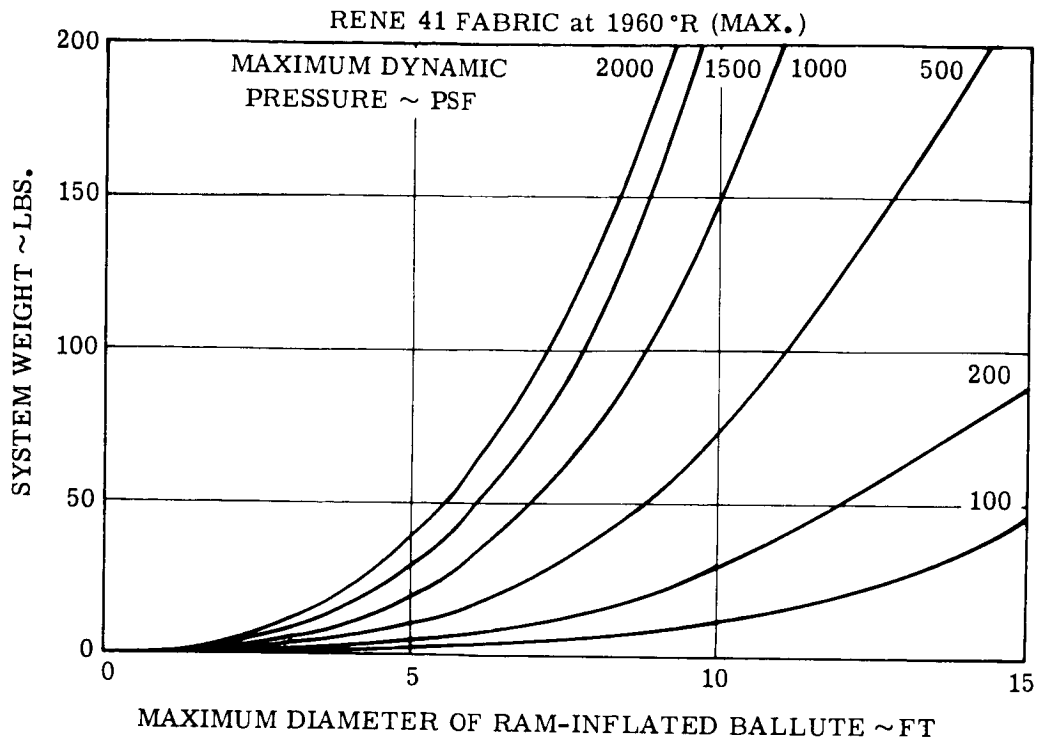


Figure 1.3.5-9. System Weight vs. Maximum Diameter of 80° Ram-Inflated Ballute

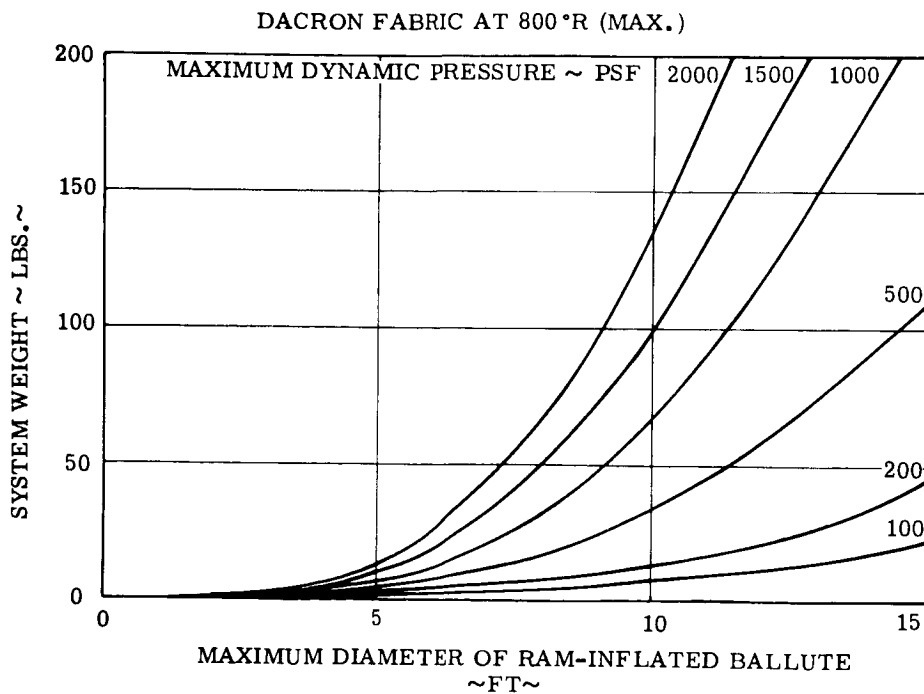


Figure 1.3.5-10. System Weight vs. Maximum Diameter of 80° Ram-Inflated Ballute

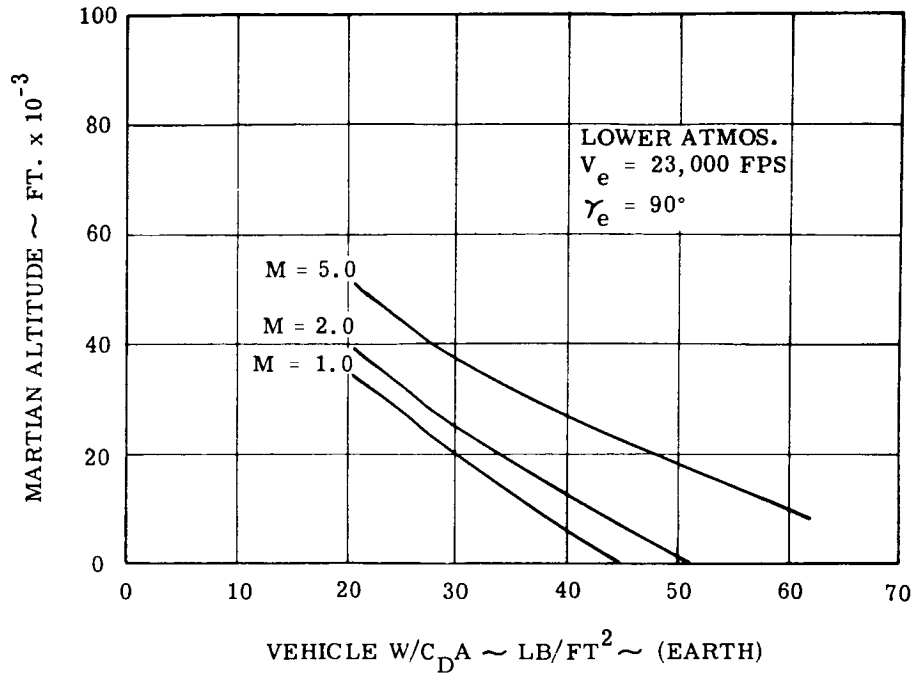


Figure 1.3.5-11. Altitude vs. Vehicle $W/C_{D,A}$ for Mach 1.0, 2.0 and 5.0

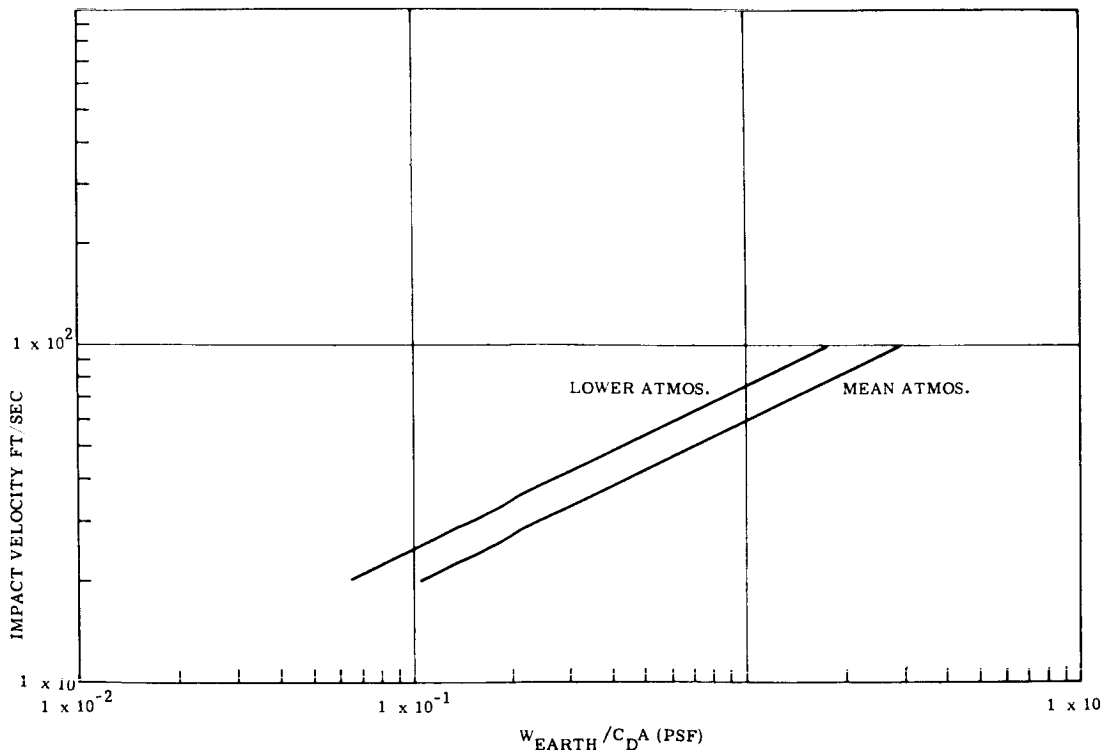


Figure 1.3.5-12. Martian Impact Velocity vs. Earth $W/C_{D,A}$ in Final Descent with Surface Density as a Parameter

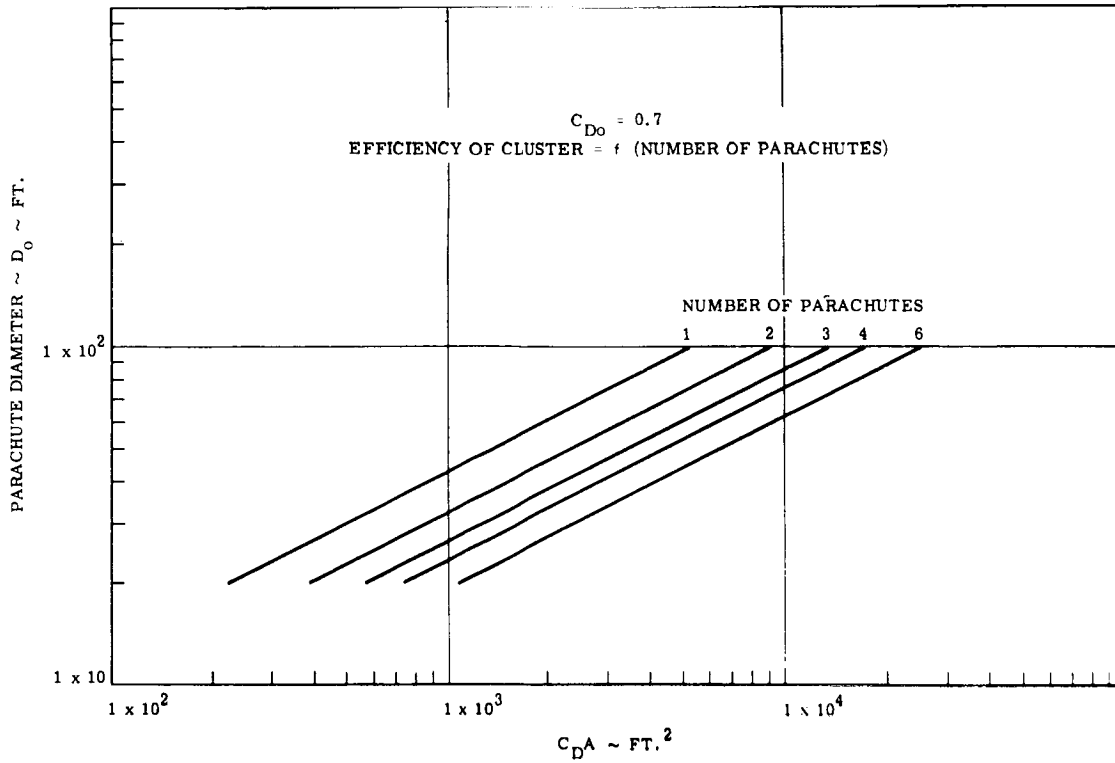


Figure 1.3.5-13. Drag Area of Main Descent Parachute(s)

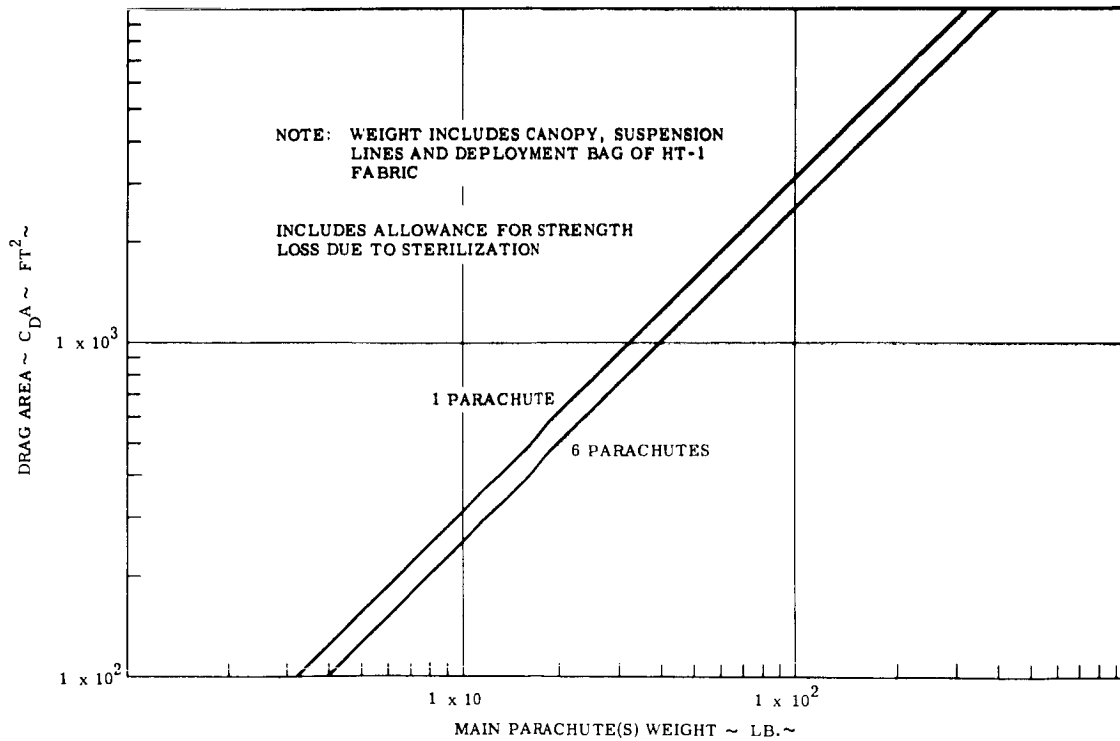


Figure 1.3.5-14. Assembly Weight of Main Descent Parachute(s)

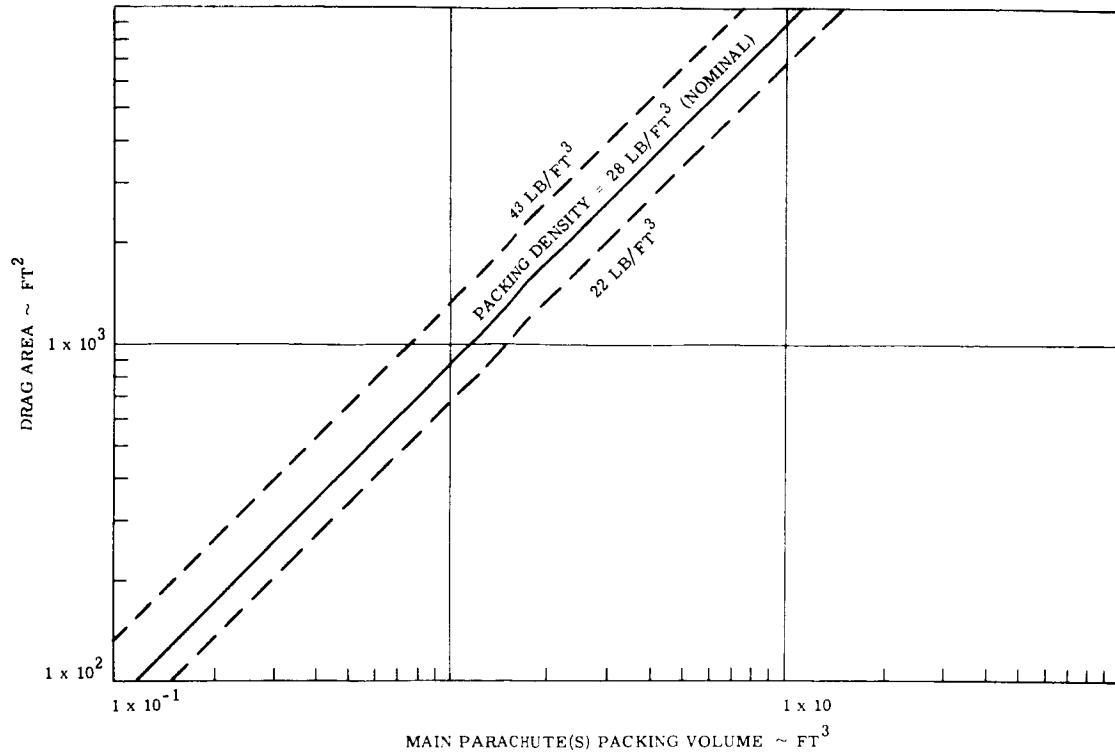


Figure 1.3.5-15. Packing Volume of Main Descent Parachute(s)

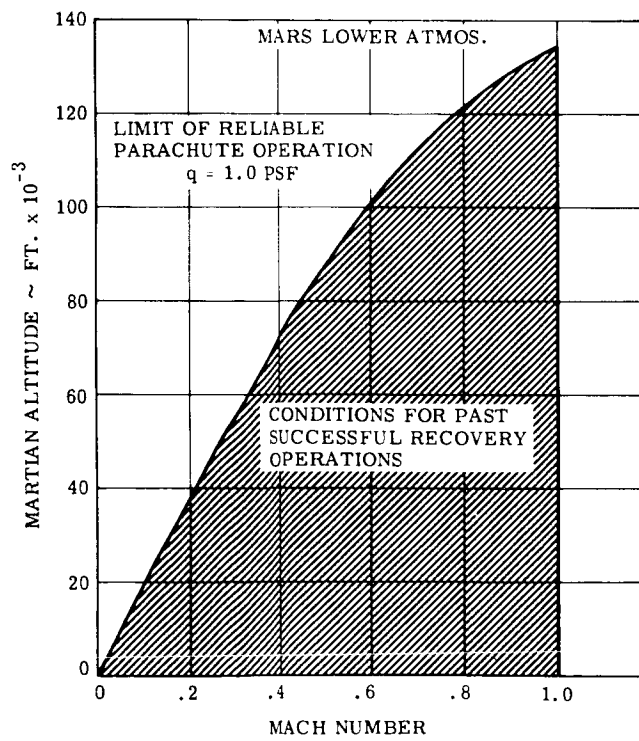


Figure 1.3.5-16. Parachute Deployment State-of-the-art Main Descent Parachutes

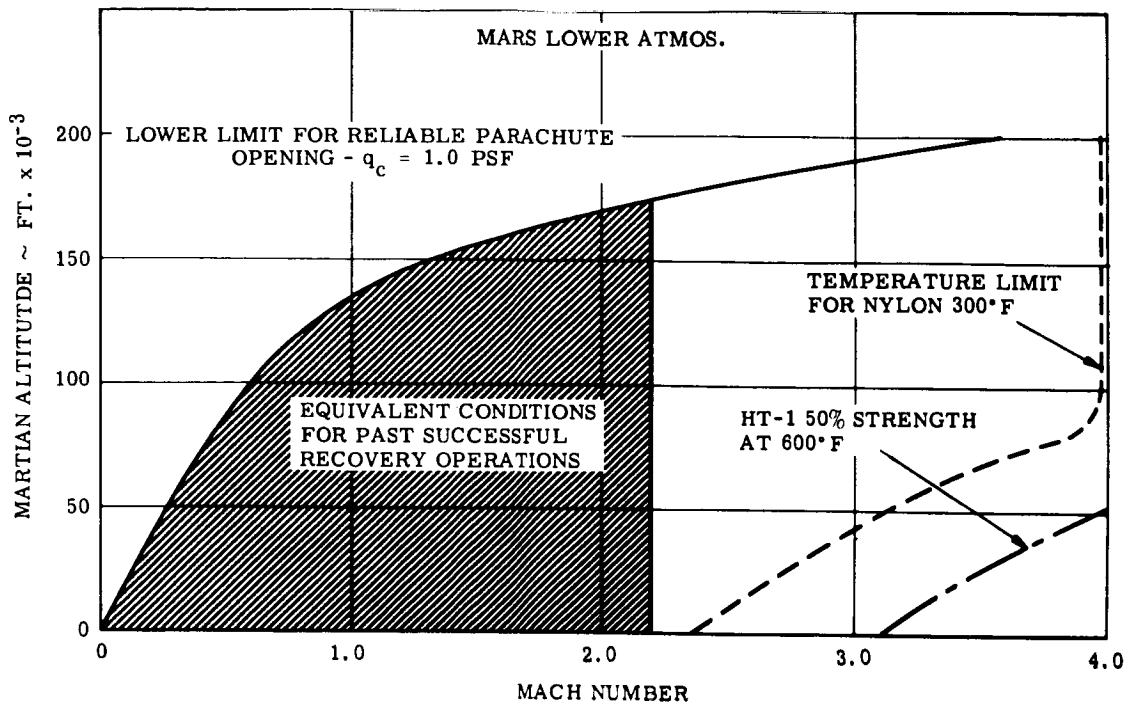


Figure 1.3.5-17. Decelerator Parachute State-of-the-art, Mars Lower Atmosphere

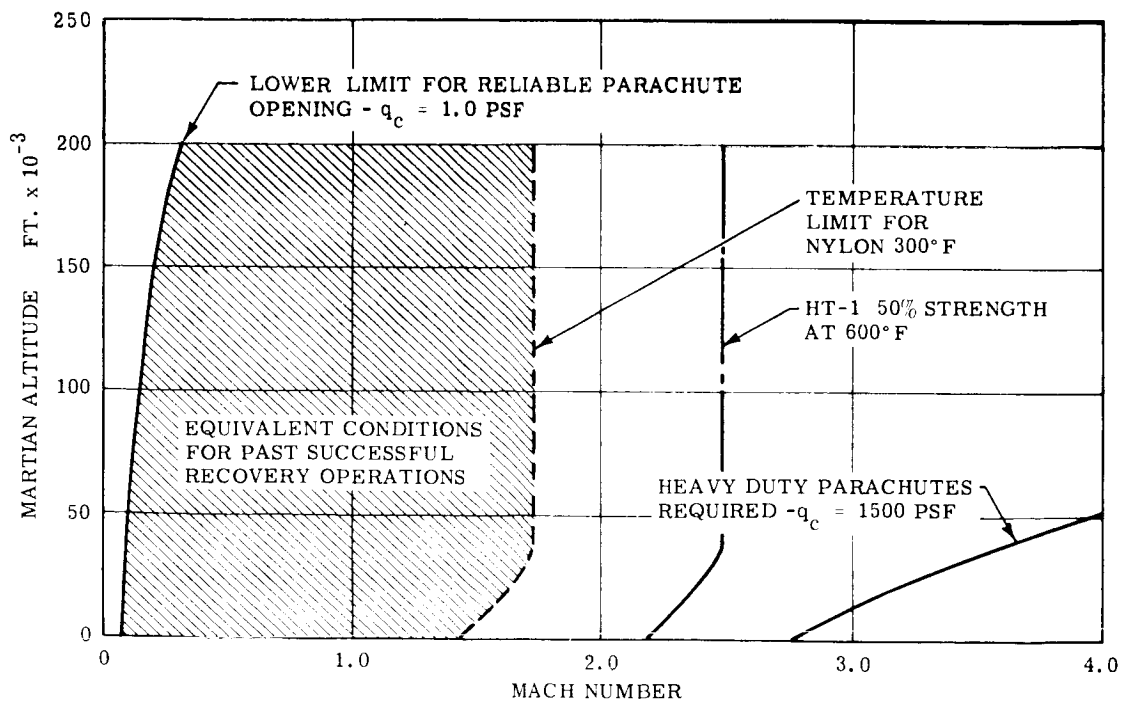


Figure 1.3.5-18. Decelerator Parachute State-of-the-art, Mars Upper Atmosphere

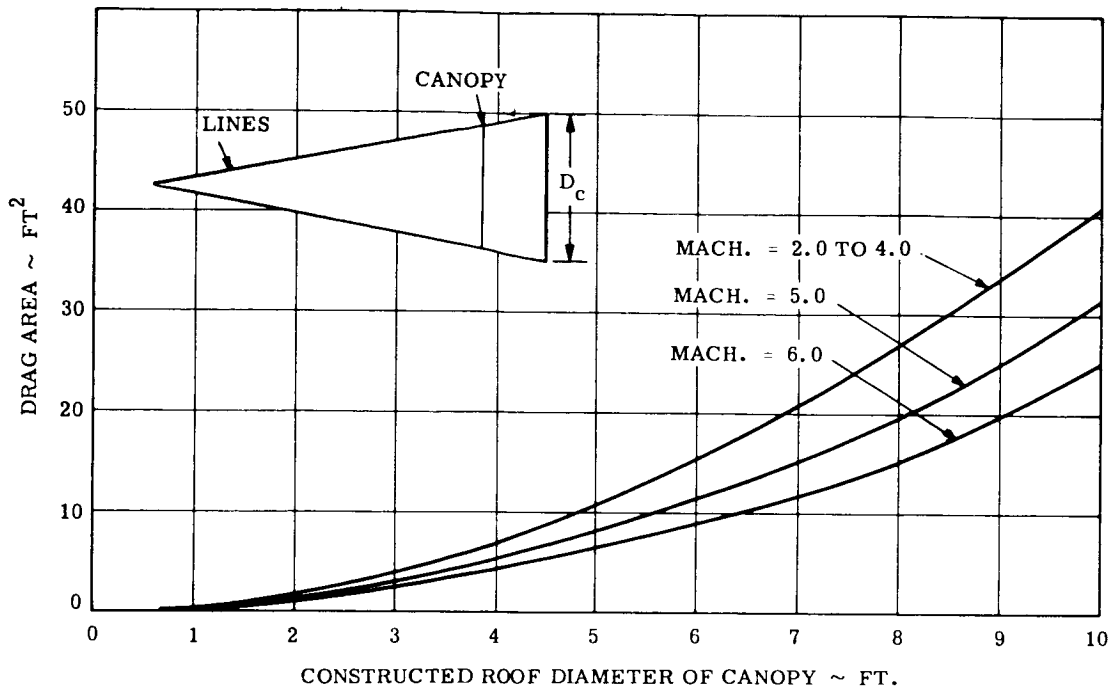


Figure 1.3.5-19. Drag Area of the Hyperflo Canopy as a Function of Constructed Diameter and Mach Number

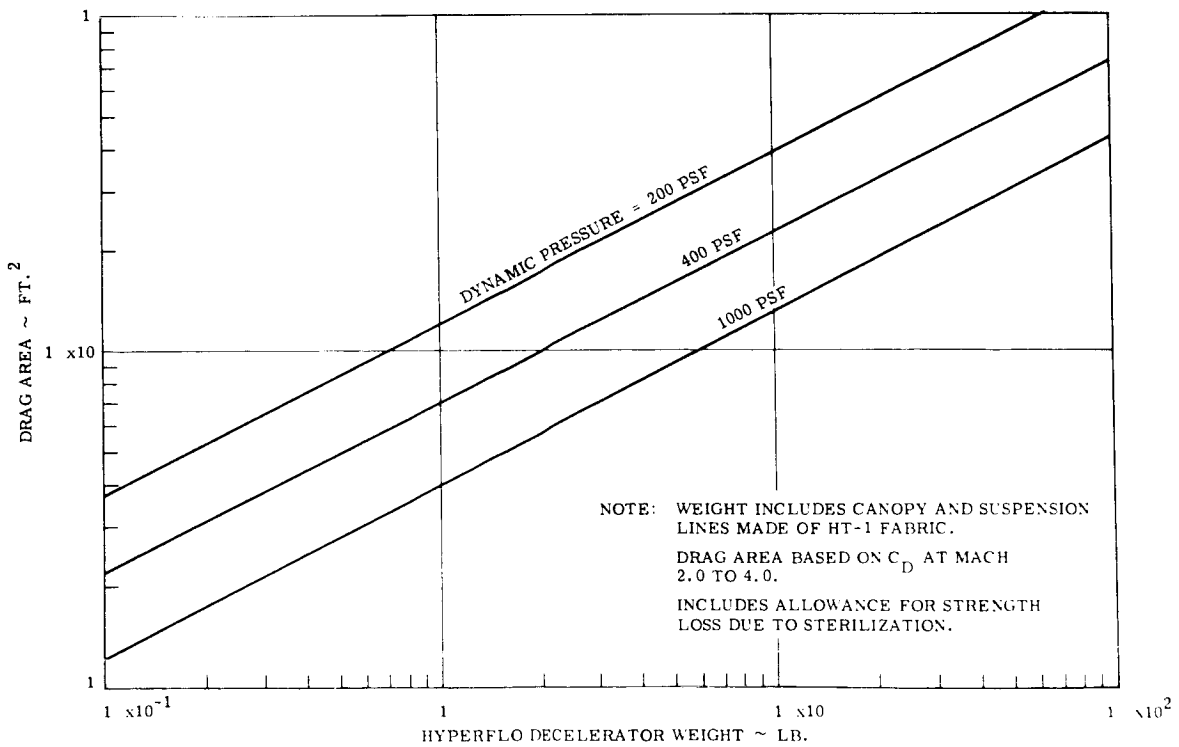


Figure 1.3.5.20. Estimated Assembly Weight of Hyperflo Decelerator Parachute

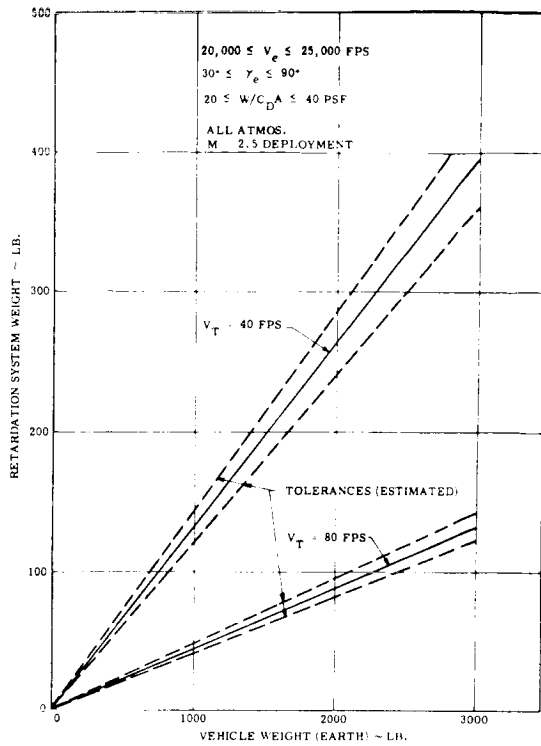


Figure 1.3.5-21. Retardation System Weight for Given Parameters

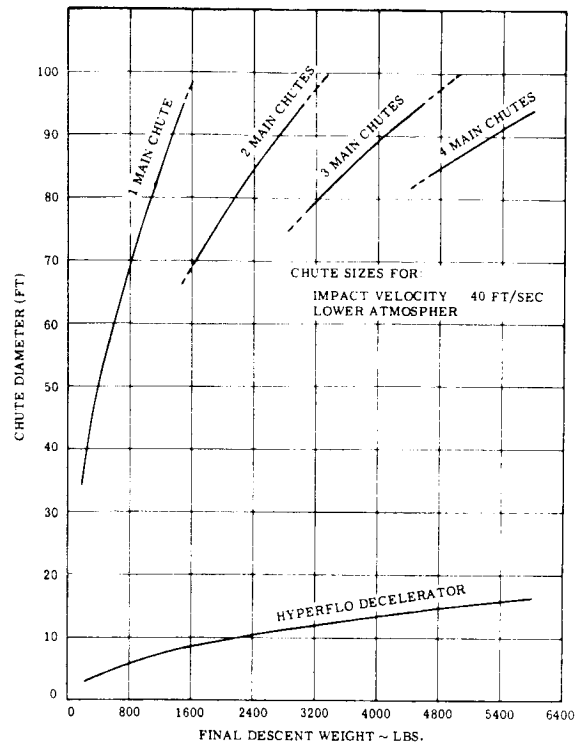


Figure 1.3.5-22. Parachute Diameters vs. Final Descent Weight

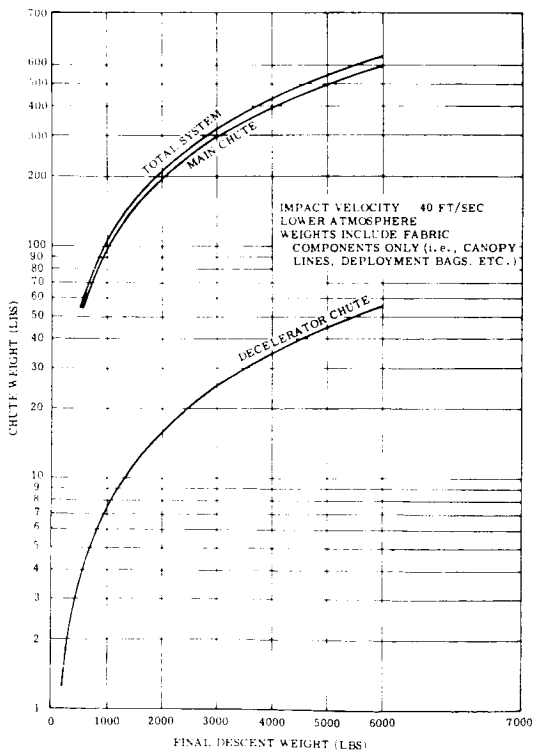


Figure 1.3.5-23. Parachute Weights vs. Final Descent Weights

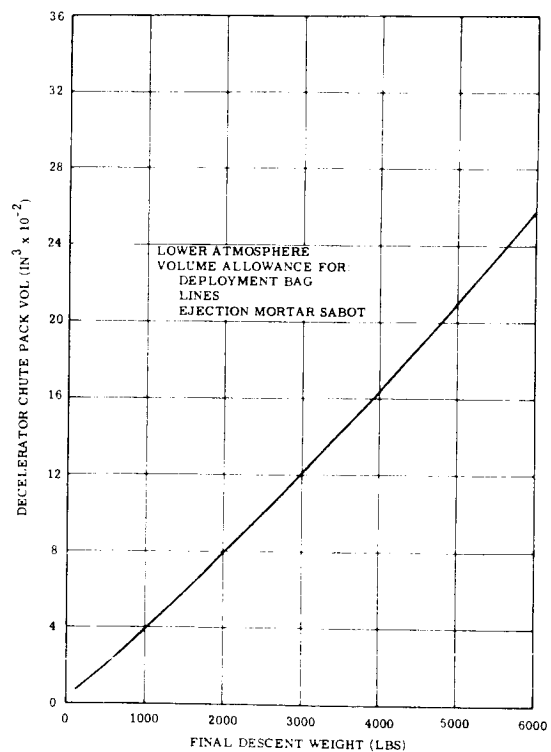


Figure 1.3.5-24. Decelerator Chute Pack Volume vs. Final Descent Weight - Mars Lander

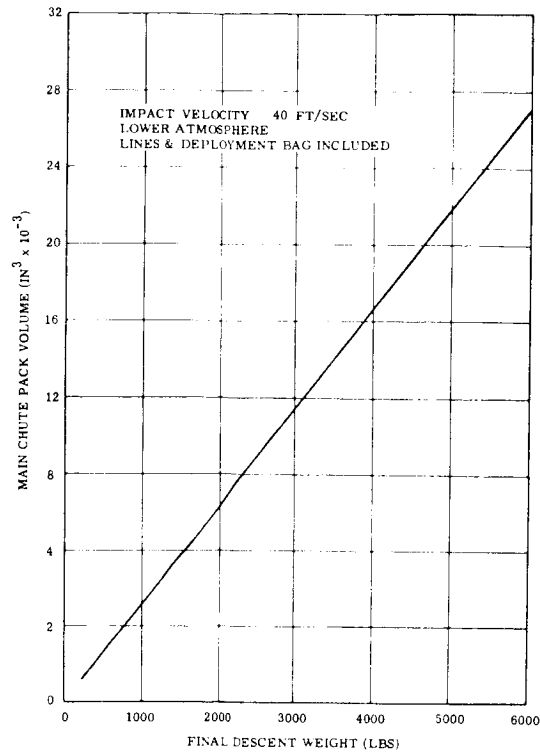


Figure 1.3.5-25. Main Chute Pack Volume vs. Final Descent Weight - Mars Lander

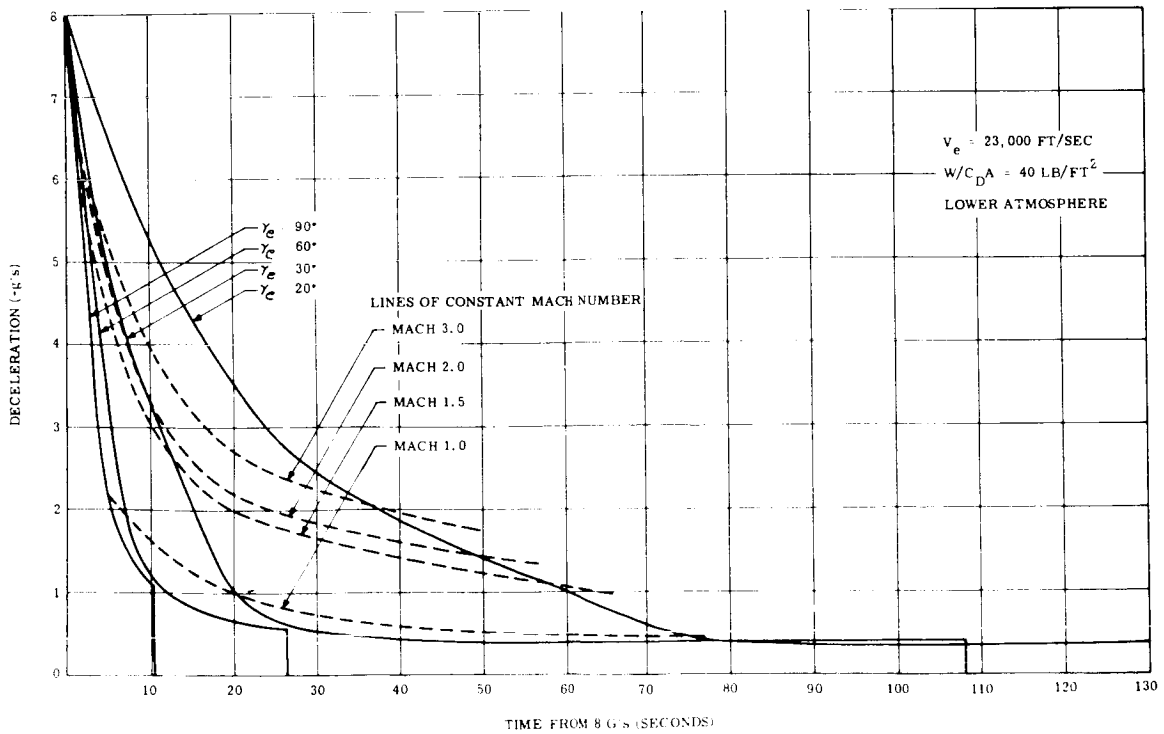


Figure 1.3.5-26. Deceleration vs. Time from 8 g's - Mars Entry

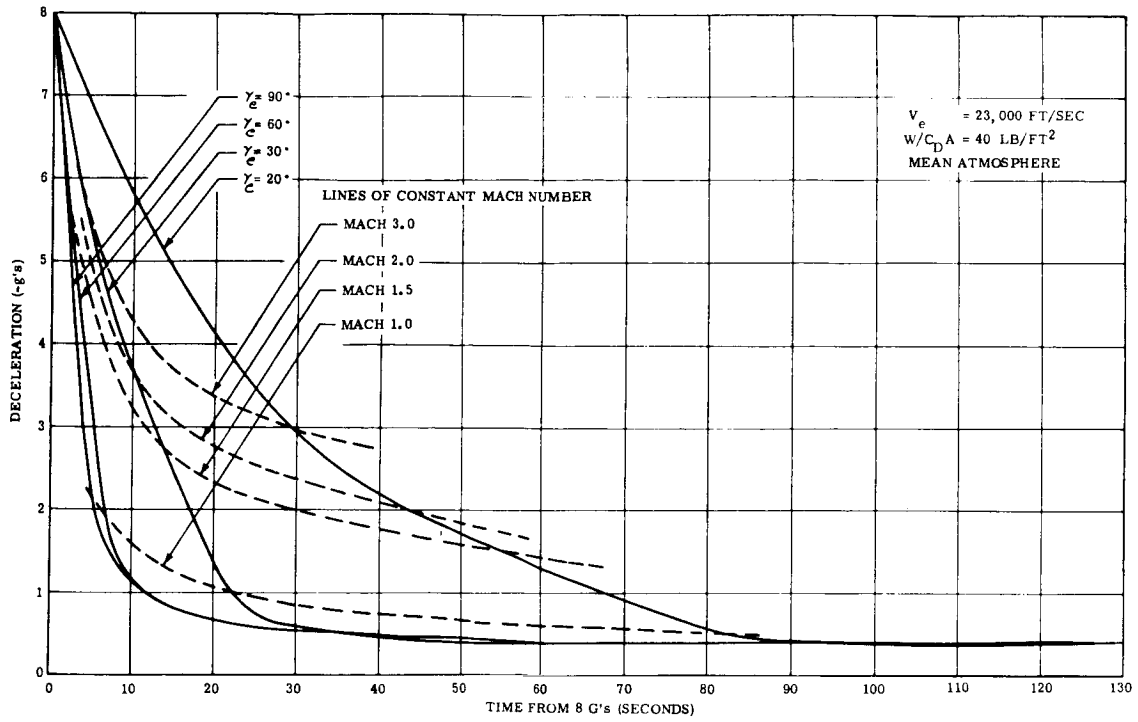


Figure 1.3.5-27. Deceleration vs. Time from 8 g's - Mars Entry

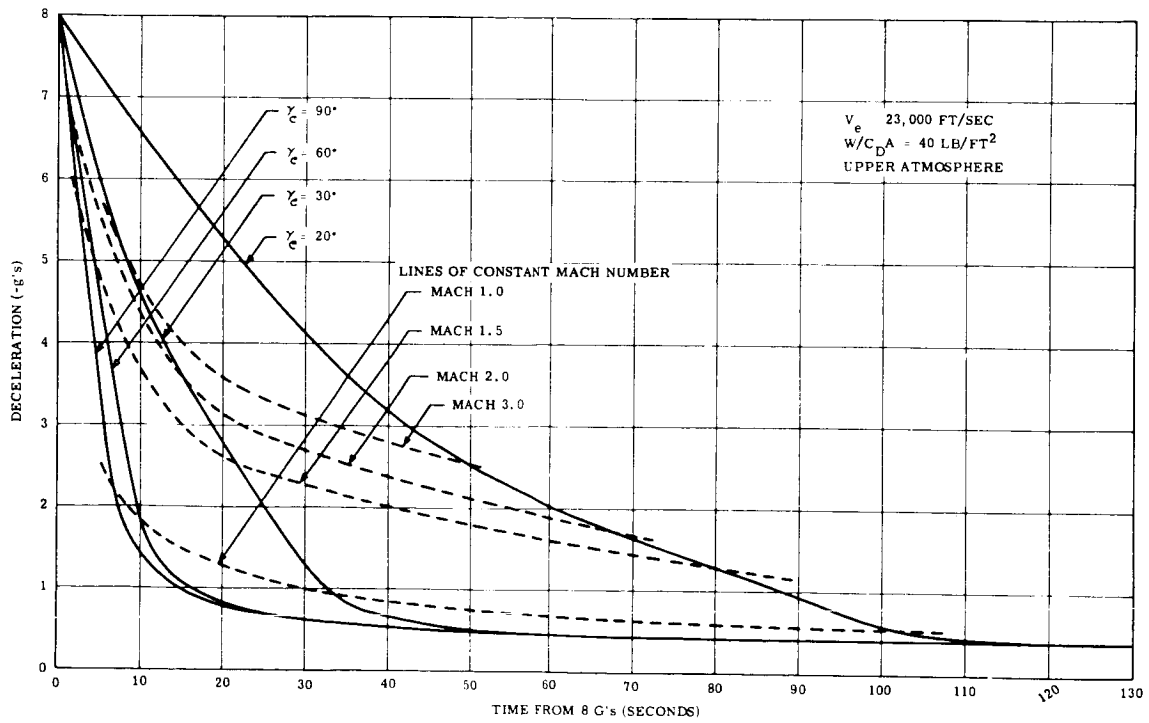


Figure 1.3.5-28. Deceleration vs. Time from 8 g's - Mars Entry

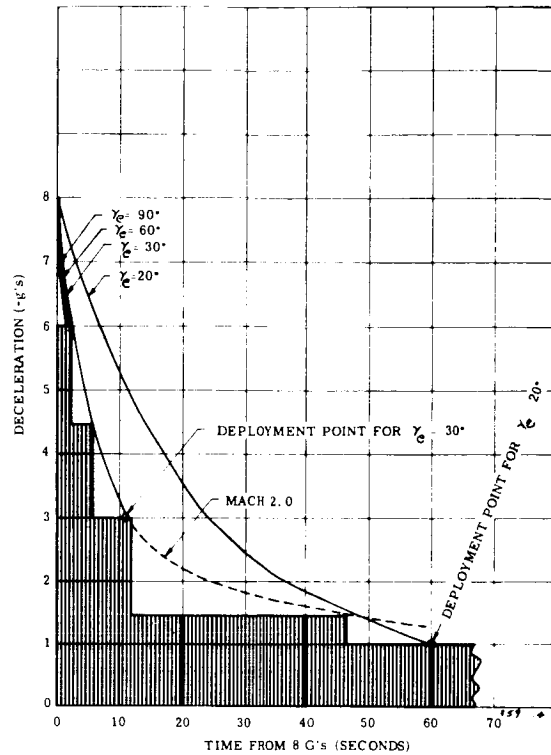


Figure 1.3.5-29. Deployment Point Diagram - Mars Entry

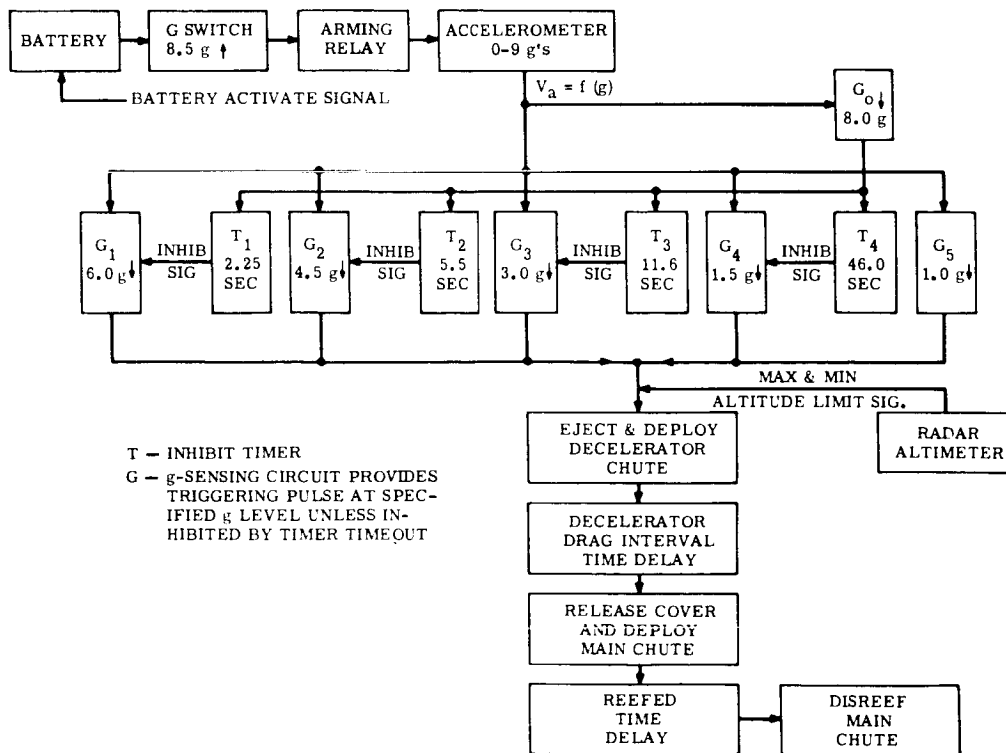


Figure 1.3.5-30. Functional Block Diagram, Retardation System

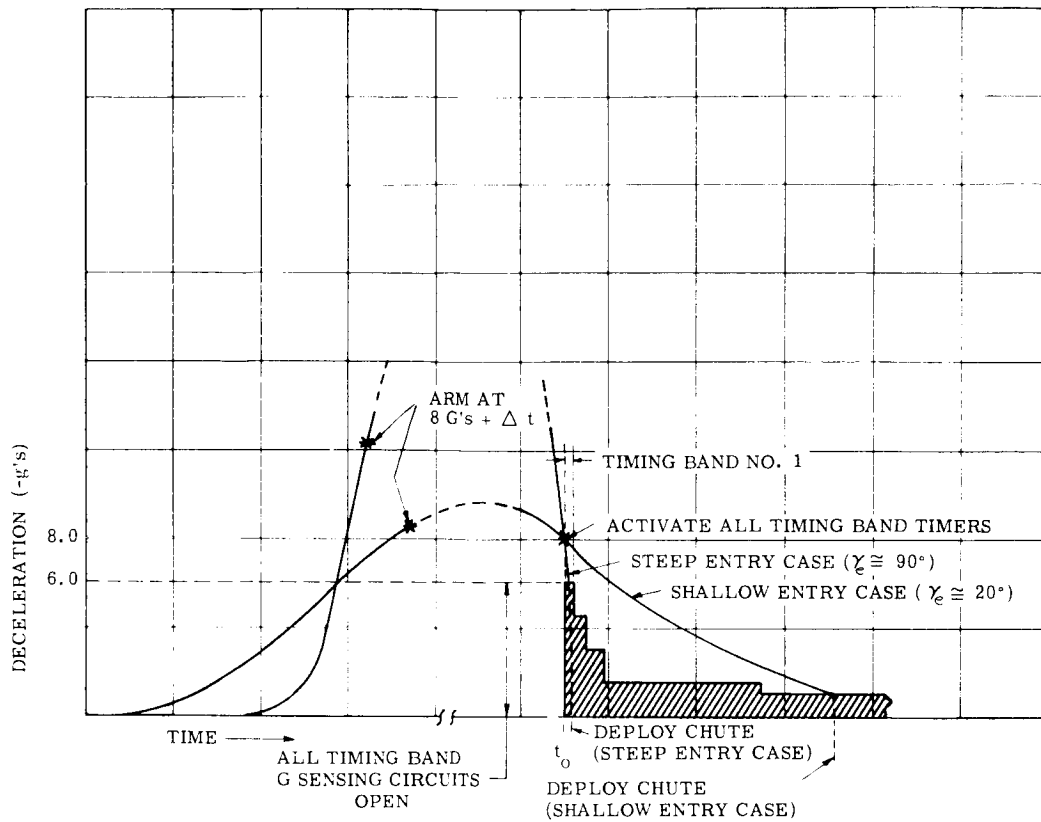


Figure 1.3.5-31. Programmer Functional Events for Mars Entry

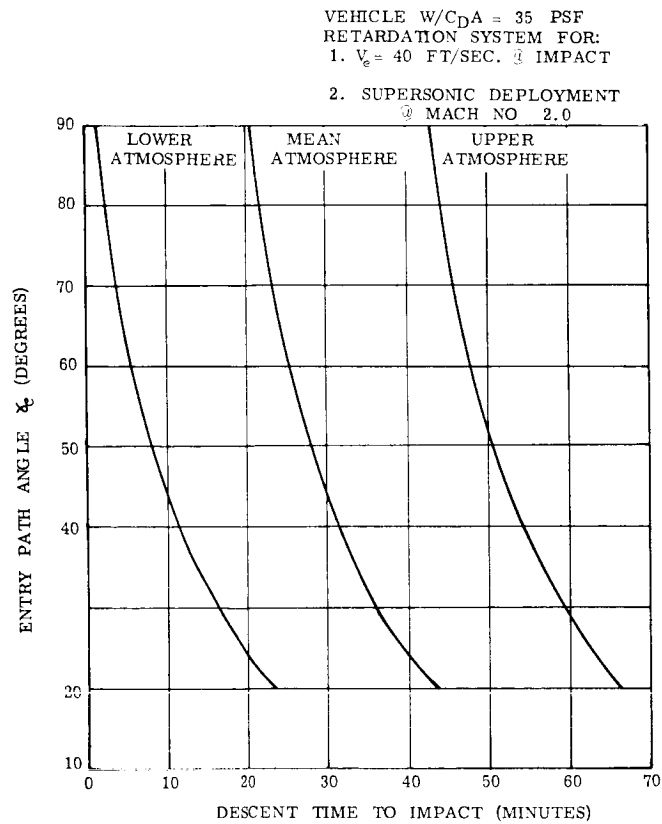


Figure 1.3.5-32. Descent Time to Impact vs. Entry Path Angle - Mars Entry

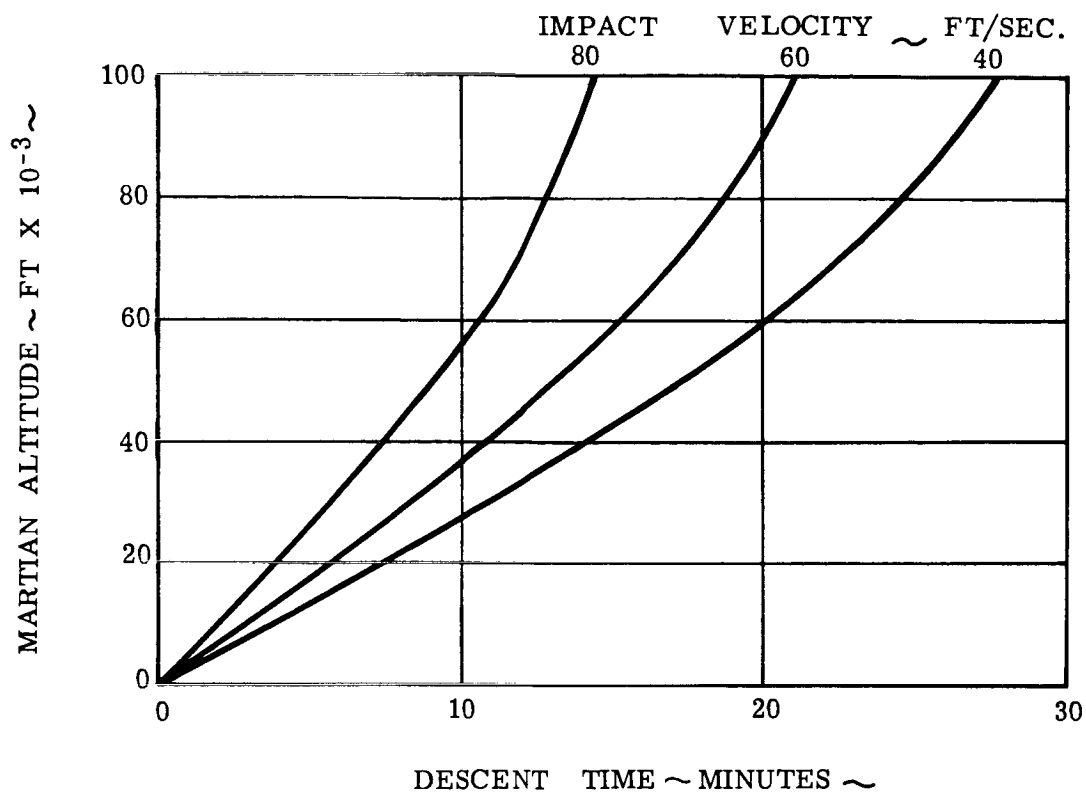


Figure 1.3.5-33. Descent Time with Main Parachute vs. Deployment Altitude - Mars Lower Atmosphere

1.3.6 THERMAL CONTROL

A. Introduction

The major portion of the operation time of the Mars Lander will be in an environment which is at a lower temperature than the desired component operational temperature. The environmental heat fluxes during transit decreases from approximately 450 Btu/hr-ft² to 195 Btu/hr-ft² in going from Earth to Mars. If the optical surface coating were selected such that the mean equilibrium temperature of the vehicle was 100°F at Earth, its mean equilibrium temperature at Mars would be -5°F or 55°F below the desired operational limit of the component temperatures. If the lander is shade-oriented, its temperature would approach that of cold space. The thermal control system for the Mars landers must be capable of adapting the thermal control system to the local conditions since the environmental conditions to which the vehicles are exposed are relatively unknown. The thermal control system must be capable of maintaining the internal payload temperature of the spacecraft between 50°F and 100°F, within the space environment of transit and on the surface of the planet. The thermal aspects of the space environment can be predicted with good accuracy; however, it is the surface environment of the planets which presents the major problem. The surface temperature of Mars may range from -184°F to a high of 117°F along with pressures ranging from nearly zero to 2 psia.

It is evident that an internal control system which is capable of heating the payload is required for the Mars lander. There are a number of ways of providing the necessary heat: electrical heaters, a chemical process, radioisotope packets, and waste energy from the electrical power supply. The heating requirements of the proposed Mars 1969 Lander could be as high as 500 watts for the lowest predicted Mars surface temperature of -184°F. Therefore the feasibility of using electrical heaters is impractical for a long period of time, since the batteries and/or increased power supply capabilities required to provide the electrical energy for a mission of one month or more is prohibitive from a weight standpoint. Similarly the weight and high reaction temperature of a chemical heat source such as hydrogen peroxide would be excessive (> 400 lbs) for a 30 day operation time on Mars. The heating of the payload using radioisotope packets distributed throughout the vehicle would result in a light weight thermal control system, however, this system provides no means to control heat. When less heating is required there is no way of cutting down the amount of energy dissipated from a radioisotope packet short of removing it from the payload. The remaining thermal control system, that of using the thermal energy dissipated from the electrical power, looks particularly attractive when the electrical power supply is a Radioisotope Thermoelectric Generator (RTG), which produces large quantities of waste thermal energy which must be rejected. Based on these conclusions the latter thermal control system is recommended. The results and conclusions to follow are based upon this type of system for the Mars Lander.

The system found to be the most satisfactory for the Mars lander was one which uses the waste thermal energy from the RTG electrical power supply to heat the payload during transit and within the low surface temperature environment. The Landers are shaded from the sun by the orbiter throughout the transit period. A liquid loop circulation system is utilized to convect the thermal from the RTG unit to the payload as required to maintain the payload temperature between 50°F and 100°F. During the transit period, the thermal energy dissipated by the RTG unit, over and above that required for temperature control, is radiated to space from a radiator in the liquid coolant loop. On the surface of Mars, the excess thermal energy is radiated directly from the RTG unit's outer surface. During powered flight and entry into Mars, the energy released from the RTG unit is absorbed by vaporization of an expendable coolant (water). The system will maintain the payload between 50°F and 100°F, except after long periods of instrumentation and component checkout on the launch pad and during the periods of time on Mars when the surface temperature may exceed 80°F. The electronic equipment may operate up to 150°F. To protect more temperature sensitive items such as the batteries and the biological culture, a heat of fusion material is used which has a melting temperature of 83°F.

The Venus Lander will be exposed to an extremely hot environment with surface temperatures ranging from 600°F to 1050°F. These temperatures exceed the maximum operating temperature of the equipment by several hundred degrees, therefore, the problem of maintaining the temperature of the payload at an acceptable level is one of cooling or removing the thermal energy from the vehicle. With the wide variation of design surface temperatures and with the variation of the solar flux from 445 BTU/hr-ft² at earth to 855 BTU/hr-ft² at Venus during the transit phase, the need for a thermal control system which may adjust itself to meet these conditions is again apparent.

There are three possible methods of providing the necessary cooling; thermoelectric, heat pump or vapor compression cycle, or an expendable coolant system. The first two methods may be eliminated by considering the coefficient of performance for a Carnot refrigerator. The maximum amount of refrigeration for each watt of input energy to the device is 0.59 watts, assuming that the energy is removed at 100°F and rejected at 1050°F. Because more is expended within the system than is removed, the system cannot cool itself. Therefore, the thermoelectric and vapor compression systems are not recommended for use within the Venus Lander vehicle. An expendable coolant system can provide the necessary cooling within the high temperature Venus environment.

An expendable coolant system using ammonia as the coolant was found to be the minimum-weight cooling system for the Venus Lander when the pressures were less than 10 atms. For atmospheric pressures greater than 10 atms, a water-ice system was found to be the best system. The expendable coolant system is activated during the entry phase into Venus when the internal vehicle temperature reaches 100°F. During the transit period, the internal vehicle temperature is maintained between 50°F and 100°F by optical surface coatings, thermal insulation, and internal electric heaters.

Prior to receipt of the study atmospheres, a thermal control system based on the 54 atmosphere surface pressure of the old Venus Extreme I atmosphere had been completed. The results of this study are included for completeness and to illustrate the effect of high design surface pressures on the thermal control system.

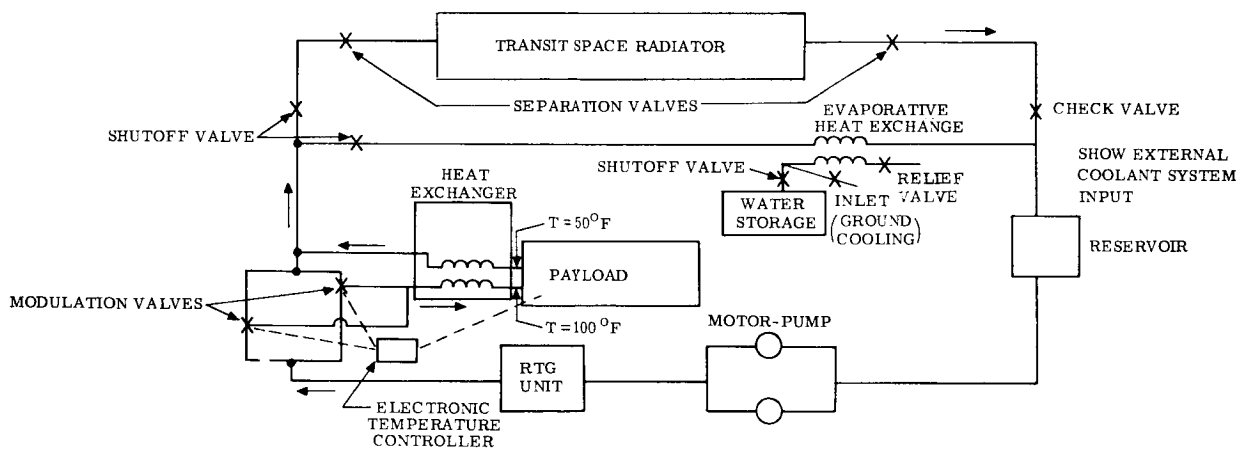
B. Prelaunch and Powered Flight Thermal Control for the Mars Lander

The temperature of the electronic equipment within the Mars lander during the prelaunch and launch phase can be maintained within acceptable limits by utilizing the thermal mass of the payload and adjacent structure. This is based on the fact that the allowable component temperatures may be 150°F and that the equipment is to be non-operative except during checkout. The thermal mass of the Mars 1969 vehicle is sufficient to absorb approximately 200 watts-hours of thermal energy assuming the initial temperature is 100°F.

The thermal energy dissipated by the RTG unit during the prelaunch and the powered flight phase is removed by the vaporization of water within an evaporative heat exchanger, which is located within a liquid coolant loop. The coolant is circulated through a heat exchanger located within the RTG unit, thus removing the dissipated thermal energy. The coolant is heated to a temperature of approximately 400°F. This energy is removed from the coolant within the evaporative heat exchanger by the vaporizing water. During the prelaunch phase, the water is supplied from an external source. During the power flight and entry into Mars phases, the water coolant is supplied from a storage tank within the Lander. Approximately 10 pounds of water is required to provide sufficient cooling for the 83 watt RTG unit during the launch phase and the longest predicted entry into Mars. The storage vessel and the water expulsion system would weigh an additional 3 pounds. The expulsion of the water can be accomplished by the expansion of a compressed spring behind a diaphragm within the water container.

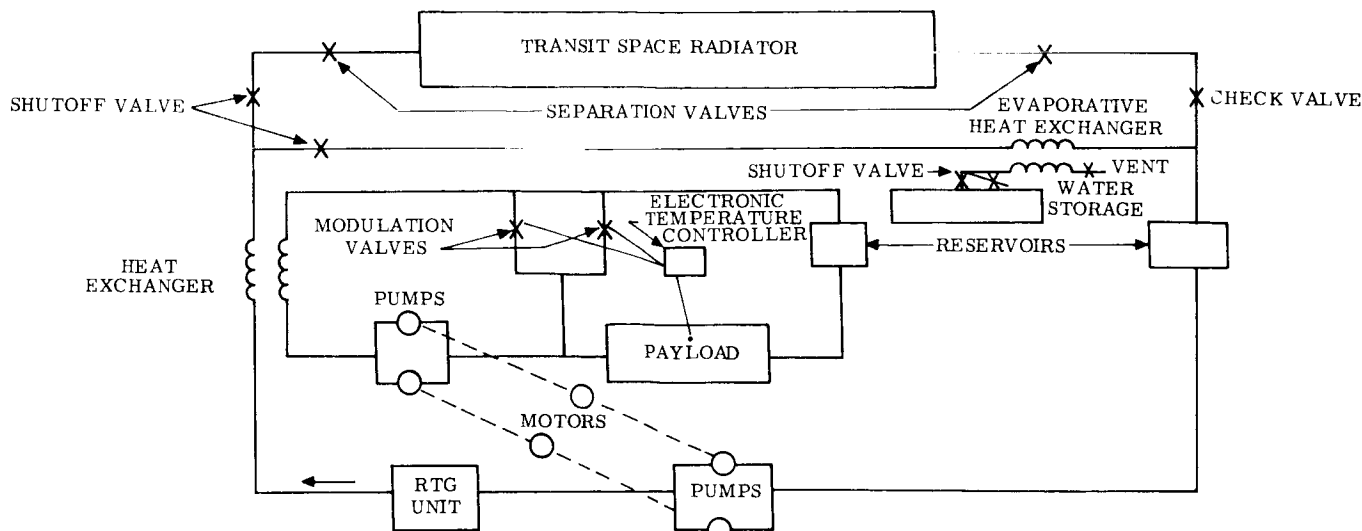
C. Transit Thermal Control of the Mars Lander

The lander vehicles are shaded from the sun by the orbiter at all times. Therefore, without internal heating of the vehicle, its temperature would tend to approach that of cold space. This heating can be provided by electrical heaters located within the payload or by utilizing the thermal energy dissipated by the RTG unit. The latter choice is the most desirable since the thermal energy dissipated by the unit must be rejected to space anyway. The amount of energy required to maintain the payload at 75°F depends on the optical surface properties of the external surface and the overall thermal conductance of the vehicles. For instance, the Mars 1969 Lander, having a wall thermal conductance of .053 BTU/ft-hr °F based on 4.5" Fiberglass and 15 lb/ft³ and a surface emissivity of 0.8 (organic paint), would require an energy input of 3.5 watts per square foot of radiating surface area to maintain a payload temperature at 75°F. The resulting surface temperature would be -150°F. The amount of energy radiated to space may be decreased by decreasing the emissivity of the surface coating or by insulating the shell of the vehicle. However, since the energy required to heat the payload is waste energy being dissipated by the RTG unit, there is no major advantage in decreasing the amount of energy lost from the vehicle. The energy is transferred from the RTG unit by a liquid transport loop. The quantity of the fluid allowed to circulate through the payload and, therefore, the amount of energy transported to it is controlled by a modulation valve. A schematic diagram of the system is shown below:



The modulation valve receives a signal from the electronic temperature controller which is sensing the temperatures of the payload equipment. A system operating in this fashion can maintain the temperature of any desired component within $\pm 25^\circ\text{F}$ of the desired nominal operation temperature of 75°F.

The coolant being discharged from the 83 watt RTG unit will be approximately 450°F at a flow rate of 130 lb/hr. Since this temperature is 350°F above the desired inlet temperature to the payload it is necessary to utilize a regenerative heat exchange to lower the coolant temperature. The temperature of the coolant is decreased by transferring the thermal energy to the low temperature (50°F) coolant being discharged from the payload. An alternate system would be to use a two loop system where the thermal energy would be transferred from the RTG circulation loop to a payload loop through a liquid to liquid heat exchanger. A schematic diagram of this system is shown below:



This latter system has the disadvantage of requiring an additional pump and a second coolant storage reservoir or accumulator for the thermal expansion of the coolant in the payload loop. This system, however, does offer the advantage of using two different coolants; a high temperature coolant such as Dow Therm in the RTG loop, and a low temperature coolant in the payload loop. With the single loop system having the regenerative heat exchanger, a single coolant is required to operate over the entire temperature range from 50°F to 450°F. A tabulation of several possible coolants is shown in Table 1.3.6-1. The thermal and transport properties are shown graphically in Figures 1.3.6-1 to 1.3.6-16.

Examining these properties, we find two liquid coolants (Monoisopropylbiphenyl and OS-45 Type IV) which have a sufficiently broad temperature operating range that they may be used within the single loop system. The Monoisopropylbiphenyl has excellent nuclear radiation resistance properties which may be desirable since the fluid is to pass through an RTG unit. Another factor which must be considered in the selection of the coolant is its influence on the performance and life of the circulation pump. For the low flow rates and long life requirement (up to 18 months) for the Mars mission, a positive displacement gear pump appears to be the only practical choice. To ensure long term operation of the liquid loop thermal control system, redundant pumps and modulation valves have been placed within the system. Only one pump and one modulation valve would function at a time. If the first one fails the next one would be activated and thus the system would continue to perform its task.

The 83 watt RTG unit dissipates approximately 1970 watts and since the 1450 pound Mars Lander requires only about 250 watts to maintain the internal temperature at 75°F during transit, the remaining 1730 watts must be radiated to space. The excess energy is transported by the liquid coolant to a space radiator on the adapter section between the lander and the orbiter. The coolant temperature is decreased to approximately 350°F within the radiator. Due to the blockage of the radiator by the Landers and the Orbiter, the surface area of this radiator is approximately twice the actual required area of 13 ft². The radiator design is based on a radiator effectiveness of 0.7 and an emissivity of 0.80 which may be attained by using a coating of titanium dioxide silicone acrylic, zinc sulphide-silicone, or a number of other high temperature coatings.

The pressure drop within the system varies from about 10 to 15 psia depending on the amount of coolant circulating through the payload loop. At a flow rate of 130 lb/hr this

TABLE 1.3.6-1. TABULATION OF COOLANTS

Coolants	Freezing Point (°F)	Flashability: (a) Fire Point (b) Self-Ignition Point (°F)	Thermal Stability (°F)	Chemical Stability	Density (lb/in ³) (lb/ft ³)	Boiling Point at 1 atm (°F)	Heat of Vaporization at Boiling Point	Remarks
1. Silicone Oil SF 96 (S)	-120	(a) 275 (b) 280	589	Inert, except with acid or base of 10% conc. At high temp. with P ₂ O ₅ , S, T.	51.2	--	--	The thermal stability of silicone fluids make exceptionally useful as heat transfer media. They are relatively non-flammable with a spontaneous ignition temperature in the 600°F range.
2. Silicone Oil SF 96 (L)	-100	(a) 410 (b) 470	--	At higher temp. polymerization to higher weight material which remains in solution may take place.	58.7	--	--	Dowtherm A is a eutectic mixture containing 75.5% diphenylacetate and 26.5% diphenyl. It may be employed for heat transfer application either in the liquid or vapor state. Dow Chemical Company suggests use of the fluid in the temperature range between 450 to 750°F.
3. Dowtherm A	Freezing Point -35.6	(a) 255 (b) 275 (c) 1150	When heated near the upper limit of its recommended temp. range, it tends to slowly decompose.	At higher temp. polymerization to higher weight material which remains in solution may take place.	66.3	406.8	124.3 BTU/lb	Dowtherm E is a grade of O-Dichlorobenzene which has been purified to remove all moisture. It is used in the liquid or vapor state. The recommended operating temperature range is 300 to 500°F.
4. Dowtherm E	Freezing Point -7	(a) 155 (b) 235 (c) Above 932	When heated above 500°F, decomposition may occur.	It is believed the aluminum catalyzes thermal break-down.	78.1	352	100.25 BTU/lb	Water is an unequaled heat transfer medium.
5. H ₂ O	Freezing Point -32	Nonflammable	Water has the highest boiling point of any liquid at 1 atm. It is thermally stable for prolonged periods at elevated temps., moisture contaminant should be kept at a minimum.	It has excellent chemical stability.	62.2	212	970.3 BTU/lb	OS-39 can be used effectively as a coolant-dielectric fluid at temperatures from below -60°F to 1000°F. The primary application of OS-39 is within sealed transformers or similar applications.
6. OS-39	-85	(a) 370	OS-39 attacks most seal materials used in pumps.	OS-39 attacks most seal materials used in pumps.	55.7	700 (With decomposition)	--	OS-39 is within sealed transformers or similar applications.
7. Coolanol 25 (Formerly OS-139)	-100	(a) 340 (b) 385	--	Coolanol 25 does not react with most organic acids, alcohols, and esters. It is more resistant to oxidation than conventional petroleum hydraulic fluids. It is compatible with most seal materials and O-rings. Coolanol 25 is not advised.	55.8	600	--	Coolanol 25 is a synthetic fluid formulated for use as a -100°F to 600°F coolant. It has excellent stability and compatibility with existing materials.
8. Coolanol 35	-85	(a) 375	--	In general, OS-45 is compatible with all common seal materials. It is not advised for use in machinery.	55.1	600	--	Coolanol 35 is similar to Coolanol 45 except for a lower viscosity at sub-zero temperatures to -85°F.
9. OS-45 Type IV	-85	(a) 370	--	Water contamination must be avoided. It is compatible with all common seal materials. It is not advised for use in machinery.	55.7	600	--	OS-45 Type IV conforms to military hydraulic fluid designations and is recommended for operation in systems over the temperature range of -80 to 500°F.
10. Coolanol 45	-85	(a) 370	The maximum recommended operating temperature is 400°F.	Water contamination must be avoided. It is compatible with all common seal materials. It is not advised for use in machinery.	55.7	600	--	Coolanol 45 is a fluid having a silicate ester base. It is intended to be used as a liquid coolant. It has an extremely wide temperature range, -85°F to 400°F.
11. FC-75	-80	Nonflammable	No degradation at 570°F for 157 hr at 1000 psi. No degradation at 570°F for 157 hr at 1000 psi.	Chemically inert. However, reactions with acids, alkalis, peroxides, alcohols, and esters should be avoided. It is not advised for use in machinery.	100	214	37.8 BTU/lb	FC-75 is a fully fluorinated product composed primarily of a mixture of 8 carbon materials. It has high thermal stability and electrical insulating properties which are far superior to hydrocarbon oils and esters.
12. FC-43	-40	Nonflammable & nonexplosive	Specified thermal stability during prolonged exposure at temps. up to 617°F. When the solution is heated above a temp. of about 220°F, it may decompose to form a sludge which has a tendency to form a troublesome sludge unless a stabilizer is added.	Chemically inert. However, reactions with acids, alkalis, peroxides, alcohols, and esters should be avoided. It is not advised for use in machinery.	116.7	250	28.2 BTU/lb	FC-43 is a fully fluorinated product composed primarily of a mixture of 8 carbon materials. It has high thermal stability and electrical insulating properties which are far superior to hydrocarbon oils and esters.
13. Ethylene Glycol 100% (By Weight)	Freezing Point -9	(a) 245 (b) 250	--	Ethylene glycol, by itself, in aqueous solutions, is stable. It is not advised for use in machinery.	64.4	387	--	Ethylene glycol solutions are excellent heat carriers over a wide range of temperatures between -50°F to about 400°F.
14. Ethylene Glycol 60% (By Weight)	Freezing Point -74	--	--	Chemically inert. However, reactions with acids, alkalis, peroxides, alcohols, and esters should be avoided. It is not advised for use in machinery.	64.5	--	--	FC-43 is a fully fluorinated product composed primarily of a mixture of 8 carbon materials. It has high thermal stability and electrical insulating properties which are far superior to hydrocarbon oils and esters.
15. Ethylene Glycol 50% (By Weight)	Freezing Point -5	--	--	Chemically inert. However, reactions with acids, alkalis, peroxides, alcohols, and esters should be avoided. It is not advised for use in machinery.	64.5	--	--	FC-43 is a fully fluorinated product composed primarily of a mixture of 8 carbon materials. It has high thermal stability and electrical insulating properties which are far superior to hydrocarbon oils and esters.
16. Ortho-terphenyl	Freezing Point -119	(a) 340 (b) 380	Pyrolytic and radiolytic breakdown follow similar patterns, resulting in similar decomposition products. The decomposition products are stable at higher temperatures at which pyrolysis becomes significant for nuclear applications, constant regeneration and partial replacement of the coolant is recommended. (See remarks.)	No hazardous chemical reactions take place between ortho-terphenyl and water and hydrocarbons. Terphenyls do not react with acids, alkalis, peroxides, alcohols, and esters. Ortho-terphenyl is not advised for use in machinery.	65 (at 200°F)	--	--	Ortho-terphenyl may be used as a heat transfer fluid up to about 600°F. Only minor weight loss occurs at 600°F. Ortho-terphenyl has properties which have favored their use as coolants in nuclear reactors. Terphenyls are stable under neutron capture cross-sections. Para-terphenyl has the best radiolysis stability.
17. Meta-terphenyl	Freezing Point -189	(a) 405 (b) 445	Thermally stable to temp. around 500°F.	No information	64.4 (at 200°F)	--	--	Thermal Stability - At temperatures higher than 750°F, polymerization to higher molecular weight polyphenyls slowly takes place. This increases the viscosity and reduces heat transfer. For example, polymer by weight is formed. Hydrogen gas is a by-product of the polymerization reaction.
18. Para-terphenyl	Freezing Point -113	(a) 405 (b) 460	Thermally stable to temp. around 500°F.	No information	64.4 (at 200°F)	--	--	Monoterprenylphenyl and diterprenylphenyl may be used in a nuclear radiation environment.
19. Monoterprenylphenyl (MTPB)	-70	(a) 315 (b) 240 (c) 285	--	No information	61.2	543	--	--
20. Dinitroterphenyl (DNP)	-24	(a) 315 (b) 240 (c) 285	--	No information	61.2	543	--	--
21. OS-124	40	(a) 550 (b) 600 (c) 1135	OS-124 is stable to approximately 847°F.	OS-124 is stable in water, alcohols, bases, and oxygen at temps. considerably higher than any presently used heat transfer media.	74.6	982	--	The use of polyphenyl ethers for high temperature heat transfer is a new development. The thermal stability of polyphenyl ethers compares favorably with that of silicones, silicones, hydrocarbons, ethers and other commonly used heat transfer media. OS-124 is a mixed isomeric five ring polyphenyl ether.

gives an ideal pumping requirement of 2 watts for the system using Monoisopropylbiphenyl as the coolant. The flow rate of 130 lb/hr is determined by the maximum payload inlet temperature of 100°F and the minimum outlet temperature of 50°F and the maximum amount of energy lost from the vehicle. The combined motor-pump efficiency in this low pressure rise and mass flow rate region is low, ranging from 5 to about 15%. However, with the development of high performance brushless D.C. electric motors, combined efficiencies of 15% and perhaps higher should be attainable. Assuming an efficiency of 15% the required electrical input to the pump is 13.5 watts at the maximum system pressure drop of 15 psia. The modulation valve and electronic controller requires an additional 3 watts of electrical power.

At the start of entry into Mars, the transit space radiator is separated from the vehicle by explosive separation valves which also seal the cut coolant lines. In addition to the sealing-separation valves, two backup sealing valves are provided. Once the space radiator has been separated from the vehicle, the thermal energy from the RTG unit is removed by vaporizing an expendable water coolant within the evaporative heat exchanger located in the radiator by-pass line. This is the same system that was used during the power flight phase. This expendable system continues to operate until the vehicle impacts on Mars and is oriented so that the surface mode of the thermal control system can be activated.

D. Surface Thermal Control for Mars Lander

The forward nose portion of the entry vehicle which covers the RTG unit must separate from the vehicle to expose the RTG unit because of safety requirements. Therefore, the thermal energy dissipated within RTG may be radiated to space and the surrounding Mars environment. The surface temperature of the 83 watt RTG unit will reach a temperature of approximately 560°F. This operation temperature is achieved by adding 10 fins to the basic RTG unit, which is a cylinder 10 inches in diameter and 10 inches long. The required emissivity is 0.8. If the power dissipation within the RTG unit were increased to any great extent, it would be necessary to remove the thermal energy from the RTG, using the coolant loop, and reject it from a radiator. The density of the atmospheric gases on Mars are so low that natural convection may be neglected in comparison to radiation even at a moderate surface temperature of 100°F. Any attempt to utilize forced convection to transport energy from the RTG unit to the payload appeared impractical, since the blower or fan requirements were 3 to 4 times that required for the pump in the liquid loop. Therefore, the liquid loop system as described in this section (C.) would be used to provide the heating within the payload during the low temperature conditions on Mars.

The design of the internal thermal control system for operation on the surface of Mars is complicated by the large variation in the environmental temperature (-184 to 117°F). At the low temperatures of a -184°F considerable heating is required to maintain the payload at 50°F. At the high temperature condition of 117°F the thermal resistance of the heat transfer paths from the equipment to the radiating surface must be held to a minimum, in order to release the heat dissipated by the electronic equipment and hold the operating temperature of the electronic equipment to 150°F or less. The thermal conductance path through the side of the vehicle is set by the insulating effect of fiberglass honeycomb, which was designed for impact not thermal control. However, the thermal conductance of the aft bulkhead may be set such that the major portion of the thermal energy dissipated by the payload may be radiated from the surface of this bulkhead. Components required to operate during the hottest portion of a Mars day should be located on the aft bulkhead. Since the temperature variation during a single day on Mars is approximately 108°F (See Figure 1.3.6-17 for the Mars surface temperature as a function of time of day) the minimum temperature corresponding to the 117°F condition would be 9°F. Therefore, it is possible to utilize the thermal inertia of the vehicle to smooth the temperature variation of the payload and reduce temperature extremes. An analog computer run was made to determine the maximum temperature and length of time the payload temperature exceeded 100°F. The results indicated that for the Mars 1969 the maximum mean temperature of the payload was 125°F and it could exceed 100°F for 10 hours. Since the

maximum temperature did not exceed 150°F, the electronic equipment should not present a problem, provided the high thermal dissipating equipment is located on the aft bulkhead.

Any payload elements requiring temperature control below 100°F, for example batteries and biological cultures, can be controlled by using a phase change paraffin heat sink which has a melting temperature near these temperatures. One such paraffin is Octadecane, which melts at 83°F and has a heat of fusion of 105 BTU/lb. Approximately 10 pounds of Octadecane would be required to limit the maximum temperature of the biological culture and batteries proposed for the Voyager Mars 1969 mission to 90°F.

Should the vehicle be exposed to the extreme cold environment of a 184°F approximately 500 watts of thermal energy would be required to maintain the payload at 75°F. The increase of 250 watts over the transit requirement is the loss from the aft bulkhead which was not exposed to space during transit. The thermal energy required to hold the payload at 75°F is provided by the RTG. The energy is transported from the RTG to the payload by the same liquid loop used during transit.

A summary of the Mars thermal control follows:

1.	Temperature Control	
	RTG	450 to 600°F
	Electronic Equipment	50 to *150°F
	Batteries and Biological Culture	75 to 90°F
2.	Possible Coolants	Monoisopropylbiphenyl or OS-45 Type IV
3.	Coolant Flow Rate	**130 lb/hrs.
4.	System Pressure Drop	10 to 15 psi
5.	System Power Consumption	16.5 watts
6.	Transit Radiator Surface Area	26 ft ²
7.	Mean Radiator Temperature	400°F
8.	System Weight (1450 lb. Mars 1969 Veh.)	90 lbs.
	2 Modulation Valves	6 lbs.
	1 Reservoir	1.5 lbs.
	1 Electronic Temp. Controller	1.5 lbs.
	2 Motor-Pumps	6 lbs.
	2 Separation Valves	6 lbs.
	4 Shutoff Valves + Relief Valve	6 lbs.
	1 Liquid to Liquid Heat Exchanger	5 lbs.
	1 Evaporative Heat Exchanger	5 lbs.
	1 Transit Space Radiator	18 lbs.
	1 Water Storage Vessel + Water	13 lbs.
	Insulation + Tubing + Coolant	12 lbs.
	Paraffin (Octadecane)	10 lbs.

*The maximum temperature of 150°F for the electronic equipment would occur only at the extreme surface temperature of 117°F.

**Monoisopropylbiphenyl coolant and 83 watt RTG unit.

E. Prelaunch and Launch Thermal Control for Venus Lander

When the total thermal energy dissipated on the pad is small, the passive thermal inertia of the vehicle can be used to absorb the heat generated during checkout. The thermal control of the Venus Lander during the prelaunch and launch phase is simplified by the fact that the contained electronic equipment within the vehicle is primarily non-operative. The equipment will be in operation only for short periods of time for check-out purposes only. The thermal energy dissipated during the check period can be removed from the electronic equipment by conduction to the structure of the vehicle. The thermal mass of payload and adjacent structure is sufficient to absorb approximately 300 to 500 watt-hours of thermal energy without exceeding the 150°F temperature limitation of the electronic equipment. This is based on a mean internal temperature of the payload of 100°F before the check-out phase begins. The temperature of the vehicle should be 100°F or less on the launch pad since it can be protected by a white aerodynamic fairing.

F. Transit Thermal Control for Venus Lander

Two vehicle (Orbiter-Lander combination) orientations have been investigated: sun-oriented and shade-oriented. The case of a random-oriented vehicle was not investigated. Since the spacecraft Orbiter vehicle is powered by solar cells, it must have a specified orientation throughout the transit period and because of space limitations the Lander will be shade-oriented. The Lander will remain attached to the Orbiter to within a few hours of entry into Venus. With these restrictions placed upon the orientation of the vehicle, along with the internal dissipation being zero, it is possible to utilize optical surface coatings and insulation for the major portion of the thermal control. In the case of the sun-oriented vehicle, it is possible to maintain the vehicle temperature between 18°F and 100°F without any additional equipment other than the optical surface coatings. To achieve this control, a continuous variation in α/ϵ (ratio of solar absorptivity to emissivity) from 0.4 to 1.1 is required for a Lander having a 30 degree cone angle. The α/ϵ requirements is given as a function of the angle between the surface and the solar rays as shown in Figure 1.3.6-18. The low temperature of 18°F occurs when the vehicle is near earth. Assuming the internal insulation is a Micro-Quartz insulation three inches thick, approximately 0.7 watts of internal dissipation per square foot of vehicle surface is required to maintain the payload at 50°F when the vehicle is near earth. The required dissipation decreases to zero at about the half-way point in the transit period to Venus. The control of the electrical heaters is accomplished by bi-metallic switches located within the payload.

The shade-oriented landing vehicle is protected from the sun's radiation by the Orbiter. The Orbiter must be of sufficient size and/or shape so that it completely protects the Lander from the solar flux during the entire transit period. The reason for this requirement is that the surface coatings of a shade-oriented vehicle are completely different from that of a sun-oriented vehicle. The optical surface coatings of a shade-oriented vehicle normally have a low emissivity to reduce the amount of heating required to maintain the payload at an acceptable temperature. To reduce the amount of heating required and to maintain a reasonable ablation shield surface temperature (0 to 50°F), it is desirable to enclose the entire shade oriented vehicle within a radiation barrier bag. The required thickness of the insulated bag as a function of the available energy for heating is shown in Figure 1.3.6-19. If 30 watts of electrical energy is available for heating and the vehicle surface area is 100 ft², then an insulated bag having a thickness of .28 inches would be required assuming a surface emissivity of 0.1. Based on an insulation density of 4.7 lb/ft³, the bag would weigh approximately 13 pounds for a Venus-sized system. The results shown in Figure 1.3.6-19 are based on using NRC-aluminized mylar insulation for the bag material. The thermal conductivity of the insulation has been derated by a factor of three from the predicted value: this is to allow for edge effects and other unaccountable heat leaks.

G. Entry and Surface Thermal Control for Venus Lander

Since the external environmental temperatures of Venus are considerably above the desired operational temperatures of the equipment to be included within the Lander, a means of cooling the payload must be devised. There are two practical systems which are capable of providing the low temperature (between 50 and 100°F) needed on the surface of Venus where the external temperature ranges from 450°F to 1050°F. These two systems are the expendable coolant system and the vapor compression system. The expendable coolant system is limited by the amount of coolant which may be carried within the vehicle, however, its power requirement is negligible. The vapor compression system may operate indefinitely, provided there is a source of power available to operate the compressor. The amount of power required to drive the compressor would be large for the Venus Lander, even if the efficiency of the motor and compressor were 100 per cent, it would require 1.85 watts of electrical power to remove 1 watt at 50°F if the rejection temperature were 1050°F. Actually, the efficiency of the motor and the compressor are each about 60 to 70 per cent for the size that would be needed for the Venus Lander. This increases the required power input to 3.78 watts per 1 watt of thermal energy removed at 50°F. Considering the power requirements of the vapor compression system, this approach was dropped in favor of the expendable coolant system.

Selection of the working fluid for the expendable coolant thermal control system involves finding a fluid that has a phase change within the control temperature range at the design planetary surface pressure levels. Early work done on Voyager Lander thermal control systems was done using the old high pressure (54) atmosphere. The conclusions drawn from the work done with the high pressure atmosphere are included for completeness and to illustrate the system effects of designing to high pressure atmospheres.

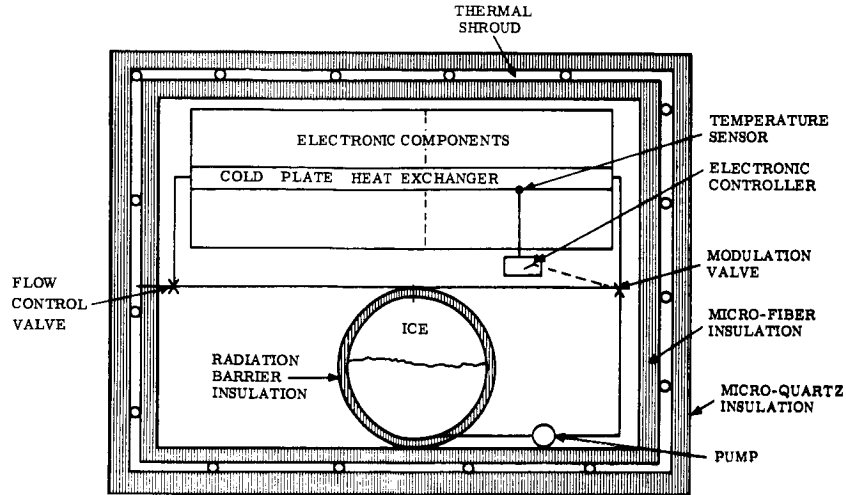
The table below lists several potential expendable coolant and some of the characteristics at 54 atmospheres pressure.

<u>COOLANT</u>	<u>HEAT REMOVAL</u>	<u>SINK TEMPERATURE</u>
Hydrogen	1,500 BTU/lb.	50°F
Nitrogen	160 BTU/lb.	50°F
Ammonia	332 BTU/lb.	200°F
Water	690 BTU/lb.	517°F

The coolants hydrogen and nitrogen must be stored in their liquid state at temperatures of -424°F and -320°F, respectively, to obtain the high heat removal per pound. Extensive insulation is required to limit their boiloff during the transit phase from Earth to Venus (assumed to be 130 days). The amount of insulation was determined by minimizing the overall weight of the system.

The expendable coolant system depending on the boiling of a fluid is pressure sensitive and this is an undesirable feature. However, the melting or sublimation temperature of a solid is relatively independent of pressure. After, examining various materials which sublime or melt within the 0 to 100°F temperature range, it becomes obvious that the ice is probably the best expendable coolant because of its high latent heats. It melts at 32°F and has a high latent heat of fusion (144 BTU/lb.). In addition to the heat absorbed during melting of the ice, approximately 68 BTU/lb. may be removed in heating the water from 32°F to 100°F. Therefore, 212 BTU's of thermal energy may be removed from the payload for each pound of ice consumed. After the water has reached 100°F, a portion of it is pumped back to the ice storage vessel where it is cooled down to approximately 32°F, the remaining portion of the water is transferred into a thermal shroud around the payload.

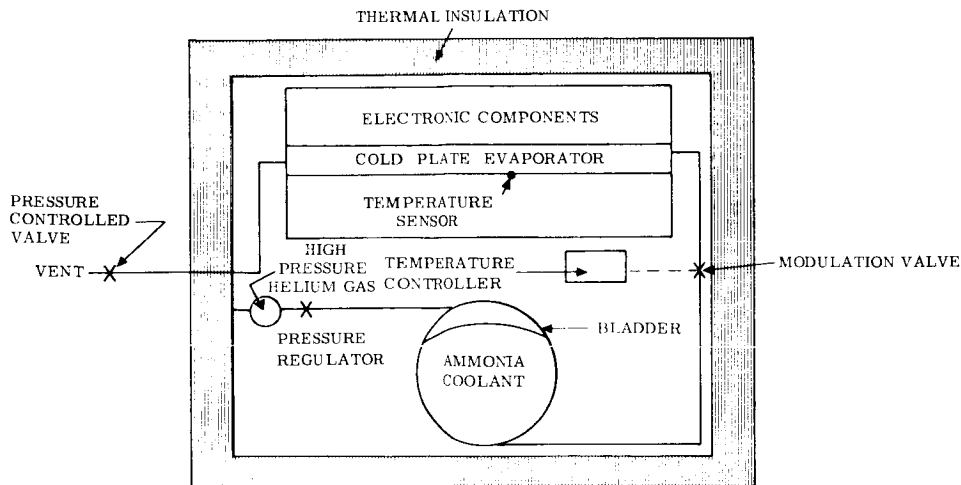
The water is heated from 100 to 517°F within the shroud and finally vaporized. A sketch of the system is shown below:



Shown in Figure 1.3.6-20 are the weights of the environmental control system including coolant boiloff, coolant storage, container insulation, and the vehicle insulation (based on a 100 ft.² of surface area) as a function of time. The results shown in this figure are those obtained when a vehicle is exposed to an atmospheric pressure and temperature of 54 atm and 890°F, respectively.

The weight of the water-ice system as a function of survival time and power dissipation is shown in Figure 1.3.6-21. The quantity of ice required as a function of survival time, surface area, and power dissipation is shown in Figure 1.3.6-22. Examination of Figure 22 shows that for large vehicles, the internal power dissipation is relatively unimportant in the sizing of an expendable coolant system. For smaller vehicles, Venus 72 (130 feet²), the internal power dissipation still accounts for only about 25 per cent of the thermal control system.

Should the atmospheric pressure on Venus be 10 atm or less, the ammonia expendable coolant system has a weight advantage and is simpler because the ammonia vaporizes within the control temperature range (80°F). Such an ammonia system is shown below:



The ammonia cooling system, as would the ice system, would be activated during entry into Venus when the internal component temperature exceeded 100°F. During the descent phase, the ammonia is expelled by high pressure helium gas or ammonia vaporized by an electrical heater. The helium gas is stored in a separate pressure vessel at approximately 6000 psia. A pressure regulator located in the line between the helium and ammonia containers maintains a constant pressure on the ammonia expendable coolant. To insure positive expulsion of the coolant regardless of the vehicle orientation, a bladder is used to expel the ammonia. The rate of discharge of the helium gas is sufficiently low that the temperature of the stored gas is essentially that of the payload. At an initial storage pressure of 600 psia, approximately 0.42 cubic feet of helium gas is required to expel 10 cubic feet of ammonia. This high pressure gas expulsion system would weigh approximately 35 lbs., assuming the pressure vessel is made of stainless steel having an allowable design stress of 50,000 psi. The weight of the expulsion system does not change appreciably with initial storage pressure. A system having an initial storage pressure of 2500 psia weighed 36.5 pounds; however, its volume was 0.825 ft³. Therefore, from a volume consideration, it is desirable to store at high pressures.

The expulsion of the ammonia coolant may also be accomplished by the vaporization of a small amount of ammonia located behind the bladder using an electrical heater. The electrical input to the heater is controlled by a pressure sensor within the storage vessel. The system required to expel the 10 cubic feet of ammonia would need approximately 7 pounds of liquid ammonia behind the bladder. The electrical input would amount to 1000 watt-hrs. or about 12 pounds of silver zinc batteries. Therefore, the total weight of this expulsion system including the two pound pressure sensor and controller is 21 pounds. Although this system is lighter in weight than the high pressure helium system, it is more complex and could present some reliability problems such as the burn-through of the bladder if it should come in contact with the electrical heater. It is for this reason that the high pressure gas expulsion system is recommended.

The flow rate of the ammonia into the cold plate evaporators, upon which the components are mounted, is controlled by the modulation valves. The modulation valves receive their signals from the temperature controllers which sense the actual temperature of the components. The liquid ammonia is vaporized within the cold plate evaporators removing approximately 500 BTU's per pound. The ammonia vapor is then vented overboard in the Venus atmosphere. Figures 1.3.6-23 and 1.3.6-24 show the weights of the ammonia expendable coolant system including the thermal insulation for both the optimum insulation thickness and for a constant insulation thickness of 3 inches. The weights are shown as a function of operation time and the insulated vehicle area. The temperature and pressure were assumed to be 1050°F and 10 atm, respectively. The weight of the ammonia coolant for the optimum insulation thickness and the 3 inch thickness is shown in Figures 1.3.6-25, and 1.3.6-26.

To reduce the amount of thermal energy conducted (this can account for 90% of the heat removed) into the payload section from the high temperature (450 to 1050°F) external environment, the payload must be insulated. Due to the high surface temperatures and a gaseous atmospheric environment, a high temperature insulation having a low thermal conductivity is needed. One such insulation is a Micro-Quartz insulation made by Johns-Manville. This insulation can operate at temperatures up to 2000°F. The average thermal conductivity of Micro-Quartz insulation is 0.0435 BTU/ft²hr °F at a mean temperature of 500°F. The heat leak into the vehicle was based on thermal conductivity, 1.5 times the reported value for the insulation. This is to allow for attachment heat leaks. The density of this insulation is 3 lb/ft³. The thicker the insulation the smaller the amount of heat conducted into the vehicle, therefore, the amount of coolant required for a given period of operation time is decreased. However, there is a trade off between the weight of coolant and the weight of the insulation, with the optimum value occurring when the weight of the coolant and storage vessel equals the insulation weight. Figure 1.3.6-27 shows the

optimum insulation thickness for the ammonia expendable coolant system operating at the 1050°F atmospheric temperature conditions as a function of time. Examining the optimum insulation curve, we find that the thickness becomes unrealistic from a thickness standpoint; for example, at five hours within the 1050°F environment the optimum insulation thickness is approximately 5.4 inches. The vehicle, therefore, becomes volume limited and it becomes necessary to set the insulation thickness at some maximum value and pay the additional weight penalty in coolant. The weight penalty due to limiting the insulation thickness to 3 inches is 60 pounds (340 lbs. for optimum insulation thickness and 400 lbs. for a constant 3 inch insulation thickness) for a vehicle having 100 ft² of surface area, 1000 watts of internal dissipation, and an operation time of 5 hours in the design environment.

A summary of the water-ice system and the ammonia system follow:

	Water-Ice	Ammonia
Maximum Atmospheric Pressure	Independent of Pressure	10 atm
Temperature range at maximum pressure	32 to 100°F	80 to 100°F
System Weight (Area = 100ft ² , Power dissipation = 1000 watts, Time = 5 hrs.)	*450	**429 lbs.
(a) Insulation	90 lbs.	75 lbs.
(b) Coolant	280	270
(c) Coolant Vessel + Insulation	36	42
(d) Thermal Shroud	35	—
(e) Pump + Valves + Controller	9	7
(f) Helium Expulsion System	—	35
Type of System	Active System (requires pump)	Semi-active System
Electrical Power Consumption	26 watts	6 watts

*The system weight is based on an environmental temperature of 890°F and a payload temperature of 100°F. The internal insulation thickness was 3 inches and the external insulation thickness was 0.6 inches.

**The system weight is based on an environmental temperature of 1050°F and a payload temperature of 100°F. The vehicle insulation thickness was 3 inches.

H. Problem Areas and Further Work

The thermal control system described within this report for the Mars lander is an active system and, therefore, has a number of moving parts which will wear out with time. This problem is further aggravated by the fact that the coolant being circulated is at a high temperature (350 to 450°F) and that the system must operate continuously for approximately 18 months. More work is required in the area of developing pumps, motors, and valves which can operate at these temperatures for extended periods of time with a high reliability.

The performance of insulations such as Micro-Quartz and Micro-fiber should be evaluated within a high temperature and a high pressure gaseous environment such as that which may be present on Venus. This information is required before a fully optimum thermal design can be made for the Venus vehicle.

I. Summary of Internal Thermal Control Systems for Mars and Venus Landers

To maintain the payload temperature of the Mars vehicle at an acceptable level (50 to 100°F) during transit and for most surface operation on Mars, heating is required. The thermal control system described within this report is based on the availability of waste thermal energy from an RTG electrical power supply. However, if some other form of power supply is used, such as solar cells, it would be necessary to utilize electrical heaters. The basic concepts of the Mars Lander thermal control system are:

1. Thermal energy available from electrical power supply for payload heating.
2. The Landers are shade-oriented during transit period.
3. The thermal mass of the payload and adjacent structure is sufficient to provide the necessary heat sink requirements for electronic equipment during check-out on launch pad and equipment operation during entry.
4. Power supply cooling during launch and entry is provided by an expendable coolant system.
5. Maximum thermal insulation thicknesses is determined for maximum power dissipation level and maximum anticipated ambient environmental temperatures.
6. Excess thermal energy dissipated from RTG unit may be radiated to the surrounding environment directly from the extended surface of RTG unit. If the power level is increased appreciable (>100 watts) it would be necessary to utilize a radiator or deploy the RTG unit from the vehicle.
7. Atmospheric gas density on Mars is so low that it is impractical from a power consumption standpoint to use forced convection to transfer heat using the Mars atmosphere. Natural convection may be neglected in comparison to radiation from a black body at 100°F.
8. The temperature of sensitive equipment, such as the batteries and biological cultures may be provided by using a solid material which has its melting temperature in the operating range of sensitive equipment.

The thermal control of the Venus Lander is one of heating during transit and cooling during surface operation on Venus. The required heating during transit may be kept to minimum by utilizing proper optical surface coatings and thermal insulation. The thermal control of a Lander on the surface of Venus within the predicted 450 to 1050°F ambient environmental temperatures requires a means of removing or absorbing thermal energy within the payload. The basic concepts of the Venus Lander thermal control system are:

1. The ambient surface environment temperatures range from 450 to 1050°F and the pressure ranges from 6.3 to 54 atm.
2. The amount of electrical power available for temperature control is limited. The vehicle does not include a nuclear turboelectric power supply. Therefore, an expendable coolant system is the only type of system practical.
3. For atmospheric pressures less than 10 atm an expendable ammonia system is the lightest weight system. When the atmospheric pressure exceeds 10 atm, the most favorable system from a weight standpoint is an ice system if the electronic equipment must be maintained at temperatures less than 100°F. The ice system is relatively insensitive to atmospheric pressure in regard to the payload temperature control capability.

4. The thermal insulation requirements become excessive from a volume standpoint and, therefore, it may be necessary to go from an optimum insulation design.
5. The thermal mass of the payload and adjacent structure is sufficient for equipment checkout on launch pad.
6. The vehicle is either shade-oriented or sun-oriented during the transit period but not a random-oriented vehicle. This permits a given type of design, so that selection of the proper optical surface properties and thermal insulation requirements can proceed.

The specific numbers stated in the text of the thermal control portion of this report apply to a given vehicle design such as the 1450 pound Mars 1969 vehicle. However, the general concepts of the environmental control system will apply to any Mars or Venus landing vehicle having temperature control requirements between 50 and 100° F and the power supplies that are stated within this report. In the case of the Venus vehicle, a number of vehicle sizes and power dissipation levels were investigated and the results are shown parametrically in Figures 18 through 26. The design of Mars environmental control system is such that it is relatively independent of the internal power dissipation and vehicle size except for the determination of the thermal insulation requirements.

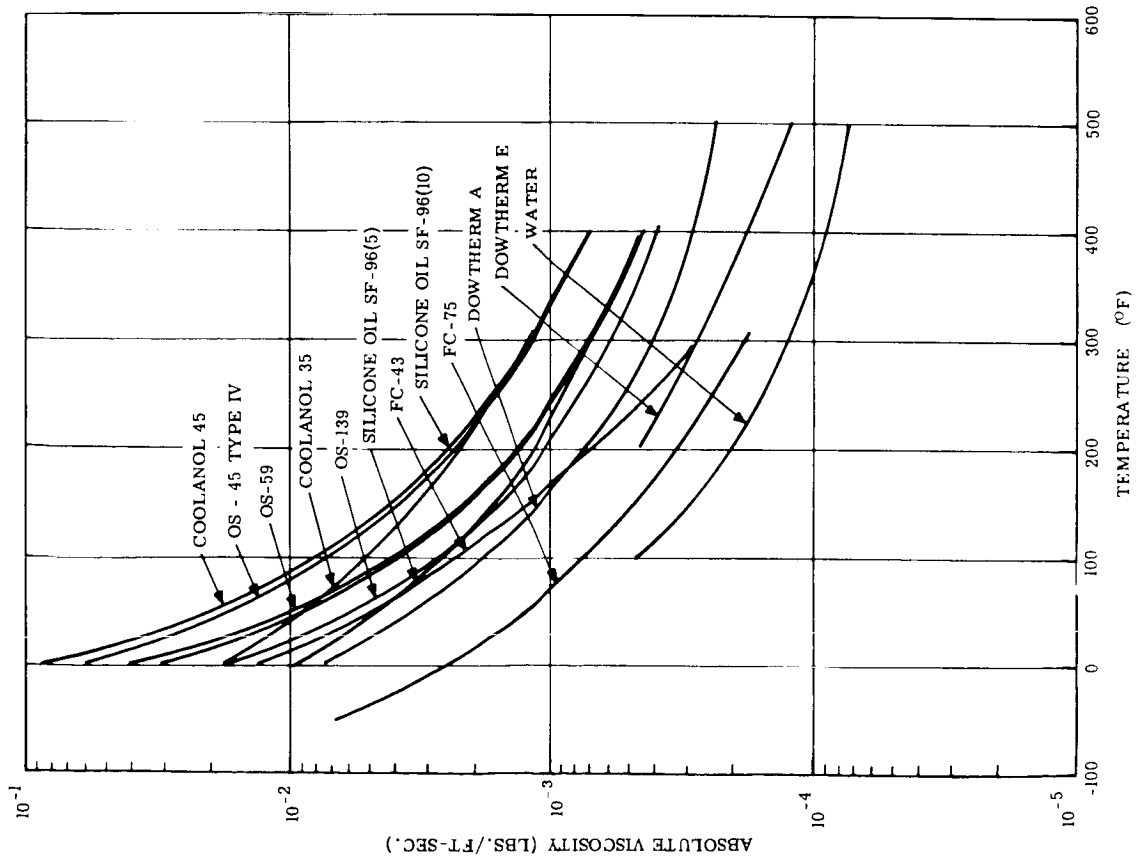


Figure 1.3.6-1. Absolute Viscosity vs. Temperature

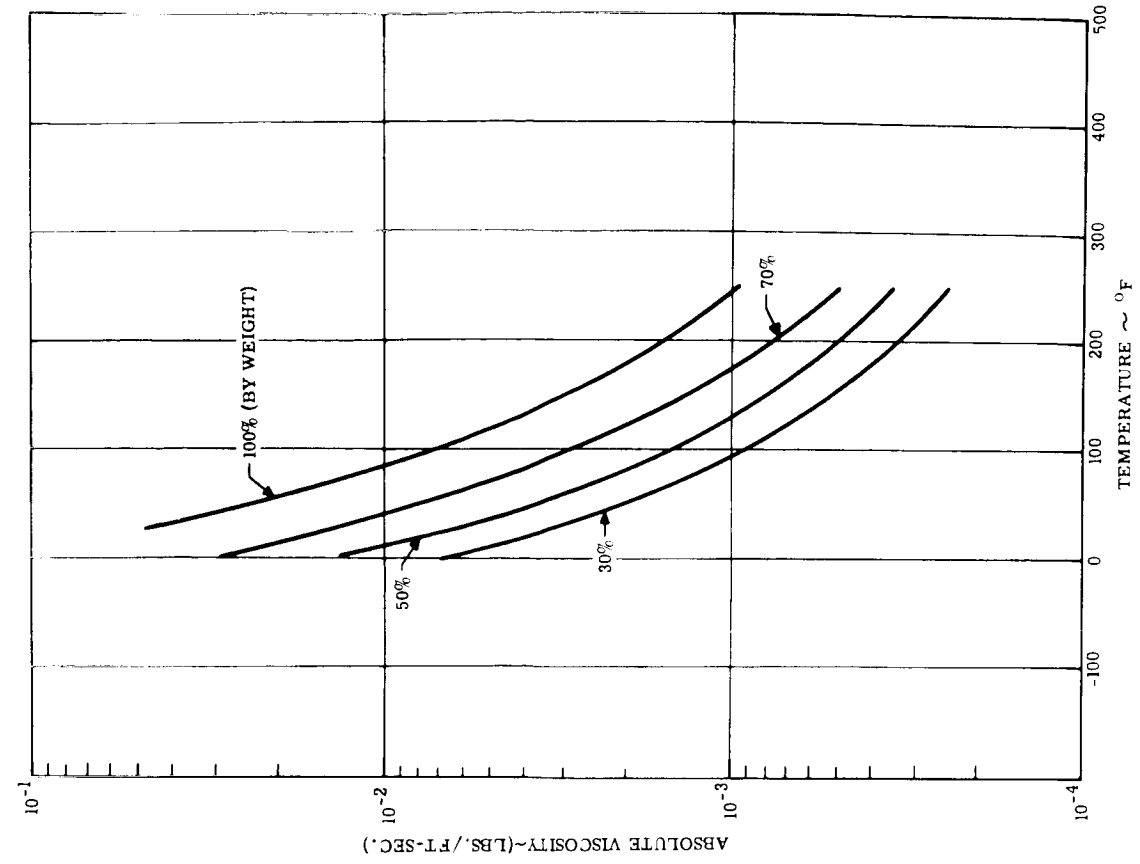


Figure 1.3.6-2. Absolute Viscosity of Ethylene Solutions

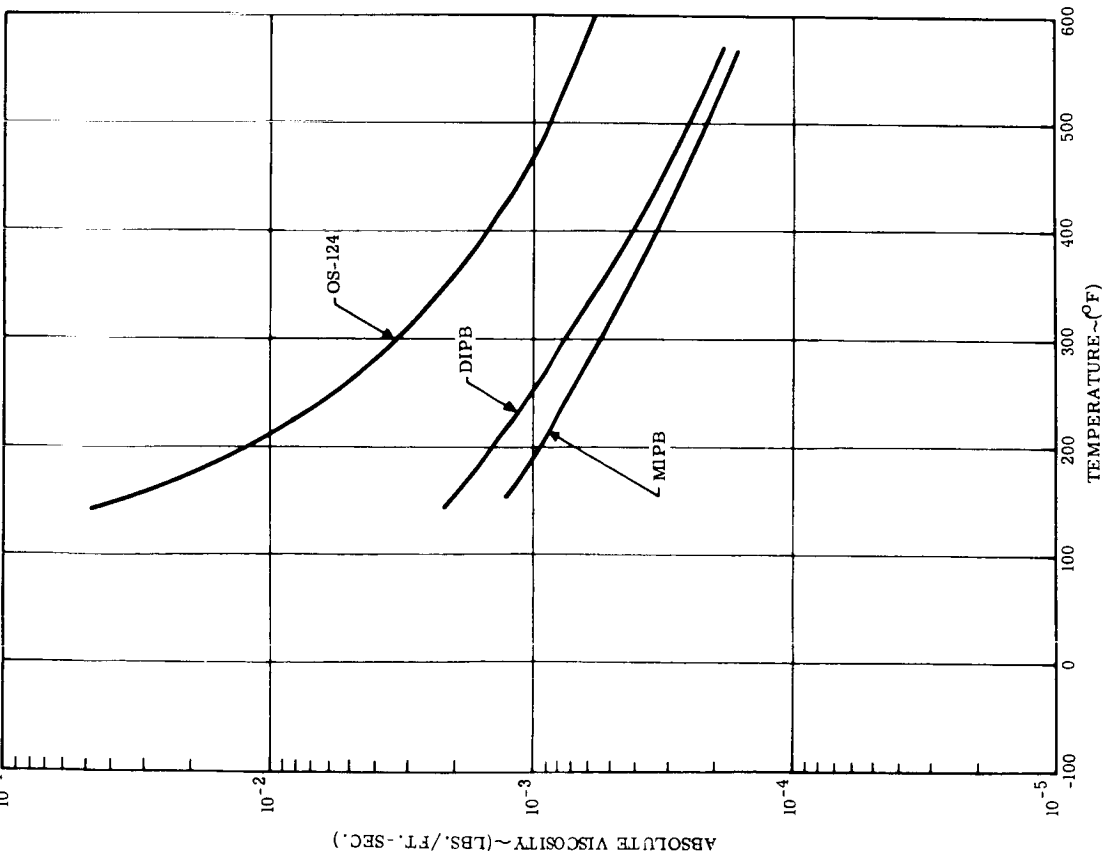


Figure 1.3.6-3. Absolute Viscosity vs. Temperature

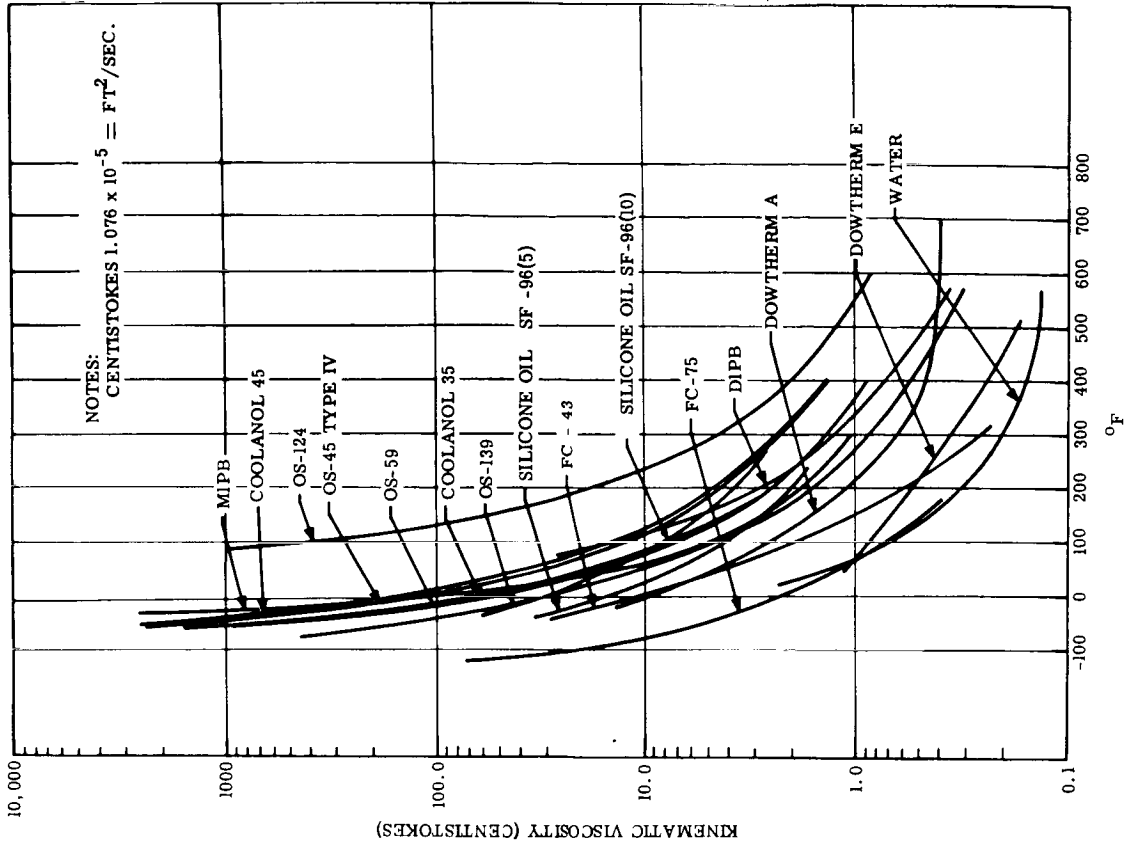


Figure 1.3.6-4. Kinematic Viscosity vs. Temperature

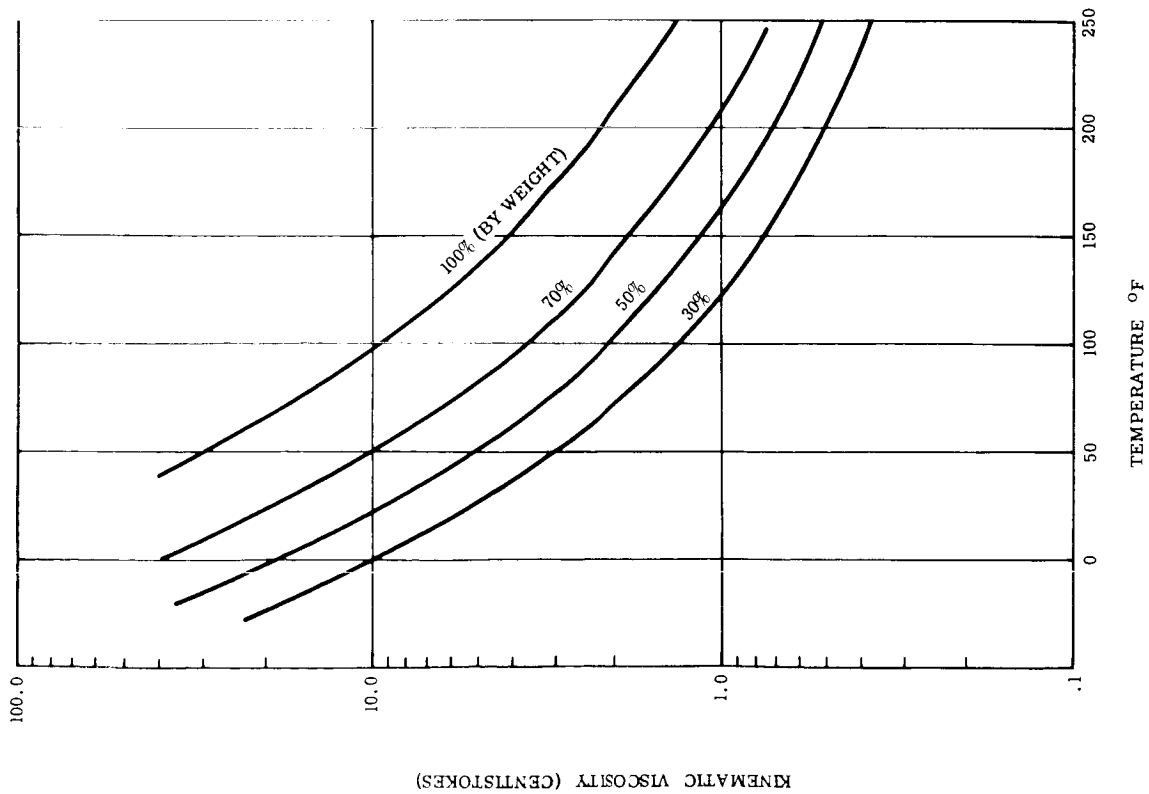


Figure 1.3.6-5. Kinematic Viscosity of Glycol Solutions

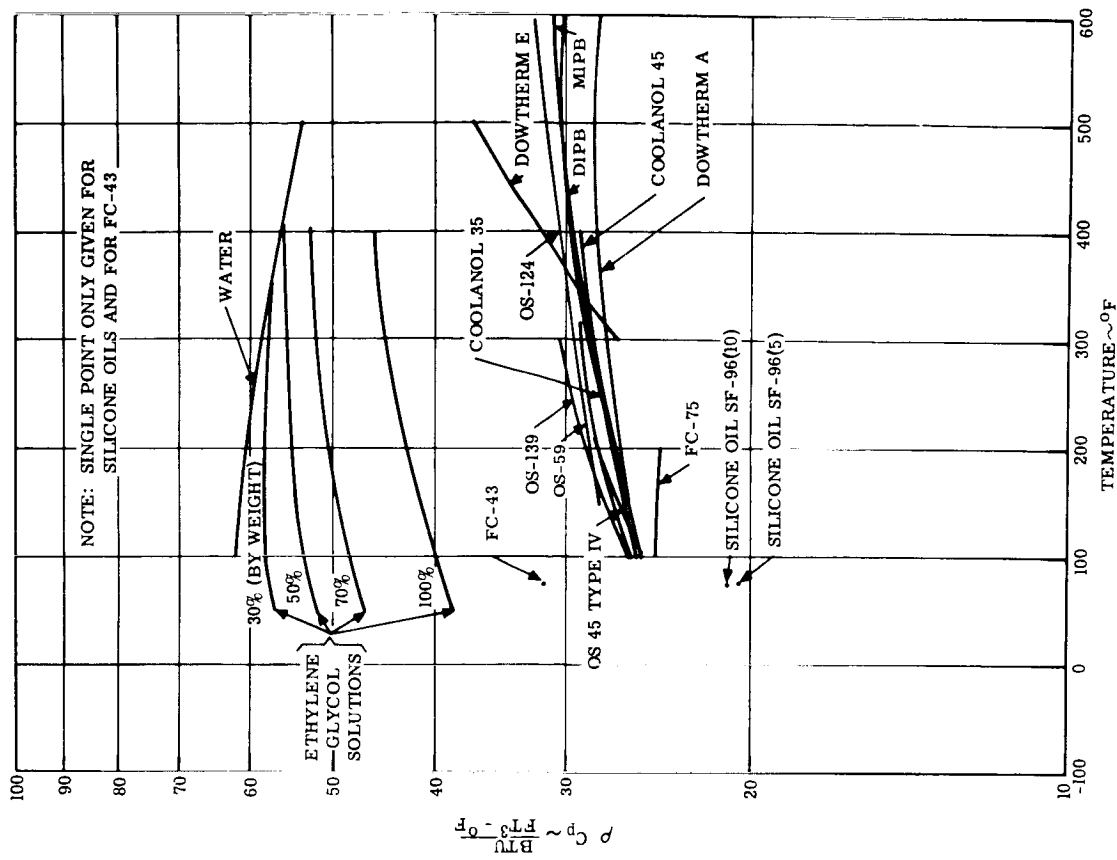


Figure 1.3.6-6. C_p vs. Temperature

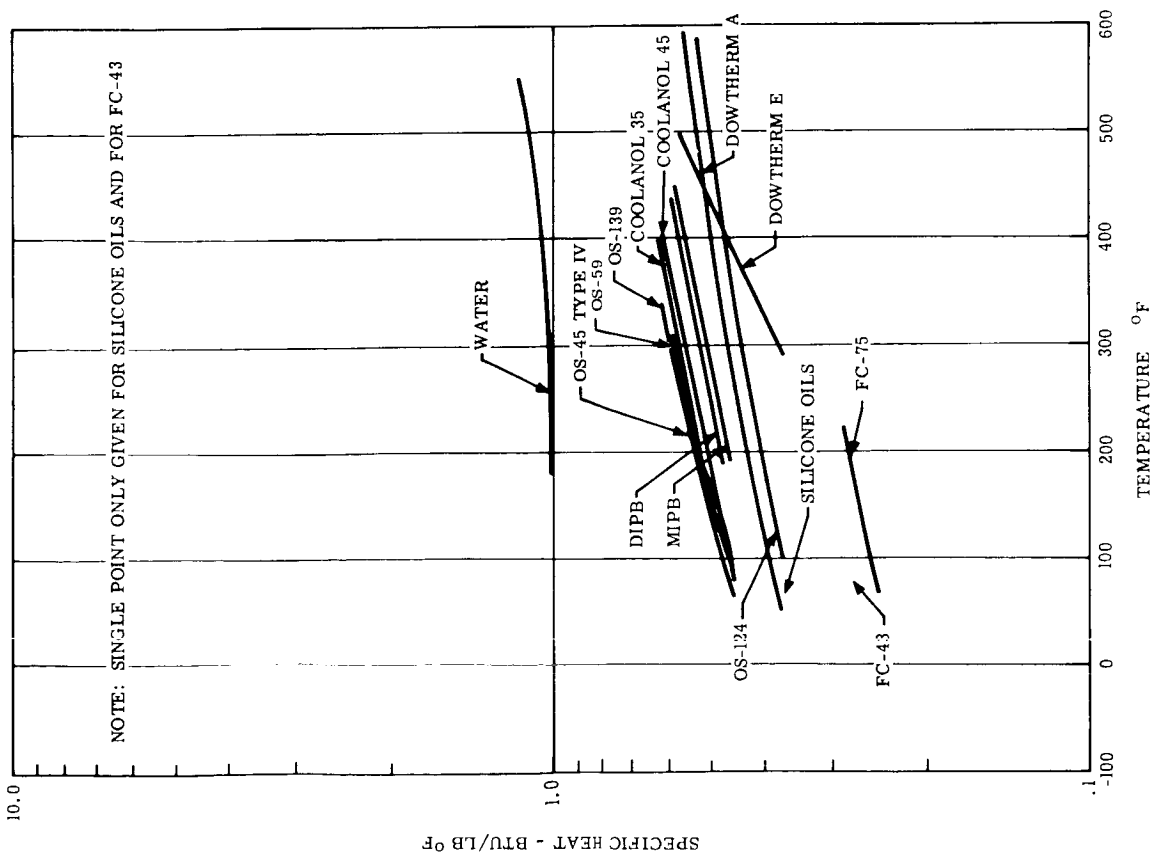


Figure 1.3.6-7. Specific Heat vs. Temperature

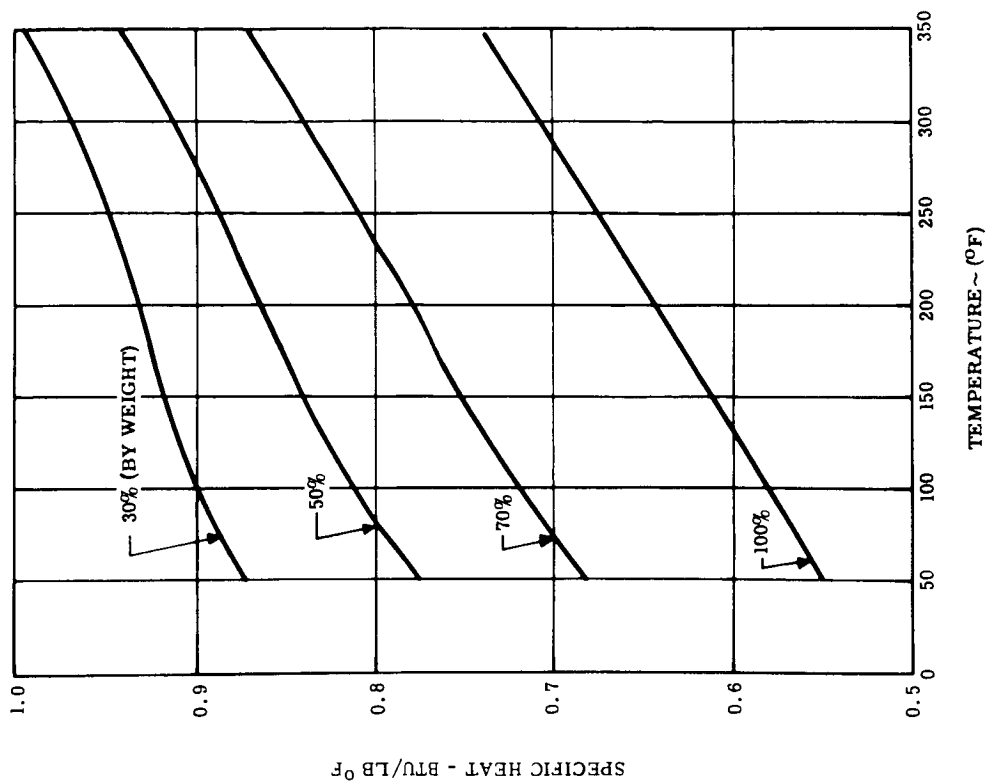


Figure 1.3.6-8 Specific Heat of Ethylene Glycol Solutions

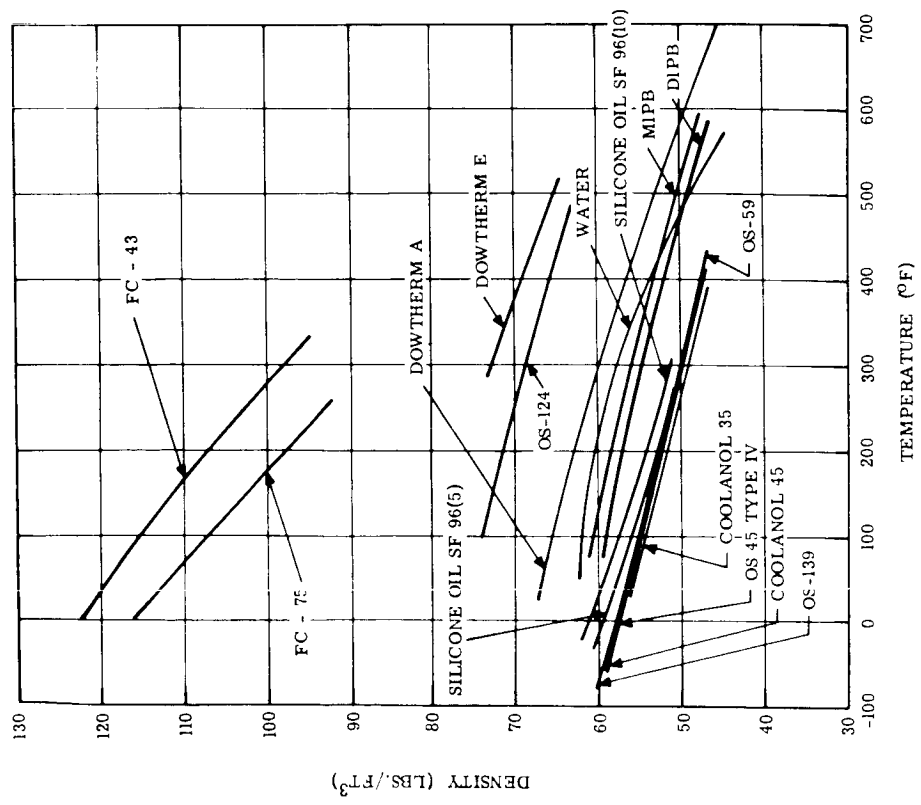


Figure 1.3.6-9. Density vs. Temperature

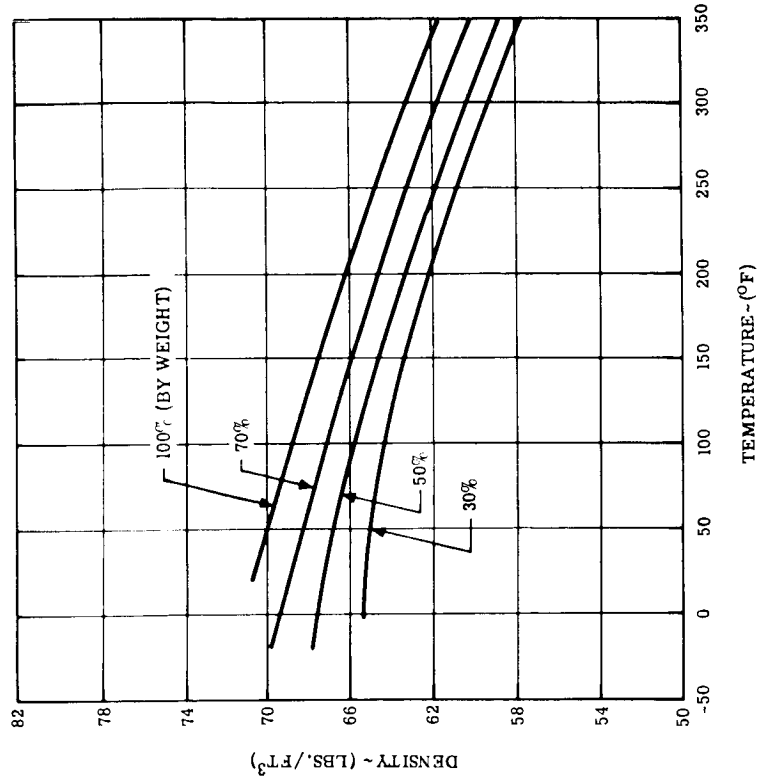


Figure 1.3.6-10. Density vs. Temperature for Ethylene Glycol Solutions

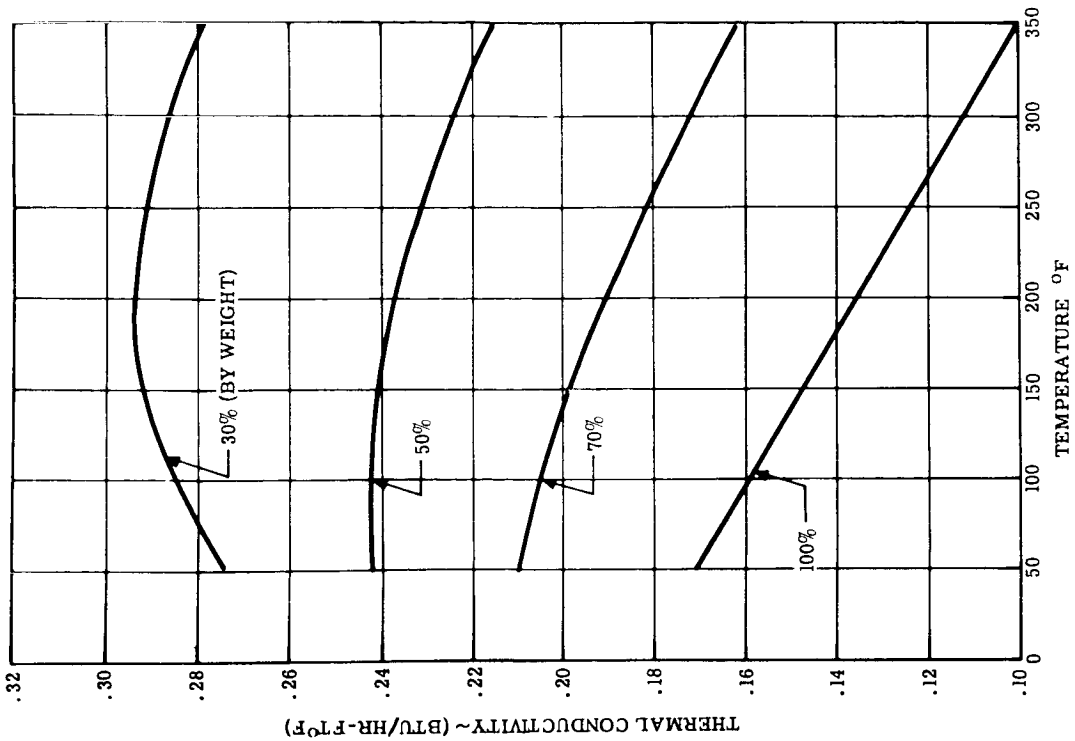


Figure 1.3.6-12. Thermal Conductivity of Ethylene Glycol Solutions

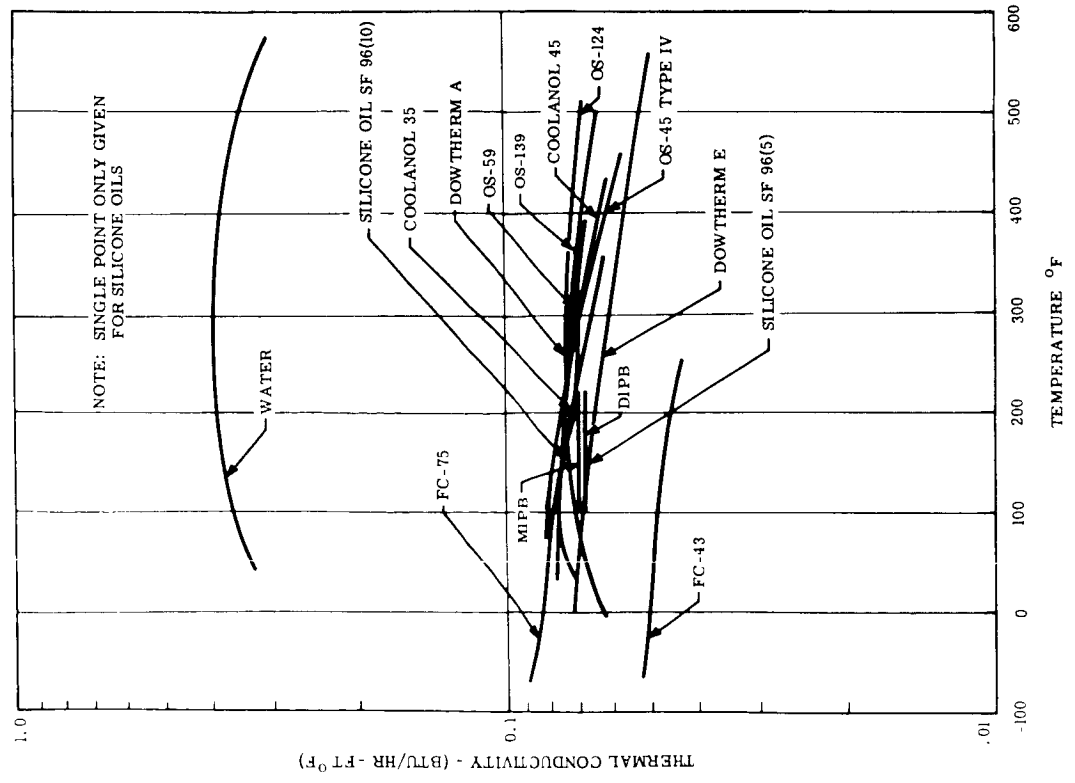


Figure 1.3.6-11. Thermal Conductivity vs. Temperature

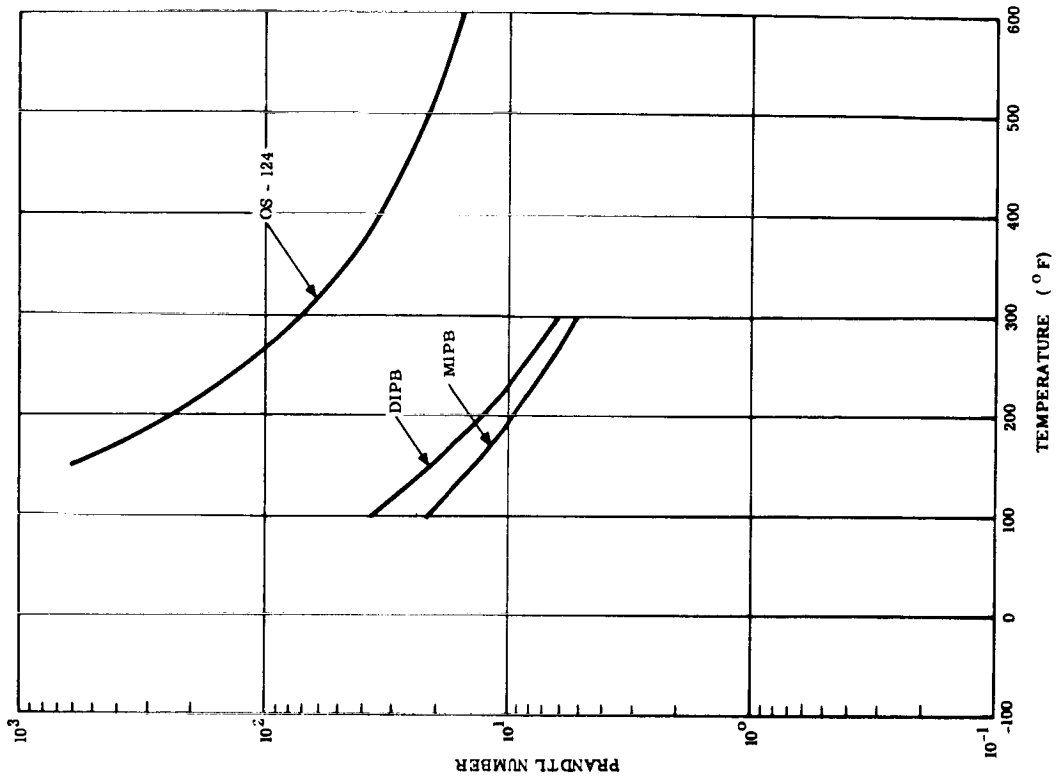


Figure 1.3.6-14. Prandtl Number vs. Temperature

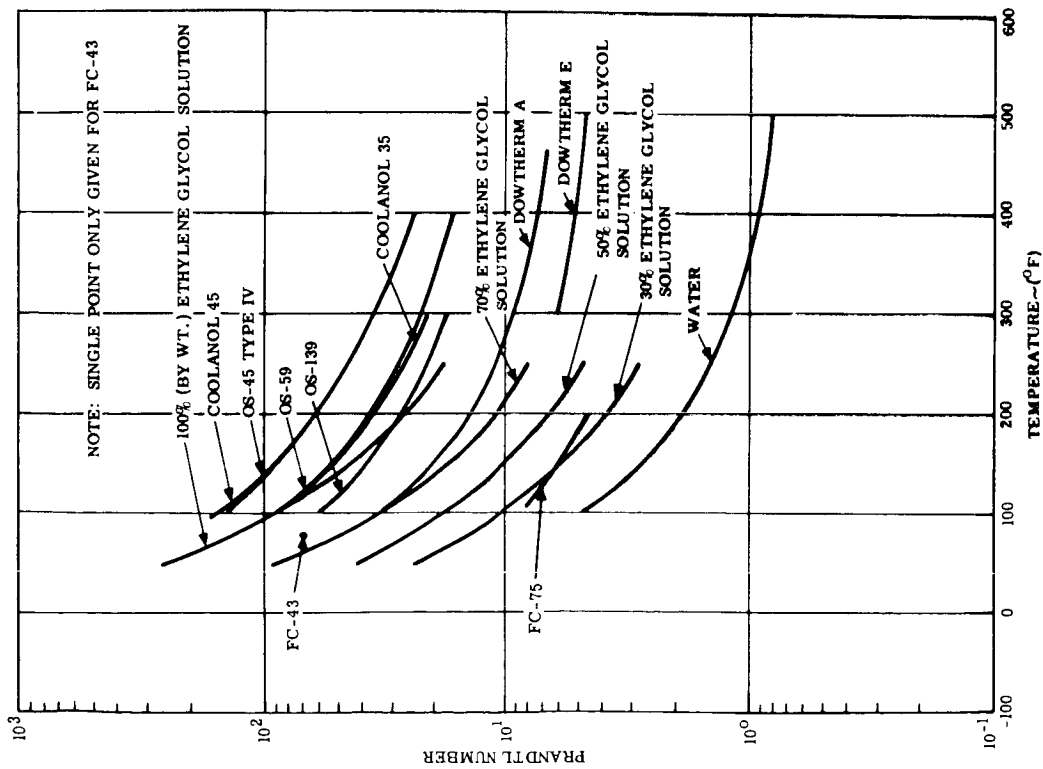


Figure 1.3.6-13. Prandtl Number vs. Temperature

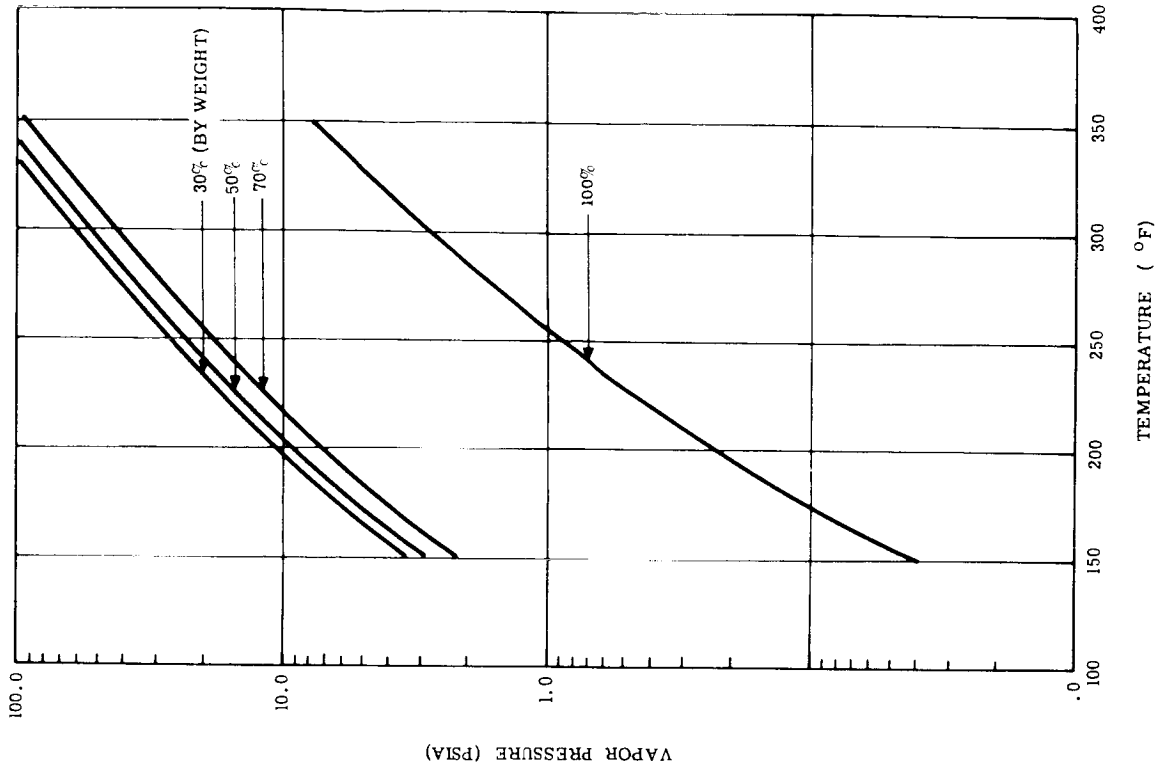


Figure 1.3.6-16. Vapor Pressure of Ethylene Glycol Solutions

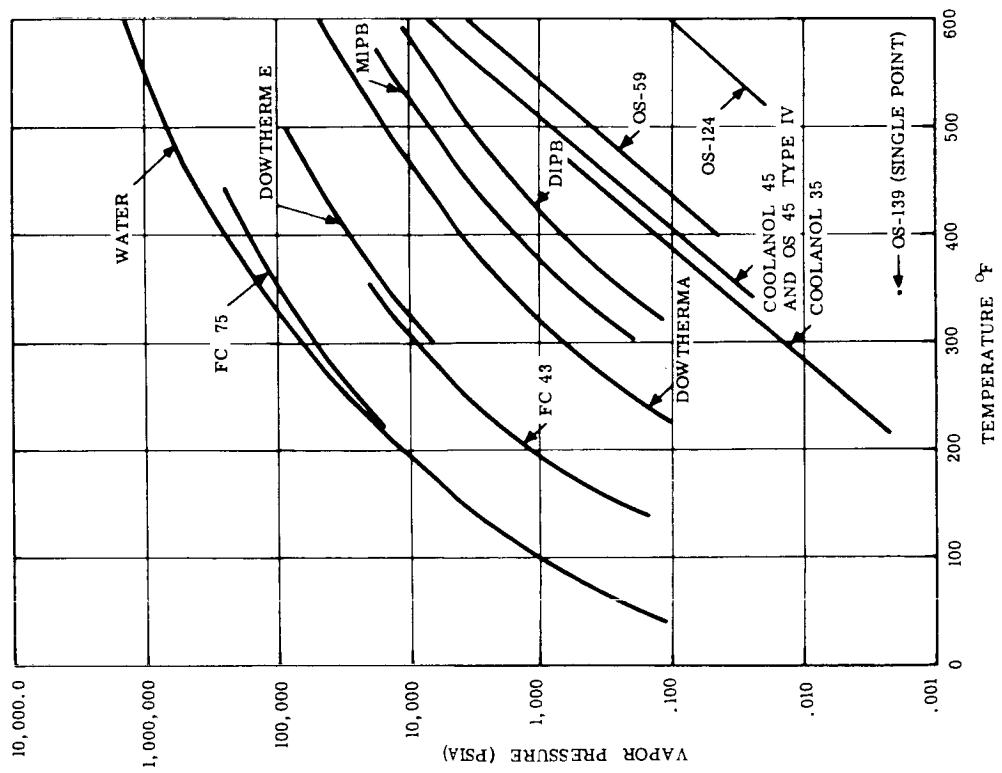


Figure 1.3.6-15. Vapor Pressure vs. Temperature

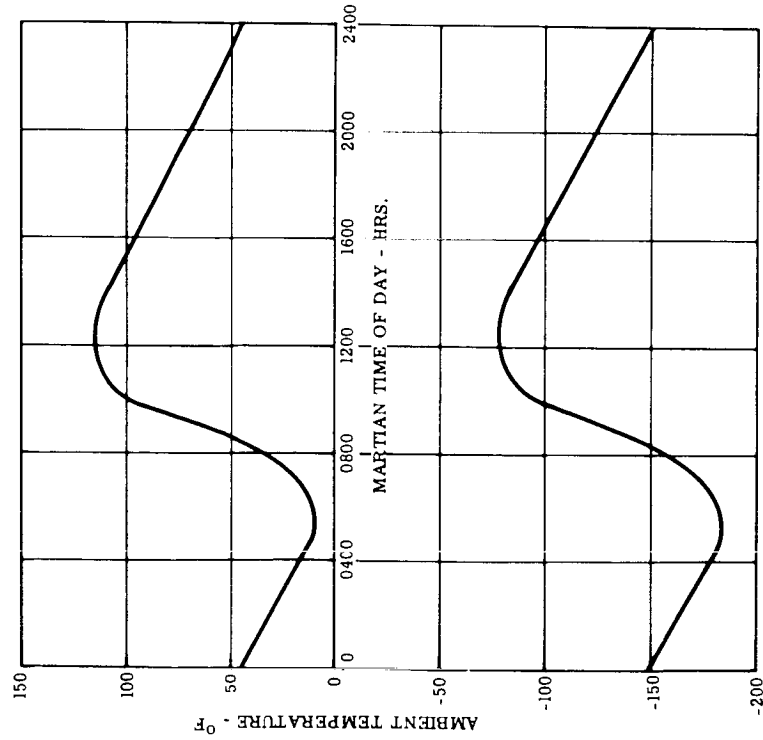


Figure 1.3.6-17. Mars Design Surface Temperatures

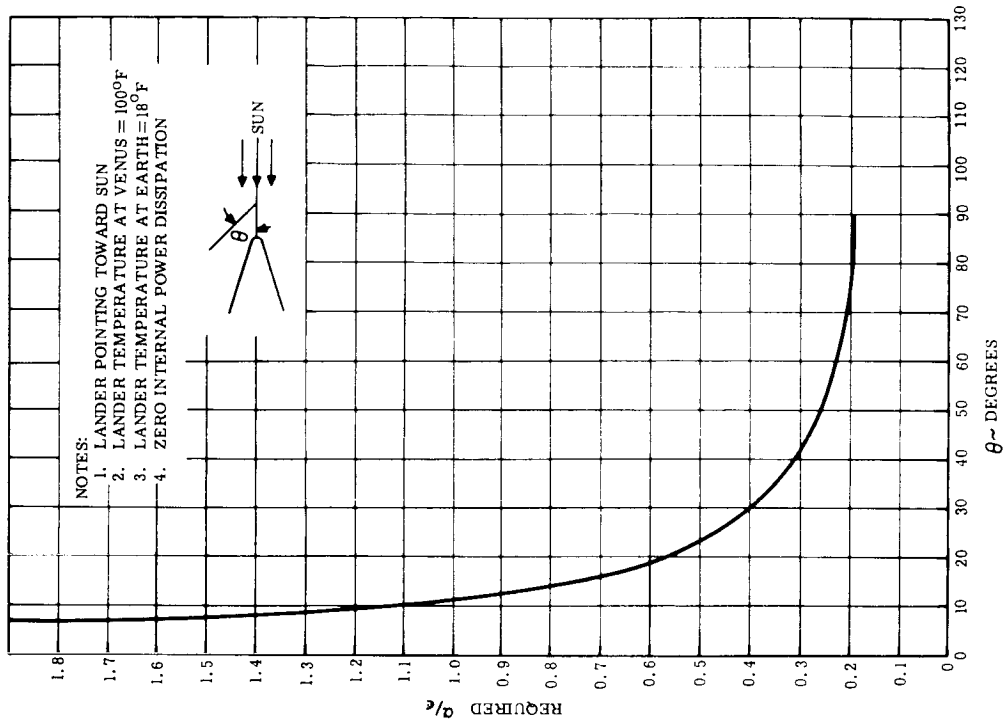


Figure 1.3.6-18. Required Optical Surface Properties for Temperature Control During Transit from Earth to Venus with Sun Orientation

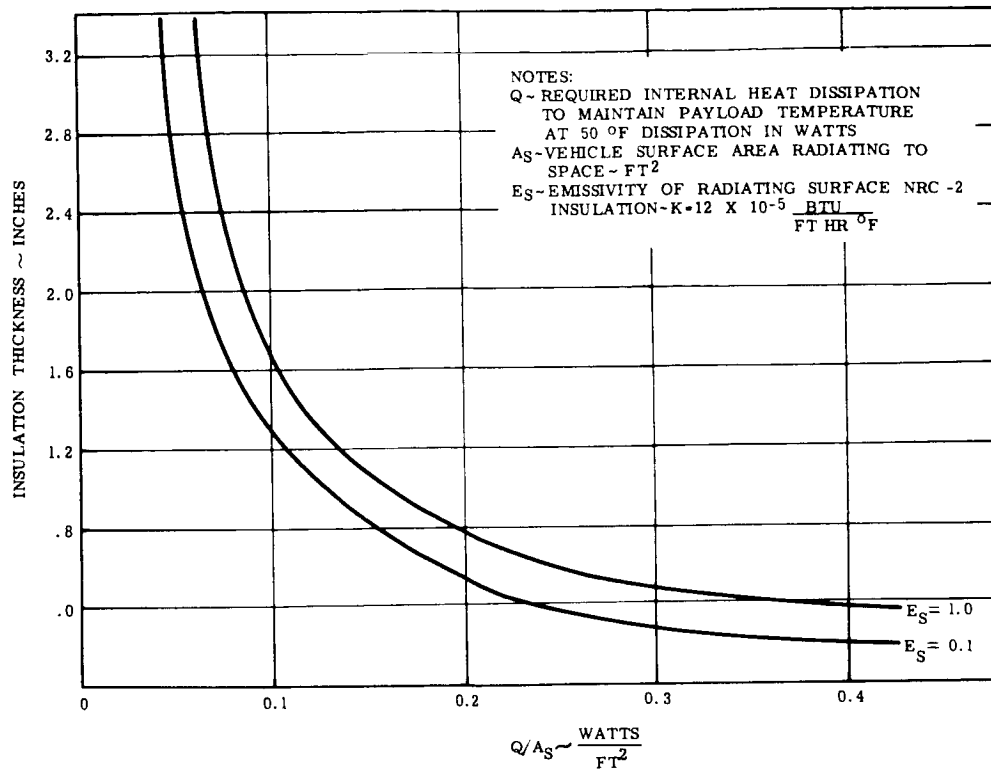


Figure 1.3.6-19. Thermal Shroud Insulation Thickness for Shade-Oriented Vehicle

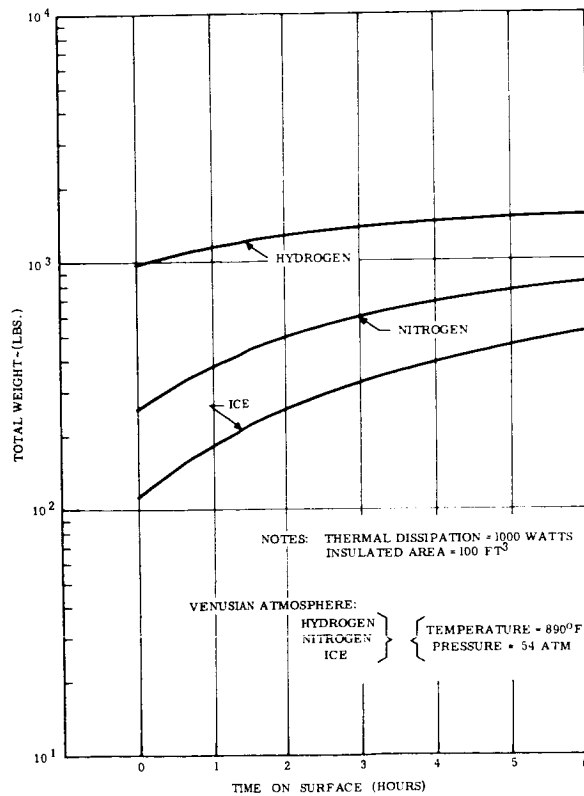


Figure 1.3.6-20. Weight of Environmental Control Systems for Venus Lander

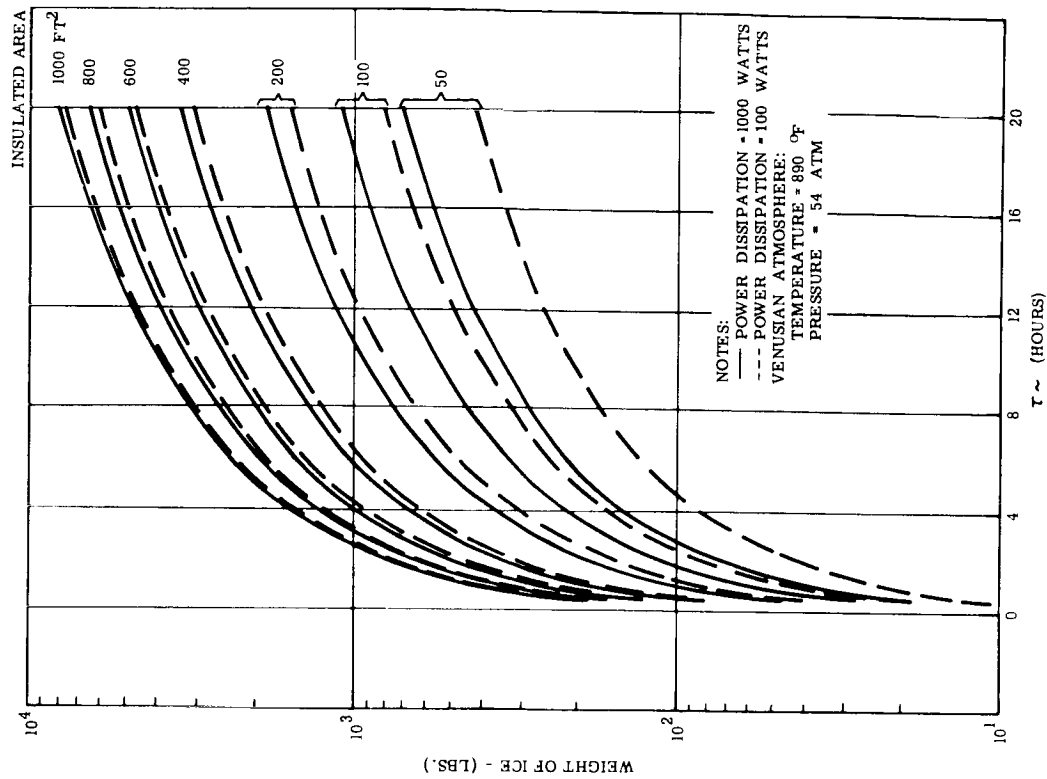


Figure 1.3.6-22. Weight of Expendable Coolant for Venus Lander

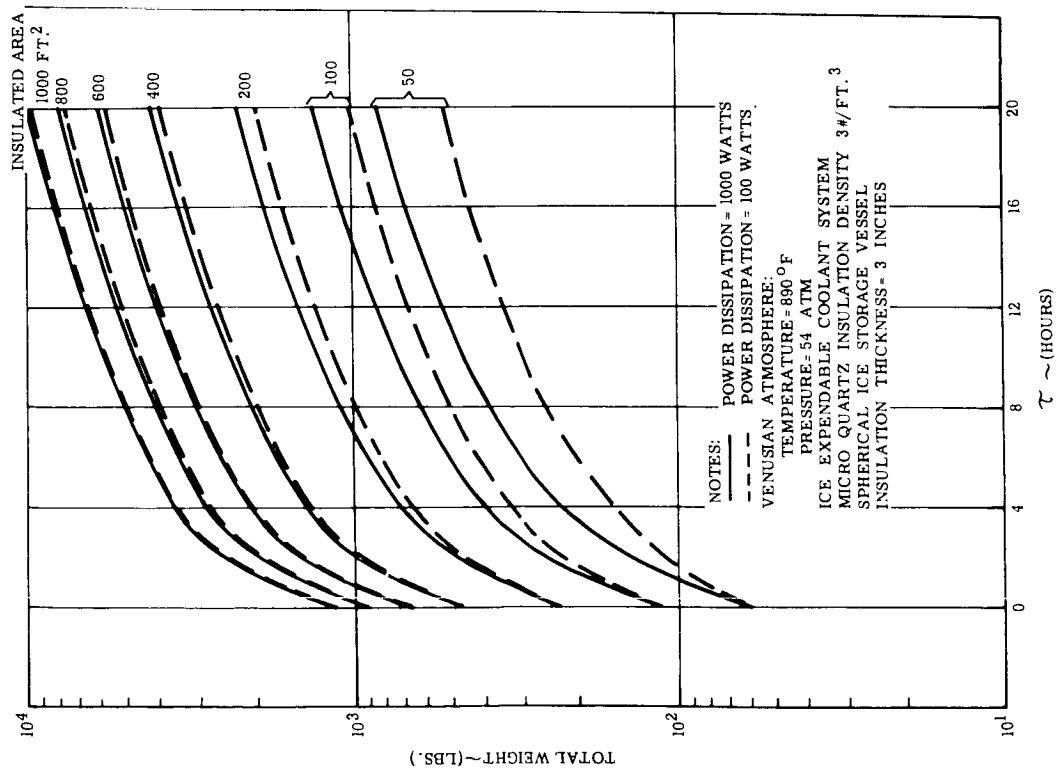


Figure 1.3.6-21. Weight of Environmental Control Systems for Venus Lander

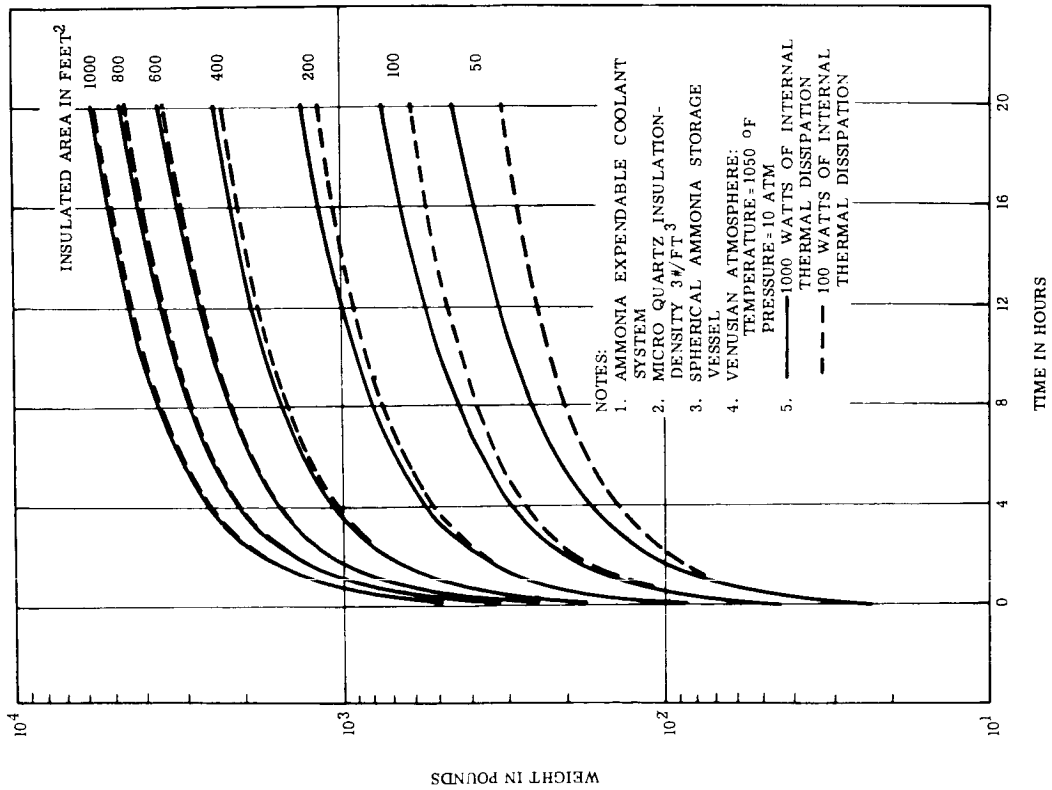


Figure 1.3.6-23. Weight of Internal Thermal Environment for Optimum Insulation Thickness

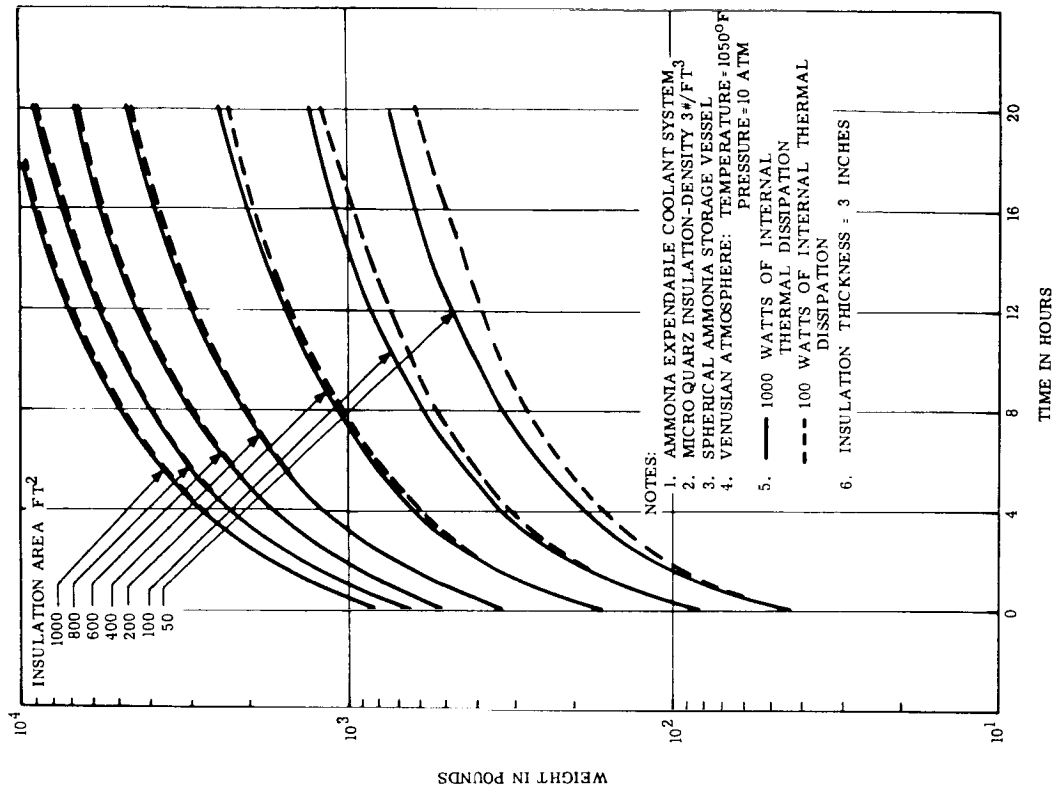


Figure 1.3.6-24. Weight of Internal Thermal Environment System for Constant Insulation Thickness

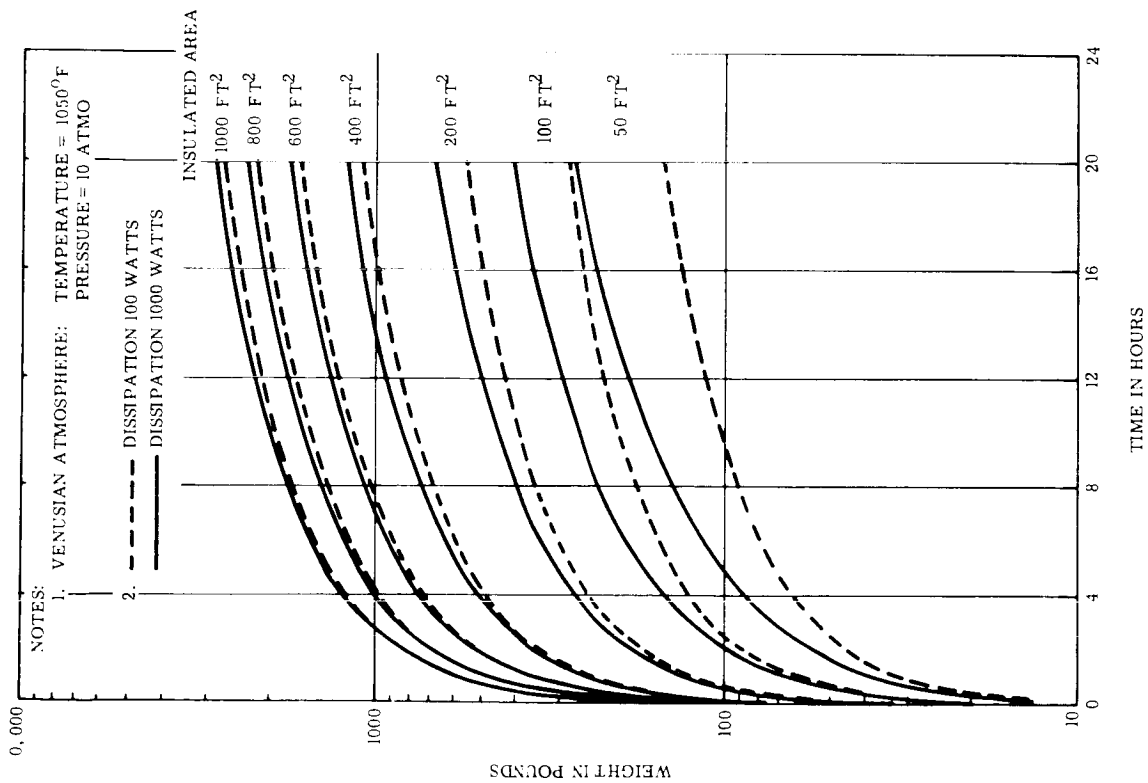


Figure 1.3.6-25. Ammonia Expendable Coolant Weight (Optimum Insulation Thickness)

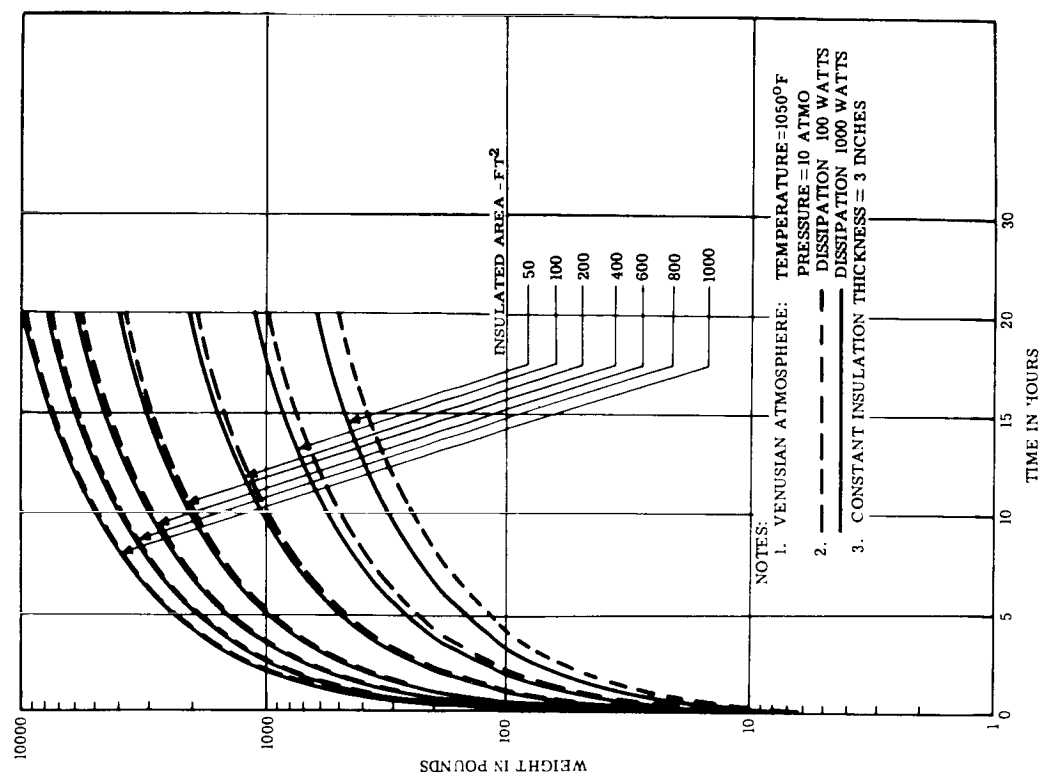


Figure 1.3.6-26. Ammonia Expendable Coolant Weight (Constant Insulation Thickness)

NOTES:

- 1. VENUSIAN ATMOSPHERE: TEMPERATURE = 1050 °F
PRESSURE = 10 ATM
- 2. COOLANT IS AMMONIA WITH THERMAL CONDUCTIVITY
= 0.065 BTU/FT-HR-°F

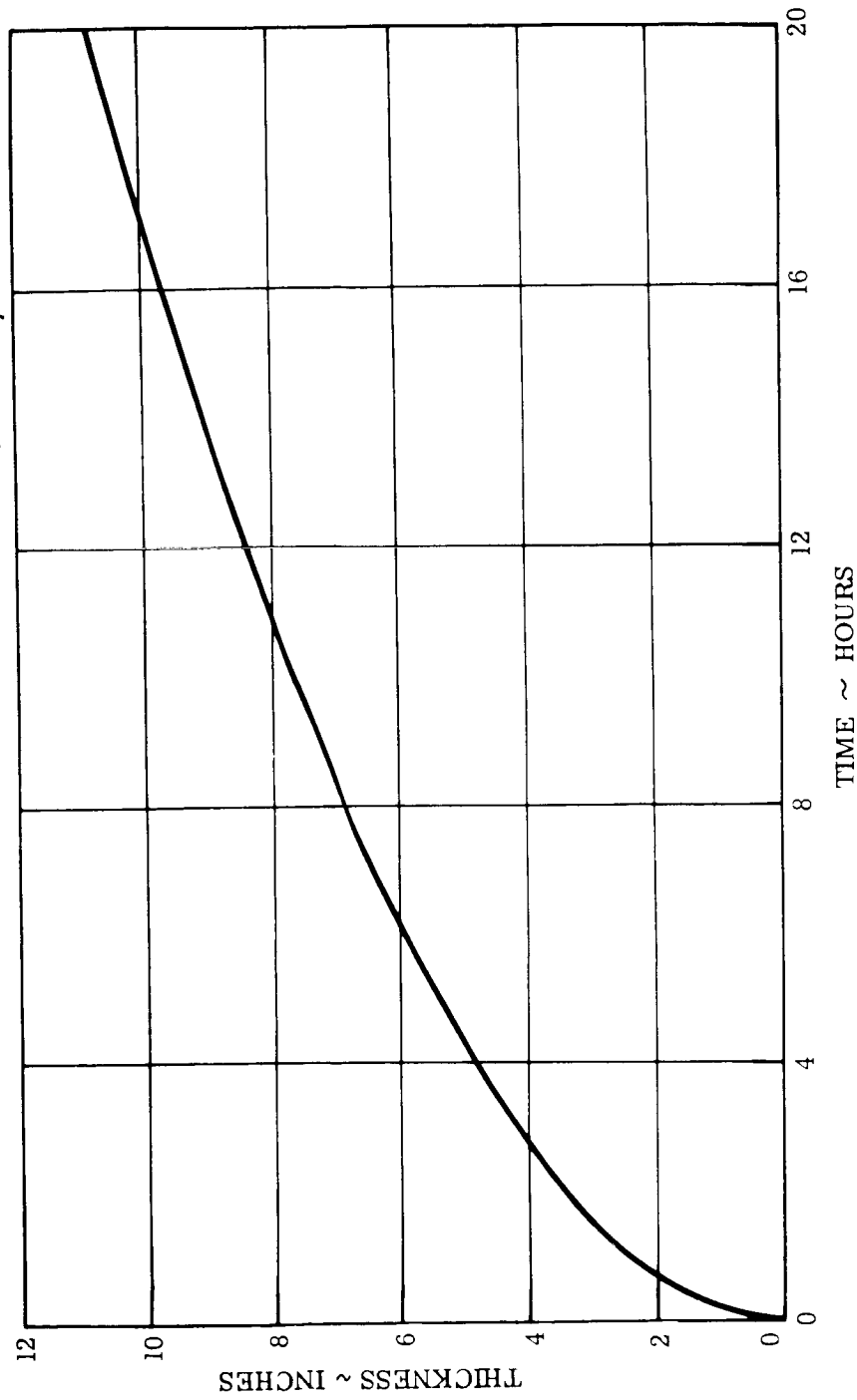


Figure 1.3.6-27. Optimum Insulation Thickness vs. Time (in Hours)

1.3.7 MATERIALS

Metallic, polymeric and ceramic materials are discussed in this section relevant to their application on the Lander vehicles. Consideration of material performance (with respect to requirements imposed by ground, transit, entry, and planetary environments) is used as the basis for material selections. Critical material requirements resulting from the mission environments have been identified and areas requiring further study or development are defined.

A. Thermal Shields and Advanced Development

(1) Summary

Organic ablative materials have been investigated with respect to mission requirements. An initial comparison of pertinent mechanical and thermal properties of various ablative materials (Table 1.3.7-1), and parametric analysis of this data to mission/entry requirements (Section 1.3.2 and 1.3.3), led to the selection of phenolic nylon and General Electric's Elastomeric Shield Material (ESM) as the prime thermal shield materials for the Venus and Mars missions, respectively. Phenolic nylon is also the choice as the primary back-up shield for the Mars mission. Phenolic refracil is selected as the primary back-up thermal shield for the Venus mission and alternate back-up shield for the Mars mission.

This section discusses material requirements, properties, and lack of data in certain areas, e.g., sterilization, transit and planetary entry environments. The discussion also includes the required investigations for advanced thermal shield materials for this mission such as graphite phenolic and advanced phenolic systems reinforced with HT-1 fibers.

(2) Phenolic Nylon (Venus)

Prior successful performance and extensive application on terrestrial re-entry vehicles, such as Mark 4 and Mark 6, coupled with desirable mechanical and thermal properties, make phenolic-nylon a prime selection for the Venus Lander. It also was selected for back-up shield material for the Mars Vehicle.

(a) Shield Requirements

The most important shield requirement is the ability of the thermal protection system to perform its function during entry into the Venus atmosphere. (This is fully described in Section 1.3.3.) In addition, the shield must withstand the ground and flight environmental requirements. However, the flight temperature extremes are kept moderate for the Venus vehicle with the use of a temperature controlling shroud. This considerably eases the mechanical requirements on the shield system. The entry conditions seem favorable for an all organic system, which will increase in performance ability with an increase in heating rate.

(b) Properties

Phenolic-nylon must, to some extent, be considered a generic term since considerable variation of mechanical properties and physical performance can result from changes in processing techniques and raw materials. Since the major portion of GE/RSD thermal shields have been produced from a single nylon cloth (Wellington-Sears, SN-19), and a single phenolic resin. (C. T. L. -91-LD), nearly all performance variability relates to the processing variables.

1) Mechanical Behavior

Typical mechanical properties of phenolic nylon thermal shields produced by various methods are shown in Table 1.3.7-2. Included are properties of phenolic nylon produced by an "ideal" or laboratory technique, which has not generally been attainable for production hardware. In Figure 1.3.7-1 typical variations of mechanical properties with temperature are depicted. Additional available mechanical performance data, of value in thermal shield design using phenolic nylon, includes the effect of strain rate on mechanical performance (Ref. 1), dynamic modulus and damping factor (Ref. 2), creep (Ref. 3) and low cycle fatigue (Ref. 4). All these properties are important in their inter-relationship in meeting design criteria.

2) Physical and Thermal Performance

Typical physical and thermal performance data for phenolic nylon are shown in Table 1.3.7-2. Ablation performance under various conditions is described in Section 1.3.3. These properties are far less sensitive to processing techniques and variables than are the mechanical properties and are, therefore, often listed for the general case.

3) Environmental Behavior

The effect of ground storage environmental aging, including humidity, has been studied and reported (Ref. 2) for highly post cured laminates. The effect of thermal aging at 250 °F on mechanical properties and shrinkage of tape wound cylinders is reported in Ref. 5 and similar information on molded parts is given in Ref. 6. Additional data, showing the effect of aging at 250 °F on laminated phenolic nylon is given in Figure 1.3.7-2 (Ref. 7). From this and other related work it can be seen that the major dimensional and mechanical property changes occur during initial aging (or post cure) at 250 °F or above.

Only limited data is available on the effect of vacuum exposure on the properties of phenolic nylon. Such information is important in assessing performance reliability after transit aging. The data of Ref. 11, which includes weight loss, mechanical and ablation performance changes for periods up to 30 days at 10^{-5} Torr and 120 °F, was obtained on relatively under-cured material. (Typical properties of these under-cured materials are listed in column 1 of Table 1.3.7-2.) During this aging period the modulus increased and strain to failure decreased (to approximately the values of a well post-cured part, column 5), and a slight overall improvement in ablation performance was noted.

Radiation effects on phenolic nylon have been determined in a general sense (Ref. 7, 8, and 9) and results indicate that changes in mechanical properties are negligible below 10^9 rads exposure.

4) Manufacturing

Forming techniques, cure and post-cure conditions, and raw material variables are all processing variables of primary importance.

The phenolic nylon material can be formed by high pressure matched metal molding (pressure limited by press size), vacuum bag autoclave techniques (pressures up to 200 psi), and by vacuum hydroclave techniques (pressures up to 3000 psi). The form of material used for matched metal molding is usually 1/2" x 1/2" chopped squares, and the resulting part is a true molding with heterogeneous reinforcement orientation. The vacuum bag autoclave and hydroclave systems require that the material be placed in or on the mold as a laminar build-up or as an oriented tape wrapping. While the orientation provided by tape wrapping is necessary for reffrasil and graphite reinforcements to prevent delamination during re-entry, it is not necessary to orient phenolic nylon materials. The phenolic resin reacts with the nylon reinforcement to some extent during cure and forms a chemical bond between the resin and reinforcement which eliminates delamination problems.

TABLE 1.3.7-1. TYPICAL MECHANICAL AND THERMAL PROPERTIES OF HEAT PROTECTION MATERIALS AT ROOM TEMPERATURE

Material	Phenolic Nylon	Phenolic Refrasil	Graphite Phenolic	ESM 1001 P-S	PD-300	Pyrolytic Graphite	Teflon	Fused Quartz
Density (lb./ft. ³)	73	105	93	40	53	137	134	131
Tensile Strength (psi x 10 ³)	5.3	5.0	5.5	.058	0.1	15 (a) 0.5 (c)	2.5	6.3
Ultimate Elongation (%)	1.0	1.0	1.0	58	15	0.2	200	---
Modulus (psi x 10 ⁶)	.55	2.0	2.0	---	.001	4.5 (c)	3.8	8.4
Compressive Strength (psi x 10 ³)	13 - 17	16	20	--	0.5	15 (a) 50 (c)	0.4	40.0
Poissons Ratio	0.23-0.37	0.4	0.4	--	0.5	-21 (a) +1.0 (c)	0.46	0.15
Thermal Conductivity (BTU/sec.-ft. °F x 10 ⁵)	4	5.5	18	2.6	3.0	8000 (a) 30 (c)	4.0	14
Specific Heat (BTU/lb.)	0.4	0.33	0.22	0.30	0.28	0.15	0.25	0.22
Coefficient of Thermal Expansion, R. T. to 200 °F (in/in/°F x 10 ⁻⁶)	18	4.5	6	100	68	0.1 (a) 15 (c)	55	0.3

(a) Parallel to surface
(c) Perpendicular to surface

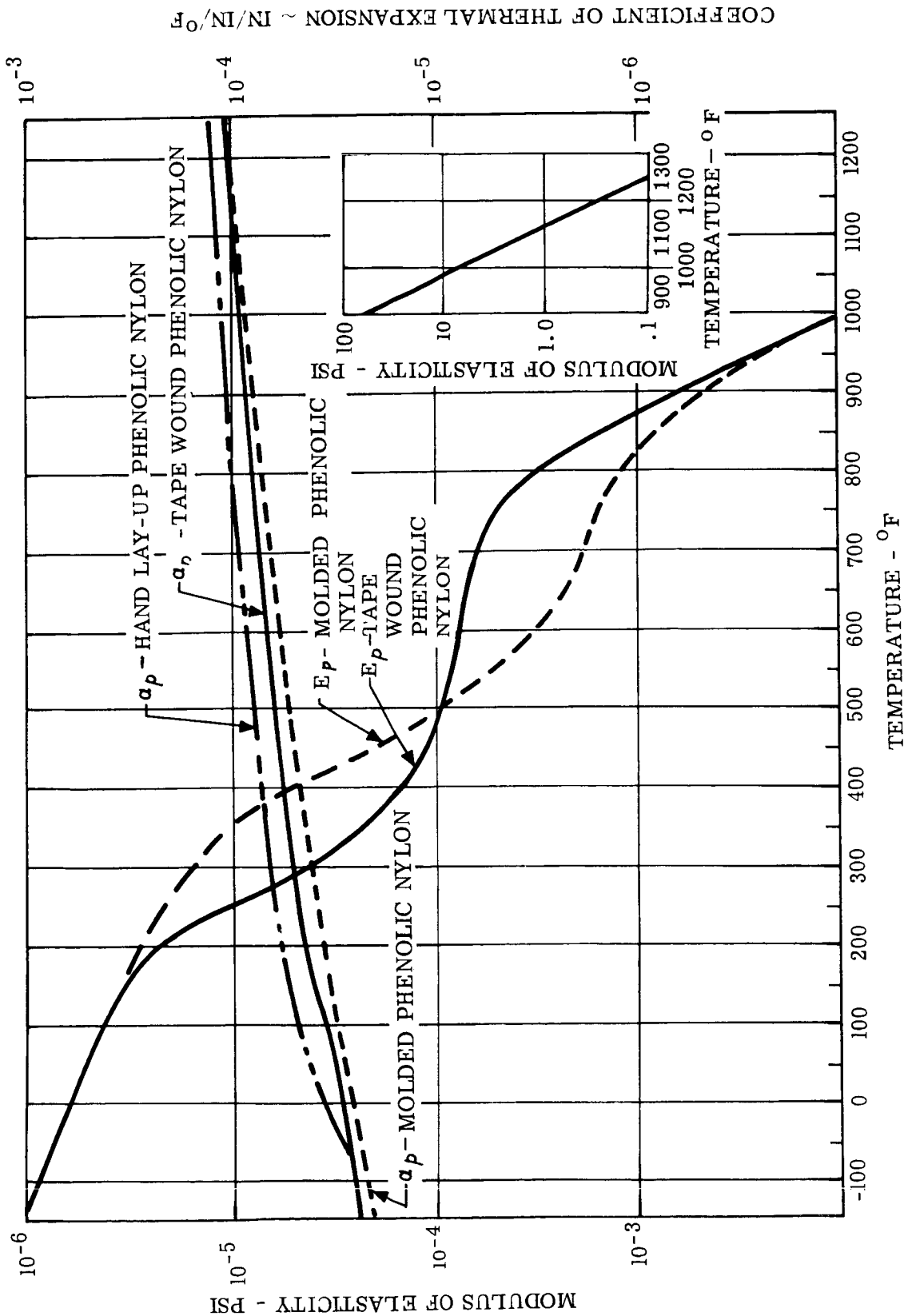
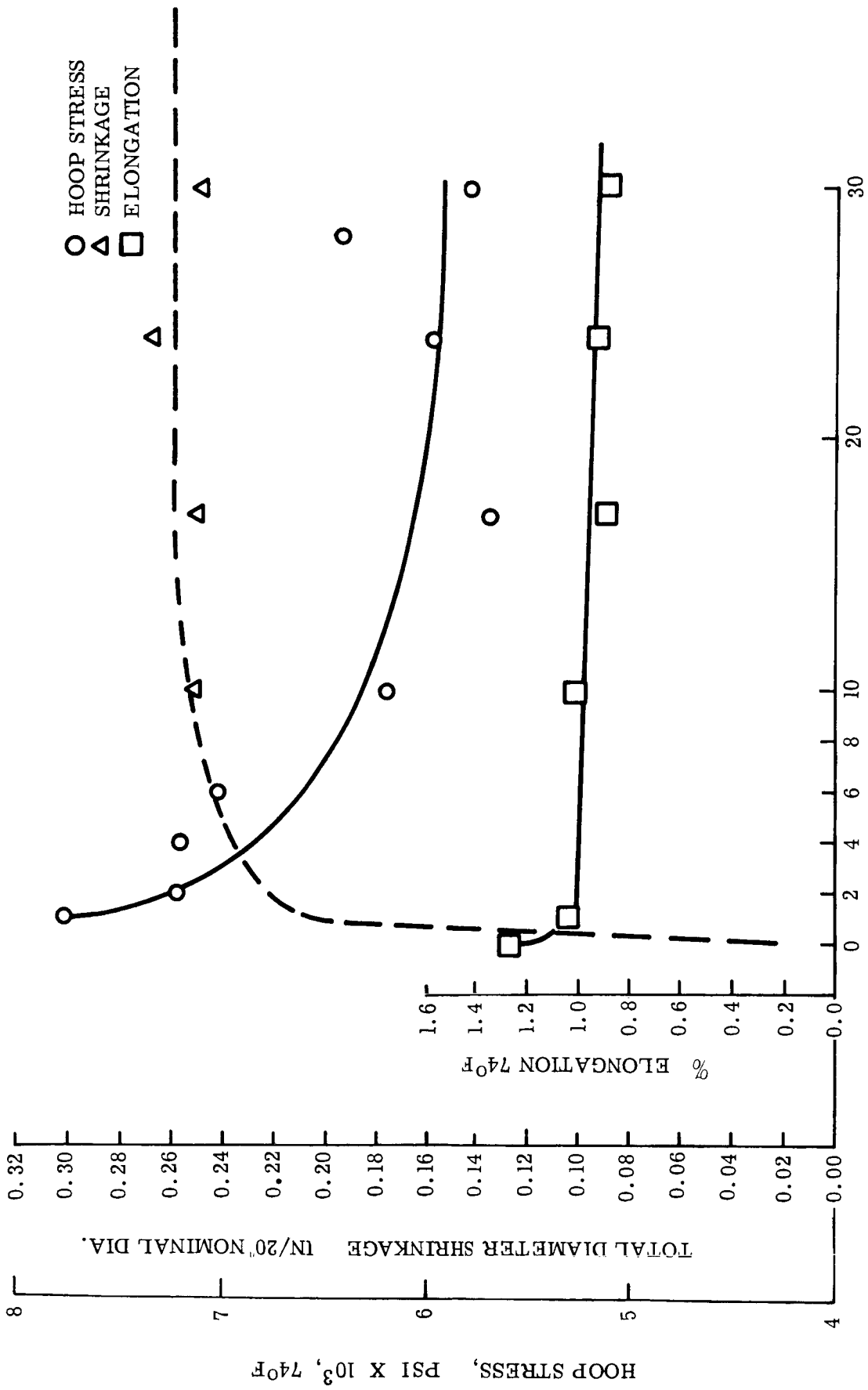


Figure 1.3.7-1. Phenolic Nylon - Modulus of Elasticity and Coefficient of Thermal Expansion



AGING TIME - DAYS AT 250°F

Figure 1.3.7-2. Effect of Aging Tape Wound Phenolic Nylon at 250°F on Room Temperature Properties

TABLE 1.3.7-2. TYPICAL PROPERTIES, PHENOLIC NYLON

Type Construction	Hand Lay-Up	Tape Wound		Molded	Press Laminate
Mold Cycle (Ref.)	(5)	(1)	(2)	(3)	(6)
Pst Cure, Hrs.** Temp. °F	None -	(1) None (1)	(2) 48 265	(3) 72 250	(6) 40 260
Tensile, Ultimate, Room Temp psi x 10 ³ -80 °F	4.3 5.0	4.6 5.0	5.6 -	4.0 -	5.8 7.3
Tensile Modulus, Room Temp psi x 10 ⁵ -80 °F	3.3 8.0	3.4 9.4	3.9 -	4.5 -	6.3 10.7
Tensile, Elongation %, Room Temp -80 °F	1.3 0.6	1.7 1.0	1.9 -	0.9 -	3.1 2.0
Coefficient Thermal Expansion Circ. (in/in/°F x 10 ⁻⁶) -6 °F to Room Temp Room Temp to +200 °F	27 40	33 35	26 25	23 -	37 47
C _p (Btu/lb-°F)	-	.35	-	.35	-
K (Btu/sec-°F/ft x 10 ⁻⁵)	-	4	-	4 to 5	6
Resin Content (%)	45	-	44.9	44.3	50.9
Specific Gravity	1.18	1.17	1.17	1.21	1.2+

(1) Ref. 5, Pg. 31, Includes various cures and post cures (4) Ref. 11, (Final cure 12 hrs. @ 250 °F, 1000 psi)

(2) Ref. 1, cure "G", Pg. 27, (Final 16 hrs. 265 °F, 150 psi) (5) MSI 24402, (Final 6 hrs. @ 250 °F, 100 psi)

(3) Ref. 1, cure "G-3", (Final 8 hrs. @ 240 °F, 4800 psi) (6) Ref. 5, Table 2 (2 hrs. @ 250 - 260 °F)

*Used on Comparative Chart, Table 1.3.8-1

**Post cure times are adjusted according to thickness of the part.

The exact method of processing a phenolic nylon part is determined by evaluating its size and shape in relation to equipment limitations, together with the economics of the process (number of parts to be made vs. tooling, labor, and material costs). Equal quality of phenolic nylon parts can be produced by any of the above techniques.

Assuming that approximately ten shields will be needed for the subject program, it is probable that a vacuum bag autoclave technique will be used. This is a state-of-the-art process and requires development work only to define a lay up pattern and a cure cycle.

The cure procedure on the proposed parts will be the most critical variable. In order to provide maximum dimensional stability during the sterilization cycles, a relatively long time, high temperature post cure will be required. Post bake cycles of extended time at temperature above 260 °F tend to increase the modulus and eventually to lower tensile strength. However, limited data indicates that with properly cured material, exposures of 100 hours at temperatures up to 300 °F produce only slight changes in mechanical properties. Because of the proposed sterilization cycle, a cure study must be made to insure optimum initial cure for the material thickness required.

5) Additional Development and Evaluation Effort

The properties, behavior and past performance of phenolic nylon substantiates its selection as the prime shield for the Venus Lander and as back-up for the Mars Lander. A review of this information in relation to the Voyager requirements indicate the following areas of development for flight qualification:

- Utilization of phenolic nylon for Venus entry is dependent on its sterilization and transit environment performance for which very little data of value is available.
- A highly post cured phenolic nylon shield system is required to minimize sterilization and transit effects on dimensions and mechanical properties. This increases thermal compatibility and bond problems due to the increased "stiffness" and lower ductility of the thermal shield.
- Considerable long term testing must be performed in order to define the long time (e.g., 1 year) transit effects on a phenolic nylon thermal shield of the type required.

(3) Phenolic Refrasil

The successful performance under severe heating requirements experienced on RVX and TVX flights makes phenolic refrasil a logical choice as the primary back-up shield for the Venus Lander and alternate for the Mars mission. Refrasil is the trade name of an acid-leached glass which has the approximate chemical and thermal properties of silica. However, during the leaching process the individual fibers are pitted and notched which considerably reduces its mechanical strength.

(a) Requirements

The shield requirements are the same as those for the prime shield selections described in Sections 1.3.3 and (4) (a) of this sub-section.

(b) Properties

Typical mechanical and thermal properties are listed in Table 1.3.7-1 with ablation performance data (discussed in Section 1.3.3). The ground and transit environmental effects on the properties of phenolic refrasil are expected to be similar to phenolic-nylon, (see

section on environmental behavior), however the effects of sterilization, transit and ground environments on dimensional stability would be minimized with phenolic reffrasil. The thermal conductivity and density of phenolic reffrasil are higher than for phenolic nylon. In general, the performance conclusions for phenolic-nylon are applicable to phenolic-reffrasil.

(c) Manufacturing

The manufacture of thermal shields to required specifications of reffrasil reinforcement impregnated with phenolic resin is "state-of-the-art". The processing of phenolic reffrasil can be accomplished by matched metal molding, vacuum bag autoclaving, or hydroclaving. The quality of the parts produced by any of the processes is comparable. Unlike phenolic nylon, however, only two types of reinforcement orientation can be used: (a) random orientation produced by matched metal molding of 1/2" x 1/2" chopped squares, and (b) a shingled orientation produced by wrapping a mandrel at an angle. The shingle-wrapped mandrel material can be molded and cured by all of the processes. The exact system to be used, as with phenolic nylon, is selected by evaluating the size and shape of the part versus equipment limitations, and economical methods, i.e., (number of parts required versus tooling costs, labor and materials.

(d) Additional Effort

The analysis and qualification effort would be very similar to that required for phenolic nylon.

(4) Elastomeric Shield Material (ESM 1000)

(a) Mars Lander Thermal Shield Requirements

It is highly desirable for the Mars Lander to have a thermal shield system possessing the following capabilities:

- (1) Mechanical compatibility with structures over a wide temperature range.
- (2) Ease of manufacture with adaptability to design changes with inexpensive tooling and equipment.
- (3) Resistance to service damage that might occur during flight or prior to launch.
- (4) Resistance to micrometeorite and other particle damage.
- (5) Ease of repair
- (6) Resistance to ground environmental factors and radiation and other space environmental conditions.
- (7) Good insulating characteristics.
- (8) High temperature bond systems allowing fuller utilization of the high temperature capability of the substructure material.
- (9) High heat of degradation for the low-flux long-term entry condition, leading to an efficient low weight shield.
- (10) Capability of use as radome material.

(b) Recommended System

1) Material Description

Elastomeric Shield Materials (ESM 1000) is a generic nomenclature applied to a series of modified, foamed, silicone elastomer formulations ranging in density from 20 lbs/ft³ to 77 lbs/ft³. Considerable variation in mechanical and thermal properties can be achieved by variations in density, matrix, fillers and base resin selection. Test emphasis has been on a 40 - 45 lb/ft³ formulation which has been flight tested on Mercury and ICBM flights and is under active consideration for use on earth orbital flights.

ESM has been chosen as the primary shield material for the Mars Lander since it more closely meets the general vehicle requirements for the Mars Lander than any other available shield system. The following sections substantiate the selection with a discussion of tests and properties and tasks necessary for design and qualification for flight.

2) Properties

a) Mechanical and Thermal Behavior

A summary of the data is presented in Table 1.3.7-3. This shows the maintenance of desirable mechanical properties of the shield and bond system over a wide temperature range for mechanical compatibility and its insulating characteristics. Additional data would have to be generated to assure flight reliability.

b) Ablation Characteristics

Ablation characteristics of ESM series material have been determined in arcs and in the Malta Rocket Exhaust Test Facility over a wide range of heating rate, shear and enthalpy environments. Figure 1.3.7-3 presents a summary of the ablative performance for some of the ESM Series materials. Ablation characteristics of ESM, phenolic nylon and phenolic graphite are compared in Reference 10. The ESM material shows substantially improved performance over other shield materials for the low flux-long term, entry conditions of the Mars Lander. Further ablation testing is required to provide quantitative, statistical, design data for the specific Mars Lander entry conditions.

c) Environmental Effects

Specimens of ESM material have been subjected to continuous exposure of 5×10^{-5} Torr at 250 °F for 14 days with no significant change in mechanical properties. Additional long term aging data is needed for design.

The effects of radiation on polymeric materials have been discussed in detail by various authors (Ref. 7, 8, 9). Most of the radiation damage will occur in the thermal control coatings used on the outer surface of the thermal shield (Section E.) The thermal shield materials should not seriously degrade unless the flight occurs during a period of high solar flare activity.

The base polymer for this resin system has been subjected to temperatures and times in excess of the sterilization conditions with no change in properties. Although no properties determinations (others than vacuum/temperature aging) have been made on the specific shield formulation, the proposed method of sterilization should have no deleterious effect on ESM. Properties determinations after sterilization, including ethylene oxide exposure, should be made for reliability assurance.

It has been demonstrated in several micrometeorite simulation penetration studies that the ESM class of material does not have a catastrophic failure on particle impact.

TABLE 1.3.7-3. TYPICAL PROPERTIES OF ESM 1001P-S

Tensile	600 °F	300 °F	200 °F	75 °F	-35 °F	-130 °F	-240 °F
Ultimate Stress (psi)	15	35	32	58	35	125	625
Strain to failure (%)	14	18	13	58	16	12	0.3
Bond Tensile (to phenolic-glass)	600 °F		400 °F		200 °F		75 °F
Ultimate Strength (psi)	11		26		47		60
Specific Heat	100 °F	200 °F	300 °F	400 °F	500 °F	600 °F	
BTU/lb/°F	0.30	0.32	0.34	0.36	0.37	0.38	
Thermal Conductivity	100 °F - 600 °F						
BTU/ft/hr/ft ² /°F	0.10 - 0.085						
Density		40 - 45					
lbs/ft ³							
Thermal Coef. of Expansion	0° to + 300 °F		0° to -40 °F*		-40 °F to -240 °F		
in/in/°F	10 x 10 ⁻⁵		15 x 10 ⁻⁵		3.5 x 10 ⁻⁵		

*crystalline phase change

(glass transition temp. ~ -175 °F)

d) Radome

Preliminary samples of ESM modifications for radomes were fabricated and screened in ablation tests at heating rates of 6 and 79 BTU/ft²-sec. in the hypersonic arc tunnel. The surface layer formed in these tests appears to be non-carbonaceous. Transmission tests at 2400 mc indicated less than 1-db loss in transmission through the degraded material as compared with the material before thermal exposure.

Material Density - 43 lb/ft³

Dielectric Constant - 2.32 @ 2400 mc

Power Transmission through 0.5 inch thick flat panels at 2400 mc

Before Arc Tunnel Exposure - 99%

After 6 BTU/ft²-sec. for 840 seconds - 97%

Although feasibility was shown in these tests, complete definition and properties evaluation tests would have to be made to provide complete material characterization for design purposes.

Formulation modifications have to be developed and qualified to the higher heating conditions of the stagnation area of the Mars Lander. Formulation optimization should further improve the electrical performance.

e) Manufacturing

A series of thermal cycle specimens were prepared which successfully survived thermal cycle and soak conditions from -300 °F to +300 °F. Large scale, sections even complex curves and shapes, have been fabricated by a relatively simple process. A conical shield-structure section of a full scale-vehicle is currently being fabricated for thermal cycle qualification.

f) Development Areas

A review of the available information with respect to the Voyager Program indicates that additional data and further evaluation would be required in the following areas:

- (1) Develop, define and qualify material for radome.
- (2) Determine complete mechanical, thermal and ablation properties to mission requirements for statistical design analysis.
- (3) Conduct environmental aging studies of shield-bond system by accelerated aging of ablation and mechanical specimens to ground and orbital mission requirements.
- (4) Define joint and sealant techniques, window and cut-out fabrication and application.
- (5) Development and application of repair procedures.
- (6) Development, application and qualification of emissive and other coatings.
- (7) Develop, design, fabricate and qualify ablation, temperature, motion and pressure sensors.
- (8) Define and fabricate full scale prototype vehicle for engineering test program with associated engineering, manufacturing and quality control specifications.
- (9) Perform materials performance analysis effect on structure, temperature history and gradients, shield thicknesses and amount degraded over body stations.
- (10) Perform thermal stress analysis and conduct cycle test to verify analysis.
- (11) Determine thermodynamic properties of the char and individual species of the gaseous products.
- (12) Calculate energy, mass, momentum and species equations for thermodynamic analyses.
- (13) Define and conduct shield-bond studies originating from special vehicle requirements.

(5) Aft Cover Thermal Protection

Either the syntactic silicone foam, PD 300, or the foamed elastomeric series, (ESM 1000) would be suitable for thermal protection of the aft cover. These materials are filled foamed silicones formulated for maximum char integrity and insulating characteristics as outlined in the previous sub-section.

(a) Requirements

A good insulating, low density material is desirable for this application. Wake heating for the Mars aft cover is low compared to the Venus vehicle. The selected material must also withstand the ground and flight environmental conditions.

(b) Properties

Table 1.3.7-1 lists typical mechanical and thermal properties of various heat protection materials. In addition to the flight proven performance of PD-300, ablation performance of both these materials systems for this type environment have been demonstrated in arc-driven test facilities and in the Malta Rocket Exhaust Facility over a wide range of heating rates, shear, and enthalpy conditions. The materials are adaptable to modifications of density, filler type and concentrations, etc., to meet the design requirements for both types of re-entry condition.

(c) Additional Effort

In addition to design qualification to the flight environment, trade-off studies are necessary to select an optimum material based on weight, performance and fabricability.

(6) Advanced Materials

(a) Graphite-Phenolic and Other Low Shape Change Ablative Materials

An advanced material study currently in progress at GE-RSD is concerned with the development of refractory reinforced ablative materials having substantially improved performance under very high heating rates and very high aerodynamic shear forces. Recent ablative testing has indicated that graphite cloth reinforced phenolics may have ablative performance significantly greater than that of phenolic nylon under severe high heat flux, high shear entry conditions (Ref. 10). The use of similar graphite-reinforced ablative materials as rocket nozzle insulation has also been reported (Ref. 12 and 13).

Studies are currently underway aimed at development and improvement of this class of materials for advanced high performance ballistic re-entry vehicles. Available materials are being screened at present, and orientation determined and processing techniques developed to provide a material for flight test to begin in February 1964. In addition, advanced development work is being carried out aimed at improving and optimizing the performance of this class of refractory reinforced materials for ballistic re-entry vehicles. This development work is initially covering the comparison of carbon with graphite reinforcements as they effect ablative performance and insulation effectiveness, the effects of resin content and fiber orientation, and the utilization of new fibrous refractory reinforcements such as zirconia, alumina, carbides, nitrides, etc. Results to date indicate that this class of materials may provide an alternate material superior to phenolic Refrasil for the severe entry conditions to be encountered in the Voyager Venus entry mission. Development and flight testing of this class of material appears to be properly timed to have significance in the Voyager program. Development, optimization and materials characterization should be carried out which is aimed at the specific needs of the Voyager program. This effort, however, will be guided by the data available from current programs.

(b) Organic Fiber Reinforced Ablative Materials

Although extensive data is available for reliably predicting the performance of phenolic-nylon thermal shield materials, there are several areas in which improvements should be sought for lengthy missions in the space environment such as will be encountered by the Voyager vehicles. These areas of possible improvement would include reduced coefficient of thermal expansion, higher elongation and improved dimensional stability during aging under temperature and/or vacuum exposure. Included in this investigation would be the use of the newly developed high temperature stable HT-1 polyamide fiber, Dacron fibers, and inorganic fibers such as glass or silica in combination with the organics.

Such a study should lead to a general upgrading of the overall reliability of the thermal shield system in relation to its extended mission requirements.

REFERENCES

1. Parker, J., "Short Time Behavior of Molded and Tape Wound Phenolic Nylon," GE TIS 60SD397, June 28, 1960.
2. Lazar, L. and Bainton, G., "Aging of Phenolic Nylon," PIR 2243-510, May 25, 1962.
3. Mehan, R., "Creep of Phenolic Nylon, and Relation to Other Viscoelastic Properties," PIR MPL-8155-179, February 11, 1963.
4. Mehan, R., "Low Cycle Fatigue Behavior of Phenolic Nylon," Unpublished report.
5. Ludwig, R., "State-of-the-Art, Phenolic Nylon for Thermal Shield," GE TIS 61SD174, December 19, 1961.
6. Smith, J., "Post Cure Cycle Evaluation, Mark 6 Nose Shields," PIR 8382-83, March 21, 1962.
7. Jaffee, L.D. and Rittenhouse, J.B., "Behavior of Materials in Space Environments" JPL Tech. Report No. 32-150, November 1961.
8. Battelle Memorial Institute, "Effect of Nuclear Radiation on Elastomeric and Plastic Materials," REIC Report #21, September 1961.
9. Lockheed Missiles and Space Company, "Space Materials Handbook," 1962.
10. Bierman, R.L., "Evaluation of Phenolic Graphite, T-R4, T-24WFAG and ESM 1003 in the Malta Pit #1 Rocket Exhaust Facility, GE TIS 63SD257, April 5, 1963.
11. Smith, J., "Part Thickness and Physical Properties of Thermal Nylon," PIR 8382-233, October 9, 1962.
12. AD 286, 218, "Plasma Arc Evaluation of Reinforced Plastic, Phase I," Aerojet General Corp., October 15, 1962.
13. AD 286, 219 "Preliminary Evaluation of the Mechanical, Physical and Thermal Properties of Thirteen Reinforced Plastic Materials, Phase I," Aerojet General Corp., October 15, 1962.

B. Structure Metals

(1) General

The structure for the lander must be the lightest unit possible, consistent with minimum development time and cost that will withstand ground and transit environments, entry loads, and will maintain integrity after impact.

(2) Summary

The materials for structural use in the Venus and Mars re-entry vehicles are discussed, with consideration given to availability, fabrication requirements, ground and transit environments, and entry and surface conditions. Aluminum honeycomb is recommended for the Mars vehicle, because of easy availability, fabrication experience, tolerance for heat sterilization, and proven entry performance.

Stainless steel honeycomb is recommended for the Venus lander because of fabrication experience, and ability to survive entry and surface conditions. Magnesium, titanium, and beryllium are discussed as alternatives, in terms of availability, state-of-the-art fabrication abilities, and probable development required.

(3) Mars Lander

It is anticipated that the structure will operate at a maximum of about 300 °F during entry, and that the structure is to be of adhesive bonded honeycomb. Aluminum or magnesium alloys are the most practicable choice. Alloys with optimum strength/weight ratios for short time service at 300 °F, and a tolerance for the sterilization and adhesive bonding thermal cycles are required.

(a) Aluminum

For maximum strength honeycomb face sheets, 2020-T6 aluminum is recommended. Design properties have not yet been established, but some data are available (Table 1.3.7-4 and Ref. 1). 2020 is a high-strength alloy which will suffer slight degradation of properties from exposure to bonding and sterilization cycles, and which exhibits excellent strength retention for short-term 300 °F service. The alloy has low resistance to crack propagation, but no state-of-the-art advances are required to insure that this characteristic is not detrimental to structural integrity.

Where maximum tensile properties are not the controlling factor, more common sheet alloys will suffice. 7075-T6 aluminum is recommended in this case. 7075-T-6 will be affected by exposure to adhesive bonding and sterilization cycles, to the extent of approximately a 10% drop in room temperature tensile properties; however, room temperature compression properties will be little affected.

5052-H39 aluminum is the recommended core material for aluminum honeycomb. This choice is based on ease of availability, very minor loss of properties due to bonding and sterilization, and good (90%) strength retention at 300 °F.

Ring and other necessary forgings can be made of a wide variety of alloys. The primary selection is 7079, which combines availability with good strength and toughness. Mechanical stress relief treatments will be specified wherever possible to reduce residual stresses and distortion without impairing mechanical properties.

For use in such devices as a tipover bar, 2219 has the best combination of shear strength and weldability.

(b) Magnesium

Magnesium honeycomb could be used in place of aluminum honeycomb. On a strength/density basis, magnesium offers no advantage over aluminum in 300 °F service. The advantage of magnesium lies in the ability to use thicker sections for equivalent weight, thus increasing stiffness slightly. Magnesium honeycomb core is not in production, and would be a development item (Ref. 2). Very small quantities have been produced on a development basis, but work is needed on surface preparation and bonding of the core and of the sandwich.

(c) Problem Areas

The use of 2020-T6 for honeycomb face sheets will necessitate a testing program to generate reliable design data, unless such data are released soon.

Use of magnesium honeycomb will require immediate development effort to obtain production quantities of core material and to solve the surface preparation and bonding problems.

The compatibility of ethylene oxide sterilant with aluminum and magnesium constructions should be confirmed. It has been reported that highly oxidized surfaces may catalyze polymerization of Ethylene oxide (Ref. 3).

TABLE 1.3.7-4. PRELIMINARY DATA ALUMINUM 2020-T6

Test Temp. (°F)	Time At Temp. Hrs.	Ult. Strength (psi)	0.2% Yield (psi)	Elong. (%)
R. T.	--	87,000	79,000	6
212	--	81,000	76,000	9
300	1/2	74,000	71,000	7
	1000	69,000	67,000	8
350	1/2	68,000	65,000	8
	1000	42,000	38,000	19
400	1/2	60,000	59,000	7
	1000	32,000	28,000	22
500	1/2	34,000	32,000	12
	1000	19,000	17,000	24

Recent reports indicate that the reaction occurring at the aluminum surface has no detrimental effect on the metal, although the reaction may have had an effect on Ethylene-oxide performance (Ref. 4). Current reports should be more thoroughly investigated before additional compatibility programs are initiated.

(4) Venus Lander

The much higher structure temperature which will be encountered in the Venusian entry and surface environments preclude the use of materials with effective service temperature less than 1000 °F. Precipitation hardened stainless steels or titanium alloys are recommended as materials for fabrication of brazed honeycomb structures.

(a) Stainless Steel

The recommended alloy for brazed honeycomb is PH 14-8 Mo, an alloy recently introduced to replace PH 15-7 Mo for supersonic transport use. The mechanical properties of PH 14-8 Mo are essentially identical to those of PH 15-7 Mo, but the resistance to crack propagation has been increased. Although the newer alloy also has improved elevated temperature stability, this characteristic is of no great importance considering the short elevated temperature exposures involved in entry (Ref. 5). The fabrication of brazed honeycomb of PH 14-8 Mo material will require no advances in basic technology, the techniques having been established in the B-58 and RS-70 programs.

Forgings can be made from several alloys, e.g., AM355, PH 13-8 Mo, 18% nickel maraging steel, etc., depending on predicted thermal and stress environments for each item.

(b) Titanium

The "super-alpha" alloys presently being developed offer good elevated temperature properties after exposure to a brazing cycle. Titanium - 8 aluminum - 1 Molybdenum - 1 Vanadium, one such alloy, is in current production and available in thin sheets. This alloy is recommended for face sheet use. The 8-1-1 alloy is not available in foil form for honeycomb core use, but very possibly will be in the near future. However, Titanium - 6 aluminum - 4 Vanadium can be obtained in foil form and offers better elevated temperature properties than the commercially pure foil often used for core production. Non-erosive brazing alloys capable of 1000 °F service temperatures are available, such as the Silver-aluminum Manganese types (Ref. 6).

The tooling designs and basic procedures established for stainless steel panels are directly applicable to titanium, but further development remains to be done. Parameters such as starting material condition, optimum braze alloy composition, brazing temperature and time, cooling cycle, methods of preplacing the braze alloy, flow control, etc., must be investigated. The comparatively extreme curvature of the Voyager structure may introduce an excessive flow condition similar to that experienced in early stainless steel work, in which the braze alloy "puddled" at the lowest point.

A destructive testing program to establish reproducibility of properties in large panels will be required, as will a concurrent effort to establish exact non-destructive testing procedures (Ref. 7).

Some work on core fabrication may be required. Diffusion bonding of the core may prove better than resistance welding, and should be investigated (Ref. 2).

There are a variety of alloys available for forgings and other fittings, e.g., Ti-8 Al- 1 Mo- 1V, Ti-7 Al - 4 Mo, Ti-6 Al - 6V - 2 Sn. Final alloy choices will depend on service conditions.

(c) Beryllium

A beryllium structure would probably be the lightest possible unit for 1000°F service. Berylco I-400 material in the form of cross-rolled sheets would have an excellent strength/weight ratio and high elastic modulus, and structure stiffness would benefit from the ability to use thicker sections for equivalent weight. However, it is felt that the construction of a high reliability vehicle of beryllium would require an extensive development program in all phases of the project; material, forming, joining and fastening, structure design, surface treatments, etc. Beryllium is the object of intensive research effort at the present time. Solution strengthening and reduction procedures are under investigation in an attempt to alleviate the problems of extreme notch sensitivity and low ductility, which apparently are due largely to the preferred grain orientation presently needed for strength (Ref. 8). Considerable design effort would be required to minimize the notch sensitivity and ductility problems, especially around fasteners. A structure breakage hazard due to high impact loads definitely exists, particularly if the structure happens to be comparatively cool upon impact, although additional crush-up material may eliminate this problem. It is felt that a reliable structure could not be built within present state-of-the-art limitations.

(d) Problem Areas

The use of titanium honeycomb will involve a fabrication development program to establish material and process parameters for brazing and may require brazing alloy development effort. Destructive and non-destructive testing programs will have to be carried out. Some core bonding studies should be performed.

The use of beryllium will require a full-scale development and test program in nearly all phases of application.

The interactions of chemical sterilants with the structure materials should be evaluated (Refs. 3 and 4).

(5) Transit Environment

Space vacuum, and radiation from the radioisotope thermionic generator and from solar activity is essentially the transit environment. No detrimental effects are anticipated with any of the structural metals from either condition, with the possible stipulation that exposed magnesium surfaces should be hard-coated to reduce any slight evaporation.

REFERENCES

1. Personal communication, Aluminum Company of America.
2. Personal communication, Hexcel Products Inc.
3. Matheson Gas Data Book, The Matheson Co., Inc. 1961.
4. Willard, M., "Surveyor Sterilization, Part I, Compatibility of Materials and Components with Heat and Ethylene Oxide From 12," Hughes Aircraft Company, RS-277, Jan., 1962.
5. Armco Product Data Report S-12, 1963.
6. DMIC Memo 45, "Recent Developments in Titanium Brazing"
7. WADD TR-60-393, "Evaluation of Brazed Honeycomb Structures"
8. ASD-TDR-62-509, Vol. II, "Beryllium Research and Development Program"

C. Bond Systems

(1) ESM 1000 (MARS)

Recent developments in silicone technology have greatly increased the adhesion characteristics of the silicone systems. The shield material is fabricated in shape conforming sections and bonded to the substrate with the base elastomer.

(a) Bond Requirements

The bond system must have sufficient tensile stress-strain characteristics at the high side of the temperature cycle and shear stress-strain at the high and low temperature extremes. These requirements depend on the differential coefficient of expansion of shield and structure, the stress-strain characteristics of the shield material, the vehicle size and shape and the manner in which the shield segments are joined.

(b) Bond Properties

The tensile strength of this bond system to a phenolic-glass substrate is reported in Table 1.3.7-3. Other tensile and shear tests have been made on aluminum, beryllium and stainless steel substrates over the temperature range of the Mars flight environment. All ultimate failures have occurred cohesively in the bond material. By using the same base resin in the bond as in the shield material, the low temperature capability of the shield system is maintained through the bond.

(c) Manufacturing

Both shield and structure bonding surfaces are thoroughly cleaned by organic solvents and protected from contamination. Before bonding, a thin continuous priming coat is applied over the structure surface and air dried. The base resin of the elastomeric system is catalyzed and applied over both bonding surfaces. The shield is placed on the structural surface and slight pressure is applied to assure contact on all bonding surfaces through the 72 hour, 125 °F curing cycle.

(2) Phenolic-Nylon (Venus)

(a) Silicone Tubing Bond System

The proposed bonding system for phenolic-nylon consists of wound silicone tubing bonded both to substrate and shield with an elastomeric silicone bond. This system is particularly characterized by its adaptability to widely varied requirements and its serviceability over a broad temperature range from less than -100°F to $+700^{\circ}\text{F}$ (Ref. TIS 63SD265).

1) Bond Requirements

Even though a shroud is employed to reduce the temperature extremes for the flight mission, a discontinuous, compressible bonding system is required to compensate for the thermal coefficient of expansion between the shield and structure. It is also highly desirable to have a bond system which is a good insulator and which has a high temperature capability for the transient high temperature entry conditions.

2) Bond Properties

The apparent modulus may be varied over a wide range by using tubing of various diameters, wall thicknesses and spacing. A typical commercially available tubing of 0.135" outside diameter and 0.015" wall thickness was chosen for design data generation and scale-up. The data is tabulated in Table 1.3.7-3. The silicone adhesive system and techniques are similar to those detailed for ESM 1000 with its low and high temperatures capability. The material acts as an excellent insulator as it is essentially a dead air space between the shield and structure. A system of this type would be mandatory without a temperature controlling shroud. A 30" tall conical section has been fabricated by this process and thermal cycled three times up to 170°F with no failures. Under a soak condition of 170°F , the bond system was roughly under 50% tensile and 75% shear strain. The generated mechanical data indicates a capability of 76% tensile and 115% shear strain at 170°F for this size test unit.

3) Manufacturing

The application of the tubing is essentially the winding of a continuous length of silicone tubing on a substrate coated with a silicone elastomer adhesive. After the tubing has been wound and cured on the substructure, a partial vacuum is pulled on the system to flatten the tubing. The adhesive coated shield is then fitted over the flattened tubing. The tubing is then inflated by low nitrogen pressure (5-15 psi) which both ensures good wetting to the silicone adhesive and ensures good contact to those areas of oversized bond gap. The inflation step also provides an automatic self-centering process whereby the bond gap tends to become equalized around the structure. The inflation pressure is maintained during the cure cycle.

(b) Foam Bond System for Phenolic-Nylon

An alternate compressible bonding system is available for phenolic-nylon which may possess certain advantages. This would involve the use of a layer of low density (20 lb./ft^3) unsupported ESM material as the compressible bond between shield and structure. The material would be fabricated in pre-foamed sheets and cut to desired thickness. The process would be similar to the pre-foamed bonding process currently in use for the Mark 6 vehicle. In this case, however, the adhesive would again be the base elastomer which is fully described for ESM 1000 in this section. While providing good insulation and the necessary compressible bond for the differential coefficient of expansion of shield and structure, it would provide a secondary thermal protection system for vehicle survival from the point of initial re-entry to and after landing. At this time, there is no additional data to support this approach although it appears feasible. A development program would have to be conducted to define and qualify this bonding method to the mission requirements.

(c) Rigid Bond System for Phenolic-Nylon

If the vehicle temperature exposure were mild and reliably controlled by the protective shroud, a rigid bond system might be usable.

(3) Alternate Shield Materials

If one of the alternate shield systems were selected for one of the missions, a rigid bond system might be applicable due to the increased thermo-mechanical compatibility of the shield and structure. Ambient or medium temperature cured adhesive systems are commercially available which will not deteriorate in the sterilization process. Qualification and testing of a number of variations of this class of adhesive have been carried out by GE for phenolic-refrasil and phenolic-graphite. If a rigid bond system were selected, additional evaluation tests and thermal stress analysis must be conducted to establish the performance reliability of the shield-bond-structure system.

D. Retardation Materials

In selecting a material or combination of materials to be used in the fabrication of drag devices for the Voyager vehicles, the following basic material properties have been considered:

- Structural integrity
- Flexibility for ease of storage
- Resistance to elevated temperatures
- Compatibility with sterilization requirements
- Stability to long-term exposure in hard vacuum

The flexibility requirement can best be met by utilizing a fabric woven from continuous filaments whose properties satisfy the environmental requirements. Table 1.3.7-5 lists the room temperature properties of several single filaments (Ref. 1). (Note: Translation of filament strength to fabric strength results in a reduction in the woven fabric strength-to-weight ratio, e.g., HT-1, Nylon Bright, Polybenzimidazole (PBI), best meet the high impact resistance and flexibility requirement at minimum weight penalty (high drag area-to-weight ratio). The results of the study conducted in Ref. 1 indicate that the HT-1 nylon fiber, although having properties at room temperature similar to 66-nylon and "Dacron" polyester yarns, retains 60% of its room temperature tensile strength at the melting temperatures of these yarns (~ 482 °F). At 660 °F, the tensile strength of HT-1 fiber is reduced to 85% of its room temperature value. The sterilization requirement will present no problem for the HT-1 fiber and it is anticipated that long-term exposure to hard vacuum will have a negligible effect upon its desirable properties. If aerodynamic heating causes equilibrium temperatures to exceed 600 °F (present requirements do not) during descent, then one must consider utilizing the higher-modules, lower impact strength, ceramic fibers, metal wires, or possibly, the organic Polybenzimidazole fiber which is reported in Ref. 1 to have strength to 800 °F but is presently in the research stage.

The drag device utilized for Venus re-entry will have higher operating temperature requirements since the free stream temperature (maximum temperature extreme) may be as high as 925 °F at 50,000 feet increasing to 1052 °F at the planetary surface (Ref. 2). A drag plate fabricated from stainless steel or titanium alloy is the preferable retardation device. If a flexible chute is desired, then fabrics woven from silica or glass fibers and metal wires may be necessary for a Venus entry drag device, however, a definite weight penalty will be encountered when using these lower strength-to-weight ratio fibers compared to HT-1 fibers. It should be noted that these fibers are optimum in the sense that they are the only flexible-type fibers which can survive at elevated temperatures, e.g., glass fabric has a useful temperature up to 1200 °F, Rene 41 wire mesh has a useful

TABLE 1.3.7-5. ROOM TEMPERATURE PROPERTIES OF SINGLE FILAMENTS

Material	Dia. in Mil	Modulus (E) x 10 ⁶ psi	Average Tensile Strength x 10 ³ psi	Specific Gravity Gm./cc
"E" Glass - Spool	.40	10.5-11.5	331	2.55
"E" Glass - Fork	.38	10 -11	501	2.55
X-37B Glass - Spool	.35	12 -13	435	2.57
X-37B Glass - Fork	.40	11.5-12.5	446	2.57
Zinc Coated "E" Glass	.53	11.5-13	104	3.76
Yarn - GE Silica	.38	10.0	184	2.20
Spool - GE Silica	.38	10.3	306	2.20
Fork - GE Silica	.42	10.3	423	2.20
HT-1	.67	3.4	84	1.38
Nylon Bright	.66	1.1	86	1.14
PBI	1.83	2.2	68	1.32
Elgiloy	.50	34.0	341	8.30
Evanohm	.50	31.0	-	8.10
Rene 41 as received	.50	28 -32	197	8.25
Rene 41 annealed	.50	28 -32	178	8.25
Rene 41 Hard	.50	28 -32	339	8.25
Tungsten	.20	54 -56	457	19.3
Gold Plated Tungsten	1.0	49	393	19.3
Gold Plated Molybdenum	1.2	42	128	10.2
Hastelloy	1.0	22	-	8.23
Chromel A	0.7	32.7	162	7.85

Reproduced from Ref. 1

temperature up to 2000 °F. Ablative coatings such as silicone rubber, teflon and neoprene may be used to depress the operating temperature of the glass or metal fabric and thereby possibly increase the effective strength-to-weight ratio of the coated fabric.

References

1. Schulman, S., "Elevated Temperature Behavior of Fibers", ASD-TDR-63-62, April, 1963.
2. Chamberlain, S., "Venus Model Atmosphere", PIR 8021-049, May 1963.

E. Energy Absorbing Materials

(1) General

The requirement for effecting a soft landing on planetary surfaces may be met by the selection of an efficient energy absorbing material. The ideal cushioning or energy absorbing material from the standpoint of energy dissipation is one which will crush inelastically to

a very small volume at constant stress, viz - the load-deformation curve of the energy absorber should be as flat as possible and its elastically recoverable energy (rebound) should be a minimum.

Structural materials that appear best to meet the above requirements are metallic and reinforced plastic honeycombs. The reinforced plastic honeycomb, e.g., phenolic fiberglass, polybutadiene-fiberglass, also appear to have the additional characteristic of having a low loss factor in the S-band (1500-5200 mc) range. Thus, these materials may possibly be transparent to radio frequency transmission and therefore compatible for use with a radar altimeter on the Mars Lander. An initial investigation into the development of RF transparent energy absorbing structural elements is presently in progress at MSD (Ref. 1).

In addition to the load bearing requisite, a light density material of sufficient strength to meet the aerodynamic loading requirement is also necessary. Ideally, this material should disintegrate if impacted upon landing so that the peak deceleration energy is absorbed through the honeycomb materials positioned at strategic load bearing points on the capsule. Materials to be considered for use in these areas are low density metallic or reinforced plastic rigid foams.

The materials considered for use must meet the impact load attention and aerodynamic load bearing requirements after their subjection to sterilization, transit and entry environments.

(2) Development

A review of data available from various sources (Refs. 1 - 6) indicated that little or no work has been performed on the determination of dynamic response characteristics of materials in the elevated temperature ranges to be encountered by these materials during planetary entry. In order to properly meet Voyager mission requirements, materials development and evaluation programs should be instituted for the respective Venus and Mars missions.

(a) Venus Lander

It is expected that the crushable structure will experience the high temperatures in the Venusian atmosphere after entry. The use of high temperature alloys of Titanium or stainless steel are recommended for a honeycomb crushable structure. Development and evaluation programs to be considered are:

- Fabrication development of honeycomb cores and panels with varying densities and cell sizes;
- Evaluation of dynamic loading characteristics from room temperature to 1100 °F, with force vectors normal and oblique to the honeycomb surface.
- Evaluation of the effect of chemical sterilization procedures on material properties.

(b) Mars Lander

Ambient temperature energy absorption characteristics have been determined for various configurations of aluminum structures (cylinders, cellular and trussgrid honeycomb). Only sparse information is presently available for fiberglass reinforced plastic honeycomb materials. There is a lack of adequate dynamic response design data for these materials in the 300 °F -500 °F temperature range. Development and evaluation programs must include:

- Fabrication techniques
- Dynamic response characteristics at elevated temperatures (to 500 °F)
- Evaluation of RF properties of reinforced plastic honeycomb at elevated temperature (to 500 °F)
- Dynamic and static characteristics of the light density, aerodynamic load bearing materials should be established to develop confidence that impact loads will not be transmitted to the structure
- Evaluation of thermal and chemical sterilization procedures upon the mechanical properties of the selected materials.

REFERENCES

1. GE S.D. Proposal, N-200760 Feb. 22, 1963. "RF Transparent Energy Absorbing Structural Elements".
2. "Cushioning for Air Drop, Part VIII, Dynamic Stress Strain Characteristics of Various Materials," Abmin Ali, The University of Texas Structural Mechanics Research Laboratory; Prepared for Quartermaster Research and Development Command, Contract DA 19-129-QM-150, Project No. 7-87-03-004B, June 3, 1957.
3. Thompson, J.N. and Ripperberger, E.A., "Shock, Vibration and Associated Environments, Part III", Bulletin No. 30, Office of the Secretary of Defense, February, 1962.
4. "Design Criteria for Plastic Package Cushioning Materials", Plastic Report No. 4, December, 1961.
5. Daigle, D.L. and Lonborg, J.O., "Evaluation of Certain Crushable Materials," Tech. Rept. No. 32-120, JPL, Jan. 13, 1961.
6. Shield, R. and Covington, C., "High-Velocity Impact Cushioning," "Part VI 108C and 100C Foamed Plastics" University of Texas, Structural Mechanics Research Laboratory, Sept. 1960, Contract DA-19-129-QM-1383, AD 250550.

F. Thermal Control Coatings

The Voyager lander may be shade- or sun-oriented during transit. While system trade-offs favor shade-orientation, each method is discussed for both Venus and Mars missions.

(1) Venus Sun Orientation

The sun oriented orbiter-lander requires passive thermal control due to its specified orientation and zero internal dissipation during the transit period. The coatings required must provide a continuous variation of α_S/ϵ_H in the range 0.2 to 1.1 (Ref. 1), be applicable to ablative substrates, and survive the transit environment.

Coatings such as the "C" Series Silicone-Acrylic (Refs. 2 and 3) and Pyromark Standard (Ref. 3) appear feasible in view of mission requirements. In addition, air-cure methyl silicones and inorganics should be investigated further for use on phenolic-nylon and phenolic-refrasil substrates.

(2) Venus Shade-Oriented

The shade-oriented Lander is protected from the sun's radiation by the orbiter, and further, will be enclosed within a radiation barrier bag of super insulation. The bag surface

should be aluminum, having an emittance of approximately 0.1, and will require no additional thermal control coatings.

(3) Mars Sun-Oriented

Thermal control coatings for the Mars Lander must be applicable to ablative substrates such as ESM, phenolic-nylon or phenolic-refrasil, and should provide a continuous α_S/ϵ_H variation in the range 0.2 to 2.5, and must also be resistant to the intense ultra-violet and ionizing radiation encountered during the transit phase.

A continuous variation of α_S/ϵ_H in the range 0.2 to 2.5 using a single coating system is unrealistic, insomuch as the range of organic (Refs. 2 and 3) and inorganic (Ref. 4) blended coatings vary in the range from 0.2 to 1.1. Recent work (Ref. 5) at Wright Patterson AFB, over a fairly narrow loading range, claims a ratio to 1.4 by means of the incorporation of leafing aluminum paste into a black paint. General Electric formulations over a wider aluminum loading range do not, at present, substantiate this claim. A ratio of 2.5, using, for instance, a black paint with α_S of 0.95 would require an ϵ_H of 0.38. The emittance of non-metallic filled resins, regardless of color, generally lies in the range 0.80 to 0.95. By means of the addition of metallic powder or paste, emittances in the range of 0.38 may be achieved, however, the solar absorptance also decreases at a somewhat similar rate, to yield a relatively constant α_S/ϵ_H approximating 1.0.

For the α_S/ϵ_H range 0.2 to 1.1, coating efforts similar to those proposed for the Venus mission are applicable. Coatings for ESM such as GE PD-115 elastomeric coatings are also applicable in this α_S/ϵ_H range.

Coating ratios in the range 1.1 to 2.5 are possible, however, they involve more complicated coating systems than that of a uniform paint coating. Mosaics or stripes of high ratio and lower ratio surfaces may be used to yield a composite α_S/ϵ_H ratio of the desired value. Vacuum deposited gold will yield ratios in the range 6.0 to 10.0 or greater, and in combination with black or white paint may be utilized to provide ratios in the range 1.1 to 2.5. Table 1.3.8-7 gives two examples of possible combinations.

TABLE 1.3.7-6. COMPOSITE RATIOS

Gold Area % (Nominal Ratio 6.0)	Black Area % (Nominal Ratio 1.0)	White Area % (Nominal Ratio 0.2)	Composite Ratio
30.0	70.0	—	2.5
40.0	—	60.0	2.52

The black-gold approach would appear to be more feasible than white-gold, in that the total gold area is maintained as small as possible. Techniques are available for the deposition of gold on plastic substrates, and a recent communication (Ref. 6) indicates that the application of vacuum deposited or sputtered gold on silicone rubber substrates such as ESM are practical. Table 1.3.7-7 lists a possible black-gold system ratios in the range 1.0 to 2.5.

TABLE 1.3.7-7. BLACK-GOLD COMPOSITE RATIOS

Gold Area % (Nominal Ratio 6.0)	Black Area % (Nominal Ratio 1.0)	Composite Ratio
30.0	70.0	2.5
25.0	75.0	2.25
20.0	80.0	2.0
15.0	85.0	1.75
10.0	90.0	1.5
5.0	95.0	1.0

(4) Mars Shade-Oriented

(a) Lander

Thermal control coatings are required for application to an ESM shield to provide an ϵ_H as low as possible (~ 0.1). The coating has no α_S requirement due to the shade-orientation. The Lander may be shrouded during the ascent and transit phase, and therefore, eliminating powered flight heating or ultra-violet/radiation requirements.

The extremely low ϵ_H required negates the use of the majority of organic coatings, however, silicone-base aluminum paints may yield ϵ_H in the range of 0.14 to 0.16 (Refs. 7 and 8). ϵ_H values less than 0.1 are obtained by gold plating or vacuum deposition (0.03 to 0.11), or by the deposition of metals such as silver, rhodium, or platinum. Other treatments reported (Ref. 9) to yield ϵ_H of 0.1 or less are very thin resin films over polished aluminum (approx. ~ 0.05), adhesive-backed aluminum foil and aluminized mylar (0.03 to 0.09), and chemical treatments for aluminum such as Alodine 1200 approx. ~ 0.06). A "wall-paper" approach using aluminum foil or metallized ESM films would appear most practical.

(b) RTG Radiator

Thermal control coatings would be required for metallic high temperature radiator fins of an RTC assembly. Operating temperatures are in the range 450 to 600°F. (Ref. 10).

Possible substrates are aluminum, stainless steel, or beryllium. The coatings must provide a nominal ϵ_H of 0.85 or greater. Due to shade-orientation, there are no α_S or ratio requirements, however, α_S values as low as practical are desirable.

Oven-cured silicone coatings (Ref. 11) would be most applicable in this area for service at elevated temperatures for extended time periods. Investigation is required of coating adhesion to stainless steel, aluminum, and beryllium at high temperature for extended periods.

Anodizing of beryllium to provide proper emittance may also prove desirable. Inorganic coatings offering long term stability should also be investigated.

(5) Required Testing

The coatings should be evaluated for elevated temperature stability, thermal cycle stability, resistance to ionizing radiation, applicability for instrumental color blending, stability to

sterilization, reflectance measurements, application techniques, and physical properties. Ultra-violet exposure should receive particular attention in that the irradiation exposure will be intense. Considerable industry effort is currently focused on this problem (Refs. 12, 13 and 14) and it is recognized that ultra-violet stability is an essential facet of thermal control coating performance.

REFERENCES

1. PIR HTT-8151-128, "Thermal Control System for Venus Lander", P.B. Cline, 8/22/63.
2. RSD-TM-CFF-4, "Thermal Control Coatings Program for Project 201-Phase I", C. F. Foster, 1/15/62.
3. RSD-TM-8158-105, "Thermal Control Coatings - Plastic and Metallic Substrater", R. R. Hockridge, 6/4/63.
4. Lockheed, MSD, "Variable Absorptance Coating Systems", M. E. Sibert, 1963.
5. WADD, ASD-TDR-62-917, "Improved Organic Coatings for Temperature Control in a Space Environment", H. H. Hormann, February 1963.
6. Private Communication 7/18/63 with Mr. R. F. Horan, Quantum, Inc., Wallingford, Conn.
7. "Thermal Radiation Properties Survey", Gubareff, Janssen and Toborg, Honeywell Research Center, 1960.
8. "Thermal Radiative Properties of Selected Materials", Vol. I, II, Defense Metals Information Center, DMIC # 177, 11/15/62.
9. "Thermal Radiative Control Surfaces for Spacecraft", Lockheed MSD #704014, March 1961.
10. PIR TCSD-8151-152, "Mars Voyager Thermal Control System Study", S. Shenkman, 7/26/63.
11. RSD-TM-8158-106, "Development of High Temperature Resistant Coatings for Application to Titanium Alloy 6AL-4V", C. F. Foster, May 31, 1963.
12. "Development of Stable Temperature Control Surfaces for Spacecraft", Jet Propulsion Laboratory Technical Report 32-340, W. F. Carroll, Nov. 20, 1962.
13. "The Effects of High Vacuum and Ultra-Violet Radiation on Plastic Materials", N. E. Wall, and R. R. Lapp, WADD Technical Report 60-125, July 1960.
14. "The Ultra-Violet Degradation of Organic Coatings", A. L. Alexander et al, WADD Technical Report 60-703, Nov. 1960.

G. Encapsulants, Sealants, Adhesives

In addition to the normal mechanical, physical and electrical criteria used for the selection of organic encapsulants, the Voyager mission has the added criteria that materials be compatible with the sterilization procedures and stable throughout and after exposure to the transit environment. Test results reported on Surveyor material compatibility studies indicate that thermosetting resins suitable for high temperature applications may be compatible with thermal and chemical sterilization procedures (Ref. 1).

Various authors have reported on polymer stability under simulated spatial environmental conditions. Several excellent summaries of work performed in this area have been prepared (Refs. 2, 3). Additional work has also been recently completed at General Electric's Missile and Space Division on another program (Ref. 4). In general, these reports indicate that polymeric materials suitable for high temperature applications will exhibit the greatest stability in the spatial environments.

For the present, it does not appear that a material development program is required unless it becomes desirable to incorporate sporicides in the base resin systems. Evaluation programs, however, should be undertaken to establish material performance characteristics; particularly desirable are long-term vacuum aging studies so that outgassing characteristics may be established.

REFERENCES

1. Willard, M., "Surveyor Sterilization, Part I, Compatibility of Materials and Components With Heat and Ethylene Oxide - Freon 12", Report RS-277, Hughes Aircraft Co., Jan. 1962.
2. Jaffe, L. D., "Effects of Space Environment Upon Plastics and Elastomers", Chemical Engineering Progress Symposium Series, No. 40, Vol. 59, 1963.
3. Clauss, F. J., "Evaluation of Materials for Spacecraft Applications," Lockheed Aircraft Corporation, Missiles and Space Division, Tech. Rpt. 5-10-61-11, 1961.
4. Kulp, J. F. and Gaskins, P. T., "Outgassing of Organic Materials Employed In Process 206 Vehicle," General Electric, Advanced Spacecraft Department, Aerospace Physics and Matls. Component, Engineering Memo #1145-008, May 8, 1963.

H. Lubricants

The choice of effective anti-friction surfaces to cover all devices and component parts is an extremely complex problem. Conventional lubricants, in general, breakdown, evaporate, or suffer radiation damage and film disruption without self-healing in a space environment. A large number of lubricants must be considered and evaluated on the basis of suitability for applications involving sliding and rolling friction under specific service conditions. The entry and surface survival factors of each mission (Mars and Venus), impose separate requirements on the lubricants.

(1) Mars

(a) Coolant As Lubricant

A thermal control system coolant, such as monoisopropylbiphenyl or OS-45, can also provide lubrication for the pumps. Stainless steel bearings (440C) with molybdenum disulfide solid films bonded to the surfaces with silicone resins would provide excellent dual source of lubrication.

(b) Composite Bearings

Metal matrix composite bearing materials of Ag - PTFE- WS_{e2} and Bronze - PTFE- WS_{e2} have been successfully used in the following conditions:

1. Moderate Loads and Speeds
2. Heavy Loads and Low Speeds

for extended periods of time in high vacuum (10^{-9} torr) in the temperature range of -160°F to $+300^{\circ}\text{F}$ (Ref. 1). Bearing starts have also been made at temperatures as low as -320°F . The composite bearings are very effective for the extreme bearing problems in that they provide a reservoir of dry lubricants, and distribute the load-bearing dry powder component on the metal surfaces with a very effective film former in the mixture. A unique method of supplying additional lubricant to any system is by use of idler gears, sleeves or retainer rings as composites of teflon and molybdenum disulfide (85 PTFE - 15 Mo S₂) held in contact with the bearing surface.

(c) Dry Lubricant Powders and Plastics

Plastics materials with various powder lubricant fillers exhibit good wear and friction characteristics. Tests conducted on the plastic composites in vacuums with rubbing velocities of 460 ft/min, temperature 150°F and loads of 150 psi showed adequate performance capabilities. A composite of teflon containing glass fibers and MoS₂ powder filler is capable of withstanding high temperatures (500°F) and medium loads. The teflon composite needle bearings would satisfy the requirements for large moving parts, such as a rotating aft bulkhead.

(d) Metallic Films

This metallic films show promise as effective lubricants in high vacuum environments. Plated films of gold alloy, e.g., Au (Ni, In, Co), deposited on stainless bearings (44OC) have been proven effective in the Explorer VIII program. This application is for a high speed low load capability with a miniature ball bearing.

Stainless steel ball bearings (44OC) with alloy gold platings were used in the solar paddle supports. Gold was found to be ideal for high vacuum conditions, is less sensitive to varying temperatures, and has a significantly better bearing surface than silver. Some background information was also available on the electric field meter flown on the Explorer VIII where the following solid film lubricants were used:

- (a) Molybdenum Disulfide Brushes
- (b) Gold Plated Aluminum Main Housing
- (c) Gold Plated Aluminum Rotor and Stator
- (d) Gold Plated (44OC) Stainless Steel Ball Bearings

Explorer VIII experience showed that:

- (1) Thin metallic films have great potential for many applications in vacuum environments.
- (2) Pure Gold plating is not as effective as the co-deposited alloy gold plate Au + (Ni, In, Co).
- (3) Fully machined retainers provide good performance, and the use of relatively hard retainer materials significantly extends the useful life of the bearings.
- (4) The bearing failures tend to be catastrophic rather than gradual.
- (5) A run-in period to compress and improve the gold surface is required for improved performance.
- (6) Long life is obtained with the use of a silver undercoat under the alloyed gold plate.
- (7) The anodized aluminum retainer was less satisfactory than the gold plated components.

(e) Problem Areas-Radiation

In general the thin metallic film lubricants were successful because metallic films are radiation resistant. The Zero G effect is not expected to be of major importance in the solid film systems but it could be a significant factor if a wet lubricant is to be contained in a system.

(f) Hermetic Seals

Hermetic seals minimize evaporation problems when using oils or greases.

(g) Ceramics

The Boron Nitrides, oxide coatings and graphite combinations with plastics have been evaluated and were not satisfactory. There appears to be a chemical breakdown or side reactions with some of the composites that have not been fully explained or understood. Adsorbed gaseous films are considered essential to the proper functioning of these lubricants.

There has been sufficient data presented to indicate that graphite is not a satisfactory lubricant in high vacuum due to the loss of adsorbed water vapor.

(h) Specific Applications

Lubricants that can be used to overcome the friction and wear, seizure, outgassing, heat transfer, viscosity-shear relationship, and metal corrosion problems have been classified in these five basic categories.

- (1) Low Vapor Pressure Oils and Greases - Examples; - Paraffinic Mineral Oils, Silicone containing fluids, Aliphatic and Aromatic Esters: Applications; - Hydraulic, Gyroflotation, Valves, Instruments, Bearings, Damping.
- (2) Solid Film Lubricants or Laminar Solids - Examples; - MoS₂, WSe₂, PbO: Applications; Bearings, Solar Paddles
- (3) Metallic Films - Example - Gold; Application, High Speed Bearing
- (4) Plastics - Examples - Teflon (impregnated or Composite); Application, Low load bearing
- (5) Ceramics - Graphites, Boron Nitrides, Oxides. Not recommended for high vacuum environments.

(i) Development

A great deal of development has been accomplished in the lubrication systems described, but the breadth of lubrication requirements for the Voyager Mission would require refining the current "state-of-the-art" materials. The severe environmental conditions would require a complete development to prove out most of the lubricants for compatibility in each specific application.

(2) Venus

The higher temperature requirements of the Venus entry surface survival and long vacuum exposures would limit the selection of lubricants. The outgassing problem could be more severe and necessitate an upgrading of the composite type of bearing.

(a) Hermetic Seals

It may be necessary for entire components or units to be sealed in the Landers to enable dual lubrication systems to be effective. However, the higher temperatures anticipated would require materials that are capable of withstanding this environment as a precautionary back-up design requirement.

(b) Low Vapor Pressure Oils and Greases

Paraffinic Mineral Oils - Capability of the best of these lubricants is 350°F and any usage of the organic liquids on instruments and guidance controls or in applications within the vehicle would require shielding.

Polyaromatics - These are the most thermally stable fluids, but current studies to develop other aromatic type structures are in progress.

(c) Liquid Metals

Development of the liquid metals as lubricants or coolants would require accurate information on the operating conditions. Containment of the liquid metals and protection against corrosion, and compatibility with the component materials are aspects which require thorough evaluation.

<u>Examples</u>	<u>Liquid Metal Fluids (Lubricants & Coolants)</u>
Metal	Fluid Range °F
Cesium	85° to 1300°F
Rubidium	85° to 1200°F
Potassium	150° to 1400°F
Sodium	180° to 1600°F
Lithium	360° to 2400°F
Gallium	85° to 3600°F

Under pressure the upper temperature range can be increased considerably.

There are many new techniques of lubricating in the temperature region in excess of 1000°F (Venus Conditions). These differ somewhat from the Mars lubrication systems in that the low friction and improved wear aspects may be in narrow high temperature regions as in the following example.

(d) Phthalocyanines as High Temperature Lubricants

Metal-free phthalocyanine, a solid organic compound, has been used successfully in the range of 800°/1300°F to lubricate rolling and sliding contact bearings. The phthalocyanine has a planar structure and very good thermal stability. Solid lubricant films of this type must adhere tenaciously to the substrate, to prevent penetration or stripping of the film, and the lubricant crystallite must be oriented in the film correctly to give good cohesiveness and to shear easily to insure low friction.

Ball bearing materials are AISI 440C stainless steel, M1 tool steel, Iron-base alloy (Timken 16-25-6), and TiC-Ni-Mo Cermet. All bearings were coated with the PCH₂ - (metal free phthalocyanine) plus polyisobutylene, and sliding friction tests were run with similar bearing materials coated with Molybdenum Disulfide plus Chlorofluorocarbon, with graphite and chlorofluorocarbon, and with lead oxide.

The most striking result is the remarkably lower wear and coefficient of friction of TiC-Ni-Mo Cermet, when lubricated with metal-free phthalocyanine, compared with the Molybdisulfide or lead oxide. The appearance of the TiC-Ni-Mo cermet and 440C stainless steel is of special interest in that pretreatment with metal-free phthalocyanine did not produce any visible adherent films on the 440C steel, while extremely thick and adherent films formed very readily on the Cermet. Apparently, chelation or other surface reactions of the lubricant with various substrates are different.

Experimental data have shown that metal-free phthalocyanine is a potential lubricant for extreme conditions of load and temperature. A development program would be required to develop this type of system since the mechanism of lubrication with phthalocyanines is not known. It is believed that the lubrication processes are similar to those of other planar structure solid lubricants, and that strongly adherent and protective lubricating films are formed by chelation of metal-free phthalocyanines with metal substrates.

Many other types of laminar structure materials have been investigated as solid film lubricants. However, combinations of the oxides, sulfides, selenides, and nitrides generally gave more wear and higher coefficients of friction.

(e) Miscellaneous Techniques

Many techniques have been developed to meet the high temperature, high vacuum environments. Such techniques include "flame" lubrication, use of glasses, liquid propellants, in-situ films, electromagnetic bearings, and gas-bearings. Because of the wide variety of techniques currently under investigation to meet the high temperature conditions, it is impossible to give a totally comprehensive picture. However, most of the methods have been discussed.

SUMMARY

Specific areas of materials application for the Lander have been investigated. While no insurmountable problem areas have been found, extensive development and evaluation work is required in many areas. Emphasis must be placed on providing reliable materials which do not degrade Lander performance during the varied mission environments.

REFERENCES

1. Bowen, P. H., Technical Document Report Number AEDC-TDR-63-166, Westinghouse Research.
2. Lewis, P., Report 61-GL-48x, GE Co., 1961.
3. Adamezak and Benzing, "Lubrication in Space Environments", ASD Report
4. Evans, E., Flatley, T., "Bearings for Vacuum Operation Goddard Space Flight Return".
5. Heckman, Bowen, "Dry Lubricating Materials", Westinghouse Research.
6. "Development of Lubricants for High Speed Bearings", WAD Report TR-60-732.
7. Cosgrove, S. L., and Krause, H. H., "Phthalocyanines - High Temperature Lubricants", Battelle Memorial Institute Report.

1.3.8 CONFIGURATION OPTIMIZATION

A. Configuration Trade-Off Study

In evaluating the sphere-cone configuration matrix, trade-offs can be performed which will indicate the efficiency of the configurations and the payload carrying capability for the Lander mission from an entry technology viewpoint. The effect of trajectory variables (γ_e , V_e), atmospheric model, and ballistic coefficient have been discussed in prior sections as they relate to each technical discipline. In this section worst-case design conditions have been utilized. For example, the structural requirements are based on the maximum load trajectory ($\gamma_e = 90^\circ$, Lower Limit atmosphere) and the thermal protection requirements are based on the maximum heating trajectory ($\gamma_e = 20^\circ$, Upper Limit atmosphere). This phase of the study evaluates the relationship between the ballistic coefficient (W/C_{DA}) and geometric configuration variables (R_N/R_B , θ_c) over a range of vehicle weights. The results can be analyzed to determine near optimum configurations (i.e., maximum payload) from purely technological grounds. In addition, if system design considerations require "non-optimum" configurations, the penalty in payload weight can be evaluated. Items included in the trade-offs are:

1. Ablation requirements
2. Insulation requirements
3. Structural requirements
4. Retardation system requirements
5. Primary and secondary impact attenuation requirements
6. Vehicle aft cover and allowances for miscellaneous hardware

Components related to the scientific payload and therefore subject to change with varying mission requirements have been grouped as part of the gross vehicle payload.

1. Thermal control
2. Telemetry and power
3. Scientific payload
4. Supporting structure.

Emphasis has been placed on the Mars mission; however, shield-structure optimization for the Venus mission has also been presented in section 1.3.8.C.

It should be noted that the absolute values of the weight figures presented in the trade-off studies are not necessarily precise, but for comparative purposes and trends the weight figures are quite adequate.

B. Shield Bond Temperature Optimization

Optimization of the shield-structure bond temperature can be obtained by determining the total shield insulation and structure weight as a function of the bond temperature. The shield and structure materials and construction considered are ESM and aluminum honeycomb as selected in previous sections. Since insulation requirements of the shield are reduced as the bond temperature rises, the weight of insulation material will decrease with increasing bond temperature. At the same time the weight of the structure will increase with increasing bond temperature due to its decreasing strength. It can then be expected that the total insulation - structure weight will reach a minimum at some bond temperature. This type of optimization is presented as an example of an analytical technique and could be modified for specific design applications which may equally well apply to the crush-up material between the vehicle shield and structure.

Figures 1.3.8-1 through 1.3.8-9 present the combined insulation - structure weight as a function of bond temperature for the matrix of Mars entry configurations. The three

vehicle weight classes have been considered. Insulation - structure weight is optimized for all configurations considered at a bond temperature of approximately 300° F. The optimum temperature of 300° F does not appear to vary significantly with configuration or vehicle size.

C. Shield and Structure Optimization

Combining the insulation - structure weight, at the optimum bond temperature, with the weight of required ablation material results in the total shield - structure weight. The ratio of shield and structure weight to total weight is presented in Figures 1.3.8-10, 1.3.8-11 and 1.3.8-12 as a function of vehicle configuration and weight class. For entry vehicles whose mission requirements do not include retardation and surface impact, these results could form the basis of a configuration selection tradeoff. For this study additional trade-offs must be made prior to final optimization; however, certain trends can be established based on the shield-structure data.

In general, the effect of a high-drag shape tends to dominate the results. Large bluntness ratios appear more desirable, particularly at the lower cone angles. As the cone angle is increased, bluntness ratio is reduced in significance and in fact appears to optimize near 0.6 for a 40 degree half cone angle. A continuous decrease is noted in shield-structure weight with increasing cone angle; however, the effect of cone angle is decreasing at higher values. Both the heat shield and structural studies have been conducted on the basis of zero angle of attack trajectories where the rate of convergence of vehicle oscillation is not considered. In view of the questionable damping characteristics of high-cone angle configurations, angle of attack effects will probably provide an upper limit on the cone angle. A detailed study of this nature would be realistic only after a parametric experimental program followed by extensive multi-degree of freedom trajectory analyses.

The optimum shield-structure configuration over the range of variables considered is a half cone angle of 40 degrees and a bluntness ratio of 0.6. The optimum shape is independent of vehicle weight class; however, approximately a two percent increase in the shield-structure weight ratio is noted between succeeding heavier weight classes. The absolute values of shield-structure weight ratios are probably slightly optimistic in view of angle of attack effects.

(1) Venus Configurations

Comparable results have been obtained for the Venus configurations for both Titanium and Stainless Steel structures combined with a phenolic nylon heat shield as shown on figures 1.3.8-13 through 1.3.8-18. The optimum shape appears to be a 40 degree half-cone angle with approximately a 0.5 bluntness ratio. The higher bluntness ratios strongly indicate the effect of the more severe Venusian entry, while the lower bluntness ratios provide insufficient drag to reduce the ballistic coefficient similar to the Mars case. The resulting variation with bluntness ratio provides a more pronounced minimum. The higher cone angles show a decided advantage at lower bluntness ratios, but are less desirable at high bluntness ratios. The penalty for using a stainless steel as opposed to Titanium, structure varies from 2 to 5 per cent of total vehicle weight depending on weight class. The optimum Venus shield-structure (stainless) is 5 to 10 per cent of total vehicle weight higher than the Mars optimum, again varying with weight class. The fact that the configurations for entry to both planets optimize near the same shape suggest the possibility of a dual purpose Lander. It should be noted that different ablation and structural materials have been utilized in the analyses of Mars and Venus entry vehicles.

D. Retardation and Impact Structure Optimization

Impact survival after planetary entry requires retardation of the Lander vehicle and absorbing the impact energy without subjecting the payload to excessive loads. Thus a retardation system (Section 1.3.5) and an impact attenuation system (Section 1.3.4-C) are

needed. Each of these subsystems will represent a significant portion of the total lander weight. Both of these subsystem weights will vary with the impact velocity, i. e., increasing impact velocity results in decreasing retardation weight and increasing impact attenuation weight. Thus, it would appear that for a given type of retardation (parachutes - Mars) and impact attenuation (material deformation), a design planetary model atmosphere (lower) and permissible load levels (125g axial; 200g lateral) an optimum impact velocity exists which represents the lowest overall weight or volume.

Figures 1.3.8-19, 1.3.8-20 and 1.3.8-21 present the combined weight of retardation and attenuation systems as a function of impact velocity for vehicle weights of 300, 1500 and 2500 pounds respectively. The effect of varying vehicle bluntness ratio is shown in these figures. The effects of vehicle cone angle on the attenuation weight for primary impact were found to be of a secondary nature. The weight of retardation and primary impact attenuation systems are minimized at near 7 per cent of the total vehicle weight for an impact velocity of approximately 75 feet per second for all configurations considered. Consideration of the vehicle volume required for these systems, Figures 1.3.8-22, 1.3.8-23 and 1.3.8-24 indicate that the minimum total volume occurs at somewhat lower impact velocities than the 75 feet per second optimum based on weight. This lower velocity for optimum volume is the result of attenuation stroke requirements which increase rapidly with increasing impact velocity. Also, a more pronounced effect of vehicle bluntness ratio can be seen in these figures. The overall optimum impact velocity can then be seen to be a function of the relative importance of overall weight and volume to the mission or payload packaging. For purposes of configuration tradeoffs, an impact velocity of 75 feet-per-second has been chosen on the basis of overall vehicle minimum weight.

An additional consideration in the optimization of a configuration is secondary impact which can occur when a vehicle falls over on its side or back after primary impact due to impacting on a sloped surface, having a horizontal velocity at impact, or a combination of these conditions. If these conditions are sufficiently severe it can be anticipated that complete tumbling of the vehicle can occur. Therefore, allowance must be made for attenuating loads encountered upon secondary impact. The following assumptions have been made with regard to secondary impact for the matrix of vehicle configurations under consideration:

- The maximum horizontal velocity to be encountered corresponds to a wind velocity of 40 mph.
- The maximum energy to be absorbed on secondary impact is the kinetic energy of the vehicle due to its own mass and the 40 mph wind velocity.
- The maximum allowable lateral load at impact is 200g.

The weight of attenuation material for secondary impact is then based on distribution of sufficient energy absorption material (aluminum honeycomb) around the vehicle to satisfy impact requirements for any vehicle roll orientation. The weight of this material is presented in Figure 1.3.8-25 as a function of wind velocity and vehicle weight. A wind of 40 mph requires approximately 7 per cent of the total vehicle weight in secondary impact material, equalling the percentage of total weight required for retardation and primary impact attenuation.

E. Payload Fraction Optimization

Combining the results of the tradeoffs on shield-structure and retardation-impact attenuation optimization with aft cover weight and a miscellaneous hardware allowance, results in the entry vehicle shell weight for the configuration matrix. The bond line temperature has been held constant at the optimum 300° F and the vertical and horizontal impact velocities at 75 and 58.6 f.p.s., (40 mph) respectively.

The resulting gross payload fractions are presented in Figures 1.3.8-26, 1.3.8-27 and 1.3.8-28 as a function of configuration variables for the various weight classes. Since the retardation tradeoffs were essentially independent of configuration and the impact attenuation was a weak function of bluntness ratio, the results are dominated by the shield-structure tradeoffs. The optimum configuration over the range of variables considered is a half-cone angle of 40 degrees and a bluntness ratio of approximately 0.6. The optimum shape is independent of vehicle weight class; however, a slight decrease in payload fractions is noted with increasing vehicle weight. For a 40 degree half-cone angle, the payload fraction is relatively insensitive to bluntness ratio (approximately 6 per cent decrease from the maximum at the lowest bluntness ratio). While the results are probably optimistic due to lack of angle of attack considerations, it is interesting to note that more than 60 per cent of the total vehicle weight is available for gross payload.

F. Design Restraints to Configuration Selection

Configuration optimization data must be integrated with design restraints to provide realistic vehicles for specific missions. Consideration must be given such factors are:

1. Payload - Unusual sizes, shapes or functions can force the design to deviate from optimum to accommodate the payload. The bottomsides sounding rockets are a good example of this category of payload.
2. Packaging density - The final design must have a packaging density less than 20 lb/ft³ in the payload compartment (Section 1.3.9).
3. Ballistic parameter - The ballistic parameter must be restricted to 35 lbs/ft² or lower for the Mars retardation system (Section 1.3.5).
4. Orientation - Very high cone angles and bluntness ratios forbid the use of the side orientation system (Section 1.3.9).

These factors can impose constraints on the range of configuration variables. The prior configuration selection trends become very useful in determination of the penalty for deviation from "optimum." Tradeoff curves showing ballistic coefficient, volume and vehicle density for the matrix of configurations and weight classes are shown in Figures 1.3.8-29 through 1.3.8-35 to assist in design applications.

A conceptual example of the design application of configuration selection is shown in Figure 1.3.8-36 with several design restraints included. The packaging density becomes too high at half cone angles slightly above 40 degrees. Side orientation limits the bluntness ratio, particularly for the higher cone angles. The best configuration, when design restraints are considered, is a bluntness ratio of 0.4 and a half cone angle of 40 degrees. The penalty induced by the orientation restraint is a reduction in gross payload weight of approximately one per cent of total vehicle weight.

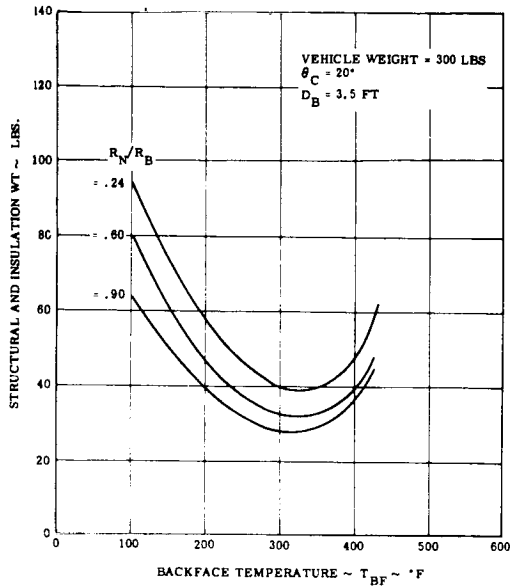


Figure 1.3.8-1. Variation of Structural and Insulation Weight with Backface Temperature

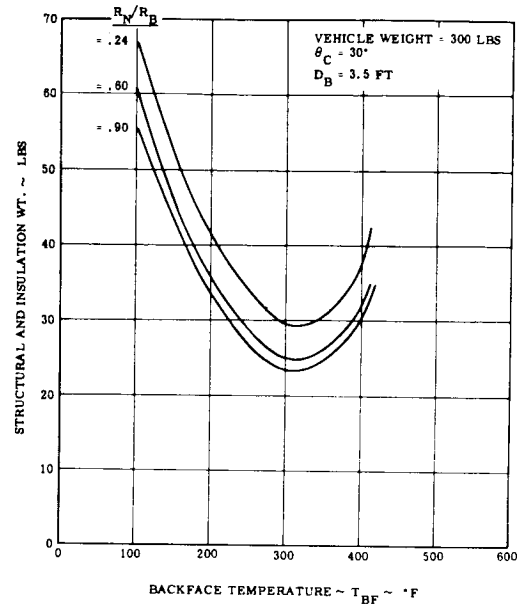


Figure 1.3.8-2. Variation of Structural and Insulation Weight with Backface Temperature

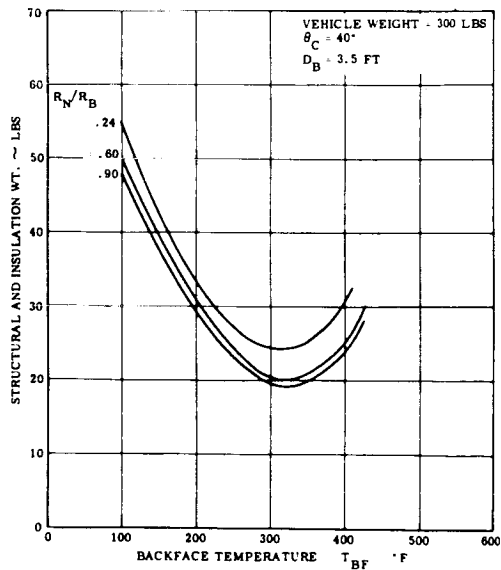


Figure 1.3.8-3. Variation of Structural and Insulation Weight with Backface Temperature

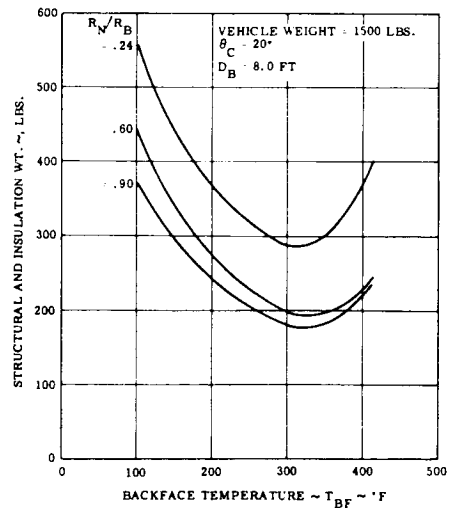


Figure 1.3.8-4. Variation of Structural and Insulation Weight with Backface Temperature

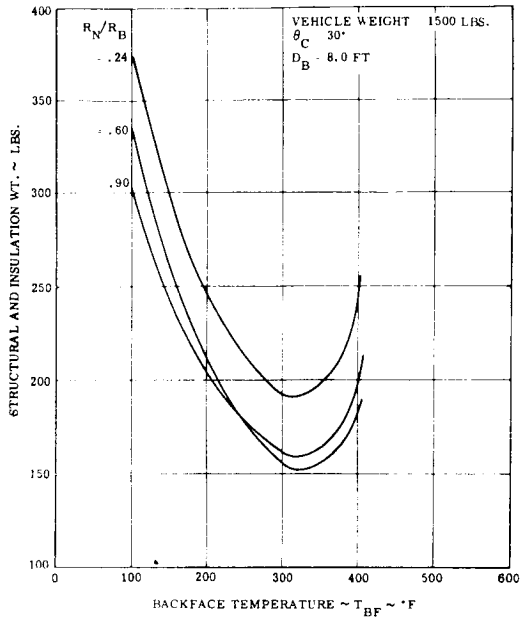


Figure 1.3.8-5. Variation of Structural and Insulation Weight with Backface Temperature

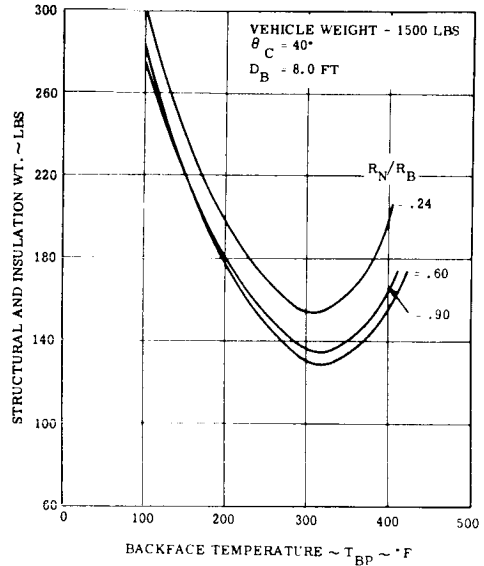


Figure 1.3.8-6. Variation of Structural and Insulation Weight with Backface Temperature

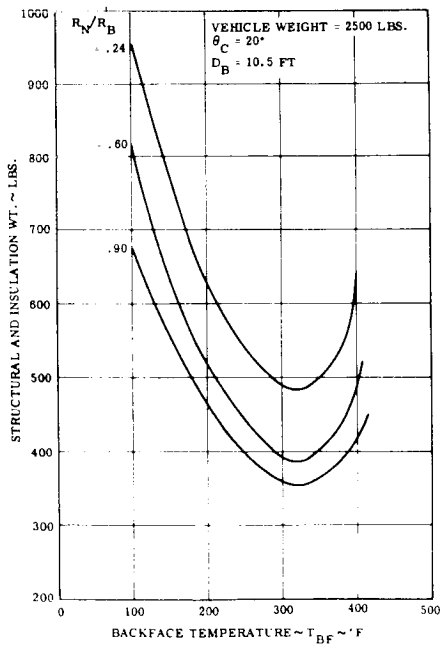


Figure 1.3.8-7. Variation of Structural and Insulation Weight with Backface Temperature

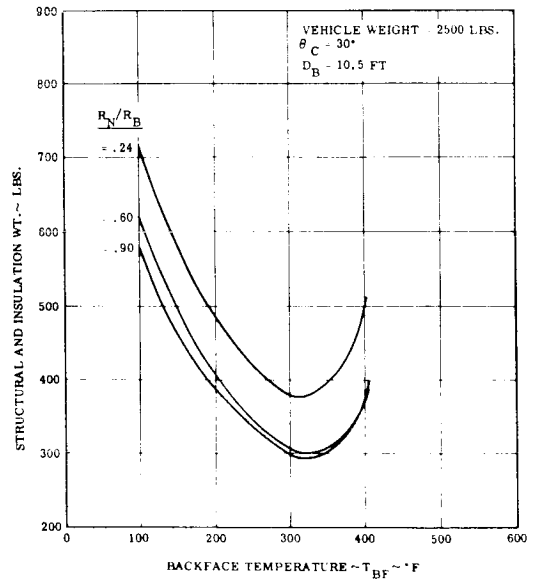


Figure 1.3.8-8. Variation of Structural and Insulation Weight with Backface temperature

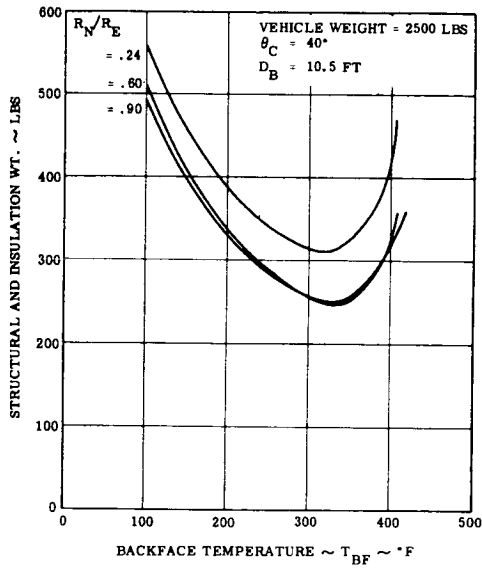


Figure 1.3.8-9. Variation of Structural and Insulation Weight with Backface Temperature

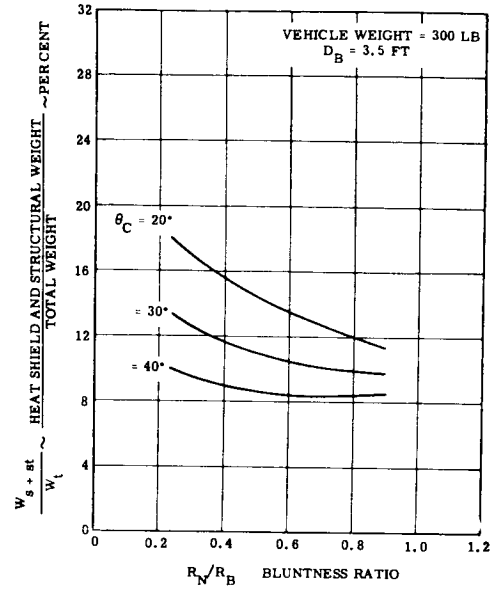


Figure 1.3.8-10. Shield Structure Optimization

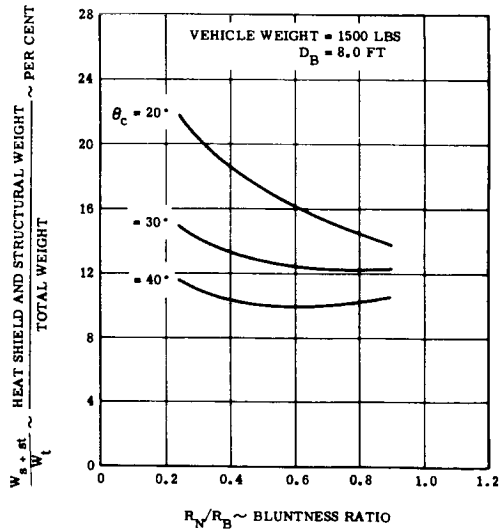


Figure 1.3.8-11. Shield Structure Optimization

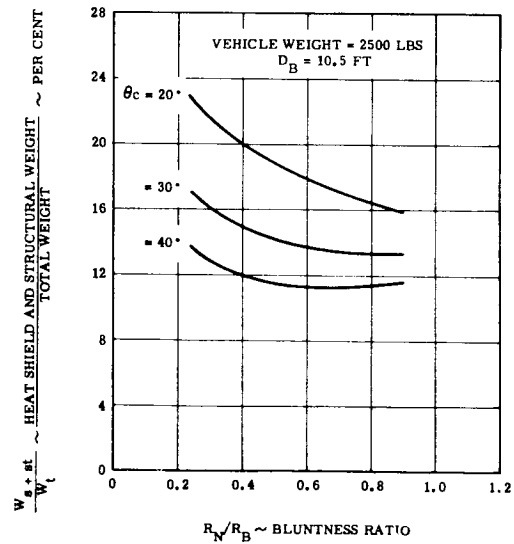


Figure 1.3.8-12. Shield Structure Optimization

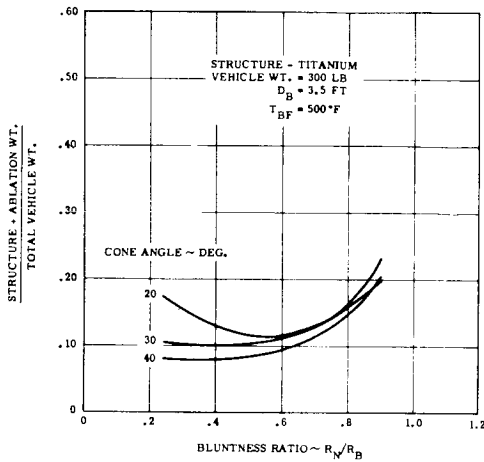


Figure 1.3.8-13. Bluntness Ratio vs. Weight - Venus Entry

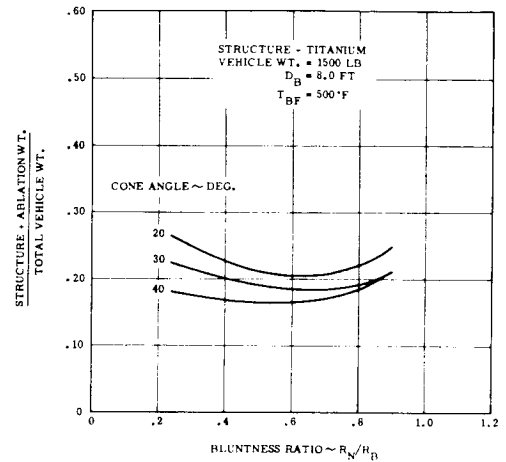


Figure 1.3.8-14. Bluntness Ratio vs. Weight - Venus Entry

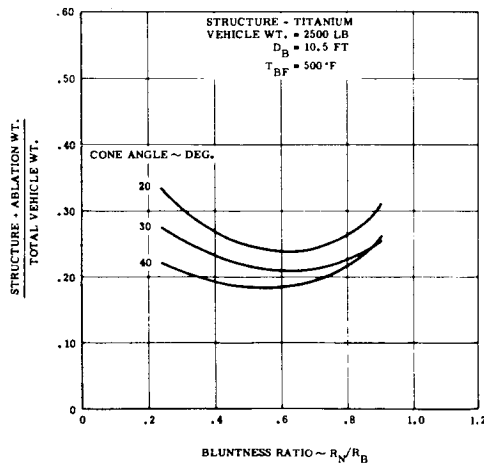


Figure 1.3.8-15. Bluntness Ratio vs. Weight - Venus Entry

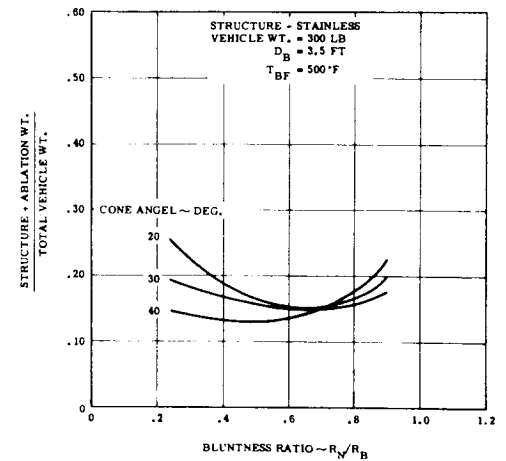


Figure 1.3.8-16. Bluntness Ratio vs. Weight - Venus Entry

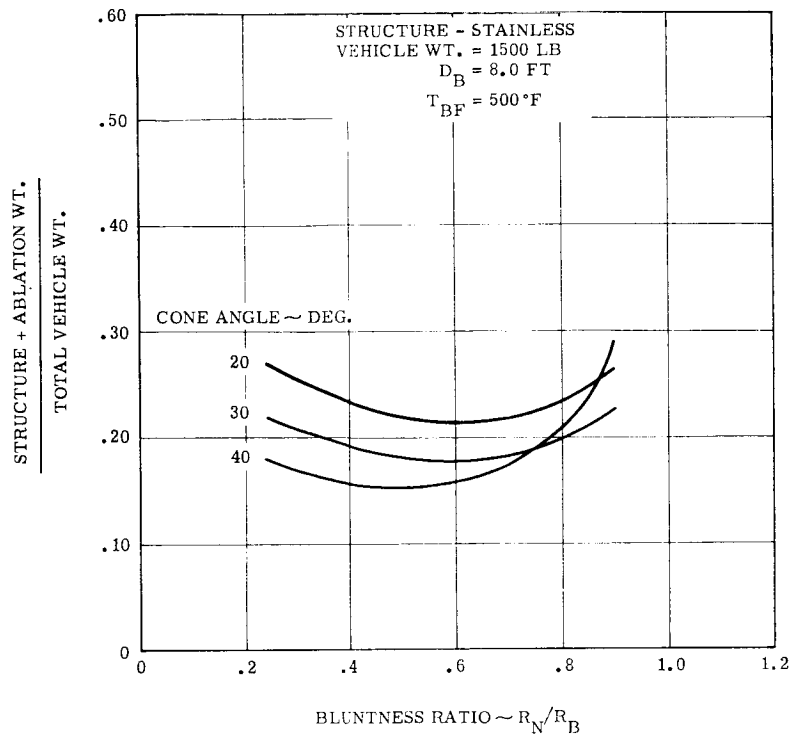


Figure 1.3.8-17. Bluntness Ratio vs. Weight - Venus Entry

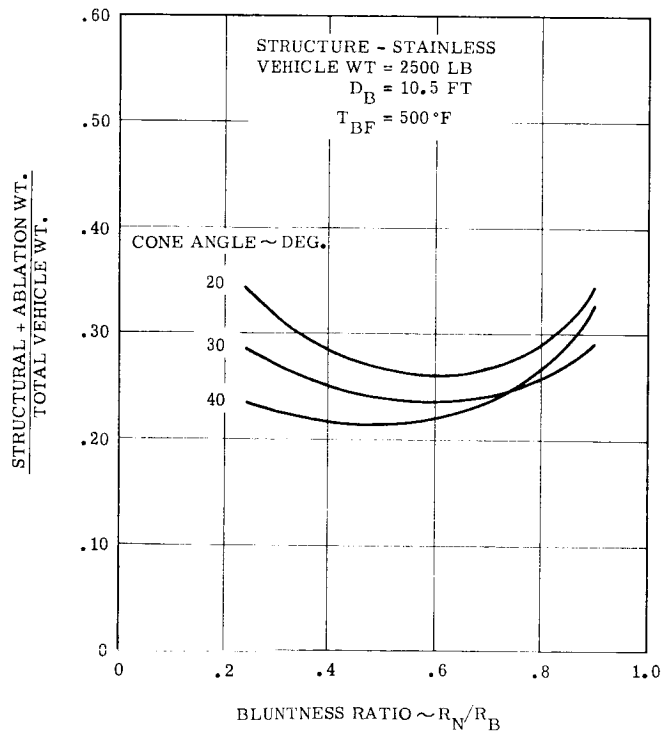


Figure 1.3.8-18. Bluntness Ratio vs. Weight - Venus Entry

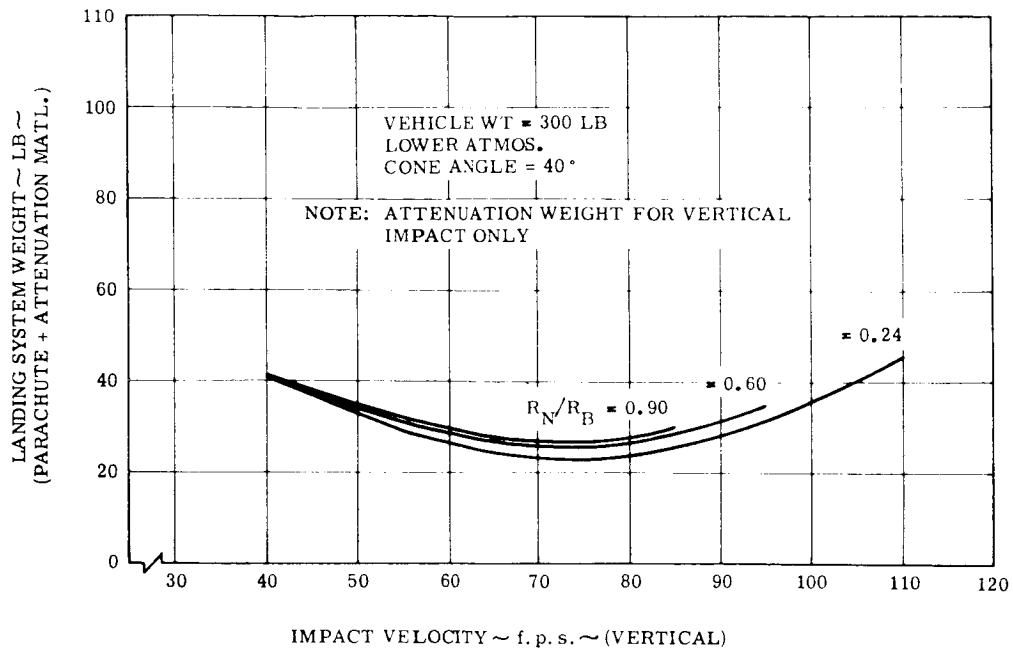


Figure 1.3.8-19. Impact Velocity Optimization on the Basis of Weight (Vehicle Weight = 300 lbs)

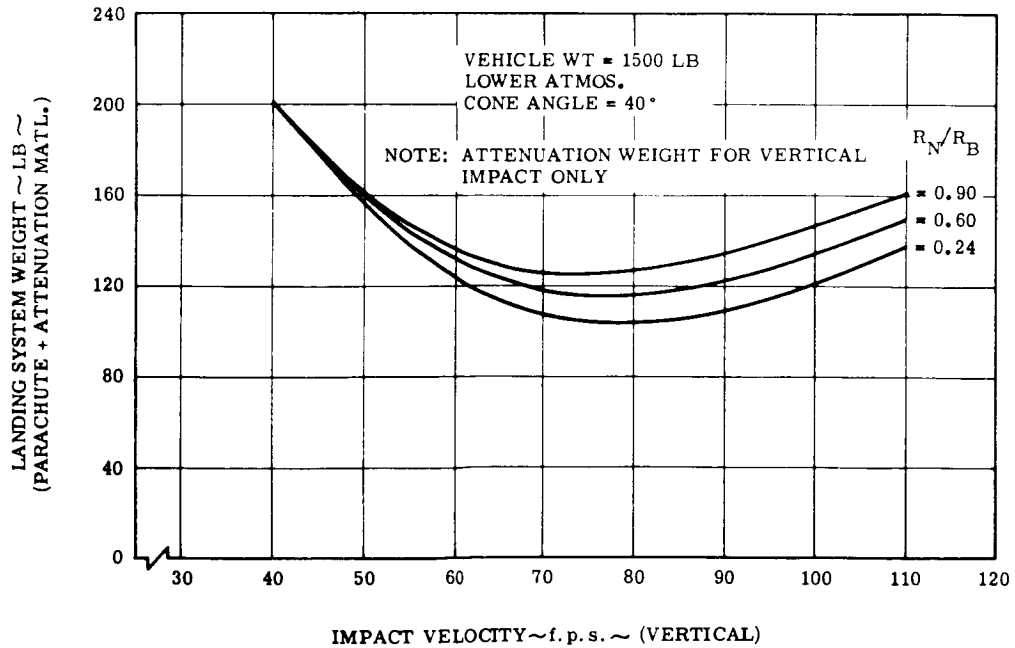


Figure 1.3.8-20. Impact Velocity Optimization on the Basis of Weight (Vehicle Weight = 1500 lbs)

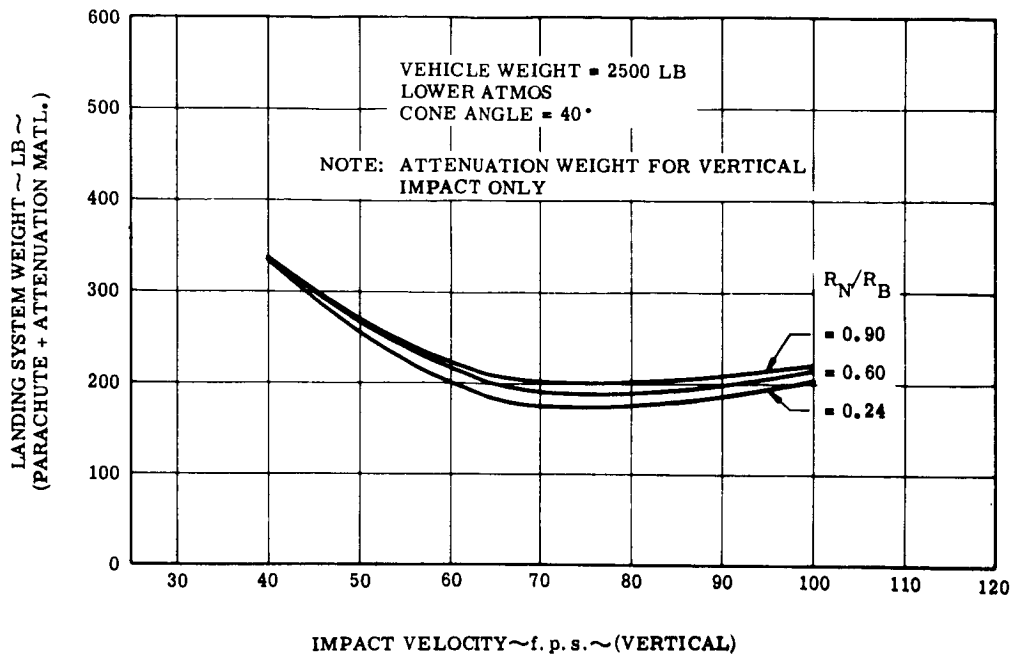


Figure 1.3.8-21. Impact Velocity Optimization on the Basis of Weight (Vehicle Weight = 2500 lbs)

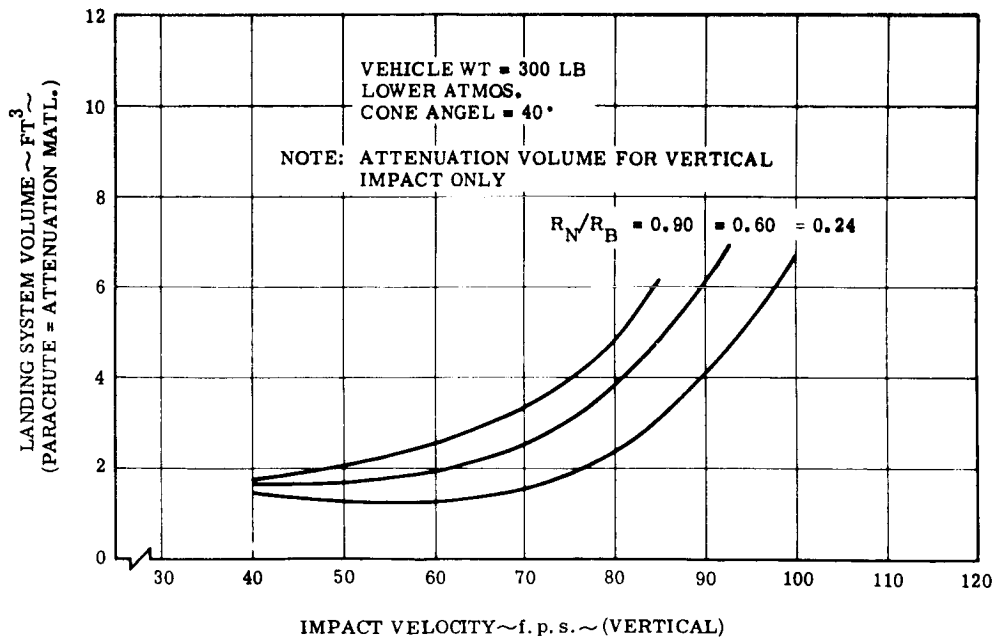


Figure 1.3.8-22. Impact Velocity Optimization on the Basis of Volume (Vehicle Weight = 300 lbs)

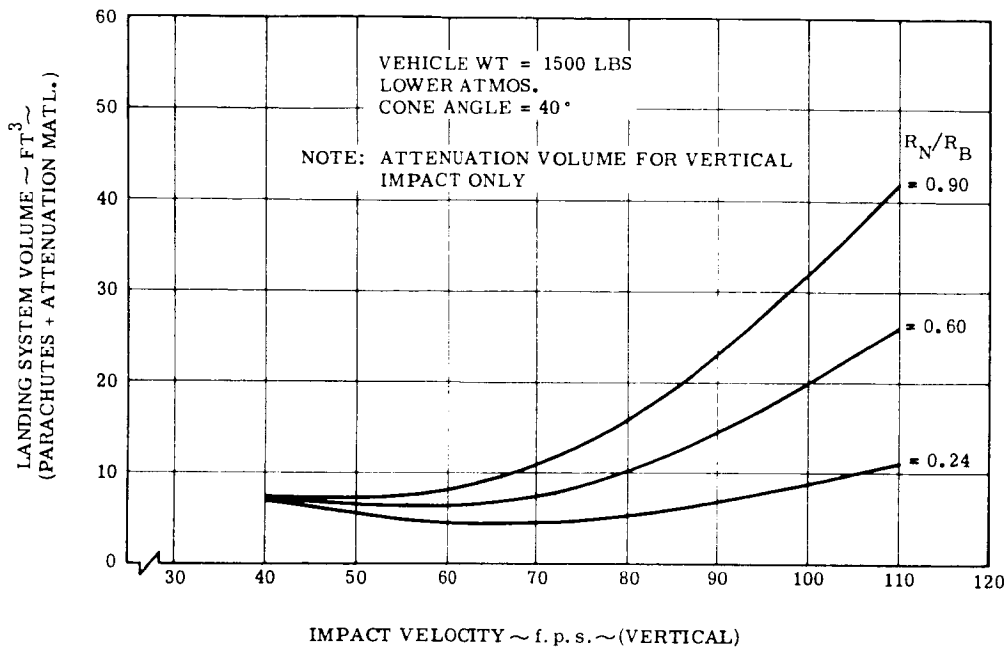


Figure 1.3.8-23. Impact Velocity Optimization on the Basis of Volume (Vehicle Weight = 1500 lbs)

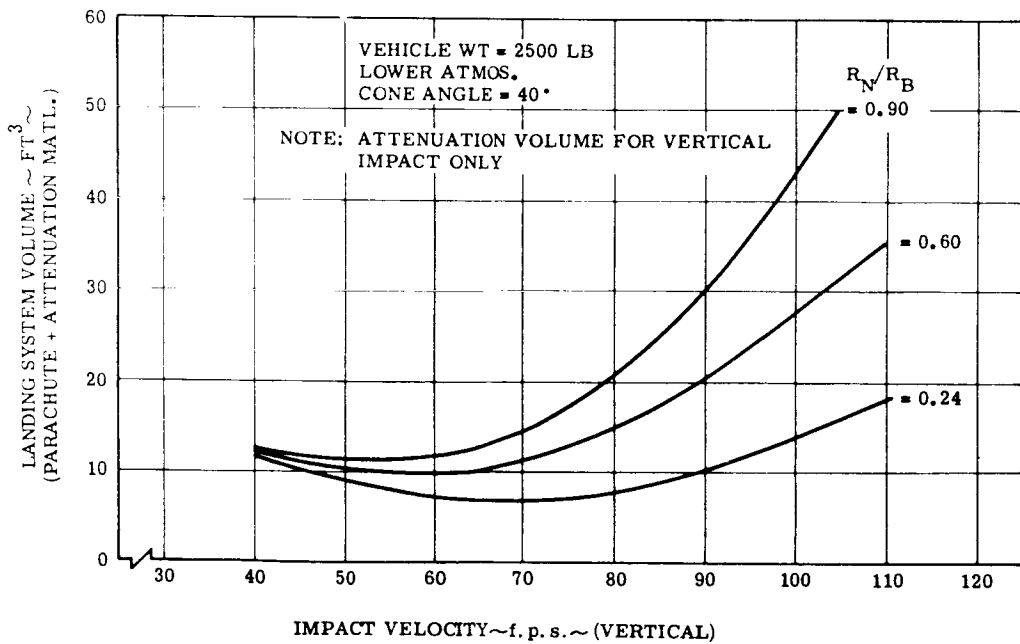


Figure 1.3.8-24. Impact Velocity Optimization on the Basis of Volume (Vehicle Weight = 1500 lbs)

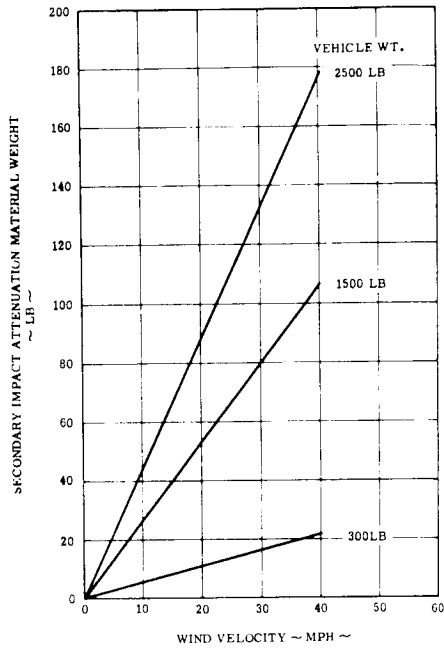


Figure 1.3.8-25. Secondary Impact Attenuation Weight vs. Wind Velocity

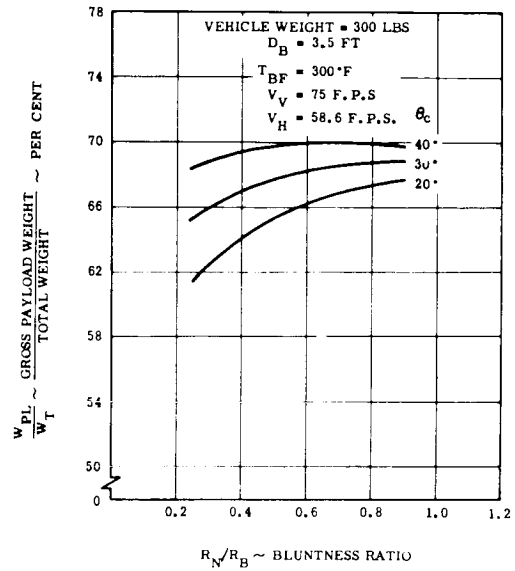


Figure 1.3.8-26. Payload Fraction Optimization (Vehicle Weight = 300 lbs)

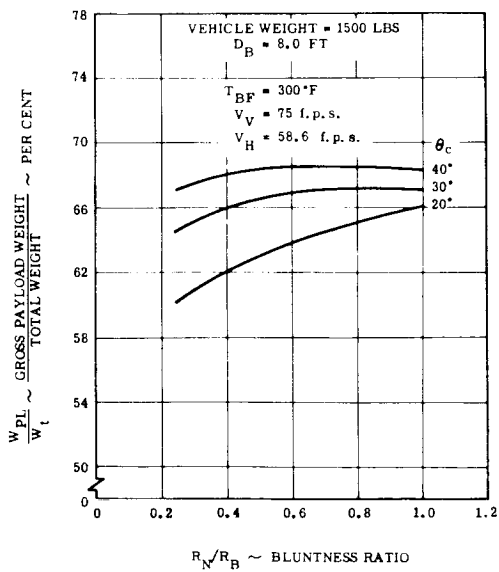


Figure 1.3.8-27. Payload Fraction Optimization (Vehicle Weight - 1500 lbs)

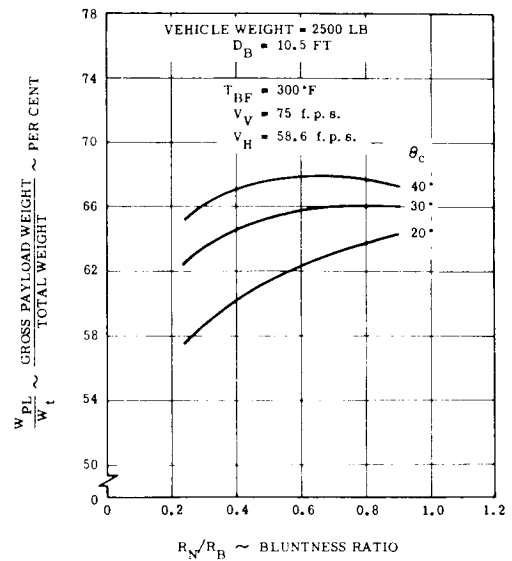


Figure 1.3.8-28. Payload Fraction Optimization (Vehicle Weight = 2500 lbs)

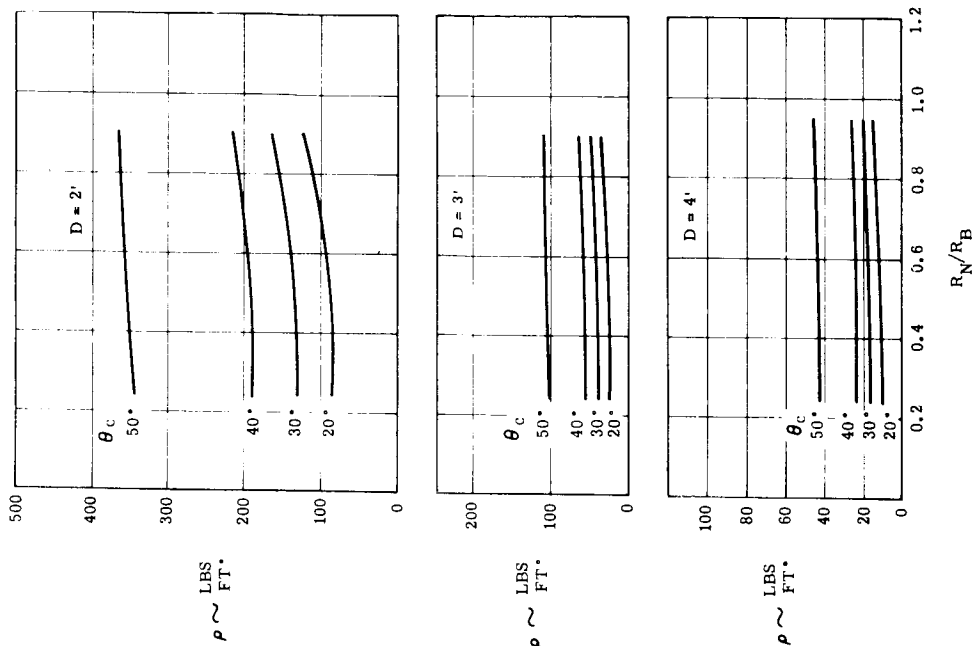


Figure 1.3.8-30. Variation of Entry Vehicle Density with Configuration (Vehicle Weight = 300 lbs)

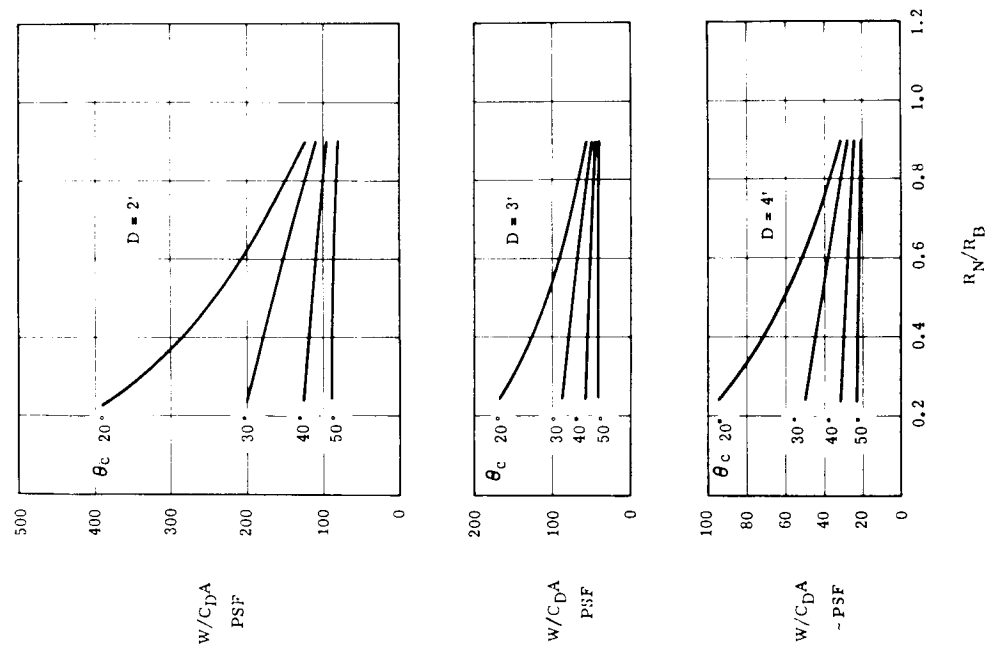


Figure 1.3.8-29. Variation of $W/C_D A$ with Configuration (Vehicle Weight = 300 lbs)

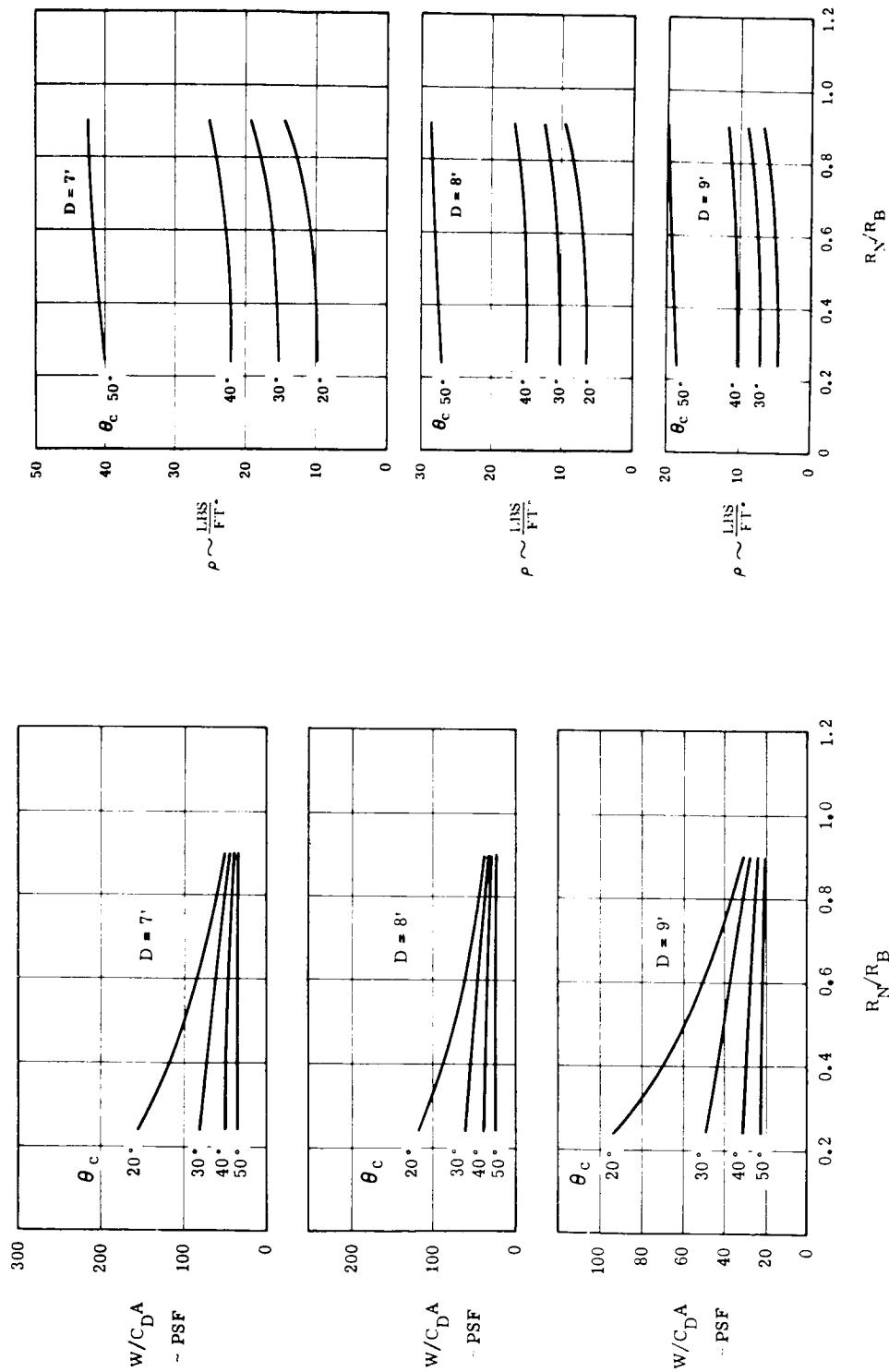


Figure 1.3.8-31. Variation of W/C_{DA} with Configuration (Vehicle Weight = 1500 lbs)

Figure 1.3.8-32. Variation of Entry Vehicle Density with Configuration (Vehicle Weight = 1500 lbs)

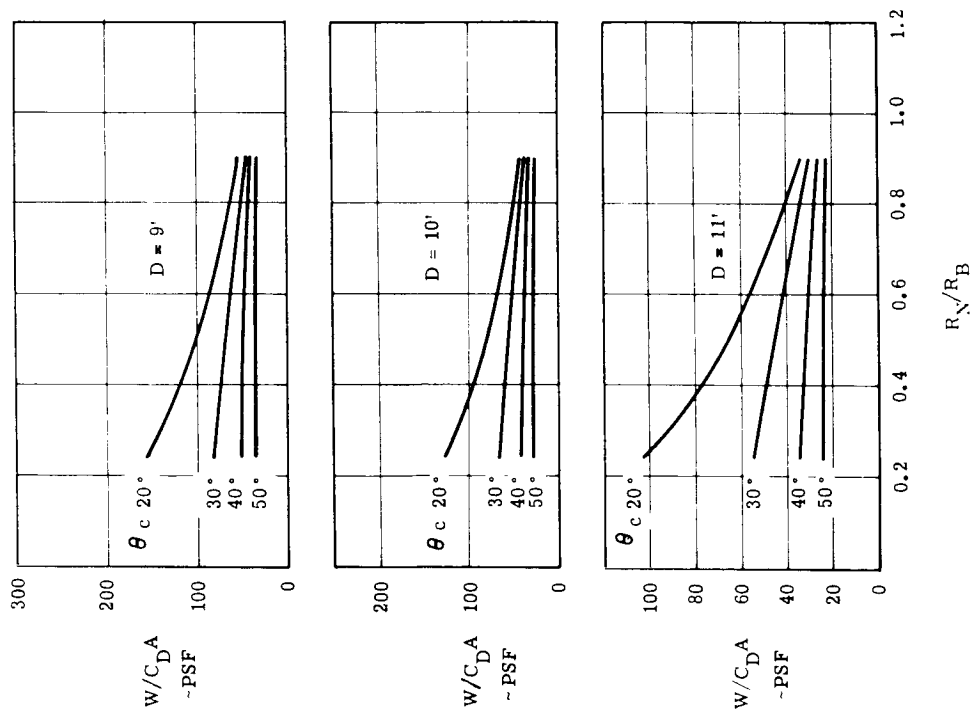


Figure 1.3.8-33. Variation of W/C_D^A Configuration (Vehicle Weight = 2500 lbs)

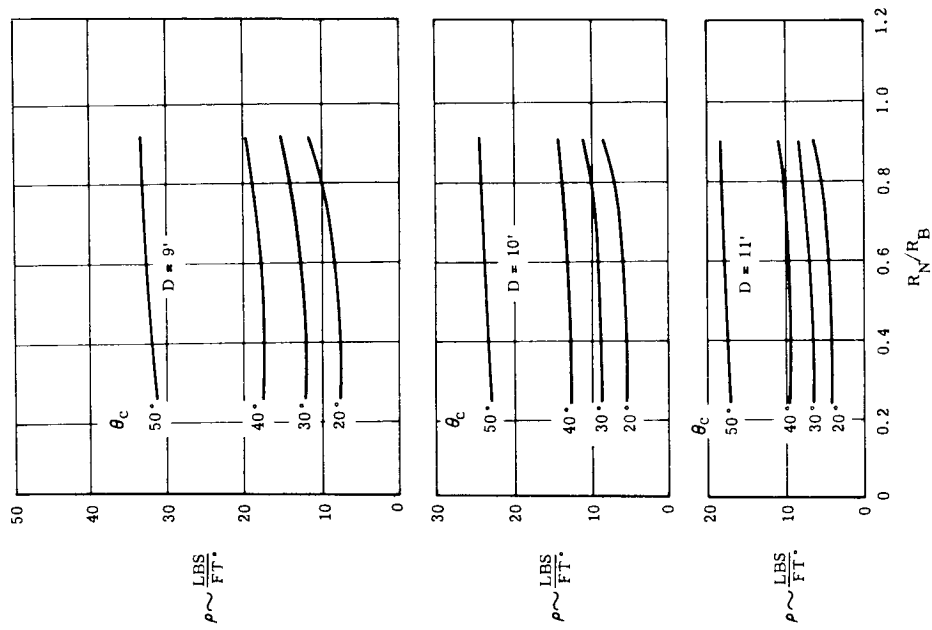


Figure 1.3.8-34. Variation of Entry Vehicle Density with Configuration (Vehicle Weight = 2500 lbs)

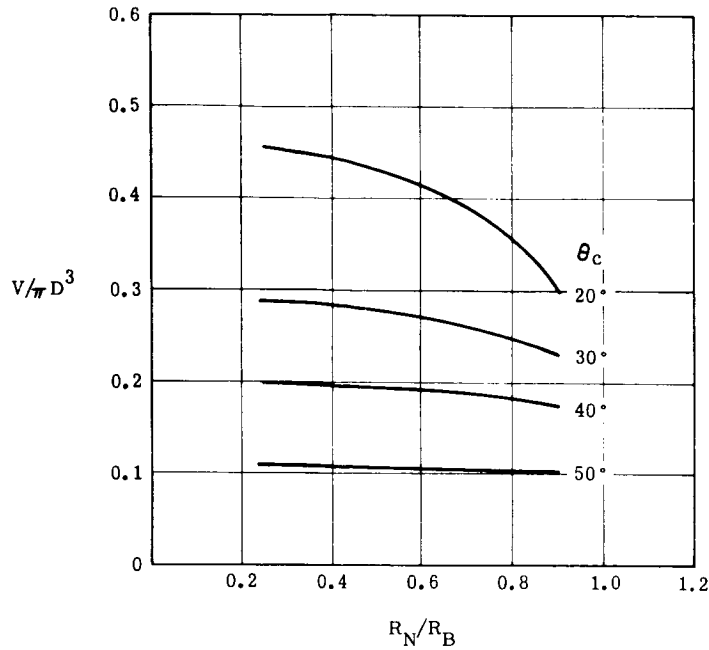


Figure 1.3.8-35. Variation of V/D^3 with Configuration

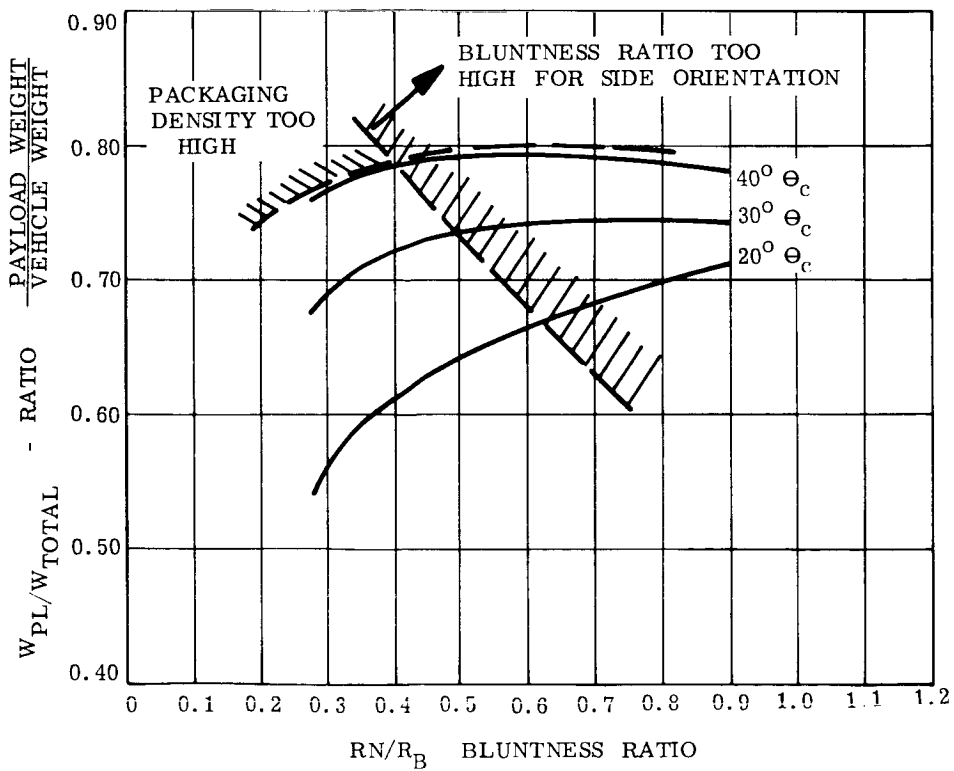


Figure 1.3.8-36. Design Restraints on Configuration Optimization

1.3.9 VEHICLE DESIGN

A. Structural Selection

As discussed in section 1.3.4 the typical Venus or Mars Lander shield and structure will consist of a heat shield which is bonded to a crushable material which is in turn bonded to the primary structure. Many factors influence the selection of the materials and basic type of construction. A matrix of these factors is shown in Table 1.3.9-1. Since the operational environment for the two planets is so different, completely different vehicle structures are proposed for Venus and Mars. The high temperature environment (1050°F surface temperature) on Venus requires the use of a high temperature material, either titanium or stainless steel. The structure used for Mars on the other hand will not be subjected to high temperatures, so lightweight alloys of magnesium, aluminum and beryllium can be considered.

(1) Mars Structure

The Mars heat shield has been designed to maintain the shield crush-up interface to 300°F to protect the fiber glass crush-up structure. Due to the insulating value of the 4-5 inch deep crush-up structure, the primary structure will not be heated above 100°F during entry. As pointed out above, any of the lightweight materials can be used for the structure. As shown in Table 1.3.9-1 beryllium monocoque and magnesium honeycomb are the most efficient structures, but when development costs, state-of-the-art and generic material characteristics are considered, aluminum honeycomb becomes very competitive and in the final analysis is the material that has been selected.

Magnesium honeycomb was not used due to the development required for its use. This would increase its costs and also the time required for procurement. This material should not be entirely eliminated at this time but should be considered as a back-up material. Magnesium can be used for structural elements in the vehicle, such as rings and fittings, where minimum machining thicknesses or stiffness dictate the gage, thus taking advantage of its low density.

(2) Venus Structure

The critical design structural loads occur during peak entry deceleration, at which time the structure is cool due to vehicle thermal inertia and the short deceleration periods, which are characteristic of Venus entries. Impact, however, will occur after the vehicle has soaked-up to the surface ambient temperature of 1050°F. Because of the high surface temperatures, the Venus crush-up and primary structure must utilize high temperature materials such as titanium or stainless steel. As shown in Table 1.3.9-1, titanium is desirable based on weight considerations alone, but, when other considerations are included, stainless steel was selected for the Venus vehicle. It is to be noted from the matrix that there is a weight penalty associated with the use of this material. When other factors such as producibility and development required are considered the choice of stainless steel Honeycomb becomes evident. Titanium may be used for internal structure and fittings where a weight savings is realized. This is a possibility where stiffness or minimum machining thicknesses are the design criteria.

(3) Design Modification

Since the mission of the Voyager program is primarily one of research, design modification must be easily accommodated. Changes to the structural shell will be virtually impossible after the crush-up material and heat shield are assembled to it. Therefore, all the equipment and experiments carried by the vehicle will be mounted on one of the bulkheads. If a major modification is required, the entire bulkhead may be re-designed and substi-

TABLE 1.3.9-1. MATRIX OF VEHICLE STRUCTURES

	Material	*Weight	Cost	Advantages	Disadvantages
VENUS Titanium Honeycomb	6AL - 4V (Faces & Core Brazed)	135 lbs	3 +	1. Light Weight 2. Double Skin, Impact Protection	1. Long Delivery Time 2. High Cost 3. Brazing Process Must be Developed 4. Special Equipment Required for Brazing In Inert Atmosphere 5. Material Sources Relatively Scarce 6. Brittleness & Notch Sensitivity
Stainless Steel Honeycomb	PH-14-8 Mo. (Faces & Core Brazed)	145 lbs	1	1. Low Cost 2. Manufacturing Process Devel- oped to Same Degree as Aluminum 3. Existing Tooling Concepts Adequate 4. Material and Process Specs Presently Available 5. Double Skin, Impact Protection	1. Weight Penalty = 10 lbs
MARKS Aluminum Honeycomb	7075-T6 5052-H38 Core (Bonded)	96 lbs	1	1. Low Cost 2. Double Skin-Impact Protection 3. High Reliability - State of Art 4. Minimum Delivery Time - 12 Months	1. Weight Penalty - 20 lbs
Magnesium Honey- comb	HK 31A Faces HK 31A Core (Bonded)	77 lbs	4	1. Light Weight 2. Double Skin-Impact Protection	1. High Material Cost 2. Longer Delivery Time Than Aluminum 3. Development Required to Pro- duce Thin Sheets
Circum. Corr. Stiffened Shell	7075-T6	92 lbs	5	1. Same Weight as Aluminum Honeycomb)	1. Weight Penalty = 16 lbs 2. Difficult Analysis 3. Corr. Forming Development Necessary 4. Spot Welding Tech. Devel. Necessary
Beryllium Monocoque	Y5804 QMV-5	76 lbs	15 +	1. Light Weight	1. Expensive 2. Difficult to Form 3. Brittle, Notch Sensitive 4. Sheet Size Limited 5. Development Time 30 Months (Forming & Fastening Tech.)

NOTE: *Weights shown are for 1500 lbs Vehicle. At 100° F.
The relationship does not change for other weight
vehicles.

tuted for the original bulkhead. For minor modifications a change can be made to the honeycomb bulkhead by means of a mechanical fastener (for a light component) or injection of plastic into the honeycomb to create a hard point for mounting a heavy component. The honeycomb bulkhead may also be strengthened by the addition of a doubler attached by means of blind fasteners.

(4) Sterilization

It is not anticipated that the sterilization cycling will change the material properties of any of the materials discussed with the exception of 7075-T6. For this material the three temperature cycles of 145°C for 36 hours each will reduce the room temperature yield strength by 9% and the room temperature ultimate strength by 10%.

B. Orientation

The importance of the orientation sub-system cannot be over-emphasized. Since one of the prime purposes of the flight is the collection and transmission of surface data of the planets, the inability to perform either function, especially the latter, would mean mission failure. Data collection and transmission both depend on Lander orientation on the surface of the planet to allow various experiments and antennas (Section C.) to be properly deployed.

The basic problem of impact survival is the unknown surface composition and topography of Mars and Venus. It became apparent early in the study that any condition chosen as the mean could be subject to local extremes; e.g., a ground slope of 20° could be up to 90° locally. Therefore, it is not practical to assign arbitrary surface conditions and limits and then design to these. Instead, orientation sub-systems were designed and limitations then investigated.

There are three basic Lander positions with respect to the planet surface that are possible and were considered. These are the nose-up, nose-down, and side-orientation. Each one has certain advantages and disadvantages as well as different terrain limitations. Therefore, each position has had some study work done and a preliminary design completed. At the end of the system descriptions there is a section on system selection. The most promising method, naturally, is the one that combines the lightest weight with the highest success probability. However, in this instance another consideration is the terrain limitation which may take precedence over the other two factors since any system that requires tight bounds of slope and soil texture to perform is too restrictive to be considered.

From an intuitive study of the configuration, it is reasonable to assume that barring a very soft, high energy absorbing surface with a low wind condition, the Lander is not likely to come to rest in a nose down attitude. It is even doubtful that it would come to rest on its aft end. Therefore, the side orientation scheme is most probable, although, provision must be made to overcome the vehicle's coming to rest on its base or its nose. The following discussion presents three alternative orientation schemes, their ramifications and inherent limitations.

(1) Side Orientation

Figure 1.3.9-1 shows the Lander with the orientation system for a side orientation. A rocket mounted to the tip-over bar is fired in the event the Lander vehicle comes to rest nose-down (View A). This rocket will produce an overturning moment that causes the vehicle to fall onto its side. In the event the vehicle comes to rest nose up, an actuator drives the Y-shaped tip-over bars out again causing the Lander to tip over onto its side (View B). Once the vehicle is on its side, it is in a state of neutral equilibrium and its "at rest" position will be a function of the terrain and topography.

When the vehicle comes to rest on its side it must be rotated to the final desired position. The reason for this is that an "up" and "down" direction is specified by the payload and communications system. One orientation leg is deployed and the orientation rockets are fired (View C). These rotate or spin the vehicle about the axis of symmetry until stopped by the extended leg hitting the planet surface. At this time, a second orientation leg is deployed, stabilizing the vehicle in the desired position.

This system is limited by ground slope or local protuberances such as rocks or outcroppings. If the Lander has rolled against an obstruction of this type, it would be stopped in its rotation unless sufficiently high impulse rockets are used to spin the vehicle to a high enough rate capable of overriding a rock as well as rolling up a slope. There is also the possibility of the vehicle over-riding the extended leg stop resulting in a misorientation.

Figure 1.3.9-1 (View D), however, shows a side orientation that overcomes the above in that local slope or texture of terrain is of no consequence to the successful orientation of deployable items. Once again, the vehicle is provided with a rocket to overcome a nose-down attitude and tip-over bars to overcome a nose-up attitude. After the vehicle has achieved a state of rest on its side, pins are pulled on the aft bulkhead and a motor is started. The motor, as shown in the figure, is mounted to the bulkhead which itself is supported in bearings. A track or gear ring is mounted to the supporting structure and the motor then "walks" along the track, thereby rotating the bulkhead. This continues until the correct position is reached as indicated by a gravity sensing switch. The motor is stopped and locked, thereby maintaining the bulkhead attitude. The tip-over bar is again extended and two harpoons located on the end are now driven into the ground. Deployment of experiments and antennas may now be accomplished. In this manner, regardless of vehicle orientation; i. e., up hill, down hill, etc., the correct position for operation is achieved.

(2) Nose Up Orientation

Another orientation system that was considered is shown in Figure 1.3.9-2. In this system, the vehicle is set onto its base and the payload exposed by ejecting the shield and primary structure. One big advantage to this system is that all soil analyzing equipment is interconnected in what remains as the final surface vehicle. That is, flexible sample handling equipment is required since the drill is mounted to the aft bulkhead and feeds the analyzing components directly; whereas in side orientation, the drill must be deployed so that wiring and conveyor equipment have to be run through a center-line mounted conduit and then distributed. Also, thermal control of this equipment is simplified. The system operates as follows.

As in the other systems, a rocket is provided to upset the nose-down position (View A). With the vehicle on its side, two approaches are shown to right the vehicle onto its base. The first approach uses a pendulum harpoon, which is mounted on the aft bulkhead and is free to rotate (View B). The pendulum will seek the position minimum energy and will come to rest in a down position relative to the vehicle. Harpoons that telescope from the tubes fire into the surface. These harpoons have a swivel joint in them that will act as the pivotal point of the vehicle. A spring-loaded, on-impact-firing projectile is launched from the aft bulkhead and is anchored some distance from the vehicle. Attached to this projectile is a cable that unwinds from a reel. A spring winds the reel which will then pull the vehicle to an erect position on the surface. The alternative method is to use a pendulum tip-over bar, which anchors itself into the surface (View C). Attached to the tip-over bar is a cable that unwinds from a reel. As before, a spring winds the reel thus, pulling the vehicle onto its base. When the vehicle has been stabilized on its base, an explosive tension bolt is sheared and three mortars of different intensity are then fired simultaneously. These will separate and eject the shield and structure from the payload,

permitting the antennas and TV camera to be erected. The three mortars are employed for redundancy, since, should only the lightest charge fire, this will still cause the shield to pivot clear about the other two points. Firing of any two will separate and eject to a clear distance as would also occur if all three should fire.

(3) Nose-Down Orientation

There is a definite advantage to deployment of antennas and the television camera in a nose-down orientation. However, this is the most difficult attitude to achieve and maintain. The reasons are fairly obvious ones and include the following. Since primary impact is nose first but most probably not at zero degrees, the nose will crush at some angle. A nose-down orientation then requires balancing and stabilizing of the vehicle on what is essentially a line or even point contact on an unknown slope. In addition, the nose-down attitude is the least stable position even if the nose were symmetrically crushed, and to maintain this attitude when considering slope of terrain requires a complicated system of support lines.

Since RTG cooling is accomplished by direct radiation to the atmosphere, and RTG exposure is required to satisfy a failure mode safety requirement, this type of orientation is incompatible with the overall systems requirement and will not be considered.

(4) Orientation Selection

In both orientation positions, nose-up, and side, as an intermediate step, the vehicle is tipped onto its side. This, of course, is not true for the coincidental case where the vehicle comes to rest in the desired position. With the vehicle on its side, local terrain and slope is relatively unimportant since it will roll to a neutral position or minimum energy position within limitations due to local obstructions or sufficiently high coefficient of friction. As previously explained, the side orientation scheme that rotates the vehicle is dependent on its success to slope, coefficient of friction, and local obstruction. Since these are all non-definable conditions, the probability of success is undefinable.

With the system descriptions in mind, a study of the various events to effect orientation for the side and nose-up system is in order.

Nose-Up

1. Impact
 2. Upset to side (fire rocket) if nose-down
 3. Unlock parallel harpoons or pendulum tip-over bar
 4. Fire harpoons
 5. Deploy cable carrying stake
 6. Stake cable
 7. Reel cable
 8. Fire explode bolt
 9. Fire shield, structure ejection mortars
- { Parallel harpoons only
}

Side-Oriented (Rotating Bulkhead)

1. Impact
2. Upset to side:
 - (a) Rocket if nose-down
 - (b) Tip-over bar if nose-up
3. Unlock bulkhead
4. Operate motor until correct rotation of bulkhead is reached
5. Deploy tip bar further to touch surface
6. Fire small stakes on tip bar

A careful perusal of the number and complexity of events indicates that all items in the rotating bulkhead system have counter parts in the nose-up scheme and that the latter system has several additional items. The one major item of concern is the possibility of jamming of the bulkhead track and motor due to impact deflection. However, careful design of the crush-up material to absorb impact and tumble, together with careful track clearance design, should be able to overcome this. Therefore, the recommended system for orientation of this vehicle is the rotating bulkhead on a side-lying vehicle.

The Lander vehicle designed for the Venus 1972 opportunity will utilize the same orientation system as does the Mars vehicle. The Venus 1970 Lander does not require orientation other than its being positioned on its side. A rocket mounted on the aft bulkhead is fired in the event of either a nose-down or nose-up landing attitude. The resulting overturning moments, in either case, will cause the vehicle to fall on its side.

C. Deployment

Several categories of experiments and equipment are carried in the Lander. An appraisal of these experiments, the number that have to be deployed vertically and those that have to make contact with the surface, follows.

The experiments carried by the Lander are grouped below with respect to their operational requirements.

Category I — Experiments requiring direct exposure to sky light or atmosphere

Temperature	- Operate during descent and on the ground
Pressure	- Operate during descent and on the ground
Density — Ray	- Operate during descent and on the ground
Solar UV Spectrum	- Operate during entry
UV Photometer	

Electron Density (Langmuir Probe)	- Operate during approach and initial entry
Surface radioactivity	- Requires view of surface
Sample Gatherer	- Atmospheric sample — on surface
Surface Sounts	- Operates on surface
Fixed TV Camera	- 525 lb. Venus Vehicle

These experiments will be mounted on the aft bulkhead or aft cover. They require no orientation except for the Surface Radioactivity experiment. This experiment will be a fixed installation on the aft bulkhead and will view the ground after the aft bulkhead is rotated.

The fixed TV camera installation in the Venus 1970 vehicle will look out the aft bulkhead and a sweep capability will be built into the lens system.

Category II — Experiments housed inside the lander
requiring samples of atmosphere or surface soil

Gas Chromatograph	- Requires atmospheric sample
Special Atmosphere Composi- tion Group	
Soil Moisture	
Radioisotope Growth Detector	- Requires soil or atmospheric sample
Turbidity and PH Growth Detector	
Photoautotroph Detector	
Microscopic Analysis	

These experiments are housed inside the Lander and require no deployment, but do require a sample of atmosphere or soil delivered to them. For this reason, they are mounted on the aft bulkhead of the Mars Lander to simplify the distribution of the sample to them. On the Venus 1970 vehicle the situation is more complex since these experiments are located on a fixed bulkhead and the sample gathering system is located on the rotating bulkhead. In this case, the sample gathering system will utilize flexible tubing to accomplish transfer of the sample.

Category III — Experiments requiring direct contact with the surface

Surface Penetrability
Seismometer
X-ray Diffraction
Particle Scattering

Thermal conductivity of Surface

Electrical Conductivity of Surface

Drill and Pulverizer

Several systems were considered for deploying these experiments. If the entire Lander were not oriented, these experiments could be mounted on a flat plate and this plate ejected onto the surface of the planet. The probability that this plate would lie on one of its flat surfaces is high. In this case, the experiments would have to be arranged so as to operate through either surface of the plate. This system would be heavy due to the weight of the plate and also the ejection system.

The surface penetrometer requires a measurement at several locations on the surface. For this instrument, it is proposed that it be mounted in a weighted ball with an offset c.g. This ball will then be ejected from the lander by means of a spring and pulled back to the vehicle in increments by means of a lanyard attached to it. Since the ball has an offset c.g., it will orient itself to bring the instrument into contact with the surface.

Mindful of these experiments and other considerations (antenna and TV camera deployment and orientation reliability), it was decided that the aft bulkhead would be oriented. In this case, the tip-over bar located on the bottom of the aft bulkhead can be deployed to bring it into contact with the surface. Category III experiments are mounted on it. Due to surface irregularities, the tip-over bar may not lie flat on the surface. Additional provisions are added to the installations to allow the instruments to be lowered to the ground on vertical tracks, or to free fall.

The anchoring event is considered to be a necessary one in view of surface winds (40 MPH) predicted for the Martian surface. The anchoring would be used primarily to resist small rocking motions or overturning and not to retard translation or rotation of the vehicle. Under the presently assumed surface winds of 40 MPH, vehicle translation and rotation is not likely to occur. Figure 1.3.9-3 shows representative wind loads as a function of surface pressure for a typical Mars 1969 Lander configuration. Figure 1.3.9-4 shows loadings for an aft bulkhead facing the wind.

Category IV — Experiments housed inside the vehicle

Radar Altimeter (Mars Vehicle)

Surface Gravity

TV camera for Microscopic Analysis

These experiments are housed inside the vehicle and require no deployment.

Category V — Experiments and equipment that require exposure to outside of lander plus further orientation to maximize their capability

Communication Antennas - Deployed vertical

Panorama Television - Scan horizon

Radar Altimeter (Venus) - Used during descent

Light Levels	-	Deployed vertical
Light intensity and Polarization	-	Deployed vertical
Insolation	-	Deployed vertical
Ionosphere Profile (Bottom Side Sounder)	-	Antenna deployed on surface of planet
Insect Attractor	-	In sight of TV camera
Meteorite Trails		
Distance and Eclipse of Phobos		
Sounding Rockets	-	Deployed vertical
Wind speed and direction	-	Deployed vertical
Precipitation Indicator	-	In sight of TV camera

The communication antennas and panorama television must be erected above the Lander and have line of sight from horizon to horizon. With the oriented bulkhead the booms on which these experiments are mounted are actuated by means of a torque motor which is controlled by a vertical sensor located on the boom. Other experiments which require an unobscured view of the sky will also be mounted on these booms. These include the light level, wind indicator, insolation and light intensity and polarization experiments.

The television camera, in addition to scanning horizon to horizon, must be capable of being depressed so as to look at the tip-over bar where experiments such as the insect attractor and precipitation indicator are located. The television cameras are also used to view the eclipse of Phobos.

The radar altimeter used for the Mars Lander is located in the nose and looks through the ESM shield and fiber glass impact structure, both of which are radar transparent. Due to the high "g" entry conditions and high surface temperatures on Venus, the materials (heat shield and crush-up structure) used, are not radar transparent. Therefore, the radar dish antenna cannot be located in the nose but must be deployed over the side at the aft end during descent. This is done by means of tracks and a torque motor. Two antennas are deployed so that no aerodynamic unbalance exists. The two antennas allow doppler capability and provide horizontal range and velocity information as well as altitude data.

The Ionosphere Profile (bottomside sounder) consists of an electronic box (located inside the vehicle) and a 400 foot wire antenna. This antenna and reel are located on the tip-over bar. The antenna is deployed by means of mortar shells. These are attached to the antenna and are fired away from the vehicle, deploying the antenna.

The sounding rockets used in the Mars 1973 vehicle, are mounted on the tip-over bar. They are required to be launched vertically. Torque motors, controlled by a vertical sensor on the package, will erect the cluster of rockets. Special precautions must be made to avoid damage to the vehicle from the rocket blast.

D. Packaging

(1) Packaging Density

Since much of the payload (scientific experiments and communications equipment) for the Voyager lander is still in the research and development stage, accurate weights and sizes

for a majority of these items is still unknown. Early in the study program it was decided to assume a packaging density based on experience gained on other programs such as Bios and Nerv and update this assumption as information became available.

Electronic component weight densities, on an average are about 60 lbs/ft.³. Due to the nature of the payload, the necessity for deployment, the requirement of some experiments to have samples of soil or atmosphere delivered to them, and results of updating as weights and volumes became available, the packaging density for this study has been limited to 20 lbs/ft.³. A detailed packaging study has been made for the Mars 1969 and Venus 1970 Lander vehicles.

(2) Packaging Considerations

(a) Radioisotope Thermoelectric Generator Unit

For the Mars Landers, the proper location of the RTG unit was of prime importance. A number of design and operational considerations led to the installation of the generator in the nose section of the vehicle. Other locations were investigated but were found undesirable because of limited accessibility to the RTG.

The primary consideration of the placement of the RTG unit was dictated by the system's requirement of maintaining the RTG in a safe and integral condition in case of failure.

The overheating of an RTG unit leads to the buildup of pressure due to the release of helium atoms. To safeguard and prevent a rupture of the pressure vessel and radioactive contamination of the planet, cooling of the RTG can be made by direct radiation to the environment. This, of course, necessitates direct exposure to the atmosphere. By positioning the RTG in the nose section, the opportunity exists for separating the nose cap and providing the RTG with this exposure.

Several systems have been investigated to provide primary cooling of the RTG unit on the planetary surface, see Section 1.3.6 for further analysis. The system's requirement calls for the RTG unit to be provided with cooling for 10 half-lives of the isotope.

For power supply units of the size proposed for Mars Landers, the best thermal control approach appears to be through direct radiation. To accomplish this, segments of the nose cap section are separated from the vehicle thus exposing the RTG to the planetary environment, see Figure 1.3.9-5. This, of course, is completely compatible with the above safety requirement. Direction radiation cooling becomes less feasible as the size of the RTG increases. Therefore, for any projected vehicle which would require extended surface life and, hence, larger power supplies, a closed liquid loop thermal control system would replace the radiation method. However, the safety requirement still stands and the requirement for a separable segmented nose section still exists.

Because of potential radiation danger to personnel during assembly and checkout of the vehicle, the isotope will be installed in the generator unit on the launch pad as one of the final operations prior to prelaunch checkout. This late assembly requires that the generator unit be located in an accessible and convenient position. The nose section provides both the needed accessibility and the added convenience. The forward section of the nose cap is removable. A breech ring type joint is provided for attaching the nose section to the vehicle after the isotope is installed in the RTG unit. The attachment mechanism will also engage a lip on the RTG unit and will provide forward structural support.

Another consideration is the desirability of thermally isolating the RTG unit from the payload compartment. With the RTG installed in the nose, it may be isolated from the payload by means of an insulated bulkhead, thus facilitating temperature control of the payload compartment.

(b) Communications Equipment and Scientific Experiments

A number of the communication packages are directly connected to the antennas with coaxial cable. Since all of the deployable antennas are mounted on the rotating bulkhead, these communication packages are also mounted on the bulkhead so that there will be no twisting of the coaxial cable. All other electrical wiring from the fixed bulkheads to the rotating bulkhead will be run through a tube in the center of the vehicle and will be capable of twisting 180° (the limit of rotation of the aft bulkhead). Also, the thermal control system tubing can be made of flexible material in the form of a coil and mounted off-center on the rotating bulkhead to facilitate twisting without kinking.

Although the sample handling equipment has not been designed yet, it is expected to be made of flexible tubing. The tubing will be used to transport the specimen from the end of the tip bar to the experiments. These experiments have also been placed on the aft bulkhead.

Those components which give off excessive heat have been placed on the aft bulkhead. This was done for two reasons: (1) the excessive heat will complement the thermal control system during the periods which require heating, and (2) during the hot part of the day on Mars when cooling is required, excess heat can be conducted through the aft bulkhead since the heating system will be inoperative at this time.

(c) Sterilization

The design goal of the Lander is to eliminate all the components that cannot take the heat sterilization (Volume V). If this is not completely achieved then sensitive components will be sterilized separately from the vehicle and will then be attached to the sterilized bulkheads. The bulkheads will then be assembled to the vehicle. By mounting the components to the bulkheads, the necessity of attaching to the interior walls of the vehicle where accessibility is poor, is eliminated. One component that cannot be handled in this fashion is the radioisotope power supply.

A number of methods of installing the radioisotope into the vehicle under sterile conditions have been investigated and are given in Volume V.

E. Vehicle Description and General Arrangement

The proposed Mars 1969 vehicle, shown on Figure 1.3.9-6 is a sphere cone shape with a $W/C_D A$ equal to 35 psf. It has a base diameter of 92 inches, nose radius of 16.1 inches, cone angle of 40° and a length of 45.9 inches. The gross weight is 1450 lbs. as it leaves the orbiter and weighs 1271 lbs. when it enters Mars. This difference in weight is the result of the ejection of the adaptor-radiator section which includes the ΔV rocket motor and the spin and separation system.

The basic structure of the vehicle is aluminum honeycomb. The aluminum honeycomb frustum and nose structure has been designed to withstand the aerodynamic and inertial forces during entry and the shock loads which occur upon impact. The internal structure consists of aluminum rings and fittings and three aluminum honeycomb bulkheads.

The shield material is ESM, .31 inch thick on the frustum section and a maximum of .55 inches thick on the nose. Crush-up material, is located between the heat shield and the basic structure. Fiber glass honeycomb is oriented with the longitudinal direction of honeycomb perpendicular to the surface of the vehicle. High density honeycomb is used in the nose and at bulkhead locations and low density honeycomb used elsewhere. The aft end of the vehicle is protected from entry heat by means of an aluminum cover. This aft cover is protected by an ablative coating of PD 300.

In general, the electronic components and scientific experiments have been located with due regard to their operating function and their environmental restrictions. Referring to

Figure 1.3.9-6, it can be seen that all components making up the payload are mounted on bulkheads or on the tip-over bar. The one exception to this is the Langmuir probe (item 17) which is mounted on the base of the vehicle.

The radar altimeter antenna (item 2) is mounted in a fixed position within the honeycomb crush-up material between the heat shield and the aluminum honeycomb primary structure. The radar dish will be looking through fiber glass crush-up and ESM shield material, both of which are radar transparent.

The RTG unit is shown as item 22. Note the cooling fins surrounding the generator. As was mentioned before, the isotope is installed into the generator unit prior to prelaunch checkout. The removable nose cap (item 88) is then attached by means of a breech-lock joint. Just aft of the nose cap can be seen the heat shield structure segments which will separate from the vehicle after surface orientation to expose the RTG. The six segments can be separated by means of shaped explosive charges.

Item 5 is the forward bulkhead on which the RTG and most of the thermal control system components are located. Details of the rotating bulkhead, bearing arrangement, and gear motor are shown in detail "B" on Figure 1.3.9-6. The motor-gear combination (item 23) is rigidly fastened to the rotating bulkhead (item 6). A gear ring is attached to the vehicle structure. When the motor is started, the bulkhead will rotate relative to the stationary gear ring. Items 12 and 16 show the tip-over bar and electric actuator in an undeployed position. On signal, the actuator will extend, thus, driving the bar out of the vehicle. The actuator is also capable of pulling the tip-over bar back into the vehicle. This is necessary since in the orientation sequence, the tip-over bar is deployed either to overturn the vehicle from a nose-up position or, since the tip-over rockets are located on the bar (for additional moment arm) to upset the vehicle in the event of a nose down landing.

The main and decelerator parachutes are stored in the retardation system cannister (item 15). The main chute is stowed in an annulus surrounding a tube which contains the decelerator chute, drogue slug, and mortar charge. This cannister is mounted on the aft cover which is separated from the vehicle when the main chute is deployed. Explosive bolts are used to attach the aft cover to the vehicle.

The ΔV rocket adapter section and space radiator is shown as item 18. The adapter is constructed of four aluminum longerons which carry the moment and longitudinal load from the lander to the orbiter. The shear is carried by means of an aluminum skin and stiffeners. This adapter is attached to the Lander by means of explosive thruster bolts. The radiator, used to cool the RTG unit during transit, is mounted to the skin of the adapter by means of bolts with insulating stand-offs. Insulation is installed between the radiator and structure to protect the structure from the heat generated from the radiator. The adapter and radiator are shed as an integral unit just prior to entry. Detail "C" shows the installation of the thruster bolt which not only severs the tie with the entry vehicle but also provides enough thrust to separate the adapter from the vehicle. Item 13 is the nitrogen gas torus reservoir which provides storage for the spin and separation cold gas system. The spin nozzles (item 7) and separation jets (item 8) are located on the skin of the adapter. Aluminum parachute fittings are provided at four locations on the aft end of the vehicle. These fittings are located at the points where the longerons from the adapter are attached.

The ΔV rocket (item 14) is a solid bi-propellant motor which produces a relative velocity of 400 f.p.s. This motor provides the impulse necessary to effect planetary entry and also insures that the Lander will be on the surface and ready to communicate with the orbiter on the first orbit.

View A-A shows the general arrangement of the aft end of the rotating bulkhead. Note that the television camera and VHF TURNSTILE antenna (items 37 and 36) are mounted on the same deployment stand. Item 33 is the direct earth link antenna in the stowed position.

Figures 1.3.9-7 and 1.3.9-8 show the proposed Mars 1971 and 1973 Entry/Lander, respectively. These vehicles are built up from a Mars 1969 vehicle to which has been added a 9.5 inch long conical frustrum extension. The extension results in a base diameter of 108 inches which increases the W/C_{DA} to 35.5 psf. The conversion can be made simply and without major modification, but with some loss of structural efficiency.

Referring to Figure 1.3.9-7, the rotating bulkhead and structural ring of the Mars 1969 vehicle are replaced by a fixed type bulkhead (Item 35) and an appropriate ring (Item 34). The aft structural ring is replaced by a new structural ring (Item 36) which accommodates a new rotating bulkhead (Item 1). The extension (Item 37) can now be fitted to the basic vehicle using the new aft ring as a splicing member. The extension section is attached by means of bolts. The extension is structurally identical to the basic Mars 1969 vehicle; aluminum honeycomb primary structure, fiberglass honeycomb crush-up, and ESM heat shield. The parachute fittings are removed from the 1969 vehicle and are relocated on the extension section. The procedure is the same for modifying a 1969 vehicle to a Mars 1973 Lander.

View A-A on Figure 1.3.9-7 shows the placement of scientific experiments and communication equipment for the Mars 1971 Lander. The tip-over bar has been made larger to accommodate more ground oriented experiments.

View A-A on Figure 1.3.9-8 shows the placement of scientific experiments and communications equipment for the Mars 1973 Lander. Here too, the tip-over bar has been made larger to hold more experiments. Note especially the sounding rockets (Item 2) which are mounted to the end of the tip-over bar. The Mars 1973 Lander is characterized by the S-Band helix array antenna (Item 16) used for primary direct link communications.

The radiator-adapter section for all vehicles has been sized so as to fit a common bolt circle on the Orbiter. Therefore, the sides of the radiator-adapter for the Mars 1971 and 1973 vehicles are cylindrical rather than conical as on the Mars 1969 Lander. The construction of this adapter is the same for all three vehicles.

The Venus Lander proposed for a 1970 mission is shown of Figure 1.3.9-9. A sphere cone configuration, it has a W/C_{DA} of 45 psf, a bluntness ratio of 0.35, base diameter of 58 inches, semi cone angle equal to 30° , and a length of 40.5 inches. The gross weight of the vehicle is 525 lbs. and the entry weight is 447 lbs. The difference in weight between gross and entry configuration is contributed to by the spin and separation system, the ΔV rocket, and the radiator-adapter section.

The primary structure of the vehicle is a stainless steel honeycomb shell with titanium rings and two stainless steel honeycomb bulkheads. The shield material is Phenolic Nylon, 0.42 inches thick on the frustrum section and a maximum of 0.65 inches thick on the nose. Crush-up material is located between the heat shield and is made of stainless steel honeycomb. High density crush-up is used at the nose and bulkhead stations and low density material is used elsewhere. The aft end of the vehicle is protected from entry heat by means of a titanium cover. This cover is protected by an ablative coating of PD 300.

Since surface life for the Venus Landers is short compared to the Mars vehicle, electrical power is supplied wholly by battery instead of an RTG. Thermal control during transit is accomplished by use of optical surface coatings, thermal insulation, and internal electric heaters. Because of the high surface temperatures on Venus, thermal control becomes one of cooling rather than heating as is the case for a Mars mission vehicle. Cooling during the entry phase and surface operations is accomplished by an expendable coolant system using ammonia as the coolant (assuming surface pressure is less than 10 atms.) Referring to Figure 1.3.9-9, the ammonia storage tank is shown as Item 10. Two and one-half inches of thermal insulation (Item 4) is bonded to the structural shell and completely insulates the payload compartment. When internal temperatures reach 100°F

(beginning of entry), the ammonia liquid flows into the cold-plate bulkhead (Item 12), evaporates, and cools the components mounted on the plate. This will continue until all of the coolant is expended, a total of 45 minutes.

The Venus 1970 vehicle does not require orientation other than being placed on its side. Tip rockets mounted on the aft bulkhead (Item 9) are provided to overturn the vehicle in the event of a nose down or nose up landing.

The television package (Item 34) utilizes a fixed camera with a rotating mirror placed in front of it. The mirror is capable of rotating about two axes, thus providing hemispherical picture coverage.

Retardation is accomplished mainly by aerodynamic drag of the vehicle. Additional retardation, to reduce impact velocity, is gained by deploying the aft thermal cover (Item 5) at an altitude of 5000 feet. On signal, a mortar charge deploys a drogue plate (Item 13) which is attached to the aft cover by a riser line. Simultaneously, explosive bolts will be fired to allow the aft cover to follow the drogue plate. The cover is attached to the vehicle by means of four harnesses.

The ΔV rocket adapter section (Item 43) is constructed of four aluminum tubes which support the rocket casing (Item 6). The supports are attached to a cylindrical channel onto which the cold gas spin nozzles (Item 8) are mounted. Separation nozzles (Item 7) are mounted directly to the adapter structure as are the two separate nitrogen storage tanks.

As mentioned in Section C, the radar antennas have been moved from the nose section on the Mars Lander to a position under the aft cover on the Venus vehicles. The antennas (Item 23) are deployed through slots provided in the aft cover.

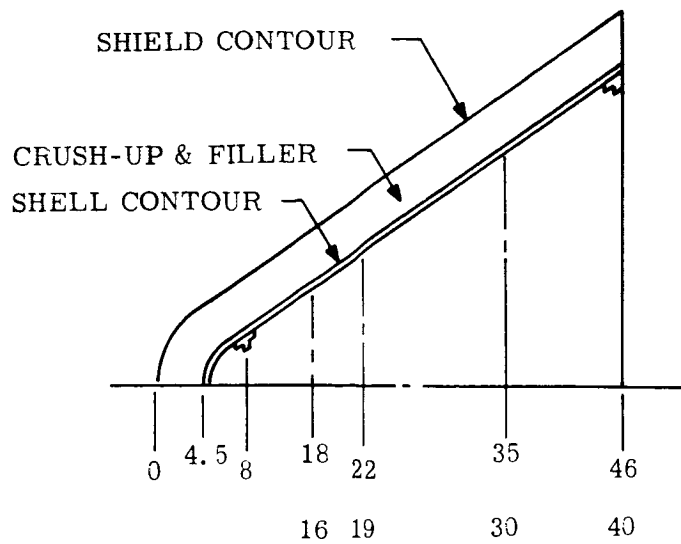
Component placement is shown in section views A and B and in the end view. Electronic components and scientific experiments have been located with due regard to their peculiar operating function and environmental restrictions.

A preliminary vehicle design study was made of an Entry/Lander vehicle for a 1972 Venusian mission. The configuration, a sphere cone with $W/C_{DA} = 44$ PSF, has a gross weight of 2,600 lbs., and entry weight of 2,213 lbs., a bluntness ratio of 0.35, a base diameter of 123 inches, and a semi-cone angle of 35° . The 1972 vehicle will be similar to the Venus 1970 Lander in that it will be made of stainless steel honeycomb with similar crush-up material, have a Phenolic Nylon heat shield, and will contain a similar thermal control system. The difference in weight between the 1970 and 1972 vehicle is mainly due to the system requirement of 5-1/2 hours surface life. The length of surface life is directly reflected in the amount of ammonia coolant which must be carried and hence, the weight and volume of the thermal control system. Because of the size of the vehicle, the type of scientific payload, and the mission, an orientation system similar to the Mars vehicles is used.

F. Structural Analysis of Mars 1969 Vehicle

(1) Shell Analysis

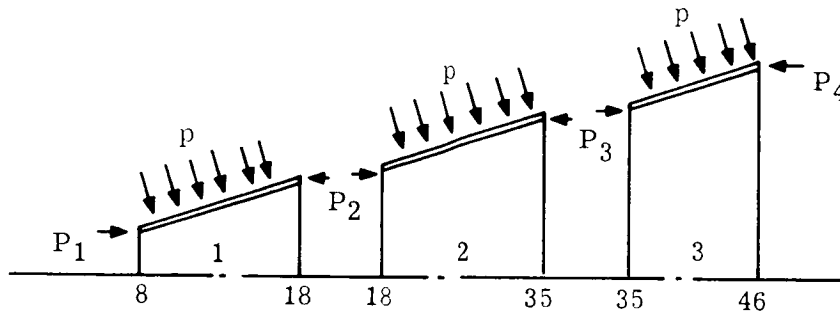
The shell geometry of the 1450 pound Mars vehicle is as follows.



The weight distribution on each bulkhead was assumed to be

bulkhead station	weight
18	100
22	100
35	230

The pressure (p) and axial load (P) condition on the shell is given in Figure 1.3.9-10 maximum axial "g" entry condition. For the purpose of this analysis, the conical shell was considered in three distinct sections as follows



The method of analysis presented in the previous section 1 was utilized to obtain the following results.

Conical Section	Face Thickness Required (limit loads)	Face Thickness Used
1	.006	.012
2	.009	.012
3	.011	.012

Corresponding to the .012 faces, the respective core depths of Sections 1, 2 and 3 were found to be .10, .30 and .40 inches.

Therefore, a shell using .012 faces and .40 depth was used for the conical shell. This analysis is based on an outside temperature of 300°F and an inside face temperature of 100°F. The spherical nose cap is designed by the impact force and is discussed in Section 1.3.4.

(2) Bulkhead Analysis

(a) Stations 18 and 22 Bulkheads.

These bulkheads were sized to withstand a uniform loading of 1.5 (100 pounds) (113 g's). A simply supported circular plate analysis was used. The maximum moment on this structure is

$$M_{\max} = \frac{W}{16 \pi m} \cdot (3m + 1)$$

where

W = total weight

m = reciprocal of Poisson's ratio

$$M_{\max} = \frac{17000}{(16)(3.3)} (10.9) = 1110 \frac{\text{in-lbs}}{\text{in}}$$

$$d_c t_f = \frac{M_{\max}}{\sigma} = \frac{1110}{62,000} = .018 \text{ in}^2$$

where

d_c = depth of core

t_f = thickness of face σ = design stress

$$t_f = \frac{.018}{.75} = .024 \text{ in.}$$

use

$$t_f = .024 \text{ in.}$$

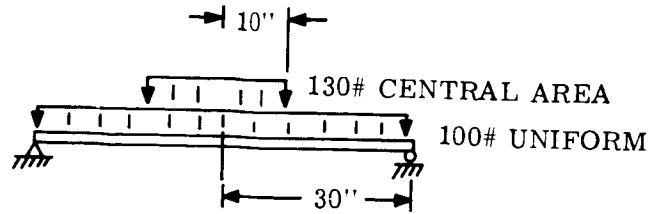
$$d_c = .75 \text{ in.}$$

(b) Station 35 Bulkhead

This bulkhead was checked for two loading conditions:

- (1) Peak axial "g" entry loads,
- (2) Tip-over bar reaction during on-ground deployment.

Considering entry loads, the bulkhead loading is as follows:



$$\begin{aligned}
 M_{\max} &= M_{\max}(\text{unif load}) + M_{\max}(\text{central load}) \\
 &= \frac{1.5(100)(113)}{16(3.3)} 10.9 + \frac{1.5(130)(113)}{4(3.3)} \left[3.3 + 4.3 \log \frac{30}{10} - 2.3 \frac{100}{3600} \right] \\
 &= 1110 + 2700 = 3810 \frac{\text{in-lbs}}{\text{in}}
 \end{aligned}$$

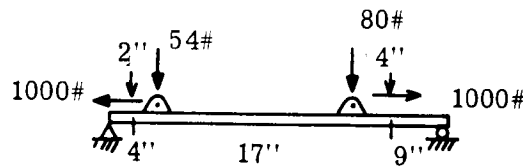
$$d_c t_f = \frac{M_{\max}}{\sigma} = \frac{3720}{62,000} = .060$$

use

$$d_c = 1.50 \text{ in.}$$

$$t_f = .040 \text{ in.}$$

Condition (2) resulted from the on-ground orientation system and were found to be as follows



Considering the above system as a simple beam, the maximum moment occurs just left of the right loading point and equals

$$M_{\max} = -9(129) + 400 = 2840 \frac{\text{in-lbs}}{\text{in}}$$

using a 1.5 load factor

$$d_c t_f = \frac{(1.5)2840}{63000} = .067 \text{ in}^2$$

for a 1.5 depth of sandwich,

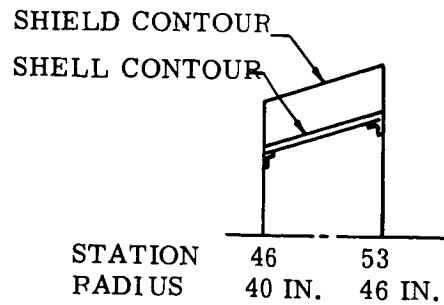
$$t_f = .045 \text{ in.}$$

Therefore, increased face thickness to .045 must be provided at peak moment locations to take the locally applied loads.

A more precise analysis must be conducted to further evaluate this condition, however, the above is considered satisfactory for the preliminary studies conducted.

(3) Growth to 2000 lb. Vehicle

The extended structure which is added to the primary 1450 pound to provide for the 2000 pound configuration is as follows.



At the peak entry load condition, the external pressure is 25 psi. This results in the following applied loads.

Station	Axial Load (lbs/in)	Hoop Load (lbs/in)
46	214 (tension)	1000
53	0	1150

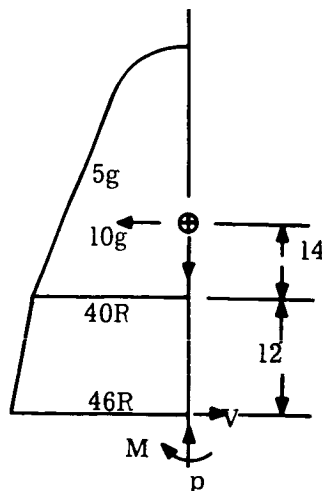
This load condition (Station 53 being critical) results in a face thickness requirement of .014 for the 300°F outside, 100°F inside face temperature. A core depth of .80 inch is required for stability using an external pressure of (1.25) (25 psi).

The bulkhead loadings remained constant and the sizes calculated previously are applicable.

(4) Adapter Analysis

(a) 1450 Pound Vehicle.

The following loading and geometry were used in this analysis.



Adapter Loading.

$$M = 5(1460)(12 + 14) = 190,000 \text{ in-lbs}$$

$$V = 5(1460) = 7300 \text{ lbs}$$

$$P = 10(1460) = 14,600 \text{ lbs}$$

A semi-monocoque structure consisting of an .020 shell plus four 1" x 1" x .125" \angle longerons is being used.

Assuming the condition of "stiffeners with inefficient skin" for bending and neglecting the moment of inertia of the angles, we get

$$I_s = \frac{4AR^2}{2} = 3200A$$

and the bending stress is:

$$f_b = \frac{My}{I} = \frac{1680}{A}$$

The axial stress is:

$$f_a = \frac{3650}{A}$$

and the total combined stress is:

$$f_c = f_a + f_b = \frac{5330}{A} = 22,800 \text{ psi}$$

The critical buckling stress (aluminum at 300°F) is

$$\sigma_{cr} = \frac{\pi^2 EI}{l^2 A} = 58,000 \text{ psi}$$

The yield strength,

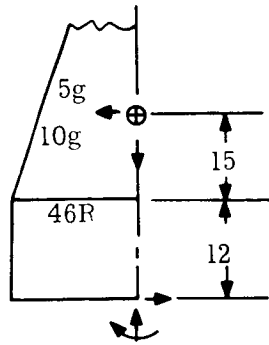
$$\sigma_{yp} = 45,000 \text{ psi}$$

Thus,

$$MS = \frac{45000}{22800} - 1 = .97$$

(b) 2000 Pound Vehicle

This geometry is as follows.



$$M = 5(12 + 15) (2000) = 270,000 \text{ in-lbs}$$

$$V = 5(2000) = 10,000 \text{ lbs}$$

$$P = 10(2000) = 20,000 \text{ lbs}$$

Again using an .020 shell and four 1" x 1" x 0.125" (<) longerons of 7075-T6 aluminum alloy at 300°F, we have

$$f_c = f_a + f_b = \frac{5000}{A} + \frac{(270,000) (.707) 46}{4200 A} = \frac{7090}{A} = 30,000 \text{ psi.}$$

The critical buckling stress is

$$\sigma_{cr} = 58,000 \text{ psi}$$

The yield strength is

$$\sigma_{yp} = 45,000 \text{ psi}$$

Thus,

$$MS = \frac{45000}{30000} = .50$$

The shearing stress in the .020 skin is only 4000 psi giving a very large MS.

G. Weight Analysis — Trends

During this study, weight estimates were made for Landers of various diameters and gross weights. The vehicle weights ranged from 525 lbs to 4000 lbs. A table of design parameters is shown in Table 1.3.9-2. It will be noted that the Mars vehicles all have a $W/C_{DA} = 35$ PSF and the Venus vehicles have a $W/C_{DA} = 45$ PSF. In addition, each of the vehicles has a payload density, in the payload compartment, of approximately 20 lbs/ft³. Figure 1.3.9-11 presents the effect of gross weight on the base diameter for both Mars and Venus Landers.

Figure 1.3.9-12 shows the c.g. location, measured from the nose, as a function of vehicle length for the gross and entry weight of the Mars and Venus vehicles. It can be seen that the c.g. moves progressively forward for the longer vehicles. The curves for the entry configuration show c.g.'s closer to the nose. This reflects the fact that all the items that are jettisoned before entry, are attached to the aft end of the vehicle.

Figures 1.3.9-13 and 1.3.9-14 show the vehicle pitch, roll and yaw moments of inertia as a function of the vehicle gross weight for the gross weight configuration and entry configuration, respectively. The divergence of the pitch or yaw moment of inertia for

large vehicles is due to the heavier aft mounted ΔV rockets and space radiators needed for the larger Entry/Lander. The convergence of the moments of inertia for the smaller vehicles reflect compactness in design.

Figure 1.3.9-15 shows the relationship between the payload compartment volume and base diameter. The volume shown is not the total volume of the vehicle but is only the volume of the payload compartment. It can be seen that the volume-wise, the larger vehicles become a more efficient.

Total heat shield weight as a function of Lander gross weight is shown on Figure 1.3.9-16. The comparison is made between the Mars and Venus vehicles. The difference between the two curves are part of the weight penalty which must be paid if commonality of Landers is sought. The Mars vehicle would have to fly with a shield designed for a Venus entry.

Figure 1.3.9-17, Structural Weight vs. Lander Gross Weight, is a comparison of the structural weights of the Mars and Venus vehicles. Again, the difference between the two curves would be the weight penalty incurred on a Mars Lander by using a common structure.

Retardation and crushup material weight as a function of vehicle gross weight is illustrated on Figure 1.3.9-18. The significantly higher retardation weight for the Mars vehicle is the result of using a parachute system whereas, the Venus vehicle uses the aft cover as a drag device, thus most of the weight shown on this figure is crushup material.

Each of the systems is designed for a vertical impact velocity of 40 feet per second with a horizontal wind of 40 mph.

Figure 1.3.9-19, Ground Orientation System Weight vs. Lander Gross Weight, shows that the orientation system is a function of the vehicle gross weight. Variation in gravity and temperature effects of the two give rise to differences in orientation system weights for similar vehicles, however, these are not strong parameters and do not reflect in the curves.

Payload weight as a function of gross vehicle weight for Venus Landers is shown in Figure 1.3.9-20. Payload, here, is defined as including the scientific experiments and their associated deployment and installation equipment, the electrical power supply, and communications equipment including antennas. The payload weight does not include the thermal control system weight since this is strongly dependent on surface life for the Venus Landers.

Figure 1.3.9-21 shows payload weight vs. gross vehicle weight for Mars Landers. Here, the payload includes the thermal control system.

Tradeoffs between scientific payload, communications, electrical power supply, and the thermal control system have been made. In all cases, the payload was optimized to provide the maximum number of high priority scientific experiments consistent with required relay and direct link communications and a reasonably sized electrical power supply.

Figure 1.3.9-22 shows the dependence of insulation area on vehicle gross weight for Venus Landers. Figure 1.3.9-23 shows the ammonia thermal control system weight as a function of insulated area and surface life. Using both figure 1.3.9-22 and 1.3.9-23 a thermal control subsystem weight can be determined for a specific surface life and gross weight vehicle.

The adapter section structure and radiator weight as a function of vehicle gross weight is shown on Figure 1.3.9-24 for both Mars and Venus Landers. Since an RTG unit and, thus, a transit radiator is used on all Martian missions, the weight difference between the Mars and Venus vehicles can be explained.

Figure 1.3.9-25, Propulsion System Weight vs. Gross Vehicle Weight, shows the weight of the ΔV rocket, spin system, Lander separation system, and adapter separation system. This weight assumes

$$\Delta V = 400 \text{ f.p.s.}$$

$$\text{Spin-up} = 80 \text{ rpm}$$

$$\text{Vehicle separation rate} = 1 \text{ f.p.s.}$$

The ΔV case is identical for all vehicles. The amount of propellant is varied for each mission.

Using Figures 1.3.9-16 through 1.3.9-19, 1.3.9-21, 1.3.9-24 and 1.3.9-25, a weight breakdown of the various subsystems can be determined for a specific gross weight Mars Lander.

Figures 1.3.9-16 through 1.3.9-20, 1.3.9-22, 1.3.9-23, 1.3.9-24 and 1.3.9-25 can be used to determine a weight breakdown for a specific gross weight Venus Lander.

The reader is again reminded that the weight estimates are based on a Martian Lander with a $W/C_D A = 35 \text{ lb/ft}^2$.

Table 1.3.9-3 is a summary weight breakdown of the five vehicles presented in this report. Figure 1.3.9-26 and 1.3.9-27 are the detailed weights breakdown for the Mars 1969 and Venus 1970 Landers.

TABLE 1.3.9-2. DESIGN PARAMETERS FOR VEHICLES PRESENTED IN THIS STUDY

Mars	'69	'71, '73, and '75	'69
Wt ~ LBS	1450	2000	4000
D_B - in.	92	108	142
R_N ~ in.	16.1	16.1	17.8
R_N/R_B	.35	.30	.40
$W/C_D A$ LBS/FT ²	35	35.5	35
θ_c ~ deg.	40	40	47
L - in.	45.9	55.4	59.5
Venus	'70	'72	
Wt. ~ LBS	525	2600	
D_B - in.	58.0	123.5	
R_N - in.	10.0	21.6	
R_N/R_B	.35	.35	

TABLE 1.3.9-2. Continued

Mars	'69	'71, '73, and '75	'69
c	.35	.35	
$W/C_D A - \text{LBS/FT}^2$	45	44	
$\theta_c \sim \text{deg}$	30	35	
L - in.	40.5	71.5	

TABLE 1.3.9-3. LANDER SUMMARY WEIGHT BREAKDOWN

	M'69	M'71	M'73	V'70	V'72
Shield	84.2	128.5	128.5	97.5	365.2
Structure	233.0	389.7	389.7	105.7	534.4
Aft Cover and Separation	63.0	63.0	63.0	25.0	151.0
Retardation and Crush Up	288.2	360.5	360.5	35.9	156.4
Thermal Control	72.0	72.0	72.0	40.0	618.0
Electrical Power	106.5	106.5	106.5	20.0	30.0
Communications	141.5	141.5	141.5	41.5	117.0
Orientation	67.0	86.0	86.0	8.0	93.0
Scientific Payload	159.4	238.2	299.2	54.1	216.9
Payload Deploy and Installation	56.0	182.1	121.0	19.0	76.1
Total Entry Lander	1270.8	1768.0	1768.0	446.7	2358.0
Spin and Separation	26.0	30.0	30.0	16.3	30.0
ΔV Rocket	97.0	127.0	127.0	46.0	160.0
Adapter and Radiator	56.2	75.0	75.0	16.0	52.0
Total Lander	1450.0	2000.0	2000.0	525.0	2600.0
Lander Suspended	1213.8	1711.0	1711.0	446.7	2213.0

H. Floating Vehicles

A floating vehicle was studied for use on the early Venus missions. This system was proposed as an alternate means of investigating the surface of Venus, while at the same time avoiding the problems associated with ground impact and orientation. Such a vehicle would be supported by a gas filled balloon and hover at some predetermined altitude while photographing the surface of the planet.

Both a cold gas balloon, utilizing Helium, and a hot gas balloon, using Butane and Oxygen, were investigated. An initial study indicated that the cold gas system had weight advantage. The following analysis is based on using a cold gas balloon.

At equilibrium condition, the lift of the balloon equals the total weight of the system.

It can be shown that the total lift equals the mass of the lifting gas times the product of the ratio of the molecular weight of the atmosphere to the lifting gas times the gravity constant on the plant. The total weight must equal the total lift, therefore, the weight

of gas necessary at equilibrium equals:

$$W_g = W_t \frac{\text{Mol Gas}}{\text{Mol A}}$$

Since the molecular weight of the Venusian atmosphere is assumed to be 29.6 and the molecular weight of helium is 4, the weight of gas is

$$W_g = W_t \times \frac{4}{29.6} = .135 W_t$$

The weight of the balloon skin will depend on the volume that the required weight of the will occupy (at temperature and pressure conditions on the planet).

Assuming that the balloon is spherical in shape:

$$W_{\text{Balloon}} = \rho_{\text{skin}} A_{\text{skin}}$$

$$A_{\text{skin}} = 4.84 (V)^{2/3}$$

$$W_{\text{Balloon}} = 0.037 (V)^{2/3}$$

Assume:

$$\rho_{\text{skin}} = 0.00764 \text{ lbs/ft}^2$$

It can also be shown that

$$V = \frac{W_t}{P_a}$$

where

P_a is the pressure of the atmosphere

Thus

$$W_{\text{Balloon}} = 0.037 \left(\frac{W_t}{P_a} \right)^{2/3}$$

Now assuming that the weight of the lines and balloon are equal to the weight of the balloon (conservative), the total lifting system equals:

$$W_{\text{lifting system}} = 0.135 W_t + 2 \left(0.037 \right) \left(\frac{W_t}{P_a} \right)^{2/3}$$

At higher altitudes the balloon becomes heavier than the lifting capability of the helium. This ceiling occurs when the lifting system equals the total system weight (W_t). At this point there is no payload.

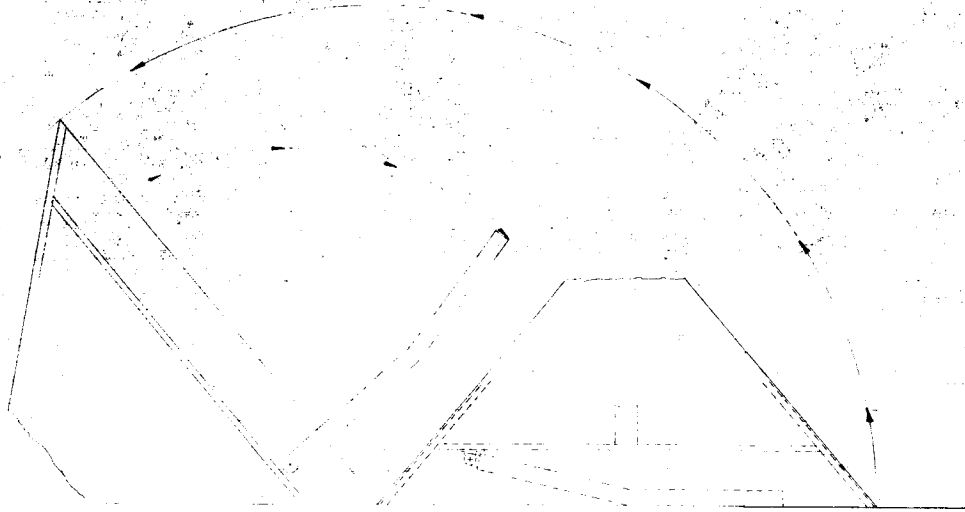
$$0.135 W_t + 0.074 \left(\frac{W_t}{P_a} \right)^{2/3} = W_t$$

$$P_a = \frac{0.00062}{W_t} \text{ lbs/ft}^2$$

For this study it was assumed:

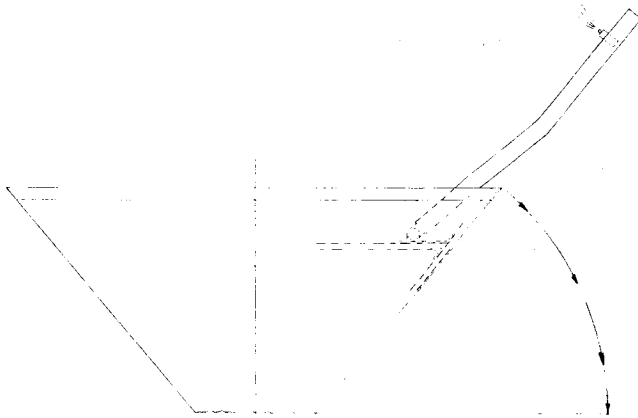
- 1) Vehicle gross weight = 450 lbs.
- 2) Component operating temperature to be maintained at or below 100° F.
- 3) No thermal control system
- 4) Gas bottle is assumed to be dropped along with structure therefore does not appear in the above equation.

Using all the available weight (450 lbs the theoretical limiting case) in the lifting system, the ceiling occurs at 190,000 feet with $T = 569^{\circ}\text{F}$ for the Venus Extreme atmosphere or 170,000 feet with $T = 349^{\circ}\text{F}$ for the Venus Standard Atmosphere. These temperatures are excessive for balloon materials. Considering a more realistic case where a payload is carried, the altitude of hover would decrease with a corresponding increase in ambient temperatures. For this reason, considering state-of-the art materials development, the floater concept was eliminated.



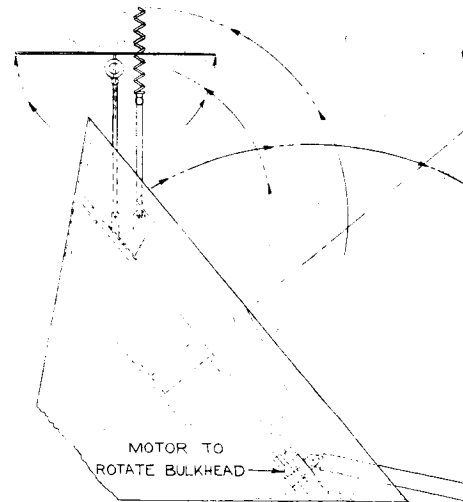
TIP BAR ACTUATES TO TIP VEHICLE FROM BASE
(IF NECESSARY)

B



ROCKET FIRES TO TIP VEHICLE FROM NOSE
(IF NECESSARY)

A



EXPERIMENTS ON TIP BAR & COMMUNICATIONS EQUIPMENT

D

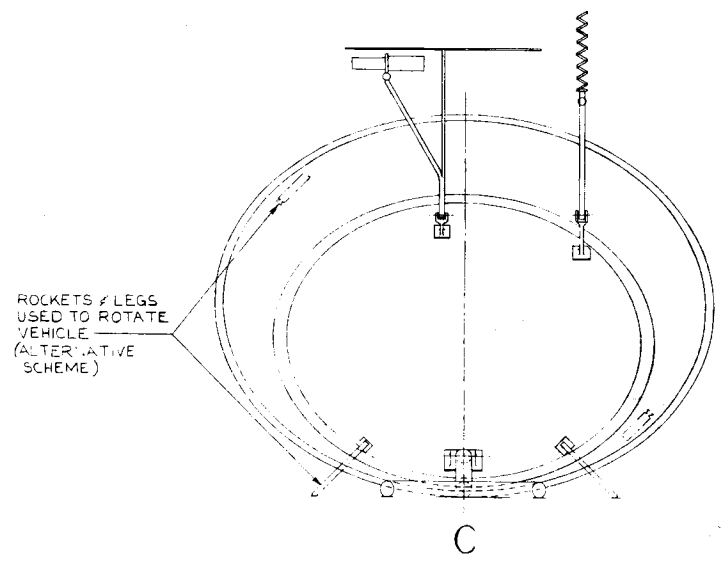
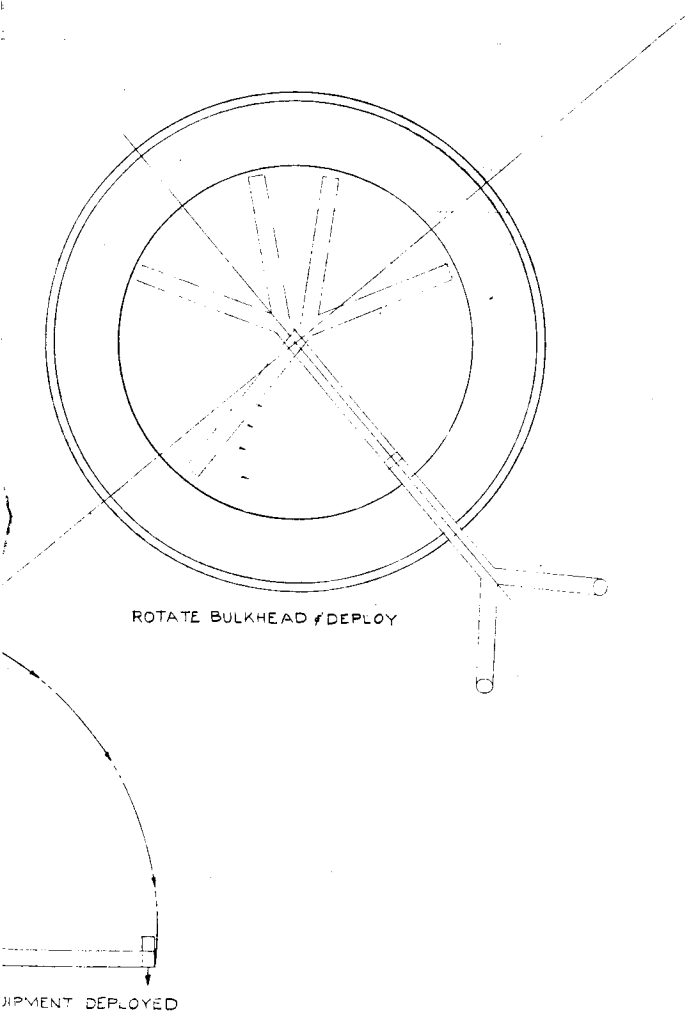
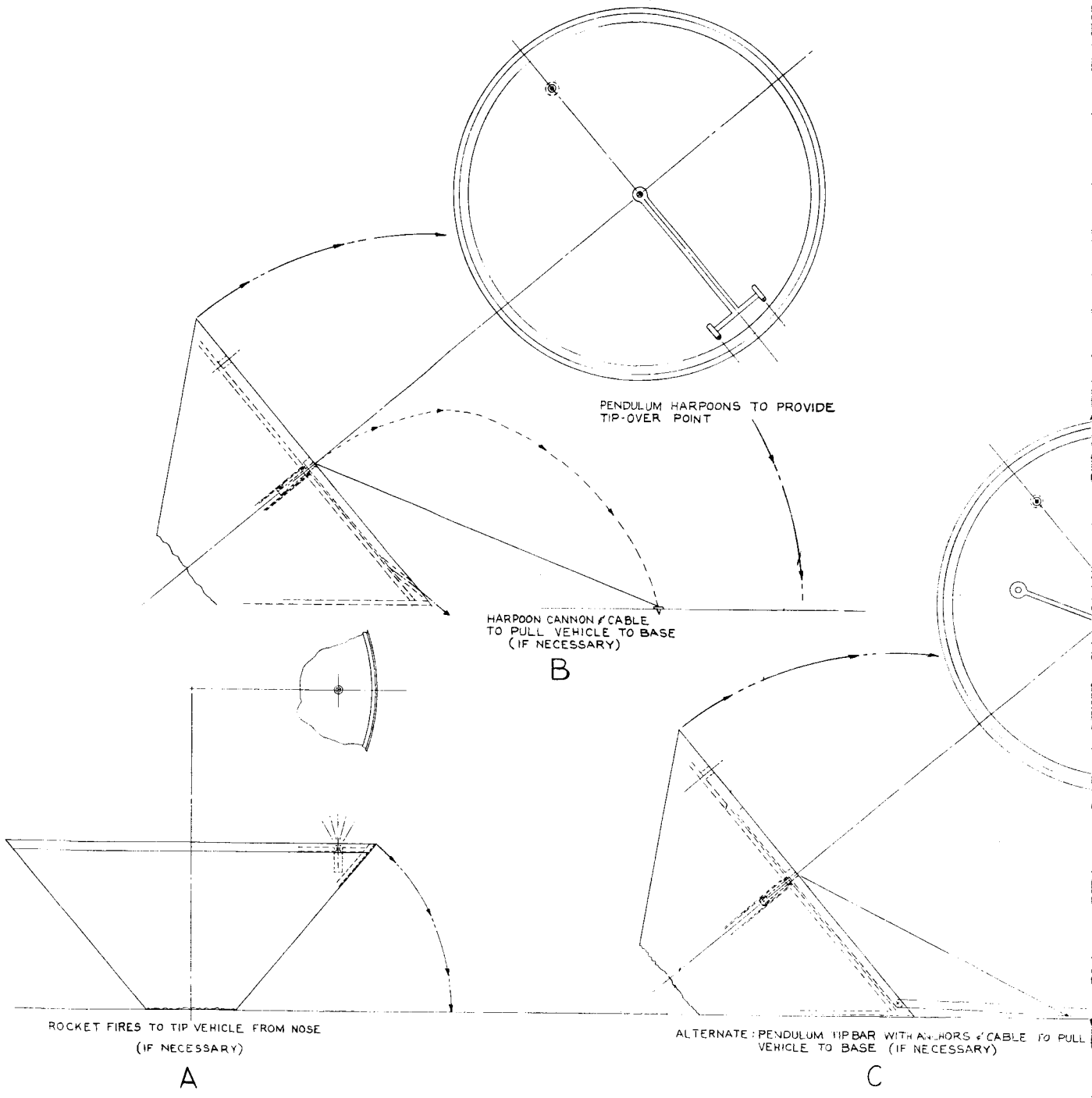


Figure 1.3.9-1. Entry/Lander-Side Orientation Scheme



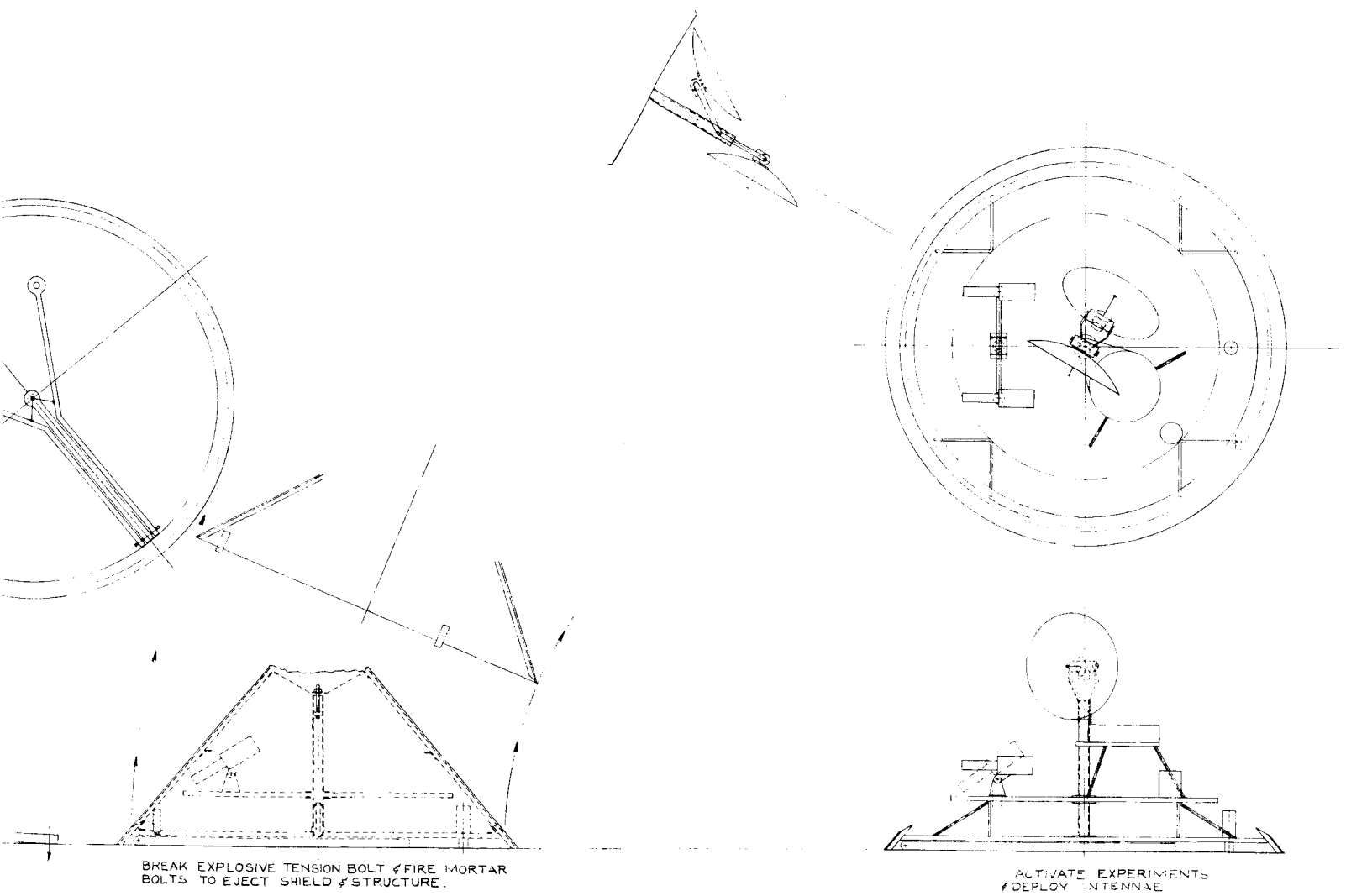


Figure 1.3.9-2. Entry/Lander-Nose-Up Orientation Scheme

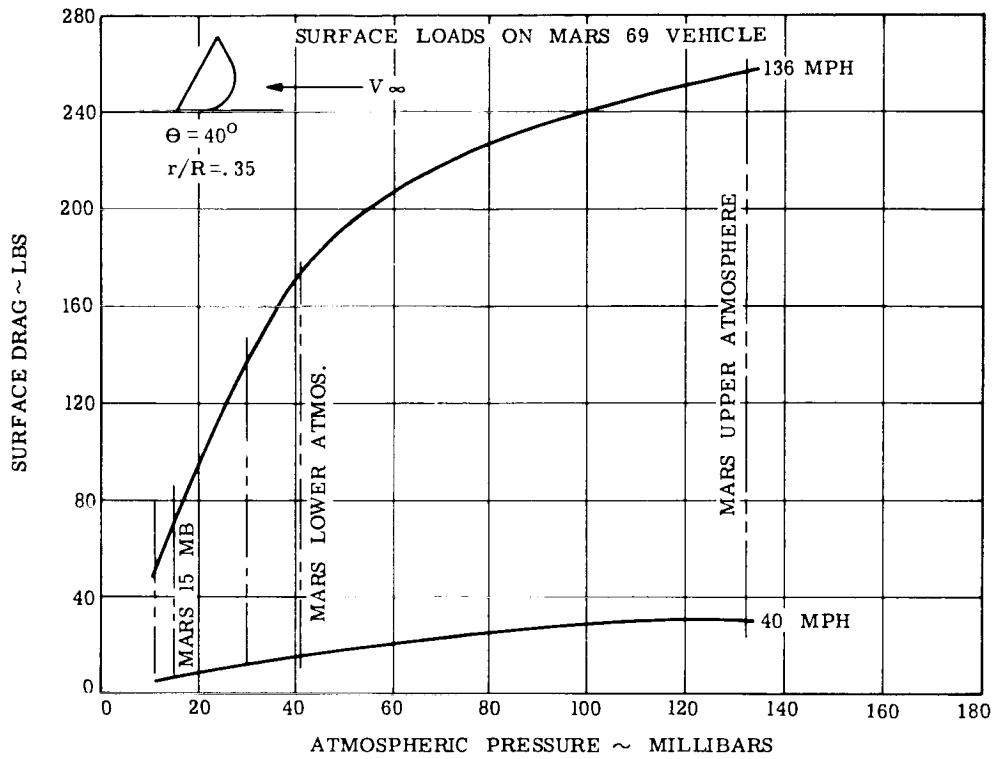


Figure 1.3.9-3. Surface Loads on Mars '69 Vehicle - Nose in Wind

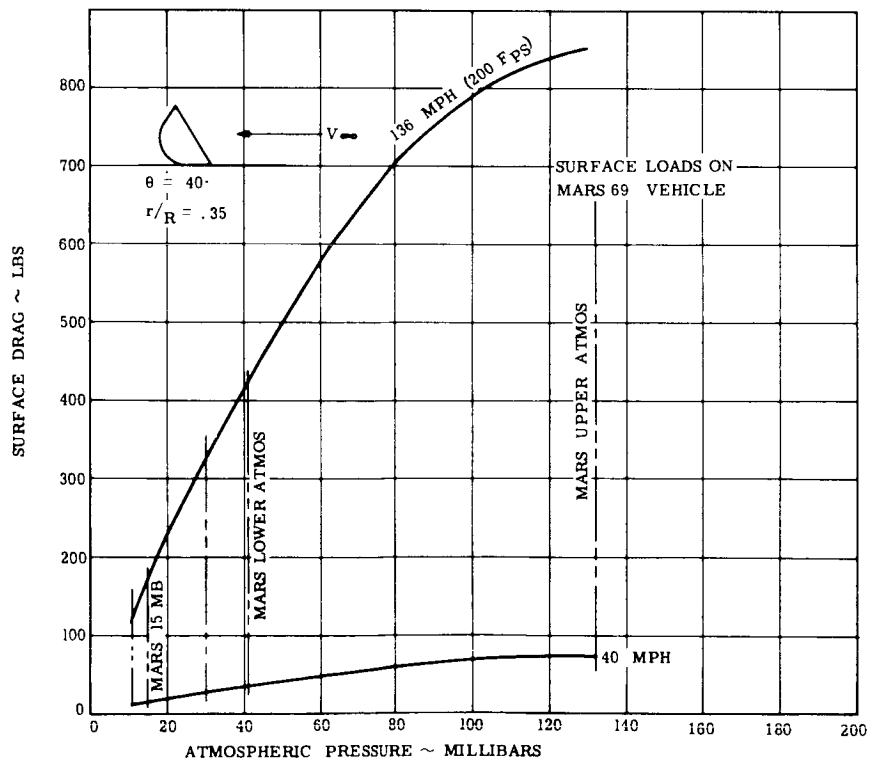


Figure 1.3.9-4. Surface Loads on Mars '69 Vehicle - Base in Wind

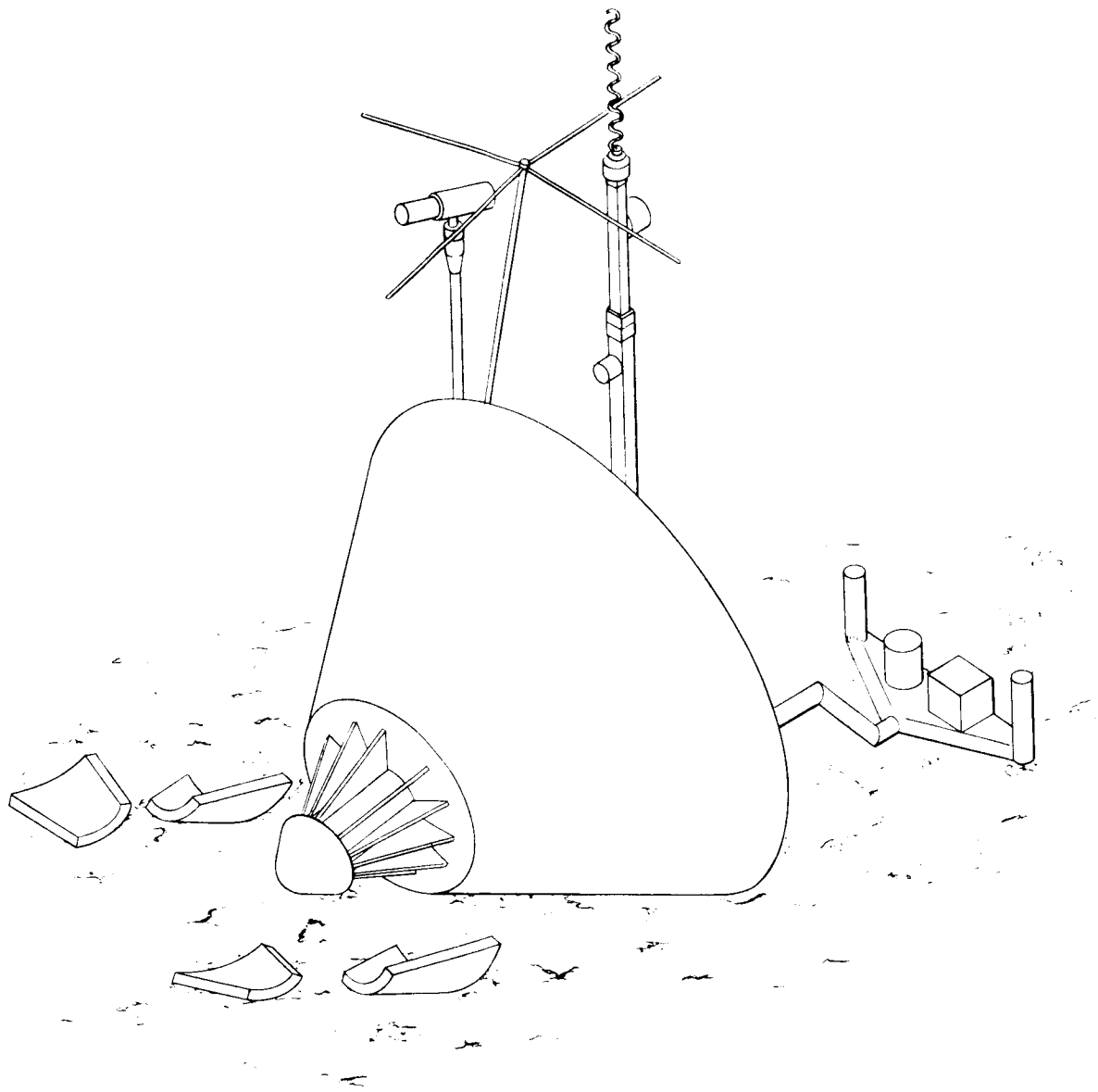
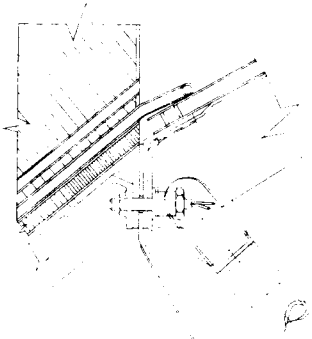
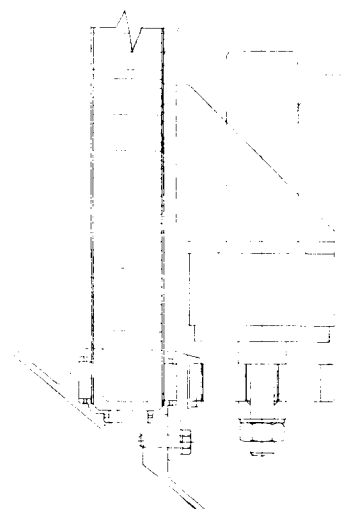


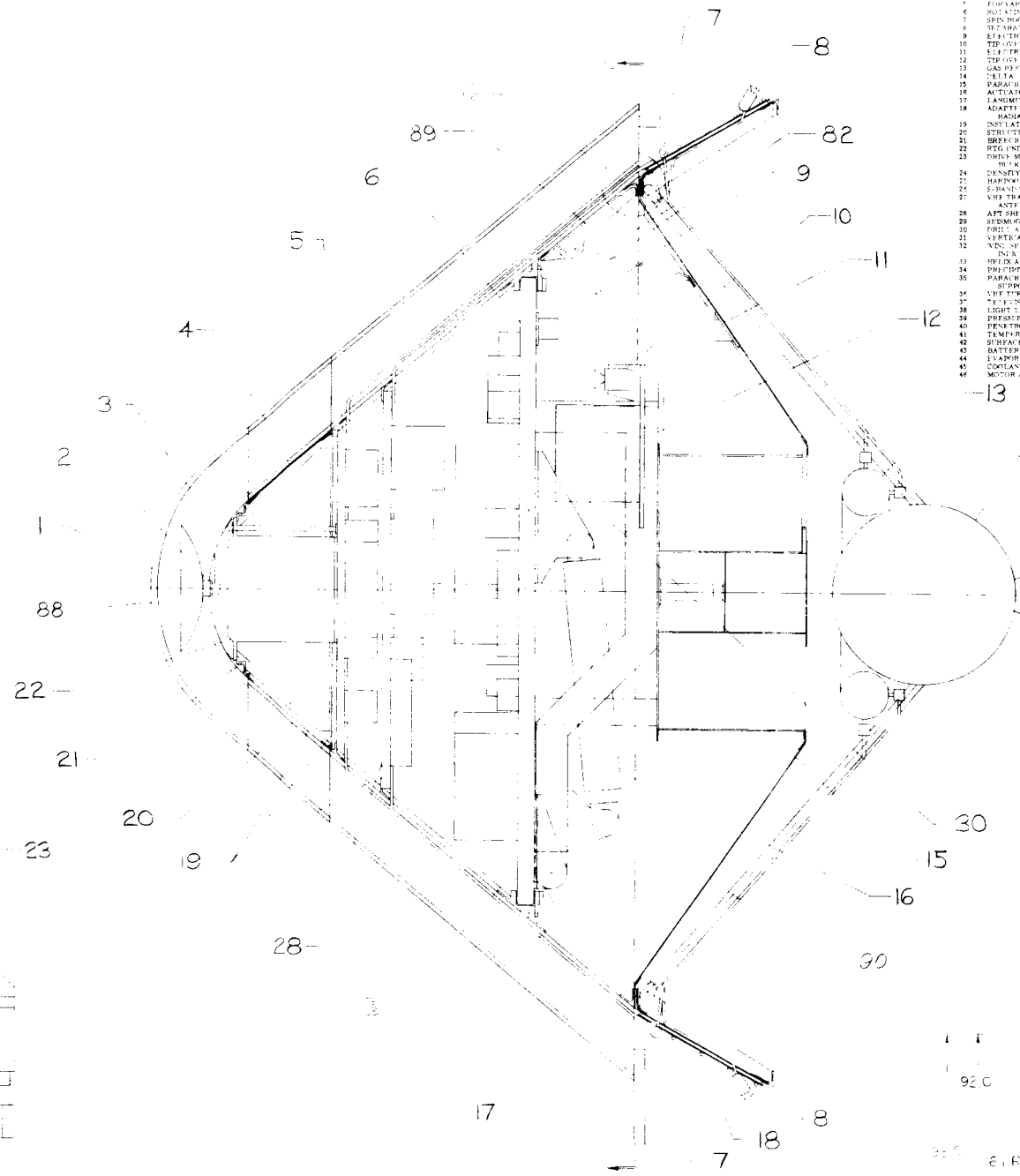
Figure 1.3.9-5. Mars Vehicle Oriented and Deployed



DETAIL C



DETAIL B



ITEM	DESCRIPTION
1	HEAD SHIELD
2	HEADREST
3	FRONT SEAT
4	FRONT SEAT
5	FRONT SEAT
6	FRONT SEAT
7	FRONT SEAT
8	FRONT SEAT
9	FRONT SEAT
10	FRONT SEAT
11	FRONT SEAT
12	FRONT SEAT
13	FRONT SEAT
14	FRONT SEAT
15	FRONT SEAT
16	FRONT SEAT
17	FRONT SEAT
18	FRONT SEAT
19	FRONT SEAT
20	FRONT SEAT
21	FRONT SEAT
22	FRONT SEAT
23	FRONT SEAT
24	FRONT SEAT
25	FRONT SEAT
26	FRONT SEAT
27	FRONT SEAT
28	FRONT SEAT
29	FRONT SEAT
30	FRONT SEAT
31	FRONT SEAT
32	FRONT SEAT
33	FRONT SEAT
34	FRONT SEAT
35	FRONT SEAT
36	FRONT SEAT
37	FRONT SEAT
38	FRONT SEAT
39	FRONT SEAT
40	FRONT SEAT
41	FRONT SEAT
42	FRONT SEAT
43	FRONT SEAT
44	FRONT SEAT
45	FRONT SEAT
46	FRONT SEAT

92 C

61 B

ITEM	DESCRIPTION
41	BATTERY
42	WATER
43	RADAR DREAMPHESTER
44	TELEVISION ELECTRONICS
45	VIDEO VOLTAGE POWER SUPPLY
46	POWER CONTROL AND CONVERTER UNIT
47	PROGRAMMER
48	AMPLIFICATION CONVERTER
49	RADAR RECEIVER
50	RADAR SIGNAL DATA CONVERSION
51	ACTUATOR
52	TELEVISION ELECTRONICS
53	DATA HANDLING PROCESSOR
54	MODULATION VALVE
55	LIQUID HEAT EXCHANGER
56	TEMPERATURE CONTROL
57	MODULATION VALVE
58	REFRIGERATION UNIT
59	MULTIPLE CHAMBER GROWTH DETECTOR
60	TELEVISION ELECTRONICS
61	SOIL MOISTURE
62	MICROSCOPIC ANALYSIS WITH TV
63	REFLECTOR
64	COMMAND DEMODULATOR
65	TURBIDITY AND PH-GROWTH DETECTOR
66	ELECTRON
67	S-BAND DUPLEXER
68	VHF DUPLEXER
69	S-BAND TRANSMITTER
70	COMMAND DEMODULATOR
71	VHF TRANSMITTER
72	TV BOX
73	VHF TRANSMITTERS IN ANTENNA TOWER
74	MASS SPECTROMETER
75	PARABOLIC LENS
76	RADAR ELECTRONICS
77	STRIFE GRAVITY
78	RADIOISOTOPE GROWTH DETECTOR
79	GAS CHROMATOGRAPH
80	LANDING PROBE ELECTRONICS
81	REMOVABLE NESE CAP
82	PARABOLIC FITTING 4
83	AFT COVER

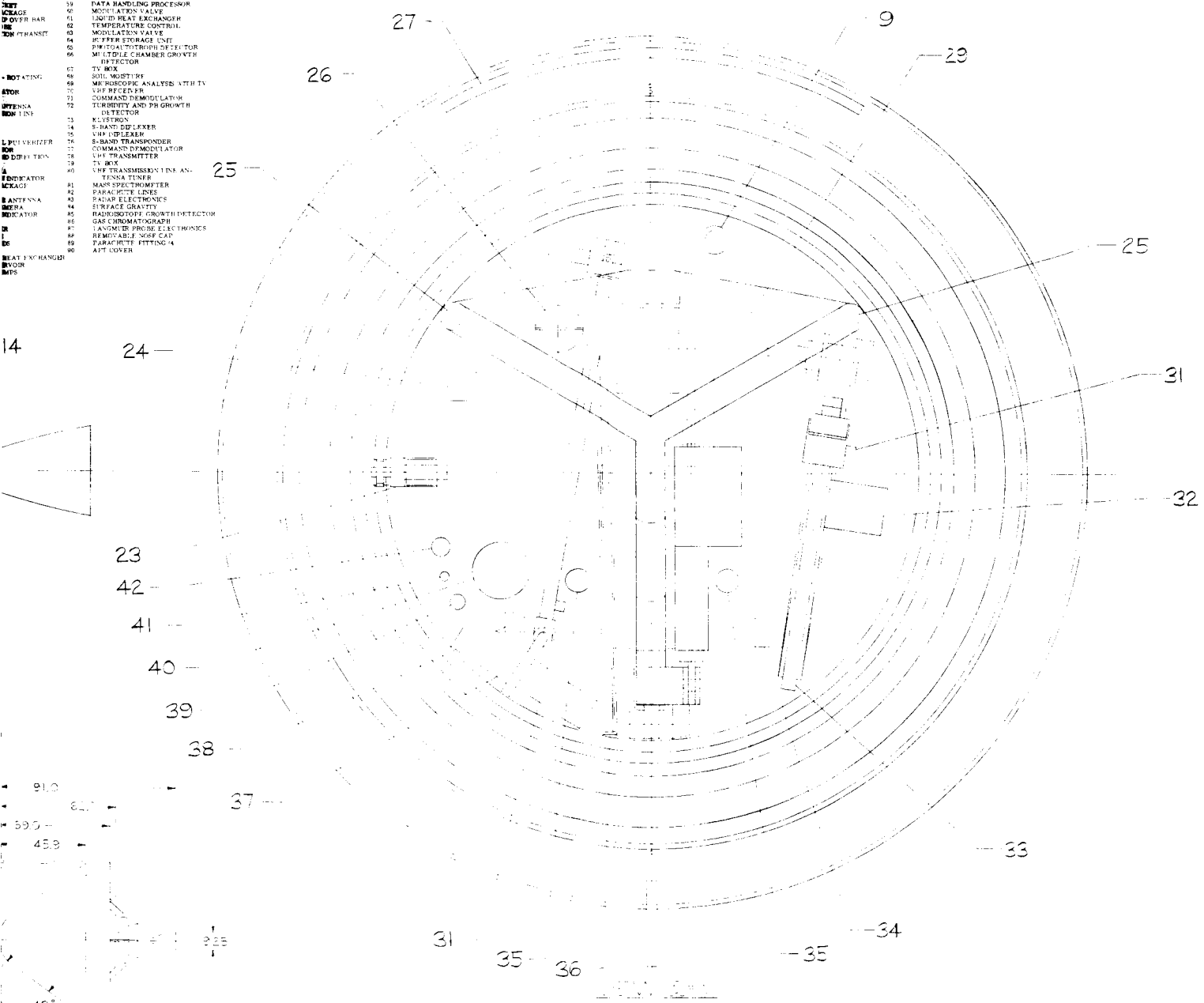
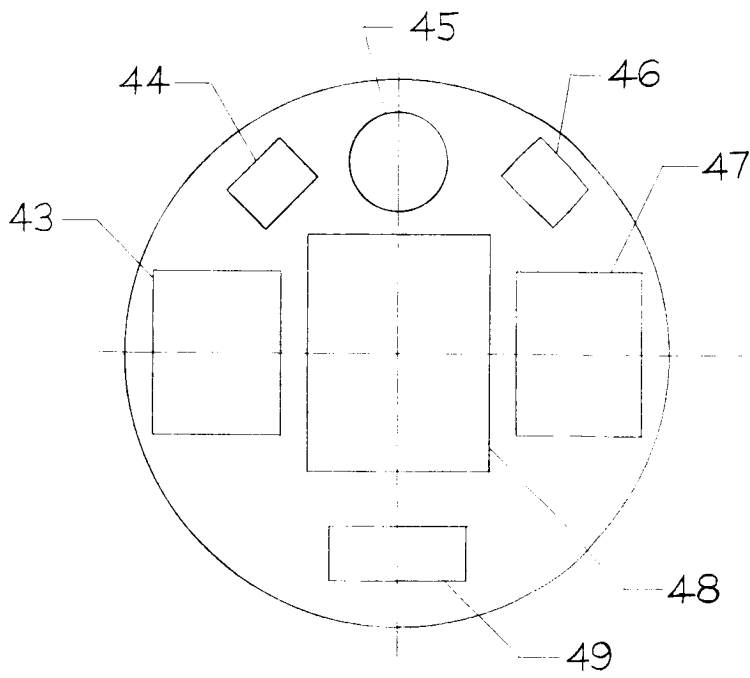
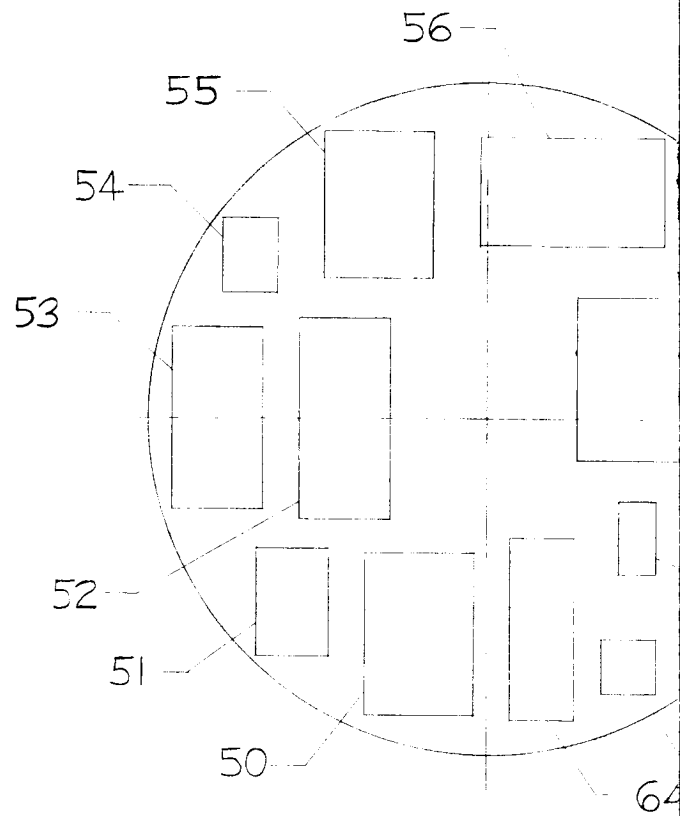


Figure 1.3.9-6. Mars 1969 Entry/Lander



VIEW LOOKING FORWARD
AT FORWARD SHELF



VIEW LOOKING FORWARD
AT AFT SHELF

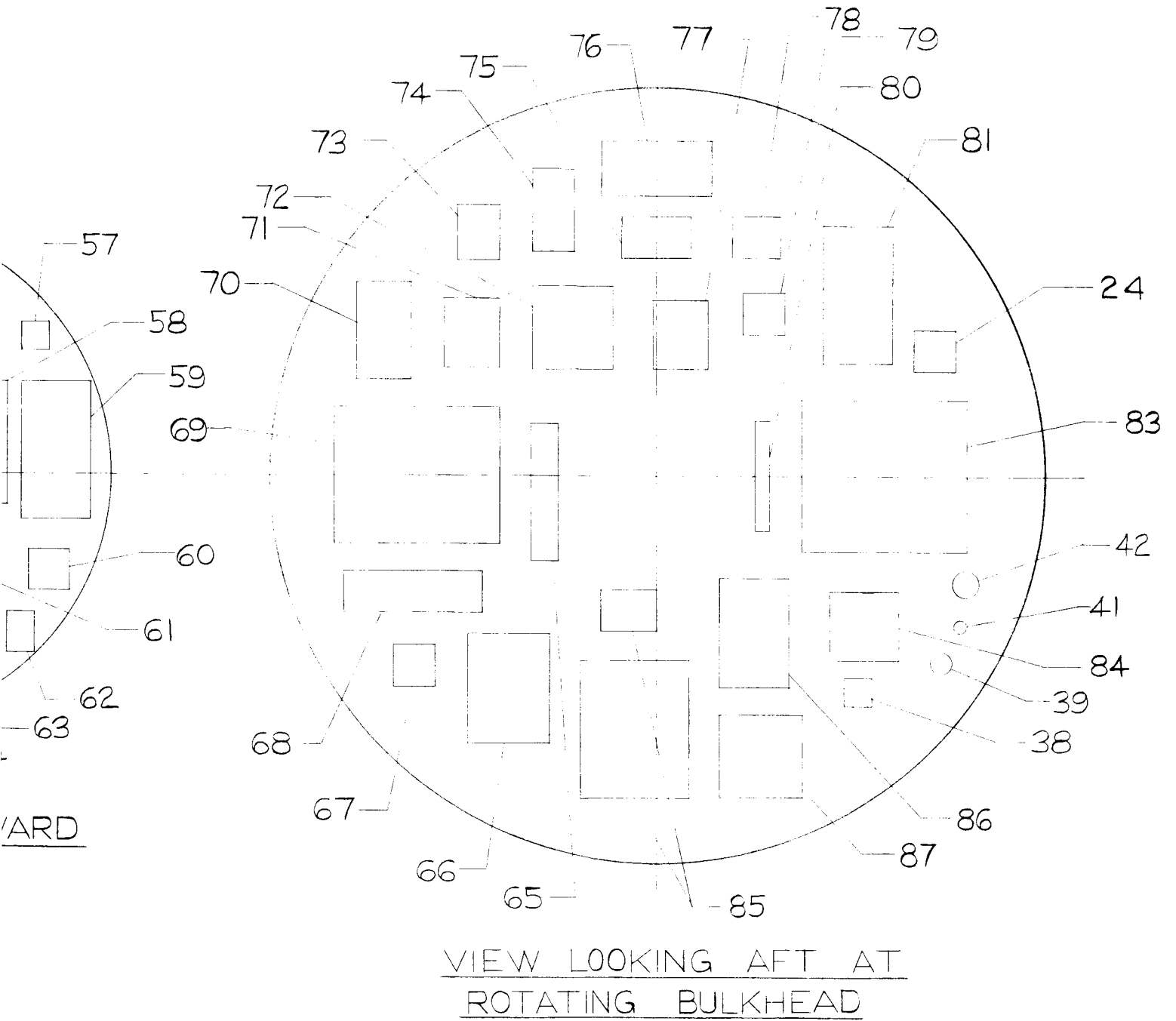
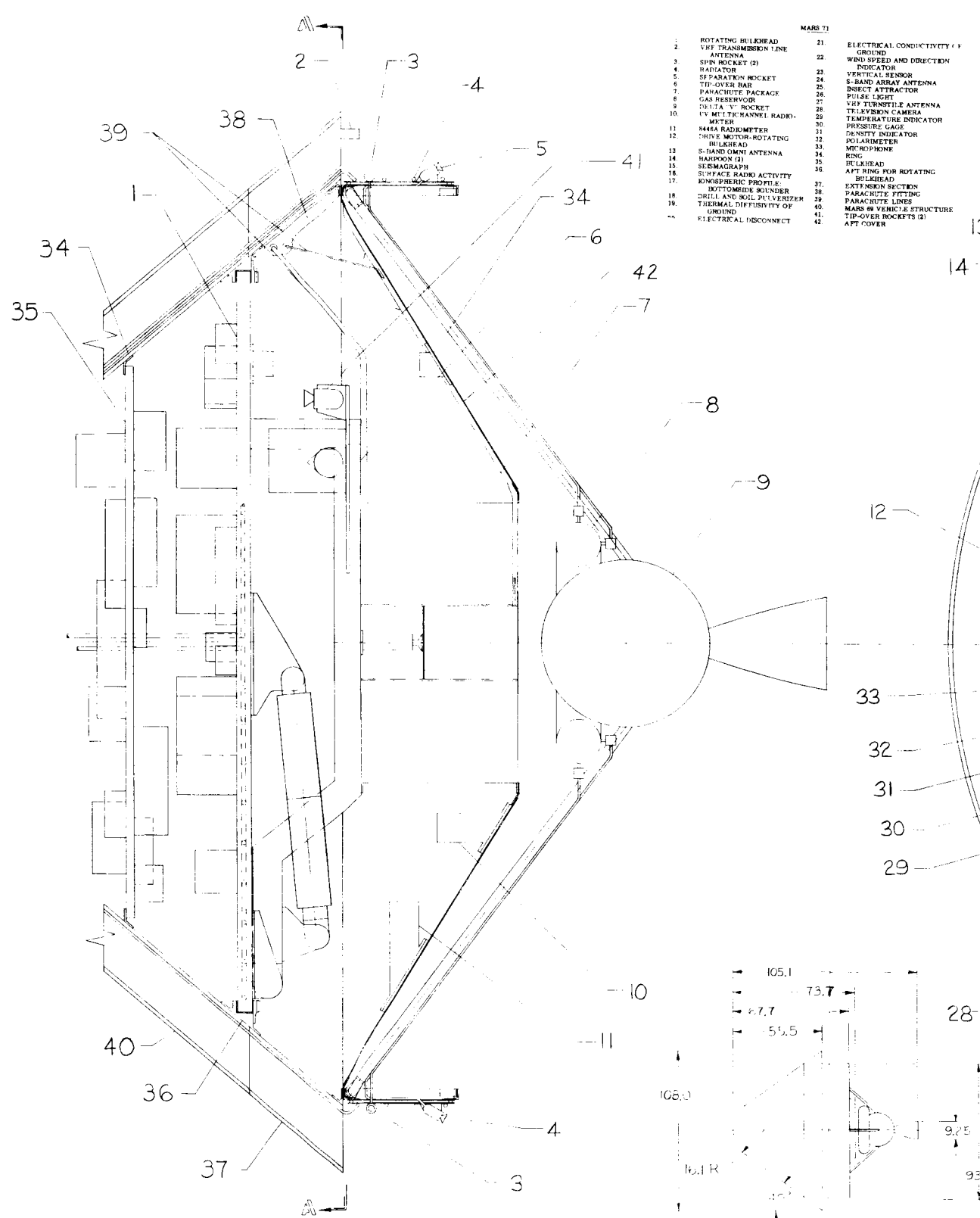
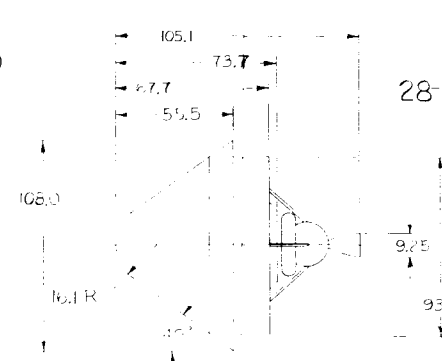


Figure 1.3.9-6. Mars 1969 Entry/Lander(Cont'd)



MARS 71

1	ROTATING BULKHEAD	21	ELECTRICAL CONDUCTIVITY OF
2	VHF TRANSMISSION LINE	22	GROUND
3	ANTENNA	23	INDICATOR
4	SPIN ROCKET (2)	24	WIND SPEED AND DIRECTION
5	RADIATOR	25	INDICATOR
6	SEPARATION ROCKET	26	VERTICAL SENSOR
7	TIP-OVER BAR	27	S-BAND ARRAY ANTENNA
8	PARACHUTE PACKAGE	28	INSECT ATTRACTOR
9	GAS RESERVOIR	29	PULSE LIGHT
10	DELTA V ROCKET	30	VHF TERNSTILE ANTENNA
11	UV MULTICHANNEL RADIO-	31	TEMPERATURE INDICATOR
12	METER	32	PRESSURE GAGE
13	MARS RADIONOMETER	33	DENSITY INDICATOR
14	CHUCK MOTOR-ROTATING	34	POLARIMETER
15	BULKHEAD	35	MICROPHONE
16	S-BAND OMNI ANTENNA	36	RING
17	HARPOON (2)	37	BULKHEAD
18	SEISMOGRAPH	38	AFT RING FOR ROTATING
19	SURFACE RADIO ACTIVITY	39	BULKHEAD
20	ATMOSPHERIC PROFILE	40	EXTENSION SECTION
21	BOTTOMSIDE SOUNDER	41	PARACHUTE FITTING
22	DRILL AND SOIL PULVERIZER	42	PARACHUTE LINES
23	THERMAL DIFFUSIVITY OF		MARS 66 VEHICLE STRUCTURE
24	GROUND		TIP-OVER ROCKETS (2)
25	ELECTRICAL DISCONNECT		AFT COVER



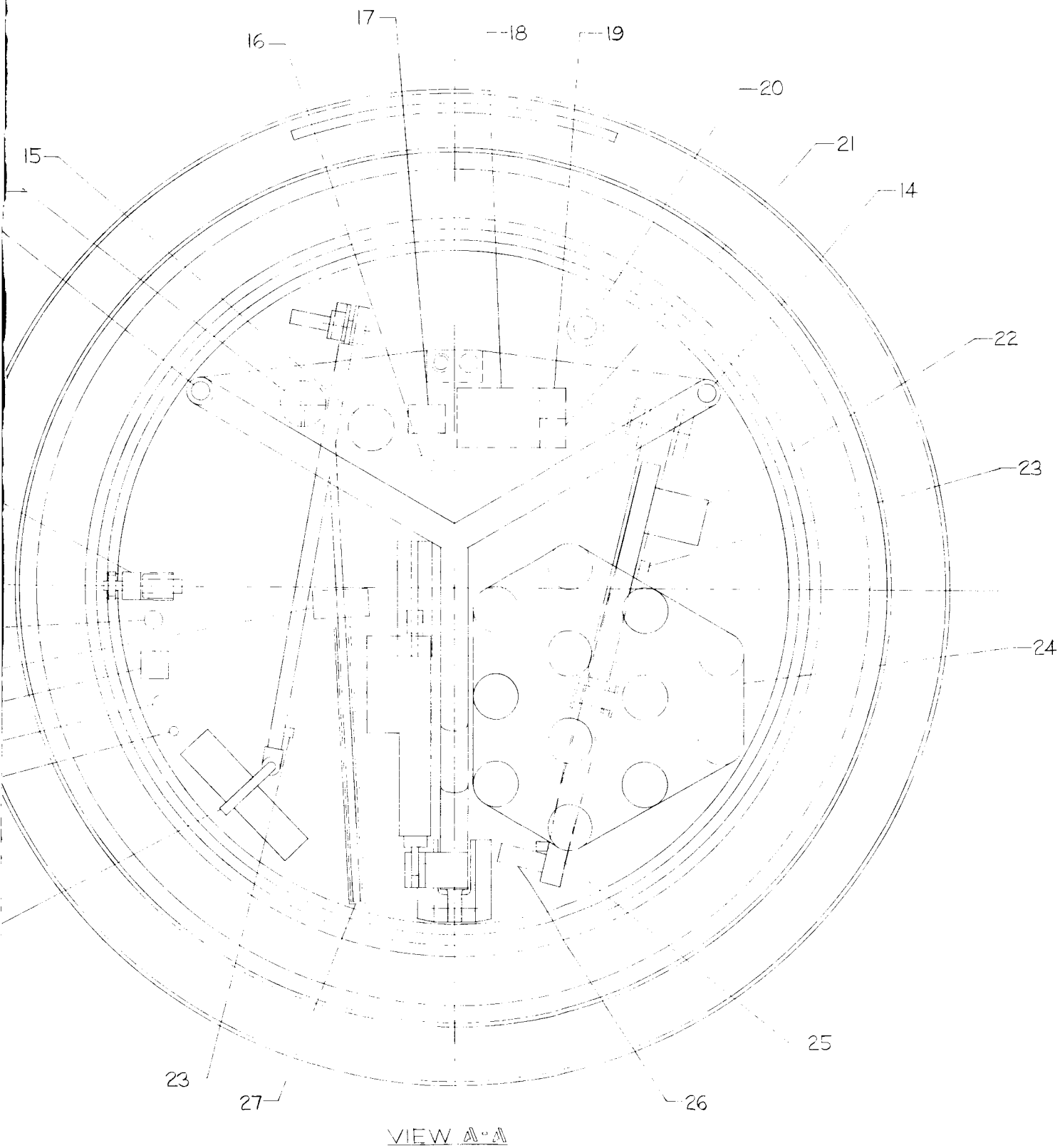
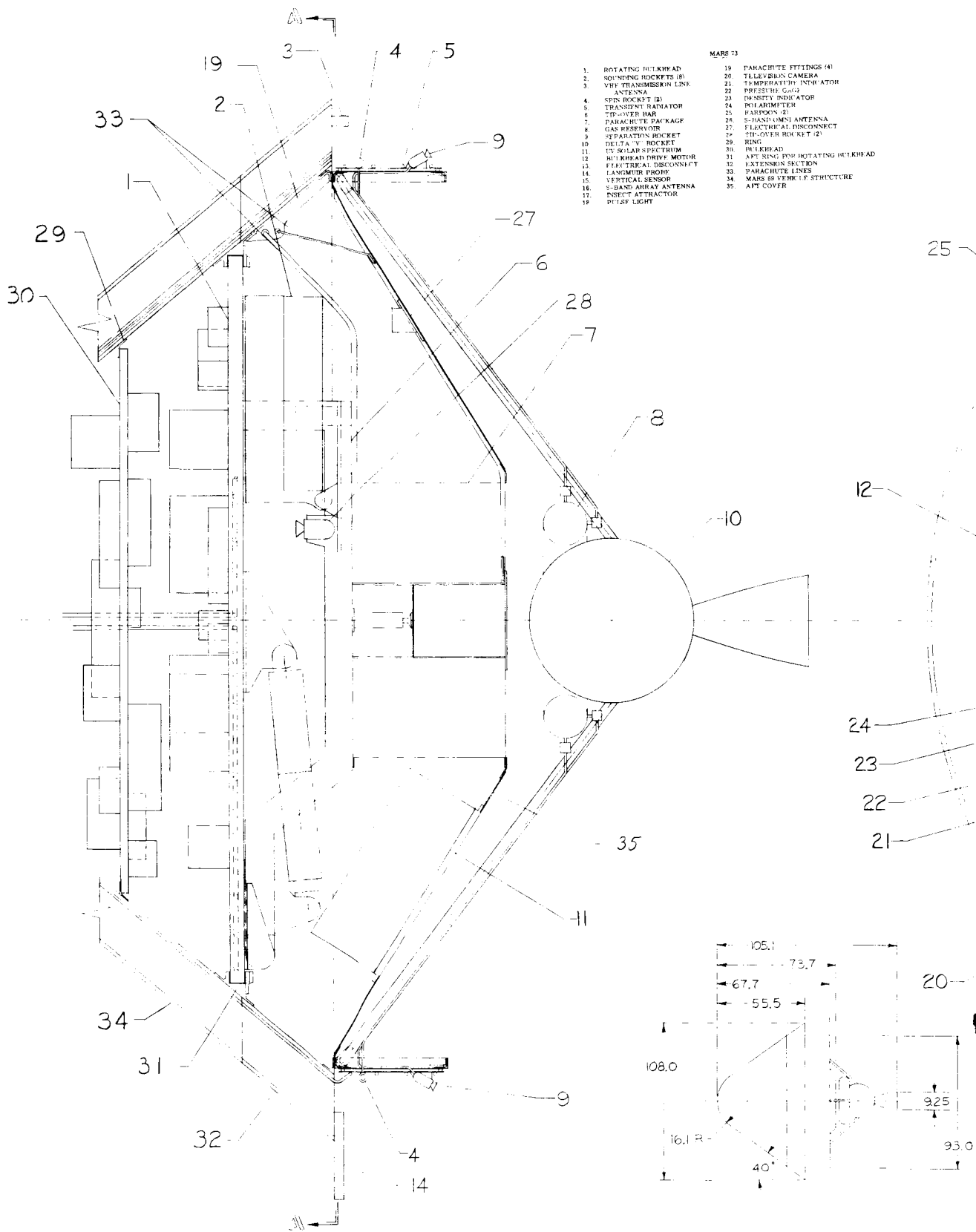


Figure 1.3.9-7. Mars 1971 Entry/Lander



- MARS 73
- | | |
|---------------------------|------------------------------------|
| 1. ROTATING HULKHEAD | 19. PARACHUTE FITTINGS (4) |
| 2. SOUNDING ROCKETS (8) | 20. TELEVISION CAMERA |
| 3. VHF TRANSMISSION LINE | 21. TEMPERATURE INDICATOR |
| 4. ANTENNA | 22. PRESSURE GAUGE |
| 5. SPIN ROCKET (2) | 23. PRESSURE INDICATOR |
| 6. TRANSPARENT BARRIER | 24. BAROMETER |
| 7. TIP-OVER BAR | 25. PARPOON (2) |
| 8. PARACHUTE PACKAGE | 26. S-HAND LUMIN. ANTENNA |
| 9. GAS RESERVOIR | 27. ELECTRICAL DISCONNECT |
| 10. SEPARATION ROCKET | 28. TIP-OVER ROCKET (2) |
| 11. DELTA V ROCKET | 29. RING |
| 12. U.S. SCLAR SPECTRUM | 30. HULKHEAD |
| 13. HULKHEAD DRIVE MOTOR | 31. APT RING FOR ROTATING HULKHEAD |
| 14. ELECTRICAL DISCONNECT | 32. EXTENSION STRUCTURE |
| 15. LANGMUIR PROBE | 33. PARACHUTE LINES |
| 16. VERTICAL SENSOR | 34. MARS 69 VEHICLE STRUCTURE |
| 17. SIDE-ARRAY ANTENNA | 35. APT COVER |
| 18. INSECT ATTRACTOR | |
| 19. PULSE LIGHT | |

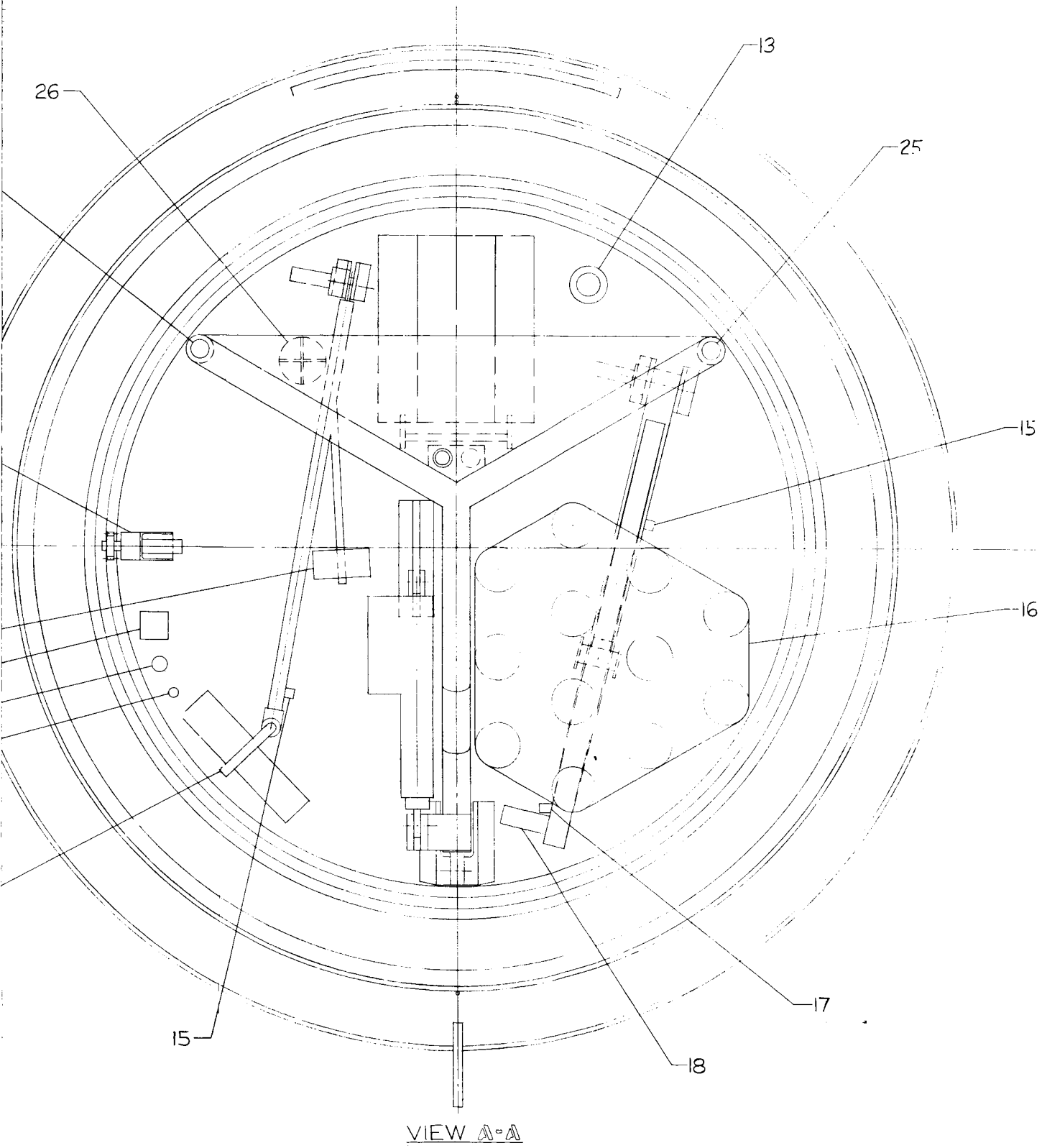
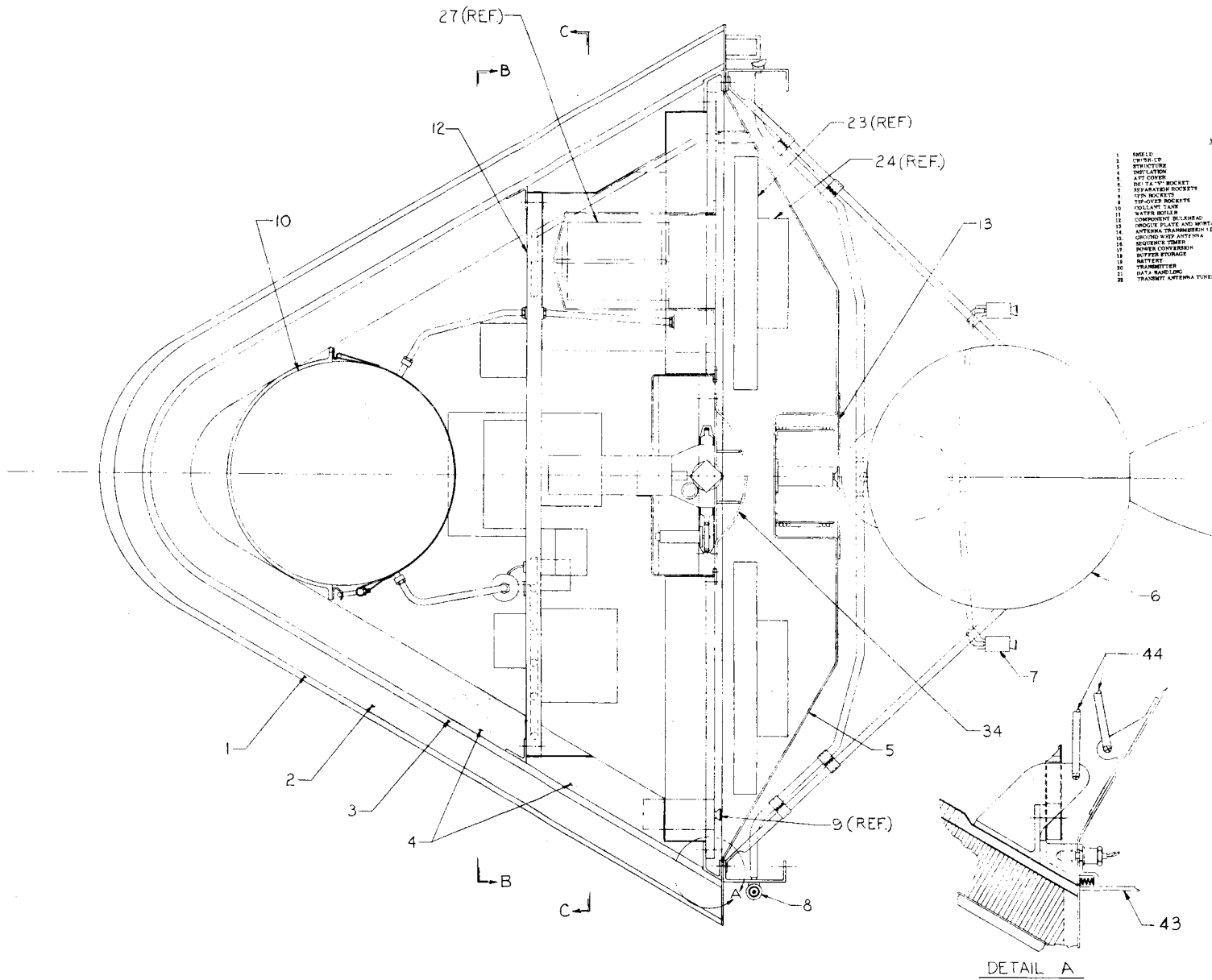


Figure 1.3.9-8. Mars 1973 Entry/Lander



- 1 SHIELD
- 2 CHINESE
- 3 DISPLAY
- 4 ANT COVER
- 5 DELTA "W" SOCKET
- 6 DELTA "W" SOCKET
- 7 DELTA "W" SOCKET
- 8 TIP SOCKET
- 9 TIP SOCKET
- 10 COLLAR TANK
- 11 WATER BULB
- 12 COMMONLY BELIEVED
- 13 CIRCUIT BOARD AND WPTA
- 14 ANTENNA TRANSDUCER
- 15 CIRCUIT BOARD ANTENNA
- 16 RECORDER
- 17 POWER CENTER
- 18 BATTERY STORAGE
- 19 BATTERY
- 20 TRANSMITTER
- 21 DATA HANDLING
- 22 TRACKER ANTENNA TUNER

DETAIL A

1. RADAR ALTIMETER ANTENNA
 2. PRE-AMPLIFIER
 3. ELECTRONIC POWER SUPPLY AND
 MODULATOR
 4. REMOTE DATA CONVERTER
 5. WIND SPEED AND DIRECTION
 ELECTRONICS
 6. CLOUD PROPERTIES
 7. CLOUD PROPERTIES ELECTRONICS
 8. SURFACE SOUND
 9. SURFACE SOUND ELECTRONICS
 10. TELEVISION PACKAGE
 11. TV DATA HANDLING
 12. TV ELECTRONICS
 13. LENSES
 14. TEMPERATURE
 15. PRESSURE
 16. SENSITIVITY AND POLARIZATION OF
 RETURN
 17. SPECIAL COMPONENTS OF
 TELEVISION
 18. ADAPTER SECTION
 19. DRAG PLATE FITTINGS AND LEADS

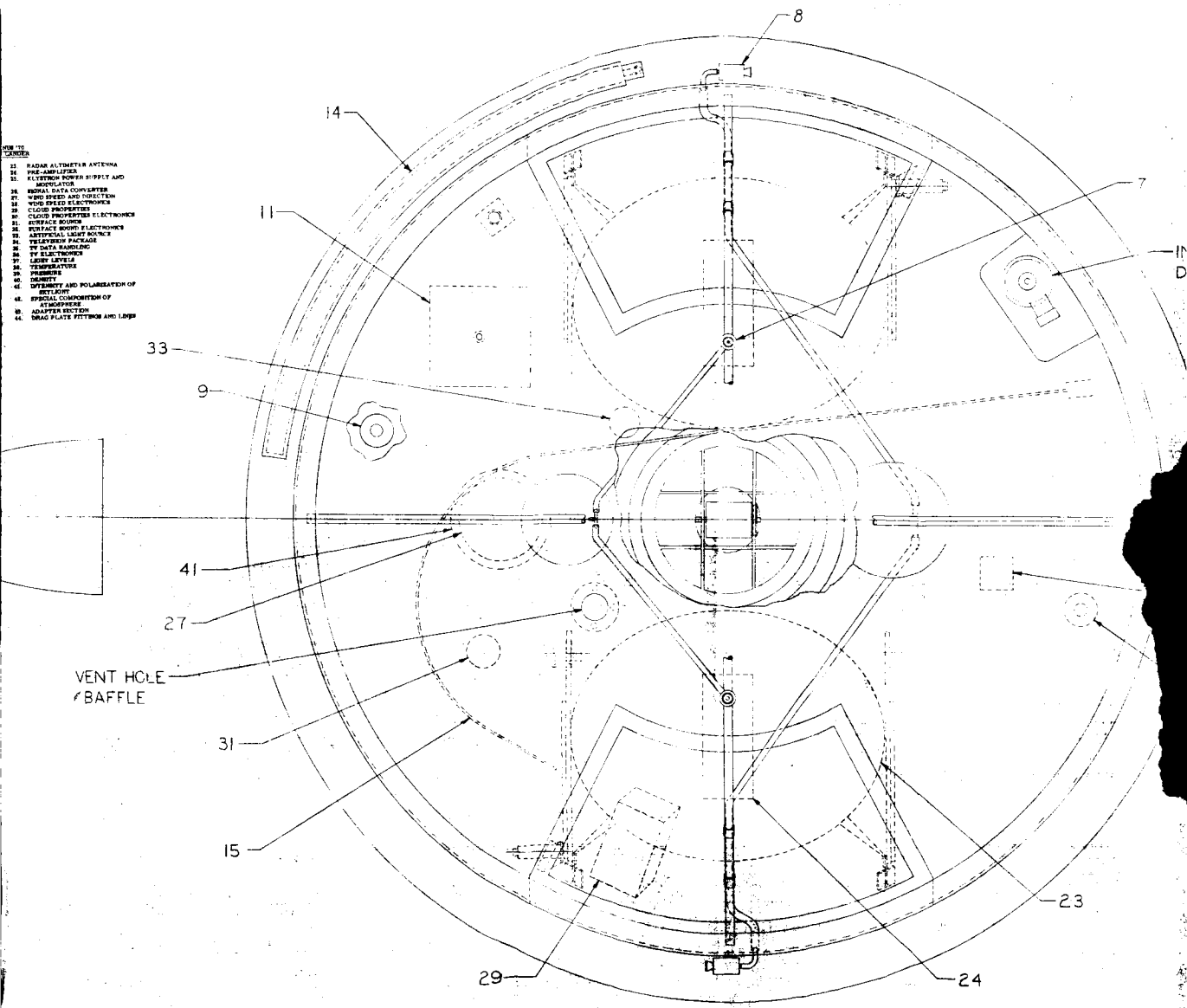
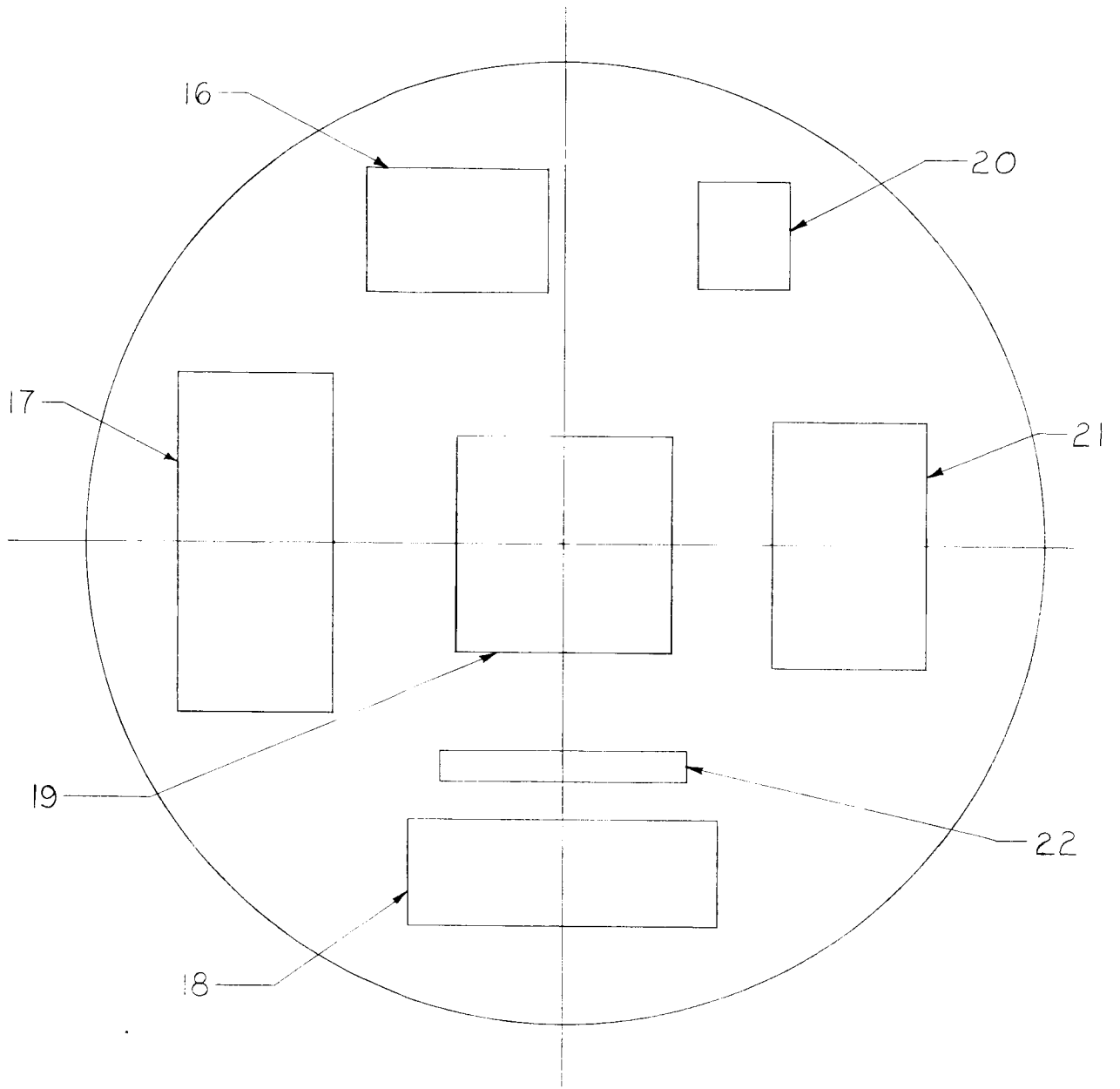


Figure 1.3.9-9. Venus 1970 Entry/Lander



VIEW B-B

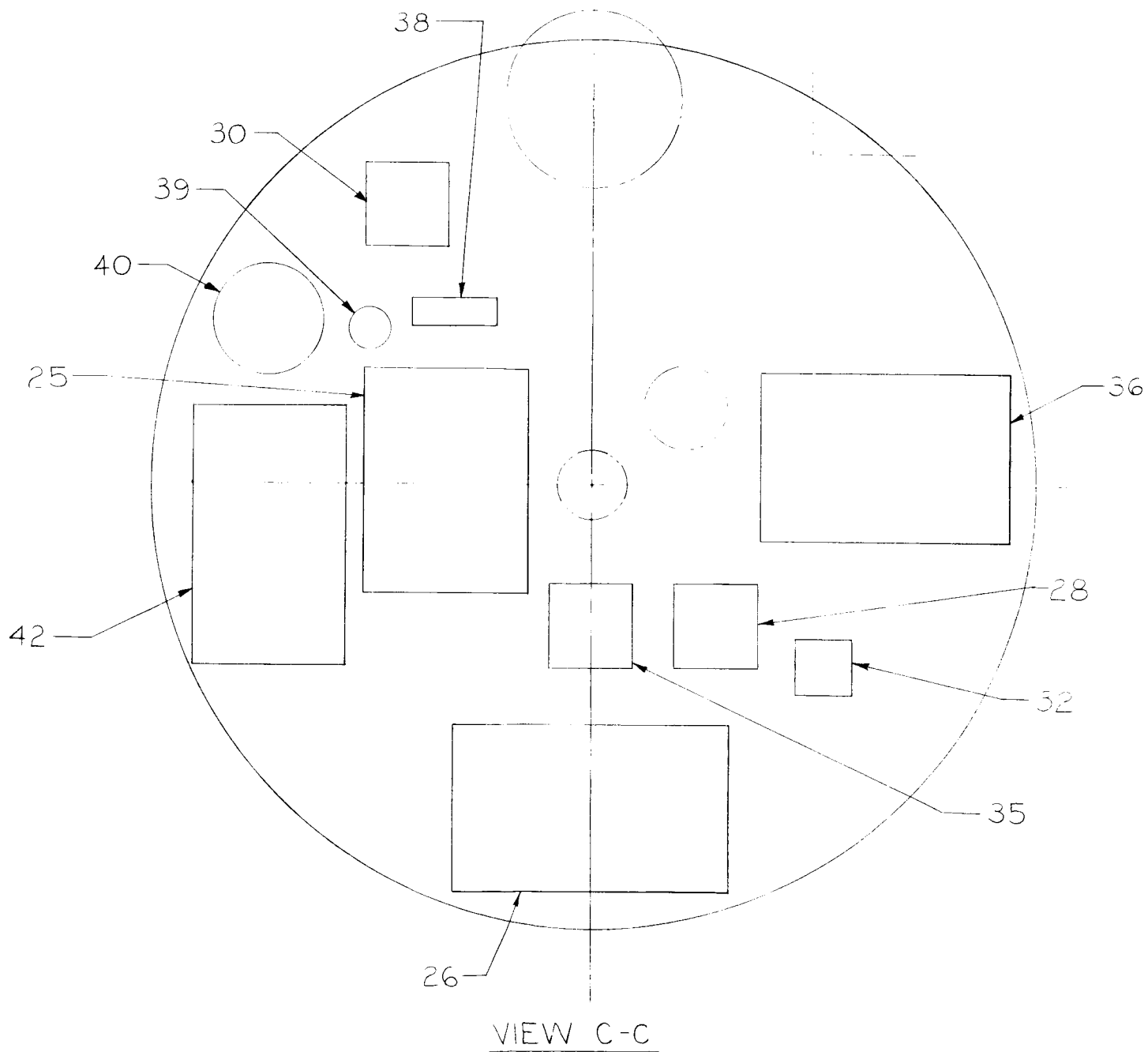


Figure 1.3.9-9. Venus 1970 Entry/Lander(Cont'd)

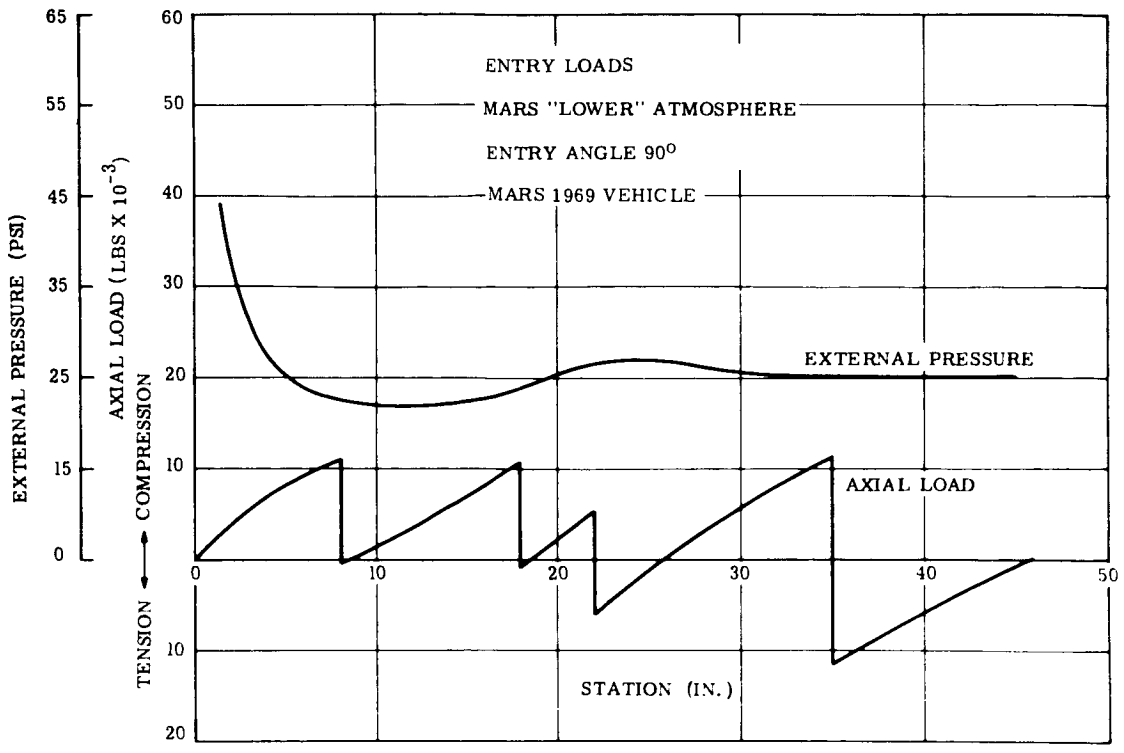


Figure 1.3.9-10. Entry Loads - Mars 1969 Vehicle

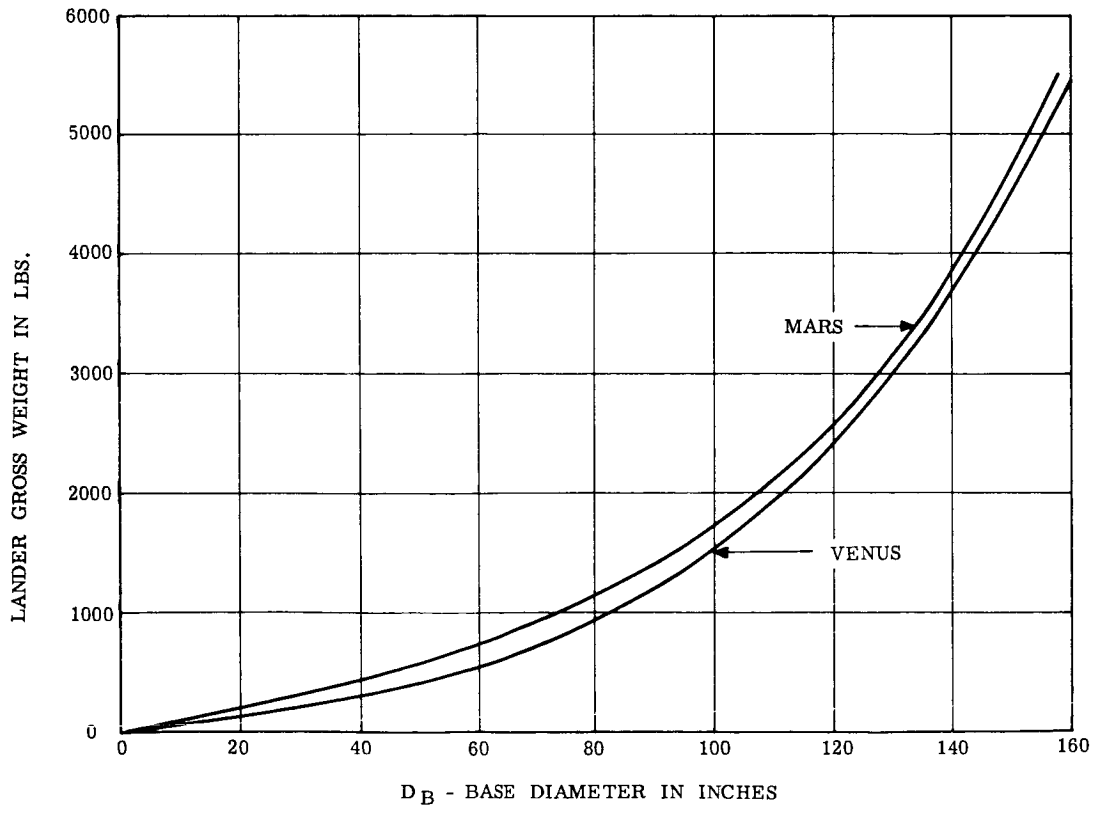


Figure 1.3.9-11. Lander Gross Weight vs. Base Diameter

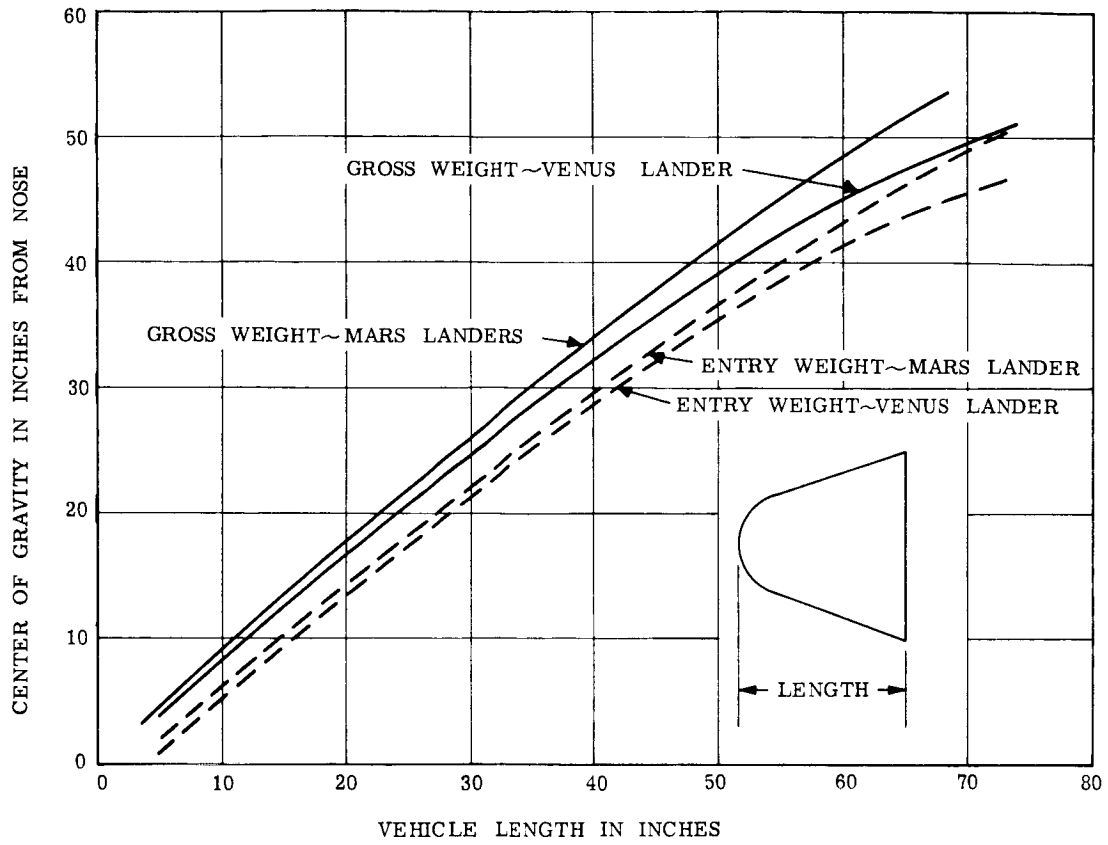


Figure 1.3.9-12. Center of Gravity vs. Vehicle Length

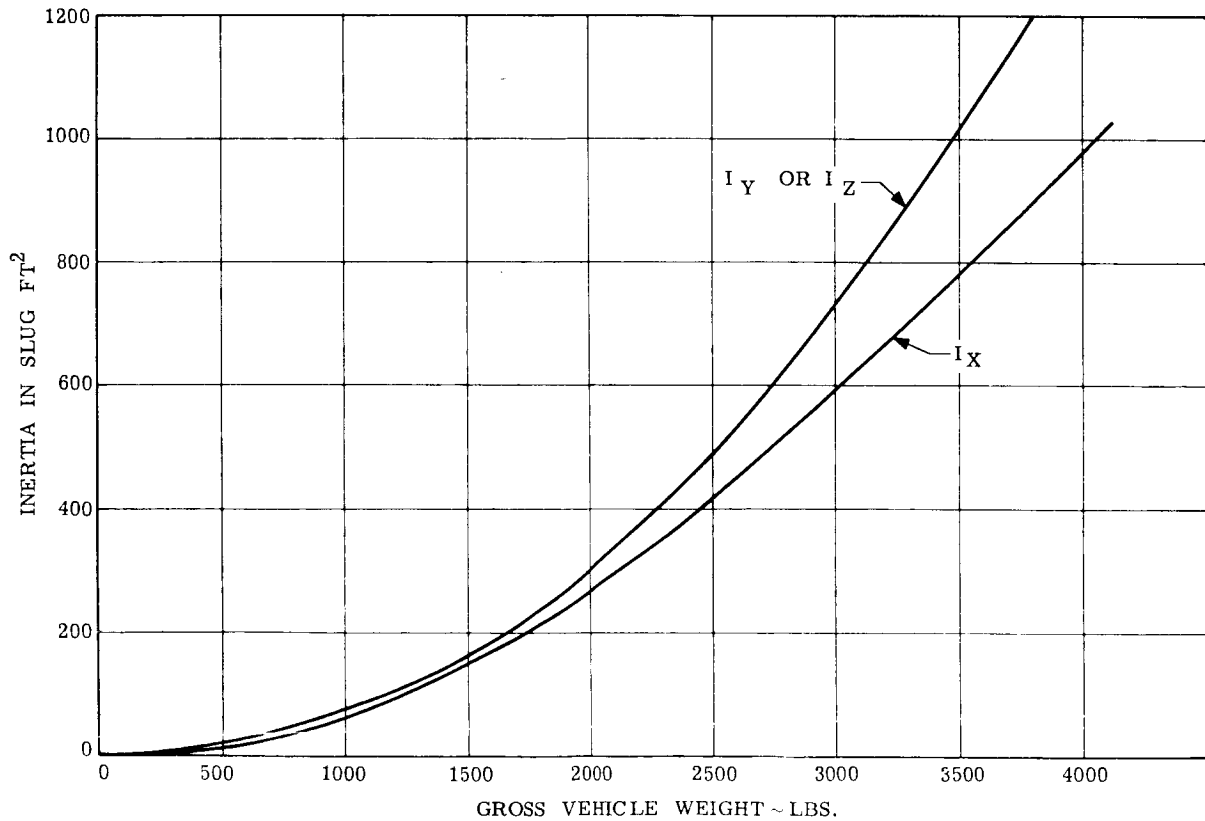


Figure 1.3.9-13. Mars Lander-Vehicle Inertia (Gross Weight Configuration) vs. Gross Weight

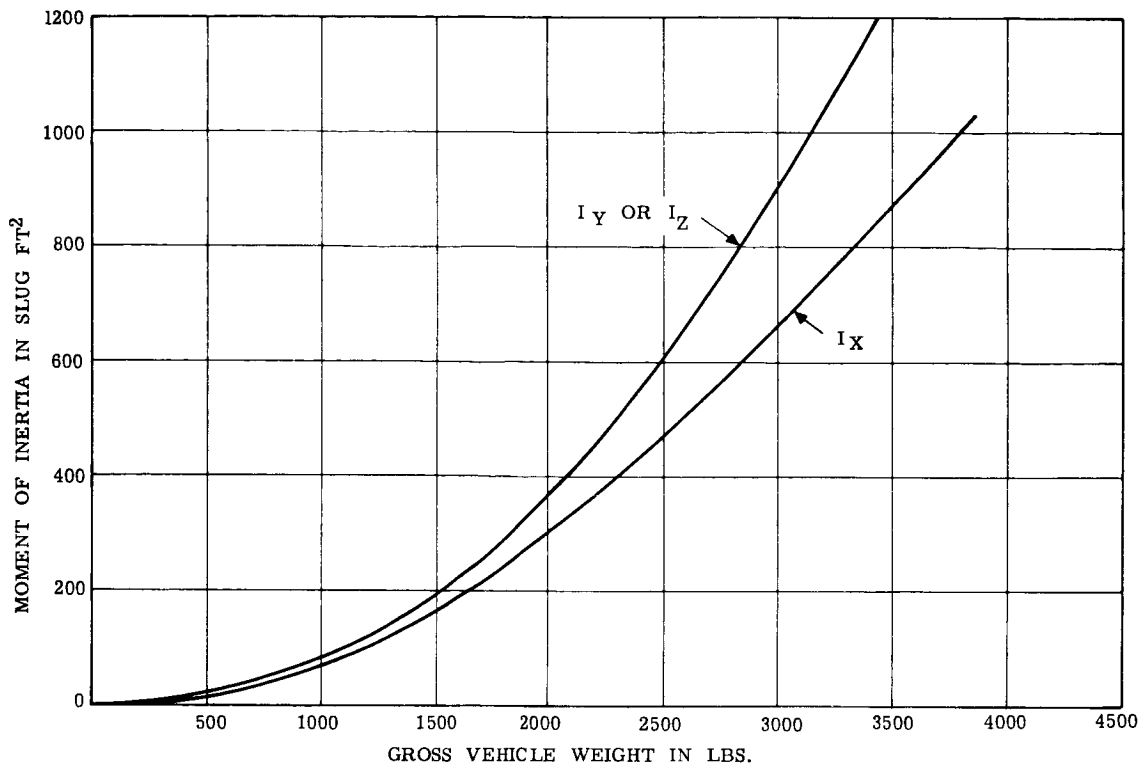


Figure 1.3.9-14 Mars Lander - Vehicle Inertia (Entry Configuration) vs. Gross Weight

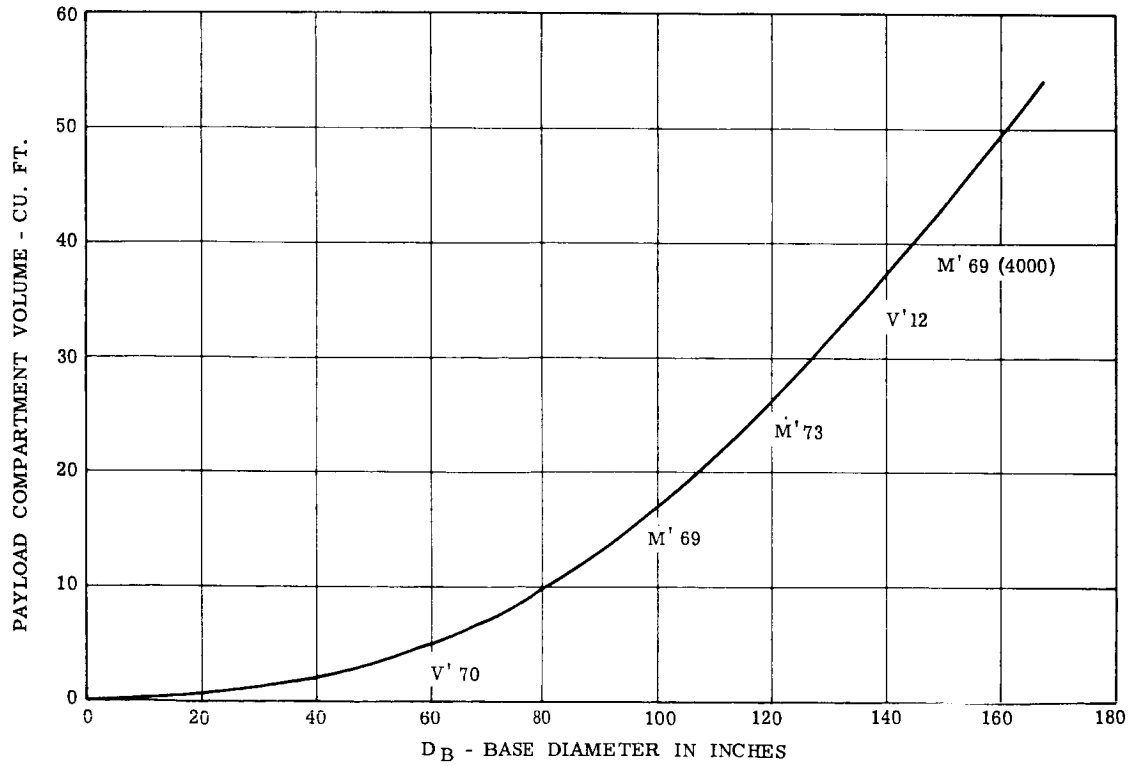


Figure 1.3.9-15 Payload Compartment Volume vs. Base Diameter

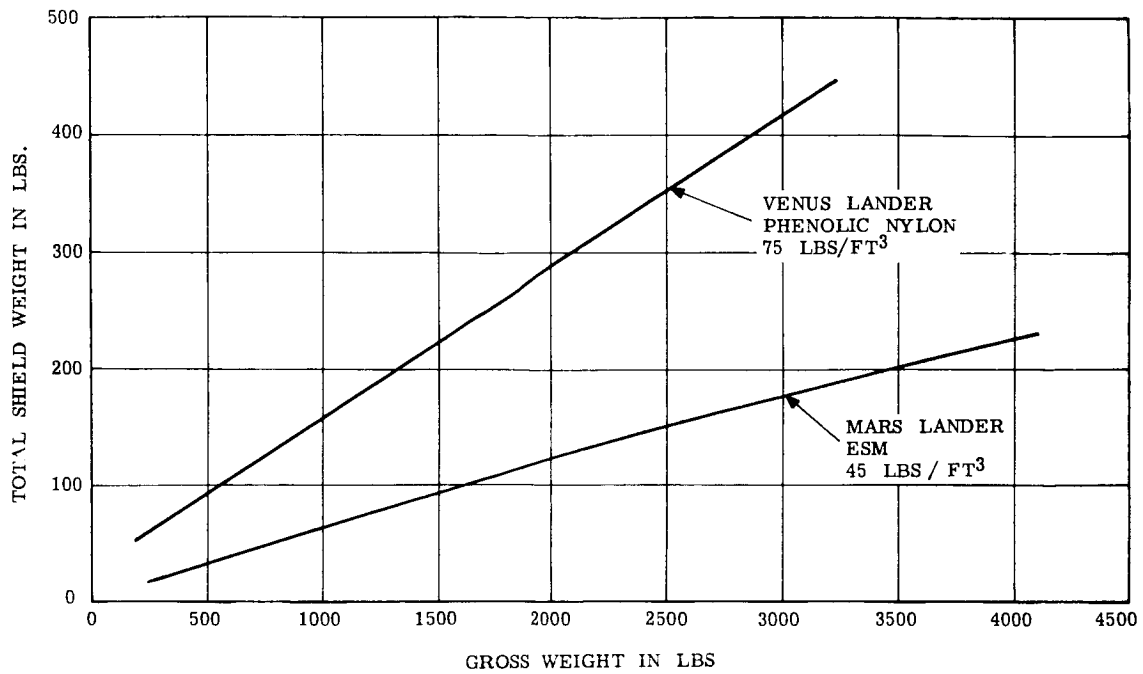


Figure 1.3.9-16. Gross Weight vs. Total Shield Weight

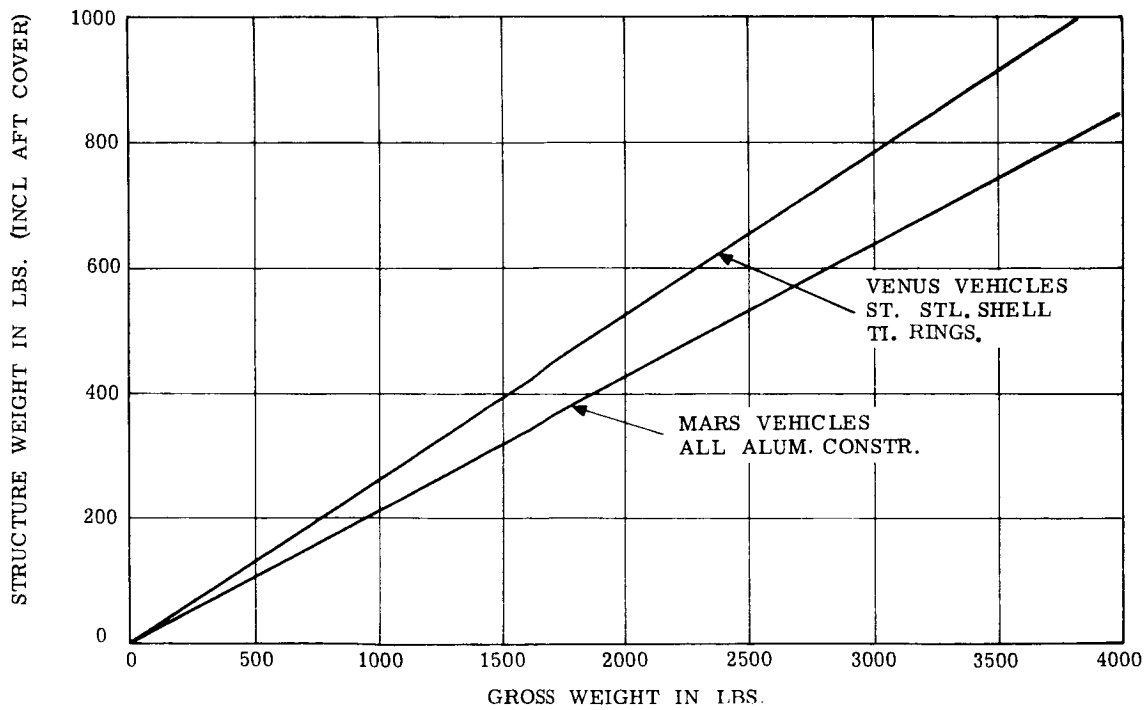


Figure 1.3.9-17. Structural Weight vs. Gross Weight

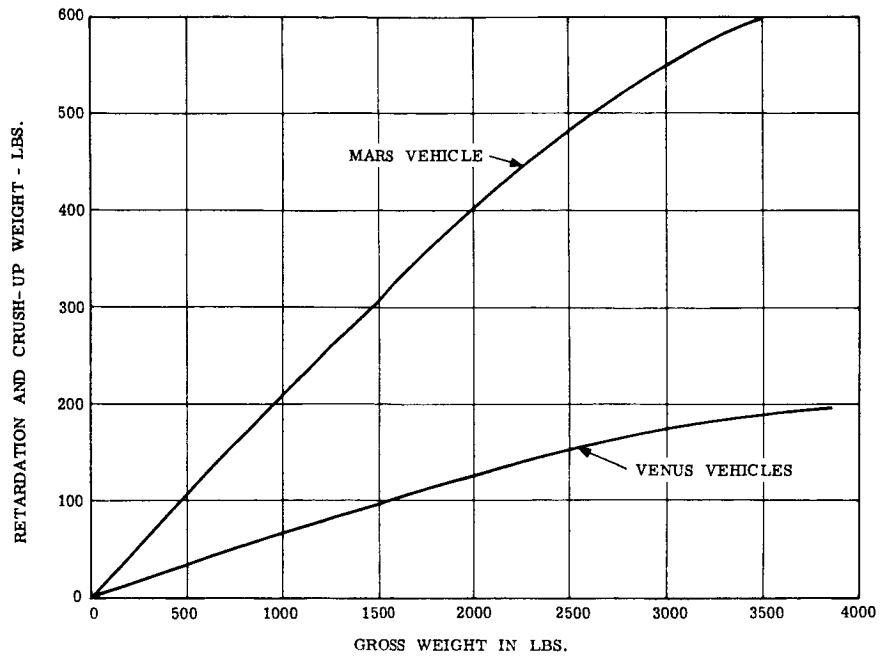


Figure 1.3.9-18 Retardation Weight vs. Gross Weight

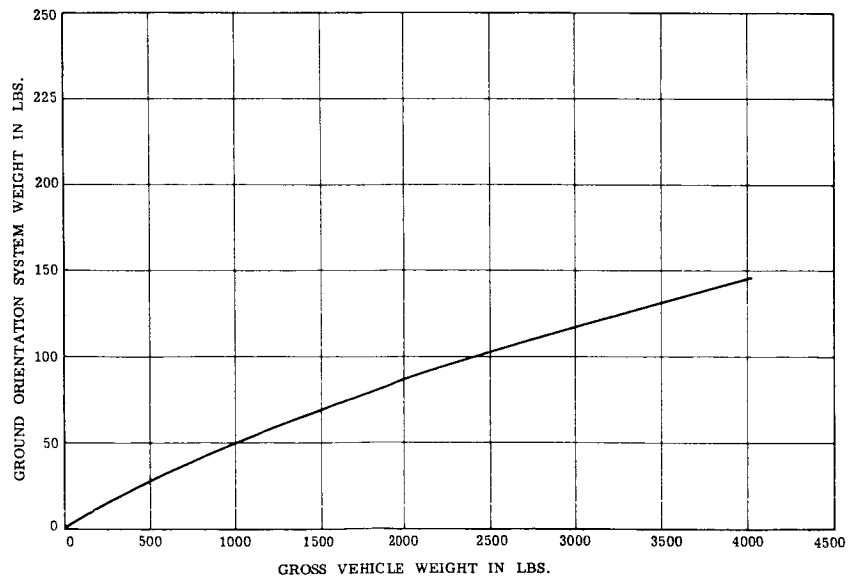


Figure 1.3.9-19 Ground Orientation System Weight vs. Gross Weight

- PAYLOAD WEIGHT INCLUDES:
1. SCIENTIFIC PAYLOAD
 2. DEPLOYMENT & INSTALLATION EQUIPMENT
 3. ELECTRICAL POWER
 4. COMMUNICATIONS EQUIPMENT

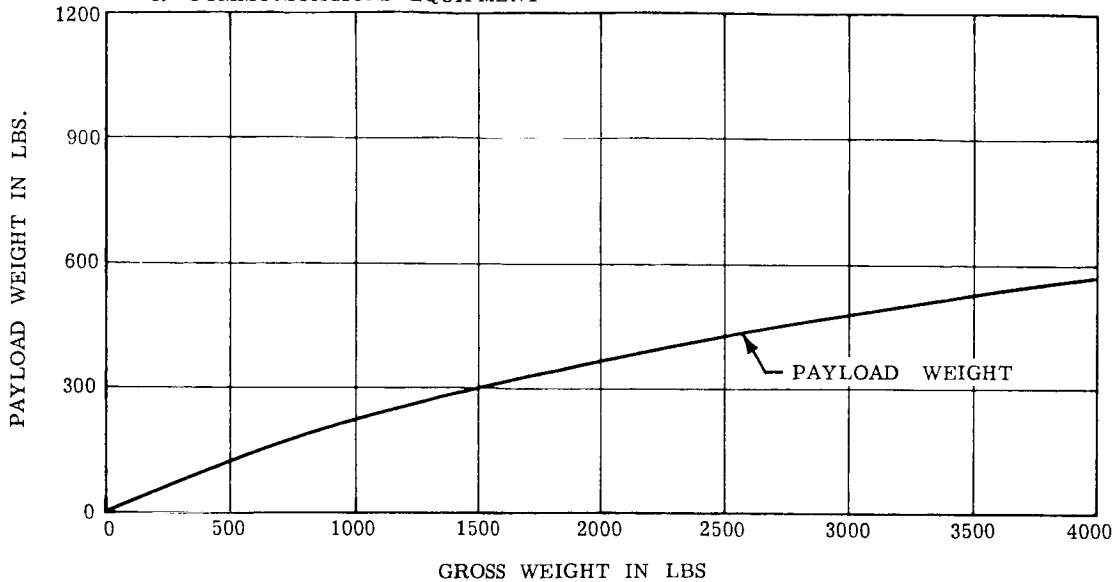


Figure 1.3.9-20 Gross Weight vs. Payload Weight - Venus Landers

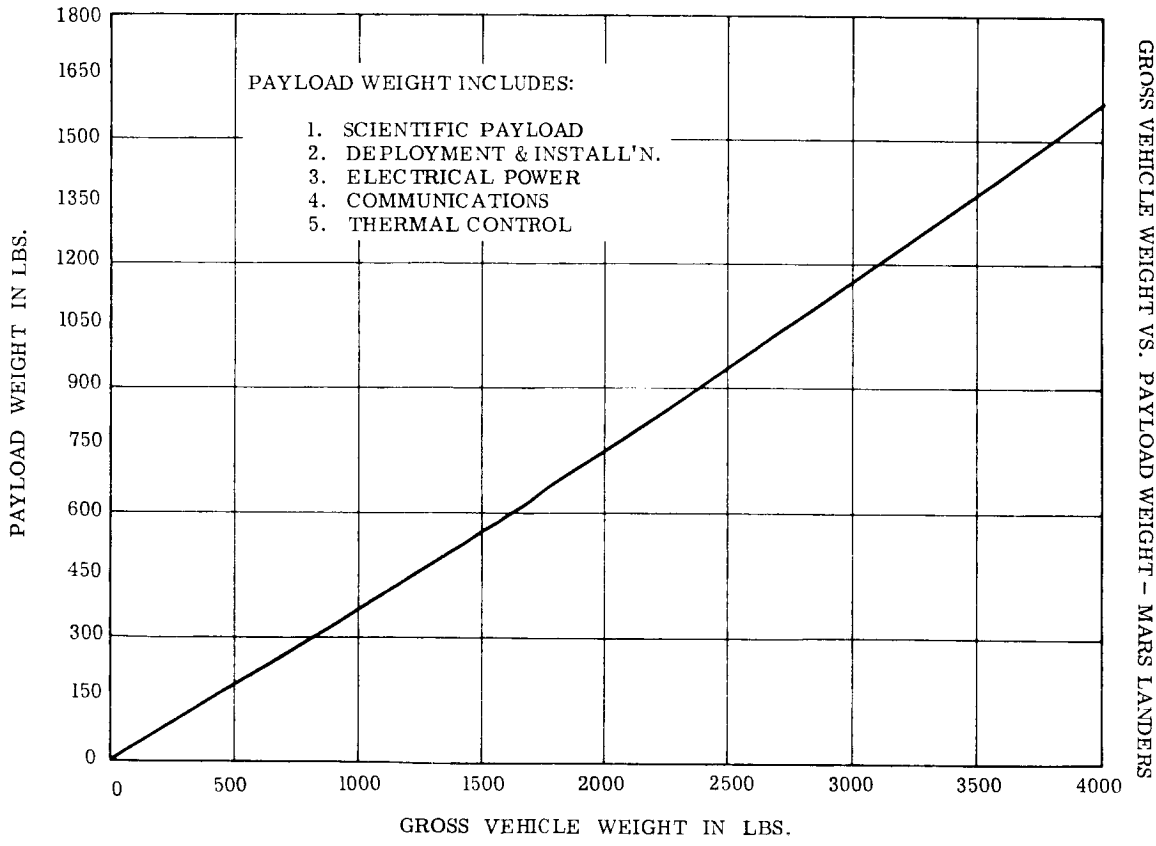


Figure 1.3.9-21 Gross Weight vs. Payload Weight - Mars Landers

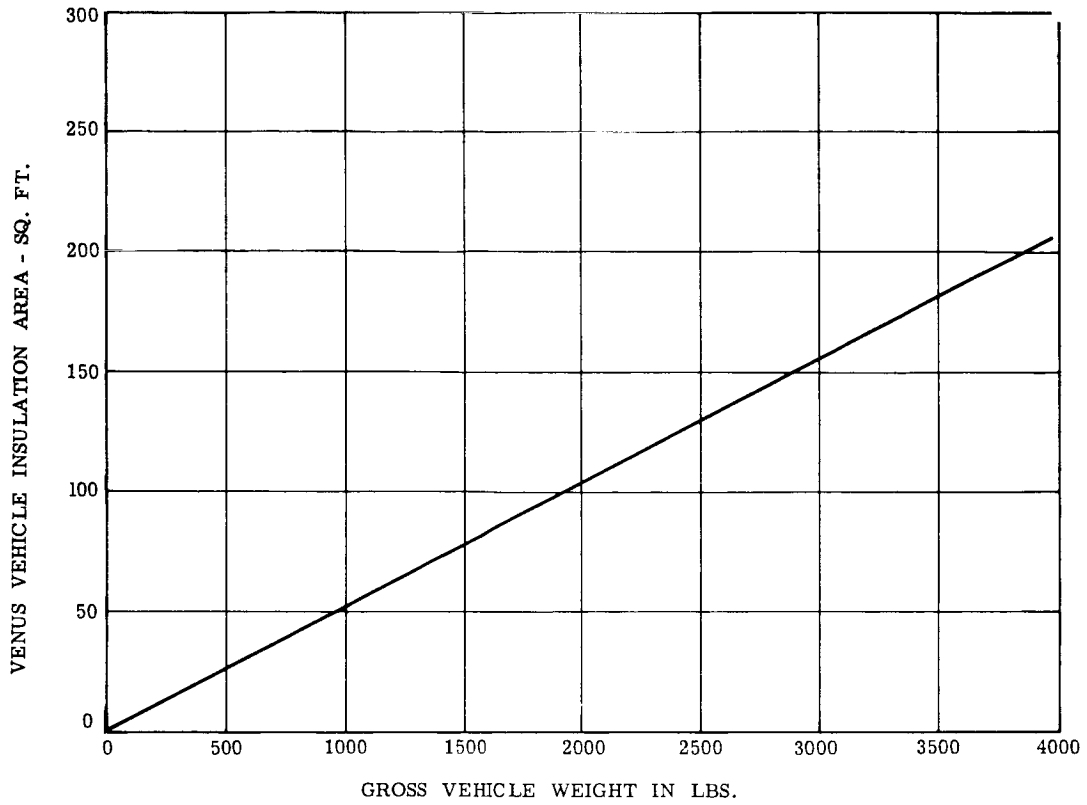


Figure 1.3.9-22 Venus Lander - Insulation Area vs. Gross Vehicle Weight

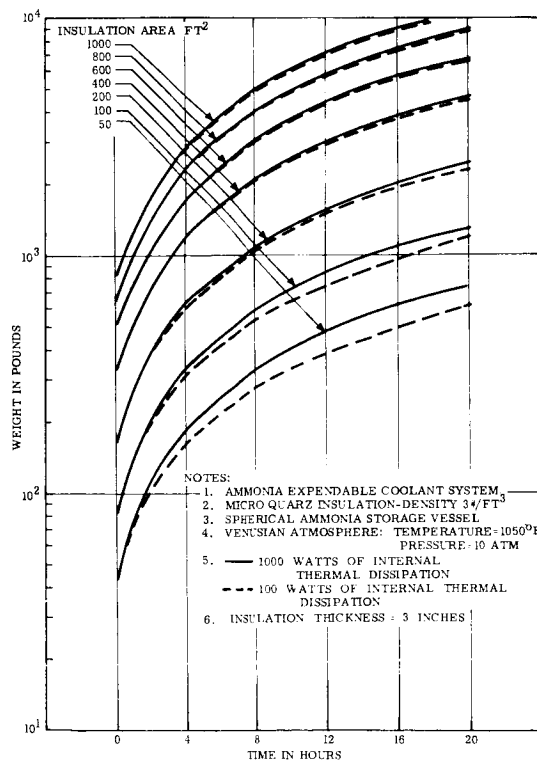


Figure 1.3.9-23 Thermal Control System Weight

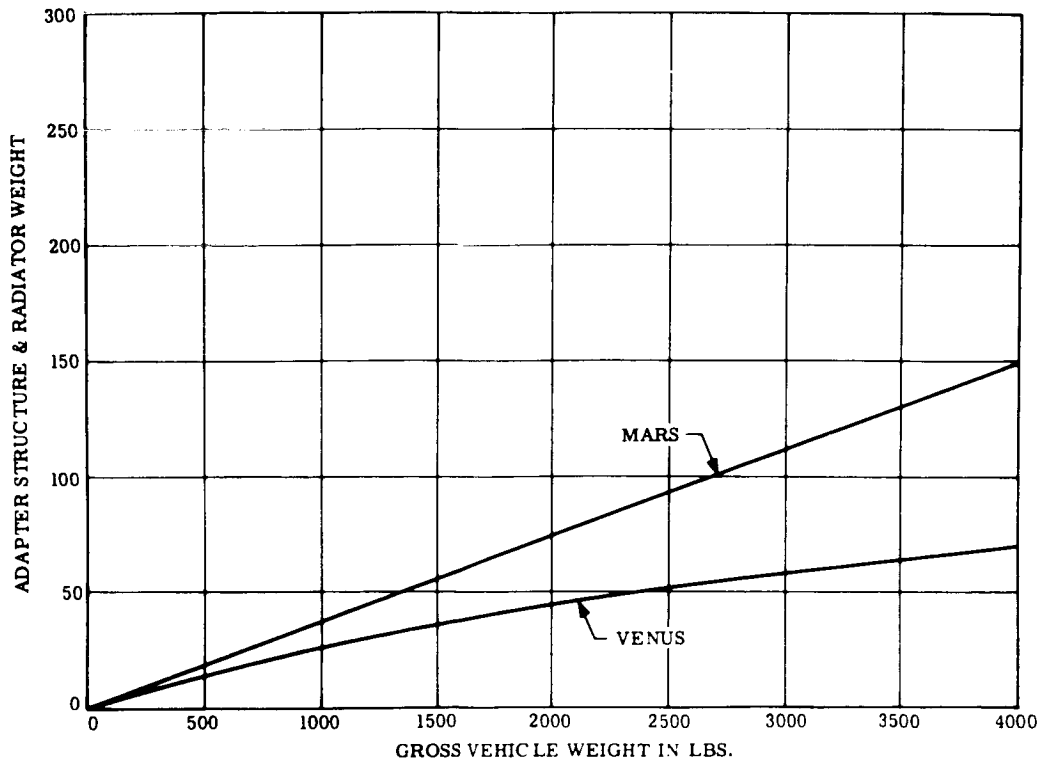


Figure 1.3.9-24. Adapter Structure and Radiator Weight vs Gross Vehicle Weight

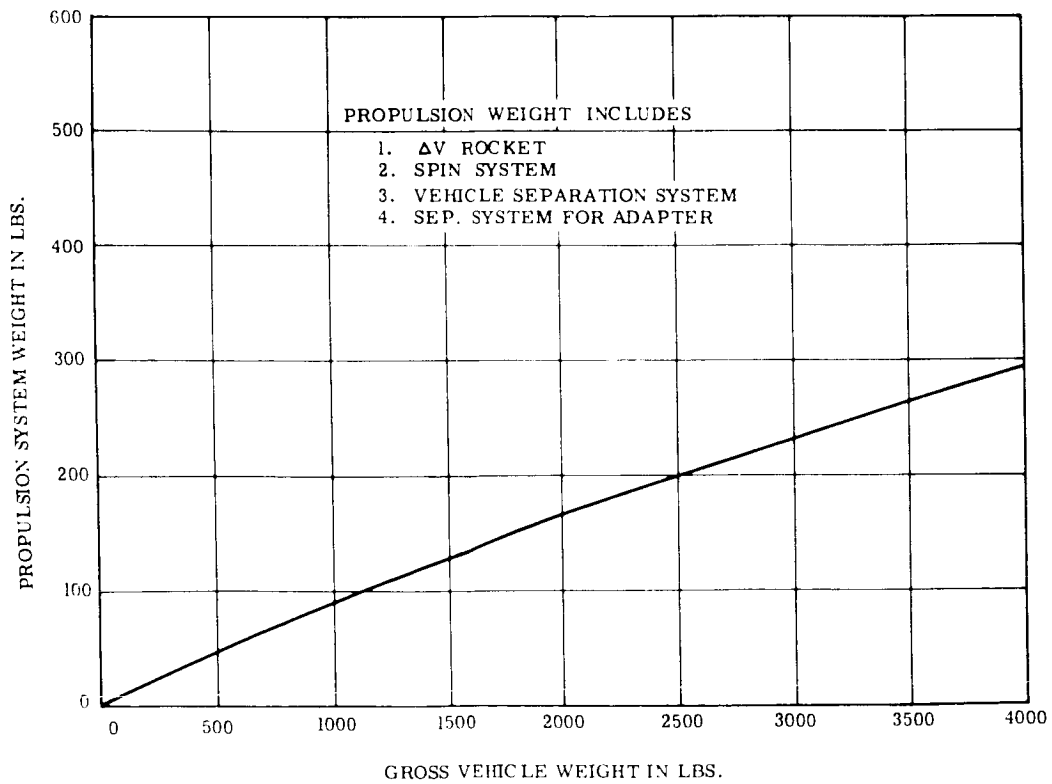
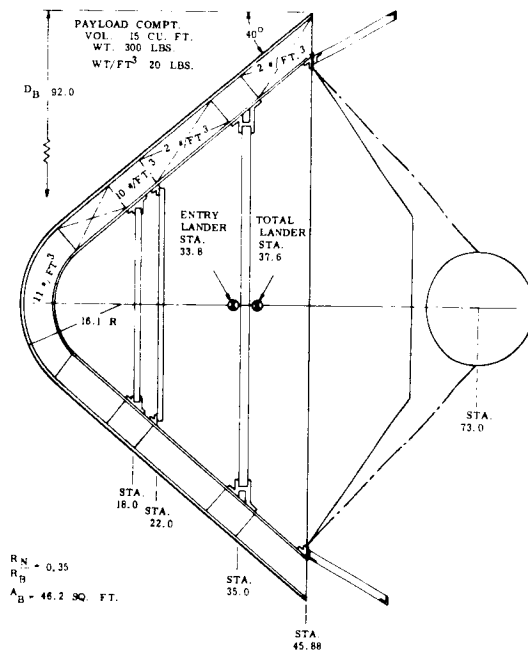


Figure 1.3.9-25. Propulsion System Weight vs Gross Vehicle Weight



WEIGHT AND BALANCE MARS 1969 LANDER

	Weight	C.G. STA.
<u>Shield - ESM 45 Lbs/Ft³</u>	(84.2)	26.7
Nose (.55 to .31)	7.2	2.5
Frustum - .31 constant	77.0	29.0
<u>Structure - Al. Alloy</u>	(233.0)	29.0
Nose	6.0	6.0
Frustum .40 H.C., .012 Faces, 6Lb Core	51.2	30.0
Ring Sta. 8.0/1.0 x 1.0 x .10 Al.	1.0	8.0
Ring Sta. 18.0 (Breech) 1 sq. in. Al.	12.0	18.0
Ring Sta 22.0 1.5 x 1.5 x .125 Al.	4.3	22.0
Ring Sta 35.0 (Rot. Blkhd)	25.4	35.0
Ring Sta 45.9 1.5 x 1.5 x .188 Al.	12.8	45.9
Blkh'd Sta. 18.0 .75 Th.H.C. .024 Faces, 10 Lbs Core	12.8	18.0
Blkh'd Sta. 22.0 .75 Th.H.C. .024 Faces, 10 Lbs Core	14.5	22.0
Blkh'd Sta. 35.0/1.5 Th.H.C. .024 Faces, 10 Lbs Core	61.0	35.0
Fittings for Chute (4)	8.0	45.9
Nose Cap Separation	16.5	7.0
Hardware	7.5	30.0
<u>Aft Cover</u>	(57.0)	52.2
Skin .040 A1.	22.4	53.0
Doublers, Reinf 20% Skin	4.5	53.0
Angle at Attachment	9.5	46.0
Shield PD300 .10 Thick	14.5	54.0
Bolts Nuts Etc.	6.1	54.0

Retardation

CRUSH UP (Total Wt. = 133.5 Lbs)

- STA 0-8 16 Lbs. Den.
- STA. 8-15 2 Lbs. Den.
- STA 15-19 16 Lbs. Den.
- STA 19-32 2 Lbs. Den.
- STA 32-37 16 Lbs. Den.
- STA 37-46 2 Lbs. Den.
- Chute Installation (Inc. decelerator = 8.)
- Chute Support Housing
- Equip. (Battery, G-Switch, Prog.)
- Harness, Cabling
- Hardware

Scientific Payload




Instrumentation (Total Wt. = 159.4 Lbs)

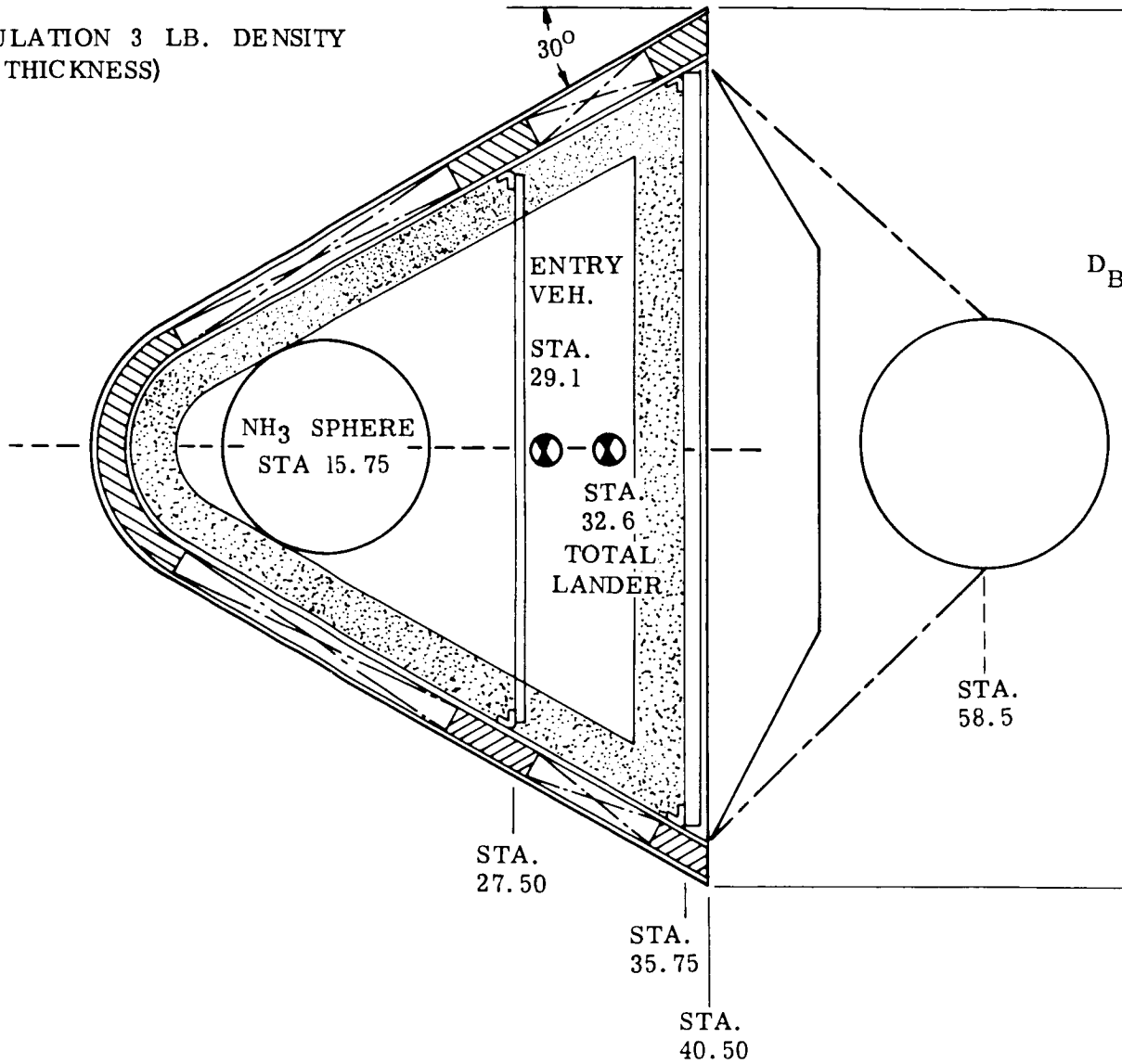
- Temperature
 - Pressure
 - Density
 - Mass Spectrometer
 - Gas Chromatograph
 - Wind Speed (on Hel. Ant.)
 - Fixed T. V.
 - Deployed T. V.
 - Radar Altimeter (Electronics)
 - Radar Altimeter - Dish (Fixed)
 - Langmuir Probe
 - Precipitation
 - Surface Sounds (incl. Elec.)
 - Light Level Indicator
 - Surface Penetrability
 - Soil Moisture
 - Seismic Activity
 - Surface Gravity
 - Radioisotope Growth Dept.
 - Turbidity and PH Growth Det.
 - Multiple Chamber Growth Det.
 - Photoautotroph Detector
 - Microscopic Analysis
 - Drill (On Tip-Over Bar)
 - Pulverizer (On Tip-Over Bar)
 - Sample Handling Equip. (On Tip-Over Bar)
- Deployment and Installation (Total Wt. =)
- TV Deployment, Incl. Motor and Mech.
 - Surface Hardness Deployment
 - Ablation Sensors
 - Temperature Sensors
 - Accelerometers
 - Ablation Converter
 - Hardware
 - Harness Cabling

		<u>Thermal Control</u>	(72.0)
		Modulation Valves (2)	6.0
		Reservoir (Coolant)	1.5
		Electronic Temp. Controller	1.5
		Motor, Pumps (2)	6.0
(288.2)	41.0	Separation Valves (2)	6.0
17.7	4.0	Shut Off Valves (3)	6.0
4.7	11.0	Heat Exchanger, (Liquid to Liq.)	5.0
30.0	17.5	Heat Exchanger (Evaporative)	5.0
12.7	26.0	Water Vessel (incl. 11 Lbs. H ₂ O)	13.0
52.0	33.5	Coolant	4.0
16.4	41.5	Plumbing Fittings, Hardware	6.0
127.2	55.0	Battery Coolant	10.0
12.0	55.0	Insulation (Fw'd and Aft Blkh'd 1")	2.0
8.0	50.0		
4.5	50.0	<u>Electrical</u>	(106.5)
3.0	52.0	RTG Unit	54.0
		Battery	28.0
(215.4)	35.3	Regulator - Battery	3.0
0.3	35.0	Power Control Unit	9.0
0.3	35.0	In Flight Disconnect	1.5
1.5	35.0	Cabling Harness	5.0
6.0	33.5	Hardware, Supports	6.0
7.0	32.5	<u>Ground Orientation</u>	(67.0)
2.0	38.0	Tip Over Bar	10.0
10.0	32.5	Fitting-Tip-Over Bar	3.0
10.0	40.0	Actuator	16.0
17.0	25.5	Fittings for Actuator	4.0
4.0	5.0	Switches	1.0
3.0	33.5	Rotating Mechanism	17.0
1.0	38.0	Rollers	3.0
1.0	35.0	Gear	2.0
0.3	35.0	Motor	5.0
1.0	38.0	Motor Support	1.0
2.0	34.0	Retainer	6.0
8.0	45.0	Harness, Cabling	8.0
3.0	32.5	Harpoons (2)	3.0
6.0	32.5	Hardware	5.0
4.0	32.0		
4.0	32.0	<u>Communication</u>	(141.5)
3.0	34.0	<u>Orbiter Link</u>	
15.0	32.5	VHF Antenna - Turnstile 5'	7.0
20.0	44.0	VHF Antenna - Quadriloop	3.0
10.0	44.0	VHF Diplexer	1.0
20.0	41.0	VHF Transmitter	2.5
		VHF Receiver	2.0
		Command Demodulator	3.0
10.0	38.0	<u>Earth Link</u>	
3.0	39.0	S-Band Antenna	4.0
1.0	28.0	S-Band Omnidirectional Antenna	2.0
0.5	28.0	S-Band Diplexer	0.5
2.0	24.0	Transponder	5.4
1.5	30.0	Power Amplifier (Klystron)	4.0
8.0	32.0	High Voltage Power Supply	5.0
30.0	34.0	Command Demodulator	3.0

21.4			
24.0			
20.0			
23.0			
20.0	<u>Command</u>		
24.5	Programmer Unit	14.0	25.0
20.0	Power Conversion and Control	7.0	24.5
24.5	<u>Data Storage and Processing</u>		
20.0	Data Processing Unit	16.0	25.5
20.0	Buffer Storage Unit	3.5	24.0
20.0	Thermo Plastic Recorder	25.0	32.0
21.0	<u>Antenna Controls</u>		
20.0	Omni Switch	2.0	38.0
28.0	Sun Sensor	2.3	38.0
	Electronic Gimbal Control	1.4	36.0
17.0	Amplifier	1.4	37.0
13.0	Drive Motors	4.0	35.0
20.0	Mode Control Electronics	0.5	37.5
20.0	Vertical Switch	2.0	38.0
24.5	Supports, Brackets	4.0	30.0
54.0	Harness Cabling	7.0	31.0
18.0	Deploy Mechanisms	6.0	42.0
16.0	Hardware	3.0	40.0
40.6	Separation System (Aft Cover)	(6.0)	46.0
45.0			
38.0	Total Entry Lander	1270.8	33.8
42.0	Suspended Weight	1213.8	
40.0			
42.0	<u>Adapter</u>		
36.0	<u>Structure</u>	(30.7)	54.2
	Skin .020 A1.	8.1	54.0
	Longerons (4) .060	0.7	53.0
	Stiffeners (20) .032	1.2	53.0
	Fw'd Angle .125 A1.	6.1	46.0
	Aft Angle .125 A1.	7.3	59.0
42.0	Support Tubes for ΔV Rocket	2.4	60.0
42.0	Fittings for Support Tubes	2.4	60.0
41.0	Hardware	2.5	51.0
31.8	<u>Thermal Control</u>	(18.0)	53.6
	Skin, .010 A1.	4.1	54.0
39.0	Insulation and Mylar Shield	2.5	54.0
46.5	Spacers	2.6	53.0
33.5	Tubing	2.3	54.5
33.5	Fittings and Connections	1.5	53.5
34.0	Coolant	2.5	54.0
33.0	Hardware	2.5	52.0
	ΔV Rocket 400 Ft/Sec, (Prop = 80 Lb)	97.0	73.0
38.0	Separation System (Adap. and Lander)	6.0	50.0
38.0	Spin System	12.0	56.0
34.0	Push Away	8.0	59.0
34.0	Harness Cabling	5.0	54.0
33.5	Hardware	2.5	54.0
25.0			
33.0	Total Mars 1969 Lander	1450.0	37.6

Figure 1.3.9-26. Detailed Weight Breakdown
Mars 1969 Lander

-  CRUSH-UP 10 LB. DENSITY (1.8 INCH THICKNESS)
-  CRUSH-UP 2 LB. DENSITY (1.8 INCH THICKNESS)
-  INSULATION 3 LB. DENSITY (3" THICKNESS)



WEIGHT AND BALANCE VENUS 1970

<u>Shield</u> - Phenolic Nylon 75 lb/cu ft.	(97.5)	24.2
Nose .65 at Stag. Pt., 146 at T.P.	7.3	2.0
Frustum .42 Constant Thickness	84.7	26.0
Bond (Soft)	5.5	25.5
<u>Structure</u>	(105.7)	28.6
Nose	6.0	4.0
Frustum - St. St'l Honeycomb	36.5	26.0
Ring Sta 7 1 x 1 x .060 Ti.	1.0	7.0
Ring Sta 27.5 1.5 x 1.5 x .08 Ti.	4.6	27.5
Ring Sta 35.8 1.5 x 1.5 x .08 Ti.	9.6	35.8
Blkh'd sta 27.5 St. St'l Honeycomb	16.7	27.5
Blkh'd Sta 35.75 St. St'l Honeycomb	22.9	35.8
Fittings For Retard Cables	2.0	40.0
Plate at Sta 40.5 .030 Ti.	2.6	40.5
Bolts, Nuts, Etc.	3.8	28.0
<u>Aft Cover</u> (Used for Retardation)	(20.0)	44.0
Skin .020 Ti.	8.4	
Doublers 20% Skin	1.6	
PD 300 Shield .10	8.3	
Hardware	1.7	
<u>Retardation</u>	(35.9)	32.5
Crush Up (Total = 23.9 Lbs)		
Sta 0-5 11 Lb Density	2.6	2.5
Sta 5-24 2 Lb Density	3.4	17.0
Sta 24-29 10 Lb Density	7.5	27.0
Sta 29-37 2 Lb Density	2.7	34.0
Sta 37-40.5 10 Lb Density	7.7	38.0
Equipment (Prog. Switch, Etc.)	5.0	43.0
Cables, Etc.	2.0	43.0
Drogue	2.5	45.0
Hardware	2.5	41.0
<u>Thermal Control</u>	(40.0)	21.1
Sphere 500 cu in.	5.5	16.0
Support for Sphere	2.0	12.0
NH ₃ - Coolant	9.5	16.0
Boiler - H ₂ O Pressurizing	5.0	20.0
Insulation 28 Sq. Ft., 2.6 Th, 3 Lbs/Ft ³	14.0	29.0
Hardware Tubing Valves	4.0	18.0
<u>Electrical</u>	(20.0)	29.7
Batteries	8.5	26.0
Supports	1.0	26.0
In-Flight Disconnect	1.5	40.5
Power Control Unit	5.0	30.0
Harness Cabling	3.0	25.0
Hardware	1.0	26.0
Ground Orientation (Tip-Over Rockets)	(8.0)	40.0
Separation System (Aft Cover)	(5.0)	41.0

58.0

<u>Scientific Payload (Instrum. = 54.1 Lbs)</u>	(73.1)	34.0
Temperature	0.3	29.5
Pressure	0.3	29.5
Density	1.5	29.5
Cloud Properties	5.0	36.0
Radar Altimeter (Electronics)	17.0	30.8
Radar Altimeter (Dish)	4.0	37.5
Surface Sounds	1.0	33.0
Television Panorama	16.0	37.0
Wind Speed	2.0	32.0
Television Light Source	2.0	39.0
Atmospheric Composition	5.0	33.0
Deployment for Cloud Properties	4.0	36.0
Deployment for Radar Altimeter	4.0	37.5
Deployment for Wind Speed	2.0	32.0
Brackets Supports	2.5	30.0
Harness Cabling	6.5	31.0
<u>Communications</u>	(41.5)	27.6
Transmitter	2.5	25.5
Data Handling Processor	11.0	23.5
Sequence Timer	4.0	24.5
Power Conversion	7.0	26.0
Buffer Storage	3.5	26.0
Antenna - Quadriloop	3.0	42.0
Antenna - Whip (Inc. Release)	3.0	37.5
Harness Cabling	5.5	28.0
Hardware	2.0	29.0
Total Entry Vehicle	446.7	29.1
Suspended Weight	446.7	29.1
<u>Adapter</u>		
Structure 1 x 1 x 4.0 x .080 Ti	13.0	43.0
Tube Supports For ΔV Rocket	2.0	48.0
Δ V Rocket	46.0	58.5
Spin System, Push Away	12.0	48.0
Separation System	4.3	40.5
Hardware	1.0	44.0
Total Venus '70	525.0	32.6

Figure 1.3.9-27. Detailed Weight Breakdown - Venus 1970 Lander

SECTION 2. ORBITER SYSTEM INTRODUCTION

SECTION NO. 2. ORBITER SYSTEM

The design criteria used for the Voyager Orbiter systems design may be divided into three general categories. The first of these are the functional requirements as dictated by the Voyager Mission Analysis. The second is the subsystem operating requirements and environments. The third is the structural design criteria which is dictated by launch vehicle environment, ground handling, and the limitations of manufacturing.

Table 2-1 gives in condensed form the Mission Analysis requirements for the Orbiter System. The main points of design interest are:

1. Two Landers required on four of six missions
2. A 10 ft. diameter Earth communications antenna required
3. VHF contact required with the Landers
4. The requirements of Orbiter sterilization for Mars 1973
5. The requirement for Radar Mapping for Venus 1970
6. Varying amounts of fuel and oxidizer required
7. Varying amounts of power required.

Subsystem requirements imposed the following constraints on the Orbiter System:

1. During transit, Entry-Landers must be either completely Sun-oriented or shade-oriented
2. The spacecraft must have maximum capability of adaption to other years and missions with minimum changes
3. Internal units and subsystem components must have ready accessibility
4. Thermal control of the spacecraft requires, if possible, that panels on which subsystem components are mounted view free space
5. Assuming use of solar power, the spacecraft will be either:
 - a) Sun-oriented with a planet oriented package
 - b) Planet-oriented with sun-oriented solar paddles
6. Manufacturing techniques to be used should be considered state-of-the-art as of 1966.

The structural design criteria used for the Voyager Spacecraft Orbiter is listed in Section 2. 5. This section includes the vibration and g levels which the various subsystems must withstand plus the associated environment.

The spacecraft is mounted on an adapter which will provide a transition structure between the Voyager Spacecraft and the launch vehicle. This adapter is not a subject for the Voyager Systems Study. However, during the study thought should be given to structural load paths through the adapter and into the launch vehicle structure.

Load introduction from the Voyager Spacecraft to the launch vehicle will be distributed by the adapter to a level capable of being withstood by the launch vehicle. The adapter will attach to the instrument unit which is mounted on the top of the launch vehicle.

Figure 2-1 shows a preliminary shroud envelope which is being considered for the Saturn C-1B launch vehicle and the Voyager Spacecraft.

The Voyager System requirements dictate the general design of the Orbiter. The launch vehicle requirements and environment essentially dictate the structure and structure assembly. These requirements, in conjunction with the individual subsystem constraints will dictate specific detail design and component location.

Based on the requirements indicated above, the Orbiter System and configuration evolved.

TABLE 2-1. MISSION ANALYSIS REQUIREMENTS

	M-69	M-71	M-73	M-75	V-70	V-72
Injected Weight	7030	7320	6000	5500	7260	7350
Orbiting Weight	2059	2102	1402	1335	2145	1804
Lander/s	2 @ 1450	2 @ 2000	2 @ 2000	2 @ 2000	1 @ 525	1 @ 2600
Fuel Midcourse & Orbit Injection	2071	1218	698	165	4590	2946
Communication (Prime)	Relay	Relay	Direct	Direct	Relay	Relay
Mission	TV Mapping	TV Mapping	Upper Atmos Determination	Fly-By	Radar Mapping	Particle & Field Measurement
Sterilize	No	No	Yes	No	No	No
PHP	Yes	Yes	No	No	Yes	Yes
Antennas	Yes	Yes	Yes	Yes	Yes	Yes
VHF Omni	Yes	Yes	No	No	Yes	Yes
VHF Yagi	10 ft dia	10 ft dia	10 ft dia	3-10 ft dia	7-10 ft dia	7-10 ft dia
Parabolic Dish	Yes	Yes	Yes	Yes	Yes	Yes
DSIF Omni	3 mo	3 mo	10 days	Flyby	3 mo	3 mo
Lifetime	-	-	-	-	10 ft dia	-
Radar Antenna	440 w	446 w	155 w	130 w	589 w	300 w
Solar Power	Yes	Yes	Yes	No	Yes	Yes
Magnetometer	Yes	Yes	No	No	Yes	Yes
Bi-Static Radar	Yes	Yes	No	No	Yes	Yes
Micrometeoroids	Yes	Yes	No	No	Yes	Yes

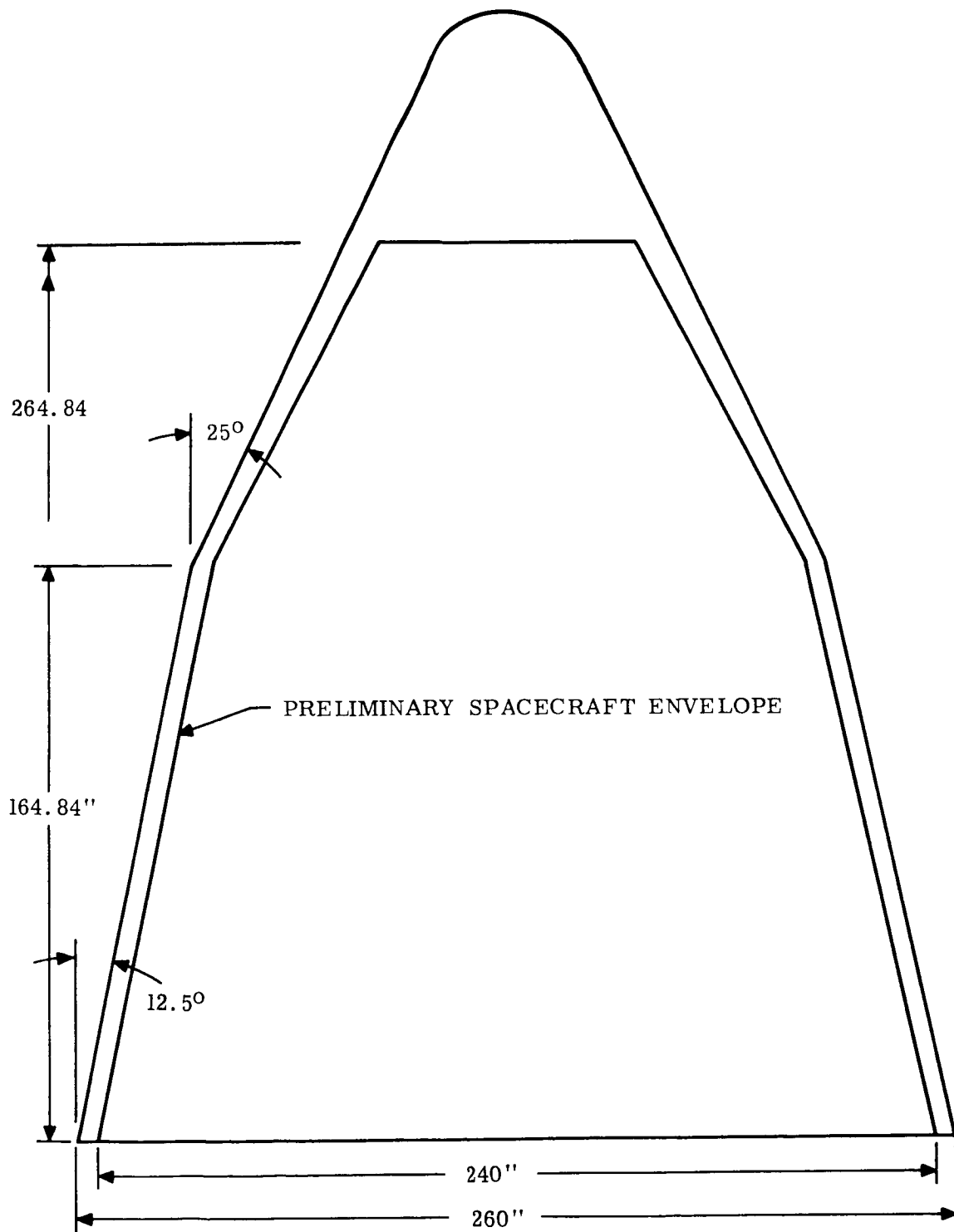


Figure 2-1. Saturn C-1B+SVI Preliminary Nose Fairing and Spacecraft Envelope

2.1 SUMMARY

The Orbiter is designed so that it is capable of carrying a variety of different payloads and sizes of Entry/Landers with a minimum amount of modification. Structural support for the Landers is provided by four points per Lander at a 91-inch diameter. These points are capable of supporting Landers varying in weight from 1,200 to 2,200 pounds. Any adaptation required to match these permanent pick-up points will be made in the lander adapter. Single Landers are capable of being attached easily to the Orbiter. A single Lander requires only an adapter in order to maintain clearance between the Entry/Lander rocket engine and the upper surface of the Orbiter. Mounting location is above the spacecraft center of gravity and along the X-axis. Capability can be built into the Orbiter to mount single Landers from 525 to 4,000 pounds.

The Orbiter structure consists of two main beams of sandwich construction which support the required fuel and oxidizer tankage and one-half the lander load; four main machined fittings which support the remaining half of the Lander loads; sandwich panels which provide support for the fittings and mountings areas for the payload packages; and miscellaneous fittings and brackets necessary to any configuration.

CONFIGURATION

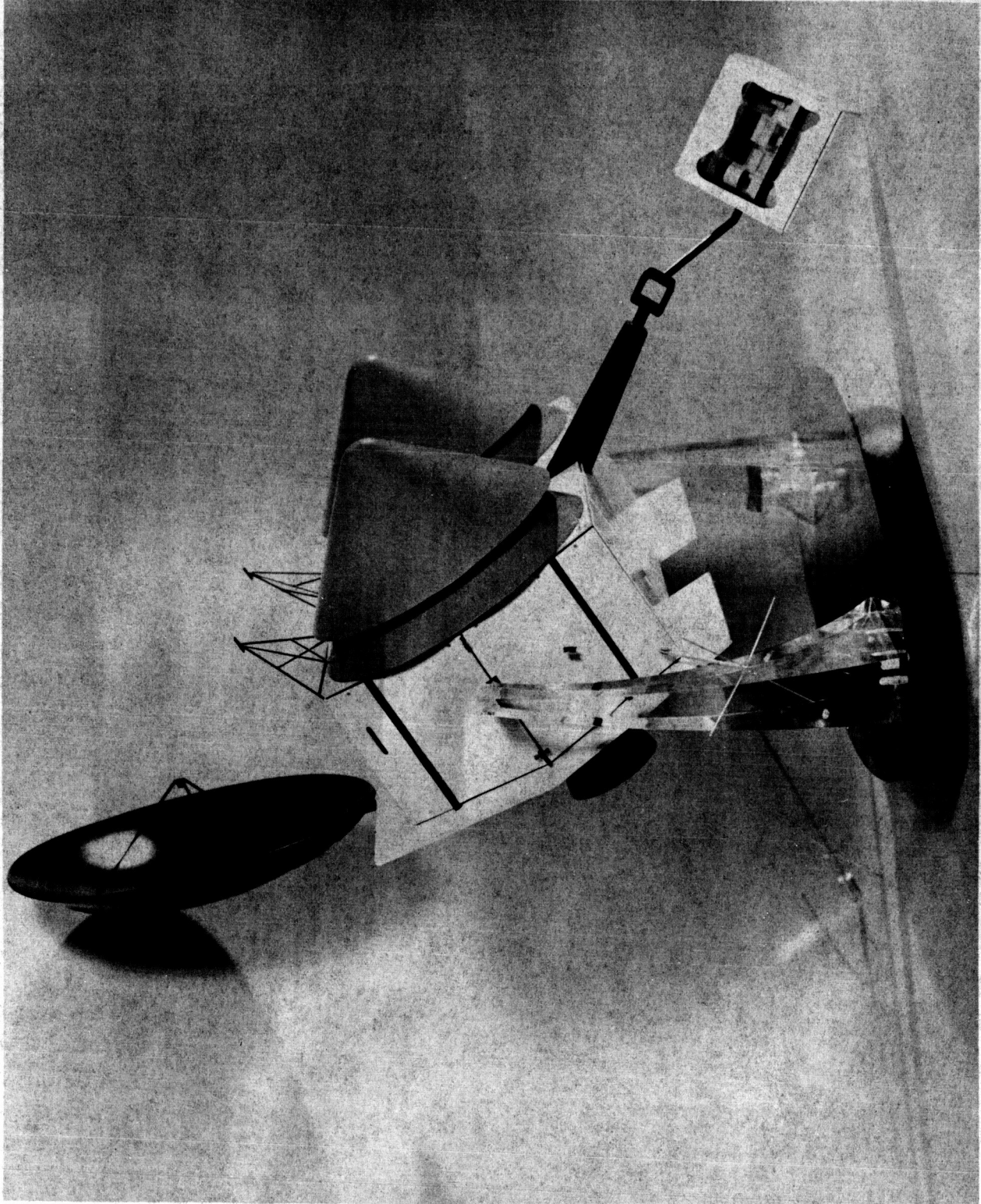
Mounted on the external surface of the Orbiter is the Planet Horizontal Package (PHP), the 10-foot diameter high gain antenna, the magnetometer and magnetometer boom, the VHF omni antenna, the DSIF omni antenna, Landers, the main engine, and solar cells.

The PHP is a self-contained structure capable of viewing the planet at all times during the orbit. The Mars 1969 PHP is at present designed to have two degrees of freedom. A further sophistication of the design is in progress in order to give three degrees of freedom if it is decided that the additional sophistication is necessary. Normal operation has the PHP stowed at the side of the Orbiter and mounted to the Orbiter during the boost phase. After injection into orbit about the planet, the PHP is deployed and, by means of sensors mounted within the PHP, pointed at the planet. The PHP total weight is 360 pounds which consists of structure, thermal control and items such as TV cameras, IR sensors, an ultraviolet radiometer, an IR spectrometer, and other scientific instrumentation. Thermal control is provided for the instruments such that an operating environment of 30°F to 100°F will be maintained.

Mounted upon the PHP is a VHF yagi antenna which is used for communications with the Lander during the orbit lifetime of the Orbiter. This antenna is stowed during transit. After the PHP is released and extended, the communications is switched from the VHF body-mounted antenna to the VHF yagi antenna on the PHP.

Power for the Orbiter is provided by means of solar panels and batteries. The solar panels are mounted on the base of the orbiter such that the structure serves a dual purpose of carrying Orbiter loads and of supplying a base on which to mount solar cells. The total area available for body-mounted cells is 82 sq. ft. Any additional wattage required above what can be provided by the body-mounted cells will be furnished by either extended fixed panels around the periphery of the Orbiter. Fixed panels around the periphery of the Orbiter are capable of supplying a maximum of 220 additional watts of power. For a requirement in excess of this value, the use of deployable panels or a small Radiosotope Thermoelectric Generator (RTG) would have to be examined.

The high gain antenna is nominally located during launch and transit in a vertical position at the side of the Orbiter. Support is by means of a hinge mechanism attached on the base of the Orbiter and by two brackets at the upper surface of the Orbiter which help to reduce vibration amplitudes during the boost phase. After injection into transit trajectory, the high gain antenna will be released and deployed while close to the Earth in order that all



Voyager Spacecraft Model

systems may be checked out. After this time, the antenna will be stored in the launch position for approximately 187 days, at which time it will be deployed and become the standard method of communications between the Earth and the spacecraft. At this time, the requirement for data rate precludes the use of the DSIF omni antennas. In addition, there is a potential problem of the antenna sensors viewing the Sun. These several factors combine to select the period of 187 days as the time of high gain antenna deployment.

Location of the antenna in this launch position allows the antenna to have a fixed feed. A capability is built into the antenna structure such that it may withstand maximum expected loads from the main engine, regardless of antenna position.

Mounted on the sun side of the Orbiter is a three-axis magnetometer and a 13-foot boom. Provisions are made such that the boom may be deployed and erected in orbit. Capabilities are built into the system to rotate the boom 180 degrees per day. Time of rotation will be approximately 0.1 second. Mounted on the magnetometer boom is a 3-foot x 10-foot dipole antenna which will be used as the antenna for the Radio Propagation Experiment. The magnetometer and boom will be stowed during transit and will be deployed only after the orbit is obtained.

Located on both the sun side and the shaded side of the Orbiter are DSIF omni antennas. These antennas are located such that communication may be maintained between Earth and the spacecraft regardless of orientation.

In addition to the DSIF omni antenna, a VHF antenna is mounted externally to the Orbiter. This antenna will be deployed immediately after the Landers are ejected and will provide communications between the Landers and the spacecraft during entry and descent. While in orbit, the VHF yagi antenna on the PHP will be used.

The main engine, which is used for mid-course corrections and for orbit insertion, is located on the base of the Orbiter, opposite the Landers. The engine is gimballed and provisions made for thrust vector control by means of hydraulic actuators. Two degrees of freedom of movement are provided, to the extent of $\pm 7^\circ$. The engine is located such that thrust vector control will be minimized. It is expected that the maximum static c. g. shift requiring thrust vector control will be in the order of plus or minus 1/2 inch, which is equivalent to ± 1 degree of engine gimbaling.

The Entry /Landers are mounted side by side on the shaded side of the Orbiter. Attachment is by means of four explosive bolts per Lander. These bolts will be bonded to the biological barrier such that a sterile interface will be maintained between the Orbiter and Landers.

Other than the four structural attachments of the Landers to the Orbiter, there will be only an electrical connector which breaks the biological barrier. An in-flight disconnect is built into the Entry/Lander structure. This in-flight disconnect will be separated just prior to firing of the four explosive bolts. Since the separation is within the sterilized area, there will be no contamination of the Entry/Landers.

LANDER SEPARATION

The separation method selected for the Landers is as follows: Upon command, the explosive bolts are fired releasing the structural tie between the Landers and the Orbiter. Cold gas jets or hot gas rockets mounted on the Lander will be fired to impart a translation to the Lander. These rockets are located such that there will be no impingement of the gases on the Orbiter. After a translation of about 3 feet, spin rockets will be actuated on the Lander in order to spin the Lander. After the first Lander is ejected, the Orbiter is reoriented to a preselected angle and the remaining Lander is ejected.

PACKAGING

The overall packaging of the Orbiter is as follows: The main mass items, which are the fuel and oxidizer tanks, are mounted between two main sandwich beams extending from side to side of the Orbiter. This gives a stiff, low deflection structure and results in a resonant point at high frequencies. Allowance is provided for growth of the fuel tanks to a maximum of 40 inches in diameter. Tanks are located such that they will give minimum c. g. shift about the yaw and pitch axes of the spacecraft. However, considered in the c. g. calculation is a potential 3% differential usage rate between fuel and oxidizer tanks.

Freon tanks for attitude control and helium tanks for pressurization purposes are mounted outboard of the fuel area with one trunnion attaching to the same beam that supports the fuel tanks and the other trunnion attaching to separate structure provided for this support.

The main electronic payload packages of the Orbiter, with the exception of those in the PHP are mounted on the two ends of the Orbiter. These payloads for the various subsystems are mounted on a sandwich panel which views free space. Each panel on which payload packages are mounted is provided with quick release structural fasteners, thus giving ready accessibility to any subsystem unit. Thermal control, both active and passive, is provided in order to maintain a transit temperature of 0°F to 100°F and an operating temperature of 30°F to 100°F.

Also mounted within the orbiter is a separate Image Orthicon Camera provided for use in terminal guidance observation. This camera will take pictures of the target planet and star background and, from this information, final trajectory corrections will be made. Capability is built into the mounting provisions of the camera for repositioning to required coordinates at any time during the prelaunch period.

Sensors required on the spacecraft are grouped in general terms as follows: fine and coarse sun sensors and star trackers on the orbiter, Earth sensors on the high gain antenna, planet sensors on the PHP, temperature sensors for the thermal control shutters and diagnostic sensors as required.

Two Canopus trackers are installed on the Voyager Orbiter. One tracker is considered "prime" and is used for orientation of the spacecraft when the Southern Hemisphere of Mars is to be mapped. Assuming both launches during the Mars 1969 window to be successful, it is desirable to be able to put the second Orbiter in an orbit such that the Northern Hemisphere of Mars can be mapped. By switching to the secondary Canopus tracker, the second Orbiter will be oriented in the correct attitude to map the Northern Hemisphere.

SEPARATION AND ACTUATION

The main method of separation considered is by means of explosive actuators. Pyrotechnic devices will be used to separate the attachments on the high gain antenna, the Planet Horizontal Package, the magnetometer boom and the Landers.

Actuation of the required components will be provided by both spring actuators and motor drives. The PHP and the high gain antenna will operate by motor drives and the magnetometer boom will be actuated by springs. In addition, the magnetometer boom will have an energy absorption device in order to precisely locate the boom at the point desired.

GROWTH CAPABILITY

Capability for other years and other missions has been one of the prime factors in the Orbital design. The orbiter is designed such that dual Landers in the range of about 1,200 to 2,200 pounds each may be mounted on the Orbiter by means of an adapter.

Single Landers can be mounted on the upper surface of the Orbiter above the center of gravity and along the X-axis. An adapter is required which will maintain clearance between the Entry/Lander rocket engine and the Orbiter. Single Landers, varying in weight from 525 to 4,000 pounds, can be carried to the selected planet.

Revisions in payload are accommodated by changing packages in the payload mounting area for various missions. Changes in the PHP necessitate only revisions to the attachment fittings and a check of the repackaging in order to keep the c. g. shift to a minimum.

CONSTRUCTION

The Orbiter structure is of semi-monocoque construction, with loads introduced along sheet stiffened longerons. The choice of semi-monocoque construction was dictated by efficiently designing for the expected vibration environment, which by and large is the limiting condition. Additionally, this type of construction enhances thermal control and affords greater flexibility for packaging efficiency. The structure does not have the familiar appearance of the sheet-stiffener shell. This was because simplicity, and hence reliability, was stressed in all phases of design, manufacture and performance. The goal of simplicity was achieved in design by the use of simple tension-compression members and avoiding complex load paths wherever possible. Also, elastic shear buckling and diagonal tension was eliminated as a failure mode. This latter condition was deemed necessary in view of the non-linearity effects which would result under dynamic loads. As a result, all primary shear webs are honeycomb panels designed to be shear stable.

Simplicity in manufacturing (where no significant weight savings can be obtained) led to the use of flat, rather than curved, panels; the use of familiar aircraft materials, fabricating techniques, and fasteners and fastening techniques. The structure appears as a box; however, it should be pointed out that the Orbiter structure is a network of deep beams capable of reacting both vertical and side loads plus overturning moments. The configuration was not designed for volumetric efficiency, but rather for a low silhouette and minimum contour dimensions which would still allow two landers to be supported side by side.

An area where manufacturing simplicity has been compromised for structural efficiency has been in the use of high strength alloys in the "foil size" gages. Usually, the only alloys available for thin face sheets (0.012"t) are the softer aluminums with a maximum allowable strength of 20,000 psi. The present design calls for chemical milling of .012 in. thick 7075-T6 aluminum sheet ($F_{cy} = 60,000$ psi) to the thinner gages thereby resulting in honeycomb panels of three times the strength of the equivalent panels used in the past.

THERMAL CONTROL

The temperature control of the major Voyager Orbiter subsystems is achieved by simple, lightweight and reliable means which are feasible in view of the present state-of-the-art. Future developments in thermal hardware, and in analytical techniques capable of increasing the quality of the thermal design have not been overlooked. An integrated structural-thermal design has evolved which places a minimum of constraints on the spacecraft mission.

Four major subsystems have been considered in the thermal studies: (1) Planetary Horizontal Package (2) the Orbiter payload components (3) the fuel tanks and (4) the solar cells.

The Voyager temperature control system utilizes a combined active and passive design concept for the first two subsystems and an entirely passive one for the last two. The

active control consists of thermally actuated louvers which will be employed to vary the effective emittance of electronic component panels and therefore, maintain adequate temperature limits under various load rejection levels. The passive control is composed of optical coatings to be applied to particular internal and external surfaces, of multiple reflective radiation shields to minimize heat gains and losses, and of heaters designed to compensate for temperature changes resulting from the continuous decrease in solar input and/or from variable power loads.

The Planetary Horizontal Package has been assumed to be in a dormant state from launch until orbit injection, and will therefore, have a large portion of its periphery insulated to keep internal heater power requirements to a minimum. The lower temperature of the external PHP surfaces during transit has been established at 0°F , and their temperature range in orbit between 30° and 100°F when the PHP is deployed and in operation. In order to meet this range, the non-insulated external surface will consist of louvers, completely closed in transit, but activated in orbit when the PHP components must dissipate energy. Since camera lenses and some scientific instruments are exposed to direct normal solar energy in transit, a fixed sun shield prevents the formation of local hot spots and yet allows some of the energy absorbed by the shield to be reradiated to the lenses which in turn reduces heater requirements.

Payload components will be thermally isolated from the effects of solar distance variation. In order to meet this goal, an insulation shielding will extend over all component surfaces exposed to internal sections of the vehicle; one blanket will cover all components located on one vehicle panel, allowing some radiation heat transfer between black boxes. Heat dissipating components will be mounted on the vehicle skin, and will therefore, possess one surface facing a near black space environment. This surface will be covered with thermally controlled louvers through which internally generated energy will be discarded. When the equipment is non-operating, the louver will be fully closed, allowing component heat leaks to be at a minimum. Heaters will supply enough energy to maintain black box skins above 0°F . When the equipment is operating, base plate temperature limits are 30° to 100°F .

The various tanks which are mounted aboard the Voyager each have their own temperature limitations. To meet these requirements, desirable internal compartment sink temperatures during transit were obtained by proper choice of emittances for orbiter external side surfaces. Since the heat input to the tanks emanates from the rear surface of the spacecraft's sun side, the changing solar constant in turn affects the compartment sink temperatures as the mission progresses. When a tank lower temperature limit is reached, heaters are turned on to prevent subcooling. Those tanks which eventually will demand heater power will be wrapped in a lightweight insulation blanket to make effective use of this power.

The Voyager Orbiter electrical power is collected by solar cells mounted on the sun side of the spacecraft. To optimize this power output, the cells are oriented normal to the sun rays during the entire mission except for spacecraft reorientations of short duration. Since the solar cells have a fixed solar absorptance to emittance ratio, their equilibrium temperature will depend largely on the quantity of incident solar energy present at any particular position in space. This temperature level will always be below that resulting when cells are mounted on a panel with an adiabatic back face, as some heat is transferred to the internal compartments of the spacecraft as mentioned above.

Other thermal considerations taken into account are listed below.

1. Spacecraft surfaces are coated with materials chosen to exhibit long term stability of their radiative characteristics, and to reduce thermal gradients in a particular subsystem. Coatings of low ratio of solar absorptance to infrared emittance are employed only when no alternative exists, due to their instability when exposed to UV radiation.

2. Scientific instruments and electrical components will perform satisfactory if mounted on a heat sink maintained within the temperature limits of 30°F to 100°F. Certain components, such as the communication power amplifiers and sun sensors, have wider limits of permissible temperature; the battery, on the other hand, must be kept between 40°F and 90°F during operation.
3. The high gain antenna will experience a change in temperature as a function of solar distance, and must endure large temperature gradients. The use of a low ratio of solar absorptance to emittance coating will tend to reduce the temperature gradients along the antenna honeycomb faces.

VOYAGER WEIGHTS

The subsystem weights are tabulated on the following pages. Also shown are the mass properties of the Mars 1969 Voyager system. The mass moments of inertia shown are based on a 3% differential usage rate of fuel and oxidizer. The 1.10 inches of center of gravity shift indicated is a maximum for static conditions. Figure 2.1-1 indicates the selected Voyager spacecraft axes.

VOYAGER WEIGHTS (LBS), MARS 1969

STRUCTURE		419
Orbiter Str	316	
Hardware	40	
PHP Str	57	
Hardware	6	
HARNESSING - VEHICLE		107
POWER SUPPLY		217
Batteries	21	
Electronics	16	
Harness (Solar Array)	7	
Fixed Array	173	
GUIDANCE AND CONTROL		225
Electronics	149	
(F-14) Tank & Gas	52	
Hardware	24	
COMMUNICATIONS		291
Electronics	259	
Antenna (10ft. Dish)	32	
DIAGNOSTIC INSTRUMENTATION		30
THERMAL CONTROL		87
PAYLOAD		215
Scientific	91	
TV	124	

VOYAGER WEIGHTS (LBS.), MARS 1969

PROPULSION	467
Fuel System	364
Pressurization System	103
ORBITING WEIGHT	2058
ORBIT INSERTION FUEL	1862
LANDER WEIGHT 2 @ 1450 LBS.	2900
MIDCOURSE FUEL	210
TOTAL WEIGHT	7030 lbs.

MASS PROPERTIES MARS 1969

Orbiter	2058 lbs
Landers	2900 lbs
Fuel	2072 lbs
	<hr/>
	7030 lbs

	Wt. lbs	X in.	Z In.	Y In.	Iox Slug- ft ²	Ioz Slug- ft ²	Ioy Slug- ft ²
After Launch	7030	40.67	-.02	-.03	4294	2275	4442
After Midcourse	6820	41.17	-.03	-.19	4270	2238	4427
After Antenna Deployed	6820	40.87	-.03	-.13	4393	2345	4406
After Landers Ejected	3909	21.38	+.05	+.15	2230	1244	1425
After Orbit Insertion	2048	17.52	+.12	-.95	1914	992	1476
Max Δ =		23.65	.15	1.10			

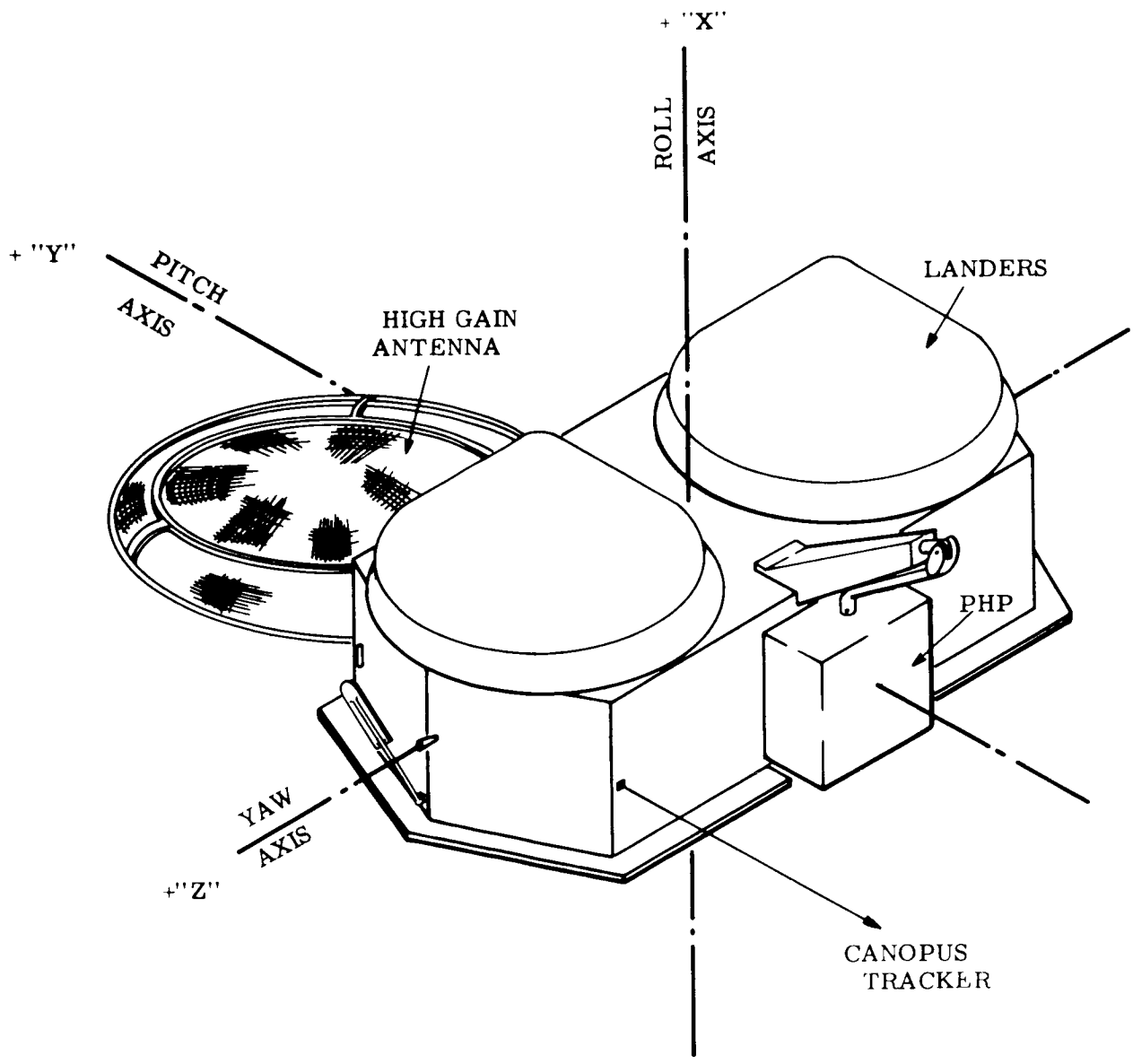


Figure 2.1-1. Voyager Orbiter Axes

2.2 CONFIGURATION SELECTION AND SEQUENCE OF EVENTS

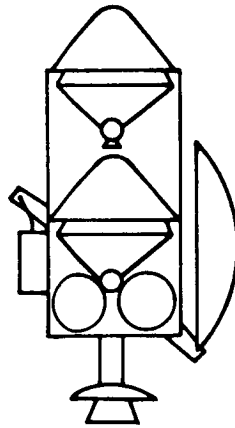
The selection of a specific configuration is normally an iterative process, varied over time by subsystem inputs. As indicated in Section 2., there are three main inputs to the Orbiter System.

1. Mission Analysis Requirements
2. Launch Vehicle Environment
3. Subsystem Requirements

The first and third of these are variables, while the second is essentially a constant.

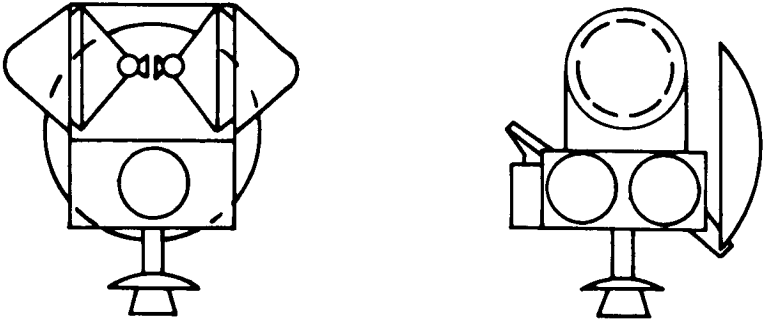
In order to acquaint the reader with a general awareness of the process followed in selecting a configuration, four general configurations considered during the System Study are shown and commented upon:

1. The first configuration considered consisted of one Lander mounted above the other Lander. This configuration was not carried further due to the reliability problem associated with the possibility of the upper Lander not releasing, and thus, interfering with the ejection of the second Lander. A failure mode is possible in which the first Lander is explosively "blown" free, but this could still interfere with free exit of the second Lander.

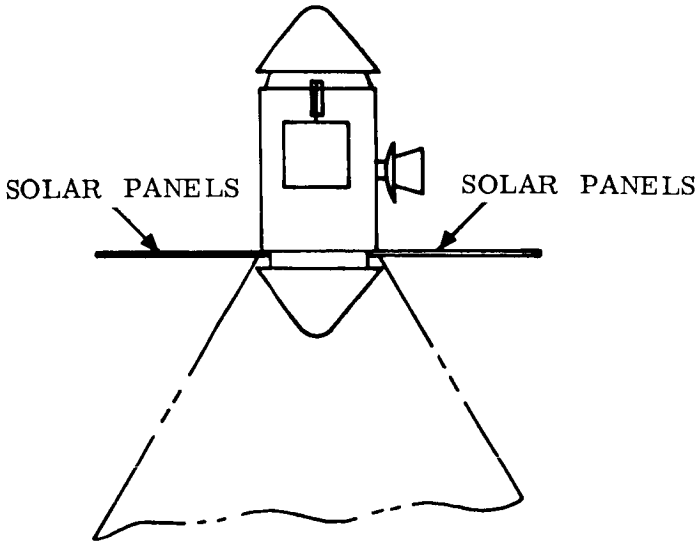


2. The second major configuration considered mounted the Landers on edge, and facing outboard. This allowed one Lander to be Sun oriented and one shade oriented. The structure above the Orbiter was required to hold the Landers during launch. At this point in time, there was sufficient subsystem definition to indicate that solar power would be used to supply the Voyager power requirements. A major drawback to this configuration is

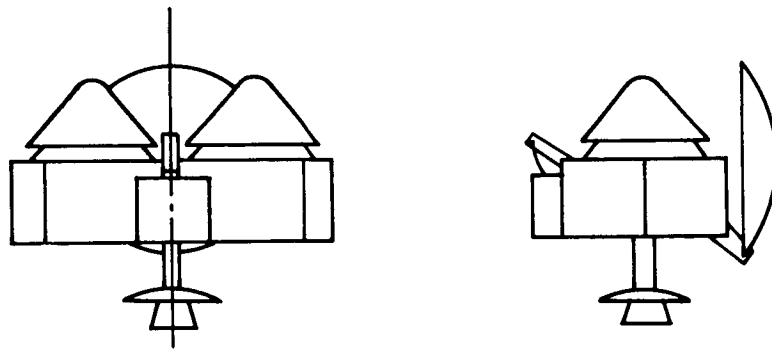
the difficulty of mounting solar panels. In addition, little growth is possible because of possible Lander interference with the shroud. Mounting one Lander would be extremely difficult.



3. The third configuration considered mounted the Landers on top and bottom of the Orbiter. The Orbiter structure was considered to be a right circular cylinder with subsystem components mounted internally. With this configuration, solar cells would have to be mounted on paddles with the Planet Horizontal Package and the Earth High Gain Antenna mounted on the external surface.



4. The fourth configuration mounted the Landers side by side with the Orbiter beneath the Landers and of a shape necessary to adequately mount all subsystem components. Solar cells may be mounted on existing panels, thus eliminating the need for deployable paddles. The structure provides convenient mounting surfaces for the PHP and the 10-foot diameter Earth antenna. Interior packaging density is low, thus allowing for expedient relocation of internal subsystem components as required for other years and missions.

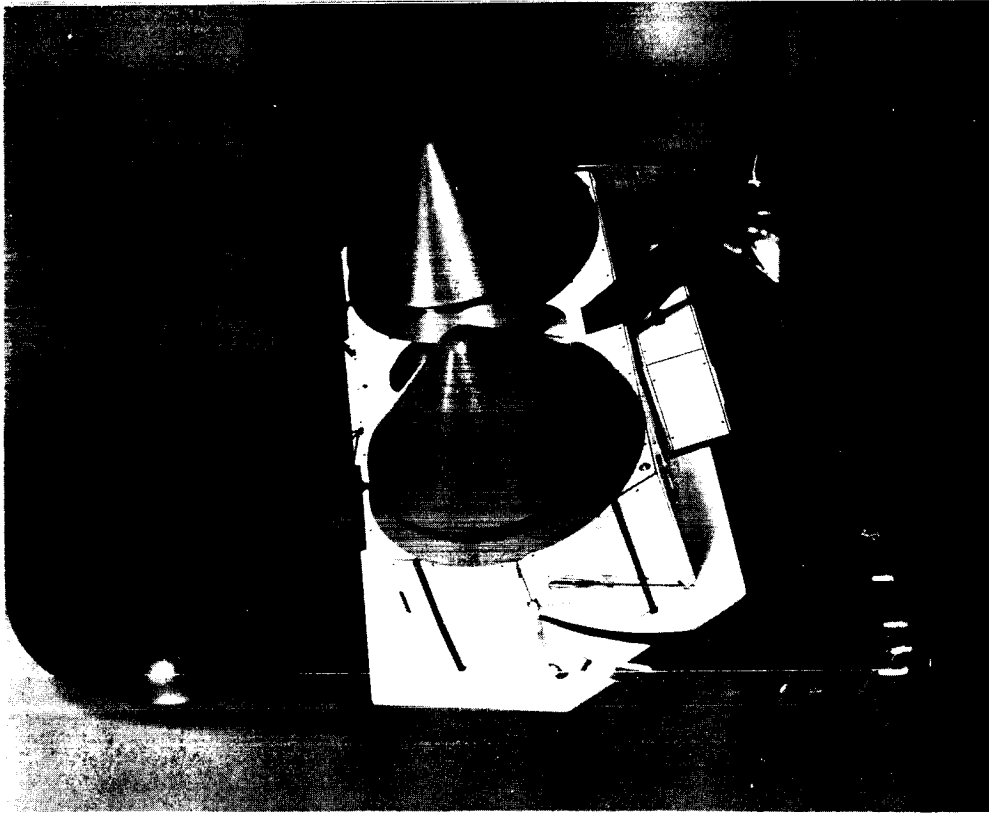
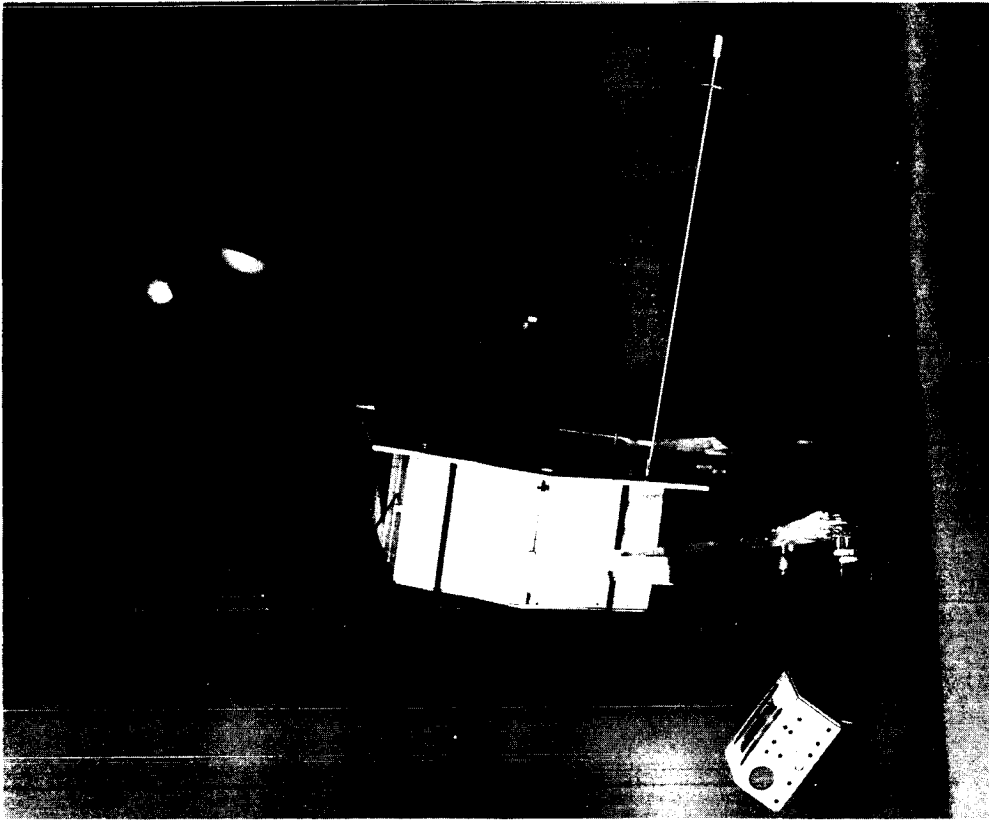


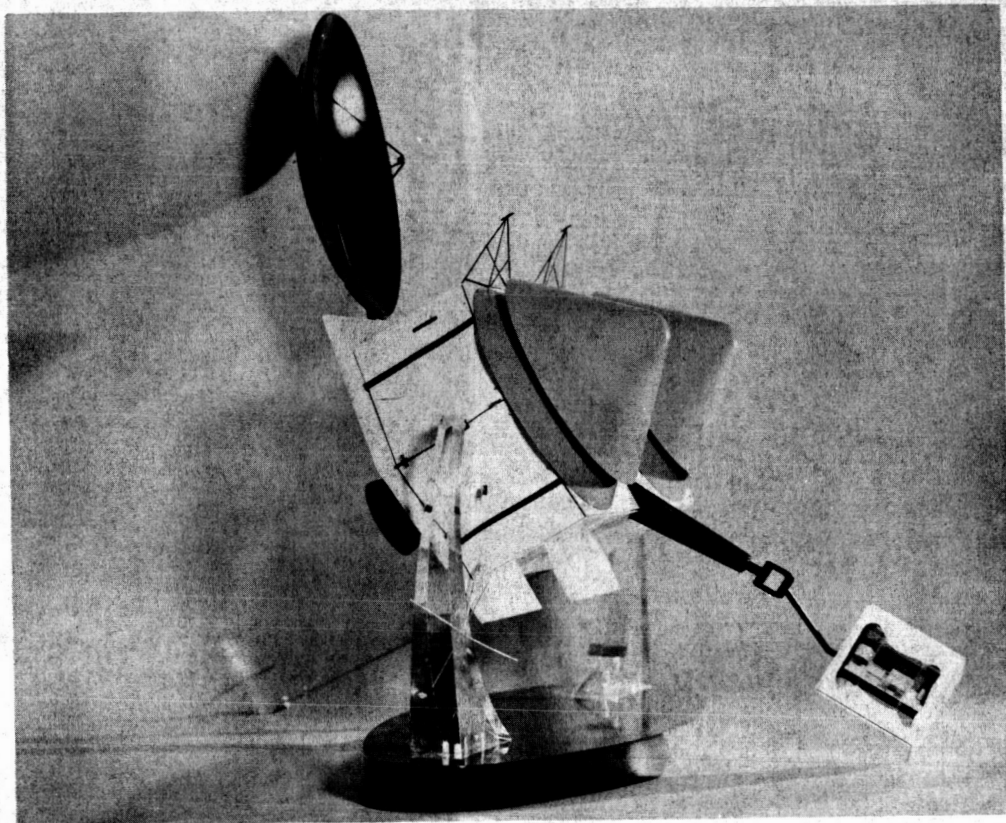
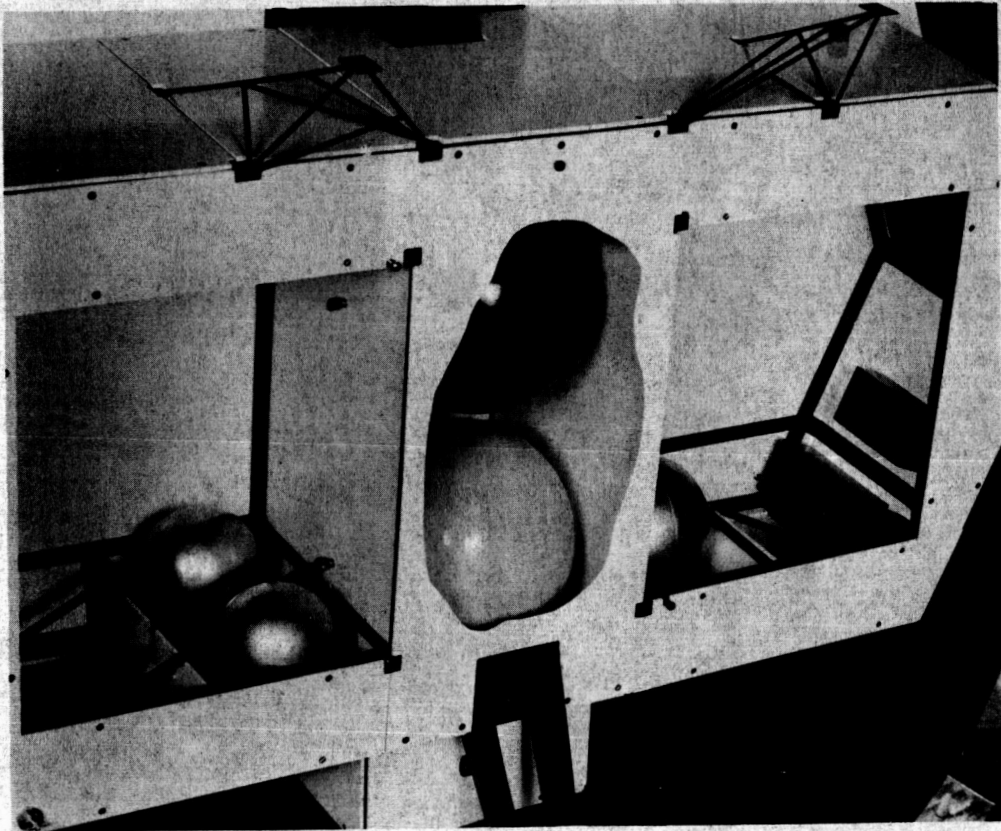
A decision as to the Orbiter System Configuration narrowed down to a consideration of configuration No. 3 and No. 4.

Item	Configuration No. 3.	Configuration No. 4.
Propulsion	Required four (4) tanks.	Required only two (2) tanks. (Better)
Communication	<p>PHP and 10-ft. dia. antenna require cutouts in Lander Adapter.</p> <p>View angles need only short PHP boom. (Better)</p>	<p>PHP and 10-ft. dia. antenna easily mounted on structure. (Better)</p> <p>View angles required long PHP boom.</p>
Power	Required deployable Solar Panels.	Can use fixed body mounted cells. (Better)
Guidance and Control	Lander ejected by force through c. g. (Better)	Landers ejected by force eccentric to c. g.
Thermal Control	Internally mounted, completely shielded components.	Internally mounted, completely shielded components.
Science	Requires jointed magnetometer boom.	Capable of mounting fixed magnetometer boom. (Better)

The final decision was made to select configuration No. 4 as the Voyager configuration. However, if major changes in subsystem selection occur, then configuration No. 3 should be reviewed in the light of these potential changes.

The following views show various arrangements of the selected Voyager configuration.





2.2.1 SEQUENCE OF EVENTS

In order to effectively create an Orbiter System, a knowledge of the events necessary to be performed is mandatory. The sequence of events for the Voyager Spacecraft from trajectory injection to Orbit insertion is shown below.

The basic assumption is that a successful ascent and injection into transit trajectory, with successful separation from the launch vehicle adapter will have been made.

Launch Date: January 10, 1969		Time to Complete Operation	Time to Begin Operation
Operation Sequence			
A.	Entry Into Transit Mode -----		Time 0 (Immediately after separation from launch vehicle.)
	1. Turn on transponder	1 min	
	2. Establish round trip phase lock	5 min	
	3. Turn on attitude control subsystem	1 sec	
	4. Orient to Sun	16 min	
	5. Deploy High-Gain Antenna and preprogram to point in Earth direction.	10 min	
	6. Switch to High-Gain from Omni by means of Earth Communication	1 sec	
	7. Orient to Canopus	48 min	
	8. Earth verification of reference acquisition	60 min	
	9. Switch to Omni	1 sec	
	10. Stow Antenna	10 min	
	11. Shut down Gyros	1 sec	
B.	First Mid-Course Correction-----		Time 0 + 1-2 weeks
	1. Switch on Gyros	1 sec	
	2. Commands received from Earth, acknowledged and verified by spacecraft and stored in the Programmer	7 min	
	3. Orientation of spacecraft by means of attitude control subsystem to required spatial orientation	12 min	
	4. Firing of Main Engine	1 min	
C.	Reorientation to the Sun-----		Immediately following engine firing
	1. Commands read out by Programmer	10 sec	
	2. Orientation to Sun and verification	6 min	

		<u>Time to Complete Operation</u>	<u>Time to Begin Operation</u>
	3. Orientation to Canopus and verification	6 min	
	4. Sensor errors telemetered to Earth upon completion	5 min	
	5. Shut down Gyros	1 sec	
D.	Second Mid-Course Correction-----		Time 0 + 5-8 weeks
	1. Switch on Gyros	1 sec	
	2. Commands received from Earth, acknowledged and verified by spacecraft and stored in the Programmer	12 min	
	3. Orientation of spacecraft by means of attitude control subsystem to required spatial orientation	12 min	
	4. Firing of Main Engine	1 min	
E.	Reorientation to the Sun-----		Immediately following engine firing
	1. Commands read out by Programmer	10 sec	
	2. Orientation to Sun and verification	6 min	
	3. Orientation to Canopus and verification	6 min	
	4. Sensor errors telemetered to Earth upon completion	10 min	
	5. Shut down Gyros	1 sec	
F.	High-Gain Antenna Deployment-----		Time 0 + 187 days
	1. Commands transmitted to spacecraft and verified	30 min	
	2. High-Gain Antenna pointed to Earth using sensor corrected on programmed angles	10 min	
	3. Switch to High-Gain Antenna	1 sec	
G.	Terminal Guidance Observation (2×10^6 nm from Planet)---		Time 0 + 258 days
	1. Commands transmitted to the spacecraft and verified	40 min	
	2. Body mounted I.O. camera turned on	5 min	
	3. TV pictures taken of planet and background		

		<u>Time to Complete Operation</u>	<u>Time to Begin Operation</u>
H.	Final Trajectory Correction (1 x 10 ⁶ nm from Planet)-----		Time 0 + 264 days
	1. Switch on Gyros	1 sec	
	2. Command transmitted to spacecraft and verified	40 min	
	3. Switch to Omni	1 sec	
	4. Store High-Gain Antenna	10 min	
	5. Orientation of spacecraft by means of attitude control subsystem to required orientation	12 min	
	6. Firing of Main Engine	1 min	
I.	Reorientation to Sun-----		Immediately after engine firing
	1. Commands read out by Programmer	10 sec	
	2. Orientation to Sun and verification	6 min	
	3. Orientation to Canopus and verification	6 min	
	4. Deploy High-Gain Antenna	10 min	
	5. Switch to High-Gain Antenna	1 sec	
	6. Sensor angles telemetered to Earth	10 min	
	7. Shut down Gyros	1 sec	
	8. TV pictures taken of planet and background		
J.	Lander Ejection (150,000 nm from planet)-----		Time 0 + 269 days
	1. Switch on Gyros	1 sec	
	2. Command transmitted to the spacecraft and verified	40 min	
	3. Orientation of spacecraft to desired spatial orientation	12 min	
	4. Physical attachment of Lander to Orbiter broken	1 sec	
	5. Lander is separated from Orbiter $\Delta V = 1$ ft/sec	1 sec	
	6. Lander spin up to 60 RPM	30 sec	

		<u>Time to Complete Operation</u>	<u>Time to Begin Operation</u>
	7. Orbiter is reoriented for second Lander ejection	6 min	
	8. Second Lander is ejected	1 min	
	9. Lander ΔV rocket engine fires. Distance from Orbiter approximately 1000 ft.	15 sec	
	10. Second Lander ΔV rocket engine fires	15 sec	
K.	Orbiter Reorientation to the Sun-----		Immediately following Lander ejection
	1. Commands read out by Programmer	10 sec	
	2. Orientation to Sun and verification	6 min	
	3. Orientation to Canopus and verification	6 min	
	4. Sensor angles telemetered to Earth	10 min	
L.	Orbiter Orientation and Injection into Orbit-----		50 minutes before retro engine firing
	1. Commands transmitted to spacecraft and verified		
	2. Switch to Omni Antenna	1 sec	
	3. Stow High-Gain Antenna	10 min	
	4. Orientation of spacecraft to required orientation	10 min	
	5. Firing of Main Engine	5 min	
M.	Orbiter In Orbit-----		Time 0 + 270 days
	1. Commands read out by Programmer	10 sec	
	2. Orientation to Sun and verification	4 min	
	3. Orientation to Canopus and verification	6 min	
	4. Deploy High-Gain Antenna	10 min	
	5. Switch to High-Gain Antenna	1 sec	
	6. Sensor angles telemetered to Earth	15 min	
	7. Deploy PHP	10 min	
	8. Switch to VHF Yagi Antenna on PHP	1 sec	
	9. Deploy any other instrumentation required for the specific mission	10 min	
	10. Shut off Gyros	1 sec	

Figure 2.2.1-1 graphically portrays the sequence of events previously presented. Each item from injection into trajectory, to Orbit injection provides inputs for the Orbiter system selection and configuration design.

Figure 2.2.1-2 portrays the block diagram for the Voyager Orbiter indicating actions, components, and subsystem interconnections necessary to accomplish the sequence of events.

Figure 2.2.1-3 indicates the final configuration axes as used in Volume IV.

2.2.2 SHROUD CLEARANCES

Figure 2.2.2-1 shows the Voyager Spacecraft mounted to a 45-inch high adapter within the preliminary shroud configuration delineated by JPL. It is required that a vertical section of 60 inches be made available at the base of the shroud in order to clear the Spacecraft. This effectively changes the point at which the 12.5° shroud angle begins.

All spacecraft appendages are confined within the shroud and adapter sections.

Another possible configuration is shown in Figure 2.2.2-2. In this sketch, the Spacecraft has been lowered into the booster approximately 36 inches. The adapter section is replaced by a toroidal-shaped Booster Instrument Section with the Spacecraft Engine and Radiation Shield located in the center of the Torus. The advantages to this system are:

1. The spacecraft center of gravity has been lowered 36 inches reducing the launch vehicle bending loads.
2. The adapter weight is utilized for a stiff booster toroidal upper section to allow for introduction of the spacecraft loads.
3. The required shroud vertical section has been reduced to 24 inches.
4. The spacecraft to booster load path is more direct and minimizes bending at the launch vehicle top plane.

2.2.3 CONCLUSIONS AND RECOMMENDATIONS

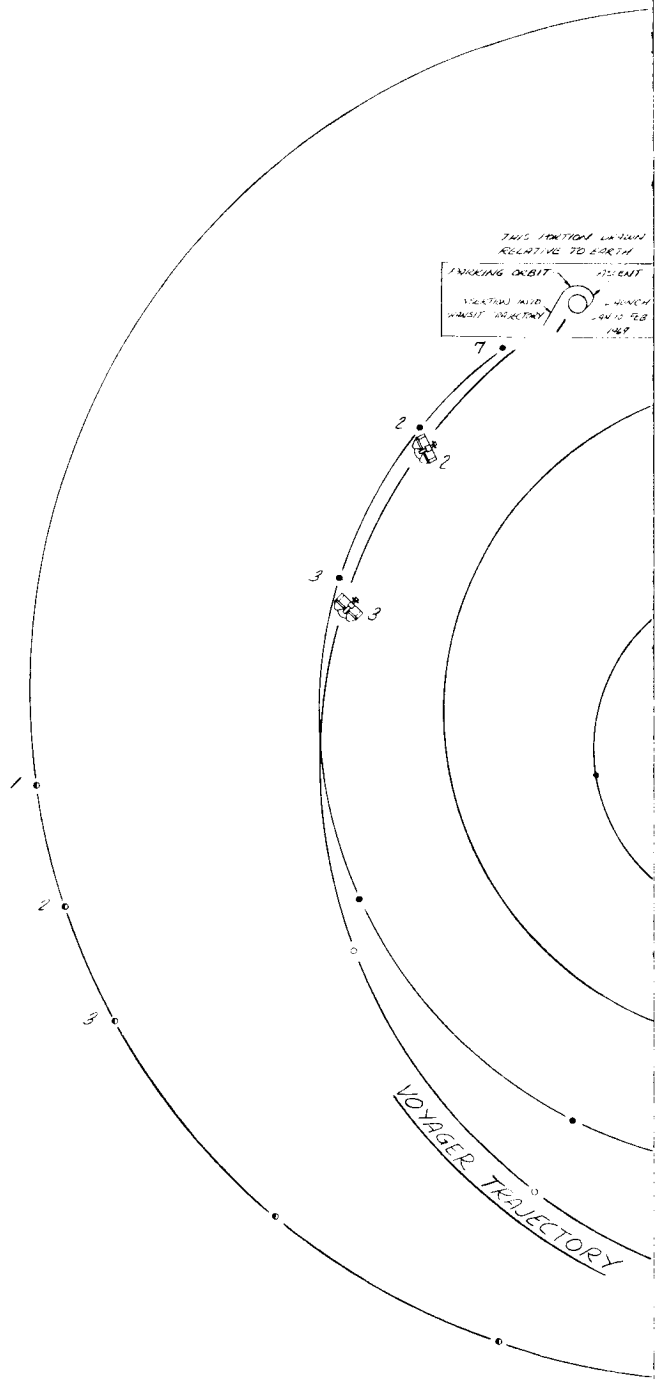
The final conclusions concerning the Voyager Orbiter can be separated into two general statements:

1. The Voyager spacecraft and required components are feasible in concept and application.
2. Development problems in several areas require advance analysis and testing prior to finalization of the design.

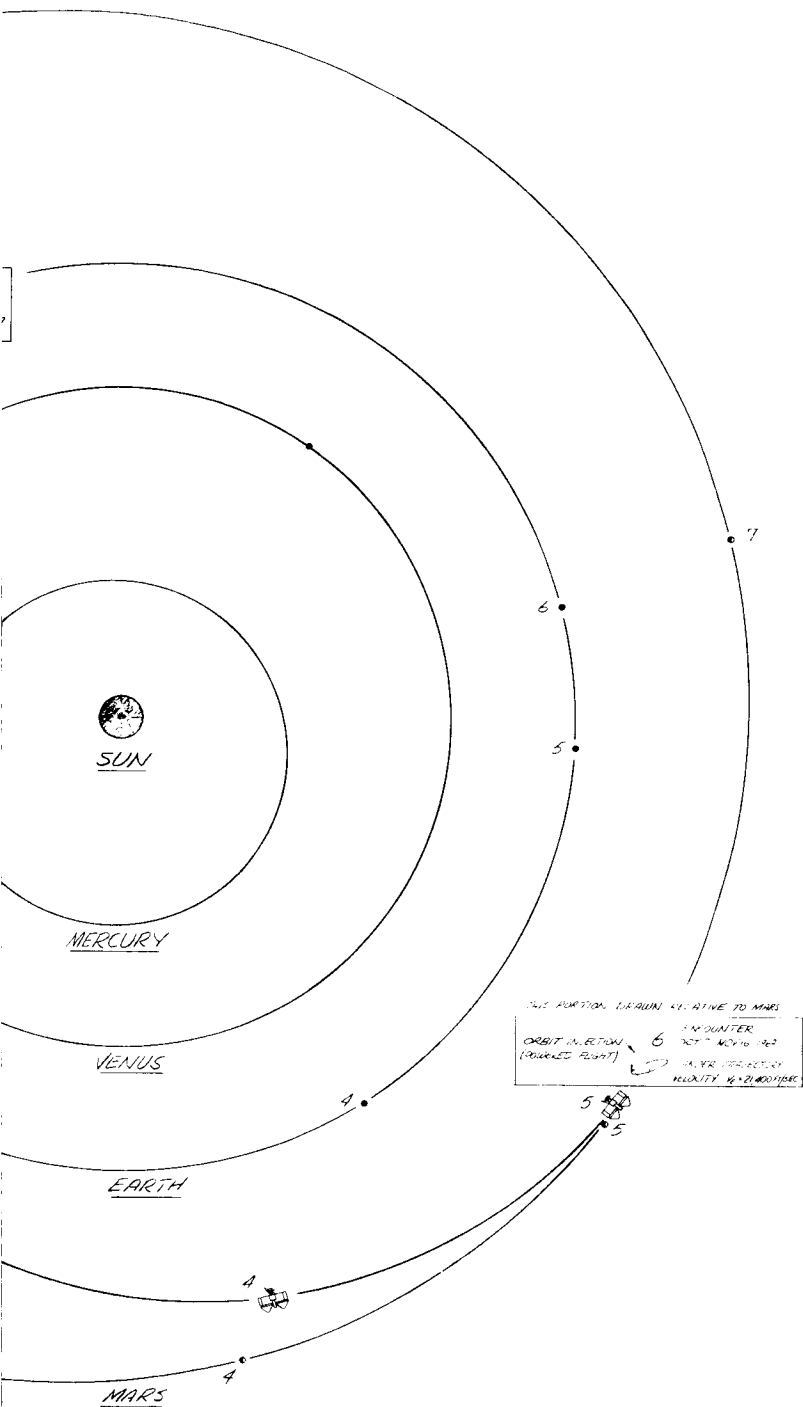
It is recommended that the following technology areas be investigated in order that early answers required for Voyager can be obtained:

1. Thermal control of the Orbiter and PHP, particularly for Venus. This will include evaluation of coatings, design of active control louvers, and means of thermal modeling.
2. Materials development (bearings and seals) consistent with long-time space exposure and their operation.

3. Design and testing of a separation system capable of separating the Lander from the Orbiter with minimum perturbations.
4. Design and development of pyrotechnic devices required to give reliable operation after long-time space exposure.
5. Investigation of residual magnetic fields and their effect on the Magnetometer.
6. Development of methods of magnetic field "shielding" in order to obtain measurements on earth to an accuracy of 0.1 gamma.



1

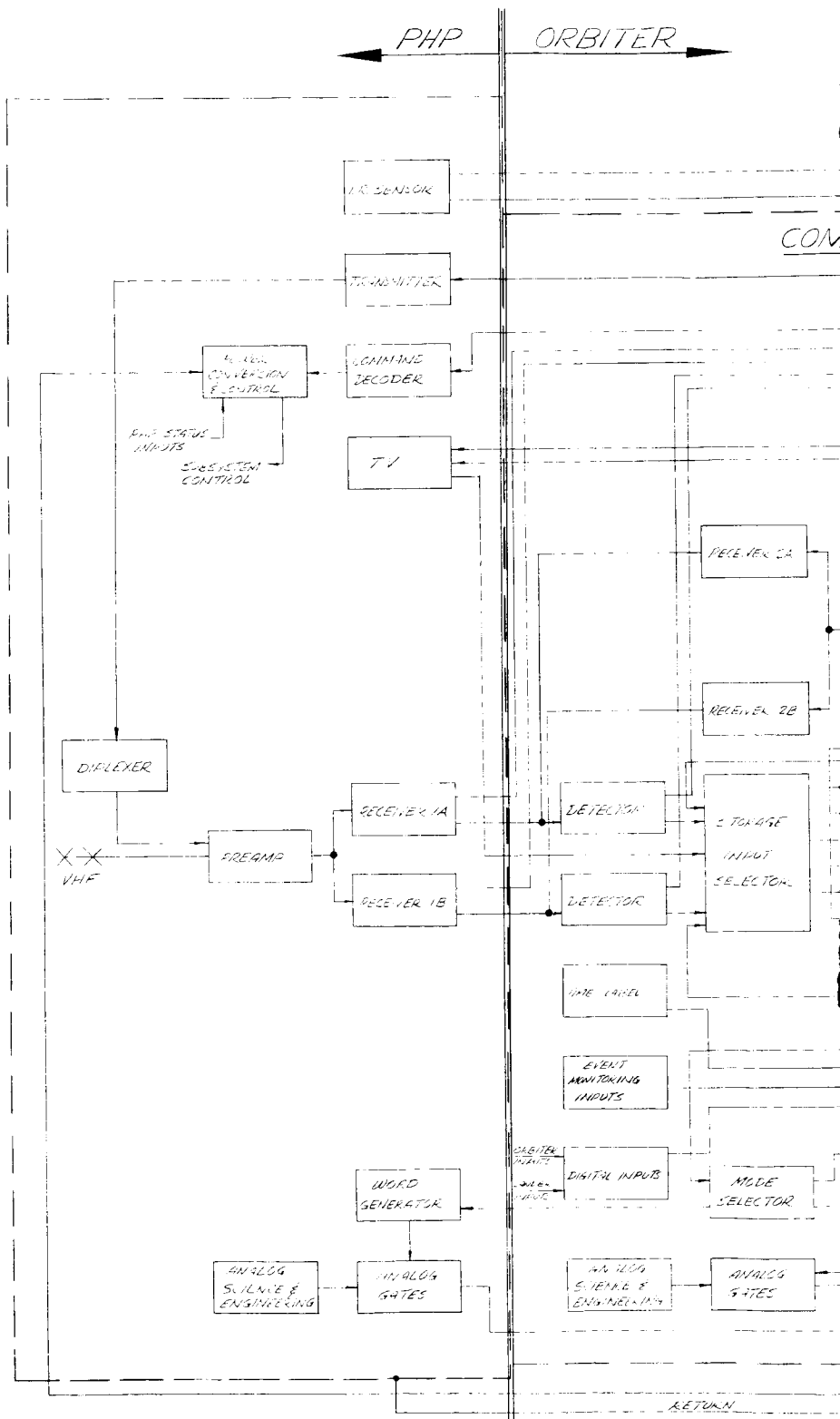


POSITION	EVENT
1	LAUNCH
2	1 ST MID-COURSE CORRECTION
3	2 ND MID-COURSE CORRECTION
4	HIGH-GAIN ANTENNA DEPLOYMENT
5	TERMINAL GUIDANCE OBSERVATION
6	PLANET ENCOUNTER
7	90 DAYS AFTER ENCOUNTER

VOYAGER TRAJECTORY
MARS 69-1B

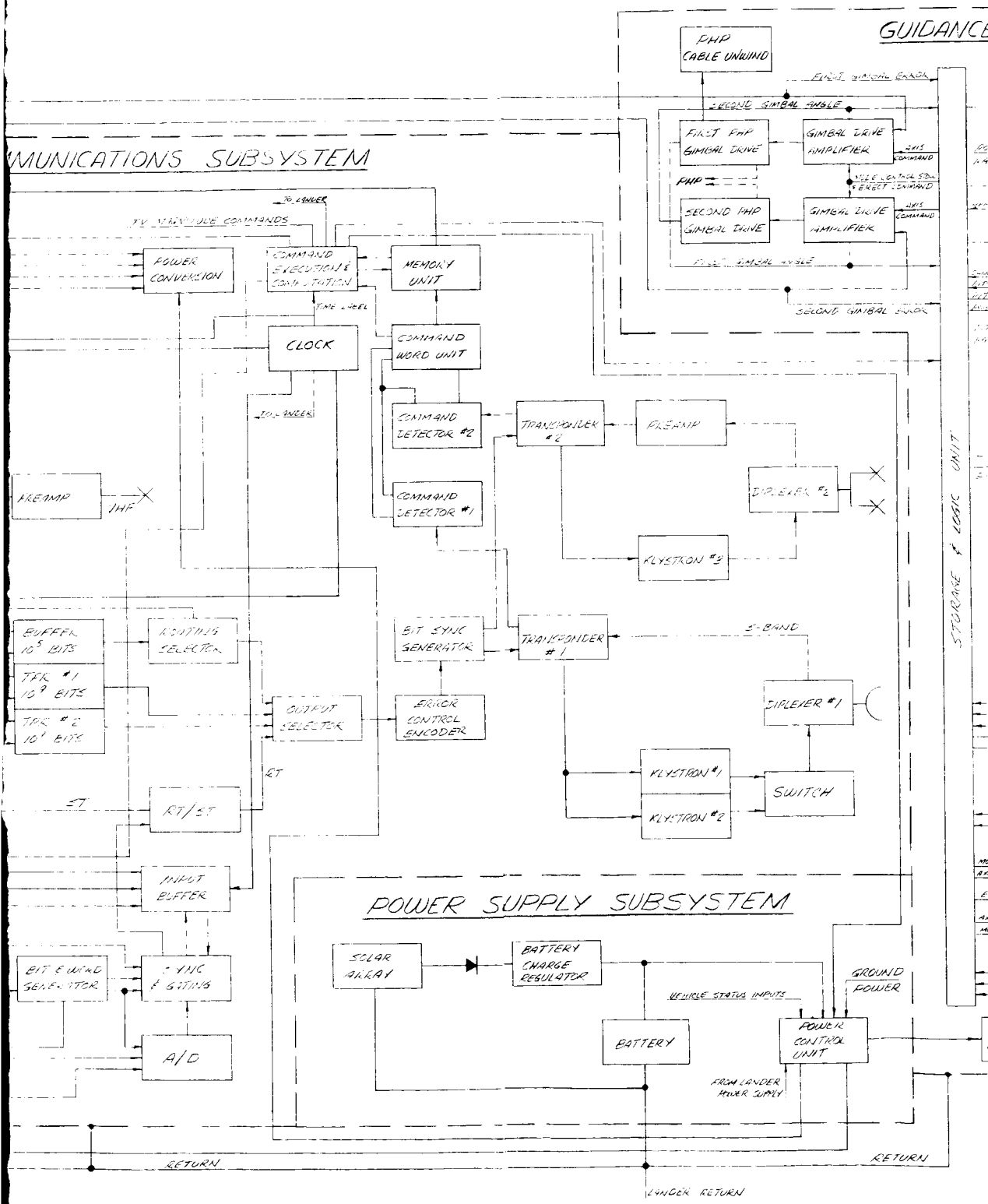
DRAWN BY M ALLEN
DATE 13 SEPT 1969

Figure 2.2.1-1. Sequence of Events -
Mars 1969

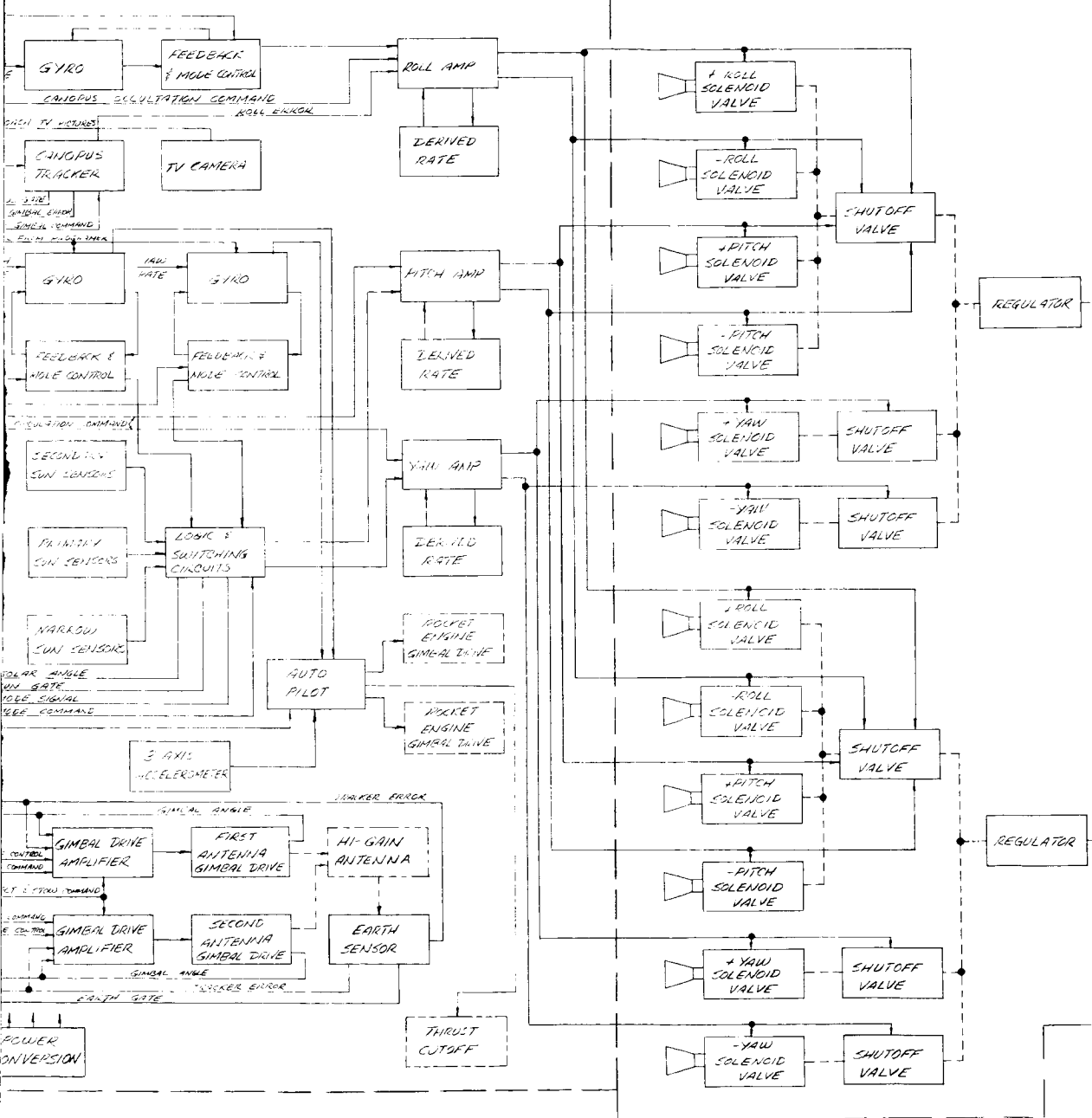


COMMUNICATIONS SUBSYSTEM

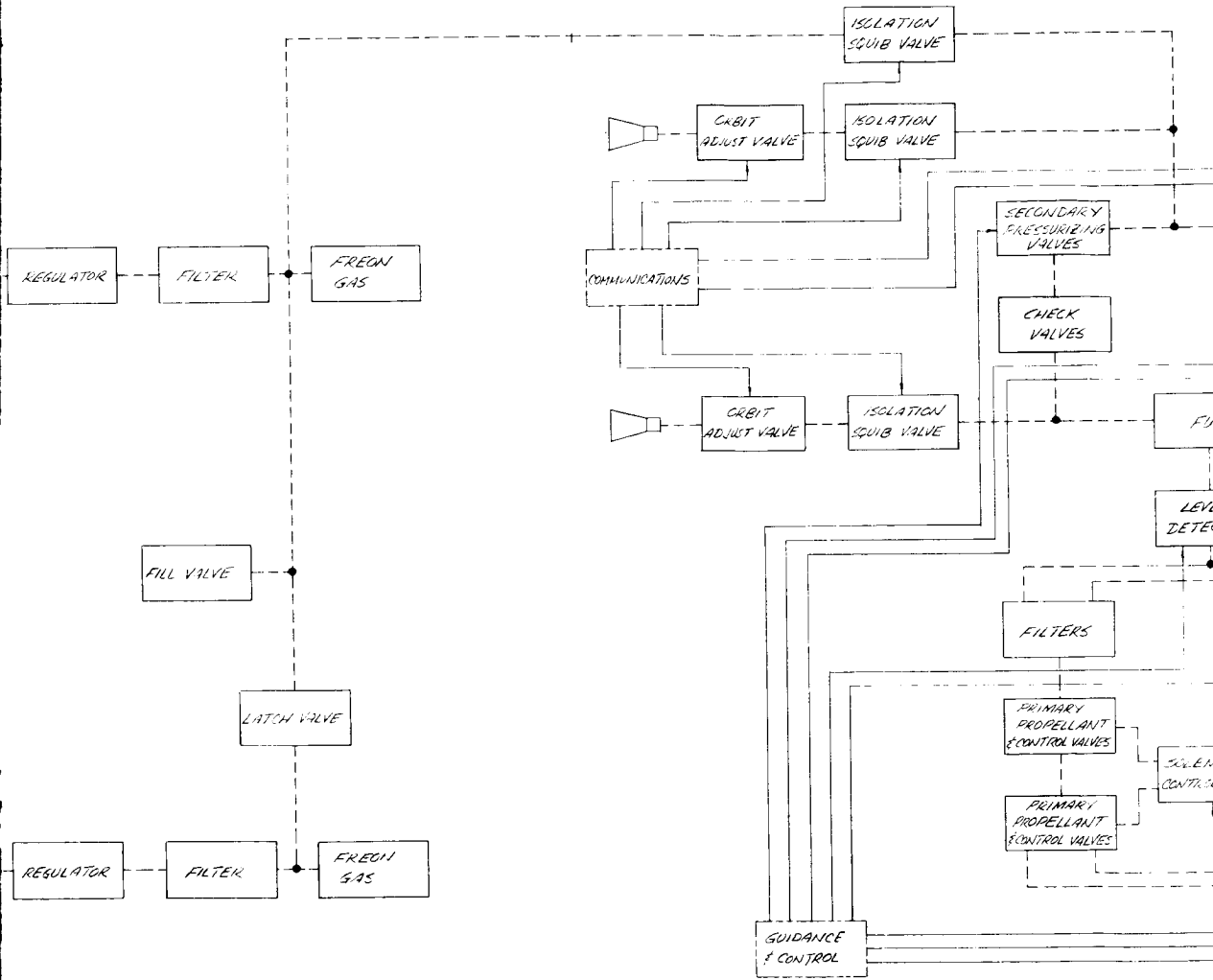
GUIDANCE



CONTROL SUBSYSTEM



PROPULSION SUBSYSTEM



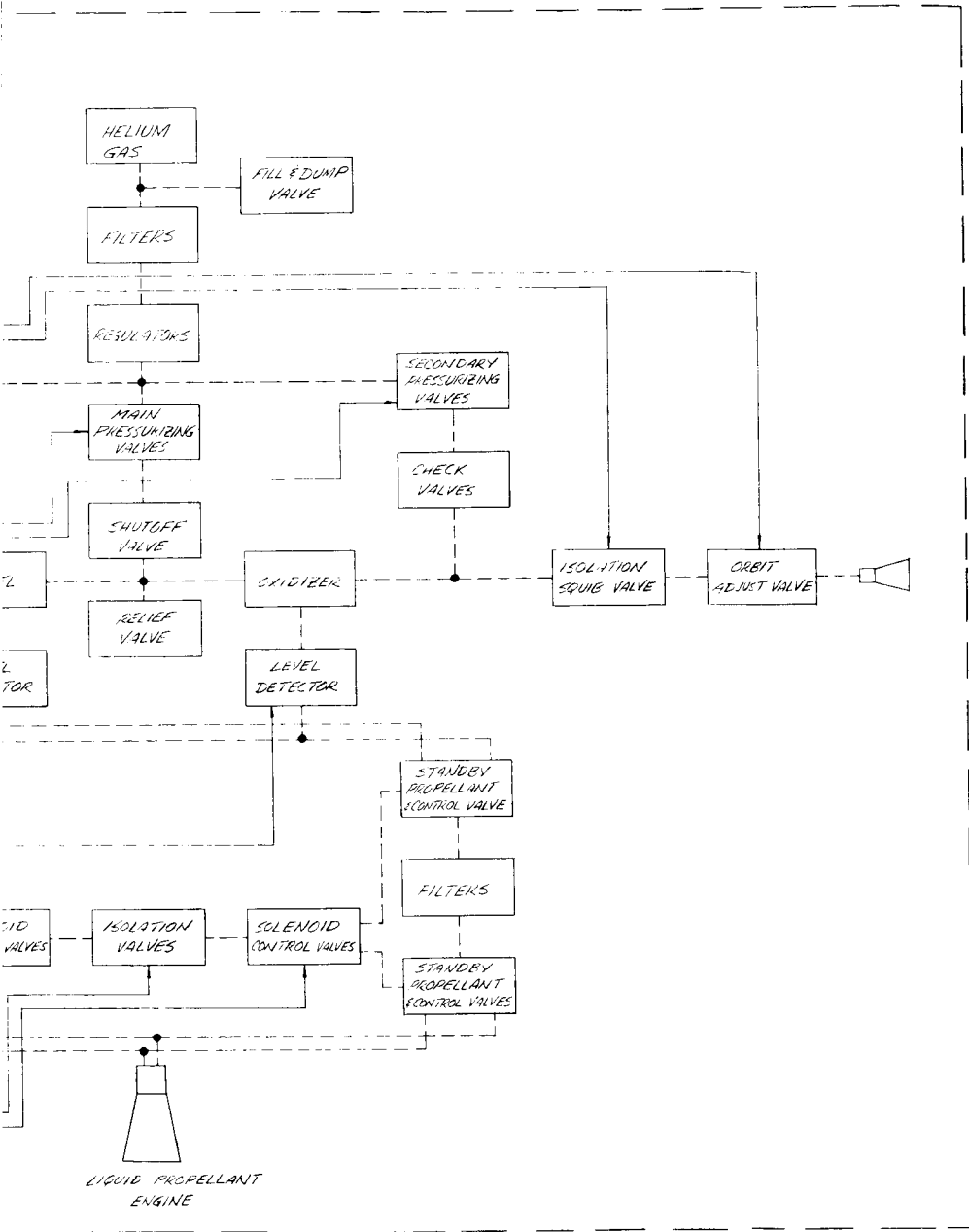


Figure 2. 2. 1-2. Voyager Orbiter System Block Diagram

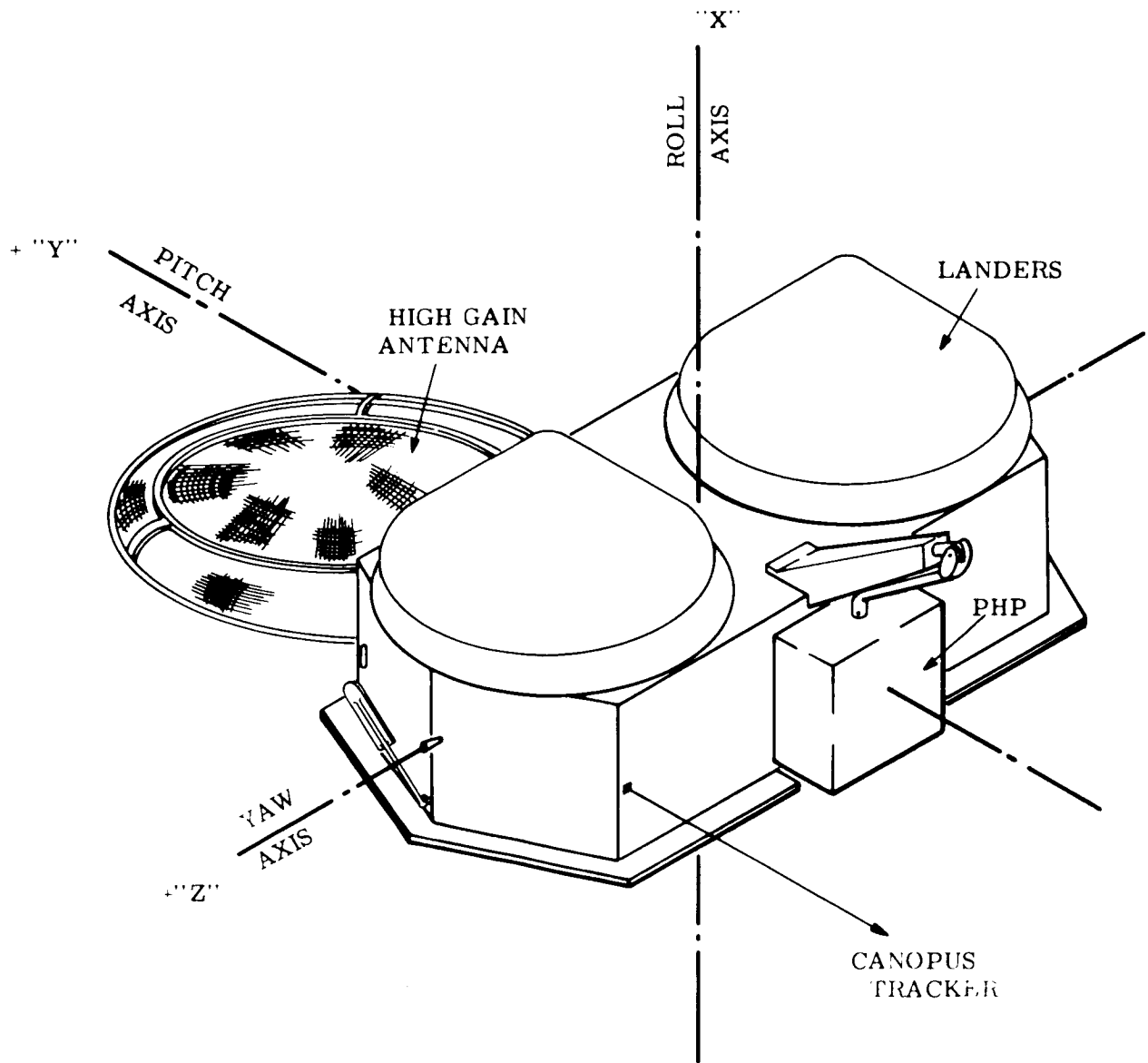


Figure 2.2.1-3. Voyager Orbiter Axes

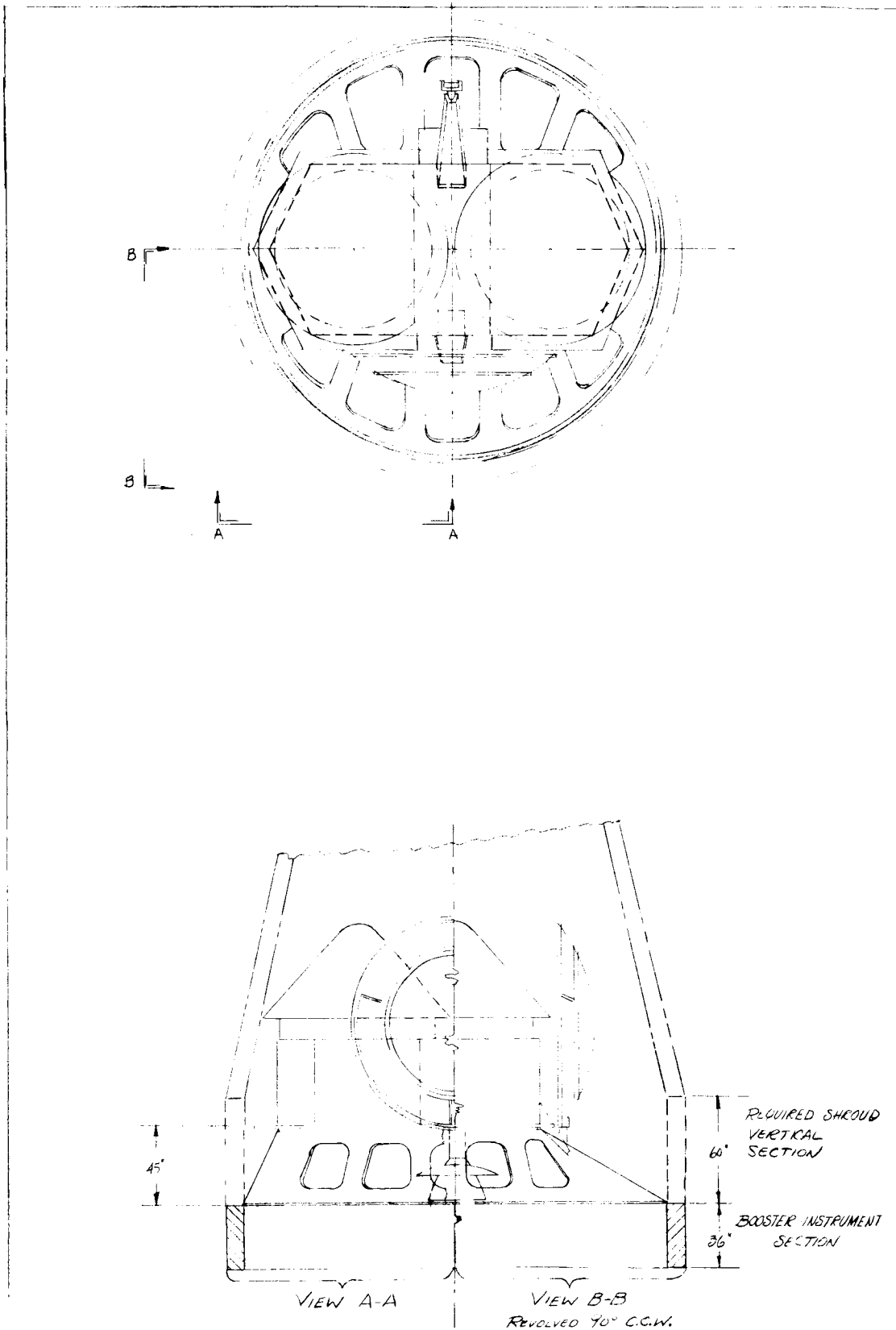


Figure 2.2.2-1. Voyager plus 45 in. Adapter Within Saturn Shroud.

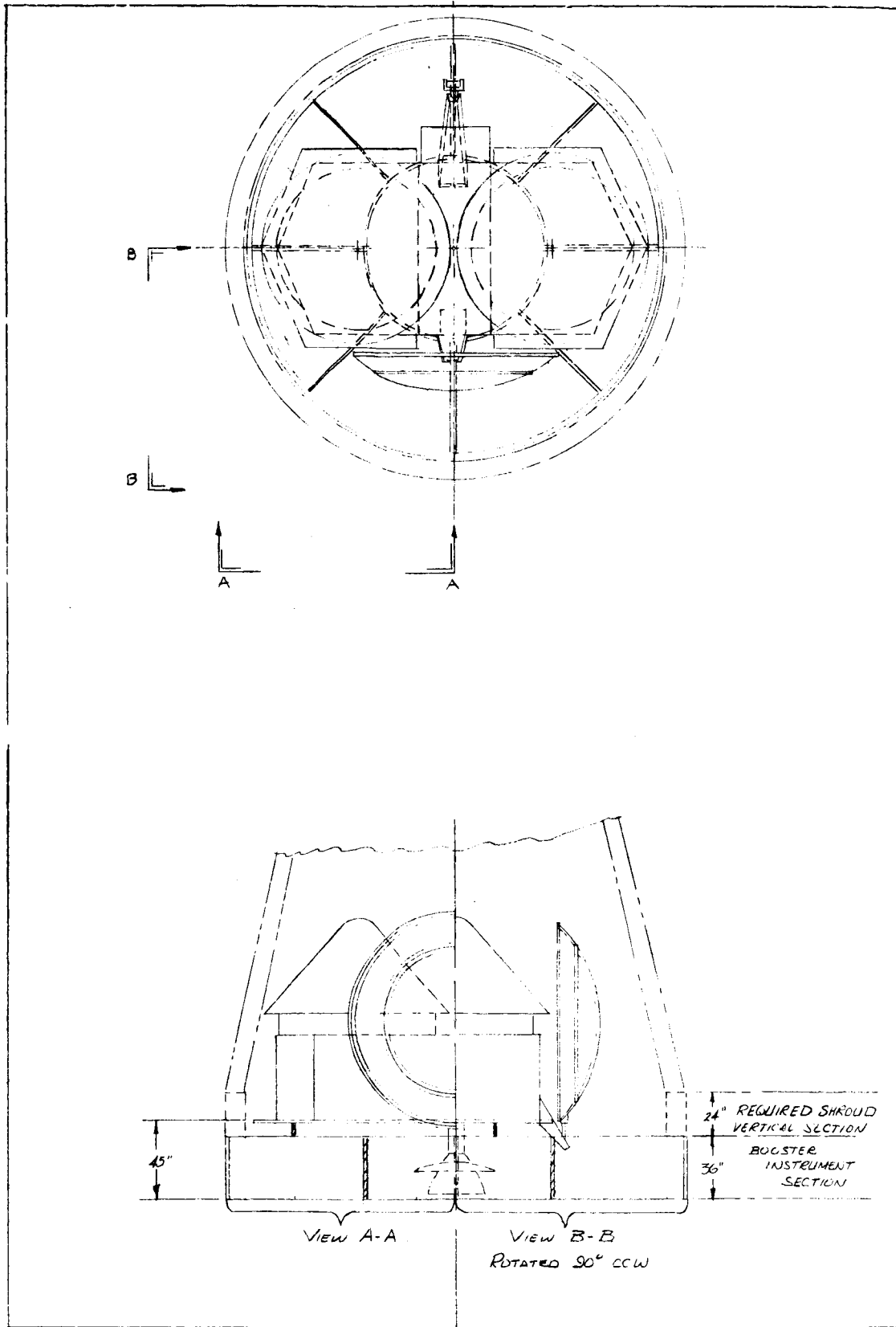


Figure 2.2.2-2. Voyager Mounted on Combined Instrument Unit-Adapter Within Saturn Shroud

2.3 ORBITER CONFIGURATION DESIGN AND INTEGRATION

2.3.1. GENERAL

The Voyager Spacecraft consists of an Orbiter, Lander(s), and a transition section (adapter) between the Orbiter and the booster. The Orbiter will separate from the adapter upon insertion into the transit trajectory and transport the Lander(s) to the proper spatial location and orientation for ejection into the desired planet impact trajectory(ies). The Orbiter will have the capability to support the following Landers for Mars and Venus opportunities:

<u>No. of Landers</u>	<u>Weight (lbs)</u>	<u>Planet Opportunity</u>
2	1450	Mars 1969
2	2000	Mars 1971
2	2000	Mars 1973
2	2000	Mars 1975
1	525	Venus 1970
1	2600	Venus 1972

The Orbiter will be launched with the above equipment secured to the vehicle. Upon injection and transit, the Orbiter will orient to the Sun. With the exception of mid-course maneuvers, Lander ejection, and Orbit insertion; the Orbiter will remain Sun/Canopus oriented (solar cells facing the Sun).

2.3.2 ORBITER DESCRIPTION

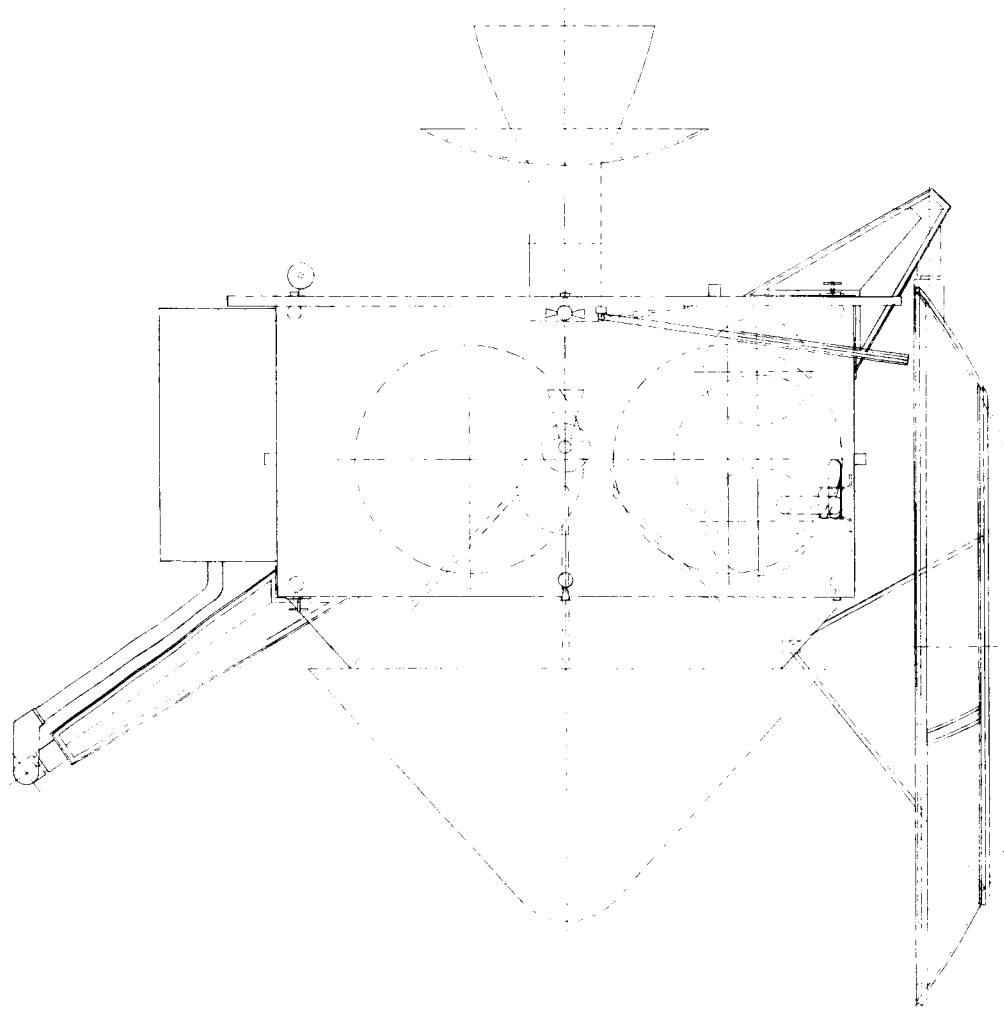
The Orbiter configuration (See Figures 2.3.2-1 and 2.3.2-2) chosen is a six sided polygon containing scientific, propulsion, guidance, power, and communications subsystems. These subsystems will enable the Orbiter to perform the dual mission of collecting scientific information and acting as a communications and command relay link for the Lander(s) which will have been conducting planet surface experiments and measurements. The support structure for these subsystems consists of a framework of extruded sections (angles, tees, etc.) machined fittings and honeycomb panels, which have been stiffened at local attachment points. Twenty honeycomb panels are removable in areas where accessibility to components is required for harnessing, repairs, and replacement. The basic size of the Orbiter is 200 inches long, 96 inches wide, and 50 inches high. The following paragraphs describe the Mars 1969 Orbiter.

Science — Most of the Orbiter scientific payload is located in the Planet Horizontal Package (PHP), a planet oriented package. The control for this package consists of a two-axis dual horizontal scanner and control drive motors. The remaining science payload is mounted to the Orbiter structure.

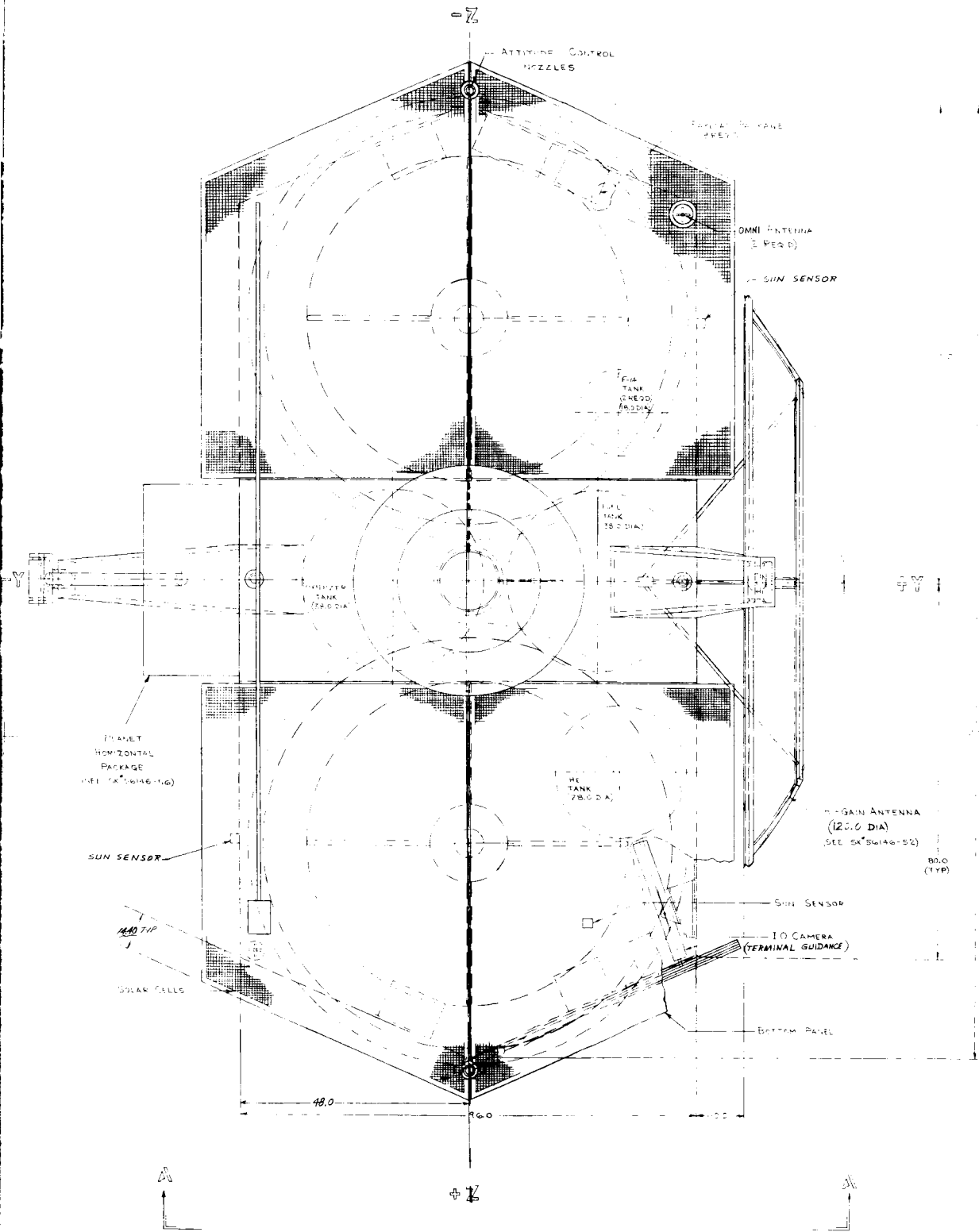
Propulsion — The propulsion subsystem consists of fuel, oxidizer, and helium pressurization tanks, and a hydraulically actuated, thrust vector controlled engine for mid-course corrections and orbit injection. An orbit-trim nozzle, connected to the propulsion pressurization system, is included in the event the orbit becomes synchronous with the planet's rotation about its own axis.

Guidance and Control (G & C) — The G & C subsystem consists of two nitrogen storage tanks, attitude control jets, gyro stabilization sensors, Earth sensors, Sun sensors, star-trackers, and an image orthicon camera for observation of the planet and star background plus all associated electronics required.

Power Supply — The power supply subsystem consists of a body mounted solar array, storage batteries and associated electronics.



VIEW A-A



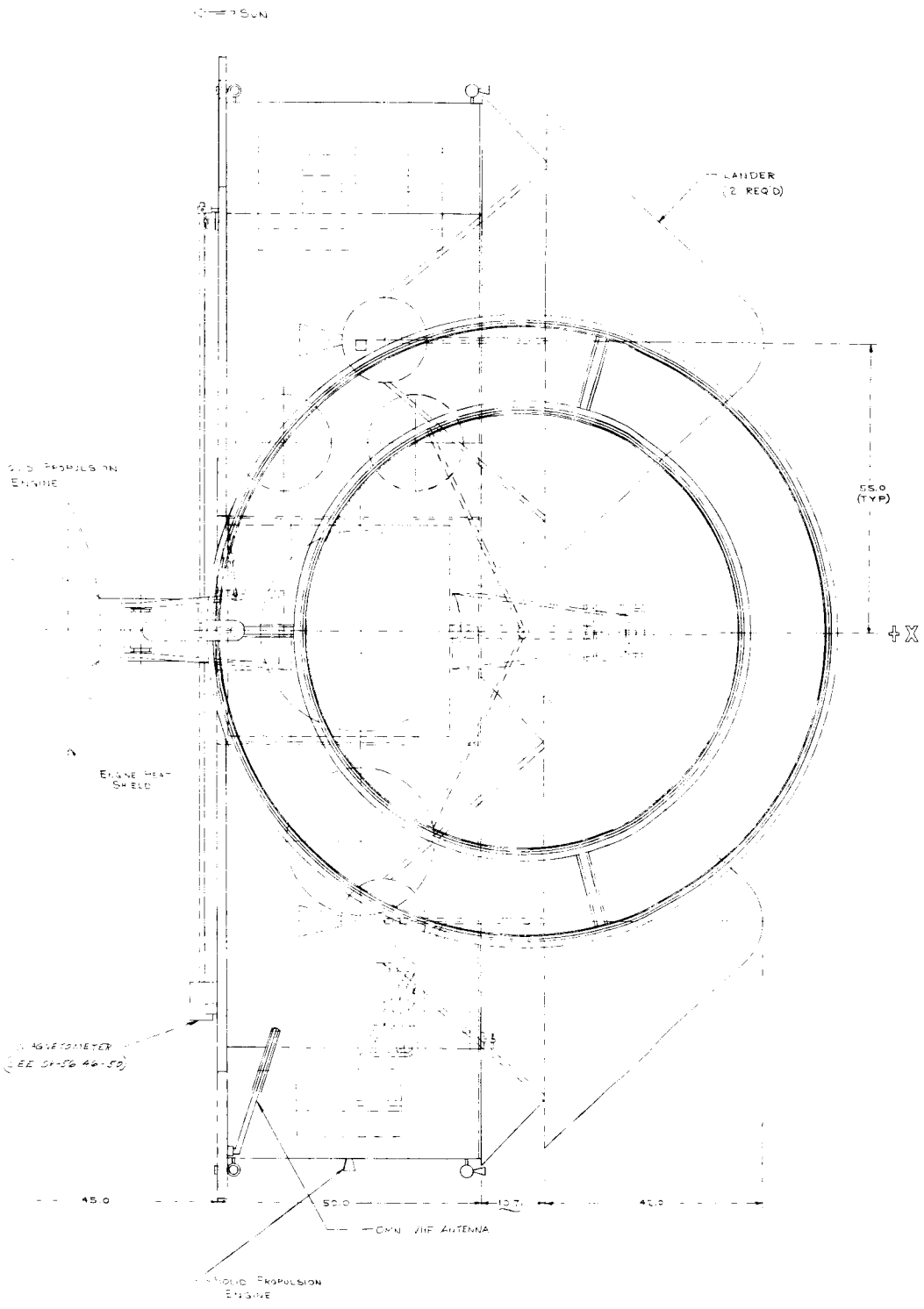
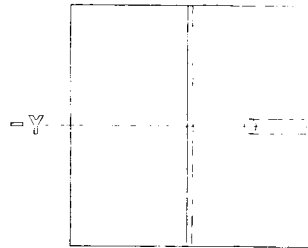
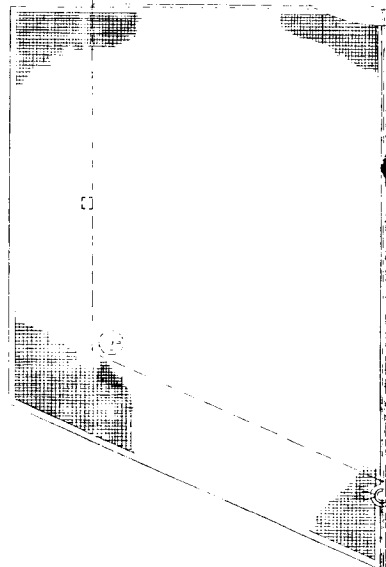
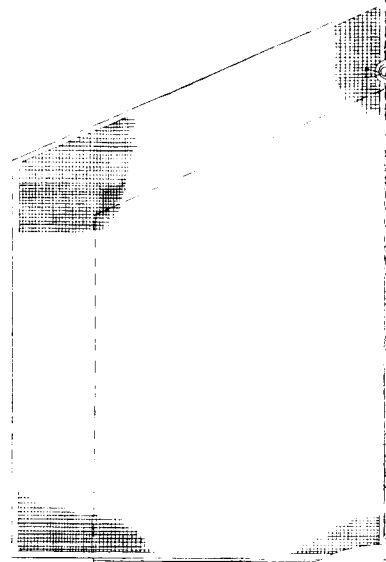


Figure 2.3.2-1. Voyager Launch Configuration

3

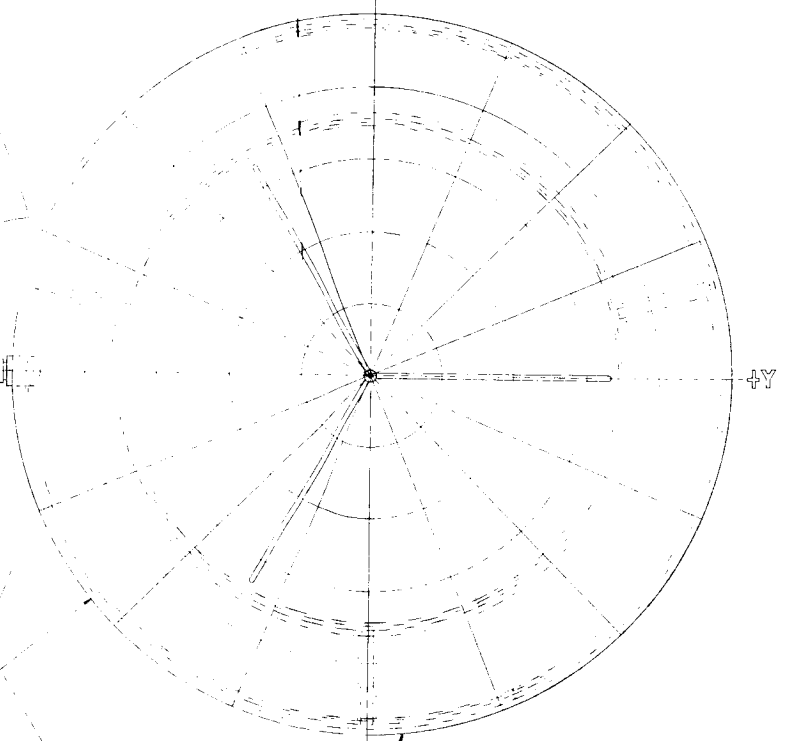
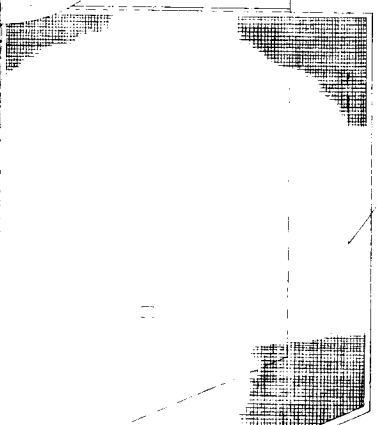
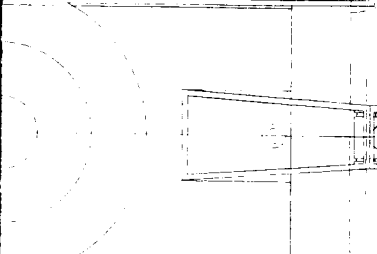
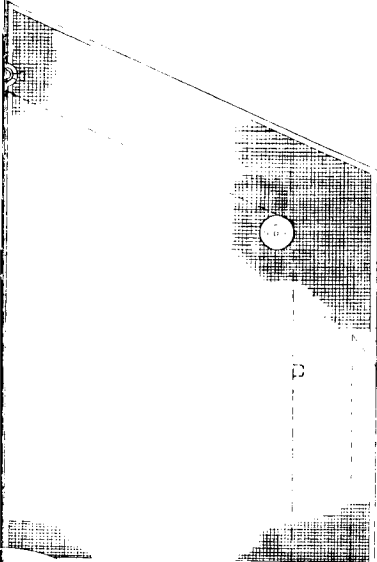


PLANET HORIZONTAL PACKAGE
- (STOWED DURING TRANSIT)
- (DEPLOYED DURING ORBIT)



Z

MAGNETOMETER
(STOWED DURING TRANSIT)
(DEPLOYED DURING ORBIT)
SEE SK-56146-5



H-GAIN ANTENNA
(STOWED & DEPLOYED DURING TRANSIT)
(DEPLOYED DURING ORBIT)
SEE SK-56146-52

133.0

30°

SUN

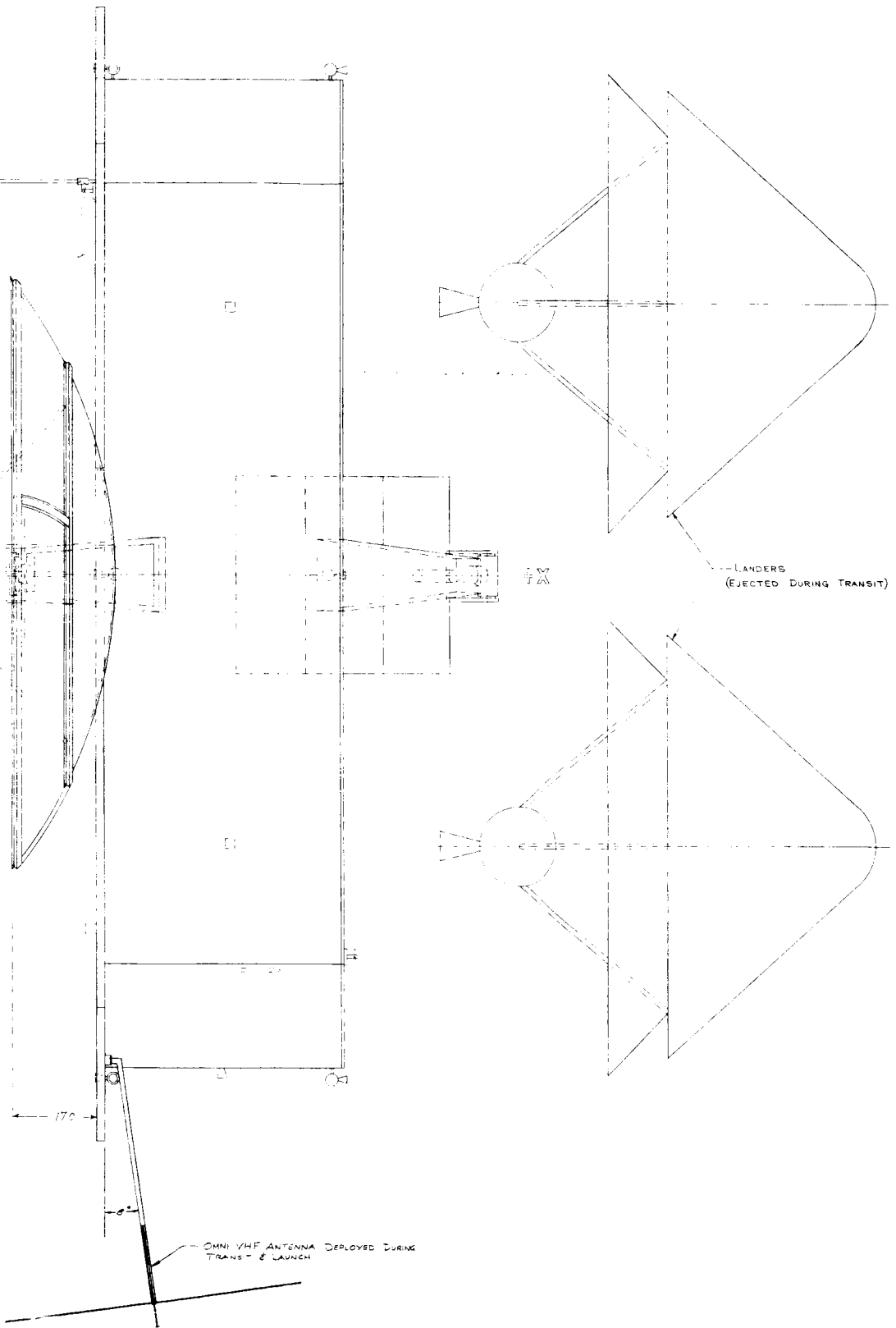


Figure 2.3.2-2. Voyager Transit Configuration

Communication — The communication subsystem consists of: a 10-foot diameter parabolic antenna, two DSIF omnidirectional antennas for Earth communication, an omnidirectional VHF antenna, and a VHF antenna mounted to the PHP for Lander communications. The electronics for the Earth and Mars communication system is located in the Orbiter and PHP. The Venus 1970 Orbiter will carry a 10-foot Cassegrain antenna to perform its radar mapping mission.

2.3.3 VIEW ANGLES

A. General

The main body of the Orbiter is a Sun/Canopus oriented vehicle at all times during orbit and transit with the exception of Engine Firing and lander ejection. The Planet Horizontal Package and the High Gain Antenna are oriented to the orbited planet and Earth through their respective sensing devices. The Image Orthicon Camera and VHF Antenna that are mounted to the Orbiter are located at the correct angle to view Mars throughout the terminal guidance phase. In addition, two Earth Communication Omnidirectional Antennas have been fixed to the orbiter structure such that Earth is "visible" from one of the omnidirectional antennas at any given time. The liquid propellant engine may be gimballed $\pm 10^\circ$ to achieve thrust vector control.

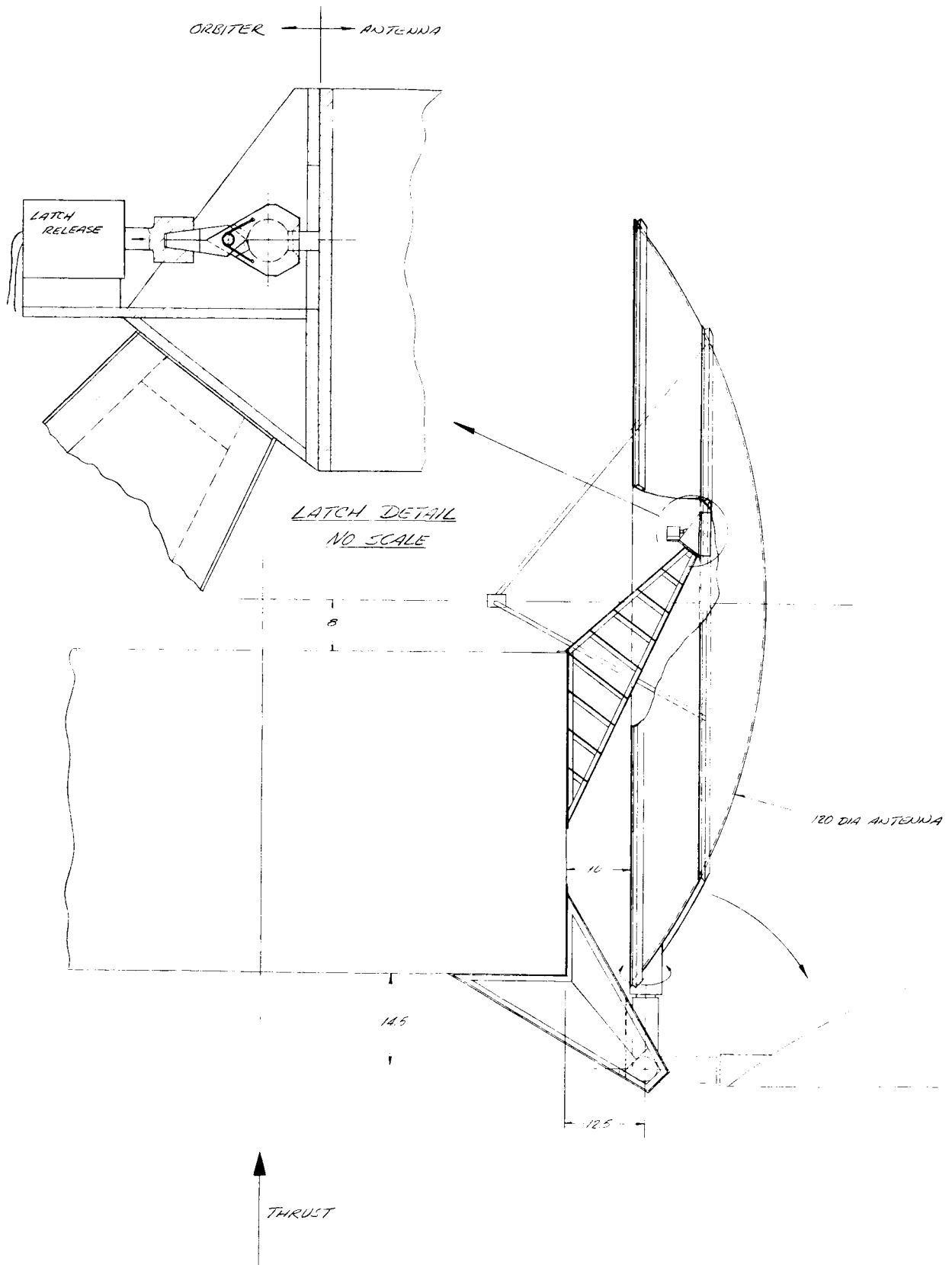
B. High Gain Antenna

The High Gain Earth Antenna (See Figure 2.3.3.-1) is secured to the vehicle at three points (120° apart) on its inner structural ring. Two of these three attachments are an electro-mechanical locking device which may be operated repeatedly during the transit phase of the trip. The third point is the hinge about which the antenna rotates. Guides are employed to secure the antenna in its stored position. The loads imposed by the guides upon the motor gear train result in slipping of the gear train clutch detent mechanism. A fixed feed is used on the Mars 1969, Venus 1970 antennas and a folded feed for Mars 1971, 1973, Venus 1972, where a fixed feed would interfere with the Landers. The folded feed is deployed by a spring-latch assembly which is actuated by antenna motion.

An alternate method of mounting the High Gain Antenna has been studied as a solution to folding the feed. This would involve rotation of the antenna such that the concave surface is facing away from the Orbiter. (Opposite to that shown in Figure 2.3.3.-1). This approach requires that the antenna support and hinge be moved further from the vehicle and that the attachments be made to the convex surface. Another advantage to a reversed storage position of the antenna would be a lessening of the effects of gas impingement during attitude control maneuvers. The impingement of gas is not expected to be a serious effect in either case due to the distances involved. Since this required more structural weight, it was set aside in favor of the approach shown in Figure 2.3.3.-1. Further work would be required in this area before a specific detail decision could be made.

The Earth oriented antenna rotation requirements are dependent upon the angular motion of Earth with respect to the: (1) spacecraft (during transit), (2) Mars (during orbit), and (3) during the Lander(s) ejection maneuver (when the spacecraft is not oriented to the Sun). These three phases are discussed below:

- (1) The Earth Antenna is stored during the launch and insertion into transit. Approximately seventy-one minutes after insertion into the transit trajectory, the antenna is deployed, used to verify the Sun/Canopus orientation (approximately 5 1/2 hours after deployment), and is stored until the 187th day of transit. The antenna is then deployed and used for all communications except during engine firings when it is again stored. Figure 2.3.3.-2 indicates the angular motions to perform these maneuvers. Angle θ (elevation) defines the "out-of-plane" position of the spacecraft relative to the Sun-Earth ecliptic plane.



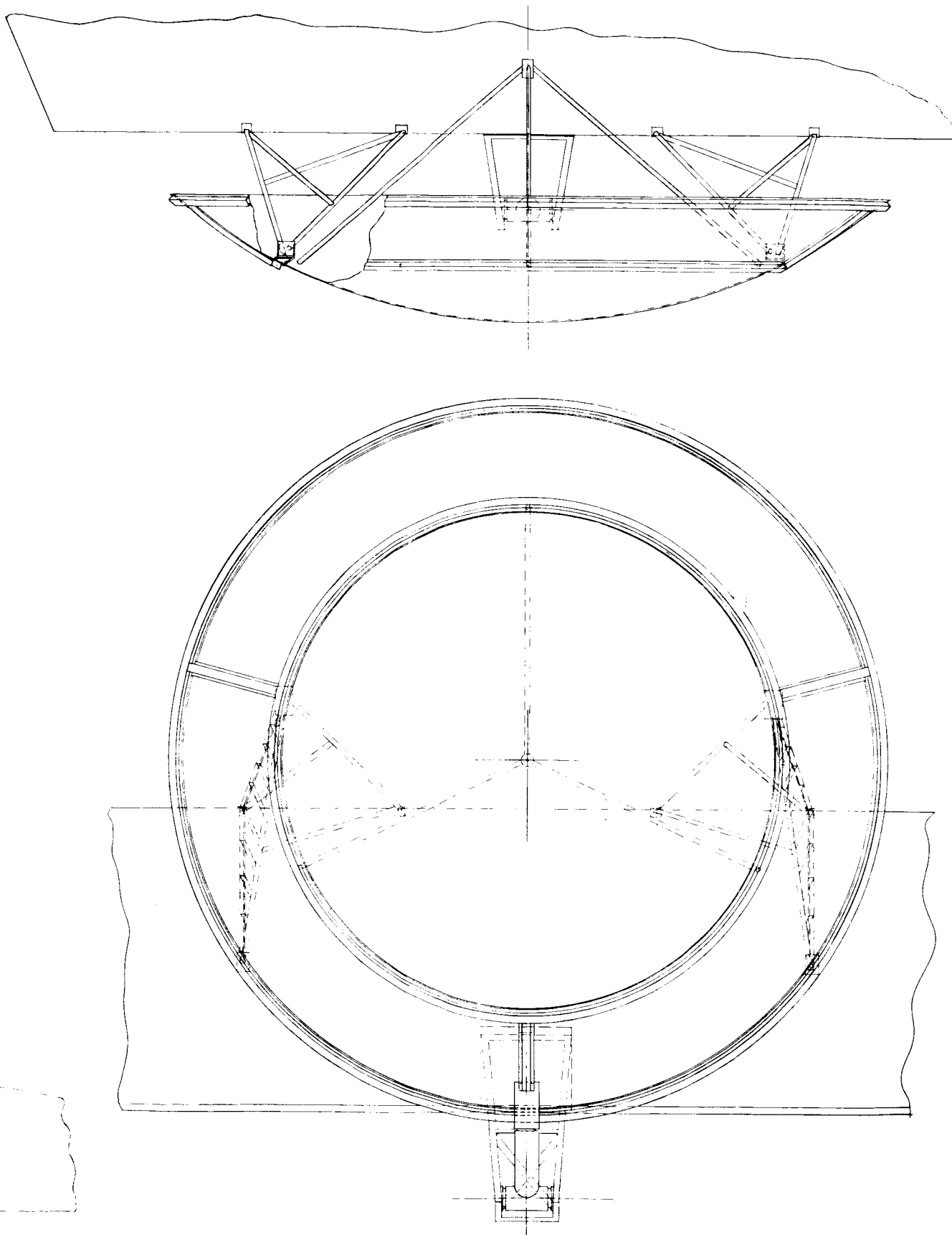


Figure 2.3.3-1. High Gain Antenna

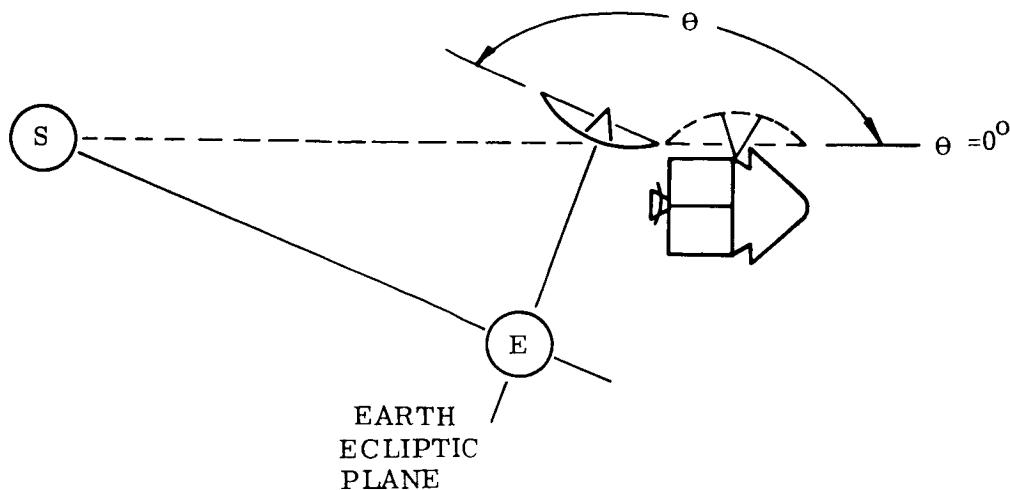


Figure 2.3.3-2. Antenna Elevation Angle (θ)
in Relation to Earth Ecliptic Plane

This angle will vary from $\theta = 0$ during a stored condition to $\theta = 90 \pm 3^\circ$ during transit usage (dependent upon launch date). Angle α defines the angle between the Sun, spacecraft, and Earth (azimuth angle) and will vary from $\alpha = 0^\circ$ during the stored condition to $\alpha = 144.3^\circ$ at encounter with Mars (See Figure 2.3.3.-3) Since the trajectory of the spacecraft never exceeds 5° out-of-plane relative to the Earth ecliptic plane, the drive motor (α) is electrically limited to operation during the elevation angle (θ) in excess of 85° . The drive motor (θ) is electrically limited to operation when the azimuth angle (α) is equal to 0° or 180° . This limitation shortens the rotation arms of the antenna with no physical interferences with the vehicle.

- (2) During the orbiting period, the Orbiter remains Sun oriented and therefore the antenna line of sight to Earth becomes a function of the Earth-Sun-Mars angles. These angles vary from $\theta = 0^\circ$, $\alpha = 90 \pm 3^\circ$ and $\alpha = 144.3^\circ$ at encounter to $\alpha = 154^\circ$ after 360 days from launch when the vehicle is launched at the middle of the launch window. (See Figures 2.3.3.-4, 5.)
- (3) During the Lander ejection maneuver the Orbiter assumes two orientations to the Sun. The first Lander is ejected in the Sun-Orbiter plane and the second 43.5 - 58 degrees from the Sun-Orbiter plane (dependent upon launch date). Translating the spacecraft rotation into antenna rotation angles (the spacecraft always remaining sun oriented) yields a required $\alpha = 160^\circ$, $\theta = 42$ (max.) as a limiting case. Since $\theta < 90$ is not a tolerable condition with α equal to anything but zero or 180° , the antenna would either:
 1. Not be used during this maneuver or;
 2. The spacecraft would be programmed to roll 90° about the Sun line such that the angular requirements would be $\alpha = 42^\circ$ and $\theta = 160^\circ$. This requires an expenditure of attitude control gas and would lose the line of sight from the Image Orthicon Camera on the Orbiter to the Planet. For these reasons, it has been decided to relax the requirement that the antenna "see" Earth during second Lander ejection.

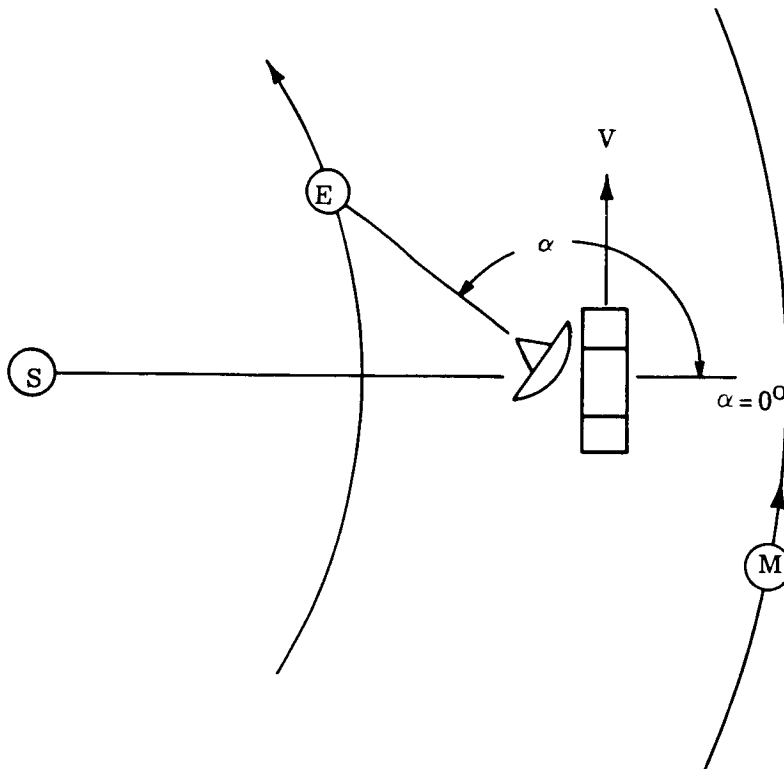


Figure 2.3.3-3. Antenna Azimuth Angle (α) in Relation to Vehicle Sun Line

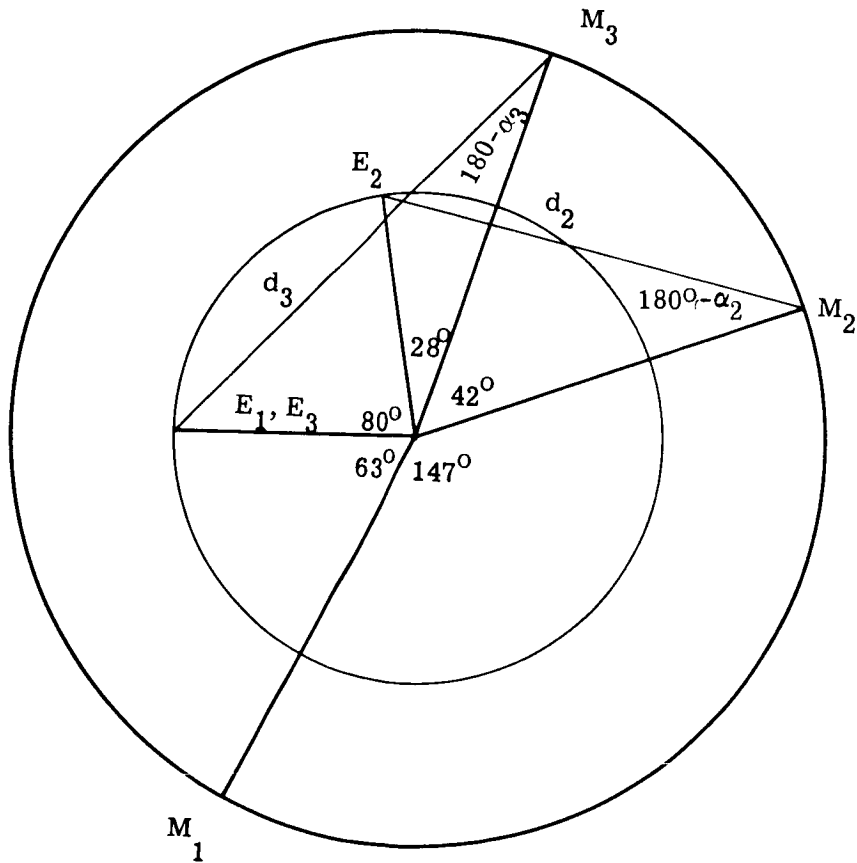
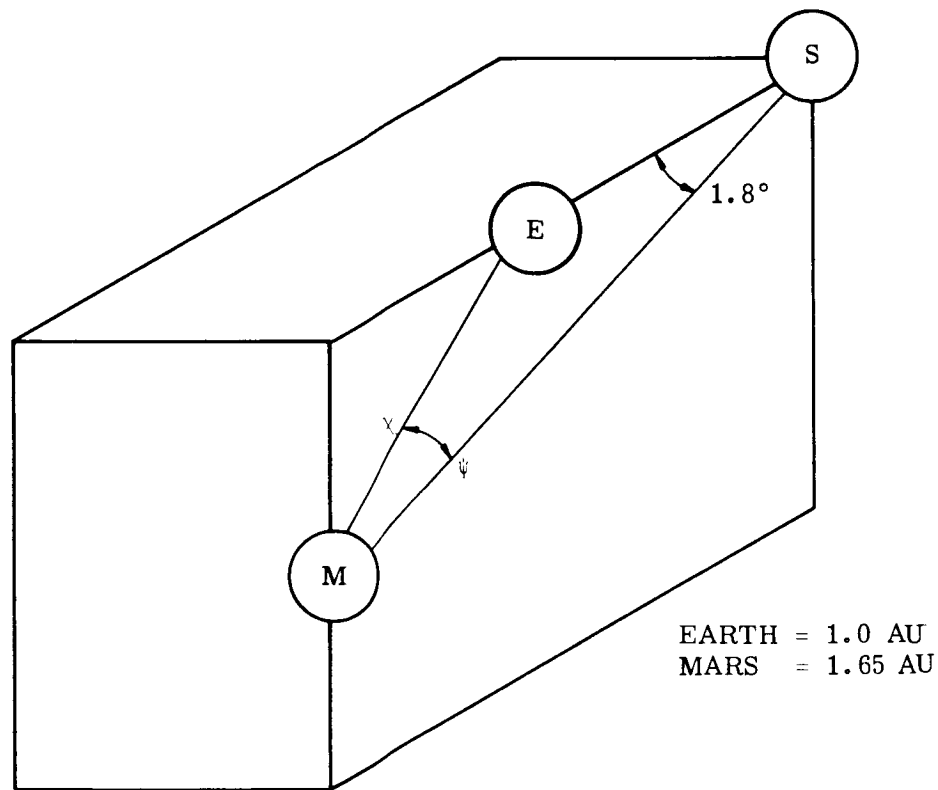


Figure 2.3.3-4. Earth, Sun, Mars Angles, Launch Through 360 Days

The Mars orbit plane is inclined 1.8° to the Earth ecliptic plane. The limiting case for the angle θ is determined by placing Earth as close to Mars as possible (in plane) as shown below. This distance (x) is:

$$x = \sqrt{(1.0)^2 + (1.65)^2 - 2(1.0)(1.65) \cos 1.8^\circ}$$



This 3° angle (ψ) is the worst out-of-plane condition of the spacecraft relative to Earth during the 360-days following launch. An additional 2° should be added to account for spacecraft orientation errors relative to the Sun. The 5° angle was used as a design parameter for the Earth antenna elevation angle.

Figure 2.3.3-5. Determination of Angle θ (Limiting Case)

$$\frac{1}{\sin \psi} = \frac{.663}{\sin 1.8^\circ}$$

$$\sin \psi = \frac{\sin 1.8^\circ}{.663} = .0527$$

$$\psi \approx 3^\circ$$

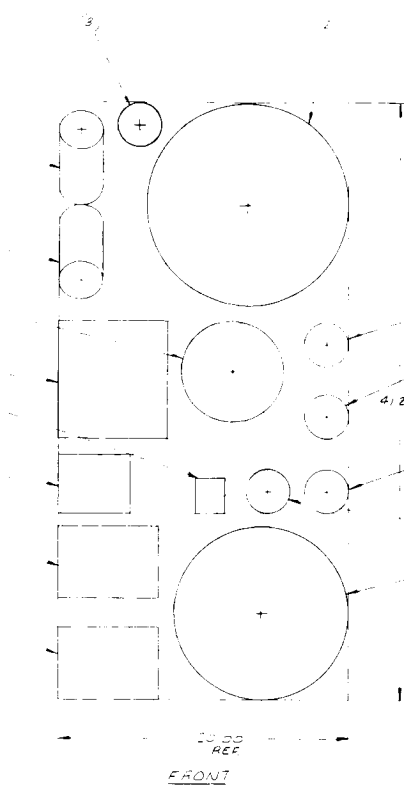
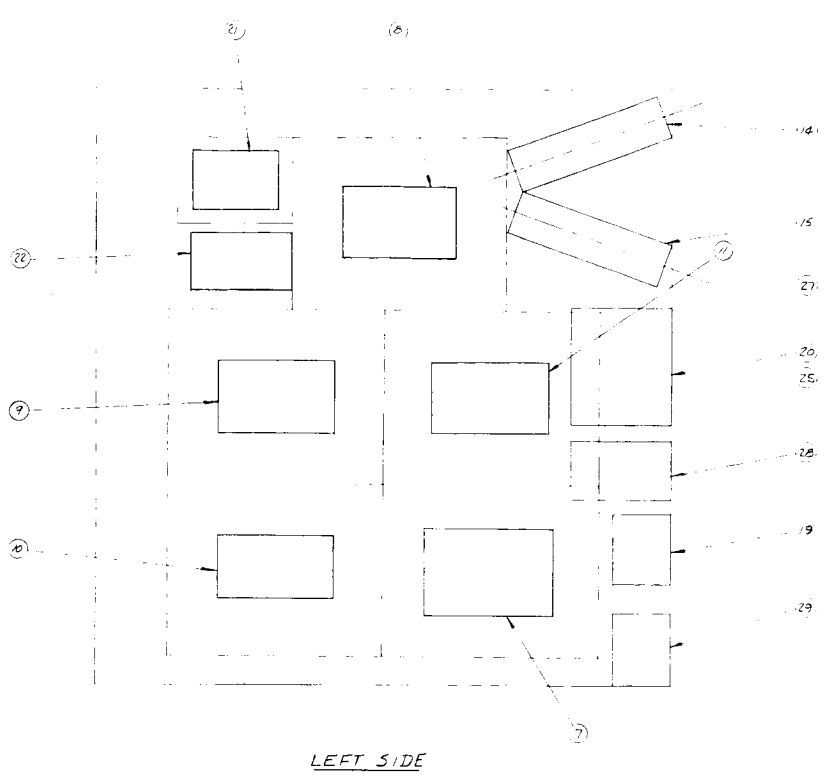
C. PHP

The Planet Horizontal Package contains the scientific, communications, and guidance equipment required to photograph the planet, obtain scientific data, receive data from either Lander, and control the orientation of the PHP (See Figure 2.3.3.-6). A 1,000 x 19,000 nautical miles, 27.3 hour orbit was chosen for the Mars 1969 mission. A curve showing angular position and altitude is shown in Figure 2.3.3.-7. Pictures of the planet are taken at altitudes of less than 4,000 nautical miles in a preprogrammed cyclical sequence. Pictures may also be taken at any altitude by command from Earth.

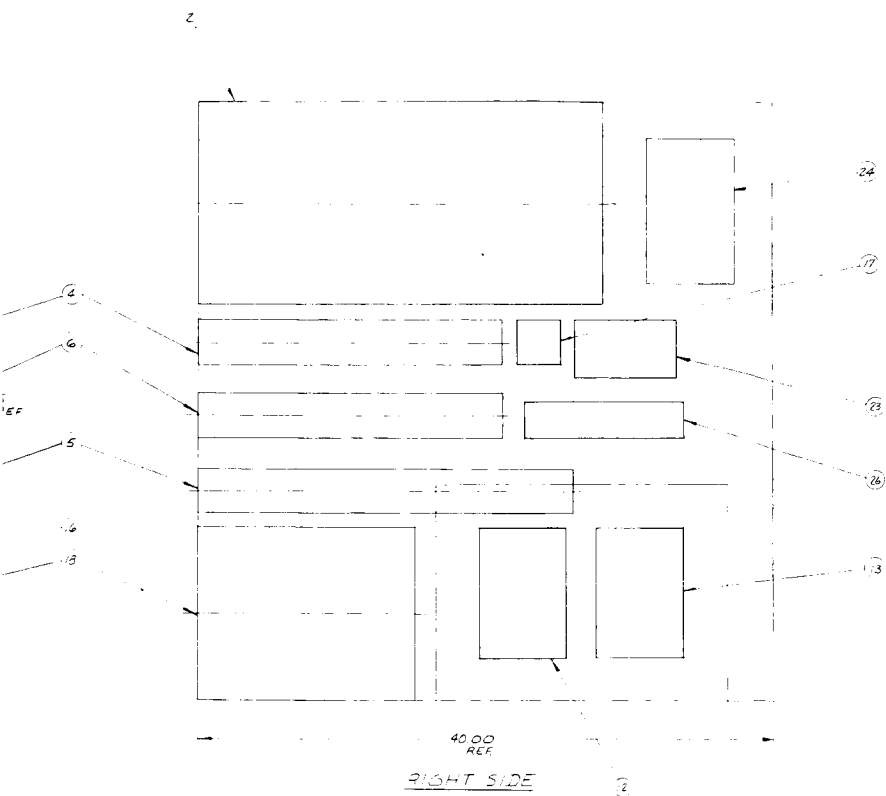
The PHP is stored from launch through orbit insertion and is then deployed for the life of the orbiter. Two surfaces of the PHP are actively temperature controlled through the use of bimetallic actuated louvers. The remainder of the surfaces are insulated to minimize heat flow to or from the PHP. The angular motions of the PHP are controlled through a two-axis, motor driven system. Upon initial usage (arrival) the PHP is deployed such that the orbital plane is normal to the rotating arm (see Figure 2.3.3.-8), and a single axis rotation is all that is required. The orbit plane precession (modal regression due to oblateness) is an $1/12^\circ$ (max.) per day, and seasonal motion of the planet is approximately $1/2^\circ$ per day, requiring rotation of the rotating arm of approximately 45° . The exact variation of this angle is sensed by a two-axis horizon scanner and the error is fed to a second drive motor system which continually rotates the view of the PHP as the orbiter traces its path over the planet. The PHP mounting and axes control have been selected as the least "control" upon arrival at Mars and an increasing amount of control thereafter. Since 90% of the mission has been accomplished in the first four days, it is felt this is a desirable approach.

In the process of rotating the PHP, a problem arises regarding the electrical interface with the spacecraft. The PHP must have the capability of transmitting and receiving diagnostic, command, and high frequency data to and from the Orbiter through a rotating joint. The three methods studied for transmitting this data were:

1. Flexible Cable
2. Slip Rings
3. RF Transmission across the rotating joint



/



NOTES:

1. COMPONENTS ARE SHOWN ONLY IN THOSE VIEWS WHICH SHOW THE EXTERIOR SURFACE TO WHICH THEY MOUNT.
2. PHANTOM LINES AROUND COMPONENTS SHOW SURFACE AREA REQUIRED FOR THERMAL RADIATION.

Figure 2.3.3-6. PHP Component Layout

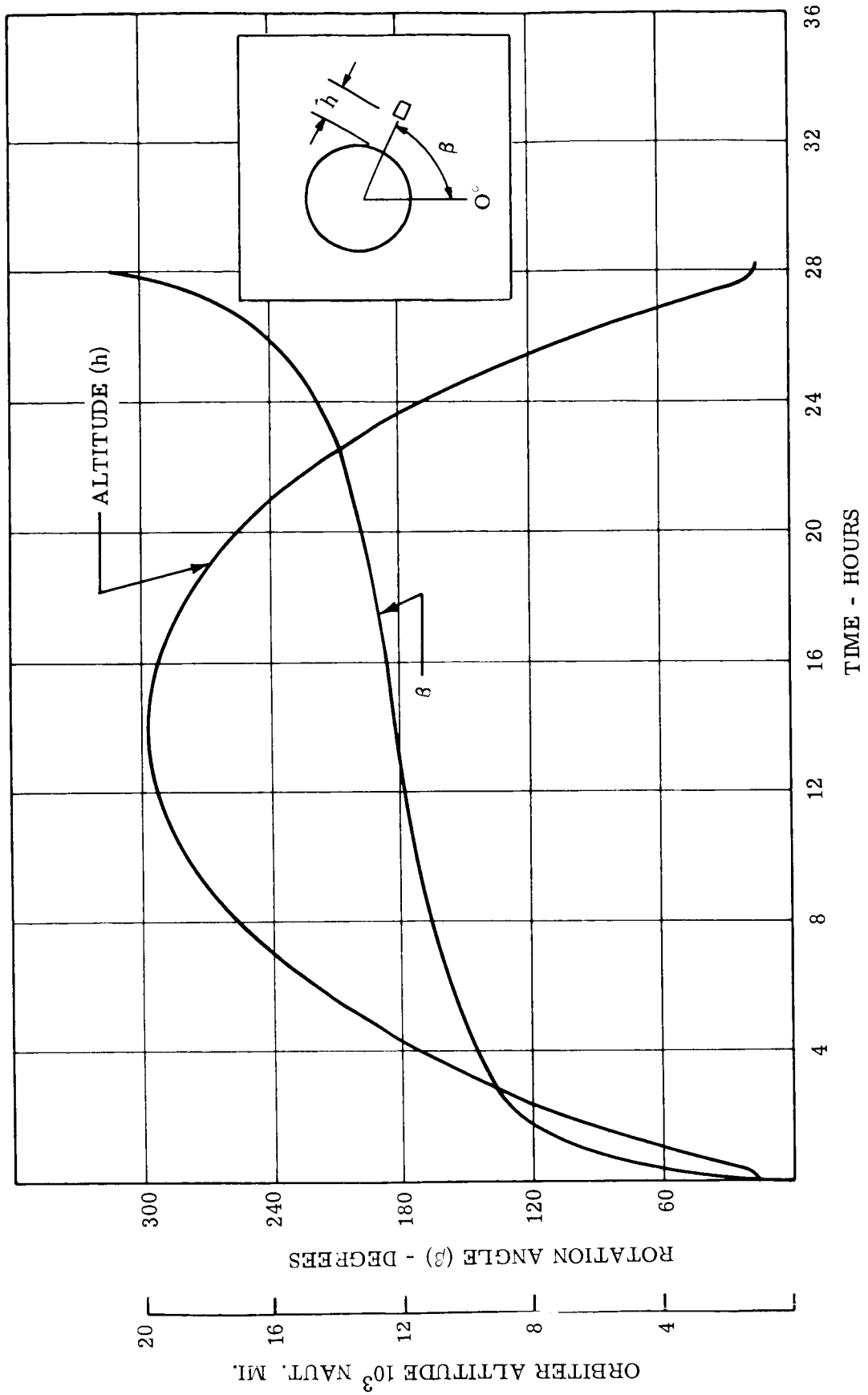
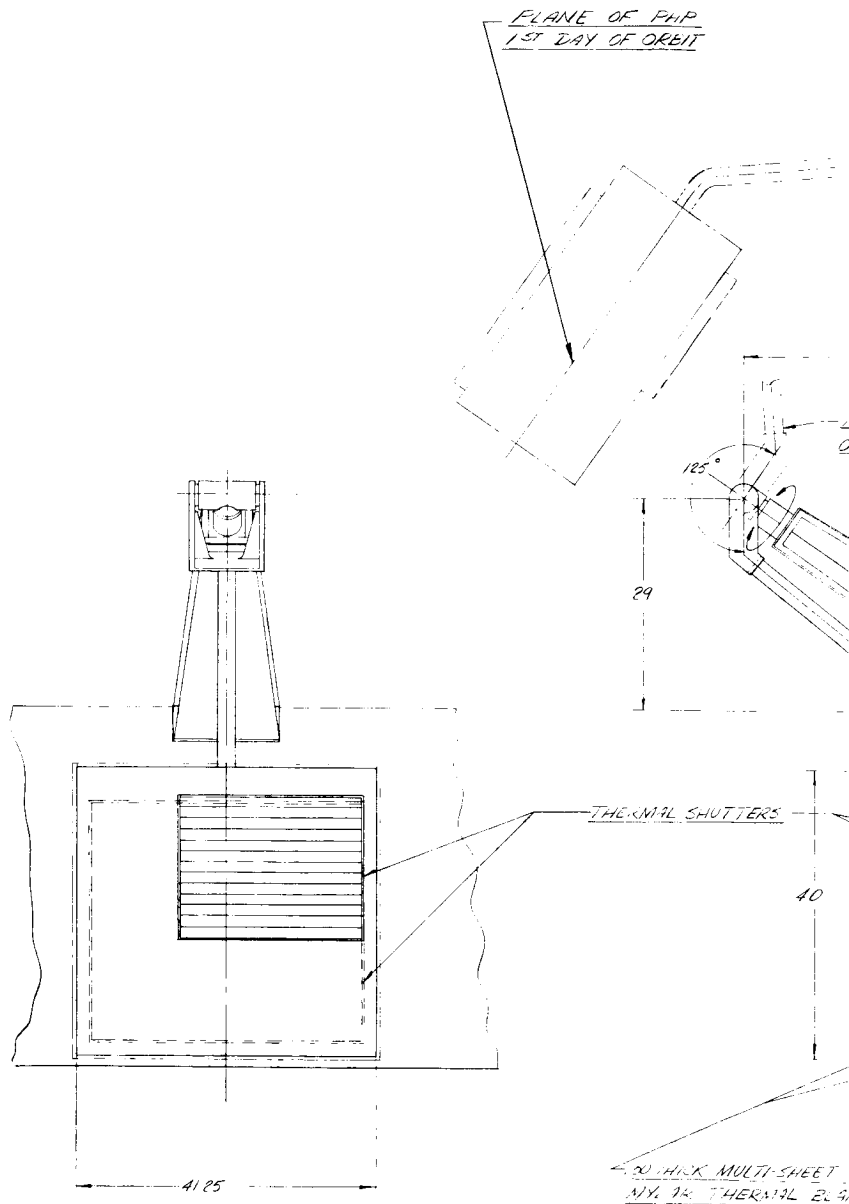
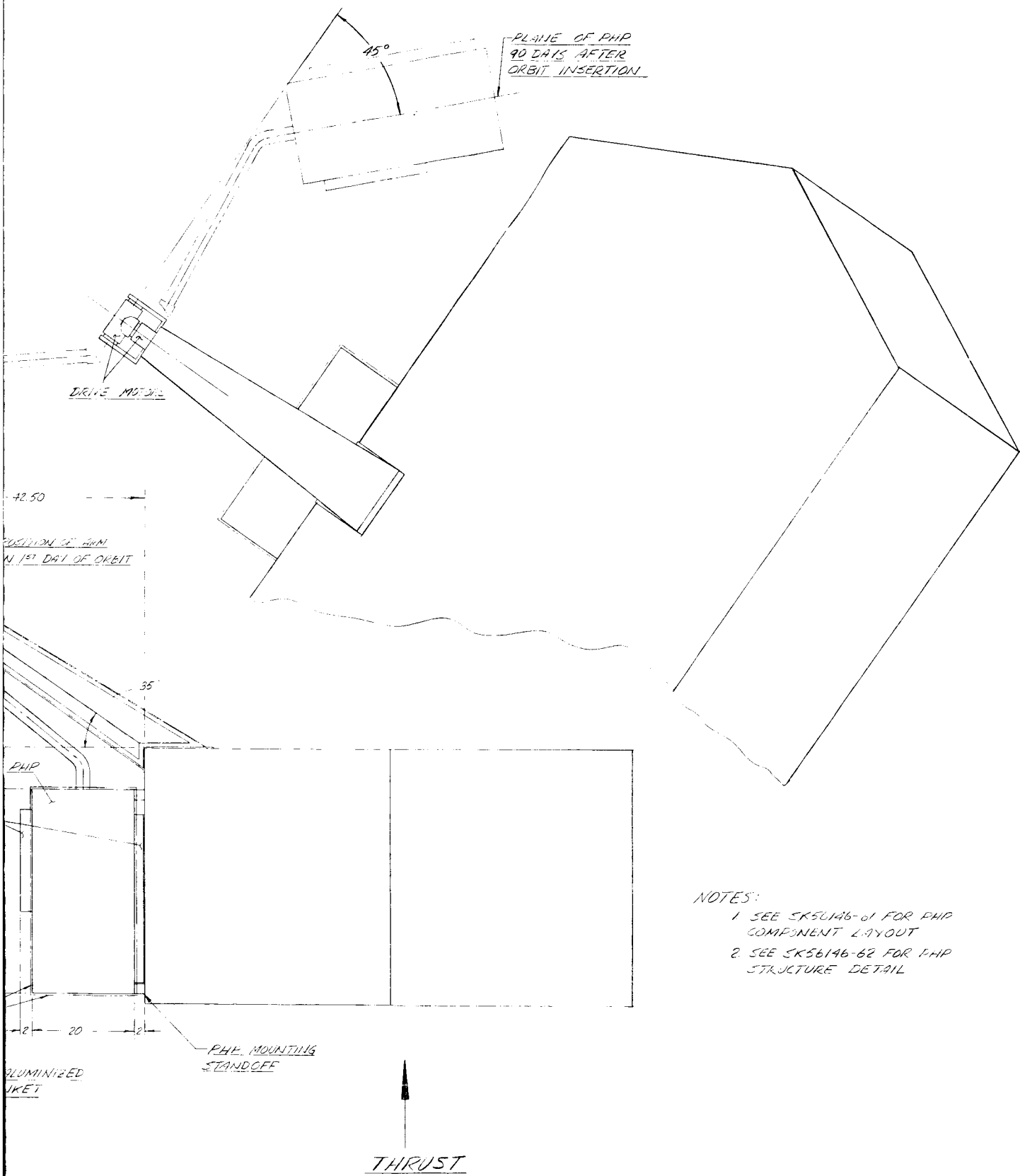


Figure 2.3.3-7. Angular Position and Altitude of Orbiter in Relation to Mars

PLANE OF PHP
1ST DAY OF ORBIT





NOTES:
 1 SEE SK56146-61 FOR PHP
 COMPONENT LAYOUT
 2 SEE SK56146-62 FOR PHP
 STRUCTURE DETAIL

Figure 2.3.3-8. PHP Support and Drive Mechanism

The method chosen as the lightest and most reliable was use of a flexible cable. In conjunction with this approach, unwinding of the cable must be preprogrammed into the PHP. In order to minimize the thermal control requirement of alternating thermal loads imposed by a single unwinding, it was decided to preprogram two unwinding cycles at 166° apart in the orbiting cycle. This approach allows the same surface of the PHP to "see" the Sun at the time the cameras are on or off. The points selected for this maneuver are at 4,000 nautical miles, $\alpha = 97^\circ$ and at 4,000 nautical miles, $\alpha = 263^\circ$ (see Figure 2.3.3.-7). The total number of unwinding cycles would be two per orbit, 24/27.3 orbits/day, and 90 days design life or 158 cycles. Tests have been run at MSD, under radiation 2.4×10^6 rads. and vacuum 10^{-5} mm Hg to 3,600 cycles without cable damage, indicating the feasibility of this approach.

D. Image Orthicon Camera on Orbiter

An image orthicon camera is mounted to the Orbiter body to photograph the planet and star background during the terminal guidance phase. The camera is mounted to a frame which may be rotated prior to launching to the optimum location for viewing the planet (varies with launch date). The frame has the capability of rotating 3° in one plane and 35° in the other (See Figure 2.3.2-1).

E. VHF Antenna on Orbiter

The VHF Omnantenna mounted to the Orbiter body is positioned to communicate with the landers from the time of separation from the Orbiter to impact with the planet. The position of the landers relative to the Orbiter Roll Axis (+ X) is approximately 143° during Orbiter orientation to the Sun and approximately 53° during the Orbiter insertion maneuver. Figure 2.3.3.-9 defines the Lander angular location and range as a function of time from lander separation to entry into Mars atmosphere. The antenna is deployed to an angular location of 98° to the roll axis (+ X) and is therefore 45° to the landers in either the Sun oriented or orbit insertion Orbiter orientation. The antenna consists of folded 5-foot dipoles on a 5-foot boom. Both the boom and dipoles are spring actuated to the operating position.

F. Magnetometer

(1) General Description

The magnetometer (see Figure 2.3.3.4-10) is secured to the vehicle base at its hinge and at the opposite end of the 160-inch beam throughout the transit phase and orbit insertion. Upon a given signal, an explosive actuator releases the magnetometer and a spring extends it to its operating position. It is locked in this position by a spring-loaded pin in its hinge and a key on the hinge shaft. Because of the extreme sensitivity of the magnetometer to stray magnetic fields, the magnetometer boom configuration proved to be a major configuration problem. Especially difficult to solve was the calibration requirement which called for physical polarity reversal of each of the three sensors daily without using magnetic field producing devices. The requirement for physical isolation from other vehicle components resulted in a boom approximately 13 feet long. Non-magnetic elgiloy springs are utilized in the deployment hinge. The magnetometer sensors are mounted in three orthogonal axes at the free end of the boom. A sun shade protects the sensors and mechanism from solar rays. Two of the sensors are fixed to the boom at right angles to each other and perpendicular to the longitudinal axis of the boom. The third sensor is mounted on a non-metallic gear with its axis parallel to the boom axis. A flywheel-gear arrangement, mounted at the free end of the boom, drives the gear-mounted sensor by inertia forces resulting from a spring actuated boom rotation of 180 degrees. A pair of opposing springs, mounted in the housing on the vehicle body at the base of the boom, provides the necessary energy to rotate the entire boom 180 degrees in approximately 0.1 second, thus providing the acceleration and sudden stop necessary to create inertia forces in the pure copper inertia wheel-gear drive sufficient to rotate

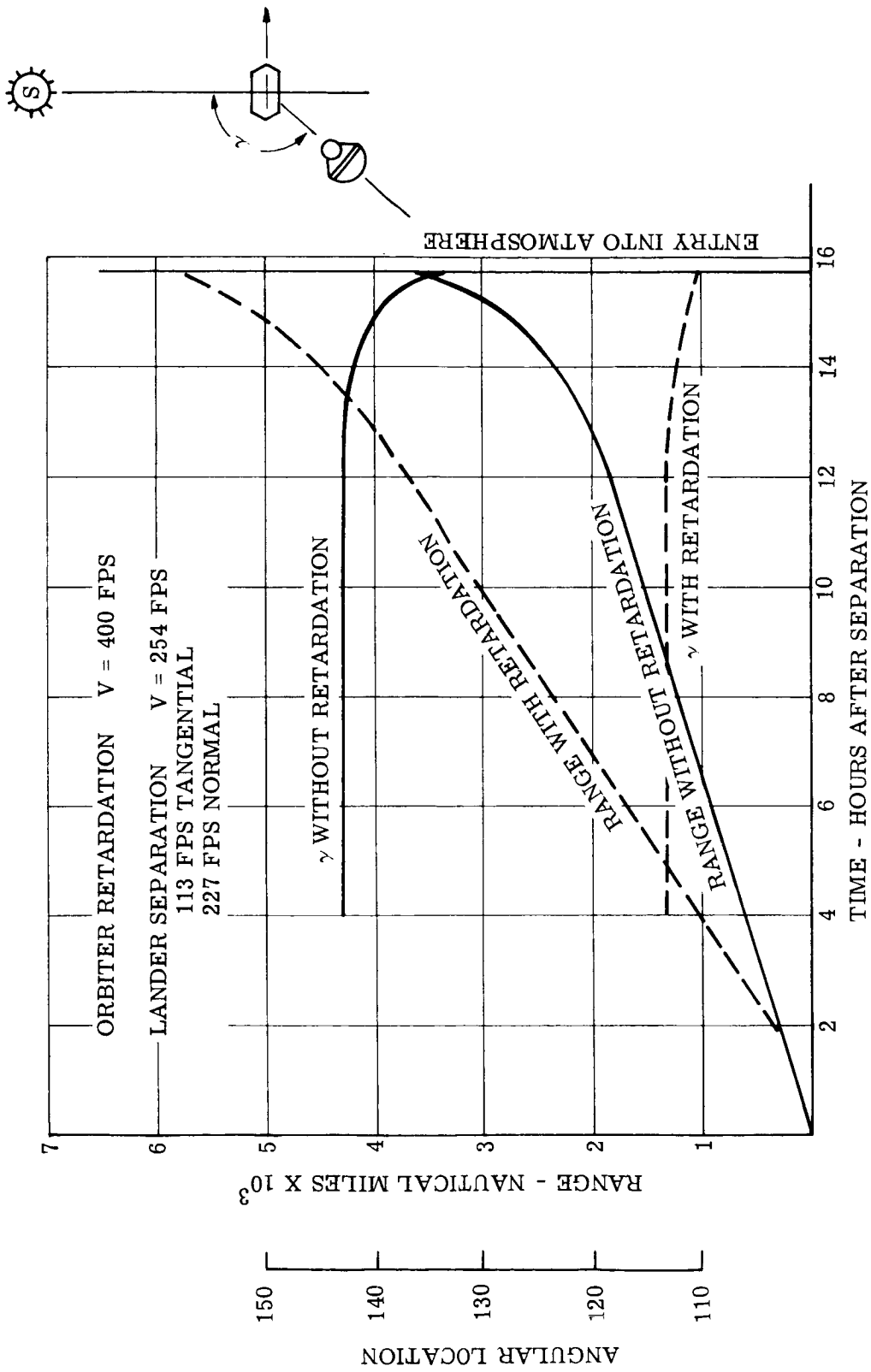


Figure 2.3.3-9. Lander Flight Path

the third sensor. The inertia wheel is damped and locked at the completion of each 180-degree rotation. The two other sensors rotate 180 degrees with the boom. The major advantage of this method of rotating the third axis of a three-axis magnetometer is that there are no motors or other devices in the area of the sensor to create a magnetic field.

Admittedly, there are many problems involved in the development of this device, but the excellent experimental data resulting from the ability to mechanically rotate the sensors for accurate calibration appears to be well worth the development effort.

Other methods considered for rotating the axes of the magnetometer sensors were:

1. Flex cable through boom

Advantages

- Simple

Problems

- Cable should be non-metallic and non-magnetic
- Routing cable through boom hinges along with electrical harness

2. Push-Pull Cable Arrangement

Advantages

- Conventional and straightforward

Problems

- Maintaining cable tension
- Non-magnetic parts and cable required
- Routing and pulley problems at hinges

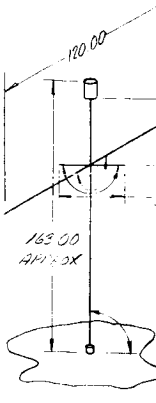
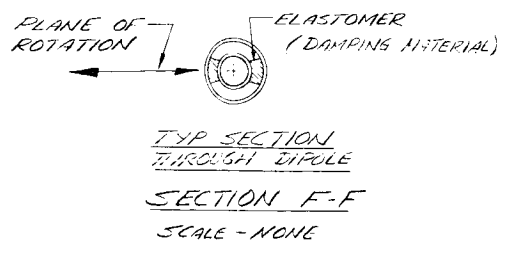
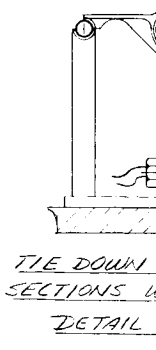
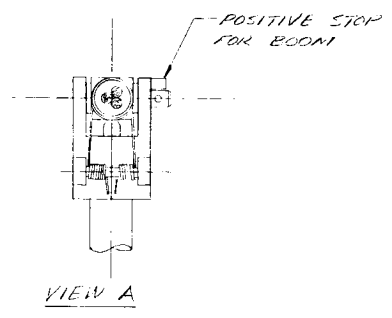
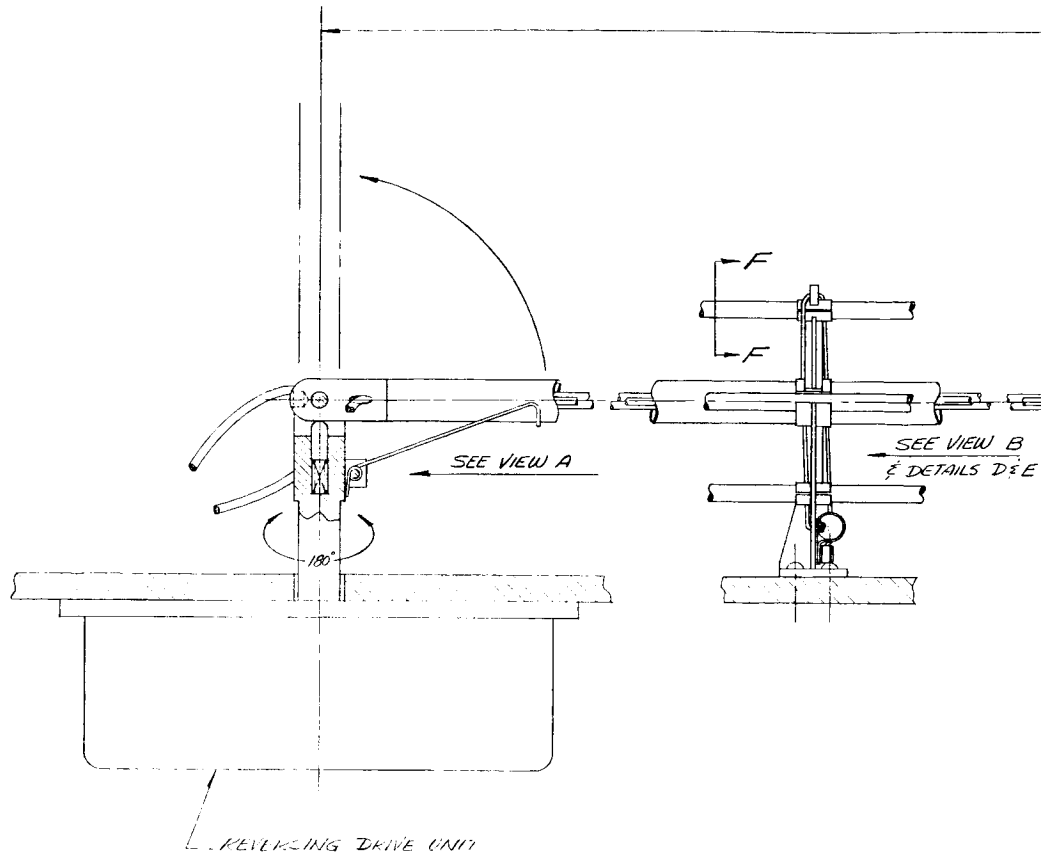
- (2) Thermal Considerations

Warpage of the magnetometer boom as a result of differential temperatures across the boom was a major concern, especially in view of the fact that the entire boom is rotated 180 degrees daily. Excessive warpage would create dynamic forces during rotation which could disturb the vehicle orientation. More detailed study is required to evaluate the problem thoroughly, but preliminary calculations indicate that a completely insulated boom would maintain a uniform temperature (less than 1° F differential) circumferentially, and detrimental warpage would not occur. Longitudinal expansion would have very negligible effect on the vehicle orientation.

- (3) Boom Length

An evaluation of the effect on the magnetometer of magnetic fields from several spacecraft component sources was made. The 13-foot boom was chosen as the optimum length. Extreme care in the Orbiter design is necessary as exemplified by the following:

1. The solar array will require a design reversing the direction of adjacent current loops; it is quite feasible to reduce the field from each loop in the array to less than one-tenth gamma.



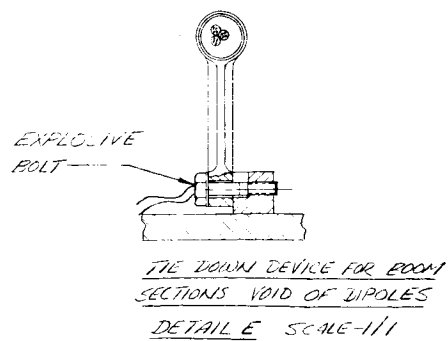
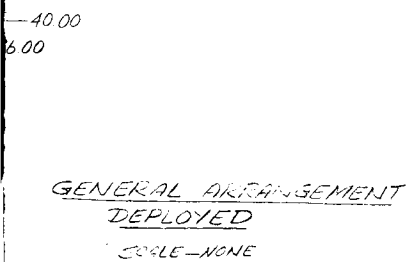
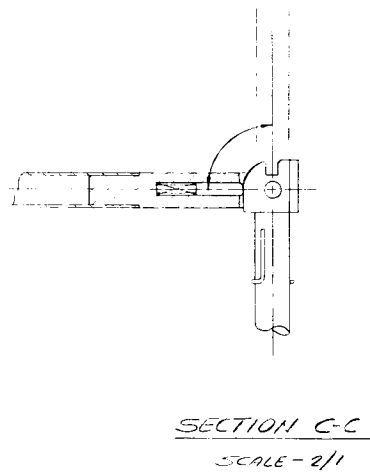
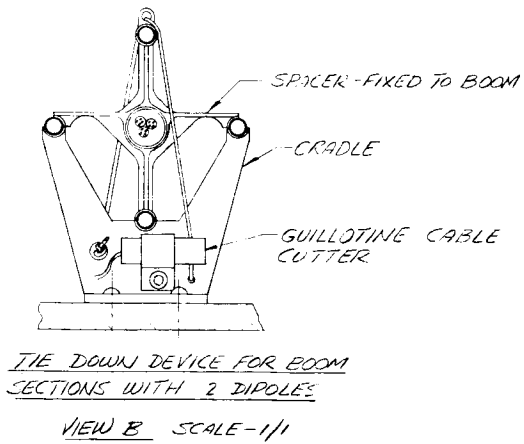
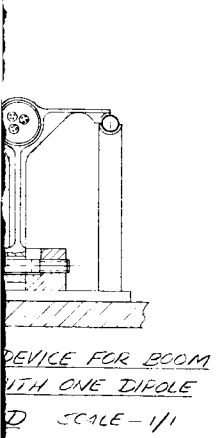
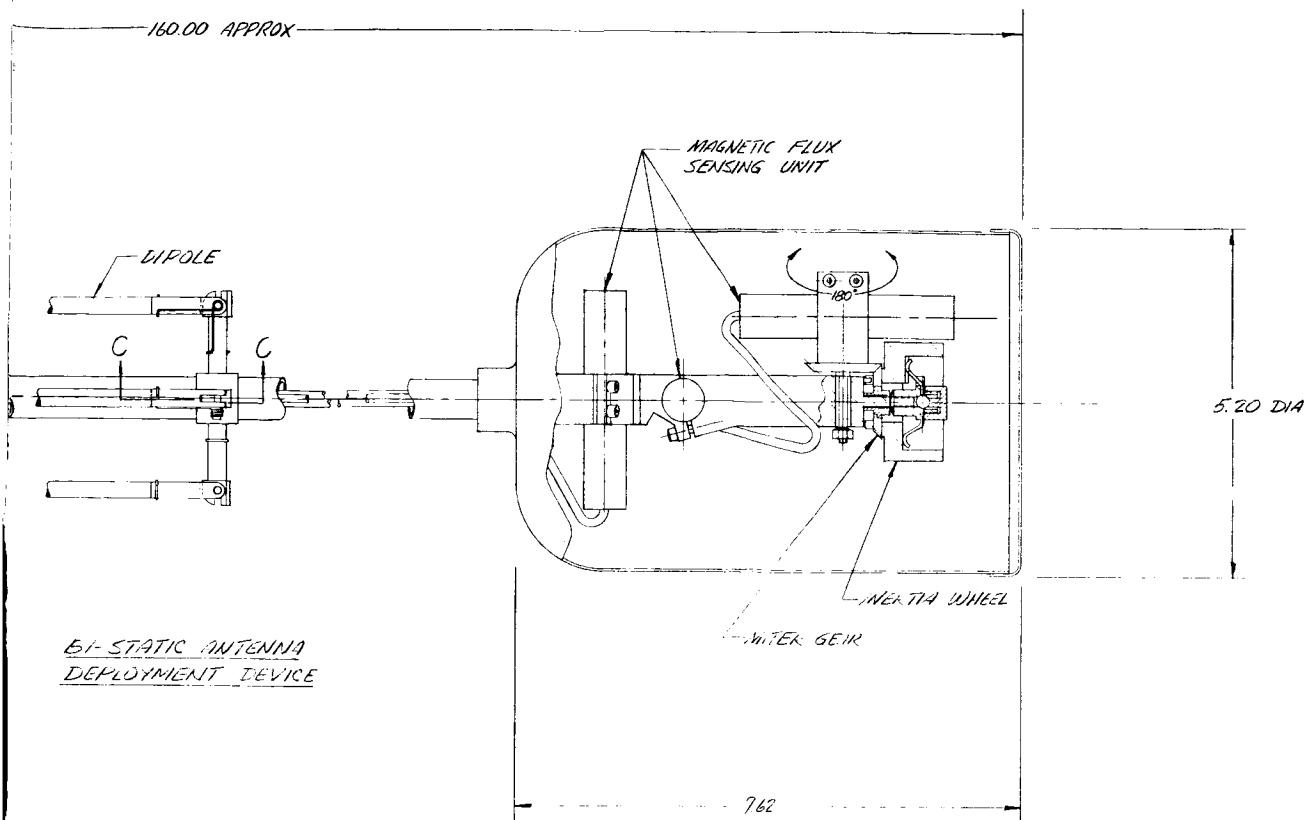


Figure 2.3.3-10. Magnetometer

2. Care must be used where large area current loops can be produced; e.g., a common ground loop serving the various components and connecting to the main power supply. Direct two wire connection should be made between the main power supply and each component.
3. If possible, all magnets should be toroidal; power supplies and other critical components will probably require shielding.

Effective degaussing can be achieved by orienting equipment to obtain field cancellation.

Contamination of structural materials by ferromagnetics, particularly the magnetometer boom, must be avoided.

A radio propagation experiment antenna is attached to the magnetometer boom and deployed when the magnetometer boom is unfolded and locked. The radio propagation experiment antenna consists of 10-foot and 3-foot elements which are spring loaded to the boom. The inertia oscillation of these elements during rotation of the boom is damped by damping strips on each element (see Figure 2.3.3-10).

G. Landers

The following methods were studied for separating the Lander from the Orbiter.

1. The Lander will have a rocket or cold gas system capable of separating it from the Orbiter with a minimum tumble rate to the Lander and no gas impingement on the Orbiter. When the Lander is approximately 3 feet from the Orbiter, a separate spin-up system shall be activated. The advantages of this system are as follows:
 - a. There is a minimum amount of tumbling force imparted to the Orbiter and Lander.
 - b. The separation system weight is not carried into orbit, thus saving additional fuel.
 - c. The linear impulse imparted to the Lander can be accurately calculated and tested.
 - d. A hot gas spin-up system may be employed with a potential weight savings.
2. The Orbiter will have the separation rockets to provide the required separation velocity prior to Lander spin-up. The advantage listed above (1. a) is lost, but the following advantages are added:
 - a. No separation impulse is imparted to the Lander and therefore the angular error of the spin axis is further reduced.
 - b. Canting of the Orbiter rockets will provide ΔV to the orbiter. At the time the Lander ΔV engine fires, the thrust direction is no longer in line with the Orbiter.
3. A four-spring system shall be located on the Orbiter to provide the separation velocity and distance prior to Lander spin-up. The advantages are listed above (1. a, 1. c, 1. d). The disadvantages are listed below:
 - a. A tumbling force is imparted to the Orbiter beyond the control capacity of the present system. Additional control system capacity would cost approximately 15 lbs.

- b. The spring assemblies and support structure would weigh about 6 lbs.
 - c. The additional fuel required to orbit this weight is approximately 18 lbs.
4. Canted jets shall be located on the Lander to provide instantaneous separation and spin-up. The advantages to this system are:
- a. The utilization of a single system to provide dual purpose functions.
 - b. Spin-up starts before any sizable Lander separation angular error accrues.
 - c. Other advantages are listed above (1. a, 1. b, 1. c).
 - d. The disadvantage is the unknown tumbling force imparted to the Orbiter from the spin-up gas impingement.

The assumptions made in all of the systems described above are that the angular errors due to Orbiter motion prior to separation, and the impulses due to separation are subjects which require additional study.

The system selected for the Voyager study is the one utilizing cold gas spin rockets on the Lander for separation and a Lander spin-up system (described in Paragraph 1.0 above). The other systems worthy of study are listed in descending order of preference.

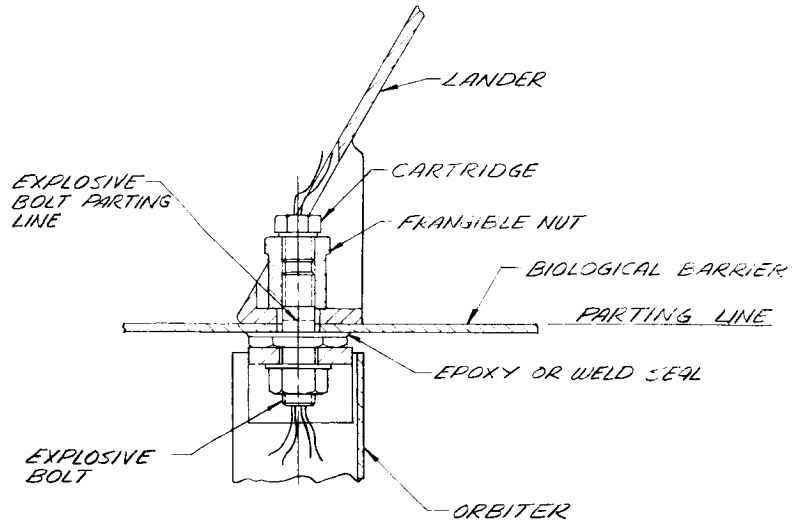
The method of securing the Landers through the powered flight environments and separating them are shown in Figure 2.3.3.-11. The bolted connection is made in four locations 90° apart.

Also shown in Figure 2.3.3.-11 is a biological barrier between the Orbiter and Lander. The barrier provides the interface for the in-flight disconnect and the explosive bolts. All surfaces on the Lander side of the barrier will be sterilized. As described in Volume V, the Entry-Lander will be mounted on the Orbiter after being encased in a biological barrier and being sterilized. Provisions have been made for physical and electrical attachment of the Lander to the Orbiter without contamination of the Entry-Lander. Removal of the upper portion of the biological barrier at the time of shroud separation is the first phase of Lander separation. At the time of Lander ejection, the in-flight disconnect is separated, and the explosive bolts attaching Landers to Orbiter are fired. Each of these physical motions occur in a sterilized area, thus leaving all unsterilized and contaminated material with the Orbiter.

The portion of the biological barrier remaining with the Orbiter is used to help provide proper thermal control of the Orbiter internal subsystem components.

H. VHF Antenna

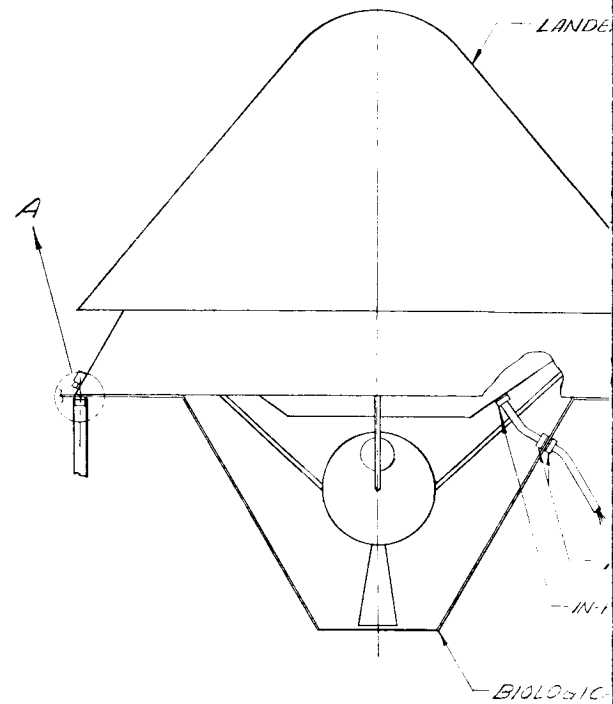
Figure 2.3.3.-12 shows the method of securing and deploying the VHF Antenna. The antenna consists of five sets of crossed dipoles on a telescoping beam. The dipoles are folded 90° and inserted into holes in the PHP. The telescoping beam is driven by a friction wheel.



SEPARATION INTERFACE

DETAIL-A

SCALE 1/1



LAUNCH & TRANSIT CONFIGURATION

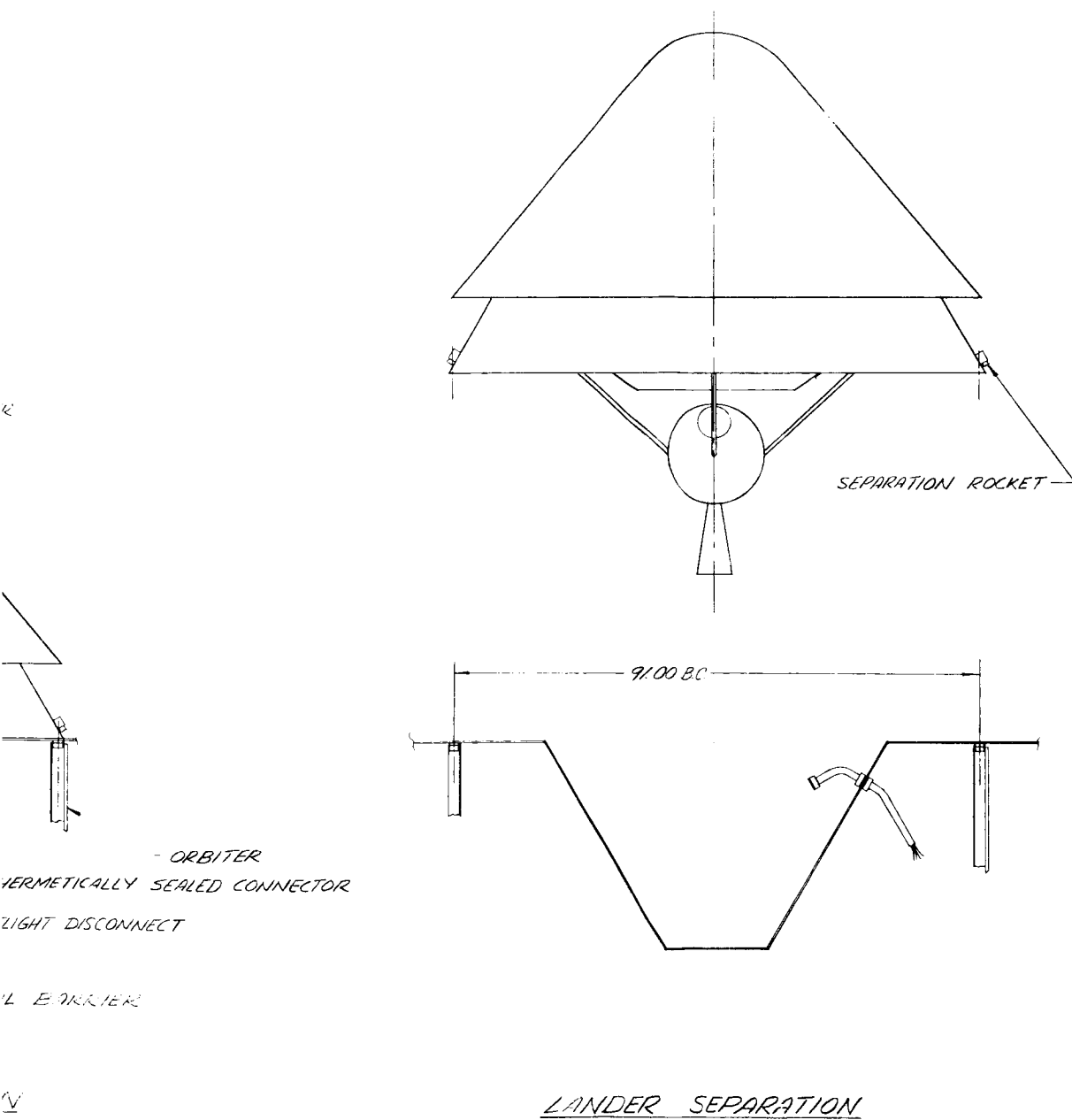
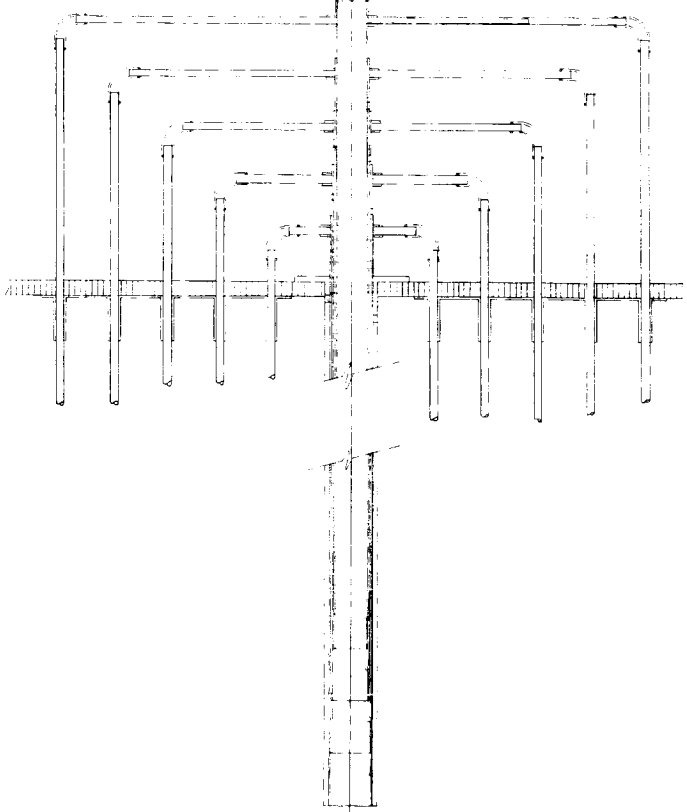
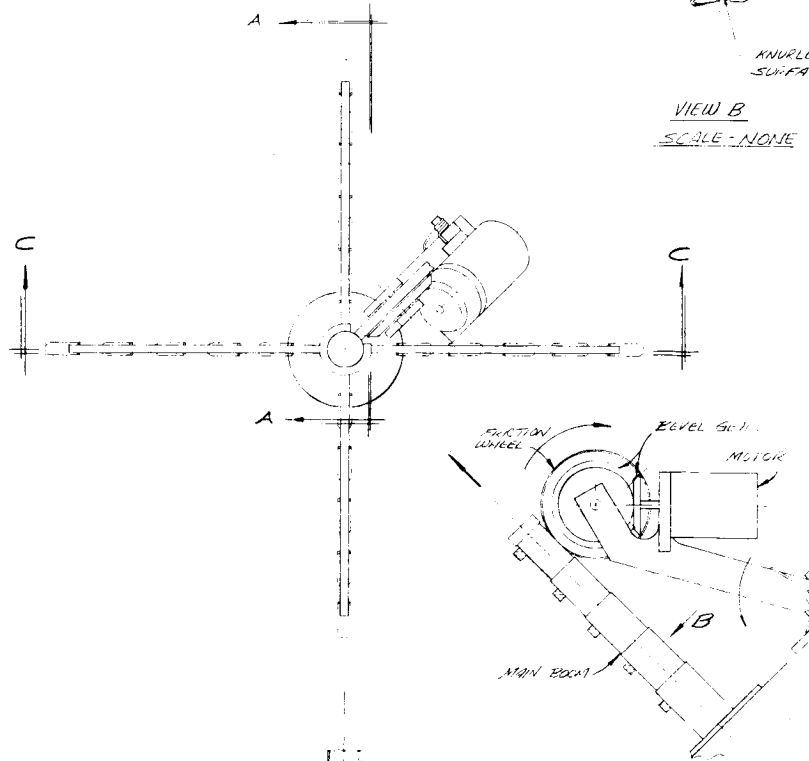


Figure 2.3.3-11. Lander/Orbiter Interface



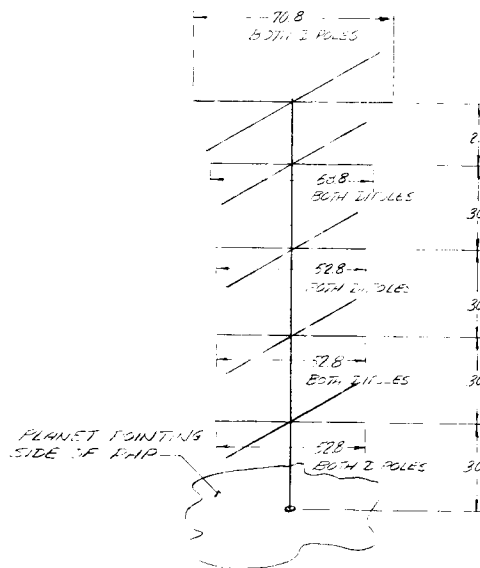
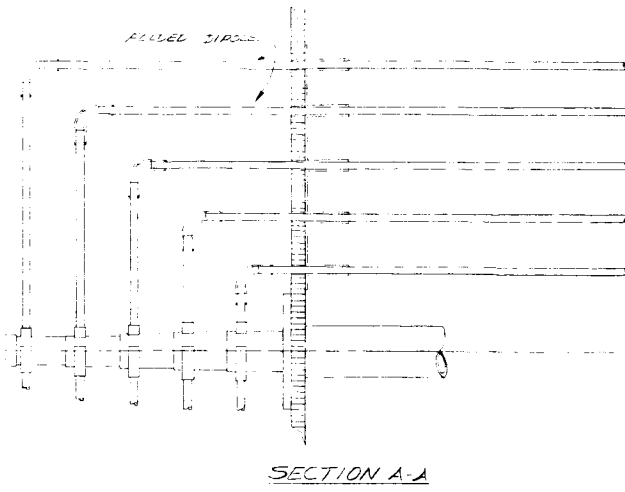
KNURLED SURFACE

VIEW B
SCALE - NONE

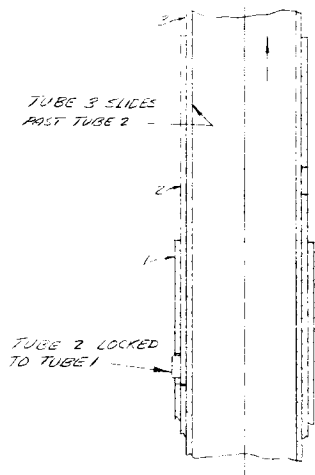


SECTION C-C

FRUCTION



GENERAL ARRANGEMENT
 DEPLOYED
 SCALE - NONE



ENLARGED
 DETAIL OF
 LOCK & RELEASE
 MECHANISM
 SCALE - NONE

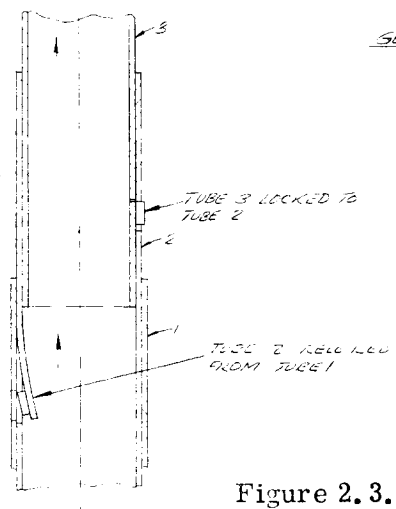


Figure 2.3.3-12. VHF Antenna Deployment Mechanism

I. Solar Panels

The total power required for the Mars 1969 mission is 440 watts. The configuration selected permitted mounting of solar cells on a structural panel at a small increased structural weight. This area provides a power of approximately 280 watts. Three approaches have been studied to determine the lightest method of providing the required area for the additional 160 watts.

1. Fixed (body mounted platforms)
2. Deployable (hinged platforms)
3. RTG mounted on the Orbiter

Figure 2.3.3.-13 shows the active cell area for 160 watts to be 43.5 feet and the required overhang to be 13.4 inches. Adding one inch as a handling edge results in a 14.4 inch overhang. The approach selected was the fixed array. Substantiating this decision were the following factors.

1. Higher reliability for a fixed array than for one which depends upon operation of moving mechanisms and explosive devices after a 280-day space environment.
2. Manufacturing Ease - Use of a fixed array allows the manufacture of four identical panels (determined by practical honeycomb panel size) for the total required array, in lieu of four or eight hinged panels plus four fixed panels.

The Solar Cells are fabricated in sub-modular form and bonded to 10 cm x 80 cm epoxy glass sections. The sections are then bonded to the structural panels. In this manner, damaged cells may be removed, repaired and replaced without disturbing the remainder of the panel.

An alternate method studied for supplying power was a 90-pound, 180 watt Radioisotope Thermoelectric Generator. The advantages derived from this consideration are: (1) reduction of storage battery requirements, (2) more time permitted for maneuvers (Sun time becoming less critical), (3) deployable platforms or an overhanging fixed array is not required.

The problem areas using this power combination are:

1. Location of RTG to minimize thermal effects on other components and/or subsystems.
2. Procurement of the Isotope.

J. Fuel Tanks

The propellant tanks are located within the two main orbiter beams in such a manner that equal volumetric flow rates of fuel and oxidizer will result in a zero cg shift. The ratio of fuel to oxidizer weight is 1:1.65 for equal volume tanks. Each tank is a 38-inch diameter titanium sphere, pressurized to 200 psi by a helium storage tank. The tanks are attached by a fixed trunnion on one side and a floating trunnion on the other. The floating feature permits expansion and contraction of the tanks under pressure and temperature variation. Through the trunnion fittings are a fill (exhaust) port and a pressure and temperature sensor on the opposite port. The tanks have a growth capability (diameter) within the existing support beams to carry an additional 25% of fuel or

oxidizer. Due to a possible usage differential between the two tanks (3% estimated) at the end of the orbit injection, the vehicle cg could shift 0.24 inch. The unused helium gas trapped in the helium, fuel and oxidizer tanks will be valved to an orbit trim nozzle and expended only if the Orbiter is in a synchronous orbit.

K. Engine Thrust Vector Control

Thrust vector control is accomplished through hydraulic actuators and an engine gimbaling system. The total cg shift from launch through orbit insertion firing does not exceed the 14° cone capability in the gimbaling system (see Figure 2.3.3.-14).

L. Attitude Control Jets

The Attitude Control System utilized a pair of nozzles to rotate the spacecraft about any of its geometric axes. Freon gas is used to supply the required impulse. The following torque is available for 1 pound of force at each nozzle.

$$M_x = 200 \text{ in. lbs. Roll}$$

$$M_y = 200 \text{ in. lbs. Pitch}$$

$$M_z = 90 \text{ in. lbs. Yaw}$$

M_x and M_y nozzles are located in a cluster such that a single line (multiple valves) may be utilized, saving weight and lessening gas losses.

M. Payload Packages

The payload packages are mounted to four removable panels in the Orbiter. The criteria for their location was a tradeoff between weight balance and thermal balance. The exterior of these panels are covered by an active temperature control system (louvers). The interior of the panel is insulated such that intercomponent radiation is possible. The remainder of the payload is mounted in the PHP (see Figure 2.3.3.-6).

N. Omni (DSIF) Antenna

Two Omnidirectional Antennas are positioned on the Orbiter to "see" Earth in any Orbiter orientation. These antennas are used for communication early in transit period and as a backup emergency mode in the event of High Gain Antenna failure.

O. Sensors

1. Sun Sensors are located in three positions on the Orbiter such that the direction of error may be determined as one sensor loses the Sun and another sees it. The sensors are both coarse and fine, dependent upon location and accuracy required.
2. An Earth sensor is located on the High Gain Antenna as a supplement to the preprogrammed positional orientation.
3. Planet sensors (horizon scanners) are located in the PHP. They are two-axis dual scanners which direct the aiming of the PHP to the planet. During the 180 "flip" of the PHP (see Paragraph 2.3.3C) the error signal is controlled through a resolver system.

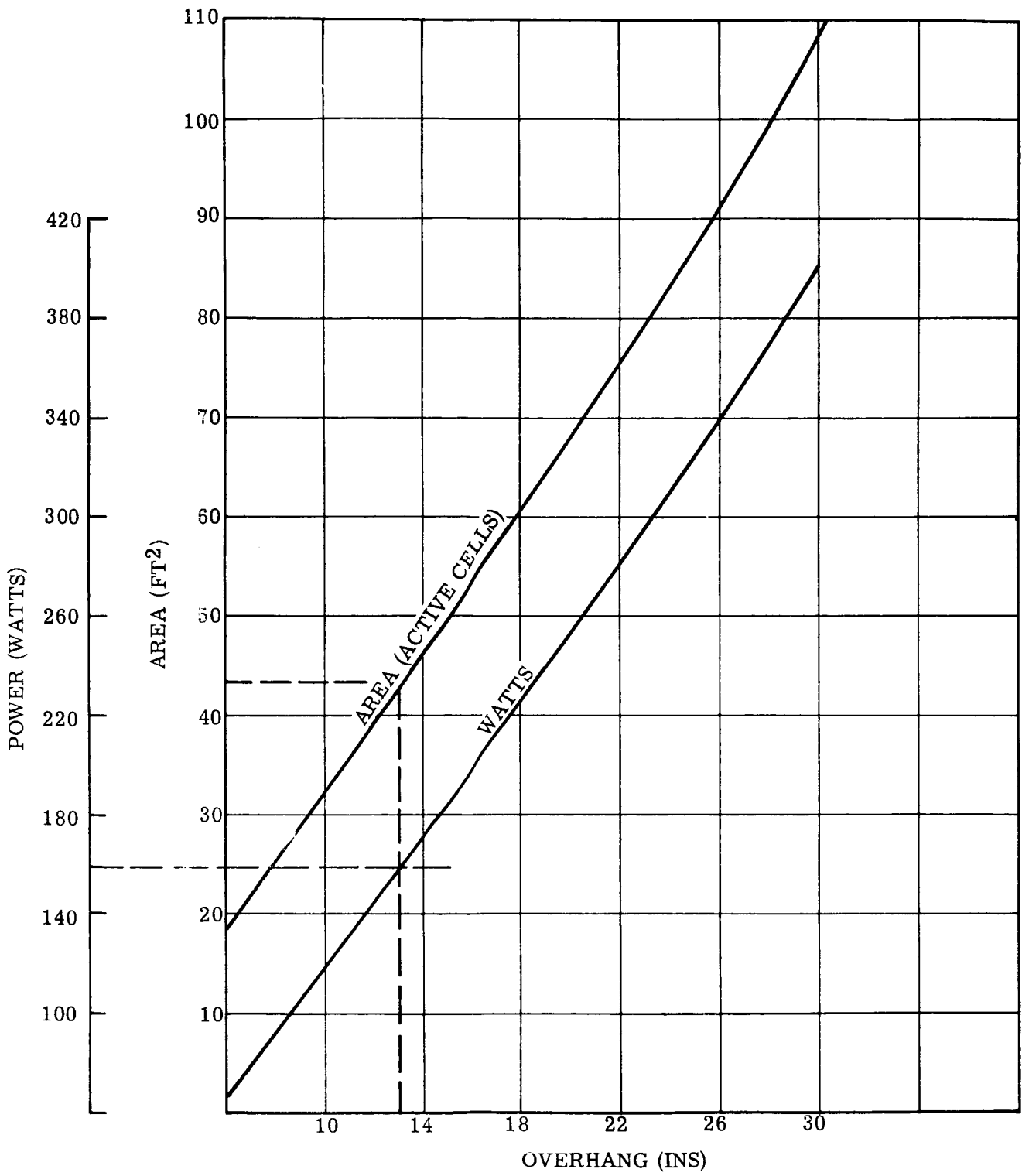
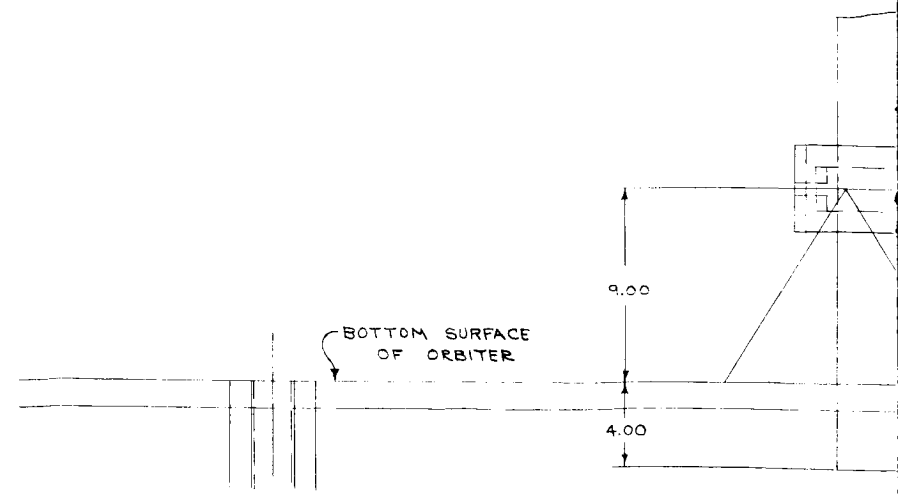
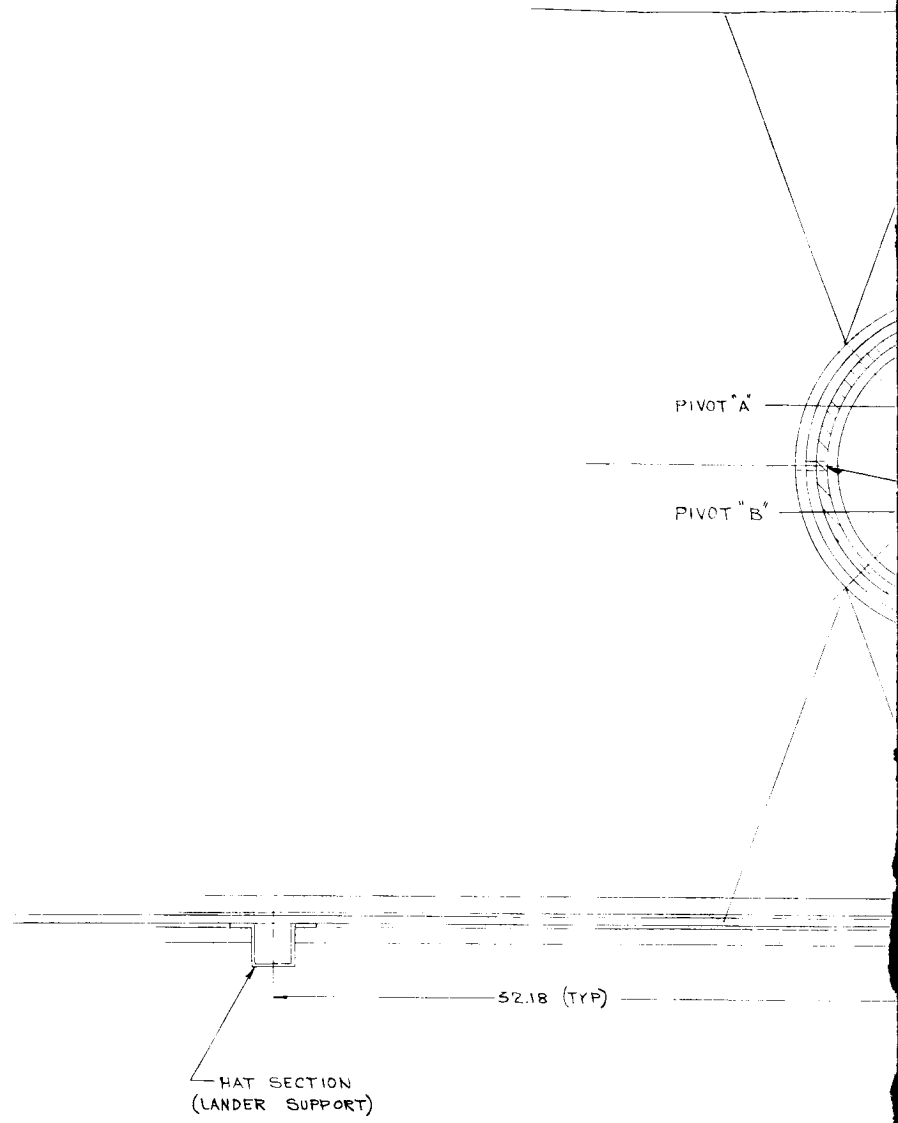


Figure 2.3.3-13. Active Cell Area vs Overhang



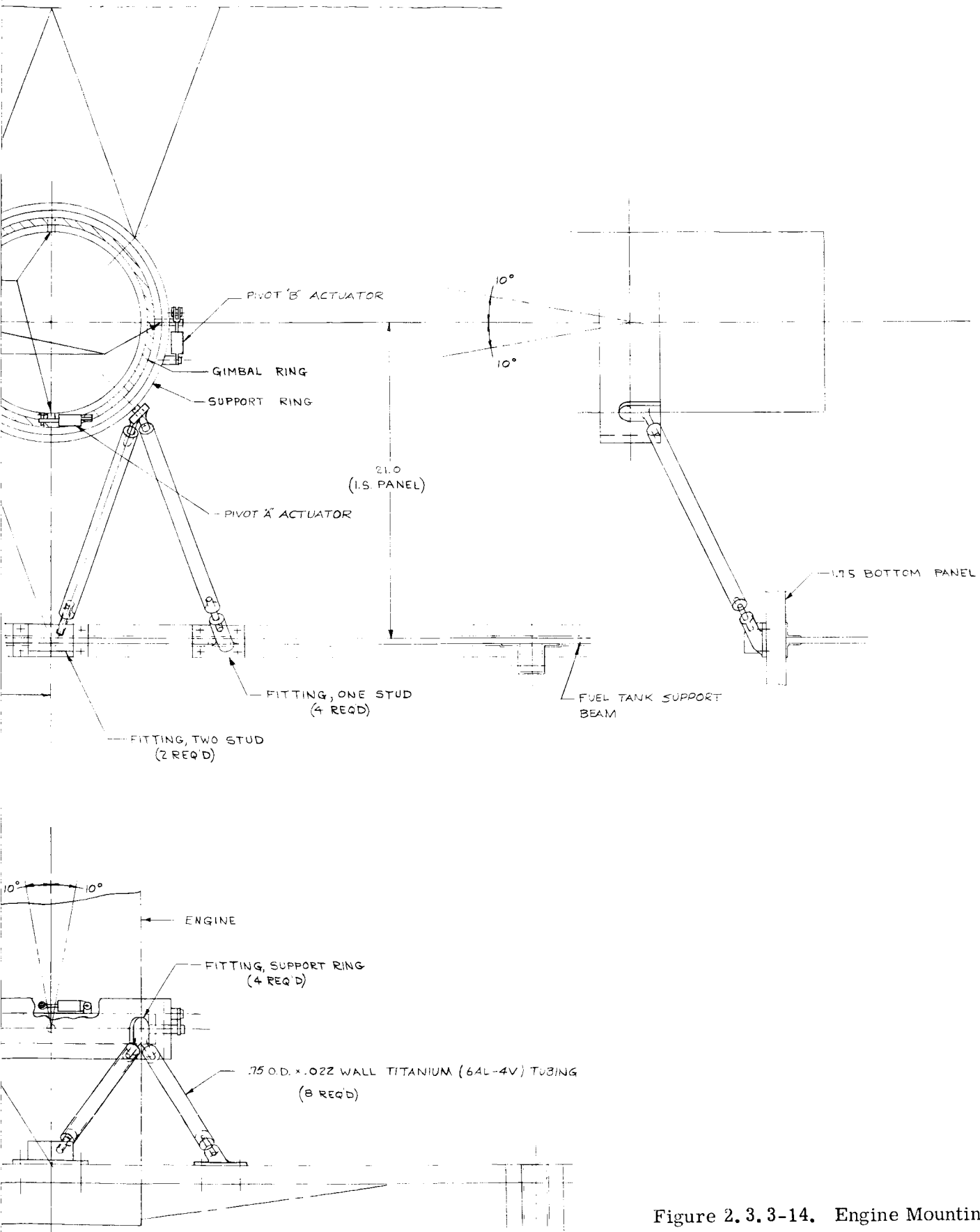


Figure 2.3.3-14. Engine Mounting

4. A Startracker is used to find the star Canopus as a fixed reference for vehicle orientation and guidance. A second startracker is mounted on an opposite surface to the above for use if an orbit of the Northern Hemisphere is desired. This would be possible if both launches are successful. In order to provide Northern Hemisphere mapping, the appropriate Canopus tracker would be actuated. This provides a spacecraft orientation such that in a Northern Hemisphere orbit, the PHP is free to view the planet.

P. Explosive Devices

Explosive mechanisms (pin pullers, bolts, nuts) are used extensively in all of the deployable parts of the vehicle. In order to insure a .999 reliability and 95% confidence level, the following program will be followed.

1. All devices will utilize a common squib design in order to gain large quantity statistical performance data.
2. A Bruceton and/or Probit Analysis will be performed using environmental extremes as dictated by analysis and past performance information available.
3. Each squib shall have hermetically sealed (to prevent outgassing and moisture penetration) dual firing circuits.
4. Multiple squibs will be utilized for each device. Any single squib will be capable of performing the desired function.
5. Fragmentation will not be permitted for any device. This will include expulsion of gases on devices which are in close proximity to optics or sensing devices which may be coated by such gas residue.

Q. Vibration Damping

Various techniques for solving vibration problems have been investigated for application in the following areas of the design:

The Magnetometer, Radio Propagation Experiment, VHF omni, and VHF antenna on PHP are erected into their operating positions by torsion springs. The energy imparted to the boom must be transferred to the vehicle with minimum boom oscillation. Dashpot damping is one technique for solving this problem. The energy of the boom is transferred into fluid motion through an orifice. The damping force created is proportional to the square of the velocity. Other possibilities are damped structural members (booms, etc.) and crushable materials to absorb energy. Fluid displacement dampers are useful in limiting vibration loads of columns (Truss Tubes) where damping is desired at low frequencies and high restraint at a higher frequency.

2.3.4 REVISIONS FOR OTHER YEARS

The following changes are required to adapt the Mars 1969 Orbiter for missions in other years. The missions discussed are Mars 1971, 1973, and 1975, and Venus 1970, 1972.

A. Mars 1971 (Figure 2.3.4.-1)

The most notable changes between the Mars 1969 and Mars 1971 missions are the allowable injected weight and the fuel required for midcourse corrections and orbit insertion. The Voyager spacecraft allowable launch weight is 7,320 pounds, an increase of 290 pounds over Mars 1969. In addition, the fuel requirements have decreased approximately

40 percent. The available weight has been added to the Landers, increasing them to 2000 pounds each. The capability to support two 2000-pound Landers has been built into the Mars 1969 Orbiter; therefore, no major changes will be required for this mission.

B. Mars 1973 (Figure 2.3.4.-2)

The Voyager spacecraft injected weight for Mars 1973 is 6,000 pounds, which includes two 2000-pound Landers, a 1402-pound Orbiter and 698 pounds of fuel. The reduction in Orbiter weight (657 lbs) is accomplished primarily by removal of the PHP (50%), Propulsion System reduction (25%), Power Supply reduction (15%), with the remainder split among the remaining subsystems. The vehicle is rebalanced by relocating the subsystem components. New fuel and oxidizer tanks will be required since it would not be feasible to use tanks with a 2071 pound capacity for a 698 pound requirement. These revised tanks can be mounted in the same area by means of brackets added to the existing structure. In addition, the orbit considered for this mission requires that the Orbiter be sterilized. This factor creates a sterilization interface with the launch vehicle.

C. Mars 1975 (Figure 2.3.4.-2)

The Mars 1975 vehicle is essentially the same as the Mars 1973 with the exception that the Orbiter (1973) becomes a fly-by. The effects are a reduction of fuel to 165 pounds and deletion of the sterilization requirements. With the reduction in fuel requirements, new tanks will be required.

D. Venus 1970 (Figure 2.3.4.-3)

The primary changes required to adapt the Mars 1969 Orbiter to the Venus 1970 mission are the addition of a 10-foot diameter Radar Mapping antenna and an increase in fuel from 2071 to 4590 pounds. The Radar Mapping function is combined with the PHP requirements in a Cassegrain antenna with the PHP in front of the subreflective surface of the antenna. Three degrees of rotational freedom are required to perform the Radar Mapping function. The increased fuel requirements results in the addition of two supplemental tanks. Additional structural beams are required to support the new tanks. These tanks will be mounted in the volume previously occupied by the Entry Lander engine. The increased fuel weight results in a single 525 pound Lander in lieu of two 1450 pound Landers (Mars 1969). The 525 pound Lander is located along the X axis ($\frac{1}{2}$ of Lander at $Y = 0, Z = 0$) on a short adapter required to provide necessary clearances.

E. Venus 1972 (Figure 2.3.4.-4)

The notable difference between the Venus 1972 and Mars 1969 vehicle is the combining of two Landers into a single larger Lander (2600 lbs.) with a life expectancy of 5 1/2 hours on the ground. The Orbiter change required is addition of an adapter and centrally locating the Lander.

2.3.5 TITAN III-C CONCEPTUAL CONFIGURATIONS

Figures 2.3.5.-1 and 2.3.5.-2 show conceptual designs for the Titan III-C. Figure 2.3.5.-1 indicates a design for an Orbiter. Since there will be no Lander attached to the Orbiter, the PHP can be mounted for launch above the Orbiter. The High-Gain Antenna is mounted below the structure and has a maximum size of 9 feet in diameter because of shroud limitations. Fuel and oxidizer tanks are mounted around the central thrust cone, and subsystem components are mounted within the thrust cone of the main engine.

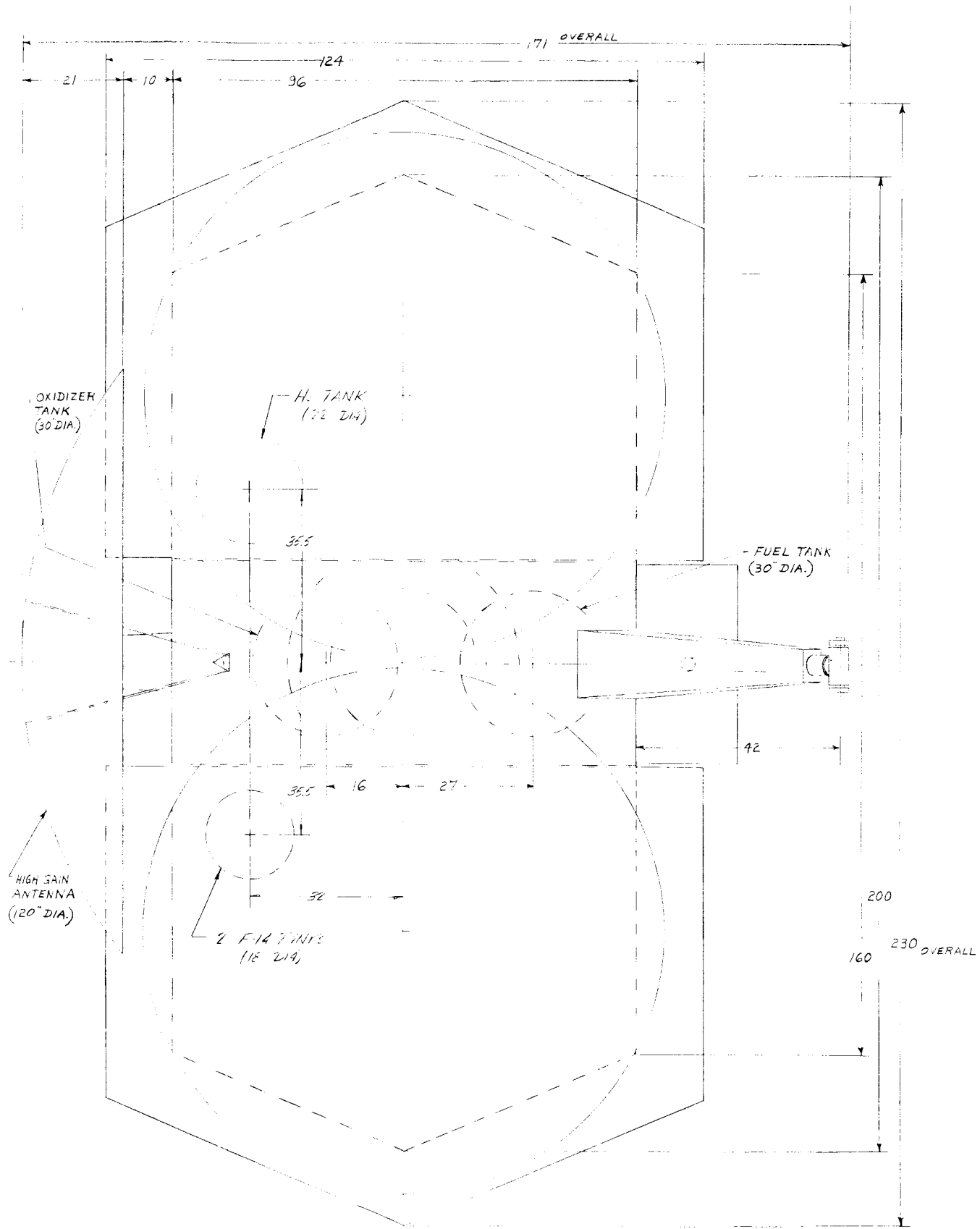
Figure 2.3.5.-2 indicates design of a fly-by bus. The same external structure previously used for the Orbiter is used for the bus. However, the High-Gain Antenna is replaced by a 3-foot diameter antenna which is sufficient for transmittal of information from the

spacecraft to Earth. A minimum number of subsystem components are mounted with the fly-by bus, principally Guidance and Control Components. Revisions are made to the tank sizes, since only mid-course fuel will be required.

2.3.6 SATURN 5 CONFIGURATION

Figure 2.3.6-1 shows a possible configuration for a 60,000-pound spacecraft. The system considered is composed of two Landers at 12,000 pounds each, 24,000 pounds of fuel and oxidizer, and an orbiter weight of 12,000 pounds. All units are to be mounted with a volume 260 inches in diameter and 55 feet high.

As shown in Figure 2.3.6-1, solar paddles could be mounted if required for power. The use of RTG power would eliminate the necessity of deploying solar panels. The conclusion reached is that a Voyager System as described above is feasible. Only the concept has been studied, with no effort expended to study individual items.



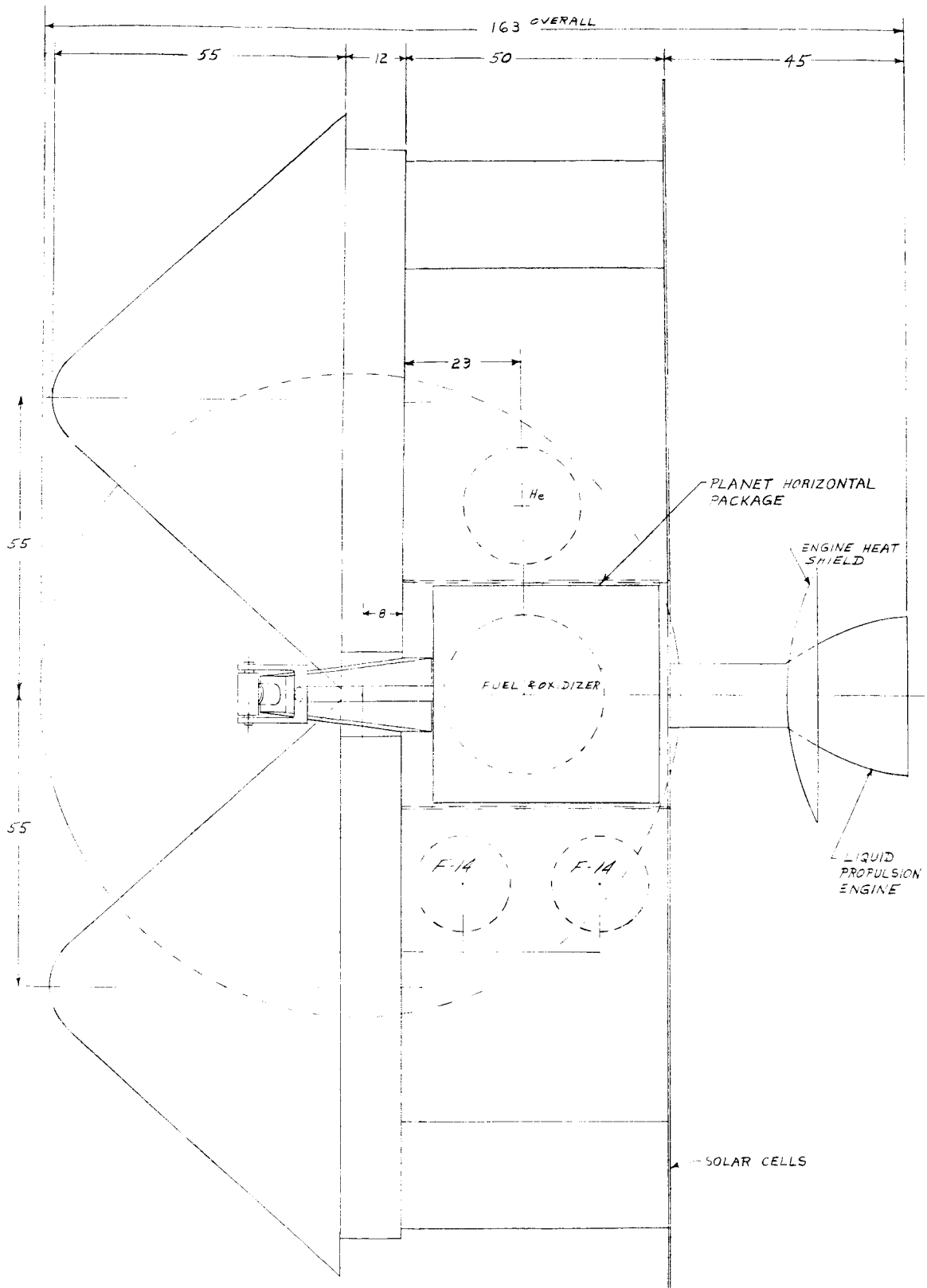
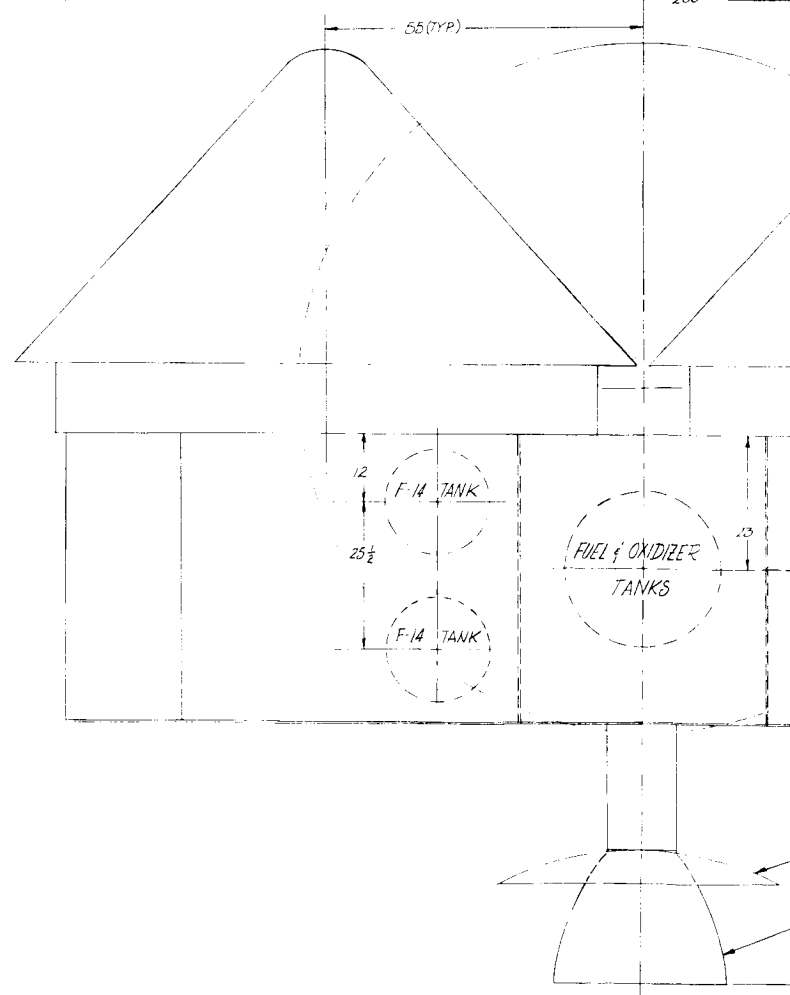
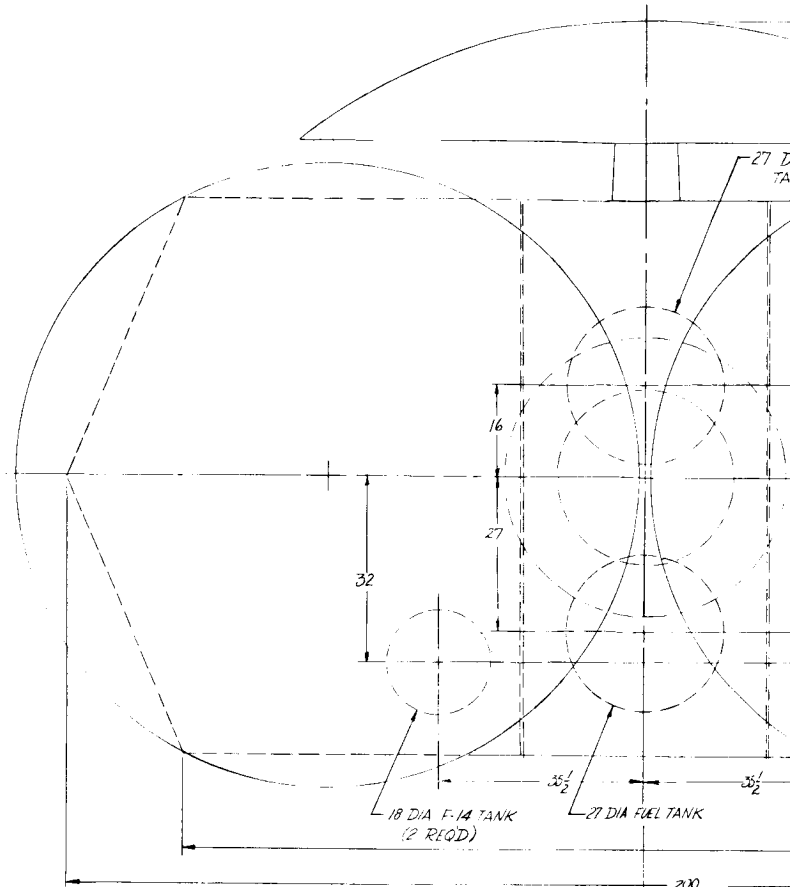
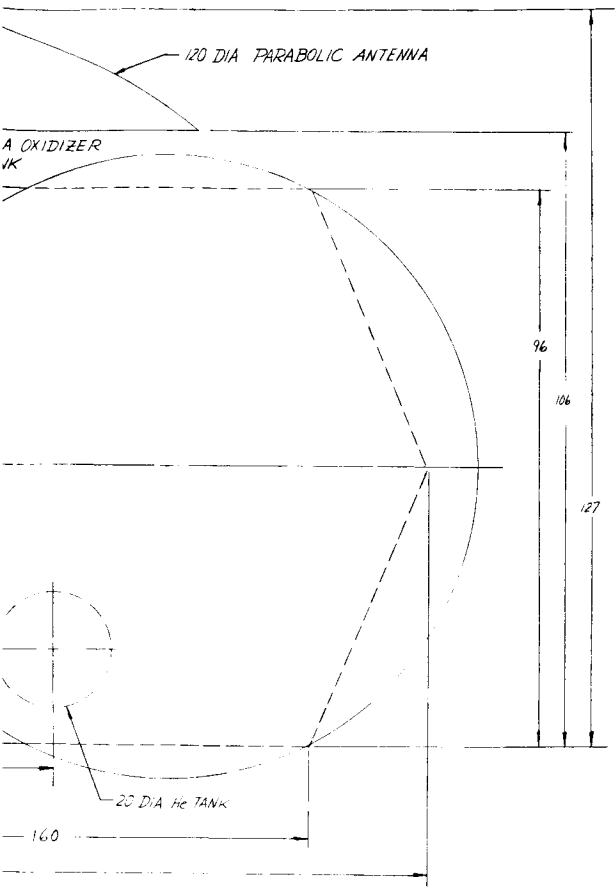


Figure 2.3.4-1. Mars 1971 Voyager Configuration





GENERAL NOTES

1. ORBITER STRUCTURE SIMILAR TO THAT SHOWN IN MARS '69

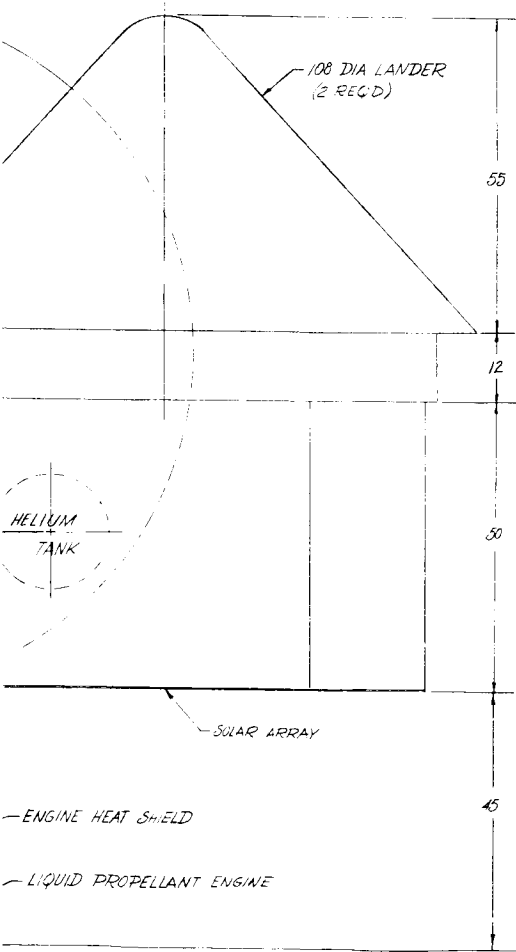
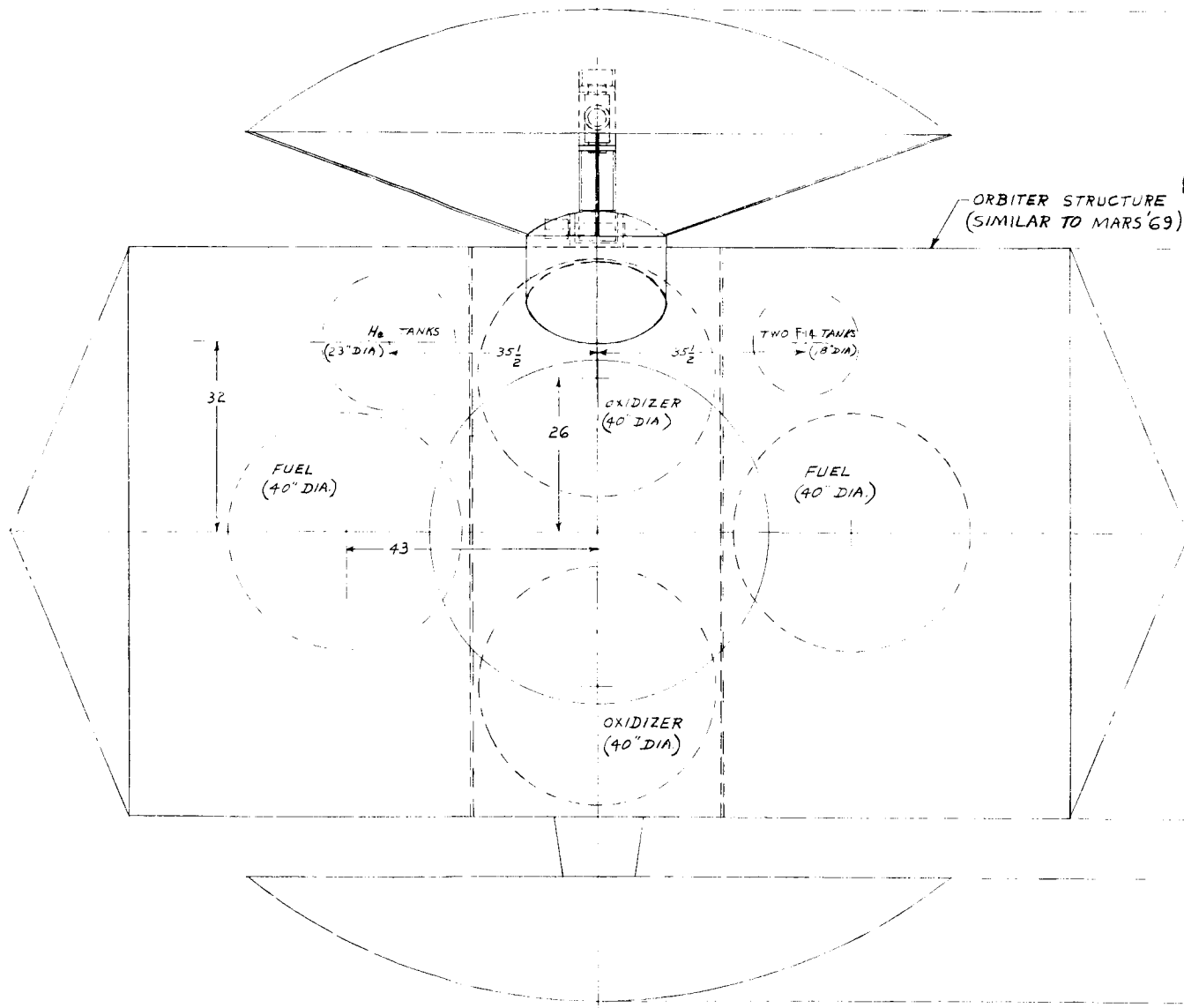


Figure 2.3.4-2. Mars 1973 Voyager Configuration



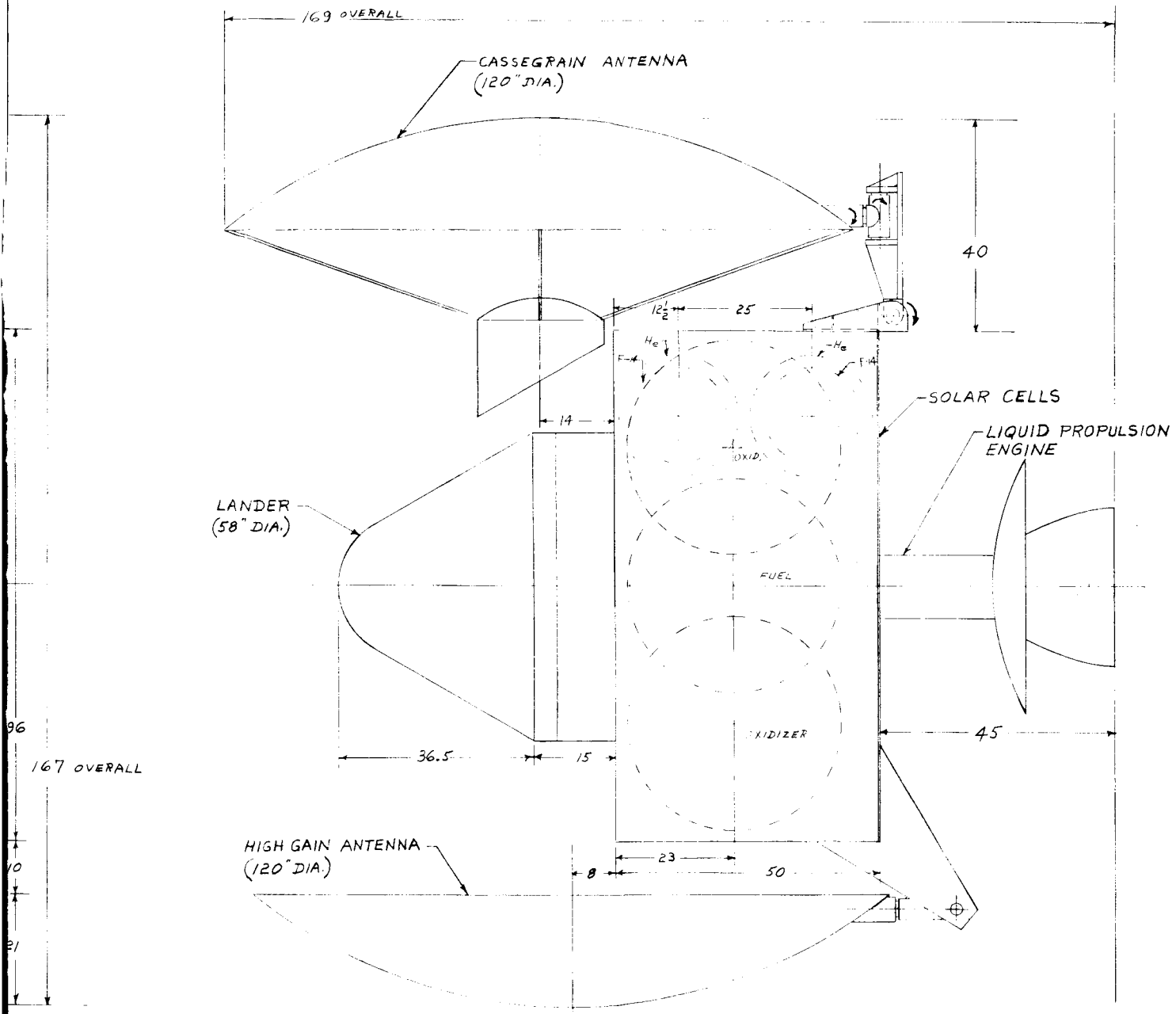
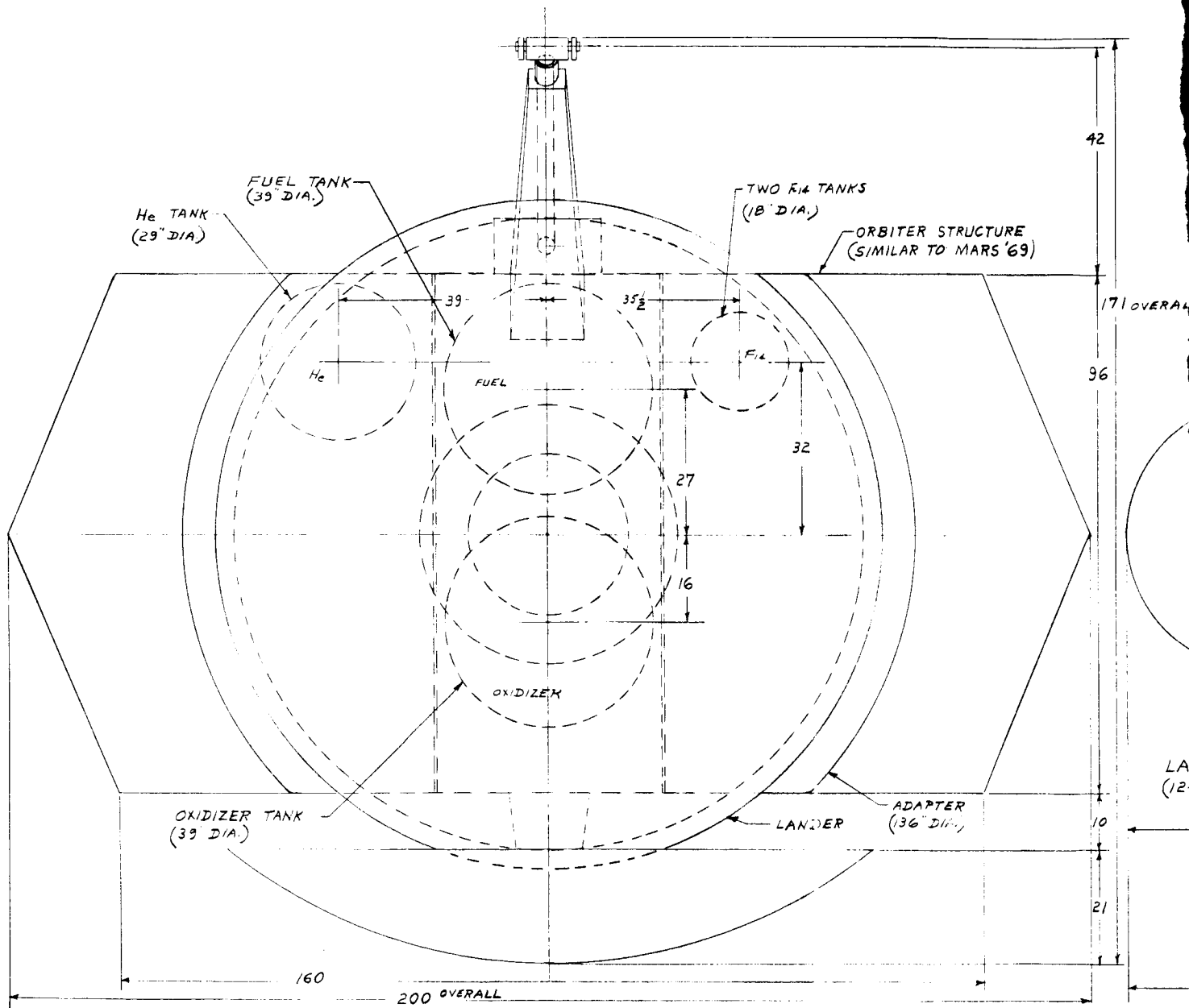
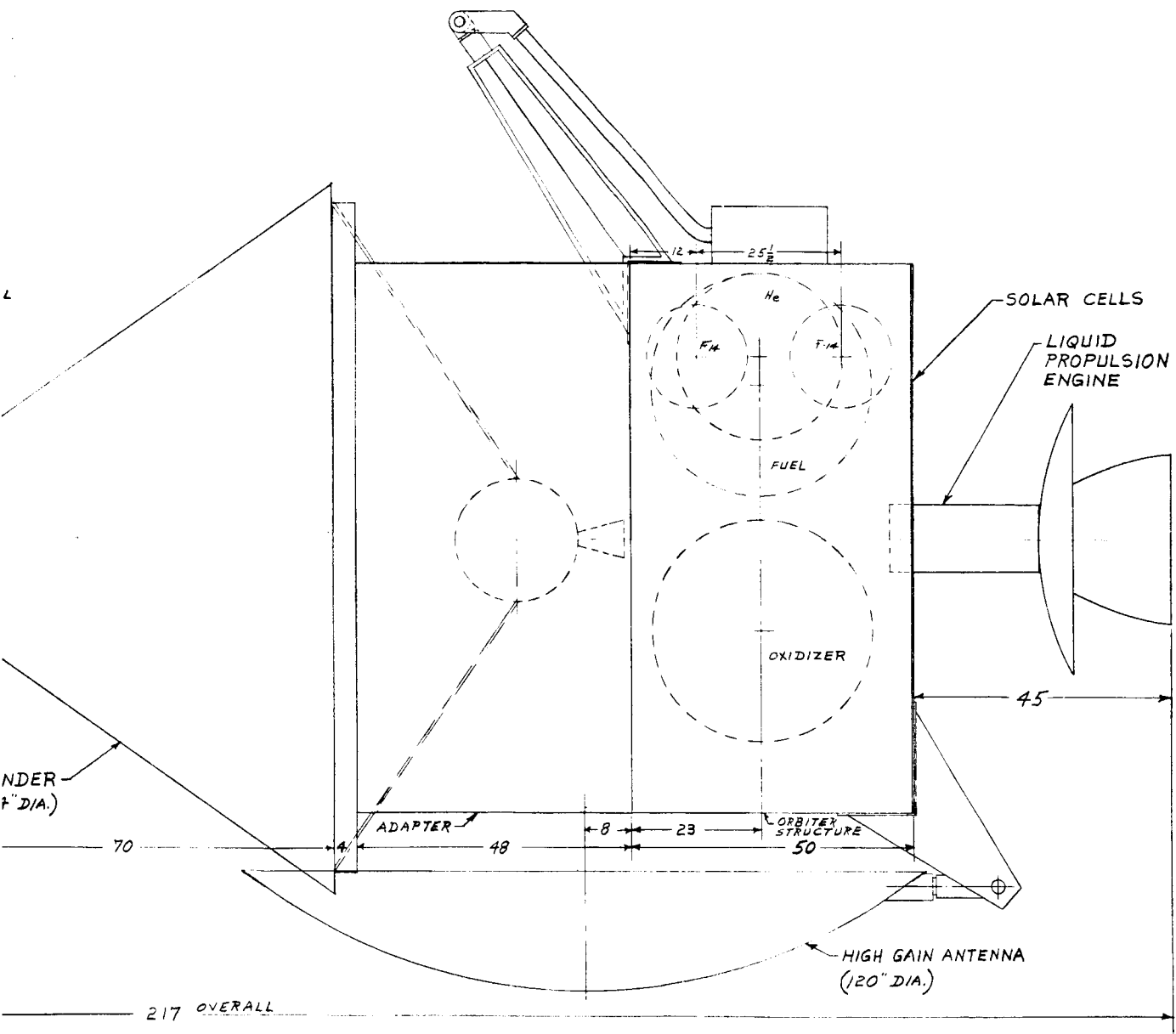


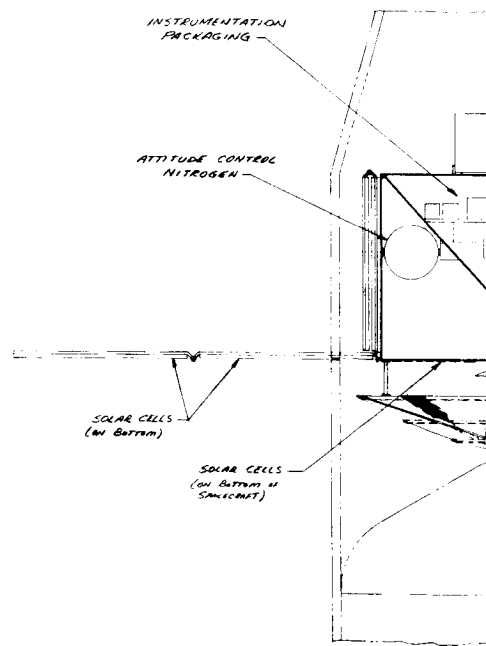
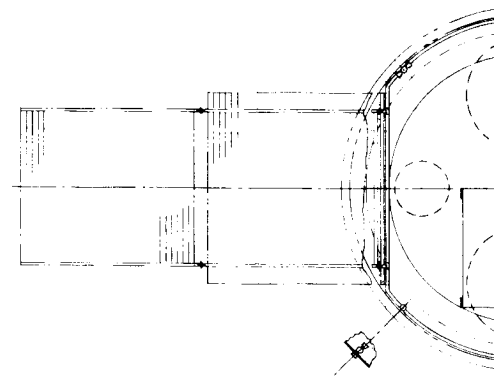
Figure 2.3.4-3. Venus 1970 Voyager Configuration





SCALE 1/10

Figure 2.3.4-4. Venus 1972 Voyager Configuration



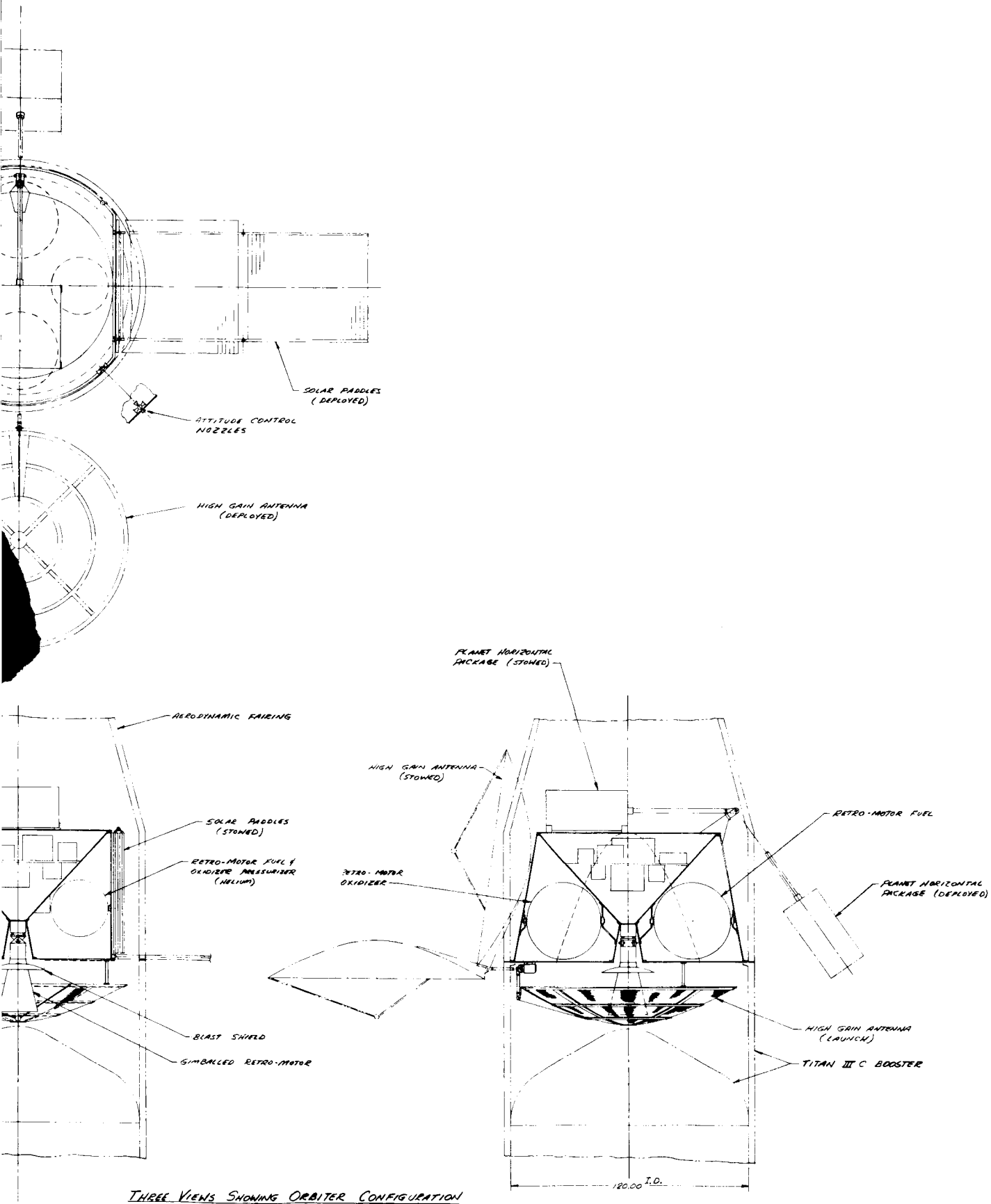
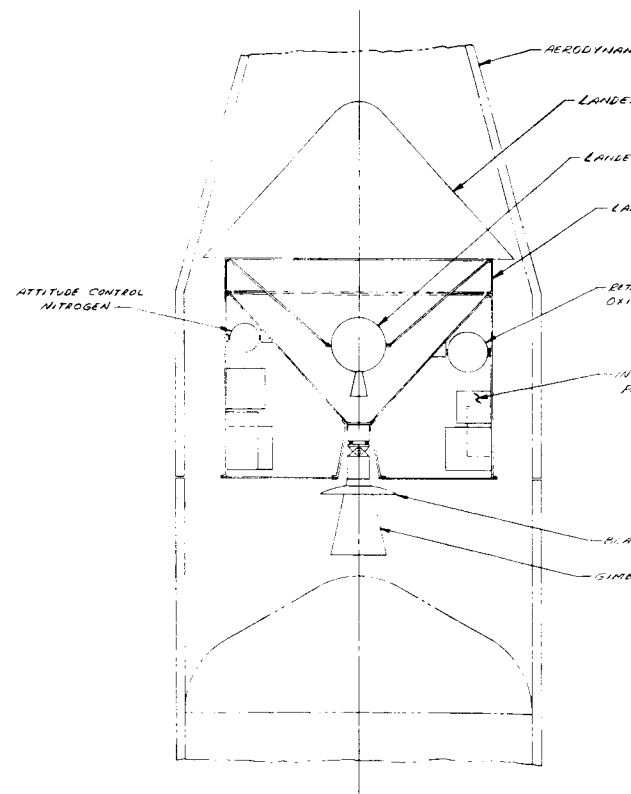
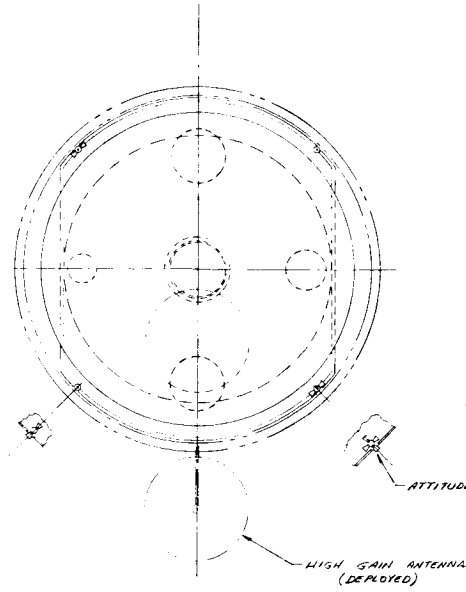


Figure 2.3.5-1. Titan IIIc Orbiter



THREE VIEW

CONTROL NOZZLES

IC FAIRING

2 PROPULSION

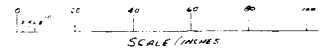
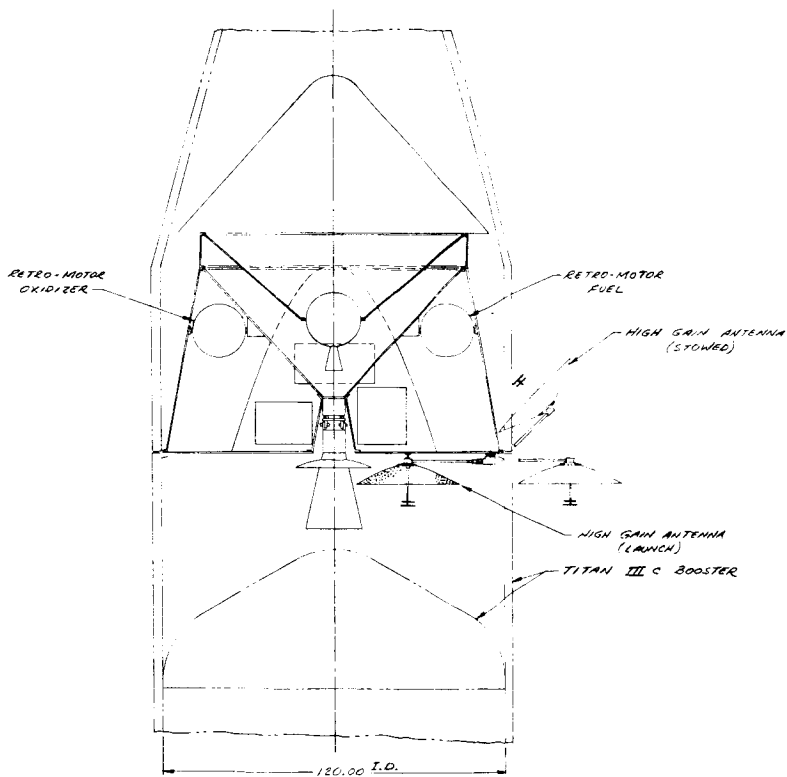
IDER ADAPTER

0. MOTOR FUEL &
NIZER PRESSURIZER
HELIUM)

TRUMENTATION
CKAGING

T SHIELD

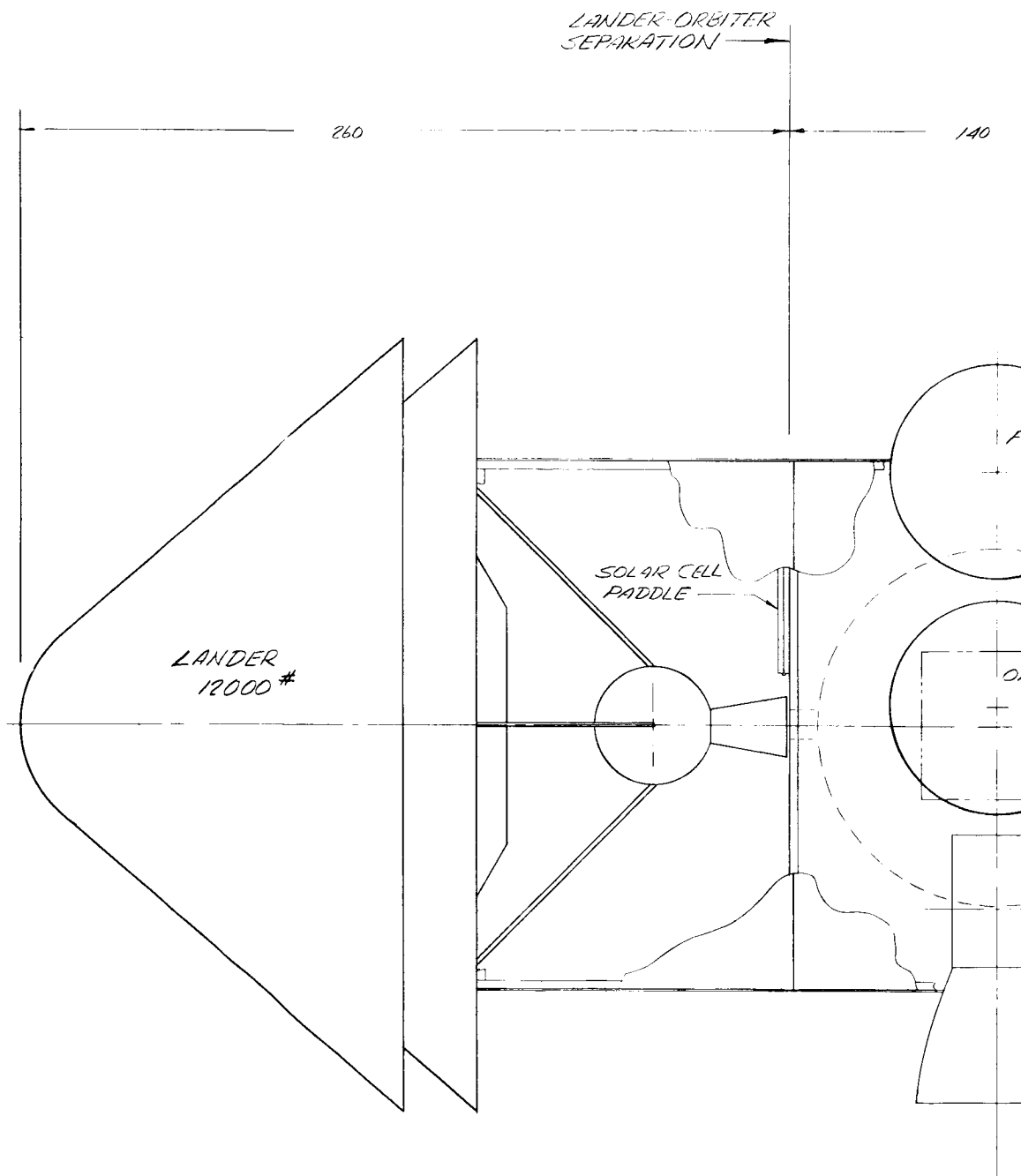
ALLED RETRO-MOTOR

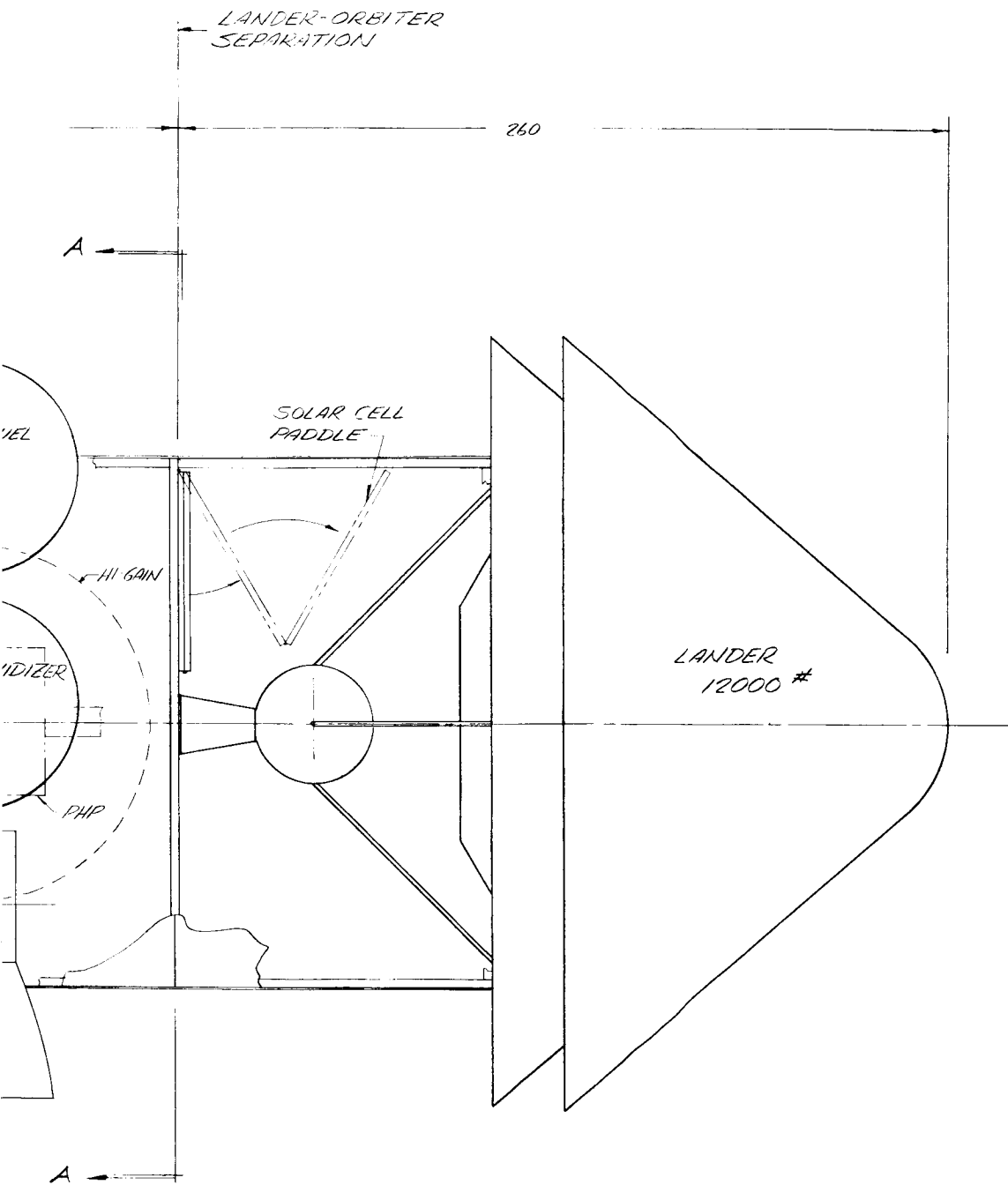


VOYAGER CONFIGURATIONS
 TITAN III C
 MARS '69
 DRAWN I.P. DATE 9-9-63

SHOWING BUS/LANDER CONFIGURATION

Figure 2.3.5-2. Titan IIIc Fly-By Bus





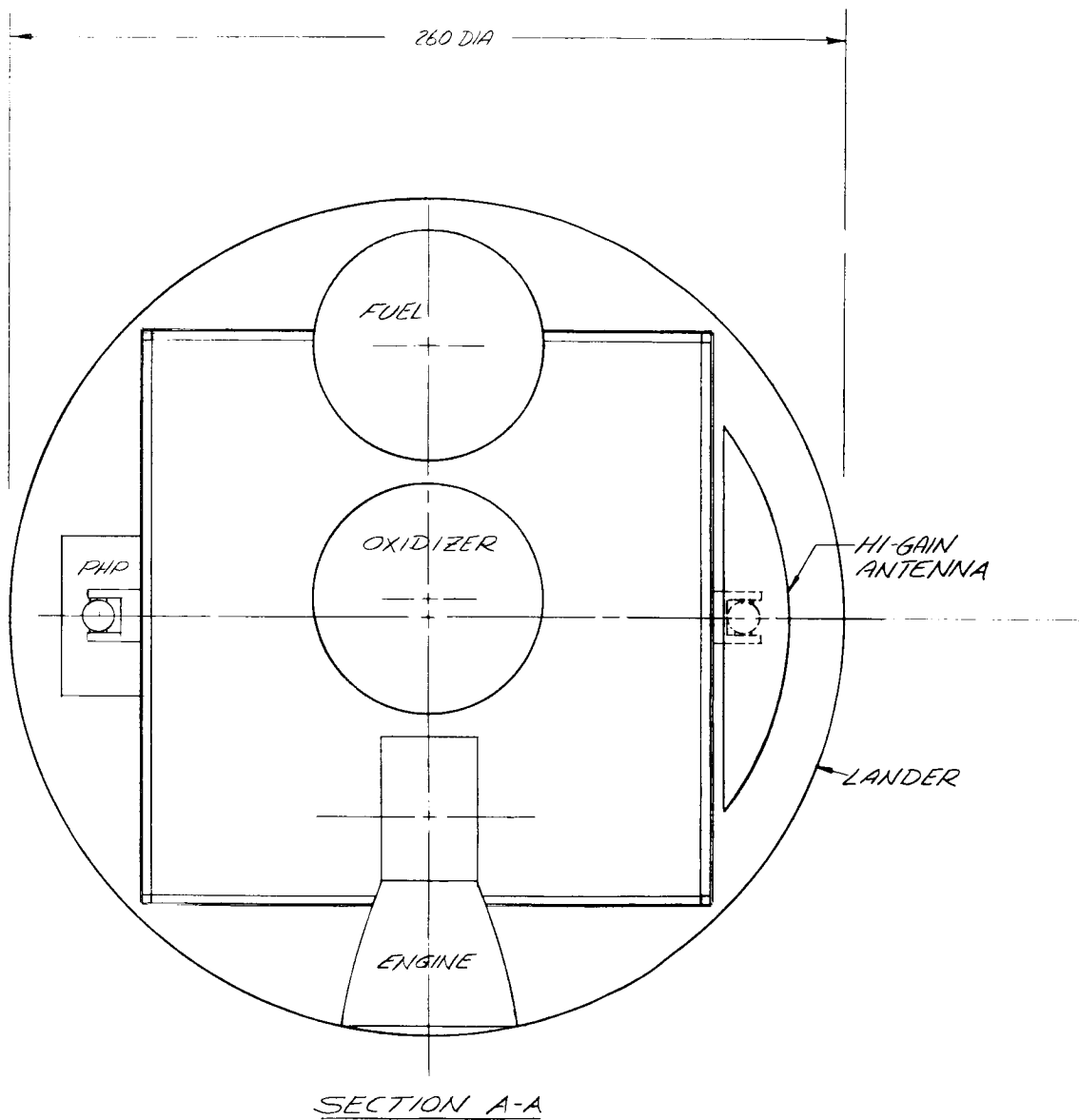


Figure 2.3.6-1. Saturn 5 Voyager Configuration

2.4 THERMAL CONTROL

2.4.1 ORBITER (MAIN BODY)

The major function of the Orbiter temperature control system is to regulate its subsystem's temperatures between limits which will assure operation during the entire mission length. During the transit phase for a Mars mission, the solar constant will change approximately 50 percent from 445 to 226 Btu/hr ft² if we consider the Mars 1969 Voyager trajectory. Other Voyager spacecraft, designed for later missions, can experience even greater variations in the solar constant, depending on chosen trajectories to Mars.

An attempt to isolate all temperature sensitive components from the effects of solar radiation would therefore certainly prevent natural temperature changes from occurring. Unfortunately, the spacecraft shell size required to mount the Landers and the nature of some of the components to be thermally controlled do not lend themselves readily to such isolation. In addition, without a solar input, electronic components must be turned on, and those devoid of internal heat generation must be continually heated to avoid subcooling. In light of these predicaments, a compromise was struck whereby indirect solar energy would be used to maintain some major Orbiter subsystems within tolerable temperature limits. As a result, the hottest spacecraft environment is experienced at Earth departure and continually decreases as the distance from the Sun increases. If a specified lower temperature limit for any component is to be exceeded, additional energy must be locally supplied from the vehicle electrical system. The penalties created by a deficiency in solar energy take the form of strip heaters, wiring and multi-layer insulation.

A sketch of the Voyager configuration is outlined on Figure 2.4.1-1. Since solar energy is to play an active role in the spacecraft temperature control, the majority of the solar cells are mounted on the vehicle surface normal to the sun's rays; a fixed paddle of narrow width completes the required solar array. The thermal interaction between the sides of the spacecraft which are parallel to the sun's rays and the paddle is therefore minor, allowing a near black space sink temperature over large skin sections of the spacecraft.

A large portion of the solar energy incident on the sun oriented surface is absorbed, and then reradiated both externally and internally. The latter supplies energy to meet the temperature levels required for all fuel and attitude control tanks, piping, wiring and components such as the image orthicon camera used in terminal guidance.

The scientific instruments and electronic components are themselves isolated from incoming solar energy by a blanket of insulation. The distribution of the components over the four small side panels of the spacecraft is dictated by weight and balance requirements. When inoperative, these components require energy to maintain their average temperature at approximately 0°F. Provisions for heaters are then necessary since to leave the electronic equipment turned on for the entire transit phase could impair their operation in orbit and would greatly reduce the overall systems reliability.

To reject heat dissipated by the equipment when it is turned on, a system of louvers mounted on the side panels are opened and in effect, view a 0°R sink temperature.

A. Payload Components

As mentioned previously, payload scientific instruments and electronic components are to be distributed over the four small sides of the spacecraft which always lie parallel to the sun's rays. It is assumed for thermal purposes that one-fourth of the load to be rejected when the equipment is operating is allocated to each of the four sides. A further assumption is that the power dissipated in each component is relatively evenly distributed over its base area; such a condition can be met through efficient packaging, as has been obtained in the design of the Advent Satellite electronic components.

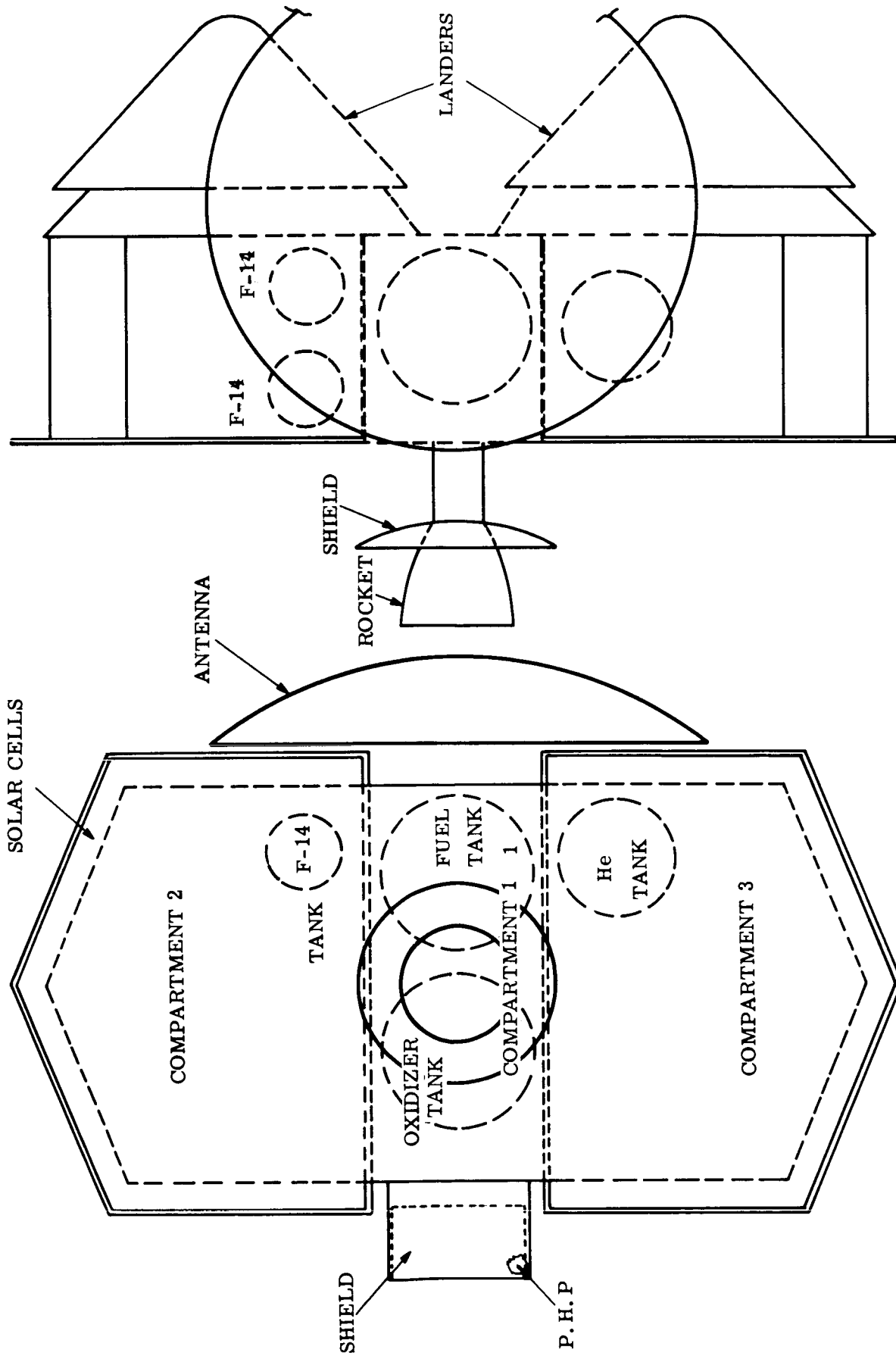


Figure 2.4.1-1. Voyager Configuration

Planetary and albedo fluxes for $(1 \times 19) 10^3$ NM orbit around Mars have been calculated, and impose a negligible load on the payload panels.

(1) General Assumptions (Mars 1969)

Solar Flux in Transit	Max: 445 BTU/hr ft ² Min: 226
Nominal Solar Flux at Orbit Injection	226 BTU/hr ft ²
Mars Average Surface Temperature	415 ^o R
Mars Surface Emittance	1
Mars Average Albedo	0.15
Nominal Voyager Inclination to the Ecliptic at Mars	31 ^o
Worst Average Geometric View Factors	
From Payload sides to Mars for $\pm 90^{\circ}$ from periapsis:	
Planetary	< .104 (Ref. Figure 2.4.1-2)
Albedo	< .067 (Ref. Figure 2.4.1-3)

The requirement for an active control of the radiation heat balance on the payload components is readily shown by examining their temperature limits and their power dissipation level listed on Tables 2.4.1-1 and 2.4.1-3 respectively. In order to satisfy these temperature ranges, the components will be completely insulated from the internal environment of Compartments 2 and 3 (Reference Figure 2.4.1-1); the internal average temperature "seen" by the component insulation will vary from 150 to 0^oF during the transit phase of the mission. The spacecraft skin used for mounting the equipment has a high emittance coating needed to radiate heat dissipated in orbit. To maintain heating requirements to a minimum when components are inactive, it is necessary to decrease this emittance. The emittance variation is accomplished by means of a louver system which covers the radiation surfaces.

(2) Insulation

A highly effective insulation has been developed at General Electric which offers low conductivity values and weighs less than 5 lb/ft³. This insulation is composed of a multi-layer of aluminized mylar sheets, 1/4 mil thick. The conductivity of the insulation is a function of the number of layers, and of the temperatures at both outer layers. For the purpose of insulating the payload components, 10 layers of mylar will be attached to a lightweight structure covering all components located on one panel. A conservative value of conductance of 0.008 Btu/hr ft² has been selected for design purposes, after review of Advent and Nimbus insulation test data. Thus, maximum heat leaks in or out of the payload will be on the order of 1 to 2 Btu/hr ft².

(a) Louver System

Individually actuated louvers will be mounted on each of the four external side panels (see Figure 2.4.1-4). Bimetallic coils will be utilized to rotate the center-pivoted louvers from the fully closed or minimum heat loss condition with a corresponding coil temperature change of 25^oF. The complete louver system including all hardware is expected to weigh on the order of 1 to 1.3 pound per square foot.

TABLE 2.4.1-1. ORBITER AND PLANETARY HORIZONTAL PACKAGE
TEMPERATURE LIMITS

Item	Mode	Temp. Limits (°F)
Payload Components	Off	-10 - 0° (1)
	On	30 - 100 (2)
Fuel Tanks	--	40 - 110
F-14, He Tanks	--	70 - 175
PHP Components	Off	-10 - 0 (1)
PHP Components	On	30 - 100 (2)

(1) -10°F for reorientation periods; 0°F for normal cruise (2) Component base plates

TABLE 2.4.1-2. SUMMARY OF MAXIMUM HEATER REQUIREMENTS
DURING NORMAL CRUISE (WATTS)

Component	Power*	Power**
Payload Electronics and Instruments	35	35
F-14 Tank No. 1	0	2.8
F-14 Tank No. 2	4	6.2
He Tank	2	6
PHP (Folded) (0° Minimum)	6	15
Totals	47	65.0

*Required at 1969 Furthest Distance From Sun = 1.4 Au.

**Required at Mars Aphelion

TABLE 2.4.1-3. ORBITER COMPONENT POWER DISSIPATIONS

Orbiter Components	Maximum Heat Dissipation (watts)
Attitude Control Subsystem	
Switching Amplifier & Logic Subsystem	3
Gyro Module	9
Gyro Control Electronic Module	7.5
Accelerometer and Electronics	2
Auto Pilot	5
Power Converter Subassembly	3
Communications	
Transponder	2
Command Demodulator	1.75
Power Amplifier	100
Power Amplifier Filament	6
High Voltage Power Supply	50
Power Control and Conversion	5
Very High Frequency Receiver (2)	1.5 (each)
Data Processor	2.5
Multicoder	1
Buffer	0.5
Programmer	6.4
Thermoplastic Recording Unit (2)	25 (each)
Battery	13.8
Science	
Ionspheric Profile	2
Ionization Chamber	1
Micrometeoroids Detector	0.5
Antenna Drive Electronics	10
PHP Drive Electronics	15

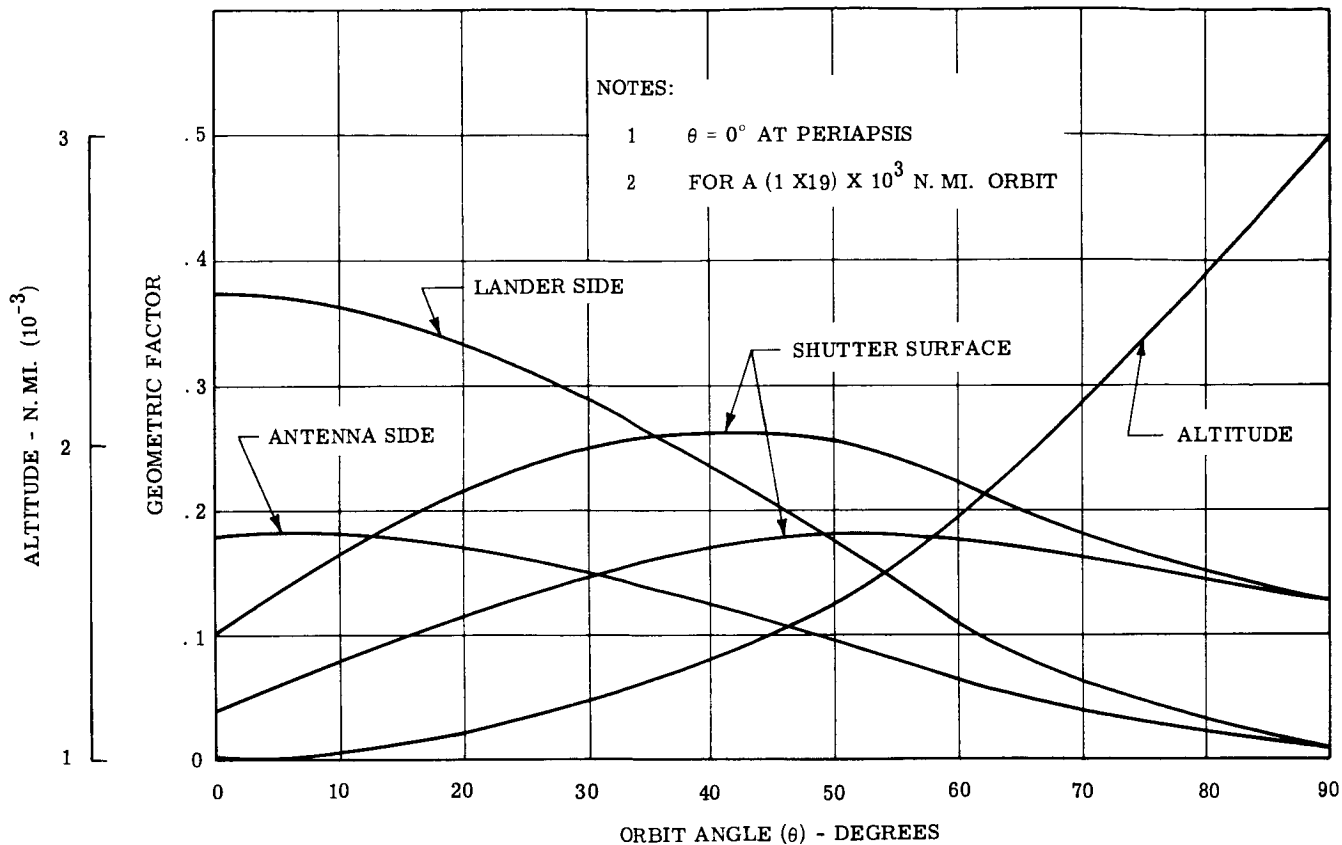


Figure 2.4.1-2. Planetary Geometric Factors (Orbiter Sides to Mars)

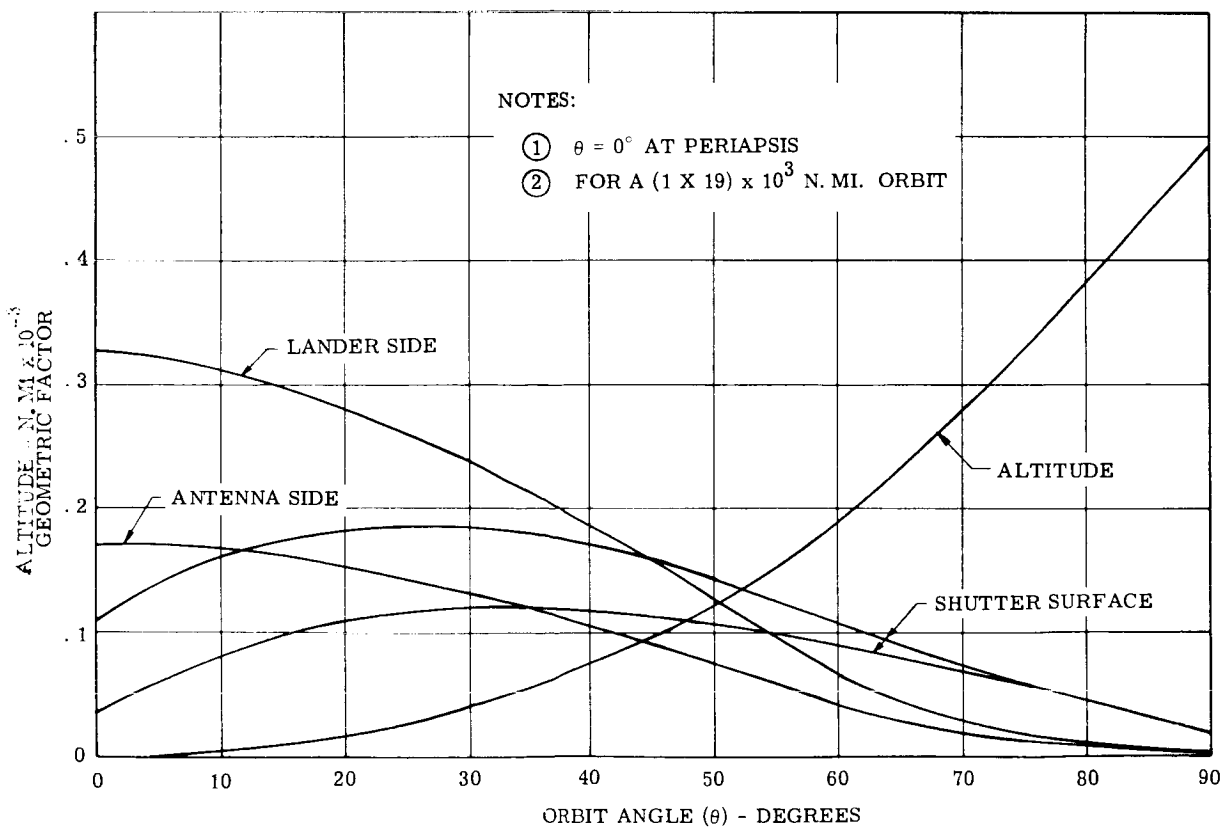
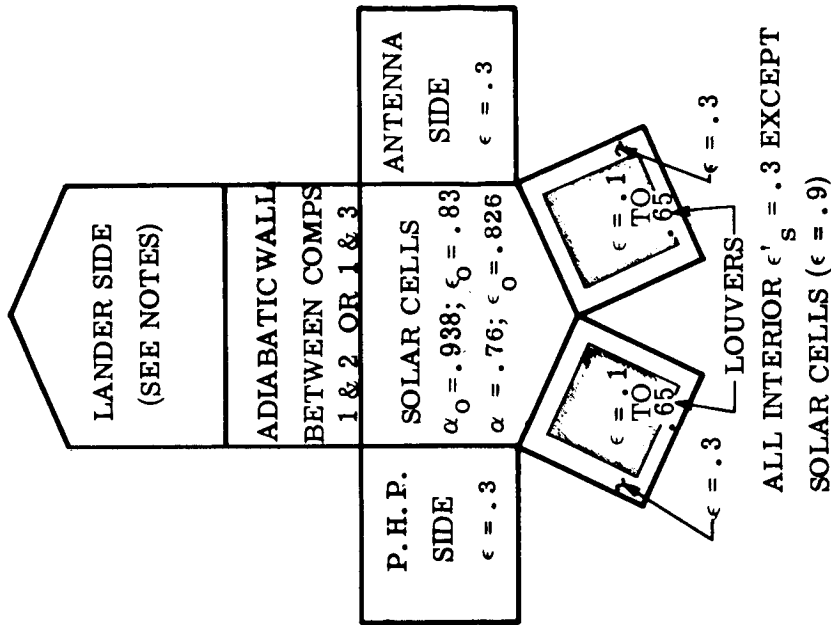
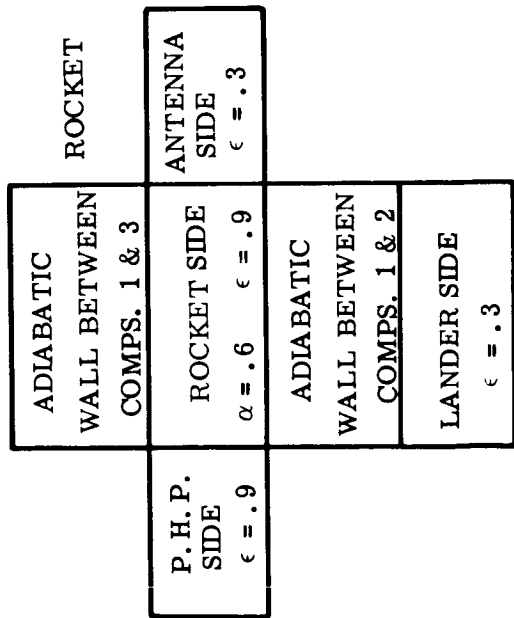


Figure 2.4.1-3. Albedo Geometric Factors (Orbiter Sides to Mars)

COMPARTMENT 2 OR 3



COMPARTMENT 1



ALL INTERIOR $\epsilon'_s = .3$

NOTES:
 1 LANDER SIDE OF COMPS. 2 OR 3 IS ADABATIC WHILE LANDERS ARE ATTACHED, BUT WHEN DETACHED THERE IS A BIOLOGICAL BARRIER (ϵ INSIDE = .2, ϵ OUTSIDE = .1)

Figure 2.4.1-4. Orbiter Surface Coating Pattern

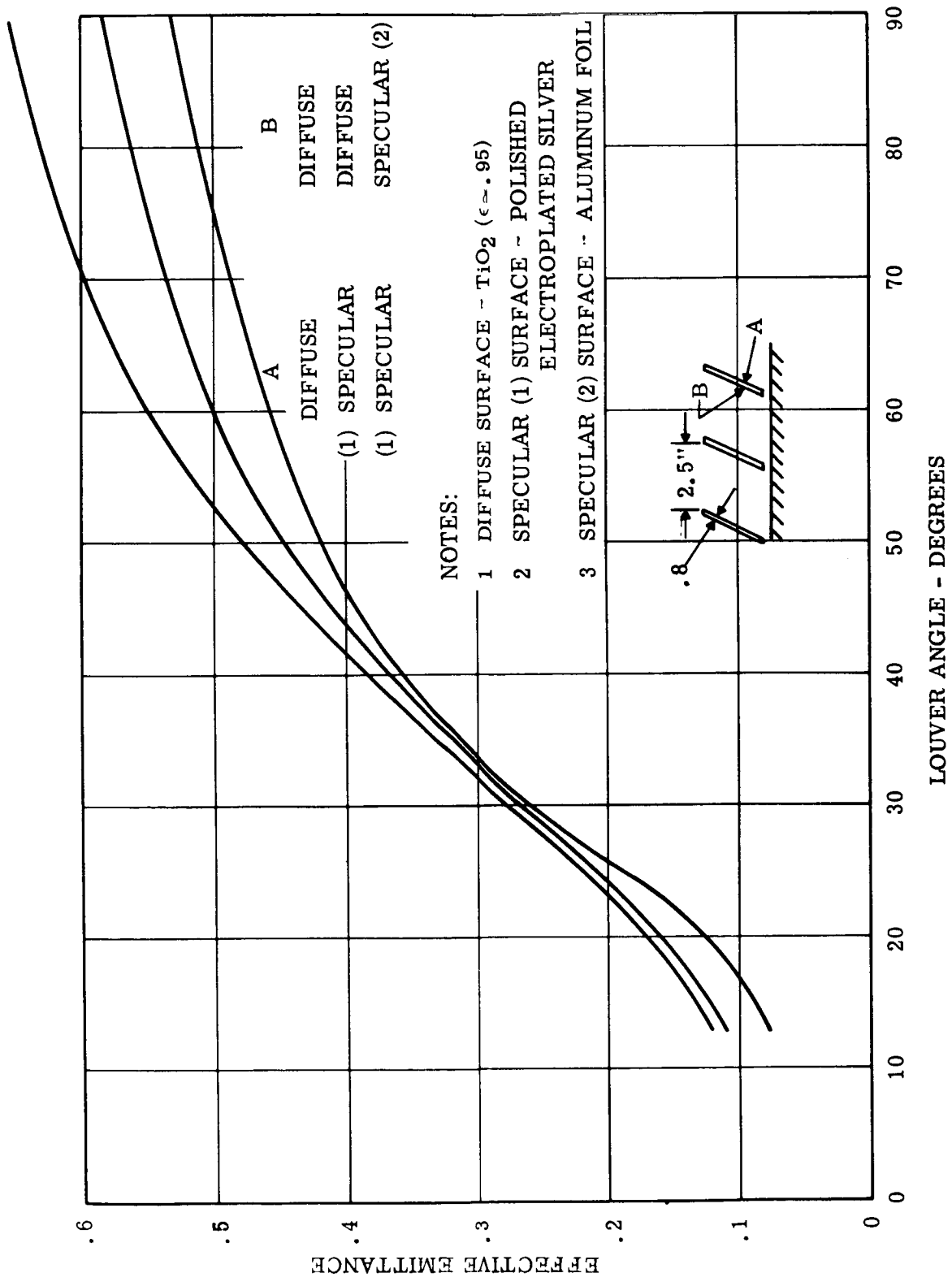


Figure 2.4.1-5. Effective Emittance vs. Louver Angle

Each louver unit will consist of the louver blade, support bearings at each end, and fittings, a bimetallic spring, and stops to limit the fully closed and open positions. The blades will be constructed from lightweight, 0.005-0.008 inch aluminum formed sheets, spotwelded together along the two edges. The surfaces are bare, specular reflectors. An emittance of 0.05 or less will be obtained; this characteristic can be met by vacuum deposition of aluminum.

The nominal settings for the bimetallic actuation were taken to be 55 to 80°F, for design purposes. Efforts will be made to distribute the sensing elements over each of the four equipment panels. The bimetal springs will be in good thermal contact with the panel, and will be enclosed in an insulated housing to minimize external thermal environment effects.

Louver dimensions will be approximately 1.5 inches in width, and 0.2 inch or less in thickness. The ratio of width to length must be kept above 5 in order to obtain near maximum effective emittances, when the louvers are fully opened.

Tests of louvers assemblies have been conducted at General Electric to determine their thermal performance; agreement has been generally good with analytical results. Although these assemblies are not duplicate hardware of those developed by JPL and STL for their interplanetary probes and OGO programs respectively, louver characteristics have been reasonably well correlated.

Figure 2.4.1-5 shows Advent Program experimental results of effective emittance vs. louver angle from various coating properties of the blades. Each louver blade was composed of multilayer insulation 0.8 inch thick, and the blade width was 3.3 inches; effectively then, each blade represents an adiabatic surface as far as incoming radiation from the panel proper. The greatest effective emittance at the fully opened position (90°) is observed to be 0.65 when both sides of the blade consist of highly specular surfaces. If one defines louver "efficiency" as to the ratio of effective panel emittance with to that without louvers for a given panel temperature, it is then 68 percent for the specular-specular case. Since the percent blockage attributed to blade thickness when louvers are fully opened differs from that reported by STL on their louver assemblies, (Reference 1, see Paragraph 2.4.4) the above efficiency has been prorated accordingly for comparison purposes. The corrected Advent louver efficiency is then approximately 79 percent vs. 76 percent reported by STL. This small disagreement may be caused by differences between the louver assemblies in general, and between the various testing techniques.

Since the Voyager Orbiter louver system will be similar to that developed by STL, the quoted 76 percent efficiency has been prorated to 74 percent to agree with the anticipated louver blockage (≈ 13.5 percent). With negligible albedo flux to be received at Mars, the base panel for the louver assemblies need only require a high emittance. Series Silicone Black Paint has such a characteristic, $\epsilon = 0.92 \pm 0.02$, and represents the type of coating that will be used on the Orbiter louver bases. A nominal 0.65 maximum effective emittance is therefore chosen for design purposes.

The effective emittance of fully closed louvers can theoretically be ≈ 0.03 , if the louver specular surfaces have an emittance of 0.05 - 0.06. Since heat leaks can occur at the edges of louver assemblies, and at overlapped joints, an effective emittance of 0.1 has been selected to calculate heat leaks from closed louvers.

From the power dissipation schedule shown on Table 2.4.1-3, and average watts dissipated/component mounting base area, a required louver covered area is estimated to be 12 ft². The vehicle skin structure for mounting components will be an aluminum honeycomb sandwich, with 32 and 12 mil for the inside and outside faces respectively. This honeycomb will act as a fin for most of the equipment. For those components which cannot be mounted

directly on the panel, and which must reject some energy, a conduction path will be provided to them into the radiating skin.

(b) Particular Components

The elevated power density which is characteristic of the Klystron tube, a unit of the communication equipment, necessitates additional fin area to maintain its base area temperature between 75 and 100°C. In operation, this tube dissipates 100 watts. Combinations of fin areas and thickness required have been calculated, and are presented on Figure 2.4.1-6. Since the most efficient fin from a weight standpoint does not have the least radiation area (reduces heating required in transit), a compromise had to be made. The area of chosen fin is 2.36 ft², and its thickness 0.1 inch. Since only one of the Klystron tubes will be operating at a time, they can all be mounted on the same fin, as close to its center as possible.

B. Solar Cells

The solar cells selected for the Mars 1969 mission are the silicon type. The temperature of the solar array is an important factor in its efficiency of operation, and is a preponderant item in the heat balance of Compartments 2 and 3. The general steady state thermal balance equation for a unit solar array operating in space can be written as:

$$S \left[Z \alpha_o + (1-Z) \alpha_F \right] = \sigma \left[Z \epsilon_c + (1-Z) \epsilon_F \right] T^4 + Q_B + SZ \eta'_D \quad (1)$$

\longleftarrow I \longrightarrow \longleftarrow II \longrightarrow

where

- P = Power output of array per unit area = $SZ \eta'_D$
- I = Solar radiation input
- II = Heat radiated from cells, uncovered front areas and back
- S = Incident Solar Flux
- Z = Ratio of active solar cell area to frontal area of array (packing factor)
- α_S = Solar absorptance of surface
- ϵ = Effective emittance of surface
- σ = Stefan-Boltzmann Constant
- T = Temperature - °R
- η'_D = Cell absolute efficiency
- $\eta'_D = \eta_{SC} \eta_T \eta_D$
- η_D = Ratio of composite cell to base cell efficiency
- η_{SC} = Cell standard efficiency to air mass = 0 sun (at 85°F)
- T = Temperature-efficiency dependence of solar cell
- Q = Heat loss

Subscripts

- o = Glass/cell properties referred to zero air mass spectrum
- F = Inactive front array surface
- B = Rear array surface
- C = Glass/cell properties

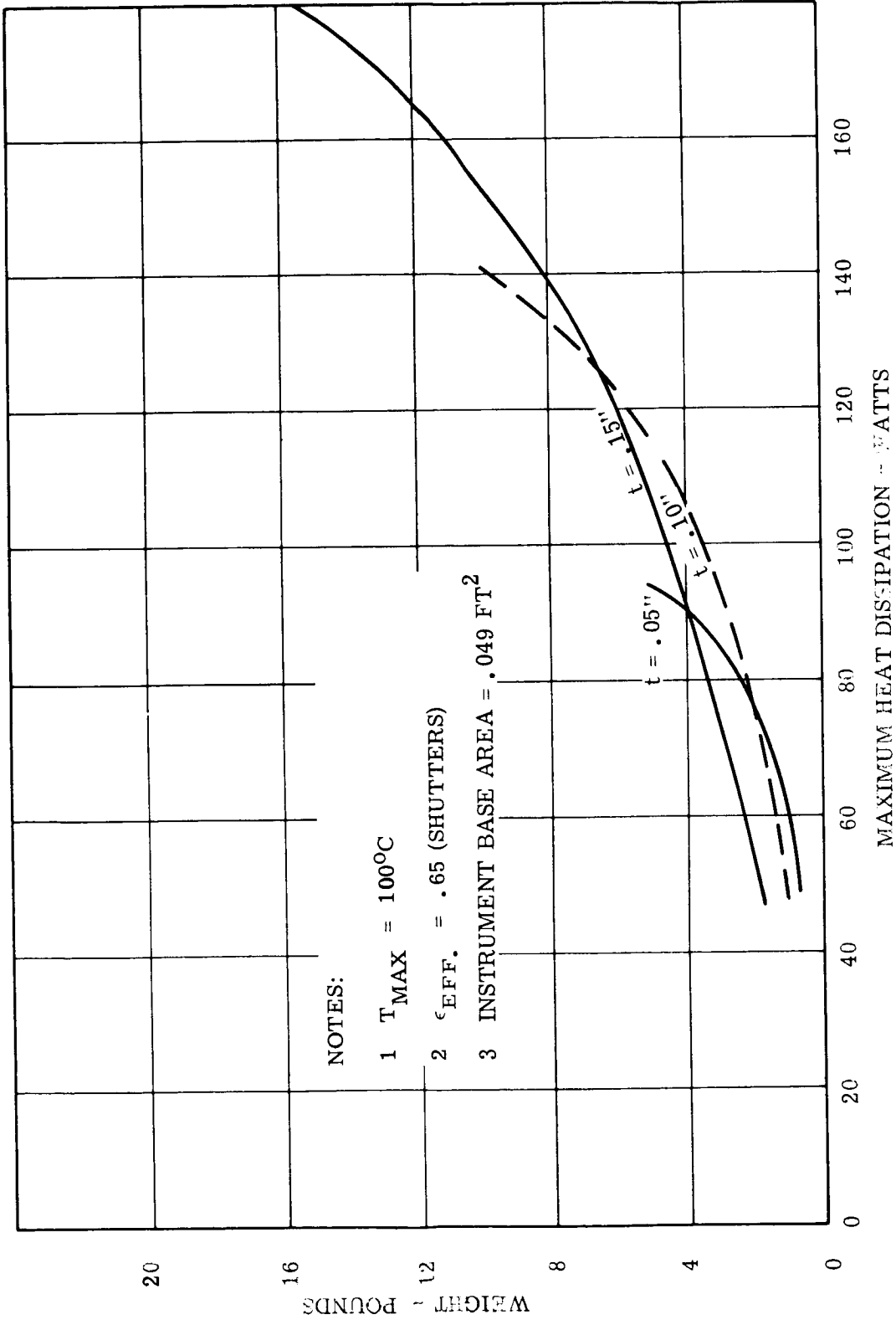


Figure 2.4.1-6. Base Plate Weight vs. Heat Dissipation

TABLE 2.4.1-4. STANDARD VALUES OF SOLAR ARRAY THERMAL CONSTANTS

$\eta_{SC} = 0.115$	$\epsilon_C = 0.83$ (glass solar cell covers)
$\eta_D = 1.00$	$\epsilon_F = 0.88$
$\eta_T = 2.26 - 0.00231 (T)$	$S = \text{varies with 1969 spacecraft position}$
$\alpha_o = 0.938$	
$\alpha_F = 0.1$ (This is an optimistic coating)	

A steady state heat balance may be used to calculate solar cell temperature since the solar constant changes slowly with time during the Orbiter mission. Albedo and planetary terms were omitted from Equation (1) in view of their negligible effects. The array is always treated as a "thin skin," that is the temperature drop across the array structure is negligible.

For the paddle temperatures vs. distance from the sun plotted on Figure 2.4.1-7, $Q_B = \sigma \epsilon_B T^4 - Q_W$ in Equation (1). ϵ_B represents the emittance of the rear of the array; this surface will be coated with Series Silicone Flat Black. The term Q_W accounts for heating effects caused by the spacecraft's sides. For the Mars missions, the cells are devoid of selective filters.

For the spacecraft mounted array, Q_B is obtained by performing a complete radiation heat balance about Compartment 2 or 3; array temperatures as a function of distance from the sun are presented on Figure 2.4.1-8. The rear of the array is again coated with Series Silicone Black paint.

C. Fuel Tanks

The temperature limits of fuel and oxydizer are on Table 2.4.1-1. In order to meet these requirements, a radiation heat balance for Compartment 1 was performed on the Analog computer. The coating properties were varied on each of the available external surfaces, and the corresponding temperature effects on the tanks were obtained. Using these results, coatings were chosen.

The general type of nodal equation which may be programmed on the analog is,

$$W_i c_{p_i} \frac{dT}{dt} = Q_i(t) + \sum C_{ij} (T_j - T_i) + \sum (F_A F_E)_{ij} \sigma (T_j^4 - T_i^4) \quad (2)$$

where

- c_{p_i} = heat capacity of i^{th} node
- C_{ij} = conductance between nodes
- $(F_A F_E)_{ij}$ = radiant interchange factor
- T_i, T_j = node temperatures
- Q_i = heat input
- t = time

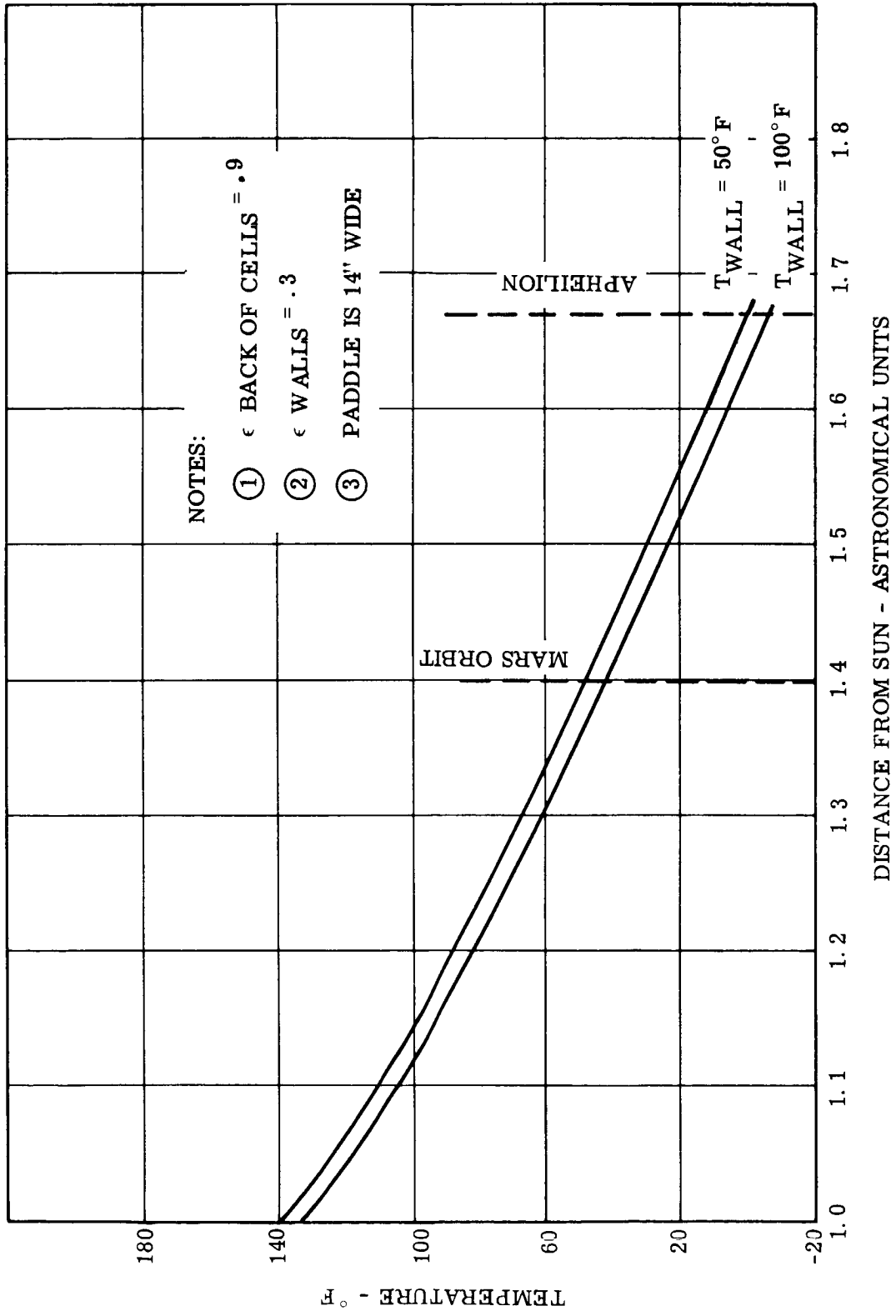


Figure 2.4.1-7. Paddle Temperature vs. Distance from Sun

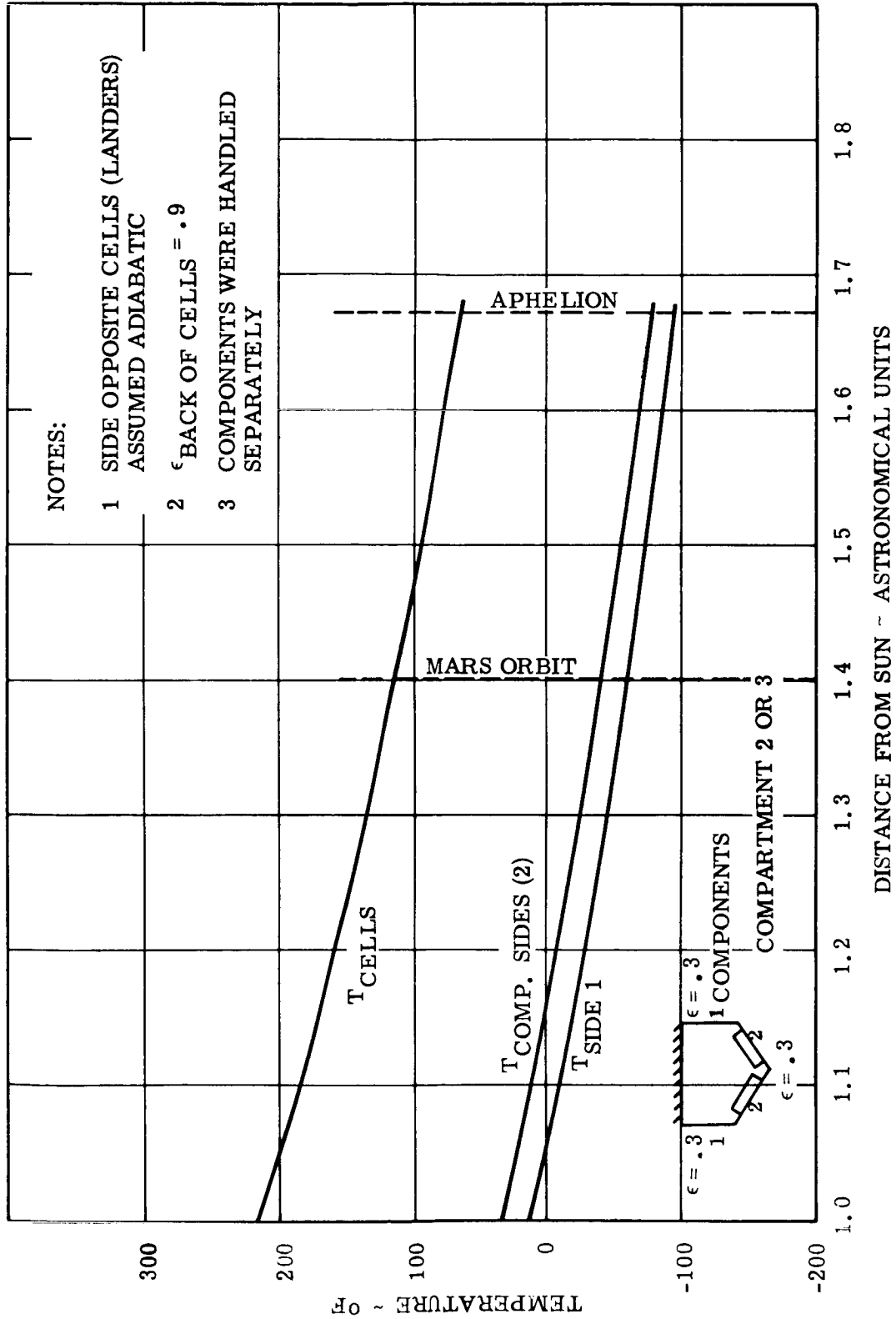


Figure 2.4.1-8. Wall Temperatures of Compartments 2 and 3 vs. Distance from Sun

All compartment heat balances were obtained on a steady state basis, again due to the small change in the solar constant with mission time. Q_i was used to represent heat inputs from the sun's rays and from Lander radiators, assumed at an average temperature of 450°F . Any conduction effects were neglected at this time, but will be included in future work, as the structural design becomes more defined. Each spacecraft wall was assumed a lumped mass, as were the tanks, and the reflective shield of the rocket nozzle.

A mean tank temperature of 110°F is obtained at Earth departure, where the antenna is in its folded position. Temperatures of Compartment 1, including tanks are shown on Figure 2.4.1-9. In order to strive for minimum thermal gradients along tank walls, all compartment internal surfaces will be covered with a low emittance coating. D4D paint, with a nominal $\epsilon = 0.3$, has been proven very stable by tests simulating the space environment conditions, such as those which will be encountered by Voyager.

D4D paint will also be employed to coat both tanks located in Compartment 1. The optical properties of that surface of Compartment 1 exposed to solar energy are,

$$\begin{aligned}\text{Solar absorptance } (\alpha_s) &= 0.6 \\ \text{Emittance } (\epsilon) &= 0.9\end{aligned}$$

This combination is required in order to maintain tanks within their temperature limits. A checkered coating pattern composed of two materials has been chosen to obtain these properties; approximately 50 percent of the surface will be covered with Series Silicone Flat Black ($\alpha = \epsilon = 0.92$), and the balance with $\text{ZNO}_2/\text{K}_2\text{S}_1\text{O}_3$ ($\alpha/\epsilon = 0.3/0.85$ - conservatively degraded).

D. F-14 and He Tanks

The temperature limits of F-14 and He tanks are shown in Table 2.4.1-1. Both F-14 tanks are located in Compartment 2, while the He tank is in Compartment 3.

A radiation heat balance was performed for each compartment, in the same manner as was done for Compartment 1. The side on which the Landers are mounted is assumed to be adiabatic; the louvers are in their closed position. The only heat flux input is due to the reradiation from the rear of the solar array. All internal and external surfaces are to be coated with D4D paint ($\epsilon = 0.3$), except for the rear of the array, which will have a high emittance coating such as Series Silicone Flat Black. This coating pattern for both Compartments 2 and 3 will tend to increase inter-reflections, which in turn will decrease temperature gradients along tank walls; in addition, the array temperature is 25°F lower than it would be with an adiabatic back face while orbiting Mars.

A decrease in the solar array temperature means a greater electrical power output for a given weight/ft² of array. Compartments 2 and 3 have similar wall temperatures, and these are shown on Figure 2.4.1-8 as a function of distance from the sun. Corresponding equilibrium temperatures for the F-14 and He tanks are presented on Figure 2.4.1-10. Analyses have shown that, substituting the Lander adiabatic wall by a surface consisting of an aluminized biological barrier, has a negligible effect on compartment temperatures (see Figure 2.4.1-10).

One can readily see that energy must be supplied to tanks in order to meet their temperature requirements listed on Table 2.4.1-1. Strip heaters will be attached to the external periphery of tanks; then, both heaters and metallic shell will be wrapped in a blanket of multilayer type insulation, similar to that employed for the payload components. When lower temperature limits of tanks are reached, a signal from a temperature sensing device will energize the heater circuits. In most Voyager missions, tank temperatures will not reach upper specified limits when the maximum amount of watts required is

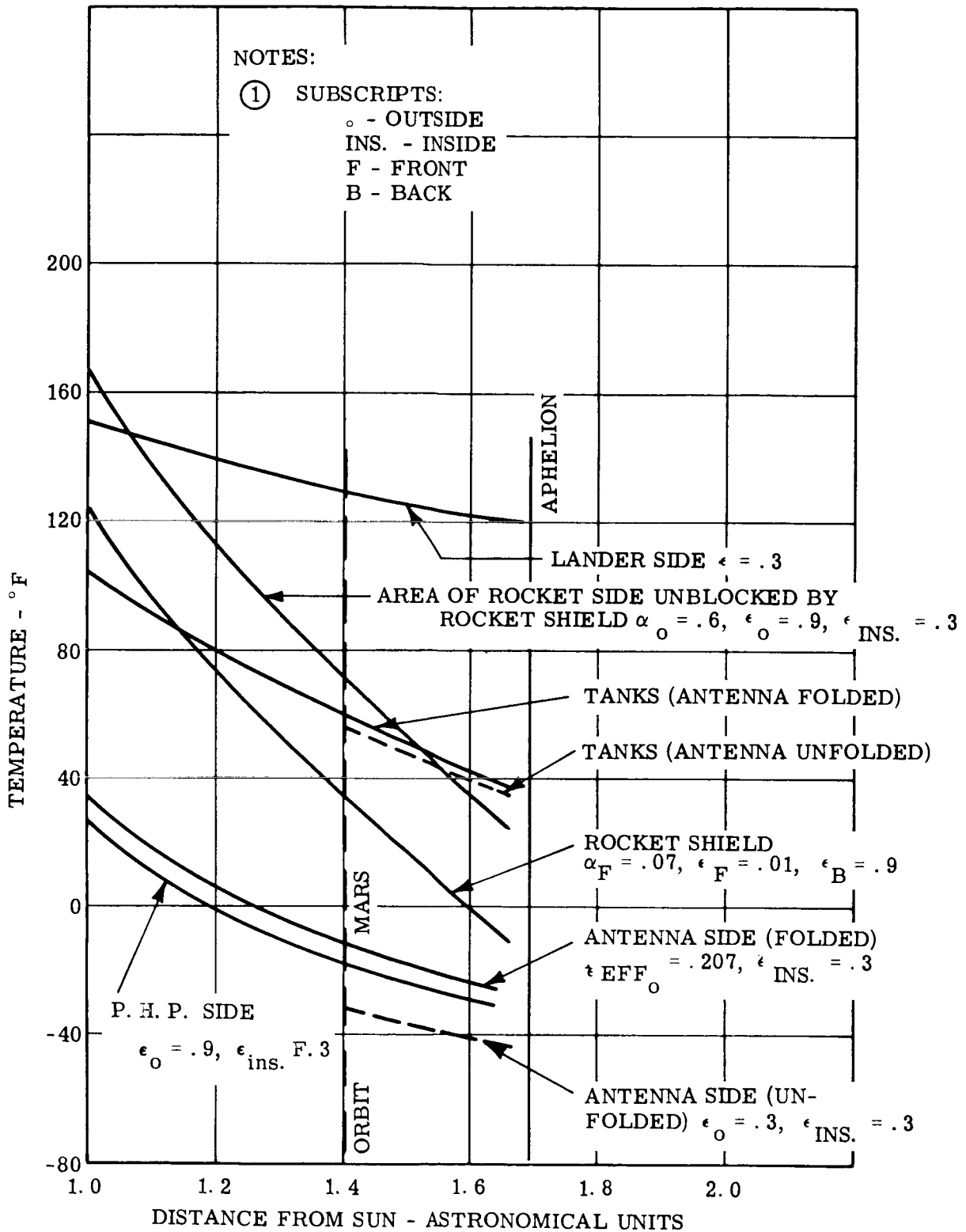


Figure 2.4.1-9. Wall Temperature of Compartment 1 vs Distance from Sun

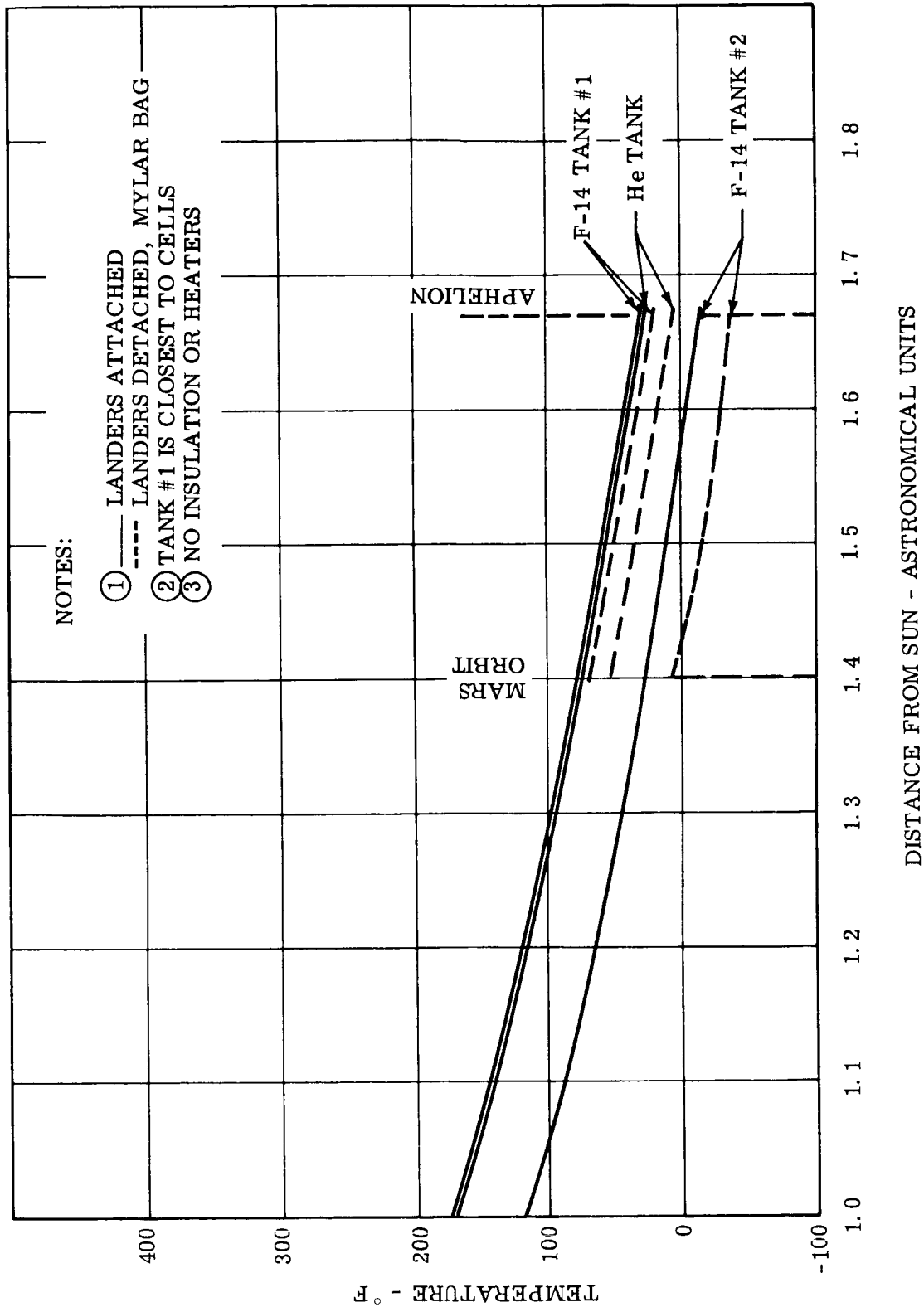


Figure 2.4.1-10. Tank Temperature vs Distance from Sun

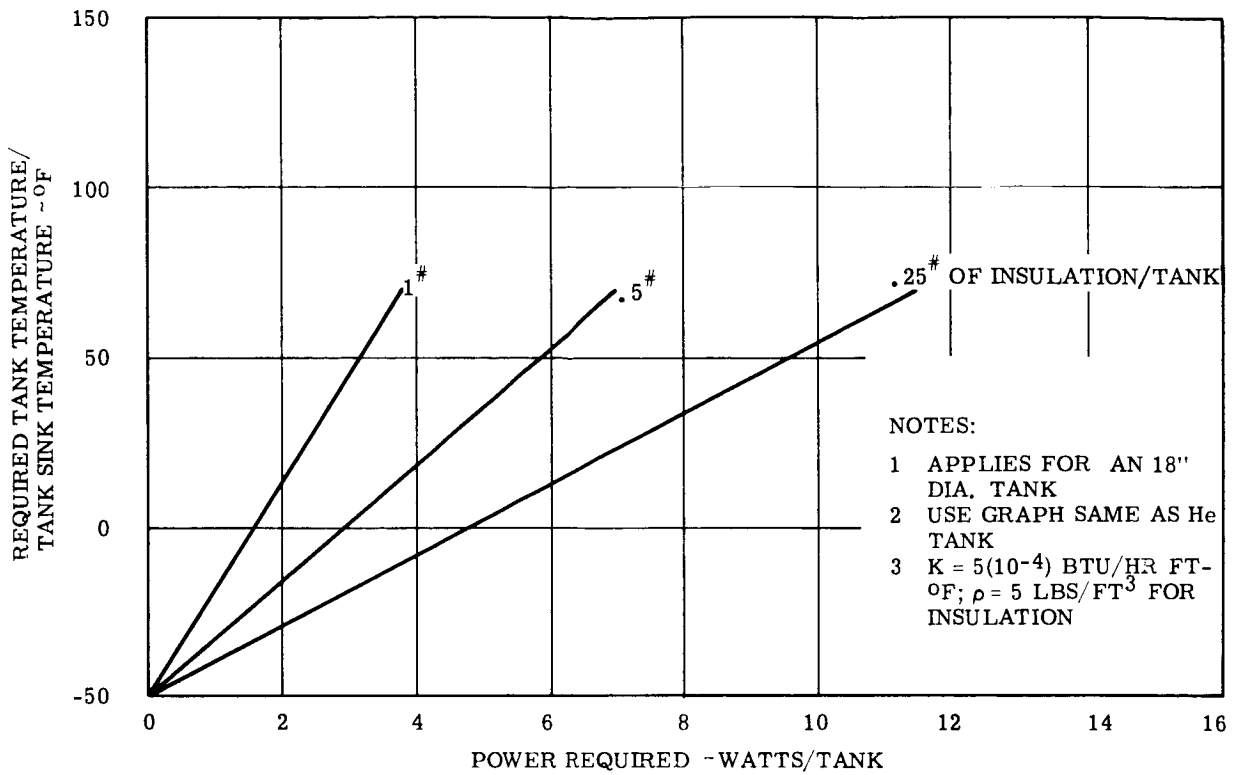


Figure 2.4.1-11. F-14 Tank Temperature vs Power Required

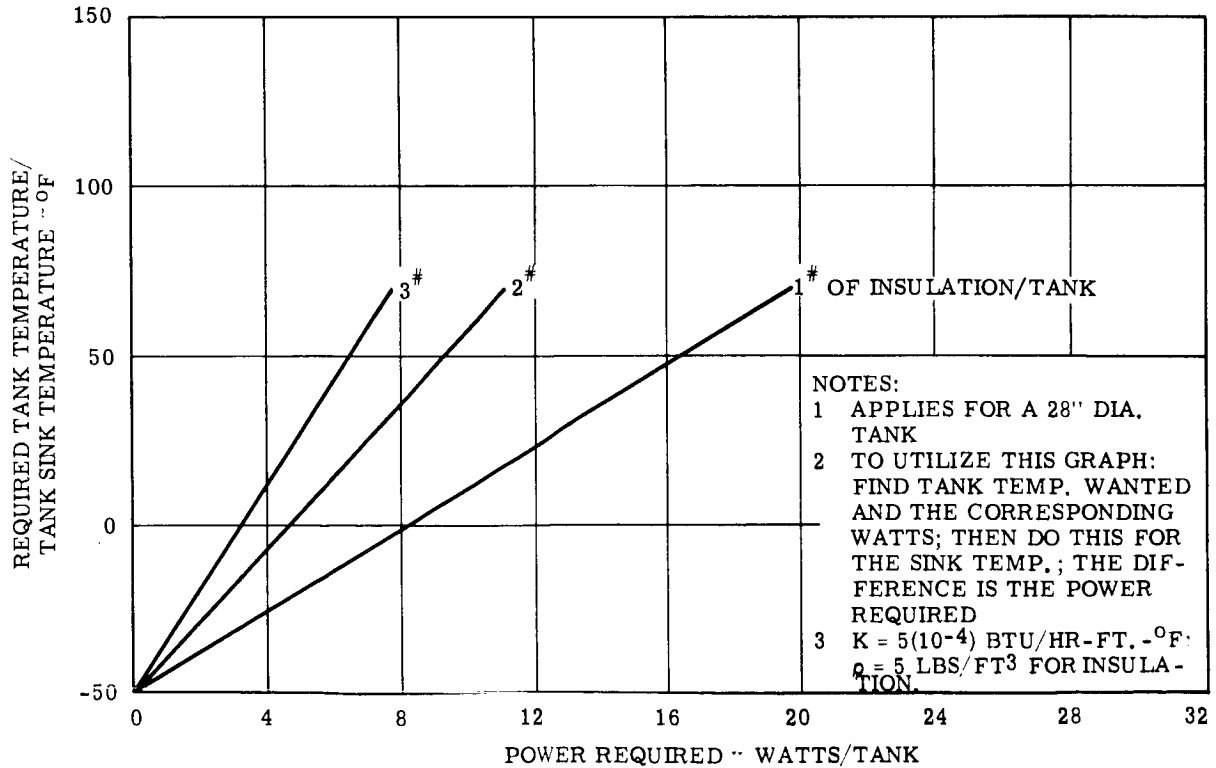


Figure 2.4.1-12. He Tank Temperature vs Power Required

immediately supplied on reaching lower temperature limits. Should the spacecraft's distance from the sun be as great as 1.67 AU, then maximum heating cannot be supplied in one step as above. Either heating is stepped up from none to maximum in two distinct steps, which can be controlled by temperature sensing device, or a time clock; or power can be proportionally controlled by a temperature sensing device. Lightweight and reliable circuits can be designed to accomplish either task.

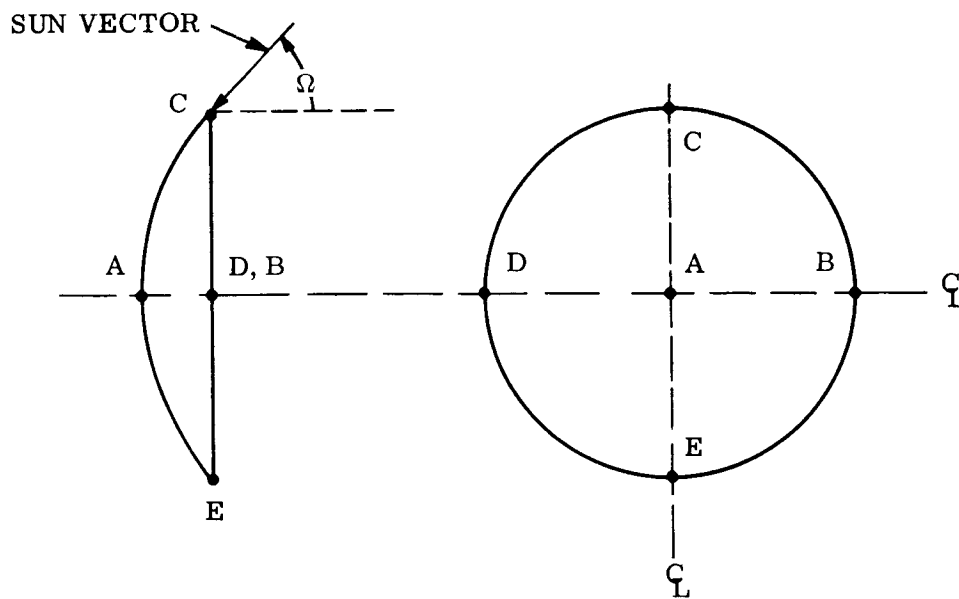
The amount of heat required for each tank depends on its location within the compartment, heat leaks through insulation and protuberances such as attachment fixtures and piping, and the spacecraft's distance from the sun. For nominally chosen insulation thickness, maximum Mars 1969 heater requirements in watts are listed on Table 2.4.1-2. Figures 2.4.1-11 and 2.4.1-12 have been plotted to indicate the approximate number of watts necessary to maintain the F-14 and He tanks within specified temperature limits. These two figures must be used in conjunction with Figure 2.4.1-10, which shows tank temperatures (with no heating) as a function of distance from sun.

In order to increase the usefulness of the gas when being used, it is desirable to raise the He temperature from 70° to 170° F. Therefore, provision is made to furnish 10 watts in addition to that required to prevent subcooling. The additional wattage will then be supplied for a period of six days immediately preceding the gas usage. A time clock will be needed to energize the heater circuit.

E. High Gain Antenna

The temperature control design of the dish antenna serves two purposes: 1) minimize the thermal distortions produced by temperature gradients in the antenna; 2) limit the concentration of radiant energy at the feed tube. The antenna structure consists of a thin faced aluminum honeycomb sandwich panel.

The approximate temperature pattern experienced by a 10 foot diameter parabolic dish ($y^2 = 14x$) is shown below. The antenna is deployed, and solar orientations are listed.



The letters indicate positions at which the local temperatures were determined. The antenna is coated on both sides with Series Silicone Black Paint. Local temperatures are shown in Table 2.4.1-5.

TABLE 2.4.1-5. LOCAL ANTENNA TEMPERATURES

Solar Orientation: $\Omega = 46^\circ$ (187 days from boost; 1.3 AU)

Position	A	B	C	D	E
Temp. ($^\circ\text{F}$)	20	-12	-101	-12	63

Solar Orientation: $\Omega = 36^\circ$ (Mars Encounter)

Temp. ($^\circ\text{F}$)	21	-10	-65	-10	47
----------------------------	----	-----	-----	-----	----

Solar Orientation: $\Omega = 26^\circ$ (90 days after Mars encounter)

Temp. ($^\circ\text{F}$)	33	1	-29	1	46
----------------------------	----	---	-----	---	----

F. Thermal Coatings

The spacecraft areas which require thermal control coatings have already been mentioned. For a system of coatings capable of maintaining the vehicle subsystem temperatures within the desired range, the radiation characteristics should have a minimum of degradation with time. Generally speaking, all surfaces and surface coatings tend to darken with exposure to ultraviolet, charged particles and other radiation. The solar absorptance is affected to a much greater extent than is the infrared emittance. Some materials are more stable under ionizing radiation than others. Since coating development is an area which is receiving considerable attention in both government facilities and industry, improvements in the state-of-the-art both in development of new materials and in knowledge of limitations of existing ones can be expected at a rapid pace. Consequently, the coatings that would be recommended now, especially on the surfaces where solar absorptance plays an important role, may be superseded by the time coatings are actually specified for Voyager.

(1) Coatings with a Low Solar Absorptance to Infrared Emittance Ratio

In addition to this property, the coatings require:

1. Good adhesion
2. Temperature stability in vacuum from -50 to 200°F
3. To withstand without appreciable degradation:
 - (a) Up to 1×10^6 rads. of charged particles corresponding to accumulative integrated dose rate derivable from the Ames Solar Probe radiation environment spectrum
 - (b) Up to 10,000 hours of 1AU ultraviolet radiation which corresponds to the integrated exposure over the vehicle mission.

The majority of the coatings reviewed have been irradiated with nuclear particle dosages far above standard environment without excessive degradation.

A number of materials have a sufficiently low ratio of solar absorptance to emittance to qualify for this application. Some are listed in Table 2.4.1-6.

TABLE 2.4.1-6. NOMINAL COATING PROPERTIES

Coating	Solar Absorptance - α_s	Emittance - ϵ	α_s/ϵ
Anodized Aluminum			
0.33 mils thick	0.12	0.69 (150°F)	0.17
0.52 mils thick	0.17	0.75 (150°F)	0.22
Fused Silica			
25 mils thick	0.10	0.80	0.125
Dow-Corning			
Pyro Mark Standard White	0.21	0.85	0.25
Tempil Corporation			
"B" Series Silicone White	0.23	0.88	0.26
Spec. MSD #171A8256			
ZnO ₂ /K Silicate/Al	0.19	0.94	0.20

A review of the materials shown in Table 2.4.1-6 either have good adhesion at present or there is good evidence that adequate adhesion can be developed. The inorganic coatings have poorer mechanical flexibility than the silicone material, but several of the inorganics may be sufficiently flexible to meet the distortion requirements. Most of the inorganic coatings listed have excellent temperature characteristics in the desired range.

The fused silica coating is expected to have very good radiation damage resistance. The solar absorptance of anodized aluminum increases appreciably with ultraviolet radiation ("Anodized aluminum coating for Temperature Control of Space Vehicle," ASD-TDR-62-918). Radiation test results on the other coatings are listed in Table 2.4.1-7.

TABLE 2.4.1-7. IRRADIATED COATING PROPERTIES

Material	Radiation Dose	Absorptance α_s	Emittance ϵ	α_s/ϵ
Pyromark White	10 ⁸ rad. of 0.9 MEV electrons 2400 hrs. 1 AU ultraviolet	0.22	0.88	0.25
		0.30		
Silicone White	10 ⁸ rad. of 0.8 MEV electrons 2400 hrs. of 1 AU ultraviolet	0.24	0.87	0.28
		0.30		
ZnO ₂ /K Silicate/Al	3100 hrs. ultra-violet at 1 AU intensity	0.21	0.90	0.23
Fused Silica	10 ⁹ rads. of cobalt 60 gamma	No Change Noted		

ZnO₂/K silicate coating for aluminum appears to have the most desirable radiation resistant properties. It is therefore, recommended as the coating to be applied to sun exposed surfaces requiring a low α_s/ϵ characteristic. For design purposes, α_s and ϵ are taken to be 0.3 and 0.8 respectively, until more confidence can be obtained with future tests.

(2) Coatings with High α_s and ϵ_s Characteristics

This coating has the least stringent requirements. In all applications except for the antenna, the only property of interest is the emittance ϵ , which should be 0.9 or above. The coating will require to withstand temperatures between -50 and 250°F , and must be reasonably flexible. Also, it should not deteriorate mechanically with charged particle radiation to 10^6 rads., but any change in optical characteristics due to ionizing radiation damage would be expected to increase both α_s and ϵ .

"B" Series Silicone Black (MSD Specification #171A8256) is one tested paint that satisfies above requirements. Measured properties are:

$$\alpha_s = 0.94 \pm 0.02, \epsilon = 0.92 \pm 0.02.$$

(3) Coating with an Emittance of 0.3

This emittance is required for a majority of the spacecraft's external and internal side panels. The temperature range for these panels will be approximately -100 to 150°F . Ultraviolet radiation will only be received from reflected solar energy, which should be a negligible amount in view of the chosen configuration, and from direct sunlight only during reorientations. The degradation of α_s is therefore of little interest, on the other hand, the stability of ϵ cannot be overlooked.

D4D leafing aluminum pigmented silicone alkyd paint has been selected as the coating revealing a very stable emittance under simulated radiation space environment. A comprehensive test program has been undertaken at MSD to investigate the effects of radiation on D4D paint, among others, for the Nimbus Project. D4D proved to be the most radiation-stable of the thermal coatings tested. Some of the results are presented in Table 2.4.1-8.

TABLE 2.4.1-8. IRRADIATION TEST RESULTS FOR D4D ON ALUMINUM

Radiation Exposure	Dose ergs/gm(1)	α_s	ϵ
None	None	0.26 - 0.27	0.27 - 0.28
UV { 1,000-2,000 Å ^o Lyman: 1216 Å ^o	$10^{14} - 10^{15}$	0.33	0.27
UV: 2,000-4,000 Å ^o	----	0.32 - 0.35	0.27
(2) Protons: 400 KEV	2×10^{13}	0.29	0.27

(1) 100 ergs/gm of absorbed ionizing radiation = 1 rad.

(2) Radiation intensity = 10^7 ergs/cm²-sec

The emittance of D4D paint has been taken as 0.3 ± 0.03 for design purposes, from repeated normal emittance measurements performed with a Beckman DKII, reflectometer and a magnesium oxide integrating sphere.

2.4.2 PLANETARY HORIZONTAL PACKAGE

The temperature limits specified for the Planetary Horizontal Package have been listed in Table 2.4.1-1. Since none of the PHP components will dissipate heat during the

transit phase of the mission, energy must be supplied by other means to maintain internal temperatures at approximately 0°F. In order to keep this need to a minimum, it becomes essential to insulate the entire PHP periphery.

When orbit injection is achieved, the PHP is deployed and its components are activated. At this point, energy dissipated by the equipment must be rejected to space, while maintaining the PHP internal honeycomb surfaces between 100 and 30°F. A breakdown of the component heat dissipation is presented on Table 2.4.2-1.

A completely insulated PHP could not discard its heat in orbit, and remain within desired temperature limits; it is therefore mandatory to be able to increase the emittance characteristics of a portion of the PHP external surface. Up to now, the demands placed on the temperature control design of the PHP are very similar to those already discussed for the orbiter payload components. They radically diverge when one investigates the "in orbit" sink temperature levels corresponding to each PHP external surface. Where, as stated earlier, Orbiter payload radiator surfaces effectively "see" a near perfect black space environment, those on the PHP are not able to do so. The reason lies in the attitude of the PHP with respect to Mars and the Sun, as it orbits the former. A planet oriented vehicle such as the PHP, whose orbit plane is inclined 25° to the ecliptic (Mars 1969), has its periphery exposed to changing solar fluxes. A pictorial representation of the PHP (with two degrees of freedom) is shown in Figure 2.4.2-1.

The configuration which is selected for the PHP is a parallelepiped. This choice is made for the following reasons:

1. A parallelepiped leaves one of its surfaces always occulted from the sun's rays, which is not feasible with a cylinder.
2. The components experiencing the greatest dissipation (i. e. , camera electronics) are black boxes, and can therefore be easily mounted to a parallelepiped surface to obtain maximum thermal conductance.
3. Anticipated active temperature control mechanics are more readily attached to a flat than to a curved surface.

The dimensions of the PHP configuration are largely dependent on component sizes and component viewing requirements. Both cameras and certain scientific instruments must continually face the planet. (See Figure 2.4.2-1.) As mentioned above, emittance control is required to reject energy in orbit. An ideal surface on which to mount thermally controlled louvers of the type indicated for the Orbiter payload, is Side 1 shown in Figure 2.4.2-1. This side is in shadow during the period of maximum heat dissipation or $\pm 90^\circ$ from periapsis. Unfortunately, this side lacks the area necessary to reject the entire heat load generated. To enlarge the configuration would tend to increase weight and offer an inefficient usage of existing volume; therefore additional surface must be sought.

The logical choice for more emittance control is Side 2 which lies opposite 1. The reasons for the selection are:

1. Side 2 experiences a constant incident solar flux $\approx 95 \text{ Btu/hr-ft}^2$ during $\pm 90^\circ$ periapsis travel. Other available sides have a sinusoidal solar flux variation, peaking at 205 Btu/hr-ft^2 .
2. Has negligible planetary and albedo geometric view factors, for $1 \times 19 (10^3 \text{ NM})$ orbit.

TABLE 2.4.2-1. PHP COMPONENT POWER DISSIPATIONS

<u>Component</u>	<u>Maximum Heat Dissipation ~ watts</u>
Image Orthicon Camera (20 M)	2
Image Orthicon Camera (140 M) (3)	2 (each)
Image Orthicon Camera Electronics (4)	25 (each)
Vidicon Camera (3)	0.6 (each)
Vidicon Camera Electronics (3)	25 (each)
VHF Diplexer	--
Infrared Spectrometer	7
Multichannel Radiometer	3
Horizon Scanner	8
VHF Transmitter	5
VHF Receiver (Video and TV) (2)	2.5 (each)
Multicoder	1
Command Decoder	0.3
Power Converter and Control	10
Infrared Flux Detector	3
Polarimeter	5
Far Ultraviolet Radiometer	3
Data Processing Units (7)	1 (each)

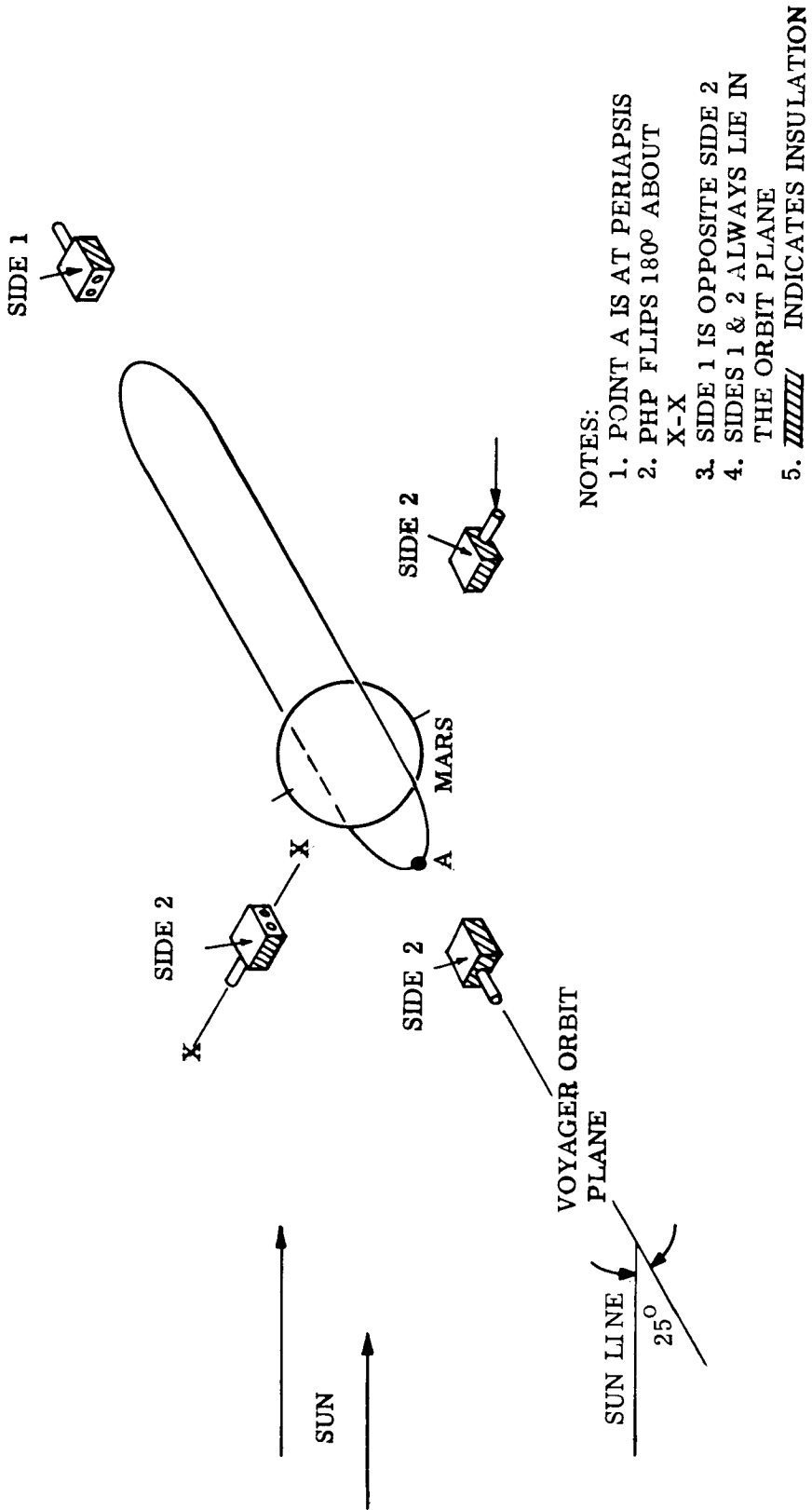


Figure 2.4.2-1. PHP Positions in Mars 1969 Orbit

3. Facilitates component layout within PHP, and maintains structure weights to a minimum.

A. Active Temperature Control Design Studies

The emittance control for Side 1 will be achieved by means of louvers identical to those employed for the Orbiter, which were discussed previously in Section 2.4.1-A.

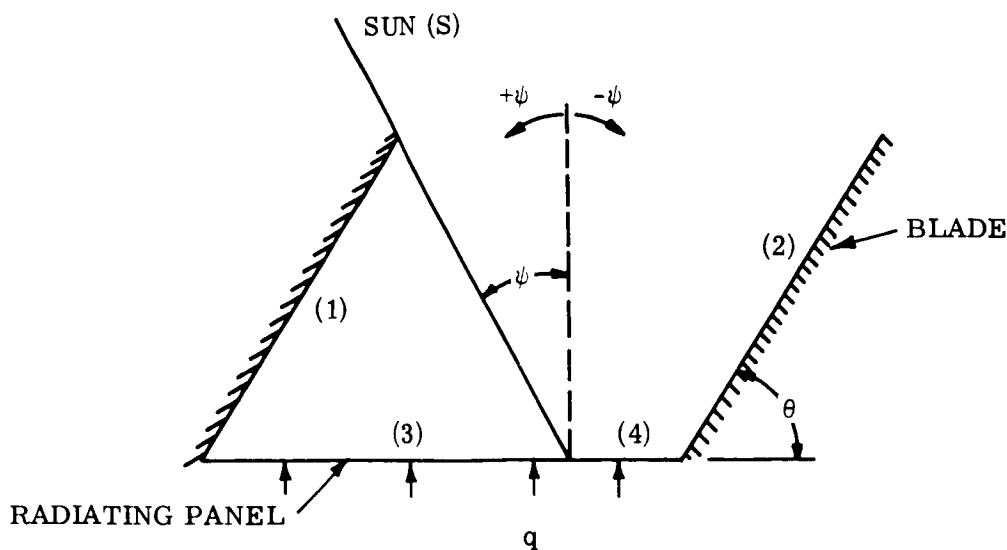
Preliminary studies have been made to assess the effect of incident solar energy on the heat rejection capability of a louver system. This problem presents itself in the allocation of louver surface area on Side 2 of the PHP.

An accurate determination of this heat rejection capability becomes an extremely complex problem to solve in view of the many variables involved and of the inherent difficulties in thermal analyses of systems with specular surfaces. Preliminary work on this subject is summarized below.

(1) Analysis for Diffuse-Diffuse Shutter Blades with Incident Sun

The following assumptions were made in the analysis:

1. Steady state conditions exist
2. Blockage from shutter thickness is neglected
3. Shutter surfaces are adiabatic
4. Diffuse surfaces behave according to Lambert's cosine law
5. Shutter is infinitely long (analyses have shown that this condition is essentially valid when shutter length/width ≥ 5)
6. Shutter width = base radiator width
7. The solar vector has been given only one degree of freedom as shown in the following sketch.



In handling this type of problem, it is necessary to separate thermal interactions due to solar and infrared energies. The radiosity technique is employed.

The solar energy leaving each surface is:

$$J_{S1} = \rho_1 (F_{1(3)} J_{S3} + F_{1(4)} J_{S4} + F_{1(2)} J_{S2}) \quad (1)$$

$$J_{S2} = \rho_2 (F_{2(1)} J_{S1} + F_{2(3)} J_{S3} + F_{2(4)} J_{S4} + S_2) \quad (2)$$

$$J_{S3} = \rho_3 (F_{3(1)} J_{S1} + F_{3(2)} J_{S2}) \quad (3)$$

$$J_{S4} = \rho_4 (F_{4(1)} J_{S1} + F_{4(2)} J_{S2} + S_4) \quad (4)$$

Solving the above equations simultaneously yields:

$$J_{S1} = \frac{a J_{S2} + F_{1(4)} \rho_4 S_4}{b} \quad (5)$$

$$J_{S2} = \frac{b \left[S_2 + (b F_{2(4)} + c F_{1(4)}) \rho_4 S_4 \right]}{bd - ac} \quad (6)$$

where:

$$a = \rho_2 F_{1(3)} F_{3(2)} + \rho_4 F_{1(4)} F_{4(2)} + F_{1(2)}$$

$$b = \frac{1}{\rho_1} - F_{1(3)} F_{3(1)} \rho_3 - F_{1(4)} F_{4(1)} \rho_4$$

$$c = \rho_1 F_{2(4)} F_{4(1)} + F_{2(3)} F_{3(1)} \rho_3 + F_{2(1)}$$

$$d = \frac{1}{\rho_2} - F_{2(4)} F_{4(2)} \rho_4 - F_{2(3)} F_{3(2)} \rho_3$$

By computing J_{S1} and J_{S2} in Equations (5) and (6), J_{S3} and J_{S4} can be calculated using Equations (3) and (4). The incident solar energy can then be calculated.

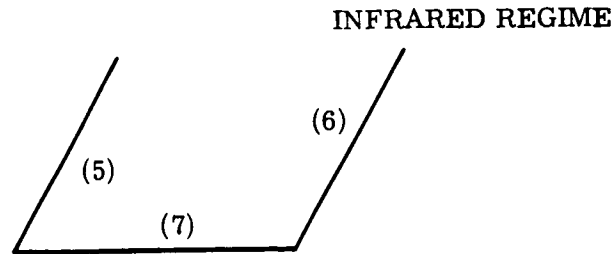
$$G_{S1} = \frac{J_{S1}}{\rho_1} \quad (7)$$

$$G_{S2} = \frac{J_{S2}}{\rho_2} \quad (8)$$

$$G_{S3} = \frac{J_{S3}}{\rho_3} \quad (9)$$

$$G_{S4} = \frac{J_{S4}}{\rho_4} \quad (10)$$

Infrared Regime



In reference to preceding sketch:

Surfaces (1) and (5) are identical

Surfaces (2) and (6) are identical

Surfaces (3) and (4) combined are identical to (7)

The infrared energy leaving each surface is:

$$J_5 = Q_5 + F_{5(7)} J_7 + F_{5(6)} J_6 \quad (11)$$

$$J_6 = Q_6 + F_{6(5)} J_5 + F_{6(7)} J_7 \quad (12)$$

$$J_7 = Q_7 + F_{7(6)} J_6 + F_{7(5)} J_5 \quad (13)$$

$$J_7 = \epsilon_7 B_7 + (1-\epsilon_7) (F_{7(5)} J_5 + F_{7(6)} J_6) \quad (14)$$

where Q is the external heat input to each body.

Solving (11), (12), and (13) simultaneously:

$$J_5 = \frac{Q_5 + F_{5(6)} J_6 + (F_{5(7)} + F_{5(6)} F_{6(7)}) J_7}{1 - F_{5(6)} F_{6(5)}} \quad (15)$$

$$J_6 = \frac{Q_6 + F_{6(5)} J_5 + (F_{6(5)} F_{5(7)} + F_{6(7)}) J_7}{1 - F_{5(6)} F_{6(5)}} \quad (16)$$

$$J_7 = \frac{(1-F_{5(6)} F_{6(5)}) Q_7 + (F_{7(6)} + F_{7(5)} F_{5(6)}) Q_6 + (F_{7(6)} F_{6(5)} F_{7(5)}) Q_5}{1-F_{5(6)} F_{6(5)} - F_{7(6)} (F_{6(5)} F_{5(7)} + F_{6(7)}) - F_{7(5)} (F_{5(6)} F_{6(7)} + F_{7(5)})} \quad (17)$$

The total heat input to each body is:

$$Q_5 = \alpha_1 G_{S1} \quad (18)$$

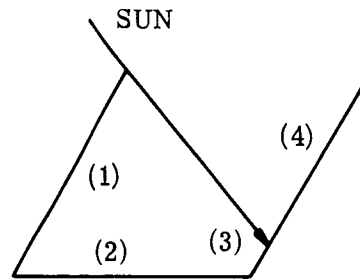
$$Q_6 = \alpha_2 G_{S2} \quad (19)$$

$$Q_7 = q + \frac{A_3}{A_7} (\alpha_3 G_{S3}) + \frac{A_4}{A_7} (\alpha_4 G_{S4}) \quad (20)$$

Having computed all values of J_S , G_S , J , G , and Q , Equations (14) and (20) can be used to find T_7 or q .

Figure 2.4.2-2 shows the variation of heat rejection as a function of solar angle ψ and radiator base temperature T_0 . Results are only developed for the case when the shutters are fully opened.

For high enough solar angles, the base radiator is shadowed from the sun. In this case, the configuration shown in the sketch below should be used for calculating the solar heat inputs.



To calculate the IR radiation interchange, with S_2 set to zero,

$$Q_5 = \alpha_1 G_{S1} \quad (21)$$

$$Q_6 = \frac{A_3}{A_6} (\alpha_3 G_{S3}) + \frac{A_4}{A_6} (\alpha_4 G_{S4}) \quad (22)$$

$$Q_7 = q + \alpha_2 G_{S2} \quad (23)$$

NOTE:

- 1.) S AT MARS = 226 BTU/HR FT²
- 2.) S AT EARTH = 474 BTU/HR FT²
- 3.) SHUTTERS IN FULL OPEN POSITION
- 4.) α FOR ALL SURFACES = 0.25
- 5.) ϵ FOR ALL SURFACES = 0.90
- 6.) RADIATING SURFACE TEMPERATURE, T_o

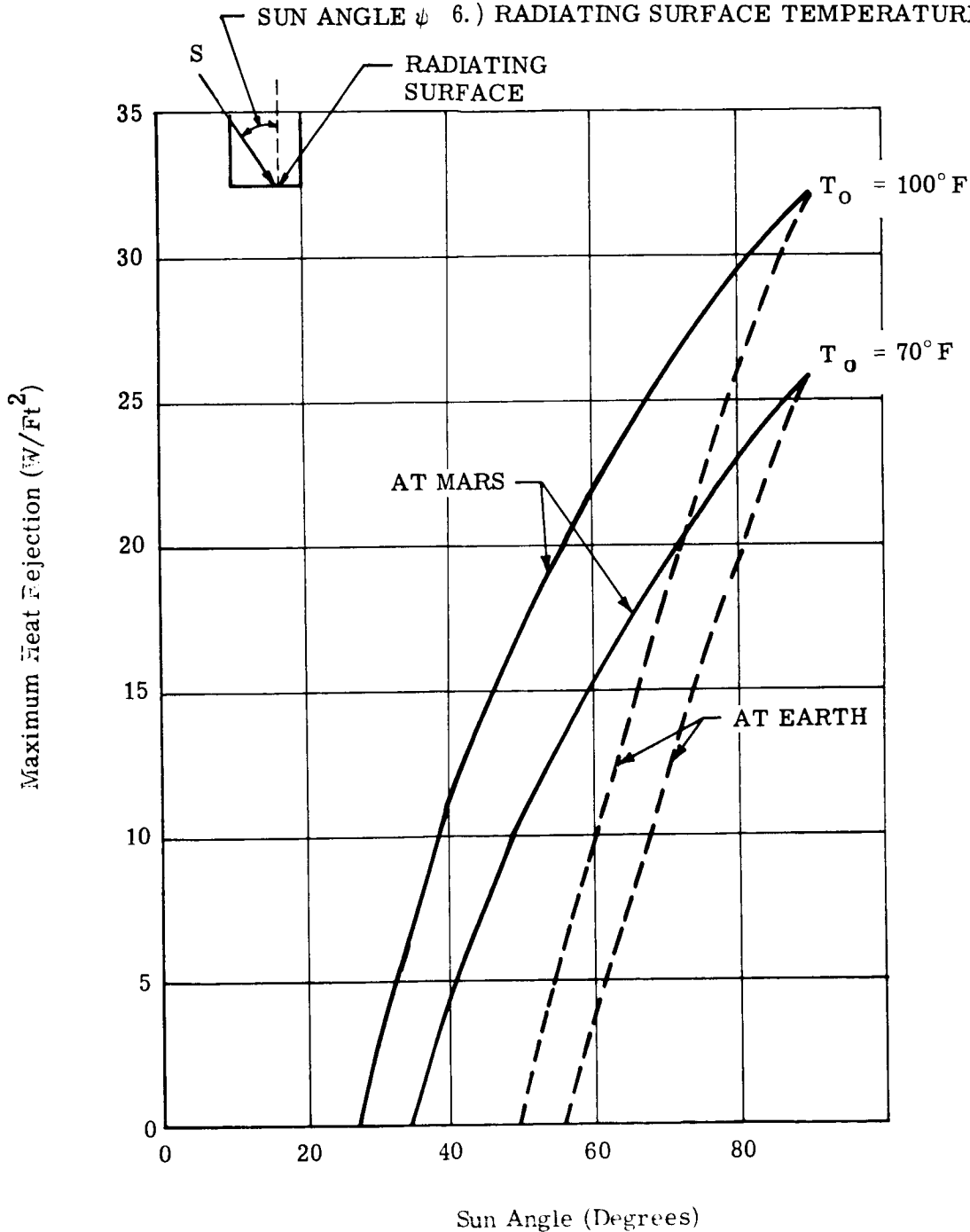


Figure 2.4.2-2. Sun Angle vs Maximum Heat Rejection

Nomenclature:

J = Energy leaving a surface per unit area, or radiosity

G = Energy incident upon a surface per unit area, or irradiance

T = Absolute temperature of a surface

A = Area

ϵ = Emittance

α = Solar absorptance

ρ = $(1 - \alpha)$

Q = External heat input per unit area

q = Component heat dissipation, per unit area of base area

B = Black body emission per unit area

Subscripts

1, 2, 3 etc. - surface identification

s - pertaining to solar regime

non-subscripted energy terms pertain to infrared energy, except for α and ρ .

(2) Analysis for Specular-Diffuse Shutter Blade with Incident Sun

The heat rejection capability of a shutter system was extended to include effects of sun incidence for the case where one side of the blade is specular and the other diffuse. The assumptions given previously still hold for this analysis; one may add that specular surfaces are taken to be perfectly flat.

Since this type of analysis is very lengthy when performed by hand, results will only be obtained for a sun angle $\psi = 65^\circ$. The method of attack employed is that described by Prof. Sparrow (Reference 2). The configuration drawn below led to a higher rejection rate, at corresponding sun angles and base radiator mean temperatures (T_0) than that already calculated for the totally diffuse system. Table 2.4.2-2 compares results obtained to date.

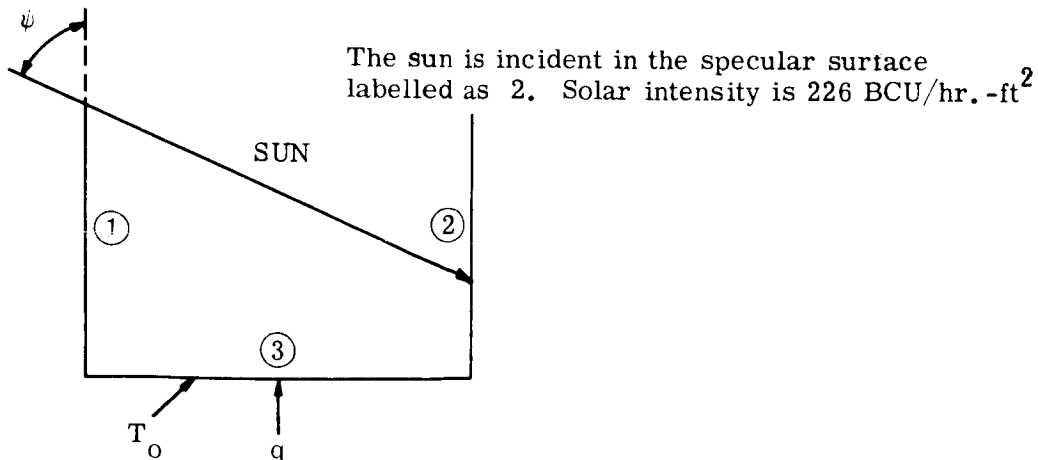


TABLE 2.4.2-2. MAXIMUM HEAT REJECTION RATE
(WATTS/FT² BASE RADIATOR) AT MARS

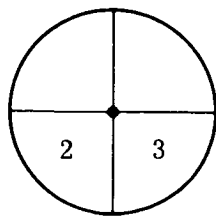
LOUVER OR SHUTTER SURFACE CHARACTERISTICS	SUN ANGLE = 65°		SUN ANGLE = 90°	
	T _o = 70°F	T _o = 100°F	T _o = 70°F	T _o = 100°F
All Surfaces Diffuse	17.3	24.0	26.0	32.2
One Blade Specular; all other surfaces diffuse.	24.1	31.8	30.9	38.4

Further work accomplished to date indicates that even greater heat rejection rates than those listed above can be obtained by making both blade surfaces specular. No definite answer can be given at this time as to which of the above configurations optimizes heat rejection rates. Future analyses will hopefully embrace all possible solar angles incident on a louver system. Up to now, the sun vector has always been assumed in the plane of the paper, and the louver blockage has been taken as zero.

Results seem to indicate that, at a solar angle of 65° in a Mars orbit, reasonable power densities can exist at component base plates, and still maintain base plate mean temperatures between 70 and 80°F. A louver system is therefore selected for Side 2 of the PHP, blade surfaces being specular. The emittance of the fully closed louver system is again chosen as 0.1 for preliminary design purposes. A low α_s/ϵ coating is required for the base radiator area, such as ZNO₂/K₂SiO₃ already discussed in Section 2.4.1(F).

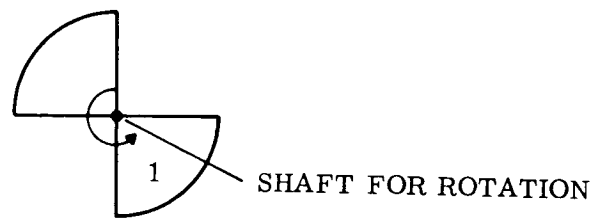
(3) Analysis of Pinwheel Temperature Controller

The pinwheel temperature control device was investigated for use on Side 2 of the PHP before undertaking the above louver studies for a Mars orbit. The pinwheel is connected to a bimetallic coil able to sense radiating panel or component temperatures. Rotation of the wheel is effected as the coil temperature changes in a specified range. A basic pinwheel configuration is shown below:



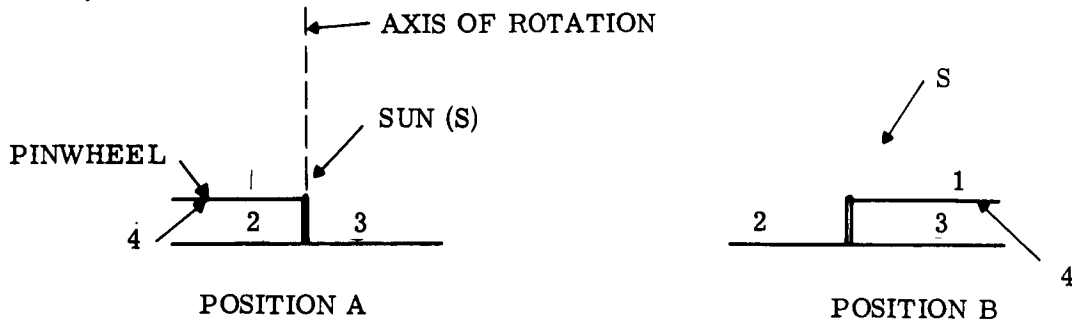
VEHICLE RADIATING SURFACE

(pinwheel shaft through center of disc)



PINWHEEL

The equations below are written to obtain the range of effective α_s and ϵ which are obtainable with this system. The following sketch shows a cross section of half of the total assembly.



The heat absorbed by the assembly for Position A is:

$$Q_{IN(A)} = \frac{1}{2} \alpha_{S_3} S + \frac{\frac{1}{2} F_{(e)24} \alpha_{S_1} S}{F_{(e)24} + \epsilon_1} - \left[\frac{1}{2} \epsilon_3 + \frac{1}{2} \frac{F_{(e)24} \epsilon_1}{F_{(e)24} + \epsilon_1} \right] \sigma T_2^4$$

assuming that $T_1 = T_4$ and $T_2 = T_3$.

Then the effective solar absorptance and infrared emittance of the system in Position A may be written as:

$$\alpha_{S_e(A)} = \frac{1}{2} \left[\alpha_3 + \frac{\alpha_1}{1 + \frac{\epsilon_1}{F_{(e)24}}} \right]$$

$$\epsilon_{e(A)} = \frac{1}{2} \left[\epsilon_3 + \frac{\epsilon_1}{1 + \frac{\epsilon_1}{F_{(e)24}}} \right]$$

where

$$F_{(e)24} = \frac{1}{1/\epsilon_2 + 1/\epsilon_4 - 1}$$

A similar development will yield absorptance and emittance for Position B.

The greatest variation in radiative characteristics which can be obtained by a pinwheel arrangement is found to be:

$$\Delta \alpha = \left(\alpha_{S_e} \right)_A - \left(\alpha_{S_e} \right)_B = \frac{1}{2} \left[\alpha_3 - \alpha_2 + \frac{\alpha_1}{\left(1 + \frac{\epsilon_1}{F_{(e)24}} \right)} - \frac{\alpha_1}{\left(1 + \frac{\epsilon_1}{F_{(e)24}} \right)} \right]$$

$$\Delta \epsilon = \left(\epsilon_e \right)_A - \left(\epsilon_e \right)_B = \frac{1}{2} \left[\epsilon_3 - \epsilon_2 + \frac{\epsilon_1}{\left(1 + \frac{\epsilon_1}{F_{(e)24}} \right)} - \frac{\epsilon_1}{\left(1 + \frac{\epsilon_1}{F_{(e)24}} \right)} \right]$$

From these equations it is apparent that the maximum value of ($\Delta \alpha_S$) is 0.50 and the maximum ($\Delta \epsilon$) is 0.50.

The objective of the pinwheel design for Side 2 of the PHP is to prevent heat leaks during transit (low emittance), and maximize heat loss during orbit dissipation (low solar absorptance and high emittance). The following coatings are therefore chosen for surfaces shown on the preceding sketch.

	α_S	ϵ
Surfaces 1 and 3, $ZnO_2/K_2 S_i O_3$,	$.2 \longrightarrow .3$	$.85 \longrightarrow .90$
Surfaces 2 and 4, electro deposited gold,	$.24 \longrightarrow .3$	$.02 \longrightarrow .04$

In view of the possible range in coating properties, theoretical effective absorptances and emittances of interest are:

$$\text{Max. } \alpha_{S_A} = .15, \text{ Min. } \epsilon_A = .43$$

$$\text{Max. } \alpha_{S_B} = .15, \text{ Min. } \epsilon_B = .02$$

The maximum heat rejection rate for this system is found to be only 60 to 70 percent of that attainable with the diffuse-specular louver system (Sun at 65° inclination) for the case listed on Table 2.4.2-2.

B. Planetary Horizontal Package - Thermal Requirements

The PHP thermal requirements result from analyses conducted for the transit and orbit mission phases.

(1) Transit Phase

The folded PHP has one of its sides sun oriented during transit. This side (3) will eventually point at the planet in orbit, and therefore consists of several apertures for camera lenses and scientific instruments. The total aperture area accounts for approximately 1.7 ft². A large portion of the heat leakage out of the PHP is then experienced through these apertures, as well as through the louver system mounted on Side 2. To counterbalance this leakage, and meet PHP temperature requirements, solar energy will be indirectly absorbed on the sun oriented openings. To accomplish this task, a sun shield is fitted approximately 6 inches from Side 3. This fixed shield is coated with Series Silicone Black Paint on both sides, and can be made of a thin sheet of fiberglass or aluminum. A sun shield will prevent direct solar impingement from creating local hot spots at the apertures, which may damage the equipment.

A heat balance was performed on the PHP during transit to obtain a mean internal temperature. Results are presented on Figure 2.4.2-3. All PHP surfaces except louvers and apertures are covered with a 1/2 inch blanket of insulation, similar to the type employed for the payload components.

Emittance of closed louvers is taken as 0.1. The heat loss from Side 1, which is folded against the Orbiter side wall, has been assumed negligible. Beyond 1.27 AU, the indirect solar energy can no longer maintain the mean PHP temperature above 0°F and additional energy must be supplied by strip heaters. Power requirements in watts are shown on Figure 2.4.2-3.

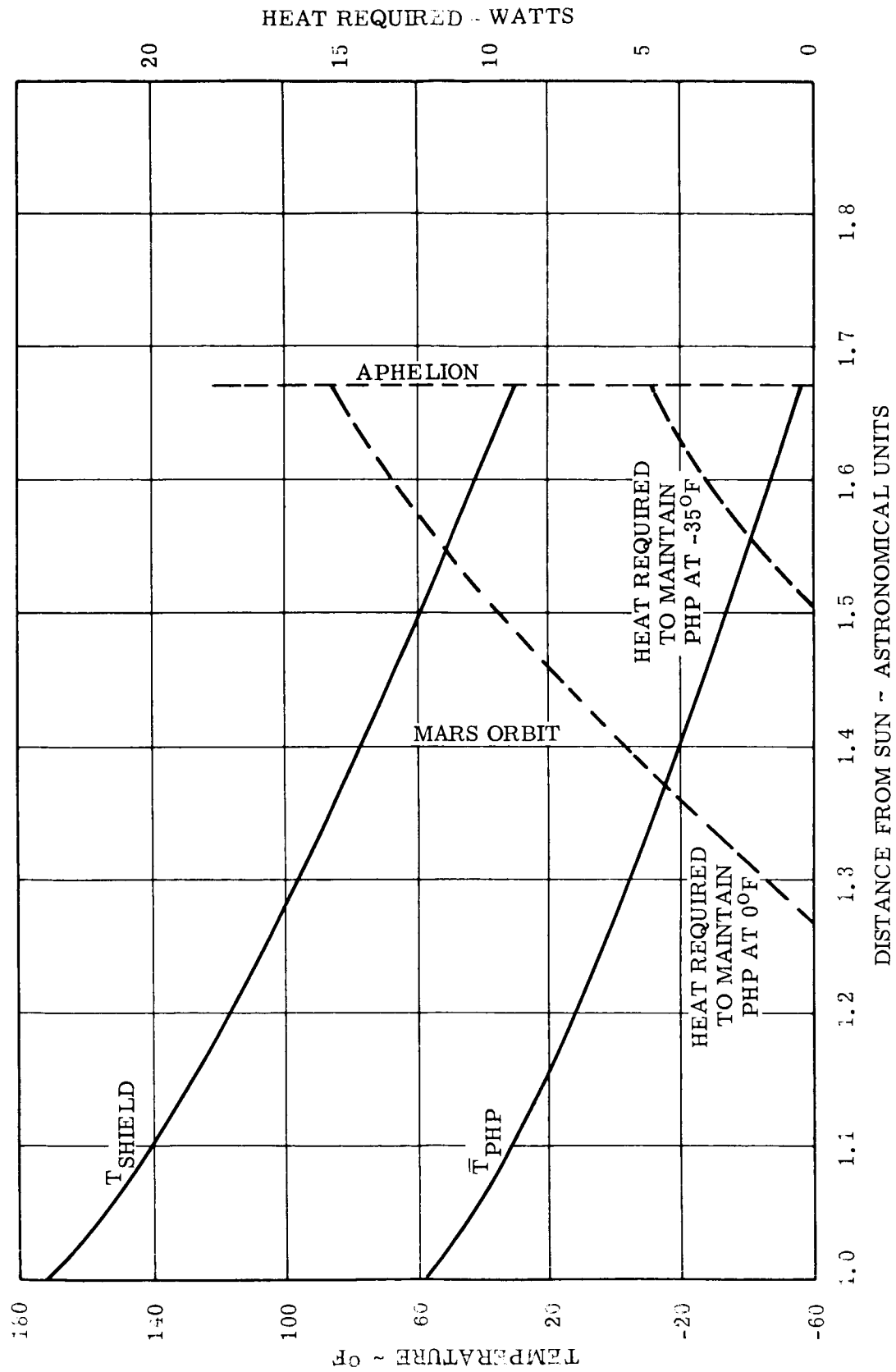
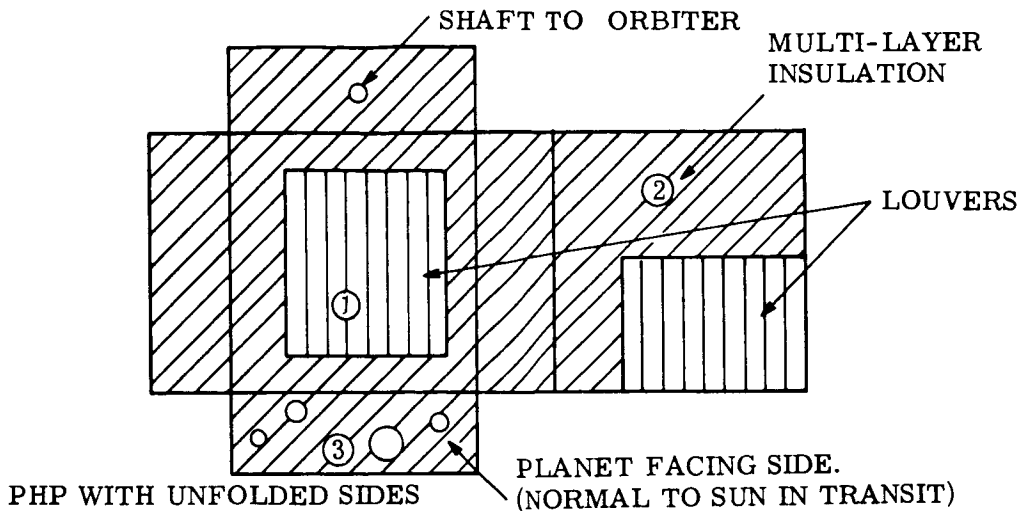


Figure 2.4.2-3. Distance from Sun vs PHP Temperature and Heat Required



Temperature gradients within the PHP will be small since the radiation h_r factor to space is \ll than the internal conductance provided by structural members.

(2) Orbit Phase

Solar and planetary characteristics for a $(1 \times 19) 10^3$ NM orbit around Mars have been stated in Section 2.4.1-A. Geometric view factors from PHP Sides 1 and 2 to Mars are calculated to be negligible thermal inputs; planetary and albedo view factors to Mars from the planet facing side are shown on Figure 2.4.2-4 for $+90^\circ$ from periapsis. The resulting average albedo flux over this two hour period is 4.8 watt/ft^2 and the average planetary flux 1.9 watt/ft^2 . Since the remaining PHP sides are completely insulated, their corresponding planetary and albedo fluxes represent inconsequential effects on the thermal balance of the PHP.

An analysis has been performed with the use of the analog computer to determine mean temperatures of the PHP radiating surfaces, which are: openings for lenses and scientific instruments, portions of Sides 1 and 2 which are actively temperature controlled.

The attitude of the PHP in orbit is shown on Figure 2.4.2-1; the maximum power dissipation is experienced during the two hour travel from -90° to 90° from periapsis (Ref. Table 2.4.2-1). Other assumptions are listed below:

Louver Area, Side 1 = 10 ft^2	W_{c_p} for each node = $12 \text{ Btu/}^\circ\text{F}$
Pinwheel Area, Side 2 = 4 ft^2	Conductance (C) between each node = 3
Aperture Area, Side 3 = 1.7 ft^2	Q_{int} (during $\pm 90^\circ$ from periapsis) = 240 watts
Aperture Emittance = 0.8	
Solar Flux at 25° to the ecliptic	Q_{int} (other times) = 15 watts
A maximum of two (2) vidicons turned "on"	

As pictured on Figure 2.4.2-1, the PHP flips 180° each time it passes by the -97° and $+97^\circ$ positions from periapsis. These reorientations cause Side 1 to be in the sun only during periods of reduced internal dissipation or $+83^\circ$ from the point where the PHP is furthest from the planet. Side 2 then receives incident solar energy only during those periods when Side 1 is in the shadow. A minimum solar load is created on radiating surfaces during maximum dissipation periods.

The active temperature control characteristics chosen in the analysis were:

	<u>Fully Opened</u>		<u>Fully Closed</u>	
	<u>ε</u>	<u>T^oF</u>	<u>ε</u>	<u>T^oF</u>
Louvers	.65	85	.1	65
Pinwheels	.43	85	.13	65

The controller is programmed to respond linearly to temperature changes between 65 and 85°F. The relatively high temperature chosen for the lower limit increases the capability of the PHP to retain energy during the 24 hour period of low heat generation. The coating properties assumed for the pinwheel system have been described in a previous section. Solar absorptance of closed louvers is taken as 0.2 (polished aluminum) for design purposes.

Mean temperatures in orbit of lumped portions of the PHP are shown on Figure 2.4.2-5. The solar input on the closed louvers mounted on Side 1, and the 15 watts internally generated are not sufficient to avoid continuous cooling of the PHP until it reaches the position -90° from periapsis. Specified lower temperature limits are not exceeded during this 24-hour period due to the substantial heat capacity of the PHP.

In view of the encouraging preliminary results which were obtained for the heat rejection capability of louvers exposed to sunlight, louvers will be mounted on Side 2 rather than pinwheels; analyses are of course needed in this area. The higher emittance variation characteristic of louvers means less radiating surface and therefore less leakage when closed than for a pinwheel system. For the dissipations shown on Table 2.4.2-1, Sides 1 and 2 will possess 8.5 and 3.5 square feet of louvers respectively (Ref. para. 2.4.2B (1) louver details are described in Section 2.4.1A. PHP radiating panels will be coated with ZnO₂/K₂SiO₃ paint which exhibits a low α_s/ε ratio.

The location of louvers on Sides 1 and 2 has been integrated with the packaging arrangement of PHP components to insure adequate internal temperature levels during periods of maximum thermal dissipation. All black boxes constituting camera electronics will be intimately attached to the PHP skin; each box requires approximately 180 in² of radiative area composed of base plate and fin. Heat generated within the Vidicon Cameras (0.6 watts) will be conducted to the instrument casing and then radiated internally in the PHP.

For the Image Orthicon Cameras (2 watts) a conduction path will be provided from the generating element to a nearby point on the external skin; when feasible, heat will be radiated from the camera casing directly to an actively temperature-controlled skin section. PHP component casings will generally be painted black to reduce temperature gradients between boxes.

Although only 15 watts were assumed generated in the PHP during the 24 hour periods when the Orbiter is furthest from Mars, there exists the capability to reject more energy. Camera electronics will seldom be turned on, and then only for periods lasting 5 to 10 minutes. Inherent heat capacities will prevent the louvers on Side 1 from opening at this point.

2.4.3 VENUS THERMAL STUDIES

The conditions imposed on the temperature control of spacecraft designed to orbit Venus become notably more severe than those already discussed for the Mars Voyager. Complications in design arise due to the following reasons:

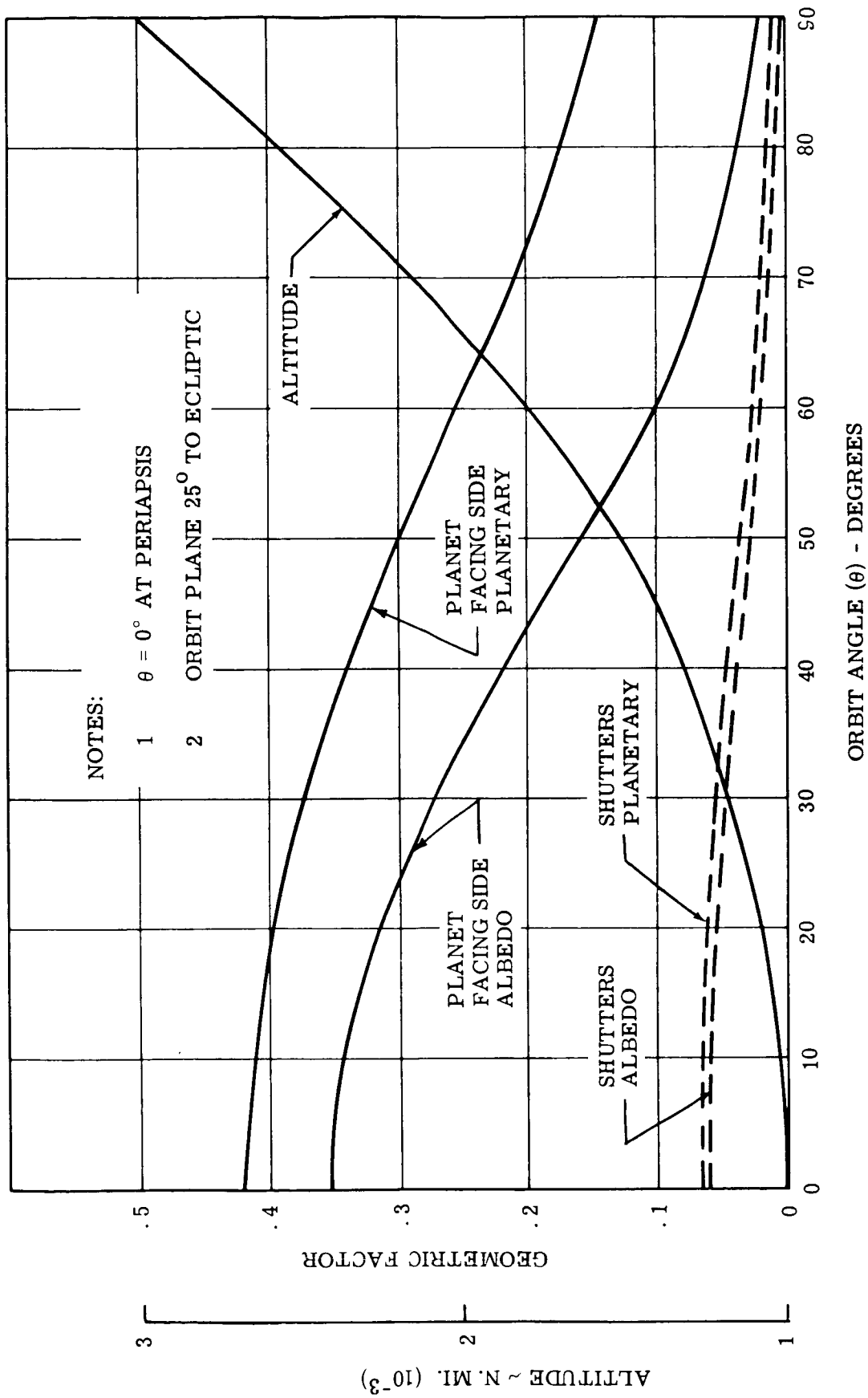
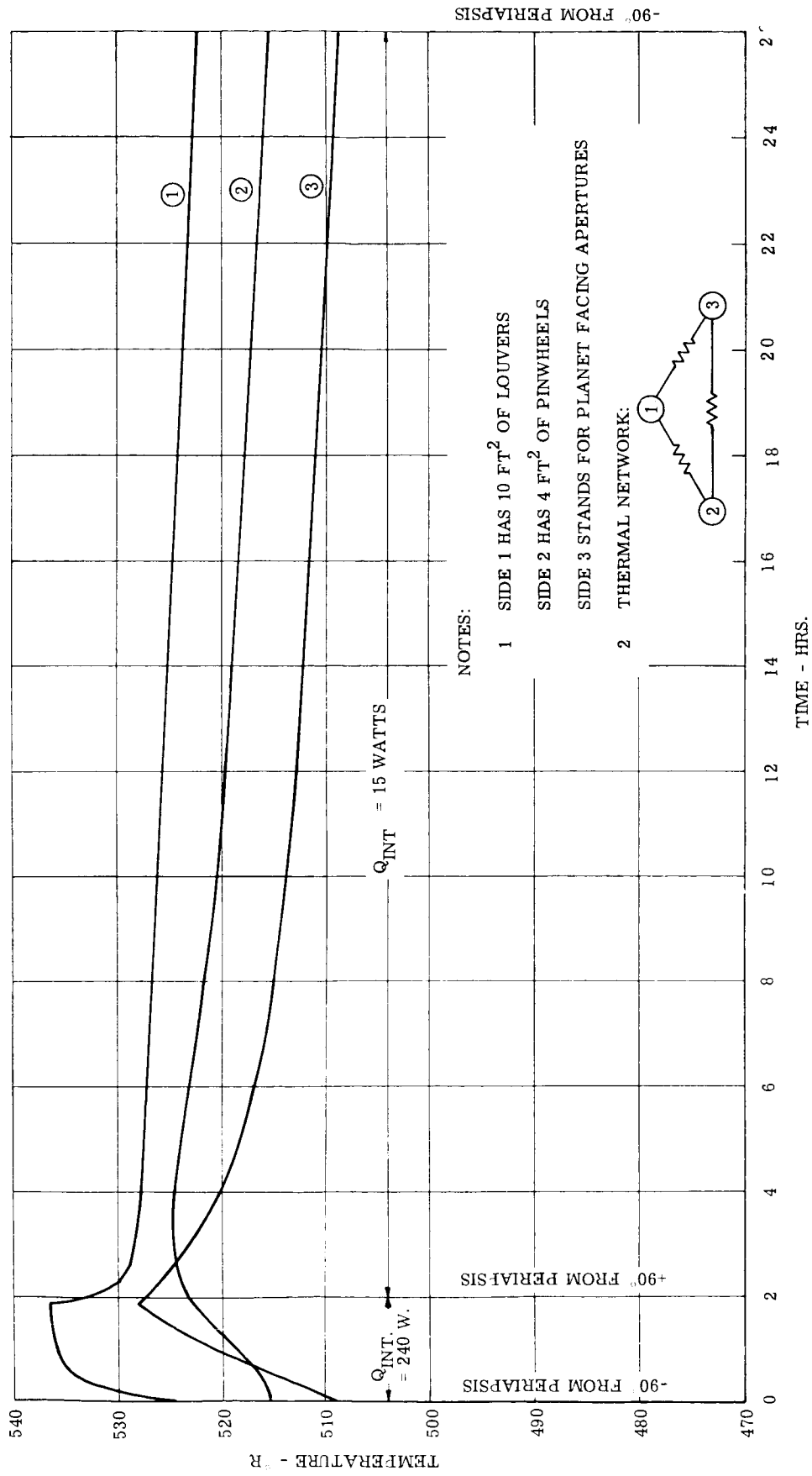


Figure 2.4.2-4. PHP Geometric Factors for Mars $1 \times 19 \times 10^3$ NM Orbit



-90° FROM PERIAPSIS

Figure 2.4.2-5. PHP Temperature History in a Mars 1 x 19 x 10³ NM Orbit

1. The solar intensity at Venus is approximately twice that at Earth.
2. Venus albedo is taken as 0.7; reflected solar energy is therefore more pronounced than at Mars or at Earth for given orbiting altitudes.
3. Prediction of spacecraft orbit inclination to the Venus orbit plane is not ascertainable, since the inclination of the Venus equator to this plane is not known.

The additional ultraviolet radiation, which accompanies an increase in solar intensity, tends to accelerate the deterioration of coating optical properties, which may compromise the temperature control. In orbits of 5000NM radius or less, reflected solar radiation can impose large heat loads on orbiter and PHP component radiating panels. High gain antenna temperature gradients may become severe enough to necessitate a meshed rather than a solid dish to distribute incident solar rays. Finally, the inability to predict an orbit inclination to the Venus orbit plane dictates a PHP thermal design which is flexible enough to meet specified temperature requirements regardless of the spacecraft's orbit attitude with respect to the sun's rays.

Preliminary investigations show that the configuration drawn in Figure 2.4.1-1 may lend itself to a Venus mission from a thermal standpoint. Since solar cells will most likely be covered with a blue-red filter to reduce the amount of solar energy absorbed ($\alpha_s = 0.57$, $\eta_D = 0.85$; refer to Paragraph 2.4.1B), a favorable heat balance can be obtained for attitude control tanks in transit from Earth to Venus. Approximate equilibrium temperature of solar cells mounted as in Figure 2.4.1-1 are:

at 1.0 AU	$T = 147^{\circ}\text{F}$
at 0.72 AU	$T = 255^{\circ}\text{F}$

A constant solar array power output of 6.95 watt/ft² is assumed at both conditions. Slight cell temperature reductions at 0.72 Au are needed to meet tank temperature limits; an emittance greater than 0.3 for Orbiter external surfaces might be sufficient to lower internal wall temperatures of Compartments 2 and 3 (Refer to Figure 2.4.1-8).

The temperature control of a PHP for Venus presents certain difficulties mentioned above. Preliminary thermal studies are discussed below.

A. Passive Temperature Control Analyses for a Venus PHP

With no orbit inclination predictions, it becomes necessary to consider all possible angles in determining the feasibility of a passive temperature control for the PHP. The angle θ has therefore been varied from 0 to 90°, where β is that angle between the Voyager orbit plane and a planet-sun line in a plane normal to the orbit plane.

Several decisions and assumptions were made, which are both valid and logical in view of possible future designs. The PHP has three degrees of freedom, is in a 1000 NM circular orbit, and has the shape of a rectangular parallelepiped. This configuration is arrived at from the standpoints of weight, electronic packaging and thermal control. (See Figure 2.4.3-1)

Since one of the sides always faces the planet and the velocity vector is normal to another side, thus defining the orientation, the Orbit Heat Flux Digital Computer Program as used at GE could be utilized. The output from this program listed the incident solar, albedo and planetary emission fluxes incident on each of the PHP sides for the several β angles chosen. Only the average values over each orbit were used in the analysis because of the relatively short orbit time (assumed 2 hours or less). The average fluxes and the constants for the orbits are listed in Table 2.4.3-1.

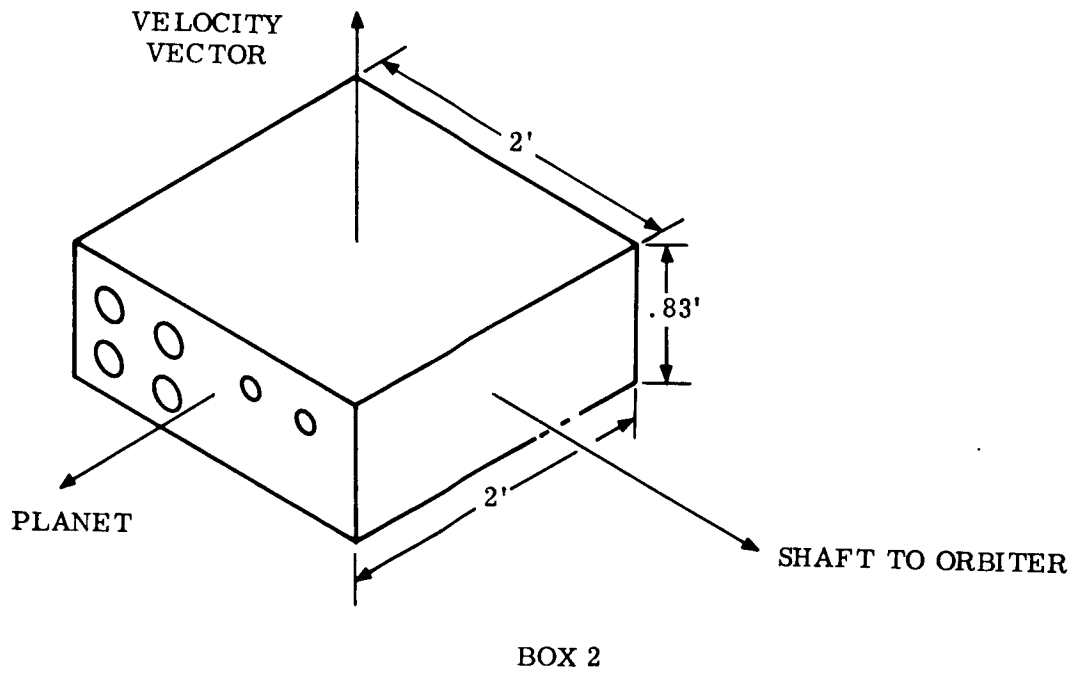
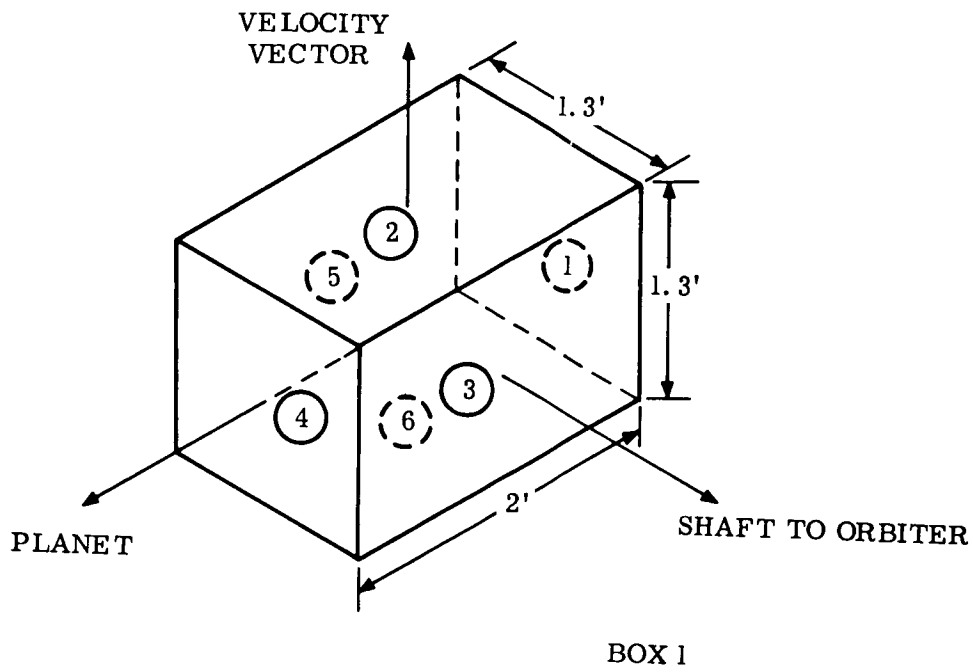


Figure 2.4.3-1. Venus PHP Configurations Chosen for Passive Temperature Control Analysis

TABLE 2.4.3-1. CONSTANTS AND FLUXES FOR VENUS PHP

Side	Average Incident Solar and Albedo Fluxes (Btu/hr-ft ²)					Average Planetary Flux (Btu/hr-ft ²)	
	$\beta = 0^\circ$	$\beta = 36^\circ$	$\beta = 45^\circ$	$\beta = 54^\circ$	$\beta = 90^\circ$	$\beta = 0^\circ$	$\beta = 90^\circ$
1	272	220	195	160	4	0	
2	243	214	195	174	4	10	
3	23	413	633	705	855	10	
4	172	172	195	225	4	44	
5	23	19	18	14	0	10	
6	243	214	195	174	4	10	

Solar = 850 Btu/hr-ft²

Albedo Factor = 0.7

Planetary Thermal Emission = 50.3 Btu/hr-ft²

Component Heat Dissipation = 30 watts

An analog circuit was designed which considered each side of the PHP as a lump-mass node, and which represented the components and instruments as one central node. The circuit used is shown in Figure 2.4.3-2.

With passive temperature control as an objective, a high and then a low emittance value were successively assigned to each of the PHP sides. The many combinations of emittances were analyzed by varying one side's emittance while keeping the others constant.

The central node is influenced by radiation and conduction from the sides. Both the radiation and conduction assumed values were included as an effective conductance in the analog analysis. Several realistic values of this conductance were chosen and are listed in Table 2.4.3-2 together with the emittances and the solar absorptances of the sides. The conductances were varied in the same manner as the emittances.

TABLE 2.4.3-2. PASSIVE PHP PARAMETER VALUES

Side	Conductances to Center Btu/Hr-F ⁰	Maximum Emittance	Minimum Emittance	Max. Solar Absorptance	Min. Solar Absorptance
1	(0.2)(1.0)(4.0)	.8	.2	.55	.33
2	(0.2)(1.0)(4.0)	.8	.2	.55	.33
3	(0.2)(1.0)(4.0)	.85	.85	.55	.3
4	(0.2)(1.0)(4.0)	.8	.2	.55	.33
5	(0.2)(1.0)(4.0)	.85	.85	.55	.3
6	(0.2)(1.0)(4.0)	.8	.2	.55	.33

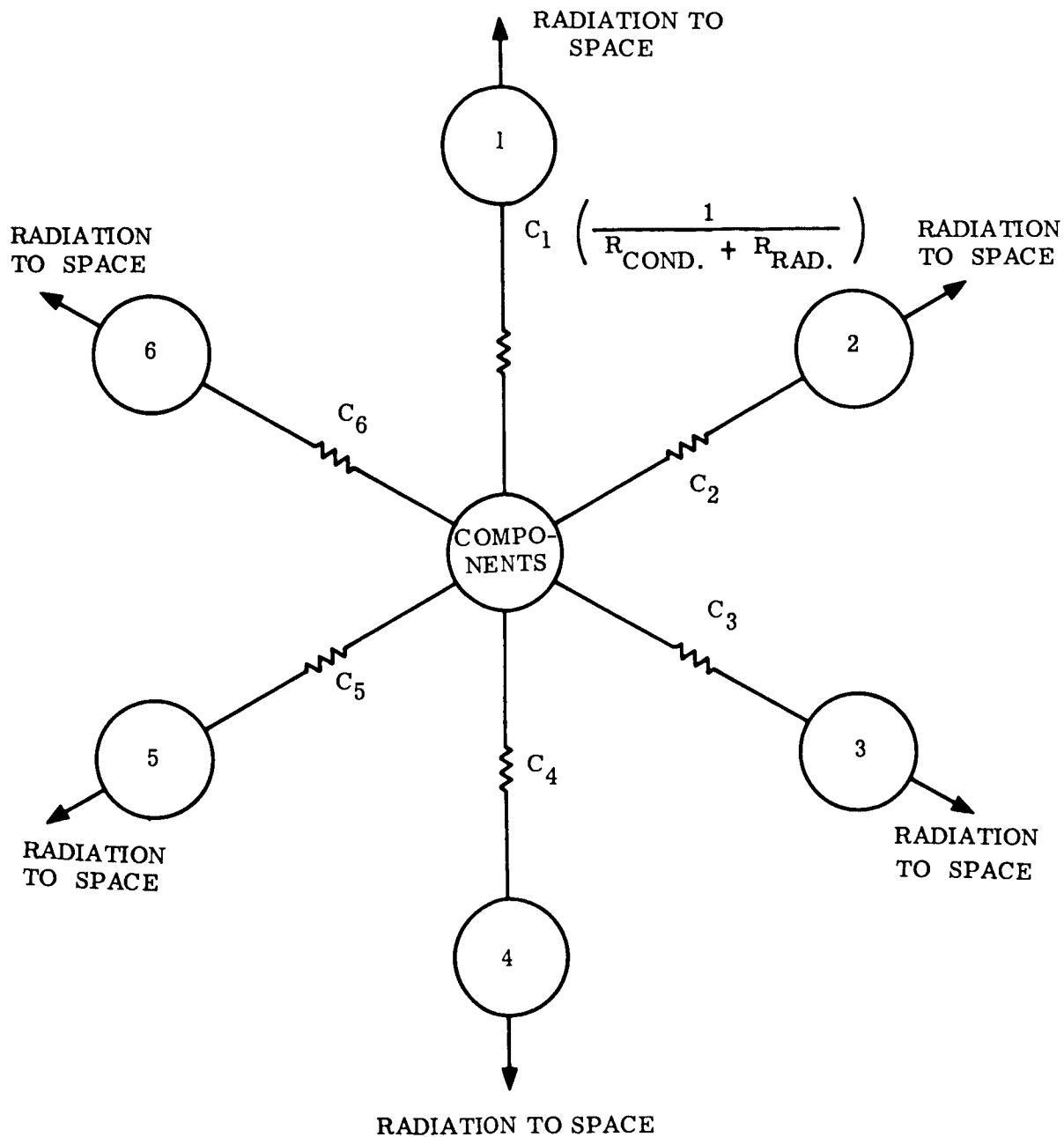


Figure 2.4.3-2. Venus PHP Analog Circuit for Passive Temperature Control Studies

The first orbit considered had a β angle of 90° during which the PHP lies continuously in the sunlight. Box 1 (shown in Figure 2. 4. 3-1) was chosen as the configuration. All possible combinations of listed emittances and conductances were analyzed.

The primary interest is in maintaining the central node between the temperature limits of 30° to 100°F . Due to this fact, all combinations which did not satisfy these limits were eliminated from further analysis. Trials at $\beta = 90^\circ$ considerably reduced the number of cases to be analyzed for the following orbit condition which was a β angle of 0° . This orbit angle has the maximum shadow time for a 1000 NM orbit. For this orbit, solar absorptances were also varied between min and max values. Applying the same temperature limits listed above, the number of remaining combinations were reduced further.

This procedure was followed for the other β angles listed until either parametric combinations or β angles were exhausted. Results for Box 1 showed that no parametric combination could satisfy the temperature limits for all β angles.

The above procedure was followed for a PHP in the shape of Box 2 of Figure 2. 4. 3-2. Studies again indicated that a passive temperature control technique could not maintain the electronic packages within the specified temperature limits. Presentation of numerical results is cumbersome, and has therefore been omitted.

A PHP active temperature control design therefore becomes mandatory in view of the above analysis. Preliminary work accomplished with the analogue computer indicated the following requirements for the PHP configuration:

1. All sides insulated except 2 and 6 (see Figure 2. 4. 3-2).
2. Distance between Sides 2 and 6 must be kept small (≈ 12 inches) to allow component heat to be totally rejected from either of these sides, and thus keep the conduction paths weight penalties to a minimum.
3. Cover surfaces 2 and 6 with a system of louvers able to alter effective emittances.
4. Since simultaneous solar incidence on Sides 2 and 6 is impossible in view of chosen assumptions, at least one of the louver system will be occulted from the sun at any given position in orbit. The other system will then be exposed to solar rays. With the built-in capability of total heat rejection from either of the two sides covered with louvers, the side in the sun will have its louvers fully closed, the other partially or fully opened. In this manner the solar load on the PHP will be reduced appreciably, and component temperature limits can be met.

Actuation of louvers can be accomplished by designing two opposed-action bimetallic sensing elements: one, exposed to external fluxes but insulated from the interior of the PHP; the other well insulated from the external thermal environment but able to sense internal temperatures. By proper adjustment of the opposing motions of the elements, those louvers exposed to solar and albedo fluxes will have a tendency to close as the fluxes increase, with component dissipation being rejected from the shadowed side. (For bimetallic element design see Paragraph 2. 4. 1. A.)

The conclusions reached from the analysis of the Venus PHP indicate that considerable work remains to be done on the analysis and design of a Venus Thermal Control Subsystem. The analysis completed specifies a concept by which thermal control of a Venus PHP could be controlled. Further work is definitely required.

2.4.4 REFERENCES, THERMAL CONTROL

1. "Orbiting Geophysical Observatory Temperature Control System Design" by J. E. Vehrencamp, presented at A. S. M. E. - A. I. Ch. E. Heat Transfer Conf. in Boston, Mass., August 1963
2. "An Enclosure Theory for Radiative Exchange Between Specularly and Diffusely Reflecting Surfaces" by E. M. Sparrow, E. Eckert and V. Jonsson ASME Paper 61-WA-167

2.5. STRUCTURAL & DYNAMIC CRITERIA OF ORBITER

This section presents the structural and dynamic criteria considered for the Voyager Orbiter system. An analysis is shown for the Solar Cell Mounting Panel which is indicative of the complete analysis. The total analysis performed substantiates the structural weight figures used throughout this report and is available in PIR 9731-329-089. The analysis covers the main structural components only and is performed in a conservative vein to further add confidence to the feasibility of design. Material allowables have been used which are well substantiated by aircraft practice (i. e. , MIL-HDBK-5) and state-of-the-art analytical methods. Minimum margins of safety selected as design parameters are also in keeping with general aircraft practices.

2.5.1 STRUCTURAL DESCRIPTION (Reference Figures 2.5-1 and 2.5-2)

A. General

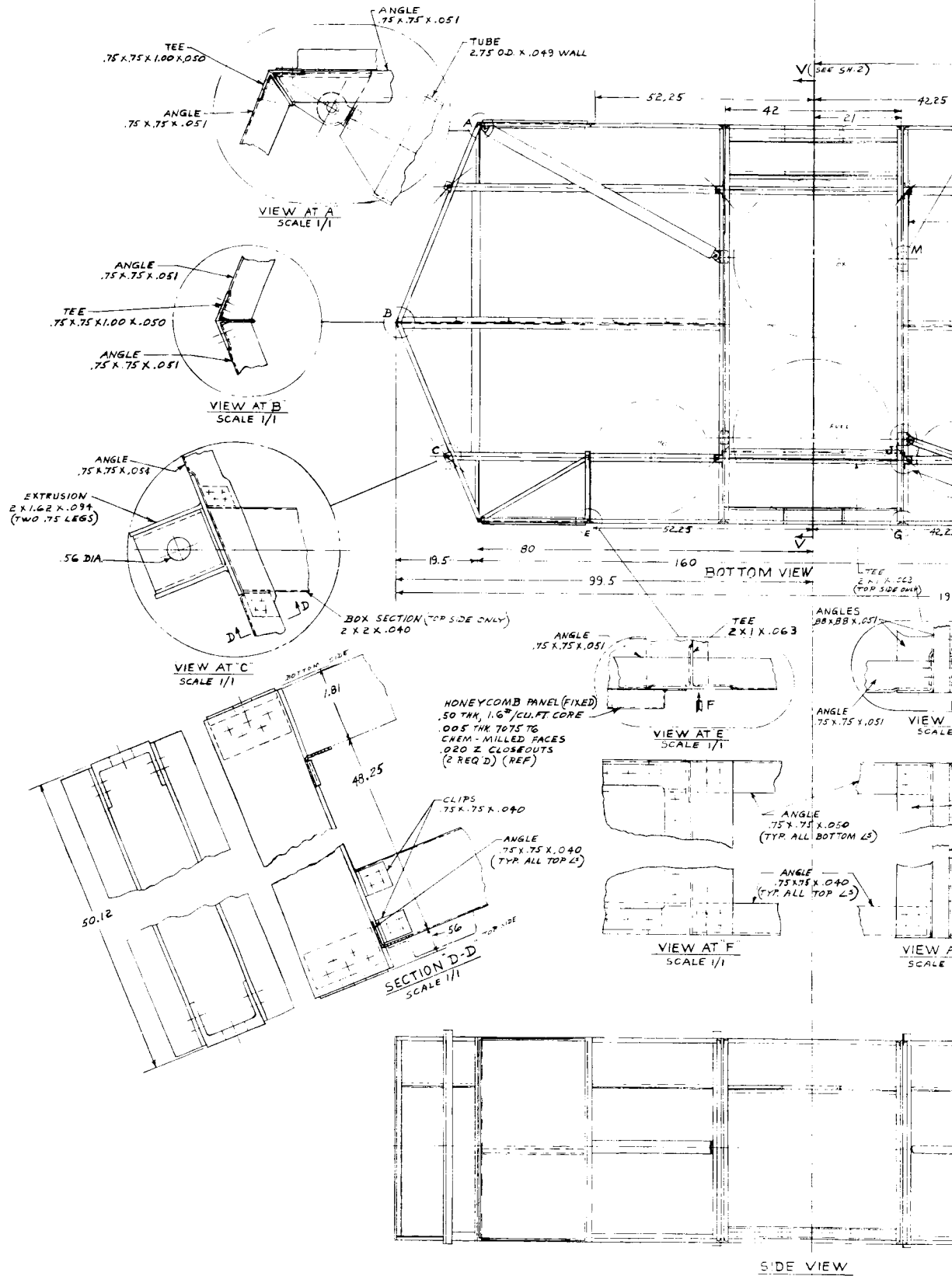
The Orbiter structure supports the entry vehicles during boost and transit in addition to the propulsion system and the orbiting equipment.

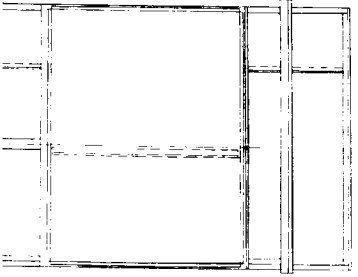
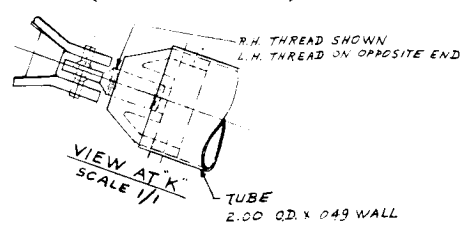
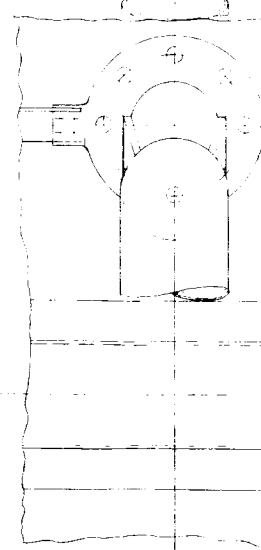
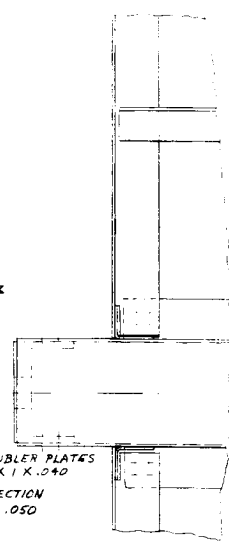
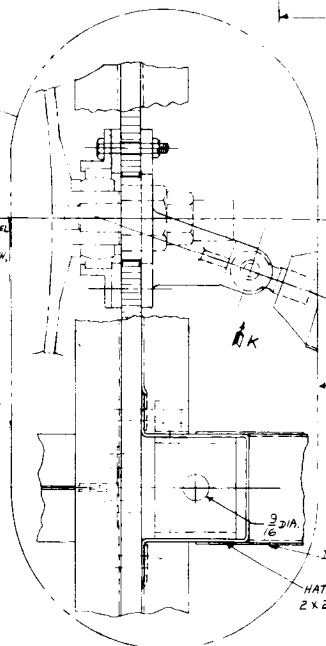
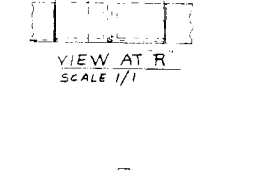
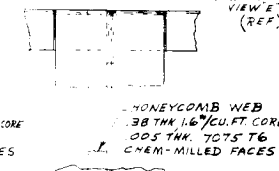
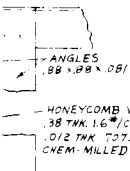
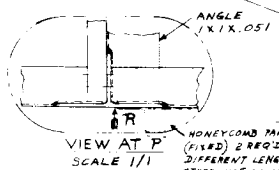
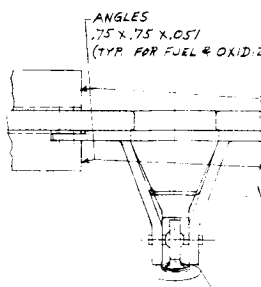
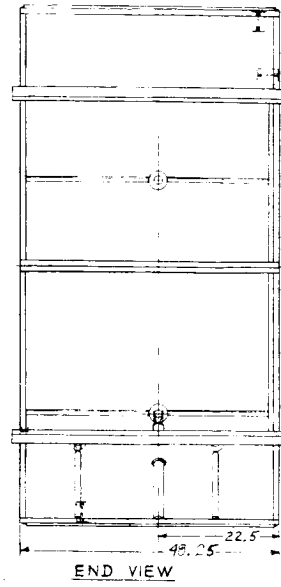
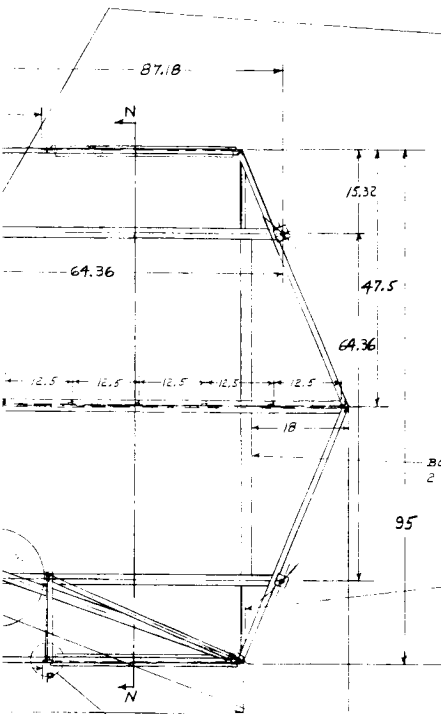
Since the Voyager vehicle is designed for a variety of missions, the overall design philosophy adhered to in the Orbiter development was that of adaptability of design to other missions. Another concept which influenced the design to a large extent was that of allowing the jettisonable booster adapter to provide as much of the structure necessary for distributing loads to the booster as possible. As a result, the Orbiter is supported at a minimum of 8 points at the lower periphery, with a capability of being supported at 14 points.

The Orbiter structure is of semimonocoque construction, with loads introduced along sheet stiffened longerons. The choice of semimonocoque construction was dictated by efficiently designing for the expected vibration environment, which by and large is the limiting condition. This is discussed fully in Section 2.5.3. Additionally, this type of construction enhances thermal control and affords greater flexibility for packaging efficiency. The structure does not have the familiar appearance of the sheet-stiffener shell. This was because simplicity, and hence, reliability was stressed in all phases of design, manufacturing and performance.

The goal of simplicity in design was achieved by the use of simple tension-compression members and avoiding complex load paths wherever possible. Also, elastic shear buckling and diagonal tension was eliminated as a failure mode. This latter condition was deemed necessary in view of the non-linear deformations which would result under dynamic loads. As a result, all primary shear webs are honeycomb panels designed to be shear stable.

Simplicity in manufacturing (where no significant weight savings can be obtained) led to the use of flat (rather than curved) panels, the use of familiar aircraft materials, fabricating techniques, fasteners and fastening techniques. The structure appears as a box; however, it should be pointed out that structurally speaking, the Orbiter structure is a network of deep beams capable of reacting both vertical and side loads plus overturning moments. The configuration was not designed for volumetric efficiency, but rather for a low silhouette and minimum contour dimensions which would still allow two Landers to be supported side by side.





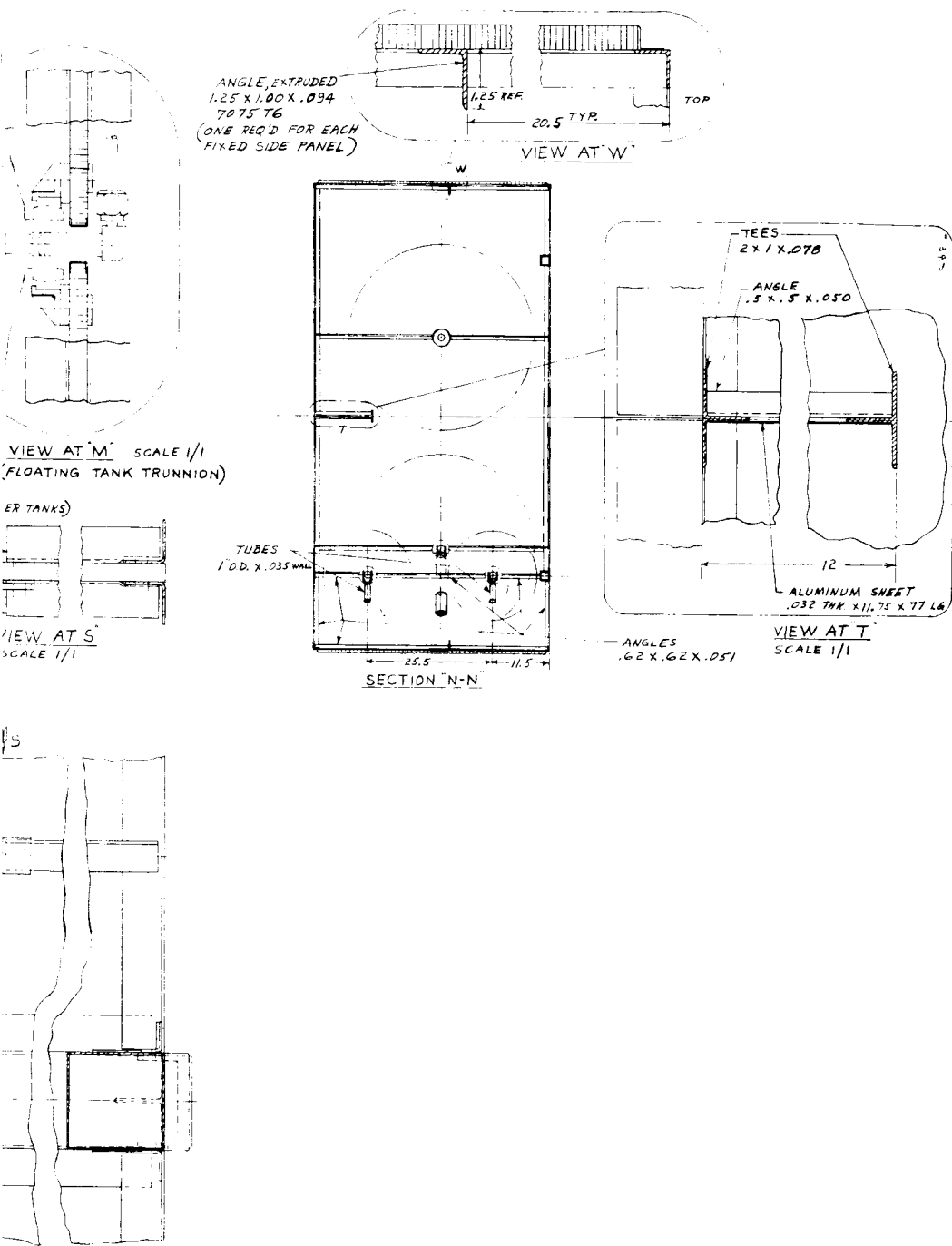
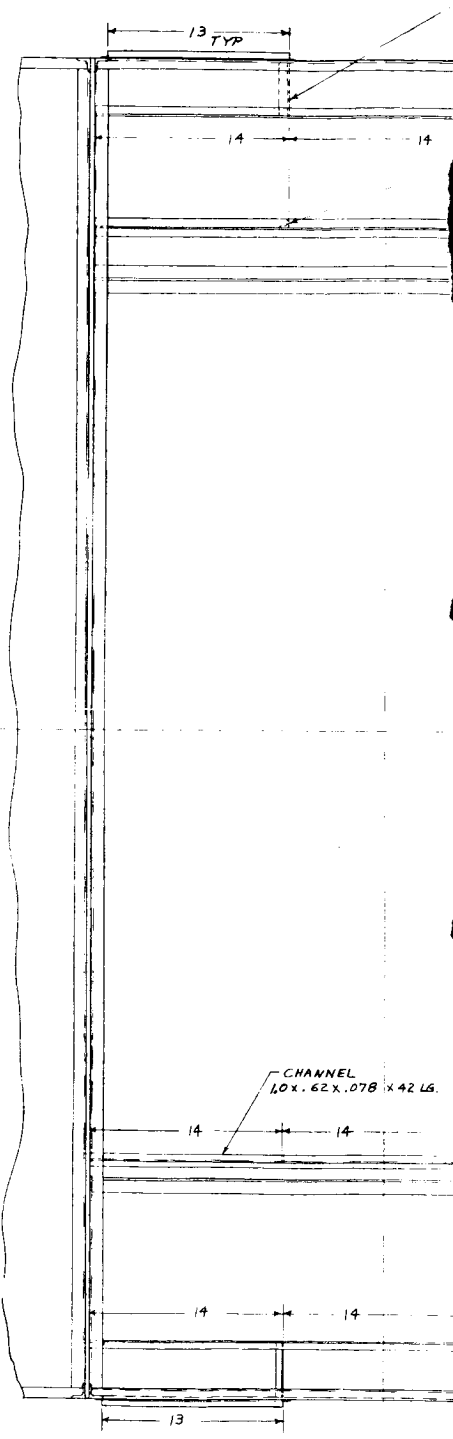


Figure 2.5-1. Voyager - Mars 1969 Orbiter Structure, F-14 Tank Mtg. (1 of 3)



VIEW AT W
SCALE 1/4

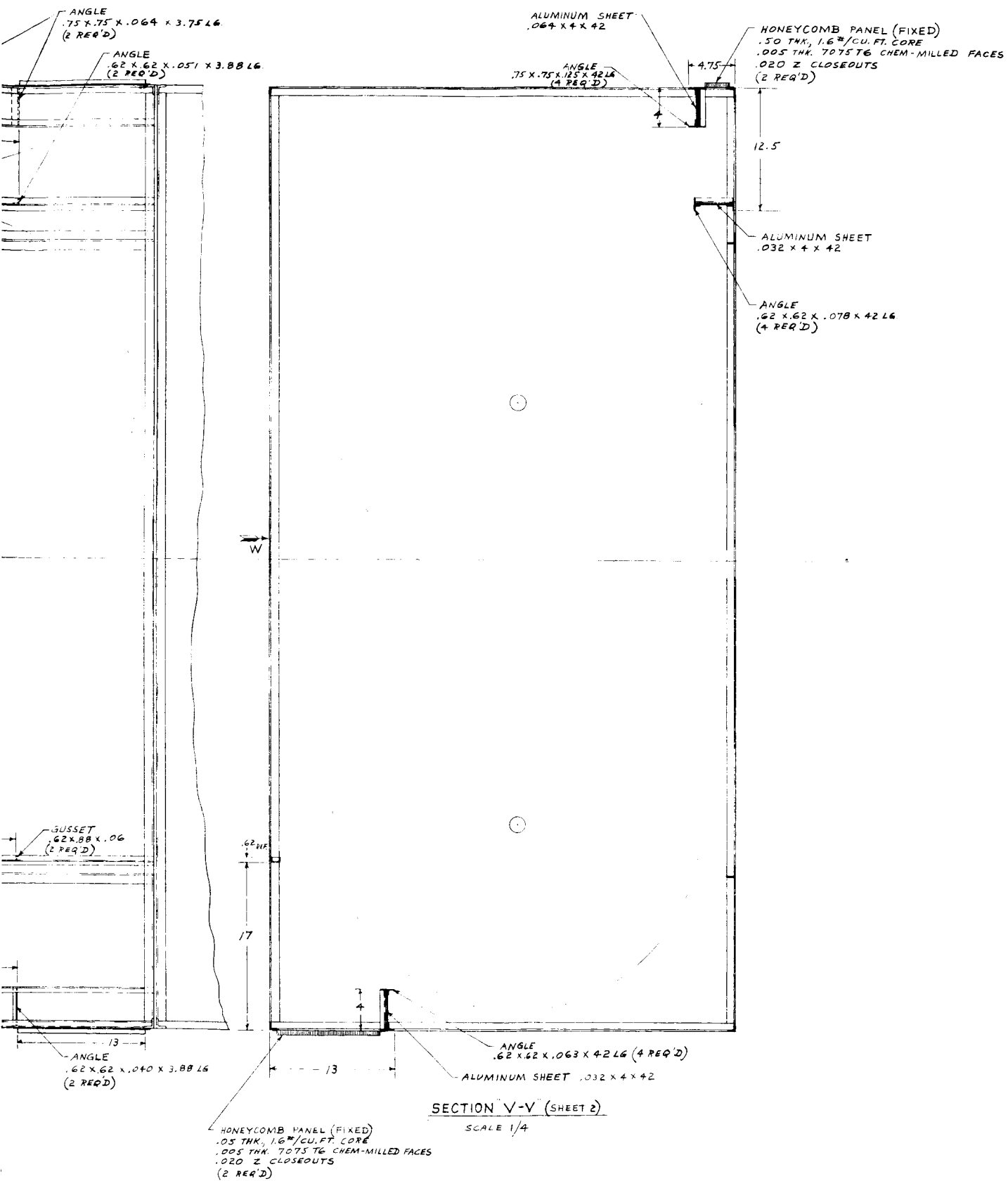
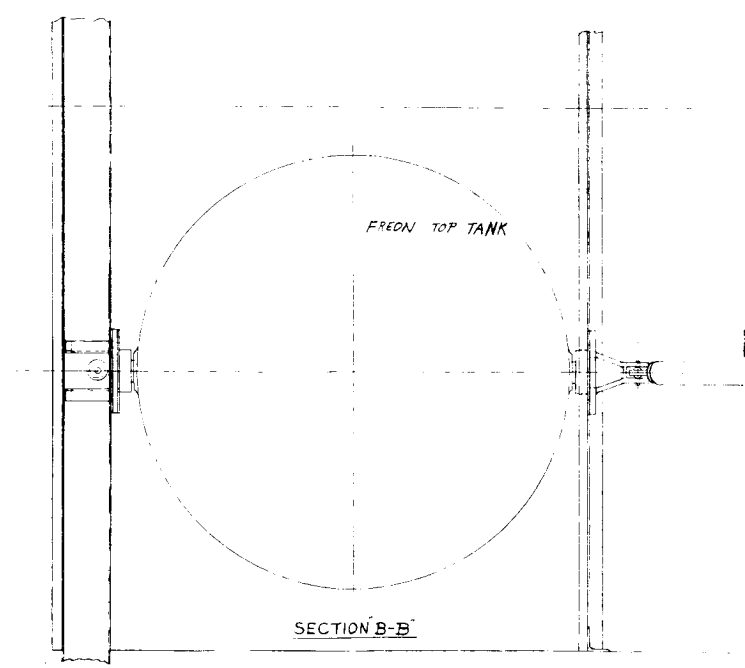
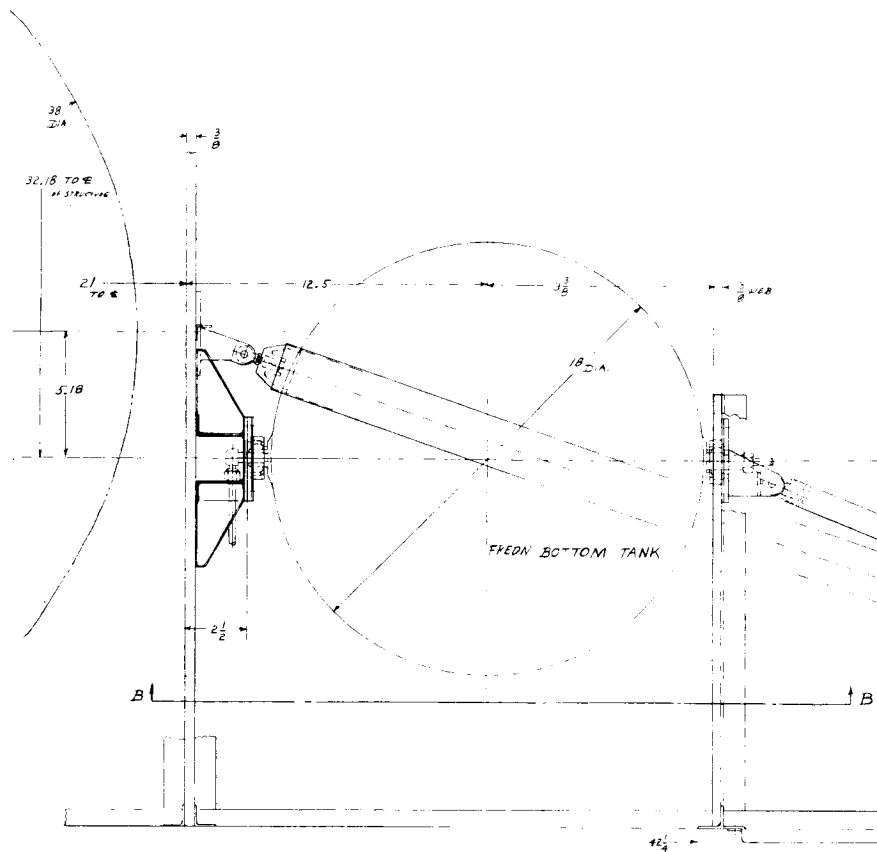
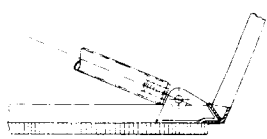
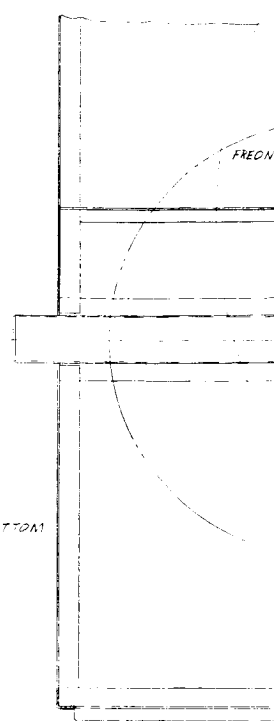
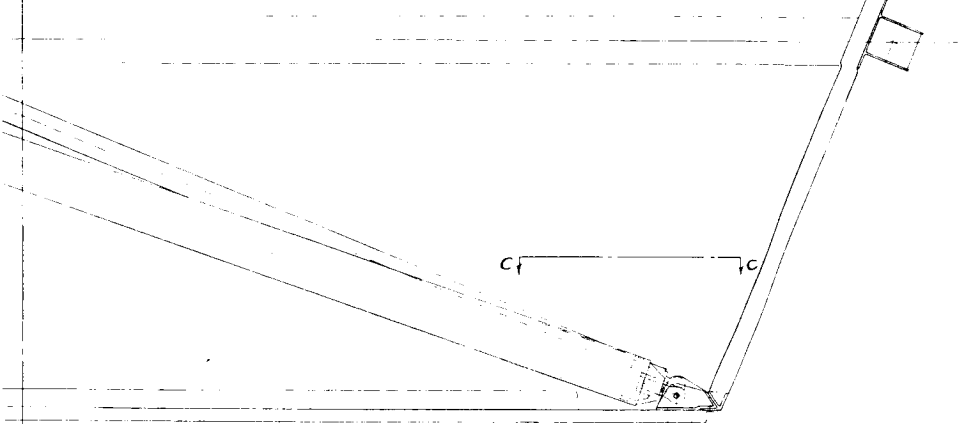
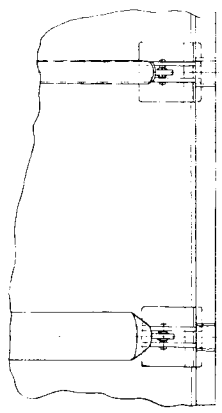


Figure 2.5-1. Voyager - Mars 1969 Orbiter Structure, F-14 Tank Mtg. (2 of 3)



A
A



SECTION D-D



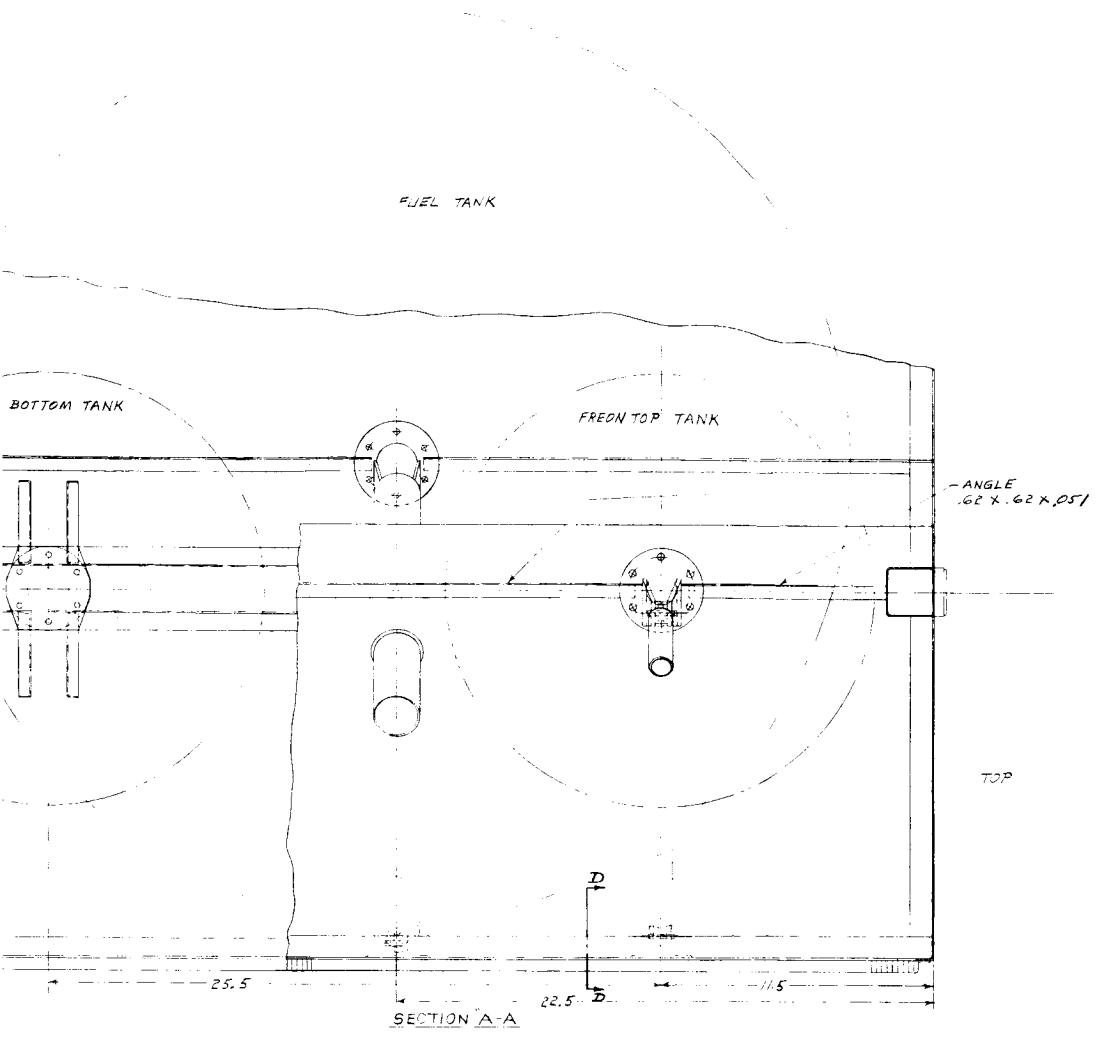
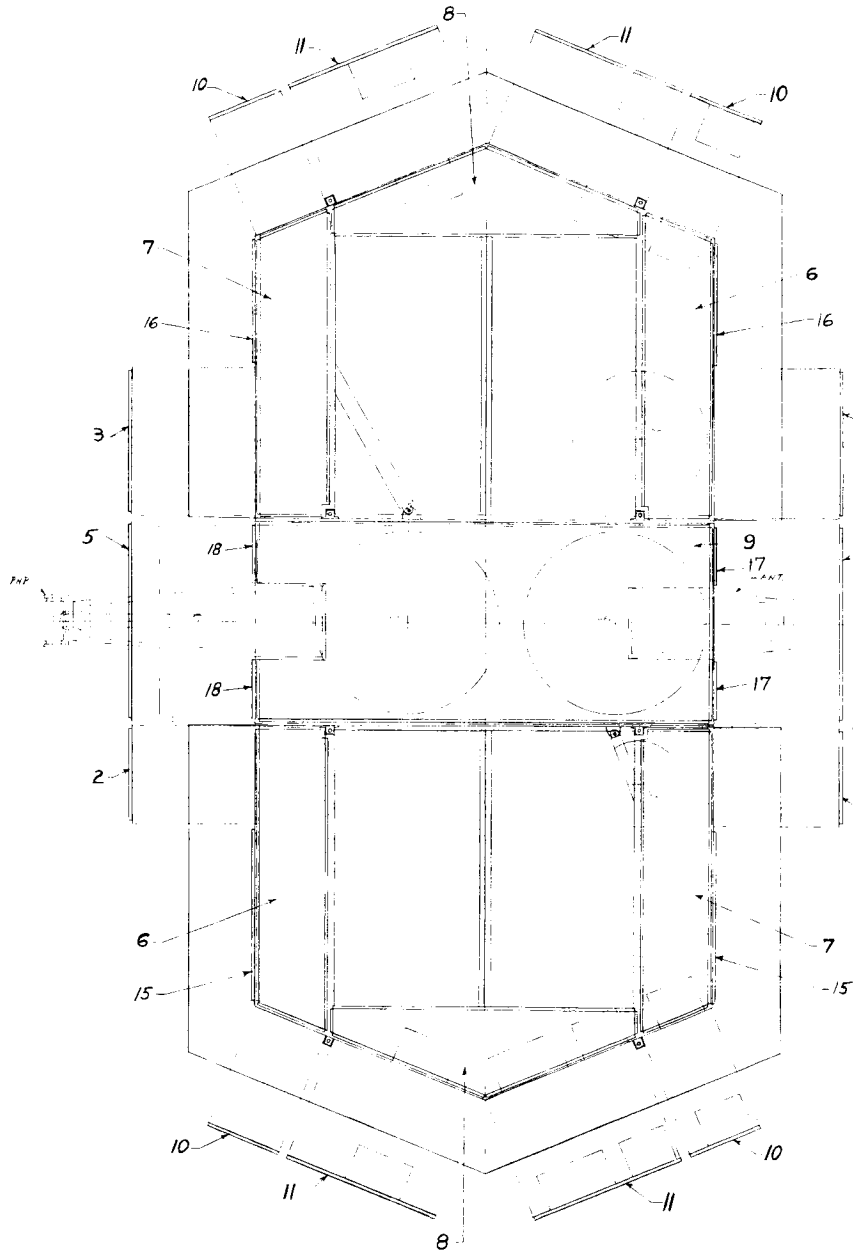
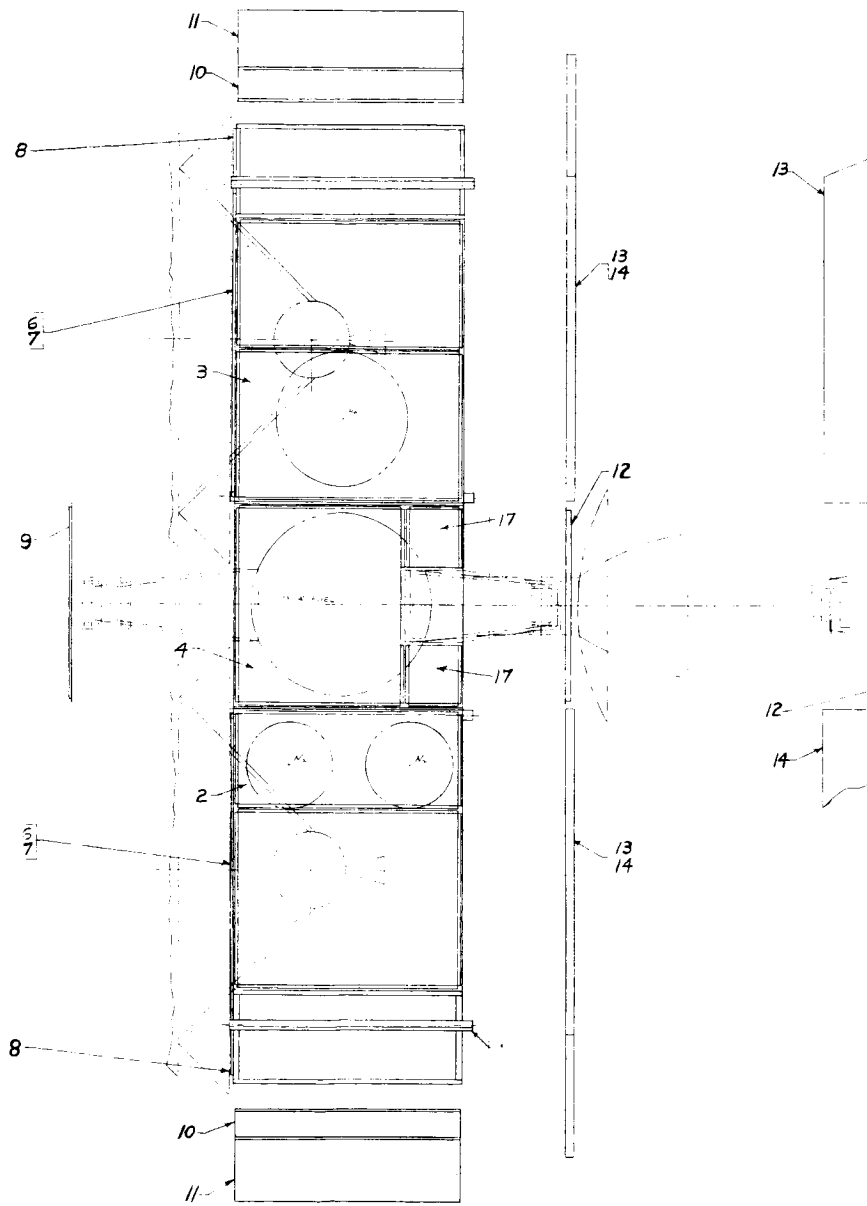


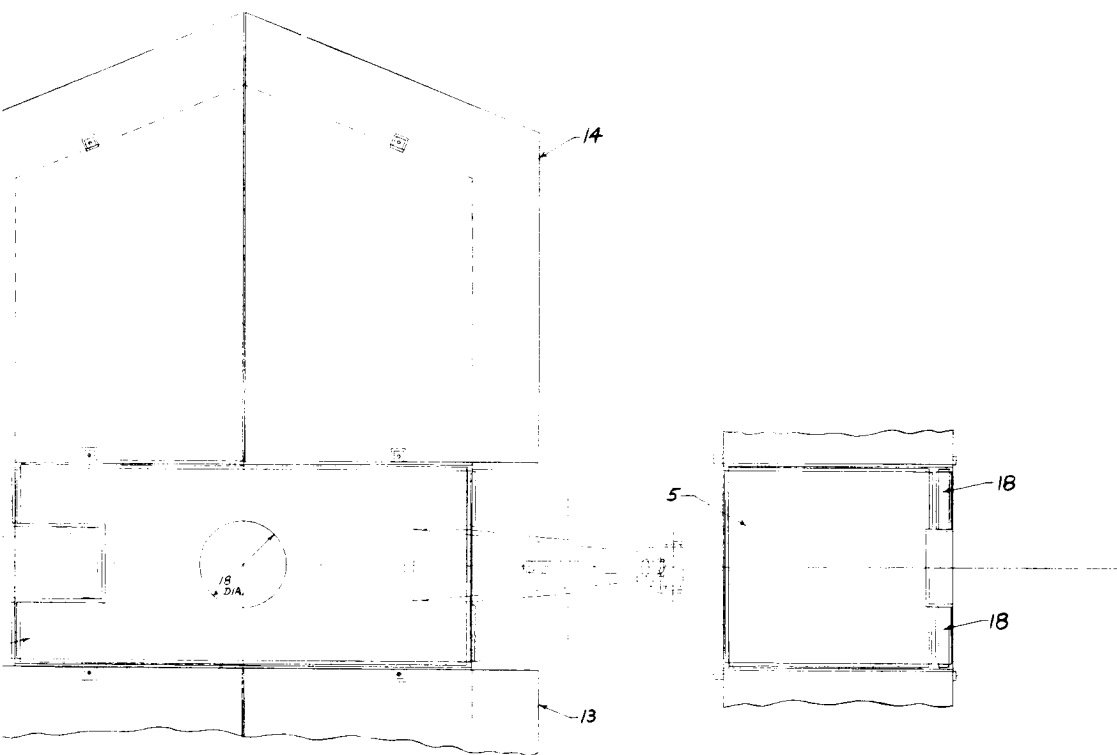
Figure 2.5-1. Voyager - Mars 1969 Orbiter Structure, F-14 Tank Mtg. (3 of 3)



1

3
4
2





NOTES

1. REMOVABLE HONEYCOMB PANELS (ITEMS 2, 3, 4, 5, & 9)
TO BE .375 THICK, 1.6"/CU FT. CORE, .005" THICK 7075 T6
CHEM-MILLED FACES, .025 Z CLOSEOUTS.
2. REMOVABLE HONEYCOMB PANELS (ITEMS 10 & 11)
TO BE .75 THICK, 1.6"/CU. FT. CORE, .012 THK (OUTSIDE) &
.032 THK (INSIDE) 6061 T6 FACES.
3. REMOVABLE HONEYCOMB PANEL (ITEM 12)
TO BE 1.00 THICK, 1.6"/CU. FT. CORE, .008 THICK 7075 T6 FACES.
4. REMOVABLE HONEYCOMB PANEL (ITEMS 13 & 14)
TO BE 1.75 THICK, 1.6"/CU. FT. CORE, .012 THICK 7075 T6 FACES.
5. FIXED HONEYCOMB PANELS (ITEMS 6, 7, 8, 15, 16, 17, & 18)
TO BE .375 THICK, 1.6"/CU. FT. CORE, .005" THICK 7075 T6
CHEM-MILLED FACES, .020 Z CLOSEOUTS.

2	18	PANEL, FIXED SIDE	SEE NOTE 5		
2	17	FIXED SIDE	A	5	
2	16	FIXED SIDE		5	
2	15	FIXED SIDE		5	
2	14	REMOVABLE BOTTOM		4	
2	13	REMOVABLE BOTTOM		4	
1	12	REMOVABLE BOTTOM		3	
4	11	REMOVABLE END		2	
4	10	REMOVABLE END		2	
1	9	REMOVABLE TOP		1	
2	8	FIXED TOP		5	
2	7	FIXED TOP		5	
2	6	FIXED TOP		5	
1	5	REMOVABLE SIDE		1	
1	4	REMOVABLE SIDE		1	
2	3	REMOVABLE SIDE		1	
2	2	PANEL, REMOVABLE SIDE		1	
1	1	ORBITER STRUCTURE	SEE NOTE 1		
ORBITER STRUCTURE IDENTIFICATION NO.	FORM NO.	DESCRIPTION	STACK SIZE	MATERIAL	REMARKS
13-000000-54	1	ORBITER STRUCTURE			

Figure 2.5-2. Voyager - Mars 1969 - (Orbiter Structure and Panel Assembly)

An area where manufacturing simplicity has been compromised for structural efficiency is in the use of high strength alloys in the "foil size" gages. Usually, the only alloys available for thin face sheets ($t < .012$ ") are the softer aluminums with a maximum allowable strength of 20,000 psi. The present design calls for chemical milling of .012" thick 7075-T6 aluminum sheet ($F_{cy} = 60,000$ psi) to the thinner gages, thereby resulting in honeycomb panels of three times the strength of the equivalent panels used in the past.

Another basic philosophy that has been adhered to is the requirement that this vehicle be as structurally efficient as possible for withstanding the mission associated environments, with no compromises made for ground handling loads. Other than supplying local hardware at appropriate hoist locations, all other members will be designed by mission environmental loads only.

B. Load Paths

(1) Primary Structure (Lander and Fuel Tank Supports)(Reference Figure 2.5-1)

On the Lander mating plane, four pickup points per Lander are provided. These are located at 90° spacing to support the Landers through their parachute lug support structure. The 1,450 lb. and 2,000 lb. Landers utilize the same pickup points, revising the Lander fairing to suit. A larger Lander can be supported at the outer periphery of the Orbiter if required by mission Analysis. For supporting the larger Lander, the lightweight tees, which serve as framing for the access panels, would be replaced by larger fittings capable of transmitting the loads directly to the adapter. At the same time, the existing Lander fittings would be replaced by lighter framing members.

Two full depth honeycomb beams divide the structure transversely across the short dimension (parallel to the Y axis). These beams support the fuel and oxidizer tanks and shear loads from four of the eight Lander reaction points to the outer periphery. The honeycomb construction stabilizes the beam webs however, the loads are introduced through angle and hat section stiffeners to avoid local stress concentrations. The Lander loads at the four remaining fittings are fed directly (through column action) to the adapter. The smaller freon and helium tanks are supported partially by these beams and partially by additional full depth webs. (Reference Figure 2.5-1) Side loads on the tanks are introduced as shear loads in the side panels by tension-compression thrust tubes at one trunnion. In this manner, the tanks are free to grow under pressure and do not become truss members themselves.

Side loads on the Landers are reacted by the top panels through stiffeners. Angle members and other extrusions form a framework through which shear loads are transmitted from panel to panel to adapter reaction points. The side panels (with the exception of the end panels which are used for component mounting) are designed for shear loads only. As a result, minimum gage face sheets consistent with careful handling can be used, provided that the core is sufficient to stabilize the panel.

The component mounting panels, besides being loaded by overall racking shears, also react local shear and bending loads from the components mounted on the panels. While a heavier gage panel is required, the inside face sheet gage and material has been selected primarily for efficiency as a thermal path. Aluminum alloy 6061-T6 has been chosen here as the sheet material for both inner and outer faces since its combination of strength and thermal conductivity is superior to other, either high strength or highly conductive, alloys.

(2) Solar Cell Support Structure

The lower deck of the structure is a honeycomb panel which supports the solar cells. While this may outwardly appear to be an inefficient method of support since the panel is

subjected to high bending loads in the boost direction, the bending stiffness required is obtained rather cheaply with a thick core. The advantages obtained from this method of solar cell mounting are:

1. The panels can be sun oriented without inducing thermal gradients on the Landers.
2. Sun oriented panels can be non-deployable saving the deployment linkage weights and increasing reliability.
3. Transverse shear structure is required at the base of the vehicle under any circumstance to react racking shears and to stabilize the lower beam caps.

(3) Rocket Engine Support

The rocket engine is supported by an eight tube titanium truss. The truss design was chosen here because no adequate backup structure was available for introducing shell loads uniformly. The truss is more adaptable for introducing the rocket engine thrust loads through the main transverse beams.

Titanium was chosen as the tube material because of the high temperatures expected during rocket firing.

(4) PHP Structure

The Planet Horizontal Package (PHP) structure is basically a box structure formed by honeycomb panels tied together through framing members. The vertical loading is reacted by shear flows. Local moments are taken by panel bending. The two interior honeycomb webs support components that are not high heat dissipators and stiffen the box to reduce dynamic amplifications. The inside face sheet gages of the front and back panels are designed by thermal considerations. The Package is tied into the Orbiter structure transverse beams through four corner fittings which would be sufficiently preloaded so that local shock loading does not occur. The boom structure is for planet orientation purposes only and offers no support to the PHP during the boost and transit phases.

(5) High Gain Antenna and Support Structure

The ten foot diameter parabolic antenna is of honeycomb construction utilizing chemical milled 7075-T6 face sheets. A stiffening outer ring, a mid ring, and additional backup structure are provided to help distribute loads to the reaction points. Vertical loads are taken by the two beams of the antenna support structure which tie into the main structure transverse beams. (Reference Figure 2.3.3-1) The hinge fitting at the base takes side loads. In its present position, local bending loads are more apt to occur under a side load condition. On a system trade-off basis, however, this packaging arrangement enabled the outer contour and the height of the orbiter structure to be reduced resulting in a lighter structural subsystem weight. Initially, it was planned to support the antenna peripherally at the base of the vehicle concave up, since the internal loads would be primarily membrane forces. However, in this position, if deployment failed to occur prior to rocket engine firing, the antenna would be destroyed by the plume of the rocket.

2.5.2 STRUCTURAL LOADS CRITERIA

A. General

This section presents all environmental conditions deemed significant to structural design. The powered flight data has been based on information available for the Saturn, and third

stage boosters of the Agena or Centaur variety. While the third (S-VI) stage is still undefined for this program, the loads given can be considered to be representative of the expected loads. The system vibration levels are derived considering that the environment from the third stage booster will be limiting, since the mass of the third stage booster will tend to damp out the vibratory loads from the Saturn booster.

The component qualification test levels have been obtained from P & VE-S-62-7 "Vibration and Shock Specifications for Components on Saturn, C-1 Block II Vehicles". The levels given are for components housed in the payload compartment designated zone 16 in the referenced document. These levels would be adequate for qualification of components to withstand the vibration environment expected from a third stage booster of a type considered.

B. Load Factors

All load factors given in this section are limit. For design purposes:

Yield Loads = 1.0 Limit Loads (Structure not critical for component alignment)

Yield Loads = 1.15 Limit Loads (Structure critical for component alignment)

Ultimate Loads = 1.25 Limit Loads (Powered flight and orbit)

Ultimate Loads = 1.50 Limit Loads (Handling and transportation)

Ultimate Loads = 2.00 Limit Loads (Pressure Vessels)

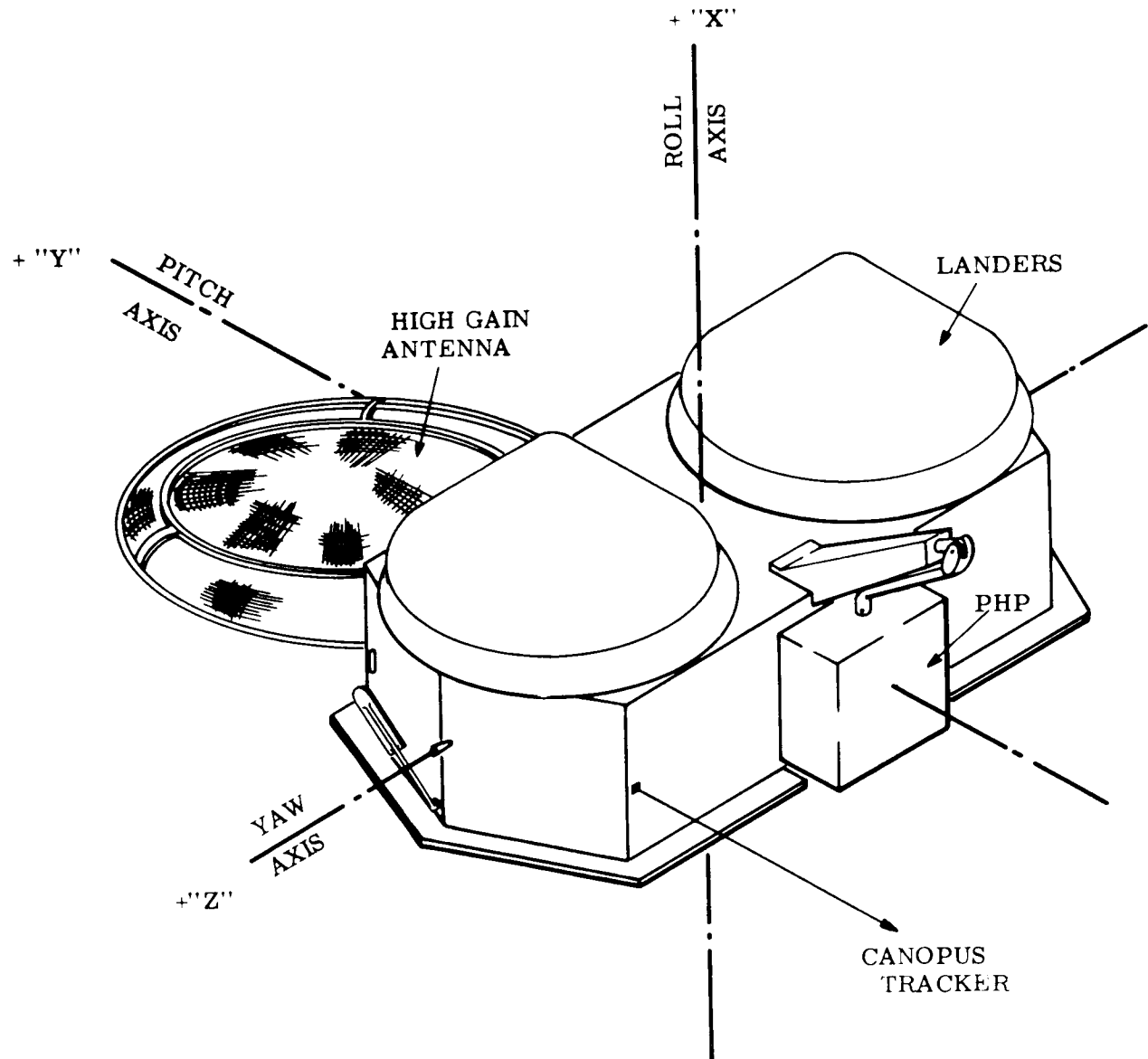
Additional margins of safety, as shown below, will be specified on specific areas in keeping with the emphasis on high reliability.

Fasteners in Shear	Required M. S. = + .15
Bolts in Tension (Eccentric Load Only)	+ .50
Fittings	+ .15
Lugs	+ .30
Welds-Electron Beam	+ .15
All Others	+ .50

An exception to the general arrangement of safety factors and margins of safety would be in the treatment of the vehicle flight proofing qualification test dynamic loads. These are actually ultimate loads but can be considered as limit to avoid yielding at test levels. In consideration of this conservative approach, some of the above factors would not be considered applicable.

(1) Axis Orientation

The limit load factors given are oriented in respect to the axes shown below:



C. Pre-Launch (Shipping, Handling and Storage)

(1) Steady State Accelerations

	N_x	N_y	N_z
1. Hoist	+3.0	±0.5	±0.5
2. Air Transportation	±3.62	±1.82	±3.62
3. Ground Transportation — Special Handling procedures will be adhered to so that above load factors are not exceeded.			

NOTE: The spacecraft is not complete when shipped (i. e., Landers are shipped separately, fuel tanks empty, etc.)

(2) Shock

Shock loading transmitted to the spacecraft from the shipping container shall be attenuated such that the loads in the vehicle structure do not exceed the powered flight and air transportation steady state loads.

Allowable load limits will be based on fatigue considerations. A free drop of 1/2 inch maximum can be expected on the complete spacecraft under normal handling conditions.

(3) Vibration

Vibration loads will also be attenuated by the shipping container so that the structural member loads do not exceed those experienced under the launch load conditions.

(4) Temperature

Temperature extremes of -80°F to 125°F are to be expected during all phases of shipping, handling and storage. For the specific components that cannot withstand this environment, special handling techniques and packaging specifications that limit the temperature from -35°F to +125°F will be specified.

(5) Pressure

Stored in container at 2.5 psig and 5% relative humidity referred to 70°F.

15.4 to 10.2 psia (0-10000 ft.)

10.2 to 1.69 psia (10000-50000 ft.) (air transport)

D. Powered Flight (Launch)

(1) Steady State Accelerations

Listed in Table 2.5-1 are maximum steady state accelerations. The lateral and longitudinal loads may act independently or in combination, and may have any values up to the given maximums. The lateral loads can act in any direction in the Y-Z plane.

TABLE 2.5-1. MAXIMUM STEADY STATE ACCELERATIONS

<u>Launch</u>	
Condition a - 3rd stage booster burnout	
N_x	= -5.6 g's
N_{yz}	= ±0.5 g's
Condition b - Saturn booster burnout, engine hard over	
N_x	= -5.3 g's
N_{yz}	= ±0.7 g's
θ	= ±.745 rad/sec ² = .92 g's N_{yz} at spacecraft cg
Max. N_{yz}	= ±0.7 g's ±.92 g's

(2) Dynamic Loads

Listed in Table 2.5-2 are expected flight vibration and flightproof test levels. The flightproof test conditions are listed as powered flight loads since the vehicle must survive these loads while in the powered flight condition.

The vibration loads experienced during flight occur in combination with steady state accelerations. However, as has been done in the past, it is expected that the vehicle will be qualified by vibration testing to an envelope of peak levels, which are more severe than the combined loads expected during flight. Listed below are expected vibration test loads which should not be combined with steady state loads and can be assumed larger than expected flight vibration loads.

TABLE 2.5-2. EXPECTED FLIGHT VIBRATION AND FLIGHT PROOF TEST LEVELS

<u>Vehicle Operative Acceptance Test</u>			
Inputs parallel to "X" axis			
Frequency	5-50 cps	50-2000 cps	
Sinusoidal	1 grms	2 grms	
Random	-	.01 g ² /cps	
Duration 10 minutes			
<u>Vehicle Flight Proofing Qualification Test (prototype only)</u>			
Inputs parallel to "X" axis			
Frequency	5-50 cps	50-100 cps	100-2000 cps
Sinusoidal	1.25 grms	2.5 grms	3.5 grms
Random	.015 g ² /cps	.015 g ² /cps	.035 g ² /cps

- NOTES: 1. All vibration should be limited to 0.4 inch double amplitude.
2. Gaussian random to be rolled off at 12 db/octave (on an acceleration basis) from 1200 to 2000 cps.
3. Tolerance on power spectral density: $\pm 50\%$.

Lateral vibration testing has not been specified for qualification with this type booster; however, it is planned to perform lateral testing as part of the engineering development program.

TABLE 2.5-3. COMPONENT QUALIFICATION TESTS

Sweep test (10 minute sweeps along 3 mutually perpendicular axes)	
16 - 42	cps @ 2 g's peak
42 - 95	cps @ .022 in. double amplitude
95 - 2000	cps @ 10 g's peak
Resonant Test (dwell at resonant frequencies for 5 minutes)	
16 - 42	cps @ 1 g peak
42 - 95	cps @ .011 in. double amplitude
95 - 2000	cps @ 5 g's peak
Shock Test (3 shocks in each direction along 3 mutually perpendicular axes - 18 shocks total)	
35 g's peak with any of the following pulse shape-time combinations:	
1.	Triangular pulse - 10 milliseconds duration
2.	half sine pulse - 8 milliseconds duration
3.	rectangular pulse - 5 milliseconds duration.

(3) Shock

Shocks caused by ignition and engine cut-off will occur during boost flight. Excitations of equipment and structure are considered to be covered by the environments specified in Tables 2.5-2 and 2.5-3.

(4) Temperature

Factors which affect the temperature distributions and are to be factored into the design on an individual basis are:

1. Solar Irradiation
2. Earth Flux
3. Albedo (reflection of solar flux by Earth atmosphere)

4. Effect of Thermal Control Devices
5. Aerodynamic Heating
6. Internal Power Dissipation
7. Thermal Radiation to Cold Walls and Free Space

(5) Acoustical Field

Maximum sound pressure levels of 145 db at lift-off may be encountered. The sound will be quite random over a broad spectrum with the octave spectral maximum at about 100 cps. Levels inside spacecraft compartments may be about 10 db less.

(6) Pressure

1. Aerodynamic Pressure at maximum q (estimated at 975 lb/ft.²) will be taken by the shroud and is not applicable for spacecraft design.
2. Internal pressure will reduce from 15.4 psia to a vacuum of 10^{-6} mm. Hg during boost.

(7) Separation Loads

Separation from the booster will be at a rate which minimizes the effect of separation loads on the design.

E. Planetary Transit and Orbital Environment

(1) Steady State Acceleration, Vibratory and Shock Loads Orbit Injection - Retrorocket Firing

Steady State

$$N_x = 1.67 \text{ g's}$$

$$N_{yz} = \text{negligible}$$

Vibratory and shock loads during orbit injections rocket engine firing are assumed less severe than during boost flight. Exceptions are for deployed and unstowed equipment.

Other minor vibrations and accelerations as excited during PHP and Antenna orientation maneuvers and attitude and control gas jet firing will be encountered. These are not considered to be significant in the structural design of the vehicle.

(2) Life Time

The operational life of the Orbiter is considered to be 270 days for transit and 90 days for planetary orbit.

(3) Thermal

Component thermal environment will be passively and actively controlled to maintain temperature within specified design limits.

Extremes of -100°F to +250°F can be expected on structural items. Actual temperature distributions will be a function of:

1. Spacecraft Orientation
2. Solar Irradiation
3. Planetary Flux
4. Planetary Albedo
5. Internal Power Dissipation
6. Thermal Radiation to Cold Walls and Free Space.

(4) Vacuum

The spacecraft will be designed to operate at pressures less than 10^{-10} mm. Hg.

(5) Charged Particles

Charged particles, resultant X-rays, and gamma rays associated with Van Allen radiation belts and solar flares will be encountered. Cosmic rays are considered to have negligible effect. Some of the constituent protons will penetrate the structure to the equipment. Some of the energetic protons striking the structure may cause penetrating gamma rays of energy approaching their incident energies. Almost all of the electrons will be absorbed with generation of ion pairs, X-rays, or Gamma rays of smaller individual energy (per particle).

(1) Radiation

TABLE 2.5-4. RADIATION

Energy (E) MEV	Average Flux Particles/cm ² -sec.	Energy (E) MEV	Average Flux Particles/cm ² -sec.
0-50	3×10^{10}	0-10	No Significant Information
50-500	$3.7 \times 10^{15} E^{-3}$	10-20	10^4
500	3×10^7	20-75	10^2
500-13,000	$7.5 \times 10^{12} E^{-2}$	75	0

(2) Solar Flares

Table 2.5-5 lists the total dose expected from two flares of approximately the size of the May 1959 flare.

TABLE 2.5-5. SOLAR FLARES

Energy (E) MEV	Average Flux Particles/cm ² - Mission
30	8.5 x 10 ¹⁰
50	1.2 x 10 ¹⁰
100	7.5 x 10 ⁸
300	9 x 10 ⁶

(6) Micrometeoroids

Micrometeoroids are unlikely to penetrate the vehicle and be a hazard to internal components. Micrometeoroids striking outside may be expected to have the following characteristics, (above 80 km altitude).

TABLE 2.5-6. MICROMETEORIDS

Material Density	Velocity	Space Density	Direction
Geminid 3.4 $\frac{\text{grams}}{\text{cm}^3}$	36 km/sec	4 x 10 ⁻¹⁹ $\frac{(10^{-3})}{(\text{m})}$.66 cm ⁻³	In the plane of the earth's orbit
Sporadic 3.4 $\frac{\text{grams}}{\text{cm}^3}$	11-70 km/sec	$\frac{3.5 \times 10^{-22} \text{ cm}^{-3}}{\text{m}}$	Any direction except from approximately the direction of the earth

Where 10⁻¹³ < mass < 10⁻³ grams

2.5.3 LOADS ANALYSIS

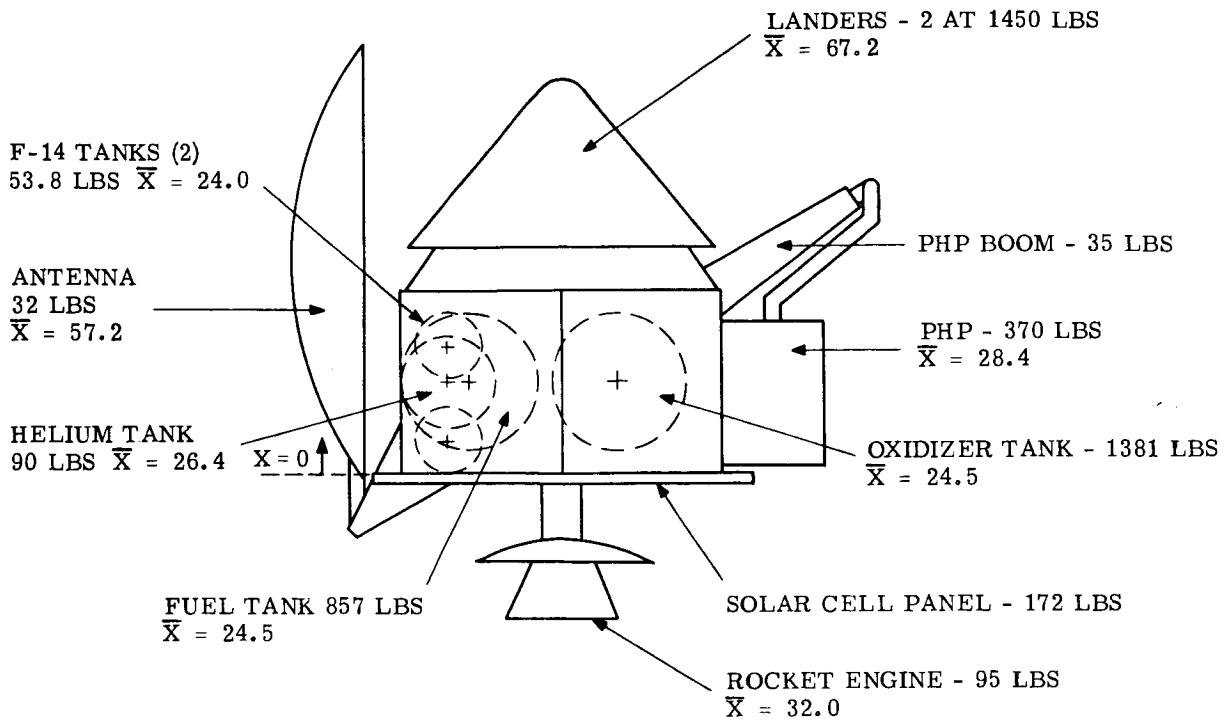
A. General

This subsection discusses the external loads acting on the vehicle structure due to critical steady state and dynamic environments selected from the structural loads criteria. For presentation, these loadings are categorized into separate classes: powered flight steady state loads, powered flight vibratory loads, orbit injection and orbital loads and ground handling loads. Only loads from the critical loading environment for each particular structural item are considered for analysis purposes.

B. Orbiter Load Distribution

Weights of major items and their locations are given in Figures 2.5-3 and 2.5-4. These values have been obtained from the weight analysis presented in Section 2.6.

For analysis purposes, the unitemized weights of small components, propulsion hardware, electrical harnessing and structure is applied as a uniform running load on the internal and external vertical panels.



$$W_{TOTAL} = 7030 \text{ LBS.}$$

$$\text{C.G. AT } X = 40.67$$

Figure 2.5-3. Major Mass Item Weight and Location, End View

The structural subsystem weight is distributed evenly over the beams. The miscellaneous items are mostly concentrated on the center transverse beams, therefore, 70% of this weight is applied to these beams with the remainder distributed over the outer periphery.

Running Length of Transverse Beams

$$= 2(96.0) = 192 \text{ in.}$$

Running Length of Outer Panels

$$2(160) + 4(52) = 528 \text{ in.}$$

W Structure = 419 lbs

$$w \text{ structure} = \frac{419}{192+528} = .582 \text{ lbs/in.}$$

W Miscellaneous = 230 lbs

$$w \text{ miscellaneous} = \frac{230(.7)}{192} = .839 \text{ lbs/in. on center beams}$$

$$w \text{ miscellaneous} = \frac{230(.3)}{528} = .131 \text{ lbs/in. on outer panels}$$

Total Distributed Load

$$= .839 + .582 = 1.421 \text{ lbs/in. - center beams}$$

$$= .582 + .131 = .713 \text{ lbs/in. - outer panels}$$

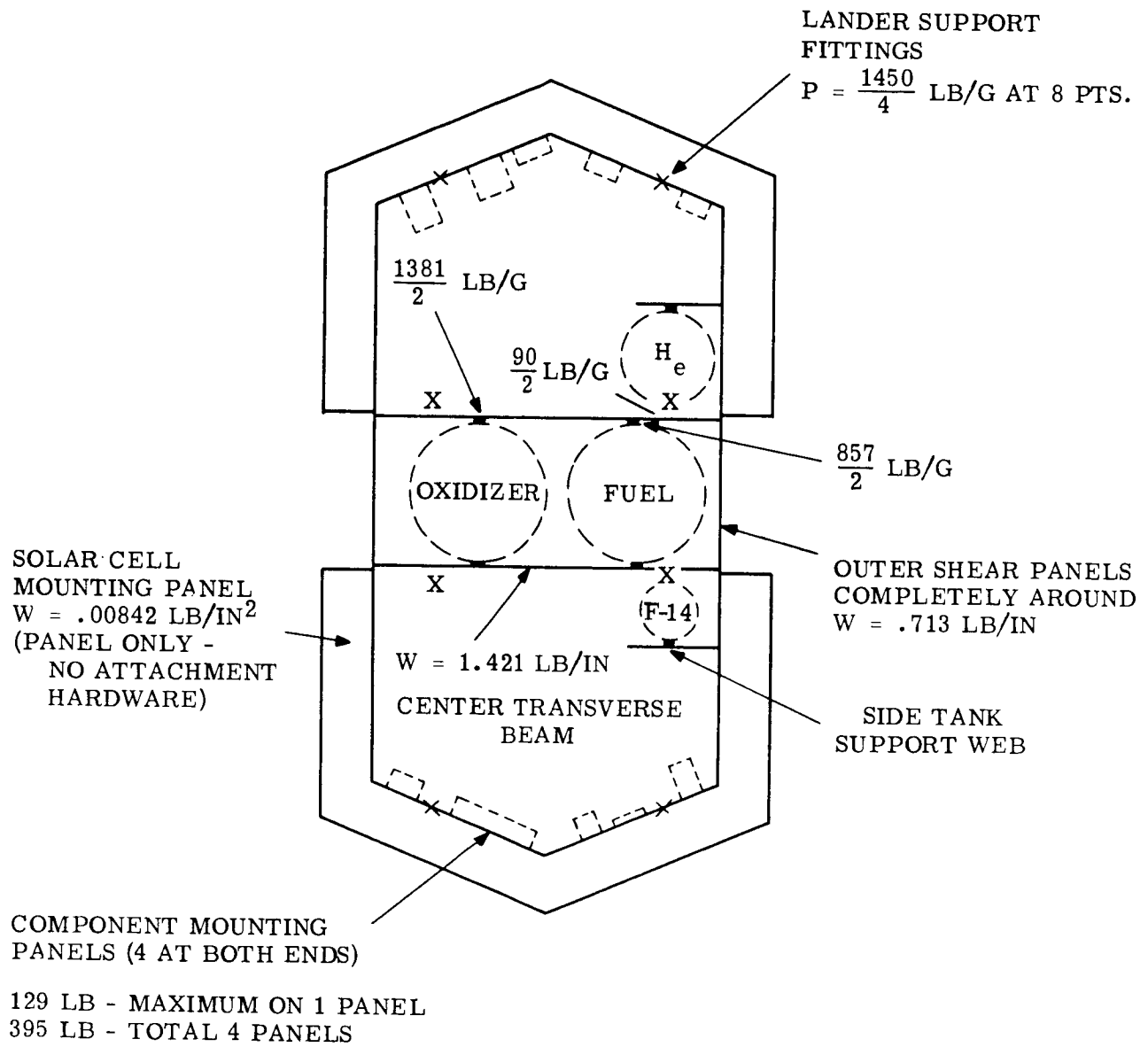


Figure 2.5-4. Major Mass Item Weight and Location, Plan View

C. Steady State Accelerations

The steady state accelerations are critical for overturning moments and side load on the complete vehicle. The dynamic test environment specifies inputs in the X direction only with only local side loads induced as a function of shaker "cross talk" and individual member mode shapes. Therefore, the steady state accelerations are used to size the vehicle hard point tie down structure, the side shear panels and most of the framing members.

The critical condition is condition "b" of Table 2.5-1, Paragraph 2.5.2.D.

$$N_x = -5.3 \text{ g's}$$

$$\text{Max. } N_{yz} = \pm 1.62 \text{ g's}$$

The above loads may act in combination, but as discussed in the design criteria section, they are not combined with the vibratory loads for design purposes.

D. Vibratory Loads

Load distribution throughout a structure due to vibratory inputs is dependent on the dynamic characteristics of the structure. Individual members and components generally reach their critical load levels at one or more discrete frequencies within the applied dynamic spectrum, usually related to the natural frequency of the individual member, the applied load frequencies and the dynamic characteristics of the structure surrounding it. Structural amplifications at different points in the spectrum vary greatly, and it is impractical to show structural loads with balanced reactions through the complete system. As a result, critical vibratory loads are applied to individual members only, and do not apply for the entire vehicle at any one instant of time. For this reason, the dynamic loads acting on the structure are given as "g" loadings for individual items.

(1) Dynamic Load Factors

As part of the structural development of the vehicle, dynamic analyses were performed on various configurations utilizing different construction techniques. (A brief outline of the method of analysis is given in the following paragraph.) A good comparison was obtained between two specific Orbiters each capable of supporting the same major components. One was a semimonocoque shell composed of riveted sheet and stiffeners, and the other was a space framework utilizing pin-ended tubular members. The results of the dynamic studies are summarized in Figure 2.5-5.

The curves presented compare dynamic transmissibility (or amplification) factors through the primary structure for the two types of construction. It is evident that the shell structure reduces transmissibility by 50% with the response being 6.25 times the input load as against 12.5 for the truss structure.

The analysis was based on a modal damping factor of 5%. Previous testing has shown that this figure is conservative for bolted honeycomb panel construction. This type of construction was utilized on the Advent Communications Satellite, and damping factors in the order of 13% were measured during testing. Consequently, the transmissibility factor of 6.25 used in the subsequent structural analyses for the Lander and Tank Support Structure, the Planet Horizontal Package Structure and the Side Component Mounting Panel Structure is conservative.

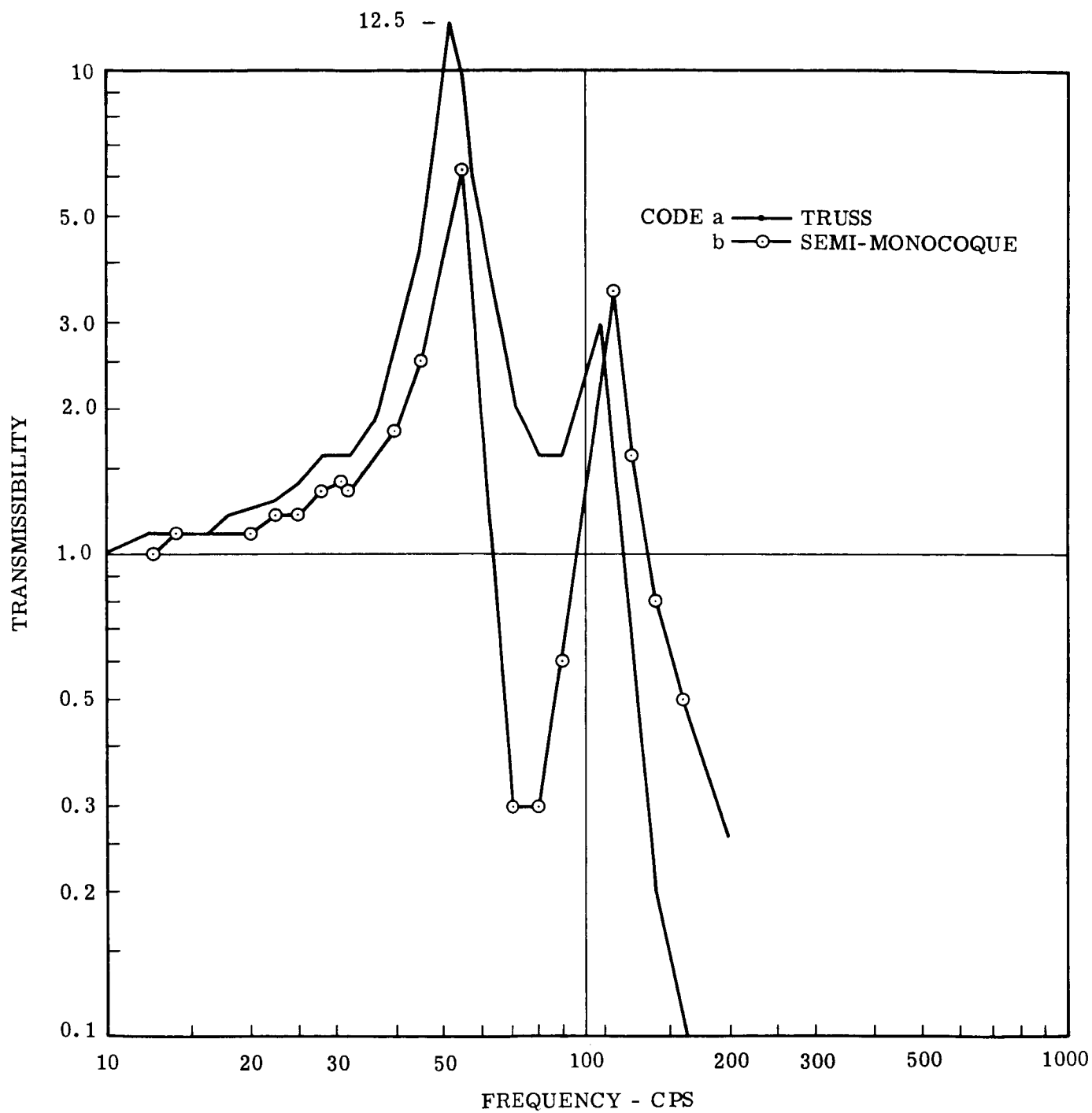


Figure 2.5-5. Dynamic Transmissibility Factors vs Frequency (cps)

For the Rocket Engine Structure which is a truss, a transmissibility factor of 15.0 is used. The conservatism of the above factor diminishes, if main structural assemblies are dynamically coupled. Therefore, a further criterion is a stiffness requirement such that the natural frequencies of the major components do not couple. This is particularly important for the solar cell mounting panel and the rocket engine support.

The High Gain Antenna Structure and the Solar Cell Mounting Support Structure are checked against response factors which also consider additional amplifications due to local resonances. For instance, at the center of the Solar Cell Panel which is under plate bending action, a total amplification factor of 30 is used for design purposes. This is also somewhat conservative because previous testing of honeycomb beam solar cell modules (not as inherently stiff as continuously supported panels) indicated a maximum response factor of 20.

A factor of 20 is used for the antenna structure. This is adequate for designing the support structure, but the design condition for the antenna itself considers the addition of a dynamic side load. The anticipated mode shapes indicate that a dynamic side load can be expected on the antenna structure. A factor of 5.0 g's is used which must also be considered a maximum expected limit. This dynamic "cross talk" factor is also used to size the propellant tank thrust tubes.

(2) Method of Analysis

1. The vehicle is represented by a mathematical model consisting of lumped masses separated by "structure". On the basis of this model, a stiffness and mass matrix is determined.
2. The natural frequencies and corresponding mode shapes are determined. This is basically an eigenvalue problem. The mode shapes are examined for dominant mass motions, and modal damping coefficients are assumed on the basis of past experience with similar structures.
3. On the basis of the information gathered in Step 2, the response of the various lumped masses are determined in the form of complex transfer functions whose absolute values represent the magnification of the base motion, and whose angles with the real axis represent the phase relation.
4. The transfer functions determined in Step 3 may then be utilized in determining the total response of the vehicle to both the sinusoidal and random vibrations. The response is in terms of peak accelerations of the various masses.

(3) Response Levels

The actual design levels assume a system resonance at a frequency between 50 and 100 cps. Referring to Table 2.5-2 of Paragraph 2.5.2.D, the input g's at these frequencies during flight proof qualification testing are:

Sinusoidal	2.5 g rms.
Random	.015 g ² /cps.

An equivalent peak g loading is obtained by using the method on pages 24-27 of reference in Paragraph 2.5.5 for finding the sinusoidal equivalent of random vibration. For a flat spectrum

$$\ddot{X}_r = \left[\frac{\pi}{2} \left(W_e(f) \right) \text{fnQ} \right] \frac{1}{2} g$$

where

$$\begin{aligned} \ddot{X}_r &= \text{rms acceleration response} \\ W_e(f) &= \text{mean-square acceleration density} \\ &= .015 \text{ g}^2/\text{cps.} \\ f_n &= \text{natural frequency of responding system} - \text{taken as 75 cps.} \\ Q &= \text{amplification factor (transmissibility)} \\ &= 6.25 \text{ based on previous analysis.} \\ \ddot{X}_r &= \left[\frac{\pi}{2} (.015) (75) (6.25) \right]^{\frac{1}{2}} \text{ g} \\ \ddot{X}_r &= 3.32 \text{ g's} \\ \text{Equivalent rms input g's} &= \frac{\text{Response}}{Q} = \frac{3.32}{6.5} = .53 \\ \text{Total input g's} &= \left[(\text{grms sin})^2 + (\text{grms equiv. sin})^2 \right]^{\frac{1}{2}} \\ &= \left[(2.50)^2 + (.53)^2 \right]^{\frac{1}{2}} = 2.56 \text{ g's rms} \\ \text{0 to Peak g's} &= 1.414 (2.56) = 3.62 \text{ g's} \end{aligned}$$

TABLE 2.5-7. PEAK DYNAMIC LOAD FACTORS (ULTIMATE)

Item	Transmissibility Factor	Peak g's (X)	Peak g's (Y, Z)
Lander, Tank and Component Mounting structure	6.25	22.6	5.0 (Tanks only)
Planet Horizontal Package	6.25	22.6	—
Antenna	20.0	72.4	5.0
Rocket Engine Support	15.0	54.3	—
Solar Cell Panel	30.0	108.6	—

(4) Effect of Increasing Vibration Loads

The vibratory design loads listed in the previous table are, of course, order of magnitude values since the vibration environment from the third stage booster has been estimated. To give some indication of how the structural weight would change as the vibration test loads change, Figure 2.5-6 is presented.

This curve presents estimated Orbiter structure weights as a function of qualification test input g's (rms) at vehicle resonance. It is assumed in all cases that the vehicle resonance occurs between 50 and 100 cps. The input g's rms can be considered to be equivalent g's derived from a combined sinusoidal and random vibration.

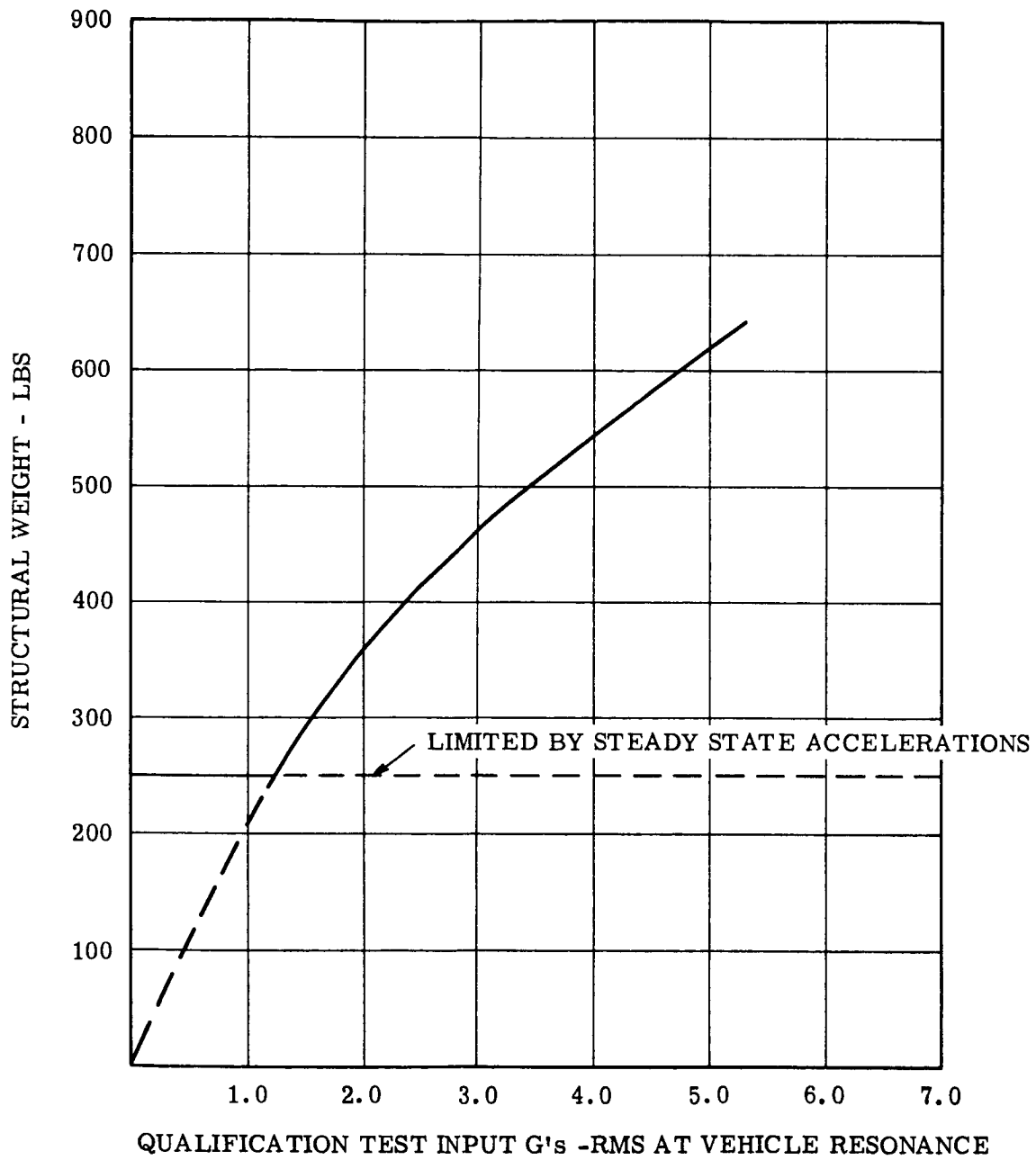


Figure 2.5-6. Qualification Test Input G's (RMS) at Vehicle Resonance

(5) Component Design Loads

It is not in the scope of this section to show analyses for individual electronic and payload package structure. However, since the weight figures for these components does include a portion for structure based upon surviving the qualification requirements, a justification of the adequacy of this environment seems proper.

The structure in the smaller components and electronic equipment will be designed to withstand the component qualification test environment specified in Table 2.5-3 of Paragraph 2.5.2D.

The test criteria specifies dynamic inputs along three mutually perpendicular axes. Since the vibratory loads experienced by the complete system are introduced parallel to the X(Roll) axis, the component qualification test levels are obviously conservative in the Y and Z directions. In the X direction, however, it is possible for the components to be subjected to higher input g's during the system qualification test than during component qualification testing.

The curves presented in Figure 2.5-7 show that the component structural response is more severe during component qualification testing, and therefore, limiting in component structural design and qualification. The curves are based on an expected component resonant frequency of 150 cps and a component modal damping factor of 0.02. This is in agreement with results obtained in the past on other spacecraft components and a minimum component natural frequency of 150 cps would be a design parameter for this program.

Curve (a) (Figure 2.5-7) shows the expected component mounting panel response vs. frequency during system qualification. This would be the input level to the component. Curve (b) (Figure 2.5-7) shows the component structure's dynamic response to these levels. Curves (c) and (d) (Figure 2.5-7) present the input "g" levels and the expected structural response vs frequency during qualification testing. A comparison of curves (b) and (d) (Figure 2.5-7) shows that the peak loads that the component would be designed to withstand occur during this latter test.

E. Orbit Injection and Orbital Loads

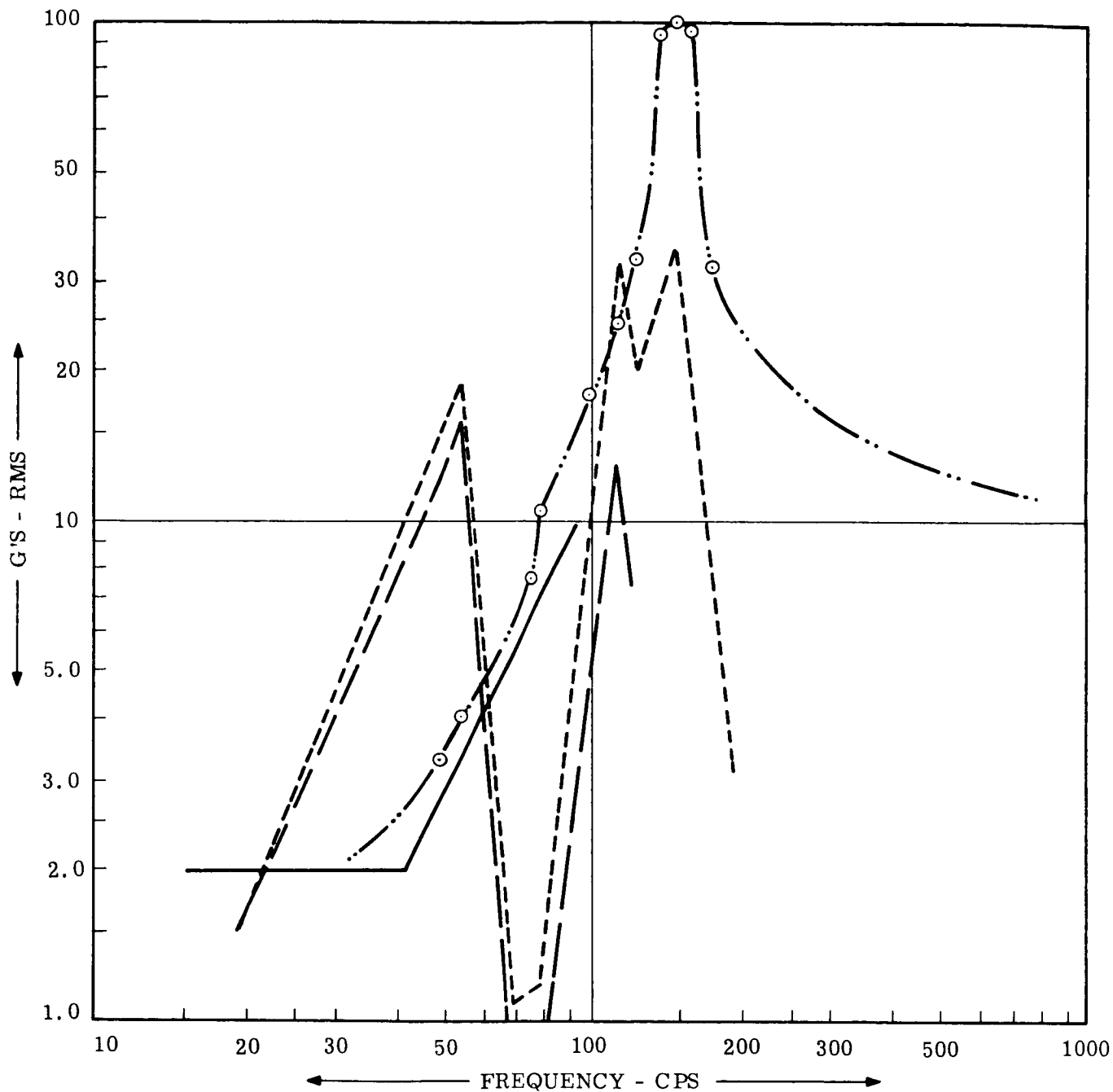
The rocket engine has a thrust capability of 2,200 lbs. During orbit injection, the maximum "g" loading of -1.67 g's (see Paragraph 2.5.2.E) does not load the primary structure more severely than the boost loads. This loading is only significant for the design of the rocket engine support. It is additionally considered that the rocket engine support structure reaches a temperature of 700°F during firing.

F. Ground Handling Loads

As per the philosophy discussed in Paragraph 2.5.1, structural members will be supported or protected in such a manner that the internal member loads induced during handling and transportation maneuvers are less than those felt during the launch and orbit phases. While this condition will be checked during a hardware program, the loads occurring under this environment are not considered significant for this structural subsystem design.

2.5.4 STRESS ANALYSIS

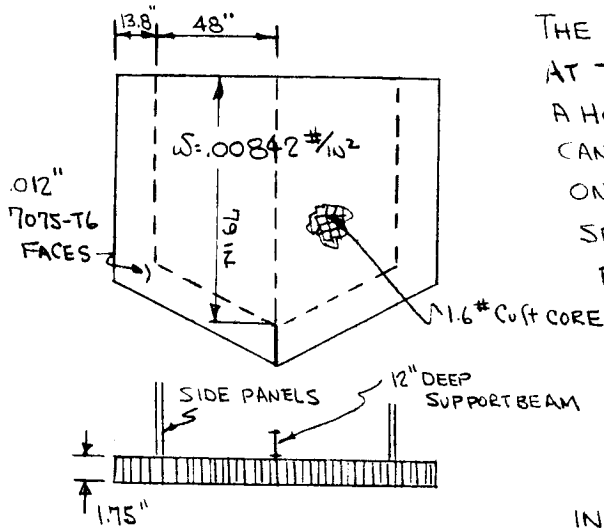
This section presents a typical analysis for the Solar Cell Mounting Panel. Loads are determined for the structure utilizing the design loading environments specified in the previous sections. Information concerning analysis of other structure may be obtained from PIR 9731-329-089.



CODE: a — — COMPONENT MOUNTING PANEL RESPONSE - VEHICLE QUALIFICATION
 b - - - COMPONENT RESPONSE - VEHICLE QUALIFICATION
 c — — INPUT LEVEL - COMPONENT QUALIFICATION
 d - · - · - ○ COMPONENT RESPONSE - COMPONENT QUALIFICATION

Figure 2.5-7. Dynamic Responses in G's (RMS) vs Frequency (cps)

SOLAR CELL MOUNTING PANEL



THE SOLAR CELLS ARE SUPPORTED AT THE BASE OF THE VEHICLE BY A HONEYCOMB PANEL. THE PANEL CANNOT BE MANUFACTURED IN ONE PIECE, AND, RATHER THAN SPLICE, AN ADDITIONAL SUPPORT BEAM IS PROVIDED AT THE CENTER. ANALYSIS SHOWS THAT THE WEIGHT REQUIRED TO MAKE AN ADEQUATE SHEAR AND MOMENT SPLICE IS MORE ECONOMICALLY EXPENDED IN A MID SUPPORT WHICH REDUCES AMPLITUDES UNDER DYNAMIC LOADING.

FOR ANALYSIS THE PANEL IS DIVIDED INTO TWO PARTS (A) THE CANTILEVERED OVERHANG AND (B) THE SIMPLY SUPPORTED INTERIOR PANEL. THIS IS JUSTIFIED ON THE BASIS THAT WHILE THE EDGE MOMENTS ON THE INTERIOR PANEL WILL DECREASE MOMENTS AT THE PANEL CENTER, THE FLEXIBILITY OF THE MID SUPPORT BEAM INDUCES SECONDARY MOMENTS WHICH ADD TO THESE MOMENTS.

A. CANTILEVERED OVERHANG

$$M_{max} = \frac{wL^2}{2} \quad N_x = 108.6 \text{ g's}$$



$$M = \frac{.00842 (13.8)^2 (108.6)}{2} = 87.1 \frac{\text{IN-LBS}}{\text{IN}}$$

$$f_b = \frac{M}{ht} = \frac{87.1}{1.75(.012)} = 4150 \text{ PSC}$$

M.S. = AMPLE

BY
CK.
DATE REV.

GENERAL ELECTRIC

PAGE
MODEL
REPORT

NATURAL FREQUENCY

AN IMPORTANT DESIGN CONSIDERATION (WHICH BECAME LIMITING FOR THE SOLAR CELL MOUNTING PANEL) IS THAT MAXIMUM AMPLITUDES AT RESONANCE DURING VIBRATION SHOULD NOT BE OF SUFFICIENT MAGNITUDE TO CAUSE BREAKS IN THE ELECTRICAL WIRING SOLDER JOINTS. AS A RESULT A STIFFNESS REQUIREMENT IN THE FORM OF A MINIMUM f_n OF 70 CPS WAS ADHERED TO.

$$\omega_n = A \sqrt{\frac{EI}{\mu L^4}} \quad (\text{REF C, Pg I-14})$$

$$= 3.52 \left[\frac{10.5(10)^6 (.01863)(386)}{.00842(13.8)^4} \right]^{\frac{1}{2}}$$

$$= 497.3 \text{ RADIANS/SEC}$$

$$f_n = \frac{497.3}{2\pi} = 79.1 \text{ CPS}$$

A = MODAL FACTOR = 3.52 (1st MODE)

μ = MASS/UNIT LENGTH

$$I = \left[\frac{t_o^3 - t_c^3}{12} \right] = \left[\frac{[1.774]^3 - [1.75]^3}{12} \right]$$

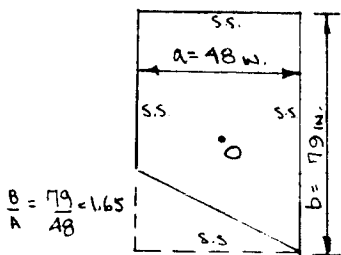
$$= .01863 \text{ IN}^4$$

THE ABOVE NEGLECTS CORE SHEAR DEFORMATION. REDUCING BY A 5% FACTOR

$$f_n = 75 \text{ cps}$$

B. INTERIOR PANEL

USING PANEL DIMENSIONS AS SHOWN



$$M_o = M_{max} = \beta g a^2 = .0885 (.00842)(108.6)(48)^2$$

$$= 186.5 \text{ IN-LBS/IN} \quad (\text{REF. C})$$

$$f_b = \frac{186.5}{1.75(.012)} = 8881 \text{ psi}$$

M.S. = AMPLE.

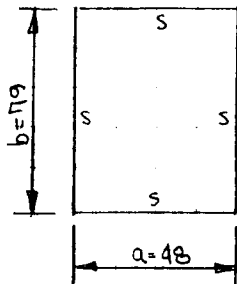
BY
CK.
DATE

REV.

GENERAL ELECTRIC

PAGE
MODEL
REPORT

NATURAL FREQUENCY (REF C, Pg 7-32)



$$\omega_n = A \sqrt{\frac{Dg}{\gamma h a^4}}$$

A = MODAL FACTOR
= 13.6 ($\frac{b}{a} = 1.65$)
FOR 1ST MODE

γh = DENSITY X PLATE THICKNESS
= $W \times 1/16^2 = .00842$

$$\omega_n = 13.6 \sqrt{\frac{.2126(10)^6 (386)}{.00842 (48)^4}}$$

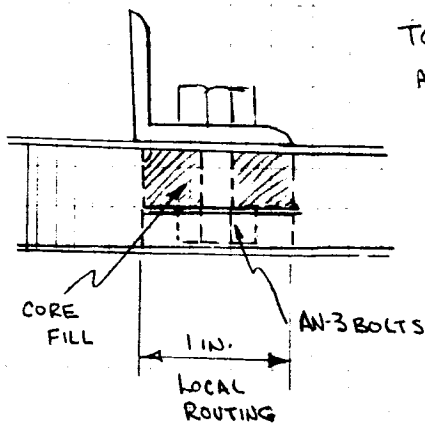
$$D = \frac{E f [t^3 - t_c^3]}{12 \Delta t}$$

$$= .2126(10)^6$$

$$\omega_n = 591.3 \text{ RAD/SEC}$$

$$f_n = \frac{591.3}{2\pi} = 94.1 = 90 \text{ CPS (COMPENSATING FOR CORE DEFORMATION)}$$

ATTACHMENTS.



TO MAINTAIN PANEL CONTINUITY AND TO OBTAIN AS HIGH AN EDGE FIXITY AS POSSIBLE THE HONEYCOMB WILL BE ROUTED OUT LOCALLY, CORE FILLED AND BOLTED AS SHOWN. WITH BOLT SPACING @ 2.5" PITCH

M.S. = AMPLE
BY INSPECTION

2.5.5 REFERENCES

The following are references for Section 2.5, Structural and Dynamic Analysis:

- (a) MIL-HDBK-5 "Strength of Metal Aircraft Elements", March 1961.
- (b) ANC-23 "Sandwich Construction for Aircraft" Part II Second Edition - 1955.
- (c) S. Timoshenko and S. Woinowsky-Krieger "Theory of Plates and Shells" Second Edition McGraw-Hill Book Co.
- (d) General Electric Co. — MSVD Structures Manual.
- (e) C. M. Harris and C.E. Crede "Shock and Vibration Handbook" Volumes I and II McGraw-Hill Book Co.
- (f) Forest Products Lab Report 1857-A "Elastic Buckling of a Simply Supported Rectangular Sandwich Panel Subjected to Combined Edgewise Bending and Compression" Nov. 1956.
- (g) Hexcel Products Inc. "Design Data and Test Methods for Honeycomb Sandwich"
- (h) R. J. Roark "Formulas for Stress and Strain" McGraw-Hill Book Co. 1954.
- (i) D. J. Peery "Aircraft Structures" McGraw-Hill — 1950.

2.6 WEIGHT ANALYSIS

2.6.1 SUMMARY

Detailed weight analysis of the Voyager system has been performed for each Launch date in order to demonstrate that useful and realistic payloads, and lander weights are possible within the maximum launch weight capabilities.

The weights of the Mars 1969 system have been used as a basis for calculating all other launches. Therefore, detailed calculations of the Mars 1969 configuration have been made and changes required due to revised launch dates were added or subtracted as necessary to obtain other configurations.

Reference axes and nomenclature for all analyses are shown in Figures 2.6.1-1 and 2.6.1-2.

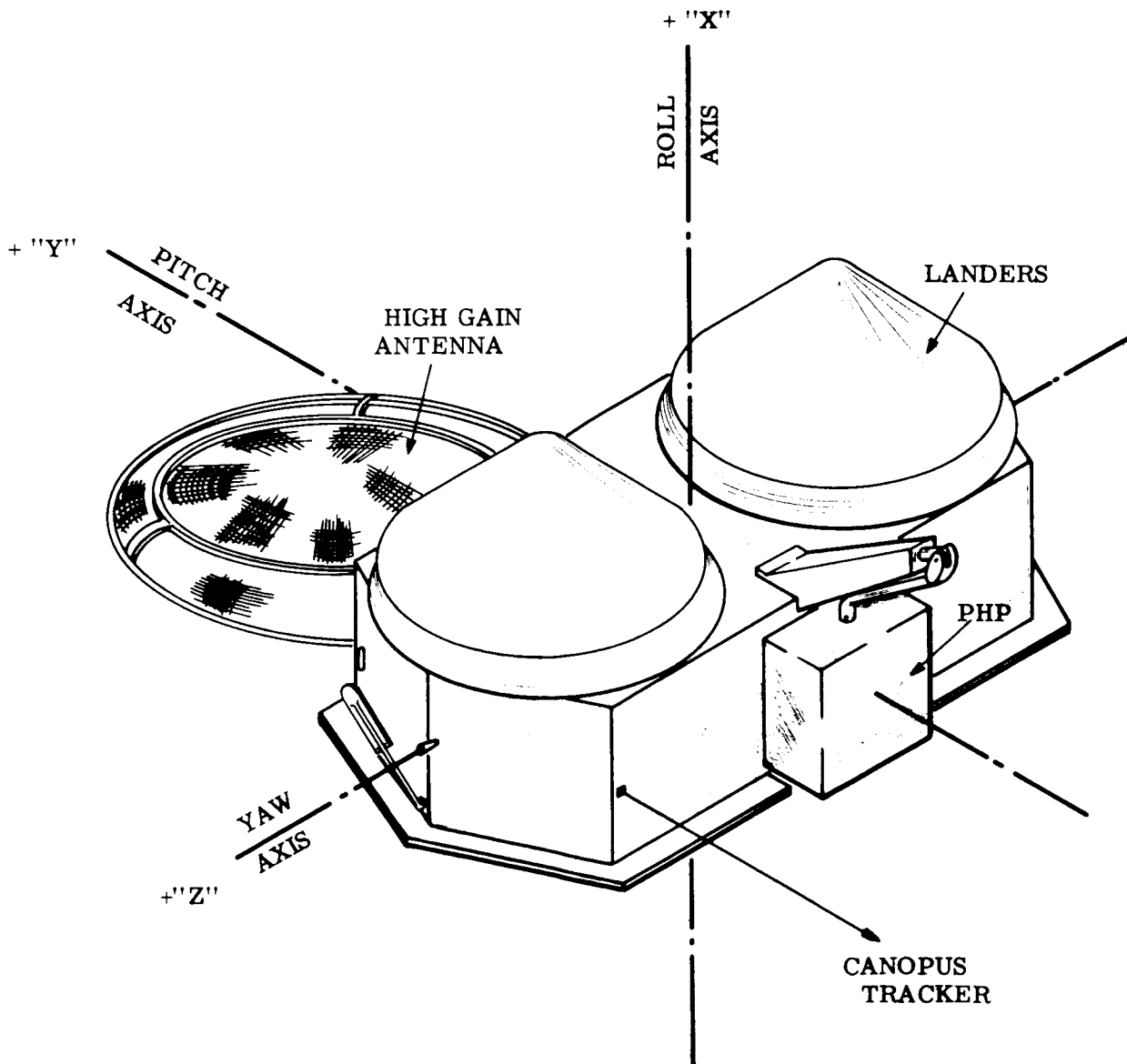


Figure 2.6.1-1. Orbiter Axes

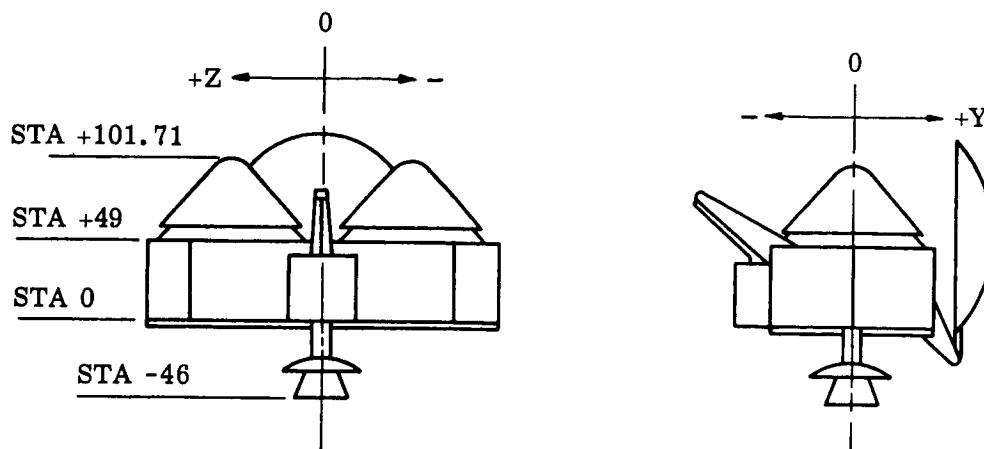


Figure 2.6.1-2. Orbiter Reference Data

Table 2.6.1-1 presents weight, center of gravity, and moment of inertia information for the Mars 1969 vehicle from launch through lander ejection, orbit injection and equipment deployment. Similar information is shown in Table 2.6.1-3 for the Mars 1971 configuration which incorporates the two heavier (2000#) landers. In each case, vehicle packaging has been selected to minimize center of gravity travel during the sequence of events shown. Tables 2.6.1-2 and 2.6.1-4 show the same information for Mars 1969 and Mars 1971 but include the effects of a conservative estimate (3% off optimum) of fuel-oxidizer burning ratio for the propulsion system.

Table 2.6.1-5 presents a breakdown of the system into subsystem weights for all of the Mars and Venus missions considered.

TABLE 2.6.1-1. WEIGHT, CENTER OF GRAVITY, AND INERTIA VARIATION, MARS 1969

Position No.	Configuration Description	Weight (Pounds)	Center of Gravity			Mass Moments of Inertia About C. G. (Slug-Ft ²)		
			X	Z	Y	I _{OX}	I _{OZ}	I _{OY}
1.	Launch with 2 Landers & all equipment stowed	7,030.0	40.67	-0.02	-0.03	4,294	2,275	4,442
2.	After mid-course correction: 79.2 lbs. fuel used, 130.8 lbs. oxidizer used	6,820.0	41.17	-0.03	-0.04	4,272	2,241	4,427
3.	Position 2. with antenna deployed	6,820.0	40.87	-0.03	0.29	4,395	2,348	4,406
4.	Position 3. with 20% freon used	6,809.3	40.89	0.03	0.24	4,390	2,345	4,403
5.	Position 4. with Lander ejected.	3,909.3	21.38	0.05	0.42	2,233	1,247	1,426
6.	Position 5. with antenna stowed	3,909.3	21.91	0.05	-0.16	2,110	1,157	1,464
7.	After orbit insertion, additional 702.6 lbs. of fuel used & 1,159.2 lbs of oxidizer used	2,047.5	19.55	-0.04	-0.44	1,917	962	1,443
Maximum C. G. shifts for above Positions.			21.62	0.09	0.86			

TABLE 2.6.1-2. MARS 1969 3% OFF-RATIO - PROPULSION SYSTEM

Position No.	Configuration Description	Weight (Pounds)	Center of Gravity			Mass Moments of Inertia About C. G. (Slug-Ft ²)		
			X	Z	Y	I _{OX}	I _{OZ}	I _{OY}
1.		7,030.0	40.67	-0.02	-0.03	4,294	2,275	4,442
2.		6,820.0	41.17	-0.03	-0.19	4,270	2,238	4,427
3.		6,820.0	40.87	-0.03	-0.13	4,393	2,345	4,406
4.		6,809.3	40.89	0.03	0.09	4,388	2,342	4,402
5.		3,909.3	21.38	0.05	0.15	2,230	1,244	1,425
6.		3,909.3	20.85	0.05	-0.42	2,107	1,193	1,502
7.		2,047.5	17.52	0.12	-0.95	1,914	992	1,476
Maximum C. G. shifts for 3% Off-Ratio Position.			23.65	0.15	1.10			

TABLE 2.6.1-3. WEIGHT, CENTER OF GRAVITY AND INERTIA VARIATION, MARS 1971

Position No.	Configuration Description	Weight (Pounds)	Center of Gravity			Mass Moments of Inertia About C. G. (Slug-Ft ²)		
			X	Z	Y	I _{OX}	I _{OZ}	I _{OY}
1.	Launch with 2 Landers & all packages stowed	7,320.0	41.33	0	0	5,375	2,215	5,398
2.	After mid-course correction, used 83.03 lbs. fuel & 136.07 lbs. of oxidizer	7,100.0	41.84	0	0	5,353	2,127	4,841
3.	Same as case 2. but with antenna deployed	7,100.0	41.55	0	0.31	5,476	2,288	5,364
4.	Same as 3. but with 20% Freon used	7,089.2	41.44	0.05	0.26	5,471	2,285	5,360
5.	Landers ejected	3,089.2	19.69	0.11	0.61	2,330	1,166	1,649
6.	Same as 5. but with antenna stowed	3,089.2	20.36	0.11	-0.12	2,199	1,018	1,574
7.	After insertion used 376.76 lbs. fuel and 621.54 lbs. oxidizer	2,090.9	18.38	0.16	-0.28	2,093	968	1,548
Maximum C. G. shifts for above cases			22.46	0.16	0.89			

TABLE 2.6.1-4. MARS 1971 3% OFF-RATIO PROPULSION SYSTEM

Position No.	Configuration Description	Weight (Pounds)	Center of Gravity			Mass Moments of Inertia About C. G. (Slug-Ft ²)		
			X	Z	Y	I _{OX}	I _{OZ}	I _{OY}
1.		7,320.0	41.33	0	0	5,375	2,215	5,398
2.		7,100.0	41.84	0	-0.09	5,351	2,126	4,840
3.		7,100.0	41.56	0	0.22	5,475	2,124	5,363
4.		7,089.2	41.58	0.05	0.18	5,469	2,121	5,361
5.		3,089.2	20.02	0.11	0.41	2,329	994	1,640
6.		3,089.2	20.69	0.11	-0.32	2,205	905	1,565
7.		2,090.9	18.86	0.16	-0.58	2,162	798	1,552
Maximum C. G. shifts for 3% off ratio			22.98	0.16	0.99			

TABLE 2.6.1-5. SUBSYSTEM WEIGHTS MATRIX (POUNDS)

SUBSYSTEM WEIGHTS	MARS 1969	REMARKS	MARS 1971	REMARKS	MARS 1973	REMARKS	MARS 1975	REMARKS	VENUS 1970	REMARKS	VENUS 1972	REMARKS
Structure	418.88		418.88		338.81		337.44		414.55		405.98	
Orbiter Str.	316.45		316.45		302.60		302.60		339.37		341.45	
Hardware	40.03		40.03		36.21		34.84		41.74		42.53	
PHP Str.	56.73		56.73		NONE		NONE		30.40		20.00	
Hardware	5.67		5.67		NONE		NONE		3.09		2.00	
Harnessing (Veh.)	106.26		106.26		61.07		54.70		76.95		78.76	
Power Supply	217.66		252.11		106.76		87.09		202.59		131.20	
Batteries	21.30		21.30		22.70		8.60		46.80		25.00	
Electronics	16.10		16.25		10.67		10.26		17.55		11.75	
Harness	7.18		8.23		2.77		2.30		5.67		2.89	
Fixed Array	173.08		206.33		70.62		65.93		132.57		91.56	
Guidance & Control	225.85		225.85		190.35		190.35		231.05		231.05	
Electronics	149.15		149.15		113.65		113.65		149.15		149.15	
F-14 Tank & Gas	52.30		52.30		52.30		52.30		57.50		57.50	
Hardware	24.40		24.40		24.40		24.40		24.40		24.40	
Communications	291.15		291.15		217.15		217.15		226.65		231.05	
Electronics	259.15		259.15		185.15		185.15		194.65		216.15	
Antenna	32.00		32.00		32.00		32.00		32.00		32.00	
(10 Ft dish)												
Diagnostic Instr.	30.00		30.00		15.00		15.00		30.00		30.00	
Thermal Control	87.00		87.00		65.50		65.50		87.00		87.00	
Payload	214.62		223.04		100.31		60.56		137.00		61.00	
* Unidentified	11.82		25.24		72.31		60.56		NONE		NONE	
Scientific	78.50		73.50		28.00		NONE		37.50		46.00	
TV	124.30		124.30				NONE		10.50		15.00	
Radar Mapper	NONE		NONE				NONE		57.00		NONE	
Antenna	NONE		NONE				NONE		32.00		NONE	
Propulsion	467.41		467.41		307.21		307.21		739.21		530.41	
Fuel System	364.00		364.00		258.80		258.80		541.80		405.00	
Pressurization	103.41		103.41		48.41		48.41		197.41		125.41	
System												
Orbiting Weight	2058.83		2101.70		1402.16		1335.00		2145.00		1803.55	
Orbit Insertion Factor		0.904		0.475		0.298				1.962		1.574
Orbit Insertion Fuel	1861.77	1 x 19 n.mi. x 1000 ΔV = 6400 ft/sec	998.30	1 x 19 n.mi. x 1000 ΔV = 3850 ft/sec	417.84	0.2 x 9 n.mi. x 1000 ΔV = 2550 ft/sec	NONE	Fly-By	4372.00	1 x 4.3 n.mi. x 1000 ΔV = 10920 ft/sec	2725.45	1 x 7.3 n.mi. x 1000 ΔV = 9130 ft/sec
Lander Weight	2900.00	2 @ 1450	4000.00	2 @ 2000	4000.00	2 @ 2000	4000.00	2 @ 2000	525.00	One Lander	2600.00	One Lander
Midcourse Fuel	210.00		220.00		180.00		165.00		218.00		221.00	
TOTAL	7030.00		7320.00		6000.00		5500.00		7260.00		7350.00	

*Includes Wire Weight

2.6.2 SUBSYSTEM DETAIL WEIGHTS (MARS 1969)

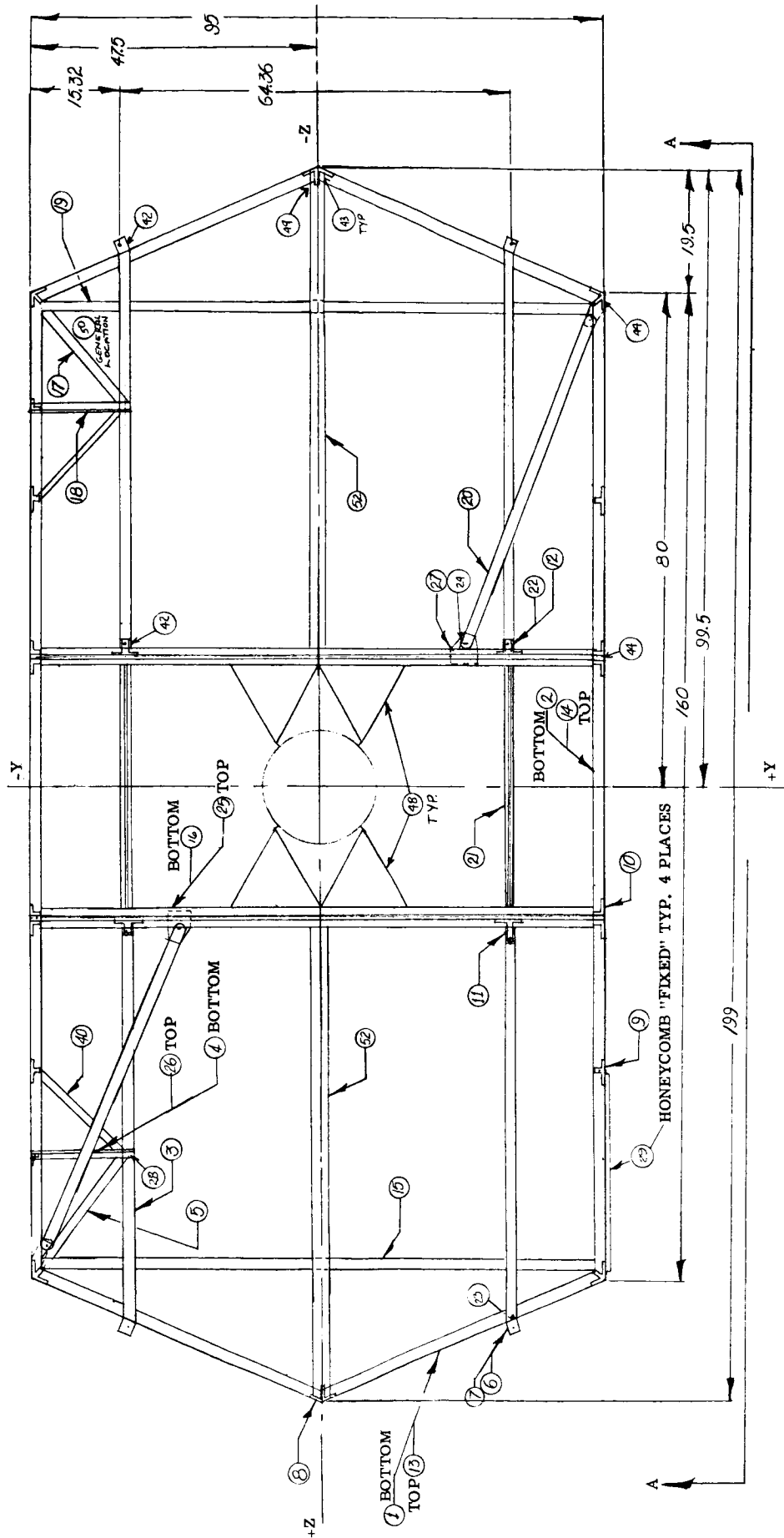
The subsystem weights are broken down into detail component and part weights in the following tabulations.

1. Guidance and Control		225.85
Image Orthicon		22.00
Optics	5.00	
Head	4.00	
Electronics	<u>13.00</u>	
Switching Amp.		1.00
Gyro Control		1.10
Auto Pilot		2.00
Antenna Drive Electronics		2.00
Actuator Hinge (Ant.)		7.50
Actuator Elevation (Ant.)		4.00
Logic, Storage and Relays		14.25
Power Supply		20.00
Earth Sensor		6.50
Canopus Scanner (+ Pitch)		5.50
Canopus Scanner (- Pitch)		5.50
Horizon Scanner		13.00
Gyro (Roll)		2.00
Gyro (Yaw)		2.00
Gyro (Pitch)		2.00
Accelerometer		3.00
Sun Sensors (Fine and Coarse) (7)		.80
Payload Compartments Str.		18.00
PHP Drive Electronics		2.00
Actuator		7.50
Actuator		7.50
a. Pneumatic System		<u>76.70</u>
Regulators (2)	3.50	
Solenoid Valves (12)	6.00	
Latching Solenoid Valves (2)	1.60	
Filters (2)	.62	
Fill and Check Valves (2)	1.00	
High Pressure Transducer	.30	
Low Pressure Transducer (2)	.60	
Temp. Sensors (3)	.15	
Nozzles (12)	3.00	
Tubing	3.00	
Fittings and Bracketry	4.63	
	Hardware Total	<u>24.40</u>
	Tankage } Gas F-14 }	<u>52.30</u>
2. Orbiter Power Supply		217.66
Secondary Battery		21.30
Regulator (Pwr. Control)		3.52
Charge Control (Based on 14 pounds/Kw)		7.08
Diodes		1.00

Inflight Disconnect (3)		4.50	
Harness (Solar Array)		7.18	
Solar Array		<u>173.08</u>	
Honeycomb (Ref. Paragraph 2.6.5)	=	88.77	
Cell (Ref. Paragraph 2.6.5)	=	71.81	
Additional Structure (Ref. Para. 2.6.5)	=	<u>12.50</u>	
3. Communications			291.15
S-Band Diplexer (2)		1.00	
Omnidirectional Antenna (2)		4.00	
Transponder (2)		10.80	
Power Amplifier (3)		12.00	
High Voltage Power Supply (2)		10.00	
Command Demodulator (2)		6.00	
Power Divider (2)		1.00	
VHF Antenna Yagi		16.00	
VHF Antenna Turnstile		10.00	
VHF Diplexer		1.00	
VHF Transmitter		2.00	
VHF Receiver (4)		10.00	
Data Demodulator (2)		10.00	
Data Processor		12.25	
Multicoder		10.00	
Buffer Unit		3.50	
Thermoplastic Recording Unit (2)		50.00	
TV Data Processing Unit (8)		4.00	
Command Decoder		4.00	
Programmer Unit		20.00	
Power Conversion and Control (Orbiter)		12.00	
Power Conversion and Control (PHP)		2.00	
Coaxial Cabling		24.60	
High Gain Antenna		32.00	
Payload Compartments Package Structure		<u>23.00</u>	
4. Diagnostic Instrumentation			30.00
5. Payload			214.62
Scientific			78.50
IR Multichannel Radiometer	3.00		
IR Spectrometer	29.00		
Magnetometer	5.00		
Micrometeoroid Sensor	8.00		
BS Radar and Antenna	13.00		
Ionization Chamber	5.50		
Polarimeter	6.00		
Far UV Radiometer	6.00		
Multichannel Radiometer	<u>3.00</u>		
Television			124.30
Image Orthicons (4)	95.80		
Optics 20m (1)	18.80		
Optics 140m (3)	3.00		
Camera Heads (4)	16.00		
Electronics (4)	52.00		
Mirror (1)	2.00		
Misc. Controls	<u>4.00</u>		

Vidicons (3)		<u>28.50</u>	
Optics (3)	3.00		
Camera Heads (3)	7.50		
Electronics (3)	12.00		
Misc. Controls	<u>6.00</u>		
Unidentified (Scientific)			<u>11.82</u>
6. Propulsion			467.41
Fuel and Oxidizer Sys. (Dry)		364.00	
Tanks 2 @ 38 in. dia.	103.00		
Residual	64.20		
Thrust Chamber	95.00		
Filters (4)	.60		
Main Valves (4)	10.00		
Fill and Purge Valves (12)	6.00		
Filters and Orifices (4)	2.50		
Latch Valves (4)	4.50		
Transducers (8)	3.20		
Shielding	4.00		
Harness	3.00		
Lines	8.00		
Brackets	10.00		
Gimbal System	<u>50.00</u>		
Includes:			
Hyd. Pwr. Pk.			
Actuators			
Servo Valves			
Accumulator			
Plumbing			
Oil			
Ring			
Bearings			
Pressurization System		<u>103.41</u>	
Tank	80.00		
Gas (He)	8.00		
Tubing and Connectors	10.00		
Clamps	.10		
Regulator	3.25		
Filter	.25		
Relief Valve	.31		
Squib Valve Norm. Open (2)	.75		
Squib Valve Norm. Close (2)	<u>.75</u>		
7. Thermal Control			87.00
Insulation:			
F-14 Tank		1.50	
He Tank		2.00	
Orbiter		8.00	
Active Control Orbiter		20.00	
Biological Barrier		12.00	
PHP Insulation		6.00	
PHP Active Control		15.50	
Timers		1.00	
Paint		5.00	
Grease		2.00	

Heaters (@ .1 pound ea.)	5.00	
Misc.	4.00	
Pwr. Amp. Heat Sink	<u>5.00</u>	
8. Vehicle Harnessing		106.26
9. Structure		418.88
Orbiter Body (Ref. Figures 2.6.2-1 through 2.6.2-4)		356.48
Framing L's ① ② ⑩ ⑬ ⑭ ⑯ ⑳	14.29	
T's ⑧ ⑨ ㉑	8.10	
Channels C's ⑥	13.00	
Hats ⑪	7.52	
Tubes ⑰ ⑳	.88	
Box Sections ③ ⑮ ⑲ ㉒	12.67	
Tank Supports (Less Ftgs.)	18.87	
④ ⑤ ⑱ ㉓ ㉔ ㉕		
Fittings ⑦ ⑫ ㉖ ㉗ ㉘ ㉙	7.28	
Clips, Gussets, Supports ㉚ ㉛ ㉜ ㉝	5.80	
Antenna Support Str. ㉞ ㉟	21.41	
PHP Support Str. ㊱ ㊲ ㊳	13.85	
Honeycomb ㉞ ㉟ ㊴ ㊵ ㊶ ㊷ ㊸		
⑳ ㉑ ㉒ ㉓ ㉔ ㉕	177.60	
Solar Array Joint, Support ㉖	14.86	
Hardware ㉗	<u>40.03</u>	
PHP (Ref. Figure 2.6.2-3)	62.40	
Framing L's ① ⑩	4.20	
Honeycomb ② ③ ④ ⑤ ⑥ ⑦ ⑧ ⑨	32.80	
Fittings ⑫ ⑬ ⑭	11.00	
Clips, Gussets, Supports ⑪ ⑮	6.90	
Tubes ⑯	1.83	
Hwd. ⑰	5.67	



BOTTOM VIEW (VIEW A-A SHOWN ON FOLLOWING PAGE)

Figure 2.6.2-1. Parts Location for Detail Weight Analysis - Orbiter-Structural Arrangement

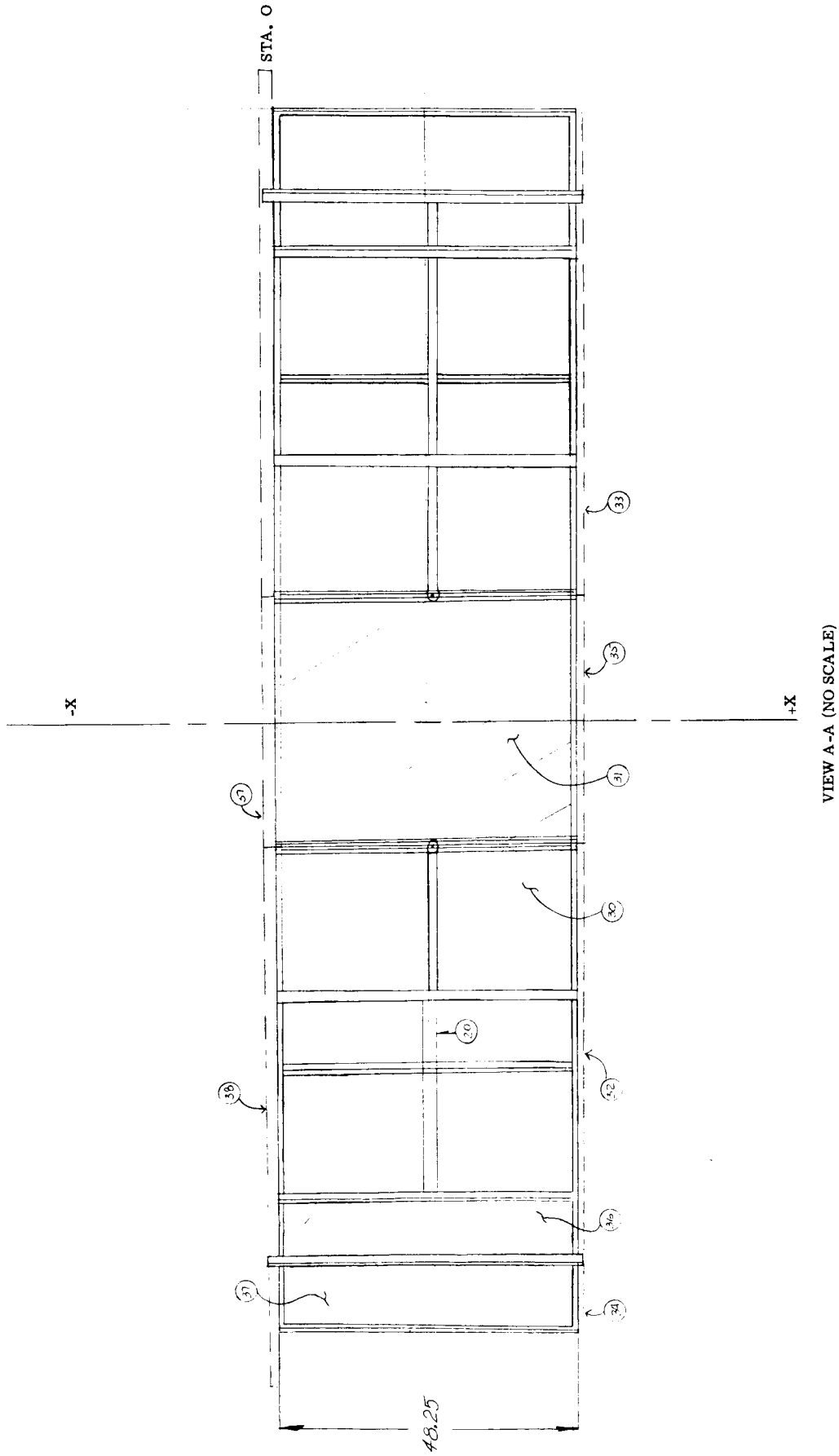


Figure 2.6.2-2. General Location of Removable Honeycomb Panels

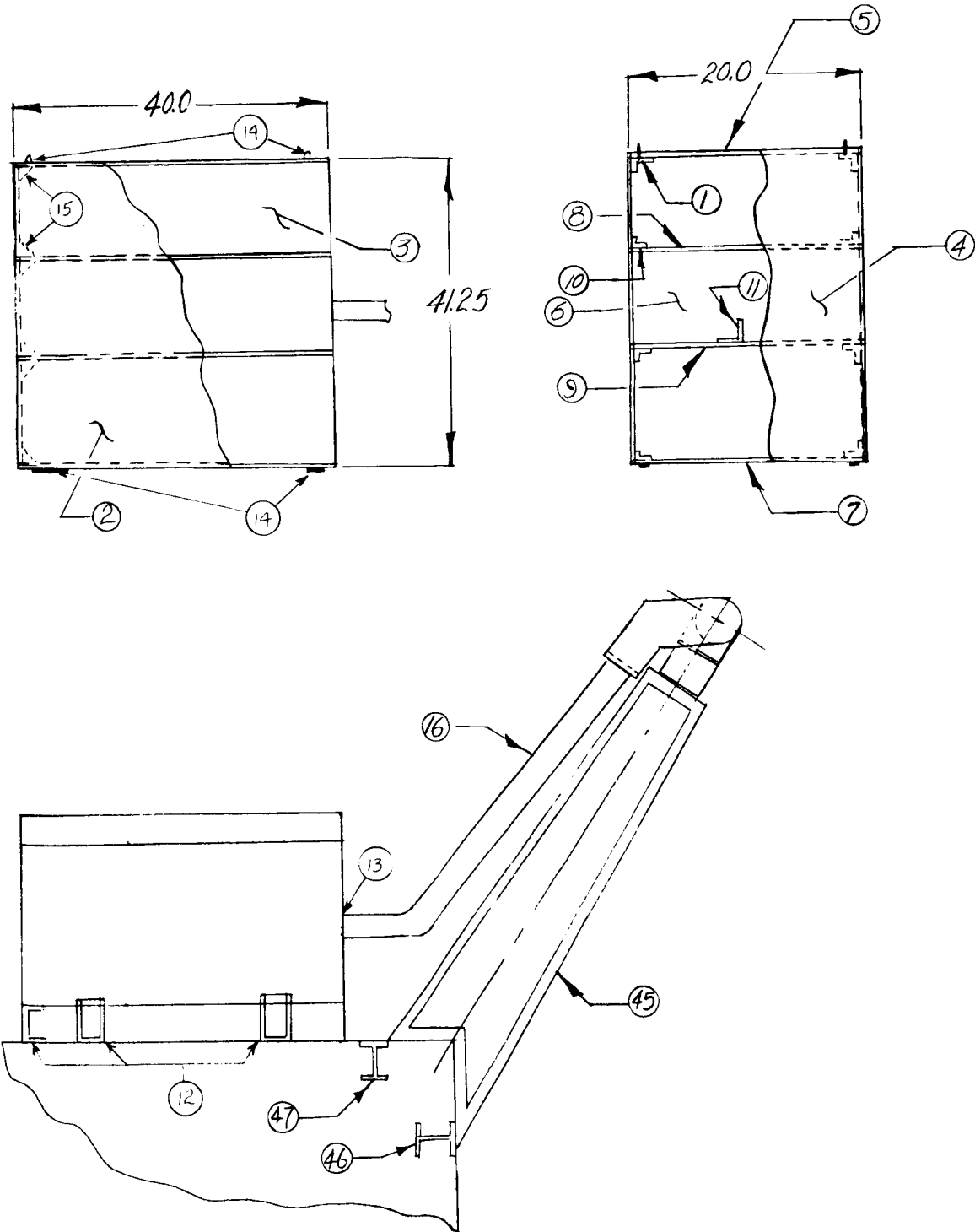


Figure 2.6.2-3. Parts Location for Detail Weight Analysis PHP Structural Arrangement
No Scale

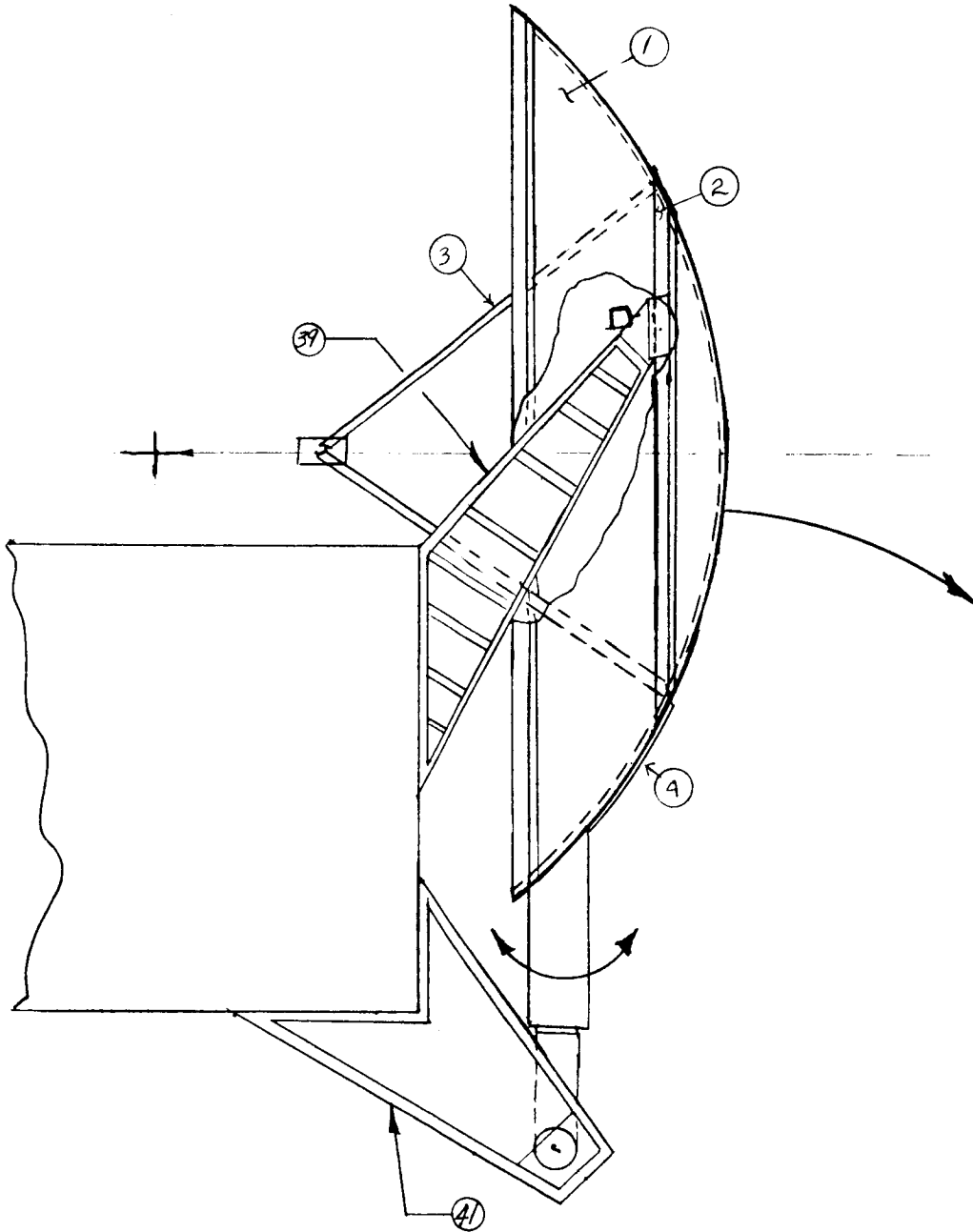


Figure 2.6.2-4. Parts Location for Detail Weight Analysis
High Gain Antenna Structural Arrangement

2.6.3 STRUCTURE DETAIL PARTS

The weight and size of the structure are given by reference numbers in circles. These reference numbers correspond to circles shown in Figures 2.6.2-1 thru 2.6.2-4. Weight is expressed in pounds. All material is aluminum unless otherwise specified.

ORBITER STRUCTURE

Ref. No.	Identification - Size and Gage	Weight Totals (Pounds)
①	Angles 3/4 in. x 3/4 in. x (0.050 in. th)	1.50
②	Angles 3/4 in. x 3/4 in. x (0.050 in. th)	2.40
③	Box Section 2 in. ² x (0.040 in. th)	8.08
④	Tank Support Frame 1 in. x 1 in. x (0.050 in. th)	0.56
⑤	Frame Tube 1 in. O.D. x (0.028 in. th wall)	0.26
⑥	Extrusion Area 0.640 in. ²	13.00
⑦	Lander and Adapter ftgs.	0.64
⑧	Tee's 3/4 in. x 3/4 in. x (0.050 in. th)	3.60
⑨	Tee's 2.0 in. x 1.0 in. x (0.063 in. th)	3.64
⑩	Angles 7/8 in. x 7/8 in. x (0.081 in. th)	5.47
⑪	Hat Section Area 0.365 in. ²	7.52
⑫	Hat Section ftgs.	0.90
⑬	Angles 3/4 in. x 3/4 in. x (.040 in. th)	1.20
⑭	Angles 3/4 in. x 3/4 in. ² x (0.040 in. th)	1.92
⑮	Box Section 2 in. ² x (0.040 in. th)	3.97
⑯	Tee's 3/4 in. x 3/4 in. x (0.050 in. th)	1.48
⑰	Frame Tubes 1 in. O.D. x (0.035 in. th wall)	0.78
⑱	Tank (F-14) Frame Angles 5/8 in. x 5/8 in. x (0.051 in. th)	0.75
⑲	Box End Angles 3/4 in. x 3/4 in. x (0.063 in. th)	0.52
⑳	Tank Thrust Stiffeners 1.25 in. x 1.0 in. x (0.094 in. th)	1.99
㉑	Tee's 2.0 in. x 1.0 in. x (0.078 in. th)	0.98
㉒	Box End Doublers 2.0 in. x 1.0 in. x 0.040 in.	0.10

Ref. No.	Identification - Size and Gage	Weight Totals (Pounds)
(23)	Clips 3/4 in. x 3/4 in. x (0.040 in. th)	0.43
(24)	Thrust Tube Ftgs.	0.84
(25)	Bulkheads - Honeycomb 1.6 lbs /ft ³ 3/8 in. th core, 0.012 in. th Skins = 0.456 lbs/ft ²	29.02
	Tee's 7/8 in. x 7/8 in. x (0.051 in. th)	6.80
(26)	Honeycomb Panel 1.6 lbs/ft ³ 3/8 in th Core, 0.005 in. th Skins = 0.254 lbs/ft ²	2.72
(27)	Tank Bearings and Supports	2.91
(28)	Angle 1.0 in. x 1.0 in. x (0.051 in. th)	0.32
(29)	Honeycomb Panel - Fixed Sandwich - same as (26) Closure 0.020 in. th sheet	10.20 1.88
(30)	Honeycomb Panel - Removable Sandwich - same as (26) Closure 0.025 in. th sheet	7.96 2.13
(31)	Honeycomb Panel - Removable Sandwich - same as (26) Closure 0.025 in. th sheet	6.22 1.31
(32)	Honeycomb Panel - Fixed Sandwich - same as (26) Closure 0.020 in. th sheet	5.66 0.88
(33)	Honeycomb Panel - Fixed Sandwich } Same as (32) Closure }	5.66 0.88
(34)	Honeycomb Panel - Fixed Sandwich - same as (26) Closure 0.020 in. th sheet	2.52 0.84
(35)	Honeycomb Panel - Removable Sandwich - same as (26) Closure 0.025 in. th sheet	6.87 1.02

Ref. No.	Identification - Size and Gage	Weight Total (Pounds)
(36)	Honeycomb Panel - Component Mounting	
	1.6 lbs/ft ³ 0.75 in. th Core, 0.012 th Skin Outside 0.50 th Skin Inside = -.053 lbs/ft ² Closure 0.050 in. th sheet	} 19.93 4.32
(37)	Honeycomb Panel - Component Mounting	
	Sandwich } Same as (36) Closure }	43.32 5.48
(38)	Solar Cell Panel. (Ref. 2.6.5) Honeycomb	
	1.6 lbs/ft ³ 1.75 in. Core th, 0.012 th Skins = 0.6397 lbs/ft ² Closure, (see Paragraph 2.6.5)	
(39)	Antenna Support Str. Upper	
	Angles 1.25 in. x 1.25 in. x (0.063 in. th) 1.25 in. x 1.25 in. x (0.094 in. th) 0.75 in. x 0.75 in. x (0.040 in. th) 0.75 in. x 0.75 in. x (0.063 in. th)	0.82 2.30 0.32 1.20
	Tubes 7/8 in. OD x (0.028 in. wall th) 1/2 in. OD x (0.022 in. wall th)	0.48 0.38
	Skin 0.051 in. th	3.00
	Latch Plate and Gussets	1.00
	Weld and Hardware	0.92
(40)	Lateral Support Tube 7/8 in. OD x (0.028 in. th wall)	0.10
(41)	Antenna Support Str. Lower	
	Angles 5/8 in. x 5/8 in. x (0.040 in. th) 5/8 in. x 5/8 in. x (0.063 in. th) 5/8 in. x 5/8 in. x (0.032 in. th) 3/4 in. x 3/4 in. x (0.040 in. th)	0.04 0.63 1.00 0.83
	Channel 1.0 in. x 5/8 in. x (0.078 in. th)	0.71
	Sheet 0.032 in. T	2.37
	0.040 in. T	5.41
(42)	Tiedown Fittings GSE	1.40
(43)	Corner Gussets	1.20
(44)	GSE Fittings, Handling Plus Hard Points	3.00
(45)	PHP Support (Hinge)	
	Angles 3/4 in. x 3/4 in. x (0.051 in. th) 5/8 in. x 5/8 in. x (0.040 in. th) 5/8 in. x 5/8 in. x (0.032 in. th)	1.44 1.25 0.30
	Sheet 0.040 in. th	4.37
	0.020 in. th	2.14

Ref. No.	Identification - Size and Gage	Weight Totals (Pounds)
④⑥	Support Beam (PHP)	
	Angles 5/8 in. x 5/8 in. x (0.078 th)	0.76
	5/8 in. x 5/8 in. x (0.051 th)	0.09
	Sheet 0.051 in. th	0.87
④⑦	Support Beam (PHP)	
	Angles 3/4 in. x 3/4 in. x (0.125 in. th)	1.40
	3/4 in. x 3/4 in. x (0.064 in. th)	.15
	Sheet 0.064 in. th	1.08
④⑧	Engine Support Tubes	
	3/4 in. OD x (0.022 th Wall-Titanium)	12.40
④⑨	Orbit Trim Nozzle Support Fitting	0.50
⑤⑩	I. O. Camera Support Shelf - Sheet 0.063 in. th	2.27
⑤⑪	Honeycomb Panel - Fixed	
	1.6 lbs/ft ³ in. th Core, 0.008 th Skins =	
	0.423 lbs/ft ²	11.51
	Closure 0.012 in. th sheet	0.66
⑤⑫	Solar Panel Joint - Support Beam	
	Tee's 2.0 in. x 1.0 in. x (0.078 in. th)	7.30
	Angles 1.0 in. x 1.0 in. x (0.050 in. th)	1.56
	Sheet 0.032 in. T	6.00
⑤⑬	Misc. Supports	1.90
⑤⑭	Orbiter Hardware (Includes Solar Array Str. Hdw.)	40.03

Planet Horizontal Package Structure - (Ref. Figure 2.6.2-3)

Ref. No.	Identification - Size and Gage	Weight Totals (Pounds)
①	Angles 1.0 in. x 1.0 in. x (0.040 in. th)	3.24
② ③	Honeycomb Component Panels	
	1.6 lbs/ft ³ 1/2 in. th Core, 0.032 th in. Inside	
	Skin 0.012 in.thOutside Skin = 0.761 lbs/ft ²	18.76
	Close Out 0.012 in. th Sheet	0.58

Ref. No.	Identification - Size and Gage	Weight Totals (Pounds)
④	Honeycomb Panel - Fixed 1.6 lbs/ft ³ 1/2 in. th Core, 0.005 in. th Skins, = 0.271 lbs/ft ² Close Out 0.020 in. th Sheet	1.55 0.38
⑤	Honeycomb Panel - Fixed Sandwich - same as ④ Close Out 0.020 in. th Sheet	1.51 0.36
⑥	Honeycomb Panel - Removable 1.6 lbs/ft ³ 1.2 in. th Core, 0.012 in. th Skins, = 0.473 lbs/ft ² Close Out 0.012 in. th Sheet	2.71 0.22
⑦	Honeycomb Panel - Removable Sandwich - same as ⑥ Close Out 0.012 in. th Sheet	2.63 0.22
⑧	Honeycomb, Internal Bulkhead 1.6 lbs/ft ³ 1/4 in. th Core, 0.008 in. th Skins, = 0.324 lbs/ft ² Close Out 0.008 in. th Sheet	1.80 0.14
⑨	Honeycomb, Internal Bulkhead Sandwich - same as ⑧ Close Out 0.008 in. th Sheet	1.80 0.14
⑩	Angles 1.0 in. x 1.0 in. x (0.040 in. th)	0.96
⑪	Component Bracketry	6.30
⑫	Tie Down Structure	4.00
⑬	Boom Attachments, Mechanism, Clips	4.00
⑭	GSE Fittings	3.00
⑮	Gussets 0.040 in. th Sheet	0.60
⑯	PHP Boom (Tube) 2.25 in. OD x (0.049 in. the Wall)	1.83
⑰	PHP Hardware	5.67

Antenna Structure -- (Ref. Figure 2.6.2-4)

Ref. No.	Identification - Size and Gage	Weight Totals (Pounds)
①	Honeycomb Dish	
	1.6 lbs/ft ³ 1/4 in. th Core, 0.002 in. th Skins, = 0.152 lbs/ft ²	13.37
	Closure 0.020 in. th Ring	2.00
②	Ring-Box 2 in. ² ft x 0.040 in. th Wall	8.53
	Doubler 3 in. x 0.020 in. th Ring	1.60
③	Feed Tubing 1.25 in. OD x (0.022 in. th Wall) } Dobblers and Center Joint	2.25
④	Structure at Hinge and Tie Down	4.25

2.6.4 EQUIPMENT PACKAGING

The prime objective of the packaging study was to minimize the displacement of the system center of gravity from the thrust (X-X) axis. A secondary objective was to keep components of a given subsystem as close together as possible, compatible with the balance requirements. Consideration was given to thermal and electrical requirements in the selection of component locations. In estimating the dimensions to be used, a packing factor (density) of 0.025 lbs/in.³ was assumed. All boxes were considered to be 8 inches deep (dimension from outer surface toward center of vehicle) and of square plan form. Figure 2.6.4-1 shows the Mars 1969 packaging arrangement.

Equipment Packaging, Mars 1969		
Equipment Weight Distribution		366.60 lbs.
<u>Box I</u>	<u>Guidance and Control</u>	51.80 lbs.
	Switching Amp.	1.00
	Gyro Control	1.10
	Auto Pilot	2.00
	Logic Storage and Relays	14.25
	Power Supply	20.00
	Gyro	2.00
	Roll	2.00
	Yaw	2.00
	Pitch	2.00
	Accelerometer	3.00
	Structure	4.15
	Insulation	0.30
	Σ	51.80 lbs., Vol. = 2,100 in. ³ , 8 in. x 16.2 in. x 16.2 in.
	CG Location	X = 14.5 Z = -78.0 Y = 35.8

Box II	Orbiter Power Supply	35.18 lbs.
	Secondary Battery	21.30
	Charge Control	6.16
	Diodes	1.00
	Inflight Disconnect (3)	4.50
	Structure	2.10
	Insulation	0.12
	Σ	35.18 lbs., Vol. = 1,400 in. ³ , 8 in. x 13.3 in. x 13.3 in.
		CG Location X = 27.6 Z = 80.5 Y = 33.5
Box III	Orbiter Power Supply	6.00 lbs.
	Regulator	4.50
	Structure	1.40
	Insulation	0.10
	Σ	6.00 lbs., Vol. = 240 in. ³ , 8 in. x 5.4 in. x 5.4 in.
		CG Location X = 327. Z = -92.0 Y = 8.0
Box IV	Communications	80.10 lbs.
	S-Band Diplexers (2)	1.00
	Transponders (2)	10.80
	Power Amplifiers (3)	12.00
	High Volt. Power Supply (2)	10.00
	Command Demodulator (2)	6.00
	Power Divider (2)	1.00
	VHF Receiver (4)	5.00
	Data Demodulator (2)	10.00
	Data Processor	12.25
	Buffer Unit	3.50
	Structure	6.45
	Insulation	2.10
	Σ	80.10 lbs., Vol. = 3,200 in. ³ , 8 in. x 20 in. x 20 in.
		CG Location X = 36.8 Z = -80.5 Y = 33.5
Box V	Recorder and Data Proc.	57.90 lbs.
	Thermo. Plastic Rec. Units (2)	50.00
	T. V. Data Proc. Unit (1)	0.50
	Structure	6.00
	Insulation	1.40
	Σ	57.90 lbs., Vol. = 2,320 in. ³ , 8 in. x 17 in. x 17 in.
		CG Location X = 11.3 Z = 84.0 Y = 32.0
Box VI	Programmer and Power Converter	36.00 lbs.
	Programmer Unit	20.00
	Power Conv. and Cont.	12.00
	Structure	3.00
	Insulation	1.00

		Σ 36.00 lbs., Vol. = 1,450 in. ³ , 8 in. x 13.5 in. x 13.5 in. CG Location X = 42.8 Z = 80.5 Y = 33.5
Box VII	Diagnostics	17.60 lbs.
	Diagnostic Inst.	15.00
	Structure	2.00
	Insulation	0.60
		Σ 17.60 lbs., Vol. = 700 in. ³ , 8 in. x 8.8 in. x 8.8 in. CG Location X = 18.1 Z = -84.0 Y = -32.0
Box VIII	Scientific Payload	10.25 lbs.
	Micrometeoroid Sensor	8.00
	Structure	2.00
	Insulation	0.25
		Σ 10.25 lbs., Vol. = 410 in. ³ , 8 in. x 7.2 in. x 7.2 in. CG Location X = 16.3 Z = -92.0 Y = -8.0
Box IX	Unidentified Payload	17.46 lbs.
	Payload	11.76
	Structure	5.00
	Insulation	0.70
		Σ 17.46 lbs., Vol. = 700 in. ³ , 8 in. x 9.4 in. x 9.4 in. CG Location X = 10.4 Z = -92.0 Y = 8.0
Box X	Miscellaneous, Distributed Throughout Vehicle	28.31 lbs.
	Sun Sensors (7)	0.80
	Harness Subassembly	7.18
	Timers	1.00
	Paint	2.50
	Grease	1.00
	Heaters	2.50
	Misc.	4.00
	Power Amp. Ht. Sink	5.00
	Misc. Structure	2.90
	Misc. Insulation	1.43
	Avg	CG Location X = 24.5 Z = \pm 50.0 Y = \pm 40.0

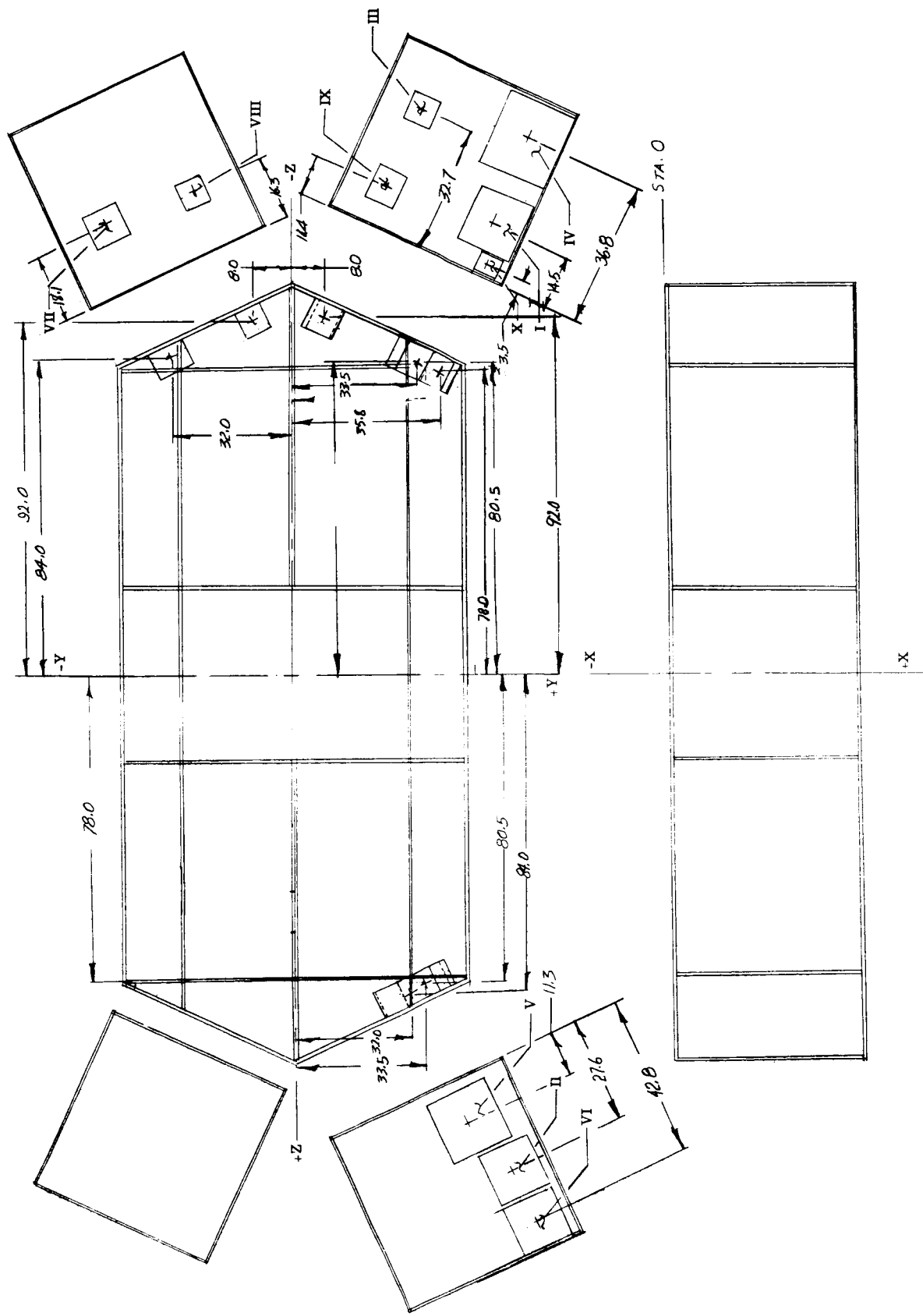


Figure 2.6.4-1. Payload Packaging Arrangement (No Scale) Mars - 1969

2.6.5 POWER SUPPLY AND SOLAR ARRAY WEIGHTS

This section describes the methods and presents the calculations used in computing the weights of the Power Supply Electronics and Solar Array for any mission and launch year. (Ref Table 2.6.5-1)

A. Solar Array Weights

Figure 2.6.5-1 defines the areas used in calculating solar array weights. The active body cell areas, with and without the shelf, are developed and used in determining the cell area required for a given power requirement. Figure 2.6.5-2 presents a cross-section through a typical solar cell and its supporting honeycomb structure. To obtain the solar array weights, a packing factor of 0.90 has been applied to the solar cell areas.

(1) Active Cell Areas

(a) Active Area if Shelf is Used (Ref. Figure 2.6.5-1)

$$\begin{array}{rcl}
 \text{Gross Area} & = & 96.0 (58.0 + 79.0) = 13,152 \text{ in.}^2 = 91.32 \text{ ft}^2 \\
 \\
 \text{Less: Fastener Area } \textcircled{1} & & \\
 & 96.0 \times 2.0 & = 192.0 \text{ in.}^2 \\
 \\
 \text{Splice Area } \textcircled{2} & & \\
 & 79.0 \times 1.0 \times 4 & = 316.0 \text{ in.}^2 \\
 \\
 \text{Shield Area } \textcircled{3} & & \\
 & 17.35 \text{ in.} \times 5.0 \text{ in.} \times 4 & = 694.0 \text{ in.}^2 \\
 \\
 \text{Fastener Area } \textcircled{4} \text{ (3 in. spacing/in.}^2\text{)} & & \\
 & 514.2/3 = 171.4 \times 1.0 \text{ in.}^2 & = \underline{171.4 \text{ in.}^2} \\
 \\
 \text{Sub-Total} & & \underline{1,373.4 \text{ in.}^2} \\
 & & \underline{\underline{-9.54 \text{ ft}^2}} \\
 \\
 \text{Net Total Active Cell Area} & & = \underline{\underline{81.78 \text{ ft}^2}}
 \end{array}$$

(b) Active Area if No Shelf is Used:

$$\text{Total Area, Above} = 81.78 \text{ ft}^2$$

$$\begin{array}{l}
 \text{Item } \textcircled{4} \text{ Panel Fastener Area will have no cells.} \\
 (58.0 + 79.0) \times 4 \times 1 \text{ in.}^2 / 144 = 3.81 \text{ ft}^2 \\
 3.81 \text{ ft}^2 - \textcircled{4} \text{ above (1.19 ft}^2\text{)} = -2.62 \text{ ft}^2
 \end{array}$$

$$\text{Total Cell Area} = 79.16 \text{ ft}^2$$

(2) Solar Cell Multiplying Factor

When body mounted solar cells are needed, the following factors have been used to obtain required Solar Cell Area.

MARS	1969	-	3.40	watts/ft ²
	1970	-	3.02	watts/ft ²
	1973	-	3.20	watts/ft ²
	1975	-	3.23	watts/ft ²
Venus	1970	-	5.95	watts/ft ²
	1972	-	5.95	watts/ft ²

B. Power Supply Electronics Weights

(1) Solar Array Harness

This weight is assumed to be 10% of the solar cell weight (less structure).

(2) Charge Control

This weight is calculated from $1.15 \times (\text{array power})$ (14 lbs/KW).

(3) Power Control Regulator

The weight of this component is calculated as the peak power load $\times 8$ lbs/KW.

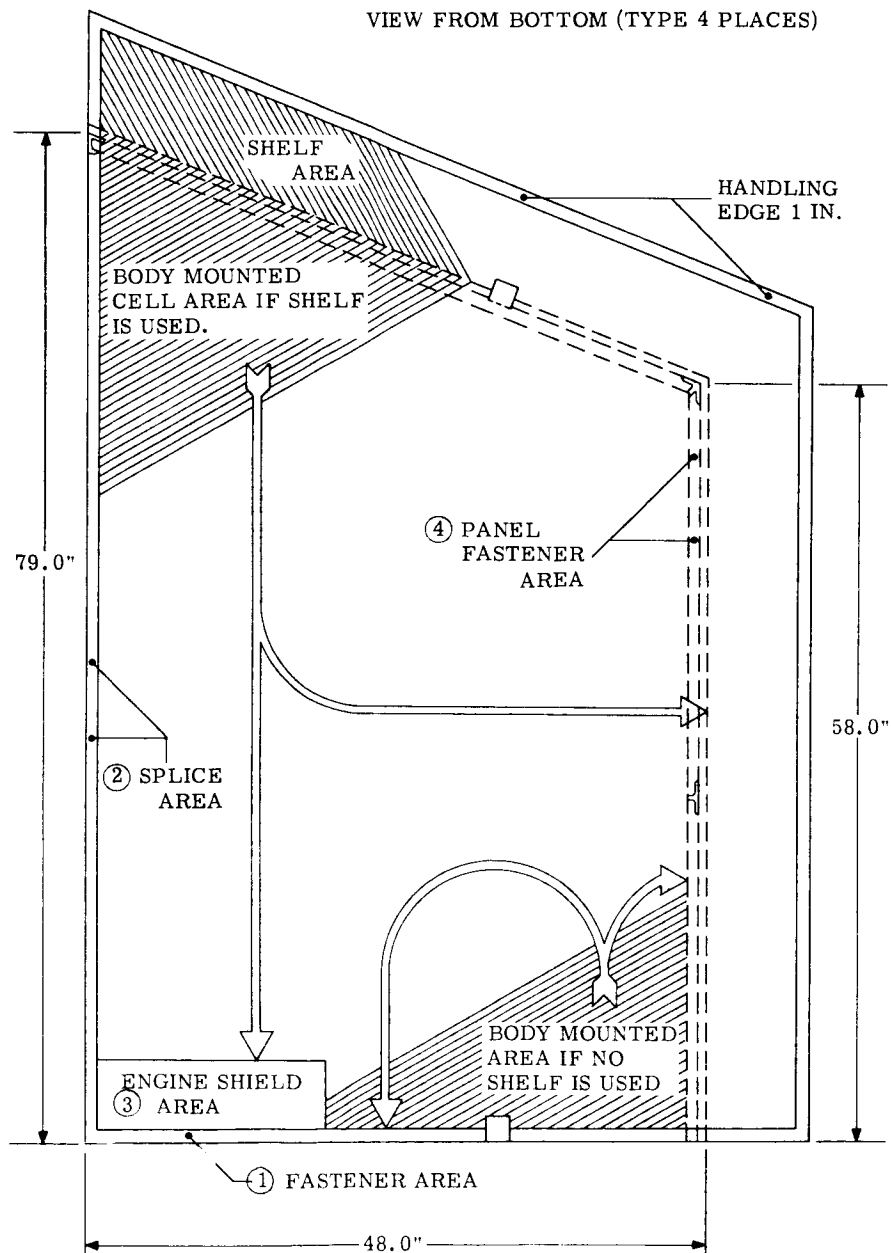
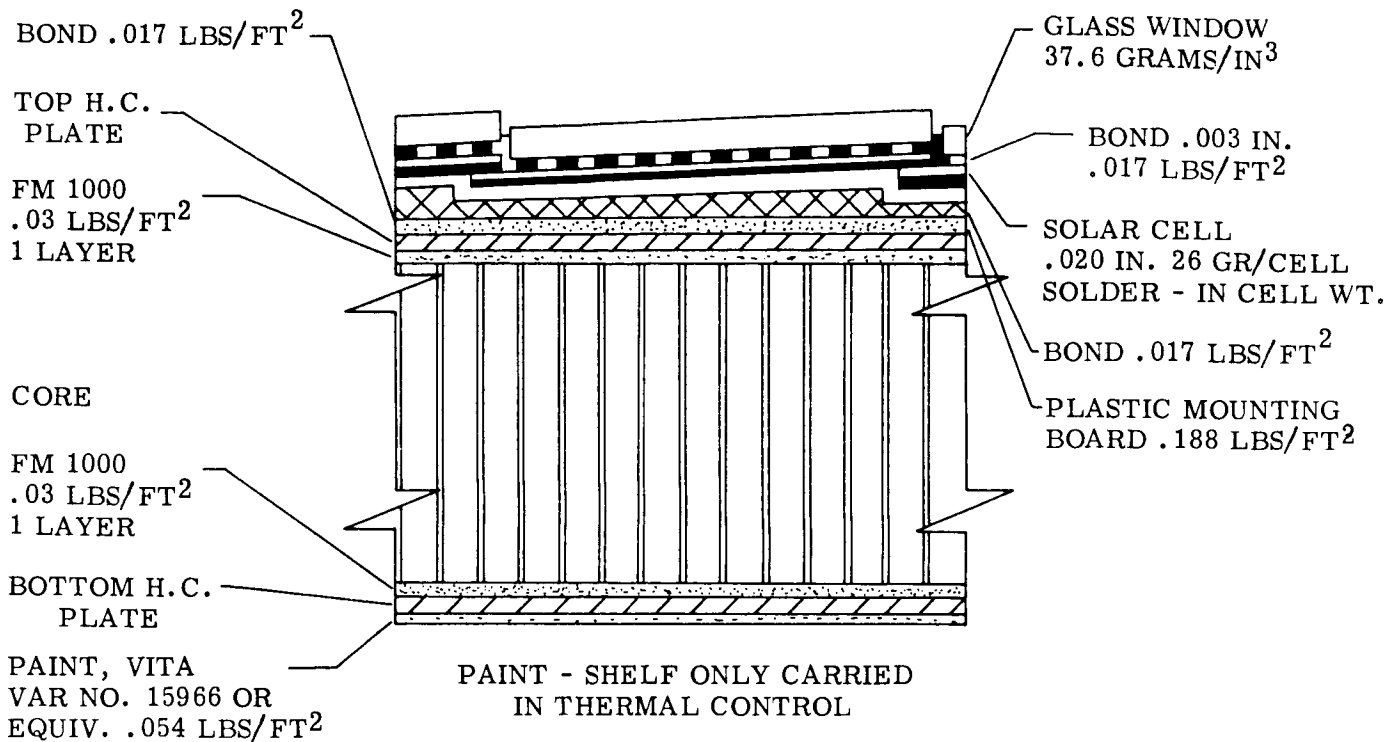


Figure 2.6.5-1. Definition of Area Used in Calculating Solar Array Weights



GLASS .006 IN. THICK 37.6 x 144.0022 x .006	→	=	.0715 LBS/FT ²
BOND .003 IN. THICK 68 LBS/FT ³ /144 x .003	→	=	.0170 LBS/FT ²
CELLS ACTUAL WT. .26 GR/CELL, .26 x *489 x .0022		=	.2797 LBS/FT ²
BOND .003 IN. THICK 68 LBS/FT ² /144 x .003	→	=	.0170 LBS/FT ²
PLASTIC MOUNTING BOARD		=	.1880 LBS/FT ²
BOND .003 IN. THICK 68 LBS/FT ³ /144 x .003	→	=	.0170 LBS/FT ²
RIBBON & TERMINALS, (RIBBON-CELL TO CELL)		=	.0417 LBS/FT ²
			.6359 LBS/FT ²

$.6359 \text{ LBS/FT}^2 \times .9 \text{ (PACKING FACTOR*)} = .5724 \text{ LBS/FT}^2$

$*489 \text{ CELLS/FT}^2 = 100\% \text{ PACKING FACTOR.}$

Figure 2.6.5-2. Typical Solar Cell Construction

TABLE 2.6.5-1. POWER SUPPLY WEIGHT MATRIX

	Mars 1969	Mars 1971	Mars 1973	Mars 1975	Venus 1970	Venus 1972
Solar Array Power at Load	440 watts	446 watts	155 watts	130 watts	589 watts	330 watts
Fixed Array Power Factor	3.40 watts/ft ²	3.02 watts/ft ²	3.20 watts/ft ²	3.23 watts/ft ²	5.95 watts/ft ²	5.95 watts/ft ²
Overhand Array Power Factor	3.71 watts/ft ²	3.21 watts/ft ²	Not req'd	Not req'd	5.95 watts/ft ²	5.95 watts/ft ²
Total Area Req'd (ft ²)	138.77	157.94	48.44	40.25	111.11	50.42
Fixed Array Area	91.32	91.32	48.44	40.25	91.32	50.42
Overhang Array Area	47.45	66.62	None req'd	None req'd	19.79	None req'd
Total Array Weight (lbs)	173.08	206.33	70.62	65.93	132.57	91.56
Honeycomb Panel	88.77***	101.03***	38.63*	38.63*	71.08***	58.44**
Closure Member	5.25	6.00	4.26	4.26	4.83	4.26
Overhang Support Structure	7.25	17.00	None	None	None	None
Cell Weight	71.81	82.29	27.73	23.04	56.66	28.86
Power Supply Electronics (lbs)	44.58	45.73	36.14	21.16	70.02	39.64
Array Harness	7.18	8.23	2.77	2.30	5.67	2.89
Charge Control	7.08	7.18	2.50	2.09	9.48	4.83
Power Control Regulation	3.52	3.57	2.67	2.67	4.07	2.92
Inflight Disconnects	4.50	4.50	4.50	4.50	3.00	3.00
Diodes	1.00	1.00	1.00	1.00	1.00	1.00
Secondary Batteries	21.30	21.30	22.70	8.60	46.80	25.00
Total Power Supply Weight (lbs)	217.66	252.11	106.76	87.09	202.59	131.20

* Honeybomb Required:

Skin = $144 \times 0.008 \times 0.1 = 0.115 \times 2 = 0.230$
 Core = $1.6 \text{ lbs/ft}^3, 1 \text{ in. Th} = 2 \times 0.133 = 0.266$
 Bond = $0.06 \text{ lbs. (2 layers)/ft}^2 = 0.122$
 0.432 lbs/ft²

** Ref: para 2.6.5 (1) Gross Area
 para 2.6.3 (38)

*** Ref: para 2.6.3 (38)